



ISSN 1580-3155

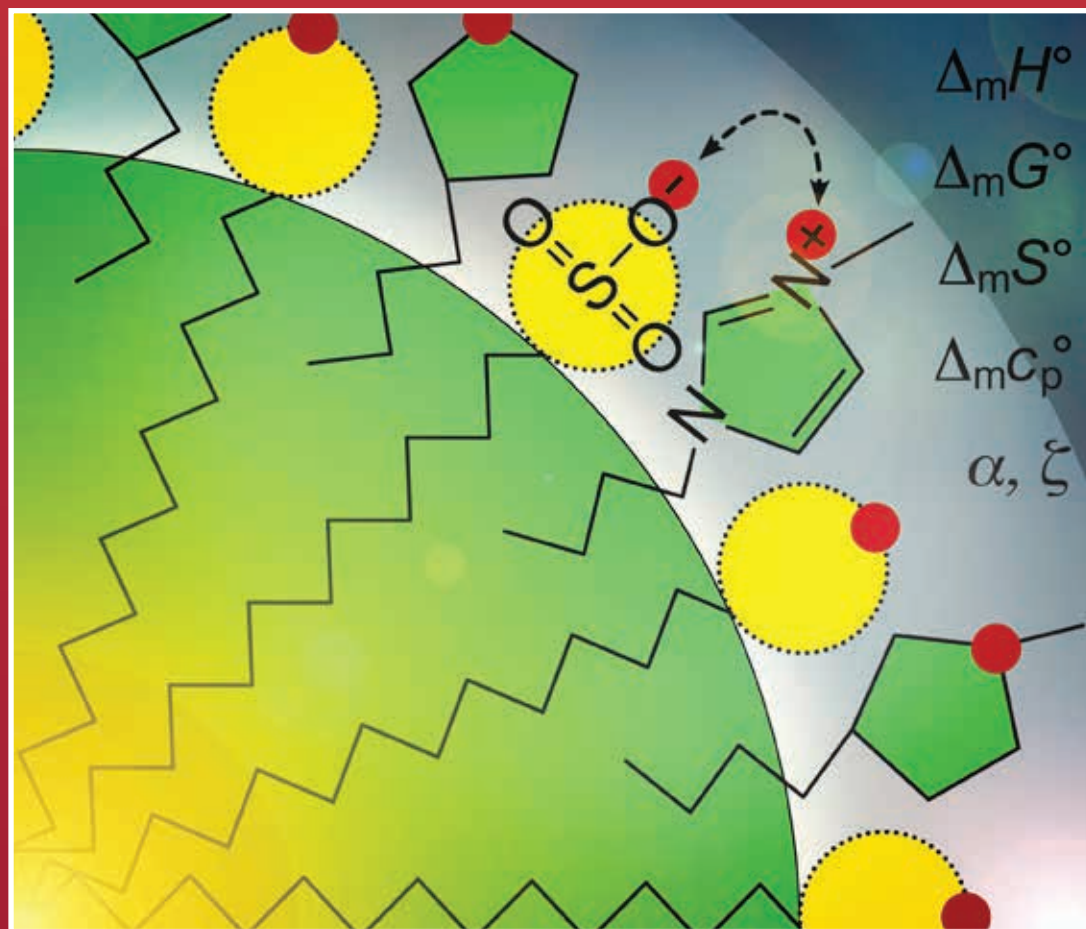
Pages 683–992 ■ Year 2020, Vol. 67, No. 3

Slovensko kemijsko društvo
Slovenian Chemical Society



Acta Chimica Slo Acta Chimica Slo Slovenica Acta C

3



67/2020

EDITOR-IN-CHIEF

KSENIJA KOGEJ

University of Ljubljana, Faculty of Chemistry and Chemical Technology, Večna pot 113, SI-1000 Ljubljana, Slovenia

E-mail: ACSi@fkt.uni-lj.si, Telephone: (+386)-1-479-8538

ASSOCIATE EDITORS

Alen Albreht, National Institute of Chemistry, Slovenia

Aleš Berlec, Jožef Stefan Institute, Slovenia

Janez Cerkovnik, University of Ljubljana, Slovenia

Mirela Dragomir, Jožef Stefan Institute, Slovenia

Ksenija Kogej, University of Ljubljana, Slovenia

Krištof Kranjc, University of Ljubljana, Slovenia

Matjaž Kristl, University of Maribor, Slovenia

Franč Perdih, University of Ljubljana, Slovenia

Aleš Podgornik, University of Ljubljana, Slovenia

Helena Prosen, University of Ljubljana, Slovenia

Irena Vovk, National Institute of Chemistry, Slovenia

ADMINISTRATIVE ASSISTANT

Marjana Gantar Albreht, National Institute of Chemistry, Slovenia

EDITORIAL BOARD

Wolfgang Buchberger, Johannes Kepler University, Austria

Alojz Demšar, University of Ljubljana, Slovenia

Stanislav Gobec, University of Ljubljana, Slovenia

Marko Goličnik, University of Ljubljana, Slovenia

Günter Grampp, Graz University of Technology, Austria

Wojciech Grochala, University of Warsaw, Poland

Danijel Kikelj, University of Ljubljana

Janez Košmrlj, University of Ljubljana, Slovenia

Blaž Likozar, National Institute of Chemistry, Slovenia

Mahesh K. Lakshman, The City College and

The City University of New York, USA

Janez Mavri, National Institute of Chemistry, Slovenia

Friedrich Sreenc, University of Minnesota, USA

Walter Steiner, Graz University of Technology, Austria

Jurij Svete, University of Ljubljana, Slovenia

Ivan Švancara, University of Pardubice, Czech Republic

Jiri Pinkas, Masaryk University Brno, Czech Republic

Gašper Tavčar, Jožef Stefan Institute, Slovenia

Christine Wandrey, EPFL Lausanne, Switzerland

Ennio Zangrando, University of Trieste, Italy

ADVISORY EDITORIAL BOARD

Chairman

Branko Stanovnik, Slovenia

Members

Udo A. Th. Brinkman, The Netherlands

Attilio Cesaro, Italy

Vida Hudnik, Slovenia

Venčeslav Kaučič, Slovenia

Željko Knez, Slovenia

Radovan Komel, Slovenia

Stane Pejovnik, Slovenia

Anton Perdih, Slovenia

Slavko Pečar, Slovenia

Andrej Petrič, Slovenia

Boris Pihlar, Slovenia

Milan Randić, Des Moines, USA

Jože Škerjanc, Slovenia

Miha Tišler, Slovenia

Đurđa Vasić-Rački, Croatia

Marjan Veber, Slovenia

Gorazd Vesnaver, Slovenia

Jure Zupan, Slovenia

Boris Žemva, Slovenia

Majda Žigon, Slovenia

Acta Chimica Slovenica is indexed in: *Academic Search Complete*, *Central & Eastern European Academic Source*, *Chemical Abstracts Plus*, *Chemical Engineering Collection (India)*, *Chemistry Citation Index Expanded*, *Current Contents (Physical, Chemical and Earth Sciences)*, *Digitalna knjižnica Slovenije (dLib.si)*, *DOAJ*, *ISI Alerting Services*, *PubMed*, *Science Citation Index Expanded*, *SciFinder (CAS)*, *Scopus and Web of Science*. Impact factor for 2019 is IF = 1.263.



Articles in this journal are published under the
Creative Commons Attribution 4.0 International License

Izdaja – Published by:

SLOVENSKO KEMIJSKO DRUŠTVO – SLOVENIAN CHEMICAL SOCIETY

Naslov redakcije in uprave – Address of the Editorial Board and Administration

Hajdrihova 19, SI-1000 Ljubljana, Slovenija

Tel.: (+386)-1-476-0252; Fax: (+386)-1-476-0300; E-mail: chem.soc@ki.si

Izdavanje sofinancirajo – Financially supported by:

Slovenian Research Agency, Ljubljana, Slovenia

National Institute of Chemistry, Ljubljana, Slovenia

Jožef Stefan Institute, Ljubljana, Slovenia

Faculty of Chemistry and Chemical Technology, University of Ljubljana, Slovenia

Faculty of Chemistry and Chemical Engineering, University of Maribor, Slovenia

University of Nova Gorica, Nova Gorica, Slovenia

Slovensko kemijsko društvo
Slovenian Chemical Society



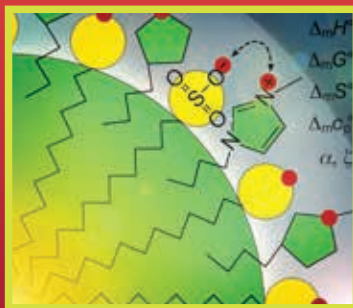
Acta Chimica Slovenica izhaja štirikrat letno v elektronski obliki na spletni strani <http://acta.chem-soc.si>. V primeru posvečenih številčk izhaja revija tudi v tiskani obliki v omejenem številu izvodov.

Acta Chimica Slovenica appears quarterly in electronic form on the web site <http://acta.chem-soc.si>. In case of dedicated issues, a limited number of printed copies are issued as well.

Transakcijski račun: 02053-0013322846 Bank Account No.: SI56020530013322846-Nova Ljubljanska banka d. d., Trg republike 2, SI-1520 Ljubljana, Slovenia, SWIFT Code: LJBA SI 2X

Oblikovanje ovitka – Design cover: KULT, oblikovalski studio, Simon KAJTNA, s. p. Grafična priprava za tisk: Majanafin, d. o. o.

Graphical Contents



ActaChimicaSlo
ActaChimicaSlo
SlovenicaActaC

Year 2020, Vol. 67, No. 3

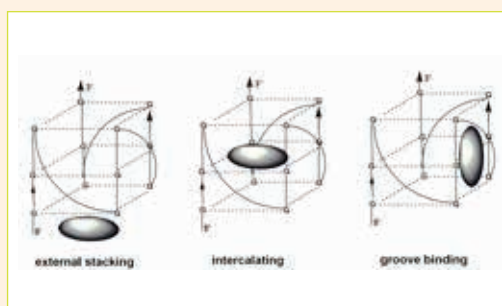
FEATURE ARTICLE

683–700

Review articles

G-Quadruplexes: Emerging Targets for the Structure-Based Design of Potential Anti-Cancer and Antiviral Therapies

Petar M. Mitrasinovic



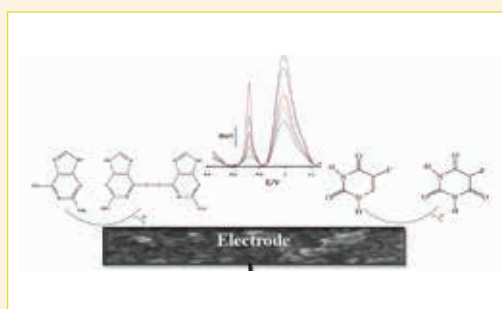
SCIENTIFIC PAPER

701–709

Analytical chemistry

A Novel Electrochemical CuO-Nanostructure Platform for Simultaneous Determination of 6-thioguanine and 5-fluorouracil Anticancer Drugs

Masoud Fouladgar

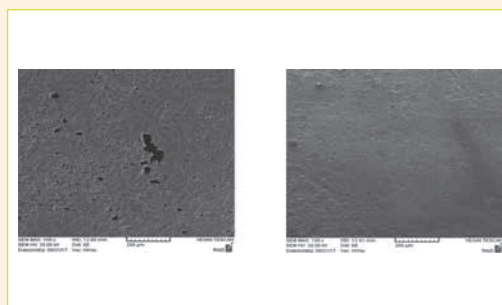


710–719

Analytical chemistry

Metoprolol: New and Efficient Corrosion Inhibitor for Mild Steel in Hydrochloric and Sulfuric Acid Solutions

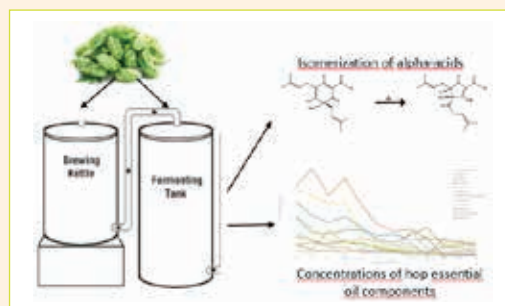
Fatemeh Mohammadinejad, Seyyed Mohammad Ali Hosseini, Mehdi Shahidi Zandi, Mohammad Javad Bahrami and Zahra Golshani



720–728 Analytical chemistry

Dynamics of Isomerization of Hop Alpha-Acids and Transition of Hop Essential Oil Components in Beer

Miha Ocvirk and Iztok J. Košir



729–738 Analytical chemistry

Low-level Electrochemical Analysis of Ketoconazole by Sepiolite Nanoparticles Modified Sensor in Shampoo Sample

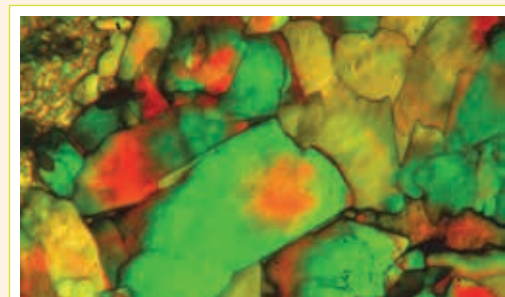
Sevda Aydar, Dilek Eskiköy Bayraktepe, Hayati Filik and Zehra Yazan



739–747 Organic chemistry

The Effect of Hydrogen Bonding and Azomethine Group Orientation on Liquid Crystal Properties in Benzylidene Aniline Compounds

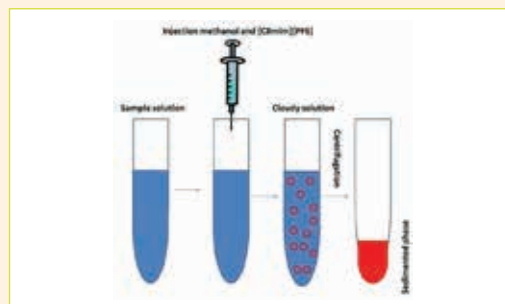
Abdullah Hussein Kshash



748–756 Analytical chemistry

Ionic Liquid-Based Dispersive Liquid-Liquid Microextraction for the Simultaneous Determination of Carbamazepine and Lamotrigine in Biological Samples

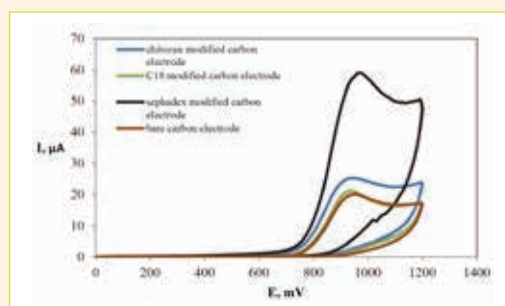
Salumeh Ranjbar, Ameneh Porgham Daryasari and Mojtaba Soleimani



757–763 Biochemistry and molecular biology

Voltammetric Determination of Sulfaclozine Sodium at Sephadex-modified Carbon Paste Electrode

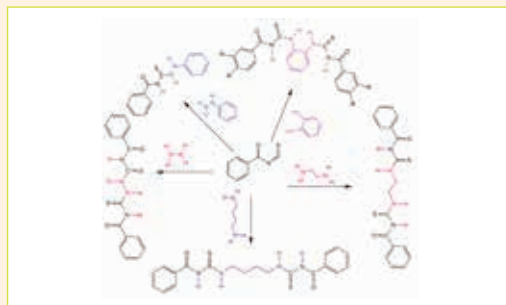
Emad Mohamed Hussien, Hanaa Saleh, Magda El Henawee, Afaf Abou El Khair and Neven Ahmed



764–777 Organic chemistry

Synthesis, Characterization and Biological Activity of Some Dithiourea Derivatives

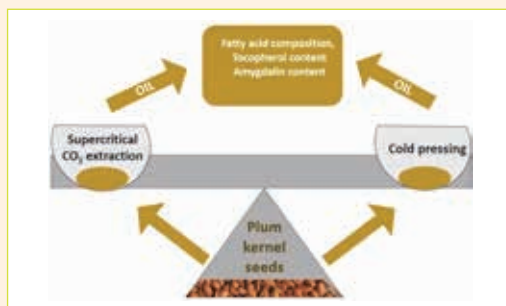
Felix Odame, Eric Hosten, Jason Krause, Michelle Isaacs, Heinrich Hoppe, Setshaba D. Khanye, Yasien Sayed, Carminita Frost, Kevin Lobb and Zenixole Tshentu



778–784 Chemical, biochemical and environmental engineering

Alternative to Conventional Edible Oil Sources: Cold Pressing and Supercritical CO₂ Extraction of Plum (*Prunus domestica* L.) Kernel Seed

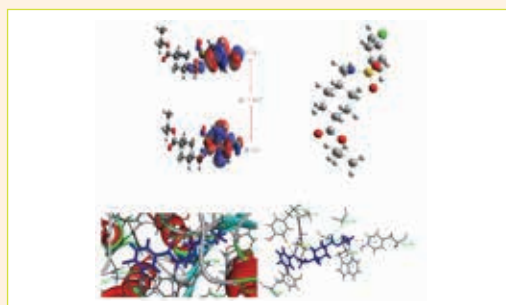
Jelena Vladić, Aleksandra Gavarić, Stela Jokić, Nika Pavlović, Tihomir Moslavac, Ljiljana Popović, Ana Matias, Alexandre Agostinho, Marija Banožić and Senka Vidović



785–798 Organic chemistry

Sulfonamide Derived Esters: Synthesis, Characterization, Density Functional Theory and Biological Evaluation through Experimental and Theoretical Approach

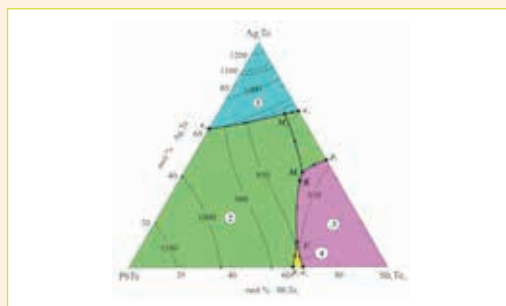
Muhammad Danish, Ayesha Bibi, Muhammad Asam Raza, Nadia Noreen, Muhammad Nadeem Arshad and Abdullah Mohamed Asiri



799–811 Materials science

Phase Equilibria in the Ag₂Te-PbTe-Sb₂Te₃ System and Thermodynamic Properties of the (2PbTe)_{1-x}(AgSbTe₂)_x Solid Solutions

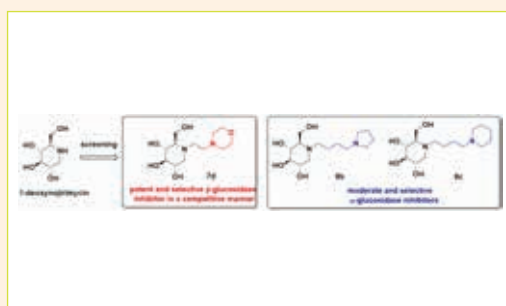
Leyla Farhad Mashadiyeva, Shabnam Hamlet Mansimova, Dunya Mahammad Babanly, Yusif Amirali Yusibov, Dilqam Babir Tagiyev and Mahammad Baba Babanly



812–821 Organic chemistry

Study on the Synthesis and Biological Activities of N-Alkylated Deoxynojirimycin Derivatives with a Terminal Tertiary Amine

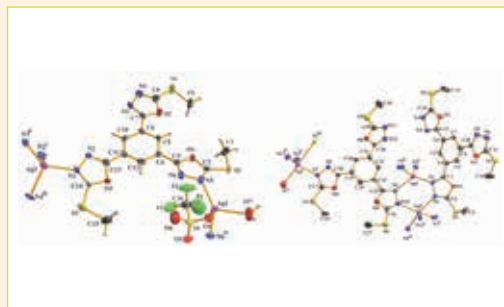
Lin Wang and Zhijie Fang



822–829 Inorganic chemistry

Structural Diversity in Oxadiazole-Containing Silver Complexes Dependent on the Anions

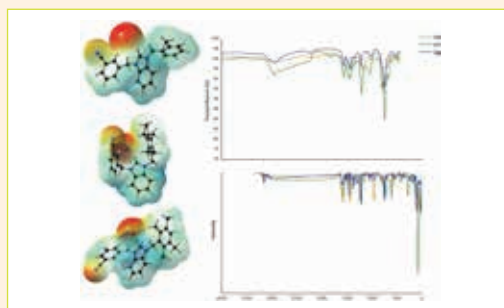
Long Zhao, Long-Yan Xie, Xiu-Li Du, Kai Zheng, Ting Xie, Rui-Rui Huang, Jie Qin, Jian-Ping Ma and Li-Hong Ding



830–841 Applied chemistry

Prediction of Biological Activities, Structural Investigation and Theoretical Studies of *meta*-cyanobenzyl Substituted Benzimidazolium Salts

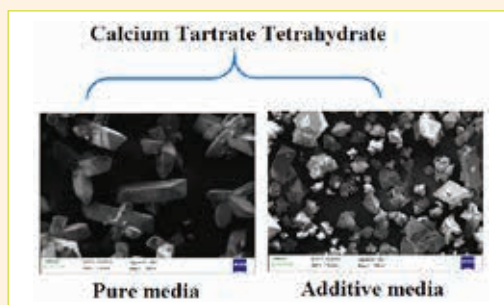
Duygu Barut Celepci and Aydın Aktaş



842–852 Chemical, biochemical and environmental engineering

Effects of Amino Acids on the Crystallization of Calcium Tartrate Tetrahydrate

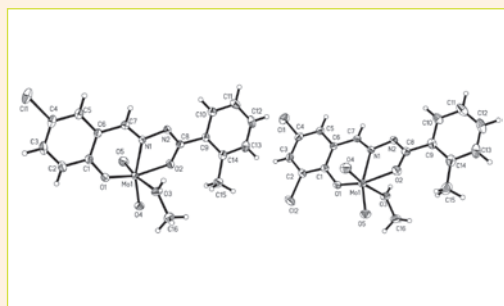
Sevgi Polat, Elif Aytan-Goze and Perviz Sayan



853–859 Inorganic chemistry

Synthesis, Crystal Structures and Catalytic Property of Dioxidomolybdenum(VI) Complexes with Tridentate Hydrazones

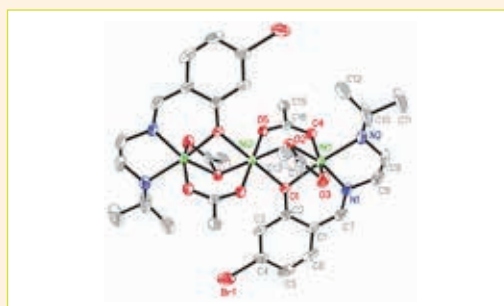
Xiao-Qiang Luo, Yong-Jun Han and Ling-Wei Xue



860–865 Inorganic chemistry

Synthesis and X-Ray Crystal Structures of Trinuclear Nickel(II) Complexes Derived from Schiff Bases and Acetate Ligands with Biological Activity

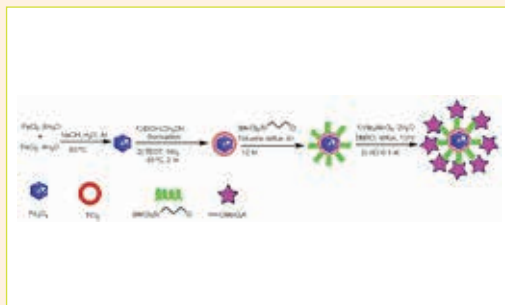
Jin-Long Hou, Hong-Yuan Wu, Cheng-Bin Sun, Ye Bi and Wei Chen



866–875 Organic chemistry

Molybdic Acid-Functionalized Nano- $\text{Fe}_3\text{O}_4@ \text{TiO}_2$ as a Novel and Magnetically Separable Catalyst for the Synthesis of Coumarin-Containing Sulfonamide Derivatives

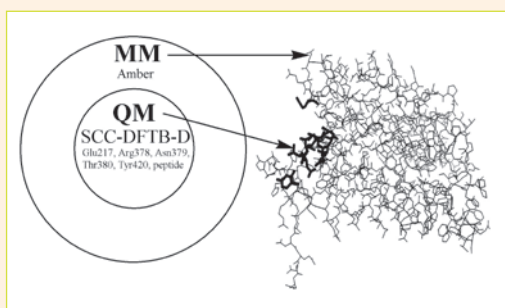
Jamileh Etemad Gholtash, Mahnaz Farahi, Bahador Karami and Mahsa Abdollahi



876–884 Biochemistry and molecular biology

Quantum Mechanics/Molecular Mechanics Study on Caspase-2 Recognition by Peptide Inhibitors

Petar M. Mitrasinovic



885–895 Biochemistry and molecular biology

Antimüllerian Hormone and Oxidative Stress Biomarkers as Predictors of Successful Pregnancy in Polycystic Ovary Syndrome, Endometriosis and Tubal Infertility Factor

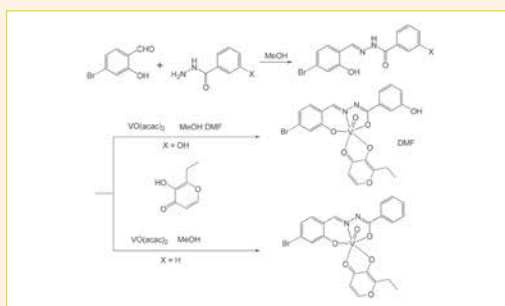
Teja Fabjan, Eda Vrtačnik-Bokal, Irma Virant-Klun, Jure Bedenk, Kristina Kumer and Joško Osredkar



896–903 Inorganic chemistry

Syntheses, Crystal Structures and Catalytic Property of Oxidovanadium(V) Complexes Derived from Tridentate Hydrazone Ligands

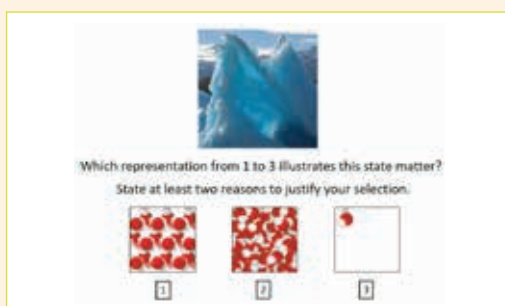
Ya-Jun Cai, Yuan-Yuan Wu, Fei Pan, Qi-An Peng and Yong-Ming Cui



904–915 Chemical education

Students' Achievements in Solving Authentic Tasks with 3D Dynamic Sub-Microscopic Animations About Specific States of Water and their Transition

Miha Slapničar, Valerija Tompa, Saša A. Glažar, Iztok Devetak and Jerneja Pavlin

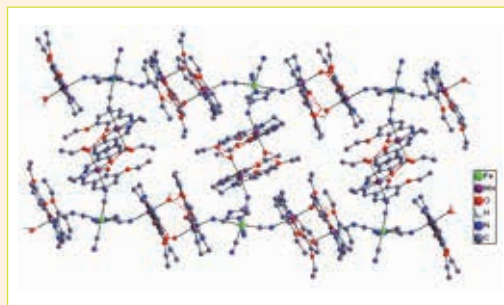


916–926

Inorganic chemistry

Cyanide-Bridged Polynuclear and One-Dimensional Fe^{III}-Mn^{III/II} Bimetallic Complexes Based-on Pentacyanoferrite(III) Building Block: Synthesis, Crystal Structures, and Magnetic Properties

Xiaoyun Hao, Yong Dou, Tong Cao, Lan Qin, Zhen Zhou, Lu Yang, Dacheng Li, Qingyun Liu, Yueyun Li and Daopeng Zhang

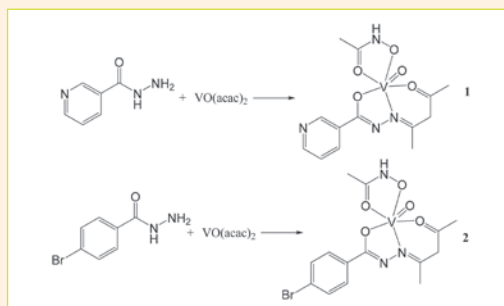


927–933

Inorganic chemistry

Synthesis, Crystal Structures and Catalytic Property of Oxidovanadium(V) Complexes with *N*'-(4-Oxopentan-2-ylidene)nicotinohydrazide and 4-Bromo-*N*'-(4-oxopentan-2-ylidene)benzohydrazide

Qiwen Yang, Pu Wang and Yan Lei

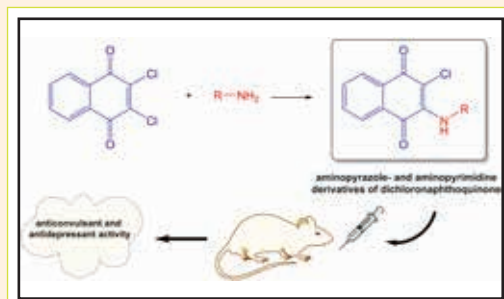


934–939

Biomedical applications

Synthesis and Evaluation on Anticonvulsant and Antidepressant Activities of Naphthoquinone Derivatives Containing Pyrazole and Pyrimidine Fragments

Nataliia Polish, Mariia Nesterkina, Nataliia Marintsova, Andriy Karkhut, Iryna Kravchenko, Volodymyr Novikov and Andrei Khairulin

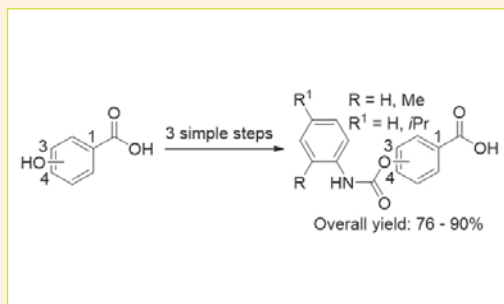


940–948

Organic chemistry

A Simple and Effective Synthesis of 3- and 4-((Phenylcarbamoyl)oxy)benzoic Acids

Urban Kořak and Stanislav Gobec

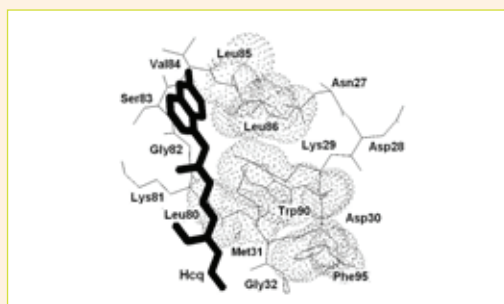


949–956

Biomedical applications

Prediction of Single Point Mutations in Human Coronavirus and Their Effects on Binding to 9-O-Acetylated Sialic Acid and Hydroxychloroquine

Petar M. Mitrasinovic

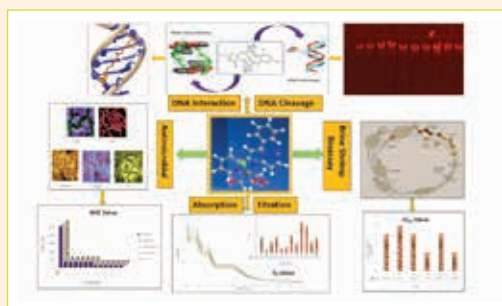


957–969

Biomedical applications

Synthesis, Characterization and Biological Application of Pyrazolo[1,5-a]pyrimidine Based Organometallic Re(I) Complexes

Reena R. Varma, Juhee G. Pandya, Foram U. Vaidya, Chandramani Pathak, Bhupesh S. Bhatt and Mohan N. Patel

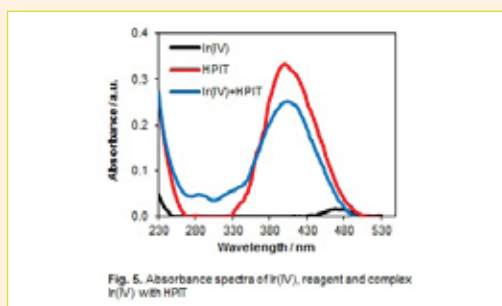


970–976

Analytical chemistry

A New Reagent for Spectrophotometric Determination of Ir(IV): 5-[2-(4-Hydroxyphenyl) hydrazineylidene]-4-iminothiazolidin-2-one (HPIT)

Oleksandr Tymoshuk, Lesia Oleksiv, Orest Fedyshyn, Petro Rydchuk, Vasyl Matiychuk and Taras Chaban

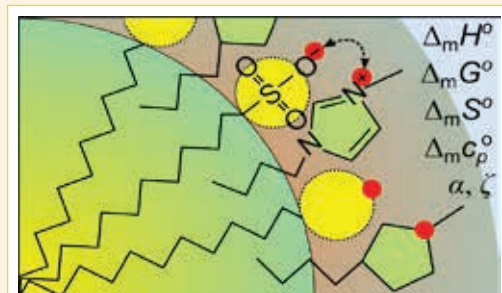


977–984

Physical chemistry

The Influence of Ionic Liquids on Micellization of Sodium Dodecyl Sulfate in Aqueous Solutions

Bojan Šarac and Marija Bešter-Rogač



SHORT COMMUNICATION

985–991

Analytical chemistry

Arsenic in Sediments, Soil and Plants in a Remediated Area of the Iron Quadrangle, Brazil, and its Accumulation and Biotransformation in *Eleocharis geniculata*

Maria Ângela de B. C. Menezes, Ingrid Falnoga, Zdenka Šlejkovec, Radojko Jaćimović, Nilton Couto, Eleonora Deschamps and Jadran Faganeli



Review article

G-Quadruplexes: Emerging Targets for the Structure-Based Design of Potential Anti-Cancer and Antiviral Therapies

Petar M. Mitrasinovic*

Center for Biophysical and Chemical Research, Belgrade Institute of Science and Technology, 11060 Belgrade, Serbia

* Corresponding author: E-mail: pmitrasinovic.ist-belgrade.edu.rs@tech-center.com

Received: 01-10-2020

Abstract

G-quadruplexes (G4s) are noncanonical secondary structures that fold within guanine (G) rich strands of regulatory genomic regions. Recent evidences suggest their intimate involvement in important biological processes such as telomere maintenance, end-capping and protection, chromosome stability, gene expression, viral integration, and recombination. Mechanistic details of how and why G4 structures influence biological function indicate a rationale for treating G4s as emerging molecular targets for future therapeutics. In other words, the structural heterogeneity with well-defined binding sites, thermal stability and abundance of G4s in telomeres, oncogene promoter regions, and viral genomes make G4s attractive targets for small molecules, aimed to selectively recognize them over all other nucleic acids structures, particularly duplex forms that are most abundant in the genome. Herein, a critical survey of well-characterized G4-interactive ligands as potential tools in anti-cancer and antiviral therapies is presented. Effects that these ligands selectively exert *in vitro* and *in vivo* models are summarized. Unique ligands involved in specific G4 recognition are put forward. A key question, how to design and develop new G4 specific ligands that conform to the structural and physicochemical requirements for optimal biological activity, is discussed by considering both remarkable advances over the last few years and our recent contributions.

Keywords: Anti-cancer and antiviral therapies, gene expression, G-quadruplex, ligand, structure-based drug design, target

1. Introduction

Even though nucleic acids structures are usually imagined as a double-helical DNA that is most abundant in the genome and plays a crucial role in genetic information storage,¹ only 3% of the human genome is expressed in proteins.² Nucleic acids are essentially dynamic structures that influence important biological functions.^{3–5} Besides folding into canonical duplex structures, single-stranded DNA may form various noncanonical structures, such as hairpin, triplex, G-quadruplex (or G-tetraplex), and i-motif structures. G-tetrad structure, defined by four Hoogsteen G-G base pairs (Figure 1a), was firstly noticed in 1910⁶ and identified about fifty years later.⁷ G4s fold within G-rich tracts and consist of two or more stacked G-tetrads, being selectively stabilized by centrally coordinated potassium ions to O6 of the guanines at concentrations (10–50 mM) that are substantially below the 120 mM of KCl observed in most cells types.^{8–11} Stabilizing preference for monovalent cations follows the order K^+

$> Na^+ > Li^+$.¹² The intracellular monovalent cation concentration and the localized ion concentrations determine the formation of G4s and can potentially dictate their regulatory roles.^{13,14} G4s can be assembled in an intramolecular (backfolded) way or from two-, three-, or four DNA strands in intermolecular structures (Figure 1b) able to adopt a large diversity of conformations and folding energies.⁸ Most intramolecular G4 structures that are deposited in the public domain have been determined by nuclear magnetic resonance spectroscopy in solution.^{1,15} G4s are more compact structures than duplex DNAs and contain well-defined binding sites for selective recognition by small molecules.

The presence and function of G4s *in vivo* are not quite clear.⁸ While consensus sequence for G4 folding is not experimentally established, approximately 370,000 G-rich sequences that contain putative G4-forming motif (PQS) are present in the human genome,^{8,16,17} dispersed throughout regulatory genomic regions (human telomeres, oncogene promoter regions, immunoglobulin

switch regions, ribosomal DNA)^{18–21} and some regions of RNA.^{22,23} Because of the self-complementary nature of duplex DNA, approximately the same number of cytosine

(C)-rich motifs is present in the human genome and capable of folding into i-motif tetraplexes under slightly acidic conditions (pH=6).^{8,16,17} The biological relevance of i-mo-

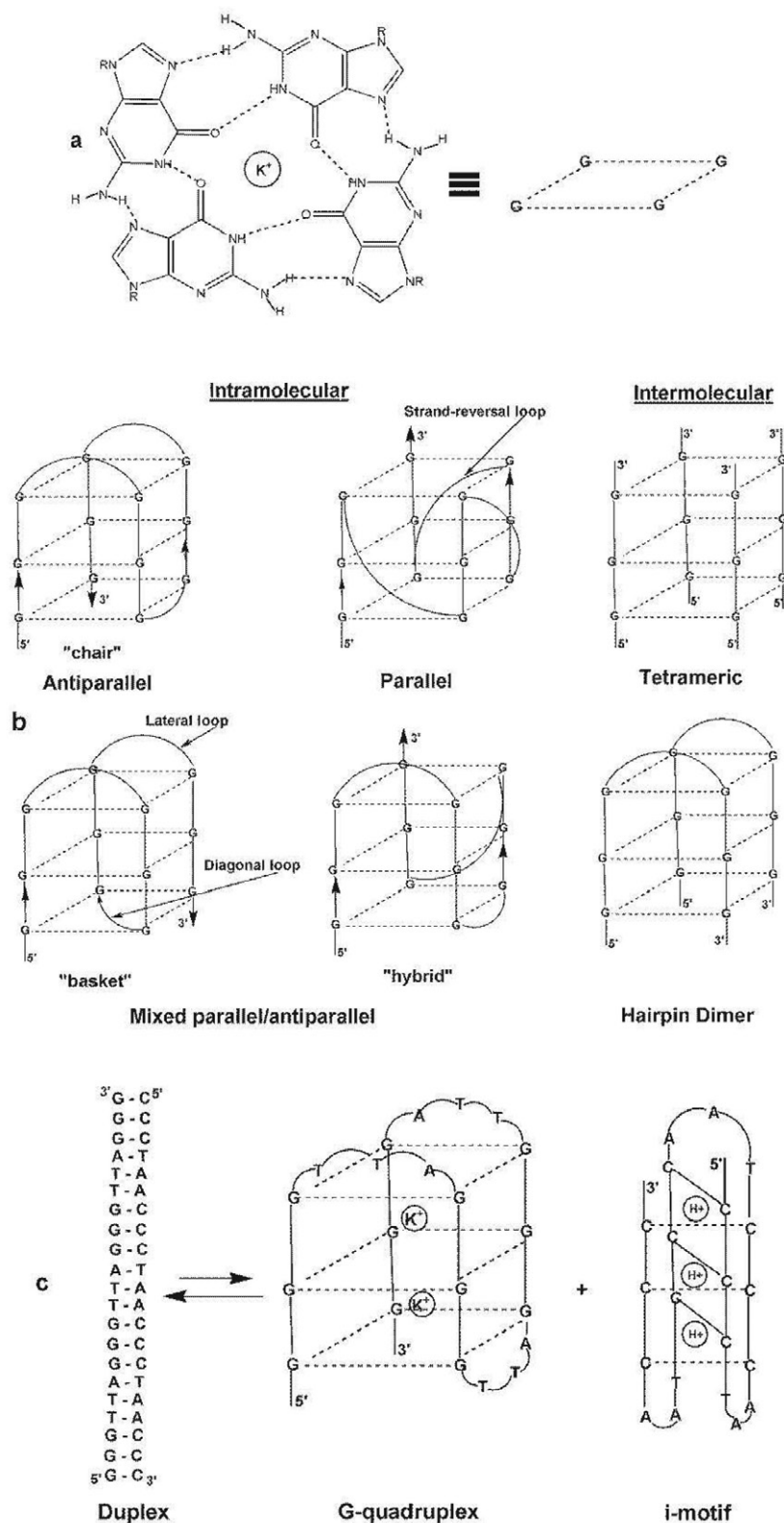


Figure 1. (a) G-tetrad structure. (b) Various G4 folding topologies. (c) One of several ways^{24,26–34} to affect the structural equilibrium between duplex and G4/i-motif is by small-molecule binding.^{8,27–29}

tif DNA *in vivo* is mainly unknown, but the possibility of having i-motifs formed under physiological conditions due to molecular binding and/or crowding interactions has

been highlighted.^{8,24,25} When G-C rich sequences exist as a mixture of G4/i-motif and canonical duplex DNA *in vitro*, the structural equilibrium (Figure 1c) can be affected in

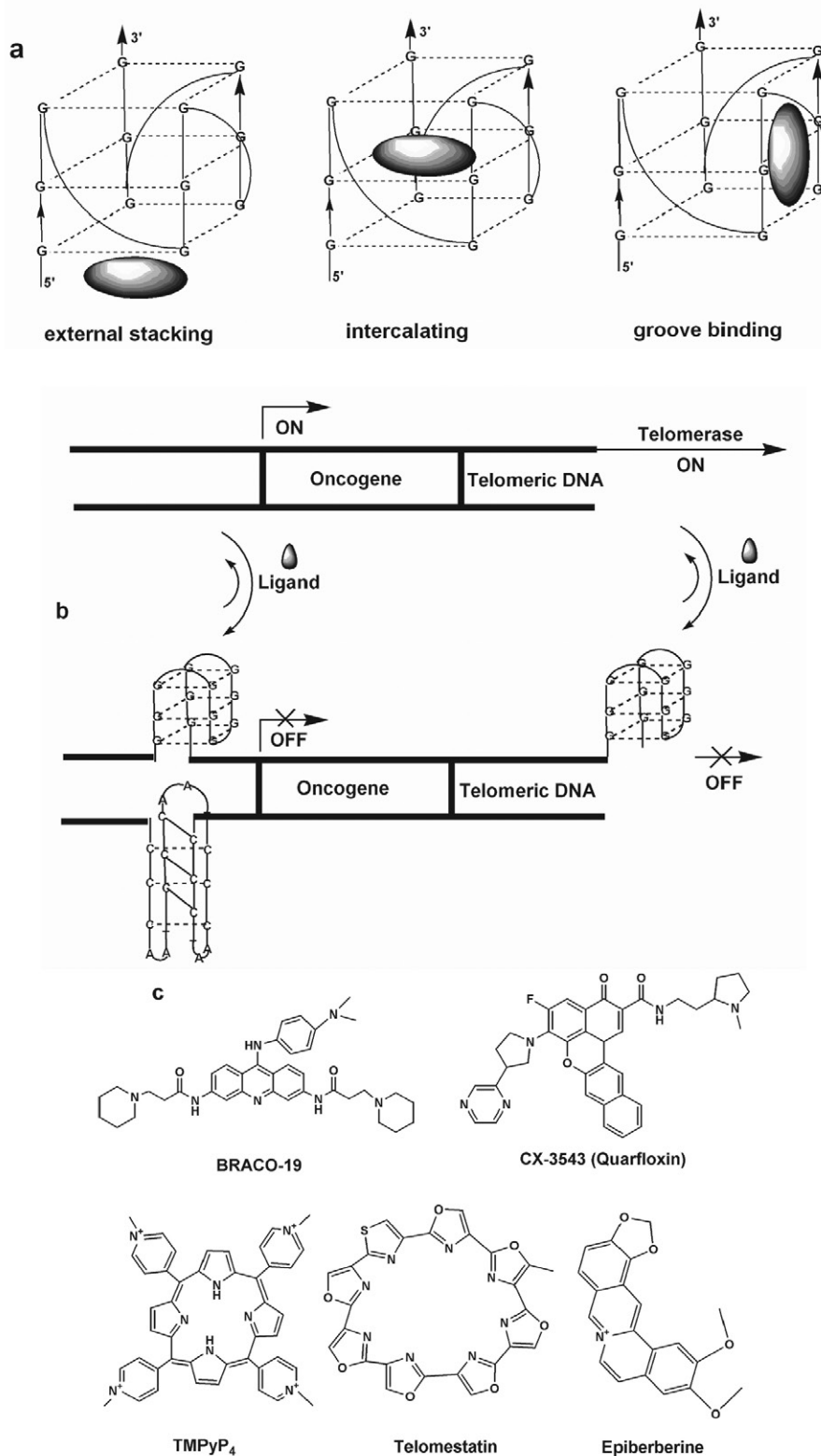


Figure 2. (a) Different modes of noncovalent interaction between small molecules and G4. (b) Regulation of gene expression and/or inhibition of telomerase activity by G4 stabilization upon ligand binding.⁸ (c) Well-characterized G4 ligand structures having fused aromatic rings that are capable of stacking with the terminal G-tetrad.

different ways, using DNA binding proteins,²⁶ small-molecule binding,^{27–29} negative supercoiling,^{29–33} changes in pH and temperature,³⁴ and molecular crowding.²⁴ Thus, cell-permeable and selective ligands may be viewed as potential tools for exploring the biological relevance and/or controlling the function(s) of one or more of these structures.⁸

It is widely accepted that predicting or controlling quadruplex folding is a mainly intractable problem.³⁵ G-rich DNA sequences are often intrinsically polymorphic *in vitro* and sensitive to pH variations, cation concentrations, or crowding conditions. An interest in the resolution of this issue is dictated by potential implementation of targeted design of quadruplexes in material, biotechnological, and therapeutic applications.^{35–37} Methodological advances at a much higher resolution and throughput in the identification and characterization of G4s *in vivo* as well as *in vitro* have well expanded the knowledge of G4 structure and function.³⁸ Recent evidences have suggested involvement of G4s in key genome functions such as transcription, replication, genome stability, and epigenetic regulation, with many links to cancer biology.^{39,40} As far as folding topology (Figure 1b) is concerned, intramolecular G4 structures have been suggested to implicate in the regulation of gene expression and chromosome stability, while intermolecular G4s have been primarily seen as intermediates or precursors of recombination and/or viral integration.⁸ The mechanistic insights into G4 biology and protein interaction partners^{38,39} have helped to design and develop an arsenal of molecular and chemical tools for biomedical applications,³⁸ with highlighting new opportunities for drug discovery.⁴¹

A growing number of predicted (either intramolecular or intermolecular) DNA/RNA quadruplex structures, being deposited into the public domain, enable the structure-based design of G4-interactive ligands on a continuous basis.^{42–46} Ligands with specificity toward certain G4s relative to others are useful for exploring the features and functions of individual G4s in the genome.⁴⁴ Knowing that some small molecules directly bind to G4 and some others interfere with the binding between G4 structure and related binding proteins, tells that the insights into interaction with nucleic acids and into nucleic acid-protein interaction are very important.⁴⁷ Most G4 studies consider only intramolecular G4 folding, but the potential prevalence of intermolecular DNA–RNA G4s in humans has been found by bioinformatics searches,⁴⁸ indicating an urgent need for innovative research in order to be able to detect and characterize intermolecular G4 motifs *in vivo*.³⁸ In other words, great experimental effort and robust analysis platforms are needed to reveal their structural conformational exchange with intramolecular G4s or other structural motifs, and their potential functions in cells,³⁸ such as in transcription.⁴⁸ A wide variety of experimental and computational methods are used to study biomolecular interactions. Experimental techniques include isothermal titration calo-

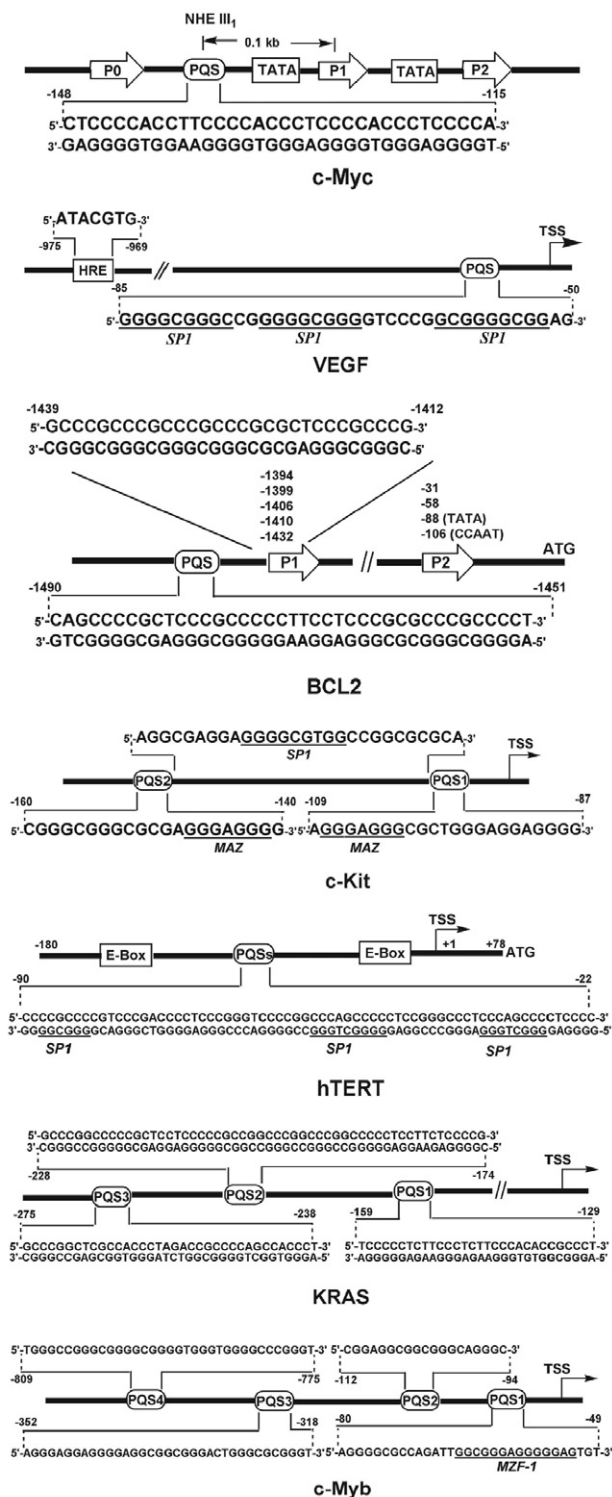


Figure 3. Gene promoters (Ps) with G4 folds.⁴³ c-Myc has one putative G4-forming sequence (PQS) and one nuclease hypersensitive element (NHE III₁). VEGF has one PQS that is close to the transcription start site (TSS) and one hormone response element (HRE) for regulating the transcription (SP1 – specific protein). BCL2 has two G4-forming elements that attenuate the BCL2 promoter activity. c-Kit has two PQSs that interact with transcription factors (MAZ, SP1). hTERT has a few PQSs, where the presence of two tandemly positioned G4s is proposed. KRAS has three PQSs, of which PQS1 acts as a stronger transcriptional suppressor. c-Myb has several PQSs (MZF1 – protein).

rimetry (ITC), electrospray ionization-mass spectrometry (ESI-MS), X-ray crystallography, nuclear magnetic resonance (NMR), circular dichroism (CD), ultraviolet (UV) and fluorescence spectroscopies.^{49–55} Relevant computational approaches comprise virtual screening (VS), molecular docking, molecular mechanics (MM), molecular dynamics (MD), statistical thermodynamics, and bioinformatics.^{56–59} Taking into account that various conformations in static structures may be due to differences in experimental conditions or procedures, the applications of MD simulations have become particularly attractive,^{60–64} enabling to correlate substantial G4 domain motions and binding site rearrangements with complex formation.^{65–68}

The structural heterogeneity, thermal stability and abundance of G4s in telomeres, oncogene promoter regions, and viral genomes make them appealing targets for future therapeutics. In this paper, an up-to-date survey of well-characterized G4s and G4-preferred ligands as potential targets and tools in anti-cancer and antiviral therapies is given. Effects that these ligands selectively exert *in vitro* and *in vivo* models without appreciably affecting normal cells are summarized. Unique ligands involved in specific G4 recognition through different modes of noncovalent interaction (Figure 2a) are put forward. Future perspective in conjunction with a daunting challenge – how to design small molecules that can bind selectively to each of the many possible G4 structures is, to some extent, addressed too.

2. G4-Preferred Ligands: Potential Tools in Anti-Cancer Therapy

The visualization of G4s by immunofluorescence has been enabled by the development of specific antibodies with extremely high affinity to G4s, and has shown the presence of G4s not only in human single-stranded telomeres, but also in duplex regions.⁴⁴ G4-forming sequences are observed in the promoter regions of cancer-related genes such as *c-Myc*,^{69–72} *VEGF*,⁷³ *BCL2*,⁷⁴ *c-Kit*,⁷⁵ *hTERT*,⁷⁶ *KRAS*,^{77,78} and *c-Myb*⁷⁹ (Figure 3).

The ends of linear chromosomes are protected by telomeres from unwanted DNA processing events that influence genome stability. Human telomeric DNA consists of 5–30 kb tandem repeats of (TTAGGG)_n, which end up by a single-stranded, from-35-to-600 bases long 3' overhang.^{1,80–82} Telomere binding proteins protect G-rich telomere repeat sequences that are prone to fold into G4 structures. Small energy differences between telomeric G4 structures have been generally observed.^{83,84} An intrinsic polymorphism of telomere DNA is particularly reflected through conformations adopted by the TTA loop segments.⁸⁵ The highly conserved telomeric sequence in higher eukaryotes means that potential formations of multiple G4s may be implicated in specific recognition of different structures by different proteins with the aim to con-

trol biology.¹ In the majority of human cancers cells as highly proliferative cells, telomeres are maintained by telomerase. Telomerase and its telomere substrates are potential targets for developing novel anti-cancer drugs (Figure 2b). The discovery of the naturally occurring macrocyclic compound Telomestatin (Figure 2c) with telomerase-inhibiting activity due to binding to telomeric G4 structures indicated the existence of G4s *in vivo*.⁴⁴ Telomere function, besides the inhibition of telomerase, might be influenced by targeting telomeric G4-DNA. The importance of telomere structure and its position during telomerase function, as well as its associated binding proteins has been experimentally dissected.²⁰ Many proteins that bind to double-stranded and/or single-stranded regions of the telomeric DNA make a nucleoprotein complex that maintains the structural integrity of telomeres *in vivo*. The effect of telomere destabilization due to small-molecule binding to DNA and consequent displacement of proteins from the complex is known as possible genotoxicity, being in relation to many G4 ligands. How this effect might be cancer-specific is unclear.⁸

Contrary to the formation of telomeric G4s in the single-stranded 3' overhang of telomeres, promoter G4s fold in the regions of double-stranded DNA. G4 formation in promoter regions is related to genes that are responsible for cell growth and proliferation (Figure 3). The clustering of putative G4-forming sequences (PQSs) is within 1 kb upstream of the transcriptional start site (TSS). The oncogene promoters are typically TATA-less with G-rich regions in vicinal promoters. Unlike telomeric DNA, the PQSs are substantially more diverse and frequently have more than four G-tracts. A sequence is capable of forming multiple G4s through a wide variety of combinations of G-tracts or different loop isomers. The presence of the G3NG3 motif is a conspicuous feature that might have been naturally selected as a basis for G4 formation. Since the determination of *c-Myc* G4, parallel G4 folds have been commonly detected; most of them contain three G-tetrads and three loops (the first and the third are 1 nucleotide long, the middle loop is of variable length). In other words, each parallel G4 structure is likely to adopt unique capping and loop structures by way of its specific variable middle loop and flanking segments. The propensity of promoter sequences to form multiple and stable G4s at equilibrium is quite intriguing. For example, in the overlapping region of *BCL2*, the presence of two distinct conformationally interchangeable G4s suggests a mechanism for the regulation of gene transcription through specific recognition of different G4 structures by different proteins.¹ Many proteins with binding affinity to G4s have been identified.⁸⁶ Modulation of gene expression may also be influenced using different small molecules in order to recognize distinct G4s. Thus, the targeting of G4s by small molecules, aimed to disrupt the interactions between G4s and their binding proteins, emerges as a potential anti-cancer strategy.⁶¹

The different modes of noncovalent G4-ligand interaction include external stacking, intercalation, and groove/loop binding (Figure 2a). Experimental^{87,88} and computational⁶¹ reports have identified the π - π stacking of ligand at the end of G4 as the most stable mode. Grooves/loops have been suggested to be viable binding sites of particular importance for blocking the interaction between G4 and its binding proteins in aqueous solution.⁶¹ The challenge of designing specific groove/loop binders stems from the groove/loop interaction mode dependence on the particular topology of groove/loop residues. However, grooves/loops offer distinct environments to gain specificity among many types of G4s by way of subtle variations of G4 topologies, groove widths, and loop sequences without affecting binding affinity.^{44,61}

There are two distinct mechanisms to inhibit cancer growth through the selective stabilization of G4s by ligand molecules (Figure 2b). The first refers to the inhibition of the over-expression of oncogenes by promoter deactivation,^{8,89} while the second refers to the inhibition of telomerase, a ribonucleoprotein complex that catalyzes the 3' extension of telomeric DNA.^{8,90–95} The second mechanism has been more extensively studied.⁸

Well-characterized G4-interactive ligands, BRACO-19, CX-3543 (Quarfloxin), TMPyP4, and Telomestatin that have modest binding affinities to duplex DNAs⁴⁴ are given in Figure 2c. The chemical structure of BRACO-19 is composed of fused aromatic rings that are capable of stacking with the terminal G-tetrad and of three side chains that branch out of its heteroaromatic core. Many similar ligands (like CX-3543) have one or more cationic side chains that are inclined to interact with G4 grooves/loops. An early idea that an optimal G4-preferred ligand structure contains large, planar, symmetric and cyclic rings, such as those of TMPyP4 and Telomestatin (Figure 2c) in order to maximize stacking interactions with the external G-tetrad has been closely associated with low specificity among intramolecular G4s.¹ BRACO-19 is one of the most studied G4 ligands so far. The studies of BRACO-19 have greatly contributed to the treatment of telomeric G4s as potential therapeutic targets. BRACO-19 has shown high anti-cancer activities *in vivo*, such as in a UXF1138L uterus carcinoma xenograft and in a DU-145 prostate cancer xenograft. Despite all these favorable functional features, the lack of membrane permeability and small therapeutic window have been identified as the major limitations of BRACO-19, which must be resolved before any attempt to develop an effective clinical agent.⁴² Quarfloxin was the first-in-class ligand with considerable therapeutic window that had completed Phase II trials as a drug candidate, well-tolerated in patients against neuroendocrine tumors, carcinoid tumors, and lymphoma. Quarfloxin targets a G4 from the *c-Myc* promoter region to disrupt the G4-nucleolin complexes, and its G4-binding was reported as inhibiting RNA biogenesis. The Phase III of human cancer clinical trials is not currently proceeding due to high albumin binding.⁴³

G4s and G4-interactive ligands as potential targets and tools in anti-cancer therapy are given in Table 1. Besides small molecules, G4-binding metal complexes have been recognized as promising anti-cancer drugs.⁹⁶ In general, ligand-mediated stabilization of the G4 structure(s) effectively inhibits telomerase activity or oncogene over-expression and, when applied to cells, most G4 ligands initiate antiproliferative effect (apoptosis) and/or replicative senescence.⁸ Ni-P, Quercetin, TH3, IZCZ-3, Benzofuran derivative, and Furopyridazinone derivative cause negligible cytotoxicity to normal somatic cells *in vivo*. By avoiding many of the problems underlying the therapeutic use of oligonucleotides, the G-rich VEGFq oligonucleotide has contributed to a novel approach to specific inhibition of gene expression *in vivo*, which can be applied to the wide array of genes whose promoters contain quadruplex-forming sequences.⁹⁷ The chemical structure of each ligand, underlined with its respective target topology is displayed in Figure 4. Among these fifteen ligands, eleven prefer parallel, three prefer hybrid, and one prefers dimeric G4 binding. It is known that the induction of a quadruplex or change of a quadruplex conformation upon binding may be one of the most powerful methods to exert a desired biological effect.⁵¹ If a ligand selectively interacts with different G4 topologies, the particular ligand is expected to easily regulate the conformational switch by surpassing the energy barriers between distinct G4 structures in Na⁺ or K⁺ solution. An NMR structural analysis has revealed that a berberine derivative, epiberberine (Figure 2c), discriminates a hybrid type 2 telomere G4 from the other adoptable topologies and promoter G4s (*c-Myc*, BCL2, and PDGFR).⁹⁸ Also the ability of epiberberine to convert the other conformations, such as telomere G4 hybrid type 1 and antiparallel (basket type) G4s, into the type 2 hybrid topology has been reported.^{43,98} It has been recently concluded that specific targeting of G4s by small molecules represents a promising strategy to study the function of targets inside a living cell without influencing their intact states.⁴⁴

The way in which CM03 (Figure 4) has been designed to target multiple effector pathways in pancreatic ductal adenocarcinoma (PDAC) deserves more attention.⁹⁹ The co-crystal structure of MM41 (Figure 4) with an intramolecular human telomeric parallel G4 has been the starting point for CM03 design. Even though the nature and structures of target G4s are unknown, NMR and crystal structures illustrate that some features are common to all G4s, particularly a core of stacked G-tetrads with small-molecule binding at the end of the core. The chromophore of MM41 has been somewhat asymmetrically stacked to the terminal G-tetrad. Indeed, one of the four substituent chains has not been positioned as the other three side chains with respect to G4 due to its orientation away from the G4 surface. The particular side chain has not been capable of making effective contacts with a G4 groove, so that its contribution to overall bind-

Table 1. G4 ligands with anti-cancer activities. Updated data reported previously.⁴³

Target	G4 topology	Cell Line	Cancer Type	Ligand ^{Ref.}	Effect
telomere	hybrid	MDA-MB-231 MCF-7	breast cancer (adenocarcinoma) breast cancer (adenocarcinoma)	Ni-P ^{107,108}	Cancer stem cell-specific apoptosis, bulk cancer-specific apoptosis and senescence, negligible cytotoxicity to normal somatic cells
telomere	dimeric G4s	SiHa	squamous cell carcinoma	IZNP1 ¹⁰⁹	Apoptosis, senescence
telomere	parallel	A549 MCF-7 MIA PaCa-2 PANC-1	lung adenocarcinoma breast cancer (adenocarcinoma) pancreatic ductal adenocarcinoma	MM41 ⁹⁹ CM03 ⁹⁹	Antiproliferative activity (apoptosis), BCL2 and KRAS as secondary targets
c-Myc	parallel	HeLa	cervical cancer	Quercetin ¹¹⁰	Apoptosis, mild cytotoxicity to normal cell line
c-Myc	parallel	A549 HeLa	lung cancer cervical cancer	TH3 ¹¹¹	Antiproliferative effect (apoptosis), negligible cytotoxicity to normal somatic cells
c-Myc	parallel	SiHa HeLa Huh7 A375	squamous cell carcinoma cervical cancer liver cancer malignant melanoma	IZCZ-3 ¹¹²	Antiproliferative effect (apoptosis), negligible cytotoxicity to normal somatic cells
c-Myc	parallel	L363, MM1S, MM1R etc.	myeloma	Benzofuran derivative ¹¹³	Antiproliferative effect (apoptosis), negligible cytotoxicity to normal cells
c-Myc	parallel	HCT116	colorectal carcinoma	Tz 1 ¹¹⁴	Apoptosis
VEGF	parallel	A549	lung cancer	VEGFq ⁹⁷	Autophagic apoptosis
BCL2	hybrid	Jurkat	human acute T cell leukemia	Fuopyridazinone derivative ¹¹⁵	Antiproliferative effect (apoptosis), negligible cytotoxicity to normal cells
c-Kit	parallel	MCF-7 HGC-27	breast adenocarcinoma gastric carcinoma	AQ1 ¹¹⁶	Antiproliferative effect (apoptosis)
hTERT	hybrid with stem loop	MCF7	breast adenocarcinoma	GTC365 ¹¹⁷	Apoptosis, senescence
KRAS	parallel	HCT16 SW620	colorectal carcinoma	Indoloquinoline derivatives ¹¹⁸	Apoptosis
c-Myb	parallel	MCF7	breast adenocarcinoma	Topotecan ¹¹⁹	Repressed expression, uncertain specificity

ing has been minimal. Relative to MM41, an optimal compound has been hypothesized to contain three substituents and to bind with similar affinity, as well as to have the advantage of lower molecular weight and reduced overall cationic charge. Thus, MM41 has been a suboptimal drug candidate due to its higher molecular weight and four positive charges, while CM03 has been an improved rationally designed derivative of MM41 and a novel lead candidate compound for potential therapy against human PDAC. Particular promoter G-quadruplexes have not been assumed as targets. Global genome

transcriptome profiling has been employed to determine which genes are affected by the rationally designed G4-interactive small molecule. Consequently, potential targets at the whole genome level in two pancreatic cancer cell lines have been determined. With *in vitro* cell assays and *in vivo* models for human PDAC, CM03 has been identified as a highly selective and potent G4-binding ligand.⁹⁹

The dynamics of noncovalent interaction between a structurally representative set of small molecules (BRA-CO-19, TMPyP₄, CX-3543, 10074-G5, Telomestatin, Tet-

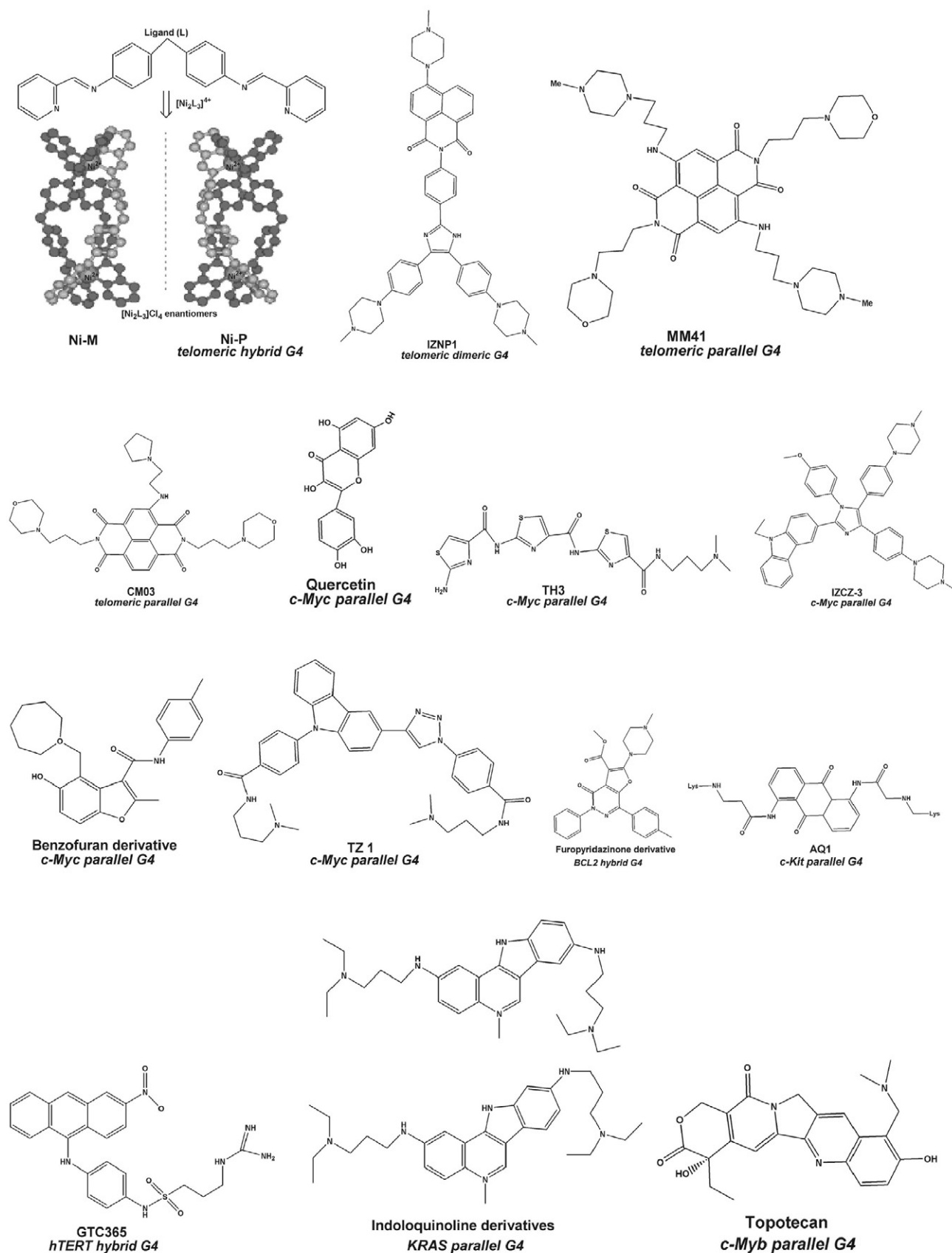


Figure 4. Chemical structures of G4 ligands (with denoted target topologies by italics) that exhibit anti-cancer activities (Table 1).

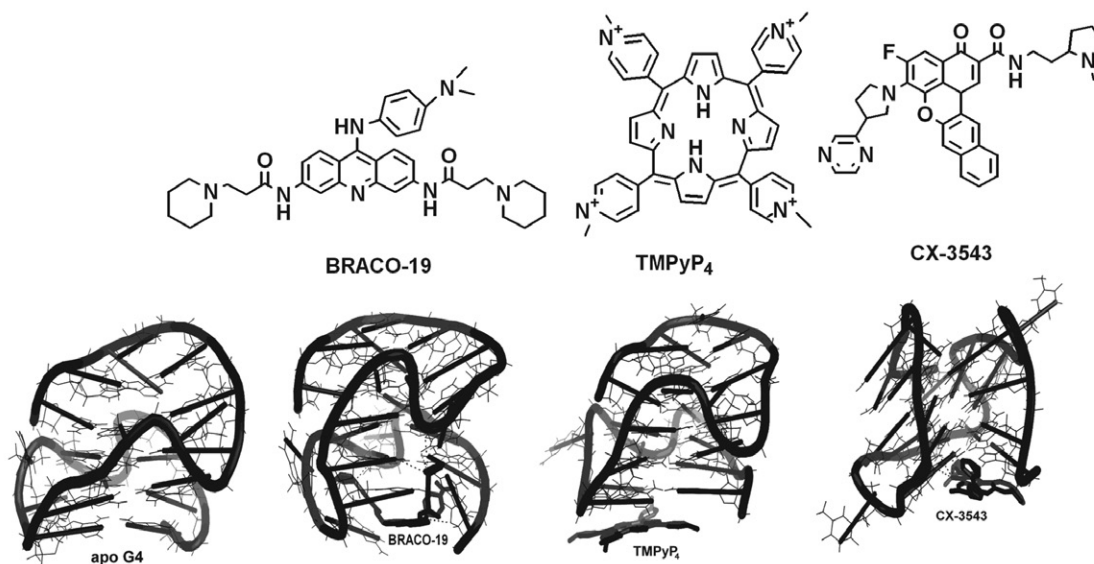


Figure 5. External stacking of BRACO-19, TMPyP₄ and CX-3543 to apo (ligand-free) G4 from the c-Myc promoter in the stable regime of molecular dynamics (MD) simulation. In a representative set of structurally diversified ligands, these three molecules were established to have the highest affinity for G4. Only BRACO-19 was shown to be a thermodynamically favorable binder by increasing the conformational flexibility of G4 in the asymptotic ($t \rightarrow \infty$) regime of MD simulation.⁶⁸

rahydropalmatine, Sanguinarine, Hoechst 33258, Benzophenanthridine derivative, Nitidine Chloride, Piperine, 12459, Quercetin, Quindoline, Berberine, and Flavopiri-

dol) and a G-quadruplex formed in the c-Myc oncogene promoter region was recently explored in a systematic fashion from a rigorous biophysical point of view.⁶⁸ In fact,

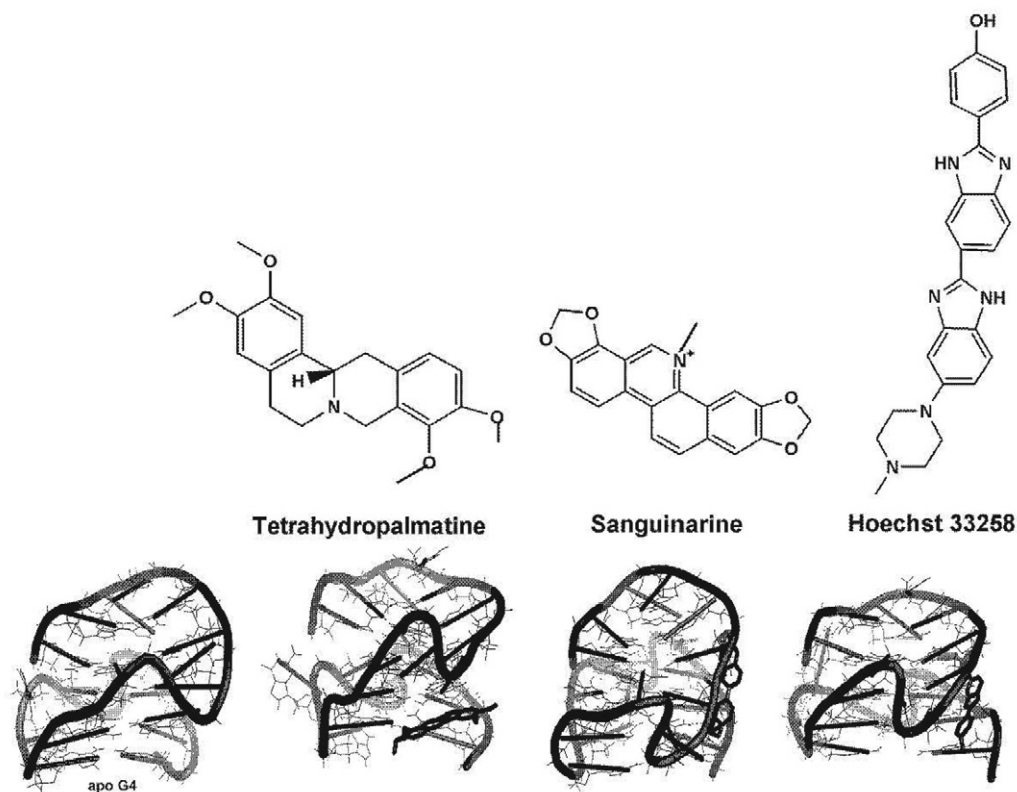


Figure 6. Groove binding of Tetrahydropalmatine, Sanguinarine and Hoechst 33258 to apo (ligand-free) G4 from the c-Myc promoter in the stable regime of molecular dynamics (MD) simulation. In a representative set of structurally diversified ligands, these three molecules were established to have the highest affinity for G4. Only Tetrahydropalmatine was shown to be a thermodynamically favorable binder by increasing the conformational flexibility of G4 in the asymptotic ($t \rightarrow \infty$) regime of MD simulation.⁶⁸

the thermodynamic consequences of apo (ligand-free) G4 conformational flexibility change upon ligand binding have been investigated in the asymptotic regime ($t \rightarrow \infty$) of MD simulation, obtained by extrapolating the stable regime to infinitely long MD simulation. BRACO-19, TMP-yP₄ and CX-3543 have shown the highest affinity to the G4 by stacking to the bottom G-tetrad of G4 (Figure 5). However, only BRACO-19 has been found to be a thermodynamically preferable binder by increasing the conformational flexibility of G4 (Figure 5), with a somewhat larger (by about 3 kcal mol⁻¹) contribution to the additional flexibility of G4 from the sugar-phosphate backbone than from the complete system of nucleobases. In addition, Tetrahydropalmatine, Sanguinarine and Hoechst 33258 have exhibited the highest affinity to the target by groove binding (Figure 6). However, only Tetrahydropalmatine has been found to be a thermodynamically favorable binder by increasing the conformational flexibility of G4 (Figure 6), mainly through the complete system of nucleobases. Therefore, two distinct mechanisms by way of which small molecules interact with G4 are associated with increased conformational flexibility and increased conformational rigidity of apo G4 upon ligand binding respectively.⁶⁸

Even though pure tetrad-binding mode is more stable than groove/loop binding mode, grooves/loops are viable binding sites that are of interest for the structure-based drug design. Grooves/loops with distinct environments help in tuning ligand specificity among many types of G4s without affecting binding affinity.⁴⁴ Thus, multiple binding

modes, which include external stacking and/or intercalation and/or groove/loop binding of two or more ligands simultaneously, have attracted certain attention.⁶¹ This type of binding is less stable than external stacking, likely due to the ability of groove/loop-binding ligands to induce loop rearrangements and destabilize the overall binding by displacing the interaction of the side chains of G-tetrad-binding ligands with the grooves/loops of G4. There are indications that a combined – G-tetrad and groove binding of ligands enhances G4 conformational rigidity, reflected through the decreased conformational flexibility of both G-tetrads and the backbone.⁶¹ For rationalizing this aspect in the case of G4 from the c-Myc promoter region, a relevant structural basis was proposed to include two unique – thermodynamically preferred small molecules: the external stacking of BRACO-19 and the groove binding of Tetrahydropalmatine simultaneously.⁶⁸

Binding sites defined by the surface features of the groove/loop regions can be used to stimulate selective binding interactions, even between closely related G4 structures.⁸ Subtle variations of G4 topologies, groove widths, and loop sequences are associated with a highly dynamic nature of G4 structures, which have propensity to lose conformational entropy upon ligand binding.¹⁰¹ This factor in determining specificity is important in order to distinguish G4s with lower ligand affinities that exist as a dynamic mixture of conformations in the unbound state (human telomere) from G4s that adopt a single conformation.⁸ A small molecule, with binding affinity to increase the conformational entropy of G4 by stacking at the end of

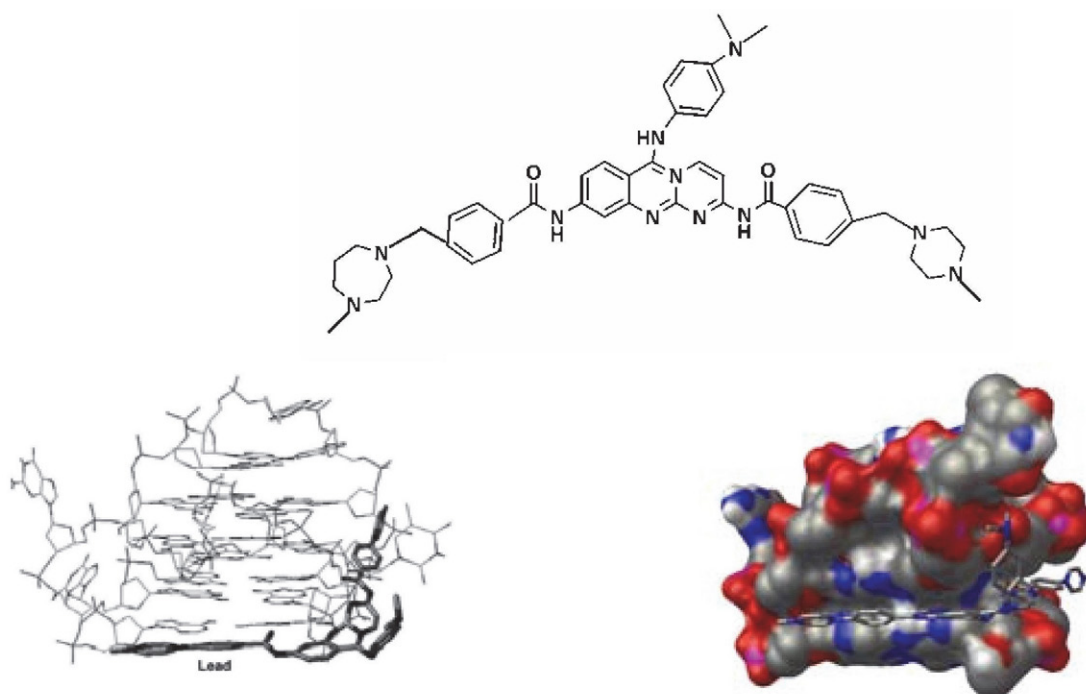


Figure 7. Proposal of lead candidate structure to interact with the c-Myc promoter G4 through external stacking and groove binding simultaneously. This proposal was based on HTVS experiments employing the key pharmacophore features of BRACO-19 for the search of the KEGG databases.¹⁰⁰

Table 2. G4s that are identified in viral genomes and their active ligands. Updated data reported previously.⁴⁶

Virus	Name	Size (nm)	Genome	No. of G4s ^{Ref.}	Active Ligands ^{Ref.}
Human Immunodeficiency Virus 1	HIV-1	ø 120	(+)ssRNA 9.75 kb	12 ¹²⁰	BRACO-19 ^{120–122} TMPyP4 ^{122,123} PIPER ¹²³ c-exNDI ¹²⁴ Nitidine Chloride ¹⁰⁵ Benzophenanthridine derivative ¹⁰⁵
Herpes Simplex Virus 1	HSV-1	ø 125	dsDNA 152 kb	316 ^{125,126}	BRACO-19 ¹²⁶ c-exNDI ¹²⁷
Epstein-Barr Virus	EBV	ø 120–180	dsDNA 172 kb	13 ¹²⁵	BRACO-19 ¹²⁸ PDS ¹²⁹ PhenDC3 ¹³⁰
Kaposi's Sarcoma associated Herpes Virus	KSHV	ø 125	dsDNA 170 kb	52 ^{125,131}	PhenDC3 ¹³¹
Human Herpes Virus 6	HHV-6	ø 200	dsDNA 162 kb	43 ¹²⁵	BRACO-19 ¹³²
Hepatitis C Virus	HCV	ø 60	(+)ssRNA 9.6 kb	2 ¹³³	TMPyP4 ¹³³ PDP ¹³³
Human Papilloma Virus	HPV	ø 60	circular dsDNA 8 kb	8 ¹³⁴	
Zika Virus	ZIKV	ø 50	(+)ssRNA 11 kb	8 ¹³⁵	
Severe Acute Respiratory Syndrome Corona Virus	SARS CoV	ø 200	(+)ssRNA 30 kb		
Hepatitis B Virus	HBV	ø 42	partially circular dsDNA 3.2 kb	1 ¹³⁶	TMPyP4 ¹³⁶ PDS ¹³⁶
Ebola Virus	EBOV cylindrical	ø 80	(-)ssRNA 18.9 kb	1 ¹³⁷	TMPyP4 ¹³⁷

G4 from an oncogene promoter region, can be hypothesized as a unique, specific pharmacophore for the identification of new lead candidates by high-throughput virtual screening (HTVS).^{68,100} A lead candidate compound (Figure 7), predicted to recognize the c-Myc promoter G4 through external stacking and groove binding at the same time, was designed by HTVS experiments in combination with analog design.¹⁰⁰ The key pharmacophore features of BRACO-19 have been used for the search of the Kyoto Encyclopedia of Genes and Genomes (KEGG) databases in order to generate hit-to-lead candidates. Two crucial features rationalize the visible G4-stabilizing advantages of the concomitant external stacking and groove binding of the lead candidate over the external stacking of BRACO-19. The first is a flexible aromatic core of the lead candidate relative to a rigid one of BRACO-19. The second is a more polar surface of the lead candidate (by about 51 Å²)

than that of BRACO-19. The conformational flexibility of small molecules is generally more preferable compared to their locking in a presumed bioactive G4 conformation.¹⁰⁰ Structure-based virtual screening and cell-based screening approaches, as well as biophysical and/or biological assays define an acceptable framework for the determination of completely new types of bioactive G4-interactive ligands.^{44,102}

3. G4-Preferred Ligands: Potential Tools in Antiviral Therapy

The presence of G4s in viruses has attracted more attention during the last few years. The viruses include those involved in recent epidemics, such as the Zika and Ebola viruses. Putative G4-forming sequences are usually located

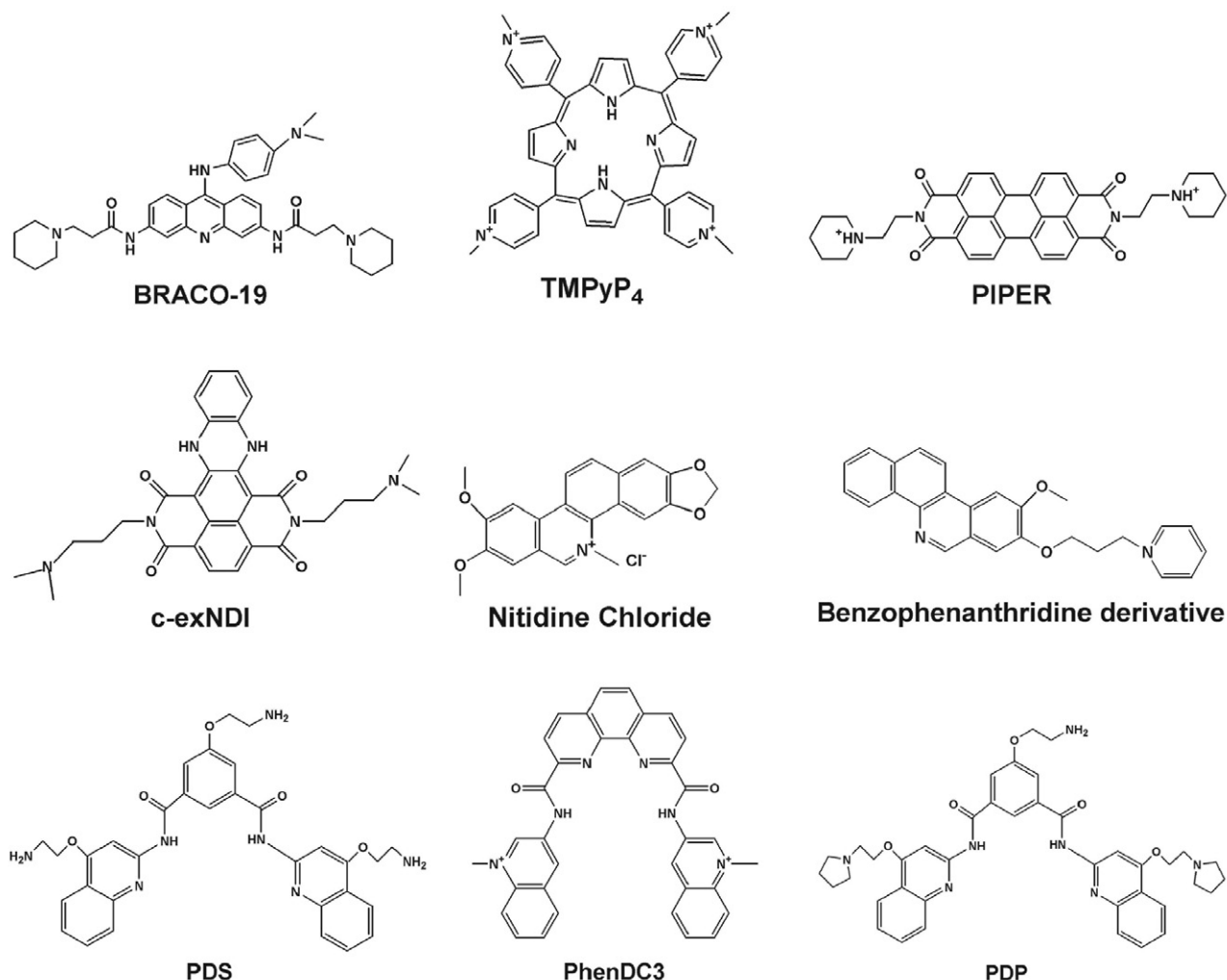


Figure 8. Chemical structures of ligands that prefer G4s in viral genomes.

ed in regulatory regions of the viral genomes and implicated in key viral processes; in some cases, their involvement in viral latency has been reported too.⁴⁶ G4 ligands are tools that have been developed and tested in order to study the complexity of G4-mediated mechanisms in the viral life cycle. They have also been viewed as potential therapeutic agents.⁴⁶ G4s that are identified in viral genomes, as well as their active ligands are summarized in Table 2. The chemical structures of the ligands are shown in Figure 8. Promising antiviral effects of G4 ligands have been generally related to G4-mediated mechanisms of action both at the genome level and at transcriptional level.⁴⁶ G4-forming oligonucleotides as potential antiviral agents have been previously reviewed in great detail,^{103,104} so that they are not considered in the present review article.

Experimental research based on ESI-MS, CD spectrometry, and DMS footprinting has indicated the formation of a G4 within a G-rich sequence that is located between -76 and -57 bp in the HIV-1 promoter.¹⁰⁵ The CD melting experiment has also shown that, among eight natural small molecules (Nitidine Chloride – NC, Benzo-

phenanthridine derivative – BPD, Jatrorrhizine, Tetrahydropalmatine, Toddalolactone, Coptisine, Piperine, and Astragaline), NC and BPD have the highest and nearly equal affinities to the HIV-1 promoter G4.¹⁰⁵ The binding modes of NC and BPD have been elaborated using sophisticated computational methods,⁶⁶ demonstrating that NC is a thermodynamically unfavorable binder by increasing the conformational rigidity of apo G4 and that BPD is a thermodynamically favorable binder by increasing the conformational flexibility of apo G4 in the asymptotic ($t \rightarrow \infty$) regime of MD simulation (Figure 9).

In addition to HTVS methods or structure-based design with ahead-presumed features, fragment-based drug discovery (FBDD) may be a valuable approach to the generation of new pharmacophores that specifically recognize G4 structures. This approach is based on the generation of molecular fragment small libraries screened against the receptor in order to further synthetically elaborate them into lead compounds. For example, one of the heterocyclic molecules (Figure 10) has been shown to specifically recognize G4 from the HIV-1 long terminal repeat (LTR) pro-

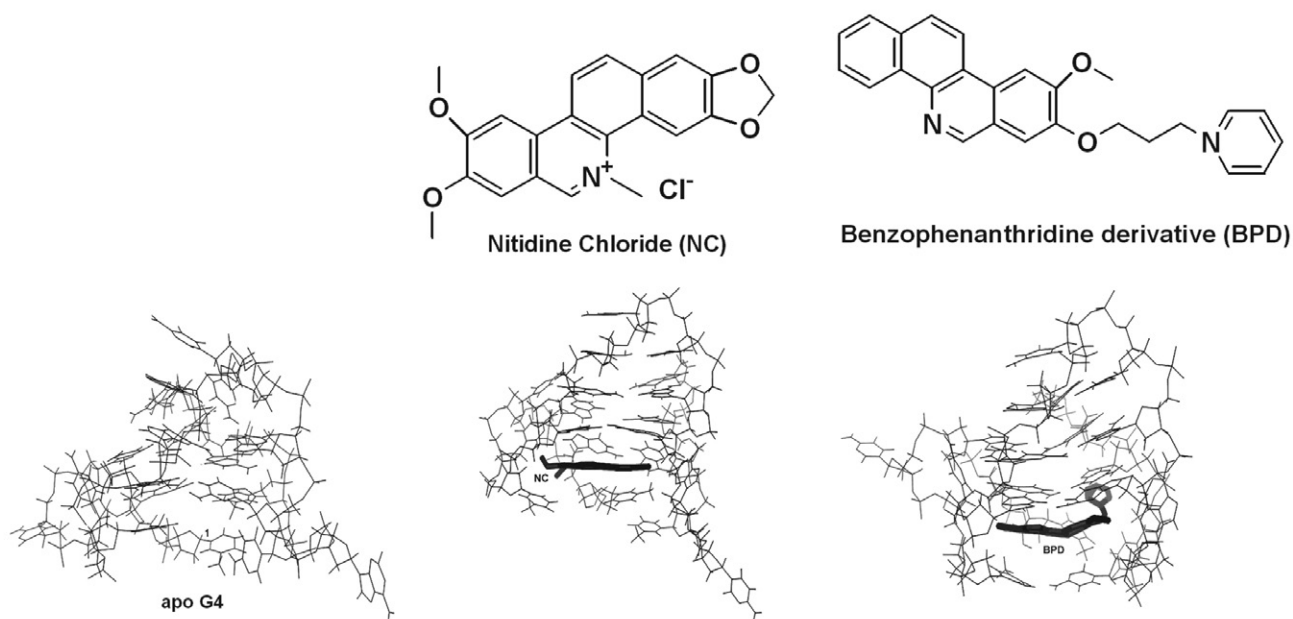


Figure 9. Among eight natural small molecules, NC and BPD were shown to have the most pronounced (and mutually comparable) affinity for G4 from the HIV-1 promoter.¹⁰⁵ NC is a thermodynamically unfavorable binder by increasing the conformational rigidity of apo G4, while BPD is a thermodynamically favorable binder by increasing the conformational flexibility of apo G4 in the asymptotic ($t \rightarrow \infty$) regime of MD simulation.⁶⁶

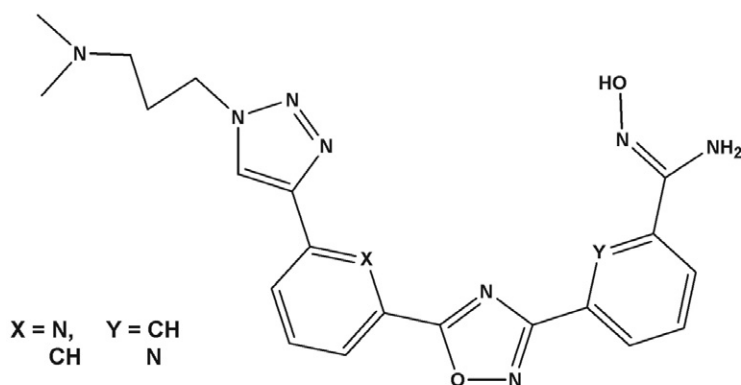


Figure 10. One of the heterocyclic molecules was shown to prefer G4 from the HIV-1 LTR promoter region and to represent a potential pharmacophore for the development of novel ligands with unexpected chemical features. These compounds were developed using a FBDD approach.¹⁰⁶

moter region and to represent a potential pharmacophore for the development of novel ligands with unexpected chemical features.¹⁰⁶ Size and poor pharmacokinetics are the main obstacles in the development of G4-interactive ligand. FBDD can be a relevant approach to the development of compounds that have smaller sizes and more drug-like properties.

4. Conclusions and Future Perspective

G-quadruplexes are naturally forming structures under physiological conditions, stabilized by monovalent cations present in cells. Over two hundreds quadruplex structures, either intramolecular or intermolecular, are currently deposited in the public domain such as the Pro-

tein Data Bank. Most G4 studies consider only intramolecular G4 folding. However, the potential prevalence of intermolecular DNA/RNA G4s in humans has been indicated by bioinformatics searches. It means that innovative research is urgently needed with the aim to detect and characterize intermolecular G4 motifs *in vivo*, that is, their structural conformational exchange with intramolecular G4s or other structural motifs, and their potential functions in cells.³⁸ The structural diversity, thermal stability and abundance of G4s in telomeres, oncogene promoter regions, and viral genomes make them attractive targets for potential anti-cancer and antiviral therapies.

Although the nature and structures of target G4s are unknown, NMR and crystal structures show that some features are common to all G4s; e.g. a core of stacked

G-tetrads with small-molecule binding at one of the ends of the core. One of the features has been recently revealed by molecular dynamics simulations,^{66,68} because distinct conformations that are often observed in static, experimentally determined structures may be the consequences of the differences in experimental conditions or procedures. The thermodynamic consequences of apo (ligand-free) G4 conformational flexibility change upon complex formation have been observed in the asymptotic regime ($t \rightarrow \infty$) of MD simulation. Two dissected mechanisms of G4-small molecule interaction are associated with increased conformational flexibility and increased conformational rigidity of apo target upon ligand binding, thereby being thermodynamically favorable and unfavorable respectively. A small molecule with binding affinity to increase the conformational flexibility of G4 through π - π stacking at the end of G4 can be conceivable as a unique, specific pharmacophore for designing novel lead candidate compounds by high-throughput virtual screening.^{66,68} Virtual screening has been demonstrated to be effective in reducing the initial number of potential candidates.⁴⁴ In this way a lead candidate structure has been predicted to target a G4 from the c-Myc promoter region through external stacking and groove binding simultaneously.¹⁰⁰ This approach would have useful implications for overcoming the challenge of designing specific groove/loop binders, which stems from the groove/loop interaction mode dependences on the particular G4 topologies, groove widths, and loop sequences. Therefore, the use of grooves/loops offers distinct environments aimed to gain specificity among many types of G4s without influencing binding affinity.⁴⁴

In contrast to HTVS methods or structure-based design with pre-set features, fragment-based drug discovery, which is based on the generation of molecular fragment small libraries screened against the receptor to further synthetically convert them into lead compounds, may be a valuable approach to the generation of new pharmacophores that specifically recognize G4 nucleic acid structures. The sizes and poor pharmacokinetic properties of G4-interactive ligands are the main glitches in their development. By adding up fragments to singly recognize the target, FBDD can be seen as a relevant approach to the development of compounds that have smaller sizes and more drug-like properties.¹⁰⁶

An appropriate framework for identifying totally new types of bioactive G4-interactive ligands is currently defined by structure-based virtual screening methods and cell-based screening approaches.^{44,106} Specific targeting of G4s by small molecules is and will be a promising tool for studying the behavior of targets inside a living cell without influencing their intact states.⁴⁴

Particular promoter G4s should not be assumed as prior targets, indicating that single G4 promoter targeting strategy is not quite a suitable approach. In fact, the knowledge of potential targets at the whole genome level is need-

ed. Global genome transcriptome profiling can be exploited for the determination of which genes are affected by a rationally designed G4-interactive small molecule. As a consequence, the selectivity and potency of a new G4-preferred compound can be evaluated using *in vitro* cell assays and *in vivo* models. A relevant example is the successful design, synthesis and identification of CM03 as a novel lead candidate for the potential therapy against human pancreatic cancer.⁹⁹

This review article is imagined to inspire ongoing efforts of modern chemists and pharmacists to target G4 structures.

5. References

1. B. Onel, C. Lin, D. Z. Yang, *Sci. China Chem.* **2014**, *57*(12), 1605–1614. DOI:10.1007/s11426-014-5235-3
2. B. E. Bernstein, E. Birney, I. Dunham, E. D. Green, C. Gunter, M. Snyder, *Nature* **2012**, *489*(7414), 57–74. DOI:10.1038/nature11247
3. P. M. Mitrasinovic, *J. Chem. Inf. Model.* **2015**, *55*(2), 421–433. DOI:10.1021/ci5006965
4. A. Rakic, P. M. Mitrasinovic, *J. Serb. Chem. Soc.* **2008**, *73*(1), 41–53. DOI:10.2298/JSC0801041R
5. P. M. Mitrasinovic, *J. Struct. Biol.* **2006**, *153*(3), 207–222. DOI:10.1016/j.jsb.2005.12.001
6. I. Bang, *Biochemische Zeitschrift* **1910**, *26*, 293–311.
7. M. Gellert, M. N. Lipsett, D. R. Davies, *Proc. Natl. Acad. Sci. U. S. A.* **1962**, *48*(12), 2013–2018. DOI:10.1073/pnas.48.12.2013
8. N. W. Luedtke, *Chimia* **2009**, *63*(3), 134–139. DOI:10.2533/chimia.2009.134
9. N. V. Hud, F. W. Smith, F. A. L. Anet, J. Feigon, *Biochemistry* **1996**, *35*(48), 15383–15390. DOI:10.1021/bi9620565
10. T. G. Voss, C. D. Fermin, J. A. Levy, S. Vigh, B. Choi, R. F. Garry, *J. Virol.* **1996**, *70*(8), 5447–5454. DOI:10.1128/JVI.70.8.5447-5454.1996
11. A. Risitano, K. R. Fox, *Biochemistry* **2003**, *42*(21), 6507–6513. DOI:10.1021/bi026997v
12. D. Sen, W. Gilbert, *Nature* **1990**, *344*(6265), 410–414. DOI:10.1038/344410a0
13. D. Miyoshi, A. Nakao, N. Sugimoto, *Nucleic Acids Res.* **2003**, *31*(4), 1156–1163. DOI:10.1093/nar/gkg211
14. D. Bhattacharyya, G. Mirihana Arachchilage, S. Basu, *Front. Chem.* **2016**, *4*, 38. DOI:10.3389/fchem.2016.00038
15. G. Marsico, V. S. Chambers, A. B. Sahakyan, P. McCauley, J. M. Boutell, M. Di Antonio, S. Balasubramanian, *Nucleic Acids Res.* **2019**, *47*(8), 3862–3874. DOI:10.1093/nar/gkz179
16. J. L. Huppert, S. Balasubramanian, *Nucleic Acids Res.* **2005**, *33*(9), 2908–2916. DOI:10.1093/nar/gki609
17. A. K. Todd, M. Johnston, S. Neidle, *Nucleic Acids Res.* **2005**, *33*(9), 2901–2907. DOI:10.1093/nar/gki553
18. M. Kaushik, S. Kaushik, A. Bansal, S. Saxena, S. Kukreti, *Curr. Mol. Med.* **2011**, *11*(9), 744–769. DOI:10.2174/156652411798062421

19. G. Wu, L. Chen, W. Liu, D. Yang, *Molecules* **2019**, *24*(8), 1578. DOI:10.3390/molecules24081578
20. L. I. Jansson, J. Hentschel, J. W. Parks, T. R. Chang, C. Lu, R. Baral, C. R. Bagshaw, M. D. Stone, *Proc. Natl. Acad. Sci. U. S. A.* **2019**, *116*(19), 9350–9359. DOI:10.1073/pnas.1814777116
21. A. Küçükakdağ Doğu, Ö. Persil Çetinkol, *Turk. J. Chem.* **2019**, *43*(4), 1040–1051. DOI:10.3906/kim-1903-6
22. S. K. Wang, Y. Wu, T. M. Ou, *Curr. Topics Med. Chem.* **2015**, *15*(19), 1947–1956. DOI:10.2174/1568026615666150515145733
23. R. Tippana, M. C. Chen, N. A. Demeshkina, A. R. Ferré-D'Amaré, S. Myong, *Nature Comm.* **2019**, *10*(1), 1855. DOI:10.1038/s41467-019-09802-w
24. D. Miyoshi, S. Matsumura, S. Nakano, N. Sugimoto, *J. Am. Chem. Soc.* **2004**, *126*(1), 165–169. DOI:10.1021/ja036721q
25. X. Li, Y. H. Peng, J. S. Ren, X. G. Qu, *Proc. Natl. Acad. Sci. U. S. A.* **2006**, *103*(52), 19658–19663. DOI:10.1073/pnas.0607245103
26. M. Fry, *Front. Biosci.* **2007**, *12*, 4336–4351. DOI:10.2741/2391
27. H. Y. Han, C. L. Cliff, L. H. Hurley, *Biochemistry* **1999**, *38*(22), 6981–6986. DOI:10.1021/bi9905922
28. A. De Cian, J. L. Mergny, *Nucleic Acids Res.* **2007**, *35*(8), 2483–2493. DOI:10.1093/nar/gkm098
29. D. Y. Sun, K. X. Guo, J. J. Rusche, L. H. Hurley, *Nucleic Acids Res.* **2005**, *33*(18), 6070–6080. DOI:10.1093/nar/gki917
30. F. Kouzine, D. Levens, *Front. Biosci.* **2007**, *12*, 4409–4423. DOI:10.2741/2398
31. P. Rawal, V. B. Kummarasetti, J. Ravindran, N. Kumar, K. Halder, R. Sharma, M. Mukerji, S. K. Das, S. Chowdhury, *Genome Res.* **2006**, *16*(5), 644–655. DOI:10.1101/gr.4508806
32. F. Kouzine, S. Sanford, Z. Elisha-Feil, D. Levens, *Nat. Struct. Mol. Biol.* **2008**, *15*(2), 146–154. DOI:10.1038/nsmb.1372
33. A. K. Shukla, K. B. Roy, *J. Biochem.* **2006**, *139*(1), 35–39. DOI:10.1093/jb/mvj009
34. A. T. Phan, J. L. Mergny, *Nucleic Acids Res.* **2002**, *30*(21), 4618–4625. DOI:10.1093/nar/gkf597
35. S. A. Dvorkin, A. I. Karsisiotis, M. Webba da Silva, *Sci. Adv.* **2018**, *4*(8), eaat3007. DOI:10.1126/sciadv.aat3007
36. S. Asamitsu, M. Takeuchi, S. Ikenoshita, Y. Imai, H. Kashiwagi, N. Shioda, *Int. J. Mol. Sci.* **2019**, *20*(12), E2884. DOI:10.3390/ijms20122884
37. J. Ida, S. K. Chan, J. Glökler, Y. Y. Lim, Y. S. Choong, T. S. Lim, *Molecules* **2019**, *24*(6), E1079. DOI:10.3390/molecules24061079
38. C. K. Kwok, C. J. Merrick, *Trends Biotech.* **2017**, *35*(10), 997–1013. DOI:10.1016/j.tibtech.2017.06.012
39. J. Spiegel, S. Adhikari, S. Balasubramanian, *Trends Chem.* **2020**, *2*(2), 123–136. DOI:10.1016/j.trechm.2019.07.002
40. K. G. Zyner, D. S. Mulhearn, S. Adhikari, S. Martinez Cuesta, M. Di Antonio, N. Erard, G. J. Hannon, D. Tannahill, S. Balasubramanian, *Elife* **2019**, *8*, e46793. DOI:10.7554/eLife.46793
41. J. Bidzinska, G. Cimino-Reale, N. Zaffaroni, M. Folini, *Molecules* **2013**, *18*(10), 12368–12395. DOI:10.3390/molecules181012368
42. D. Yang, K. Okamoto, *Future Med. Chem.* **2010**, *2*(4), 619–646. DOI:10.4155/fmc.09.172
43. S. Asamitsu, S. Obata, Z. Yu, T. Bando, H. Sugiyama, *Molecules* **2019**, *24*(3), e429. DOI:10.3390/molecules24030429
44. S. Asamitsu, T. Bando, H. Sugiyama, *Chem. Eur. J.* **2019**, *25*(2), 417–430. DOI:10.1002/chem.201802691
45. D. Musumeci, C. Riccardi, D. Montesarchio, *Molecules* **2015**, *20*(9), 17511–17532. DOI:10.3390/molecules200917511
46. E. Ruggiero, S. N. Richter, *Nucleic Acids Res.* **2018**, *46*(7), 3270–3283. DOI:10.1093/nar/gky187
47. Z. Y. Sun, X. N. Wang, S. Q. Cheng, X. X. Su, T. M. Ou, *Molecules* **2019**, *24*, 396. DOI:10.3390/molecules24030396
48. K. W. Zheng, S. Xiao, J. Q. Liu, J. Y. Zhang, Y. H. Hao, Z. Tan, *Nucleic Acids Res.* **2013**, *41*(10), 5533–5541. DOI:10.1093/nar/gkt264
49. B. Pagano, S. Cosconati, V. Gabelica, L. Petraccone, S. De Tito, L. Marinelli, V. La Pietra, F. S. di Leva, I. Lauri, R. Trotta, E. Novellino, C. Giancola, A. Randazzo, *Curr. Pharm. Des.* **2012**, *18*(14), 1880–1899. DOI:10.2174/138161212799958332
50. A. Nuthanakanti, I. Ahmed, S. Y. Khatik, K. Saikrishnan, S. G. Srivatsan, *Nucleic Acids Res.* **2019**, *47*(12), 6059–6072. DOI:10.1093/nar/gkz419
51. M. Chen, G. Song, C. Wang, D. Hu, J. Ren, X. Qu, *Biophys. J.* **2009**, *97*(7), 2014–2023. DOI:10.1016/j.bpj.2009.07.025
52. V. Viglasky, L. Bauer, K. Tluczkova, P. Javorsky, *J. Nucleic Acids* **2010**, *2010*, Article ID 820356. DOI:10.4061/2010/820356
53. R. D. Gray, L. Petraccone, R. Buscaglia, J. B. Chaires, *Methods Mol. Biol.* **2010**, *608*, 121–136. DOI:10.1007/978-1-59745-363-9_8
54. B. DeMarco, S. Stefanovic, A. Williams, K. R. Moss, B. R. Anderson, G. J. Bassell, M. R. Mihalescu, *PLoS ONE* **2019**, *14*(5), e0217275. DOI:10.1371/journal.pone.0217275
55. M. I. Umar, D. Ji, C. Y. Chan, C. K. Kwok, *Molecules* **2019**, *24*, 2416. DOI:10.3390/molecules24132416
56. R. C. Monsen, J. O. Trent, *Biochimie* **2018**, *152*, 134–148. DOI:10.1016/j.biochi.2018.06.024
57. S. Haider, *J. Ind. Institute Sci.* **2018**, *98*(3), 325–339. DOI:10.1007/s41745-018-0083-3
58. V. Brazda, J. Kolomaznik, J. Lysek, M. Bartas, M. Fojta, J. Stastny, J. L. Mergny, *Bioinformatics* **2019**, *35*(18), 3493–3495. DOI:10.1093/bioinformatics/btz087
59. A. Pavlov, P. M. Mitrasinovic, *Curr. Org. Chem.* **2010**, *14*(2), 129–137. DOI:10.2174/138527210790069866
60. L. Petraccone, N. C. Garbett, J. B. Chaires, J. O. Trent, *Biopolymers* **2010**, *93*(6), 533–548. DOI:10.1002/bip.21392
61. Q. Hou, S. B. Chen, J. H. Tan, H. B. Luo, D. Li, L. Q. Gu, Z. H. Huang, *J. Comput. Aided Mol. Des.* **2012**, *26*, 1355–1368. DOI:10.1007/s10822-012-9619-1
62. J. Husby, A. K. Todd, J. A. Platts, S. Neidle, *Biopolymers* **2013**, *99*(12), 989–1005. DOI:10.1002/bip.22340
63. F. S. Di Leva, E. Novellino, A. Cavalli, M. Parrinello, V. Limongelli, *Nucleic Acids Res.* **2014**, *42*(9), 5447–5455. DOI:10.1093/nar/gku247
64. J. K. Zhou, D. Y. Yang, S. Y. Sheu, *Phys. Chem. Chem. Phys.* **2015**, *17*(19), 12857–12869. DOI:10.1039/C5CP00378D
65. F. Moraca, J. Amato, F. Ortuso, A. Artese, B. Pagano, E. Novel-

- lino, S. Alcaro, M. Parrinello, V. Limongelli, *Proc. Natl. Acad. Sci. U. S. A.* **2017**, *114*(11), E2136–E2145. DOI:10.1073/pnas.1612627114
66. P. M. Mitrasinovic, *J. Biomol. Struct. Dyn.* **2018**, *36*(9), 2292–2302. DOI:10.1080/07391102.2017.1358670
67. B. Machireddy, H. J. Sullivan, C. Wu, *Molecules* **2019**, *24*(6), E1010. DOI:10.3390/molecules24061010
68. P. M. Mitrasinovic, *Croat. Chem. Acta* **2019**, *92*(1), 43–57. DOI:10.5562/cca3456
69. C. L. Grand, T. J. Powell, R. B. Nagle, D. J. Bearss, D. Tye, M. Gleason-Guzman, L. H. Hurley, *Proc. Natl. Acad. Sci. U. S. A.* **2004**, *101*(16), 6140–6145. DOI:10.1073/pnas.0400460101
70. A. Siddiqui-Jain, C. L. Grand, D. J. Bearss, L. H. Hurley, *Proc. Natl. Acad. Sci. U. S. A.* **2002**, *99*(18), 11593–11598. DOI:10.1073/pnas.182256799
71. E. V. Prochownik, P. K. Vogt, *Genes & Cancer* **2010**, *1*(6), 650–659. DOI:10.1177/1947601910377494
72. S. Balasubramanian, L. H. Hurley, S. Neidle, *Nat. Rev. Drug Discov.* **2011**, *10*(4), 261–275. DOI:10.1038/nrd3428
73. D. Sun, K. Guo, J. J. Rusche, L. H. Hurley, *Nucleic Acids Res.* **2005**, *33*(18), 6070–6080. DOI:10.1093/nar/gki917
74. T. S. Dexheimer, D. Sun, L. H. Hurley, *J. Am. Chem. Soc.* **2006**, *128*(16), 5404–5415. DOI:10.1021/ja0563861
75. S. Rankin, A. P. Reszka, J. Huppert, M. Zloh, G. N. Parkinson, A. K. Todd, S. Ladame, S. Balasubramanian, S. Neidle, *J. Am. Chem. Soc.* **2005**, *127*(30), 10584–10589. DOI:10.1021/ja050823u
76. S. L. Palumbo, S. W. Ebbinghaus, L. H. Hurley, *J. Am. Chem. Soc.* **2009**, *131*(31), 10878–10891. DOI:10.1021/ja902281d
77. S. Cogoi, F. Quadrioglio, L. E. Xodo, *Biochemistry* **2004**, *43*(9), 2512–2523. DOI:10.1021/bi035754f
78. R. K. Morgan, H. Batra, V. C. Gaerig, J. Hockings, T. A. Brooks, *Biochim. Biophys. Acta (BBA) Gene Regul. Mech.* **2016**, *1859*(2), 235–245. DOI:10.1016/j.bbagr.2015.11.004
79. R. G. Ramsay, T. J. Gonda, *Nat. Rev. Cancer* **2008**, *8*(7), 523–534. DOI:10.1038/nrc2439
80. R. K. Moyzis, J. M. Buckingham, L. S. Cram, M. Dani, L. L. Deaven, M. D. Jones, J. Meyne, R. L. Ratliff, J. R. Wu, *Proc. Natl. Acad. Sci. U. S. A.* **1988**, *85*(18), 6622–6626. DOI:10.1073/pnas.85.18.6622
81. W. E. Wright, V. M. Tesmer, K. E. Huffman, S. D. Levene, J. W. Shay, *Genes Dev.* **1997**, *11*(21), 2801–2809. DOI:10.1101/gad.11.21.2801
82. A. J. Sfeir, W. H. Chai, J. W. Shay, W. E. Wright, *Mol. Cell* **2005**, *18*(1), 131–138. DOI:10.1016/j.molcel.2005.02.035
83. J. Dai, M. Carver, C. Punchihewa, R. A. Jones, D. Z. Yang, *Nucleic Acids Res.* **2007**, *35*(15), 4927–4940. DOI:10.1093/nar/gkm522
84. L. Petraccone, C. Spink, J. O. Trent, N. C. Garbett, C. S. Mekmaysy, C. Giancola, J. B. Chaires, *J. Am. Chem. Soc.* **2011**, *133*(51), 20951–20961. DOI:10.1021/ja209192a
85. J. Dai, M. Carver, D. Yang, *Biochimie* **2008**, *90*, 1172–1183. DOI:10.1016/j.biochi.2008.02.026
86. V. Brázda, L. Hároniková, J. C. Liao, M. Fojta, *Int. J. Mol. Sci.* **2014**, *15*(10), 17493–17517. DOI:10.3390/ijms151017493
87. B. J. Chen, Y. L. Wu, Y. Tanaka, W. Zhang, *Int. J. Biol. Sci.* **2014**, *10*(10), 1084–1096. DOI:10.7150/ijbs.10190
88. S. Neidle, *Curr. Opin. Struct. Biol.* **2009**, *19*, 239–250. DOI:10.1016/j.sbi.2009.04.001
89. Y. Qin, L. H. Hurley, *Biochimie* **2008**, *90*(8), 1149–1171. DOI:10.1016/j.biochi.2008.02.020
90. D. J. Patel, A. T. Phan, V. Kuryavyi, *Nucleic Acids Res.* **2007**, *35*(22), 7429–7455. DOI:10.1093/nar/gkm711
91. L. Oganessian, T. M. Bryan, *Bioessays* **2007**, *29*(2), 155–165. DOI:10.1002/bies.20523
92. J. L. Mergny, J. F. Riou, P. Mailliet, M. P. Teulade-Fichou, E. Gilson, *Nucleic Acids Res.* **2002**, *30*(4), 839–865. DOI:10.1093/nar/30.4.839
93. J. Cuesta, M. A. Read, S. Neidle, *Mini Rev. Med. Chem.* **2003**, *3*(1), 11–21. DOI:10.2174/1389557033405502
94. A. De Cian, L. Lacroix, C. Douarre, N. Temime-Smaali, C. Trentesaux, J. F. Riou, J. L. Mergny, *Biochimie* **2008**, *90*(1), 131–155. DOI:10.1016/j.biochi.2007.07.011
95. M. A. Shamma, R. J. Shmookler Reis, C. Li, H. Koley, L. H. Hurley, K. C. Anderson, N. C. Munshi, *Clin. Cancer Res.* **2004**, *10*(2), 770–776. DOI:10.1158/1078-0432.CCR-0793-03
96. S. N. Georgiades, N. H. Abd Karim, K. Suntharalingam, R. Vilar, *Angew. Chem. Int. Ed.* **2010**, *49*, 4020–4034. DOI:10.1002/anie.200906363
97. D. Muench, F. Rezzoug, S. D. Thomas, J. Xiao, A. Islam, D. M. Miller, K. C. Sedoris, *PLoS ONE* **2019**, *14*(1), e0211046. DOI:10.1371/journal.pone.0211046
98. C. Lin, G. Wu, K. Wang, B. Onel, S. Sakai, Y. Shao, D. Yang, *Angew. Chem. Int. Ed.* **2018**, *57*, 10888–10893. DOI:10.1002/anie.201804667
99. C. Marchetti, K. G. Zyner, S. A. Ohnmacht, M. Robson, S. M. Haider, J. P. Morton, G. Marsico, T. Vo, S. Laughlin-Toth, A. A. Ahmed, G. Di Vita, I. Pazitna, M. Gunaratnam, R. J. Besser, A. C. G. Andrade, S. Diocou, J. A. Pike, D. Tannahill, R. B. Pedley, T. R. J. Evans, W. D. Wilson, S. Balasubramanian, S. Neidle, *J. Med. Chem.* **2018**, *61*(6), 2500–2517. DOI:10.1021/acs.jmedchem.7b01781
100. P. M. Mitrasinovic, *Acta Chim. Slov.* **2020**, *67*, 1–10. DOI:10.17344/acsi.2019.5105
101. G. Sattin, A. Artese, M. Nadai, G. Costa, L. Parrotta, S. Alcaro, M. Palumbo, S. N. Richter, *PLoS ONE* **2013**, *8*(12), e84113. DOI:10.1371/journal.pone.0084113
102. R. Rocca, F. Moraca, G. Costa, M. Nadai, M. Scalabrin, C. Talarico, S. Distinto, E. Maccioni, F. Ortuso, A. Artese, S. Alcaro, S. N. Richter, *Biochim. Biophys. Acta (BBA) Gen. Subj.* **2017**, *1861*(5PtB), 1329–1340. DOI:10.1016/j.bbagen.2016.12.023
103. D. Musumeci, C. Riccardi, D. Montesarchio, *Molecules* **2015**, *20*(9), 17511–17532. DOI:10.3390/molecules200917511
104. C. Platella, C. Riccardi, D. Montesarchio, G. N. Roviello, D. Musumeci, *Biochim. Biophys. Acta (BBA) Gen. Subj.* **2017**, *1861*(5PtB), 1429–1447. DOI:10.1016/j.bbagen.2016.11.027
105. W. Wang, Y. Sui, L. Zhang, W. Tan, X. He, X. Xie, *Can. J. Chem.* **2016**, *94*(1), 60–65. DOI:10.1139/cjc-2015-0215
106. M. Tassinari, A. Lena, E. Butovskaya, V. Pirota, M. Nadai, M.

- Freccero, F. Doria, S. N. Richter, *Molecules* **2018**, *23*(8), 1874. DOI:10.3390/molecules23081874
107. H. Yu, X. Wang, M. Fu, J. Ren, X. Qu, *Nucleic Acids Res.* **2008**, *36*(17), 5695–5703. DOI:10.1093/nar/gkn569
108. H. Qin, C. Zhao, Y. Sun, J. Ren, X. Qu, *J. Am. Chem. Soc.* **2017**, *139*(45), 16201–16209. DOI:10.1021/jacs.7b07490
109. M. Hu, S. Chen, B. Wang, T. Ou, L. Gu, J. Tan, Z. Huang, *Nucleic Acids Res.* **2016**, *45*(4), 1606–1618. DOI:10.1093/nar/gkw1195
110. A. Tawani, S. K. Mishra, A. Kumar, *Sci. Rep.* **2017**, *7*(1), 3600. DOI:10.1038/s41598-017-03906-3
111. D. Dutta, M. Debnath, D. Müller, R. Paul, T. Das, I. Bessi, H. Schwalbe, J. Dash, *Nucleic Acids Res.* **2018**, *46*(11), 5355–5365. DOI:10.1093/nar/gky385
112. M. Hu, Y. Wang, Z. Yu, L. Hu, T. Ou, S. Chen, Z. Huang, J. Tan, *J. Med. Chem.* **2018**, *61*(6), 2447–2459. DOI:10.1021/acs.jmedchem.7b01697
113. K. M. Felsenstein, L. B. Saunders, J. K. Simmons, E. Leon, D. R. Calabrese, S. Zhang, A. Michalowski, P. Gareiss, B. A. Mock, J. S. Jr. Schneekloth, *ACS Chem. Biol.* **2015**, *11*(1), 139–148. DOI:10.1021/acschembio.5b00577
114. D. Panda, P. Saha, T. Das, J. Dash, *Nat. Commun.* **2017**, *8*, 16103. DOI:10.1038/ncomms16103
115. J. Amato, A. Pagano, D. Capasso, S. Di Gaetano, M. Giustini-ano, E. Novellino, A. Randazzo, B. Pagano, *ChemMedChem* **2018**, *13*(5), 406–410. DOI:10.1002/cmdc.201700749
116. E. Zorzan, S. Da Ros, C. Musetti, L. Z. Shahidian, N. F. R. Coelho, F. Bonsembiante, S. Létard, M. E. Gelain, M. Palumbo, P. Dubreuil, M. Giantin, C. Sissi, M. Dacasto, *Oncotarget* **2016**, *7*(16), 21658–21675. DOI:10.18632/oncotarget.7808
117. H. Kang, Y. Cui, H. Yin, A. Scheid, W. P. Hendricks, J. Schmidt, A. Sekulic, D. Kong, J. M. Trent, V. A. Gokhale, *J. Am. Chem. Soc.* **2016**, *138*(41), 13673–13692. DOI:10.1021/jacs.6b07598
118. J. Lavrado, H. Brito, P. M. Borralho, S. A. Ohnmacht, N. Kim, C. Leitão, S. Pisco, M. Gunaratnam, C. M. Rodrigues, R. Moreira, S. Neidle, A. Paulo, *Sci. Rep.* **2015**, *5*, 9696. DOI:10.1038/srep09696
119. F. Li, J. Zhou, M. Xu, G. Yuan, *Int. J. Biol. Macromol.* **2018**, *107*(PtB), 1474–1479. DOI:10.1016/j.ijbiomac.2017.10.010
120. R. Perrone, M. Nadai, I. Frasson, J. A. Poe, E. Butovskaya, T. E. Smithgall, M. Palumbo, G. Palu, S. N. Richter, *J. Med. Chem.* **2013**, *56*(16), 6521–6530. DOI:10.1021/jm400914r
121. R. Perrone, E. Butovskaya, D. Daelemans, G. Palu, C. Pan-necouque, S. N. Richter, *J. Antimicrob. Chemother.* **2014**, *69*(12), 3248–3258. DOI:10.1093/jac/dku280
122. D. Piekna-Przybylska, G. Sharma, S. B. Maggirwar, R. A. Bambara, *Cell Cycle* **2017**, *16*(10), 968–978. DOI:10.1080/15384101.2017.1312225
123. R. Perrone, M. Nadai, J. A. Poe, I. Frasson, M. Palumbo, G. Palu, T. E. Smithgall, S. N. Richter, *PLoS ONE* **2013**, *8*(8), e73121. DOI:10.1371/journal.pone.0073121
124. R. Perrone, F. Doria, E. Butovskaya, I. Frasson, S. Botti, M. Scalabrin, S. Lago, V. Grande, M. Nadai, M. Freccero, S. N. Richter, *J. Med. Chem.* **2015**, *58*(24), 9639–9652. DOI:10.1021/acs.jmedchem.5b01283
125. B. Biswas, M. Kandpal, U. K. Jauhari, P. Vivekanandan, *BMC Genomics* **2016**, *17*(1), 949. DOI:10.1186/s12864-016-3282-1
126. S. Artusi, M. Nadai, R. Perrone, M. A. Biasolo, G. Palu, L. Flamand, A. Calistri, S. N. Richter, *Antiviral Res.* **2015**, *118*, 123–131. DOI:10.1016/j.antiviral.2015.03.016
127. S. Callegaro, R. Perrone, M. Scalabrin, F. Doria, G. Palu, S. N. Richter, *Sci. Rep.* **2017**, *7*(1), 2341. DOI:10.1038/s41598-017-02667-3
128. J. Norseen, F. B. Johnson, P. M. Lieberman, *J. Virol.* **2009**, *83*(20), 10336–10346. DOI:10.1128/JVI.00747-09
129. P. Murat, J. Zhong, L. Lekieffre, N. P. Cowieson, J. L. Clancy, T. Preiss, S. Balaswvvubramanian, R. Khanna, J. Tellam, *Nat. Chem. Biol.* **2014**, *10*(5), 358–364. DOI:10.1038/nchembio.1479
130. M. J. Lista, R. P. Martins, G. Angrand, A. Quillevere, C. Daskalogianni, C. Voisset, M. P. Teulade-Fichou, R. Fahraeus, M. Blondel, *Microb. Cell* **2017**, *4*(9), 305–307. DOI:10.15698/mic2017.09.590
131. A. Madireddy, P. Purushothaman, C. P. Loosbroock, E. S. Robertson, C. L. Schildkraut, S. C. Verma, *Nucleic Acids Res.* **2016**, *44*(8), 3675–3694. DOI:10.1093/nar/gkw038
132. S. Gilbert-Girard, A. Gravel, S. Artusi, S. N. Richter, N. Wallaschek, B. B. Kaufer, L. Flamand, *J. Virol.* **2017**, *91*(14), e00402–17. DOI:10.1128/JVI.00402-17
133. S. R. Wang, Y. Q. Min, J. Q. Wang, C. X. Liu, B. S. Fu, F. Wu, L. Y. Wu, Z. X. Qiao, Y. Y. Song, G. H. Xu, Z. G. Wu, G. Huang, N. F. Peng, R. Huang, W. X. Mao, S. Peng, Y. Q. Chen, Y. Zhu, T. Tian, X. L. Zhang, X. Zhou, *Sci. Adv.* **2016**, *2*(4), e1501535. DOI:10.1126/sciadv.1501535
134. K. Tluckova, M. Marusic, P. Tothova, L. Bauer, P. Sket, J. Plavec, V. Víglašky, *Biochemistry* **2013**, *52*(41), 7207–7216. DOI:10.1021/bi400897g
135. A. M. Fleming, Y. Ding, A. Alenko, C. J. Burrows, *ACS Infect. Dis.* **2016**, *2*(10), 674–681. DOI:10.1021/acsinfecdis.6b00109
136. B. Biswas, M. Kandpal, P. Vivekanandan, *Nucleic Acids Res.* **2017**, *45*(19), 11268–11280. DOI:10.1093/nar/gkx823
137. S. R. Wang, Q. Y. Zhang, J. Q. Wang, X. Y. Ge, Y. Y. Song, Y. F. Wang, X. D. Li, B. S. Fu, G. H. Xu, B. Shu, P. Gong, B. Zhang, T. Tian, X. Zhou, *Cell Chem. Biol.* **2016**, *23*(9), 1113–1122. DOI:10.1016/j.chembiol.2016.07.019

Povzetek

G-kvadrupleksi (G4) so nekanonske sekundarne strukture, ki se zvijejo znotraj vijačnic, bogatih z gvaninom (G), v regulatornih genskih regijah. Nedavni dokazi kažejo na njihovo tesno vključenost v pomembne biološke procese, kot so vzdrževanje telomer, zaščita koncev vijačnic, stabilnost kromosomov, izražanje genov, integracija virusov in rekombinacija. Mehanične podrobnosti, kako in zakaj strukture G4 vplivajo na biološko funkcijo, kažejo na utemeljenost obravnave G4 kot potencialnih molekularnih tarč za bodoče terapije. Z drugimi besedami, strukturna heterogenost z natančno določenimi vezavnimi mesti, termična stabilnost in pogostost G4 v telomerih, onkogenih promotorskih regijah in virusnih genomih naredijo G4 za privlačne tarče za majhne molekule, katerih cilj je selektivno prepoznavanje med vsemi drugimi strukturami nukleinskih kislin, zlasti dupleksne oblike, ki so v genomu najbolj pogoste. V članku je predstavljen kritičen pregled dobro opisanih ligandov, ki interagirajo z G4, kot potencialnih orodij za zdravljenje raka in protivirusnih terapij. Učinki, ki jih ti ligandi selektivno izvajajo v *in vitro* in *in vivo* modelih, so povzeti. Predstavljeni so edinstveni ligandi, ki sodelujejo v specifičnem prepoznavanju G4. Ključno vprašanje, kako oblikovati in razviti nove G4 specifične ligande, ki ustrezajo strukturnim in fizikalno-kemijskim zahtevam za optimalno biološko aktivnost, je obravnavano ob upoštevanju izjemnega napredka v zadnjih nekaj letih in naših nedavnih prispevkov.



Except when otherwise noted, articles in this journal are published under the terms and conditions of the Creative Commons Attribution 4.0 International License

Scientific paper

A Novel Electrochemical CuO-Nanostructure Platform for Simultaneous Determination of 6-thioguanine and 5-fluorouracil Anticancer Drugs

Masoud Fouladgar¹¹ Department of Biochemistry, Falavarjan Branch, Islamic Azad University, Isfahan, Iran.

* Corresponding author: E-mail: Fouladgar@iaufala.ac.ir;

Tel: +98 9131295016

Received: 01-23-2019

Abstract

Analysis of anticancer drugs is very important and necessary for the correct administration of them in the human body. Electrochemical behavior of 6-thioguanine (6-TG) has been studied using a carbon paste electrode modified by 1-ethyl-3-methylimidazolium tetrafluoroborate (ionic liquid) (1E3MIBF4) and CuO nanoparticles (CuO/1E3MIBF4/CPE). Using square wave voltammetry showed the linear relation between net anodic current and concentration of 6-TG in the range of 70 nmol L⁻¹ to 520 μmol L⁻¹ 6-TG with the detection limit of 20 nmol L⁻¹ 6-TG. The proposed modified electrode had excellent repeatability (RSD = 1.31%, n = 5) and long term stability (2.9% deviation in 25 days). The diffusion coefficient of 6-TG on the CuO/1E3MIBF4/CPE was found to be 1.54 × 10⁻⁵ cm²s⁻¹. The CuO/1E3MIBF4/CPE was successfully applied for the determination of 6-TG in real samples. In addition, the anodic peaks of 6-TG and fluorouracil (5-FU) in their mixture can be well separated using CuO/1E3MIBF4/CPE and simultaneous determination of them was studied.

Keywords: 6-Thioguanine; 5-Fluorouracil; CuO nanoparticles; 1-ethyl-3-methylimidazolium tetrafluoroborate; voltammetry

1. Introduction

6-Thioguanine (6-TG) is a common anticancer and antitumor drug which is an analogue of the physiological purines, guanine and hypoxanthine. In addition, thioguanine has been applied for treatment of hematological malignancies, psoriasis and inflammatory bowel disease, such as Crohn's disease. It has interaction with DNA and RNA and using it may have several side effects. Its main side effects are on the liver and it can cause hemotoxicity as well.¹ Oral administration of 6-TG is poorly absorbed and about 30% of administered dose being bioavailable. In hepatic metabolism of 6-TG, a methyl group is added to the sulfhydryl group of 6-TG.²

5-Fluorouracil (5-FU) is an antimetabolite agent same as 6-thioguanine that is being used for treatment of cancer. This group of drugs disrupts nucleic acid synthesis and is toxic to normal cells. It is a fluorinated pyrimidine and inhibits synthesis of DNA by blocking thymidylate synthetase. It is used in treatment of small tumors for which surgery is contraindicated. Particularly it is em-

ployed for the treatment of metastatic carcinomas of the breast, gastrointestinal tract, head and neck, and pancreas. Administered 5-Fluorouracil undergoes hepatic metabolism and about 10% of administered dose excretes unchanged in urine.² Both 6-TG and 5-FU are in the list of World Health Organization's List of Essential Medicines.³

Control of the adverse side effects of drugs and determination the pharmacokinetics properties are the important reasons to measurement the drugs in pharmaceutical samples and in biological samples too. In this regard many analytical methods have been reported to analysis drug samples including electrochemical methods.^{4,5} Many modified electrochemical sensors have been suggested for determination and studying interactions of 6-TG. Madueno et al. have been studied electrochemical oxidation of this anticancer drug (6-TG) including adsorption and phase formation on the mercury electrode.⁶ Wang et al. could measure 6-TG by modified gold electrode with DNA. Potassium ferricyanate was used as an electroactive indicator to probe the interaction between 6-TG and DNA.⁷ Ensafi et al. used the ability of 6-TG to form com-

plex with Cu(II) and cathodic stripping on the mercury electrode.⁸ Beitollahi et al. reported application of 2,7-bis(ferrocenyl ethyl)fluoren-9-one as a modifier of carbon paste electrode. They determined 6-TG based on electrocatalytic effect of modifier.⁹ Eksin et al. studied interaction between 6-TG and ss-DNA on the pencil graphite electrode and obtained data confirmed interactions between 6-TG and ss-DNA.¹⁰ Beitollahi et al. reported determination of 6-TG and folic acid using amplified sensors with ZnO-CuO nanoplates and 2-chlorobenzoyl ferrocene.¹¹

To improve the analytical features of the electrochemical methods, applied electrodes have been modified with different materials.^{12–14} In recent years, nanomaterials have been widely used in electrochemical analysis methods.^{15–20} Electrochemical sensors amplified with conductive materials help to improving sensitivity of electroactive materials sensors and also increase the diversity of them.^{21–26} In between, nanomaterials with different and unique properties showed more attention for modification of electrochemical sensors.^{27–31} One of the effects of application of nanomaterials is due to the change in the active surface area of electrodes.^{32–34} This effect and some other effects that appear when the size of particles decreases to nanoscale, cause to improve performance of electrochemical methods.³⁵ However, application of nanoparticles may have disadvantage effect on the electrochemical signals and increases background currents. Copper oxide nanoparticles are semiconductor metal that not only have special electrical and magnetic properties but also have great biological properties including effective antimicrobial action. Wide applications of CuO nanoparticles has caused significant advance in synthesis approaches of CuO nanoparticles.³⁶ Zeta potential values of CuO nanoparticles are negative or positive depending on pH of solution and can effect adsorption of electroactive species and improve electrochemical signals.³⁷

In addition, using electrically conducting liquids especially ionic liquids in the structure of paste electrodes, improves the sensitivity of the electrodes.^{38–46} 1-ethyl-3-methylimidazolium tetrafluoroborate is a room temperature ionic liquid that has suitable electrochemical stability for voltammetric aspects. It has wide voltage range of the electrochemical window, which allows electrochemical studies on various electroactive compounds.^{47,48}

In this work, synthesized CuO nanoparticles and 1E3MIBF₄ were used for amplification of modified sensor. Composition of CuO/1E3MIBF₄/CPE was optimized and CuO/1E3MIBF₄/CPE was suggested to determine 6-TG in real samples. In addition, simultaneous determination of 6-TG and 5-FU was investigated using modified electrode.

2. Experimental

2.1. Materials and Devices

All chemical compounds (6-thioguanine, 5-fluorouracil, phosphoric acid, 1-ethyl-3-methylimidazolium

tetrafluoroborate, copper(II) acetate, paraffin oil, sodium hydroxide and graphite powder) were purchased from Sigma-Aldrich Company in analytical grade and they were used as received without any further purification. Ultrapure water (18.2 MΩ cm, Mili-Q) was used for preparation of solutions. Phosphate buffer solutions were prepared by mixing adequate amounts of 0.1 mol L⁻¹ sodium dihydrogen phosphate and 0.1 mol L⁻¹ sodium hydrogen phosphate solutions. To prepare 6-TG standard solution (1 × 10⁻³ mol L⁻¹), adequate amount of 6-TG was dissolved in warm (35–40 °C) 1:1 (v/v) water-ethanol solution.

Electrochemical measurements were executed by Autolab PGSTAT 101 potentiostat/galvanostat (Metrohm, Netherlands) in a conventional electrochemical cell (50 ml). An Ag/AgCl electrode and a platinum wire electrode were applied as reference electrode and counter electrode, respectively. CuO/1E3MIBF₄/CPE was used as working electrode.

2.2. Real Sample Preparation

To prepare the tablets sample, five tablets were exactly weighed. Then the tablets were grinded and were completely homogenized. Then a required amount of the powder was transferred to the 100 ml beaker and about 80 ml of warm (35–40 °C) 1:1 (v/v) water-ethanol solution was added. The mixture was stirred magnetically and ultrasonicated (15 min) till the powder was dissolved. Afterward, the solution was filtered by filter paper and transferred to a flask and diluted to 100 ml with water-ethanol solution. For electrochemical measurement, adequate amount of resultant solution was transfer to electrochemical cell containing 10 ml of phosphate buffer solution (pH = 7.0).

The spiked dextrose-saline solution was prepared by mixing dextrose-saline solution with the same volume of phosphate buffer solution (pH = 7.0). Then 10 ml of resultant solution was added to the electrochemical cell and adequate amount of standard solution of 6-TG was added.

2.3. Nanoparticle Synthesis

200 ml of 0.2 mol L⁻¹ copper(II)acetate mixed with 2 ml acetic acid solution and mixture was heated until it came to boil. Then 30 ml of 0.8 mol L⁻¹ NaOH were added to the mixture. The color of the solution changed from blue to black. Afterwards, the mixture was boiled for 2 h. After cooling the mixture in the air, it was centrifuged into solid and water and the obtained solid was separated and washed.

2.4. Fabrication of CuO/1E3MIBF₄/CPE

The composition of CuO/1E3MIBF₄/CPE was optimized and optimum composition contained 10% 1E

3MIBF₄ and 6% nanoparticles. Accordingly, a mixture including 10% 1E3MIBF₄ as ionic liquid, 6% CuO nanoparticles and 84% graphite powder was prepared. About 1 ml of diethyl ether was added to the mixture and the mixture was mixed until a uniform mixture obtained. After vaporization of diethylether, a suitable amount of viscose paraffin was added to the mixture and components were mixed and the obtained paste was inserted into the glass tube in the presence of copper wire.

2. 5. Recommended Procedure

Prepared modified electrode was polished with a white and clean paper. To measure blank signal, ten milliliters of buffer solution (pH = 7.0) were transferred to the electrochemical cell. Then, the square wave voltammogram was recorded from 0.35 to 1.25 V *vs.* Ag/AgCl (Frequency 10 Hz). Afterward, different amounts of standard solutions of 6-TG and/or 5-FU were added to the cell and square wave voltammograms were recorded again to get the analytical signal. The difference between the blank and the analytical signal was obtained as a net peak current. Calibration plot was constructed by plotting net currents *vs.* concentration of drugs.

3. Results and Discussion

3. 1. Investigation of Synthesized Nanoparticles

Scanning electron microscopy (SEM) of synthesized nanoparticles confirmed synthesis of uniform spherical particles with nanoscale size (Figure 1.a). In addition, obtained Energy-dispersive X-ray (EDX) spectrum from synthesized nanoparticles confirmed the existence of only oxygen and copper in the composition of nanoparticles (Figure 1.b).

3. 2. pH effect

According to the previous electrochemical reported papers for analysis of 6-TG,⁴⁹ we guessed the pH dependent electro-oxidation mechanism for determination of 6-TG at a surface of electrode. Therefore, linear sweep voltammograms of 6-TG (100 μmol L⁻¹) were recorded in the pHs range of 5–8. As can be seen in Figure 2 (inset), increasing pH of solution causes the shift of oxidation peak potential to negative potentials. The slope of plot of potential versus pH was -61.2 mV/pH, which is close to anticipated Nernstian value (Figure 2). Consequently, this indicates that the electro-oxidation of 6-TG occurred in the presence of equal value of proton and electron. The obtained result agrees with the suggested mechanism for electro-oxidation of 6-TG (Scheme 1).⁴⁹

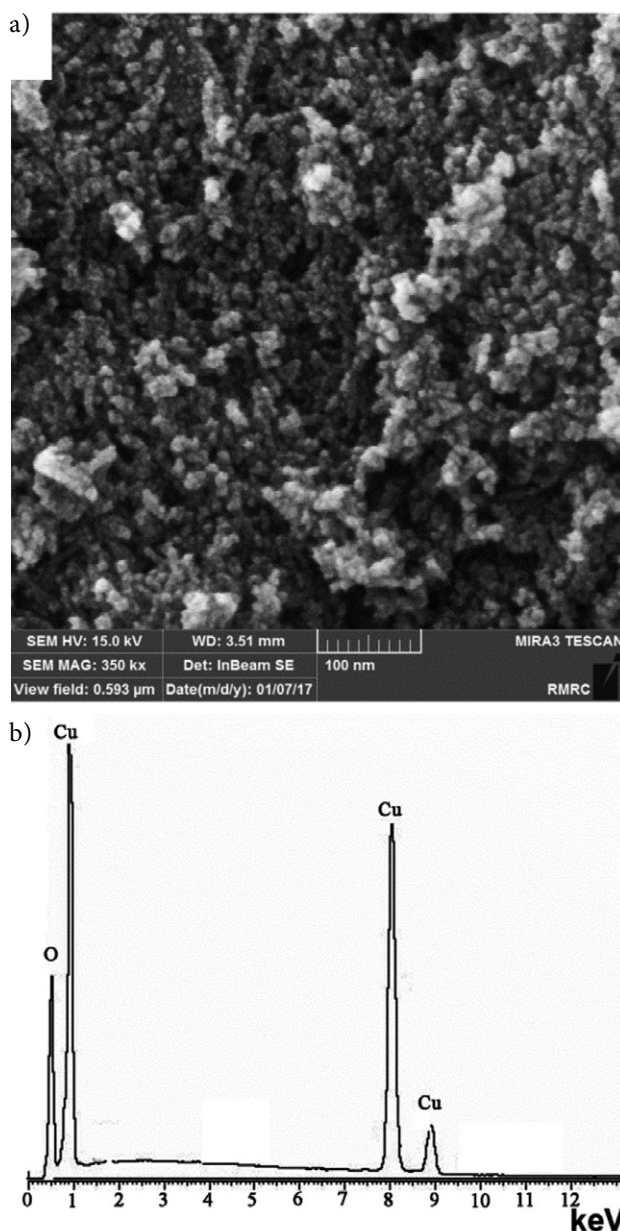


Figure 1. a) SEM image b) EDX spectrum of synthesized CuO nanoparticles

3. 3. Effect of Modification

In this step, we investigated the synergic effect of modifiers on the 6-TG electro-oxidation signal by recording the linear sweep voltammograms 6-TG (100 μmol L⁻¹) at a surface of CuO/1E3MIBF₄/CPE (curve a), 1E3MIBF₄/CPE (curve b), CuO/CPE (curve c) and CPE (curve d). As can be seen in Figure 3, addition of CuO nanoparticles caused increasing oxidation current and shifting peak potential toward lower potentials. Addition of ionic liquid into the carbon paste had similar effects. Synergy between effects of addition of nanoparticles and ionic liquid caused to achieve maximum peak current and lower overpotential (Figure 3. a). In addition, the current density in-

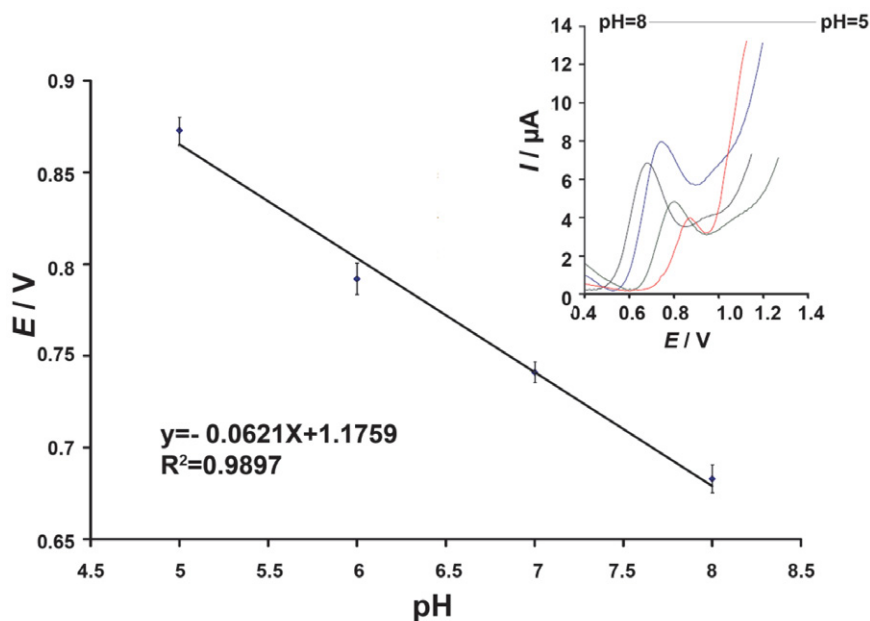
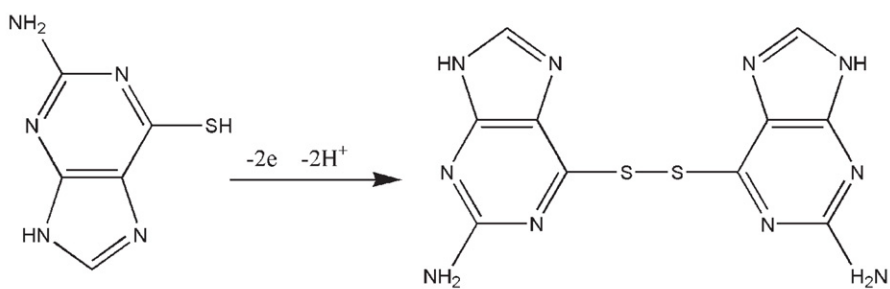


Figure 2. Plot of potential vs. pH for the electrooxidation of $100 \mu\text{mol L}^{-1}$ 6-TG at CuO/1E3MIBF₄/CPE. Inset: Linear sweep voltammograms of $100 \mu\text{mol L}^{-1}$ 6-TG with different pHs (scan rate = 100 mV s^{-1}).



Scheme 1. Proposed mechanism for oxidation of 6-TG on the electrode.

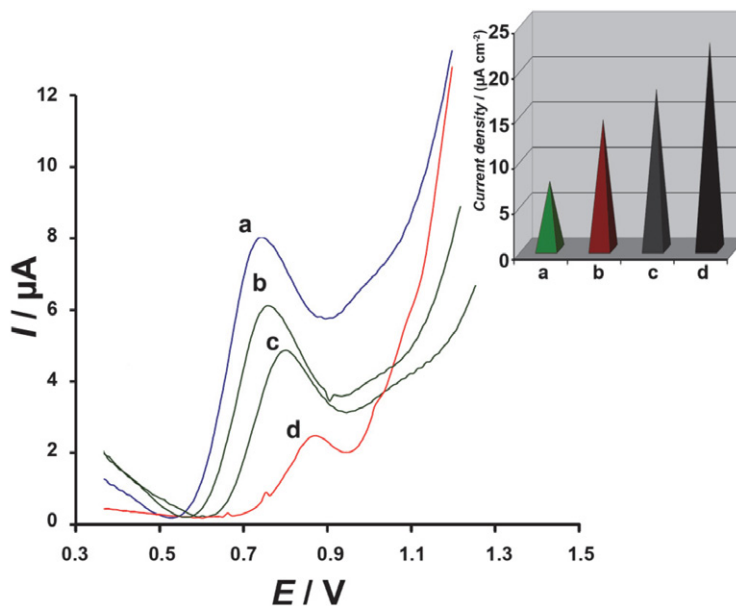


Figure 3. Linear sweep voltammograms of (a) CuO/1E3MIBF₄/CPE, (b) 1E3MIBF₄/CPE, (c) CuO/CPE, and (d) CPE in the presence of $100 \mu\text{mol L}^{-1}$ 6-TG at pH 7.0. Inset: the current densities derived from voltammograms responses at same electrodes.

creased by moving CPE to CuO/1E3MIBF₄/CPE (Figure 3. inset).

These effects may be relative to the conductivity effect of CuO nanoparticles and 1E3MIBF₄ at a surface CPE. In addition, the active surface area of modified and non-modified electrodes CuO/1E3MIBF₄/CPE, 1E3MIBF₄/CPE, CuO/CPE and CPE was obtained based on the Randles–Sevcik equation (in the presence of 1 mM K₄Fe(CN)₆).³² The active surface areas of CPE, CuO/CPE, 1E3MIBF₄/CPE and CuO/1E3MIBF₄/CPE were calculated equals; 0.28, 0.31, 0.32 and 0.33 cm², respectively.

3. 4. Electrochemical Investigations

Linear sweep voltammograms of 6-TG (300 μmol L⁻¹) at CuO/1E3MIBF₄/CPE were recorded in the scan range between 10-100 mVs⁻¹ (Figure 4-a inset). Linear relation between peak currents and square root of scan

rates confirmed that the electrode process was controlled under the diffusion step. In addition, a kinetic limitation can be observed in this investigation due to shifted oxidation peak potential toward positive value. Also, the value of charge transfer coefficient (α) was obtained ~ 0.8 using slope of Tafel plot (Figure 4-b).

Chronoamperometry was also employed for investigation of 6-TG (300 and 500 μmol L⁻¹) electro-oxidation at CuO/1E3MIBF₄/CPE by applying single potential step 800 mV at CuO/1E3MIBF₄/CPE. From the slopes of plots of I (current) versus $t^{1/2}$ (Figure 5), the average of diffusion coefficient of 6-TG was found to be 1.54×10^{-5} cm²s⁻¹ (Cottrell equation). Since electrode reaction is diffusion-controlled, anodic current is controlled by diffusion and hence depends on the diffusion coefficient. Modification of electrode causes increasing diffusion coefficient which in turn leads to increasing anodic current.

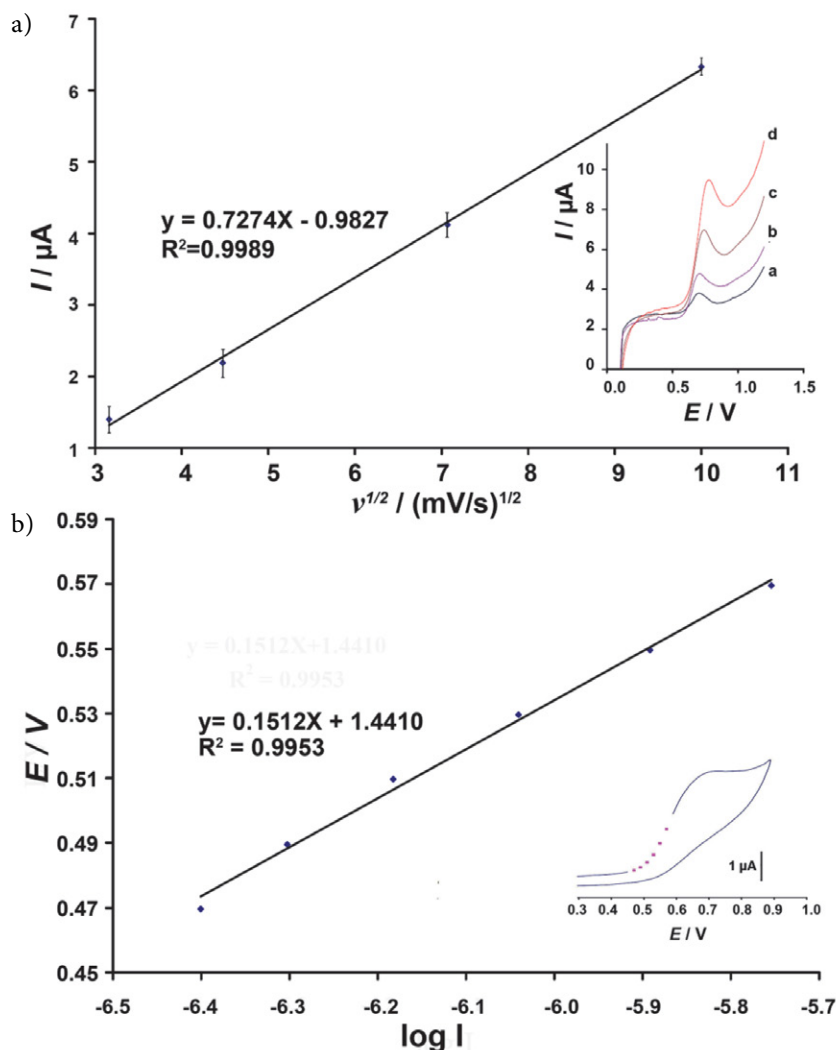


Figure 4. a) The Plot of I_{pa} vs. $v^{1/2}$ for electro-oxidation of 300 μmol L⁻¹ 6-TG (pH = 7.0). Inset; linear sweep voltammograms of CuO/1E3MIBF₄/CPE containing 300 μmol L⁻¹ 6-TG at various scan rates; a-d correspond to 10, 20, 50 and 100 mVs⁻¹, respectively. b) Tafel plot for 300 μmol L⁻¹ (pH = 7.0) 6-TG at CuO/1E3MIBF₄/CPE. Inset: Corresponding cyclic voltammogram

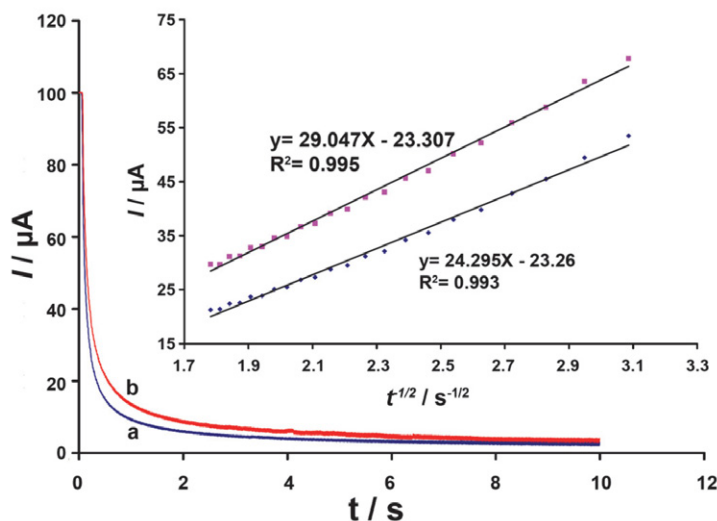


Figure 5. Chronoamperograms obtained at CuO/1E3MIBF₄/CPE in the presence of a) 300; and b) 500 μmol L⁻¹ of 6-TG in the buffer solution (pH 7.0). Inset: Cottrell's plot for the data from the chronoamperograms.

4. Analytical Features

In order to obtain calibration curve, square wave voltammograms (SWV) of solutions with different 6-TG concentrations were recorded at CuO/1E3MIBF₄/CPE. Plot of net oxidation peak current versus concentration was linear in the range of 70 nmol L⁻¹ to 520 μmol L⁻¹ 6-TG with the regression equation being $I_p(\mu\text{A}) = 0.076C_{6\text{-TG}} + 0.174$ ($R^2 = 0.998$) and detection limit of the method 20 nmol L⁻¹ 6-TG ($3S_b/m$). This value of linear dynamic range or limit of detection compared with previous electrochemical sensor and results showed better analytical ability for proposed sensor (Table 1).

The relative standard deviation for square wave signals of 25 μmol L⁻¹ 6-TG at the surface of CuO/1E3MIBF₄/CPE was 1.31% ($n = 5$), which confirmed excellent repeatability. The stability of CuO/1E3MIBF₄/CPE was checked

by recorded square wave voltammograms of 25 μmol L⁻¹ 6-TG over a period of 25 days. Compared to its first oxidation current, only 2.9% deviation was recorded when CuO/1E3MIBF₄/CPE was used daily and stored in the laboratory. This suggests that CuO/1E3MIBF₄/CPE possesses long-term stability.

Table 2. Interference study for analysis of 50 μmol L⁻¹ 6-TG

Species	Tolerance limits (mole ratio)
Glucose	850
Na ⁺ , Br ⁻ , Cl ⁻ , K ⁺ , Ascorbic acid*	550
Phenyl alanine, Glycine, Methionine	400
Starch	Saturation

* After addition of 1 mmol L⁻¹ ascorbic oxidize

Table 1. Characteristics of several electrochemical methods for determination of 6-TG

Technique	Electrochemical Method	Linear dynamic range	Detection limit	Ref.
Study self-assembled monolayer of 6-TG on mercury electrode	cyclic and ac voltammetry	–	–	6
DNA-modified gold electrode	differential pulse stripping voltammetry	2×10^{-8} – 8×10^{-7} mol L ⁻¹	6×10^{-9} mol L ⁻¹	7
Complex formation and adsorption on mercury electrode	cathodic adsorptive stripping	0.15–180 nmol L ⁻¹	0.08 n mol L ⁻¹	8
Electrocatalyst	differential pulse voltammetry	0.06–10 μmol L ⁻¹ and 10–160 μmol L ⁻¹	22 nmol L ⁻¹	50
Study interaction between 6-TG and DNA	differential pulse voltammetry, electrochemical impedance spectroscopy	–	–	10
Electrocatalyst and using ZnO-CuO nanoplates	square wave voltammetric	0.05 to 200 μmol L ⁻¹	25 n mol L ⁻¹	11
Modification of carbon paste with CuO nano particles and ionic liquid	square wave voltammetric	0.07 to 520 μmol L ⁻¹	20 n mol L ⁻¹	this work

Table 3. Determination of 6-TG in real samples (n = 5)

Sample	Added ($\mu\text{mol L}^{-1}$)	Expected ($\mu\text{mol L}^{-1}$)	Founded ($\mu\text{mol L}^{-1}$)	Recovery %	Published method ($\mu\text{mol L}^{-1}$)
Tablet*	–	5	4.92 ± 0.35	98.4	4.95 ± 0.28
	10	15	15.63 ± 0.75	104.2	15.74 ± 0.98
Intravenous solution**	–	–	< Limit of detection		
	20	20	20.75 ± 0.82	103.7	19.75 ± 1.01

±Shows the standard deviation * Kwaliti Pharmaceuticals limited, India. **Dextrose (3.33 %), saline (0.3 %), I.P.P.C.(Iranian Parenteral & Pharmaceutical Co), Tehran, Iran.

To study the influence of various substances which may potentially interfere with the determination of 6-TG, the oxidation current of $50 \mu\text{mol L}^{-1}$ 6-TG was measured in the presence of different concentrations of interfering species and was compared with current that obtained from 6-TG solution by acceptable error $\pm 5\%$. The results are shown in Table 2 and confirm selectivity of CuO/1E-3MIBF₄/CPE for the analysis of 6-TG.

To study the application of CuO/1E3MIBF₄/CPE for analysis of 6-TG in real samples, the CuO/1E3MIBF₄/CPE was applied for the determination of 6-TG in tablets and intravenous dextrose-saline solutions (Table 3).

In addition, changing the concentration of each one had no effect on the peak current of another one. Therefore, simultaneous determination was performed by simultaneously changing the concentrations of 6-TG and 5-FU and recording the SWVs. Figure 6 shows the calibration curves of 6-TG and 5-FU. The current sensitivities towards 6-TG in the presence and in the absence of 5-FU were found to be approximately equal which confirms that the oxidation processes of 6-TG and 5-FU at CuO/1E3MIBF₄/CPE are independent and simultaneous or independent measurements of two compounds are, therefore, possible without any interference.

5. Simultaneous Determination of 6-TG and 5-FU

Square wave voltammogram of a solution containing 6-TG and 5-FU showed two distinguished peak currents.

6. Conclusion

As a conclusion, we fabricated a novel electrochemical modified sensor amplified with CuO nanoparticles and 1E3MIBF₄ for the determination of 6-TG in the presence

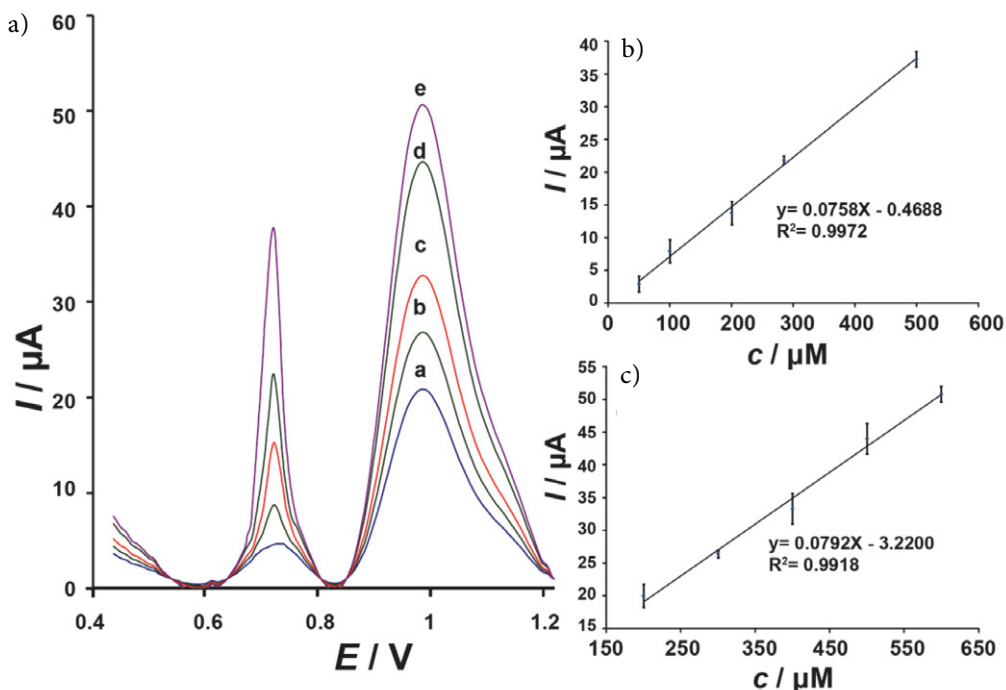


Figure 6. Inset; SWVs of CuO/1E3MIBF₄/CPE (PBS buffer, pH 7.0) containing different concentrations of 6-TG and 5-FU in $\mu\text{mol L}^{-1}$. (a–e) 50 + 200; 100 + 300; 200 + 400; 285 + 500 and 500 + 600, respectively. B) plot of the current as a function of 6-TG concentration. C) plot of the current as a function of 5-FU concentration.

of 5-FU, as two important anticancer drugs. The CuO/1E-3MIBF₄/CPE showed good analytical ability for nanomolar determination of 6-TG. The CuO/1E3MIBF₄/CPE resolved overlapping signal of 6-TG and 5-FU at an optimum condition. The CuO/1E3MIBF₄/CPE was used for the analysis of 6-TG in real samples.

Acknowledgements

The author gratefully acknowledges Islamic Azad University, Falavarjan branch research council for support of this work.

7. References

- J. K. Aronson, Book Meyler's side effects of drugs: the international encyclopedia of adverse drug reactions and interactions, Elsevier, 2015.
- S. Enna and D. Bylund, Book xPharm: The Comprehensive Pharmacology Reference, Elsevier, 2008.
- A. Attaran, *Health Aff.* **2004**, *23*, 155–166. DOI:10.1377/hlthaff.23.3.155
- J. G. Manjunatha, *J. Surface Sci. Technol.* **2018**, *34*, 74–80. DOI:10.18311/jsst/2018/15838
- J. G. Manjunatha, *Sens. Biosensing Res.* **2017**, *16*, 79–84. DOI:10.1016/j.sbsr.2017.11.006
- R. Madueno and T. Pineda, *J. Electroanal. Chem.* **2004**, *565*, 301–310. DOI:10.1016/j.jelechem.2003.10.024
- S. F. Wang, F. Xie, R. F. Hu and H. C. Cai, *Anal. Lett.* **2006**, *39*, 1041–1052. DOI:10.1080/00032710600620328
- A. A. Ensafi and R. Hajian, *J. Brazil. Chem. Soc.* **2008**, *19*, 405–412. DOI:10.1590/S0103-50532008000300006
- H. Beitollahi, J.-B. Raoof and R. Hosseinzadeh, *Anal. Sci.* **2011**, *27*, 991–991. DOI:10.2116/analsci.27.991
- E. Eksin, G. Congur, F. Mese and A. Erdem, *J. Electroanal. Chem.* **2014**, *733*, 33–38. DOI:10.1016/j.jelechem.2014.08.012
- H. Beitollahi, S. G. Ivari and M. Torkzadeh-Mahani, *Mater. Sci. Eng., C* **2016**, *69*, 128–133. DOI:10.1016/j.msec.2016.06.064
- N. S. Prinith and J. G. Manjunatha, *Mater. Sci. Technol. Energy* **2019**, *2*, 408–416. DOI:10.1016/j.mset.2019.05.004
- J. G. Manjunatha, B. E. K. Swamy, G. P. Mamatha, C. Raril, L. N. Swamy and S. Fattepur, *Materials Today: Proceedings* **2018**, *5*, 22368–22375. DOI:10.1016/j.matpr.2018.06.604
- C. Raril and J. G. Manjunatha, *Anal. Bioanal. Electrochem.* **2018**, *10*, 372–382.
- G. Tigari, J. G. Manjunatha, C. Raril and N. Hareesha, *Chemistry Select* **2019**, *4*, 2168–2173. DOI:10.1002/slct.201803191
- N. S. Prinith, J. G. Manjunatha and C. Raril, *Anal. Bioanal. Electrochem.* **2019**, *11*, 742–756.
- J. G. Manjunatha, *Open Chem Eng J.* **2019**, *13*, 81–87. DOI:10.2174/1874123101913010081
- S. Cheraghi, M. A. Taher and H. Karimi-Maleh, *J. Food Compos. Anal.* **2017**, *62*, 254–259. DOI:10.1016/j.jfca.2017.06.006
- B. J. Sanghavi, G. Hirsch, S. P. Karna and A. K. Srivastava, *Anal. Chim. Acta* **2012**, *733*, 37–45. DOI:10.1016/j.aca.2012.05.029
- J. G. Manjuntha and G. K. Jayaprakash, *Eurasian J. Anal. Chem.* **2019**, *14*, 1–11.
- H. Karimi-Maleh and O. A. Arotiba, *J. Colloid Interface Sci.* **2020**, *560*, 208–212. DOI:10.1016/j.jcis.2019.10.007
- H. Karimi-Maleh, F. Karimi, M. Alizadeh and A. L. Sanati, *Chem. Rec.* **2020**. DOI:10.1002/tcr.201900092
- H. Karimi-Maleh, C. T. Fakude, N. Mabuba, G. M. Peleyeju and O. A. Arotiba, *J. Colloid Interface Sci.* **2019**, *554*, 603–610. DOI:10.1016/j.jcis.2019.07.047
- F. Tahernejad-Javazmi, M. Shabani-Nooshabadi and H. Karimi-Maleh, *Composites Part B: Engineering* **2019**, *172*, 666–670. DOI:10.1016/j.compositesb.2019.05.065
- A. Khodadadi, E. Faghieh-Mirzaei, H. Karimi-Maleh, A. Abbaspourrad, S. Agarwal and V. K. Gupta, *Sens. Actuators, B* **2019**, *284*, 568–574. DOI:10.1016/j.snb.2018.12.164
- Z. Shamsadin-Azad, M. A. Taher, S. Cheraghi and H. Karimi-Maleh, *J. Food Meas. Charact.* **2019**, *13*, 1781–1787. DOI:10.1007/s11694-019-00096-6
- H. Karimi-Maleh, M. Shafeizadeh, M. A. Taher, F. Opoku, E. M. Kiarii, P. P. Govender, S. Ranjbari, M. Rezapour and Y. Orooji, *J. Mol. Liq.* **2020**. DOI:10.1016/j.molliq.2019.112040
- H. Karimi-Maleh, M. Sheikhshoaei, I. Sheikhshoaei, M. Ranjbar, J. Alizadeh, N. W. Maxakato and A. Abbaspourrad, *New J. Chem.* **2019**, *43*, 2362–2367. DOI:10.1039/C8NJ05581E
- M. Miraki, H. Karimi-Maleh, M. A. Taher, S. Cheraghi, F. Karimi, S. Agarwal and V. K. Gupta, *J. Mol. Liq.* **2019**, *278*, 672–676. DOI:10.1016/j.molliq.2019.01.081
- S. Malekmohammadi, H. Hadadzadeh, S. Rezakhani and Z. Amirghofran, *ACS Biomater. Sci. Eng.* **2019**, *5*, 4405–4415. DOI:10.1021/acsbomaterials.9b00237
- Y. Akbarian, M. Shabani-Nooshabadi and H. Karimi-Maleh, *Sens. Actuators, B* **2018**, *273*, 228–233. DOI:10.1016/j.snb.2018.06.049
- M. Fouladgar and S. Mohammadzadeh, *Anal. Lett.* **2014**, *47*, 763–777. DOI:10.1080/00032719.2013.855782
- M. L. Yola and N. Atar, *Electrochim. Acta* **2014**, *119*, 24–31. DOI:10.1016/j.electacta.2013.12.028
- L. Shang, F. Zhao and B. Zeng, *Food Chem.* **2014**, *151*, 53–57. DOI:10.1016/j.foodchem.2013.11.044
- C. Jianrong, M. Yuqing, H. Nongyue, W. Xiaohua and L. Sijiao, *Biotechnol. Adv.* **2004**, *22*, 505–518. DOI:10.1016/j.biotechadv.2004.03.004
- M. E. Grigore, E. R. Biscu, A. M. Holban, M. C. Gestal and A. M. Grumezescu, *Pharmaceuticals* **2016**, *76*, 75–89. DOI:10.3390/ph9040075
- A. El-Trass, H. ElShamy, I. El-Mehasseb and M. El-Kemary, *Appl. Surf. Sci.* **2012**, *258*, 2997–3001. DOI:10.1016/j.apsusc.2011.11.025
- W. Sun, M. Yang and K. Jiao, *Anal. Bioanal. Chem.* **2007**, *389*, 1283–1291. DOI:10.1007/s00216-007-1518-2
- H. Khani, M. K. Rofouei, P. Arab, V. K. Gupta and Z. Vafaei, *J. Hazard. Mater.* **2010**, *183*, 402–409. DOI:10.1016/j.jhazmat.2010.07.039

40. M. Fouladgar, *Measurement* **2016**, *86*, 141–147.
DOI:10.1016/j.measurement.2016.02.057
41. Y. Zhang and J. B. Zheng, *Electrochim. Acta* **2007**, *52*, 7210–7216. DOI:10.1016/j.electacta.2007.05.039
42. W. Sun, Y. Li, M. Yang, S. Liu and K. Jiao, *Electrochem. Commun.* **2008**, *10*, 298–301.
DOI:10.1016/j.elecom.2007.12.012
43. S. Negahban, M. Fouladgar and G. Amiri, *J. Taiwan Inst. Chem. Eng.* **2017**, *78*, 51–55. DOI:10.1016/j.jtice.2017.05.032
44. M. Ashjari, H. Karimi-Maleh, F. Ahmadpour, M. Shabani-Nooshabadi, A. Sadriani and M. A. Khalilzadeh, *J. Taiwan Inst. Chem. Eng.* **2017**, *80*, 989–996.
DOI:10.1016/j.jtice.2017.08.046
45. M. Fouladgar, *J. Electrochem. Soc.* **2016**, *163*, B38–B42.
DOI:10.1149/2.0611603jes
46. M. Fouladgar, *Sens. Actuators, B* **2016**, *230*, 456–462.
DOI:10.1016/j.snb.2016.02.094
47. M. Shamsipur, A. A. M. Beigi, M. Teymouri, S. M. Pourmortazavi and M. Irandoust, *J. Mol. Liq.* **2010**, *157*, 43–50.
DOI:10.1016/j.molliq.2010.08.005
48. J. Fuller, R. T. Carlin and R. A. Osteryoung, *J. Electrochem. Soc.* **1997**, *144*, 3881–3886. DOI:10.1149/1.1838106
49. P. Kraske, *J. Electroanal. Chem. Interfacial Electrochem.* **1986**, *207*, 101–116. DOI:10.1016/0022-0728(86)87065-6
50. H. Karimi-Maleh, M. R. Ganjali, P. Norouzi and A. Bananezhad, *Mater. Sci. Eng., C* **2017**, *3*, 472–477.
DOI:10.1016/j.msec.2016.12.094

Povzetek

Analiza protirakovih zdravil je zelo pomembna in potrebna za njihovo pravilno uporabo v človeškem telesu. Preučevali smo elektrokemijsko obnašanje 6-tioguanina (6-TG) z uporabo elektrode iz ogljikove paste, modificirane z 1-etil-3-metilimidazolijevim tetrafluoroboratom (ionska tekočina) (1E3MIBF4) in nanodelci CuO (CuO/1E3MIBF4/CPE). Uporaba square wave voltometrije je pokazala linearno zvezo med celotnim anodnim tokom in koncentracijo 6-TG v območju od 70 nmol L⁻¹ do 520 μmol L⁻¹ 6-TG z mejo zaznave 20 nmol L⁻¹ 6-TG. Predlagana modificirana elektroda je imela odlično ponovljivost (RSD = 1,31 %, n = 5) in dolgoročno stabilnost (2,9 % odstopanje v 25 dneh). Ugotovljeno je bilo, da je koeficient difuzije 6-TG na CuO / 1E3MIBF4/CPE $1,54 \times 10^{-5}$ cm²s⁻¹. CuO/1E3MIBF4/CPE je bil uspešno uporabljen za določanje 6-TG v realnih vzorcih. Poleg tega je mogoče anodne vrhove 6-TG in fluorouracila (5-FU) v njuni mešanici dobro ločiti z uporabo CuO/1E3MIBF4/CPE in ju preučevati istočasno.



Scientific paper

Metoprolol: New and Efficient Corrosion Inhibitor for Mild Steel in Hydrochloric and Sulfuric Acid Solutions

Fatemeh Mohammadinejad,¹ Seyyed Mohammad Ali Hosseini,^{2,*}
Mehdi Shahidi Zandi,³ Mohammad Javad Bahrami⁴ and Zahra Golshani⁵

¹Department of Chemistry, Shahid Bahonar University of Kerman, P.O. Box: 76169-14111, Kerman, Iran.

²Department of Chemistry, Shahid Bahonar University of Kerman, P.O. Box: 76169 14111, Kerman, Iran.

³Department of Chemistry, Kerman Branch, Islamic Azad University, P.O. Box: 7635131167, Kerman, Iran.

⁴Department of Science, Farhangian University, P.O. Box: 76175173, Kerman, Iran.

⁵Department of Chemistry, Shahid Bahonar University of Kerman, P.O. Box: 76169 14111, Kerman, Iran.

* Corresponding author: E-mail: s.m.a.hosseini@uk.ac.ir

Tel: 0913-3412012

Received: 06-08-2019

Abstract

The inhibition behavior of metoprolol tablet on steel alloy (st37) in 1 M hydrochloric acid and 0.5 M sulfuric acid solutions were studied by three methods (potentiodynamic polarization, electrochemical impedance spectroscopy, and scanning electronic microscopy, SEM). The obtained parameters revealed that different amounts of metoprolol drug inhibited the corrosion of mild steel in the acid solutions of HCl and H₂SO₄. The corrosion resistance of the alloy increased with the increase in the concentration of metoprolol up to 300 ppm but was reduced by increasing the temperature. The derived parameters from polarization curves indicated that the drug is a mixed type inhibitor. The results obtained from the different methods are consistent with each other. The adsorption of metoprolol was found to be physical, exothermic, and spontaneous, and also fitted the Langmuir adsorption model. SEM micrographs are in accordance with the adsorption performance of the tablet.

Keywords: Corrosion Inhibitor; potentiodynamic Polarization; electrochemical Impedance Spectroscopy; mild steel; metoprolol.

1. Introduction

Corrosion is the dissolution of metals and alloys exposed to aggressive media and is very difficult to eliminate completely. Inhibition of the corroding material would be more achievable than complete elimination. Demolition of metal and alloys development could be rapid after destruction of the protective film which depends on the composition and character of metals and aggressive media. For example, formation of oxides and diffusion of metal cations into the coating matrix, local pH changes, and electrochemical potential.¹ Mild steel is an abundant and efficient building material. However, it is difficult to protect

this alloy exposed to harsh environments against corrosion.² Acidic solutions are extensively utilized in different industries for various purposes, including acid pickling, acid descaling, and oil well acidizing.³ Due to the general aggressiveness of acid media, the use of effective inhibitors is one of the reliable and economical ways for minimizing the corrosion rates and the protection of metal surfaces against corrosive media.⁴⁻⁶ Thus, reliable inhibitors for the corroding materials in reducing acids (hydrochloric acid and sulfuric acid) have attracted the wide attention of researchers.⁵ Organic compounds with π -bonds and heteroatoms (P, S, N, and O) are highly effective and available inhibitors, but most of them are expensive and toxic with

negative effect on the environment.^{7–12} These properties restrict their use to reduce the corrosion of metals and alloys. Therefore, it is very important and necessary to find out the least expensive and environmentally safe corrosion inhibitors.^{13,14} Earlier report¹⁵ indicates that the use of drugs for the protection of metals corrosion offers some advantages in comparison to the use of some organic/inorganic inhibitors due to their eco-environmental nature. Most of the drugs are nontoxic and less expensive with limited negative effects on different media, so they are suggested to replace the traditional toxic corrosion inhibitors.¹⁶ Thus, in the present investigation the effect of metoprolol tablet on the corrosion resistance of mild steel in 1.0 M hydrochloric acid and 0.5 M sulfuric acid solutions was done. The selection of this drug as corrosion inhibitor is done on the ground of its low toxicity and high solubility in acidic media. Electrochemical impedance spectroscopy (EIS), potentiodynamic polarization, and scanning electron microscopy (SEM) methods were employed to evaluate corrosion rate of the steel and inhibition efficiency of the drug.

2. Experimental

2.1. Materials and Solutions

Metoprolol tablets are commercially obtained as a trade name Lopressor, Toprol-xl by Tolidaru Company. The compound in its purest state has the molecular formula of $C_{15}H_{25}NO_3$ and melting point 120 °C. No attempt was made to eliminate the effect of excipients from the tablets. The molecular structure of metoprolol used in this study is given in Fig. 1. At first, solutions of 2.0 M hydrochloric and 1.0 M sulfuric acid were prepared for each experiment in distilled water using analytical grade 37% HCl and 98% H_2SO_4 purchased from Sigma-Aldrich. Various amounts of the tablet (1000, 800, 600, 400, and 100 ppm) were added to the acids solutions, with adequate volume of acid and inhibitor (the tablet was dissolved in distilled water and passed through the filter paper without purification) to get the desired concentration of acids (1.0 M HCl and 0.5 M H_2SO_4) and 500–50 ppm of inhibitor. Mild steel samples of the following composition were used (in wt. %): C 0.17; Si 0.5; Mn 1.4; S 0.045; Fe to balance. The specimens were mechanically cut into 1 cm² pieces. Prior to all measurements, the samples were polished using different grades of emery papers (600–3000), degreased with acetone and finally washed with distilled water and dried in air, then im-

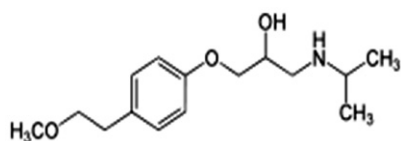


Figure 1. Molecular structure of metoprolol (RS)-1-(isopropylamino)-3-[4-(2-methoxyethyl)-phenoxy]-propan-2-ol.

mersed in the solutions for 30 min (to get stable OCP) before each EIS test.

2.2. Procedures

2.2.1. Electrochemical Measurements: Potentiodynamic Polarization and Electrochemical Impedance Spectroscopy (EIS)

The electrochemical measurements were carried out with an Autolab potentiostat/galvanostat (AUTOLAB-302N, Netherlands) by using a three-electrode cell containing Ag/AgCl as reference (with 0.197 mV), Pt electrode as counter and mild steel as working electrode used for this investigation. The potential range for potentiodynamic polarization tests was –850 to –200 mV and the scan rate was 1 mV/s. The frequency range for EIS tests was 100 mHz to 100 kHz and the EIS amplitude was 10 mV peak to peak. Before each polarization and impedance test, potential was stabilized within 30 min at 25 ± 1 °C. Finally, all of the curves were analyzed with Nova software (Utrecht, The Netherlands).

2.2.2. Effect of Temperature

The effect of temperature on the corrosion rate of mild steel in both acids solutions with and without various concentrations of inhibitor in the temperature range of $25\text{--}55 \pm 1$ °C was investigated by potentiodynamic polarization technique.

2.2.3. Scanning Electron Microscopic (SEM) Studies

The surface morphology of the working electrode was examined after immersion of the alloy for about 24 h in 1 M HCl and 0.5 M H_2SO_4 solutions at room temperature, in the absence and presence of the optimum concentration of metoprolol using scanning electron microscopy (SEM). Scans were taken with a EM3200 instrument (accelerating voltage 0–30 kV) from KYKY company, China.

3. Results and Discussion

3.1. Electrochemical Impedance Spectroscopy

Electrochemical impedance spectroscopy (EIS) has been employed in order to investigate the surface layer formed by the inhibitor. The effect of metoprolol concentrations on the impedance behavior of mild steel in 1.0 M hydrochloric acid and 0.5 M sulfuric acid solutions at 25 ± 1 °C is shown in Fig. 2. Inhibitor efficiency can also be estimated by charge transfer resistance according to the following equation:¹⁷

$$IE\% = \left(\frac{R_{ct}^i - R_{ct}^0}{R_{ct}^i} \right) \times 100 \quad (1)$$

where R_{ct}^i and R_{ct}^0 are charge transfer resistances of mild steel in the absence and presence of inhibitor, respectively. Inhibition efficiency increased with the concentration of inhibitor up to 300 ppm and further increase in the inhibitor concentration did not cause any appreciable change in the inhibition performance.

Fig. 3 illustrates the electrical equivalent circuit employed to analyze the impedance plots. In this Figure, R_s is the solution resistance and R_{ct} is the charge transfer resistance. The impedance of the constant phase element (CPE) is defined as below:¹⁸

$$Z_{CPE} = A^{-1}(i\omega)^{-n} \quad (2)$$

where A is proportionality coefficient, ω is angular frequency (in rad./s) and $i = -1$ is the imaginary number. The correct equation to convert the CPE constant, A , into the double layer capacitance, C_{dl} , is:¹⁹

$$C_{dl} = \frac{1}{2\pi\omega_{max}R_{ct}} \quad (3)$$

where ω_{max} is the frequency at which the imaginary component of the impedance is maximum. The electrochemical pa-

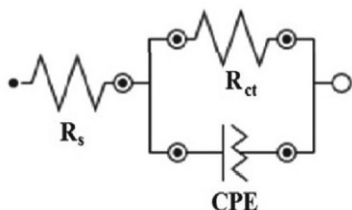


Figure 3. Equivalent circuit to estimate impedance diagrams.

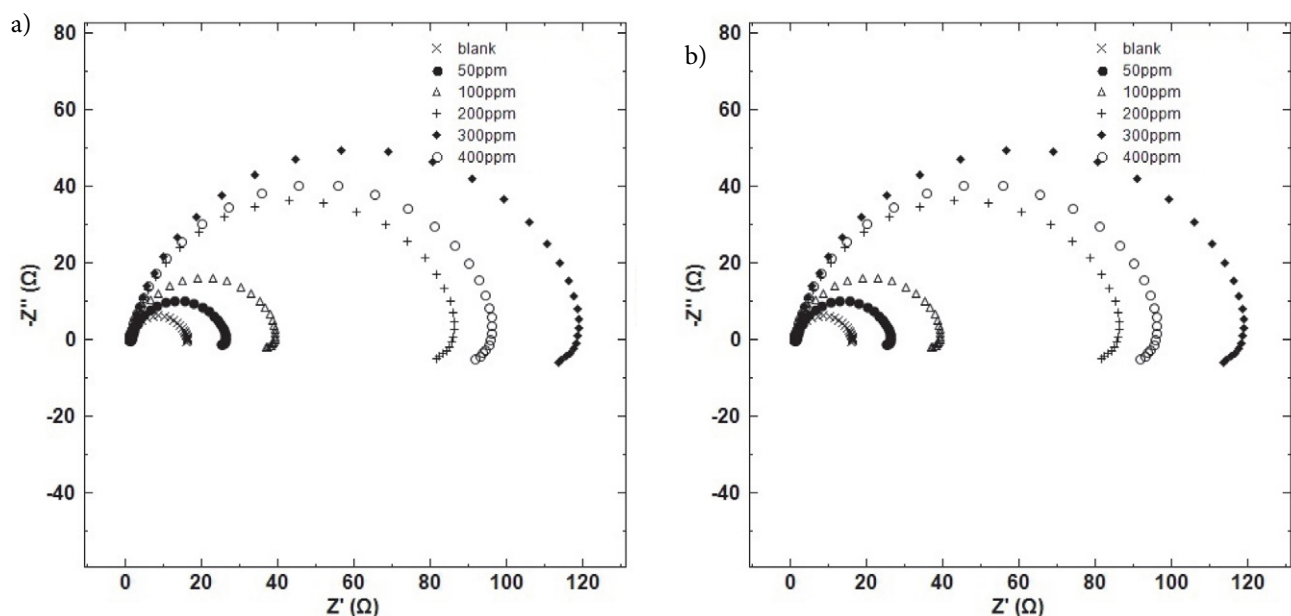


Figure 2. Nyquist curves for mild steel in a) 1 M hydrochloric acid solution and b) 0.5 M sulfuric acid solution in absence and presence of different concentrations of inhibitor at 25 ± 1 °C. (The experiments were repeated at least two times)

rameters, obtained from fitting of the recorded EIS data are listed in Table 1. In this table, the calculated double-layer capacitance (C_{dl}) values derived from the CPE parameters are also given and standard deviation (S.D.) and mean (\bar{X}) values are calculated.

Table 1. Corrosion parameters derived from Nyquist curves for mild steel in a) hydrochloric acid and b) sulfuric acid solution in absence and presence of different concentrations of inhibitor at 25 ± 1 °C. (Results derived from at least two repeats of experiment.)

a)

inhibitor concentration (ppm)	$C_{dl}/ \mu\text{F}/\text{cm}^2$	$R_{ct}/ \Omega \text{ cm}^2 \pm \text{S.D.}$	IE%	\bar{X}
Blank	368	15.0 ± 0.00	–	15.0
50	299	25.0 ± 1.53	40	25.3
100	196	38.0 ± 2.08	60	36.7
200	116	86.0 ± 2.00	82	88.0
300	62	121.0 ± 1.53	87	122.3
400	103	97.0 ± 2.08	84	98.7

b)

inhibitor concentration (ppm)	$C_{dl}/ \mu\text{F}/\text{cm}^2$	$R_{ct}/ \Omega \text{ cm}^2 \pm \text{S.D.}$	IE%	\bar{X}
Blank	607	16.0 ± 0.00	–	16.0
50	506	26.0 ± 1.53	37	26.3
100	318	31.0 ± 1.53	50	32.3
200	190	40.0 ± 1.53	58	41.3
300	136	55.0 ± 1.53	70	56.3
400	241	41.0 ± 1.53	60	40.6

3. 2. Potentiodynamic Polarization

Fig. 4 presents the potentiodynamic polarization curves of mild steel in 1 M HCl and 0.5 M H₂SO₄ in the blank and solution containing various concentrations of tablet. The relevant parameters are gathered in Table 2, i.e. corrosion current density (i_{corr}), corrosion potential (E_{corr}), surface coverage (θ), anodic and cathodic Tafel slopes (β_a , β_c). The corrosion current density decreased as the concentration of inhibitor increased up to 300 ppm, then decreased. Addition of inhibitor to acid media affected both cathodic and anodic

branches of the polarization curves. But the corrosion potential did not change noticeably. Therefore, metoprolol behaved as mixed-type inhibitor. In addition to the above parameters, Table 2 depicts the values of corrosion inhibition efficiencies (IE) that were calculated using the appropriate equation:²⁰

$$\text{IE}\% = \left(\frac{i_{\text{corr}} - i_{\text{inh}}}{i_{\text{corr}}} \right) \times 100 \quad (4)$$

where i_{corr} and i_{inh} are the corrosion current densities in the experiments without and with inhibition, respectively.

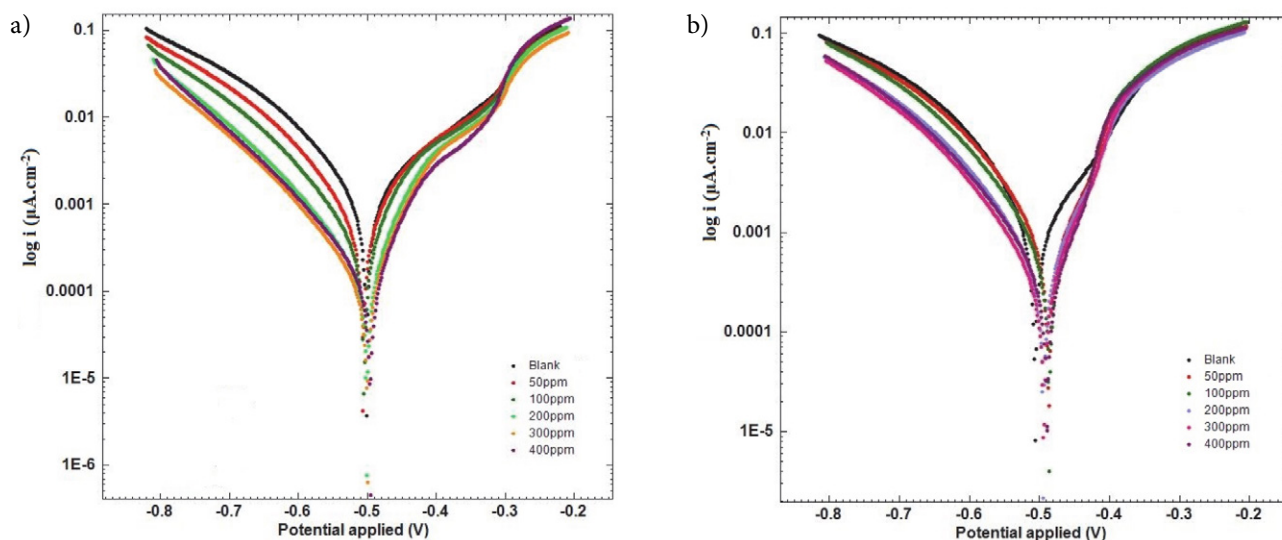


Figure 4. Polarization curves for mild steel in a) 1 M hydrochloric acid and b) 0.5 M sulfuric acid solution in absence and presence of different concentrations of inhibitor at 25 ± 1 °C. (The experiments were repeated at least two times)

Table 2. Corrosion parameters derived from polarization curves for mild steel in a) hydrochloric acid and b) sulfuric acid solution in absence and presence of different concentrations of inhibitor at 25 ± 1 °C. (Results derived from at least two repeats of experiment.)

a)							
inhibitor concentration (ppm)	$i_{\text{corr}}/\mu\text{A}/\text{cm}^2 \pm \text{S.D.}$	$-E_{\text{corr}}/\text{mV}$	$\beta_c/\text{mV}/\text{dec}$	$\beta_a/\text{mV}/\text{dec}$	θ	IE%	\bar{X}
Blank	1553.0 ± 1.41	503	176	142	–	–	1552.0
50	568.0 ± 6.03	508	93	101	0.63	63	574.0
100	415.0 ± 2.52	506	83	113	0.73	73	420.0
200	161.0 ± 4.70	498	74	114	0.90	90	166.0
300	99.0 ± 7.02	502	95	54	0.94	94	97.0
400	135.0 ± 5.51	498	65	107	0.91	91	141.0
b)							
inhibitor concentration (ppm)	$i_{\text{corr}}/\mu\text{A}/\text{cm}^2 \pm \text{S.D.}$	$-E_{\text{corr}}/\text{mV}$	$\beta_c/\text{mV}/\text{dec}$	$\beta_a/\text{mV}/\text{dec}$	θ	IE%	\bar{X}
blank	1823.0 ± 02.12	508	141	113	–	–	1821.5
50	739.0 ± 6.00	488	109	62	0.59	59	745.0
100	657.0 ± 6.12	487	118	57	0.64	64	662.0
200	569.0 ± 6.11	496	123	71	0.68	68	559.7
300	308.0 ± 6.36	495	67	102	0.83	83	312.5
400	480.0 ± 6.50	491	122	59	0.74	74	479.7

The IE values indicate that the inhibition is pronounced with increasing the inhibitor amount. Higher concentrations (above 300 ppm) did not affect the IE values (experiments at above 400 ppm (i.e. 500 ppm) of inhibitor were done but the results did not reveal appreciable changes, so due to overlapping of curves, these results are not given). The results show that the drug acts as an effective inhibitor. The calculated efficiencies obtained from polarization technique are in a close correlation with those obtained from charge transfer resistance.

3. 3. Effect of Temperature

The effect of temperature on the resistance performance of metoprolol on mild steel in 1 M HCl and 0.5 M H₂SO₄ was probed by potentiodynamic polarization measurements at optimum concentration of metoprolol. The

polarization curves in the absence and presence of 300 ppm metoprolol and in temperature range of 25–55 ± 1 °C are given in Fig. 5 and the corrosion parameters are listed in Table 3. The results obtained from polarization curves revealed an increase in current density and a decrease in IE values with rising temperature.

Important information on the mechanism of the inhibitor action could be obtained by comparing apparent activation energy (E_a), derived in the presence of inhibitor and its absence. E_a values were calculated from Arrhenius equation:²¹

$$i_{\text{corr}} = A \exp\left(\frac{-E_a}{RT}\right) \quad (5)$$

where i_{corr} is corrosion current, A is a constant and T is the temperature. Fig. 6 shows the Arrhenius plots for the cor-

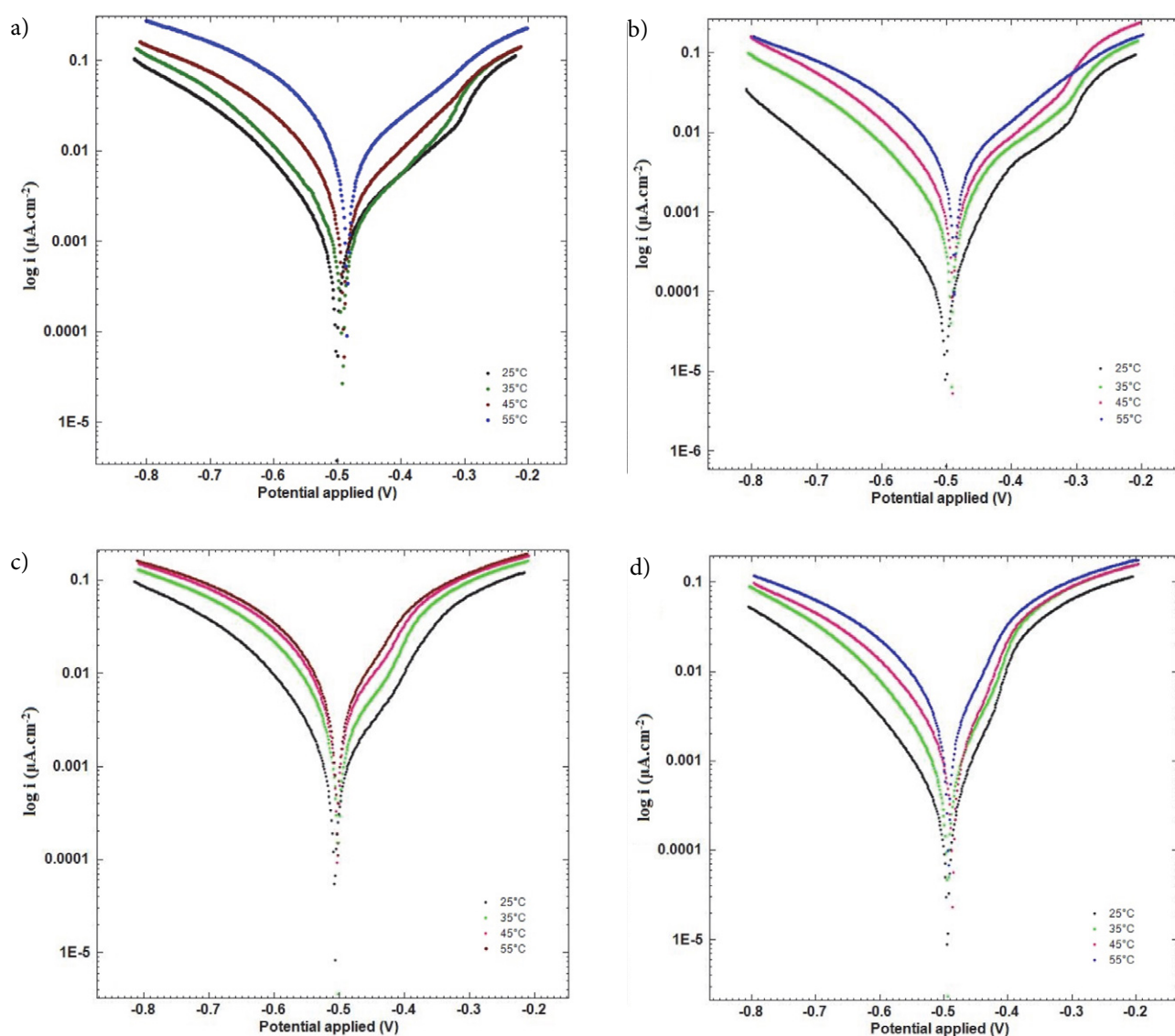


Figure 5. Effect of temperature on the polarization curves in 1 M hydrochloric acid solution a) without inhibitor b) with 300 ppm of inhibitor and 0.5 M sulfuric acid solution c) without inhibitor d) with 300 ppm of inhibitor. (The experiments were repeated at least two times.)

Table 3. Corrosion parameters calculated from polarization measurements in 1 M hydrochloric acid a) without inhibitor b) with 300 ppm of inhibitor and sulfuric acid solution c) without inhibitor d) with 300 ppm of inhibitor, at different temperatures. (Results derived from at least two repeats of experiment.)

a)				
temperature (C°)	$i_{\text{corr}}/\mu\text{A}/\text{cm}^2 \pm \text{S.D.}$	$-E_{\text{corr}}/\text{mV}$	\bar{X}	
25	1553.0 ± 1.41	502	1552.0	
35	1867.0 ± 9.90	494	1860.0	
45	2993.0 ± 7.80	492	2978.5	
55	6873.0 ± 9.20	486	6866.50	
b)				
temperature (C°)	$i_{\text{corr}}/\mu\text{A}/\text{cm}^2 \pm \text{S.D.}$	$-E_{\text{corr}}/\text{mV}$	IE%	\bar{X}
25	99.0 ± 7.02	502	94	97.0
35	830.0 ± 7.80	493	56	824.5
45	1728.0 ± 7.10	491	42	1723.0
55	4622.0 ± 7.07	498	35	4627.0
c)				
temperature (C°)	$i_{\text{corr}}/\mu\text{A}/\text{cm}^2 \pm \text{S.D.}$	$-E_{\text{corr}}/\text{mV}$	\bar{X}	
25	1823.0 ± 2.12	508	1821.5	
35	5260.0 ± 6.36	502	5255.5	
45	5268.0 ± 5.66	503	5264.0	
55	10453.0 ± 5.66	504	10457.0	
d)				
temperature (C°)	$i_{\text{corr}}/\mu\text{A}/\text{cm}^2 \pm \text{S.D.}$	$-E_{\text{corr}}/\text{mV}$	IE%	\bar{X}
25	308.0 ± 6.36	495	83	312.5
35	1450.0 ± 9.90	494	72	1443.0
45	2024.0 ± 7.80	487	62	2018.5
55	4623.0 ± 8.50	493	56	4629.0

rosion of mild steel in both solutions. The E_a values were determined from the plots ($\ln j_{\text{corr}}$ versus $1/T$) and are given in Table 4. A decrease in inhibition yield with rise in temperature with analogous increase in corrosion activation energy in the presence of inhibitor compared to its absence is frequently interpreted as being suggestive of formation of an adsorption film of physical (electrostatic) nature.

3. 4. Adsorption Isotherm

To obtain the surface coverage, θ , it was assumed that the inhibition efficiency is because of the blocking effect of the adsorbed species and hence $\theta = \text{IE} (\%)/100$. Here, an attempt was made to test the Langmuir, Temkin, and Frumkin isotherms. The Langmuir adsorption isotherm is found

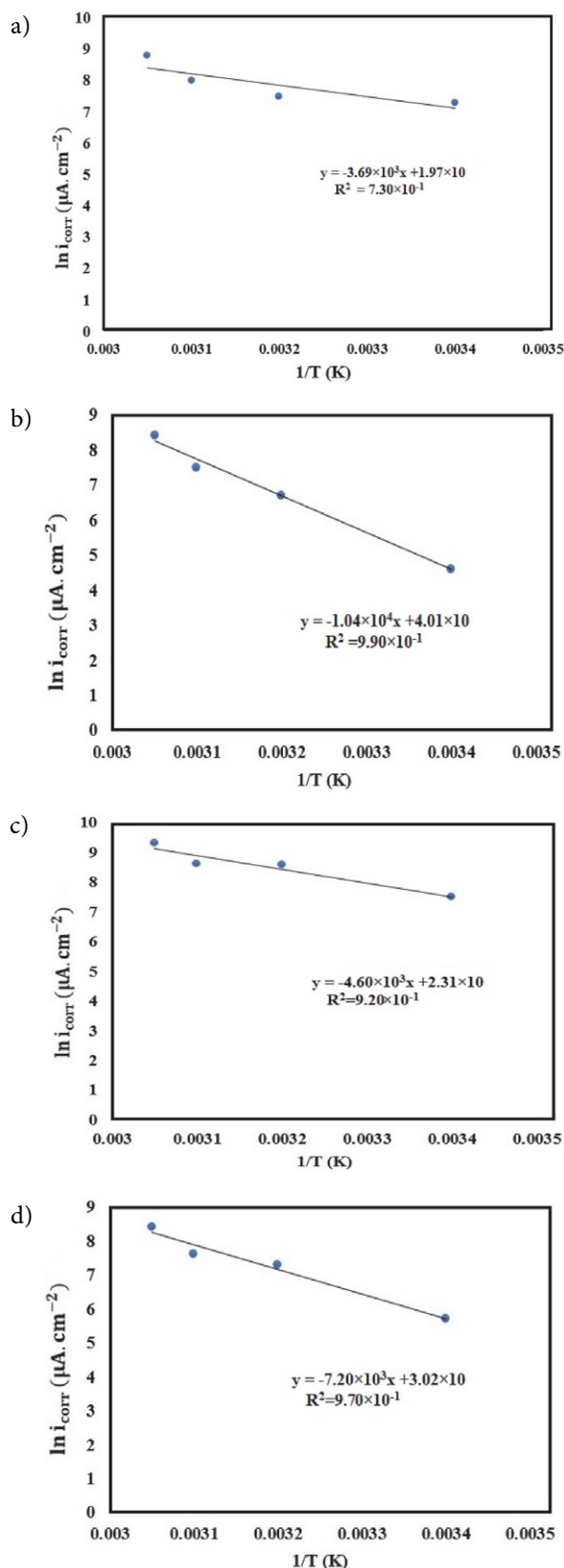


Figure 6. Arrhenius slopes calculated from corrosion current density for mild steel in 1 M hydrochloric acid, a) without inhibitor, b) with inhibitor and 0.5 M sulfuric acid solution c) without inhibitor d) with inhibitor.

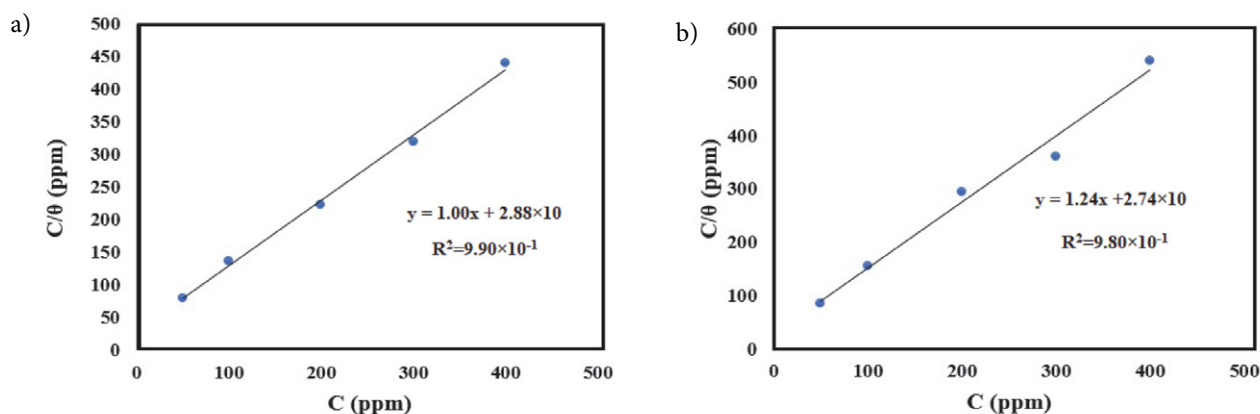


Figure 7. Langmuir adsorption isotherm on the mild steel surface in a) hydrochloric acid and b) sulfuric acid solution in the presence of inhibitor at 25 ± 1 °C.

to fit well with the experimental data (Fig. 7). This kind of isotherm is defined by the below equation:²²

$$\frac{C_{inh}}{\theta} = \frac{1}{K_{ads}} + C_{inh} \quad (6)$$

where θ is the surface coverage, C_{inh} is the inhibitor concentration, and K_{ads} is the adsorption equilibrium constant. The plot of C/θ versus C for solutions (Fig. 7) yields straight line with correlation coefficient close to 1.0 confirming the adsorption of the inhibitor on the sample fits the Langmuir isotherm. This isotherm is based on the assumptions that all the adsorption sites are equivalent and the ability of a molecule to be adsorbed at a given site is independent of the occupation of nearby sites.²³

3. 5. Thermodynamic Parameters

The adsorption equilibrium constant, K_{ads} , was calculated using equation (6). The Gibbs standard free energy of the adsorption of the inhibitor was explored by the following equation:²⁴

$$\Delta G_{ads}^{\circ} = -RT \ln(1 \times 10^6 K_{ads}) \quad (7)$$

where R is the gas constant (8.314 J/Kmol) and T is the absolute temperature (K).

Also, the value of enthalpy of adsorption, ΔH_{ads}° , was calculated from the below equation:²⁵

$$\frac{\theta}{1-\theta} = AC \exp\left(-\frac{\Delta H_{ads}^{\circ}}{RT}\right) \quad (8)$$

where θ is surface coverage, A is an independent constant, C is concentration, R is gas constant, T is absolute temperature. Fig. 8 illustrates the plot of $\ln\left(\frac{\theta}{1-\theta}\right)$ versus $1/T$, and there the value of ΔH_{ads}° was measured by the slope of the straight line.

Entropy of adsorption ΔS_{ads}° is given by the equation (9):²⁶

$$\Delta G_{ads}^{\circ} = \Delta H_{ads}^{\circ} - T\Delta S_{ads}^{\circ} \quad (9)$$

The calculated values of E_a , ΔH_{ads}° , ΔG_{ads}° , and ΔS_{ads}° for mild steel in both solutions in absence and presence of

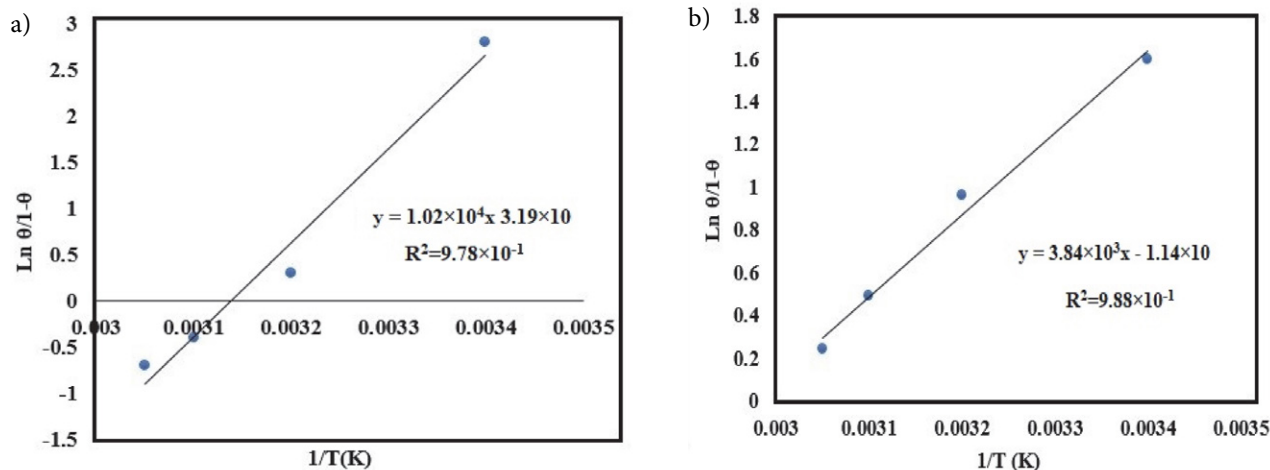


Figure 8. Plots of $\ln(\theta/(1-\theta))$ versus $1/T$ for mild steel in a) hydrochloric acid solution containing 300 ppm of inhibitor and b) sulfuric acid solution containing 300 ppm of inhibitor, at different temperatures.

the optimum concentration of the inhibitor are reported in Table 4. Generally, the values of $\Delta G_{\text{ads}}^{\circ}$ around -20 kJ/mol or less negative are consistent with the electrostatic interaction between charged molecules and the charged metal surface (physisorption); those around -40 kJ/mol or more negative involve charge sharing or transfer from organic molecules to the metal surface to form a coordinate type of metal bond (chemisorption).

The derived values of $\Delta G_{\text{ads}}^{\circ}$ for both solutions (>-40 and <-20) kJ/mol is commonly interpreted with comprehensive adsorption (physical and chemical adsorption).²⁷

For these solutions, the negative values of $\Delta G_{\text{ads}}^{\circ}$ showing the spontaneity of the adsorption process of inhibitor molecules on the steel surface. The negative signs of $\Delta H_{\text{ads}}^{\circ}$ reflect the exothermic nature of metoprolol behavior on the alloy. In this research, entropy of adsorption in both solutions is low and negative.

3. 6. SEM Observations

Scanning electron micrographs (SEM) of the surface of mild steel immersed for 24 h in 1 M HCl and 0.5 M

Table 4. Thermodynamic and kinetic parameters for adsorption of inhibitor in sulfuric acid and hydrochloric acid solutions on the metal surface. (Results derived from two repeats of experiment.)

	E_a (kJ/mol)	$\Delta H_{\text{ads}}^{\circ}$ (kJ/mol)	$\Delta G_{\text{ads}}^{\circ}$ (kJ/mol)	$\Delta S_{\text{ads}}^{\circ}$ (kJ/mol K)
Hydrochloric acid	30.9	–	–	–
Sulfuric acid	38.2	–	–	–
Hydrochloric acid and inhibitor	86.8	–84.5	–25.9	–0.197
Sulfuric acid and inhibitor	59.9	–31.9	–26.0	–0.020

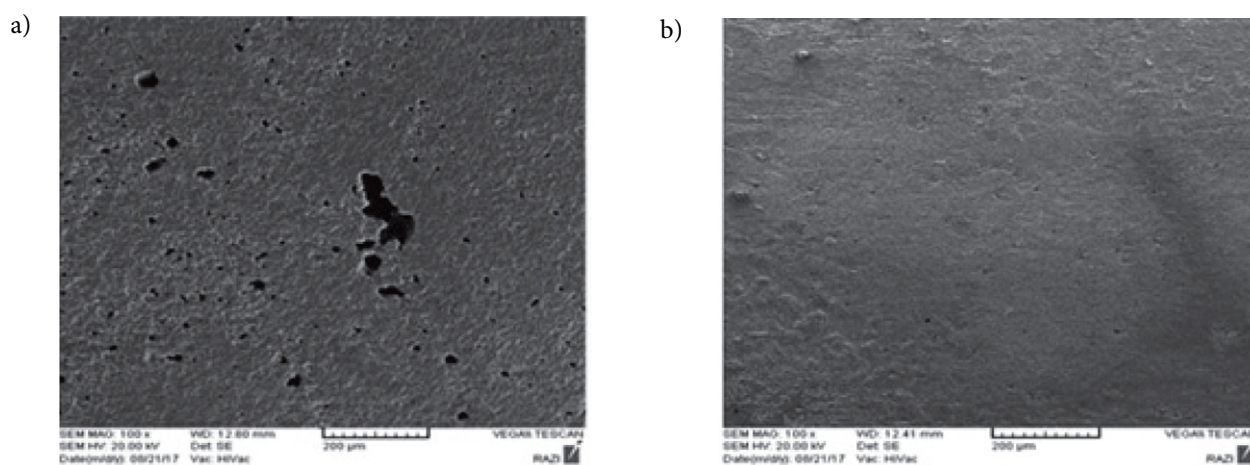


Figure 9. SEM images of mild steel in 1.0 M hydrochloric acid solution, a) blank, b) with inhibitor.

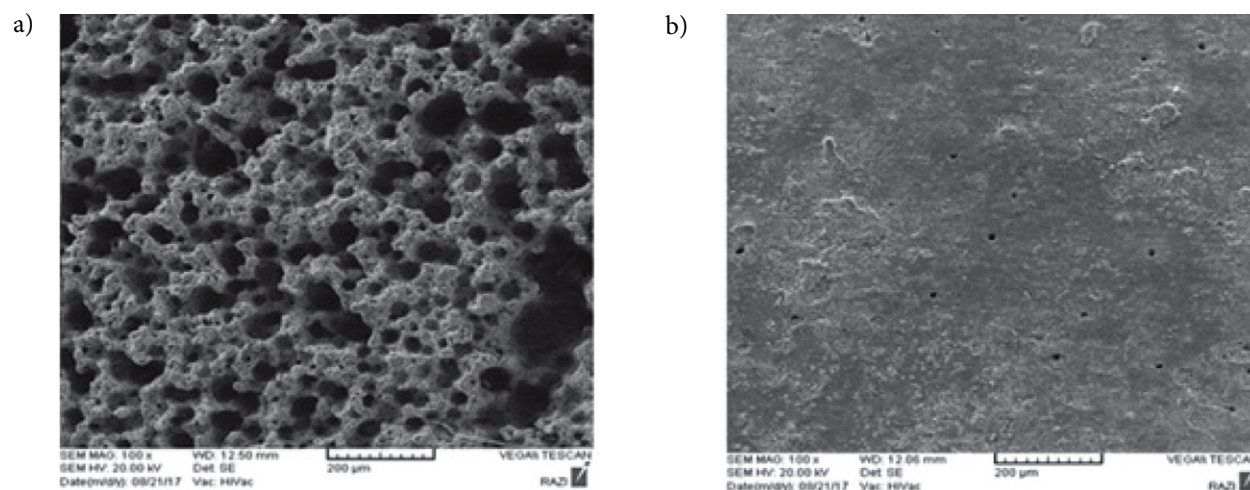


Figure 10. SEM images of mild steel in 0.5 M sulfuric acid solution, a) blank, b) with inhibitor.

H₂SO₄ solutions without and with the optimum concentration of inhibitor are shown in Fig. 9 and 10. The alloy surfaces in both blank solutions (Fig. 9a and 10a) were drastically damaged but in the presence of 300 ppm metoprolol (Fig. 9b and 10b) were protected. This demonstrates the potential of metoprolol to act as an efficient corrosion inhibitor for the mild steel in the acid media.

4. Conclusions

The below conclusions were drawn for this study:

1. Metoprolol tablet was found to be a suitable inhibitor of mild steel corrosion in acid media, especially in HCl.
2. Inhibition efficiency increased with an increase in metoprolol concentration up to 300 ppm while it decreased with increase in temperature.
3. The inhibitor concentration (300 ppm) at 25 ± 1 °C reached to a maximum inhibition efficiency.
4. The free energy of adsorption indicates that the process was spontaneous and the adsorption enthalpy indicated that the process is exothermic with negative entropy of adsorption.
5. The EIS measurements showed that with addition of the inhibitor up to 300 ppm, the charge transfer resistance enhances and the double layer capacitance (C_{dl}) reduces.
6. Potentiodynamic polarization measurements showed that the tablet acts as a mixed-type inhibitor in both solutions.
7. The results obtained from potentiodynamic polarization and EIS are consistent.
8. The adsorption of the inhibitor on the alloy surface in the solutions obeys Langmuir isotherm.
9. The SEM investigations revealed formation of a uniform and protective film on the alloy.

5. References

1. B. E. A. Rani, B. B. J. Basu, *Int. J. Corros.* **2012**, *2012*, 1–15. DOI:10.1155/2012/380217
2. X. Li, S. Deng, H. Fu, G. Mu, *Corros. Sci.* **2009**, *51*, 620–634. metoprolola fizikalna, eksotermna in spontana
3. M. J. Bahrami, S. M. A. Hosseini, P. Pilvar, *Corros. Sci.* **2010**, *52*, 2793–2803. DOI:10.1016/j.corsci.2010.04.024
4. R. M. Palou, O. Olivares-Xomelt, N. V. Likhanova, *InTech.* **2014**, 432–465.
5. S. M. A. Hosseini, M. Salari, M. Ghasemi, *Mater. Corros.* **2009**, *60*, 963–968. DOI:10.1002/maco.200905214
6. S. Bilgic, M. Sahin, *Mater. Chem. Phys.* **2001**, *70*, 290–295. DOI:10.1016/S0254-0584(00)00534-4
7. H. D. Lece, K. C. Emregul, O. Atakol, *Corros. Sci.* **2008**, *50*, 1460–1468. DOI:10.1016/j.corsci.2008.01.014
8. G. Mu, X. Li, Q. Qu, J. Zhou, *Corros. Sci.* **2006**, *48*, 445–459. DOI:10.1016/j.corsci.2005.01.013
9. E. Samiento-Bustos, J. G. Gonzalez Rodriguez, J. Uruchurtu, G. Dominguez- Patino, V.M. Salinas-Bravo, *Corros. Sci.* **2008**, *50*, 2296–2303. DOI:10.1016/j.corsci.2008.05.014
10. A. C. Bastos, M. G. Ferreira, A. M. Simoes, *Corros. Sci.* **2006**, *48*, 1500–1512. DOI:10.1016/j.corsci.2005.05.021
11. M. Sahin, G. Gece, F. Karci, S. Bilgic, *J. Appl. Electrochem.* **2008**, *38*, 809–815. DOI:10.1007/s10800-008-9517-3
12. G. Gece, *Corros. Sci.* **2008**, *50*, 2981–2992. DOI:10.1016/j.corsci.2008.08.043
13. R. T. Loto, C.A. Loto, A. P. I. Popoola, *J. Mater. Environ. Sci.* **2012**, *3*, 885–894.
14. D. G. Ladha, U. J. Naik, N. K. Shah, *J. Mater. Environ. Sci.* **2013**, *4*, 701–708.
15. N. O. Eddy, S. A. Odoemelam, *J. Mater. Sci.* **2008**, *4*, 87–96.
16. A. S. Mahdi, *Int. J. Adv. Res. Eng. Tech.* **2014**, *5*, 99–107.
17. N. S. Patel, S. Jauhari, G. N. Mehta, *Acta Chim.Slov.* **2010**, *57*, 297–304.
18. M. Outirite, M. Lagrenée, M. Lebrini, M. Traisnel, C. Jama, H. Vezin, F. Bentiss, *Electrochim. Acta.* **2010**, *55*, 1670–1681. DOI:10.1016/j.electacta.2009.10.048
19. M. S. Al-Otaibi, A. M. Al-Mayouf, M. Khan, A. A. Mousa, S. A. Al-Mazroa, H. Z. Alkhatlan, *Arabian J. Chem.* **2014**, *7*, 340–346. DOI:10.1016/j.arabjc.2012.01.015
20. A. Samide, I. Bibicu, M. Rogalski, M. Preda, *Acta Chim.Slov.* **2004**, *51*, 127–136.
21. B. El Mehdi, B. Mernari, M. Traisnel, F. Bentiss, M. Lagrenee, *Mater. Chem. Phys.* **2003**, *77*, 489–496. DOI:10.1016/S0254-0584(02)00085-8
22. L. Herrag, B. Hammouti, A. Aouniti, S. El Kadiri, R. Touzani, *Acta Chim. Slov.* **2007**, *54*, 419–423.
23. P. Atkins, J. de Paula, Oxford University Press, Oxford, USA, Physical Chemistry, Eighth, **2006**.
24. A. Pal, S. Dey, D. Sukul, *Res. Chem. Intermed.* **2016**, *42*, 4531–4549. DOI:10.1007/s11164-015-2295-8
25. Gh. Golestani, M. Shahidi, D. Ghazanfari, *Appl. Surf. Sci.* **2014**, *308*, 347–362. DOI:10.1016/j.apsusc.2014.04.172
26. H. Ashassi-Sorkhabi, B. Shaabani, D. Seifzadeh, *Appl. Surf. Sci.* **2005**, *239*, 154–164. DOI:10.1016/j.apsusc.2004.05.143
27. E. A. Noor, A. H. Al-Moubaraki, *Mater. Chem. Phys.* **2008**, *110*, 145–154. DOI:10.1016/j.matchemphys.2008.01.028

Povzetek

Proučevali smo inhibicijo korozije jeklene zlitine (st37) s tabletami metoprolola v 1 M klorovodikovi kislini in v 0,5 M žveplove kislini. Uporabili smo tri metode: potenciodinamično polarizacijo, elektrokemijsko impedančno spektroskopijo in vrstično elektronsko mikroskopijo, SEM. Pridobljeni parametri so pokazali, da različne količine metoprolola inhibirajo korozijo jekla v raztopinah kisljin HCl in H₂SO₄. Korozijska odpornost zlitine se je povečevala glede na višanje koncentracije metoprolola do 300 ppm, a se je zmanjšala pri višji temperaturi. Parametri, pridobljeni iz polarizacijskih krivulj, so pokazali, da je učinkovina inhibitor mešanega tipa. Rezultati, pridobljeni z različnimi metodami, so se med seboj ujemali. Ugotovili smo, da je adsorpcija ter da se ujema z Langmuirjevim adsorpcijskim modelom. SEM mikrografije se skladajo z adsorpcijskim obnašanjem tablete



Except when otherwise noted, articles in this journal are published under the terms and conditions of the Creative Commons Attribution 4.0 International License

Scientific paper

Dynamics of Isomerization of Hop Alpha-Acids and Transition of Hop Essential Oil Components in Beer

Miha Ocvirk¹ and Iztok J. Košir^{1,*}¹ Institute of Hop Research and Brewing, Cesta Žalskega Tabora 2, SI-3310 Žalec, Slovenia

* Corresponding author: E-mail: iztok.kosir@ihps.si

Tel: 00386 371 21 608

Received: 01-13-2020

Abstract

Hops' unique composition of essential oil components and bitter resins are crucial for beer aroma, which is important to consumers' acceptance of beer. In this experiment the same wort was divided into four portions and each was hopped differently. To determine the dynamics of isomerization rates the concentrations of alpha- and iso-alpha-acids were continuously measured. Measurements of hop essential oil components were performed during each process to understand the dynamics of the transition into beer. The maximum isomerization yield of alpha-acids (18.1%) was achieved after 100 min. Longer boiling increased the reduction of iso-alpha-acids, as well as essential oil components. Dry hopping also affected not only on beer aroma but also on beer bitterness.

Keywords: Beer; hop; aroma; isomerization; hop essential oil

1. Introduction

In the brewing process hop is a quantitatively minor ingredient, but of paramount importance to the brewing industry. With their complex chemistry, hops have been the subject of investigation for decades.¹ During the brewing process hops are added into the boiling wort to provide a bitter taste and aroma to the final product.² One of the main reasons for boiling the wort is the isomerization reaction of the hop alpha-acids into their isomerized forms. The duration of kettle hopping depends on the time required for the isomerization to take place.³ Adding hops into the boiling wort is desired with intent to achieve the desired bitterness, however it causes a reduction in the yield of essential oils in the beer due to evaporation. Consequently, these components are not present in beer in the same ratios as they are in hops. Some components are very volatile and some have low solubility in water.⁴

During other stages of the brewing process, essential oil components decrease because of adsorption of yeast cells on the trub in addition to evaporation. The CO₂ produced during alcoholic fermentation also affects the decrease of aroma compound yields in beer.^{5–8} To avoid the loss of aroma constituents and to achieve better yields dry hopping technique is in use, where hops are added at a later stages of brewing process, during fermentation or maturation.

The volatile aroma compounds of the hops are crucial for brewers, since they give beer its unique aroma. The identification of hop essential oil composition lasts for decades and the study of Roberts et.al concluded on the presence of over 1000 compounds in an oil fraction.⁹ Dried hops contain approximately 0.5–4.0% of essential oils. According to the chemical composition, compounds can be divided into three groups depending on their chemical structure: the hydrocarbon fraction which form approximately 75% of the total oil, the oxygen containing compounds forming approximately 25% of the total oil and the sulphur-containing compounds present in much lower quantities.^{2,10} Hydrocarbon fraction, consists of monoterpenes, sesquiterpenes and aliphatic hydrocarbons. Due to evaporation and low solubility in water, concentrations of these group of aroma compounds are very low in finished beer. Presence of alcohol in beer can increase solubility of monoterpenes. Oxygen containing compounds consist mostly of monoterpenic, sesquiterpenic and aliphatic alcohols and these components can be formed by the oxidation or reduction during beer production. In general, these compounds are more soluble in water compared to the hydrocarbons because of the higher polarity of the molecule.^{6,7} Generally, myrcene, which is the most abundant component in hop essential oil, is undesirable in beer, while linalool and geraniol – both from an oxygen fraction

present in lower concentrations than myrcene, present a pleasant aroma. The odour threshold is more important than the concentration level of a component in beer.¹¹

The analytical approach to determine the volatile flavour-active compounds in beer is based on different solvent extraction techniques and separation by gas chromatography with flame ionization detection (GC-FID) or gas chromatography-mass spectrometry (GC-MS).¹² A newer approach to determine the volatile aroma compound is based on a solvent-free extraction technique, head-space solid phase micro extraction (HS-SPME),^{13,8} head-space trap GC-MS analysis of hop essential oils^{14,15} and stir bar sorptive extraction.¹⁶

Much research has been done to investigate the complexity of the final flavour compounds in beer aroma, but in our study the dynamics of the transfer of hop essential oil components as well as the dynamics of the isomerization of alpha-acids were studied directly during process. The aim of this study was to explore the levels of hop essential oils and alpha-acids during short- and long-time kettle hopping. By preparing the first two beer types (A–B), we investigated the behaviour of hop essential oil components (HEOC) during short-time (A) and long-time (B) wort boiling. In preparing the second two types of beer, we investigated dry hopping techniques of beer aroma compounds originated from hops. We tried to determine the difference if hop is added at the beginning of fermentation (C), or at the beginning of maturation (D).

2. Experimental

2.1. Experimental Beer Brewing

For 90 L of wort 100 L of water and 20 kg of Pilsner Malt (Castle Malt, Belgium) were used. The mashing process started at 52 °C for 30 min, then the temperature was increased to 63 °C for 30 min, the temperature was increased once more to 72 °C for 30 min and finally the temperature was increased to 76 °C and held for 10 min. After mashing and lautering the wort was divided into four parts, 1 × 60 L and 2 × 15 L. For beers A (short time boiling) and B (long time boiling) the whole amount of hop was added at the beginning of the wort boiling and left it in for 60 min. After that, the wort was divided in 2 equal parts (30 L). The second part of the wort continued with boiling for another 60 min (120 min in total). In each 30 L 250 g of hop cones were added. For beers C and D wort was boiling without hop in the same way as in the first two trials. In one 15 L fermentation tank 125 g of hop was added and left it until the end of six days of fermentation (beer C). In the second 15 L, 125 g of hop was added after the fermentation process, at the beginning of a two week maturation (beer D). Yeast strain used in fermentation process was Saflager W34/70 (Fermentis) 1 g per L. The duration of the fermentation was 5 days at 12 °C, while maturation take place at 2 °C for 2 weeks. After adding hops into boil-

ing wort, samples were collected every 10 min. During fermentation, samples were collected on each day of fermentation and during maturation, samples were collected every week of maturation.

2.2. Beer Analyses

Basic beer characteristics were measured. Determination of extract, alcohol and degree of fermentation were carried out according to the MEBAK II, method 2.10.4.¹⁷ Determination of pH value was carried out according to the Analytica EBC, method 9.35.¹⁸ Bitterness of beer was measured according to the Analytica EBC, method 9.8.¹⁹ Measurement of CO₂ was carried out according to the Analytica EBC, method 9.28.²⁰ and the determination of beer colour was carried out according to the Analytica EBC, method 9.6.²¹

2.3. Analytical Determination of Hop Metabolites

Determination of the content of hop essential oil was carried out according to Analytica EBC, method 7.10,²² using standard steam distillation. The determination of hop essential oil components was carried out according to the Analytica EBC, method 7.12²³ using GC-FID. The determination of alpha-acids was carried out according to the Analytica EBC, method 7.4.²⁴

2.4. Determination of Hop Essential Oil Components (HEOC) in Beer

For the hop essential oil component analysis in beer, an Agilent 6890 GC, equipped with FID detector (Agilent Technologies, USA) was used. The determination of essential oils was performed on a 60 m × 0.32 mm × 0.25 μm DB-Wax capillary column (Agilent Technologies, USA) according to the MEBAK, method 2.23.^{6,25} with some modifications, where the aroma compounds are driven out of the sample by steam distillation. The extraction of aroma compounds was performed by shaking 80 mL of distillate in 100 mL glass centrifuge tubes with 1 mL dichloromethane (Sigma-Aldrich, USA). Helium 5.0 was used as a carrier gas with a constant flow of 2.8 mL min⁻¹. The temperatures of the injector and detector were set to 250 °C. The temperature program started at 60 °C for 4 min, then increased by 5 °C min⁻¹ to 220 °C and was held at 220 °C for 30 min, then increased by 20 °C min⁻¹ to 240 °C and held for 5 min at 240 °C. The sample injection volume was 4 μL. Methyl heptanoate (Sigma-Aldrich, USA) was used as an internal standard. Identifications and quantifications of all investigated compounds presented in Table 1 were performed using standards purchased through Sigma-Aldrich, USA. For all measured parameters, the repeatability, accuracy and linearity for analytes were determined. RSDs for repeatability were from 1.3 to 1.9%. All measurements were done in duplicate.

Table 1: Composition of Dana essential oil

Essential oil component	% in hop oil
Methyl hexanoate	0.4
α -Pinene	0.2
Myrcene	37.5
Linalool	1.1
Borneol	0.1
α -Terpineole	0.4
Methyl nonanoate	0.2
Nerol	0.3
β -Citronellol	0.3
Geraniol	0.5
Methyl caprate	1.0
Neryl acetate	0.2
Geranyl acetate	0.4
β -Cariophyllene	9.4
α -Humulene	21.1
β -Farnesene	5.1
Tridecanone	0.8
Geranyl iso-butyrate	1.0
Cariophyllene oxide	0.9
Farnezol	0.2
Limonene	0.3

2. 5. Alpha-Acids and Iso-Alpha-Acids Determination

To determine alpha-acids and iso-alpha-acids in wort and beer, samples were taken and frozen at $-20\text{ }^{\circ}\text{C}$ until analysis. Prior to analysis, samples were warmed to room temperature and centrifuged at 3000 rpm for 15 min in Heraeus Biofuge Primo (Switzerland) centrifuge. The clear upper phase was filtered through $0.45\text{ }\mu\text{m}$ PET filters into 2 mL glass vials. Injection of $2\text{ }\mu\text{L}$ was made with an auto sampler of an Agilent 1200 HPLC chromatograph, using HPLC grade methanol (Merck, Germany), distilled water and 85% ortho-phosphoric acid (Sigma Aldrich, USA) in a ratio of 77.5: 21: 0.9 as a mobile phase. Separation was performed on a 150 mm long Nucleodur C18 Column (Macherey Nagel, Germany). Iso-alpha-acids were recorded at wavelength 270 nm, while alpha-acids were recorded at 314 nm.

3. Results and Discussion

In each type of beer brewed, the same amount (g L^{-1}) of the traditional Slovenian variety, Dana, with the al-

pha-acids content 9.0% and 1.9 mL of hop essential oil on 100 g of dried hop was used. Basic beer specifications of all investigated beer types are presented in Table 2. Data consists of extract, alcohol, degree of fermentation, pH, bitterness, content of CO_2 and content of iso-alpha-acids.

3. 1. Isomerization of Alpha-Acids

The content of iso-alpha-acids is the sum of all three peaks of isomerized analogues of alpha-acids: iso-cohumulone ($t_R = 4.19\text{ min}$), iso-adhumulone ($t_R = 4.97\text{ min}$) and iso-humulone ($t_R = 5.42\text{ min}$). In brewing science, the iso-alpha-acids are expressed as the sum of all three components, because for brewers, the sum value is relevant. The content of alpha-acids is the sum of cohumulone ($t_R = 8.39\text{ min}$) and n+adhumulone ($t_R = 10.70\text{ min}$). In Figure 1 where the dynamics of isomerization of alpha-acids for beer type B are presented, one can see a high isomerization rate in the first 30 min.

The highest utilization of 18.1% was achieved after 100 min of boiling. Isomerization yield was calculated as the ratio of actual mass concentration of iso-alpha-acids in beer, divided by the know content of alpha-acids in hop that was added into wort. Each sample taken later had smaller concentrations of iso-alpha-acids and smaller concentrations of alpha-acids. There was also a small part (1.6% of total alpha-acids added in wort) of alpha-acids that remained un-isomerized. This is a sign that longer boiling causes further degradation of iso-alpha acids. During fermentation we can see the concentration of iso-alpha-acids decreasing but a small increase in concentration was noticed on the last, fifth day of fermentation. Concentration during the maturation process increased to the final isomerization yield of 14.6%. The rise of IAA is occurred during maturation, where all bioprocess are finished, all the components reacts between each other's and beer gets its flavour and aroma.⁶ The pattern was the same (not shown) in beer type A, with one difference. The maximum isomerization yield was achieved at the end of boiling for 60 min, but after this time there is a part (4.6% of total alpha-acids added in wort) of alpha-acids that remain un-isomerized. Again, the concentrations decreased during fermentation and slightly increased during the maturation process.

In beer C, the concentration of iso-alpha-acids decreased every day until the final isomerization yield was below 1% (Figure 2).

Table 2. Basic beer characteristics for each beer type.

Beer type	Extract (%)	Alcohol (vol. %)	Degree of fermentation (%)	pH	Bitterness (IBU)	CO_2 (g L^{-1})	Iso-alpha-acids (mg L^{-1})
A	11.8	5.1	66.2	4.7	112	3.0	98
B	12.6	6.1	67.1	4.8	120	3.1	110
C	11.3	5.2	68.8	4.7	14	4.7	6
D	11.4	5.2	69.1	4.7	8	4.8	6

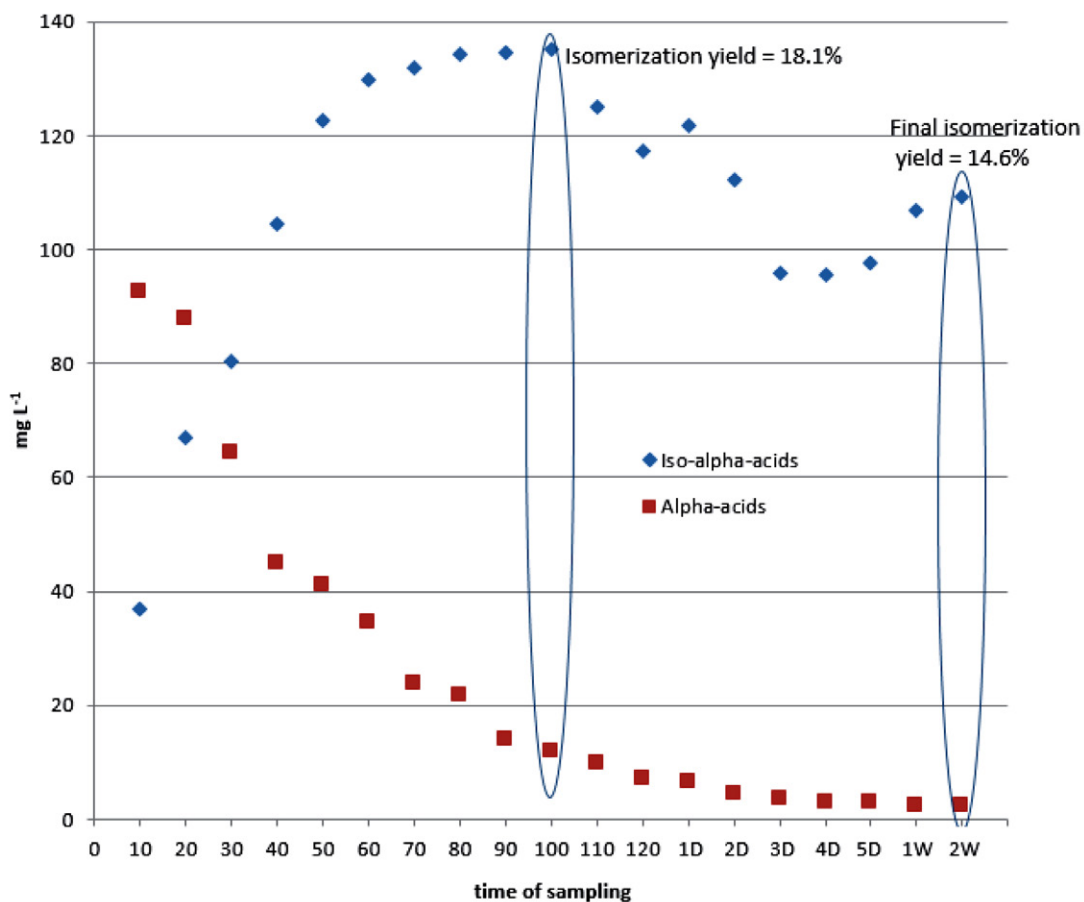


Figure 1: Dynamic of isomerization of alpha-acids in beer B. Sampling was made every 10 min during boiling, every day of fermentation and every week of maturation.

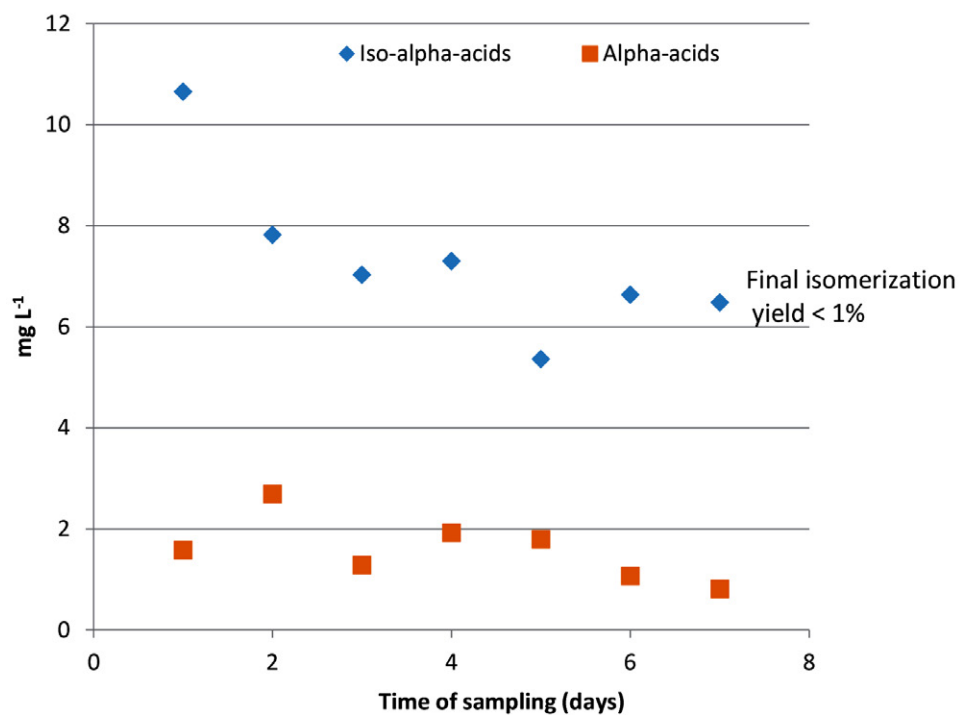


Figure 2. Dynamic of isomerization of alpha-acids in beer C.

The alpha-acid content in the beer was approximately 2 mg L^{-1} from the beginning of the process to the end of fifth day. The cause of low isomerization yield was the low temperature of the process. The cause is also limited solubility of alpha-acids in the wort and further losses of iso-alpha-acids post wort boiling; the absorption of trub and because of losses during clarification.^{26–29} Knowledge of the utilization value of iso-alpha-acids for each brewery is of crucial importance for brewers to achieve a desired level of bitterness in beer. In Table 3, where the dynamics

Table 3. Dynamics of isomerization in beer D

Time of sampling	Alpha-acids (mg L^{-1})	Iso-alpha-acids (mg L^{-1})
After 1 week of maturation	7.2	5.8
After 2 weeks of maturation	8.6	6.0

of isomerization in beer D is presented, one can see that the concentrations of alpha-acids are slightly higher than

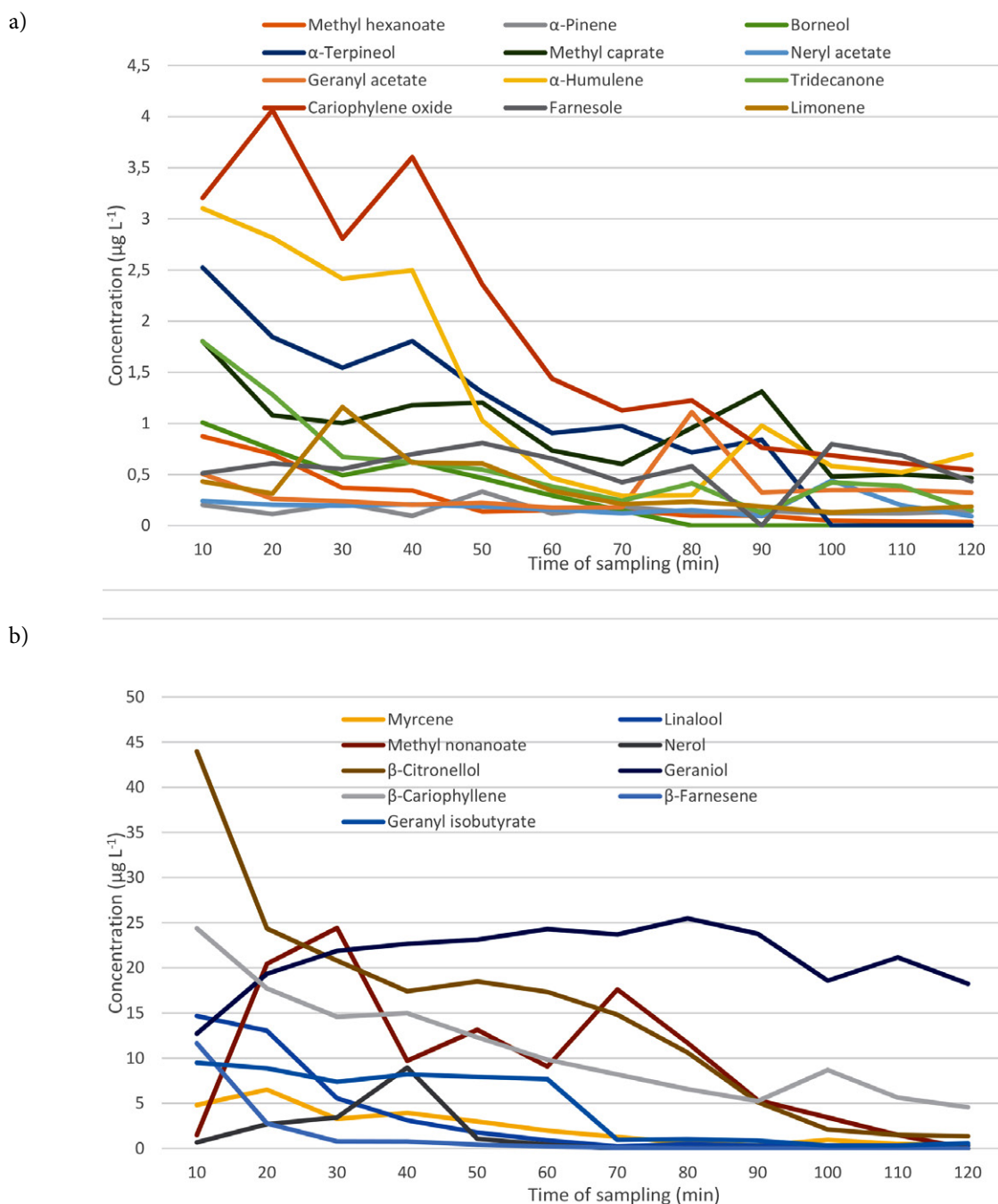


Figure 3a and 3b. Transition of hop essential oil components during wort boiling.

the concentrations of iso-alpha-acids. Both concentrations are very low, as the isomerization process depends on the temperature of the medium.

3. 2. Determination of the Transition of HEOC in Beer

The most abundant components of Dana essential oils were focused on. These components with their relative abundance in hop are presented in Table 1. Concentrations of investigated HEOC at the beginning of the hop-

ping process and at the end of the experiment are presented in Table 3. Concentrations of HEOC during wort boiling in beer types A and B (first 60 min for beers A + B and next 60 min for beer B) decreased at different rates (Figures 3a and 3b).

Some were decreased to the values < LOD. The exception is geraniol, where a small increase in concentration is noticed. It is important to know that these are not the final concentrations in beer. The literature states that later in the fermentation or maturation process concentrations of some HEOC can increase, because of thermal re-

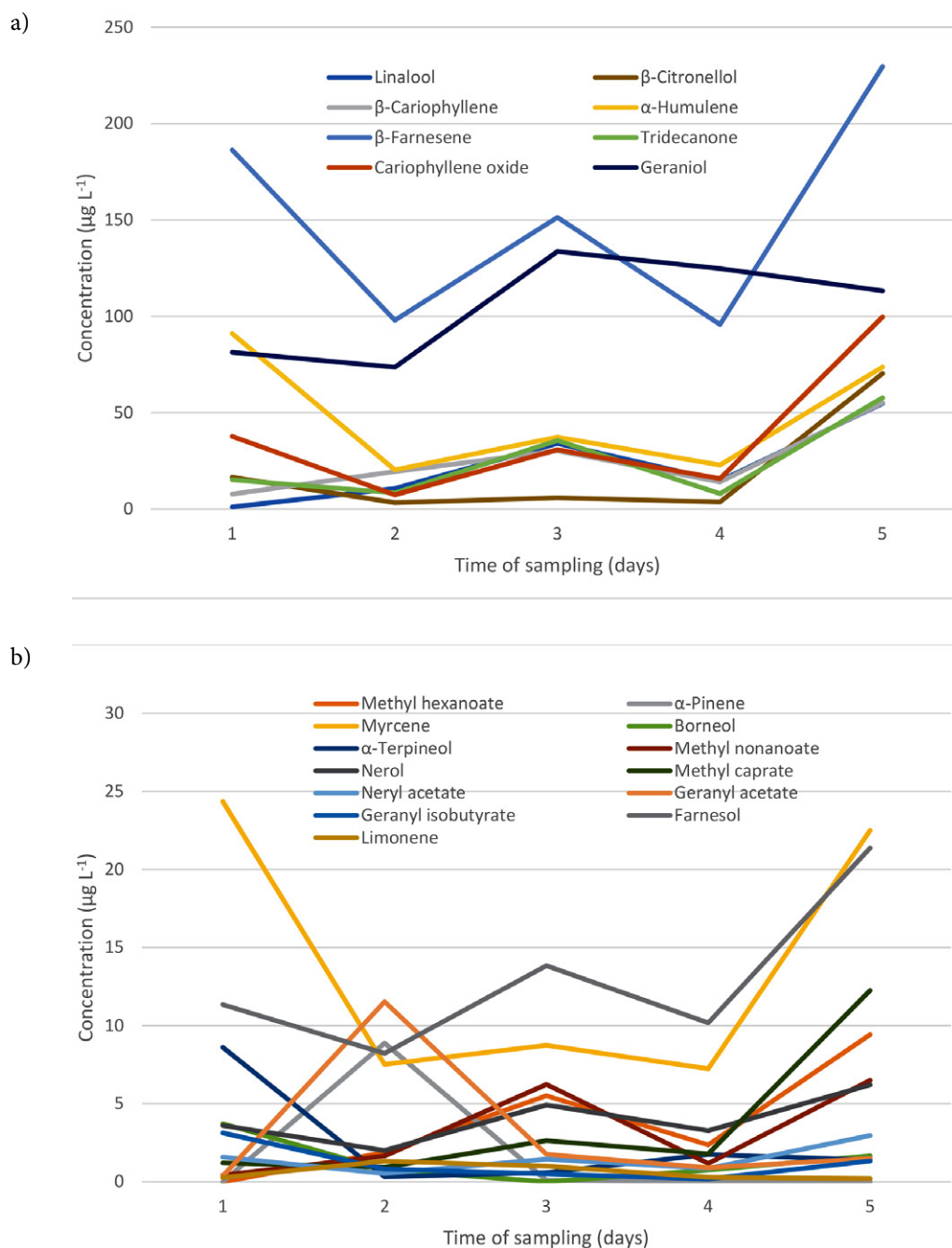


Figure 4a and 4b. Transition of hop essential oil components during fermentation.

actions or by biotransformation processes such as oxidation, reductions, isomerization or hydrolysis of volatiles that occur in beer brewing.^{30–35} Myrcene and α -humulene, which belong to the terpene hydrocarbon fraction of essential oils, are hydrophobic and would not pass from the hops through to the finished beer during the brewing process. On the other hand, hydrophilic terpene alcohols, such as linalool, are easier to retain in the beer.^{30,31} Due to evaporation during wort boiling, myrcene, although it is the most common component in essential oils, does not contribute to the beer aroma because the concentrations are normally far below the odour threshold level.³² In beer C we observed the transition of HEOC during fermentation (Figure 4a and 4b).

In general, concentrations of HEOC begin high, and then some fluctuation in concentrations is observed, until the last day of fermentation when the HEOC are again in the same range as at the beginning. One of the main reasons for such fluctuations in concentrations during dry hopping, which seems to be simple, but from a physico-chemical point of view dry hopping is very complex and complicated, is not just extraction time and amount of hops but also the presence of yeast cells and carbon dioxide which can wash out the essential components from beer.^{6,7}

It is interesting, that concentrations of limonene, α -terpineole, neryl acetate and geranyl-iso-butyrate remain almost the same as they were after the first day of dry hopping. Concentration of linalool increases around 50

times. The concentrations of HEOC in beer C are generally higher than in both “kettle hopped” beers A and B. In beer D, where hop was added only at the beginning of the maturation process, two types of HEOC dynamics are observed. In Table 4, some concentrations decrease with time while some of the concentrations increase.

Some concentrations are higher than in beer C. One of the reasons is a low temperature during the maturation process and live environment in the fermentation process. Beside extraction of HEOC in wort or beer, chemical reactions between some components can lead to an increase of concentrations. Linalool can come from nerol or geraniol, and β -citronellol can come from geraniol. Linalool could be also cyclized to α -terpineol.^{31,33} Although linalool is not abundant in hops, its contribution to beer aroma is high because of its very low odour threshold value of 2.2 $\mu\text{g L}^{-1}$.³⁴ Henke et al. also reported that concentrations of geraniol increase during fermentation, which is in line with our results.³⁵

4. Conclusions

From this experiment, it can be concluded that the optimal time of hopping to achieve high bitterness is no longer, than 100 min. Dry hopping also effects beer bitterness, but the isomerization rates are very low, and consequently higher concentrations of un-isomerized alpha-acids were detected. During brewing, severe losses, oh hop essential oils occur by evaporation in the hot part

Table 4. Concentrations of hop essential oil components in beer types A-D (LOD = 0.1 $\mu\text{g L}^{-1}$)

	A		B		C		D	
	Start [$\mu\text{g L}^{-1}$]	Final [$\mu\text{g L}^{-1}$]	Start [$\mu\text{g L}^{-1}$]	Final [$\mu\text{g L}^{-1}$]	Start [$\mu\text{g L}^{-1}$]	Final [$\mu\text{g L}^{-1}$]	Start [$\mu\text{g L}^{-1}$]	Final [$\mu\text{g L}^{-1}$]
Methyl hexanoate	0.9 ± 0.1	0.4 ± 0.1	0.9 ± 0.1	0.4 ± 0.1	< LOD	9.4 ± 0.2	4.2 ± 0.1	2.4 ± 0.1
α -Pinene	0.2 ± 0.1	0.2 ± 0.1	0.2 ± 0.1	0.1 ± 0.1	< LOD	< LOD	< LOD	< LOD
Myrcene	4.8 ± 0.1	1.9 ± 0.1	4.8 ± 0.1	0.4 ± 0.1	24.3 ± 0.3	22.5 ± 0.3	0.6 ± 0.1	1.71 ± 0.1
Linalool	14.6 ± 0.2	0.9 ± 0.1	14.6 ± 0.2	0.3 ± 0.1	1.1 ± 0.1	54.7 ± 0.8	19.7 ± 0.3	28.2 ± 0.3
Borneol	1.0 ± 0.1	0.3 ± 0.1	1.0 ± 0.1	< LOD	3.7 ± 0.1	1.7 ± 0.1	0.3 ± 0.1	0.3 ± 0.1
α -Terpineole	2.5 ± 0.1	0.9 ± 0.1	2.5 ± 0.1	< LOD	8.6 ± 0.2	1.4 ± 0.1	0.4 ± 0.1	0.6 ± 0.1
Methyl nonanoate	1.5 ± 0.1	9.0 ± 0.2	1.5 ± 0.1	< LOD	0.4 ± 0.1	6.5 ± 0.1	5.7 ± 0.1	14.9 ± 0.2
Nerol	0.7 ± 0.1	0.4 ± 0.1	0.7 ± 0.1	< LOD	3.6 ± 0.1	6.2 ± 0.1	2.9 ± 0.1	11.3 ± 0.2
β -Citronellol	43.9 ± 0.7	17.3 ± 0.4	43.9 ± 0.7	1.3 ± 0.1	16.5 ± 0.3	70.3 ± 1.1	1.3 ± 0.1	0.7 ± 0.1
Geraniol	12.7 ± 0.2	24.3 ± 1.0	12.7 ± 0.2	18.2 ± 0.3	81.3 ± 1.3	113.2 ± 1.8	4.0 ± 0.2	26.9 ± 0.4
Methyl Caprate	1.8 ± 0.1	0.7 ± 0.1	1.8 ± 0.1	0.5 ± 0.1	1.2 ± 0.1	12.2 ± 0.2	2.8 ± 0.1	1.7 ± 0.1
Neryl acetate	0.2 ± 0.1	0.1 ± 0.1	0.2 ± 0.1	1.0 ± 0.1	1.6 ± 0.1	3.0 ± 0.1	1.4 ± 0.1	0.9 ± 0.1
Geranyl acetate	0.5 ± 0.1	0.2 ± 0.1	0.5 ± 0.1	0.3 ± 0.1	0.4 ± 0.1	1.5 ± 0.1	1.1 ± 0.1	38.2 ± 0.6
β -Cariophyllene	24.4 ± 0.3	9.8 ± 0.2	24.4 ± 0.3	4.6 ± 0.1	7.8 ± 0.1	55.2 ± 0.7	5.0 ± 0.1	2.3 ± 0.1
α -Humulene	3.1 ± 0.1	0.4 ± 0.1	3.1 ± 0.1	0.6 ± 0.1	91.1 ± 1.4	73.7 ± 1.1	1.7 ± 0.1	36.5 ± 0.6
β -Farnesene	11.6 ± 0.2	0.2 ± 0.01	11.6 ± 0.2	< LOD	186.1 ± 2.7	229.6 ± 3.2	10.7 ± 0.2	39.4 ± 0.6
Tridecanone	1.8 ± 0.1	0.4 ± 0.1	1.8 ± 0.1	0.1 ± 0.1	15.2 ± 0.3	57.8 ± 1.0	10.6 ± 0.2	31.5 ± 0.5
Geranyl iso-butyrate	9.5 ± 0.2	7.7 ± 0.2	9.5 ± 0.2	0.5 ± 0.1	3.1 ± 0.1	1.3 ± 0.1	5.7 ± 0.1	< LOD
Cariophyllene oxid	3.2 ± 0.1	1.4 ± 0.1	3.2 ± 0.1	0.5 ± 0.3	37.7 ± 0.7	99.7 ± 1.8	8.6 ± 0.1	17.6 ± 0.3
Farnesol	0.5 ± 0.1	0.6 ± 0.1	0.5 ± 0.1	18.6 ± 0.3	11.3 ± 0.2	21.4 ± 0.4	4.7 ± 0.1	3.6 ± 0.1
Limonene	0.4 ± 0.1	0.3 ± 0.1	0.4 ± 0.1	0.2 ± 0.1	0.3 ± 0.1	0.2 ± 0.1	0.1 ± 0.1	3.1 ± 0.1

of the process. Losses in the cold part of beer production are mainly consequence of washing out aroma compounds by carbon dioxide and adsorption of the aroma compounds on the yeast cells. Nevertheless, oxidation and reaction between aroma compounds can lead to rise of concentration of these compounds. Dry hopping does not result in increased aroma intensity in all cases.

Funding Sources

This work was financially supported by the Slovenian Research Agency by grant 020-2/2011-3.

Abbreviations

HEOC – hop essential oil components, t_R – retention time

5. References

1. C. Almaguer, C. Schönberger, M. Gastl, K. E. Arendt, T. Becker, *Humulus lupulus* – a story that begs to be told. A review, *J. Inst. Brew.* **2014**, *120*, 289–314. DOI:10.1002/jib.160
2. K. Štěrba, P. Čejka, J. Čulík, M. Jurková, K. Krofta, M. Pavlovič, A. Mikyška, J. Olšovská, Determination of Linalool in different hop varieties using a new method based on fluidized – bed extraction with gas chromatographic mass spectrometric detection, *J. Am. Soc. Brew. Chem.* **2015**, *73*, 151–158. DOI:10.1094/ASBCJ-2015-0406-01
3. M. G. Malowicki, T. H. Shellhammer, Isomerization and degradation kinetics of hop (*Humulus lupulus*) acids in a model wort-boiling system, *J. Agric. Food Chem.* **2005**, *53*, 4434–4439. DOI:10.1021/jf0481296
4. T. Inui, F. Tsuchiya, M. Ishimaru, K. Oka, H. Komura, Different beers with different hops. Relevant compounds for their aroma characteristics, *J. Agric. Food Chem.* **2013**, *61*, 4758–64. DOI:10.1021/jf3053737
5. M. Schnaitter, A. Kell, H. Kollmannsberger, F. Schüll, M. Gastl, T. Becker, Scale-up of dry hopping trials: importance of scale for aroma and taste perceptions, *Chem. Ing. Tech.* **2016**, *88*, 1955–1965. DOI:10.1002/cite.201600040
6. N. Rettberg, M. Biendl, L. A. Garbe, Hop Aroma and Hoppy Beer Flavour: Chemical Background and Analytical Tools-A review, *J. Am. Soc. Brew. Chem.* **2018**, *76*, 151–158. DOI:10.1080/03610470.2017.1402574
7. L. Jelínek, M. Karabin, J. Müllerová, P. Dostálek, The secret of dry hopped beers-Review. *Kvasny Prum.* **2018**, *64*, 287–296. DOI:10.18832/kp201836
8. J. Dennenlöhner, S. Thörner, A. Manowski, N. Rettberg, Analysis of selected Hop Aroma Compounds in Commercial Lager and Craft Beers Using HS-SPME-GC-MS/MS. *J. Am. Soc. Brew. Chem.* **2019**. DOI:10.1080/03610470.2019.1668223
9. M. T. Roberts, J. P. Dufour, A. C. Lewis, Application of comprehensive multidimensional gas chromatography combined with time-of-flight mass spectrometry (GC/GC-TOFMS) for high resolution analysis of hop essential oil, *J. Sep. Sci.* **2004**, *27*, 473–478. DOI:10.1002/jssc.200301669
10. G. A. Fix, Wort Boiling in Principles of Brewing Science - a Study of Serious Brewing Issues 2nd ed., Brewers Publications, Boulder, USA, **1999**, pp. 53–78.
11. C. W. Bamforth, Science principles of malting and brewing, American Society of Brewing Chemists, St. Paul, **2006**.
12. M. Kovačević, M. Kač, Determination and verification of hop varieties by analysis of hop essential oils, *Food Chem.* **2002**, *77*, 489–494. DOI:10.1016/S0308-8146(02)00114-0
13. J. Hrivňák, D. Smogrovičová, P. Nádaský, J. Lakatošová, Determination of beer aroma compounds using headspace solid-phase microcolumn extraction, *Talanta*. **2010**, *83*, 294–296. DOI:10.1016/j.talanta.2010.08.041
14. G. C. da Silva, A. A. S. da Silva, L. S. N. Da Silva, R. L. D. O. Godoy, L.C. Nogouira, S.L. Quitério, R.S.L. Raices. Method development by GC-ECD and HS-SPME-GC-MS for beer volatile analysis, *Food Chem.* **2015**, *167*, 71–77. DOI:10.1016/j.foodchem.2014.06.033
15. C. Schmidt, M. Biendl, Headspace Trap GC-MS analysis of hop aroma compounds in beer, *Brewing Sci.* **2016**, *69*, 9–15.
16. T. Horak, J. Culik, V. Kellner, P. Čejka, D. Hašková, M. Jurková, J. Dvořák, Determination of selected beer flavours: Comparison of a stir bar sorptive extraction and a steam distillation procedure, *J. Ins. Brew.* **2011**, *117*, 617–621. DOI:10.1002/j.2050-0416.2011.tb00512.x
17. Destillationsanalyse (Referenzmethode – EBC – Methode), Brautechnischen Aanalysenmethoden Band II, 4. Auflage, MEBAK, Freising-Weihenstephan, **2002**, 76–78.
18. European Brewery Convention, Analytica EBC, section 9 – Beer, method 9.35, Analytica EBC, Fachverlag Hans Carl, Nürnberg, **2004**.
19. European Brewery Convention, Analytica EBC, section 9 – Beer, method 9.8, Analytica EBC, Fachverlag Hans Carl, Nürnberg, Germany **2004**.
20. European Brewery Convention, Analytica EBC, section 9 – Beer, method 9.28.3, Analytica EBC, Fachverlag Hans Carl, Nürnberg, **2007**.
21. European Brewery Convention, Analytica EBC, section 9 – Beer, Method 9.6, Analytica EBC, Fachverlag Hans Carl, Nürnberg, Germany, **2000**.
22. European Brewery Convention, Analytica EBC, section 7 – Hops, Method 7.10, Fachverlag Hans Carl GmbH, Nürnberg, Germany, **2002**.
23. European Brewery Convention, Analytica EBC, section 7 – Hops, Method 7.12, Fachverlag Hans Carl GmbH, Nürnberg, Germany, **2006**.
24. European Brewery Convention, Analytica EBC, section 7 – Hops, Method 7.4, Fachverlag Hans Carl GmbH, Nürnberg, Germany, **2000**.
25. Determination of Steam-volatile Aroma Compounds in Beer, method 2.23.6, MEBAK Wort, Beer, Beer-based Beverages, MEBAK, Freising, **2013**, pp. 405 – 412.
26. B. Jaskula, P. Kafarski, G. Aerts, L. De Cooman, A kinetic study of isomerization of Hop-acids, *J. Agric. Food Chem.* **2008**, *56*, 6408–6415. DOI:10.1021/jf8004965

27. Y. Huang, J. Tippmann, T. Becker, Kinetic modelling of hop acids during wort boiling. *Int. J. Biosci. Biochem. Bioinforma.* **2013**, *3*, 47–52.
28. S. Kappler, M. Krahl, C. Geissinger, T. Becker, M. Krottenhaler, Degradation of Iso- α -acids during wort boiling, *J. Ins. Brew.* **2010**, *116*, 332–338. DOI:10.1002/j.2050-0416.2010.tb00783.x
29. B. Jaskula Goiris, G. Aerts, L. De Cooman, Hop α -acids isomerization and utilisation: an experimental review, *Cerevisia.* **2010**, *6*, 57–70. DOI:10.1016/j.cervis.2010.09.004
30. T. Kishimoto, A. Wanikawa, K. Kono, K. Shibata, Comparison of the Odor-Active Compounds in Unhopped Beer and Beers Hopped with Different Hop Varieties, *J. Agric. Food Chem.* **2006**, *54*, 8855–8861. DOI:10.1021/jf061342c
31. K. Takoi, K. Koie, Y. Itoga, Y. Katayama, M. Shimase, Y. Nakayama, J. Watari, Biotransformation of Hop-Derived Monoterpene Alcohols by Lager Yeast and Their Contribution to the Flavor of Hopped Beer, *J. Agric. Food Chem.* **2010**, *58*, 5050–5058. DOI:10.1021/jf1000524
32. M. Coelhan, A. Aberl, Determination of Volatile Compounds in Different Hop Varieties by Headspace-Trap GC/MS In Comparison with Conventional Hop Essential Oil Analysis, *J. Agric. Food Chem.* **2012**, *60*, 2785–2792. DOI:10.1021/jf205002p
33. M. Riu-Aumatell, P. Miró, A. Serra-Cayuela, S. Buxaderas, F. Lopez-Tamames, Assessment of the aroma profiles of low-alcohol beers using HS-SPME-GC-MS, *Food Res. Int.* **2014**, *57*, 96–202. DOI:10.1016/j.foodres.2014.01.016
34. M. Steinhaus, P. Schieberle, Comparison of the most odor-active compounds in fresh and dried hopcones (*Humulus lupulus* L. variety Spalter Select) based on GC-olfactometry and odor dilution techniques, *J. Agric. Food Chem.* **2000**, *48*, 1776–1783. DOI:10.1021/jf990514l
35. S. Hanke, M. Herrmann, J. Ruckerl, C. Schönberger, W. Back, Hop Volatile Compounds (part II): Transfer Rates of Hop Compounds from Hop Pellets to Wort and Beer, *Brewing Sci.-Monatsschrift. Brauwiss.* **2008**, *61*, 140–144.

Povzetek

Edinstvena sestava eteričnega olja hmelja in grenkih smol je ključnega pomena za aromo, kar je pomembno za sprejemanje piva s strani potrošnikov. V tem poskusu je bilo isto pivo razdeljeno na štiri dele, vsak je bil hmeljen drugače. Za določitev dinamike hitrosti izomerizacije so bile izvedene kontinuirane meritve koncentracij alfa- izo-alfa-kislin. Prav tako so bile med postopkom merjene tudi koncentracije določenih komponent eteričnega olja hmelja, da bi razumeli dinamiko njihovega prehoda v pivo. Največji izkoristek izomerizacije alfa-kislin (18,1 %) je bil dosežen po 100 min varjenja pivine. Daljše vretje povečuje zmanjšanje koncentracij izo-alfa-kislin, kot tudi komponent eteričnega olja. Hladno hmeljenje vpliva ne le na aromo piva, ampak tudi na grenkobo.



Except when otherwise noted, articles in this journal are published under the terms and conditions of the Creative Commons Attribution 4.0 International License

Scientific paper

Low-level Electrochemical Analysis of Ketoconazole by Sepiolite Nanoparticles Modified Sensor in Shampoo Sample

Sevda Aydar,¹ Dilek Eskiköy Bayraktape,² Hayati Filik¹ and Zehra Yazan^{2,*}¹ Faculty of Engineering, Department of Chemistry, Istanbul University, 34320 Avcılar, Istanbul, Turkey² Ankara University, Faculty of Science, Chemistry Department, 06560 Ankara, Turkey

* Corresponding author: E-mail: zehrayazan67@gmail.com; zdurmus@science.ankara.edu.tr

Phone: +903122126720/1284 fax: +903122232395

Received: 07-11-2019

Abstract

In this study, the nano-sepiolite modified carbon paste electrode (CCPE) was prepared for the determination of ketoconazole (KC). The effects of pH, the proportion of the electrode modifier, deposition potential, and deposition time were investigated. Ketoconazole shows one irreversible oxidation peak at about the potential value of 0.6–0.7 V at different pH values. CV studies show that the modified electrode performed a catalytic effect on the peak signal of KC compared to the bare electrode. This catalytic behavior of CCPE was used for the development of a sensitive detection method. The impact of pH and scan rates on the anodic peak potentials and currents were examined, and the scan rate results show that the oxidation behavior of KC was controlled by the adsorption process at the CCPE surface. Therefore, adsorptive stripping differential pulse voltammetry (AdsDPV) and adsorptive stripping square wave voltammetry (AdsSWV) methods were developed for KC analysis. The two different linear ranges were obtained as (0.1–1.0) nM and (3.0–10.0) nM for AdsDPV, and (0.1–10.0) nM and (3.0–10.0) nM for AdsSWV, respectively. The detection (LOD) and quantification (LOQ) limits were found to be 0.017 nM and 0.056 nM for AdsDPV and 0.025 nM and 0.083 nM for AdsSWV, respectively. Besides, the proposed new sensor has obtained very high recovery values in the analysis of KC in the pharmaceutical shampoo.

Keywords: Ketoconazole; carbon paste electrode; sepiolite clay; pharmaceutical shampoo

1. Introduction

Ketoconazole is 1-acetyl-4-[4-[[[2RS,4SR)-2-(2,4-dichlorophenyl)-2-(1-*H*-imidazol-1-yl methyl)-1,3-dioxolan-4-yl] methoxy] phenyl] piperazine and an imidazole derivative.¹ Ketoconazole (KC) has a strong antifungal effect against many fungal, gram-positive microorganisms and yeasts. In addition, KC is used in oral administration as an antifungal drug due to its lower toxicity than most azole antimycotics.² The mechanism of action is caused by damage to the cytoplasmic membrane in the fungus and leads to the disruption of mitochondrial and microsomal enzymes of fungi. KC is used as an active component of antifungal formulations in creams, tablets, and anti-dandruff shampoos.³ KC can cause side effects such as urticaria, angioedema, leukopenia, hemolytic anemia, nausea, and thrombocytopenia.

Determination of ketoconazole due to its importance in biological fluids, pharmaceutical preparations,

and also cosmetic products appears to be worthwhile. Various methods have been developed for this purpose, including spectrophotometry,^{4–7} high-performance liquid chromatography,^{8–10} and liquid chromatography-triple quadrupole tandem mass spectrometry.¹¹ These methods are often time-consuming and require expensive equipment. Also, due to their low sensitivity, requiring pretreatment steps, such as extraction and separation steps are needed in an organic environment. Electrochemical methods can be considered for the detection of pharmaceutical and cosmetic drugs. Among them, adsorptive stripping voltammetry-based adsorption phenomena can be preferred for the electrochemical detection of pharmaceutical and cosmetic drugs in the terms of sensitivity, trace level analysis, and simplicity.^{12–15} Modification of electrode with nano-materials can be used for developing electrochemical nano-sensors.^{16,17} Electrode modification can

catalyze the electron transfer rate between the analyte and electrode. Sepiolite clay used as electrode modifier has ease of adsorption for the polar organic species and ions, imparts the electrical conductivity, and has a catalytic contribution to the electrochemical processes. As well, the intercalation and ion exchange capacity of sepiolite clay expands the sorption capacity and conductivity properties of the working electrodes.^{18,19}

Electrochemical sensors based on nano-sepiolite clay show trace limit of detection, higher effective surface area, conductivity, and adsorption capacity properties. In our previous studies, we have tried the sepiolite mineral alone and combined with other modifiers for inducing novel properties in carbon paste electrodes.^{12,19–21} In this regard, we have developed two different sensitive and selective adsorptive voltammetric stripping methods (AdsDPV and AdsSWV) for the determination of ketoconazole at sepiolite clay modified CPE. The developed methods were successfully applied to the determination of ketoconazole in shampoo samples containing ketoconazole. The developed AdsDPV and AdsSWV methods for determination of KC in a shampoo sample, compared to the other electroanalytical methods based on KC analysis in the cosmetic products^{1,22–24} have the widest linear working range and the lowest limit of detection.

2. Experimental

2.1. Reagents and Apparatus

Sepiolite clay, graphite powder, mineral oil, and all solvents were supplied from Sigma. Ketoconazole was also supplied from Sigma-Aldrich, and other used chemicals were analytical grade and used without a preliminary purification step. The stock solution of KC ($1.0 \cdot 10^{-3}$ M) was prepared by dissolving of KC in a few drops of 0.1 M HCl solution and water. The prepared stock solution was stored in the refrigerator at + 4 °C. 0.04 M Britton-Robinson buffer was used as the supporting electrolyte.

All electrochemical measurements (CV, SWV, DPV, and EIS) were performed by using CHI 660C (USA, Texas) and C3 cell stand (Bioanalytical Systems, Inc., USA, BASi) with a solid electrode unit. Ag/AgCl (in 3.0 M NaCl, BAS MF-2052) as reference electrode and platinum wire (BASi MW-1032) as auxiliary electrode were used for electrochemical measurements. CCPE and CPE sensors were selected as working electrodes. SEM photographs and EDX graphs were recorded by using Carl Zeiss AG, EVO[®]50 Series.

Before all assays, pH was measured with a HANNA Instruments HI2211 pH/ORPmeter. Double-distilled water was supplied *mp*MINIpure system. All assays were carried out at 25 °C.

AdsDPV and AdsSWV methods were used for the electrochemical determination of KC. For AdsDPV method, the device parameters were: amplitude: 0.05 V, pulse

width: 0.05 s, sample width: 0.0167 s, pulse period: 0.5 s. For AdsSWV; amplitude: 0.025 V, frequency 20 Hz, potential range: 0.2–0.8 V. For EIS: amplitude: 0.005 V, frequency range: 0.05– 10^5 Hz, and Nyquist plots were recorded under open circuit potential.

2.2. Sensor Preparation Procedure

30 mg of graphite powder and 10 μ L of mineral oil were mixed in a petri dish with a spatula to prepare CPE. Sepiolite clay and graphite powder were mixed to prepare CCP electrode and then mineral oil (10 μ L) was added. The mass ratios of the sepiolite clay in the mixture were changed between 3.3–10%. The electrical connection was provided by copper wire. The surface of the prepared sensors was smoothed with a smooth paper. Before each experiment, the surface cleaning process of modified CPE sensors was performed by washing with a water-ethanol mixture (1:1).

2.3. Analytical Procedure

KC ($1.0 \cdot 10^{-3}$ M) stock solution was used in all analyses. In all voltammetric methods, supporting electrolyte (0.04 M BR buffer pH 9.0) and KC stock solution were added to the electrochemical cell with a total volume of 10.0 mL. The CCPE, reference, and counter electrodes were immersed in the cell. After arranging all the electrode connections, the working solutions were purged with nitrogen gas (99.99% purity) to remove the oxygen and then the voltammograms were recorded in the potential window of 0.2 V–0.9 V by using AdsDPV and AdsSWV.

2.4. Shampoo Sample Preparation

The 0.5 g of Ketoral shampoo was weighed to produce the desired final concentration of the sample. After that, a few drops of 0.1 M HCl and a small amount of doubly distilled water were added. Then, the total volume of pure water to 100 mL was completed, and the solution was prepared to contain $1.9 \cdot 10^{-4}$ M KC. This mixture was incubated overnight at 4 °C to complete the dissolution of the KC. Appropriate volumes of the resulting solution were placed in the voltammetric cell containing 10.0 mL of BR buffer (pH 9.0), and voltammograms were recorded.

3. Results and Discussion

3.1. Surface Characterization of CPE and CCPE

The surface morphological studies of both bare CPE and sepiolite clay modified CPE (CCPE) were carried out using SEM and EDX measurements. The SEM photographs of CPE and CCPE show that the CCPE electrode

surface has a more porous structure than bare CPE surface (Fig. 1 a,b). Meanwhile, the EDX measurement was performed to confirm the elemental content of the bare CPE and sepiolite modified CPE (Fig.1 c, d). In Fig.1 c, only one peak is seen that belongs to the carbon (C) element in CP electrode and Fig.1 d shows four peaks that belong to the carbon (C), oxygen (O), magnesium (Mg), and silicon (Si), respectively. According to EDX plots and SEM measurements of the electrodes, it can be clearly said that sepiolite clay has remained successfully on the CPE surface.

Cyclic voltammetry (CV) and Electrochemical impedance spectroscopy (EIS) measurements were per-

formed using 5.0 mM $\text{Fe}(\text{CN})_6^{3-}/\text{Fe}(\text{CN})_6^{4-}$ in 0.1 M KCl solution to compare the electrochemical properties of CPE and CCPE (Fig.2 a, b). According to the obtained CV voltammograms in Fig.2a, the higher anodic and cathodic peak currents and the lower peak separation (ΔE_p) values were obtained at the CCPE electrode compared to CPE. Meanwhile, the Nyquist plots of the same electrode surfaces (Fig.2b) show that the charge transfer resistance (R_{ct}) (about 4000 ohms) of CCPE is smaller than the R_{ct} (about 7000 ohms) of CPE. CV and EIS results confirm that the sepiolite clay on the CPE surface provides an electrocatalytic effect on the electron transfer rate.

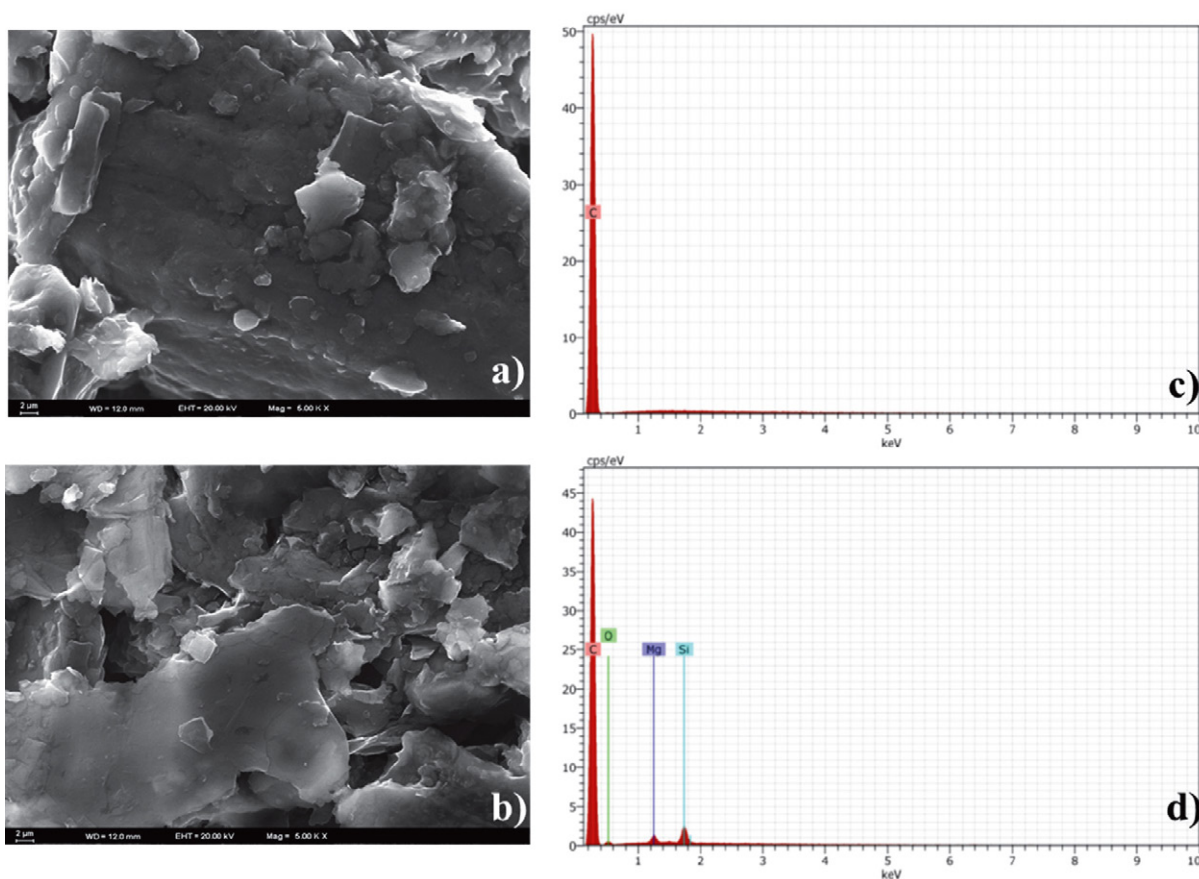


Figure 1. SEM images of CPE (a) and CCPE (b), EDX elemental mapping of CPE (c) and CCPE (d)

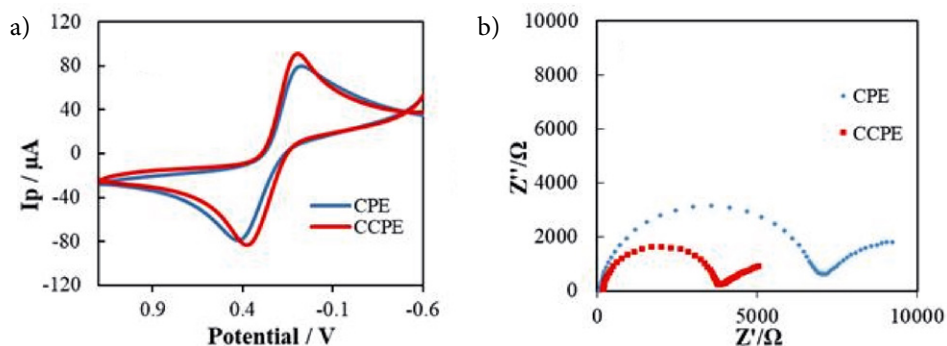


Figure 2. a) CV voltammograms b) Nyquist plots of CPE and CCPE in 5.0 mM $\text{Fe}(\text{CN})_6^{3-}/\text{Fe}(\text{CN})_6^{4-}$ in 0.1 M KCl solution.

3. 2. Optimization of Sepiolite Content

The optimum amount of sepiolite clay was determined to use in the preparation of the modified CCPE electrode. For this purpose, clay modified electrodes were prepared in such a way that the amount of sepiolite clay was 3.3%, 5.0%, 6.7%, 8.3%, and 10.0%. The signals were recorded using the CV method at a scan rate of 0.1 V/s in a BR buffer solution. The peak current of KC increased up to 6.7% and decreased sharply at the higher amount of sepiolite (Fig. 3). It indicates that 6.7% was the optimum amount of sepiolite concentration. The electrode based on nano-sepiolite clay shows the higher peak current as compared to bare CPE because of the high conductivity and catalytic effect to the electron-transfer rate of sepiolite clay.²⁰

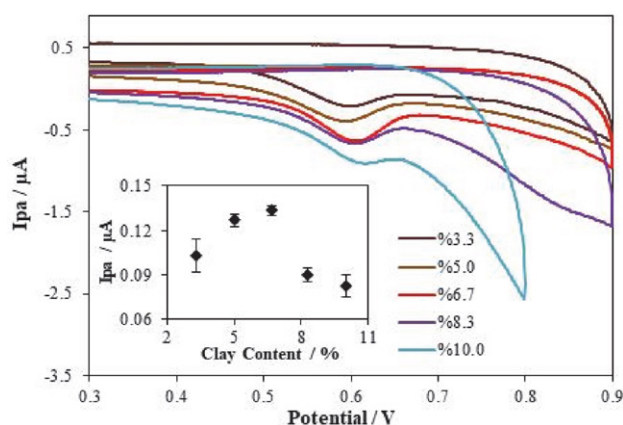


Figure 3. CVs of 1.0 μM KC in BR buffer solution on CCPE with different quantities of sepiolite clay (pH 9.0; scan rate: 0.10 V/s).

3. 3. Electrochemical Behavior of KC

The cyclic voltammograms of 1.0 μM KC demonstrated the oxidation signals of KC at 0.597 V and 0.582 V

potentials at CPE and CCPE electrodes in BR buffer solution (pH 9.0), respectively (Fig. 4). The CCPE sensor produced a better current response and sharper peak shapes compared to the bare electrode. The presence of sepiolite clay in the modified electrode improved the sensitivity of the method and the electro-catalytic effect on the redox signals of KC.

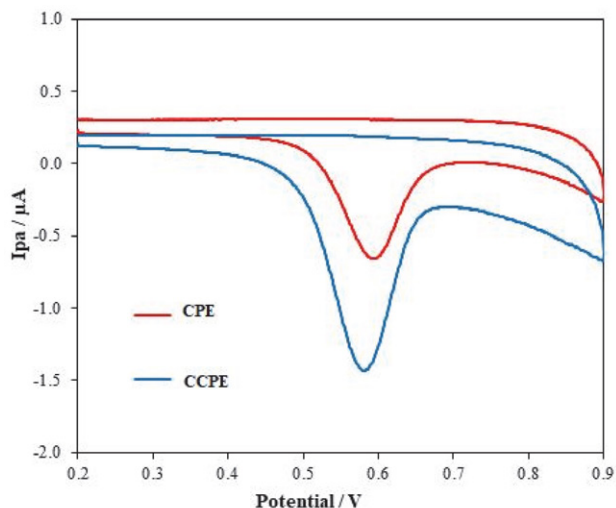


Figure 4. CVs of 1.0 μM KC at CPE and CCPE electrodes (v: 0.1 V/s, 0.04 M BR buffer, pH 9.0).

3. 4. Cyclic Voltammetric Studies

The effect of the scan rate on the redox properties of KC was investigated by using the CV method. For this purpose, cyclic voltammograms were recorded at scan rates in the range 0.005–0.4 V/s in the presence of $1.0 \cdot 10^{-6}$ M KC on scanning from 0.2 V to 0.9 V towards positive potential region on CCPE electrode (Fig. 5). These voltammograms were used for determining whether the electrochemical ox-

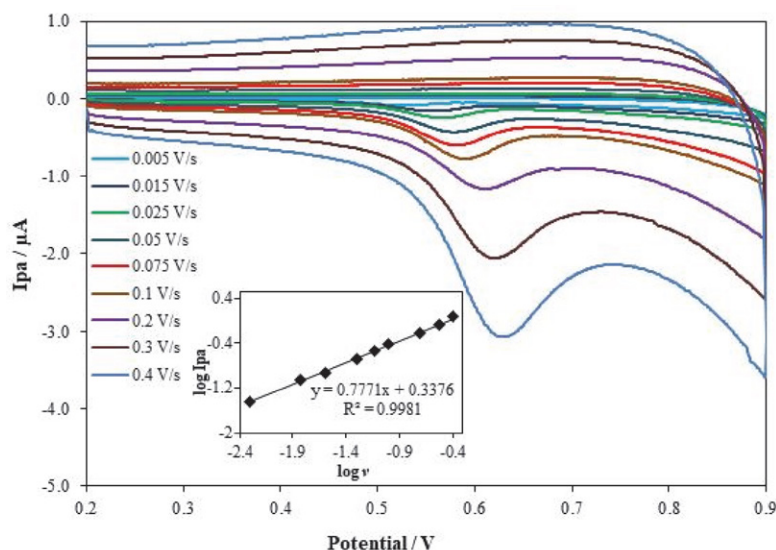


Figure 5. CVs of 1.0 μM KC with increasing scan rates in BR buffer at pH 9.0. Inset: $\log v$ - $\log I_p$ graph.

idation behaviors are reversible, irreversible, or quasi-reversible. As shown in Fig. 5, only one anodic peak at about 0.60 V was observed. No peak was observed in the reverse scan potentials. In addition, as the scan rate increased, the oxidation signal of KC is shifted to more positive potential values, and this phenomenon shows that the oxidation peak of KC exhibits irreversible redox behavior.³

To monitor the electrochemical process (adsorption or diffusion-controlled) of KC, we used CV technique. In this context, the $\log i_p - \log v$ graph was plotted, and the slope value of the $\log i_p - \log v$ graph is 0.78 for the oxidation peak of KC. According to this result, it can be said that the adsorption phenomenon is dominant in the electrochemical behavior of ketoconazole.^{2,22} The fact that pre- or post-peaks are observed in the cyclic voltammograms of KC at high scan rates is another indication that adsorption does occur on the electrode surface. I_p vs. $v^{1/2}$ graph is nonlinear, which indicates electrochemical reaction is not diffusion controlled.

3. 5. Influence of pH

The pH is a crucial parameter that can affect the peak currents and redox mechanism at the electrode surface in voltammetry. Therefore, the effect of pH on the peak current of KC was investigated by using the CV method. The oxidation peak currents of $1.0 \cdot 10^{-6}$ M KC were measured at different pH (2.0–12.0) to determine the optimum pH. Fig. 6. shows that the highest peak current was obtained at pH 9.0. This pH value was chosen to perform the electro-analytical study. To investigate the transferred electron number (n) in the electrooxidation of KC for the irreversible process, we used the following Eq. (1).²⁵

$$E_{pa} - E_{pa}/2 = \frac{47.7}{\alpha n} \quad (1)$$

Here, E_{pa} is anodic peak potential, $E_{pa}/2$ is the half peak potential, α is the electron transfer coefficient. The α is taken to be 0.5 for an irreversible process. In this study, the number of electrons transferred (n) was found to be 2.28. This result is in good accordance with the previously estimated number of electrons of KC at pH 9.0.²⁶ Therefore, the oxidation process of KC involves a two-electron transfer process, and the tentative oxidation peak of KC was attributed to the oxidation of the imidazole group with the loss of electrons to form the ketone structure.²⁶

3. 6. Optimization of Experimental Conditions for AdsDPV and AdsSWV Methods

Experimental conditions such as deposition potential and time are vital parameters affected by the electrochemical signal of organic compounds. For this purpose, deposition potentials were changed in the range 0.0–1.0 V for AdsDPV and AdsSWV methods (Fig. 7 A, C). This study has shown that 0.1 V and 0.4 V provided the highest peak current for AdsDPV and AdsSWV, respectively. Therefore, these deposition potentials were used in all subsequent experiments.

Similar trials for deposition time were evaluated in deposition time ranging from 0.0 to 180 s (keeping deposition potentials) (Fig. 7 B, D). It was observed that I_p values increase rapidly until 75 s, and then they decrease rapidly for AdsDPV method (Fig. 7B). The optimum value of deposition time was chosen as 75 s. Similarly, the deposition time where the highest peak current was observed was selected as 45 s for AdsSWV (Fig. 7D).

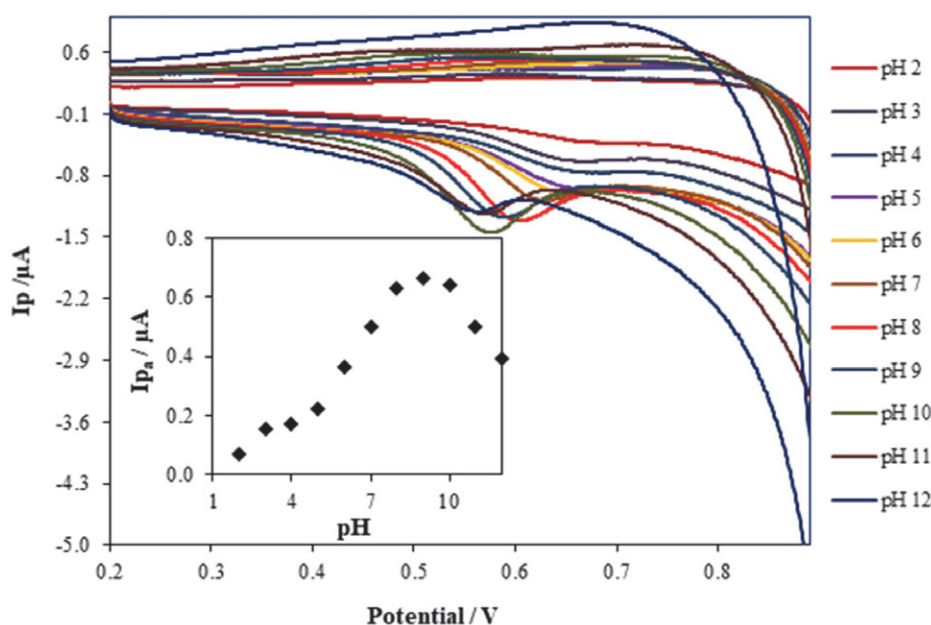


Figure 6. CVs of $1.0 \mu\text{M}$ KC in different pH values Inset: pH- i_p graph.

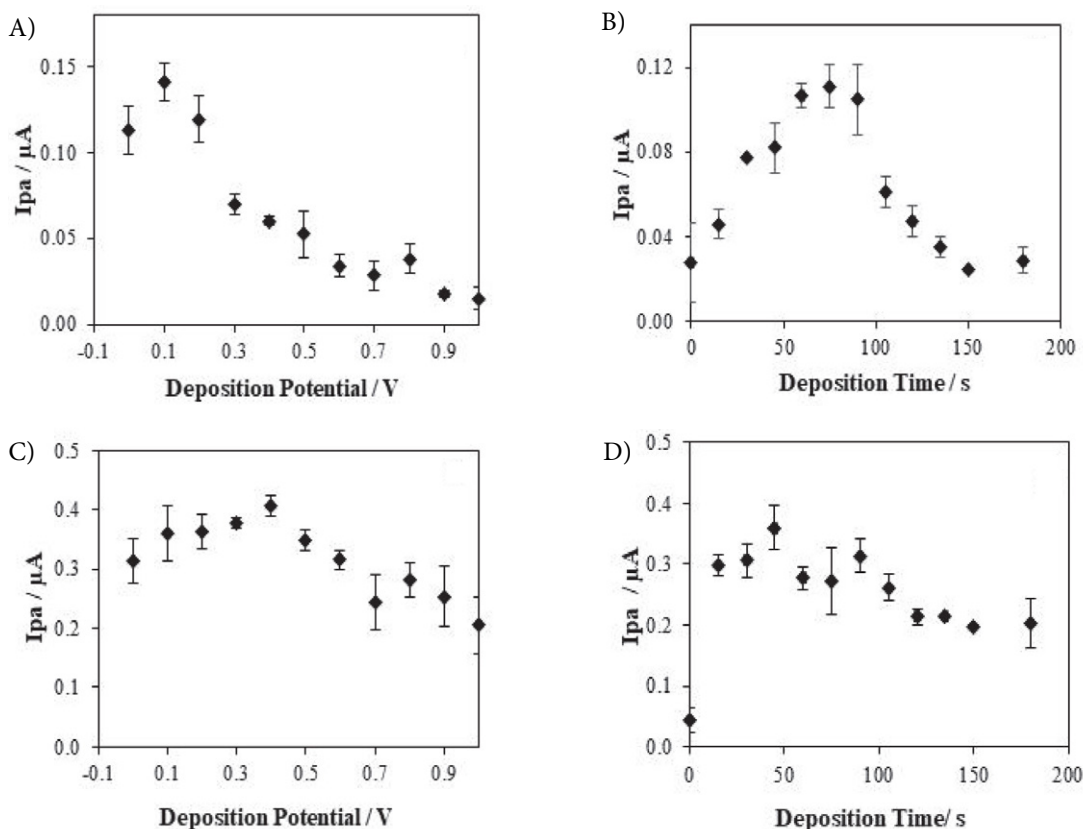


Figure 7. Effect of deposition potential and deposition time on peak current shown in AdsDPV method (A, B) and AdsSWV method (C, D) recorded in the presence of $1.0 \cdot 10^{-7}$ M KC at CCPE electrode in 0.04 M BR buffer pH 9.0.

3. 7. Calibration Studies and Validation of Optimized Methods

The applicability of AdsDPV and AdsSWV techniques as analytical methods for the analysis of KC was studied by measuring the anodic current as a function of the KC concentration. Calibration curves were constructed for both methods at pH 9.0. Considering the slopes of calibration graphs, the results obtained AdsDPV is more sensitive than by AdsSWV (Fig. 8A-B and Table 1). It was decided that the CCPE electrode could determine KC in the two different linear concentrations ranges of 0.1–1.0 nM and 3.0–10.0 nM for the AdsDPV and AdsSWV methods.

The following equations calculated the LOD and LOQ values:

$$\text{LOD} = \frac{3s}{m}, \quad \text{LOQ} = \frac{10s}{m} \quad (2)$$

Where, s is the standard deviation for the studied KC concentration ($1.0 \cdot 10^{-9}$ M), and m is the slope of the calibration chart.

The LOD and LOQ values for AdsDPV were 0.017 nM and 0.056 nM; the AdsSWV was 0.025 nM and 0.083 nM respectively (Table 1). A survey of the literature reveals

that LOD and LOQ values of KC are the lowest results so far.

AdsDPV and AdsSWV methods developed for KC determination on the CCPE electrode were compared to the results obtained by voltammetric methods in the literature (Table 2). The linear working range, LOD, and LOQ values obtained by the CCPE electrode were found to be superior to those reported methods.

The repeatability, reproducibility, and stability of the modified electrode were investigated. Reproducibility of peak current and potential values (intra-day and inter-day) were determined by using AdsSWV and AdsDPV methods. The percentage of relative standard deviation (%RSD) values is shown in Table 1. %RSD values are less than 5.0%. These results indicate excellent repeatability. However, the reproducibility of the CCPE sensor was tested using five different electrodes prepared on the same day. The %RSD values of reproducibility were calculated as 2.58% and 4.62% for AdsSWV and AdsDPV, respectively.

To investigate the stability of the CCPE sensor, we recorded the KC signals on different days. After the first ten days, it was found that the sensor signal retains 98.42% and 99.02% of the initial value. When the current and potential values of C oxidation signal obtained up to 40 days were examined, it was observed that peak current and potential values of KC decreased by 5.0% compared to its

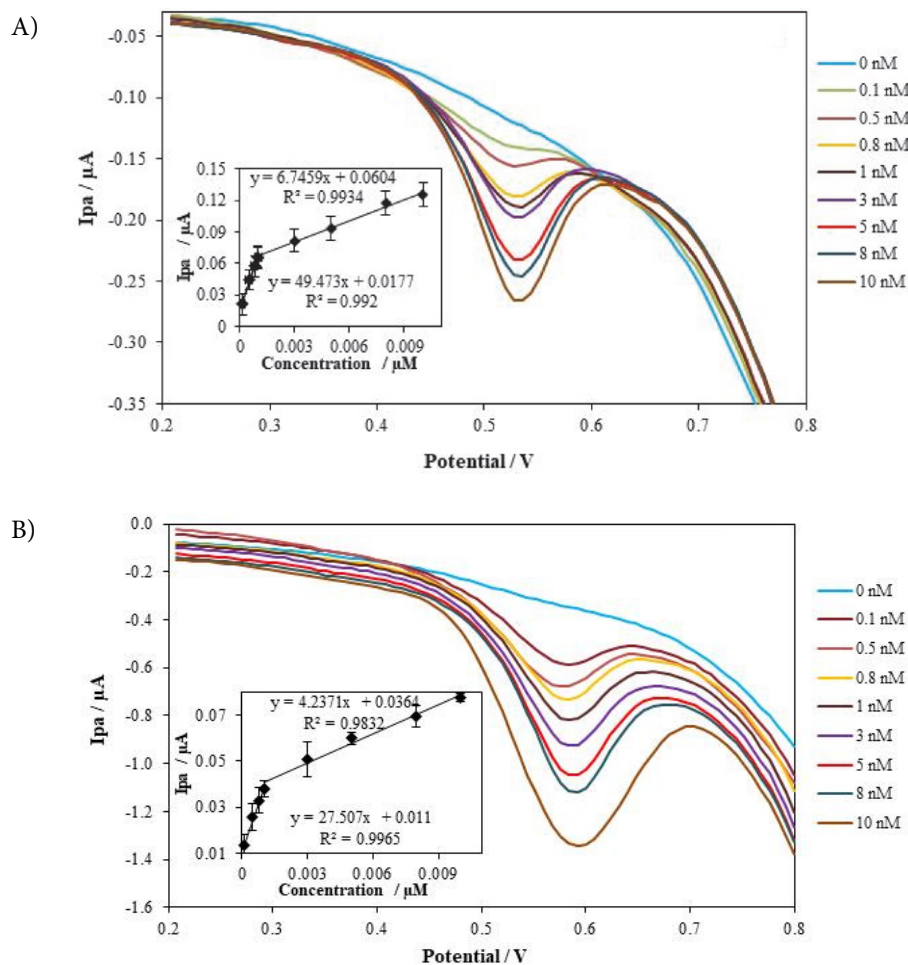


Figure 8. A. AdsDPV and B. AdsSWV voltammograms recorded in 0.04 M BR buffer (pH 9.0) for increasing KC concentrations under optimized conditions. Inset: Calibration graphs for KC.

Table 1. The statistical results of the regression analysis obtained with AdsSWV and AdsDPV methods at the CCPE electrode.

Regression parameters	CCPE	
	AdsSWV	AdsDPV
Potential, V	0.58	0.52
Linear working range, nM	0.1–1.0	0.1–1.0
	3.0–10.0	3.0–10.0
The slope of calibration graph, $\mu A/\mu M$	27.51	49.47
	4.35	6.75
The intercept of calibration graph, μA	0.011	0.018
	0.036	0.060
Limit of detection (LOD), nM	0.025	0.017
Limit of quantification (LOQ), nM	0.083	0.056
Regression coefficient (R^2)	0.997	0.992
	0.991	0.993
Repeatability of peak potential, RSD*% (intra-day)	0.76	0.68
Repeatability of peak potential, RSD*% (inter-day)	3.22	3.72
Repeatability of peak current, RSD*% (intra-day)	4.51	4.63
Repeatability of peak current, RSD*% (inter-day)	4.44	4.04
Reproducibility of peak current, RSD*%	2.58	4.62
Reproducibility of peak potential, RSD*%	0.83	0.82

*RSD is the relative standard deviation of 5 replications.

Table 2. The comparison of analytical data reported by some different electrochemical sensors with the CCPE sensor for KC analysis.

Sensor	Technique	Linearity range μM	LOD μM	Application	Reference
BDD	SWV	0.287–3.13	0.0829	Tablet	3
CDMGC	DPV	10.0–80.0	0.105	Shampoo	1
CPE	DPV	0.024–0.48	0.0233	Tablet, Cream	22
GCE	DPV	0.0001–1.0	0.00004	Tablet	27
Au disc electrode	DPV	50.0–2500	50.0	Tablet, Cream	23
AuNP/GCE		20.0–100.0	2.3	Shampoo	24
AuNPs/CPE	DPV, SWV	1.0–80.0	0.1	Tablet	26
CCPE	AdsDPV	0.0001–0.001 0.003–0.01	0.0168 nM	Shampoo	<i>This paper</i>
	AdsSWV	0.0001–0.001 0.003–0.01	0.0248 nM		

BDD: boron-doped diamond electrode; CDMGC: beta-cyclo-dextrin modified glassy carbon electrode; CPE: Carbon paste electrode; GCE: Glassy carbon electrode; AuNPs/GCE: Au nanoparticles modified glassy carbon electrode; AuNPs/CPE: Au nanoparticles modified carbon paste electrode

original values. According to this result, it can be said that the stability of the prepared clay CPE electrode is maintained for up to 40 days. The prepared sensor was kept at +4 °C after all experiments.

3. 8. Interferences

The interference effect of some electroactive species, which can be found in cream and drug substances, has been investigated in voltammetric AdsDPV and AdsSWV methods developed for the determination of KC. For this purpose, the concentration of Na^+ , Mg^{2+} , K^+ , Co^{2+} , Fe^{3+} , Cu^{2+} , Zn^{2+} , ascorbic acid, glucose, lactose, glycerin, and sodium benzoate was added to 100 times the concentration of KC. The percent changes in the peak current of KC in the presence of Na^+ , K^+ , Fe^{3+} , ascorbic acid, glucose, lactose, glycerin, and sodium benzoate was found to be less than 5% compared to its original signal. The obtained results indicate that these species did not have any interference effect. The results obtained in the presence of Mg^{2+} , Co^{2+} , Cu^{2+} , and Zn^{2+} showed that these species had a high interference effect in the electrochemical determination of KC. When these cations were added in the presence of KC, the oxidation peak of KC was observed to disappear. This result may be attributed to the formation of a complex between these metals and KC.^{28, 29}

3. 9. Real Sample Analysis and Recovery Studies

To determine the accuracy of the two methods developed, we performed a recovery study using a shampoo (Ketoral shampoo 2.0% KC). In Table 3, for AdsSWV and AdsDPV methods, the recovery values were found in the range of 99.5% to 110.4% indicating that the accuracy of the methods is really satisfactory.

To evaluate the accuracies and precisions of the two developed AdsDPV and AdsSWV methods, student *t*-test and *F*-test were applied to the data obtained from the recovery study. The results show that (Table 3) there are no meaningful differences in terms of accuracy and precision between these two methods.

4. Conclusions

This study demonstrates that the sepiolite clay modified carbon paste electrode was tested as a sensor for ketoconazole analysis. The ultra-sensitive detection of KC was carried out for the first time by using anodic adsorptive stripping methods. The effect of modifying agent combination, pH, deposition time, and potential values were in-

Table 3. Recovery results for KC in pharmaceutical shampoo (n=5)

Method	Added Amount, nM	Found Amount, nM	Average	Recovery, %	RSD, %	<i>t</i> -test	<i>F</i> -test
AdsSWV	3.0	3.3; 3.1; 2.3; 3.2; 3.1	2.98 ± 0.129	99.5	4.3	$t_{d1^*} = 1.80$ $t_{d2^*} = 0.57$ $t_{d3^*} = 1.89$	$F_{d1^*} = 1.50$ $F_{d2^*} = 3.06$ $F_{d3^*} = 2.42$
	5.0	5.1; 5.4; 5.3; 5.2; 5.0	5.23 ± 0.188	104.6	3.5		
	7.0	7.2; 7.6; 8.1; 7.3; 8.2	7.73 ± 0.438	110.4	5.6		
AdsDPV	3.0	3.1; 3.2; 2.3; 3.3; 3.1	3.14 ± 0.155	104.9	4.9	$t_{d1^*} = 1.80$ $t_{d2^*} = 0.57$ $t_{d3^*} = 1.89$	$F_{d1^*} = 1.50$ $F_{d2^*} = 3.06$ $F_{d3^*} = 2.42$
	5.0	5.2; 5.0; 5.3; 5.4; 4.7	5.13 ± 0.163	102.7	3.1		
	7.0	6.0; 7.9; 6.8; 6.9; 7.3	6.96 ± 0.591	99.42	8.4		

$t_k = 2.31$ (N-2 = 8 at 95% confidence level); $F_k = 6.39$ ($N_1-1 = 4$ and $N_2-1 = 4$ at 95% confidence level)

*1, 2 and 3 represent the data obtained at concentrations of 3.0, 5.0 and 7.0 nm, respectively.

vestigated for the determination of KC. The electrochemical determination of KC was successfully developed on the surface-modified electrode in the shampoo sample. No significant interference was found in the analysis of KC except for some cations. The linear working ranges, LOD, and LOQ values obtained by the developed methods were found to be superior to the methods in the literature. The acceptable recovery and low relative standard deviation data demonstrated that the accuracy and precision of the developed methods were satisfactory.

Acknowledgements

We gratefully acknowledge the financial support provided by Ankara University, Scientific Research Fund (Project number: 17H0430009).

5. References

1. M. El Ries, M. A. Ghany, L. Hussin, F. M. El-Anwar and A. Mohamed, *Bull. Fac. Pharm. Cairo Univ.* **2013**, *51*, 49–55. DOI:10.1016/j.bfopcu.2011.09.001
2. J. Borowiec, L. Wei, L. Zhu and J. Zhang, *Anal. Methods* **2012**, *4*, 444–448. DOI:10.1039/c2ay05615a
3. K. Mielech-Łukasiewicz and K. Rogińska, *Anal. Methods* **2014**, *6*, 7912–7922. DOI:10.1039/C4AY01421A
4. S. S. Rane and P. Padmaja, *J Pharm Anal* **2012**, *2*, 43–47. DOI:10.1016/j.jpba.2011.10.004
5. É. R. Kedor-Hackmann, M. M. Nery and M. I. R. Santoro, *Anal. Lett.* **1994**, *27*, 363–376. DOI:10.1080/00032719408001079
6. M. P. Vojić, G. Popović, D. Sladić and L. Pfindt, *J. Serb. Chem. Soc.* **2005**, *70*, 67–78. DOI:10.2298/JSC0501067V
7. S. Fraihat and K. Bahgat, *Trop J Pharm Res.* **2014**, *13*, 1511–1514. DOI:10.4314/tjpr.v13i9.18
8. O. Popovska, Z. Kavrakovski and V. Rafajlovska, *Curr Pharm Anal.* **2017**, *13*, 505–511. DOI:10.2174/1573412912666160610104703
9. S. H. Kim, A. Shrestha, N. H. Hoang, N. L. Huong and J. W. Park, *Anal. Lett.* **2014**, *47*, 1465–1475. DOI:10.1080/00032719.2013.874013
10. D. A. Hamdy and D. R. Brocks, *J Pharm Biomed Anal.* **2010**, *53*, 617–622. DOI:10.1016/j.jpba.2010.04.018
11. K. Wang, Y. Wu, Z. Chi, C. Shu, L. Li, J. Wei, L. Tao, P. Ma and L. Ding, *J Pharm Biomed Anal.* **2016**, *128*, 504–509. DOI:10.1016/j.jpba.2016.06.025
12. S. Aydar, D. E. Bayraktepe, H. Filik and Z. Yazan, *Acta Chim. Slov.* **2018**, *65*, 946–954. DOI:10.17344/acsi.2018.4615
13. P. T. Pinar, *Acta Chim. Slov.* **2020**, *67*, 212–220. DOI:10.17344/acsi.2019.5367
14. F. Öztürk, I. H. Taşdemir, D. A. Erdoğan, N. Erk, E. Kılıç, *Acta Chim. Slov.* **2011**, *58*, 830–839.
15. M. Á. Lorenzo, A. S. Arribas, M. Moreno, E. Bermejo, M. Chicharro and A. Zapardiel, *Microchem J.* **2013**, *110*, 510–516. DOI:10.1016/j.microc.2013.05.018
16. G. Xu, M. Zhang and X. Yu, *Acta Chimica Slovenica* **2018**, *65*, 502–511. DOI:10.17344/acsi.2017.3974
17. T. Dodevska, I. Shterev and Y. Lazarova, *Acta Chim. Slov.* **2018**, *65*, 970–979. DOI:10.17344/acsi.2018.4672
18. Z. Navrátilová and P. Kula, *Electroanalysis* **2003**, *15*, 837–846. DOI:10.1002/elan.200390103
19. M. Pekin, D. E. Bayraktepe and Z. Yazan, *Ionics* **2017**, *23*, 3487–3495. DOI:10.1007/s11581-017-2132-8
20. D. E. Bayraktepe, Z. Yazan and K. Polat, *J. Electroanal. Chem.* **2016**, *780*, 38–45. DOI:10.1016/j.jelechem.2016.08.035
21. D. E. Bayraktepe, T. Yanardağ, Z. Yazan and A. Aksüt, *Rev. Roum. Chim* **2015**, *60*, 287–295.
22. M. Shamsipur and K. Farhadi, *Electroanalysis* **2000**, *12*, 429–433. DOI:10.1002/(SICI)1521-4109(20000401)12:6<429::AID-ELAN429>3.0.CO;2-R
23. O. Gładysz, P. Łoś, B. Karolewicz and A. Górniak, *Int. J. Electrochem. Sci* **2016**, *11*, 1676–1690.
24. M. M. Alshalalfeh, M. Sohail, T. A. Saleh and M. A. Aziz, *Aust. J. Chem.* **2016**, *69*, 1314–1320. DOI:10.1071/CH16072
25. J. Wang, *Analytical Electrochemistry*, Wiley, New York, **2006**. DOI:10.1002/0471790303
26. T. A. Saleh, K. M. AlAqad and A. Rahim, *J. Mol. Liq.* **2018**, *256*, 39–48. DOI:10.1016/j.molliq.2018.02.006
27. T. Peng, Q. Cheng and C. F. Yang, *Fresenius J. Anal. Chem.* **2001**, *370*, 1082–1086. DOI:10.1007/s002160100773
28. E. Robles-Escajeda, A. Martínez, A. Varela-Ramirez, R. A. Sánchez-Delgado and R. J. Aguilera, *Cell Biol Toxicol* **2013**, *29*, 431–443. DOI:10.1007/s10565-013-9264-z
29. M. Navarro, E. J. Cisneros-Fajardo, T. Lehmann, R. A. Sánchez-Delgado, R. Atencio, P. Silva, R. Lira and J. A. Urbina, *Inorg. Chem.* **2001**, *40*, 6879–6884. DOI:10.1021/ic0103087

Povzetek

V predstavljeni študiji smo pripravili elektrodo iz ogljikove paste, modificirano z nano-sepiolitom (CCPE) in jo uporabili za določitev ketokonazola (KC). Raziskali smo vpliv pH, deleža elektrodnega modifikatorja, depozicijskega potenciala in časa depozicije. Ketokonazol daje samo en ireverzibilni oksidacijski vrh pri vrednosti potenciala okrog 0,6–0,7 V pri različnih vrednostih pH. CV študija je pokazala, da modificirana elektroda katalitsko učinkuje na maksimalni signal KC v primerjavi z golo elektrodo. To katalitsko obnašanje CCPE smo uporabili za razvoj občutljive metode detekcije. Raziskali smo vpliv pH in hitrosti preleta na maksimalni anodni potencial in tok. Rezultati za hitrost preleta kažejo, da je oksidacijsko obnašanje KC kontrolirano s procesom adsorpcije na površino CCPE. Zaradi tega smo za analizo KC razvili metodi adsorpcijske inverzne diferencialne pulzne voltometrije (AdsDPV) in adsorpcijske inverzne pravokotno-pulzne voltometrije (AdsSWV). Za AdsDPV smo dobili dve različni linearni območji: (0,1–1,0) nM in (3,0–10,0) nM, za AdsSWV pa (0,1–10,0) nM in (3,0–10,0) nM. Meje zaznave (LOD) in meje določitve (LOQ) smo določili kot 0,017 nM in 0,056 nM pri AdsDPV ter 0,025 nM in 0,083 nM pri AdsSWV. Predlagani novi senzor je dosegal zelo visoke izkoristke oz. točnost pri analizi KC v farmacevtskem šamponu.



Except when otherwise noted, articles in this journal are published under the terms and conditions of the Creative Commons Attribution 4.0 International License

Scientific paper

The Effect of Hydrogen Bonding and Azomethine Group Orientation on Liquid Crystal Properties in Benzylidene Aniline Compounds

Abdullah Hussein Kshash

Department of Chemistry, Education College for Pure Science, University Of Anbar, 31001, Ramadi, Anbar, Iraq

* Corresponding author: E-mail: fdrabdullahkshash@gmail.com

Tel: +964-7830818171

Received: 10-25-2019

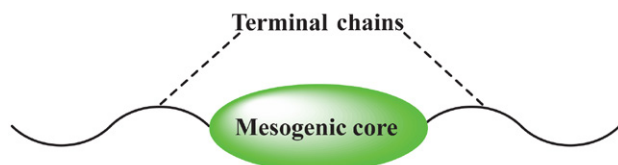
Abstract

This study examines the effects of substituents and hydrogen bonding, orientations of imine linkage on the behavior of benzylidene aniline compounds as liquid crystals (LC). Compounds 4-carboxy benzylidene-4-X-aniline (X = H, F, Cl, Br, CH₃, OCH₃) **1a–6a** were synthesized by the reaction of aniline and its substituted derivatives with 4-formylbenzoic acid. Compounds 4-X-benzylidene-4-carboxy aniline (X = H, F, Cl, Br, CH₃, OCH₃) **1b–6b** were synthesized by the reaction of benzaldehyde and its substituted derivatives with 4-aminobenzoic acid using absolute ethanol as the solvent. Synthesized compounds were characterized by FT IR and ¹H NMR spectroscopy, liquid crystal properties were investigated using differential scanning calorimetry (DSC) and polarizing optical microscopy (POM) techniques. Based on the mesomorphic properties, it was proven that the compounds **2b–4b** are dimorphic exhibiting a smectic and nematic phase, compounds **5b, 6b** are monomorphic exhibiting a nematic phase, while compounds **1a–6a** and **1b** have not shown any mesophase. For compounds **1a–6a** hydrogen bonding and reversing imine linkage (in comparison with compounds **1b–6b**) caused the absence of their mesomorphic properties.

Keywords: Benzylideneaniline, liquid crystals, hydrogen bonding, nematic phase, smectic phase, 4-formylbenzoic acid.

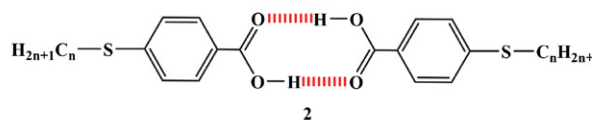
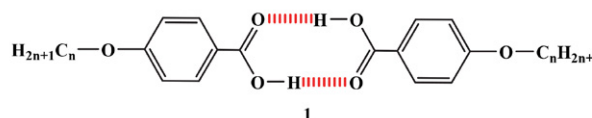
1. Introduction

Molecules of liquid crystals (LCs) with low molecular masses consist of a central core, generally containing phenyl rings linked by a double bond(s) and terminal groups such as alkyl and alkoxy chains, which promote molecular crystallinity and lower melting points.¹



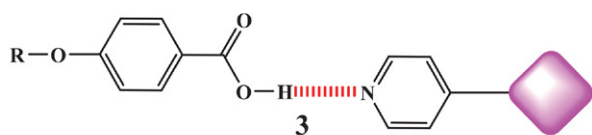
Hydrogen bonding is an intermolecular attractive interaction between the hydrogen atom of a molecule X–H, where H is less electronegative than X, and a Y atom that possesses one pair of electrons in the same or another molecule, therefore, hydrogen bond donor is X–H, and the acceptor is Y or a π-bond. Three-dots symbol (...) is usually used to depict the hydrogen bonding, such as X–

H...Y–Z, where both atoms X and Y could be F, O and N.^{2,3} The association of some molecules *via* hydrogen bonding enhances the mesogenic properties of these molecules by the formation of homodimers, heterodimers, and complex structures. The first enhancement was the homodimerization of *n*-alkoxybenzoic acids **1** and *n*-alkylthio benzoic acids **2** *via* hydrogen bonding and formation of a supramolecular nucleus.^{4,5}

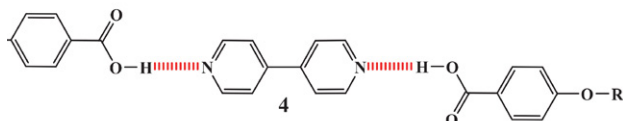


Heterodimerization can occur in different ratios to form supramolecular liquid crystals. For instance, heterocomplex **3** can be obtained in ratio 1:1 *via* the formation of

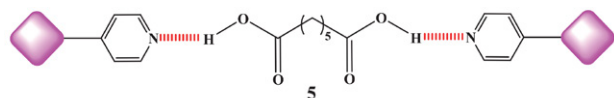
a single hydrogen bond (H...N) between 4-alkoxybenzoic acid and pyridine fragment.⁶



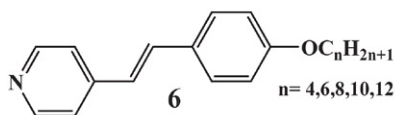
On the other hand, heterocomplex **4** is formed in ratio 2:1 *via* the formation of two hydrogen bonds between the bipyridyl fragment and two carboxylic acid molecules.⁷



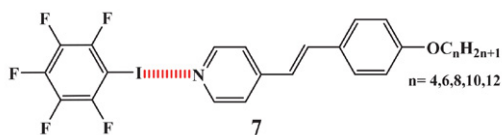
Inverted approaches of ratio 2:1 can also be found, such as in heterocomplex **5** between a dicarboxylic acid and two pyridine fragments.⁸



Halogen bonding is defined as an interaction between the halogen atom X and an electronegative atom A, which is generally depicted by the dotted line: D-X...A.⁹ The electron density around the halogen is polarized and distributed anisotropically and can additionally be amplified when halogen atom is bonded to an electron-withdrawing group.¹⁰ Nguyen and his colleagues reported that there are no mesomorphic properties of 4-alkoxy-4'-stilbazole **6**.



Nevertheless, the mixing of equimolar amounts of stilbazoles **6** and pentafluoriodobenzene can cause interactions between the nitrogen atom in the pyridine ring and the electronic iodine density by forming a halogen bond, that can also induce the formation of complex **7** which is exhibiting nematic and smectic phases.¹¹



Thus, the anisotropic complex formed by halogen bonding extends the rigid-rod motif for the molecule and induces liquid crystal properties.

Non-planar *N*-benzylidene aniline is the simplest compound of Schiff base structure; torsion angle for *N*-phenyl bond is around 55°, and about 10° for the benzylidene ring, so the π orbitals of azomethine group are

being more parallel to benzylidene ring than to the aniline ring¹² (Fig. 1).

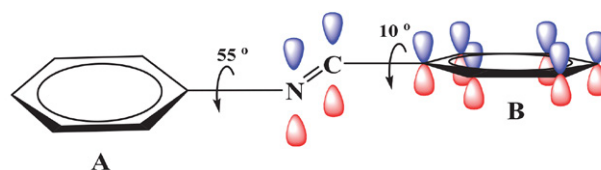


Figure 1. The torsion angle for benzylidene aniline compounds.

This study aims to investigate the influence of hydrogen bonding and the orientation of the imine linkage on liquid crystalline properties of the benzylidene aniline compounds, using 4-carboxy-benzylidene-4-*X*-aniline ($X-C_6H_4-N=CH-C_6H_4-COOH$) **1a–6a** and 4-*X*-benzylidene-4-carboxy-aniline ($X-C_6H_4-CH=N-C_6H_4-COOH$) **1b–6b** as models, where $X = H, F, Cl, Br, CH_3, OCH_3$.

2. Experimental Section

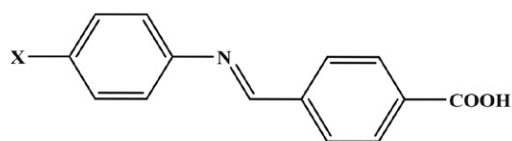
2.1. Material and Methods

All chemicals were purchased from Sigma-Aldrich. They were used without further purification. Infrared spectra were recorded as ATR using Bruker-Tensor 27 spectrometer. ¹H NMR spectra were recorded using Bruker 400 MHz spectrometer and DMSO-*d*₆ as the solvent. Measurements of phase transition temperatures were made using Mettler Toledo DSC 823 (DSC) at a heating rate of 10 °C min⁻¹, and POM equipped with hot stage.

2.2. Synthesis of Schiff Bases

To a 50 mL round-bottomed flask, that contains 20 mL of absolute ethanol, 7 mmol of aromatic aldehyde, and 5 drops of glacial acetic acid, was added 7 mmol of aromatic amine dissolved in 10 mL of absolute ethanol; the mixture was then refluxed for 3 h, thereafter cooled down to room temperature, the solid precipitate obtained was filtered, washed with cooled EtOH and recrystallized from EtOH.

The compounds of 4-carboxy benzylidene-4-*X*-aniline (Fig. 2) have been characterized as follows:



$X = H$ (**1a**), F (**2a**), Cl (**3a**), Br (**4a**), $-CH_3$ (**5a**), $-OCH_3$ (**6a**)

Figure 2. Molecular structure for compounds **1a–6a**.

4-Carboxybenzylideneaniline (1a).¹³ White solid, yield 82%; m.p. 219–221 °C, IR (ATR) cm⁻¹ 2500–3500 (O-H carboxylic acid), 3077 (C-H aromatic), 3032 (νH-CN), 1679 (C=O carboxylic acid), 1620 (ν C=N). ¹H NMR: δ

13.18 (s, 1H, H-15), 8.73 (s, 1H, H-8), 8.08 (d, $J = 8.1$ Hz, 2H, H-11, H-13), 8.06 (d, $J = 8.3$ Hz, 2H, H-3, H-7), 7.45 (t, $J = 7.7$ Hz, 2H, H-4, H-6), 7.32 (d, $J = 7.8$ Hz, 2H, H-10, H-14), 7.29 (t, $J = 7.3$ Hz, 1H, H-5).

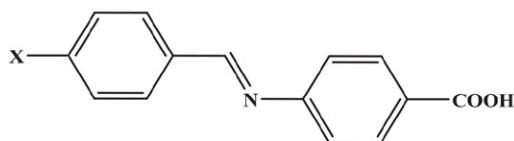
4-Carboxybenzylidene-4-fluoroaniline (2a). Pale yellow solid, yield 65%; m.p. 230–232 °C, IR (ATR) cm^{-1} 2500–3500 (O-H carboxylic acid), 3057 (C-H aromatic), 3031 (vH-CN), 1675 (C=O carboxylic acid), 1620 (v C=N). ^1H NMR: δ 13.18 (s, 1H, H-15), 8.74 (s, 1H, H-8), 8.08 (d, $J = 8.1$ Hz, 2H, H-11, H-13), 8.05 (d, $J = 8.1$ Hz, 2H, H-3, H-7), 7.28 (t, $J = 8.6$ Hz, 2H, H-4, H-6), 7.40 (m, 2H, H-10, H-14).

4-Carboxybenzylidene-4-chloroaniline (3a). Pale yellow solid, yield 69%; m.p. 235–237 °C, IR (ATR) cm^{-1} 2500–3500 (O-H carboxylic acid), 3064 (C-H aromatic), 3033 (vH-CN), 1675 (C=O carboxylic acid), 1620 (v C=N). ^1H NMR: δ 13.24 (s, 1H, H-15), 8.75 (s, 1H, H-8), 8.08 (d, $J = 8.4$ Hz, 2H, H-11, H-13), 7.50 (d, $J = 8.2$ Hz, 2H, H-3, H-7), 8.06 (d, $J = 8.1$ Hz, 2H, H-4, H-6), 7.36 (d, $J = 8.4$ Hz, 2H, H-10, H-14).

4-Carboxybenzylidene-4-bromoaniline (4a). Pale yellow solid, yield 74%; m.p. 266–268 °C, IR (ATR) cm^{-1} 2500–3500 (O-H carboxylic acid), 3061 (C-H aromatic), 3034 (vH-CN), 1680 (C=O carboxylic acid), 1621 (v C=N). ^1H NMR: δ 13.23 (s, 1H, H-15), 8.74 (s, 1H, H-8), 8.07 (d, $J = 8.7$ Hz, 2H, H-11, H-13), 7.63 (d, $J = 8.2$ Hz, 2H, H-3, H-7), 8.05 (d, $J = 8.2$ Hz, 2H, H-4, H-6), 7.29 (d, $J = 8.2$ Hz, 2H, H-10, H-14).

4-Carboxybenzylidene-4-methylaniline (5a). Pale yellow solid, yield 82%; m.p. 238–240 °C, IR (ATR) cm^{-1} 2500–3500 (O-H carboxylic acid), 3078 (C-H aromatic), 3028 (vH-CN), 1679 (C=O carboxylic acid), 1621 (v C=N). ^1H NMR: δ 13.23 (s, 1H, H-15), 8.73 (s, 1H, H-8), 8.14 (d, $J = 8.0$ Hz, 2H, H-11, H-13), 8.07 (d, $J = 8.3$ Hz, 2H, H-3, H-7), 8.03 (d, $J = 6.0$ Hz, 2H, H-4, H-6), 8.04 (d, $J = 5.9$ Hz, 2H, H-10, H-14), 2.34 (s, 3H, CH_3).

4-Carboxybenzylidene-4-methoxyaniline (6a). Pale yellow solid, yield 82%; m.p. 212–214 °C, IR (ATR) cm^{-1} 2500–3500 (O-H carboxylic acid), 3076 (C-H aromatic), 3032 (vH-CN), 1682 (C=O carboxylic acid), 1619 (v C=N). ^1H NMR: δ 12.63 (s, 1H, H-15), 8.74 (s, 1H, H-8), 8.06 (d, $J = 8.0$ Hz, 2H, H-11, H-13), 7.36 (d, $J = 8.3$ Hz, 2H, H-3, H-7), 7.01 (d, $J = 8.4$ Hz, 2H, H-4, H-6), 8.02 (d, $J = 7.9$ Hz, 2H, H-10, H-14), 3.79 (s, 3H, OCH_3).



X = H (**1b**), F (**2b**), Cl (**3b**), Br (**4b**), $-\text{CH}_3$ (**5b**), $-\text{OCH}_3$ (**6b**)

Figure 3. Molecular structures for compounds **1b–6b**.

The compounds of 4-X-benzylidene-4-carboxyaniline (Fig. 3) were characterized as follows:

Benzylidene-4-carboxyaniline (1b). Pale yellow solid, yield 71%; m.p. 194.8 °C, IR (ATR) cm^{-1} 2500–3500 (O-H carboxylic acid), 3068 (C-H aromatic), 3031 (vH-CN), 1677 (C=O carboxylic acid), 1622 (v C=N). ^1H NMR: δ 12.83 (s, 1H, H-15), 8.65 (s, 1H, H-8), 7.97 (d, $J = 8.3$ Hz, 2H, H-11, H-13), 7.56 (d, $J = 7.5$ Hz, 2H, H-3, H-7), 7.37–7.30 (m, 2H, H-4, H-6), 7.58 (d, $J = 8.1$ Hz, 2H, H-10, H-14), 7.37–7.30 (m, 1H, H-5).

4-Fluorobenzylidene-4-carboxyaniline (2b). Pale yellow solid, yield 88%; m.p. 249 °C, IR (ATR) cm^{-1} 2500–3500 (O-H carboxylic acid), 3071 (C-H aromatic), 3019 (vH-CN), 1678 (C=O carboxylic acid), 1625 (v C=N). ^1H NMR: δ 12.35 (s, 1H, H-15), 8.64 (s, 1H, H-8), 7.99 (d, $J = 8.5$ Hz, 2H, H-11, H-13), 7.32 (d, $J = 8.0$ Hz, 2H, H-3, H-7), 7.45 (t, $J = 8.6$ Hz, 2H, H-4, H-6), 7.62 (d, $J = 8.2$ Hz, 2H, H-10, H-14).

4-Chlorobenzylidene-4-carboxyaniline (3b). Pale yellow solid, yield 79%; m.p. 270.4 °C, IR (ATR) cm^{-1} 2500–3500 (O-H carboxylic acid), 3073 (C-H aromatic), 3013 (vH-CN), 1677 (C=O carboxylic acid), 1624 (v C=N). ^1H NMR: δ 12.38 (s, 1H, H-15), 8.66 (s, 1H, H-8), 7.98 (d, $J = 8.1$ Hz, 2H, H-11, H-13), 7.33 (d, $J = 7.6$ Hz, 2H, H-3, H-7), 7.93 (d, $J = 8.0$ Hz, 2H, H-4, H-6), 7.61 (d, $J = 7.9$ Hz, 2H, H-10, H-14).

4-Bromobenzylidene-4-carboxyaniline (4b). Pale yellow solid, yield 80%; m.p. 289 °C, IR (ATR) cm^{-1} 2500–3500 (O-H carboxylic acid), 3070 (C-H aromatic), 3018 (vH-CN), 1679 (C=O carboxylic acid), 1621 (v C=N). ^1H NMR: δ 12.33 (s, 1H, H-15), 8.66 (s, 1H, H-8), 7.99 (d, $J = 8.1$ Hz, 2H, H-11, H-13), 7.34 (d, $J = 8.0$ Hz, 2H, H-3, H-7), 7.91 (d, $J = 8.1$ Hz, 2H, H-4, H-6), 7.62 (d, $J = 8.2$ Hz, 2H, H-10, H-14).

4-Methylbenzylidene-4-carboxyaniline (5b). Pale yellow solid, yield 74%; m.p. 256.2 °C, IR (ATR) cm^{-1} 2500–3500 (O-H carboxylic acid), 3070 (C-H aromatic), 3032 (vH-CN), 1678 (C=O carboxylic acid), 1627 (v C=N). ^1H NMR: δ 12.50 (s, 1H, H-15), 8.59 (s, 1H, H-8), 7.98 (d, $J = 8.1$ Hz, 2H, H-11, H-13), 7.35 (d, $J = 7.7$ Hz, 2H, H-3, H-7), 7.31 (d, $J = 8.0$ Hz, 2H, H-4, H-6), 7.86 (d, $J = 7.7$ Hz, 2H, H-10, H-14), 2.39 (s, 3H, CH_3).

4-Methoxybenzylidene-4-carboxyaniline (6b). Pale yellow solid, yield 72%; m.p. 289 °C, IR (ATR) cm^{-1} 2500–3500 (O-H carboxylic acid), 3063 (C-H aromatic), 3030 (vH-CN), 1678 (C=O carboxylic acid), 1626 (v C=N). ^1H NMR: δ 12.61 (s, 1H, H-15), 8.55 (s, 1H, H-8), 7.97 (d, $J = 8.2$ Hz, 2H, H-11, H-13), 7.29 (d, $J = 8.1$ Hz, 2H, H-3, H-7), 7.09 (d, $J = 8.3$ Hz, 2H, H-4, H-6), 7.91 (d, $J = 8.2$ Hz, 2H, H-10, H-14), 3.85 (s, 3H, OCH_3).

3. Results and Discussion

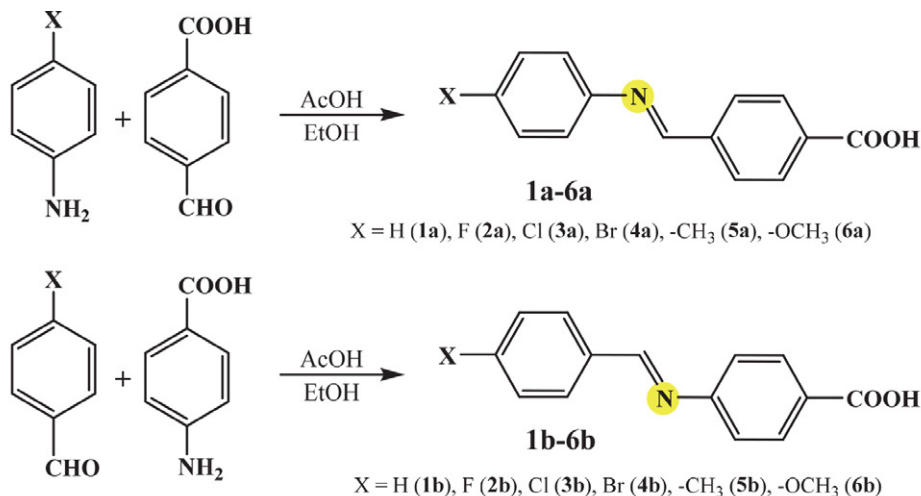
3. 1. Synthesis

Target Schiff bases were synthesized by the condensation reactions of aromatic aldehydes and aromatic amines using absolute ethanol as the solvent and glacial acetic acid as the catalyst. Compounds **1a–6a** were synthesized by the reaction of 4-formylbenzoic acid with 4-sub-

stituted aniline. Compounds **1b–6b** were synthesized by the reaction of 4-amino benzoic acid with 4-substituted benzaldehyde (Scheme 1).

3. 2. Characterization

FT IR spectra for compounds **1a–6a** and **1b–6b** showed the absence of NH₂ group stretching vibration



Scheme 1. Synthetic route for compounds **1a–6a** and **1b–6b**.

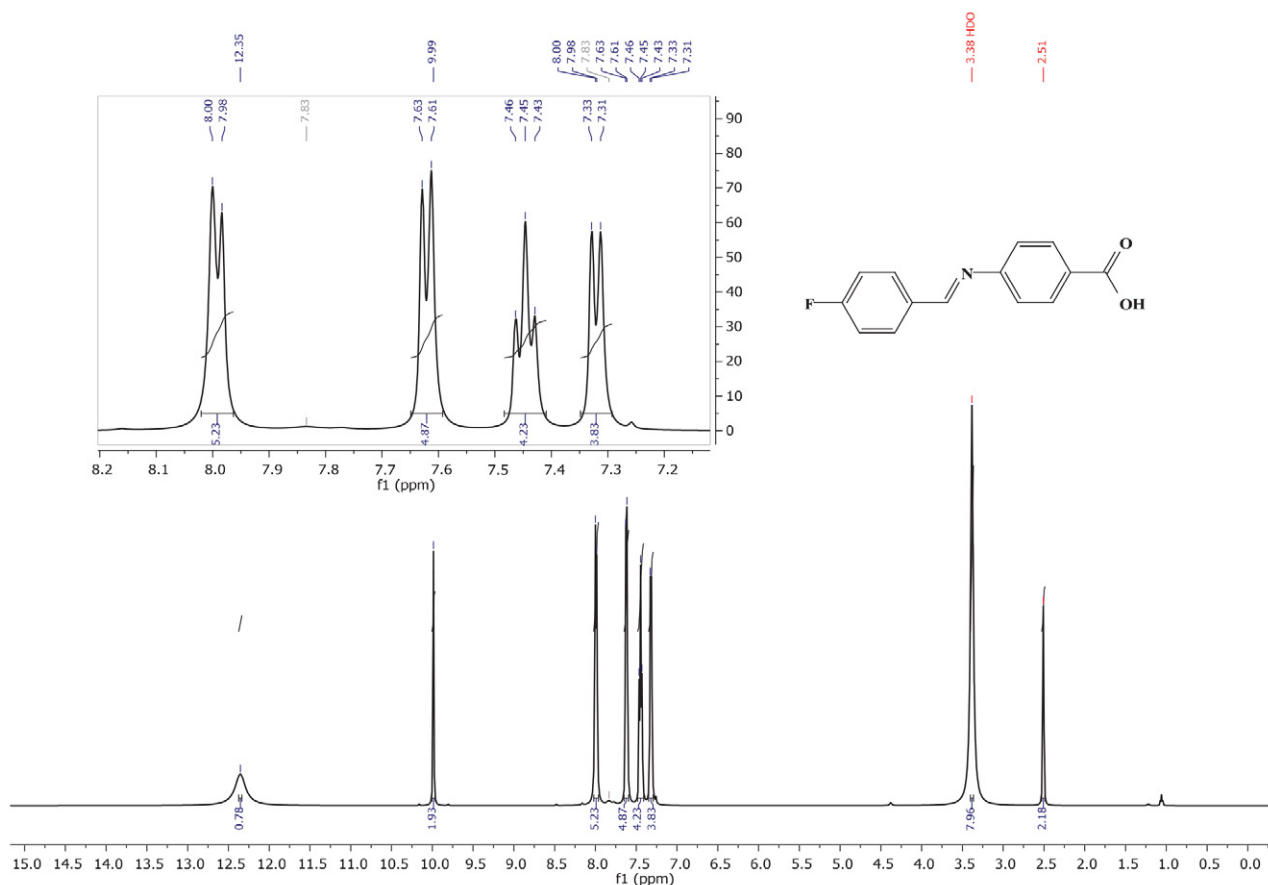


Figure 4. ¹H NMR spectrum of compound **2b**.

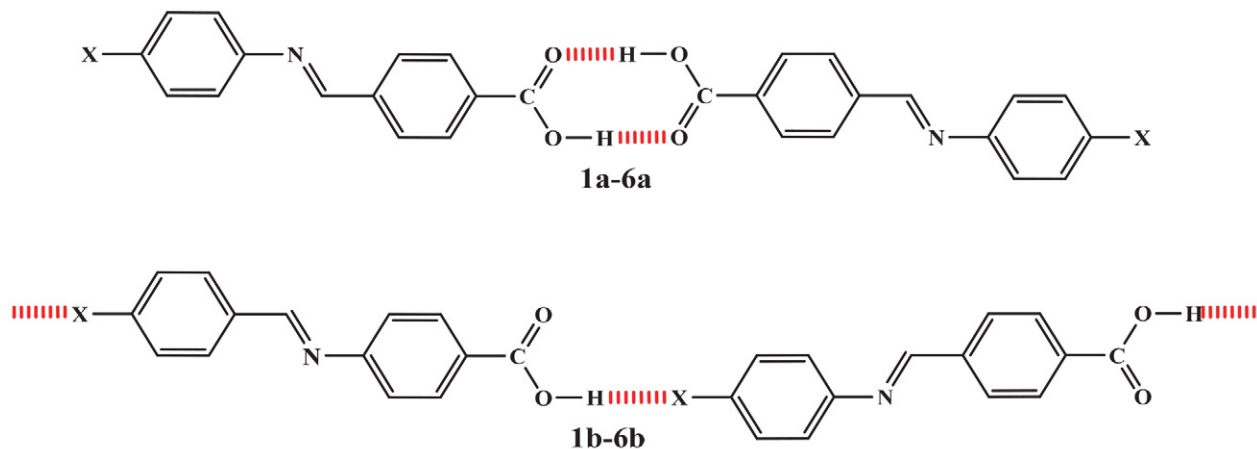


Figure 5. A schematic of the hydrogen bond in compounds **1a–6a** and **1b–6b**.

bands for aromatic amine and $\nu\text{C}=\text{O}$ group absorption band for aromatic aldehyde. FT IR spectra for compounds **1a–6a** revealed a broad absorption within the range $2500\text{--}3500\text{ cm}^{-1}$ which is attributable to the O–H group, medium absorption within the range $3057\text{--}3078\text{ cm}^{-1}$ attributable to the aromatic C–H, strong absorption band within the range $1675\text{--}1682\text{ cm}^{-1}$ attributable to the C=O group of carboxylic acid, and absorption within the range $1619\text{--}1621\text{ cm}^{-1}$ for the C=N group. FT IR spectra for compounds **1b–6b** showed the appearance of a broad absorption band within the range $2500\text{--}3500\text{ cm}^{-1}$ attributable to the O–H group, an absorption band within a range $3063\text{--}3073\text{ cm}^{-1}$ that was attributable to aromatic C–H, and a strong absorption band within the range $1677\text{--}1679\text{ cm}^{-1}$ that was attributable to C=O group of carboxylic acid, besides absorption band for C=N group observed within the range $1621\text{--}1627\text{ cm}^{-1}$. Further identification for Schiff bases was performed using ^1H NMR, spectra of compounds **1a–6a** were comprised of a singlet signal within the range $12.63\text{--}13.24\text{ ppm}$ attributed to the proton of the hydroxyl group (–COOH); a singlet signal at the down-field region within the range $8.73\text{--}8.75\text{ ppm}$ which evidenced the presence of the proton of the azomethine group ($\text{H}\text{--C}=\text{N}$) and several different signals within the range $7.01\text{--}8.14\text{ ppm}$ which are ascribed to aromatic protons. ^1H NMR spectra for compounds **1b–6b** showed a singlet signal within the range $12.35\text{--}12.83\text{ ppm}$ which is ascribed to the proton of the hydroxyl group (–COOH); a singlet signal within the range $8.55\text{--}8.66\text{ ppm}$ which was attributed to the proton of the azomethine group ($\text{H}\text{--C}=\text{N}$); and several signals within the range $7.29\text{--}7.99\text{ ppm}$ which were attributed to aromatic protons. The ^1H NMR spectrum for compound **2b** is shown in Fig. 4 as a representative illustration.

Chemical shift values ($12.63\text{--}13.24\text{ ppm}$) for the proton of the hydroxyl group in compounds **1a–6a** suggest that these compounds tend to form stabilized dimers by hydrogen bonding between carboxyl groups, while the chemical shift values ($12.63\text{--}13.24\text{ ppm}$) for

compounds **1b–6b** suggest that these compounds prefer to form weak hydrogen bonds between the carboxyl group and terminal substituent groups on the benzylidene ring (Fig. 5).

3. 3. A Study of the Mesomorphic Properties of the Synthesized Compounds

Polarised optical microscopy and differential scanning calorimetry were used to study the mesomorphic properties of synthesized compounds, employing careful monitoring by POM during heating and cooling scans and subsequently verified by the DSC measurements. The results showed that there are no mesomorphic properties for compounds **1a–6a**, owing to spontaneous carboxylic dimerization *via* intermolecular hydrogen bonding and weakness in the lateral attractive force (Fig. 5). On the other hand, it was found that the melting points of these compounds increase as the terminal halogen atom size increased (Fig. 6).

Mesomorphic properties of synthesized compounds **1b–6b** were investigated by DSC and POM and the measurements were very similar. Transition temper-

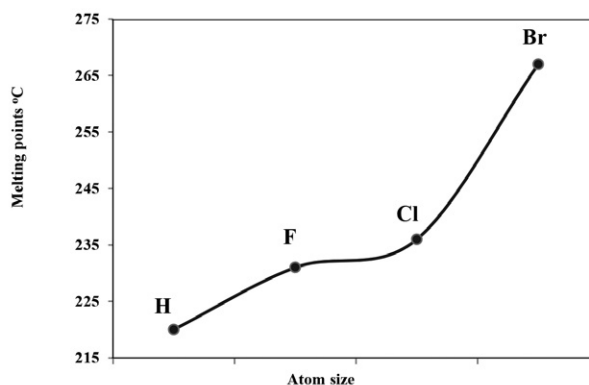


Figure 6. The dependence of melting points on the size of substituent atoms.

Table 1. Mesomorphic data and structures for compounds 1b–6b

Comp.	Transition	Peak temp. °C	DT_{Sm}	DT_N	ΔH (kJ mol ⁻¹)	ΔH (J mol ⁻¹ K ⁻¹)
1b	Cr-I	197.4	–	–	–	–
	Cr-Sm	166			0.2531	0.5766
2b	Sm-N	197.7	31.7	70.6	7.7838	16.5365
	N-I	268.3			9.1891	16.9760
3b	Cr-Sm	224			1.5491	3.1166
	Sm-N	263.5	39.5	14.5	2.8153	5.2475
	N-I	278			2.5721	4.6680
4b	Cr-Sm	225.2			1.4613	2.9332
	Sm-N	247.9	22.7	28.1	1.0373	1.9913
5b	N-I	276			0.8338	1.5186
	Cr-N	242.1		24.2	7.3093	14.1900
6b	N-I	266.3			7.3193	13.5718
	Cr-N	202.9		88.9	8.7821	18.4535
	N-I	291.8			1.0423	1.8454

atures and associated ΔH , ΔS are listed in Table 1. The investigation revealed no mesomorphic behavior for compound 1a, whereas, compounds 2b–4b were dimorphic exhibiting smectic and nematic phase, furthermore, compounds 5b and 6b were monomorphic exhibiting nematic phase. Smectic mosaic and nematic Schlieren textures were observed during POM investigation, optical photomicrographs are shown in Fig. 7 and the DSC

thermogram of 6b is shown in Fig. 8 as a representative illustration.

3. 5. Influence of Reverse Imine Linkage on Mesomorphic Properties

Despite the structural similarity of compounds 1a–6a and 1b–6b, the mesomorphic properties are quite

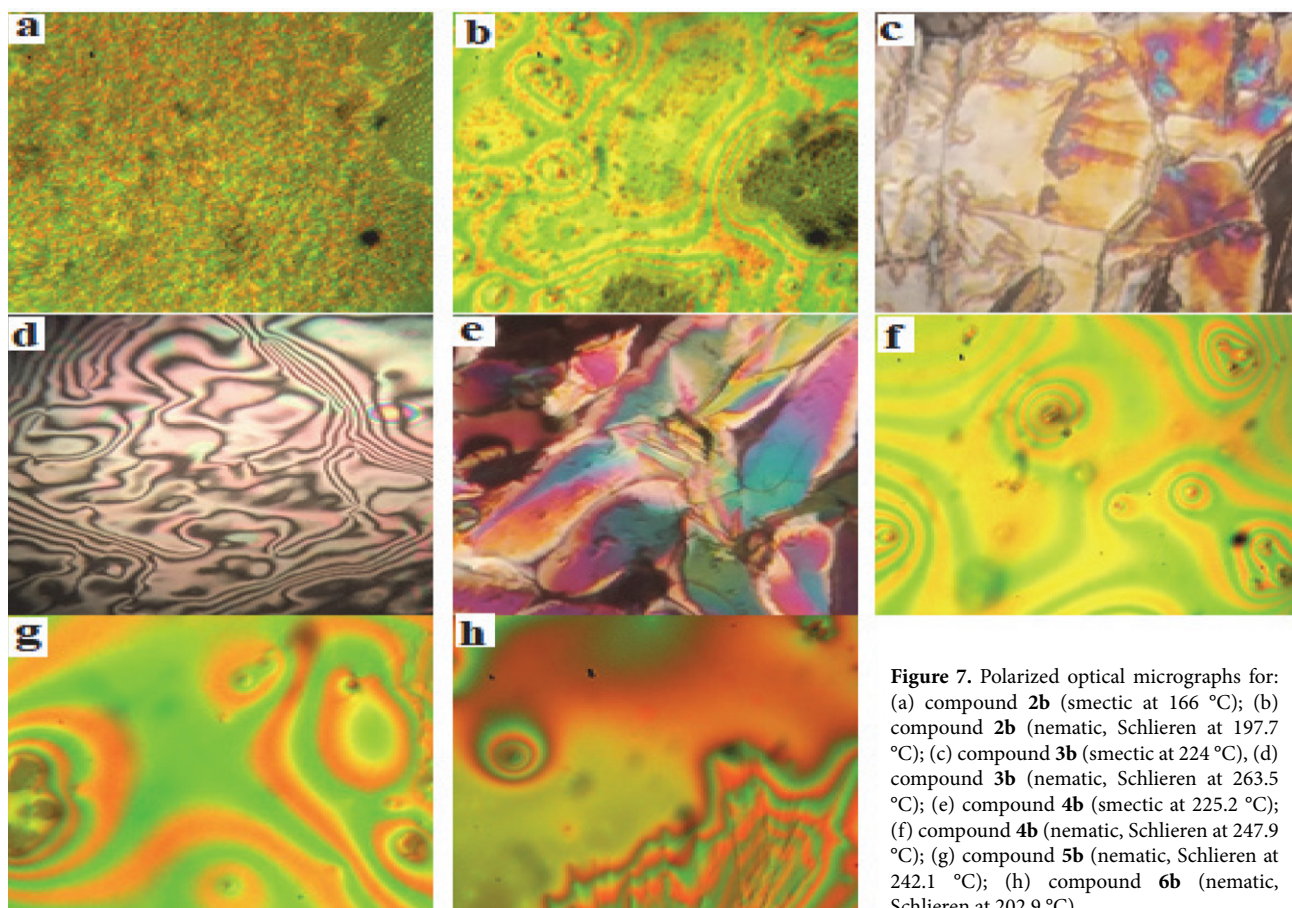


Figure 7. Polarized optical micrographs for: (a) compound 2b (smectic at 166 °C); (b) compound 2b (nematic, Schlieren at 197.7 °C); (c) compound 3b (smectic at 224 °C), (d) compound 3b (nematic, Schlieren at 263.5 °C); (e) compound 4b (smectic at 225.2 °C); (f) compound 4b (nematic, Schlieren at 247.9 °C); (g) compound 5b (nematic, Schlieren at 242.1 °C); (h) compound 6b (nematic, Schlieren at 202.9 °C).

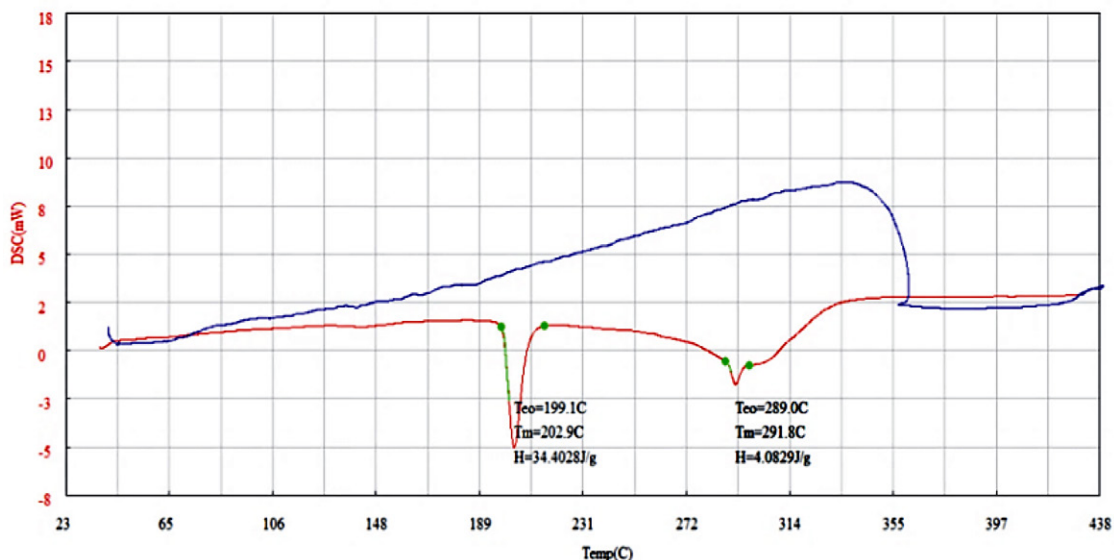


Figure 8. DSC thermogram for compound **6b**.

different. No mesomorphic properties were found for compounds **1a–6a**, while inversions of imine linkage orientation in compounds **1b–6b** enhanced the mesomorphic properties, except for compound **1b** due to the absence of a terminal group (in **1b**) and its dimerization by intermolecular hydrogen bonding. Orientations of inverted imine linkage and carboxyl group beside terminal substituents cause remarkable changes on the dipole moment and improve the polarisability of the molecule by conju-

gation between azomethine and terminal substituents *via* the phenyl ring for compounds **2b–4b**, thus, increasing the lateral attraction force to enhance the formation of smectic phase and terminal attraction force by hydrogen bonding to enhanced nematic phase formation¹¹ (Fig. 9).

The appearance of the nematic phase in compounds **5b** and **6b** was enhanced by the terminal hydrogen bonding between carboxyl and a π orbital created by hyperconjugation,¹² while in compound **6b** hydrogen bonding was between carboxyl group and the oxygen atom of the methoxy group (Fig. 10).

4. Conclusion

Benzylidene aniline compounds were synthesized and characterized. The study indicates that the hydrogen bonding and the orientation of inverted imine C=N linkage play a significant role in liquid crystals behavior, especially in compounds **1a–6a** and **1b**, which is preventing the formation of liquid crystals owing to their dimerization through hydrogen bonding, while the liquid crystal properties of compounds **2b–6b** were improved by the lateral interactions and terminal hydrogen bonding occurring between carboxyl and terminal substituent group.

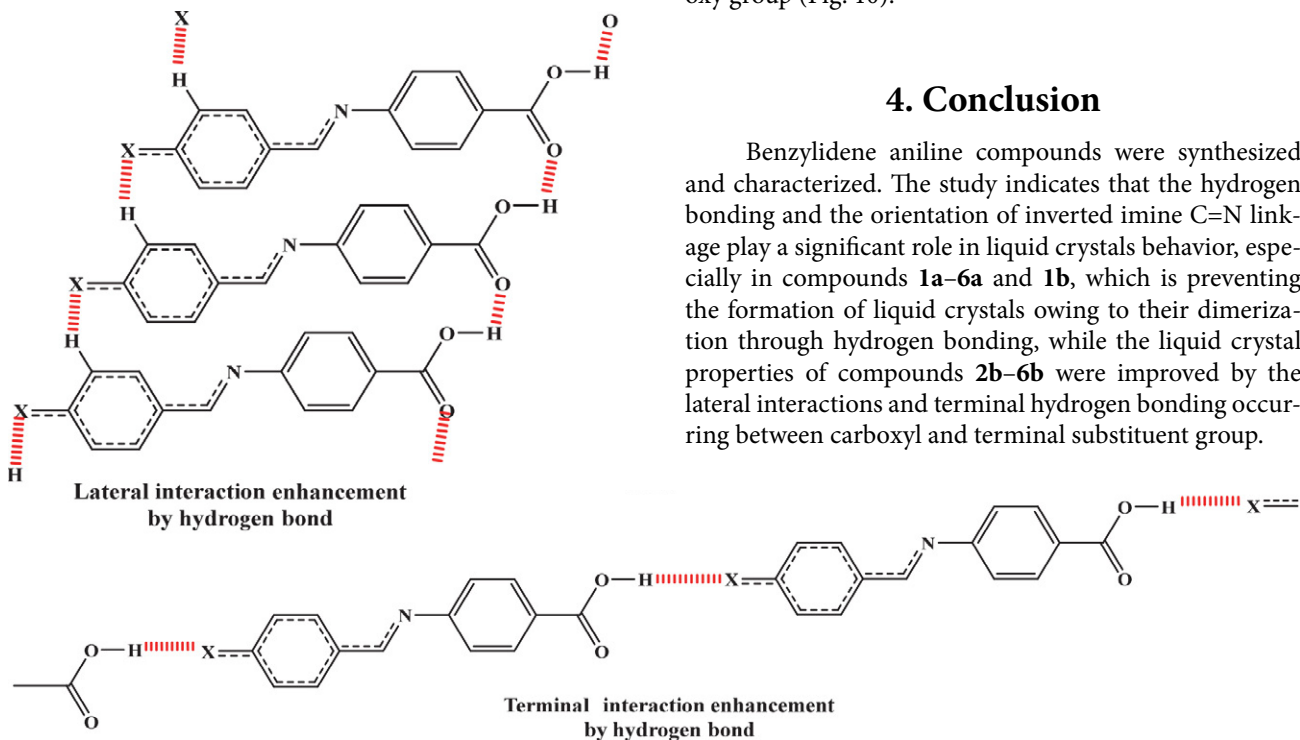


Figure 9. Hydrogen bonds for compounds **2b–4b** at the smectic and nematic phases.

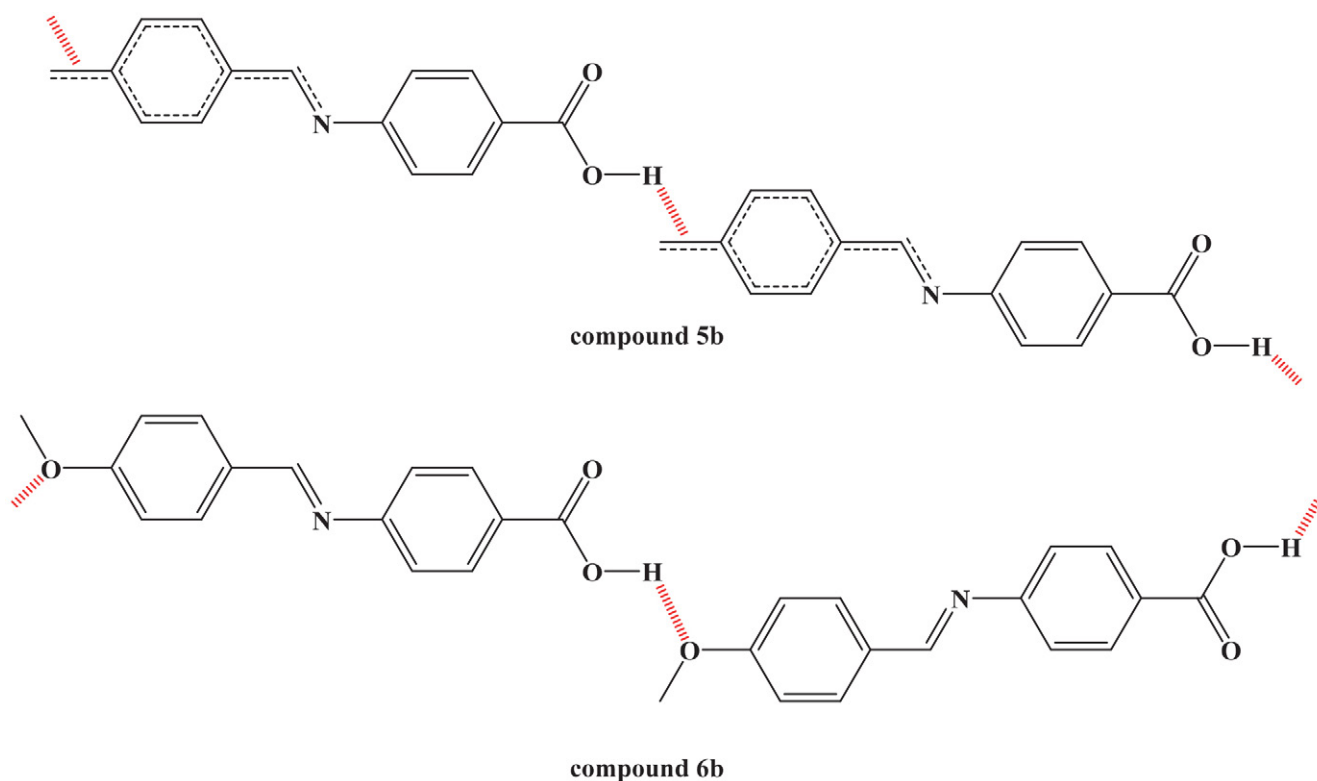


Figure 10. Hydrogen bond for compounds 5b and 6b at the nematic phase.

Acknowledgments

The author is grateful to Ms. Alaa Adnan Rashad, Al-Nahrain University, for her help in carrying out some of the measurements in this research.

5. References

- B. Bai, H. Wang, H. Xin, B. Long, M. Li, *Liq. Cryst.* **2007**, *34*, 659–665. DOI:10.1080/02678290701328118
- T. Steiner, *Angew. Chem. Int. Ed.* **2002**, *41*, 48–76. DOI:10.1002/1521-3773(20020104)41:1<48::AID-ANIE48>3.0.CO;2-U
- E. Arunan, G. R. Desiraju, R. A. Klein, J. Sadlej, S. Scheiner, I. Alkorta, D. C. Clary, R. H. Crabtree, J. J. Dannenberg, P. Hobza, H. G. Kjaergaard, A. C. Legon, B. Mennucci, D. J. Nesbitt, *Pure Appl. Chem.* **2011**, *83*, 1637–1641. DOI:10.1351/PAC-REC-10-01-02
- G. W. Gray, B. Jones, *J. Chem. Soc.* **1954**, 2556–2562. DOI:10.1039/jr9540002556
- Y. Arakawa, Y. Sasaki, K. Igawa, H. Tsuji, *New J. Chem.* **2017**, *41*, 6514–6522. DOI:10.1039/C7NJ00282C
- T. Kato, J. M. J. Frechet, *J. Chem. Soc.* **1989**, *111*, 8533–8534. DOI:10.1021/ja00204a044
- T. Kato, J. M. J. Frechet, P. G. Wilson, T. Saito, T. Uryu, A. Fujishima, C. Jin, F. Kaneuchi, *Chem. Mater.* **1993**, *5*, 1094–1100. DOI:10.1021/cm00032a012
- T. Kato, A. Fujishima, J. M. J. Frechet, *Chem. Lett.* **1990**, *19*, 919–922. DOI:10.1246/cl.1990.919
- M. Fourmigué, *Curr. Opin. Solid State Mater. Sci.* **2009**, *13*, 36. DOI:10.1016/j.cossms.2009.05.001
- B. Bankiewicz, M. Palusiak, *Struct. Chem.* **2013**, *24*, 1297–1306. DOI:10.1007/s11224-012-0157-1
- H. L. Nguyen, P. N. Horton, M. B. Hursthouse, A. C. Legon, D. W. Bruce, *J. Am. Chem. Soc.* **2004**, *126*, 16–17. DOI:10.1021/ja036994l
- H. B. Bürgi, J. D. Dunitz, *Helv. Chim. Acta*, **1970**, *53*, 1747–1764. DOI:10.1002/hlca.19700530724
- L. Óvári, Y. Luo, F. Leyssner, R. Haag, M. Wolf, P. Tegeder, *J. Chem. Phys.* **2010**, *133*, 1–8. DOI:10.1063/1.3460647

Povzetek

V tej študiji smo raziskali učinke substituentov in vodikovih vezi ter orientacije iminskih povezav na obnašanje benziliden anilinskih spojin v vlogi tekočih kristalov (LC). 4-Karboksibenziliden-4-X-aniline (X = H, F, Cl, Br, CH₃, OCH₃) **1a–6a** smo sintetizirali s pomočjo reakcije anilina in njegovih substituiranih derivatov s 4-formilbenzojsko kislino; 4-X-benziliden-4-karboksi aniline (X = H, F, Cl, Br, CH₃, OCH₃) **1b–6b** pa smo pripravili z reakcijo anilina in njegovih substituiranih derivatov s 4-aminobenzojsko kislino v absolutnem etanolu kot topilu. Pripravljene spojine smo karakterizirali s pomočjo FT IR in ¹H NMR spektroskopije, lastnosti tekočih kristalov pa smo raziskali s pomočjo diferenčne dinamične kalorimetrije (DSC) in s polarizirano optično mikroskopijo (POM). Glede na mezomorfne lastnosti smo dokazali, da so spojine **2b–4b** dimorfne in izkazujejo smektično in nematično fazo, spojini **5b, 6b** sta monofazni in izkazujeta nematično fazo, spojine **1a–6a** and **1b** pa niso pokazale mezofaznega obnašanja. Pri spojinah **1a–6a** se zaradi vodikovih vezi in inverzne iminske povezave (glede na spojine **1b–6b**) mezofazne lastnosti niso pojavile.



Except when otherwise noted, articles in this journal are published under the terms and conditions of the Creative Commons Attribution 4.0 International License

Ionic Liquid-Based Dispersive Liquid–Liquid Microextraction for the Simultaneous Determination of Carbamazepine and Lamotrigine in Biological Samples

Salumeh Ranjbar, Ameneh Porgham Daryasari* and Mojtaba Soleimani

Department of Chemistry, Lahijan Branch, Islamic Azad University, Lahijan, Iran P.O.Box 4416939515

* Corresponding author: E-mail: porgham54@gmail.com

Tel.: +981342230561; Fax: +981342224756

Received: 11-07-2019

Abstract

This paper describes a new approach for the determination of carbamazepine and lamotrigine in biological samples by ionic liquid dispersive liquid-phase microextraction prior to high-performance liquid chromatography with ultraviolet detection. The effects of different ionic liquids (ILs) on the extraction efficiency of carbamazepine and lamotrigine were investigated. The highest extraction efficiencies of carbamazepine and lamotrigine were obtained using 30 μL of 1-methyl-3-octylimidazolium hexafluorophosphate [C8MIM][PF6]. Several factors affecting the microextraction efficiency, such as the type and volume of extracting solvent, type and volume of disperser solvent, salt concentration, and pH of the sample solution have been optimized. The calibration plots were linear in the range of 0.1–20 mg L^{-1} for carbamazepine and 0.3–40 mg L^{-1} for lamotrigine with detection limits of 0.04 mg L^{-1} for carbamazepine and 0.07 mg L^{-1} for lamotrigine in plasma samples. The results confirm the suitability of the presented method as a sensitive method for the analysis of the target analytes in urine and plasma samples.

Keywords: Ionic liquids; dispersive liquid–liquid microextraction; carbamazepine; lamotrigine; human urine; human plasma

1. Introduction

One of the most common serious neurological disorders is epilepsy.¹ Anti-epileptic drugs (AEDs) are the main form of treatment for epilepsy. Carbamazepine and newer AEDs like lamotrigine (LTG) are among the first-line medicines for treatment of seizures.² Lamotrigine (LTG), chemically known as [6-(2,3-dichlorophenyl)-1,2,4-triazine-3,5-diamine], is used as monotherapy and as an adjunct with other antiepileptics for treatment of

partial and generalized toxic-clonic seizures. It's used as a tranquilizer and in the treatment of neurological lesions.^{3,4}

Carbamazepine (CBZ) (5-*H*-dibenzo[*b,f*]azepine-5-carboxamide), is a first line antiepileptic drug used in the treatment of partial and generalized tonic-clonic seizures.⁵ The chemical structures of carbamazepine and lamotrigine are shown in Figure 1.

Most biological samples have complex matrices and the analytes are typically present at low concentration levels, which are not detectable by the analytical instrument. Therefore, a sample preparation step is generally required to extract, isolate, and concentrate the analytes of interest.

Different analytical techniques that have been used for the determination of lamotrigine include planar chromatography,⁶ HPLC,⁷ TLC and HPLC,⁸ GC,⁹ HPLC and GC,¹⁰ capillary electrophoresis,¹¹ and immunoassay.¹² High performance liquid chromatography (HPLC-UV, HPLC-DAD) and immunoassay were used for determination of carbamazepine in biological materials. Also, gas chromatography with mass spectrometry and liquid chromatography with mass spectrometry have been reported.^{13–15}

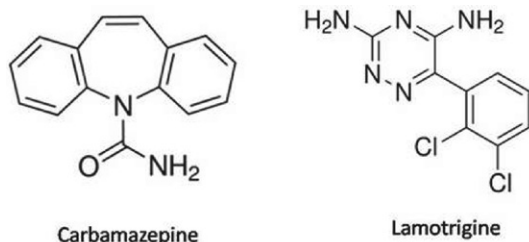


Figure 1. The structure of carbamazepine and lamotrigine

Liquid-liquid extraction (LLE),¹⁶ solid-phase extraction (SPE),¹⁷ and stir bar-sorptive extraction (SBSE)¹⁸ have been developed for the determination of CBZ in biological fluids. These methods are time consuming and require substantial amounts of toxic organic solvents. The sample preparation methods employed for lamotrigine involve SPME,¹⁹ SPE,²⁰ protein precipitation (PP),²¹ LLE,²² and microextraction by packed sorbent (MEPS).²³

A novel microextraction method called dispersive liquid-liquid microextraction (DLLME) was introduced in 2006.²⁴ DLLME utilizes an extraction solvent and a dispersive solvent to produce a cloudy solution. DLLME has become a very popular technique for the extraction of different compounds.^{25–27} Generally, the extraction solvent used in DLLME is highly toxic and not environmentally friendly.

In environmentally friendly sample preparation methods, it is important to use liquid solvents in reduced amounts, replaced with green solvents or even completely eliminated from the analytical procedure.²⁸ Ionic liquids (ILs) are considered to be “environmentally friendly solvents”.²⁹ The immiscibility of ILs in water and their capability to solubilize organic species has made them suitable to extract the compounds.³⁰ Recently, ionic liquid DLLME is very popular.³¹

In this paper, for the first time, DLLME method using IL as extraction solvent combined with high-performance liquid chromatography has been developed for the simultaneous determination of carbamazepine and lamotrigine in biological samples. The parameters affecting the extraction efficiency, such as the type and volume of extracting solvent, type and volume of disperser solvent, salt concentration, and pH of the sample solution have been optimized. The proposed method was successfully applied to determine carbamazepine and lamotrigine in biological samples.

2. Experimental

2.1. Chemicals and Reagents

Carbamazepine and lamotrigine were obtained from Sobhan Darou Company (Rasht, Iran). Acetone, acetonitrile, methanol, and sodium chloride were obtained from Merck Company (Germany). Ionic liquids (ILs) [C8MIM][PF6] and [C6MIM][PF6] were obtained from SIGMA-ALDRICH. IL [C4MIM][PF6] was obtained from Fluka. Buffer solution (disodium hydrogen phosphate – potassium dihydrogen phosphate, pH = 6.88) was obtained from Merck. Sodium dihydrogen phosphate, disodium hydrogen phosphate, sodium hydrogen carbonate, and disodium carbonate were obtained from Merck. Deionized water was used in all experiments. Stock standard solutions of the analytes were prepared by dissolution of each drug in methanol, having a concentration of 1000 mg L⁻¹. Fresh standard solutions were prepared by diluting the

standard solution of the analytes with deionized water of required concentration. All these solutions were stored at 4 °C in the absence of light.

2.2. Apparatus

Chromatographic analysis was performed using a Shimadzu (LC-20AD prominence, Japan) with a photodiode array detector (SPD-M20A). Separations were carried out on a μ Boundapak C18 column of 15 cm \times 4.6 mm with 5 μ m particles. HPLC data were acquired and processed using a Lab solution software (LC solution version 1.25 SP5). The mobile phase was phosphate buffer (pH 6.8) – methanol – acetonitrile (70:20:10, v/v/v) at a flow rate of 1.0 mL min⁻¹ under isocratic conditions. The detection was performed at the wavelength of 284 and 308 nm for carbamazepine and lamotrigine, respectively. In the measurement of lamotrigine (LTG) and carbamazepine (CBZ) in the optimization steps and also determination in real samples, the mixture of both drugs were used. The maximum wavelengths for measurement of LTG and CBZ were 308 nm and 284 nm, respectively. Unfortunately, in 308 nm and 284 nm, both of the drugs have peaks. However, CBZ at 284 nm and LTG at 308 nm have peaks with high intensities. The maximum intensity of the peaks of each drug at the selected wavelengths were used for the subsequent experiments. A centrifuge model ALC 4232 was used to perform the centrifuge process (USA). The pH-meter model 827 Metrohm (Herisau, Switzerland) was used for pH measurements.

2.3. Dispersive Liquid-liquid Microextraction procedure

Five milliliters of sample solution containing the analytes was poured into a centrifuge glass vial. The pH of the solution was adjusted to 10 by using sodium bicarbonate. A mixture containing 30 μ L of [C8MIM][PF6] (as extraction solvent) and 100 μ L of methanol (as disperser solvent) was injected into the sample solution. Cloudy solution was formed as the fine droplets of the immiscible extraction solvent dispersed in the sample. This process enlarged the contact area between the extraction solvent and sample, and the analytes were extracted into the formed fine droplets. Then it was placed in ice bath for 2 min. The cloudy solution was centrifuged at 3500 rpm for 10 min to separate the phases. Finally, 100 μ L methanol was added into the collected IL and injected into the HPLC system.

3. Results and Discussion

In the present study, the applicability of ionic liquid DLLME combined with HPLC was considered for the simultaneous determination of carbamazepine and lamo-

trigine in biological samples. There are several factors which affect the extraction process including type and volume of extracting solvent, type and volume of disperser solvent, salt concentration and pH of the sample solution. Optimization of the variables was performed using one variable at a time method. All experiments were replicated three times. The spiked concentration level in the optimization study was 5 mg L⁻¹ of carbamazepine and 20 mg L⁻¹ of lamotrigine. Enrichment factor (EF) and extraction recovery (ER) were calculated based on the following equations:

$$EF = C_{\text{sedimented}}/C_0 \quad (1)$$

$$ER(\%) = \frac{C_{\text{sedimented}} \times V_{\text{sedimented}}}{C_0 \times V_{\text{sample}}} \times 100 = EF \times \frac{V_{\text{sedimented}}}{V_{\text{sample}}} \times 100 \quad (2)$$

Where, EF, $C_{\text{sedimented}}$ and C_0 are the enrichment factor, concentration of the analyte in the sedimented phase, and initial concentration of the analyte in the sample, respectively. ER%, $V_{\text{sedimented}}$ and V_{sample} are the extraction recovery, volume of the sedimented phase, and volume of the sample, respectively. $C_{\text{sedimented}}$ is calculated from a suitable direct injection calibration curve. Blank urine and plasma was obtained from ten different healthy volunteers. Different sources of blank urine and plasma ($n = 3$) were used for testing the endogenous interferences. There were no interfering peaks at either the carbamazepine or lamotrigine retention time.

3. 1. Effect of pH

The sample pH is an important factor in the enrichment process and can affect the extraction efficiencies of the analytes. In this study, the pH values of the sample solutions were adjusted between 7 and 11 with buffers of

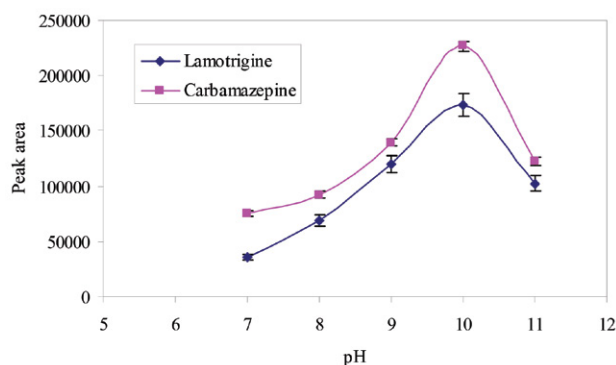


Figure 2. Effect of pH on the extraction efficiency. Extraction conditions: extraction solvent: [C4MIM][PF6], extraction solvent volume: 30 μ L; dispersive solvent: methanol; dispersive solvent volume: 100 μ L; concentration of NaCl (w/v): 1.0%

sodium phosphate and sodium bicarbonate. As seen in Figure 2, the best peak areas were obtained at pH 10. The pK_a value for CBZ is 13.13 and the pK_a value for LTG is 5.3. At the pH 10, the analytes were extracted based on hydrophobic interaction. Also, in acidic pH, the drugs were decomposed. Thus, pH 10 was selected as the optimum value.

3. 2. Selection of Extraction Solvent

In the selection of the extraction solvent, certain properties of the IL that need to be considered are: (1) to extract carbamazepine and lamotrigine well; (2) to have higher density than water; and (3) to form a cloudy solution in the presence of dispersive solvent. In this study, three ionic liquids, including [C8MIM][PF6], [C6MIM][PF6], and [C4MIM][PF6] were investigated. By comparing them as extraction solvents, it was observed that carbamazepine and lamotrigine exhibited a better affinity for [C8MIM][PF6], because of higher solubility of the mentioned drugs in [C8MIM][PF6] (Figure 3). Therefore, [C8MIM][PF6] was selected as extraction solvent in the subsequent experiments.

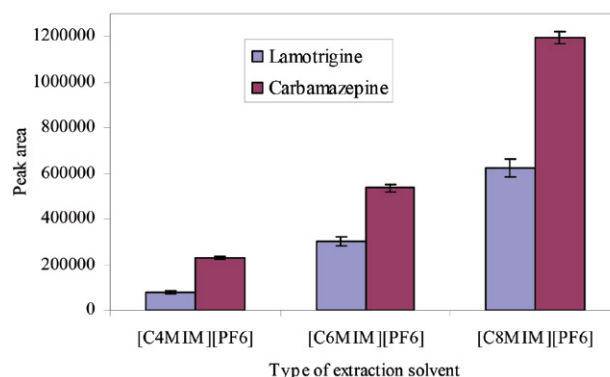


Figure 3. Effect of type of extraction solvent on the extraction efficiency. Extraction conditions: extraction solvent volume: 30 μ L; dispersive solvent: methanol; dispersive solvent volume: 100 μ L; concentration of NaCl (w/v): 1.0%, pH:10

3. 3. Effect of Extraction Solvent Volume

Optimization of the volume of the IL as an extraction solvent is a further step in the development of a IL-DLLME procedure. The volume of the extraction solvent can influence formation of dispersion and thus has to be optimized. In order to study the effect of extraction solvent volume, different volumes of [C8MIM][PF6] (20–50 μ L in 10 μ L intervals) were tested. It was observed (Figure 4) that the peak areas were increased by increasing the [C8MIM][PF6] volume up to 30 μ L for carbamazepine and lamotrigine. The peak areas of the analytes decreased by increasing the volume of [C8MIM][PF6], which was an expected result due to dilution of the extracted analytes in the extraction solvent at higher volumes. Therefore, 30 μ L of [C8MIM][PF6] was selected as the optimum volume.

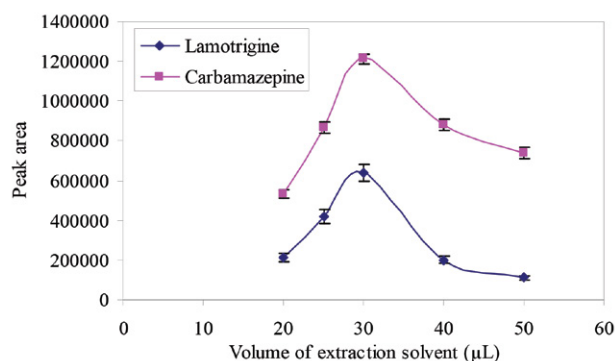


Figure 4. Effect of volume of extraction solvent on the extraction efficiency, Extraction conditions: extraction solvent: [C8MIM][PF6], dispersive solvent: methanol; dispersive solvent volume: 100 μ L; concentration of NaCl (w/v): 1.0%, pH:10

3. 4. Effect of Type of Disperser Solvent

In the IL-DLLME, the disperser solvent should be soluble in the extraction solvent and miscible in the sample solution, thus enabling the formation of fine droplets of the extraction solvent. Therefore, acetonitrile, methanol, and acetone were tested as disperser solvents. A series of sample solutions were examined using 100 μ L of each of the disperser solvents containing 30 μ L of [C8MIM][PF6]. By using acetone and acetonitrile, the cloudy solution was not formed well. It was clear that (Figure 5) the best peak areas were obtained when methanol was used as a disperser solvent. Hence, the subsequent experiments were performed using methanol as the disperser solvent.

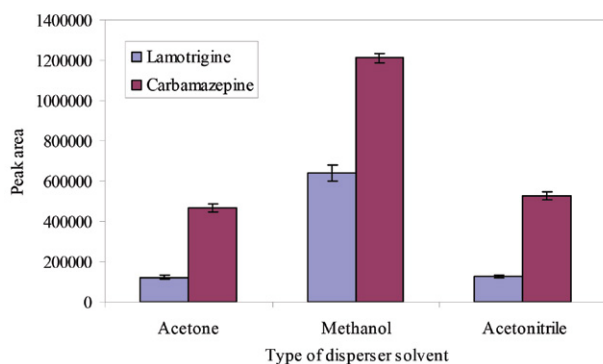


Figure 5. Effect of type of disperser solvent on the extraction efficiency, Extraction conditions: extraction solvent: [C8MIM][PF6], extraction solvent volume: 30 μ L; dispersive solvent volume: 100 μ L; concentration of NaCl (w/v): 1.0%, pH:10

3. 5. Effect of Volume of Disperser Solvent

In order to study the effect of disperser solvent volume, different volumes of methanol (50, 100, 300, 500, and 1000 μ L) were used. It is clear from Figure 6 that 100 μ L methanol gave the highest peak areas. It seems that at the volume of 100 μ L, the amount of methanol was

enough for effective forming of the cloudy solution. At lower volume of methanol, cloudy solution was not properly formed resulting in a decrease in the peak areas. At higher volume of methanol, the solubility of the analytes in the sample increased resulting in a decrease in the peak areas. Thus, 100 μ L was selected as the optimum volume of methanol.

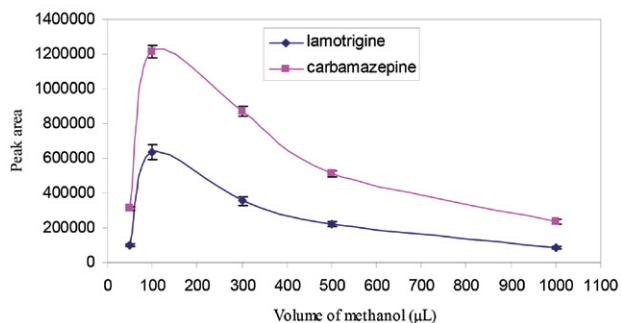


Figure 6. Effect of volume of methanol on the extraction efficiency, Extraction conditions: extraction solvent: [C8MIM][PF6], extraction solvent volume: 30 μ L; dispersive solvent: methanol; concentration of NaCl (w/v): 1%; pH: 10

3. 6. Salt Addition

Generally, salt addition can cause a decrease in the solubility of the analytes in sample solution and enhance extraction efficiency. To evaluate the possibility of salting-out effect, the extraction efficiency was studied with the sodium chloride ranging from 0.5 to 1.5% (w/v) (Figure 7). Due to the salting-out effect, the peak areas increased as the amount of NaCl increased from 0.5 to 1.0% (w/v). By increasing the ionic strength (NaCl concentration from 1.0 to 1.5% (w/v)), a reduction of the peak areas for carbamazepine and lamotrigine were observed because of dilution effect. Based on the results, 1.0% (w/v) of NaCl was added in all the subsequent experiments.

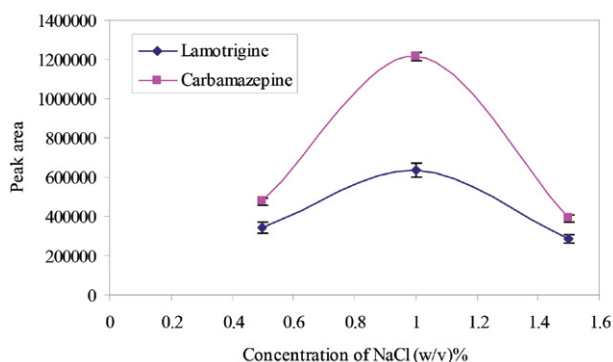


Figure 7. Effect of NaCl concentration on the extraction efficiency, Extraction conditions: extraction solvent: [C8MIM][PF6], extraction solvent volume: 30 μ L; dispersive solvent: methanol; dispersive solvent volume: 100 μ L; pH: 10

3. 7. Analytical Performance and Method Validation

Calibration data of carbamazepine and lamotrigine were obtained using IL-DLLME-HPLC system under optimum conditions. For urine samples, the linearity of calibration curve was observed in the range of 0.07–20 mg L⁻¹ for carbamazepine and 0.17–40 mg L⁻¹ for lamotrigine. The coefficients of determination (*R*²) were 0.991 and 0.997 for carbamazepine and lamotrigine, respectively. The limits of detection (LODs) based on signal-to-noise ratio (S/N) of 3, were 0.02 and 0.05 mg L⁻¹ for carbamazepine and lamotrigine, respectively. The limits of quantification (LOQs), based on signal-to-noise ratio (S/N) of 10, were 0.07 and 0.17 mg L⁻¹ for carbamazepine and lamotrigine, respectively. The relative standard deviation (RSD%, *n* = 5) at the concentration level of 5.0 mg L⁻¹ of carbamazepine and lamotrigine were 1.7% and 5.6% for carbamazepine and lamotrigine, respectively. Enrichment factors were 35 and 26 for carbamazepine and lamotrigine, respectively. Extraction recoveries were 70 and 52% for carbamazepine and lamotrigine, respectively. However, for plasma samples, linearity was observed in the range of 0.1–20 mg L⁻¹ for carbamazepine and 0.3–40 mg L⁻¹ for lamotrigine. The *R*² were 0.987 and 0.995 for carbamazepine and lamotrigine, respectively. The limits of detection (LODs) based on signal-to-noise ratio (S/N) of 3, were 0.04 and 0.07 mg L⁻¹ for carbamazepine and lamotrigine, respectively. The limits of quantification

(LOQs), based on signal-to-noise ratio (S/N) of 10, were 0.1 and 0.3 mg L⁻¹ for carbamazepine and lamotrigine, respectively. The relative standard deviation (RSD%, *n* = 5) at the concentration level of 5.0 mg L⁻¹ of carbamazepine and lamotrigine were 3.2% and 8.4% for carbamazepine and lamotrigine, respectively. Enrichment factors were 27 and 19 for carbamazepine and lamotrigine, respectively. Extraction recoveries were 54 and 38% for carbamazepine and lamotrigine, respectively.

The selectivity of the method was evaluated by analysing six blank plasma and urine samples to evaluate the existence of matrix endogenous substances at retention times that could interfere with carbamazepine (CBZ) and lamotrigine (LTG) peaks. The analysis of blank human plasma and urine samples from six healthy volunteers confirmed the absence of endogenous interferences at the retention times of carbamazepine and lamotrigine.

The stability of CBZ and LTG stock solutions were evaluated at room temperature for 8 h and 24 h and after storage at –20 °C for 10 days. Stability was calculated by comparing the pertinent responses obtained from the tested stock solution(s) with the responses of freshly prepared ones and the results are given in Table 1. According to the results obtained, CBZ and LTG was stable in human plasma and urine samples in the different storage conditions.

Absolute recoveries of the analytes were determined in triplicates at high, medium and low concentrations in plasma and urine by extracting drug-free plasma and

Table 1. Summary of stability of CBZ and LTG in stock solution and human plasma and human urine

Drug(<i>n</i> = 5)	Data on Stock Solution Stability		
	8 h at RT	24 h at RT	10 days at –20 °C
CBZ			
Precision (%)	1.2	1.8	1.5
Accuracy (%)	100.1	99.8	98.7
LTG			
Precision (%)	3.5	3.7	3.0
Accuracy (%)	99.6	99.3	98.9
Data on Stability in Plasma Samples			
CBZ			
Precision (%)	3.0	3.3	3.6
Accuracy (%)	98.1	97.9	97.2
LTG			
Precision (%)	7.8	8.0	7.6
Accuracy (%)	98.3	97.8	98.1
Data on Stability in Urine Samples			
CBZ			
Precision (%)	1.5	1.4	1.6
Accuracy (%)	98.8	99.1	97.8
LTG			
Precision (%)	4.8	5.1	5.0
Accuracy (%)	98.2	98.5	97.8

urine samples spiked with CBZ and LTG. Recovery was calculated by comparison of the analyte peak-areas of the extracted samples with those of the unextracted analyte standards, representing 94 and 88% recovery of CBZ and LTG, respectively, in plasma and 99 and 94% recovery of CBZ and LTG, respectively, in urine.

In order to evaluate the effect of matrix samples on the performance of the proposed method, determination of CBZ and LTG in human urine and plasma samples at the three different concentration levels were performed. For doing the IL-DLLME procedure on the plasma samples, some extra processes are needed. First the human plasmas were dissolved in a suitable amount of acetonitrile such as 1:1 (*v/v*) reducing the matrix effect and then the mixtures were centrifuged. Secondly, they were filtered for getting a clear solution and removing the dirty solution at the bottom of test tubes. The samples was found to be free from the drugs. Therefore, specific amounts of CBZ and LTG at the three different concentration levels were spiked to the samples and analyzed by the proposed method. The spiking recoveries of the target compounds in the urine and plasma samples are summarized in Table 2. The relative recovery (RR) is obtained from the following equation:

$$RR\% = C_{\text{found}} - C_{\text{real}} / C_{\text{added}} \times 100 \quad (3)$$

where C_{found} , C_{real} , and C_{added} are the concentrations of the analytes after the addition of a known amount of standard in a real sample, the concentration of the analytes in a real sample, and the concentration of a known amount of standard, which was spiked to the real sample, respectively. The relative recoveries were between 87–103% (Table 2) and showed that the matrix had negligible effect on the performance of the proposed method. The chromatograms of the urine and plasma sample (without spiking and spiked) are shown in Figures 8 and 9, respectively.

Table 3 compares the proposed method with the other extraction methods for the determination of the target analytes in biological samples. The comparison of extraction time of the proposed method with solid-phase microextraction (SPME),³² liquid-liquid extraction (LLE),^{33,34} and solid-phase extraction (SPE)³⁵ for the extraction of the target analytes indicates that this novel method has a very short equilibrium time comparing to the mentioned methods and the extraction time needed for the proposed method is a few seconds. Quantitative results of the proposed method are better than for SPE³⁵ and LLE^{33,34} methods. Relative standard deviation (RSD%) of the proposed method is better than for SPME³² and LLE³³ methods. Also, SPE and LLE methods are time-consuming and laborious, and the large amounts of organic solvents used in the extraction procedures cause problems with regards to health and the

Table 2. Determination of carbamazepine (CBZ) and lamotrigine (LTG) in human plasma and urine by IL-DLLME-HPLC-DAD

	Spiked concentration (mg L ⁻¹)						Relative recovery (% ± SD), <i>n</i> = 3 ^a					
	CBZ			LTG			CBZ			LTG		
Human urine	2	4	10	5	14	20	93.0 ± 3.1	103.0 ± 1.5	101.0 ± 1.2	90.0 ± 5.0	97.0 ± 3.5	99.0 ± 4.1
Human plasma	2	4	10	5	14	20	89.0 ± 5.4	94.0 ± 2.8	96.0 ± 2.5	87.0 ± 9.5	91.0 ± 4.5	93.0 ± 3.1

^a Standard deviation

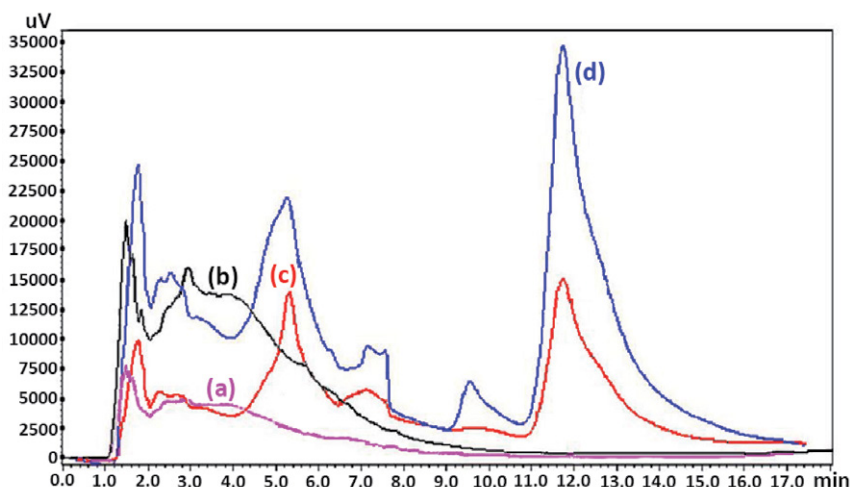


Figure 8. HPLC chromatograms, (a,b) before spiking with analytes in urine at the wavelength of 308 and 284 nm for lamotrigine and carbamazepine, respectively, (c) 14 mg L⁻¹ (lamotrigine) and (d) 4 mg L⁻¹ (carbamazepine) spiking of analytes in urine after extraction via proposed method at optimum conditions. (The retention time of LTG was 5.1 min and the retention time of CBZ was 12.1 min at the measurement in the maximum wavelengths).

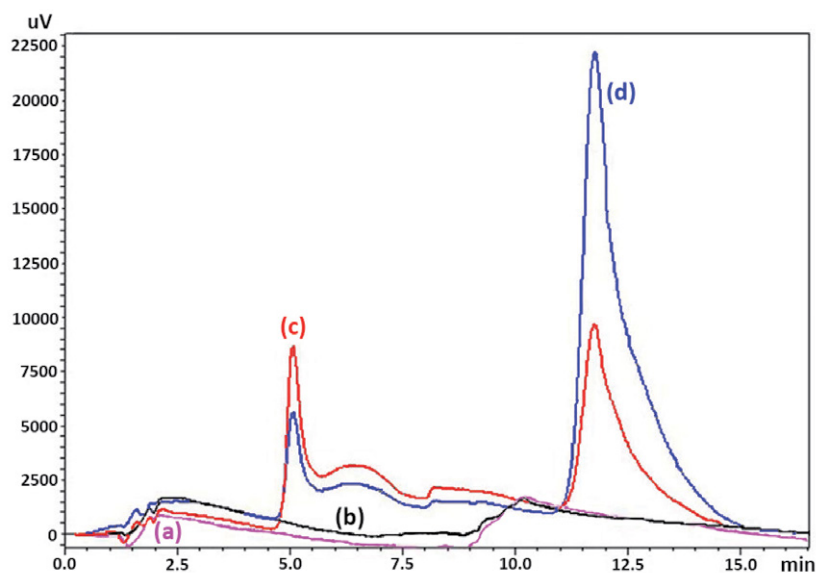


Figure 9. HPLC chromatograms, (a,b) before spiking with analytes in plasma at the wavelength of 308 and 284 nm for lamotrigine and carbamazepine, respectively, (c) 14 mg L⁻¹ (lamotrigine) and (d) 4 mg L⁻¹ (carbamazepine) spiking of analytes in plasma after extraction via proposed method at optimum conditions. (The retention time of LTG was 5.1 min and the retention time of CBZ was 12.1 min at the measurement in the maximum wavelengths).

environment. Finally, the extraction solvent used in DLLME generally is highly toxic and not environmentally friendly. Ionic liquids (ILs) are considered to be “environmental friendly solvents”. In the proposed work, in DLLME method, IL was used as extraction solvent.

4. Conclusions

A rapid and simple method using the ionic liquid-based dispersive liquid-liquid microextraction procedure was presented to the extract and concentrate carbamazepine and lamotrigine from biological samples.

Table 3. Comparison of the proposed method with other extraction methods for the determination of carbamazepine (CBZ) and lamotrigine (LTG)

Methods	Sample	R.S.D.%	Dynamic linear range (mg L ⁻¹)	Limit of detection (mg L ⁻¹)	Extraction time (min)	Ref.
SPME-GC-TSD	Plasma	<10	0.06–20 (CBZ); 0.2–10 (LTG)	0.06 (CBZ); 0.2 (LTG) (Limit of quantitation)	15	[32]
Precipitation and liquid extraction-GC-MS	Serum	<12	0.625–20 (CBZ, LTG)	–	5	[33]
LLE-HPLC-UV	Plasma	<6	1.0–30 (LTG)	0.15 (LTG)	5	[34]
SPE-HPLC-DAD	Plasma	<8	0.2–25 (CBZ)	0.02 (CBZ)	1	[35]
IL-DLLME-HPLC-DAD	Urine and plasma	Urine (1.7 (CBZ), 5.6 (LTG))	Urine (0.07–20 (CBZ), 0.17–40 (LTG))	Urine (0.02 (CBZ), 0.05 (LTG))	A few seconds	This work
		Plasma (3.2 (CBZ), 8.4 (LTG))	Plasma (0.1–20 (CBZ), 0.3–40 (LTG))	Plasma (0.04 (CBZ), 0.07 (LTG))		

The proposed microextraction method is environmentally friendly (highly toxic chlorinated solvents are not required), rapid, and with a simple set-up. The proposed method has satisfying LODs which were in the range of 0.02–0.07 mg L⁻¹, and precisions were in the range of 1.7–8.4%. The proposed method was also applied for the analysis of drugs in urine and plasma samples and the recoveries from spiked samples were in the range of 87–103%. All these results indicated that the proposed method had advantages such as good sensitivity, simplicity, easiness to operate, limited chance of exposure to the toxic solvents, and high enrichment factor. This study provides a new perspective regarding the replacement of chlorinated solvents with less-toxic solvents in DLLME and supports the use of green analytical chemistry methods. In the final experiment, the developed method was applied to the determination of carbamazepine and lamotrigine in biological samples and the acceptable results can be achieved.

Acknowledgements

Financial support by Lahijan Branch, Islamic Azad University (Lahijan, Iran) during the period of this research is gratefully acknowledged.

Compliance with Ethical Standards

Funding There is no funding for this study.

Conflict of Interest No conflict exists; author Ameen Porgham Daryasari declares that she has no conflict of interest. Author Salumeh Ranjbar declares that she has no conflict of interest. Author Mojtaba Soleimani declares that he has no conflict of interest.

Ethical approval This article does not comprise of any studies with human participants or animals performed by any of the authors.

Informed consent No humans are involved in this study.

5. References

- H. M. Neels, A. C. Sierens, K. Naelaerts, S.L. Scharpe, G. M. Hatfield, W. E. Lambert, *Clin. Chem. Lab. Med.* **2004**, *42*, 1228–1255. DOI:10.1515/CCLM.2004.245
- A. Fortuna, J. Sousa, G. Alves, A. Falcao, P. Soares-da-Silva, *Anal. Bioanal. Chem.* **2010**, *397*, 1605–1615. DOI:10.1007/s00216-010-3673-0
- A. G. Gilman, J. G. Hardman, L. E. Limbird, Goodman and Gilman's the Pharmacological Basis of Therapeutics, 10th edn (McGraw Hill, New York, USA), 539, **2001**.
- S. C. Sweetman, Martindale, The Complete Drug Reference, 34th edn (Pharmaceutical Press, London), 363, **2005**.
- M. Silanpaa, L. Haataja, T. Tomson, S. I. Johannessen, Carbamazepine, in: S. Shorvon, E. Perucca, J. Engel (Eds), The treatment of epilepsy, third ed. Blackwell Publishing LTD., Oxford, **2009**, pp. 459–474. DOI:10.1007/s00216-010-3673-0
- M. Sigrid, F. Ricardo, V. Mario, D. Marta, C. Godoy, *JPC-J. Planar Chromat.* **2011**, *24*, 222–226. DOI:10.1556/JPC.24.2011.3.9
- N. Jebabli, E. Gaies, H. Jebari, R. Charfi, M. Lakhal, A. Klouz, S. Trabelsi, I. Salouage, *Tunis Med.* **2015**, *93*, 565–568. 8. N. F. Youssef, E. A. Taha, *Chem. Pharm. Bull.* **2007**, *55*, 541–545. DOI:10.1248/cpb.55.541
- P. Nikolaou, I. Papoutsis, A. Dona, C. Spiliopoulou, S. Athanasis, *J. Pharm. Biomed. Anal.* **2015**, *102*, 25–32. DOI:10.1016/j.jpba.2014.08.034
- G. S. Elizabeth, S. Giannoutsos, D. R. Lower, M. A. Virji, M. D. Krasowski, *J. Chromatogr. Sci.* **2007**, *45*, 616–622. DOI:10.1093/chromsci/45.9.616
- R. Theurillat, M. Kuhn, W. Thormann, *J. Chromatogr. A* **2002**, *979*, 353–368. DOI:10.1016/S0021-9673(02)01257-8
- P. E. Morgan, D. S. Fisher, R. Evers, R. J. Flanagan, *Biomed. Chromatogr.* **2011**, *25*, 775–778. DOI:10.1002/bmc.1515
- S. Ghatol, V. Vithlani, S. Gurule, A. Khuroo, T. Monif, P. Partani, *J. Pharm. Anal.* **2013**, *3*, 75–83. DOI:10.1016/j.jpha.2012.09.001
- C. Linder, A. Hansson, S. Sadek, L. L. Gustafsson, A. Pohanka, *J. Chromatogr. B* **2018**, *1072*, 116–122. DOI:10.1016/j.jchromb.2017.11.005
- J. M. Juenke, K. A. Miller, M. A. Ford, G. A. Mcmillin, K. L. Johnson-Davis, *Clin. Chim. Acta* **2011**, *412*, 1879–1882. DOI:10.1016/j.cca.2011.06.009
- L. A. Romanlyshyn, J. K. Wichmann, N. Kucharczyk, R. C. Shumaker, D. Ward, R. D. Sofia, *Ther. Drug Monit.* **1994**, *16*, 90–99. DOI:10.1097/00007691-199402000-00015
- K. He, T. Yonetani, Y. Asada, S. Echigo, S. Itoh, *Mirochem. J.* **2019**, *145*, 1191–1198. DOI:10.1097/00007691-199402000-00015
- A. Klancar, M. Zakotnik, R. Roskar, J. Trontelj, *Anal. Methods* **2017**, *9*, 5310–5321. DOI:10.1039/C7AY01310H
- M. D. Cantu, D. R. Toso, C. A. Lacerda, F. M. Lancas, E. Carrilho, M. E. Queiroz, *Anal. Bioanal. Chem.* **2006**, *386*, 256–263. DOI:10.1007/s00216-006-0629-5
- S. Bompadre, A. Tagliabracci, M. Battino, R. Giorgetti, *J. Chromatogr. B Analyt. Technol. Biomed. Life Sci.* **2008**, *863*, 177–180. DOI:10.1016/j.jchromb.2007.12.020
- W. Lee, J. H. Kim, H. S. Kim, O. H. Kwon, B. I. Lee, K. Heo, *Neurol. Sci.* **2010**, *31*, 717–720. DOI:10.1007/s10072-010-0257-x
- N. R. Barbosa, A. F. Midio, *J. Chromatogr. B Biomed. Sci. Appl.* **2000**, *741*, 289–293. DOI:10.1016/S0378-4347(00)00102-X
- A. Ferreira, M. Rodrigues, P. Oliveira, J. Francisco, A. Fortuna, L. Rosado, P. Rosado, A. Falcao, G. Alves, *J. Chromatogr. B Analyt. Technol. Biomed. Life Sci.* **2014**, *971*, 20–29. DOI:10.1016/j.jchromb.2014.09.010
- M. Rezaee, Y. Assadi, M. R. M. Hosseini, E. Aghae, F. Ahmadi, S. Berijani, *J. Chromatogr. A* **2006**, *1116*, 1–9. DOI:10.1016/j.chroma.2006.03.007
- R. Rahnema, Z. C. Jojadeh, M. R. Jamali, *Acta Chim. Slov.* **2012**, *59*, 641–647.

26. M. R. Hadjmohammadi, S. S. Ghoreishi, *Acta Chim. Slov.* **2011**, *58*, 765–771.
27. S. Shariati, M. Golshekan, *Acta Chim. Slov.* **2011**, *58*, 311–317.
28. P. Anastas, N. Eghbali, *Chem. Soc. Rev.* **2010**, *39*, 301–312.
DOI:10.1039/B918763B
29. S. Xiulan, Z. Li, Y. Fang, P. Chen, G. Ren, H. Shan, *Curr. Anal. Chem.* **2010**, *6*, 249–259.
DOI:10.2174/157341110791516954
30. J. F. Liu, J. A. Jönsson, G. B. Jiang, *Trends Anal. Chem.* **2005**, *24*, 20–27. DOI:10.1016/j.trac.2004.09.005
DOI: 10.1016/j.trac.2004.09.005
31. R. Rahnama, N. Mansoursamaei, M. R. Jamali, *Acta Chim. Slov.* **2014**, *61*, 191–196.
32. M. E. C. Queiroz, S. M. Silva, D. Carvalho, *J. Chromatogr. Sci.* **2002**, *40*, 219–223. DOI:10.1093/chromsci/40.4.219
33. J. Hallbach, H. Vogel, W. G. Guder, *Eur. J. Clin. Chem. Clin. Biochem.* **1997**, *35*, 755–759. DOI:10.1515/cclm.1997.35.10.755
34. E. Greiner-Sosanko, S. Giannoutsos, D. R. Lower, M. A. Virji, M. D. Krasowski, *J. Chromatogr. Sci.* **2007**, *45*, 616–622.
DOI:10.1093/chromsci/45.9.616
35. P. Dzodic, L. Zivanovic, A. Protic, I. Ivanovic, R. Velickovic-Radovanovic, M. Spasic, S. Lukic, *J. Serb. Chem. Soc.* **2012**, *77*, 1423–1436. DOI:10.2298/JSC120106084D

Povzetek

Članek opisuje nov pristop za določanje karbamazepina in lamotrigina v bioloških vzorcih z disperzivno mikroekstrakcijo s topili ob uporabi ionskih tekočin ter v nadaljevanju s tekočinsko kromatografijo visoke ločljivosti z ultravijolično detekcijo. Raziskali smo učinek različnih ionskih tekočin (IL) na učinkovitost ekstrakcije karbamazepina in lamotrigina. Najvišjo učinkovitost ekstrakcije karbamazepina in lamotrigina smo dobili z uporabo 30 μL 1-metil-3-oktilimidazolijevega heksafluorofosfata [C8MIM][PF6]. Optimizirali smo še več drugih faktorjev, ki vplivajo na učinkovitost mikroekstrakcije, kot so vrsta in volumen ekstrakcijskega topila, vrsta in volumen disperzijskega topila, koncentracija soli in pH vzorca. Kalibracijske krivulje so bile za plazemske vzorce linearne v območju 0,1–20 mg L^{-1} za karbamazepin in 0,3–40 mg L^{-1} za lamotrigin, meje zaznave pa so bile 0,04 mg L^{-1} za karbamazepin in 0,07 mg L^{-1} za lamotrigin. Rezultati potrjujejo primernost predstavljene metode kot dovolj občutljive za analizo tarčnih analitov v vzorcih urina in plazme.



Except when otherwise noted, articles in this journal are published under the terms and conditions of the Creative Commons Attribution 4.0 International License

Scientific paper

Voltammetric Determination of Sulfaclozine Sodium at Sephadex-modified Carbon Paste Electrode

Emad Mohamed Hussien,^{1,*} Hanaa Saleh,² Magda El Henawee,²
Afaf Abou El Khair² and Neven Ahmed¹

¹ National Organization for Drug Control and Research (NODCAR), Giza, Egypt.

² Faculty of Pharmacy, Zagazig University, Zagazig, Egypt.

* Corresponding author: E-mail: emadhussien@yahoo.com

Tel.: +2 02 3749 6077

Received: 11-08-2019

Abstract

The electrochemical behavior of Sulfaclozine Sodium (SLC) was studied at a bare and sephadex-modified carbon paste electrodes by cyclic voltammetry and square wave voltammetry. The cyclic voltammetry (CV) showed a well-defined irreversible oxidation peak at 0.94 V in Britton- Robinson buffer pH 7.0. The strong affinity of SLC to sephadex allowed accumulation of SLC at the surface of electrode and thus higher electrochemical sensitivity to SLC. The influence of sephadex loading, the pH of the solution and the scan rate on the peak current was studied. A linear calibration curve covering the concentration range from 0.005 to 1 mM was obtained using SWV. The method was successfully applied for the determination of SLC in the veterinary pharmaceutical formulations with satisfactory accuracy and precision.

Keywords: Sulfaclozine Sodium; square wave voltammetry; sephadex; carbon paste electrode.

1. Introduction

Coccidiosis is a parasitic disease that attacks the intestinal tract of poultry caused by protozoan parasites of the genus *Eimeria*. This disease is of worldwide occurrence and costs the poultry industry many millions of dollars every year to control.¹ Although live vaccines were introduced, prophylactic chemotherapy is still preferred for coccidiosis control in most countries. The last half of the twentieth century marked improvements in the performance of commercially reared poultry. These improvements would not be possible without the introduction of a succession of ever more effective anticoccidial agents to control coccidiosis.²

Sulfaclozine, N¹ – (6-chloropyrazinyl) sulfanilamide (Figure 1) is a sulfonamide antibacterial that has been used

in veterinary medicine.³ It is effective in the treatment of clinical coccidiosis as well as prevention of the disease.⁴

The analytical methods which have been reported for the determination of sulfaclozine include chromatographic methods with different detectors.^{5–9} and capillary electrophoresis.¹⁰ These methods are either time-consuming or use expensive instrumentation.

In contrast to the reported techniques, the voltammetric techniques are simple and rapid with high sensitivity and selectivity for drug analysis. Moreover, the carbon paste electrodes which are used for voltammetric measurements have several advantages for the electrochemical investigation of organic compounds. They are cheap, easy to prepare and use; and offer surface regeneration and modification, low background current, a large potential domain, no memory effects and adsorption-extraction capabilities.^{11,12} Furthermore, including surfactants in the experimental protocol and modification of the carbon paste (chemically or by nanomaterials) have been reported to influence the electrochemical process occurring at the surface of the electrode.^{13,14} Sephadex is a cross-linked dextran which is used as a stationary phase in gel filtration chromatography.¹⁵ Carbon paste electrodes modified with

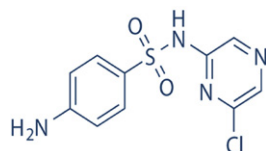


Figure 1. Chemical structure of Sulfaclozine

sephadex have been used for the sensitive determination of nifuroxazide and glibenclamide.^{16,17} Indeed, Numerous pharmaceutical compounds were analyzed using carbon paste electrodes.

The present work reports for the first time a SWV method for the determination of SLC in veterinary formulation. The proposed method utilizes the electrochemical oxidation of SLC at a carbon paste electrode modified with sephadex in a micellar medium. The effect of sephadex on the oxidation peak current was investigated. The method was validated According to the ICH guidelines.¹⁸

2. Experimental

2. 1. Reagents and Materials

Sulfaclozine sodium was obtained from Yangzhou Tianhe Pharmaceutical Co., LTD, China with potency 99.75%. Clozicoc[®] W.S.P (Each 100 g contains 32 g sulfaclozine sodium) was obtained from Pharco Pharmaceuticals, Alex., Egypt. Graphite powder, paraffin oil, Sephadex G-50, C18 silica gel and chitosan were supplied from Sigma–Aldrich. Methanol was purchased from Loba Chemie Co., India. Sodium dodecyl sulfate (SDS), Phosphoric acid and boric acid were supplied from Adwic Co., Egypt. Acetic acid was obtained from Piochem Co., Egypt. Briton Robinson buffer (BR) buffer was prepared by adding equal volumes of phosphoric acid 0.04 M, acetic acid 0.04 M and boric acid 0.04 M, the pH of the buffer was adjusted by NaOH 0.2 M to cover the pH range from 2.0 to 10.0. SDS 10.0 mM was prepared by dissolving an appropriate amount of SDS in water. Double- distilled water was used throughout the study and referred to by “water”.

2. 1. 4. Standard Solution

Sulfaclozine stock solution (10.0 mM) was prepared by dissolving 30.66 mg of SLC in 1.0 mL methanol, then diluting with water to 10 mL.

2. 2. Apparatus

Bio-logic SP 150 electrochemical work station with a three-electrode configured stand (model C-3) was used for the voltammetric measurements. The working electrode was a bare carbon paste electrode or a sephadex-modified carbon paste electrode (SMCPE); the reference electrode was Ag/AgCl/3 M KCl (BAS, USA) and the counter electrode was a platinum wire (BAS, USA).

2. 3. Procedures

2. 3. 1. Preparation of Modified Carbon- Paste Electrode

Sephadex-modified carbon paste (SMCPE) electrode was made by hand mixing of 0.4 g Sephadex and 0.8 g of

graphite powder with 0.4 mL paraffin oil. Plain (unmodified) carbon paste was made by mixing 1.0 g graphite powder with 0.6 mL paraffin oil. The paste was packed into the electrode body and smoothed on a filter paper till a shiny appearance of the electrode surface was obtained.

2. 3. 2. Analytical Procedure

The CV at the carbon paste was repeated between 0 and 1.4 V several times in the buffer solution (pH 7.0) till the CV becomes stable. Then the electrode was transferred into another cell containing BR buffer solution (pH 7.0), 0.005 mM to 1.0 mM SLC and 0.03 mM SDS. The solution was stirred for 30 s at an open circuit potential, afterwards, the CV was recorded between +0.4 and +1.4, at 100 mVs⁻¹ scan rate.

2. 3. 3. Calibration Curve of SLC

The SWV was performed to determine SLC in bulk powder and pharmaceutical formulations. Different aliquots were accurately transferred from the stock standard solution to an electrochemical cell containing 10 mL buffer (pH 7.0) and 0.03 mM SDS. The SWV was recorded at SMCPE. The peak current was plotted against drug concentration of SLC in (μM).

2. 3. 4. Application to Veterinary Pharmaceutical Formulation

An accurately weighed 0.96 g Clozicoc[®] W.S.P. containing 306.7 mg of sulfaclozine sodium was transferred into a 100-mL volumetric flask and dissolved in 10 mL methanol. The solution was sonicated for 15 min, then, the flask was completed to the mark with water to obtain 10.0 mM SLC (solution I). Further dilution was carried out from solution I into 10-mL volumetric flask to obtain 1.0 mM SLC (solution II).

The accuracy and precision of the method was studied using 0.005, 0.47 and 0.65 mM of the sample solution, each solution was prepared in triplicate. The accuracy and precision solutions were prepared by transferring 50 μL from solution I; 500 μL and 700 μL from solution II, each into an electrochemical cell containing BR pH 7 and 0.03 mM SDS. The concentration of the sample was determined by the standard addition method using the SWV.

3. Results and Discussion

3. 1. Sulfaclozine Electrochemical Oxidation Behavior

The electrochemical behavior of SLC was studied at the carbon paste by recording the CV from 0 to 1.4 V in BR pH 7. The CV (Figure 2) shows one anodic peak current

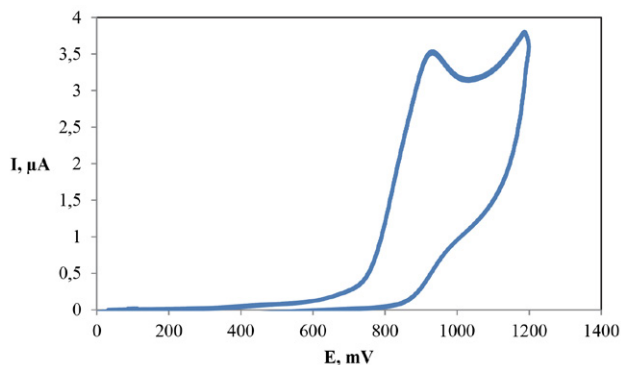


Figure 2. The results are the average of five separate determinations Cyclic voltammogram of 0.1 mM SLC in BR buffer of pH 7.0 at a bare carbon paste electrode.

((I_p) = 3.5 μ A at 0.94 V) with no cathodic peak in the reverse scan, it means that the oxidation process of SLC is irreversible. The anodic peak could be due to the oxidation of the amine group in SLC.¹⁹

3. 2. Optimization of the Experimental Conditions

3. 2. 1. Effect of pH

The electrochemical oxidation of organic compounds depends, in most cases, on the pH of the solution. Herein, the effect of changing the pH of the solution on the oxidation of SLC was studied in BR buffer over the pH range from 2.0–10.0. It was observed that the peak potential of SLC is shifted towards less positive values when the pH was increased. The relationship between the E_p and pH at the sephadex-modified carbon paste electrode was found to be linear and controlled by the equation $E_p = -51\text{pH} + 1284$ ($R^2 = 0.995$) (Figure 3a). The slope (~ 51 mV per pH) is close to the expected 59 mV per pH indicating that equal number of protons and electrons involved in the oxidation process of SLC. The highest oxidation current was obtained at pH 7 (Figure 3b), therefore, all measurements were carried out at pH 7.0.

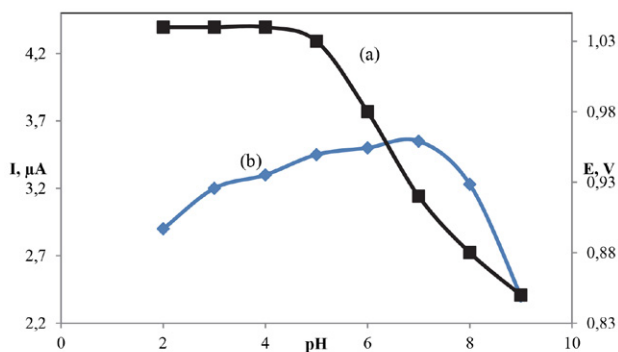


Figure 3. Dependence of peak potential (a) and peak current (b) on the pH of 0.1 mM SLC. The scan rate is 100 mV s^{-1}

3. 2. 2. Effect of Sephadex

Different materials including C_{18} modified silica, chitosan and sephadex were tested for possible enhancement of the oxidation current and, hence, increasing sensitivity of the electrode. (Figure 4) shows no difference in the electrochemical behavior of sulfaclozine when 30% C_{18} modified silica was added to the carbon paste electrode, while the addition of 30% chitosan to the paste make a little improvement in the current response. In contrast, carbon paste modified with 30% (w/w) sephadex exhibited a considerable oxidation current that indicating the high affinity of the drug to sephadex. This affinity has been utilized for preconcentration of the drug onto the electrode surface to increase the sensitivity to SLC. The effect of sephadex loading on the peak current is shown in Figure 5.

3. 2. 3. Effect of Sodium Dodecyl Sulfate

Sulfaclozine oxidation behavior in a micellar medium was also studied using SDS.

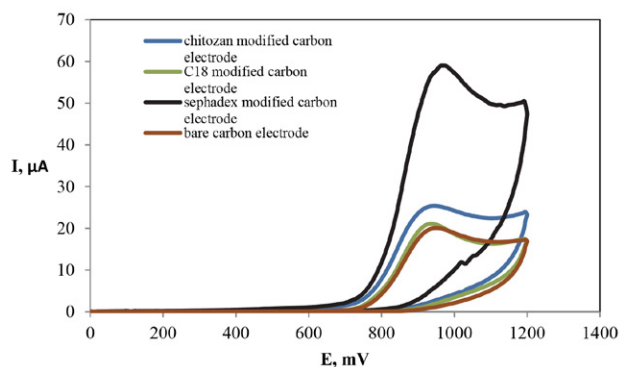


Figure 4. Cyclic voltammograms of 1.0 mM SLC in PH 7.0 using different modified and unmodified electrodes.

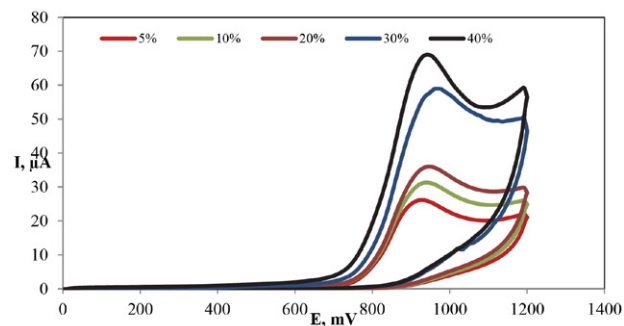


Figure 5. Cyclic voltammograms of SLC (1.0 mM) in PH 7.0 on carbon paste electrode containing different amounts of sephadex; the scan rate is 100 mV s^{-1}

SDS is a hydrophobic ionic surfactant, which can be adsorbed onto the electrode surface. As a result, the electrochemical process such as the mass and electron transfer energy at the electrode/solution interface are affected.²⁰ It

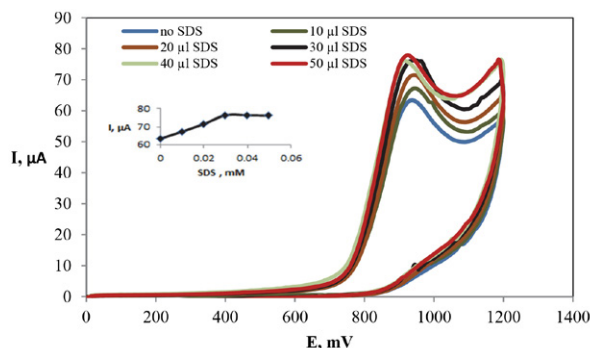


Figure 6. Cyclic voltammograms recorded in 1.0 mM SLC containing different concentrations of SDS, the measurements were carried out using 40% sephadex carbon paste electrode in BR buffer pH 7.0.

has been reported that SDS can remove the oily binder (insulator) and hence lower the uncompensated resistance at the electrode/solution interface.^{21, 22, 23} Herein, the effect of SDS was studied by the addition of different volume of 0.01 M SDS (10–50 μL) to the SLC solution of pH 7 and recording the CV. Figure 6 shows the relationship between the anodic current and the SDS concentrations. It was observed that the peak current increases with increasing SDS in the measuring solution, and the highest oxidation current was observed when the SLC solution contains 30 μL of 0.01 M SDS; no further improvement in the peak current was observed above this concentration.

3. 2. 4. Effect of Scan Rate

The effect of the scan rate (ν) on the peak potential (E_p) and the peak current (i_p) was studied between 10 mVs^{-1} and 250 mVs^{-1} in 1.0 mM sulfaclozine solution in BR buffer (pH 7.0) containing 0.03 mM SDS (Figure 7a). The relationship between the oxidation peak current of SLC and the square root of scan rate ($\nu^{1/2}$) was found to be linear, indicating that electrochemical oxidation of SLC is a diffusion controlled process.²⁴

Plotting the logarithm of the peak current against the logarithm of the scan rate resulted in a straight line with a slope of 0.47 (Figure 7b), this value is close to the theoretical value of 0.5 for a purely diffusion-controlled process.²⁴ It was also found that the E_p (oxidation peak potential) was dependent on scan rate, the peak potential was shifted to more positive values when the scan rate increased, which confirms that the oxidation process is irreversible. Furthermore, the relationship between the peak potential and the logarithm of the scan rate was found to be linear (Figure 7c) in accordance with Laviron's equation (1).²⁵

$$E_p = E^0 + \left(\frac{2.303RT}{\alpha nF}\right) \log \left(\frac{RTk^0}{\alpha nF}\right) + \left(\frac{2.303RT}{\alpha nF}\right) \log \nu \quad (1)$$

Here α is the transfer coefficient, k^0 is the standard heterogeneous rate constant of the reaction, ν is the scan

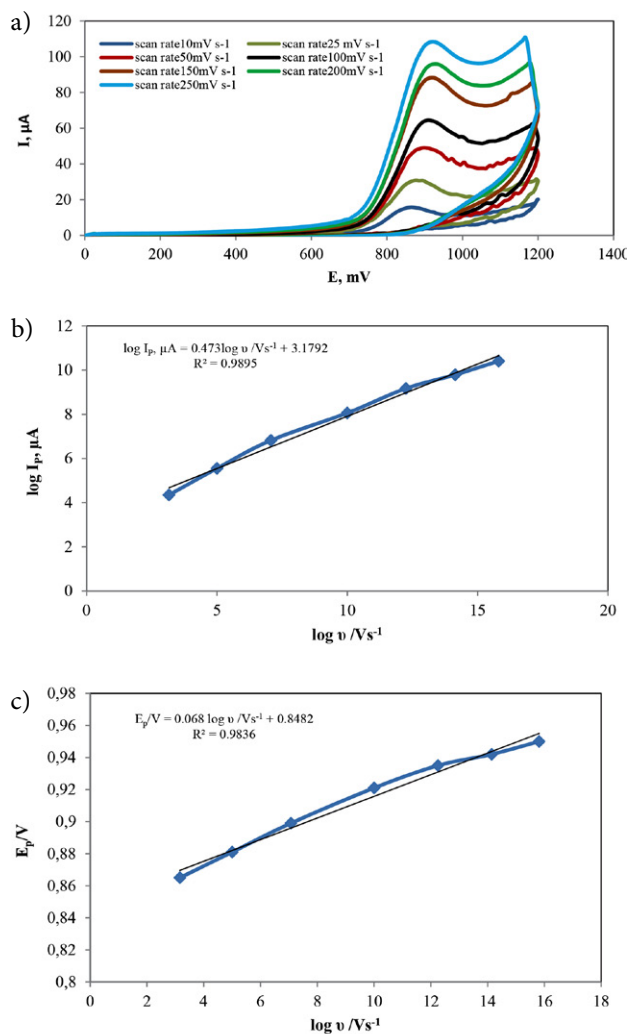


Figure 7. (a) The CV of 1.0 mM SLC containing 0.03 mM SDS in BR buffer of pH 7.0 at 40% SMCPE at different scan rates, (b) Dependence of the logarithm of peak current $I_p/\mu\text{A}$ on logarithm of scan rate (ν/Vs^{-1}). (c) Relationship between peak potential E_p/V and logarithm of scan rate $\log(\nu/\text{Vs}^{-1})$.

rate, and E_0 is the formal redox potential, n is the number of electrons transferred. So, the value of αn can be obtained from the slope of E_p vs $\log \nu$. The slope was found to be 0.068, when $T = 298\text{K}$ and $R = 8.314 \text{ J K}^{-1} \text{ mol}^{-1}$ and $F = 96485 \text{ C/mol}$, αn was found to be 0.85. According to Bard and Faulkner,²⁶ α can be calculated from the following equation (2).

$$\alpha = \frac{47.7}{E_p - E_{p/2}} \text{ mV} \quad (2)$$

k^0 value can be calculated from the intercept of the above plot if the value of $E^{0'}$ is known.

$E^{0'}$ in Eq. (1) can be obtained from the intercept of E_p versus ν curve by extrapolating to the vertical axis at $\nu = 0$.²⁷ All values of αn , α , n , $E^{0'}$ and k^0 are summarized in table 1.

Table 1. The calculated values of αn , α , n , $E^{0'}$ and k^0 for the electro-oxidation of SLC by cyclic voltammetry (CV) at SMCPE.

Parameters	SMCPE
αn	0.8476
α	0.611
n	1.38
$E^{0'}$	0.85
k^0	3.1439

3. 2. 5. Square Wave Voltammetry (SWV)

Under optimal experimental conditions, the calibration curve was constructed using the SWV over the concentration range from 0.005 to 1 mM. The parameters of SWV are 50 mV pulse height, 200 ms pulse width, 10 ms step height and 100 ms step time. The solution was stirred for 30 s at 400 rpm at an open circuit potential followed by 30 s quiescent time before any measurements.

3. 3. Calibration, Detection Limit and Reproducibility

A linear relationship between SLC anodic peak current of and its concentration was found in the concentra-

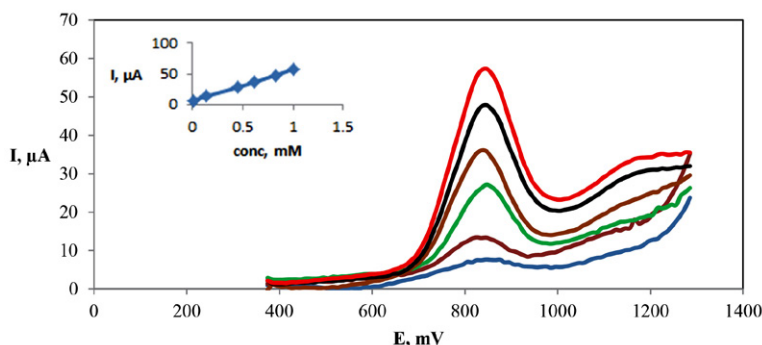
Table 2. Performance data of the proposed SWV method for determination of SLC

Parameters	SLC
Linearity range (mM)	0.005mM to 1.0 mM
Slope ($\mu\text{A} \cdot \text{mM}^{-1}$)	50.67
Intercept (μA)	5.86
Correlation coefficient (r)	0.9995
LOD (μM)	1.04
LOQ (μM)	2.99
Accuracy (mean \pm S.D.)	100.18 \pm 0.01
Precision (RSD %)	
Interday	2.08
Intraday	2.12

tion range from 0.005 mM to 1.0 mM ($R = 0.999$) with a slope of $50.67 \mu\text{A} \cdot \text{mM}^{-1}$ and a limit of detection 0.001 mM. The reproducibility (%RSD, $n = 3$) of the peak current for 0.005 mM sulfaclozine was 2.08% as shown in Table 2.

3. 4. Determination of Sulfaclozine in Veterinary Formulation

SLC was determined in Clozicoccc[®] W.S.P. using standard addition method; the obtained results were sta-

**Figure 8.** SWV of SLC over the concentration range from 0.005 to 1.0 mM in BR pH 7.0 containing 0.03 mM SDS using 40% SMCPE.**Table 3.** determination of SLC in pharmaceutical dosage form and statistical comparison of the proposed voltammetric and the published HPLC method⁵

Pharmaceutical formulation	Standard addition technique				Reference method ⁵
	Taken(mg)	Added (mg)	Found(mg)	%Recovery ^a	
Clozicoccc w.s.p batch No.564	0.015	0.015	0.0149	99.96	
	0.120	1.45	1.43	98.87	
	0.120	2.00	2.01	100.31	
Mean				99.59	99.33
S.D				1.01	1.51
n			5		
variance				1.02	2.28
Student's <i>t</i> -test (2.132) ^b				0.64	–
F-test (6.39) ^b				2.24	–

^a The results are the average of five separate determinations ^b the tabulated *t* and *F* values, respectively, at $P = 0.05$

tistically compared with those obtained by a reference method.⁵ The calculated t- and F-values are found to be less than the theoretical ones, confirming that accuracy and precision of the two methods are comparable at 95% confidence level (Table 3).

4. Conclusion

Herein, we report for the first time a novel simple and rapid SWV method for SLC determination in veterinary formulations. The method is based on a carbon paste electrode modified with sephadex. The sephadex modified carbon paste electrode showed a dramatic increase in the oxidation peak current over the plain carbon paste. The SWV method was linear over a wide concentration range of SLC from 0.005 mM to 1.0 mM with a detection limit of 1 μ M. The method was applied successfully for the determination of SLC in the veterinary formulation with satisfactory accuracy and precision. The student's t-test and F-ratio test showed no significant difference regarding the accuracy and precision between the present method and the reported method.

List of abbreviations

SLC :	Sulfaclozine Sodium
SWV :	Square wave voltammetry
SDS :	Sodium dodecyl sulfate
BR :	Briton Robinson buffer
SMCPE :	Sephadex-modified carbon paste electrode
CV :	Cyclic Voltammetry
W.S.P :	Water soluble powder

5. References

- Chapman, H. D., Chapter 53 – Coccidiosis in Egg Laying Poultry, in *Egg Innovations and Strategies for Improvements*, P.Y. Hester, Editor. **2017**, Academic Press: San Diego. 571–579. DOI:10.1016/B978-0-12-800879-9.00053-6
- Chapman, H.D., Perspectives for the control of coccidiosis in poultry by chemotherapy and vaccination in Proceedings of the IXth International Coccidiosis Conference. **2005**. Foz de Iguassu, Parana, Brazil. 99–104.
- S. C. Sweetman, R.P.S., Martindale: The Complete Drug Reference. thirty-eights ed. Vol. 1. **2014**, London: Pharmaceutical Press.
- Md. Harun-Or-Rashid, et al., *Scholars Journal of Agriculture and Veterinary Sciences*, **2016**, 3(4), 284–287.
- TANG Shu, C. J., GAO Jian-long, BAO En-dong, *Nanjing Agricultural Univeristy*, **2012**, 105–109.
- Yu, H., et al., *Journal of Chromatography B*, **2011**, 879(25), 2653–2662. DOI:10.1016/j.jchromb.2011.07.032
- Bousova, K. Senyuva, and H. Mittendorf, *Journal of Chromatography A*, **2013**, 1274, 19–27. DOI:10.1016/j.chroma.2012.11.067
- Gorissen, B., et al., *Analytical and Bioanalytical Chemistry*, **2015**, 407(15), 4447–4457. DOI:10.1007/s00216-014-8449-5
- Goodspeed, et al., *Journal – Association of Official Analytical Chemists*, **1978**, 61(5), 1050–1053.
- Su, H. X., et al., *Fenxi Ceshi Xuebao*, **2013**, 32(2), 156–161.
- Ivan Švancara, et al., *Electroanalysis with Carbon Paste Electrodes*. **2012**: CRC Press Taylor & Francis Group. DOI:10.1201/b11478
- Kalcher, K., et al., *Electroanalysis*, **1995**, 7(1), 5–22. DOI:10.1002/elan.1140070103
- Acuna, J. A., et al., *Talanta*, **1993**, 40(11), 1637–42. DOI:10.1016/0039-9140(93)80078-6
- R. Vittal, H. Gomathi, and K. J. Kim, *Adv Colloid Interface Sci*, **2006**, 119(1), 55–68. DOI:10.1016/j.cis.2005.09.004
- Gel Filtration, Theory and Practice, Pharmacia Fine Chemicals. **1976**, Uppsala: Sweden.
- Radi, A., *Analytical and bioanalytical chemistry*, **2004**, 378, 822–6. DOI:10.1007/s00216-003-2392-1
- Radi, A., *Fresenius' Journal of Analytical Chemistry*, **1999**, 364, 590–594. DOI:10.1007/s002160051391
- ICH Q2A. validation of analytical methods. *International Conference on Harmonization*. **2003**, IFPMA: Geneva.
- V. Momberg, et al., *Analytica Chimica Acta*, **1984**, 159, 119–127. DOI:10.1016/S0003-2670(00)84288-9
- Sanghavi, B. J. and A. K. Srivastava, *Electrochimica Acta*, **2010**, 55(28), 8638–8648. DOI:10.1016/j.electacta.2010.07.093
- Jayaprakash, G. K., et al., *Journal of Molecular Liquids*, **2017**, 240, 395–401. DOI:10.1016/j.molliq.2017.05.093
- Manjunatha JG, et al., *Int J Electrochem Sci*, **2009**, 4, 662–671.
- Shankar, S. S., B. E. K. Swamy, and B. N. Chandrashekar, *Journal of Molecular Liquids*, **2012**, 168, 80–86. DOI:10.1016/j.molliq.2012.01.012
- D. K. Gosser, *Cyclic Voltammetry; Simulation and Analysis of Reaction Mechanisms*. New York (N.Y.): VCH, **1993**.
- E. Laviron, *J. Electroanal. Chem.* **1979**, 101(1), 19–28. DOI:10.1016/S0022-0728(79)80075-3
- A. J. Bard and L. R. Faulkner, “*Electrochemical Methods Fundamentals and Applications*,” 2nd Edition, Wiley, Hoboken, **2004**.
- Wu, Y., X. Ji, and S. Hu, *Bioelectrochemistry*. **2004**, 64, 91–97. DOI:10.1016/j.bioelechem.2004.03.005

Povzetek

Elektrokemijsko obnašanje natrijevega sulfaklozina (SLC) je bilo proučevano na golih in sephadex-modificiranih elektrodah iz ogljikove paste s ciklično voltometrijo in kvadratno valovno voltometrijo. Ciklična voltometrija (CV) je pokazala dobro definiran nepovratni vrh oksidacije pri 0.94 V v Britton-Robinson pufru pri pH 7.0. Močna afiniteta SLC do sefadeksa je omogočila kopičenje SLC na površini elektrode in s tem večjo elektrokemično občutljivost za SLC. Proučen je bil vpliv nalaganja sefadeksa, pH raztopine in hitrost skeniranja na največji tok. Z uporabo SWV smo dobili linearno kalibracijsko krivuljo, ki pokriva območje koncentracije od 0.005 do 1 mM. Metodo smo uspešno uporabili za določanje SLC v veterinarskih farmacevtskih formulacijah z zadovoljivo točnostjo in natančnostjo.



Except when otherwise noted, articles in this journal are published under the terms and conditions of the Creative Commons Attribution 4.0 International License

Scientific paper

Synthesis, Characterization and Biological Activity of Some Dithiourea Derivatives

Felix Odame,^{1,2*} Eric Hosten,² Jason Krause,³ Michelle Isaacs,⁵
Heinrich Hoppe,⁵ Setshaba D. Khanye,⁴ Yasien Sayed,⁶ Carminita Frost,³
Kevin Lobb⁴ and Zenixole Tshentu²

¹ Department of Basic Sciences, University of Health and Allied Sciences, PMB 31, Ho, Ghana.

² Department of Chemistry, Nelson Mandela University, P.O. Box 77000, Port Elizabeth 6031, South Africa.

³ Department of Biochemistry and Microbiology, Nelson Mandela University, P.O. Box 77000, Port Elizabeth 6031, South Africa.

⁴ Department of Chemistry, Rhodes University, P.O. Box 94, Grahamstown 6140, South Africa.

⁵ Department of Biochemistry and Microbiology, Rhodes University, Grahamstown 6140, South Africa.

⁶ Protein Structure-Function Research Unit, School of Molecular and Cell Biology, University of the Witwatersrand 2050, Johannesburg 2050, South Africa.

* Corresponding author: E-mail: felixessah15@gmail.com

Received: 11-08-2019

Abstract

Novel dithiourea derivatives have been designed as HIV-1 protease inhibitors using Autodock 4.2, synthesized and characterized by spectroscopic methods and microanalysis. 1-(3-Bromobenzoyl)-3-[2-((3-bromophenyl)formamido)methanethiyl]amino]phenyl]thiourea (**10**) and 3-benzoyl-1-((phenylformamido)methanethiyl]amino]thiourea (**12**) gave a percentage viability of $17.9 \pm 5.6\%$ and $11.2 \pm 0.9\%$ against *Trypanosoma brucei*. Single crystal X-ray diffraction analysis of 1-benzoyl-3-(5-methyl-2-((phenylformamido)methanethiyl]amino]phenyl]thiourea (**1**), 3-benzoyl-1-(2-((phenylformamido)methanethiyl]amino]ethyl]thiourea (**11**), 3-benzoyl-1-((phenylformamido)methanethiyl]amino]thiourea (**12**) and 3-benzoyl-1-(4-((phenylformamido)methanethiyl]amino]butyl]thiourea (**14**) have been presented. 1-(3-Bromobenzoyl)-3-[2-((3-bromophenyl)formamido)methanethiyl]amino]phenyl]thiourea (**10**) gave a percentage inhibition of $97.03 \pm 0.37\%$ against HIV-1 protease enzyme at a concentration of 100 μM .

Keywords: Dithiourea, cytotoxicity; HIV-1 protease inhibition; *plasmodium falciparum* activity; *trypanosoma brucei* activity

1. Introduction

Thiourea derivatives have been synthesized by a variety of methods.^{1–8} A solvent-free three-component one-pot reaction between 2,6-diaminopyridine or 1,2-diaminobenzene and NH_4SCN with subsequent addition of an aroyl chloride gave bis-1-(aroyl)-3-(aryl)thioureas in excellent yields. The thiocyanate derivatives were first synthesized and then used to prepare the thiourea derivatives.¹ Benzoyl chloride has been reacted with ammonium thiocyanate in CH_2Cl_2 solution under solid–liquid phase transfer catalysis, using polyethylene glycol-400 as the catalyst, to give the corresponding benzoyl isothiocyanate.

Dropwise addition of a solution of 1,4-butylenediamine in CH_2Cl_2 yielded 3,3'-dibenzoyl-1,1'-(butane-1,4-diyl)dithiourea,² while 3,3-bis(4-nitrophenyl)-1,10-(para-phenylene)dithiourea has been prepared by the reaction of (para-nitro)benzoyl isothiocyanate with para-phenylenediamine in CH_2Cl_2 using polyethylene glycol-400 as a phase transfer catalyst.³ This reaction has been carried out using 1,6-hexyldiamine as the source diamine to give *N,N*-(1,6-hexamethylene)-bis(benzoylthiourea).⁴ Thiocarbonylhydrazide has been converted into 1-aminothiocarbonyl-4-aryloxy-3-thiosemicarbazides and 1,5-bis(aryloxythiocarbonyl)thiocarbonylhydrazides by the addition

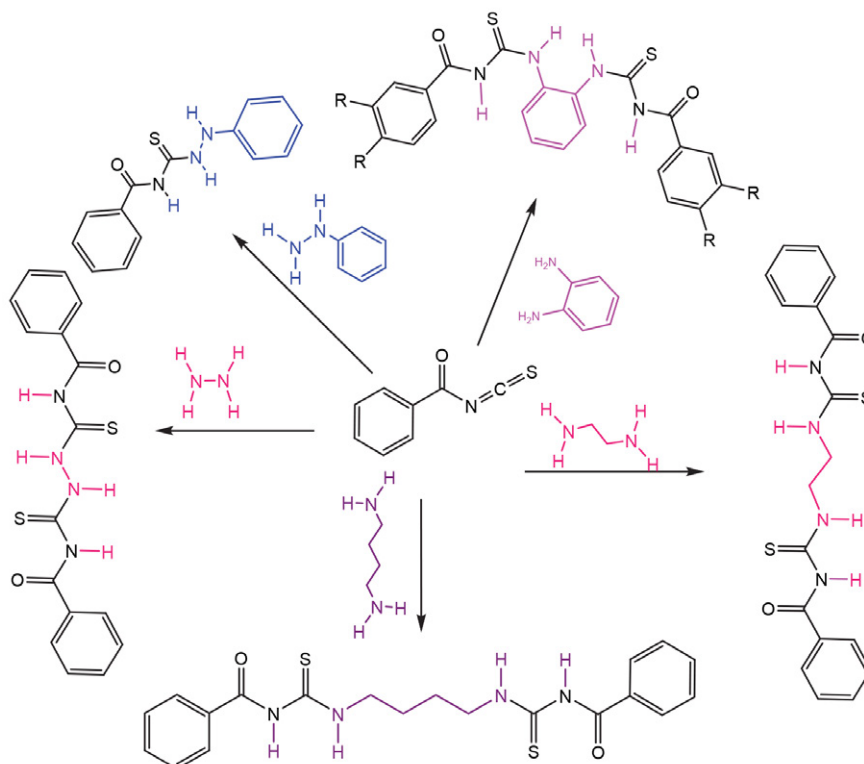
of one or two equivalents of aroyl isothiocyanate, respectively. 1-Phenyl- or 1-benzylidene-thiocarbonylhydrazide and aroyl isothiocyanates gave the appropriate mono-adduct analogues. 1-Aminothiocabamoyl-4-benzoyl-3-thiosemicarbazide is cyclised to 3-mercapto-5-phenyl-1,2,4-triazole in alkaline medium, and to 2-benzamido-5-mercapto-1,3,4-thiadiazole in acid media; the action of alkyl halides on the appropriate alcohol yields 2-benzamido-5-alkylthio-1,3,4-thiadiazoles.⁵

The reaction of benzoyl isothiocyanate with *ortho*-phenylenediamine has been done in acetone using potassium thiocyanate as a thiocyanate source.⁶ Urea attacks the benzoyl isothiocyanate on one end of the molecule. Potassium thiocyanate in acetone has been reacted with benzoyl chloride at 50 °C.⁷ 1,2-Diaminoethane, 1,3-diaminopropane or 1,4-diaminobutane dissolved in acetone were added and stirred at room temperature for 2 h.⁸

2. Results and Discussion

2.1. Synthesis and Spectroscopic Characterization

The phenyl thiourea derivatives are formed by the attack of the thione carbon of the starting benzoyl isothiocyanate by the two amino groups of the other starting molecule. Scheme 1 gives the synthetic pathway for the synthesis of the diamine derivatives.



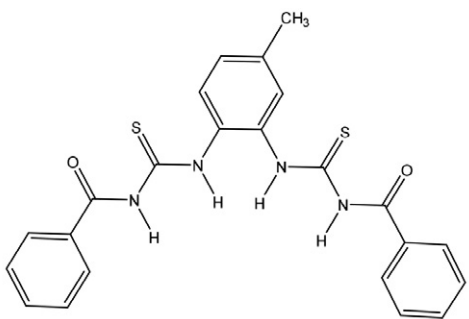
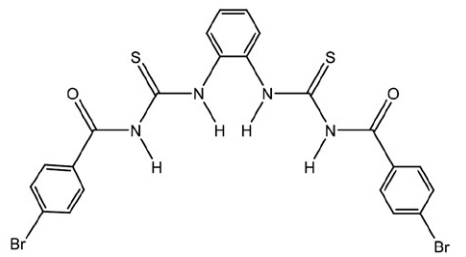
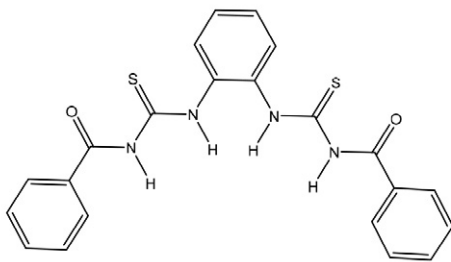
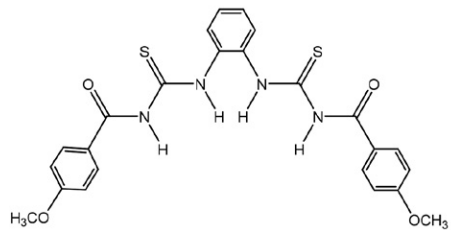
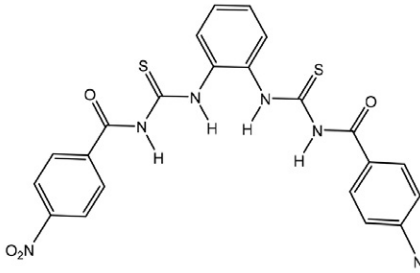
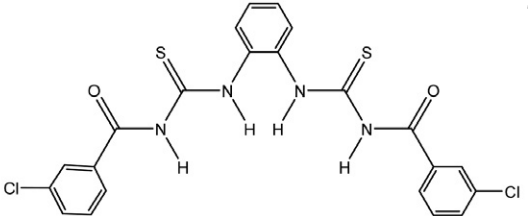
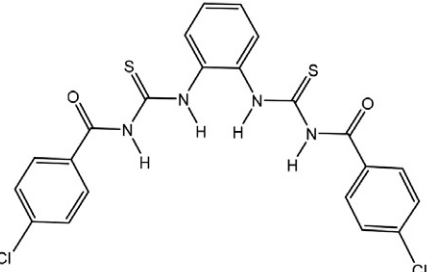
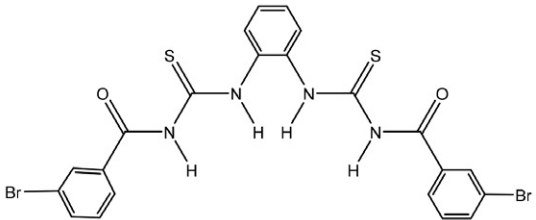
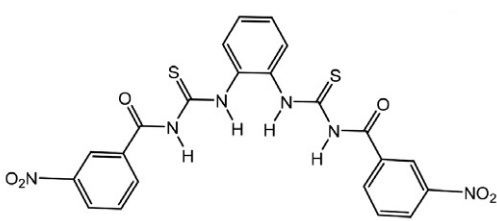
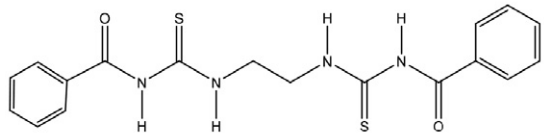
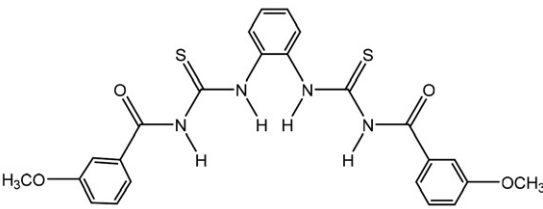
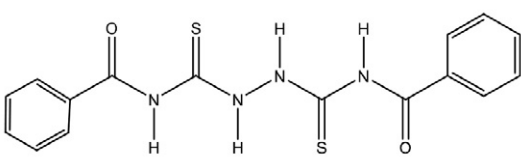
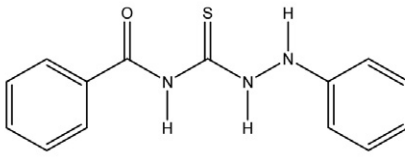
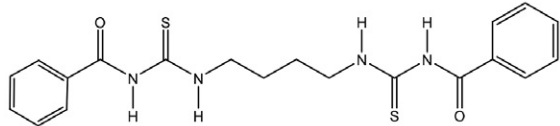
Scheme 1. Synthesis of phenylthiourea compounds and other diamine derivatives.

Spectroscopic characterization. The dithiourea derivatives were obtained by the reaction of ammonium thiocyanate with the respective benzoyl chloride in acetone and heating under reflux for 2 h to yield the benzoyl isothiocyanate derivatives. The addition of the diamines and further heating under reflux for 3 h gave the final products **1–14**. The ¹H NMR gave signals between δ 14.24 and 11.24 ppm for the NH proton of the amide. Table 1 gives the structures of all the synthesized compounds and their yields.

Aromatic protons gave signals between δ 11.72 and 7.01 ppm. In the ¹³C NMR the thione signal was observed between δ 180.8 and 171.5 ppm whilst the carbonyl occurred between δ 168.3 and 161.0 ppm. Signals for aromatic carbons were observed between δ 159.0 and 113.3 ppm. The IR gave signals for the N–H stretching between 3440 and 3071 cm^{-1} , whilst the aliphatic C–H stretching occurred between 2993 and 2727 cm^{-1} . The C=S stretching was observed between 1683 and 1670 cm^{-1} , with the carbonyl stretching occurring between 1687 and 1640 cm^{-1} and the C=C stretching observed between 1597 and 1506 cm^{-1} .

Crystal structures of compounds 1, 11, 12 and 14. Compounds **1**, **11**, **12** and **14** were recrystallized from DMSO/toluene (1:1). Compound **1** was obtained as white crystals, whilst compounds **11** and **12** were obtained as brown and light brown crystals, respectively. Compound **14** recrystallized from DMSO/toluene (1:3) as a light brown solid. The crystallographic data, selected bond

Table 1. List of synthesized compounds and their yields.

Compound	Structure	Yield (%)	Compound	Structure	Yield (%)
1		78.0	7		72.2
2		78.0	8		77.1
3		74.7	9		75.3
4		70.7	10		80.0
5		73.0	11		70.9
6		76.4	12		71.8
			13		71.6
			14		80.8

lengths and bond angles for the crystal structures of compounds **1**, **11**, **12** and **14** are provided in Tables 2 and 3. The ORTEP diagrams for compounds **1**, **11**, **12** and **14** are pre-

sented in Figures 1, 2, 3 and 4. Compounds **1**, **11** and **14** crystallized in the monoclinic space group $P2_1/c$, while compound **12** crystallized in the monoclinic space group

Table 2. Crystallographic data and structure refinement summary for compounds **1**, **11**, **12** and **14**.

Property	1	11	12	14
Formula	$C_{23}H_{20}N_4O_2S_2$	$C_{18}H_{18}N_4O_2S_2$	$C_{16}H_{14}N_4O_2S_2, 2(C_2H_6OS)$	$C_{20}H_{22}N_4O_2S_2$
CCDC Number	1448382	1919730	1919731	1919732
Formula weight	448.57	386.50	514.73	414.56
Crystal system	Monoclinic	Monoclinic	Monoclinic	Monoclinic
Space group	$P2_1/c$	$P2_1/c$	$P2_1/n$	$P2_1/c$
a [Å]	10.8288(4)	11.2036(13)	6.3738(2)	5.9962(2)
b [Å]	17.8575(7)	7.1780(8)	15.3854(5)	23.2946(10)
c [Å]	22.6276(9)	11.0901(13)	12.6585(4)	7.1680(3)
α [°]	90	90	90	90
β [°]	92.581(2)	100.783(5)	93.448(1)	103.777(2)
γ [°]	90	90	90	90
V [Å ³]	4371.2(3)	876.11(18)	1239.09(7)	972.42(7)
Z	8	2	2	2
D_{calc} [g/cm ³]	1.363	1.465	1.380	1.416
Mu(MoKa) [/mm]	0.272	0.325	0.417	0.298
$F(000)$	1872	404	540	436
Crystal size [mm]	0.23 × 0.32 × 0.54	0.14 × 0.22 × 0.25	0.15 × 0.27 × 0.33	0.06 × 0.47 × 0.58
Temperature [K]	200	200	200	200
Tot., unique data, $R(int)$	40580, 10903, 0.028	2175, 2175, 0.000	11663, 3088, 0.020	13405, 2402, 0.020
Observed data [$I > 2.0 \sigma(I)$]	7835	1986	2596	2022
N_{ref}	10903	2175	3088	2402
N_{par}	616	128	155	135
R, wR_2, S	0.0605, 0.1408, 1.08	0.1277, 0.4138, 1.17	0.0298, 0.0821, 1.03	0.0339, 0.0931, 1.06
Min. and max. resd. dens. [e/Å ³]	-0.63, 0.71	-1.59, 1.64	-0.27, 0.33	-0.20, 0.32

Table 3. Selected bond lengths (Å) and bond angles (°) for compounds **1**, **11**, **12** and **14**.

Bond Distances (Å)							
1	11	11	11	12	12	14	14
S21–C22	1.667(1)	S1–C2	1.662(1)	S1–C2	1.668(1)	S1–C2	1.673(1)
S11–C12	1.667(1)	O1–C1	1.218(1)	O1–C1	1.225(2)	O1–C1	1.223(2)
O21–C21	1.230(1)	C1–C11	1.492(1)	N1–C1	1.382(2)	N1–C1	1.374(2)
O11–C11	1.224(1)	N1–C2	1.405(1)	N1–C2	1.383(2)	N2–C2	1.321(2)
N21–C22	1.399(1)	N1–C1	1.371(1)	N2–N2_a	1.373(2)	N2–C3	1.461(2)
N22–C22	1.332(1)	C3–C3_a	1.522(1)	N2–C2	1.332(2)	N1–C2	1.390(2)
N22–C221	1.421(3)	N2–C2	1.325(2)	S2–O2	1.508(1)	C3–C4	1.521(2)
N23–C23	1.335(4)	N2–C3	1.454(2)	N2–C2	1.332(2)	C4–C4_a	1.522(2)
Bond Angles (°)							
1	11	11	11	12	12	14	14
N21–C22–N22	114.5(2)	C1–N1–C2	128.6(1)	O2–S2–C4	106.2(1)	C1–N1–C2	129.3(1)
S21–C22–N22	127.6(2)	C2–N2–C3	123.3(1)	O2–S2–C3	105.6(1)	C2–N2–C3	122.3(1)
O11–C11–N11	122.4(2)	O1–C1–N1	122.4(1)	N2_a–N2–C2	119.6(1)	O1–C1–C11	122.1(1)
N21–C21–C211	117.6(2)	S1–C2–N2	126.0(1)	N1–C1–C11	115.1(1)	N1–C2–N2	117.8(1)
N11–C12–N12	114.7(2)	S1–C2–N1	118.4(1)	N1–C2–N2	116.1(1)	S1–C2–N2	124.7(1)
S22–C23–N24	118.2(2)	N1–C1–C11	115.3(1)	S1–C2–N1	121.2(1)	N2–C3–C4	112.4(1)
S22–C23–N23	126.0(2)	O1–C1–C11	122.3(1)	C3–S2–C4	97.1(1)	S1–C2–N1	117.5(1)
O22–C24–N24	122.7(3)	N1–C2–N2	115.6(1)	C1–N1–C2	126.5(1)	N1–C1–C11	115.4(1)
O22–C24–C231	121.4(3)	N2–C3–C3_a	111.1(1)	O1–C1–N1	122.9(1)	O1–C1–N1	122.5(1)
O11–C11–C111	122.4(2)	C1–C11–C12	123.5(1)	O1–C1–C11	122.0(1)	C1–C11–C12	117.5(1)
O21–C21–C211	120.7(2)	C1–C11–C16	116.6(1)	S1–C2–N2	122.8(1)	C1–C11–C16	123.7(1)

$P2_1/n$. In compound **1** the bond distances O21–C21 and O11–C11 are 1.230(1) Å and 1.224(1) Å which are consistent with carbonyls,⁹ whilst the bond distances of S21–C22 and S11–C12 which are 1.667(1) Å and 1.667(1) Å are typical of thiones.¹⁰ The bond angles of S21–C22–N22 and O11–C11–N11 are 127.6(2)° and 122.4(2)° respectively this confirms that the carbon atoms are sp^2 hybridized. The bond distances of S1–C2 and O1–C1 in compound **11** are 1.662(1) Å and 1.218(1) Å for a thione and a carbonyl, respectively. The bond distance of C3–C3_a is

1.522(1) Å which is consistent with a carbon-carbon single bond.¹¹ The bond angles of S1–C2–N2 and S1–C2–N1 are 126.0(1)° and 118.4(1)° confirming that the carbon is sp^2 hybridized, whilst the bond angle of N2–C3–C3_a which is 111.1(1)° confirms the carbon is sp^3 hybridized. In compound **12** the bond distance S1–C2 which was 1.668(1) Å was consistent with a thione, whilst the carbonyl O1–C1 bond length was 1.225(2) Å. The N2–N2_a bond distance was 1.373(2) Å. The bond angles of O1–C1–N1 and O1–C1–C11 were 122.9(1)° and 122.0(1)°,

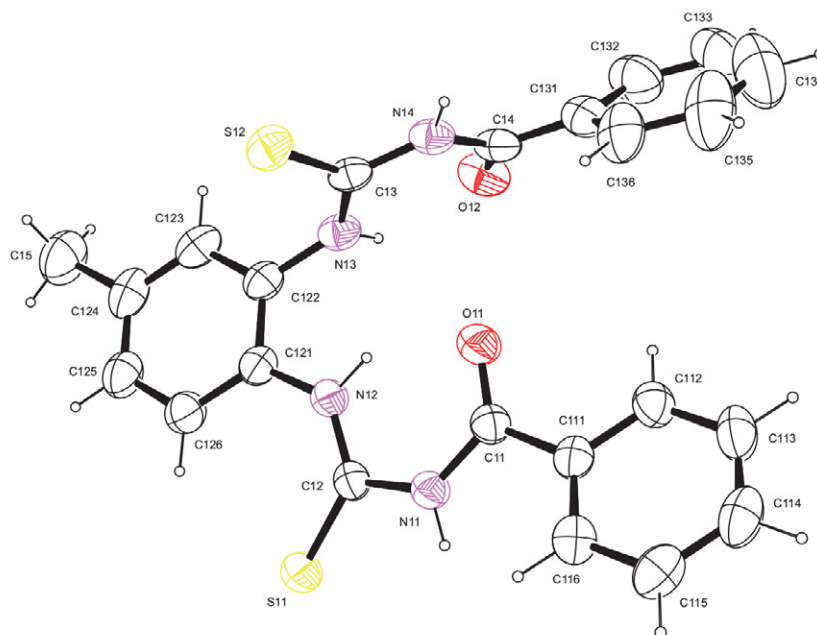


Figure 1. An ORTEP view of 1-benzoyl-3-(5-methyl-2-(((phenylformamido)methanethiolyamino)phenyl)thiourea (**1**) showing 50% probability displacement ellipsoids and the atom labelling.

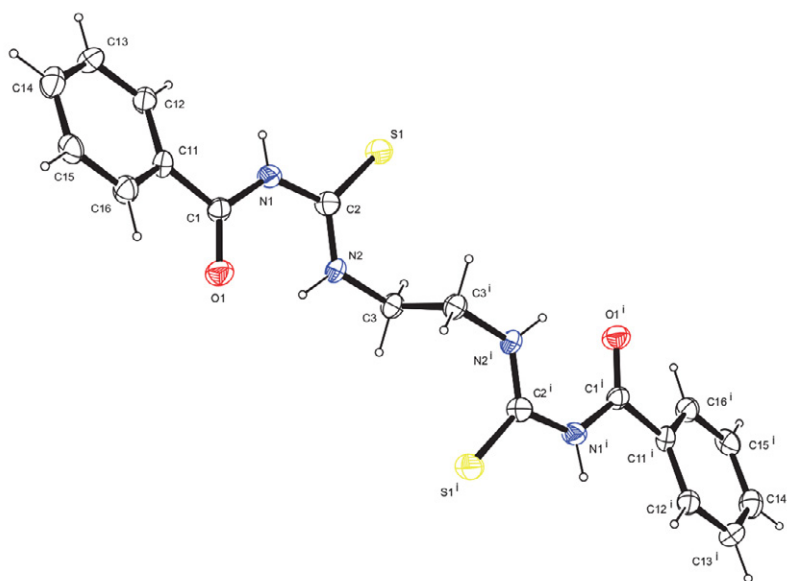


Figure 2. An ORTEP view of 3-benzoyl-1-(2-(((phenylformamido)methanethiolyamino)ethyl)thiourea (**11**) showing 50% probability displacement ellipsoids and the atom labelling.

respectively, confirming that the carbon atom involved is sp^2 hybridized.

In compound **14** the carbonyl O1–C1 bond length was 1.223(2) Å, whilst the thione S1–C2 was 1.673(1) Å. The bond angles of O1–C1–C11, N1–C2–N2 and S1–C2–N2 in compound **14** were 122.1(1)°, 117.8(1)° and 124.7(1)° which is characteristic of sp^2 hybridized carbon.

The crystal structure of compound **11** was reported at 293 K,¹² but this work gives the crystal structure at 200

K. Both measurements gave a monoclinic space group $P2_1/c$ with two molecules in the unit cell. The cell parameters obtained at 273 K were slightly higher than the measurement at 200 K.

The crystal structure of compound **12** has been reported at 273 K,¹³ whilst this work presents the crystal structure at 200 K. Both measurements gave a monoclinic space group $P2_1/n$ with two molecules in the unit cell and each molecule bonded to two molecules of dimethylsulfox-

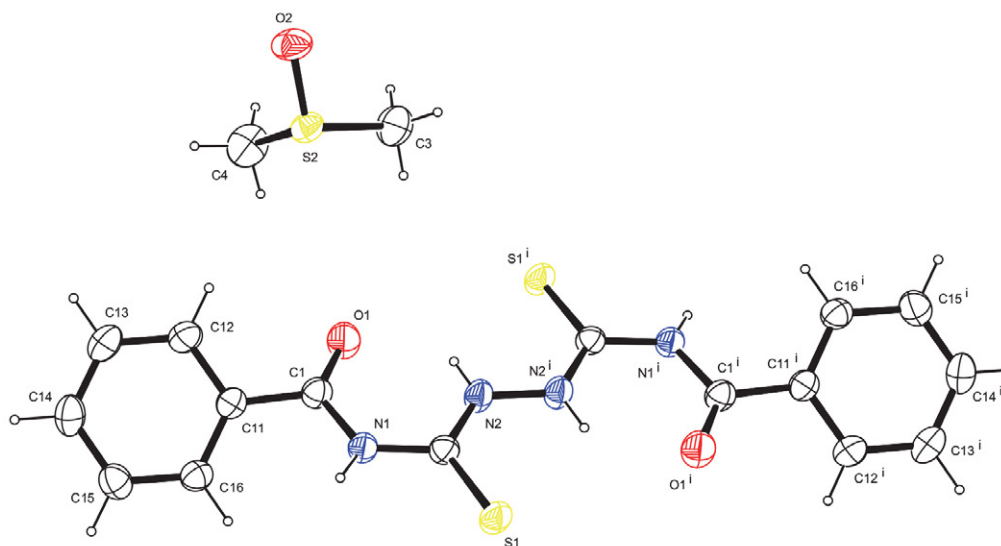


Figure 3. An ORTEP view of 3-benzoyl-1-[(phenylformido)methanethioyl]amino}thiourea dimethyl sulfoxide (**12**) showing 50% probability displacement ellipsoids and the atom labelling.

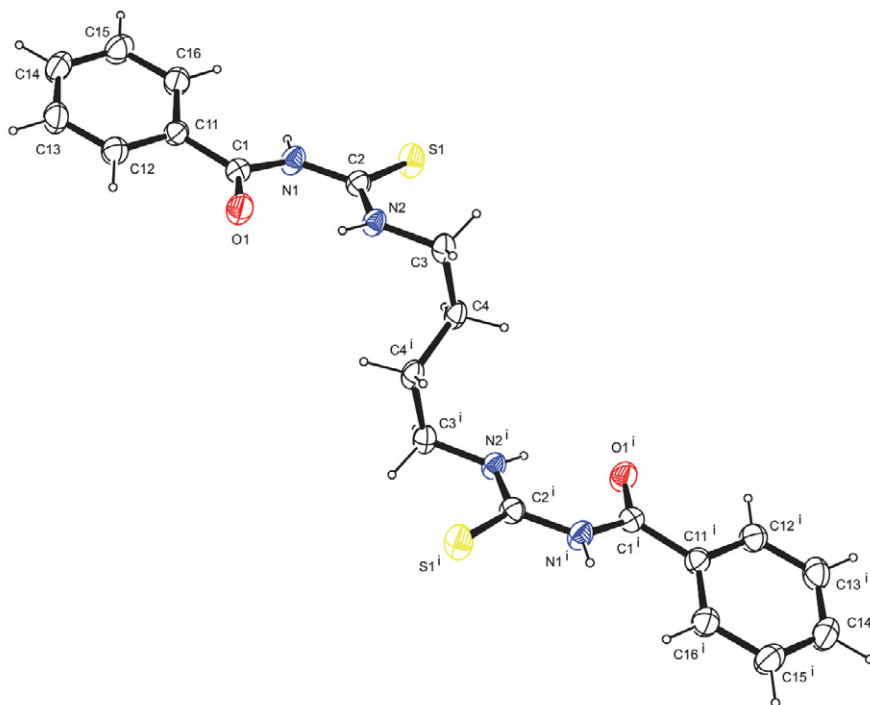


Figure 4. An ORTEP view of 3-benzoyl-1-(4-[(phenylformamido)methanethioyl]amino}butyl)thiourea (**14**) showing 50% probability displacement ellipsoids and atom labelling.

ide. The cell parameters for the determination at 273 K gave consistently higher values than the measurement at 200 K. The measurement at 273 K gave a lower density (1.347 g cm^{-3}) than the measurement at 200 K (1.380 g cm^{-3})

The crystal structure of compound 14 has been reported at 298 K,² whilst this work reports the crystal structure at 200 K. Both measurements gave a monoclinic space group $P2_1/c$ with two molecules in the unit cell. The cell parameters for the determination at 298 K gave consistently higher values than the measurement at 200 K. The measurement at 298 K gave a lower density (1.380 g cm^{-3}) than the measurement at 200 K (1.416 g cm^{-3})

3. Biological Studies

The compounds were tested for their cytotoxicity using HeLa cells, and tested against HIV-1 protease with ritonavir as a positive control and *Plasmodium falciparum* strain 3D7 (20 μM) with chloroquine as a positive control. The compounds were also tested for their activity against *Trypanosoma brucei* (20 μM) with pentamidine as a positive control.

Cytotoxicity tests. The graph (Figure 5) and table (Table 4) below give the % HeLa cell viability obtained for each tested compound (1–12). Compounds 1 and 12 were found to be cytotoxic against HeLa cells whilst all the other compounds were found to be non-cytotoxic.

HIV-1 protease activity. Table 5 and Figure 6 give the HIV-1 screening results for the diamine derivatives of benzoyl isothiocyanate and their *in silico* results. The

Table 4. % HeLa cell viability obtained for the compounds 1–12.

Compound	% Viability
1	42.48
2	68.62
3	67.55
4	67.67
5	75.44
6	91.16
7	99.55
8	72.61
9	63.29
10	65.97
11	71.01
12	49.73

screening of the compounds 1–14 was completed at 100 μM and 10 μM of inhibitor and ritonavir, respectively. The predicted inhibition constant for compound 1 (4-methyldithiourea) was 0.19 μM whilst the HIV-1 assay gave a % inhibition of $17.69 \pm 9.61\%$, compound 2 (unsubstituted) gave a predicted inhibition constant of 0.13 μM and a percentage inhibition of $10.30 \pm 6.12\%$. For compound 3 (4-nitro derivative) a predicted inhibition constant of 0.47 μM and a percentage inhibition of $31.03 \pm 0.42\%$ were obtained whilst compound 5 (3-nitro derivative) gave predicted inhibition constant of 0.11 μM and a percentage inhibition of $32.68 \pm 11.03\%$. Though the predicted inhibition constant of the 3-nitro derivative seems to be better than that of the 4-nitro, the percentage inhibition for both compounds are not too different, due to their interaction with solvent molecules which does not greatly change

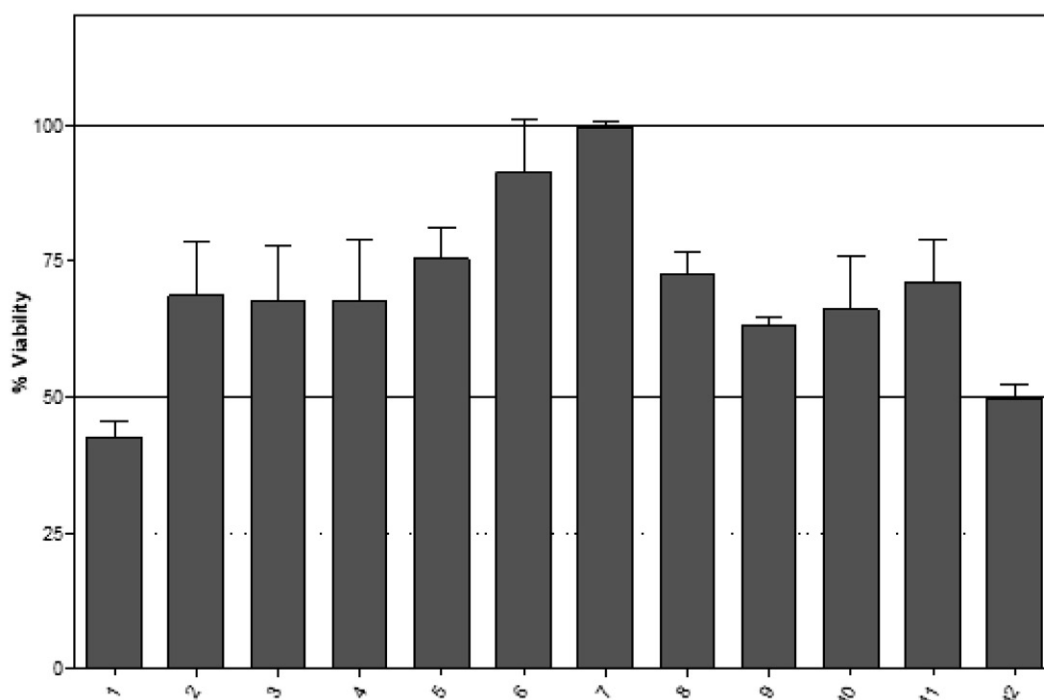


Figure 5. % HeLa cell viability \pm SD obtained for compounds 1–12.

their orientations in the active site. Compounds **4** (4-chloro derivative), **6** (3-methoxy derivative) and **8** (4-methoxy derivative) showed no activity in the HIV-1 protease assay with the predicted inhibition constants of 0.21, 1.90 and 0.81 μM , suggesting that in solution the methoxy substituent on the dithiourea makes the whole molecule inactive against HIV-1 protease at a concentration of 100 μM whilst a chloro substitution at position 4 makes the molecule ineffective at inhibiting HIV-1 protease because the chloro group interacts with the surrounding groups that interfere with its ability to fit well into the active site for effective inhibition of the protease. When the chloro group is attached at position 3, such as in compound **9** (3-chloro derivative), it gave a predicted inhibition constant of 0.06 μM which was the best predicted inhibition constant from the set and a percentage inhibition of $1.78 \pm 11\%$ confirming that the chloro group undergoes too much interaction with polar groups in solution hence the substantial departure from the predicted inhibition. Compound **7** (4-bromo derivative) gave predicted inhibition constant of 0.12 μM and a percentage inhibition of $29.62 \pm 4.10\%$ whilst compound **10** (3-bromo derivative) gave predicted inhibition constant of 0.095 μM and a percentage inhibition of $97.03 \pm 0.37\%$. Compound **10** gave the best percentage inhibition of all the compounds. In these class of compounds, a bromo substituent at position 3 gives the best percentage inhibition among this class of compounds. The size of the bromo group allows the substituent to fit the active site for effective binding to the aspartate groups and the bridging water molecules in the active site. The other diamine derivatives gave lower predicted inhibition constants than those with the phenyl backbone. In the computation, the lack of rigidity in these molecules accounts for their lower predicted inhibition constants even though their protease

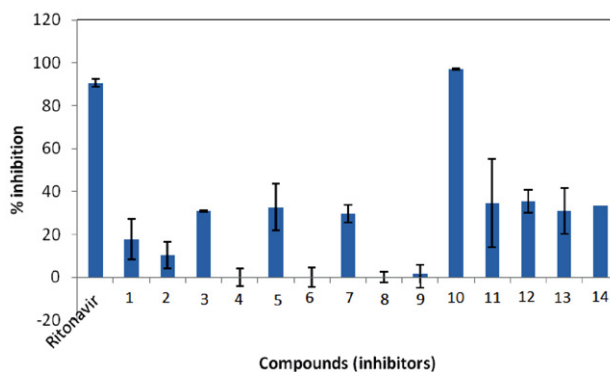


Figure 6. HIV-1 protease screening results illustrating percentage inhibition of selected diamine derivatives of benzoyl isothiocyanate (100 μM) and ritonavir (10 μM) relative to untreated control. Error bars represent standard deviation of $n = 3$.

% inhibition is comparable to the *ortho*-phenylenediamine derivatives. Compound **11** (ethanediamine derivative) gave predicted inhibition constant of 19.98 μM and a percentage inhibition of $34.53 \pm 20.69\%$. Compound **12** (hydrazine derivative) gave predicted inhibition constant of 10.98 μM and a percentage inhibition of $35.49 \pm 5.24\%$. Compound **13** (phenylhydrazine derivative) gave predicted inhibition constant of 0.25 μM and a percentage inhibition of $30.80 \pm 10.61\%$. Compound **14** (butyldiamine derivative) gave predicted inhibition constant of 10.98 μM and a percentage inhibition of $33.18 \pm 0.16\%$.

Figure 7 gives the 2D representation of compound **10** in the protease active site. The presence of a polar group on this class of compounds improves the extent of interaction at the active site both in the docking studies and the bioassays making this class of compounds active against the protease.

Table 5. HIV-1 protease screening results of the screened **1–14** diamine derivatives of benzoyl isothiocyanate.

Compound	Fluorescence	% Activity relative to untreated control	% Inhibition relative to untreated control	<i>In silico</i> results K_i (μM)
Ritonavir	36.24	9.34	90.66 ± 1.88	Unsuccessful
1	186.01	82.31	17.69 ± 9.61	0.19
2	202.70	89.70	10.30 ± 6.12	0.13
3	155.85	68.97	31.03 ± 0.42	0.47
4	402.60	103.79	0 ± 4.10	0.21
5	152.13	67.32	32.68 ± 11.03	0.11
6	243.51	107.76	0 ± 4.60	1.90
7	159.05	70.38	29.62 ± 4.10	0.12
8	446.80	115.18	0 ± 2.43	0.81
9	381.00	98.22	1.78 ± 11	0.06
10	11.522	2.97	97.03 ± 0.37	0.095
11	147.94	65.4	34.53 ± 20.69	19.98
12	145.79	64.52	35.49 ± 5.24	10.98
13	268.44	69.20	30.80 ± 10.61	0.25
14	151.00	66.82	33.18 ± 0.16	1.34

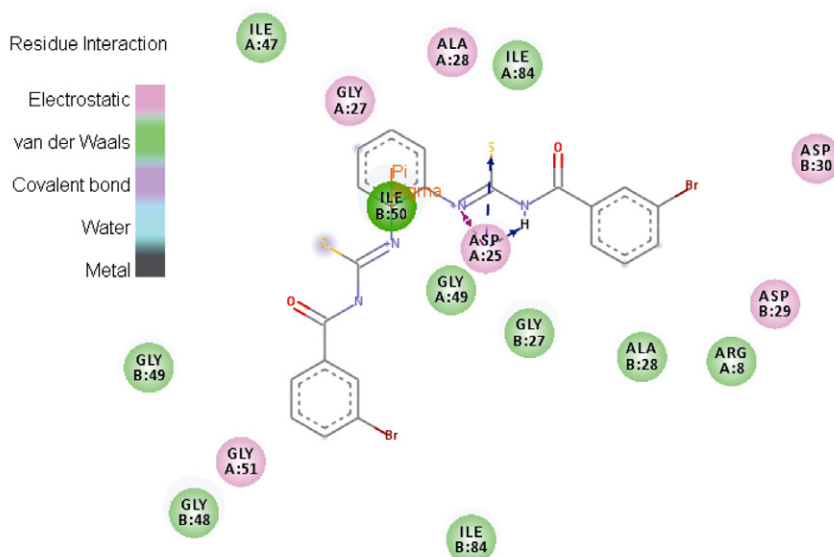


Figure 7. 2D representation of 1-(3-bromobenzoyl)-3-[2-((3-bromophenyl)formamido)methanethiyl]amino)phenyl]thiourea (**10**) in the HIV-1 protease binding site.

Anti-malaria test. The bar graph (Figure 8) and table (Table 6) below show the percentage parasite (*Plasmodium falciparum* strain 3D7) viability \pm SD obtained after a 48 h incubation with 20 μ M of the individual compounds **1**–**12**. The anti-malaria test showed varying degrees of activity, with compound **6** giving the best percentage viability of 57.2 ± 1.3 , whilst compound **11** was the least active with a percentage viability of 98.0 ± 13.4 . Chloroquine was used as the standard in the antimalarial test.

Trypanosoma brucei activity. The graph (Figure 9) and table (Table 7) below show the residual percentage parasite (*Trypanosoma brucei*) viability obtained after a 48 h incubation with 20 μ M of the individual compounds **1**–**12**. Compounds **10** and **12** gave very good activity with percentage viability of $17.9 \pm 5.6\%$ and $11.2 \pm 0.9\%$, re-

Table 6. Percentage parasite (*Plasmodium falciparum* strain 3D7) viability \pm SD obtained for the compounds **1**–**12**.

Compound	Viability %
1	65.9 ± 5.0
2	80.0 ± 6.5
3	87.8 ± 7.9
4	62.6 ± 1.8
5	80.9 ± 14.2
6	57.2 ± 1.3
7	88.1 ± 3.1
8	78.2 ± 13.2
9	89.2 ± 5.9
10	64.9 ± 2.2
11	98.0 ± 13.4
12	60.6 ± 6.3

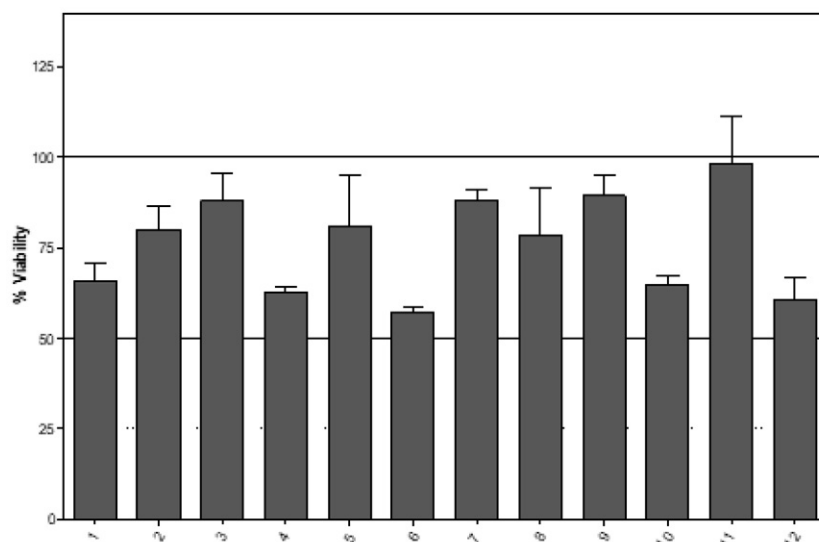


Figure 8. Percentage parasite (*Plasmodium falciparum* strain 3D7) viability \pm SD obtained for compounds **1**–**12**.

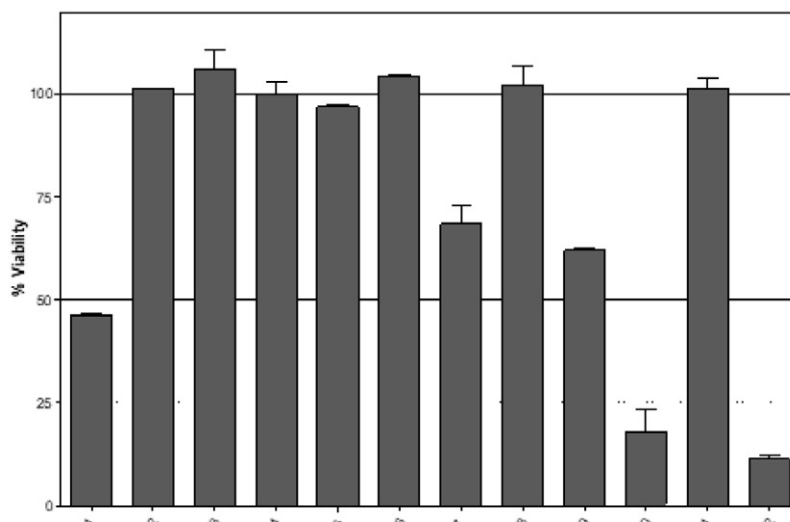


Figure 9. The residual percentage parasite (*Trypanosoma brucei*) viability \pm SD obtained for compounds 1–12.

spectively whilst the least active was compound 3 with a percentage viability $106.1 \pm 4.5\%$. Pentamidine was used as the standard.

Table 7. Percentage parasite (*Trypanosoma brucei*) viability \pm SD obtained for the compounds 1–12.

Compound at 20 μ M	Viability %
1	46.4 \pm 0.4
2	101.2 \pm 0.1
3	106.1 \pm 4.5
4	100.1 \pm 3.0
5	96.9 \pm 0.5
6	104.2 \pm 0.5
7	68.4 \pm 4.3
8	102.2 \pm 4.7
9	62.0 \pm 0.6
10	17.9 \pm 5.6
11	101.3 \pm 2.7
12	11.2 \pm 0.9

4. Experimental

Chemicals and instrumentation. Analytical grade reagents and solvents for synthesis and analysis which included 3-chlorobenzoyl chloride, 4-chlorobenzoyl chloride, 4-methoxybenzoyl chloride, 3-methoxybenzoyl chloride, 3-bromobenzoyl chloride, 4-bromobenzoyl chloride, 4-nitrobenzoyl chloride, 3-nitrobenzoyl chloride, *ortho*-phenylenediamine, 4-methyl-*ortho*-phenylenediamine, 2-(2-aminophenyl)benzimidazole ethylene diamine, hydrazine hydrate and ammonium thiocyanate were obtained from Sigma Aldrich (USA), whilst benzoyl chloride, toluene and acetone were obtained from Merck Chemicals (SA). The chemicals were used as received (*i.e.* without further purification). ^1H NMR and ^{13}C NMR spectra were recorded on a Bruker Avance AV 400 MHz spectrometer

operating at 400 MHz for ^1H and 100 MHz for ^{13}C , using deuterated dimethyl sulfoxide as the solvent and tetramethylsilane as the internal standard. Chemical shifts are expressed in ppm. Structural assignments of resonances have been performed with the help of 2D NMR gradient experiments (^1H - ^1H COSY). FT-IR spectra were recorded on a Bruker Platinum ATR Spectrophotometer Tensor 27 and the data were processed using OPUS. Elemental analyses were performed using a Vario Elementar Microcube ELIII. Melting points were obtained using a Stuart Lasec SMP30 melting point apparatus and are reported uncorrected, whilst the mass spectra were determined using an Agilent 7890A GC System connected to a 5975C VL-MS-C with electron impact as the ionization mode and detection by a triple-axis detector.

General method for the synthesis of dithiourea derivatives. The dithiourea derivatives were prepared by dissolving ammonium thiocyanate (0.04 mol, 3.05 g) in 80 mL of acetone, the respective benzoyl chloride (0.04 mol) was then added and heated under reflux at 100–120 $^\circ\text{C}$ for 2 h. The benzoyl isothiocyanate derivative (0.04 mol) obtained was filtered, 4-methyl-*ortho*-phenylenediamine, *ortho*-phenylenediamine, ethylenediamine or hydrazine hydrate (0.04 mol) was added to the filtrate and refluxed at 100–120 $^\circ\text{C}$ for 3 h.

1-Benzoyl-3-(5-methyl-2-[(phenylformamido)methanethiyl]amino)phenylthiourea (1). The product obtained was filtered and recrystallized from DMSO/toluene (1:1) as a brown solid. M.p. 172–173 $^\circ\text{C}$. Yield 78.0%. ^1H NMR (400 MHz, DMSO- d_6) δ 12.45 (s, 1H, NH), 12.41 (s, 1H, NH), 11.72 (d, 2H, $J = 8.0$ Hz, NH), 7.90 (d, 4H, $J = 8.0$ Hz), 7.77 (m, 1H, $J = 8.4$ Hz), 7.73 (s, 1H), 7.64 (t, 2H, $J = 7.2$ Hz), 7.49 (t, 4H, $J = 7.6$ Hz), 7.22 (d, 1H, $J = 8.0$ Hz), 2.31 (s, 3H). ^{13}C NMR (100 MHz, DMSO- d_6) δ 180.40 (C=S), 168.3 (C=O), 136.8 (C), 133.2 (C), 133.1 (C), 130.9

(CH), 128.5 (CH), 128.3 (CH), 127.7 (CH), 126.9 (CH), 126.5 (CH), 20.7 (CH₃). IR ν_{\max} 3186 (N–H), 2981 (C–H), 1670 (C=S), 1593 (C=O), 1512 (C=C), 1487 (C–N) cm⁻¹. Anal. calcd. for C₂₃H₂₀N₄O₂S₂: C 61.59; H, 4.49; N, 12.49; S, 14.30. Found: C 61.65; H, 4.54; N, 12.56; S, 14.46. LRMS (*m/z*, M⁺) found for C₂₃H₂₀N₄O₂S₂: 448.40, expected mass: 448.56.

1-Benzoyl-3-(2-(((phenylformamido)methanethioyl)amino)phenyl)thiourea (2). The product obtained was filtered and recrystallized from DMSO/toluene (1:1) as a light brown solid. M.p. 174–176 °C. Yield 78.0%. ¹H NMR (400 MHz, DMSO-*d*₆) δ 12.52 (s, 1H), 8.10 (d, 2H), 7.94 (d, 2H), 7.71 (m, 2H), 7.65 (m, 4H), 7.48 (m, 2H), 7.42 (m, 2H), 7.11 (m, 1H). ¹³C NMR (100 MHz, DMSO-*d*₆) δ 167.3 (C=O), 166.4 (C=O), 144.2 (C), 131.8 (C), 130.7 (CH), 129.2 (CH), 128.8 (CH), 128.5 (CH), 124.4 (CH), 113.5 (CH). IR ν_{\max} 3327 (N–H), 3262 (N–H), 3134 (N–H), 1673 (C=S), 1643 (C=O), 1596 (C=C), 1514 (C=C), 1486 (C–N), 1337 cm⁻¹. Anal. calcd. for C₂₂H₁₈N₂O₂S₂: C, 60.81; H, 4.18; N, 12.89; S, 14.76. Found: C, 60.56; H, 4.28; N, 12.78; S, 14.52. LRMS (*m/z*, M⁺) found for C₂₂H₁₈N₂O₂S₂: 434.45, expected mass: 434.53.

1-(4-Nitrobenzoyl)-3-[2-(((4-nitrophenyl)formamido)methanethioyl)amino]phenyl thiourea (3). The mother liquor was allowed to stand overnight in a fume hood. The product obtained was filtered and recrystallized from DMSO/toluene (1:1) as a yellow solid. M.p. 202–204 °C. Yield 74.7%. ¹H NMR (400 MHz, DMSO-*d*₆) δ 12.30 (s, 2H, NH), 12.13 (s, 2H, NH), 8.33 (d, 4H, *J* = 8.0 Hz), 8.09 (d, 4H, *J* = 8.0 Hz), 7.93 (m, 2H), 7.42 (m, 2H). ¹³C NMR (100 MHz, DMSO-*d*₆) δ 180.1 (C=S), 161.0 (C=O), 149.7 (C), 138.1 (C), 133.3 (C), 130.20 (CH), 127.3 (CH), 126.8 (CH), 123.2 (CH). IR ν_{\max} 3200 (N–H), 3071 (N–H), 1683 (C=S), 1662 (C=O), 1508 (C=C), 1484 (C–N) cm⁻¹. Anal. calcd. for C₂₂H₁₆N₆O₆S₂: C, 50.38; H, 3.07; N, 16.02; S, 12.23. Found: C, 50.49; H, 3.11; N, 16.17; S, 12.36. LRMS (*m/z*, M⁺) found for C₂₂H₁₆N₆O₆S₂: 524.20, expected mass: 524.53.

1-(4-Chlorobenzoyl)-3-[2-(((4-chlorophenyl)formamido)methanethioyl)amino]phenyl thiourea (4). The product obtained was filtered and recrystallized from DMSO/toluene (1:1) as a yellow solid. M.p. 173–175 °C. Yield 70.7%. ¹H NMR (400 MHz, DMSO-*d*₆) δ 8.52 (m, 2H), 7.93 (d, 2H, *J* = 7.6 Hz), 7.89 (d, 2H, *J* = 7.6 Hz), 7.81 (br, 2H), 7.65 (br, 2H), 7.55 (t, 2H, *J* = 8.0 Hz), 7.50 (t, 2H, *J* = 8.0 Hz). ¹³C NMR (100 MHz, DMSO-*d*₆) δ 143.8 (C), 132.1 (CH), 125.9 (CH), 124.0 (CH), 119.6 (CH). IR ν_{\max} 3038 (N–H), 1640 (C=O), 1578 (C=C), 1555 (C=C), 1476 (C–N), 1447 (C–N) cm⁻¹. Anal. calcd. for C₂₂H₁₆Cl₂N₄O₂S₂: C, 52.49; H, 3.20; N, 11.13; S, 12.74. Found: C, 52.56; H, 3.26; N, 11.22; S, 12.85. LRMS (*m/z*, M⁺) found for C₂₂H₁₆Cl₂N₄O₂S₂: 503.20, expected mass: 503.42.

1-(3-Nitrobenzoyl)-3-[2-(((3-nitrophenyl)formamido)methane)amino]phenyl thiourea (5). The product obtained was filtered and recrystallized from DMSO/toluene (1:1) as a yellow solid. M.p. 201–203 °C. Yield 73.0%. ¹H NMR (400 MHz, DMSO-*d*₆) δ 12.34 (s, 2H, NH), 12.18 (s, 2H, NH), 8.65 (s, 2H), 8.48 (d, 2H, *J* = 8.0 Hz), 8.31 (d, 2H, *J* = 8.0 Hz), 7.96 (m, 2H), 7.78 (dd, 2H, *J* = 8 Hz), 7.44 (t, 2H, *J* = 4.0 Hz). ¹³C NMR (100 MHz, DMSO-*d*₆) δ 180.2 (C=S), 166.4 (C=O), 147.3 (C), 135.1 (C), 133.7 (C), 133.3 (CH), 130.1 (CH), 127.4 (CH), 127.2 (CH), 126.6 (CH), 123.5 (CH). IR ν_{\max} 3351 (N–H), 3204 (N–H), 1687 (C=O), 1515 (C=C) cm⁻¹. Anal. calcd. for C₂₂H₁₆N₆O₆S: C, 50.38; H, 3.07; N, 16.02; S, 12.23. Found: C, 50.24; H, 3.20; N, 16.18; S, 12.19. LRMS (*m/z*, M⁺) found for C₂₂H₁₆N₆O₆S: 524.60, expected mass: 524.53.

1-(3-Methoxybenzoyl)-3-[2-(((3-methoxyphenyl)formamido)methanethioyl)amino]phenyl thiourea (6). The product obtained was filtered and recrystallized from DMSO/toluene (1:1) as a white solid. M.p. 164–166 °C. Yield 76.4%. ¹H NMR (400 MHz, DMSO-*d*₆) δ 12.50 (s, 2H), 11.69 (s, 2H), 7.92 (m, 2H), 7.50 (d, 2H, *J* = 7.6 Hz), 7.45 (s, 2H), 7.41 (t, 4H, *J* = 8 Hz), 7.21 (d, 2H, *J* = 8.8 Hz), 3.77 (s, 6H). ¹³C NMR (100 MHz, DMSO-*d*₆) δ 180.4 (C=S), 168.1 (C=O), 159.0 (C), 133.4 (C), 129.8 (C), 127.1 (CH), 126.6 (CH), 120.8 (CH), 119.3 (CH), 113.3 (CH), 55.5 (CH₃). IR ν_{\max} 3326 (N–H), 3184 (N–H), 3003 (N–H), 1663 (C=O), 1597 (C=C), 1506 (C=C), 1464 (C–N) cm⁻¹. Anal. calcd. for C₂₄H₂₂N₄O₄S₂: C, 58.28; H, 4.48; N, 11.33; S, 12.97. Found: C, 58.12; H, 4.29; N, 11.42; S, 12.86. LRMS (*m/z*, M⁺) found for C₂₄H₂₂N₄O₄S₂: 494.35, expected mass: 494.59.

1-(4-Bromobenzoyl)-3-[2-(((4-bromophenyl)formamido)methanethioyl)amino]phenyl thiourea (7). The product obtained was filtered and recrystallized from DMSO/toluene (1:1) as a white solid. M.p. 205–207 °C. Yield 72.2%. ¹H NMR (400 MHz, DMSO-*d*₆) δ 12.37 (s, 2H), 11.82 (s, 2H), 7.91 (m, 2H), 7.81 (d, 4H, *J* = 8.0 Hz), 7.73 (d, 4H, *J* = 7.6 Hz), 7.40 (m, 2H). ¹³C NMR (100 MHz, DMSO-*d*₆) δ 180.5 (C=S), 167.4 (C=O), 133.6 (C), 131.4 (CH), 131.2 (C), 130.6 (CH), 127.2 (CH), 127.1 (C), 126.7 (CH). IR ν_{\max} 3140 (N–H), 2993 (C–H), 1681 (C=O), 1585 (C=C), 1517 (C=C), 1429 (C–N) cm⁻¹. Anal. calcd. for C₂₂H₁₆Br₂N₄O₂S₂: C, 44.61; H, 2.72; N, 9.46; S, 10.83. Found: C, 44.70; H, 2.65; N, 9.40; S, 10.76. LRMS (*m/z*, M⁺) found for C₂₂H₁₆Br₂N₄O₂S₂: 592.20, expected mass: 592.33.

1-(4-Methoxybenzoyl)-3-[2-(((4-methoxyphenyl)formamido)methanethioyl)amino]phenyl thiourea (8). The product obtained was filtered and recrystallized from DMSO/toluene (1:1) as a white solid. M.p. 206–208 °C. Yield 77.1%. ¹H NMR (400 MHz, DMSO-*d*₆) δ 12.56 (s, 2H, NH), 11.48 (s, 2H, NH), 7.92 (m, 6H), 7.38 (m, 2H, *J* = 3.6, 5.6 Hz), 7.01 (d, 4H, *J* = 8.8 Hz), 3.82 (s, 6H). ¹³C NMR

(100 MHz, DMSO- d_6) δ 180.8 (C=S), 167.5 (C=O), 163.2 (C), 133.3 (C), 131.0 (CH), 126.9 (CH), 123.9 (CH), 113.71 (CH), 55.8 (CH₃). IR ν_{\max} 3404 (N–H), 3278 (N–H), 3001 (N–H), 2961 (C–H), 2837 (C–H), 1653 (C=O), 1594 (C=C), 1525 (C=C), 1489 (C–N) cm^{-1} . Anal. calcd. for C₂₄H₂₂N₄O₄S₂: C, 58.26; H, 4.48; N, 11.33; S, 12.97. Found: C, 58.13; H, 4.37; N, 11.29; S, 13.03. LRMS (m/z , M⁺) found for C₂₄H₂₂N₄O₄S₂: 494.20, expected mass: 494.59.

1-(3-Chlorobenzoyl)-3-[2-(((3-chlorophenyl)formamido)methanethioyl)amino]phenyl thiourea (9). The product obtained was filtered and recrystallized from DMSO/toluene (1:1) as a light brown solid. M.p. 143–145 °C. Yield 75.3%. ¹H NMR (400 MHz, DMSO- d_6) δ 12.40 (br, 2H), 11.88 (s, 2H, NH), 8.04 (m, 1H), 7.91 (d, 3H, J = 12.8 Hz), 7.83 (d, 2H, J = 7.6 Hz), 7.70 (d, 2H, J = 8.0 Hz), 7.52 (m, 2H, J = 8.0, 7.2 Hz), 7.41 (s, 2H). ¹³C NMR (100 MHz, DMSO- d_6) δ 180.4 (C=S), 167.0 (C=O), 134.3 (C), 133.2 (C), 132.8 (CH), 130.5 (CH), 128.5 (CH), 127.3 (CH), 127.1 (CH), 126.7 (CH). IR ν_{\max} 3440 (N–H), 3166 (N–H), 2971 (C–H), 1668 (C=O), 1593 (C=C), 1510 (C=C), 1471 (C–N), 1459 (C–N) cm^{-1} . Anal. calcd. for C₂₂H₁₆Cl₂N₄O₂S₂: C, 52.49; H, 3.20; N, 11.13; S, 12.74. Found: C, 52.31; H, 3.29; N, 11.22; S, 12.86. LRMS (m/z , M⁺) found for C₂₂H₁₆Cl₂N₄O₂S₂: 503.35, expected mass: 503.42.

1-(3-Bromobenzoyl)-3-[2-(((3-bromophenyl)formamido)methanethioyl)amino]phenyl thiourea (10). The mother liquor was allowed to stand overnight in a fume hood. The product obtained was filtered and recrystallized from DMSO/toluene (1:1) as a light yellow solid. M.p. 191–193 °C. Yield 80.0%. ¹H NMR (400 MHz, DMSO- d_6) δ 12.29 (s, 2H), 11.75 (s, 2H), 7.93 (s, 2H), 7.89 (m, 2H), 7.79 (d, 4H, J = 7.6 Hz), 7.44 (d, 2H, J = 8 Hz), 7.41 (m, 2H). ¹³C NMR (100 MHz, DMSO- d_6) δ 180.65 (C=S), 167.74 (C=O), 136.3 (C), 134.5 (CH), 133.8 (C), 131.5 (CH), 131.2 (CH), 127.9 (CH), 126.9 (CH), 122.1 (CH). IR ν_{\max} 3389 (N–H), 3176 (N–H), 3016 (N–H), 1662 (C=O), 1595 (C=C), 1563 (C=C), 1456 (C–N) cm^{-1} . Anal. calcd. for C₂₂H₁₆Br₂N₄O₂S₂: C, 44.61; H, 2.72; N, 9.46; S, 10.83. Found: C, 44.75; H, 2.68; N, 9.39; S, 10.70. LRMS (m/z , M⁺) found for C₂₂H₁₆Br₂N₄O₂S₂: 592.10, expected mass: 592.33.

3-Benzoyl-1-(2-(((phenylformamido)methanethioyl)amino)ethyl)thiourea (11). The product obtained was filtered and recrystallized from DMSO/toluene (1:1) as a light brown solid. M.p. 220–222 °C. Yield 70.85%. ¹H NMR (400 MHz, DMSO- d_6) δ 10.98 (s, 2H), 7.91 (d, 4H, J = 7.6 Hz), 7.61 (t, 2H, J = 7.2 Hz), 7.51 (t, 4H, J = 7.6 Hz), 3.09 (s, 4H). ¹³C NMR (100 MHz, DMSO- d_6) δ 180.8 (C=S), 167.3 (C=O), 132.9 (C), 132.2 (CH), 128.5 (CH) 43.4 (CH₂). IR ν_{\max} 3420 (N–H), 3229 (N–H), 3047 (N–H), 1664 (C=O), 1579 (C=C), 1507 (C=C), 1448 (C–N) cm^{-1} . Anal. calcd. for C₁₈H₁₈N₄O₂S₂: C, 55.94; H, 4.69; N, 14.50;

S, 16.59. Found: C, 56.03; H, 4.74; N, 14.42; S, 16.63. LRMS (m/z , M⁺) found for C₁₈H₁₈N₄O₂S₂: 386.30, expected mass: 386.49.

3-Benzoyl-1-(((phenylformido)methanethioyl)amino)thiourea (12). The product obtained was filtered and recrystallized from DMSO/toluene (1:1) as a white solid. M.p. 345–346 °C. Yield 71.8%. ¹H NMR (400 MHz, DMSO- d_6) δ 14.24 (s, 1H, NH), 12.12 (s, 1H, NH), 8.13 (d, 2H, J = 8.0 Hz), 8.01 (d, 2H, J = 8.0 Hz), 7.94 (d, 1H, J = 8.0 Hz), 7.65 (m, 1H), 7.55 (t, 3H, J = 8.0 Hz), 7.50 (m, 1H). ¹³C NMR (100 MHz, DMSO- d_6) δ 171.5 (C=O), 168.3 (C=S), 167.3 (C=O), 165.0 (C=O), 156.0 (C), 150.2 (C), 134.2 (CH), 132.8 (CH), 131.6 (CH), 131.2 (CH), 130.7 (CH), 128.8 (CH), 128.4 (CH), 128.3 (CH), 128.2 (CH), 125.4 (CH). IR ν_{\max} 2988 (C–H), 2911 (C–H), 1670 (C=O), 1658 (C=O), 1536 (C=C), 1489 (C–N), 1424 (C–N) cm^{-1} . Anal. calcd. for C₁₆H₁₄N₄O₂S₂: C, 53.61; H, 3.94; N, 15.63; S, 17.89. Found: C, 53.73; H, 4.02; N, 15.60; S, 17.78. LRMS (m/z , M⁺) found for C₁₆H₁₄N₄O₂S₂: 358.36, expected mass: 358.44.

3-Benzoyl-1-(phenylamino)thiourea (13). The product recrystallized from DMSO/toluene (1:1) as a white solid. M.p. 242–244 °C. Yield 71.6%. ¹H NMR (400 MHz, DMSO- d_6) δ 8.03 (m, 2H), 7.44 (m, 2H), 7.37 (m, 5H), 7.34 (s, 1H), 7.19 (s, 1H). ¹³C NMR (100 MHz, DMSO- d_6) δ 162.9 (C=O), 149.6 (C), 136.8 (C), 129.9 (CH), 129.4 (CH), 129.3 (CH), 128.7 (CH), 126.6 (CH), 125.1 (CH). IR ν_{\max} 3070 (N–H), 3018 (N–H), 2727 (C–H), 1591 (C=O), 1561 (C=O), 1499 (C–N), 1475 (C–N) cm^{-1} . Anal. calcd. for C₁₄H₁₃N₃OS: C, 62.31; H, 5.19; N, 14.42; S, 13.86. Found: C, 62.31; H, 5.19; N, 14.42; S, 13.86. LRMS (m/z , M⁺) found for C₁₄H₁₃N₃OS: 271.80, expected mass: 271.97.

3-Benzoyl-1-(4-(((phenylformamido)methanethioyl)amino)butyl)thiourea (14). The product was filtered and recrystallized from DMSO/toluene (1:1) as a light brown solid. M.p. 159–161 °C. Yield 80.8%. ¹H NMR (400 MHz, DMSO- d_6) δ 11.24 (s, 1H, NH), 10.94 (br, 1H, NH), 7.90 (d, 2H, J = 8.0 Hz), 7.62 (t, 1H, J = 7.2, 7.6 Hz), 7.48 (t, 2H, J = 7.6 Hz), 3.76 (m, 4H), 2.51 (br, 2H, NH), 2.06 (t, 2H, NH). ¹³C NMR (100 MHz, DMSO- d_6) δ 180.2 (C=S), 167.7 (C=O), 132.9 (C), 132.2 (CH), 128.4 (CH), 128.3 (CH), 42.6 (CH₂), 26.7 (CH₂). IR ν_{\max} 3405 (N–H), 3217 (N–H), 2929 (C–H), 1666 (C=O), 1511 (C=C), 1432 (C–N) cm^{-1} . Anal. calcd. for C₂₀H₂₂N₄O₂S₂: C, 57.95; H, 5.35; N, 13.32; S, 15.47. Found: C, 57.87; H, 5.42; N, 13.45; S, 15.36. LRMS (m/z , M⁺) found for C₂₀H₂₂N₄O₂S₂: 414.70. Expected mass: 414.54.

X-ray crystal structure determination. X-ray diffraction analyses of **1**, **11**, **12** and **14** were performed at 200 K using a Bruker Kappa Apex II diffractometer with monochromated Mo K α radiation (λ = 0.71073 Å). APEXII¹⁴ was

used for data collection and¹⁵ for cell refinement and data reduction. The structures were solved by direct methods using SHELXS-2013,¹⁴ and refined by least-squares procedures using SHELXL-2013,¹⁵ with SHELXL,¹⁴ as a graphical interface. All non-hydrogen atoms were refined anisotropically. Carbon-bound H atoms were placed in calculated positions (C–H 0.95 Å for aromatic carbon atoms and C–H 0.99 Å for methylene groups) and were included in the refinement in the riding model approximation, with $U_{\text{iso}}(\text{H})$ set to $1.2U_{\text{eq}}(\text{C})$. The H atoms of the methyl groups were allowed to rotate with a fixed angle around the C–C bond to best fit the experimental electron density (HFIX 137 in the SHELX program suite¹⁵) with $U_{\text{iso}}(\text{H})$ set to $1.5U_{\text{eq}}(\text{C})$. Nitrogen-bound H atoms were located on a difference Fourier map and refined freely. Data were corrected for absorption effects using the numerical method implemented in SADABS.¹⁶

5. Conclusions

The work involved the design and synthesis of dithioureia derivatives for HIV-1 protease inhibitors using Autodock 4.2, the compounds were characterized by spectroscopic techniques and microanalysis. 1-(3-Bromobenzoyl)-3-[2-(((3-bromophenyl)formamido)methanethiyl)amino]phenylthiourea (**10**) and 3-benzoyl-1-((phenylformido)methanethiyl)aminothiourea (**12**) gave a percentage viability of $17.9 \pm 5.6\%$ and $11.2 \pm 0.9\%$ against *Trypanosoma brucei*. The single crystal X-ray diffraction analysis of 1-benzoyl-3-(5-methyl-2-((phenylformamido)methanethiyl)amino)phenylthiourea (**1**), 3-benzoyl-1-(2-((phenylformamido)methanethiyl)amino)ethylthiourea (**11**), 3-benzoyl-1-((phenylformido)methanethiyl)aminothiourea (**12**) and 3-benzoyl-1-(4-((phenylformamido)methanethiyl)amino)butylthiourea (**14**) have been presented. 1-(3-Bromobenzoyl)-3-[2-(((3-bromophenyl)formamido)methanethiyl)amino]phenylthiourea (**10**) gave a percentage inhibition of $97.03 \pm 0.37\%$ against HIV-1 protease enzyme at a concentration of 100 μM .

Acknowledgement

We thank MRC for the research funding (MRC-SIR). F. Odame thanks the National Research Foundation of South Africa for awarding him a postdoctoral Fellowship.

Supplementary Information

Supplementary data associated with this article can be found in the online version. CCDC numbers 1448382, 1919730, 1919731 and 1919732 contain the crystal structures associated with this article.

6. References

1. R. Mohebat, G. Mohammadian, *J. Chem. Res.* **2012**, 36, 626–628. [doi:10.1039/c2cc36262g](https://doi.org/10.1039/c2cc36262g)
2. Y. J. Ding, X. B. Chang, X. Q. Yang, W. K. Dong, *Acta Cryst.* **2008**, E64, o658. Trypanosoma brucei. Predstavljeni so tudi rezultati rent
3. W. K. Dong, H. B. Yan, L. Q. Chai, Z. W. Lv, C. Y. Zhao, *Acta Cryst.* **2008**, E64, o1097. [DOI:10.1107/S160053680801430X](https://doi.org/10.1107/S160053680801430X)
4. W. K. Dong, X. Q. Yang, L. Xu, L. Wang, G. L. Liu, J. H. Feng, *Z. Kristallogr. NCS* **2007**, 222, 279–280. [DOI:10.1524/ncrs.2007.0118](https://doi.org/10.1524/ncrs.2007.0118)
5. F. Kurzer, *J. Chem. Soc. (C)*, **1971**, 2932–2938. [DOI:10.1039/j39710002932](https://doi.org/10.1039/j39710002932)
6. S. K. Kang, N. S. Cho, M. K. Jeon, *Acta Cryst.* **2012**, E68, o395. [DOI:10.1107/S1600536812000621](https://doi.org/10.1107/S1600536812000621)
7. E. I. Thiam, M. Diop, M. Gaye, A. S. Sall, A. H. Barry, *Acta Cryst.* **2008**, E64, o776. [DOI:10.1107/S1600536808008374](https://doi.org/10.1107/S1600536808008374)
8. Y. H. Lee, W. S. Han, H. J. Lee, S. M. Ahn, T. K. Hong, *J. Anal. Chem.* **2015**, 70, 621–626. [DOI:10.1134/S1061934815050172](https://doi.org/10.1134/S1061934815050172)
9. F. Odame, E. Hosten, R. Betz, K. Lobb, Z. R. Tshentu, *Acta Chim. Slov.* **2015**, 62, 986–994. [DOI:10.17344/acsi.2015.1703](https://doi.org/10.17344/acsi.2015.1703)
10. F. Odame, E. C. Hosten, Z. R. Tshentu, R. Betz, *Z. Kristallogr. NCS* **2014**, 229, 337–338.
11. F. Odame, J. Krause, E. C. Hosten, R. Betz, K. Lobb, Z. R. Tshentu, C. L. Frost, *Bull. Chem. Soc. Ethiop.* **2018**, 32, 271–284. [DOI:10.4314/bcse.v32i2.8](https://doi.org/10.4314/bcse.v32i2.8)
12. I. Samb, N. Gaye, R. Sylla-Gueye, E. I. Thiam, M. Gaye, P. Retailleau, *Acta Cryst E.* **2019**, 75, 642–645. [DOI:10.1107/S205698901900495X](https://doi.org/10.1107/S205698901900495X)
13. B. M. Yamin, M. S. M. Yusof, *Acta Cryst E.* **2003**, 59, o358–o359. [DOI:10.1107/S1600536803003635](https://doi.org/10.1107/S1600536803003635)
14. APEX2, SADABS and SAINT (2010) Bruker AXS Inc: Madison, WI, USA.
15. G. M. Sheldrick, A short history of SHELX, *Acta Cryst. A*, **2008**, 64, 112–122. [DOI:10.1107/S0108767307043930](https://doi.org/10.1107/S0108767307043930)
16. C. B. Hübschle, G. M. Sheldrick, B. Dittrich, *ShelXle: J. Appl. Cryst.* **2011**, 44, 1281–1284. [DOI:10.1107/S0021889811043202](https://doi.org/10.1107/S0021889811043202)

Povzetek

Izvedli smo načrtovanje (s pomočjo Autodock 4.2) in sintezo novih ditiosečninskih derivatov kot inhibitorjev HIV-1 proteaze. Nove spojine smo karakterizirali s spektroskopskimi metodami in z mikroanalizo. Spojini 1-(3-bromobenzoil)-3-[2-((3-bromofenil)formamido)metantioil]amino)fenil]tiosečnina (**10**) in 3-ben(**12**) sta dali $17.9 \pm 5.6\%$ in $11.2 \pm 0.9\%$ sposobnost preživetja za genske difrakcijske analize monokristalov spojin 1-benzoil-3-(5-metil-2-((fenilformamido)metantioil]amino)fenil]tiosečnine (**1**), 3-benzoil-1-(2-((fenilformamido)metantioil]amino)etil]tiosečnine (**11**), 3-benzoil-1-((fenilformamido)metantioil]amino)tiosečnine (**12**) and 3-benzoil-1-(4-((fenilformamido)metantioil]amino)butil]tiosečnine (**14**). Za spojino 1-(3-bromobenzoil)-3-[2-((3-bromofenil)formamido)metantioil]amino)fenil]tiosečnina (**10**) smo izmerili odstotno inhibicijo $97.03 \pm 0.37\%$ proti encimu HIV-1 proteaza pri koncentraciji 100 μM .



Except when otherwise noted, articles in this journal are published under the terms and conditions of the Creative Commons Attribution 4.0 International License

Scientific paper

Alternative to Conventional Edible Oil Sources: Cold Pressing and Supercritical CO₂ Extraction of Plum (*Prunus domestica* L.) Kernel Seed

Jelena Vladić,¹ Aleksandra Gavarić,¹ Stela Jokić,² Nika Pavlović,³
Tihomir Moslavac,⁴ Ljiljana Popović,¹ Ana Matias,⁴ Alexandre Agostinho,⁴
Marija Banožić² and Senka Vidović^{1,*}

¹ University of Novi Sad, Faculty of Technology, Bulevar cara Lazara 1, Novi Sad, Serbia

² J. J. Strossmayer University of Osijek, Faculty of Food Technology, Trg S. Trojstva 3, 31000 Osijek, Croatia

³ J. J. Strossmayer University of Osijek, Faculty of Medicine, Cara Hadrijana 10E, 31000 Osijek, Croatia

⁴ iBET - Instituto de Biologia Experimental e Tecnológica, Avenida da República, Estação Agronómica, 2780-157 Oeiras, Portugal

* Corresponding author: E-mail: senka.vidovic@uns.ac.rs
Tel.: +381 21 485 3603

Received: 11-08-2019

Abstract

Plum (*Prunus domestica* L.) is a fruit widely cultivated across Europe and its processing generates a considerable amount of waste in form of discharged plum kernels. This creates a new opportunity to exploit plum kernels in order to provide an alternative to conventional edible oils. The main aim of this study was to obtain high-quality oil from plum kernel seeds by applying traditional cold pressing (CP) and supercritical carbon dioxide (ScCO₂) extraction as a modern technology. The obtained oils were characterized based on the chemical composition of fatty acids and tocopherols. In obtained oils, twelve fatty acids were identified. The oleic acid was the most dominant in both oils (68.66% in oil obtained by ScCO₂, 65.86% in oil obtained by CP), followed by linoleic acid (22.24–25.44%). While total tocopherols content in oil obtained by ScCO₂ was 4 to 5.8-fold higher than CP. The results proved that the utilization of plum kernel seeds possess high potential as an alternative oil source due a high amount of oleic acid and tocopherols and a low amount of saturated fatty acids and amygdalin.

Keywords: *Prunus domestica*; supercritical carbon dioxide; cold pressing; tocopherol; fatty acid

1. Introduction

Prunus species comprises 40 different varieties. However, only two species are predominate for industrial application: the European plum (*Prunus domestica* L.) which is hexaploid tree, and the Japanese plum (*Prunus salicina* L.) which is diploid tree.¹ Plum production and processing are widely spread across Europe. Food companies producing dry and canned plum, plum juices and jam; beside, in several European countries plums are used for production of alcoholic beverages.² Through processing all are generating large amounts of waste, mostly consist of plum kernel. Apart from being use as biodiesel feed-

stock,³ cheap source of bioactive peptides,⁴ active carbons⁵ or carbonaceous adsorbents,⁶ plum kernel (plum kernel seeds) could be used as a valuable source of oils, which yield can reach above 50%.⁷

Recently, nonconventional oils have gained a lot of attention due to their useful properties.⁸ It is already known that some fruit seeds derived from citrus,⁹ grapes¹⁰ and watermelon¹¹ can be used as sources of oils, phenolics and proteins. Citrus seeds contain 20.0–78.9% of oil depending on the species and cultivation conditions.¹² Mathhaus and Ozcan¹³ reported that in 17 different citrus seeds the content of oils oleic acid was in the range from 12.8 to 70.1%, linoleic acid from 19.5 to 58.8%, and palmitic acid from 5.1

to 28.3%. Watermelon seeds have an excellent potential for application in food formulations due to the high amount of oil from 50 to 51% and proteins from 32 to 37%.¹⁴ Watermelon seed oil is reported to contain a high content of unsaturated fatty acids from 77 to 82%, a high content of linoleic acid from 59 to 67.5%, and oleic acid from 14 to 18.1%. In addition, grape seeds also contain a considerable amount of oil (14–17%) and a high content of unsaturated acids compared to sunflower and corn oils, which is the main cause for their high commercial interest. Cao and Ito¹⁵ reported linoleic acid as the most abundant fatty acid (68.10–78.18%) in grape seed oils. Plum oil is located in the plum kernel seed. According to Velickovic et al.¹⁶ the content of seed in the plum kernel is 136 g/kg for, while content of oil, determined using standard Soxhlet procedure, is 409 g of oil per kg of plum.¹⁶ Same authors identified six main fatty acids in the plum oil: oleic, linoleic, palmitic, stearic and arachidonic acid, out of which oleic (59.5%) and linoleic (27.1%) had the highest percentage.¹⁶

Several different techniques could be applied for separation of oil fraction from the seeds. Among them extraction by organic solvents, supercritical extraction by carbon dioxide (ScCO₂) and cold pressing (CP), are mostly used. Yield of separated oil, oil quality and chemical composition are dependable on applied technique. Advantage of ScCO₂ and CP is the production of safe products, as well as processing in accordance to “green technologies” concept. Therefore, the main aim of this research was to investigate the possibility to obtain high-quality oil from plum kernels seed, using traditional CP and modern technology such as ScCO₂. The oils were characterized based on the chemical composition of fatty acids and tocopherols. The characteristics of oil obtained by ScCO₂ were compared to the oil produced by CD. The outcomes may provide a preliminary estimation of the plum kernels seed as an alternative source of edible oil, based upon their fatty acid profile since it is the main quality parameter for edible oils.

2. Materials and Methods

2.1. Material

Plum kernels were obtained from fruit producer *Plemić komerc doo* (Osečina, Serbia; year of collection 2017). Material was collected in dry condition and pulverized in mill (MRC Sample mill C-SM/450-C, Holon, Israel). Sieve sets (Erweka, Germany) was employed for determination of the particle size of the grounded material and the average particle size was 0.310 mm. The purity of CO₂ used for extraction was 99.97% (w/w) and purchased from Messer, Osijek, Croatia. For determination of fatty acid composition, Food Industry FAME mix 37 standards (Cat. No. 35077) was purchased from Restek (USA). For determination of tocopherol, α -tocopherol (Dr. Ehrenstorfer Cat No. 17924300), β -tocopherol (Supelco Cat No. 46401-U), γ -tocopherol (Supelco Cat No. 4-7785) and δ -tocopherol (Su-

pelco Cat No. 4-7784) were used. Amygdalin ($\geq 99\%$) standard (A6005-1G) was purchased from Sigma-Aldrich, Cas No. 29883-15-6, USA. All other used chemicals were analytical grade and purchased from J. T. Baker (PA, USA).

2.2. Cold Pressing of Plum Kernel Oil (PKO)

The cold pressed plum kernel oil was obtained by pressing 1 kg of plum seeds using the following parameters: head presses temperature of 40 °C, frequency of 20 Hz and using a nozzle of ID 6 mm. The pressing of the seeds was performed in a screw expeller SPU 20 (Senta, Serbia) with capacity 20–25 kg/h.

2.3. Supercritical CO₂ Extraction of Plum Kernel Oil (ScCO₂)

The experiments were carried out using ScCO₂ system explained in detail elsewhere.^{17,18} The extractor vessel was filled with the 100 g of grounded dried plum. The obtained extracts (oil) were collected in glass tubes. Extraction time was 5h. After each 30 minutes, extraction process was paused and the amount of obtained extracts was weighed. The ScCO₂ extraction parameters were as follows: pressure 300 bar, temperature 40 °C, and mass flow rate of 2 kg/h. Conditions in the separator were pressure 15 bar and temperature 25 °C.

2.4. Analysis of Fatty Acids (FA) Composition

FA methyl esters were prepared according to HRN EN ISO 12966-2:2011 standard method by saponification of glycerides with NaOH in methanol and analysed by gas chromatography carried out using Gas chromatograph 7890B (Agilent Technologies, Lake Forest, USA). Gas chromatography conditions were explained elsewhere.¹⁹ Obtained results are expressed as percentage (%) of individual fatty acids to the total fatty acids. The analyses were performed in two replicates.

2.5. Determination of Content of Tocopherols

Determination of tocopherols (α , β + γ , δ) content in PKO obtained by ScCO₂ was performed according to modified HRN EN 12822:2014 standard.²⁰ Analysis was performed using reversed-phase High Performance Liquid Chromatography (HPLC) Infinity 1290 Agilent Technologies (USA) instrument equipped with fluorescence detector (FLD). The analysis was monitored at wavelengths set at 290 and 325 nm, respectively. The instrument was equipped with autosampler G4226A and 1260 FLD G1321C with quaternary pump G4204A. Used column was Zorbax Eclipse XDB, C18 with particle size 5 μ m, and 250 mm long. As a mobile phase was acetonitrile:methanol (50:50) used with gradient run time of 16 minutes, as follow: start flow 2 mL/min and holding for 7 minutes, de-

creasing to 1.5 mL/min. Injection volume was 20 μ L and column temperature was set to 25 °C. Oil for HPLC analysis was prepared as follows. First, certain amount of oil was dissolved in volume of isopropanol providing 88.00–89.00% recovery. Prepared solutions were filtered through 0.2 filters before analysis.

2. 6. Determination of Content of Amygdalin

Cold pressed PKO and ScCO₂ extracts (2 g) were weighed into a round-bottom flask, with added ethanol (50 mL). Prepared mixture was boiled under reflux for 120 min. The extracts were filtered and ethanol was completely evaporated under vacuum. Diethyl ether (10 mL) was added to the dried sample and mixture was vortexed about 1 min to precipitate amygdalin. Diethyl ether was evaporated on rotary evaporator and dissolved in water (5 mL). Sample was filtered through a 0.2 μ m PTFE filter before HPLC analysis.²¹

The method was performed with an Agilent 1290 Infinity I HPLC system equipped with Agilent DAD detector and auto-sampler using (20 μ L). The detector was set at 210 nm and the peak areas were integrated automatically, using the Agilent HPLC Data Analysis software Chemstation. Used column for separation was C18 column (4.6 \times 250 mm, 5 μ m) at 20 °C. Quantitative analysis was performed with the external standardization by measuring the peak areas. RP-HPLC analysis was performed by isocratic elution with a flow rate of 1.0 mL min⁻¹. Used mobile phase was water: methanol (75:25 v/v). The analyses were conducted in two replicates.

3. Results and Discussion

3. 1. Extraction Yield of PKO

The kernels recovered from the plum kernels are a valuable source of oil and significant variations in oil yield

have been reported in different studies.^{22–24} The causes of variations might be attributed to a different geographic origin, variety, applied extraction technique, etc. Matthäus and Özcan²² determined oil content in *P. domestica* from two different locations (47.1 and 47.8 g/100 g) using petroleum as extraction solvent. According to Gornas et al.,²³ significant impacts on the PKO yield were related to variety and applied extraction techniques. Gornas et al.²³ reported that the difference between the highest and the lowest level of oil was almost 2.5-fold, while the average content of 28 varieties of two species tested was 38.2% (w/w) where oil extraction was done using *n*-hexane. In a study by Kostic et al.,²⁴ plum kernel oil yield was 35.8%, determined by the Soxhlet extraction, while the PKO yield obtained by pressing was 25.5%, which was 71% of the oil content. Authors concluded that extraction is a more efficient method than pressing since part of oil remains in cake during pressing. However, having in mind environmental and economic disadvantages of organic solvents, pressing is a more appropriate method.²⁴

In this study, efficiency of ScCO₂ as a modern extraction technique and CP technique as a traditional one was compared. Extraction yield obtained with CP was 30.85%, whereas the total extraction yield obtained by ScCO₂ was higher, 38.70%. ScCO₂ extraction kinetics, that is, the extraction yield in function of extraction time, is presented in Figure 1.

3. 1. Composition of Fatty Acids

Seed oils from *Prunus* species have already been reported to possess a highly desirable fatty acid composition with a high content of oleic acid, variable contents of linoleic acid followed with low content of saturated fatty acids. According to fatty acid composition, that may result higher consumer preferences than for olive oil.²² Twelve fatty acids in the kernel oils of plum were identified. The oleic and linoleic acids were predominant in PKO in both cold pressed

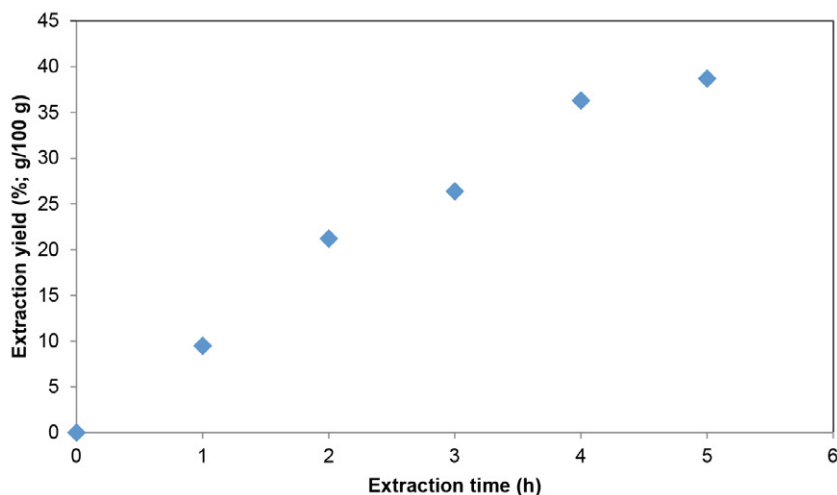


Figure 1. Extraction yield of PKO obtained by ScCO₂

and ScCO₂ extracts. These results are consistent with the ones from a published study by Kiralan et al.²⁵ where oleic acid was predominant, followed by linoleic and palmitic acids. Kamel and Kakuda²⁶ also reported oleic and linoleic acids as prevailing fatty acids in peach kernel oil. The oleic acid is 18-carbon monounsaturated fatty acid, essential and highly preferable in human nutrition. It is attributed to have positive effects such as reducing triglycerides, total cholesterol, and glycemic index in human metabolism. Moreover, the increase in oxidation stability in vegetable oil is often assigned to oleic acid presence.²⁷ The PKO is characterized with a high content of oleic acid (68.66% in PKO obtained by ScCO₂, 65.86% in PKO obtained by cold pressing) and a significantly lower amount of saturated fatty acids like palmitic acid and stearic acid (5.80% and 1.92% in PKO obtained by ScCO₂, respectively; 5.79% and 1.62% in PKO obtained by cold pressing, respectively). Similar results were obtained by Kiralan et al.²⁵ where the content of oleic acid was higher (75.43%), the content of palmitic acid was slightly higher (5.83%), and the content of stearic acid was slightly lower (1.35%) in *P. domestica* oil. The oleic (55–83%) and palmitic (7.5–20%) acids were the prevailing fatty acids in olive oils, followed by stearic acid (0.5–5.0%).²⁸ Detailed fatty acid profile is displayed in Table 2. Moreover, the composition of the obtained fatty acids has a number of similarities with other kernel oil studies.^{29,30} However, notable differences were not found in fatty acid profiles of PKO obtained by ScCO₂ and CP.

Considering its nutritional value, genus *Prunus* kernels represent an attractive oil for human consumption due to high values of oleic and linoleic acids. In a study by Matthäus and Özcan,²² the mean value for the content of oleic acid was 66.9% and for linoleic acid 22.7% which is in

agreement with our findings. Regarding fatty acid composition, the *Prunus* kernel seed oil could be compared to mid-high-oleic rapeseed oil which does not possess α -linolenic acid which is sensitive to oxidation. It is convenient that the amount of this fatty acid is low (0.09% in PKO obtained by ScCO₂, 0.07% in PKO obtained by CP). This is significant for the stability of PKO, especially if food processing requires heat. Therefore, taking into account the low amount of saturated fatty acids, the high amount of monounsaturated oleic acid, and a desirable fatty acid composition, PKO is highly recommended for human consumption as edible oil.²²

3. 2. Tocopherol Content

Tocopherol comprises several lipophilic phenolic compounds commonly found in edible oils, oil products, fatty fishes, cereals, nuts and other fat-contain products.³¹ This vitamin has 4 tocopherol homologues α -, β -, γ -, and δ -tocopherol, and 4 tocotrienol homologues, α -, β -, γ -, and δ -tocotrienol.³² Primary function of antioxidants and vitamin E is terminating free radicals *in vivo*.³² The relative reactivity of α , β , γ , and δ -tocopherol forms against oxygen radicals decreases following the order of $\alpha > \beta = \gamma > \delta$.³³ Therefore, α -tocopherol has the highest affinity to α -tocopherol transferprotein and as the consequence highest bioavailability³² and low rate of metabolism.³⁵ However, the deficiency of tocopherol in diet may cause circulatory disorders and influence on the metabolism pathway in muscles. Since vegetable oils provide humans with a significant part of their daily vitamin E dietary requirements,³⁶ it was of great importance to determine tocopherols profile for PKOs. Results of quantitative HPLC analysis of tocoph-

Table 2. Fatty acid composition of plum kernels obtained by ScCO₂ and by cold pressing

Fatty acid		Average value for ScCO ₂ -PKO [%]	Average value for CP-PKO [%]
C16:0	Palmitic acid	5.80	5.79
C16:1 (cis-9)	Palmitoleic acid	0.90	0.93
C17:1 (cis-10)	Heptadecenoic acid	0.10	0.11
C18:0	Stearic acid	1.92	1.62
C18:1 (cis-9)	Oleic acid, ω - 9	68.66	65.86
C18:2 (cis-9,12)	Linoleic acid, ω - 6	22.24	25.44
C20:0	Arachidic acid	0.13	0.11
C20:1 (cis-11)	Eicosenoic acid	0.09	0.07
C18:3 (cis-9,12,15)	Linolenic acid, ω - 3	0.09	0.07
C22:0	Behenic acid	0.02	<0.01
C20:3 (cis-8,11,14)	Eicosatrienoic acid	<0.01	<0.01
C22:1 (cis-13)	Erucic acid, ω - 9	0.01	<0.01
C24:0	Lignoceric acid	0.01	<0.01
Σ Saturated fatty acids SFA		7.90	7.52
Σ Unsaturated fatty acids UFA		92.10	92.48
Σ Monounsaturated fatty acids MUFA		69.76	66.97
Σ Polyunsaturated fatty acids PUFA		w22.33	25.51

LOD – limit of detection; <0.01

Table 3. Content of tocopherols in PKO

PKO	α -tocopherol (mg/g oil)	β + γ -tocopherol (mg/g of oil)	δ -tocopherol (mg/g of oil)
CP-PKO	0.076	1.22	0.149
ScCO₂			
after 1h	0.157	2.197	0.354
after 2h	0.092	1.46	0.217
after 3h	0.033	0.921	0.131
after 4h	0.019	0.720	0.096
after 5h	0.0063	0.532	0.067
Total	0.310	5.830	0.865

erols in PKOs, cold pressed or obtained by ScCO₂, are expressed as mg of compound per g of oil (mg/g) in Table 3.

The tocopherol homologues (α , β , γ and δ) were detected in cold pressed PKO, and also in PKO obtained by ScCO₂. Whole ScCO₂ process lasted for 5 hours and oil fractions were collected every hour of the extraction in order to determine at which extraction time the most significant solubility of tocopherols in oil is achieved. Previous researches^{37–40} showed that ScCO₂ extraction can provide satisfactory tocopherol yield from kernels and other plant by-products.

According to Hassanein,⁴¹ tocopherol content of PKO (0.71 mg/g) was distinctly higher than that of apricot (0.43 mg/g) and peach (0.52 mg/g) kernel oils, where oil was extracted using chloroform-methanol as a solvent. The oils derived from plum contained 85.5% of γ -tocopherol, apricot oil 93.5% of γ -tocopherol and peach 97.7% of tocopherol. However, α - and δ -tocopherols were detected in minor amounts. Beta-tocopherol was not detected in the three above mentioned oils. Previous mentioned three kernel oils showed to be highly resistant to autoxidation due to high content of γ -tocopherol.⁴² In our case, the majority of β + γ -tocopherols were obtained after two hours of ScCO₂. After 1h of ScCO₂, the amount of α -tocopherol is 2-fold higher than the amount obtained by cold pressing. The similar ratio is noticed after 1h of ScCO₂ in β + γ -tocopherols and δ -tocopherol amounts toward the ones obtained by traditional method. It is evident that the highest solubility of tocopherols was in the first hour of the extraction. Solubility decreases with further extraction, and after 5 hours of extraction, a 25 times lower amount of α -tocopherol was extracted in comparison with the first hour. A similar pattern of results was obtained for apricot kernels seeds in a study Pavlović et al.³⁷ where after 1 hour of ScCO₂ extraction the total content of tocopherols significantly decreased. When comparing the total tocopherols content in PKO obtained by ScCO₂ to those obtained with a conventional technique, it must be pointed out that a higher tocopherols content (4 to 5,8-fold) was obtained by applying the modern extraction technique (ScCO₂). Obtained tocopherol values correlate fairly well with Górnaś et al.⁴³ where the extraction of PKO was conducted

with hexane and assisted with ultrasound waves. Similarly to their research, γ -tocopherol was found to be predominant.

3. 3. Amygdalin Content

Stones from the *Prunus* genus fruits are low-cost and could represent considerable sources of proteins potential sources of peptides with biological activity. However, main restriction to the use of these oil sources is the presence of cyanogenic glycosides such as amygdalin.⁴⁴ Amygdalin is cyanogenic glycoside, commonly present in kernels and seeds of different fruits.⁴⁵ This glycoside is potentially toxic in the presence of enzymes (β -glucosidases and α -hydroxynitrilelyases), resulting in the release of hydrogen cyanide.⁴⁶ On the other hand, amygdalin exhibits many positive biological activities such as the anti-inflammatory and anti-cancer activity. Bolarinwa et al.⁴⁶ reported that seeds from *Rosaceae* species, especially from subspecies *Pomoideae* and *Prunoideae* contained relatively high amounts (0.1–17.5 mg/g) of amygdalin compared to seeds from non-*Rosaceae* species (0.01–0.2 mg/g). Senica et al.⁴⁷ also reported big differences in amounts of amygdalin in plum varieties. The lowest amount of amygdalin was in seeds of Valjevka variety and the highest amount of amygdalin was in seeds of Jojo variety. Before industrial application of *Rosaceae* species, it is recommended to perform a determination of amygdalin.⁴⁸ Garcia et al.⁴⁴ reported amygdalin content of 4.39 mg/g present in the plum seeds, which is 10-fold higher in comparison to amygdalin content (0.41 mg/g) found in our sample. A possible explanation for the significant differences in amygdalin content can be found in different environmental conditions, such as geographical origin, atmospheric conditions, and so on.⁴⁷ Amygdalin content in our plum seed was very low, and in both PKOs is present in traces (Table 4). Moreover, amygdalin content in both oils was significantly lower than in fresh plum kernels. The decrease in amygdalin content could be explained by enzyme degradation of amygdalin into degradation products such as cyanide. Both CP and ScCO₂ methods for obtaining plum kernel seeds oil were performed at low temperature (40 °C), avoiding inactivation of enzymes above 100 °C. With respect to differences in variety and extraction method, enzymatic degradation could be responsible for low amygdalin content. Generally, amygdalin content decreased in processed products for all *Rosaceae* and non-*Rosaceae* species.⁴⁶ However, future

Table 4. Amygdalin content in plum kernels, their oil and extract

Sample	Amygdalin content
Plum kernels	0.4100 mg/g of kernels
CP-PKO	0.0025 mg/g of oil
ScCO ₂ -PKO	0.0022 mg/g of oil

LOD (limit of detection) = 0.00024 mg/g; LOQ (limit of quantitation) = 0.00074 mg/g

work should consider the determination of enzymatic degradation products.

4. Conclusions

Despite the growing number of published papers, the fruit kernels are still considered as non-conventional potential oil sources. In view of the current desire for convenience food such as seedless fruits (citrus, grapes, watermelon, cherry, etc.) there is a tendency of growing kernel waste and further disposal issues. Dealing with the issue of pre-consumer or production food waste will be a crucial action prior to improving productivity and sustainability of the food production system. The high oil content in *Prunus* kernel seeds is comparable to commercial oils seeds such as rapeseed or sunflower seeds. Therefore kernels from genus *Prunus* are highly suitable for commercial oil production. Due to this, the utilization of kernels from this genus seems to be an interesting niche to create an extra value from a by-product.

Fatty acids composition of PKOs obtained by ScCO₂ and by cold pressing are similar, however, ScCO₂ has shown as more efficient considering notably higher yields of tocopherols, especially α -tocopherol. Additionally, obtained results justify the further processing of plum kernels as by-products of the fruit industry for the production of oil for potential food and pharmaceutical applications.

5. References

1. B. L. Topp, D. M. Russell, M. Neumüller, M. A. Dalbó, W. Liu, Springer US, **2012**, 571–621. DOI:10.1007/978-1-4419-0763-9_15
2. F. V. Dulf, D. C. Vodnar, C. Socaciu, *Food Chem.* **2016**, *209*, 27–36. DOI:10.1016/j.foodchem.2016.04.016
3. M. D. Kostić, A. V. Veličković, N. M. Joković, O. S. Stamenković, V. B. Veljković, *Wast. Manag.* **2016**, *48*, 619–629. DOI:10.1016/j.wasman.2015.11.052
4. E. Gonzalez-Garcia, M. L. Marina, M. C. García, *J. Funct. Foods*, **2014**, *11*, 428–437. DOI:10.1016/j.jff.2014.10.020
5. P. Nowicki, H. Wachowska, R. Pietrzak, *J. Hazard. Mater.* **2010**, *181(1)*, 1088–1094. DOI:10.1016/j.jhazmat.2010.05.126
6. P. Nowicki, M. Skrzypczak, R. Pietrzak, *Chem. Eng. J.* **2010**, *162(2)*, 723–729. DOI:10.1016/j.ces.2010.06.040
7. P. Górnas I. Mišina I. Grāvīte G. Lācis, V. Radenkovs A. Olšteine, D. Seglina, E. Kaufmane, E. Rubauskis, *Eur. Food Res. Technol.* **2015**, *241*, 513–520. DOI:10.1007/s00217-015-2480-4
8. P. Górnas, M. Rudzińska, *Ind. Crop. Prod.* **2016**, *83*, 329–338. DOI:10.1016/j.indcrop.2016.01.021
9. M. Gölükcü, R. Toker, H. Tokgoz, O. Çınar, *Tarim Bilim Derg.* **2016**, *22(4)*, 566–575. DOI:10.1501/Tarimbil_0000001415
10. L. Zhao, Y. Yagiz, C. Xu, J. Lu, S. Chung, M. R. Marshall, *Food Func.* **2015**, *6(7)*, 2293–2302. DOI:10.1039/C5FO00261C
11. A. Rai, B. Mohanty, R. Bhargava, *Sep. Purif. Technol.* **2015**, *141*, 354–365. DOI:10.1016/j.seppur.2014.12.016
12. N. Habila, M. H. Inuwa, I. A. Aimola, A. S. Agbaji, Z. Ladan, R. Sangodare, I. S. Williams, O. B. Odjobo, E. Ogabiela, *J. Plant Stud.* **2012**, *1(2)*, 55. DOI:10.5539/jps.v1n2p55
13. B. Matthäus, M. M. Özcan, *Grasas. Aceites.* **2012**, *63(3)*, 313–320. DOI:10.3989/gya.118411
14. T. A. El-Adawy, K. M. Taha, *J. Agric. Food Chem.* **2001**, *49(3)*, 1253–1259. DOI:10.1021/jf001117+
15. X. Cao, Y. Ito, *J. Chromatogr. A.* **2003**, *1021(1)*, 117–124. DOI:10.1016/j.chroma.2003.09.001
16. D. T. Veličković, M. S. Ristić, I. T. Karabegović, S. S. Stojičević, N. C. Nikolić, M. L. Lazić, *Adv. Technol.* **2016**, *5(1)*, 10–16. DOI:10.5937/savteh1601010V
17. S. Jokić, G. Horvat, K. Aladić, in: *Supercritical Fluid Extraction: Technology, Applications and Limitations*, L. Jason (Ed): New York, SAD: *Nova Publishers*, **2015**, 95–122.
18. S. Jokić, S. Vidović, K. Aladić, in: *J. Osborne (Ed): Supercritical Fluids: Fundamentals, Properties and Applications*, New York, SAD, *Nova Publishers*, **2014**, 205–228.
19. M. Jakovljević, T. Moslavac, M. Bilic, K. Aladić, F. Bakula, S. Jokić, *Croat. J. Food Sci. Technol.* **2018**, *10(2)*, 197–205. DOI:10.17508/CJFST.2018.10.2.08
20. C. Bele, C. T. Matea, C. Raducu, V. Miresan, O. Negrea, *Not. Bot. Horti. Agrobo.* **2013**, *41*, 93–96. DOI:10.15835/nbha4119027
21. I. F. Bolarinwa, C. Orfila, M. R. Morgan, *Food Chem.* **2014**, *152*, 133–139. DOI:10.1016/j.foodchem.2013.11.002
22. B. Matthäus, M. M. Özcan, *J. Food Lipid.* **2009**, *16(2)*, 187–199. DOI:10.1111/j.1745-4522.2009.01140.x
23. P. Górnas, M. Rudzińska, A. Soliven, *Ind. Crop. Prod.* **2017**, *100*, 77–84. DOI:10.1016/j.indcrop.2017.02.014
24. M. D. Kostić, A. V. Veličković, N. M. Joković, O. S. Stamenković, V. B. Veljković, *Waste Manag.* **2016**, *48*, 619–629. DOI:10.1016/j.wasman.2015.11.052
25. M. Kiralan, M. Kayahan, S. S. Kiralan, M. F. Ramadan, *Eur. Food Res. Technol.* **2017**, *244(1)*, 31–42. DOI:10.1007/s00217-017-2932-0
26. B. S. Kamel, Y. Kakuda, *J. Am. Oil Chem. Soc.* **1992**, *69(5)*, 492–494. DOI:10.1007/BF02540957
27. S. M. Abdulkarim, K. Long, O. M. Lai, S. K. S. Muhammad, H. M. Ghazali, *Food Chem.* **2007**, *105(4)*, 1382–1389. DOI:10.1016/j.foodchem.2007.05.013
28. M. A. L. de Oliveira, M. R. Balestros, A. Ferreira Faria, F. A. Simas Vaz, Academic Press, **2010**, 545–552. DOI:10.1016/B978-0-12-374420-3.00059-0
29. S. Turan, A. Topcu, I. Karabulut H. Vural, A. A. Hayaloglu, *J. Agric. Food Chem.* **2007**, *55*, 10787–10794. DOI:10.1021/jf071801p
30. M. M. Özcan, A. Unver, E. Erkan D. Arslan, *Sci. Hort.* **2011**, *127*, 330–333. DOI:10.1016/j.scienta.2010.10.027
31. W. M. Cort, T. S. Vicente, E. H. Waysek, B. D. Williams, *J. Agric. Food Chem.* **1983**, *31(6)*, 1330–1333. DOI:10.1021/jf00120a045
32. E. Niki, *Free Radic. Biol. Med.* **2014**, *66*, 3–12. DOI:10.1016/j.freeradbiomed.2013.03.022

33. Y. Yoshida, E. Niki, N. Noguchi, *Chem. Phys. Lipids*, **2003**, *123*, 63–75. DOI:10.1016/S0009-3084(02)00164-0
34. A. Hosomi, M. Arita, Y. Sato, C. Kiyose, T. Ueda, O. Igarashi, H. Arai, K. Inoue, *FEBS Lett.* **1997**, *409*, 105–108. DOI:10.1016/S0014-5793(97)00499-7
35. R. Brigelius-Flohé, M. G. Traber, *FASEBJ.* **1999**, *13*, 1145–1155. DOI:10.1096/fasebj.13.10.1145
36. M. Z. Tsimidou, in: *Olives and Olive Oil in Health and Disease Prevention* **2010**, Academic Press, 561–567. DOI:10.1016/B978-0-12-374420-3.00061-9
37. N. Pavlović, S. Vidović, J. Vladić, L. Popović, T. Moslavac, S. Jakobović, S. Jokić, *Eur. J. Lipid Sci. Technol.* **2018**, 1800043. DOI:10.1002/ejlt.201800043
38. E. Vági, B. Simándi, K. P. Vászárhelyiné, H. Daood, Á. Kéry, F. Doleschall, B. Nagy, *J. Supercrit. Fluid.* **2007**, *40*, 218. DOI:10.1016/j.supflu.2006.05.009
39. I. Gracia, J. F. Rodríguez, A. de Lucas, M. P. Fernández-Ronco, M. T. García, *J. Supercrit. Fluid.*, **2011**, *59*, 72. DOI:10.1016/j.supflu.2011.05.019
40. A. de Lucas, E. M. de la Ossa, J. Rincón, M. A. Blanco, I. Gracia, *J. Supercrit. Fluids*, **2002**, *22*, 221. DOI:10.1016/S0896-8446(01)00132-2
41. M. M. Hassanein, *Grasas y Aceites*, **1999**, *50(5)*, 379–384. DOI:10.3989/gya.1999.v50.i5.682
42. P. Budowski, D. Sklan, in: A. J. Vergroesen, M. Crawford, M. (Ed): *The role of fats in human nutrition*. Academic Press, New York, **1989**, 363. DOI:10.1016/B978-0-12-718051-9.50013-5
43. P. Górnaś, M. Rudzinska, M. Raczyk, I. Misina, A. Soliven, G. Lăcis, D. Seglina, *J. Agric. Food Chem.* **2016**, *64*, 898–905. DOI:10.1021/acs.jafc.5b05330
44. M. C. García, E. González-García, R. Vásquez-Villanueva, M. L. Marina, *Food Funct.* **2016**, *7(11)*, 4693–4701. DOI:10.1039/C6FO01132B
45. G. B. Donald, *Med. Toxicol. Nat. Subst.* **2009**, *55*, 336–352.
46. I. F. Bolarinwa, C. Orfila, M. R. A. Morgan, *Food Chem.* **2014**, *152*, 133–139. DOI:10.1016/j.foodchem.2013.11.002
47. M. Senica, F. Stampar, R. Veberic, M. Mikulic-Petkovsek, *J. Agric. Food Chem.* **2017**, *65(48)*, 10621–10629. DOI:10.1021/acs.jafc.7b03408
48. P. Górnas, I. Mišina I. Grāvīte, G. Lăcis, V. Radenkovs, A. Olšteine, D. Seglina, E. Kaufmane, E. Rubauskis, *Eur. Food Res. Technol.* **2015**, *241*, 513–520. DOI:10.1007/s00217-015-2480-4

Povzetek

Sliva (*Prunus domestica* L.) je pogosto gojena na območju Evrope in procesiranje plodov ustvarja znatne količine odpadnih pešk, ki vsebujejo mehko jedrce. Le-ta lahko predstavljajo alternativni vir jedilnih olj. Cilj te študije je bil pridobitev visoko kvalitetnega olja iz jedrc slivovih pešk z uporabo tradicionalne tehnike hladnega stiskanja (ang. CP) in moderne tehnologije ekstrakcije s superkritičnim ogljikovim dioksidom (ScCO₂). Pridobljena olja smo okarakterizirali na osnovi kemijske sestave maščobnih kislin in tokoferolov. Oleinska kislina je bila prisotna v najvišji koncentraciji v olju pri obeh tehnikah ekstrakcije (68.66 % v olju pridobljenem s ScCO₂, 65.86 % pridobljenem s CP), sledila pa je linolenska kislina (22.24–25.44 %). Celotna količina tokoferolov v olju pa je bila v primeru ekstrakcije s ScCO₂ 4–5.8 krat višja kot pri CP. Rezultati kažejo, da imajo jedrca slivovih pešk velik potencial kot alternativni vir olj z visokim deleže oleinske kisline in tokoferola ter nizkim deležem nasičenih maščobnih kislin in amigdalina.



Except when otherwise noted, articles in this journal are published under the terms and conditions of the Creative Commons Attribution 4.0 International License

Scientific paper

Sulfonamide Derived Esters: Synthesis, Characterization, Density Functional Theory and Biological Evaluation through Experimental and Theoretical Approach

Muhammad Danish,^{1,*} Ayesha Bibi,¹ Muhammad Asam Raza,^{1,*} Nadia Noreen,¹ Muhammad Nadeem Arshad² and Abdullah Mohamed Asiri²

¹ Department of Chemistry, University of Gujrat, Gujrat 50700 Pakistan

² Chemistry Department, Faculty of Science, King Abdulaziz University, Jeddah 21589, Saudi Arabia

* Corresponding author: E-mail: drdanish62@gmail.com and asamgcu@yahoo.com

Received: 11-19-2019

Abstract

A series of new solid esters was synthesized by using greener chemistry strategy involving simple reaction of an alcohol with sulfonamide ligand. Characterization study of these methyl (1), ethyl (2) isopropyl (3) and *n*-butyl (4) ester of 4-((4-chlorophenylsulfonamido)methyl)cyclohexanecarboxylic acid was done by using FTIR, NMR mass spectrometry and X-ray crystallography. The compounds were optimized with Gaussian software according to basis set B3LYP/6-31G(d,p) and their different parameters related to structure were calculated. Furthermore, all compounds of the series were screened for their *in vitro* biological applications involving anti-bacterial (*Chromohalobacter salixgens*, *Halomonas halofila*, *Escherichia coli*, *Staphylococcus aureus*, *Bacillus subtilis*, and *Shigella sonnei*), anti-fungal (*Aspergillus niger*), anti-oxidant (DPPH scavenging activity) and enzyme inhibition (acetylcholine esterase and butyrylcholine esterase) study. Sulfonamide based esters were also docked against selected enzymes (AChE and BChE) using MOE software for their mode of binding. Results obtained from these biological evaluations showed that such compounds have potential against targeted activity.

Keywords: Sulfonamide derived esters; DFT; docking studies; enzyme inhibition.

1. Introduction

Infectious diseases due to bacteria or fungi are the major leading causes of morbidity all over the world.^{1–4} The development of resistance (antibacterial) in microbes against the present antibiotics is growing now on a daily basis.⁵ Consequently, there is an urgent need in this area for new and improved antimicrobial agents having a broad-spectrum activity against the resistant strains. Researchers throughout the world are engaged in synthesizing and designing new drugs having widespread activity to overcome this issue.^{6–9} Sulfonamides form the foundation for the first drugs mainly employed as preventive and chemotherapeutic agents against different ailments.¹⁰ Sulfa drugs, having sulfonamide functionality, revolutionized the medicinal field due to their extensive biological activities.¹¹ Folic acid, an important compound for synthesis of bacterial nucleic acids, is inhibited by sulfonamides which ultimately leads to death of bacterial cells. Green chemistry synthesis is the current requirement as it has no haz-

ardous by-products. Carboxylate ester formation implemented simply by reacting alcohol with carboxylic acid is such an example. Besides their applications in artificial flavoring of food and in perfume making,¹² esters of various compounds are found to show promising biological applications. Variety of carboxylate esters derived from sulfonamides are found to serve in the field of health by giving meritorious biological applications. Ester derived from *para*-tolylbenzene sulfonamide of benzoic acid has been found to show inhibition activity for enzyme lipoxigenase. Carboxylate ester derived from biphenyl sulfonamide is found to show inhibitory behavior toward carbonic anhydrase enzymes as well as its isozymes, including isozymes I, II, XIV, XII and XIV.¹³ Moreover, for the treatment of obesity and to control Type 2 diabetes, esters derived from arylsulfonamide served to give such applications.¹⁴ As anti-microbial agents, esters of *N*-substituted sulfonamide are found to give anti-bacterial activity against four bacterial strains, *i.e.* *Pseudomonas aeruginosa*, *Bacillus subtilis*, *Escherichia coli* and *Staphylococcus au-*

reus.¹⁵ Due to the presence of amide and sulfonamide functional groups in carboxylate esters of sulfonamide derivatives, they are found to show anti-fungal activity against *Aspergillus niger* and *Candida albicans*.¹⁶

In current research work new methyl, ethyl, isopropyl and *n*-butyl esters derived from 4-((4-chlorophenylsulfonamido)methyl)cyclohexanecarboxylic acid were aimed to be synthesized. *In vitro* biological study, i.e. enzyme inhibition, anti-oxidant study, anti-bacterial and anti-fungal screening were also part of this research work.

2. Experimental

2.1. Chemical and Instruments

Chemicals like dimethyl sulfoxide, methanol, ethanol, isopropanol and *n*-butanol were purchased from Alfa Aesar and Merck chemical industries. These were of analytical grade. Infrared spectral study of compounds was done in mid IR region ($4000\text{--}400\text{ cm}^{-1}$) by KBr disc method using Perkin-Elmer System 100. Mass spectral study was done by ESI-MS technique.

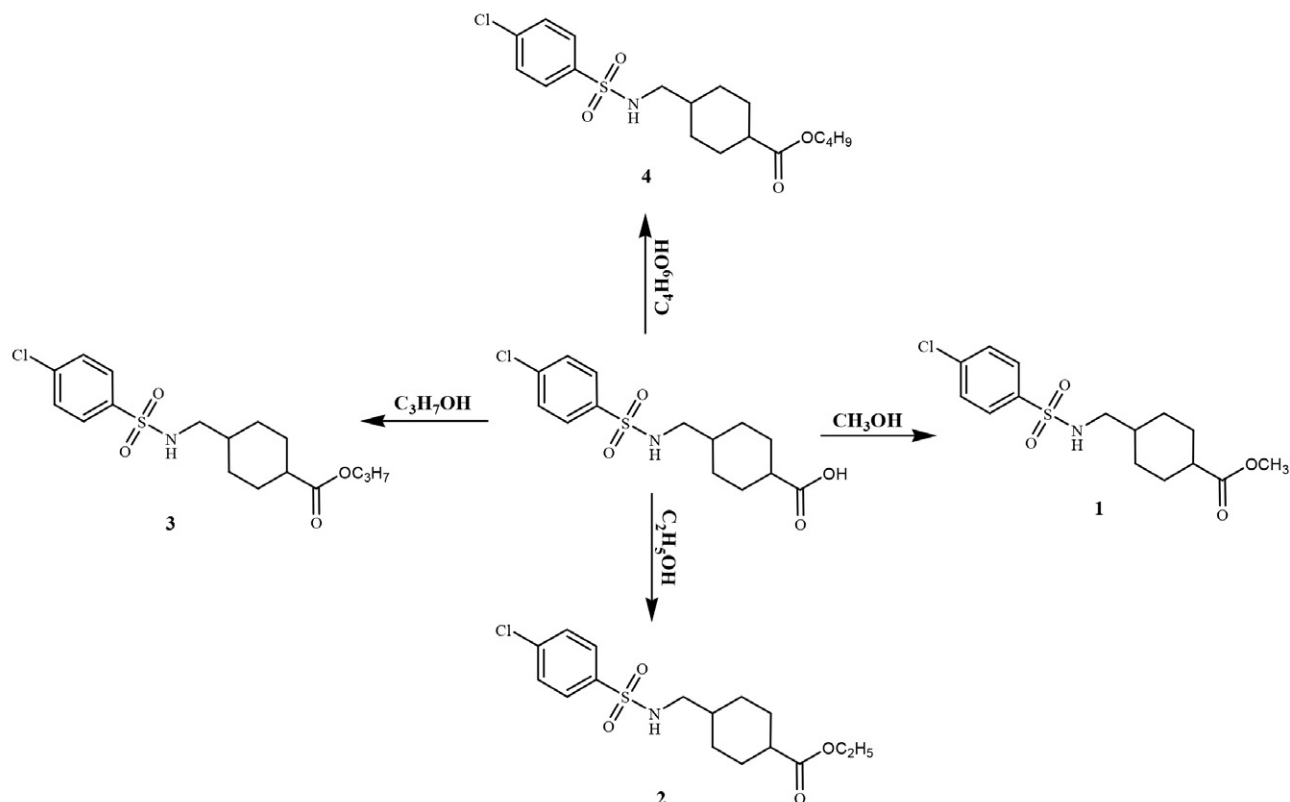
2.2. Synthesis of Carboxylate Esters of Sulfonamide

20 mL alcohol (methanol for **1**, ethanol for **2**, isopropanol for **3** and *n*-butanol for **4**) was taken and then

added 1 mL conc. H_2SO_4 as a catalyst into it. 0.5 g of 4-((4-chlorophenylsulfonamido)methyl)cyclohexanecarboxylic acid (published by our research group) was added in 20 mL alcohol till clear solution was obtained. Then added this alcoholic solution to alcohol-sulfuric acid mixture and refluxed it for about 4–6 hours. Reaction mixture was concentrated at room temperature by slow evaporation process and ester as a solid product was obtained (Scheme 1).¹⁷

2.3. Crystallography of 3

The compound **3** was re-crystallized to support the synthesis of series of compounds being presented in this manuscript. Microscope was used for screening of suitable crystal for data collection. The selected single crystal was fixed over a glass fiber tip fascinated in a wax supported by a hollow copper rod with magnetic base. This holder was mounted on Agilent SuperNova (Dual source) Agilent Technologies Diffractometer, equipped with graphite-monochromatic Cu/Mo $\text{K}\alpha$ radiation for data collection. The data collection was accomplished using Crys-AlisPro software¹⁸ at 296 K under the Mo $\text{K}\alpha$ radiation. The structure solution was performed using SHELXS-97¹⁹ and refined by full-matrix least-squares methods on F^2 using SHELXL-97 in-built with WinGX.²⁰ All non-hydrogen atoms were refined anisotropically by full-matrix least-squares methods.¹⁹ Figures were drawn using PLATON



Scheme 1. Synthesis of carboxylate esters of sulfonamide

and ORTEP-3.²⁰ All the aromatic CH hydrogen atoms were positioned geometrically and treated as riding atoms where C–H = 0.93 Å and $U_{\text{iso}}(\text{H}) = 1.2U_{\text{eq}}(\text{C})$ for carbon atoms. The C–H bond distances are 0.96 Å, 0.97 Å and 0.98 Å for methyl, methylene and methine groups, respectively. $U_{\text{iso}}(\text{H}) = 1.5U_{\text{eq}}(\text{C})$ for methyl carbon atoms, while $U_{\text{iso}}(\text{H}) = 1.2U_{\text{eq}}(\text{C})$ for methylene and methine carbon atoms. The N–H = 0.68(7)–0.94(4) Å, hydrogen atoms were located with difference Fourier map and refined with $U_{\text{iso}}(\text{H}) = 1.2U_{\text{eq}}(\text{N})$. The assigned CCDC number is 1861455.

2. 4. Biological Studies

Antibacterial Activity

Antibacterial activity was determined according to the disc diffusion method against four bacterial strains: *Chromohalobacter salexigens*, *Chromohalobacter israelensis*, *Halomonas halofila* and *Halomonas salina*.²¹ Bacterial medium was prepared and autoclaved for 20 min at 121 °C and 15 psi. 30 mL of the sterilized medium was poured in the petri plates and seeded with respective bacterial strains. 20 µL of sample (5 mg/mL) was applied on disks with the help of a micropipette. Streptomycin and ampicillin were used as reference drugs while solvents were used as negative. After incubation of 24 hours at 37 °C, the zone of inhibition was measured.

Antifungal Activity

Antifungal activity was determined against two different fungal strains: *Aspergillus flavus* and *Aspergillus niger* by using the method of Samina *et al.* (2009) with minor modification.²¹ Sterilized medium of 30 mL was poured aseptically in autoclaved petri plates and seeded with the respective fungal strain. After the solidification of the medium disks were placed on it and 20 µL of sample (5 mg/mL) was applied on each disc. The plates were incubated at 25 °C and the zone of inhibition was measured with Vernier caliper after 48 hours.

Antioxidant Activity

Antioxidant activity of synthesized compounds was checked according to the method of Shahwar *et al.* (2012) using 2,2'-diphenyl-1-picrylhydrazyl (DPPH) radical.²² DPPH solution was prepared as 0.0025 g/mL in methanol and 100 µL of sample (5 mg/mL) was mixed with 2 mL DPPH solution. Test tubes were kept in dark for half an hour and measured the absorbance at 517 nm using methanol as blank and gallic acid as reference standard. The scavenging of free radicals was calculated using following formula:

$$\begin{aligned} \% \text{ Inhibition} &= \\ &= \frac{\text{Absorbance (blank)} - \text{Absorbance (test)}}{\text{Absorbance (blank)}} \times 100 \end{aligned} \quad (1)$$

Enzyme Inhibition Studies

The AChE and BChE inhibition activities were determined according to the method of Ellman *et al.* (1961)²³ with slight modifications. 100 µL test compound (5 mg/mL) was mixed with 100 µL enzyme (AChE and BChE) and incubated at 37 °C for 10 minutes. After incubation, 0.5 mL buffer (50 mM), 50 µL DTNB followed by the addition of 50 µL substrate acetylthiocholine iodide and butyrylthiocholine iodide for AChE and BChE, respectively. After 30 minutes of incubation at 37 °C, the absorbance was measured at 410 nm using UV/VIS spectrophotometer. All experiments were carried out with their respective controls in triplicate.

The percentage inhibition was calculated by the following formula:

$$\% \text{ age inhibition} = \frac{A - B}{A} \times 100 \quad (2)$$

Where A is the optical density of blank and B is the optical density of sample.

2. 5. DFT Studies

Quantum chemical calculations were performed with Gaussian 09. The results are visualized with Gauss View 5.0. The geometries of the compounds are optimized without any symmetry constraints using the hybrid functional B3LYP method with 6-31G(d,p) basis set.^{24,25} The basis set chosen contains polarization functions on all atoms. The B3LYP method of DFT is quite reliable for the prediction of geometric and electronic properties of neutral and charged species ranging from simple molecular to polymer structures.^{26–28} For optimization, the input geometries are taken from the crystal structure (where available) in order to better match with the experimentally obtained structures. Frequency calculations are also performed at the same level in order to confirm these structures as true minima (absence of an imaginary frequency).

2. 6. Docking Studies

Docking experiments were performed *via* Molecular Operating Environment (MOE). Crystal structures of AChE and BChE with PDB codes 1EVE and 1POI, respectively, were selected for these studies. All the water molecules were removed from the protein structure, then hydrogen atoms were added and energy optimization was carried out using default force field. The three-dimensional (3D) structures of compounds were modeled through the builder program implemented in MOE. The geometrical parameters for 3D structures of the compounds were optimized, and partial charges were calculated before docking. The 3D protonation of the downloaded enzymes was done and energy minimization of the retrieved protein molecule was carried out using default parameters of

MOE energy minimization algorithm (gradient: 0.05, Force Field: MMFF94X). The resulting model was subjected to systematic conformational search at default parameters with RMS gradient of 0.01 kcal/mol using Site Finder. For 1EVE (AChE), the active site of the prepared enzyme was defined as the residues within 10 Å of the reference ligand (donepezil). However, for 1POI (BChE), the enzyme was searched for its active site and dummy atoms were created using alpha spheres as centroids. A key tryptophan residue in AChE, Trp84 (TcAChE numbering), is conserved in BChE (Trp82). The backbone and residues were kept fixed and the energy minimization was performed. The lowest energy minimized pose was used for further analysis. Ligand-interaction module of MOE was used to calculate the 2D ligand-enzyme interactions. The view of the docking results and analysis of their surface with graphical representations were done using MOE and discovery studio visualizer.²⁹

3. Results and Discussion

The reaction was carried out in acid catalyzed media by simply reacting alcohol with sulfonamide ligand. The reaction gives water as by-product, hence the strategy is a type of green synthesis which is advantageous and environmentally friendly having no hazardous or harmful effects on the environment. The structure and activity of the starting material (acid) has been already published by our group.³⁰ The reaction was monitored with TLC and after completion of the reaction, structure elucidation was done with FTIR, mass spectrometry and NMR. The exact crystal structure of **3** was confirmed with XRD analysis.

3.1. Methyl 4-((4-Chlorophenylsulfonamido)methyl)cyclohexanecarboxylate (1)

White amorphous solid; yield: 1.74 g (76%); mp: 96–97 °C; molecular formula: C₁₅H₂₀ClNO₄S; molecular mass: 345.84 g mol⁻¹; IR (KBr, cm⁻¹): ν_{max} 3270 (NH), 2922 (CH), 1320–1158 (SO₂), 1699–1432 (C=O); ¹H NMR (DMSO-*d*₆, 300 MHz): δ 7.65–7.80 (dd, 4H, aromatic), 3.56 (s, 3H, -CH₃), 2.59 (t, 2H, -CH₂), 0.79–2.24 (m, 10H, cyclohexyl); ¹³C NMR (DMSO-*d*₆, 75 MHz): δ 175.8 (C-2), 140.0 (C-4'), 137.5 (C-1'), 129.8 (C-3' and C-5'), 128.8 (C-2' and C-6'), 51.7 (C-1), 48.8 (C-3), 42.6 (C-1''), 37.1 (C-4''), 29.4 (C-2'' and C-6''), 28.5 (C-3'' and C-5''); EI-MS: *m/z* 344.25 [M - 1].

3.2. Ethyl 4-((4-Chlorophenylsulfonamido)methyl)cyclohexanecarboxylate (2)

Lustrous white amorphous; yield: 0.81 g (47%); mp: 120–122 °C, molecular formula: C₁₆H₂₂ClNO₄S; molecular mass: 359.87 g mol⁻¹; IR (KBr, cm⁻¹): ν_{max} 3298

(NH), 2934 (CH), 1321–1159 (SO₂), 1727 (C=O). ¹H NMR (CDCl₃): δ 7.5–7.8 (dd, 4H, aromatic), 4.8 (t, 3H, -CH₃), 4.1 (q, 2H, -CH₂), 1.0–2.2 (m, 10H, cyclo-H); ¹³C NMR (CDCl₃): δ 175.7 (C-3), 139.1 (C-4'), 138.5 (C-1'), 129.4 (C-3' and C-5'), 128.5 (C-2' and C-6'), 60.3 (C-1), 49.1 (C-3), 43.1 (C-1''), 37.2 (C-4''), 29.5 (C-2'' and C-6''), 28.2 (C-3'' and C-5''), 14.2 (C-2); ESI-MS: *m/z* 358.25 [M - 1].

3.3. Isopropyl 4-((4-Chlorophenylsulfonamido)methyl)cyclohexanecarboxylate (3)

Lustrous white crystalline; yield: 1.97 g (84%); mp: 111–113 °C, molecular formula: C₁₇H₂₄ClNO₄S; molecular mass: 373.89 g mol⁻¹; IR (KBr, cm⁻¹): ν_{max} 3263 (NH), 2924 (CH), 1320–1158 (SO₂), 1730–1432 (C=O), ESI-MS: *m/z* 372.25 [M - 1].

3.4. Butyl 4-((4-chlorophenylsulfonamido)methyl)cyclohexanecarboxylate (4)

Off-white amorphous solid; yield: 1.21g (59%); mp: 106–108 °C; molecular formula: C₁₈H₂₆ClNO₄S; molecular mass: 387.92 g mol⁻¹; IR (KBr, cm⁻¹): ν_{max} 3267 (NH), 2931 (CH), 1323–1159 (SO₂), 1725–1431 (C=O); ¹H NMR (DMSO-*d*₆, 300 MHz): δ 7.65–7.80 (dd, 4H, aromatic), 4.00 (t, 2H, H-4), 2.58 (t, 2H, H-6), 1.54–2.21 (m, 10H, cyclohexyl), 0.87 (t, 3H, H-1), 1.20 (m, 2H, H-2), 1.47 (m, 2H, H-3); ¹³C NMR (DMSO-*d*₆, 75 MHz): δ 175.4 (C-5), 140.0 (C-4'), 137.5 (C-1'), 129.8 (C-3' and C-5'), 128.8 (C-2' and C-6'), 63.8 (C-4), 48.9 (C-5), 42.8 (C-1''), 37.1 (C-3), 30.6 (C-4''), 29.4 (C-2'' and C-6''), 28.5 (C-3'' and C-5''), 19.0 (C-2), 14.0 (C-1); ESI-MS: *m/z* 386.33 [M - 1].

3.5. Crystallography of 3

Molecule **3** is ornamented with the methyl, methylene, methine and aromatic hydrogen atoms along with the NH group. We have observed two independent molecules [(C1–C17) and (C18–C34)] per asymmetric unit cell (Figure 1). The crystallographic parameters are given in Table 1, while the selected bond lengths and bond angles are provided in Supplementary Data (Tables S1 and S2). The cyclohexane ring adopted the chair conformation in each independent molecule and the root mean square (r.m.s) deviations for the fitted atoms of this ring are 0.2342(4) Å and 0.2298(4) Å in molecule 1 and molecule 2, respectively. The puckering parameters were determined for the cyclohexane rings in each independent molecule and the parameters in black and white are $Q = 0.5738$, $\theta = 0.69$ and $\varphi = 22.3039$ for the ring II (C8–C13), while $Q = 0.5628$, $\theta = 1.55$ and $\varphi = 40.732$ for the ring IV (C25–C30). The geometry around the S atom is distorted tetrahedral which is typical behavior of sulfonamide functional group.^{31–34} The dihedral angle between the aromatic ring I (C1–C6) and cyclohexane ring II (C8–C13)

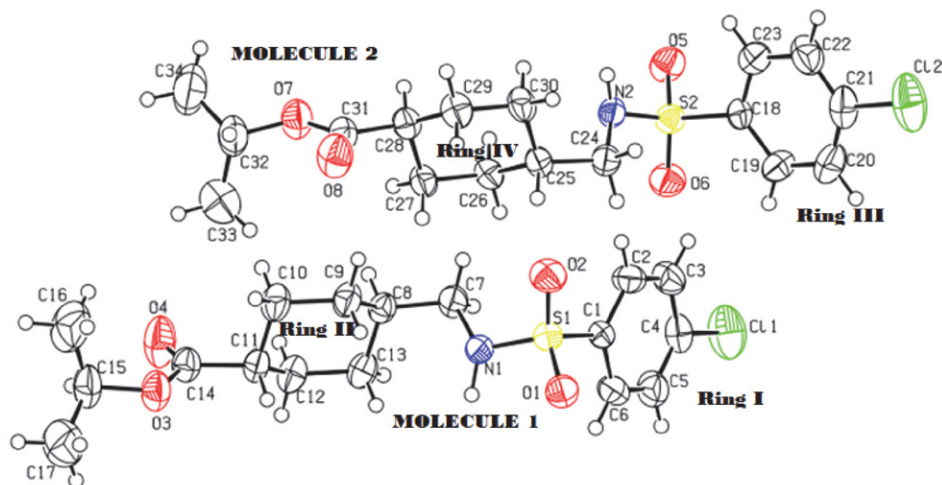


Figure 1. ORTEP diagram of 3 with thermal ellipsoids were drawn at 50% probability level

is $44.649(3)^\circ$ but the same angle between the ring III (C18–C23) and ring IV (C25–C30) is $45.663(3)^\circ$. The carboxylate and the isopropyl groups are almost perpendicular in each molecule as the dihedral angles are $78.772(7)^\circ$ and $78.906(72)^\circ$ in molecule 1 and molecule 2, respective-

ly. The carboxylate groups are twisted at dihedral angles of $68.738(3)^\circ$ and $60.883(4)^\circ$ with respect to the plane produced from the fitted atoms of cyclohexane rings in molecule 1 and molecule 2, respectively. Classical hydrogen bonding of N–H...O type connects the molecule along *b*-axis to generate the infinite long chains. The N1 acts as donor *via* H1N to the O1 following the symmetry operation $1 - x, \frac{1}{2} + y, -z$. The N2 acts as donor in the molecule 2 *via* H2N to O5 oxygen atom, where the symmetry operation is $1 - x, \frac{1}{2} + y, 1 - z$ as shown in Figure 2, Table 2.

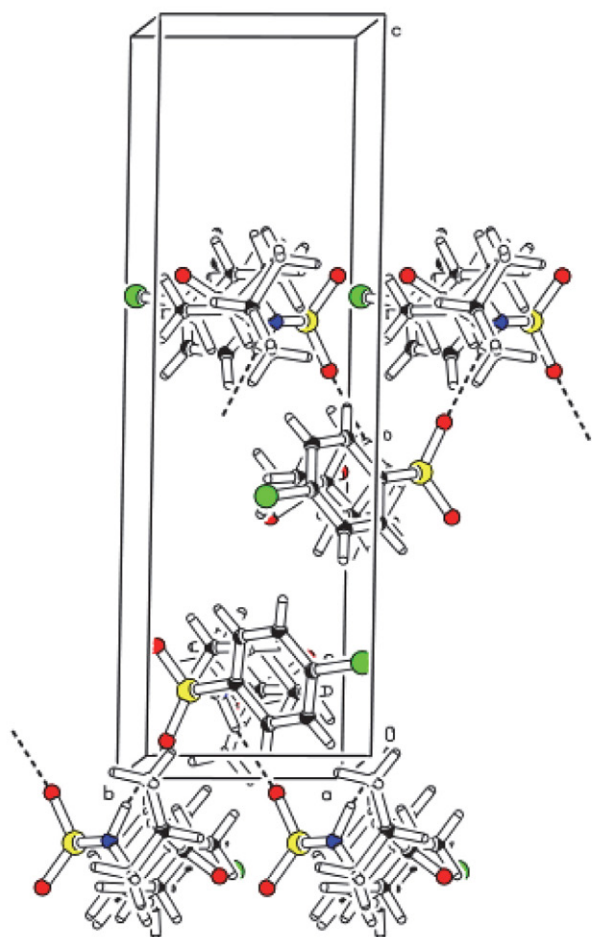


Figure 2. A unit cell view for 3 showing the intermolecular hydrogen bonding and formation of long chains along *b*-axis.

Table 1. Crystal data and structure refinement for 3

CCDC number	1861455
Empirical formula	$C_{17}H_{24}ClNO_4S$
Formula weight	373.88
Temperature/K	296(2)
Crystal system	monoclinic
Space group	$P2_1$
<i>a</i> /Å	16.9426(13)
<i>b</i> /Å	5.8454(3)
<i>c</i> /Å	20.5910(18)
$\alpha/^\circ$	90
$\beta/^\circ$	112.829(9)
$\gamma/^\circ$	90
Volume/Å ³	1879.5(3)
Z	4
ρ_{calc} /mg/mm ³	1.321
μ /mm ⁻¹	0.334
F(000)	792.0
Reflections collected	11000
Independent reflections	7495 [R(int) = 0.0379]
Data/restraints/parameters	7495/1/442
Goodness-of-fit on F ²	1.026
Final R indexes [$I \geq 2\sigma(I)$]	$R_1 = 0.0729, wR_2 = 0.1776$
Final R indexes [all data]	$R_1 = 0.0986, wR_2 = 0.2039$
Largest diff. peak/hole / e Å ⁻³	1.11/−0.31
Flack Parameters	0.02(12)

Table 2. Hydrogen Bonds for **3**

D	H	A	$d(D-H)/\text{\AA}$	$d(H-A)/\text{\AA}$	$d(D-A)/\text{\AA}$	D–H–A/ $^{\circ}$
N1	H1N	O1 ⁱ	1.01(6)	2.02(6)	2.992(6)	161(5)
N2	H2N	O5 ⁱⁱ	0.87(6)	2.12(6)	2.977(6)	169(6)

ⁱ 1 – x, –½ + y, –z ⁱⁱ 1 – x, ½ + y, 1 – z

3. 6. Antimicrobial Studies

Bacteria are necessary for life function but pathogenic bacterial species are major cause of various infections in human bodies. For the treatment of infections, different antibiotics are being sold in the market and one among them is sulfa drug. Our group is also synthesizing different sulfonamide compounds and evaluating their antibacterial potential using *in vitro* model. Here we aimed to check the anti-bacterial potential of **1**, **2**, **3** and **4** against six bacterial strains, *i.e.* *C. salixgens*, *H. halofila*, *S. aureus*, *B. subtilis*, *S. sonnei*, *E. coli*. Results obtained showed that except *C. salixgens*, all bacteria were inhibited by synthesized compounds. *Aspergillus niger* (*A. niger*) is the fungus that causes aspergillosis; a lung disease, for the person having extremely weak immune system.³⁵ It is also a common cause of fungal ear infection known as otomycosis in tropical areas.³⁶ For the treatment of these diseases, synthesis of anti-fungal agents is obvious. In current research work compounds **1**, **2**, **3** and **4** were screened for their anti-fungal potential against *A. niger*. It was found from results that **2** and **3** are more active against fungal strain (see Table 3).

3. 7. Antioxidant Potential

Reactive oxygen species (ROS) are free radicals involving hydrogen peroxide, hydroxyl ion, superoxide, hydrogen peroxide and hydroxyl free radical ($\cdot\text{OH}$, OH^- , $\cdot\text{O}_2^-$, O_2^{2-} , H_2O_2). Diseases caused by the overproduction of ROS in body involve chronic inflammation and autoimmune diseases, infectious diseases, cancer, sensory impairment, neurological disorders, fibrotic and cardiovascular diseases.³⁷ In order to treat the mentioned health disorders, use of antioxidants is imperative. The antioxidant po-

tential of all synthesized esters has been evaluated using standard protocols and results are presented in Table 4. All compounds exhibited moderate to good activity except **1** (24.1 ± 0.4), furthermore maximum radical scavenging activity was shown by **3** comparable to standard.

3. 8. Acetylcholine/Butyrylcholine Esterase Study

Acetylcholine esterase (AChE) is mainly involved in the transmission of neurotransmitter acetylcholine in brain. AChE hydrolyzes the acetylcholine into choline and acetate group. Over-activity of AChE causes deficiency of acetylcholine, hence leads to Alzheimer's disease (AD). In order to treat Alzheimer's disease, AChE activity must be inhibited. Butyrylcholine esterase also belongs to the same class of enzyme and is actively involved in Alzheimer's disease.³⁸ Our research group members are working on the synthesis of different compounds and evaluating their enzyme inhibition potential. This work is a continuation of our previous research, in which we aimed to check the inhibitory potential of **1**, **2**, **3** and **4** against both enzymes

Table 4. Enzyme inhibition and antioxidant potential of synthesized esters

Compound	Enzyme Inhibition (%)		Antiradical Scavenging (%)
	AChE	BChE	
1	47.3 ± 0.5	55.4 ± 0.7	24.1 ± 0.4
2	41.7 ± 0.9	32.2 ± 0.4	61.4 ± 1.2
3	60.4 ± 1.4	47.7 ± 1.1	77.9 ± 1.3
4	58.1 ± 1.1	54.5 ± 0.9	63.3 ± 0.9
Gallic acid	–	–	91.1 ± 0.9

Table 3. Antimicrobial potential of synthesized esters 1–4

Compound	Zone of inhibition (mm)						Fungal strain <i>A. niger</i>
	Bacterial strains						
	<i>C. salixgens</i>	<i>H. halofila</i>	<i>E. coli</i>	<i>S. aureus</i>	<i>B. subtilis</i>	<i>S. sonnei</i>	
1	NIL	12.4 ± 1.1	11.1 ± 0.5	10.0 ± 0.7	NIL	25.4 ± 0.7	NIL
2	NIL	7.3 ± 0.7	15.4 ± 0.4	12.1 ± 0.9	17.5 ± 1.1	30.1 ± 1.1	4.5 ± 0.1
3	NIL	13.7 ± 0.9	11.3 ± 0.8	12.4 ± 1.3	15.1 ± 0.8	12.5 ± 0.6	6.5 ± 0.3
4	NIL	14.1 ± 1.2	NIL	8.5 ± 0.8	NIL	15.3 ± 1.0	NIL
Ampicillin	NIL	15.6 ± 0.7	33.5 ± 1.1	39.2 ± 1.0	41.3 ± 1.3	31.5 ± 1.1	–
Fungone	–	–	–	–	–	–	30.2 ± 0.8

Chromohalobacter salixgens (*C. salixgens*), *Halomonas halofila* (*H. halofila*), *Escherichia coli* (*E. coli*), *Staphylococcus aureus* (*S. aureus*), *Bacillus subtilis* (*B. subtilis*), *Shigella sonnei* (*S. sonnei*).

Table 5. Docking results of synthesized esters

Compound	Docking Score			Binding Affinity (kcal/mol)		
	AChE	BChE		AChE	BChE	
	1EVE	1POI	4BDS	1EVE	1POI	4BDS
1	-10.2116	-9.8558	-11.6188	-6.9708	-5.2680	-5.4057
2	-10.9667	-10.5598	-11.2390	-6.5568	-5.4028	-4.7353
3	-12.6362	-10.8013	-12.4252	-6.5128	-5.0774	-4.7111
4	-11.7883	-10.4357	-12.1566	-7.3311	-5.6446	-5.5252

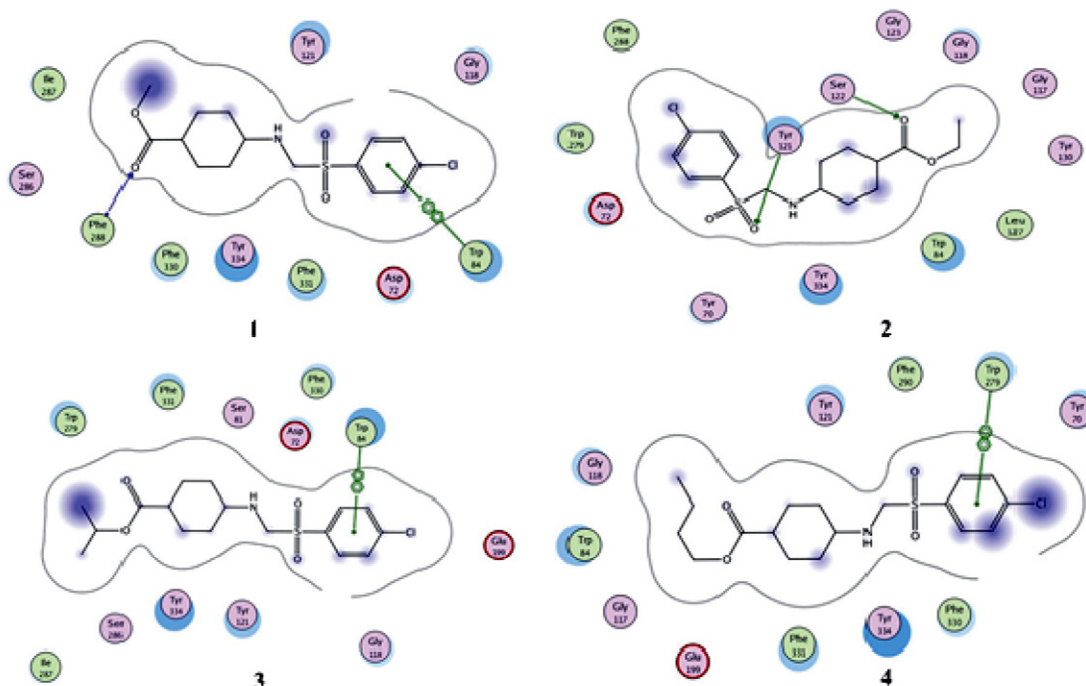


Figure 3. Interactions of synthesized esters with AChE (1EVE)

(AChE and BChE). As shown in Table 4, all the synthesized compounds gave moderate to good enzyme inhibition activity. The order of enzyme inhibition against AChE was found to be: $3 > 4 > 1 > 2$, while $1 > 4 > 3 > 2$ against BChE.

All four synthesized esters 1–4 were docked with AChE (1EVE) and BChE (1POI and 4BDS) by downloading their respective PDB files from the internet source using MOE software. The solvent molecules were eliminated and structures of enzyme and compounds were minimized before docking. The interaction of molecules with different amino acid residues at the active site are shown in Figure 3. Esters showed different types of interactions with residues such as hydrogen bonding, van der Waals, π - π interaction; among these some are weak while others bind the inhibitor to the active site rigidly. In AChE, inhibitors (esters 1–4) showed interactions with Phe288, Trp84, Tyr121, Ser122, Trp279, Phe290, Arg289, Phe331, Tyr334, His440, Asp72, Ser31, Tyr130, Gly123 and Gly118. Maximum interaction was demonstrated by 3 with docking score and binding affinity -12.6362, -6.5128, respectively, while others have

close results (Table 5). Ester 1 interacts with Trp84 at anionic site, His440 at catalytic triad and Phe288 located at acyl pocket. Phe290, Trp84, Tyr334 and Phe288 are the amino acid residues exhibiting different interactions with 2. In case of 3, the amino acid residues at peripheral anionic site (PAS) Tyr70, Asp72, Tyr334, Tyr130 interacted with inhibitor, while Trp84 and Tyr130 located at anionic site also stabilized the molecule. The 4 ester also interacted with Trp84, Tyr121, Tyr334 and His440 located at anionic, PAS and catalytic triad of the AChE (1EVE), as shown in Figure 4.

The synthesized inhibitors were also docked with BChE using PDB files; 1POI and 4BDS. It is evident from the results that 3 exhibited the highest binding score -10.8013 and -12.4252 against 1POI and 4BDS, respectively. The order (1POI) of remaining esters with respect to the binding score was $2 > 4 > 1$, while in 4BDS it was $4 > 1 > 2$ as shown in Table 7. The inhibitors showed the interactions with Trp82, Thr120, Ser198, Gly116, Trp332, His438, Gly117, Trp231, Val288, Glu197, Leu286 and Pro285 in the case of 1POI, while in 4BDS Trp82, Thr120, His438,

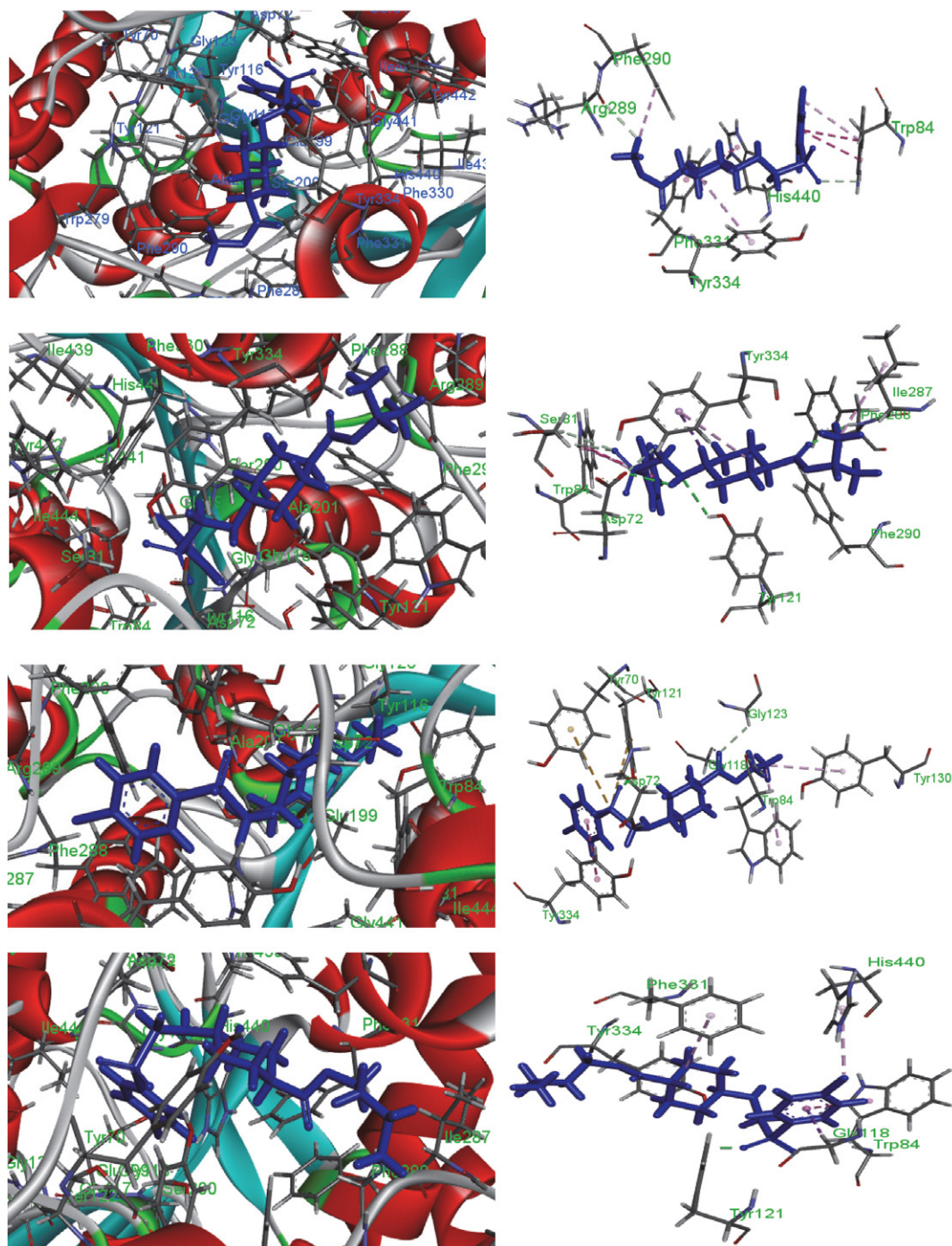


Figure 4. Best docking-poses of the synthesized compounds in the binding site of 1EVE

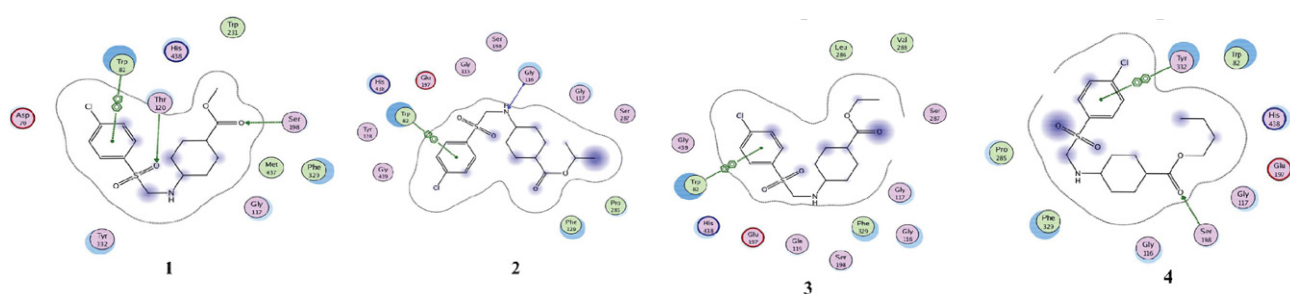


Figure 5. Interactions of synthesized esters with BChE (1POI)

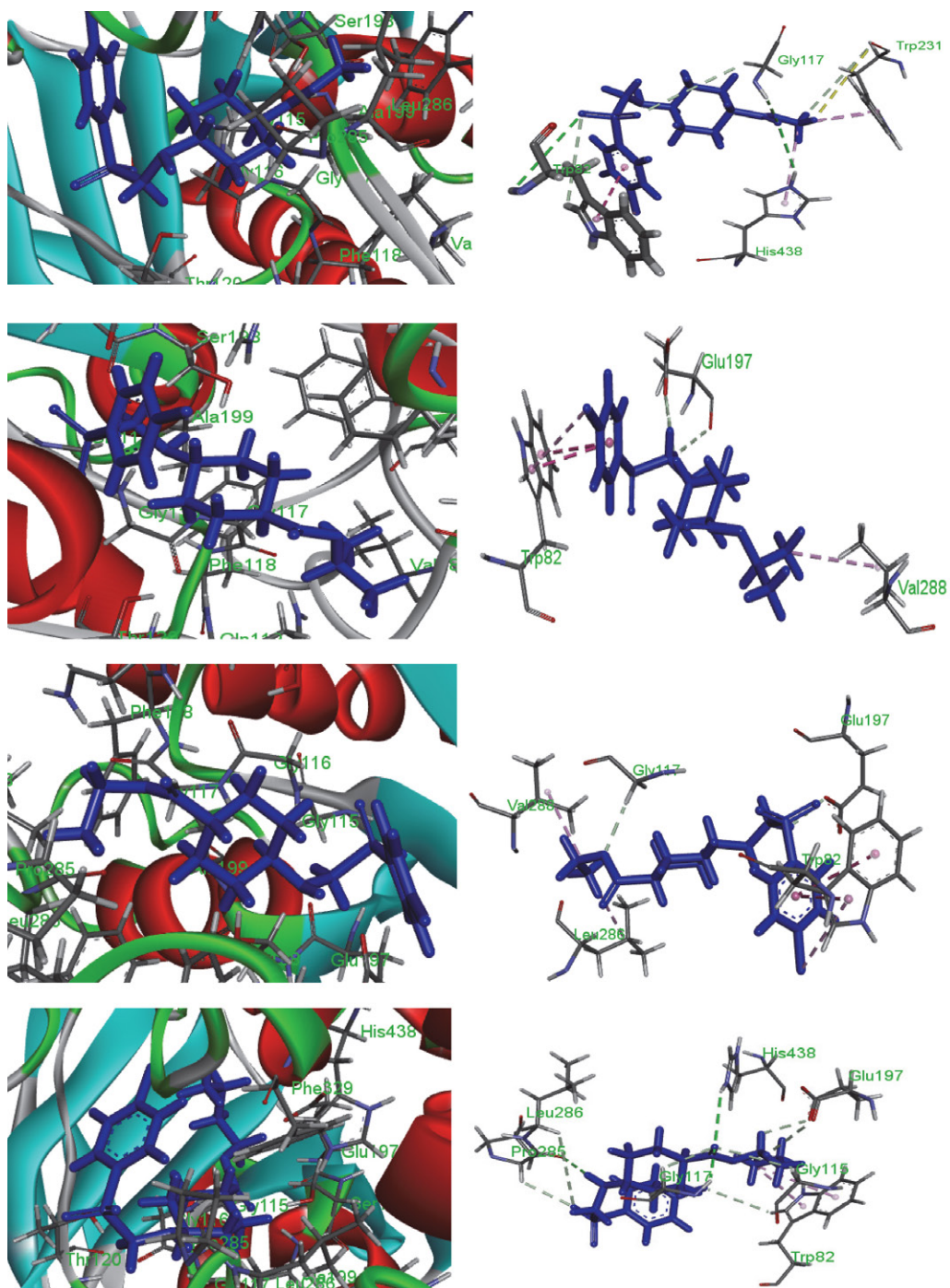


Figure 6. Best docking-poses of the synthesized compounds in the binding site of IPOI

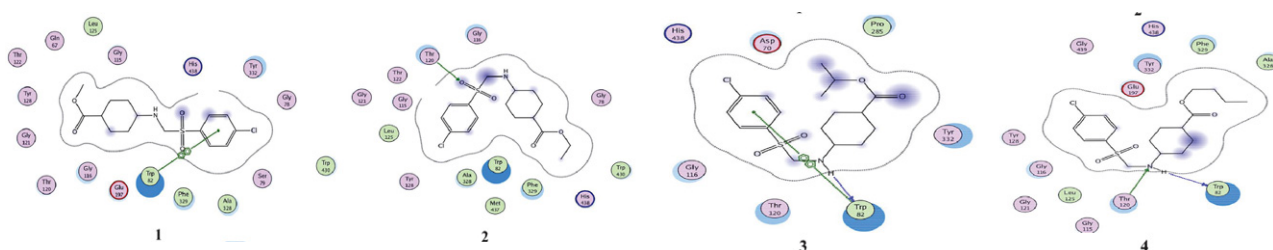


Figure 7. Interactions of synthesized esters with BChE (4BDS)

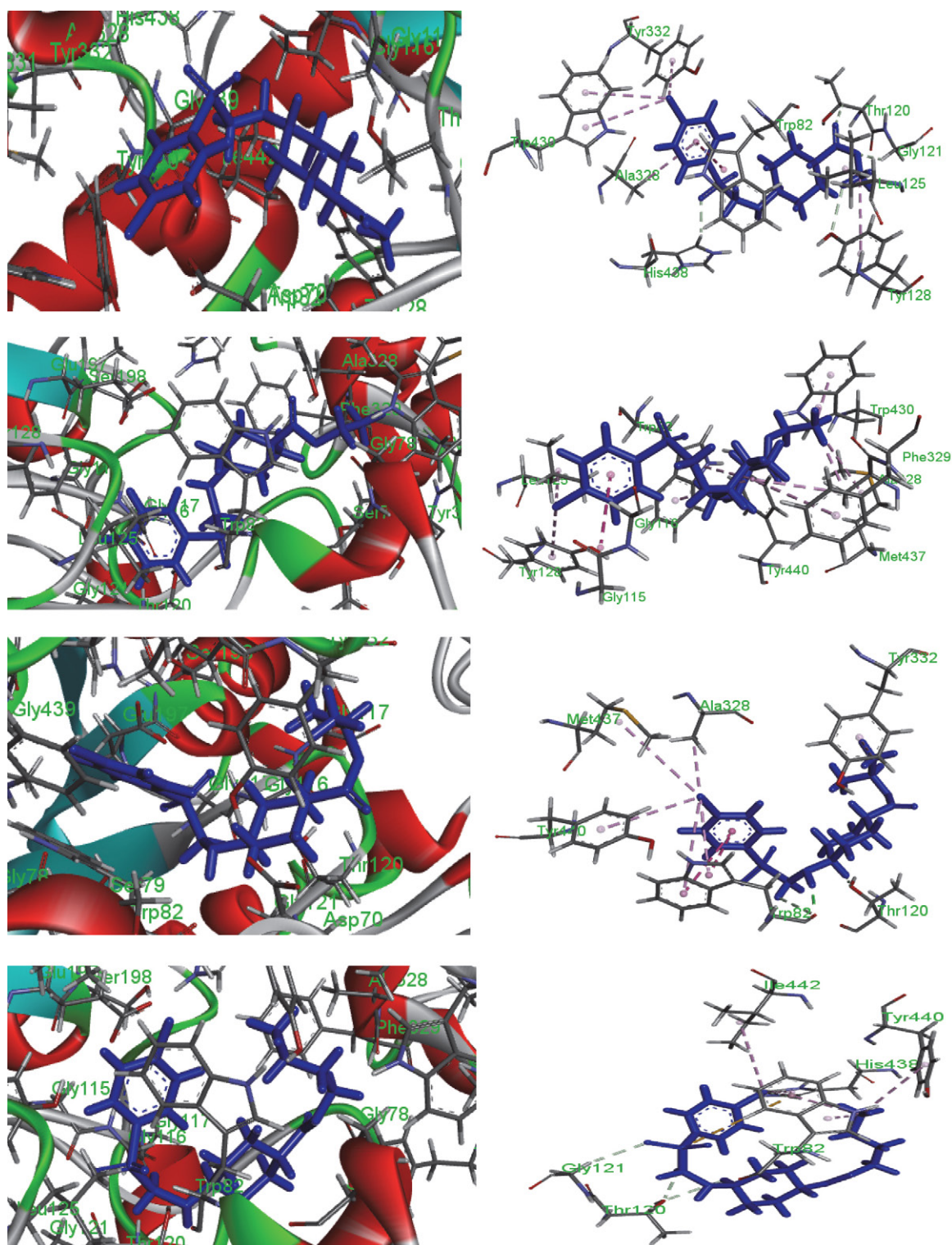


Figure 8. Best docking-poses of the synthesized compounds in the binding site of 4BDS

Gly117, Tyr440, Tyr332 and Ala328 are major residues which bind to the inhibitors (Figures 5–8). Ester **1** showed hydrogen binding with Gly117 and Trp231, while hydrophobic interaction with His438 and Trp82. Ester **2** demonstrated π - π interaction with Trp82 at anionic site, while hy-

drogen bonding with Val288 located at acyl pocket of 1POI. Similarly, Val288 and Trp82 provide the major interactions of ester **3** with the enzyme. It was observed that different residues such as Trp82, Glu197, His438, Gly117 etc. interact with hydrogen bonds with the inhibitor **4**. On

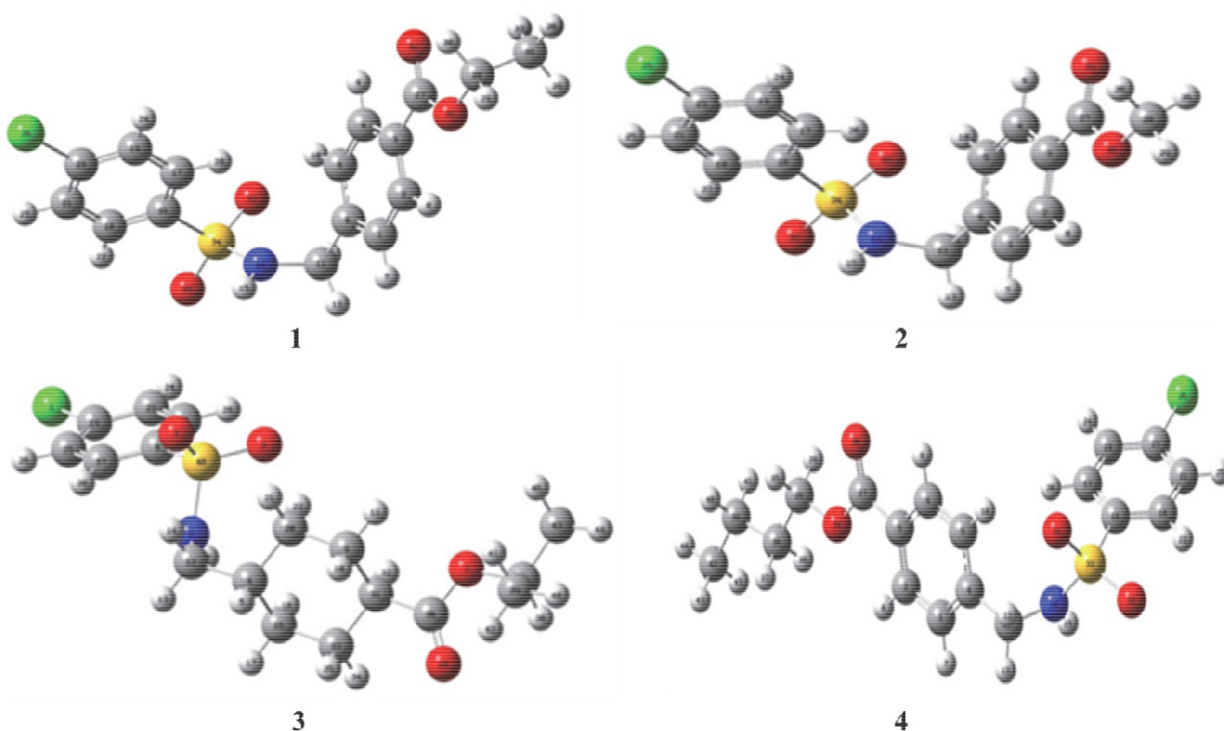


Figure 9. Optimized structures of synthesized compounds

Table 6. Global chemical reactivity indices of synthesized esters

Esters	1	2	3	4
μ (chemical potential)	-0.1402	-0.1405	-0.1540	-0.1398
η (chemical hardness)	0.2138	0.2139	0.2312	0.2137
X (electronegativity)	0.1402	0.1405	0.1540	0.1398
HOMO	-0.3540	-0.3544	-0.3852	-0.3535
LUMO	0.0736	0.0734	0.0772	0.0739
(LUMO–HOMO)	0.4276	0.4278	0.4625	0.4274
Energy (Hartree)	-1816.3955	-1777.5706	-1858.7156	-1894.0337
Ω	-0.1402	0.1405	0.154	-0.0193
IP (ionization potential)	0.3540	0.3544	0.3852	0.3535
EA (electron affinity)	-0.0736	-0.0734	-0.0772	-0.0739
Dipole moment	5.8484	5.8946	2.9289	6.2044
Nuclear repulsion energy	2111.4097	1983.1852	2359.5095	2341.0539
Gibbs free energy	-1816.1263	-1777.3305	-1858.3458	-1893.7086
Enthalpy	-1816.0521	-1777.2589	-1858.2654	-1893.6267

the active site of 4BDS, all four esters mainly interact with Trp82, Thr120, Tyr440 and **1**, **2** and **3** are further stabilized by interaction with Ala328.

3. 9. Computational Studies

DFT study of the targeted compounds was carried out using Gaussian software while optimized structures were visualized in Gauss view 5. The structures of all compounds were optimized using basis set B3LYP and bond lengths and bond angles of **3** were compared with experi-

mental data (XRD results). It was clear from the results that there is a close resemblance between experimental and theoretical results. HOMO and LUMO were also drawn and energy gap between these was calculated and it was found that **1**, **2** and **4** have very small difference in the energy gap ranging from 0.4274 to 0.4278, while **3** has 0.4625 as shown in Table 6 and Figure 10. Others parameters such as chemical potential, chemical hardness, electronegativity, Hartree energy, ionization potential, electron affinity, dipole moment, nuclear repulsion energy, Gibbs free energy were also calculated and are presented in Table 6. It was clear from

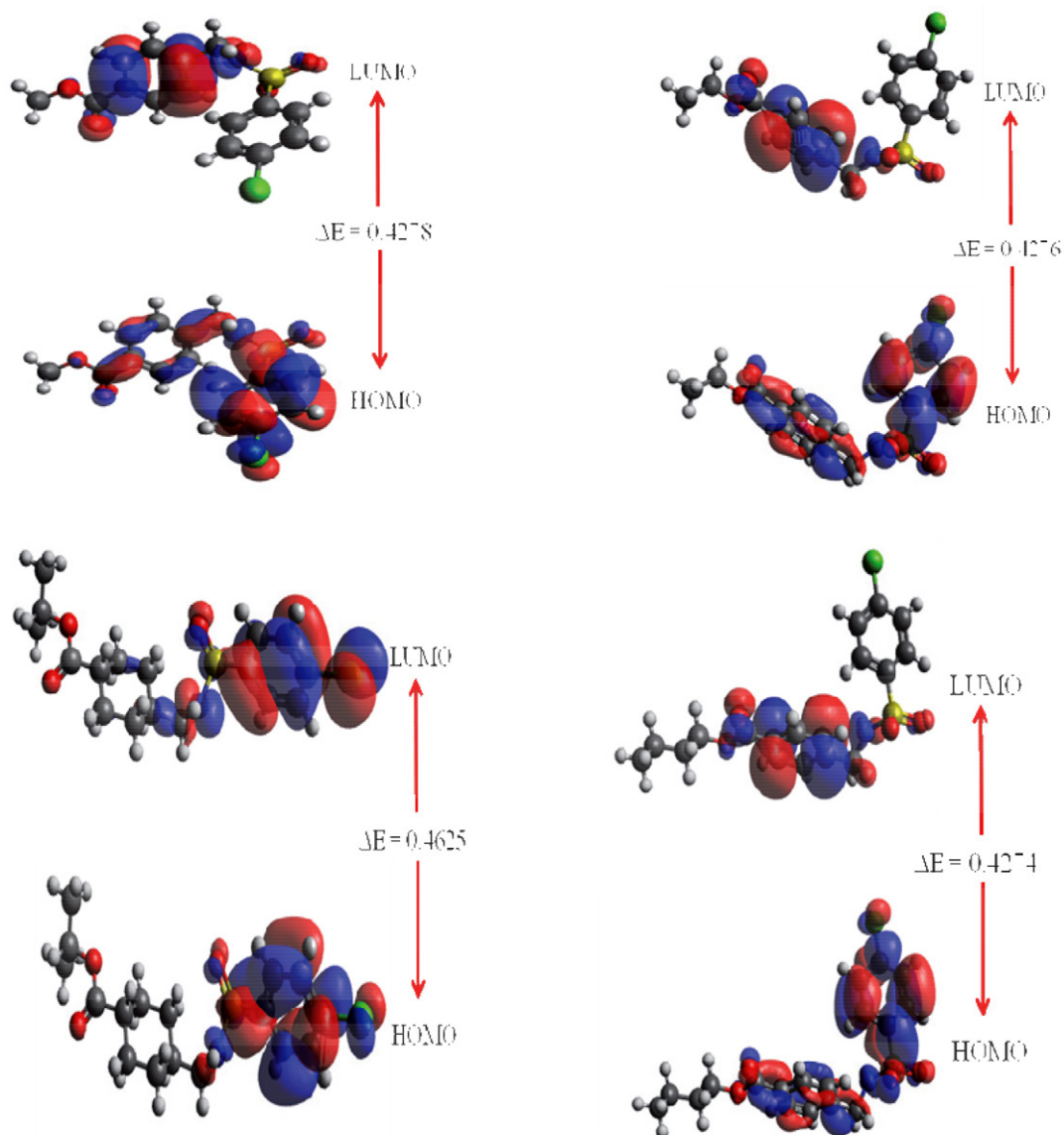


Figure 10. HOMO-LUMO energy diagram of synthesized esters

the results that there is a slight variation among the values of calculated parameters which suggested the presence of the same functionality and having similar physical and chemical properties of the molecules.

4. Conclusion

In current research work, a series of methyl (1), ethyl (2), isopropyl (3) and butyl (4) esters of 4-((4-chlorophenylsulfonamido)methyl)cyclohexanecarboxylic acid has been synthesized. Characterization of these compounds was done by FT-IR and mass spectrometry and NMR techniques while 3 was confirmed with X-ray crystallography. All compounds were screened for their biological applications involving anti-bacterial, anti-fungal, enzyme inhibi-

tion and anti-oxidant studies. Results showed that synthesized molecules have biological potential against tested activities. HOMO and LUMO was drawn after optimizing the structures with Gaussian and computational analysis was done to check binding mode of compound 3.

Conflict of Interest

All authors declared that they have no conflict of interest.

Acknowledgment

The help of Higher Education Commission is acknowledged for funding this study under the Project No. 20-2549/NRPU/R&D/HEC/12.

Supplementary Data

Selected bond lengths and bond angles for ester **3** are provided (Tables S1 and S2).

5. References

- M. Pfaller, D. Diekema, D. Gibbs, V. Newell, D. Ellis, V. Tullio, A. Rodloff, W. Fu, T. Ling, *J. Clin. Microbiol.* **2010**, *48*, 1366–1377. DOI:10.1128/JCM.02117-09
- H. S. Lee, Y. Kim, *J. Microbiol. Biotechnol.* **2016**, *26*, 610–617.
- N. Robbins, P. Uppuluri, J. Nett, R. Rajendran, G. Ramage, J. L. Lopez-Ribot, D. Andes, L. E. Cowen, *PLoS Pathogens*. **2011**, *7*, e1002257. DOI:10.1371/journal.ppat.1002257
- D. Wagner, A. Sander, H. Bertz, J. Finke, W. Kern, *Infection* **2005**, *33*, 397–400. DOI:10.1007/s15010-005-5082-4
- R. Sribalan, V. Padmini, A. Lavanya, K. Ponnuvel, *Saudi Pharma. J.* **2016**, *24*, 658–668. DOI:10.1016/j.jsps.2015.05.003
- J. N. Soni, S. S. Soman, *Eur. J. Med. Chem.* **2014**, *75*, 77–81. DOI:10.1016/j.ejmech.2014.01.026
- O. A. Phillips, E. E. Udo, M. E. Abdel-Hamid, R. Varghese, *Eur. J. Med. Chem.* **2009**, *44*, 3217–3227. DOI:10.1016/j.ejmech.2009.03.024
- O. A. Phillips, E. E. Udo, A. A. Ali, S. M. Samuel, *Eur. J. Med. Chem.* **2007**, *42*, 214–225. DOI:10.1016/j.ejmech.2006.10.005
- S.-Y. Kim, H. B. Park, J.-H. Cho, K. H. Yoo, C.-H. Oh, *Bioorg. Med. Chem. Lett.* **2009**, *19*, 2558–2561.
- A. Bendjeddou, T. Abbaz, A. Ayari, M. Benahmed, A. Gouasnia, D. Villemin, *Orient. J. Chem.* **2016**, *32*, 799–806. DOI:10.13005/ojc/320205
- A. Ali, G. K. K. Reddy, H. Cao, S. G. Anjum, M. N. Nalam, C. A. Schiffer, T. M. Rana, *J. Med. Chem.* **2006**, *49*, 7342–7356. DOI:10.1021/jm060666p
- G. Mustafa, I. U. Khan, M. Ashraf, I. Afzal, S. A. Shahzad, M. Shafiq, *Bioorg. Med. Chem.* **2012**, *20*, 2535–2539. DOI:10.1016/j.bmc.2012.02.055
- G. La Regina, A. Coluccia, V. Famigliani, S. Pelliccia, L. Monti, D. Vullo, E. Nuti, V. Alterio, G. De Simone, S. M. Monti, *J. Med. Chem.* **2015**, *58*, 8564–8572. DOI:10.1021/acs.jmedchem.5b01144
- G. R. Bebernitz, Google Patents, 2010.
- Y. Genç, R. Özkanca, Y. Bekdemir, *Ann. Clin. Microb. Anti.* **2008**, *7*, 17–21. DOI:10.1186/1476-0711-7-17
- B. Singh, A. Maheshwari, G. Dak, K. Sharma, G. Talesara, *Indian J. Pharm. Sci.* **2010**, *72*, 607–612. DOI:10.4103/0250-474X.78529
- M. Danish, A. Bibi, K. Gilani, M. A. Raza, M. Ashfaq, M. N. Arshad, A. M. Asiri, K. Ayub, *J. Mol. Struct.* **2019**, *1175*, 379–388. DOI:10.1016/j.molstruc.2018.07.116
- R. Bikas, P. M. Anarjan, S. W. Ng, E. R. Tiekink, *Acta Crystallogr. E: Structure Reports Online* **2012**, *68*, o193–o193. DOI:10.1107/S1600536811053268
- G. M. Sheldrick, *Acta Crystallogr. A: Foundations of Crystallography* **2008**, *64*, 112–122. DOI:10.1107/S0108767307043930
- L. J. Farrugia, *J. Appl. Crystallogr.* **2012**, *45*, 849–854. DOI:10.1107/S0021889812029111
- S. Shahid, M. A. Raza, S. Ur-Rehman, *Afr. J. Biotechnol.* **2009**, *8*, 5116–5121.
- D. Shahwar, M. A. Raza, *Asian Pac. J. Trop. Biomed.* **2012**, *2*, 547–550. DOI:10.1016/S2221-1691(12)60094-X
- G. L. Ellman, K. D. Courtney, V. Andres Jr, R. M. Featherstone, *Biochem. Pharmacol.* **1961**, *7*, 88–95. DOI:10.1016/0006-2952(61)90145-9
- A. D. Becke, *J. Chem. Phys.* **1993**, *98*, 5648–5652. DOI:10.1063/1.464913
- N. Kumar, V. Pruthi, N. Goel, *J. Mol. Struct.* **2015**, *1085*, 242–248. DOI:10.1016/j.molstruc.2014.12.064
- A. Ilyas, N. Muhammad, M. A. Gilani, K. Ayub, I. F. Vankelecom, A. L. Khan, *J. Membr. Sci.* **2017**, *543*, 301–309. DOI:10.1016/j.memsci.2017.08.071
- S. Sherzaman, M. N. Ahmed, B. A. Khan, T. Mahmood, K. Ayub, M. N. Tahir, *J. Mol. Struct.* **2017**, *1148*, 388–396. DOI:10.1016/j.molstruc.2017.07.054
- R. U. Nisa, K. Ayub, *New J. Chem.* **2017**, *41*, 5082–5090. DOI:10.1039/C7NJ00312A
- I. Daoud, N. Melkemi, T. Salah, S. Ghalem, *Comput. Biol. Chem.* **2018**, *74*, 304–326. DOI:10.1016/j.compbiolchem.2018.03.021
- M. Danish, R. A. Butt, M. N. Tahir, M. Ashfaq, S. T. Hafeez, M. N. Ahmed, H. Qureshi, *Chinese J. Struct. Chem.* **2017**, *36*, 1307–1314.
- M. N. Arshad, A. M. Asiri, K. A. Alamry, T. Mahmood, M. A. Gilani, K. Ayub, A. S. Birinji, *Spectrochim. Acta A: Molecular and Biomolecular Spectroscopy* **2015**, *142*, 364–374. DOI:10.1016/j.saa.2015.01.101
- M. N. Arshad, T. Mahmood, A. Faroque Khan, M. Zia-Ur-Rehman, A. M. Asiri, I. Ullah Khan, R. Un-Nisa, K. Ayub, A. Mukhtar, M. Tariq Saeed, *Chinese J. Struct. Chem.* **2015**, *34*, 15–25.
- M. N. Arshad, O. Şahin, M. Zia-ur-Rehman, I. U. Khan, A. M. Asiri, H. M. Rafique, *J. Mol. Struct.* **2013**, *54*, 437–442. DOI:10.1134/S0022476613020224
- M. N. Arshad, O. Şahin, M. Zia-ur-Rehman, M. Shafiq, I. U. Khan, A. M. Asiri, S. B. Khan, K. A. Alamry, *J. Chem. Crystallogr.* **2013**, *43*, 671–676.
- E. Schuster, N. Dunn-Coleman, J. Frisvad, P. Van Dijck, *Appl. Microbiol. Biotechnol.* **2002**, *59*, 426–435. DOI:10.1007/s00253-002-1032-6
- G. Beaney, A. Broughton, *J. Laryngol. Otol.* **1967**, *81*, 987–997. DOI:10.1017/S0022215100067955
- K. Brieger, S. Schiavone, F. J. Miller Jr, K.-H. Krause, *Swiss Med. Wkly.* **2012**, *142*, w13659.
- P. T. Francis, A. M. Palmer, M. Snape, G. K. Wilcock, *J. Neurol. Neurosurg. Psychiatry* **1999**, *66*, 137–147. DOI:10.1136/jnnp.66.2.137

Povzetek

S pomočjo zelene sintezne strategije smo z enostavno reakcijo med alkoholom in sulfonamidnim ligandom pripravili serijo novih trdnih estrov. Karakterizacijo tako pripravljenega metilnega (1), etilnega (2), izopropilnega (3) in *n*-butilnega (4) estra 4-((4-klorofenilsulfonamido)metil)cikloheksankarboksilne kisline smo izvedli s pomočjo FTIR, NMR masne spektrometrije in rentgenske kristalografije. Spojine smo optimizirali s pomočjo Gaussian programskega paketa z baznim setom B3LYP/6-31G(d,p) in izračunali nekaj parametrov, ki so povezani s strukturo. Za vse spojine smo *in vitro* izvedli nekatere biološke študije, vključno z antibakterijskim delovanjem (*Chromohalobacter salixgens*, *Halomonas halofila*, *Escherichia coli*, *Staphylococcus aureus*, *Bacillus subtilis* in *Shiegella sonnei*), delovanjem proti glivam (*Aspergillus niger*), antioksidacijskim delovanjem (aktivnost uničevanja DPPH) in encimsko inhibicijo (acetilholin esteraza in butirilholin esteraza). Da bi ugotovili način vezave, smo sulfonamidne estre sidrali v izbrana encima (AChE in BChE) s pomočjo MOE programske opreme. Rezultati bioloških študij kažejo, da pripravljene spojine izkazujejo potencialno aktivnost.



Except when otherwise noted, articles in this journal are published under the terms and conditions of the Creative Commons Attribution 4.0 International License

Scientific paper

Phase Equilibria in the $\text{Ag}_2\text{Te-PbTe-Sb}_2\text{Te}_3$ System and Thermodynamic Properties of the $(2\text{PbTe})_{1-x}(\text{AgSbTe}_2)_x$ Solid Solutions

Leyla Farhad Mashadiyeva,¹ Shabnam Hamlet Mansimova,²
 Dunya Mahammad Babanly,^{1,3} Yusif Amirali Yusibov,⁴ Dilqam Babir Tagiyev¹
 and Mahammad Baba Babanly^{1,2,*}

¹ Institute of Catalysis and Inorganic Chemistry, Azerbaijan National Academy of Science, Baku, Azerbaijan

² Baku State University, Chemistry Department, Baku, Azerbaijan

³ Azerbaijan State Oil and Industry University, Baku, Azerbaijan

⁴ Ganja State University, Chemistry Department, Ganja, Azerbaijan

* Corresponding author: E-mail: babanlymb@gmail.com

Received: 13-29-2019

Abstract

Phase equilibria in the $\text{Ag}_2\text{Te-PbTe-Sb}_2\text{Te}_3$ system were experimentally investigated by means of differential thermal analysis, powder X-ray diffraction techniques and electromotive force (EMF) measurement method. A liquidus surface projection of the system, 750 K and 300 K isothermal sections, as well as five vertical sections of the phase diagram, were constructed. The primary crystallization fields of phases and homogeneity range of phases were also determined. The character and temperature of the various nonvariant and monovariant equilibria were identified. The studied system is characterized by the formation of a wide continuous band of a high-temperature cubic structured solid solution (β -phase) between PbTe and $\text{Ag}_{1-x}\text{Sb}_{1+x}\text{Te}_{2+x}$ intermediate phase. The partial molar thermodynamic functions of lead telluride in alloys and standard integral thermodynamic functions of the β -solid solutions along the 2PbTe - AgSbTe_2 section were calculated based on the EMF measurements results.

Keywords: Ag-Sb-Pb-Te system; silver telluride; lead telluride; antimony telluride; phase equilibria; solid solution; thermodynamic functions.

1. Introduction

Complex silver-containing chalcogenides are among the advanced functional materials.^{1–3} Thanks to the mobility of silver ions, these phases have mixed ion-electron conductivity and can be widely used in semiconductors, electrochemical energy storage materials, electrodes of fuel cells and batteries, etc.^{4,5}

Alloys formed in $\text{Ag}_2\text{X-A}^{\text{IV}}\text{X-B}^{\text{V}}\text{X}_3$ systems (where $\text{A}^{\text{IV}} = \text{Ge, Sn, Pb}$; $\text{B}^{\text{V}} = \text{Sb, Bi}$; $\text{X} = \text{S, Se, Te}$) are good thermoelectric materials with a high thermoelectric figure of merit ZT .^{6–10} Besides, phases $\text{A}^{\text{IV}}\text{B}^{\text{V}}\text{X}_4$, $\text{A}^{\text{IV}}\text{B}^{\text{V}}\text{X}_7$, etc. which are formed on the boundary quasi-binary systems of the $\text{Ag}_2\text{X-A}^{\text{IV}}\text{X-B}^{\text{V}}\text{X}_3$ systems possess topological surface states and can be used in spintronics and quantum

computing.^{11–14} Great interest is complex telluride phases formed in these systems with excellent thermoelectric properties, such as Ge-Sb-Ag-Te (named as TAGS) and Pb-Sb-Ag-Te (denoted as LAST).^{15–19} It is known that the development of new multicomponent materials is based on data on the phase equilibria of the corresponding systems and thermodynamic properties of phases formed in them.^{20–24}

Herein, we present the phase relationships in the $\text{Ag}_2\text{Te-PbTe-Sb}_2\text{Te}_3$ system over the entire concentration range. Also, we report the thermodynamic properties of the $(2\text{PbTe})_{1-x}(\text{AgSbTe}_2)_x$ solid solution formed in the system. Earlier we report the self-consistent phase equilibria description and thermodynamic study result in such silver-based multi-component telluride systems

$\text{Ag}_2\text{Te-PbTe-Bi}_2\text{Te}_3$,²⁵ $\text{Ag}_2\text{Te-SnTe-Bi}_2\text{Te}_3$,²⁶ and $\text{Ag}_2\text{Te-SnTe-Sb}_2\text{Te}_3$,^{27,28} In all these studied systems, high-temperature solid solutions with a cubic structure along the $\text{A}^{\text{IV}}\text{Te-AgB}^{\text{V}}_2\text{Te}_3$ section are formed.

2. Literature Review

2.1. Starting Compounds

The starting binary compounds of the $\text{Ag}_2\text{Te-PbTe-Sb}_2\text{Te}_3$ system are well known. Ag_2Te melts congruently at 1233 K and has three polymorph modifications.²⁹ Its room-temperature modification (RT- Ag_2Te) crystallizes in the monoclinic system ($P2_1/c$ space group; lattice parameters: $a = 0.809$ nm; $b = 0.448$ nm; $c = 0.896$; $\beta = 112.55^\circ$) and remains stable up to 378 K with tellurium excess and up to 418 K with silver excess.³⁰ Intermediate-temperature modification (IT- Ag_2Te) crystallizes in the face-centered cubic system ($Fm\bar{3}m$ space group; $a = 0.6648$ nm,³¹) transforms into high temperature body-centered cubic form (HT- Ag_2Te ; $Im\bar{3}m$ space group; $a = 0.529$ nm,³²) at 1075 K. PbTe melts congruently at 1197 K,²⁹ and crystallizes in the $Fm\bar{3}m$ face-centered cubic crystal structure with cell parameter; $a = 6.6461(3)$ nm.³³ Sb_2Te_3 melts congruently at 893 K,²⁹ and crystallizes in the rhombohedral tetradymite type of structure ($R\bar{3}m$ space group) with parameters: $a = 0.4264$ nm; $c = 3.0458$ nm.³⁴

2.2. Boundary Quasi-Binary Systems

The boundary quasi-binary systems of the $\text{Ag}_2\text{Te-PbTe-Sb}_2\text{Te}_3$ system were studied well.

The $\text{Ag}_2\text{Te-PbTe}$ system has a $T-x$ diagram of eutectic type with limited mutual solubility of the components.^{35–37} The eutectic has the composition 38 mol % PbTe and crystallizes at 967 K,³⁶ (35 mol % PbTe and 973 K,³⁵). The solubility of the starting components in each other is 12–15% at the eutectic temperature.³⁷

Phase diagrams of the $\text{Ag}_2\text{Te-Sb}_2\text{Te}_3$ pseudobinary system were elaborated separately in.^{38,39} A previously reported in,⁴⁰ phase with the nominal composition of Ag_2SbTe_2 does not exist. In fact, the only ternary intermediate phase $\text{Ag}_{1-x}\text{Sb}_{1+x}\text{Te}_{2+x}$ with variable composition ($0.08 < x < 0.41$,³⁸), which crystallizes in the NaCl structure type ($Fm\bar{3}m$ space group; $a = 0.6078$ nm,³⁸) is thermodynamically stable. However, earlier reports differ about the temperature and compositional region of this phase.^{38,39} Further investigations of the Ag-Sb-Te ternary system confirmed that this phase is only stable in a limited temperature range ($633 \text{ K} < T < 847 \text{ K}$) and it decomposes into solid solutions based on starting Sb_2Te_3 and IT- Ag_2Te compounds below 633 K.^{41–43} The decomposition process was additionally confirmed by temperature-dependent X-ray diffraction analysis,⁴⁴ and electrochemical measurements.⁴⁵ The homogeneity range of the $\text{Ag}_{1-x}\text{Sb}_{1+x}\text{Te}_{2+x}$ phase varies with temperature from 35 to 45 mol% Sb_2Te_3 .

Recent works are devoted to the search for optimal compositions of this nonstoichiometric phase, which exhibits a high thermoelectric figure of merit.^{46,47} The eutectic of the $\text{Ag}_2\text{Te-Sb}_2\text{Te}_3$ system crystallizes at 70 mol% Ag_2Te and 817 K.³⁸

The phase diagram of the $\text{PbTe-Sb}_2\text{Te}_3$ boundary system reported in,⁴⁸ was characterized by formation only ternary compound $\text{Pb}_2\text{Sb}_6\text{Te}_{11}$, at approximately the eutectic composition on peritectic reaction at 860 K. Shelimova et al.,⁴⁹ showed formation in this system also PbSb_2Te_4 and PbSb_4Te_7 compounds with a layered structure. However, further studies on this system,^{50,51} have not confirmed the last compounds. These studies indicated the formation of only the $\text{Pb}_2\text{Sb}_6\text{Te}_{11}$ metastable ternary compound with a 7-layer rhombohedral structure. This metastable phase is stable at high temperatures and decomposes on cooling into PbTe and Sb_2Te_3 . However, solidification processing always yields the $\text{Pb}_2\text{Sb}_6\text{Te}_{11}$ phase as a constituent phase observable at room temperature.^{50,51} There is an eutectic reaction between $\text{Pb}_2\text{Sb}_6\text{Te}_{11}$ and Sb_2Te_3 at 855 K.⁴⁸

3. Experimental Part

3.1. Synthesis

All starting compounds Ag_2Te , PbTe , and Sb_2Te_3 of the title system were prepared by melting of elements in evacuated ($\sim 10^{-3}$ Pa) silica ampoules at temperatures ~ 50 K higher than their melting points.²⁹ High purity simple substances from the Evochem Advanced Materials GMBH Company (Germany) of were used for synthesis: silver in granules (Ag-00047; 99.999%), antimony in granules (Sb-00002; 99.999%), lead in granules (Pb-00005; 99.9995%), tellurium pieces (Te-00005; 99.9999%). Silver telluride Ag_2Te was additionally annealed at 1200 K for 3 hours and

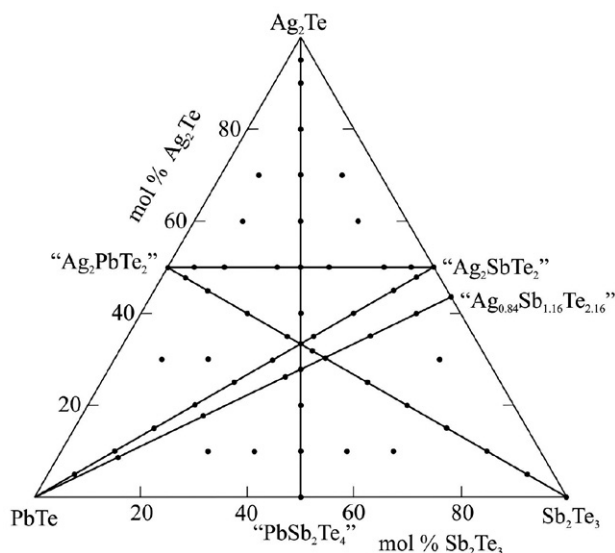


Fig. 1. Studied isopleth sections (lines) and alloys (points) of the $\text{Ag}_2\text{Te-PbTe-Sb}_2\text{Te}_3$ system

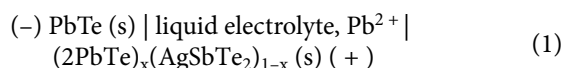
then was quenched with cold water in order to obtain a homogeneous stoichiometric composition. All starting compounds have been identified using differential thermal analysis and powder X-ray diffraction techniques.

More than sixty alloys of the $\text{Ag}_2\text{Te-PbTe-Sb}_2\text{Te}_3$ system (Fig. 1) were prepared from the pre-synthesized initial compounds also by vacuum alloying. Considering that the non-stoichiometric phase $\text{Ag}_{1-x}\text{Sb}_{1+x}\text{Te}_{2+x}$ decomposes upon cooling, 2 series of $\text{PbTe-“AgSbTe}_2\text{”}$ and $\text{PbTe-“Ag}_{0.84}\text{Sb}_{1.16}\text{Te}_{2.16}\text{”}$ alloys with the same compositions were prepared. Alloys from the first series were slowly cooled to 750 K after alloying and then annealed at this temperature for about 700 hours. Alloys from the second series were quenched in cold water after alloying and then also annealed at 750 K (700 h). All alloys after annealing were cooled to room temperature in the off-furnace mode.

3. 2. Analysis

Differential thermal analysis (DTA) and powder X-ray diffraction (PXRD) techniques were employed to analyze both starting compounds and alloys. Thermal analysis of the equilibrated alloys was carried out using a NETZSCH 404 F1 Pegasus system. The DTA measurement was performed between room temperature and ~ 1300 K with a heating and cooling rate of 10 K min^{-1} under the inert gas (Ar) flow. Temperatures of thermal effects were taken mainly from the heating curves. NETZSCH Proteus Software was used for the evaluation of the DTA data. The PXRD analysis was performed on a Bruker D8 ADVANCE diffractometer, with $\text{CuK}\alpha_1$ radiation. PXRD patterns were indexed by using TopasV3.0 software by Bruker.

The electromotive force (EMF) method with glycerol electrolyte,⁵² was used for the thermodynamic study of the $(2\text{PbTe})_x(\text{AgSbTe}_2)_{1-x}$ solid solutions. Concentration chains of the following type were constructed and their EMF was measured in the temperature range of 300–450 K:



Similar electrochemical cells were previously successfully used for thermodynamic studies of several chalcogenide and other inorganic systems.^{53–56} Equilibrium alloys $(2\text{PbTe})_x(\text{AgSbTe}_2)_{1-x}$ with compositions $x = 0.1; 0.15; 0.2; 0.4; 0.6; 0.8$ were synthesized by fusing the elementary components in the required ratios into evacuated to $\sim 10^{-2}$ Pa and sealed quartz ampoules. To maximally approximate the alloys to the equilibrium state, the cast non-homogenized samples obtained by quenching the melts from 1100 K were ground into powder, thoroughly mixed, pressed into tablets weighing 0.3–0.5 g and annealed first at 750 K (500 hours), and then at 450 K (200 h.). Synthesized alloys were identified by PXRD.

To prepare electrodes the PbTe (left electrode) and annealed alloys $(2\text{PbTe})_x(\text{AgSbTe}_2)_{1-x}$ (right electrodes) were powdered and pressed onto molybdenum current leads in the form of tablets with a diameter of ~ 0.6 cm and a thickness of ~ 0.3 cm.

A solution of KCl in glycerol with the addition of PbCl_2 was used as the electrolyte. In order to prevent the presence of moisture and oxygen in the electrolyte anhydrous, chemically pure salts were used, as well as glycerin was previously dehydrated and outgassed by pumping at ~ 400 K.

The electrochemical cell described in,⁵³ was assembled. EMF measurements were carried out in an inert atmosphere using a high-voltage digital voltmeter V7-91. Before starting the measurements, the electrochemical cell was kept at ~ 350 K for 40–60 h, after which the first equilibrium EMF values were obtained. Subsequent measurements were carried out every 3–4 hours after the establishment of a certain temperature. The EMF values, which, regardless of the direction of the temperature change did not differ from each other at a given temperature by more than 0.2 mV, were considered to be equilibrium.

Results and Discussion

We have constructed the self-consistent phase diagram of the quasi-ternary $\text{Ag}_2\text{Te-PbTe-Sb}_2\text{Te}_3$ system as well as determined thermodynamic functions of the $\text{PbTe-“AgSbTe}_2\text{”}$ solid solution by the combined analysis of all our experimental results and the data found in the literature on the phase equilibria for the boundary quasibinary systems.

4. 1. The Sections $\text{PbTe-“AgSbTe}_2\text{”}$ and $\text{PbTe-“Ag}_{0.84}\text{Sb}_{1.16}\text{Te}_{2.16}\text{”}$

As mentioned above in Experimental Part, two series of alloys were prepared along these sections. Fig. 2 shows heating curves for $\text{PbTe-“AgSbTe}_2\text{”}$ alloys of both series with compositions 60, 80 and 90 mol% PbTe . As can be seen, the melting onset temperatures of the two series of alloys are very different. For samples of the 1st series (red curves) obtained by slow cooling, the melting onset temperatures are significantly (up to 100°) lower than the samples of the 2nd series (blue curves). Increasing the annealing time up to 1000 h did not change the DTA curves of alloys of the 2nd series, whereas for alloys of the 1st series some ($\sim 10\text{--}20^\circ$) rise in the temperatures of the onset of melting was observed.

These results show that the 2nd series samples can be considered practically in equilibrium. Therefore, data from DTA curves of the 2nd series alloys were used to construct the phase diagram of the $\text{PbTe-“AgSbTe}_2\text{”}$ system (Fig. 3). The $\text{PbTe-“AgSbTe}_2\text{”}$ system is characterized by the formation of wide (up to 70 mol%) solid solutions based on PbTe (β -phase), but the system is generally

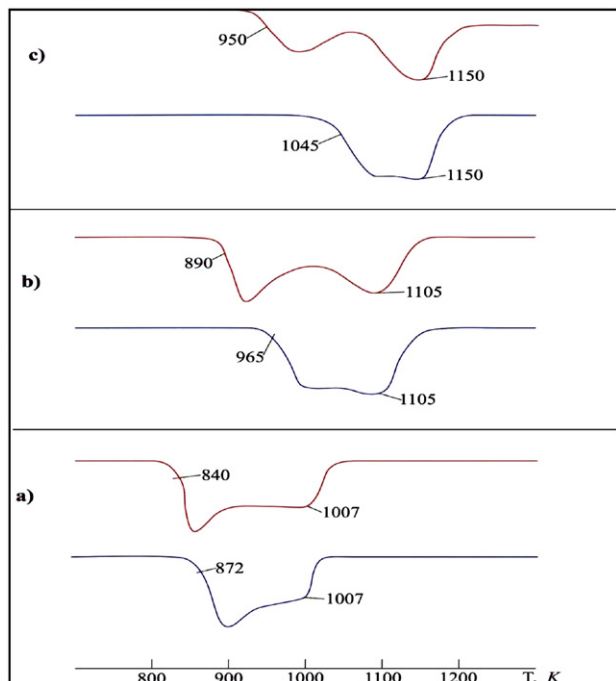


Fig. 2. Fragments of the DTA curves for the PbTe-“AgSbTe₂” system alloys with the compositions 60 (a), 80 (b) and 90 (c) mol% PbTe. DTA curves for the samples from the 1st series are red, and from the 2nd series are blue

non-quasi-binary. The reason is the non-individuality of the starting component “AgSbTe₂” which is a two-phase alloy Ag₂Te + Ag_{1-x}Sb_{1+x}Te_{2+x}.^{38,39}

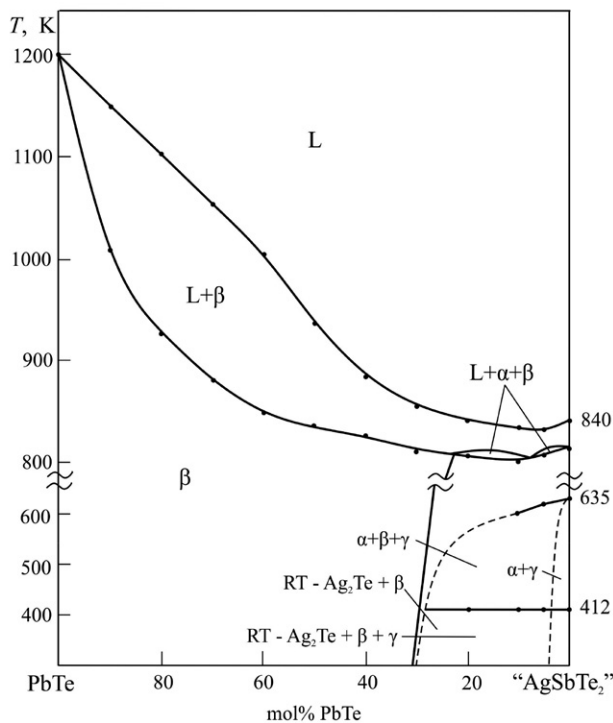


Fig. 3. PbTe-“AgSbTe₂” vertical section of the phase diagram of the Ag₂Te-PbTe-Sb₂Te₃ system

The powder X-ray analysis results confirmed the formation of a wide area (30–100 mol% PbTe) of a solid solution with a cubic structure in the studied section. PbTe-poor alloys are three-phase. For example, Fig. 4 represents a powder X-ray pattern of alloy with composition 20 mol% PbTe and 80 mol% “AgSbTe₂”. As can be seen from Fig. 4 the PXRD pattern of this alloy consists of a set of reflection lines of the RT-Ag₂Te, β -phase, and γ -phase based on Sb₂Te₃.

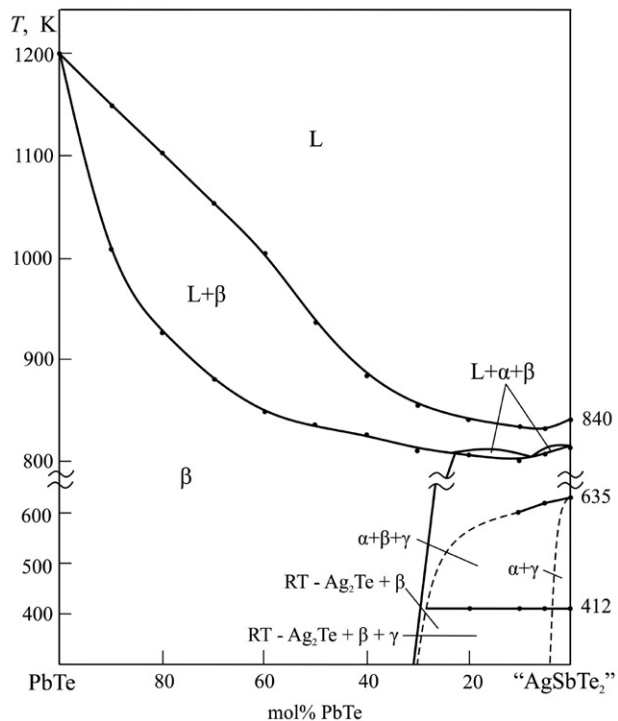


Fig. 4. PXRD patterns and phase composition for alloy with composition 20 mol% PbTe-80 mol% “AgSbTe₂”

A characteristic feature of the PbTe-“AgSbTe₂” system is a very large temperature range of crystallization (melting) of the β -phase (up to 150°). For this reason, slow cooling of melts leads to strong segregation and inhomogeneity of solid solutions in composition, which makes it difficult to achieve an equilibrium state of the samples. Inhomogeneity of solid solutions in composition in the 1st series alloys is demonstrated by a powder X-ray patterns of an alloy with a composition of 70 mol% PbTe (Fig. 5 a, b). As can be seen, X-ray patterns of samples of this alloy, obtained in two various ways, differ sharply. The sample from the 1st series has very diffuse reflection peaks, while the alloy from the 2nd series has a very high-quality X-ray pattern showing much smoother peaks with minimum noise.

The phase equilibria along the 2PbTe-“Ag_{0.84}Sb_{1.16}Te_{2.16}” section (Fig. 6) is qualitatively similar to the PbTe-“AgSbTe₂” section. The system is non-quasibinary due to the peritectic melting of the “Ag_{0.84}Sb_{1.16}Te_{2.16}”

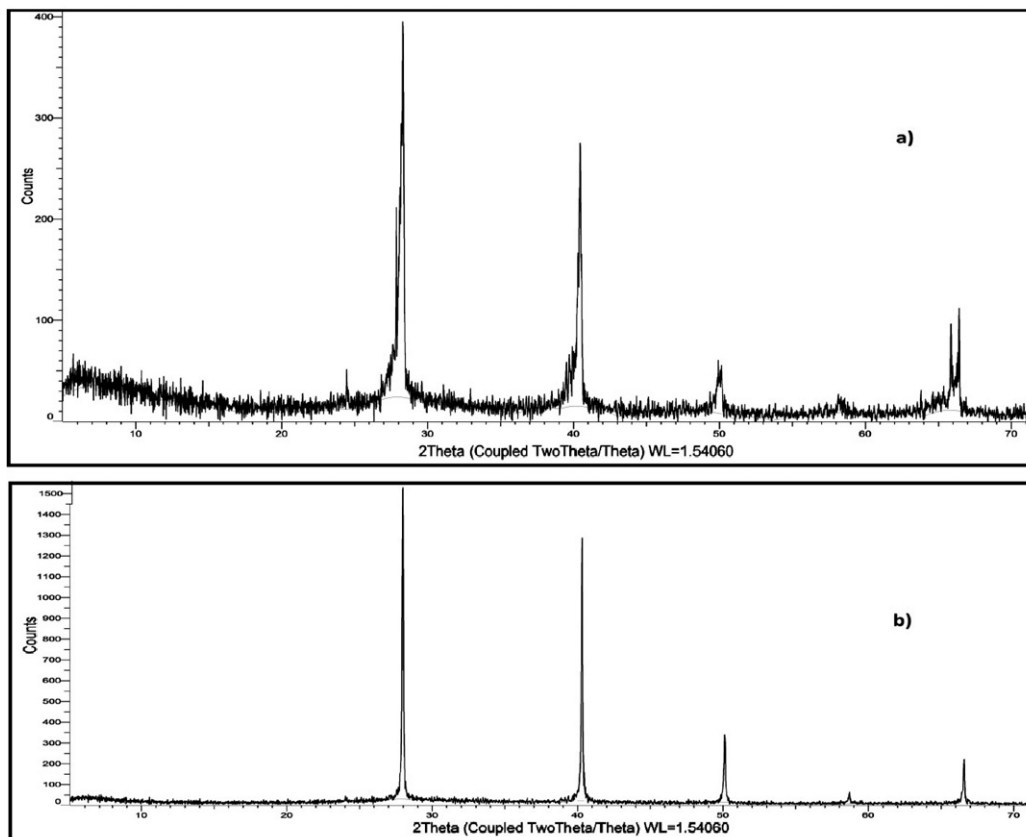


Fig. 5. Powder X-ray patterns of alloy with composition of 70 mol% PbTe: a) a sample from the 1st series; b) a sample from the 2nd series

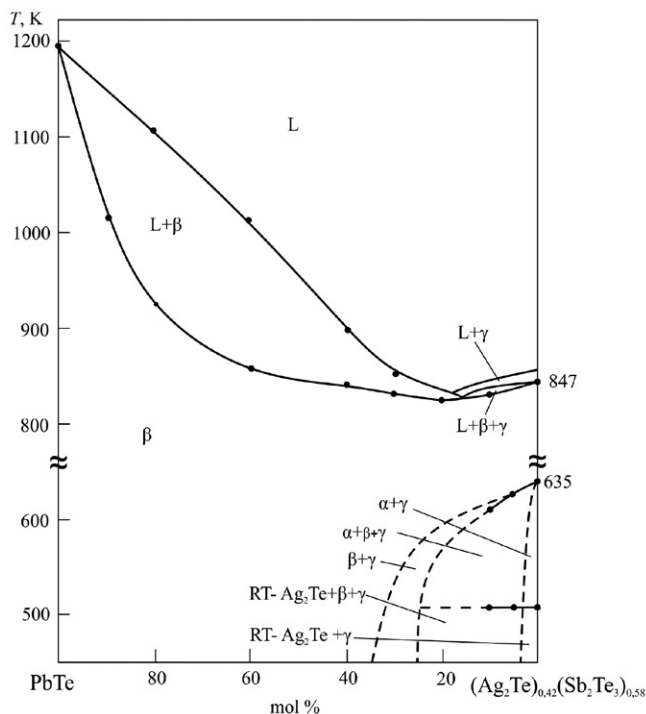


Fig. 6. 2PbTe- $\text{Ag}_{0.84}\text{Sb}_{1.16}\text{Te}_{2.16}$ vertical section of the phase diagram of the Ag_2Te -PbTe- Sb_2Te_3 system

phase and its decay into $\text{Ag}_2\text{Te} + \text{Sb}_2\text{Te}_3$ below 635 K. This, in turn, leads to the decomposition of β -solid solutions formed in this section in the 0–40 mol% PbTe composition range and, as a result, the $\alpha + \beta + \gamma$, $\beta + \gamma$, $\alpha + \gamma$, etc. fields are formed in the system (α -phase is a solid solution based on an $\text{IT-Ag}_2\text{Te}$).

Using TopasV3.0 software the lattice parameters of the β -phase were calculated (Table 1) and the concentration dependence of these parameters was plotted (Fig. 7). As can be seen from Fig. 7, the lattice parameters are a linear function of the composition. An insignificant positive deviation of this dependence on the Vegard law is probably caused by elastic deformation of the β -phase

Table 1. Crystallographic parameters of the β -solid solutions for the 2PbSe- $\text{Ag}_{0.84}\text{Sb}_{1.16}\text{Te}_{2.16}$ system

Composition, mol% $\text{Ag}_{0.84}\text{Sb}_{1.16}\text{Te}_{2.16}$	Cubic lattice parameter; a , nm
0 (PbTe)	0.6463(7)
20	0.6401(7)
40	0.6326(6)
60	0.6252(7)
80	0.6173(3)
100 ($\text{Ag}_{0.84}\text{Sb}_{1.16}\text{Te}_{2.16}$)	0.6077(8)

crystal lattice, due to the large difference in the crystal radius of antimony (0,09 nm) compared to silver (0,129 nm) and lead (0,133 nm). Crystal radii data were taken from.⁵⁷

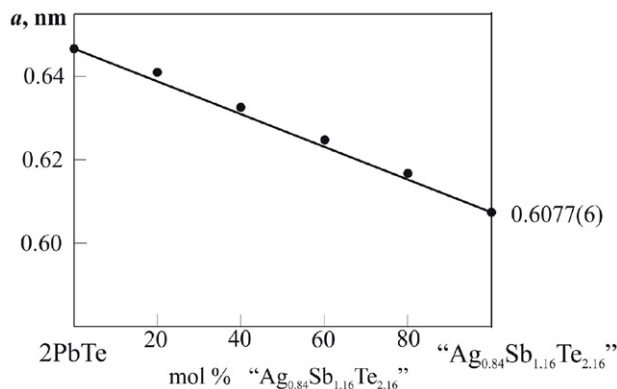


Fig. 7. Concentration dependence of cubic lattice parameter for β -phase along the $2\text{PbTe}-\text{Ag}_{0.84}\text{Sb}_{1.16}\text{Te}_{2.16}$ section

4. 2. Solid-Phase Equilibria

The isothermal sections at 750 K and 300 K of the phase diagram of the $\text{Ag}_2\text{Te}-\text{PbTe}-\text{Sb}_2\text{Te}_3$ system have been constructed.

The isothermal sections at 750 K. A homogeneity range of the intermediate phase $\text{Ag}_{1-x}\text{Sb}_{1+x}\text{Te}_{2+x}$ along $\text{PbTe}-\text{Sb}_2\text{Te}_3$ section is 40–44 mol% Sb_2Te_3 at 750 K.³⁸ A wide (up to 8 mol%) continuous band of β -solid solution is formed in the $\text{Ag}_2\text{Te}-\text{PbTe}-\text{Sb}_2\text{Te}_3$ system at 750 K (Fig. 8a). The width of a β -solid solutions is 3–4 mol% in the $\text{Ag}_2\text{Te}-\text{Sb}_2\text{Te}_3$ section and expands up to 7–8 mol% with a change in composition towards PbTe . The $\text{PbTe}-\text{Ag}_{0.84}\text{Sb}_{1.16}\text{Te}_{2.16}$ section is completely in the homogene-

ity area of the β -phase. The $\text{PbTe}-\text{AgSbTe}_2$ section in the composition range of 25–100 mol% PbTe passes through the β -phase homogeneity area, and at <25 mol% PbTe passes into the two-phase region $\alpha + \beta$. The β -phase forms connode lines with α -phase and γ -phase.

The isothermal sections at 300 K (Fig. 8b). The decomposition of the $\text{Ag}_{1-x}\text{Sb}_{1+x}\text{Te}_{2+x}$ intermediate phase below 635 K leads to partial decomposition of the β -phase in the composition range of <25 mol% PbTe and the following heterogeneous regions are formed: $\text{RT}-\text{Ag}_2\text{Te} + \beta + \gamma$ and $\text{RT}-\text{Ag}_2\text{Te} + \gamma$.

The location and borders of phase areas on the solid-phase equilibrium diagrams (Fig. 8a, b) were established by using the PXRD technique (for example, powder X-ray pattern of the alloy #1 from Fig. 8b is presented in Fig. 4) and confirmed by the DTA, as well as by the EMF technique (see sections 4.5).

4. 3. The Liquidus Surface Projection

The liquidus surface of the $\text{Ag}_2\text{Te}-\text{PbTe}-\text{Sb}_2\text{Te}_3$ system consists of 4 fields corresponding to primary crystallization of the α -, β - and γ - phases, as well as ternary compound $\text{Pb}_2\text{Sb}_6\text{Te}_{11}$ (Fig. 9). The α -phase primary crystallization area is separated from the α' -phase based on $\text{HT}-\text{Ag}_2\text{Te}$ by the dashed line. Largest crystallization field in the system belongs to β -phase (field 2 in Fig. 9). This region is divided into 2 parts by the curve M_1M_2 connecting the minimum points of M_1 and M_2 . The primary crystallization area of the ternary $\text{Pb}_2\text{Sb}_6\text{Te}_{11}$ compound is very small (field 4 in Fig. 9). Transitional equilibrium U limits the extent of this area inside the concentration triangle. This is in good agreement with data,^{50,51} on a narrow temperature range for the existence of compound $\text{Pb}_2\text{Sb}_6\text{Te}_{11}$.

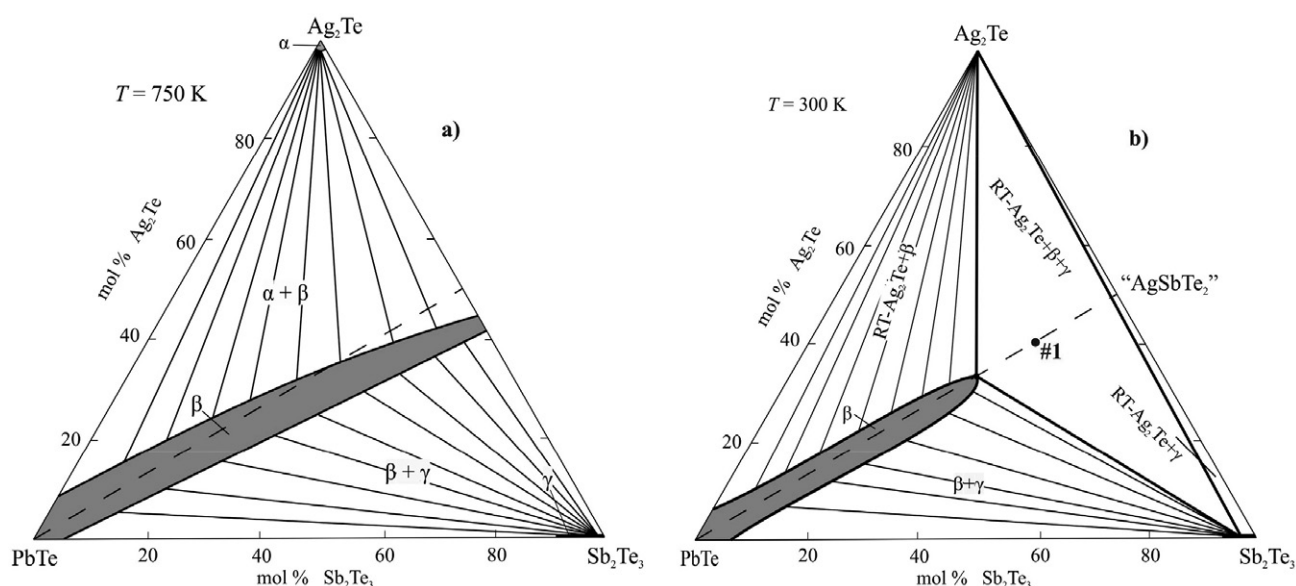


Fig. 8. (a) 750 K and (b) 300 K isothermal sections of the phase diagram of the $\text{Ag}_2\text{Te}-\text{PbTe}-\text{Sb}_2\text{Te}_3$ system

Table 2. Nonvariant and monovariant equilibria in the Ag_2Te - PbTe - Sb_2Te_3 system

Point or curve in Fig. 9	Equilibrium	Composition, mol%		T, K
		Ag_2Te	Sb_2Te_3	
P_1	$L + \beta \leftrightarrow \text{Pb}_2\text{Sb}_6\text{Te}_{11}$	–	62	860
P_2	$L + \gamma \leftrightarrow \text{Pb}_2\text{Sb}_6\text{Te}_{11}$	48	52	847
e_1	$L \leftrightarrow \text{Pb}_2\text{Sb}_6\text{Te}_{11} + \gamma$	–	66	855
e_2	$L \leftrightarrow \alpha + \beta$	62	–	967
e_3	$L \leftrightarrow \alpha + \text{Ag}_{1-x}\text{Sb}_{1+x}\text{Te}_{2+x}$	70	30	813
U	$L + \text{Pb}_2\text{Sb}_6\text{Te}_{11} \leftrightarrow \beta + \gamma$	11	59	847
M_1	$L + \gamma \leftrightarrow \beta$	42	46	825
M_2	$L \leftrightarrow \alpha + \beta$	68	27	805
$P_1\text{U}$	$L + \beta \leftrightarrow \text{Pb}_2\text{Sb}_6\text{Te}_{11}$			860–847
$e_1\text{U}$	$L \leftrightarrow \text{Pb}_2\text{Sb}_6\text{Te}_{11} + \gamma$			855–847
UK	$L \leftrightarrow \beta + \gamma$			847–830
KM_1	$L + \gamma \leftrightarrow \beta$			830–825
P_2M_1	$L + \gamma \leftrightarrow \beta$			847–825
M_1M_2	$L \leftrightarrow \gamma$			825–805
e_2M_2	$L \leftrightarrow \alpha + \beta$			967–805
e_3M_2	$L \rightarrow \alpha + \beta$			813–805

The primary crystallization fields of the phases are bordered by peritectic ($p_1\text{U}$, p_2M_1) and eutectic (e_2M_2 , M_2e_3 , $e_1\text{U}$, UM_1) curves (Fig. 9). Types and temperatures for all nonvariant and monovariant equilibria in the Ag_2Te - SnTe - Sb_2Te_3 system are listed in Table 2.

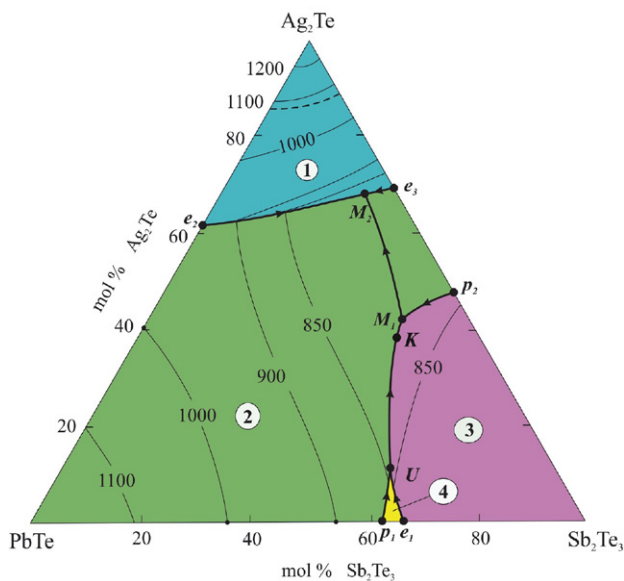


Fig. 9. The liquidus surface projection of the Ag_2Te - PbTe - Sb_2Te_3 system. Primary crystallization fields of phases: 1 – α' ; 2 – β ; 3 – γ and 4 – $\text{Pb}_2\text{Sb}_6\text{Te}_{11}$

4. 4. Isopleth Sections

In the context of a liquidus surface projection (Fig.9, Table 2) we consider three isopleth sections which almost completely cover a studied quasi-ternary system.

The section “ $\text{AgPb}_{0.5}\text{Te}$ ”-“ AgSbTe_2 ” (Fig. 10) passes through the region of primary crystallization of the

β -phase and intersects the curve M_1M_2 . Therefore, a minimum point is observed on the liquidus curve of this section. Below liquidus, crystallization proceeds according to a monovariant eutectic reaction $L \leftrightarrow \alpha + \beta$ (Fig. 10, Table 2, curves e_2M_2 , e_3M_2) and, as a result, a two-phase region $\alpha + \beta$ is formed in the subsolidus. The processes occurring in the system below 635 K and associated with the decomposition of the “ $\text{Ag}_{1-x}\text{Sb}_{1+x}\text{Te}_{2+x}$ ” phase were described above.

The section Ag_2Te -“ PbSb_2Te_4 ” (Fig. 11) passes through the areas of primary crystallization of α' , α and β phases. Below the liquidus in the composition range of 0–25 mol% Ag_2Te the univariant processes $L + \beta \leftrightarrow$

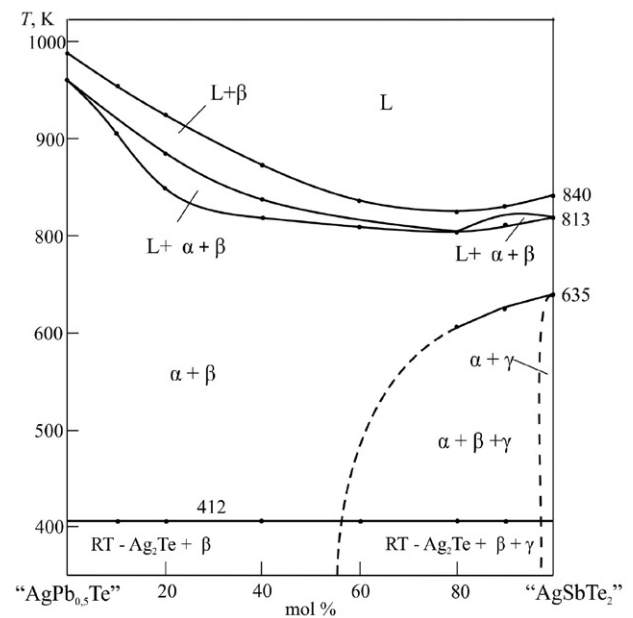


Figure 10. Isopleth section “ $\text{AgPb}_{0.5}\text{Te}$ ”-“ AgSbTe_2 ”

$\text{Pb}_2\text{Sb}_6\text{Te}_{11}$ and $L \leftrightarrow \beta + \gamma$ occur and the two-phase region $\beta + \gamma$ is formed. In the composition range 25–35 mol% Ag_2Te , crystallization continues according to the $L \leftrightarrow \beta$ scheme. In the composition range 25–35 mol% Ag_2Te , as a result of the crystallization process $L \leftrightarrow \alpha + \beta$ a two-phase region $\text{RT-Ag}_2\text{Te} + \beta$ is formed in the system due to the $\alpha \leftrightarrow \text{RT-Ag}_2\text{Te}$ phase transition. Note that due to the formation of α' and α solid solutions, the phase transition temperature $\alpha' \leftrightarrow \alpha$ (~1080 K) increases slightly compared to pure Ag_2Te , which leads to the establishment of the $L + \alpha' \leftrightarrow \alpha$ (p') peritonic equilibrium in the system.

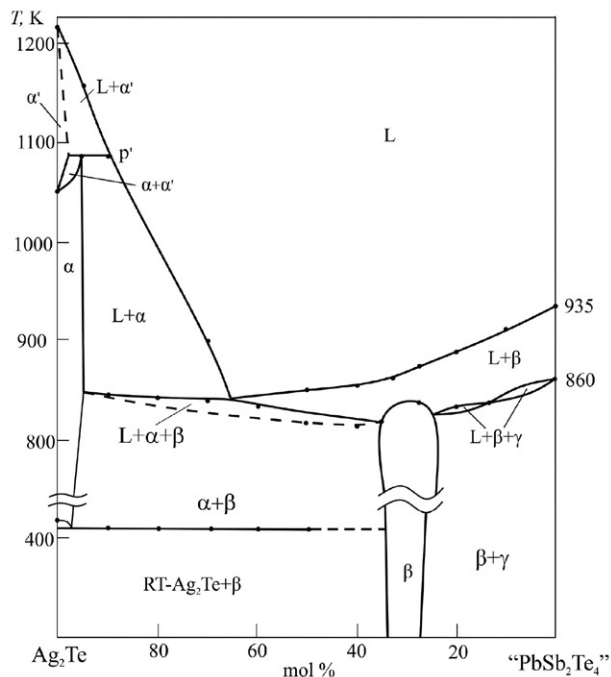


Figure 11. Isopleth section Ag_2Te -« PbSb_2Te_4 »

The section « $\text{AgPb}_{0.5}\text{Te}$ »- Sb_2Te_3 (Fig. 12) passes through the regions of primary crystallization of β and γ phases. Further, the crystallization process continues according to the monovariant reactions $L \leftrightarrow \alpha + \beta$ (0–30 mol% Sb_2Te_3), $L \leftrightarrow \beta + \gamma$ (40–90 mol% Sb_2Te_3) and $L + \gamma \leftrightarrow \beta$ (90–98 mol% Sb_2Te_3). In the range of compositions ~30–38 mol% Sb_2Te_3 , crystallization proceeds according to the $L \leftrightarrow \beta$ reaction and ends with the formation of the β -phase.

4. 5. Thermodynamic Properties of the $(2\text{PbTe})_{1-x}(\text{AgSbTe}_2)_x$ Solid Solution Obtained with EMF Measurements

Measurements of the EMF of the chains of type (1) showed that the EMF values for samples $(2\text{PbTe})_x(\text{AgSbTe}_2)_{1-x}$ with compositions $x = 0.1, 0.15$ and 0.2 are the same, and with further increase of the concentration of

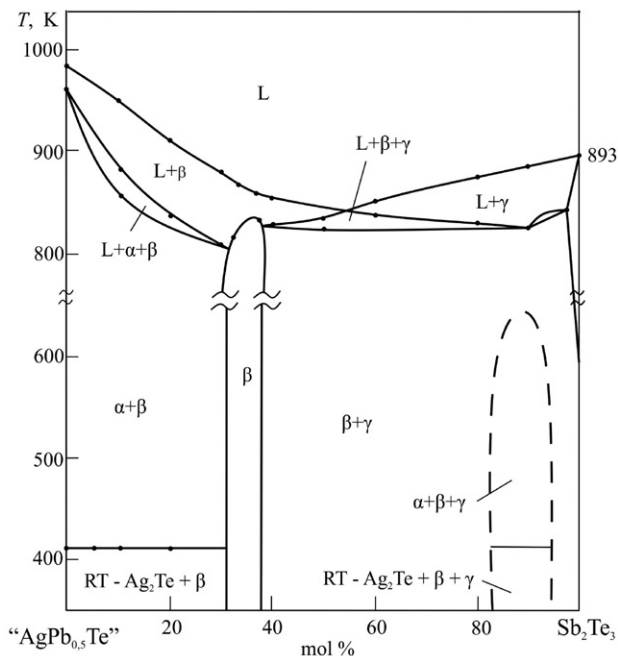


Figure 12. Isopleth section « $\text{AgPb}_{0.5}\text{Te}$ »- Sb_2Te_3

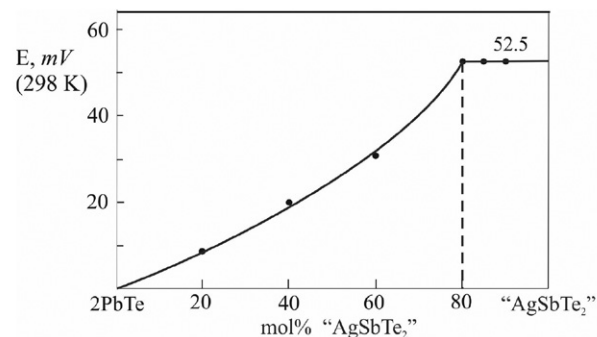


Figure 13. Concentration dependence of the EMF of chains of type (1) at 298 K for the 2PbTe -« AgSbTe_2 » alloys

PbTe the values of EMF continuously decrease (Fig. 13). This indicates that in this system up to 80 mol.% solid solutions are produced based on PbTe .

Analysis of the temperature dependences of the EMF showed that for all samples they are linear (Fig. 14). Therefore, the experimental data were processed by the least-squares method in the approximation of the linear temperature dependence of the EMF. For this purpose, the «Microsoft Office Excel 2010» software was used.

The obtained linear equations are presented in Table 3 in the following form recommended in,⁵²:

$$E = a + bT \pm t \left[\left(\frac{S_E^2}{n} \right) + S_b^2 \cdot (T - \bar{T})^2 \right]^{1/2} \quad (2)$$

Here n is the number of pairs of values of E and T ; S_E and S_b are the dispersions of individual measurements of EMF and coefficient b , respectively; \bar{T} is average absolute temperature, t is Student's test. With a confidence level of

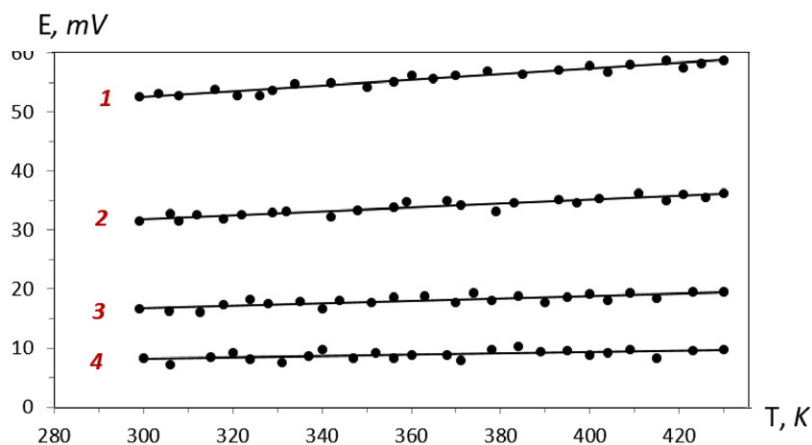


Figure 14. Temperature dependences of the EMF of chains of type (1) for the 2PbTe–“AgSbTe₂” alloys: **1** – (2PbTe)_{0.2}(AgSbTe₂)_{0.8}; **2** – (2PbTe)_{0.4}(AgSbTe₂)_{0.6}; **3** – (2PbTe)_{0.6}(AgSbTe₂)_{0.4}; **4** – (2PbTe)_{0.8}(AgSbTe₂)_{0.2}

95% and the number of experimental points $n \geq 20$ the Student’s test is $t \geq 2$.

The partial molar functions of PbTe ($\Delta \bar{Z}_{\text{PbTe}}$) in alloys at 298.15 K were calculated from the data of Table 3 according to the following relations,⁵⁸:

$$\Delta \bar{G}_{\text{PbTe}} = -zFE \quad (3)$$

$$\Delta \bar{S}_{\text{PbTe}} = zF \left(\frac{\partial E}{\partial T} \right)_p = zFb \quad (4)$$

$$\Delta \bar{H}_{\text{PbTe}} = -zF \left[E + T \left(\frac{\partial E}{\partial T} \right)_p \right] = -zFa \quad (5)$$

Table 3. Temperature dependences of the EMF of cells of type (1) for the (2PbTe)_x(AgSbTe₂)_{1-x} alloys in the 300, 450 K temperature range

Composition	$E, \text{ mV} = a + bT \pm t \times S_E(T)$
(2PbTe) _{0.2} (AgSbTe ₂) _{0.8}	$38.2 + 0.0487T \pm 2 \left[\frac{1.5}{24} + 4.8 \cdot 10^{-5}(T - 363.3) \right]^2$
(2PbTe) _{0.4} (AgSbTe ₂) _{0.6}	$23.6 + 0.0277T \pm 2 \left[\frac{1.8}{24} + 5.4 \cdot 10^{-5}(T - 362.6) \right]^2$
(2PbTe) _{0.6} (AgSbTe ₂) _{0.4}	$12.2 + 0.0167T \pm 2 \left[\frac{1.1}{24} + 3.5 \cdot 10^{-5}(T - 363.6) \right]^2$
(2PbTe) _{0.8} (AgSbTe ₂) _{0.2}	$5.8 + 0.0097T \pm 2 \left[\frac{1.2}{24} + 3.7 \cdot 10^{-5}(T - 361.7) \right]^2$

and listed in Table 4. As can be seen from Fig. 15, all these functions are continuous functions of the composition in the field $x \geq 0.2$.

The partial molar functions of PbTe are the difference between the partial molar values of lead in (2PbTe)_x(AgSbTe₂)_{1-x} solid solutions ($\Delta \bar{Z}_{\text{Pb}}$) and in pure PbTe:

$$\Delta \bar{Z}_{\text{PbTe}} = \Delta \bar{Z}_{\text{Pb}} - \Delta \bar{Z}'_{\text{Pb}} \quad (6)$$

где $Z \equiv G$ (или H).

PbTe is the only compound of the Pb-Te system and

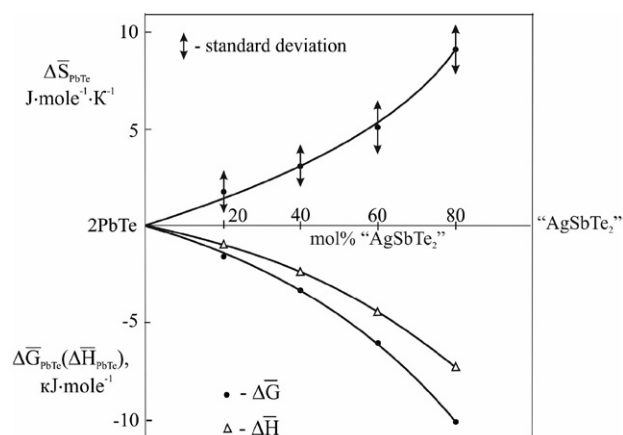


Figure 15. Concentration dependences of partial thermodynamic functions of PbTe in the 2PbTe–“AgSbTe₂” solid solutions at 298 K.

Table 4. Relative partial thermodynamic functions of PbTe in the 2PbTe–AgSbTe₂ alloys at 298 K

Composition	$-\Delta \bar{G}_{\text{PbTe}}$ $\text{kJ} \times \text{mole}^{-1}$	$-\Delta \bar{H}_{\text{PbTe}}$ $\text{kJ} \times \text{mole}^{-1}$	$-\Delta \bar{S}_{\text{PbTe}}$ $\text{J} \times \text{K}^{-1} \times \text{mole}^{-1}$
(2PbTe) _{0.2} (AgSbTe ₂) _{0.8}	10,13±0.20	7,37±0.97	9,26±2,67
(2PbTe) _{0.4} (AgSbTe ₂) _{0.6}	6,11±0.21	4,56±1,03	5,21±2,84
(2PbTe) _{0.6} (AgSbTe ₂) _{0.4}	3,27±0.17	2,35±0.83	3,09±2,28
(2PbTe) _{0.8} (AgSbTe ₂) _{0.2}	1,64±0.18	1.12±0.85	1,74±2,34

has an almost constant stoichiometric composition.³⁴ According to,⁵⁸ in such cases:

$$\Delta \bar{Z}_{Pb} = \Delta_f Z^0(PbTe) \quad (7)$$

Considering relations (6) and (7), the partial molar functions of lead in solid solutions $(2PbTe)_x(AgSbTe_2)_{1-x}$ can be calculated from the relation:

$$\Delta \bar{Z}_{Pb} = \Delta \bar{Z}_{PbTe} + \Delta_f Z^0(PbTe) \quad (8)$$

The values obtained by the relation (8) are presented in Table 5.

The calculation of standard thermodynamic functions of the formation of a solid solution of the limiting composition $(2PbTe)_{0.2}(AgSbTe_2)_{0.8}$, which is in equilibrium with Ag_2Te and Sb_2Te_3 , was performed using the following potential-forming reaction:

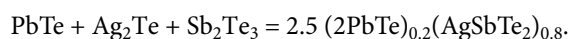


Table 5. Relative partial thermodynamic functions of lead in the $2PbTe$ – $AgSbTe_2$ alloys at 298 K

Composition	$-\Delta \bar{G}_{Pb}$ $\kappa J \text{ mole}^{-1}$	$-\Delta \bar{H}_{Pb}$ $\kappa J \text{ mole}^{-1}$	$-\Delta \bar{S}_{Pb}$ $J \times K^{-1} \text{ mole}^{-1}$
$(2PbTe)_{0.2}(AgSbTe_2)_{0.8}$	77,43±1,70	75,97±1,57	4,90±4,77
$(2PbTe)_{0.4}(AgSbTe_2)_{0.6}$	73,41±1,71	73,16±1,63	0,84±4,94
$(2PbTe)_{0.6}(AgSbTe_2)_{0.4}$	70,57±1,67	70,95±1,43	-1,74±4,38
$(2PbTe)_{0.8}(AgSbTe_2)_{0.2}$	68,94±1,68	69,72±1,45	-2,62±4,44

Table 6. Standard integral thermodynamic functions of the $(2PbTe)_{1-x}(AgSbTe_2)_x$ solid solutions

Phase	$-\Delta_f G^\circ$ (298 K) $\kappa J \text{ mole}^{-1}$	$-\Delta_f H^\circ$ (298 K) $\kappa J \text{ mole}^{-1}$	S° (298 K), $J \times K^{-1} \text{ mole}^{-1}$
$PbTe$, ⁵⁸	67.3±1.5	68.6±0.6	110.0±2.1
Sb_2Te_3 , ⁵⁸	56.9±1.0	56.5±0.4	246.4±2.1
Ag_2Te , ⁵⁹	40.2±0.3	35.0±0.5	152.0±2.0
$(2PbTe)_{0.9}(AgSbTe_2)_{0.1}$	128.5±2.8	130.0±1.2	217.6±4.1
$(2PbTe)_{0.8}(AgSbTe_2)_{0.2}$	119.0±2.5	121.9±1.1	218.4±3.9
	122.2±2.9*	122.3±2.5*	220.0±3.5*
$(2PbTe)_{0.6}(AgSbTe_2)_{0.4}$	104.3±2.0	104.2±0.9	213.7±3.4
	106.4±2.3*	105.2±2.0*	216.1±3.5*
$(2PbTe)_{0.4}(AgSbTe_2)_{0.6}$	86.3±1.6	85.4±0.9	208.2±3.5
	89.1±1.8*	86.8±1.5*	211.5±3.8*
$(2PbTe)_{0.2}(AgSbTe_2)_{0.8}$	67.3±1.1	66.0±0.7	202.2±3.0
	69.8±1.2*	67.0±0.9*	204.9±3.7*

* these values are obtained by the EMF method with solid electrolyte,⁶¹

According to this reaction, the standard Gibbs free energy of formation and the enthalpy of formation $(2PbTe)_{0.2}(AgSbTe_2)_{0.8}$ can be calculated by the relation:

$$\Delta_f Z^0[(2PbTe)_{0.2}(AgSbTe_2)_{0.8}] = 0.4\Delta \bar{Z}_{PbTe} + 0.4\Delta_f Z^0(PbTe) + 0.4\Delta_f Z^0(Ag_2Te) + 0.4\Delta_f Z^0(Sb_2Te_3) \quad (9),$$

and entropy can be calculated from the relation:

$$S^0[(2PbTe)_{0.2}(AgSbTe_2)_{0.8}] = 0.4S_{PbTe} + 0.4S^0(PbTe) + 0.4S^0(Ag_2Te) + 0.4S^0(Sb_2Te_3) \quad (10).$$

Standard integral thermodynamic functions of the formation of solid solutions with compositions $x = 0.4$; 0.6 and 0.8 were calculated by integrating the Gibbs-Duhem equation:

$$\Delta_f Z^0[(2PbTe)_x(AgSbTe_2)_{1-x}] = 2(1-x) \int_{0.2}^x \frac{\Delta \bar{Z}_{PbTe}}{(1-x)^2} dx + x\Delta_f Z^0[(2PbTe)_{0.2}(AgSbTe_2)_{0.8}] \quad (11)$$

Errors were found by the method of accumulation of errors. The first term on the right side of equation (11) was determined by integrating by means of the trapezoid method using the “Microsoft Office Excel 2010” software.

Literature data on corresponding standard integral thermodynamic functions of the Ag_2Te , $PbTe$ and Sb_2Te_3

compounds in addition to own experimental results (Table 4), were used at calculations of equations (9) and (10) (Table 6).

The values of standard enthalpies of formation and entropies for $PbTe$ and Sb_2Te_3 were taken from Ref.⁵⁸ For the Ag_2Te compound, the data of,⁵⁹ obtained by the EMF

method were used. Using the EMF method with solid Ag^+ conducting electrolyte,⁶⁰ thermodynamic data for investigated solid solutions previously were obtained in,⁶¹ and also are listed in Table 6. As can be seen, the results obtained by two modifications of the EMF method, agree within the margin of inaccuracies.

5. Conclusion

A complete description of the phase equilibria in the quasi-ternary Ag_2Te - PbTe - Sb_2Te_3 system, including 750 and 300 K isothermal sections and five isopleth sections of the phase diagram, as well as liquidus surface projection, were obtained. This system characterized by the formation of a wide continuous high-temperature solid solution (β -phase) with a cubic structure between PbTe and “ $\text{Ag}_{1-x}\text{Sb}_x\text{Te}_{2+x}$ ” intermediate phase. Below 635 K, a solid-state decomposition of the β -phase occurs and subsequently the formation of the α - and γ -phases based correspondingly on $\text{IT-Ag}_2\text{Te}$ and Sb_2Te_3 were observed.

The formation of a wide (up to 80 mol%) region of solid solutions based on PbTe along the 2PbTe -“ AgSbTe_2 ” section was confirmed by measuring EMF of the concentration chains concerning to the PbTe electrode. A new mutually agreed complex of data on standard partial thermodynamic functions of PbTe and lead, as well as integral thermodynamic functions of β -solid solutions along the above section was obtained. This data is in agreement with the results obtained earlier by the EMF method with solid Ag^+ conductive electrolyte.⁶¹

The presented results can be used for the design of new LAST alloys, which are of great interest as thermoelectric materials.

6. References

- Applications of Chalcogenides: S, Se, and Te / Ed. Ahluwalia G. K, **2016**, Cham.: Springer, 461p.
- A. V. Kolobov, J. Tominaga, Chalcogenides, **2012**, Springer.
- M. -R. Gao, Y. -F. Xu, J. Jiang, S. -H. Yu, *Chemical Society Reviews*, **2013**, 42(7), 2986. DOI:10.1007/978-3-642-28705-3
- I. Riess, *Solid State Ion.*, **2003**, 157, 1–17. DOI:10.1039/c2cs35310e
- H. Wada, M. Ishii, M. Onoda, M. Tansho, A. Sato, *Solid State Ionics*, **1996**, 86–88, 159–163. DOI:10.1016/S0167-2738(02)00182-0
- C. Gayner, K. K. Kar, *Progress in Materials Science*, **2016**, 83, 330–382. DOI:10.1016/j.pmatsci.2016.07.002
- A. V. Shevelkov, *Russ. Chem. Rev.*, **2008**, 77 (1), 1–19. DOI:10.1070/RC2008v077n01ABEH003746
- F. Tesfaye, M. Moroz, *Journal of Electronic Research and Application*, **2018**, 2 (2), 28–41. DOI:10.26689/jera.v2i2.337
- G. Tan, F. Shi, H. Sun, L. -D. Zhao, C. Uher, V. P. Dravid, M. G. Kanatzidis, *J. Mater. Chem. A*, **2014**, 2, 20849–20854. DOI:10.1039/C4TA05530F
- A. Dahshan, H. H. Hegazy, K. A. Aly, P. Sharma, *Physica B: Condensed Matter*, **2017**, 526, 117–121. DOI:10.1016/j.physb.2017.09.097
- D. Niesner, S. Otto, V. Hermann, Th. Fauster, T. V. Menshchikova, S. V. Eremeev, Z. S. Aliev, I. R. Amiraslanov, P. M. Echenique, M. B. Babanly, E. V. Chulkov, *Physical Review B*, **2014**, 89, 081404–081404–5. DOI:10.1103/PhysRevB.89.081404
- M. Papagno, S. Eremeev, J. Fujii, Z. Aliev, M. B. Babanly, S. Mahatha, I. Vobornik, N. Mam, D. Pacile, E. Chulkov, *ACS Nano*, **2016**, 10 (3), 3518–3524. DOI:10.1021/acsnano.5b07750
- T. Okuda, T. Maegawa, M. Ye, K. Shirai, T. Warashina, K. Miyamoto, K. Kuroda, M. Arita, Z. S. Aliev, I. R. Amiraslanov, M. B. Babanly, E. V. Chulkov, S. V. Eremeev, A. Kimura, H. Namatame, M. Taniguchi, *Phys. Rev. Lett. (American Phys. Soc.)*, **2013**, 111, 205803–5. DOI:10.1103/PhysRevLett.111.206803
- D. Pacile, S. V. Eremeev, M. Caputo, M. Pisarra, O. De Luca, I. Grimaldi, J. Fujii, Z. S. Aliev, M. B. Babanly, I. Vobornik, R. G. Agostino, A. Goldoni, E. V. Chulkov, M. Papagno. *Physica status solidi (RRL) – Rapid Research Letters*, **2018**, 12 (12), 1800341–8. DOI:10.1002/pssr.201800341
- I. Horichok, R. Ahiska, D. Freik, L. Nykyruy, S. Mudry, O. Matkivskiy, T. Semko, *Journal of Electronic Materials*, **2016**, 45(3), 1576–1583. DOI:10.1007/s11664-015-4122-9
- J. Liu, L. M. Peng, *Applied Mechanics and Materials*, **2014**, 456, 490–493. DOI:10.4028/www.scientific.net/AMM.456.490
- Y. Chen, B. He, T. J. Zhu, X. B. Zhao, *Journal of Physics D: Applied Physics*, **2012**, 45(11), 115302. DOI:10.1088/0022-3727/45/11/115302
- B. Kusz, T. Miruszewski, B. Bochentyn, M. Łapiński, J. Karczewski, *Journal of Electronic Materials*, **2016**, 45(2), 1085–1093. DOI:10.1007/s11664-015-4251-1
- A. Kumar, P. A. Vermeulen, B. J. Kooi, J. Rao, L. van Eijck, S. Schwarzmüller, O. Oeckler, G. R. Blake. *Inorganic Chemistry*, **2017**, 56(24), 15091–15100. DOI:10.1021/acs.inorgchem.7b02433
- M. B. Babanly, E. V. Chulkov, Z. S. Aliev, A. V. Shevel'kov, I. R. Amiraslanov, *Russ. J. Inorg. Chem.*, **2017**, 62(13), 1703–1729. DOI:10.1134/S0036023617130034
- P. Villars, A. Prince, H. Okamoto, Handbook of Ternary Alloy Phase Diagrams (10 volume set). American Technical Publishers, **1995**, 15000 p.
- G. Gottstein Physical Foundations of Material Science, Springer, **2004**, 502 p. DOI:10.1007/978-3-662-09291-0
- F. M. Mammadov, I. R. Amiraslanov, Y. A. Aliyeva, S. S. Ragimov, L. F. Mashadiyeva, M. B. Babanly, *Acta Chim. Slov.*, **2019**, 66, 1–7. DOI:10.17344/acsi.2019.4988
- S. Z. Imamaliyeva, G. I. Alakbarzade, M. A. Mahmudova, I. R. Amiraslanov, M. B. Babanly, *Acta Chim. Slov.*, **2018**, 65, 365–371. DOI:10.17344/acsi.2017.4053
- D. M. Babanly, I. I. Aliev, K. N. Babanly, Yu. A. Yusibov, *Russ. J. Inorg. Chem.*, **2011**, 56 (9), 1472–1477.

- DOI:10.1134/S0036023611090038
26. L. F. Mashadiyeva, J. O. Kevser, I. I. Aliev, Y. A. Yusibov, D. B. Taghiyev, Z. S. Aliev, M. B. Babanlı, *J. Alloys. Compd.*, **2017**, 724, 641–648. DOI:10.1016/j.jallcom.2017.06.338
27. L. F. Mashadiyeva, J. O. Kevser, I. I. Aliev, Y. A. Yusibov, D. B. Taghiyev, Z. S. Aliev, M. B. Babanlı, *Phase equilibria and diffusion*, **2017**, 38 (5), 603–614. DOI:10.1007/s11669-017-0583-2
28. L. F. Mashadiyeva, Yu. A. Yusibov, Dzh. Kevser, M. B. Babanlı, *Russ. J. Phys. Chem. A*, **2017**, 91 (9), 1642–1646. DOI:10.1134/S0036024417090187
29. T. B. Massalski (Ed.), *Binary Alloy Phase Diagrams*, second ed., ASM International, Materials Park, Ohio, **1990**, p. 3589.
30. A. Lee, A., J. L. de Boer, *Acta Cryst. C*, **1993**, 49, 1444–1446. DOI:10.1107/S0108270193003294
31. J. Schneider, H. Schulz, *Z. Kristallogr.*, **1993**, 203, 1–15. DOI:10.1524/zkri.1993.203.Part-1.1
32. A. J. Frueh, *Am. Mineral.*, **1961**, 46, p. 654–660.
33. P. B. Pereira, I. Sergueev, S. Gorsse, J. Dadda, E. Müller, R. P. Hermann, *Physica Status Solidi (b)*, **2012**, 250(7), 1300–1307. DOI:10.1002/pssb.201248412
34. T. L. Anderson, H. B. Krause, *Acta Crystallogr. B*, **1974**, 30, 1307–1310. DOI:10.1107/S0567740874004729
35. F. Wald, *J. Less Common. Met.*, **1967**, 13 (6), 579–590. DOI:10.1016/0022-5088(67)90103-8
36. R. Blachnik, B. Gather, *J. Less Common. Met.*, **1978**, 60 (1), 25–32. DOI:10.1016/0022-5088(78)90086-3
37. K. Bergum, T. Ikeda, G. Jeffrey-Snyder, *Journal of Solid State Chemistry*, **2011**, 184(9), p. 2543–2552. DOI:10.1016/j.jssc.2011.07.012
38. G. Petzow, G. Effenberg: „Ternary Alloys”, Wiley-VCH Verlag, Weinheim, **1988**, 2, p. 554
39. R. M. Marin-Ayral, B. Legendre, G. Brun, B. Liautard, J. C. Tedenac, *Thermochimica Acta*, **1988**, 131, 37–45. DOI:10.1016/0040-6031(88)80055-8
40. S. Geller, J. H. Wernick, *Acta Crystallogr.*, **1959**, 12, 46. DOI:10.1107/S0365110X59000135
41. H. J. Wu, S. W. Chen, *Acta Mater.*, **2011**, 59, 6463–6472. DOI:10.1016/j.actamat.2011.07.010
42. P. M. Wyzga, K. T. Wojciechowski, *J. Electron. Mater.*, **2016**, 45, 1548–1554. DOI:10.1007/s11664-015-4102-0
43. K. T. Wojciechowski, M. Schmidt, *Phys. Rev. B*, **2009**, 79, 184202–7. DOI:10.1103/PhysRevB.79.184202
44. B. Du, Y. Yan, X. Tang, *J. Electron. Mater.*, **2015**, 44, 2118–2123. DOI:10.1007/s11664-015-3682-z
45. M. Aspiala, P. Taskinen, *J. Chem. Thermodyn.* **2016**, 93, 261–266. DOI:10.1016/j.jct.2015.08.025
46. P. Wyzga, I. Veremchuk, U. Burkhardt, P. Simon, Y. Grin, K. Wojciechowski, *Applied Sciences*, **2018**, 8(1), 52–70. DOI:10.3390/app8010052
47. H. Matsushita, E. Hagiwara, A. Katsui, *Journal of Materials Science*, **2004**, 39(20), 6299–6301. DOI:10.1023/B:JMSC.0000043599.86325.ba
48. N. K. Abrikosov, E. L. Elagina, M. A. Popova, *Inorg. Mater.*, **1965**, 1, 1944–1946.
49. L. E. Shelimova, O. G. Karpinskii, T. E. Svechnikova, E. S. Avilov, M. A. Kretova, V. S. Zemskov, *Inorganic Materials*, **2004**, 40(12), 1264–1270. DOI:10.1007/s10789-005-0007-2
50. T. Ikeda, S. M. Haile, V. A. Ravi, H. Azizgolshani, F. Gascoin, G. J. Snyder, *Acta Mater.*, **2007**, 55, 1227–1239. DOI:10.1016/j.actamat.2006.09.036
51. T. Ikeda, J. Snyder, *MRS Proceedings*, **2010**, 1267–5. DOI:10.1557/PROC-1267-DD06-07
52. A. G. Morachevskiy, G. F. Voronin, V. A. Geyderikh, I. B. Kutsenok, *Electrochemical research methods in the thermodynamics of metal systems*, “Akademkniga”, **2003**, 334 p. (In Russian)
53. S. Z. Imamaliyeva, S. S. Musayeva, D. M. Babanlı, Y. I. Jafarov, D. B. Taghiyev, M. B. Babanlı, *Thermochimica Acta*, **2019**, 679, 178319–7. DOI:10.1016/j.tca.2019.178319
54. D. M. Babanlı, L. F. Mashadiyeva, M. B. Babanlı, *Inorganic Materials*, **2017**, 53(5), 519–524. DOI:10.1134/S002016851705003X
55. M. Rozman, U. Bren, M. Lukšič, R. F. Godec, G. Bokias, A. N. Kalarakis, E. Stathatos, *Electrochimica Acta*, **2018**, 283, 1105–1114. DOI:10.1016/j.electacta.2018.07.052
56. S. Z. Imamaliyeva, D. M. Babanlı, T. M. Gasanly, D. B. Tagiev, M. B. Babanlı. *Russian Journal of Physical Chemistry A*, **2018**, 92(11), 2111–2117. DOI:10.1134/S0036024418110158
57. R. D. Shannon, *Revised Effective Ionic Radii and Systematic Studies of Interatomic Distances in Halides and Chalcogenides*, *Acta Crystallographica*, **1976**, A32, p. 751–767 (Digital version: Database of Ionic Radii; DOI:10.1107/S0567739476001551
58. Data base of thermal constants of substances (Digital version, In: Yorish V. S., Yungman V. S. (Ed.), **2006**, <http://www.chem.msu.ru/cgi-bin/tkv>).
59. M. V. Voronin, E. G. Osadchii, E. A. Brichkina, *Physics and Chemistry of Minerals*, **2017**, 44(9), 639–653. DOI:10.1007/s00269-017-0889-y
60. L. F. Mashadiyeva, Sh. G. Mansimova, Yu. A. Yusibov, M. B. Babanlı, *Russian Journal of Electrochemistry*, **2018**, 54 (1), 106–111. DOI:10.1134/S102319351711009X
61. M. B. Babanlı, Y. A. Yusibov, N. B. Babanlı, *The EMF method with solid-state electrolyte in the thermodynamic investigation of ternary Copper and Silver Chalcogenides. Electromotive force and measurement in several systems.* / Ed. Kara S. InTech. Org. 2011. P. 57. DOI:10.5772/28934

Povzetek

Raziskovali smo fazna ravnotežja v sistemu $\text{Ag}_2\text{Te-PbTe-Sb}_2\text{Te}_3$ z metodami diferencialne termične analize, praškovne rentgenske difrakcije in meritvami elektromotorne sile (EMF). Konstruirali smo površinsko projekcijo sistema, izotermalne odseke pri 750 K in 300 K, ter pet vertikalnih odsekov faznega diagram. Določili smo primarna kristalizacijska področja in območja homogenosti faz. Identificirali smo vrsto in temperature različnih nevariantnih in monovariantnih ravnotežij. Značilnost preučevanega sistema je nastanek širokega zveznega pasu visokotemperaturne kubične trdne raztopine (β -faza) med PbTe in $\text{Ag}_{1-x}\text{Sb}_{1+x}\text{Te}_{2+x}$. Na osnovi rezultatov meritev EMF smo izračunali parcialne molarne termodinamske funkcije svinčevega telurida v zlitinah in standardne integralne termodinamske funkcije β -trdnih raztopin vzdolž odseka 2PbTe-AgSbTe_2 .



Except when otherwise noted, articles in this journal are published under the terms and conditions of the Creative Commons Attribution 4.0 International License

Scientific paper

Study on the Synthesis and Biological Activities of *N*-Alkylated Deoxynojirimycin Derivatives with a Terminal Tertiary Amine

Lin Wang and Zhijie Fang*

School of Chemical Engineering, Nanjing University of Science & Technology, Nanjing 210094, Jiangsu, P.R. China

* Corresponding author: E-mail: zjfang@njust.edu.cn

Tel: +86-25-84303232; fax: +86-25-84315520

Received: 12-14-2019

Abstract

A series of *N*-alkylated deoxynojirimycin (DNJ) derivatives connected to a terminal tertiary amine at the alkyl chains of various lengths were prepared. These novel synthetic compounds were assessed for preliminary glucosidase inhibition and anticancer activities *in vitro*. Potent and selective inhibition was observed among them. Compound **7d** ($IC_{50} = 0.052$ mM) showed improved and selective inhibitory activity against β -glucosidase compared to DNJ ($IC_{50} = 0.65$ mM). In addition, analysis of the kinetics of enzyme inhibition by using Lineweaver–Burk plots indicated that **7d** inhibited β -glucosidase in a competitive manner, suggesting that **7d** was expected to bind to the active site of β -glucosidase. Compounds **8b** and **8c** were found to be moderate and selective inhibitors of α -glucosidase. Nevertheless, none of compounds inhibited the growth of B16F10 melanoma cells.

Keywords: biological activities; glucosidase; 1-deoxynojirimycin; selective inhibition

1. Introduction

Glucosidases are enzymes which catalyze the hydrolysis of glycosidic bonds in oligosaccharides or glycoconjugates, playing a vital role in the digestion of carbohydrates and in the processing of glycoproteins and glycolipids.¹ Glucosidases are also involved in carbohydrate-mediated diseases such as diabetes,² tumor metastasis,³ viral infections,⁴ and lysosomal storage diseases.⁵ Inhibitors of α -glucosidase can significantly decrease postprandial blood glucose levels⁶ and promote glycoprotein misfolding in the endoplasmic reticulum (ER).⁷ In mammals, β -glucosidase enables hydrolysis of glucosylceramide into ceramide and glucose, which is in part performed by β -glucocerebrosidases (GBA1 or GCase)⁸ and GBA2.⁹ Gaucher disease, the most common lysosomal storage disease, is caused by mutations in the β -glucocerebrosidase (GBA1) gene. Inhibitors of β -glucosidase could reduce the biosynthesis of glycolipids to balance the deficient activity of β -Gcase.¹⁰ In tumor cells, oligosaccharides on the surface of tumor cells play an important role in expression of the malignant phenotype and the metastatic spread of tumor cells. The synthesis of these oligosaccharides in endoplasmic reticulum and Golgi is dependent on

carbohydrate processing enzymes such as glucosidases. Therefore, specific glucosidase inhibitors may be candidates for cancer chemotherapy.^{11,12}

Among the families of glucosidase inhibitors reported so far, iminosugars are particularly notable. They are carbohydrate mimetics where the endocyclic oxygen has been replaced by a nitrogen atom.^{13–15} Their structures can mimic transition-state analogues of glucosidases, which interact with two carboxylic acid units to form strong ions and catalyze the cleavage of the glycoside bonds.¹ Their most famous representative is the naturally occurring 1-deoxynojirimycin **1**.² Some *N*-alkylated DNJ derivatives, like *N*-hydroxyethyl-DNJ¹⁶ **2** (miglitol, an intestinal α -glucosidase inhibitor), and *N*-butyl-DNJ¹⁷ **3** (miglustat, a glucosylceramide synthase inhibitor) have been approved for the treatment of diabetes-type 2 and Gaucher disease, respectively. Compound **6**³ not only inhibited α -glucosidase (*Bacillus stearothermophilus*), BAEC growth and migration, but also suppressed the growth of A549 cells (Figure 1). Nevertheless, despite extensive synthesis and investigations of highly bioactive iminosugars, a remaining drawback is their limited selectivity on glucosidases, and this leads to some side effects when applied therapeutically. For example, *N*-butyl-DNJ **3** (Figure 1) can inhibit some other

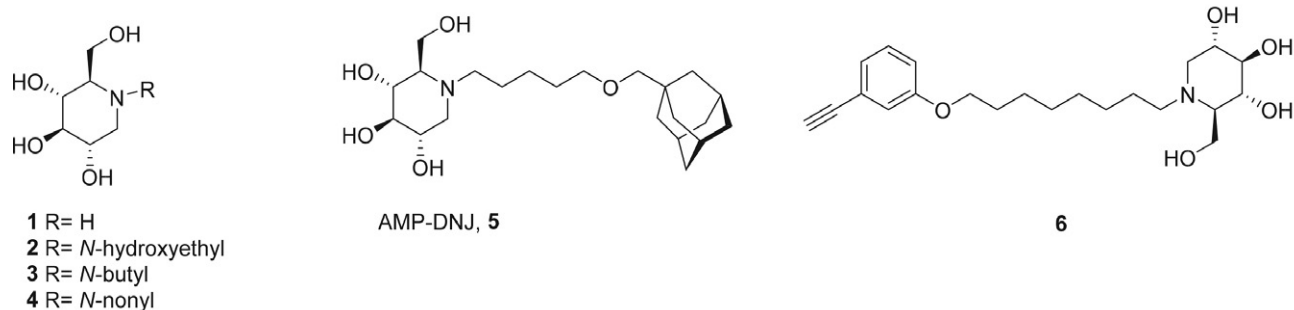


Figure 1. Known potent glycosidase inhibitors derived from 1-deoxynojirimycin.

enzymes nonrelated to lysosomal storage disease, such as sucrase, maltase, α -glucosidase I and II.¹⁸ Obviously, improving the selectivity of iminosugars as glycosidase inhibitors is a challenging goal.

Modification or variation of a known iminosugar inhibitor, especially a natural product, is a feasible strategy to obtain more selective and stronger inhibitors. Generally, there are two main strategies for modification of iminosugars: introduction of different alkyl groups on the amino group and alterations of the ring hydroxyl residues.¹⁹ It has been demonstrated that the potency of DNJ derivatives could be increased by introducing a hydrophobic group on the nitrogen atom of DNJ using a heteroatom linker and a carbon chain spacer. Moreover, lengthening of the alkyl chain and an increase in the size of the hydrophobic group would be also beneficial for the glucosidase inhibition. These types of modifications can be seen in the design of compounds **4**,²⁰ **5**²¹ and **6** (Figure 1).³

Our group had done some work on the modification of DNJ, such as the synthesis of C-6 deuterio DNJ, a potent α -glucosidase and the optimization of DNJ synthetic route.^{22,23} And as a part of our ongoing program devoted to the development of new glucosidase inhibitors, we embarked on a strategy starting from DNJ as the lead compound. The key DNJ scaffold was connected to a terminal tertiary amine through introduction of alkyl chains of various length. And the introduction of a nitrogen atom may lead to a polarization different from that of oxygen atom.^{24,25} The work reported herein describes the synthesis and biological evaluation of a small library of DNJ derivatives in which the length of the alkyl chain and the size and nature of the terminal tertiary amine substituents have been studied.

2. Experimental

2.1. Materials and Methods

All reagents and solvents were purchased from commercial suppliers and used without further purification. Reactions progression was monitored by Thin Layer Chromatography (TLC) using silica gel GF₂₅₄ plates (0.2 mm thickness), spots were detected under UV-light ($\lambda =$

254 nm). Visualization of the deprotected iminosugar was accomplished by exposure to iodine vapour. Flash column chromatography was carried out by silica gel (200–300 mesh). NMR spectra were recorded on Bruker Avance III 500 MHz spectrometer using CDCl₃ or D₂O as solvents. Chemical shifts are reported in ppm. High resolution mass spectra (HRMS) were recorded by direct injection on a mass spectrometer (Thermo Scientific LTQ Orbitrap XL) equipped with an electrospray ion source in positive mode. The following abbreviations have been used to describe the signal multiplicity: br (broad), s (singlet), d (doublet), t (triplet), q (quartet), h (hexet), m (multiplet), dd (doublet of doublets), dt (doublet of triplets).

General Procedure A

Nucleophilic substitution on a nitrogen atom. The starting material (1 mM) was mixed with *N*-bromophthalimide (2 mM) and K₂CO₃ (3 mM) in DMF (10 mL). The mixture was heated at 100 °C for 24 h. After cooling, the mixture was poured into water and extracted into ethyl acetate. The organic layer was dried over Na₂SO₄ and concentrated. The residue was purified by flash column chromatography (10:1→3:1; PE:ethyl acetate).

General Procedure B

Hydrazinolysis. The starting material (1 mM) was mixed with 80% hydrazine hydrate (0.13 mL, 2 mM) in EtOH (10 mL). The mixture was heated under reflux for 3 h. After cooling, the solid was removed by filtration. The filtrate was concentrated and the residue was purified by flash column chromatography (20:1:0.2→20:2:0.2; ethyl acetate: MeOH:NH₄OH).

General Procedure C

Reductive amination. The starting material (1 mM) was mixed with formaldehyde (178.38 mg, 37% aqueous solution, 0.22 mL, 2.2 mmol) and formic acid (0.19 mL, 5.0 mmol). The mixture was heated at 105 °C for 3 h. After cooling, the mixture was poured into water and extracted into ethyl acetate. The organic layer was washed with saturated NaHCO₃ solution, dried and concentrated. The residue was purified by flash column chromatography (20:1:0.2→20:2:0.2; ethyl acetate: MeOH:NH₄OH).

General Procedure D

Double nucleophilic substitution. The starting material (1 mM) was mixed with alkyl dibromide (2 mM) and K_2CO_3 (3 mM) in CH_3CN (10 mL). The mixture was heated at 80 °C for 12 h. After cooling, the solution was concentrated. The residue was purified by flash column chromatography (20:1:0.2→20:2:0.2; ethyl acetate: MeOH: NH_4OH).

General Procedure E

Catalytic hydrogenolysis. To a solution of the benzylated intermediate (1 mmol) in EtOH was added Pd (10%)/C (100 mg) and the mixture stirred under an atmosphere of hydrogen at room temperature for 24 h. The catalyst was filtered off, the solvents removed under reduced pressure and the residue purified by flash column chromatography (8:2:0.1→6:4:0.1; n-propanol: H_2O : NH_4OH).

2-(2-((2R,3R,4R,5S)-3,4,5-Tris(benzyloxy)-2-((benzyloxy)methyl)piperidin-1-yl)ethyl)isoindoline-1,3-dione (10a)

Prepared according to procedure A. Compound **9** (2 g, 3.8 mmol), *N*-(4-bromoethyl)phthalimide (2.1 g, 7.6 mmol), K_2CO_3 (1.6 g, 11.4 mmol), DMF (40 mL). Yield: 87% (2.4 g), colourless syrup, R_f = 0.45 (3:1, PE:ethyl acetate). 1H NMR (500 MHz, $CDCl_3$): δ 7.76 (dd, J = 5.4, 3.0 Hz, 2H, ArH), 7.65 (dd, J = 5.4, 3.0 Hz, 2H, ArH), 7.46–7.00 (m, 20H, ArH), 4.95 (d, J = 10.9 Hz, 1H, $PhCH_2$), 4.77 (ddd, J = 22.9, 15.6, 11.3 Hz, 4H, $PhCH_2$), 4.46 (d, J = 12.1 Hz, 1H, $PhCH_2$), 4.32 (dd, J = 26.1, 11.4 Hz, 2H, $PhCH_2$), 3.94 (dt, J = 13.9, 8.0 Hz, 1H, H-8a), 3.78–3.56 (m, 4H, H-6, H-8b, H-2), 3.51–3.43 (m, 2H, H-3, H-4), 3.41 (dd, J = 11.0, 4.8 Hz, 1H, H-1a), 3.23 (dt, J = 13.7, 8.2 Hz, 1H, H-7a), 2.65 (ddd, J = 13.3, 7.2, 3.4 Hz, 1H, H-7b), 2.42 (d, J = 8.8 Hz, 1H, H-5), 2.26 (t, J = 10.7 Hz, 1H, H-1b). ^{13}C NMR (126 MHz, $CDCl_3$): δ 168.35, 138.97, 138.71, 138.52, 138.07, 133.81, 132.17, 128.43, 128.37, 128.33, 128.01, 127.97, 127.94, 127.84, 127.64, 127.53, 123.16, 87.20, 78.69, 78.57, 77.33, 77.08, 76.83, 75.49, 75.20, 73.10, 72.66, 66.07, 64.50, 54.25, 49.24, 34.56.

2-(4-((2R,3R,4R,5S)-3,4,5-Tris(benzyloxy)-2-((benzyloxy)methyl)piperidin-1-yl)butyl)isoindoline-1,3-dione (10b)

Prepared according to procedure A. Compound **9** (2 g, 3.8 mmol), *N*-(4-bromobutyl)phthalimide (1.9 g, 7.6 mmol), K_2CO_3 (1.6 g, 11.4 mmol), DMF (40 mL). Yield: 85% (2.3 g), colourless syrup, R_f = 0.33 (3:1, PE:ethyl acetate). 1H NMR (500 MHz, $CDCl_3$): δ 7.83 (dt, J = 7.4, 3.7 Hz, 2H, ArH), 7.75–7.63 (m, 2H, ArH), 7.42–7.16 (m, 18H, ArH), 7.11 (d, J = 6.4 Hz, 2H, ArH), 4.95 (d, J = 11.1 Hz, 1H, $PhCH_2$), 4.86 (d, J = 10.8 Hz, 1H, $PhCH_2$), 4.80 (d, J = 11.1 Hz, 1H, $PhCH_2$), 4.72–4.60 (m, 2H, $PhCH_2$), 4.46 (s, 2H, $PhCH_2$), 4.39 (d, J = 10.8 Hz, 1H, $PhCH_2$), 3.63 (dt, J = 11.0, 5.9 Hz, 4H, H-6, H-2, H-10a), 3.56 (t, J = 9.4 Hz, 2H, H-10b, H-3), 3.45 (t, J = 9.1 Hz, 1H, H-4), 3.08 (dd, J = 11.1, 4.8 Hz, 1H, H-1a), 2.72 (m, 1H, H-7a), 2.63–2.50 (m,

1H, H-7b), 2.29 (d, J = 9.5 Hz, 1H, H-5), 2.18 (t, J = 10.8 Hz, 1H, H-1b), 1.65–1.33 (m, 4H, H-8, H-9). ^{13}C NMR (126 MHz, $CDCl_3$): δ 168.44, 139.07, 138.57, 137.80, 133.98, 132.17, 128.53, 128.44, 128.37, 127.92, 127.70, 127.58, 127.48, 123.27, 87.35, 78.61, 78.49, 77.38, 77.12, 76.87, 75.36, 75.23, 73.43, 72.79, 65.43, 63.88, 54.40, 51.76, 37.81, 26.56, 21.43.

2-((2R,3R,4R,5S)-3,4,5-Tris(benzyloxy)-2-((benzyloxy)methyl)piperidin-1-yl)ethan-1-amine (11a)

Prepared according to procedure B. Compound **10a** (1.3 g, 1.86 mmol), 80% hydrazine hydrate (0.23 mL, 3.72 mM), EtOH (10 mL). Yield: 82% (0.87 g), colourless syrup, R_f = 0.43 (20:2:0.2; ethyl acetate:MeOH: NH_4OH). 1H NMR (500 MHz, $CDCl_3$): δ 7.46–7.18 (m, 18H, ArH), 7.18–7.04 (m, 2H, ArH), 4.95 (d, J = 11.0 Hz, 1H, $PhCH_2$), 4.87 (d, J = 10.8 Hz, 1H, $PhCH_2$), 4.81 (d, J = 11.0 Hz, 1H, $PhCH_2$), 4.67 (q, J = 11.6 Hz, 2H, $PhCH_2$), 4.50 (d, J = 12.0 Hz, 1H, $PhCH_2$), 4.42 (dd, J = 11.4, 4.6 Hz, 2H, $PhCH_2$), 3.77–3.44 (m, 5H, H-6, H-2, H-3, H-4), 3.11 (dd, J = 11.4, 4.8 Hz, 1H, H-1a), 2.90–2.79 (m, 1H, H-7a), 2.79–2.64 (m, 2H, H-7b, H-8a), 2.55–2.42 (m, 1H, H-8b), 2.42–2.24 (m, 3H, H-5, NH_2), 2.20 (t, J = 10.9 Hz, 1H, H-1b). ^{13}C NMR (126 MHz, $CDCl_3$): δ 138.99, 138.53, 137.80, 128.52, 128.50, 128.43, 128.39, 127.98, 127.93, 127.79, 127.67, 127.57, 87.19, 78.55, 78.39, 77.46, 77.20, 76.95, 75.40, 75.26, 73.34, 72.92, 66.20, 64.83, 54.89, 54.27, 38.43.

4-((2R,3R,4R,5S)-3,4,5-Tris(benzyloxy)-2-((benzyloxy)methyl)piperidin-1-yl)butan-1-amine (11b)

Prepared according to procedure B. Compound **10b** (1.2 g, 1.66 mmol), 80% hydrazine hydrate (0.21 mL, 3.31 mM), EtOH (10 mL). Yield: 85% (0.84 g), colourless syrup, R_f = 0.35 (20:2:0.2; ethyl acetate:MeOH: NH_4OH). 1H NMR (500 MHz, $CDCl_3$): δ 7.39–7.18 (m, 18H, ArH), 7.18–7.06 (m, 2H, ArH), 4.95 (d, J = 11.1 Hz, 1H, $PhCH_2$), 4.87 (d, J = 10.9 Hz, 1H, $PhCH_2$), 4.80 (d, J = 11.1 Hz, 1H, $PhCH_2$), 4.67 (q, J = 11.6 Hz, 2H, $PhCH_2$), 4.53–4.37 (m, 3H, $PhCH_2$), 3.66 (dt, J = 8.7, 5.5 Hz, 2H, H-6), 3.62–3.51 (m, 2H, H-3, H-2), 3.47 (t, J = 9.0 Hz, 1H, H-4), 3.08 (dd, J = 11.2, 4.8 Hz, 1H, H-1a), 2.77–2.43 (m, 6H, H-7, H-10, NH_2), 2.32 (d, J = 9.4 Hz, 1H, H-5), 2.21 (t, J = 10.8 Hz, 1H, H-1b), 1.37 (m, 4H, H-8, H-9). ^{13}C NMR (126 MHz, $CDCl_3$): δ 138.10, 137.67, 136.86, 127.48, 127.42, 126.94, 126.73, 126.63, 126.54, 86.23, 77.61, 77.54, 76.60, 76.35, 76.09, 74.35, 74.21, 72.52, 71.83, 64.59, 62.99, 53.44, 51.27, 40.79, 30.07, 20.50.

N,N-Dimethyl-2-((2R,3R,4R,5S)-3,4,5-tris(benzyloxy)-2-((benzyloxy)methyl)piperidin-1-yl)ethan-1-amine (12a)

Prepared according to procedure C. Compound **11a** (0.3 g, 0.53 mmol), formaldehyde (37% aqueous solution, 0.12 mL, 1.17 mmol) and formic acid (0.1 mL, 2.65 mmol). Yield: 83% (0.26 g), yellow syrup, R_f = 0.83(20:2:0.2; ethyl acetate:MeOH: NH_4OH). 1H NMR (500 MHz, $CDCl_3$): δ 7.28 (m, 18H, ArH), 7.12 (d, J = 6.4 Hz, 2H, ArH), 4.95 (d,

$J = 11.1$ Hz, 1H, PhCH₂), 4.87 (d, $J = 10.8$ Hz, 1H, PhCH₂), 4.81 (d, $J = 11.1$ Hz, 1H, PhCH₂), 4.67 (q, $J = 11.6$ Hz, 2H, PhCH₂), 4.47 (s, 2H, PhCH₂), 4.40 (d, $J = 10.8$ Hz, 1H, PhCH₂), 3.74–3.54 (m, 4H, H-6, H-2, H-3), 3.46 (t, $J = 9.1$ Hz, 1H, H-4), 3.12 (dd, $J = 11.2$, 4.8 Hz, 1H, H-1a), 2.93–2.80 (m, 1H, H-7a), 2.80–2.66 (m, 1H, H-7b), 2.47–2.33 (m, 2H, H-5, H-8a), 2.29 (td, $J = 11.2$, 7.2 Hz, 2H, H-1b, H-8b), 2.16 (s, 6H, 2×CH₃). ¹³C NMR (126 MHz, CDCl₃): δ 139.05, 138.58, 137.78, 128.56, 128.48, 128.46, 128.39, 127.95, 127.93, 127.91, 127.73, 127.61, 127.52, 87.36, 78.51, 78.42, 77.39, 77.14, 76.89, 75.38, 75.24, 73.56, 72.86, 65.66, 64.07, 55.05, 54.68, 50.21, 45.91.

***N,N*-Dimethyl-4-((2*R*,3*R*,4*R*,5*S*)-3,4,5-tris(benzyloxy)-2-((benzyloxy)methyl)piperidin-1-yl)butan-1-amine (13a)**

Prepared according to procedure C. Compound **11b** (0.17 g, 0.29 mmol), formaldehyde (37% aqueous solution, 64 μL, 0.64 mmol) and formic acid (55 μL, 1.45 mmol). Yield: 90% (0.16 g), yellow syrup, $R_f = 0.75$ (20:2:0.2; ethyl acetate:MeOH:NH₄OH). ¹H NMR (500 MHz, CDCl₃): δ 7.45–7.19 (m, 18H, ArH), 7.19–7.05 (m, 2H, ArH), 4.95 (d, $J = 11.1$ Hz, 1H, PhCH₂), 4.88 (d, $J = 10.9$ Hz, 1H, PhCH₂), 4.81 (d, $J = 11.1$ Hz, 1H, PhCH₂), 4.67 (q, $J = 11.6$ Hz, 2H, PhCH₂), 4.45 (dt, $J = 10.9$, 9.9 Hz, 3H, PhCH₂), 3.72–3.61 (m, 2H, H-6), 3.57 (dt, $J = 9.8$, 5.6 Hz, 2H, H-2, H-3), 3.45 (t, $J = 9.1$ Hz, 1H, H-4), 3.08 (dd, $J = 11.2$, 4.9 Hz, 1H, H-1a), 2.68 (m, 1H, H-7a), 2.63–2.52 (m, 1H, H-7b), 2.37–2.09 (m, 10H, H-5, H-1a, H-10, 2 × CH₃), 1.54–1.20 (m, 4H, H-8, H-9). ¹³C NMR (126 MHz, CDCl₃): δ 138.09, 137.64, 136.89, 127.43, 126.89, 126.67, 126.56, 126.47, 86.41, 77.70, 77.63, 76.36, 76.10, 75.85, 74.36, 74.21, 72.48, 71.78, 64.61, 62.83, 58.56, 53.47, 51.23, 44.35, 24.49, 20.72.

(2*R*,3*R*,4*R*,5*S*)-3,4,5-Tris(benzyloxy)-2-((benzyloxy)methyl)-1-(2-(pyrrolidin-1-yl)ethyl)piperidine (12b)

Prepared according to procedure D. Compound **11a** (0.3 g, 0.53 mmol), 1,4-dibromobutane (127 μL, 1.06 mmol), K₂CO₃ (0.22 g, 1.59 mmol), CH₃CN (5 mL). Yield: 84% (276 mg), yellow syrup, $R_f = 0.55$ (20:2:0.2; ethyl acetate:MeOH:NH₄OH). ¹H NMR (500 MHz, CDCl₃): δ 7.45–7.21 (m, 18H, ArH), 7.18 (d, $J = 6.7$ Hz, 2H, ArH), 4.95 (d, $J = 10.9$ Hz, 1H, PhCH₂), 4.90 (d, $J = 10.8$ Hz, 1H, PhCH₂), 4.81 (d, $J = 11.0$ Hz, 1H, PhCH₂), 4.69 (d, $J = 1.5$ Hz, 2H, PhCH₂), 4.48 (dt, $J = 18.5$, 11.5 Hz, 3H, PhCH₂), 3.74 (qd, $J = 10.9$, 2.4 Hz, 2H, H-6), 3.59 (m, 2H, H-2, H-3), 3.50 (t, $J = 8.8$ Hz, 1H, H-4), 3.27–3.10 (m, 2H, H-1a, H-8a), 2.86 (m, 7H, H-7, H-8b, H-9, H-12), 2.39 (d, $J = 9.1$ Hz, 1H, H-5), 2.26 (t, $J = 10.8$ Hz, 1H, H-1b), 1.83–1.60 (m, 4H, H-10, H-11). ¹³C NMR (126 MHz, CDCl₃): δ 138.84, 138.46, 138.40, 137.76, 128.58, 128.52, 128.48, 128.45, 128.11, 128.02, 127.96, 127.93, 127.79, 127.76, 127.64, 86.59, 78.35, 78.02, 77.55, 77.30, 77.04, 75.40, 75.30, 73.40, 72.79, 66.28, 64.64, 55.05, 54.36, 51.99, 49.58, 23.15.

(2*R*,3*R*,4*R*,5*S*)-3,4,5-Tris(benzyloxy)-2-((benzyloxy)methyl)-1-(2-(piperidin-1-yl)ethyl)piperidine (12c)

Prepared according to procedure D. Compound **11a** (0.3 g, 0.53 mmol), 1,4-dibromopentane (143 μL, 1.06 mmol), K₂CO₃ (0.22 g, 1.59 mmol), CH₃CN (5 mL). Yield: 80% (269 mg), yellow syrup, $R_f = 0.64$ (20:2:0.2; ethyl acetate:MeOH:NH₄OH). ¹H NMR (500 MHz, CDCl₃): δ 7.42–7.19 (m, 18H, ArH), 7.14 (d, $J = 6.4$ Hz, 2H, ArH), 4.95 (d, $J = 11.1$ Hz, 1H, PhCH₂), 4.88 (d, $J = 10.8$ Hz, 1H, PhCH₂), 4.81 (d, $J = 11.1$ Hz, 1H, PhCH₂), 4.66 (q, $J = 11.6$ Hz, 2H, PhCH₂), 4.50 (d, $J = 12.1$ Hz, 1H, PhCH₂), 4.43 (d, $J = 11.4$ Hz, 2H, PhCH₂), 3.75–3.52 (m, 4H, H-6, H-2, H-3), 3.46 (t, $J = 9.1$ Hz, 1H, H-4), 3.12 (dd, $J = 11.2$, 4.8 Hz, 1H, H-1a), 2.96–2.84 (m, 1H, H-7a), 2.84–2.70 (m, 1H, H-7b), 2.53–2.21 (m, 8H, H-8, H-9, H-13, H-5, H-1b), 1.58–1.46 (m, 4H, H-10, H-12), 1.39 (m, 2H, H-11). ¹³C NMR (126 MHz, CDCl₃): δ 139.07, 138.59, 137.81, 128.59, 128.45, 128.40, 128.37, 127.92, 127.72, 127.61, 127.50, 87.31, 78.55, 78.42, 77.38, 77.13, 76.88, 75.36, 75.26, 73.54, 72.82, 65.52, 64.02, 55.02, 54.96, 54.19, 49.10, 25.75, 24.17.

4-((2*R*,3*R*,4*R*,5*S*)-3,4,5-Tris(benzyloxy)-2-((benzyloxy)methyl)piperidin-1-yl)ethyl)morpholine (12d)

Prepared according to procedure D. Compound **11a** (0.3 g, 0.53 mmol), 2-bromoethyl ether (137 μL, 1.06 mmol), K₂CO₃ (0.22 g, 1.59 mmol), CH₃CN (5 mL). Yield: 85% (287 mg), colourless syrup, $R_f = 0.73$ (20:2:0.2; ethyl acetate:MeOH:NH₄OH). ¹H NMR (500 MHz, CDCl₃): δ 7.40–7.21 (m, 18H, ArH), 7.21–7.10 (m, 2H, ArH), 4.96 (d, $J = 11.1$ Hz, 1H, PhCH₂), 4.89 (d, $J = 10.9$ Hz, 1H, PhCH₂), 4.82 (d, $J = 11.1$ Hz, 1H, PhCH₂), 4.66 (dd, $J = 27.2$, 11.6 Hz, 2H, PhCH₂), 4.52 (d, $J = 12.1$ Hz, 1H, PhCH₂), 4.45 (d, $J = 10.9$ Hz, 1H, PhCH₂), 4.38 (d, $J = 12.1$ Hz, 1H, PhCH₂), 3.72–3.52 (m, 8H, H-6, H-2, H-3, H-10, H-11), 3.46 (t, $J = 9.1$ Hz, 1H, H-4), 3.10 (dd, $J = 11.2$, 4.8 Hz, 1H, H-1a), 2.84 (m, 1H, H-7a), 2.78–2.67 (m, 1H, H-7b), 2.49–2.20 (m, 8H, H-5, H-1b, H-8, H-9, H-12). ¹³C NMR (126 MHz, CDCl₃): δ 139.03, 138.56, 137.74, 128.65, 128.47, 128.43, 128.39, 127.97, 127.93, 127.75, 127.67, 127.54, 87.33, 78.54, 78.42, 77.43, 77.17, 76.92, 75.40, 75.30, 73.53, 72.88, 66.93, 65.46, 63.89, 55.04, 54.03, 48.86.

(2*R*,3*R*,4*R*,5*S*)-3,4,5-Tris(benzyloxy)-2-((benzyloxy)methyl)-1-(4-(pyrrolidin-1-yl)butyl)piperidine (13b)

Prepared according to procedure D. Compound **11b** (0.3 g, 0.5 mmol), 1,4-dibromobutane (120 μL, 1 mmol), K₂CO₃ (0.21 g, 1.5 mmol), CH₃CN (5 mL). Yield: 81% (265 mg), pale yellow syrup, $R_f = 0.49$ (20:2:0.2; ethyl acetate:MeOH:NH₄OH). ¹H NMR (500 MHz, CDCl₃): δ 7.39–7.19 (m, 18H, ArH), 7.15 (d, $J = 6.6$ Hz, 2H, ArH), 4.96 (d, $J = 11.0$ Hz, 1H, PhCH₂), 4.89 (d, $J = 10.8$ Hz, 1H, PhCH₂), 4.81 (d, $J = 11.0$ Hz, 1H, PhCH₂), 4.67 (q, $J = 11.6$ Hz, 2H, PhCH₂), 4.52–4.39 (m, 3H, PhCH₂), 3.73–3.52 (m, 4H, H-6, H-2, H-3), 3.47 (t, $J = 9.0$ Hz, 1H, H-4), 3.07 (dd, $J = 11.2$, 4.8 Hz, 1H, H-1a), 2.78–2.43 (m, 8H, H-7, H-10, H-11, H-14), 2.30 (d, $J = 9.5$ Hz, 1H, H-5), 2.18 (t, $J = 10.8$

Hz, 1H, H-1b), 1.83 (m, 4H, H-12, H-13), 1.60–1.34 (m, 4H, H-8, H-9). ^{13}C NMR (126 MHz, CDCl_3): δ 138.99, 138.55, 137.91, 128.45, 128.38, 127.95, 127.92, 127.89, 127.73, 127.61, 127.53, 87.35, 78.67, 78.53, 77.34, 77.08, 76.83, 75.42, 75.24, 73.47, 72.80, 65.71, 64.01, 55.98, 54.33, 53.96, 51.75, 29.36, 25.92, 23.37, 21.91.

(2R,3R,4R,5S)-3,4,5-Tris(benzyloxy)-2-((benzyloxy)methyl)-1-(4-(piperidin-1-yl)butyl)piperidine (13c)

Prepared according to procedure D. Compound **11b** (0.3 g, 0.5 mmol), 1,4-dibromopentane (135 μL , 1 mmol), K_2CO_3 (0.21 g, 1.5 mmol), CH_3CN (5 mL). Yield: 82% (274 mg), colourless syrup, $R_f = 0.57$ (20:2:0.2; ethyl acetate:MeOH: NH_4OH). ^1H NMR (500 MHz, CDCl_3): δ 7.43–7.20 (m, 18H, ArH), 7.20–7.09 (m, 2H, ArH), 4.97 (d, $J = 11.0$ Hz, 1H, PhCH_2), 4.90 (d, $J = 10.8$ Hz, 1H, PhCH_2), 4.82 (d, $J = 11.0$ Hz, 1H, PhCH_2), 4.68 (q, $J = 11.7$ Hz, 2H, PhCH_2), 4.45 (t, $J = 5.3$ Hz, 3H, PhCH_2), 3.74–3.53 (m, 4H, H-6, H-2, H-3), 3.48 (t, $J = 9.0$ Hz, 1H, H-4), 3.06 (dd, $J = 11.2$, 4.8 Hz, 1H, H-1a), 2.80–2.36 (m, 8H, H-7, H-10, H-11, H-15), 2.30 (d, $J = 9.4$ Hz, 1H, H-5), 2.15 (t, $J = 10.8$ Hz, 1H, H-1b), 1.86–1.31 (m, 10H, H-8, H-9, H-12, H-13, H-14). ^{13}C NMR (126 MHz, CDCl_3): δ 138.96, 138.53, 137.99, 128.51, 128.48, 128.43, 128.37, 128.00, 127.93, 127.88, 127.78, 127.66, 127.59, 87.33, 78.68, 78.44, 77.55, 77.30, 77.04, 75.47, 75.27, 73.43, 72.77, 65.88, 64.21, 58.12, 54.24, 53.73, 51.32, 24.21, 23.17, 22.94, 22.00.

4-(4-((2R,3R,4R,5S)-3,4,5-Tris(benzyloxy)-2-((benzyloxy)methyl)piperidin-1-yl)butyl)morpholine (13d)

Prepared according to procedure D. Compound **11b** (0.3 g, 0.5 mmol), 2-bromoethyl ether (129 μL , 1 mmol), K_2CO_3 (0.21 g, 1.5 mmol), CH_3CN (5 mL). Yield: 87% (292 mg), colourless syrup, $R_f = 0.7$ (20:2:0.2; ethyl acetate:MeOH: NH_4OH). ^1H NMR (500 MHz, CDCl_3): δ 7.44–7.18 (m, 18H, ArH), 7.18–7.04 (m, 2H, ArH), 4.95 (d, $J = 11.1$ Hz, 1H, PhCH_2), 4.88 (d, $J = 10.8$ Hz, 1H, PhCH_2), 4.81 (d, $J = 11.1$ Hz, 1H, PhCH_2), 4.67 (q, $J = 11.6$ Hz, 2H, PhCH_2), 4.45 (dt, $J = 13.5$, 11.5 Hz, 3H, PhCH_2), 3.63 (m, 8H, H-6, H-2, H-3, H-12, H-13), 3.46 (t, $J = 9.1$ Hz, 1H, H-4), 3.08 (dd, $J = 11.1$, 4.9 Hz, 1H, H-1a), 2.76–2.64 (m, 1H, H-7a), 2.60 (m, 1H, H-7b), 2.48–2.16 (m, 8H, H-5, H-1b, H-10, H-11, H-14), 1.51–1.28 (m, 4H, H-8, H-9). ^{13}C NMR (126 MHz, CDCl_3): δ 139.04, 138.59, 137.86, 128.44, 128.39, 128.37, 127.92, 127.86, 127.70, 127.60, 127.50, 87.41, 78.64, 78.60, 77.36, 77.10, 76.85, 75.38, 75.24, 73.50, 72.83, 67.01, 65.52, 63.72, 58.77, 54.49, 53.72, 52.21, 24.45, 21.58.

(2R,3R,4R,5S)-1-(2-(Dimethylamino)ethyl)-2-(hydroxymethyl)piperidine-3,4,5-triol (7a)

Prepared according to procedure E. Compound **12a** (260 mg, 0.44 mmol), 10% Pd/C (100 mg), EtOH (10 mL), pH~1 with 1 M aq HCl. Yield: 91% (93 mg), pale yellow syrup, $R_f = 0.73$ (1:1:0.5; ethyl acetate:MeOH: NH_4OH). ^1H NMR (500 MHz, D_2O): δ 3.84 (dd, $J = 12.8$,

2.1 Hz, 1H, H-6a), 3.76 (dd, $J = 12.8$, 2.9 Hz, 1H, H-6b), 3.47 (td, $J = 10.2$, 4.9 Hz, 1H, H-2), 3.29 (t, $J = 9.5$ Hz, 1H, H-3), 3.18 (t, $J = 9.2$ Hz, 1H, H-4), 2.94 (dd, $J = 11.4$, 4.9 Hz, 1H, H-1a), 2.89–2.77 (m, 1H, H-7a), 2.73–2.63 (m, 1H, H-7b), 2.56–2.45 (m, 2H, H-8), 2.33–2.14 (m, 8H, H-5, H-1b, $2\times\text{CH}_3$). ^{13}C NMR (126 MHz, D_2O): δ 78.30, 69.95, 68.76, 65.22, 57.54, 55.92, 53.30, 48.79, 44.18. HRMS (ESI) m/z calcd for $\text{C}_{10}\text{H}_{23}\text{N}_2\text{O}_4^+$ (M+H) $^+$ 235.16523, found 235.16492.

(2R,3R,4R,5S)-2-(Hydroxymethyl)-1-(2-(pyrrolidin-1-yl)ethyl)piperidine-3,4,5-triol (7b)

Prepared according to procedure E. Compound **12b** (160 mg, 0.44 mmol), 10% Pd/C (80 mg), EtOH (5 mL), pH~1 with 1 M aq HCl. Yield: 95% (64 mg), yellow syrup, $R_f = 0.44$ (1:1:0.5; ethyl acetate:MeOH: NH_4OH). ^1H NMR (500 MHz, D_2O): δ 3.86 (dd, $J = 12.7$, 1.9 Hz, 1H, H-6a), 3.79 (dd, $J = 12.8$, 2.8 Hz, 1H, H-6b), 3.49 (td, $J = 10.3$, 4.9 Hz, 1H, H-2), 3.31 (t, $J = 9.5$ Hz, 1H, H-3), 3.21 (t, $J = 9.2$ Hz, 1H, H-4), 2.98 (dd, $J = 11.4$, 4.9 Hz, 1H, H-1a), 2.89 (m, 1H, H-7a), 2.81–2.68 (m, 3H, H-7b, H-8), 2.62 (m, 4H, H-9, H-12), 2.30 (t, $J = 11.1$ Hz, 1H, H-1b), 2.24 (d, $J = 9.7$ Hz, 1H, H-5), 1.74 (m, 4H, H-10, H-11). ^{13}C NMR (126 MHz, D_2O): δ 78.31, 69.97, 68.79, 65.17, 57.55, 55.92, 53.62, 50.34, 49.49, 22.73. HRMS (ESI) m/z calcd for $\text{C}_{12}\text{H}_{25}\text{N}_2\text{O}_4^+$ (M+H) $^+$ 261.18088, found 261.18057.

(2R,3R,4R,5S)-2-(Hydroxymethyl)-1-(2-(piperidin-1-yl)ethyl)piperidine-3,4,5-triol (7c)

Prepared according to procedure E. Compound **12c** (260 mg, 0.41 mmol), 10% Pd/C (100 mg), EtOH (10 mL), pH~1 with 1 M aq HCl. Yield: 92% (123 mg), yellow syrup, $R_f = 0.52$ (1:1:0.5; ethyl acetate:MeOH: NH_4OH). ^1H NMR (500 MHz, D_2O): δ 3.82 (dd, $J = 12.7$, 2.2 Hz, 1H, H-6a), 3.75 (dd, $J = 12.8$, 2.9 Hz, 1H, H-6b), 3.45 (td, $J = 10.3$, 4.9 Hz, 1H, H-2), 3.26 (t, $J = 9.4$ Hz, 1H, H-3), 3.17 (t, $J = 9.2$ Hz, 1H, H-4), 2.94 (dd, $J = 11.2$, 5.3 Hz, 2H, H-1a, H-7a), 2.71 (m, 7H, H-7b, H-8, H-9, H-13), 2.24 (dd, $J = 21.8$, 10.5 Hz, 2H, H-5, H-1a), 1.65–1.48 (m, 4H, H-10, H-12), 1.43 (m, 2H, H-11). ^{13}C NMR (126 MHz, D_2O): δ 78.25, 69.92, 68.71, 65.08, 57.45, 55.81, 54.06, 53.38, 46.94, 24.00, 22.41. HRMS (ESI) m/z calcd for $\text{C}_{13}\text{H}_{27}\text{N}_2\text{O}_4^+$ (M+H) $^+$ 275.19653, found 275.19635.

(2R,3R,4R,5S)-2-(Hydroxymethyl)-1-(2-morpholinoethyl)piperidine-3,4,5-triol (7d)

Prepared according to procedure E. Compound **12d** (270 mg, 0.42 mmol), 10% Pd/C (100 mg), EtOH (10 mL), pH~1 with 1 M aq HCl. Yield: 94% (110 mg), yellow solid, $R_f = 0.68$ (1:1:0.5; ethyl acetate:MeOH: NH_4OH). ^1H NMR (500 MHz, D_2O): δ 3.81 (dd, $J = 12.9$, 1.8 Hz, 1H, H-6a), 3.74 (dd, $J = 12.9$, 2.7 Hz, 1H, H-6b), 3.65 (m, 4H, H-10, H-11), 3.45 (td, $J = 10.1$, 4.9 Hz, 1H, H-2), 3.26 (t, $J = 9.5$ Hz, 1H, H-3), 3.16 (t, $J = 9.2$ Hz, 1H, H-4), 2.93 (dd, $J = 11.4$, 4.9 Hz, 1H, H-1a), 2.88–2.80 (m, 1H, H-7a), 2.76–2.64 (m, 1H, H-7b), 2.59–2.41 (m, 6H, H-8, H-9, H-12),

2.27 (t, $J = 11.1$ Hz, 1H, H-1b), 2.20 (d, $J = 9.7$ Hz, 1H, H-5). ^{13}C NMR (126 MHz, D_2O): δ 78.25, 69.89, 68.70, 66.06, 65.11, 57.47, 55.87, 52.88, 47.71. HRMS (ESI) m/z calcd for $\text{C}_{12}\text{H}_{25}\text{N}_2\text{O}_5^+$ ($\text{M}+\text{H}$) $^+$ 277.17580, found 277.17614.

(2R,3R,4R,5S)-1-(4-(Dimethylamino)butyl)-2-(hydroxymethyl)piperidine-3,4,5-triol (8a)

Prepared according to procedure E. Compound **13a** (200 mg, 0.32 mmol), 10% Pd/C (100 mg), EtOH (10 mL), pH~1 with 1 M aq HCl. Yield: 93% (78 mg), white solid, $R_f = 0.67$ (1:1:0.5; ethyl acetate:MeOH: NH_4OH). ^1H NMR (500 MHz, D_2O): δ 3.79 (d, $J = 12.6$ Hz, 1H, H-6a), 3.71 (d, $J = 12.4$ Hz, 1H, H-6b), 3.49–3.38 (m, 1H, H-2), 3.25 (t, $J = 9.4$ Hz, 1H, H-3), 3.14 (t, $J = 9.2$ Hz, 1H, H-4), 2.90 (dd, $J = 11.1$, 4.2 Hz, 1H, H-1a), 2.72–2.59 (m, 1H, H-7a), 2.53 (m, 1H, H-7b), 2.30 (m, 2H, H-10), 2.25–2.04 (m, 8H, H-5, H-1a, 2 \times CH $_3$), 1.36 (m, 4H, H-8, H-9). ^{13}C NMR (126 MHz, D_2O): δ 78.34, 70.07, 68.88, 64.96, 58.20, 57.52, 55.27, 51.81, 43.63, 24.18, 20.82. HRMS (ESI) m/z calcd for $\text{C}_{12}\text{H}_{27}\text{N}_2\text{O}_4^+$ ($\text{M}+\text{H}$) $^+$ 263.19653, found 263.19635.

(2R,3R,4R,5S)-2-(Hydroxymethyl)-1-(4-(pyrrolidin-1-yl)butyl)piperidine-3,4,5-triol (8b)

Prepared according to procedure E. Compound **13b** (220 mg, 0.34 mmol), 10% Pd/C (100 mg), EtOH (10 mL), pH~1 with 1 M aq HCl. Yield: 90% (88 mg), colorless syrup, $R_f = 0.37$ (1:1:0.5; ethyl acetate:MeOH: NH_4OH). ^1H NMR (500 MHz, D_2O): δ 3.80 (dd, $J = 12.7$, 1.9 Hz, 1H, H-6a), 3.72 (dd, $J = 12.8$, 2.6 Hz, 1H, H-6b), 3.48–3.37 (m, 1H, H-2), 3.26 (t, $J = 9.5$ Hz, 1H, H-3), 3.15 (t, $J = 9.2$ Hz, 1H, H-4), 2.91 (dd, $J = 11.4$, 4.9 Hz, 1H, H-1a), 2.65 (m, 1H, H-7a), 2.48 (m, 7H, H-7b, H-10, H-11, H-14), 2.25–2.08 (m, 2H, H-5, H-1b), 1.66 (m, 4H, H-12, H-13), 1.39 (m, 4H, H-8, H-9). ^{13}C NMR (126 MHz, D_2O): δ 78.37, 70.10, 68.90, 65.00, 57.59, 55.31, 55.25, 53.19, 51.86, 25.67, 22.70, 21.09. HRMS (ESI) m/z calcd for $\text{C}_{14}\text{H}_{29}\text{N}_2\text{O}_4^+$ ($\text{M}+\text{H}$) $^+$ 289.21218, found 289.21194.

(2R,3R,4R,5S)-2-(Hydroxymethyl)-1-(4-(piperidin-1-yl)butyl)piperidine-3,4,5-triol (8c)

Prepared according to procedure E. Compound **13c** (260 mg, 0.39 mmol), 10% Pd/C (100 mg), EtOH (10 mL), pH~1 with 1 M aq HCl. Yield: 95% (113 mg), yellow syrup, $R_f = 0.44$ (1:1:0.5; ethyl acetate:MeOH: NH_4OH). ^1H NMR (500 MHz, D_2O): δ 3.78 (d, $J = 11.9$ Hz, 1H, H-6a), 3.71 (dd, $J = 12.7$, 2.4 Hz, 1H, H-6b), 3.43 (td, $J = 10.0$, 5.0 Hz, 1H, H-2), 3.25 (t, $J = 9.5$ Hz, 1H, H-3), 3.14 (t, $J = 9.2$ Hz, 1H, H-4), 2.89 (dd, $J = 11.4$, 4.9 Hz, 1H, H-1a), 2.84–2.46 (m, 8H, H-7, H-10, H-11, H-15), 2.26–2.09 (m, 2H, H-5, H-1b), 1.58 (m, 4H, H-12, H-14), 1.53–1.31 (m, 6H, H-8, H-9, H-13). ^{13}C NMR (126 MHz, D_2O): δ 78.33, 70.04, 68.86, 65.01, 57.58, 57.31, 55.29, 53.29, 51.54, 23.74, 22.45, 22.30, 20.75. HRMS (ESI) m/z calcd for $\text{C}_{15}\text{H}_{31}\text{N}_2\text{O}_4^+$ ($\text{M}+\text{H}$) $^+$ 303.22783, found 303.22754.

(2R,3R,4R,5S)-2-(Hydroxymethyl)-1-(4-morpholinobutyl)piperidine-3,4,5-triol (8d)

Prepared according to procedure E. Compound **13d** (270 mg, 0.34 mmol), 10% Pd/C (100 mg), EtOH (10 mL), pH~1 with 1 M aq HCl. Yield: 96% (119 mg), pale yellow solid, $R_f = 0.59$ (1:1:0.5; ethyl acetate:MeOH: NH_4OH). ^1H NMR (500 MHz, D_2O): δ 3.73 (m, 6H, H-6, H-12, H-13), 3.41 (td, $J = 9.7$, 4.6 Hz, 1H, H-2), 3.24 (t, $J = 9.5$ Hz, 1H, H-3), 3.12 (t, $J = 9.2$ Hz, 1H, H-4), 2.89 (dd, $J = 11.4$, 4.8 Hz, 1H, H-1a), 2.73–2.40 (m, 8H, H-7, H-10, H-11, H-14), 2.25–2.08 (m, 1H, H-5, H-1b), 1.40 (m, 4H, H-8, H-9). ^{13}C NMR (126 MHz, D_2O): δ 78.25, 69.93, 68.77, 65.50, 64.97, 57.58, 57.41, 55.20, 52.21, 51.64, 22.60, 20.75. HRMS (ESI) m/z calcd for $\text{C}_{14}\text{H}_{29}\text{N}_2\text{O}_5^+$ ($\text{M}+\text{H}$) $^+$ 305.20710, found 305.20676.

2. 2. Glucosidase Inhibitory Assays

α -Glucosidase (yeast), β -glucosidase (sweet almonds), and α -mannosidase (jack bean) was purchased from Sigma. 1-Deoxynojirimycin, *para*-nitrophenyl α -D-glucopyranoside, *para*-nitrophenyl β -D-glucopyranoside and *para*-nitrophenyl α -D-mannosidase were also purchased from Sigma. Inhibitory potencies were carried out by spectrophotometrically measuring the residual hydrolytic activities of the glycosidases on the corresponding *para*-nitrophenyl glycoside substrates. The α -glucosidase,²⁶ β -glucosidase assays²⁷ were performed in 50 mM phosphate buffer, pH 6.8 at 37 °C. The α -mannosidase assay²⁸ was performed in 50 mM citrate buffer, pH 5.5 at 37 °C. The test compounds were pre-incubated with the enzyme solutions and buffered in a disposable 96-well microtiter plate at 37 °C for 15 min. Next, the reactions were initiated by the addition of 20 μL of a solution of the corresponding *para*-nitrophenyl glycoside substrates. After the reaction mixture was incubated at 37 °C for 15 min. Thereupon, it was quenched by adding 80 μL Na_2CO_3 (0.2 mol/L). Enzymatic activity was quantified by measuring the absorbance at 405 nm using a BioTek μ Quant Microplate Spectrophotometer. Each experiment was performed in triplicate. IC_{50} values were determined graphically with GraphPad Prism (version 8.0).

2. 3. Kinetics of Enzyme Inhibition

Inhibition constant (K_i) measurement was performed in 50 mM phosphate buffer (pH 6.8) at 37 °C, using *para*-nitrophenyl β -D-glucopyranoside as the substrate. The assay was initiated by adding β -glucosidase ($K_m = 3.5$ mM) to a solution of the substrate (concentrations used: 0.875 mM, 1.75 mM, 3.5 mM, 7 mM, 10.5 mM) in the presence of inhibitors (concentrations used: 0 mM, 0.1 mM, 0.2 mM). After the reaction mixture was incubated at 37 °C for 15 min, it was quenched by adding 80 μL Na_2CO_3 (0.2 mol/L). The absorbance of 4-nitrophenol released from the substrate was read at 405 nm.

2. 4. Cell Culture and Inhibition of Proliferation B16F10 Cells²⁹

The mouse B16F10 melanoma cell line, which is derived from C57BL/6 mice was purchased from KeyGen Biotech (Nanjing, China). The cell line was cultured in DMEM supplemented with fetal bovine serum (10%), penicillin (100 U/mL) and streptomycin (100 µg/mL) at 37 °C in humidified 5% CO₂ atmosphere. Media was replenished every third day. B16F10 cells were seeded on 96-well microtiter plates in DMEM supplemented with 10% FBS and incubated overnight. The compounds (1 mM, 0.05 mM) were then added to the cells and cultured for another 48 h. Each treatment was performed in six well replicates. MTT reagent (Sigma Aldrich) was added to each well incubated for 4 h at 37 °C. After the cell culture medium was removed, formazan crystals in adherent cells were dissolved in 200 µL DMSO and the absorbance of the formazan solution was measured at 570 nm.

3. Results and Discussion

3. 1. Chemistry

The target compounds were prepared from the key intermediate **11** through reductive amination or double nucleophilic substitution, respectively (Figure 2). The synthesis of compound **11** commenced from 2,3,4,6-tet-

ra-*O*-benzyl-1-deoxynojirimycin **9** which was prepared according to previously published procedures in four steps.²⁸ Treatment of *O*-benzyl protected DNJ **9** with *N*-(4-bromobutyl)phthalimide or *N*-(4-bromoethyl)phthalimide in the presence of K₂CO₃ in DMF afforded *N*-phthalyl protected DNJ **10** (Scheme 1). The intermediate **10** was then converted into primary amide **11** by a hydrazinolysis reaction using N₂H₄ in EtOH.

A generalized synthetic approach to the derivatives **7** and **8** was shown in Scheme 2. The reductive amination of **11** with HCHO-HCOOH gave compounds **12a** and **13a**. For compounds **12** and **13** which bore 5- and 6-membered rings, double nucleophilic substitution reaction was performed on primary amine **11** in basic conditions. All the intermediates **12** and **13** were obtained in good (80%) to excellent (90%) yields, independently of the chain length. Precursors **12** and **13** were then deprotected by hydrogenolysis (10% Pd/C, EtOH, 1 M HCl) to afford the target derivatives **7** and **8** in almost quantitative yield.

3. 2. Biological Evaluation

The small library of DNJ derivatives were submitted to a panel of biological evaluations, which included inhibition of glycosidases, inhibition kinetics of β-glucosidase, as well as inhibition of B10F16 cells growth. These experiments are summarized below.

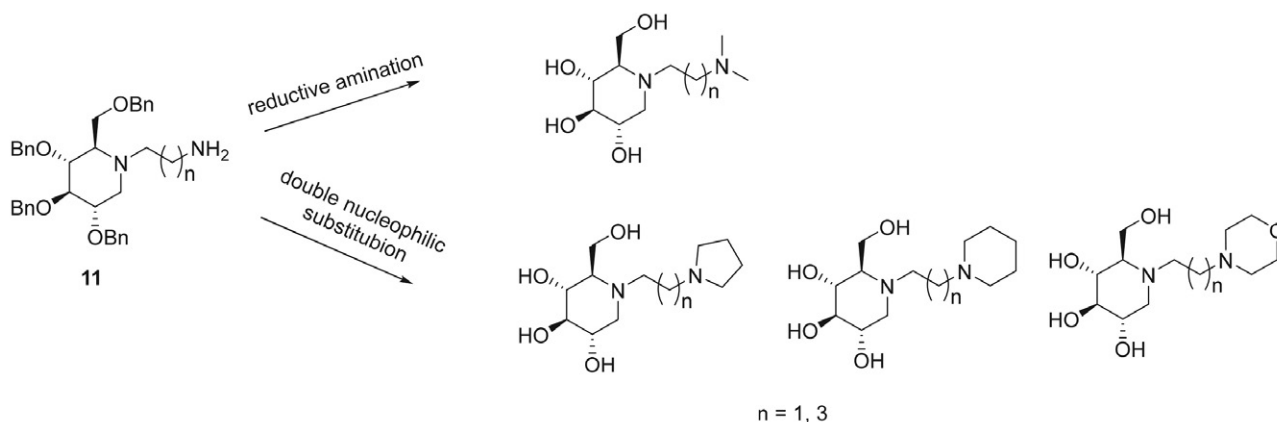
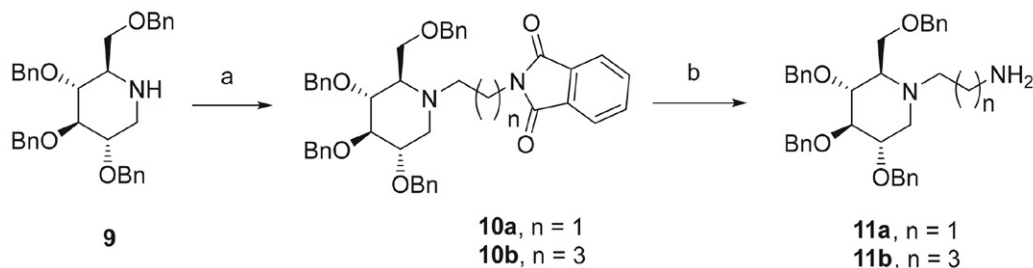
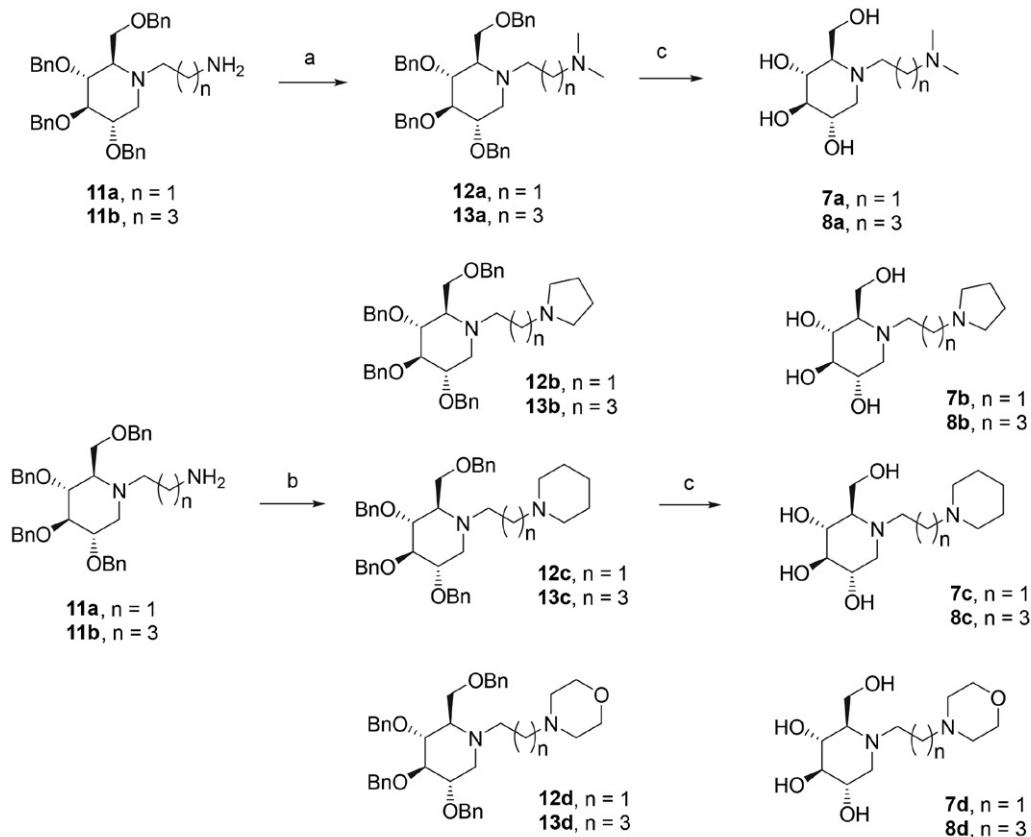


Figure 2. The key intermediate **11** and the general structures of the target compounds.



Scheme 1. Synthesis of the primary amide **11**. Reagents and conditions: (a) *N*-(4-bromobutyl) phthalimide or *N*-(4-bromoethyl) phthalimide, K₂CO₃, DMF, 100 °C, 24 h, 87% (**10a**), 85% (**10b**); (b) N₂H₄ (80%), EtOH, reflux, 3 h, 82% (**11a**), 85% (**11b**).



Scheme 2. Synthesis of *N*-alkylated derivatives of 1-deoxynojirimycin. Reagents and conditions: (a) HCHO, HCOOH, 105 °C, 3 h, 83% (**12a**), 90% (**13a**); (b) alkyl dibromide, K₂CO₃, CH₃CN, 80 °C, 12 h, 84% (**12b**), 81% (**13b**), 80% (**12c**), 82% (**13c**), 85% (**12d**), 87% (**13d**); (c) H₂, 10% Pd/C, EtOH, 1 M HCl, rt, 24 h, 91% (**7a**), 93% (**8a**), 95% (**7b**), 90% (**8b**), 92% (**7c**), 95% (**8c**), 94% (**7d**), 96% (**8d**).

3. 2. 1. Inhibition of Glucosidases

Glycosidase inhibitory activities of compounds **7** and **8** was evaluated against α -glucosidase (yeast), β -glucosidase (almonds), α -mannosidase (jack bean), with reference to the known standard DNJ. The results were expressed as the inhibition of glucosidase activity (IC₅₀) and are summarized in Table 1.

Compounds **7a**, **7b** and **7c** had weak inhibitory activities against α - and β -glucosidase at 1 mM. It was, however, interesting to note that compound **7d** bearing a morpholine ring was the only derivative in our library exhibiting higher and selective activity of β -glucosidase with an IC₅₀ of 0.052 \pm 0.004 mM compared to DNJ (IC₅₀ = 0.65 \pm 0.04 mM), while none of the other glucosidases

were inhibited by this compound (Table 1). This indicated that a much more favorable interaction with the β -glucosidase active site.

Compound **8a** also had weak inhibitory activity against α - and β -glucosidase. Derivatives **8b** and **8c** which possessed a longer alkyl chain were found to be more selective inhibitors of α -glucosidase than **7b** and **7c**, with IC₅₀ values of 0.364 \pm 0.011 mM and 0.358 \pm 0.04 mM, respectively. And they had similar potencies to α -glucosidase. Compound **8d**, which bore a morpholine ring, showed decreased inhibitory activity against α -glucosidase with an IC₅₀ of 1.385 \pm 0.137 mM compared to **8b** and **8c**. However, **8d** showed better inhibitory effect on α -glucosidase than **7d** which possessed a shorter alkyl chain (Table 1). Moreover, compounds **8a**, **8b**, **8c** and **8d** have reduced

Table 1. Glycosidase inhibitory activity values IC₅₀ (mM)

Enzyme	7a	7b	7c	7d	8a	8b	8c	8d	DNJ
α -glucosidase (yeast)	10% ^a	24%	29%	33%	49%	0.364 \pm 0.011	0.358 \pm 0.04 ^b	1.385 \pm 0.137	0.155 \pm 0.015
β -glucosidase (almonds)	22%	34%	33%	0.052 \pm 0.004	17%	40%	18%	29%	0.648 \pm 0.036
α -mannosidase (jack bean)	NI ^c	NI	NI	NI	NI	NI	NI	NI	NI

^a The inhibition rate (%) was obtained from the 1 mM of compounds. ^b IC₅₀ is defined as the compound concentration at which 50% activities of glucosidases. The values are mean \pm SD from three independent experiments. ^c NI indicated no inhibition at 1 mM of compounds.

inhibitory activity compared to DNJ. These results suggested that **8b** and **8c** which bore 5- and 6-membered rings would be beneficial for the interaction with α -glucosidase through the hydrophobic effect more than *N*-dimethyl DNJ derivative **8a**.³⁰ Compounds having $n = 3$ displayed better inhibition towards α -glucosidase than compounds having $n = 1$, with a trend correlating higher inhibition associated with increased chain length. In addition, introduction of a nitrogen atom seemed to display no or negligible inhibition against all the enzymes. Finally, none of these derivatives showed inactivation of jack bean α -mannosidase.

3. 2. 2. Inhibition Kinetics of β -Glucosidase

In order to explore further insight into how **7d** interacted with β -glucosidase (almonds), the mode of inhibition and inhibition constant of **7d** was determined by the Lineweaver–Burk plots (Figure 3). The double reciprocal plots of **7d** showed straight lines with the same v_{\max} . This indicated that **7d** ($K_i = 7 \mu\text{M}$) inhibited β -glucosidase in a competitive manner, a nearly 7-fold increase compared to DNJ²⁶ ($K_i = 47 \mu\text{M}$). Hence, this competitive inhibition indicated that **7d** was expected to bind to the active site of β -glucosidase and compete with their primary substrates. Moreover, a probable hydrogen bond acceptor was the carbonyl hydrogen atom of the catalytic acid.²⁷

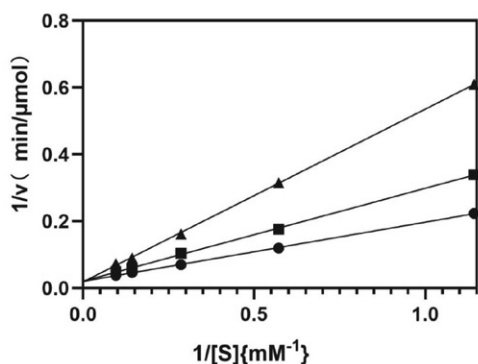


Figure 3. Double-reciprocal plot of the inhibition kinetics of β -glucosidase (almonds) by compound **7d**. Substrate concentration: 0.875, 1.75, 3.5, 7, 10.5 mM, inhibitor concentration: 0 mM (control, \blacktriangledown), 0.1 mM (\blacklozenge), 0.2 mM (\blacktriangle).

3. 3. Inhibition of B16F10 Cells Growth

The inhibition of B16F10 cells growth by compounds was determined using the MTT assay and the results are summarized in Figure 4. All compounds were inactive with no significant inhibition being observed at 0.05 mM and 1 mM. This indicated that compounds by the modification of changing length of the tether, the size and nature of the terminal tertiary amine substituents had no influence on the anticancer activity.

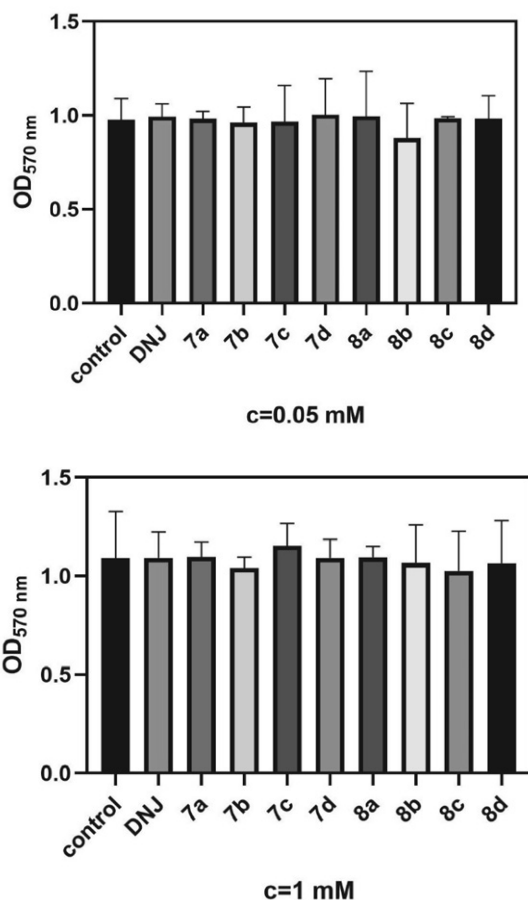


Figure 4. Effect of glycosidase inhibitors on B16F10 cells growth. Each bar represents the mean (\pm SD, $n = 6$). $P > 0.05$ comparing with control.

4. Conclusion

In summary, a series of DNJ derivatives were designed and synthesized, and the structures of synthesized compounds were confirmed by ^1H NMR, ^{13}C NMR and HRMS. Moreover, the preliminary glucosidase inhibition and anticancer activities were evaluated *in vitro*. Compound **7d** proved to be the most potent and selective β -glucosidase inhibitor in a competitive manner, and none of the other glycosidases were inhibited by this compound at micromolar level. Compounds **8b** and **8c** were moderate and selective α -glucosidase inhibitors. Nevertheless, all compounds could not inhibit the growth of B16F10 melanoma cells. The collective results indicated that a lengthening of the alkyl chain linking DNJ provide better selectivity towards α -glucosidase. The size of the hydrophobic group at the alkyl chain, especially its nature, differs greatly for the selective inhibition against α - and β -glucosidases. Compounds **7d**, **8b** and **8c** would be a lead for designing novel compounds, and further derivatives would be prepared by altering these specific molecules. In addition, our results provides useful clues for the design of selective glucosidase inhibitors.

5. References

- C. S. Rye, S. G. Withers, *Curr. Opin. Chem. Biol.* **2000**, *4*, 573–580. DOI:10.1016/S1367-5931(00)00135-6
- T. Kimura, K. Nakagawa, H. Kubota, Y. Kojima, Y. Goto, K. Yamagishi, S. Oita, S. Oikawa, T. Miyazawa, *J. Agric. Food. Chem.* **2007**, *55*, 5869–5874. DOI:10.1021/jf062680g
- Y. X. Zhao, W. J. Liu, Y. Zhou, X. M. Zhang, P. V. Murphy, *Bioorg. Med. Chem. Lett.* **2010**, *20*, 7540–7543. DOI:10.1016/j.bmcl.2010.09.065
- Y. M. Du, H. Ye, T. Gill, L. J. Wang, F. Guo, A. Cuconati, J. T. Guo, T. M. Block, J. H. Chang, X. D. Xu, *Bioorg. Med. Chem. Lett.* **2013**, *23*, 2172–2176. DOI:10.1016/j.bmcl.2013.01.108
- J. D. Diot, I. Garcia Moreno, G. Twigg, C. Ortiz Mellet, K. Haupt, T. D. Butters, J. Kovensky, S. G. Gouin, *J. Org. Chem.* **2011**, *76*, 7757–7768. DOI:10.1021/jo201125x
- G.-N. Kim, Y.-I. Kwon, H.-D. Jang, *J. Med. Food* **2011**, *14*, 712–717. DOI:10.1089/jmf.2010.1368
- A. J. Rawlings, H. Lomas, A. W. Pilling, M. J. Lee, D. S. Alonzi, J. S. Rountree, S. F. Jenkinson, G. W. Fleet, R. A. Dwek, J. H. Jones, T. D. Butters, *Chembiochem* **2009**, *10*, 1101–1105. DOI:10.1002/cbic.200900025
- A. H. Futerman, F. M. Platt, *Mol. Genet. Metab.* **2017**, *120*, 22–26. DOI:10.1016/j.ymgme.2016.11.390
- A. Massimo, S. Maura, L. Nicoletta, M. Giulia, M. Valentina, C. Elena, P. Alessandro, B. Rosaria, S. Sandro, *Neurochem. Res.* **2016**, *41*, 210. DOI:10.1007/s11064-015-1763-2
- L. Smith, S. Mullin, A. H. V. Schapira, *Exp. Neurol.* **2017**, *298*, 180–190. DOI:10.1016/j.expneurol.2017.09.010
- R. Kornfeld, S. Kornfeld, *Annu. Rev. Biochem.* **1985**, *54*, 631. DOI:10.1146/annurev.bi.54.070185.003215
- D. H. Dube, C. R. Bertozzi, *Nat. Rev. Drug Disc.* **2005**, *4*, 477. DOI:10.1038/nrd1751
- N. Asano, R. J. Nash, R. J. Molyneux, G. W. J. Fleet, *Tetrahedron: Asymmetry* **2000**, *11*, 1645–1680. DOI:10.1016/S0957-4166(00)00113-0
- C. H. Wong, D. P. Dumas, Y. Ichikawa, K. Koseki, S. J. Danishefsky, B. W. Weston, J. B. Lowe, *J. Am. Chem. Soc.* **1992**, *114*, 7321–7322. DOI:10.1021/ja00044a068
- H. Liu, L. Sim, D. R. Rose, B. M. Pinto, *J. Org. Chem.* **2006**, *71*, 3007–3013. DOI:10.1021/jo052539r
- P. Segal, P. U. Feig, G. Scherthner, K. P. Ratzmann, J. Rybka, D. Petzinna, C. Berlin, *Diabetes. Care* **1997**, *20*, 687–691. DOI:10.2337/diacare.20.5.687
- F. M. Platt, G. R. Neises, R. A. Dwek, T. D. Butters, *J. Biol. Chem.* **1994**, *269*, 8362.
- M. A. Fischl, L. Resnick, R. Coombs, A. B. Kremer, J. C. Potage, R. J. Fass, K. H. Fife, W. G. Powderly, A. C. Collier, R. L. Aspinall, *J. Acquir. Immune Defic. Syndr.* **1994**, *7*, 139–147.
- R.-W. Wang, X.-L. Qiu, M. Bols, F. Ortega-Caballero, F.-L. Qing, *J. Med. Chem.* **2006**, *49*, 2989–2997. DOI:10.1021/jm060066q
- A. Mehta, N. Zitzmann, P. M. Rudd, T. M. Block, R. A. Dwek, *FEBS Lett.* **1998**, *430*, 17–22. DOI:10.1016/S0014-5793(98)00525-0
- T. Wennekes, B. Lang, M. Leeman, G. A. v. d. Marel, E. Smits, M. Weber, J. v. Wiltenburg, M. Wolberg, J. M. F. G. Aerts, H. S. Overkleeft, *Org. Process. Res. Dev.* **2008**, *12*, 414–423. DOI:10.1021/op700295x
- W. F. Wang, F. Wang; T. T. Liang, Z. Fang, *Chem. Res. Appl.* **2017**, *29*, 793–798.
- M. Iftikhar, L. Wang, Z. Fang, *J. Chem. Res.* **2017**, *41*, 460–464. DOI:10.1016/S0928-1258(17)30358-3
- W. Yu, T. Gill, L. Wang, Y. Du, H. Ye, X. Qu, J. T. Guo, A. Cuconati, K. Zhao, T. M. Block, X. Xu, J. Chang, *J. Med. Chem.* **2012**, *55*, 6061–6075. DOI:10.1021/jm300171v
- C. G. F. Cooper, E. R. Lee, R. A. Silva, A. J. Bourque, S. Clark, S. Katti and V. Nivorozhkin, *Org. Process. Res. Dev.* **2012**, *16*, 1090–1097. DOI:10.1021/op2001222
- W. L. Dong, T. Jespersen, M. Bols, T. Skrydstrup, M. R. Sierks, *J. Biochem.* **2006**, *35*, 2788.
- N. Panday, Y. Canac, A. Vasella, *Helv. Chim. Acta* **2000**, *83*, 58. DOI:10.1002/(SICI)1522-2675(20000119)83:1<58::AID-HLCA58>3.0.CO;2-K
- P. Compain, C. Decroocq, J. Iehl, M. Holler, D. Hazelard, T. Mena Barragán, C. Ortiz Mellet, J.-F. Nierengarten, *Angew. Chem. Int. Ed.* **2010**, *49*, 5753–5756. DOI:10.1002/anie.201002802
- P. Dua, R. P. Gude, *Cancer Chemother. Pharmacol.* **2006**, *58*, 195–202. DOI:10.1007/s00280-005-0155-8
- S. M. Ding, T. Lan, G. J. Ye, J. J. Huang, Y. Hu, Y. R. Zhu, B. Wang, *Bioorg. Med. Chem.* **2018**, *26*, 3370–3378. DOI:10.1016/j.bmc.2018.05.008

Povzetek

Pripravili smo serijo *N*-alkiliranih deoksinojirimicinskih (DNJ) derivatov, povezanih s terminalno terciarno aminsko skupino na alkilni verigi različnih dolžin. Te nove sintezne spojine smo preliminarно *in vitro* analizirali za glukozidazno inhibicijo in antirakavo aktivnost. V nekaterih primerih smo opazili močno in selektivno inhibicijo. Spojina **7d** (IC₅₀ = 0.052 mM) je, v primerjavi z DNJ (IC₅₀ = 0.65 mM), pokazala izboljšano in selektivno inhibitorno aktivnost proti β-glukozidazi. Dodatne analize kinetike encimske inhibicije s pomočjo Lineweaver–Burkovich diagramov so pokazale, da **7d** inhibira β-glukozidazo na kompetitiven način, kar nakazuje, da se **7d** verjetno veže v aktivno mesto β-glukozidaze. Spojini **8b** and **8c** sta pokazali zmerno, a vendar selektivno, inhibicijo α-glukozidaze. Ne glede na to, pa nobena od spojin ni inhibirala rasti B16F10 melanomskih celic.



Except when otherwise noted, articles in this journal are published under the terms and conditions of the Creative Commons Attribution 4.0 International License

Scientific paper

Structural Diversity in Oxadiazole-Containing Silver Complexes Dependent on the Anions

Long Zhao,^{†1} Long-Yan Xie,^{†1} Xiu-Li Du,^{†1} Kai Zheng,¹ Ting Xie,¹
Rui-Rui Huang,¹ Jie Qin,^{*1} Jian-Ping Ma^{*2} and Li-Hong Ding³

¹ School of Life Sciences, Shandong University of Technology, Zibo 255049, P. R. China

² College of Chemistry, Chemical Engineering and Materials Science, Shandong Normal University, Jinan 250014, P. R. China

³ Lanzhou University of Arts and Sciences, Lanzhou, 730000, P. R. China

* Corresponding author: E-mail: qinjietutu@163.com
xxgk123@163.com; Tel.: 0086-533-2780271; Fax: 0086-533-2781329

Received: 12-17-2019

† These authors contributed equally to this work.

Abstract

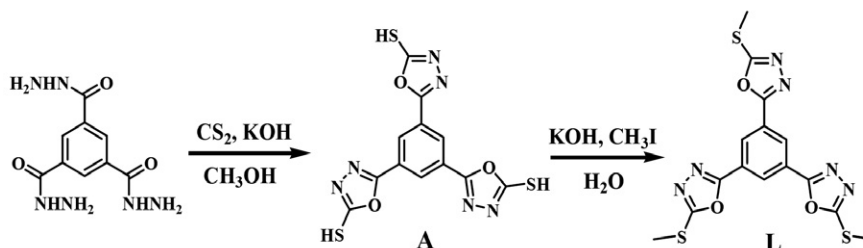
Two coordination polymers, namely $[Ag_2(L)(SO_3CF_3)(H_2O)](SO_3CF_3) \cdot CH_2Cl_2$ (**1**) and $[Ag_5(L)_4(H_2O)_2](SbF_6)_5 \cdot 5THF$ (**2**), were obtained by reacting oxadiazole-containing tri-armed ligand 1,3,5-tri(2-methylthio-1,3,4-oxadiazole-5-yl)benzene (**L**) and silver salts in CH_2Cl_2/THF medium. The two complexes crystallized in the tetragonal space group $I4_1/a$ and orthorhombic space group $Fdd2$, respectively. The Single-crystal X-ray diffraction revealed that the two complexes exhibit strikingly different 3D polymeric structures, which can be ascribed to the different counter anions. **L** in compound **1** acted as a hexa-dentate ligand, binding to two types of Ag^+ atoms to form a 3D polymeric structure. **L** in compound **2** acted as a hexa- and penta-dentate ligand, binding to three types of Ag^+ atoms to form the 3D polymeric structure. The antibacterial activity of the complexes was also investigated.

Keywords: Coordination polymers; oxadiazole-containing spacer; counter anions; antibacterial activity

1. Introduction

The design and synthesis of coordination polymers exhibiting intriguing structures and properties have attracted much attention because of their potential application in catalysis,^{1–3} magnetic properties,^{4–6} gas adsorption and separation,^{7,8} molecular sensing and luminescent materials.^{9,10} Many factors, including the nature of the metal ion, design of the organic ligand, auxiliary ligand, solvent

medium, and inorganic counter anions can affect the self-assembly process of coordination compounds.¹¹ Our research group has initiated a synthetic program for the construction of coordination polymers generated from oxadiazole-containing organic ligands.^{11,12–14} As an extension of previous studies, we expand oxadiazole-bridging double-armed ligands to the oxadiazole-containing tri-armed ligand **L**, namely 1,3,5-tri(2-methylthio-1,3,4-oxadiazole-5-yl)benzene (Scheme 1). **L** has three arms, each



Scheme 1. Synthesis of **L**.

comprising 2-methylthio-1,3,4-oxadiazole. As is known, N atoms on the 1,3,4-oxadiazole ring can bind to transition metals, and the S atom also has strong binding ability to soft metals (e.g., Ag⁺). Therefore, **L** can act as a multi-connector in the assembly of complexes with six oxadiazole N-donors and three S-donors, which may result in polynuclear or high-dimensional intricate structures. The reactions of **L** with AgSO₃CF₃ and AgSbF₆ in CH₂Cl₂/THF allow for two 3D coordination polymers, [Ag₂(L)(SO₃CF₃)(H₂O)](SO₃CF₃)•CH₂Cl₂ (**1**) and [Ag₅(L)₄(H₂O)₂](SbF₆)₅•5THF (**2**), respectively. Here, we report the synthesis and crystal structures of these compounds. Moreover, the antibacterial activities of **1** and **2** were investigated.

2. Experimental

2.1. Physical Measurements and Materials

Reagents and solvents were purchased commercially from Xiya Reagent. The reagents used in the experiment were all analytical pure, and no further purification was carried out without explanation. The intermediate **A** was synthesized according to the literature method.¹¹ Infrared spectra in the range of (400–4000 cm⁻¹) were determined by Vector22 Bruker spectrophotometer using potassium bromide tablets. The IR spectra of the synthesized compounds are given in Figure S1 of the supporting information. ¹H NMR spectra were measured on a Bruker AM 500 spectrometer.

2.2. Synthesis of L

KOH (0.2 g, 3.57 mmol) was added to a solution of **A** (0.4 g, 1.00 mmol) in water (30 mL), the mixture was

stirred for 20 minutes at ambient temperature. Then CH₃I (0.8 mL) was added, the mixture was stirred for 6 hours at 0 °C, then filtered. The product was collected and purified on silica gel by column using CH₂Cl₂/THF (5 : 1, v/v) as the eluent to afford **L** as the white crystalline solid (0.34 g). Yield 80 %. M.p. = 134–136 °C, IR (KBr pellet cm⁻¹): 3047(w), 2936(m), 1543(m), 1465(vs), 1432(s), 1323(m), 1181(vs), 1105(m), 947(s), 898(m), 781(s), 731(m), 705(s), 678(m). ¹H NMR (300MHz, CDCl₃, 25°C, TMS, ppm): 8.77(s, 3H, -C₆H₃), 2.87(s, 9H, -CH₃). Single crystals suitable for X-ray crystallographic analysis were grown by slow diffusion of ethanol into dicholmethane solution of **L**.

2.3. Synthesis of 1

A solution of AgSO₃CF₃ (19.6 mg, 0.076 mmol) in THF (10 mL) was layered carefully onto a solution of **L** (10 mg, 0.024 mmol) in CH₂Cl₂. The solutions were left at room temperature for about 1 week, and blocky colorless crystals were obtained. Yield: 55% (based on **L**). IR (KBr pellet cm⁻¹): 2939(w), 1624(m), 1554(m), 1464(vs), 1432(m), 1257(vs), 1181(vs), 1033(s), 974(m), 782(m), 730(m), 678(s), 517(m).

2.4. Synthesis of 2

A solution of AgSbF₆ (26.6 mg, 0.077 mmol) in THF (10 mL) was layered carefully onto a solution of **L** (10 mg, 0.024 mmol) in CH₂Cl₂. The solutions were left at room temperature for about 2 weeks, and claviform colorless crystals were obtained. Yield: 40% (based on **L**). IR (KBr pellet cm⁻¹): 2936(w), 1621(m), 1552(m), 1464(vs), 1431(m), 1182(s), 1105(w), 976(w), 784(m), 663(vs).

Table 1. Crystallographic data for **L**, **1**, and **2**.

	L	1	2
Empirical formula	C ₁₆ H ₁₄ Cl ₂ N ₆ O ₃ S ₃	C ₁₈ H ₁₆ Ag ₂ C ₁₂ F ₆ N ₆ O ₁₀ S ₅	C ₈₀ H ₉₂ Ag ₅ F ₃₀ N ₂₄ O ₁₉ S ₁₂ Sb ₅
Mr	505.41	1037.31	3796.60
Crystal System	triclinic	tetragonal	orthorhombic
Space group	<i>P</i> -1	<i>I</i> 4 ₁ / <i>a</i>	<i>Fdd</i> 2
<i>a</i> (Å)	12.3957(15)	29.635(2)	23.442(3)
<i>b</i> (Å)	13.1933(16)	29.635(2)	49.277(8)
<i>c</i> (Å)	14.4155(18)	15.200(2)	22.284(3)
α (°)	111.293(2)	90.00	90.00
β (°)	106.666(2)	90.00	90.00
γ (°)	94.493(2)	90.00	90.00
<i>V</i> (Å ³)	2059.9(4)	13350(2)	25741(6)
<i>Z</i>	4	4	8
ρ _c (g cm ⁻³)	1.630	2.064	1.959
<i>F</i> (000)	1032	8228	14752.0
<i>T</i> / K	173(2)	173(2)	173(2)
μ(Mo-Kα) / mm ⁻¹	0.652	1.738	2.079
GOF (<i>F</i> ²)	1.021	1.098	1.029
Data / restraints / parameters	7495 / 0 / 547	5907 / 16 / 474	11022 / 19 / 740
<i>R</i> ₁ ^a , <i>wR</i> ₂ ^b (<i>I</i> > 2σ(<i>I</i>))	0.0421, 0.1046	0.0493, 0.1046	0.0452, 0.1114

^a *R*₁ = Σ||*F*_o| - |*F*_c||/Σ|*F*_o|, ^b *wR*₂ = [Σ*w*(*F*_o² - *F*_c²)²/Σ*w*(*F*_o²)]^{1/2}

2. 5. Determination of Crystal Structures

The single crystal of the synthesized compounds were measured using Bruker Smart Apex CCD diffractometer. The collected data were reduced using SAINT,¹⁵ and multi-scan absorption corrections were performed using SADABS.¹⁶ The structures were solved by direct methods and refined against F^2 by full-matrix least-squares.¹⁷ All of the non-hydrogen atoms were refined aniso-tropically. All the hydrogen atoms were generated geometrically and refined isotropically using the riding model except the hydrogen atoms of water molecules, which were located directly from the Fourier map. Details of crystallographic parameters, data collection, and refinements are summarized in Table 1. The bond length and bond angle of the crystals are shown in Tables 2 and 3.

Table 2. Selected bond distances (Å) and angles (°) for complex 1.

Ag1-N2 ^{#1}	2.274(4)	Ag1-N4 ^{#2}	2.293(4)
Ag1-N1	2.316(4)	Ag1-N3 ^{#3}	2.311(4)
Ag2-N5	2.229(4)	Ag2-N6 ^{#4}	2.282(4)
Ag2-O4	2.566(4)	Ag2-O7	2.322(4)
N2 ^{#1} -Ag1-N4 ^{#2}	114.42(14)	O7-Ag2-O4	93.19(16)
N2 ^{#1} -Ag1-N3 ^{#3}	106.15(14)	N5-Ag2-N6 ^{#4}	138.06(14)
N4 ^{#2} -Ag1-N3 ^{#3}	106.39(15)	N5-Ag2-O7	119.72(16)
N2 ^{#1} -Ag1-N1	113.64(14)	N6 ^{#4} -Ag2-O7	94.29(15)
N4 ^{#2} -Ag1-N1	101.77(15)	N5-Ag2-O4	87.70(14)
N3 ^{#3} -Ag1-N1	114.46(14)	N6 ^{#4} -Ag2-O4	116.05(14)
Ag1-N2 ^{#1}	2.274(4)	Ag1-N4 ^{#2}	2.293(4)
Ag1-N1	2.316(4)	Ag1-N3 ^{#3}	2.311(4)
Ag2-N5	2.229(4)	Ag2-N6 ^{#4}	2.282(4)

Symmetry code: #1: $-y+7/4, x+1/4, z+1/4$; #2: $y-1/4, -x+7/4, z+3/4$; #3: $-x+3/2, -y+2, z+1/2$; #4: $-y+7/4, :x+1/4, z-3/4$

Table 3 Selected bond distances (Å) and angles (°) for complex 2.

Ag1-N2	2.257(5)	Ag1-N2 ^{#1}	2.257(5)
Ag1-N9	2.328(6)	Ag1-N9 ^{#1}	2.328(6)
Ag2-N7	2.294(6)	Ag2-N4 ^{#2}	2.374(6)
Ag2-N11 ^{#2}	2.325(6)	Ag2-O7	2.466(6)
Ag2-S1 ^{#3}	2.9549(19)	Ag3-N1	2.362(6)
Ag3-N10	2.325(7)	Ag3-N12 ^{#1}	2.384(6)
Ag3-N6 ^{#4}	2.413(7)	Ag3-N3 ^{#1}	2.548(6)
N2 ^{#1} -Ag1-N2	108.5(3)	N2 ^{#1} -Ag1-N9 ^{#1}	123.1(2)
N2-Ag(1)-N9 ^{#1}	109.6(2)	N2 ^{#1} -Ag1-N9	109.6(2)
N2-Ag1-N9	123.1(2)	N9 ^{#1} -Ag1-N9	82.1(3)
N7-Ag2-N4 ^{#2}	92.6(2)	N1 ^{#2} -Ag2-N4 ^{#2}	134.8(2)
N7-Ag2-N11 ^{#2}	129.3(2)	O7-Ag2-S1 ^{#3}	178.13(17)
N10-Ag3-N1	110.7(2)	N10-Ag3-N6 ^{#4}	82.7(2)
N10-Ag3-N12 ^{#1}	94.8(2)	N10-Ag3-N3 ^{#1}	132.2(2)
N6 ^{#4} -Ag3-N12 ^{#1}	114.5(2)	N12 ^{#1} -Ag3-N3 ^{#1}	132.76(19)
N3 ^{#1} -Ag3-N1	79.2(2)	N1-Ag3-N6 ^{#4}	152.4(2)

Symmetry code: #1: $-x+3/2, -y+3/2, z$; #2: $-x+1, -y+3/2, z+1/2$; #3: $x-1/2, y, z+1/2$; #4: $-x+7/4, y-1/4, z+1/4$.

2. 6. Antibacterial Activity Test

Four referenced bacterial strains, *B. subtilis*, *E. coli*, *P. aeruginosa* and *S. aureus* were selected. Streptomycin was used as a positive control. The IC₅₀ (half minimum inhibitory concentrations) of the test compounds were determined by a colorimetric method using the dye MTT (3-(4,5-dimethylthiazol-2-yl)-2,5-diphenyl tetrazolium-bromide). Stock solutions of the synthesized compounds (100 µg/mL) were prepared in DMSO, and sequentially diluted with Mueller-Hinton medium. The antibacterial activities were evaluated by the method reported before.¹⁸ The procedure of antibacterial activity was given in detail in *Supporting Information*.

3. Results and Discussion

3. 1. Crystal Structure Analysis

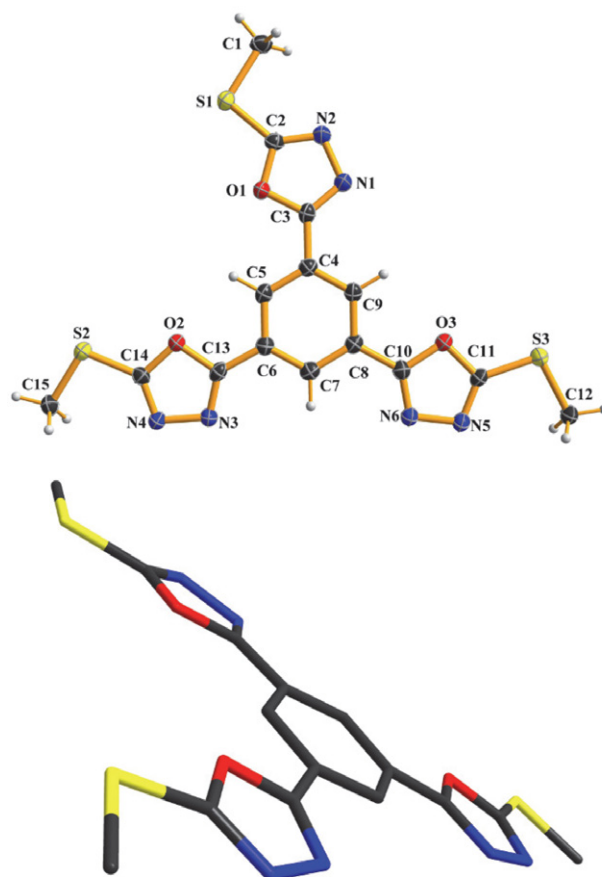


Figure 1. Molecular structure of L (50% probability displacement ellipsoids), front and side views are presented.

Colorless crystals of L suitable for X-ray structure analysis were obtained via the slow diffusion of ethanol into a dichloromethane solution of L. L crystallized in the triclinic space group $P\bar{1}$; there are two L and two CH_2Cl_2

molecules in the asymmetric unit. As shown in Figure 1, **L** has an approximately planar structure except for the methyl H atoms stretching out of the plane. The dihedral angles between the central benzene ring and surrounding oxadiazole rings are $4.371(7)^\circ$, $6.136(2)^\circ$, and $7.257(2)^\circ$, respectively.

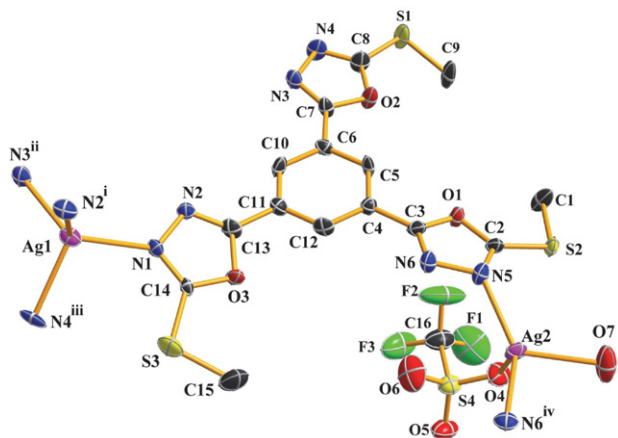


Figure 2. The coordination environment of Ag^+ in **1** at 50% probability displacement. (Solvent molecules are omitted for clarity) Symmetry codes: (i) $-y+7/4, x+1/4, z+1/4$; (ii) $-x+3/2, -y+2, z+1/2$; (iii) $y-1/4, -x+7/4, z+3/4$; (iv) $-y+7/4, x+1/4, z-3/4$.

Crystallization of **L** with AgSO_3CF_3 in a $\text{CH}_2\text{Cl}_2/\text{THF}$ mixed-solvent system at room temperature produced complex **1** with a 55% yield. **1** crystallized in the tetragonal space group $I4_1/a$. Single crystal analysis revealed that two crystallographically independent Ag^+ ions, one ligand **L**, one coordinated water molecule, one coordinated CF_3SO_3^- anion, one free CF_3SO_3^- anion and one solvent CH_2Cl_2 molecule compose the asymmetric unit of **1**. After complexation, **L** was no longer planar in complex **1**, which was evident from the dihedral angles between the central benzene ring and surrounding oxadiazole rings being $11.004(7)^\circ$, $16.914(8)^\circ$, and $21.110(5)^\circ$, respectively. As illustrated in Figure 2, the $\text{Ag}1$ and $\text{Ag}2$ coordination environments are distinct from each other. The $\text{Ag}1$ center

adopts a distorted tetrahedral coordination sphere, which consists of four $\text{N}_{\text{oxadiazole}}$ donors ($\text{N}1$, $\text{N}2^{\text{i}}$, $\text{N}3^{\text{ii}}$, and $\text{N}4^{\text{iii}}$) from four separate ligands. $\text{Ag}2$ is also four-coordinated by two $\text{N}_{\text{oxadiazole}}$ atoms ($\text{N}5$ and $\text{N}6^{\text{iv}}$) along with O atoms from a water molecule ($\text{O}7$) and CF_3SO_3^- anion ($\text{O}4$). The $\text{Ag}1$ -N bond lengths are in the range of $2.274(4)$ – $2.316(4)$ Å, which are longer than the bond lengths of $\text{Ag}2$ -N ($2.229(4)$ – $2.282(4)$) Å. The Ag-N and Ag-O bond lengths are in agreement with those values in a previous report.¹⁴

In the extended structure, neighboring $\text{Ag}1$ centers are bridged by four $\text{N}_{\text{oxadiazole}}$ atoms into a $\{\text{Ag}_2\text{N}_4\}$ dinuclear core ($\text{Ag}1\cdots\text{Ag}1$ distance of $3.8158(7)$ Å), which is similar to that found in compounds generated from oxadiazole-bridging double-armed ligands.¹⁴ Notably, the two adjacent $\{\text{Ag}_2\text{N}_4\}$ dinuclear units are almost perpendicular to each other (dihedral angle of 89.923°) and are arranged

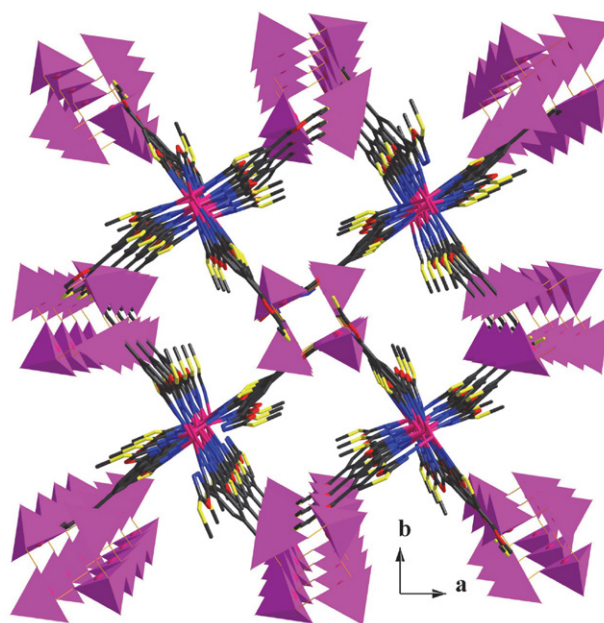


Figure 4. 3D framework of **1** (anions and CH_2Cl_2 molecules are omitted for clarity), and $\text{Ag}2$ centers are highlighted as fuchsia polyhedrons.

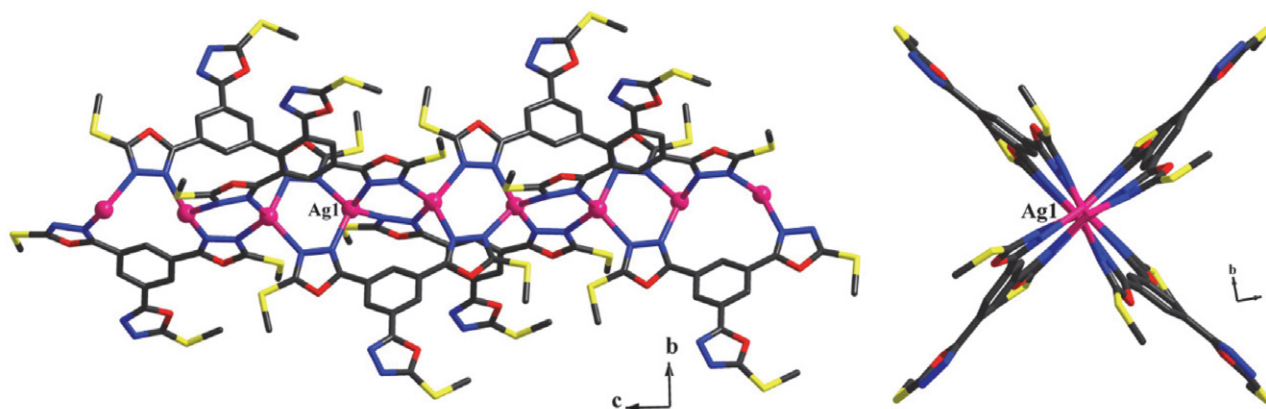


Figure 3. 1D chain structure consists of $\text{Ag}1$ in **1**.

alternately to form a 1D polymeric chain extending along the crystallographic *c* axis (Figure 3).

The remaining oxadiazole groups on these $\{\text{Ag}_2\text{N}_4\}_n$ chains adopt a $\mu_2\text{-}\eta^1\text{:}\eta^1$ bridging mode, connecting four Ag2 centers to form a twelve-membered $\{\text{Ag}_4\text{N}_8\}$ saddle-like ring (Figure S2). In the solid state, these $\{\text{Ag}_4\text{N}_8\}$ clusters are located between the $\{\text{Ag}_2\text{N}_4\}_n$ chains, and further link the 1D chains into a 3D microporous supramolecular network with rectangular channels along the *c* axis (Figure 4). The CF_3SO_3^- anions and solvent CH_2Cl_2 molecules are present in the channels. In summary, each **L** in compound **1** acts as a hexa-dentate ligand, binding to six Ag^+ atoms, in which all the $\text{N}_{\text{oxadiazole}}$ donors are utilized to bind Ag^+ ions into a 3D polymeric structure, whereas $\text{S}_{\text{methylthio}}$ donors are not involved in coordination.

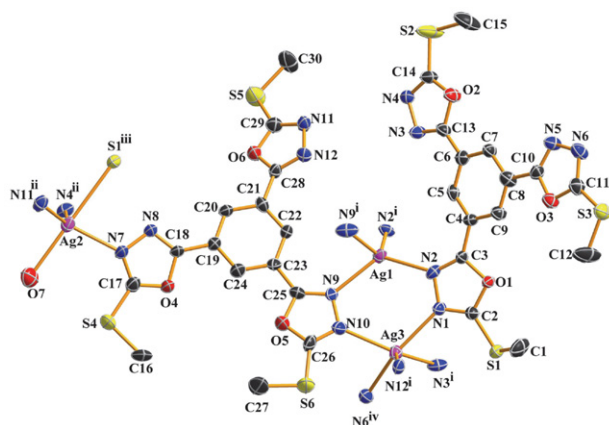


Figure 5. The coordination environment of Ag^+ in **2** at 50% probability displacement. (Anions and solvent molecules are omitted for clarity) Symmetry codes: (i) $-x+3/2, -y+3/2, z$; (ii) $-x+1, -y+3/2, z+1/2$; (iii) $x-1/2, y, z+1/2$; (iv) $-x+7/4, y-1/4, z+1/4$.

To investigate the effect of the counter anions on the structural motif of the $\{\text{Ag}^+\text{-L}\}$ coordination system, the weakly coordinated SbF_6^- anion was used instead of the strongly coordinated CF_3SO_3^- anion for the self-assembly reaction in the same $\text{CH}_2\text{Cl}_2/\text{THF}$ solvent system; this produced compound **2** with a 40% yield. Single crystal analysis revealed that five crystallographically independent Ag^+ ions, four ligands, two coordinated water molecules, five free SbF_6^- anions, and five tetrahydrofuran molecules constitute the asymmetric unit of **2**. In complex **2**, the dihedral angles between the central benzene ring and surrounding oxadiazole rings exhibit a large difference. For the central benzene ring involving C4–C9, the dihedral angles are $0.771(2)^\circ$, $8.022(4)^\circ$, and $23.962(6)^\circ$, respectively. For the central benzene ring involving C19–C24, the dihedral angles are $4.827(6)^\circ$, $18.136(8)^\circ$, and $31.515(8)^\circ$, respectively.

There are three independent Ag^+ centers in **2** (Figure 5). The first center, Ag1, is located in a distorted tetrahedral coordination sphere with four $\text{N}_{\text{oxadiazole}}$ donors (N2, N9, N2', and N9'). The Ag1–N bond lengths are 2.257(5)–2.328(6) Å. Ag2 is five-coordinated by three $\text{N}_{\text{oxadiazole}}$ donors (N7, N4ⁱⁱ, and N11ⁱⁱⁱ), one S atom and one O atom from a water molecule. The Addison distortion index, τ ($\tau = (\beta - \alpha)/60$, where α and β are the two largest coordinated angles in the complex; perfect square pyramidal, $\tau = 0$; perfect trigonal bipyramidal, $\tau = 1$),¹⁹ for Ag2 is 0.72, indicating a distorted trigonal bipyramidal coordination sphere. The axial O7–Ag2–S1ⁱⁱⁱ angle of $178.13(17)^\circ$ is slightly smaller than the ideal value of 180° . The equatorial Ag2–N bond lengths are 2.325(6)–2.374(6) Å, while the axial Ag2–O7 and Ag2–S1ⁱⁱⁱ distances are 2.466(6) and 2.9549(19) Å, respectively; thus, it is an elongated trigonal bipyramidal structure. Ag3 is also five-coordinated, with a

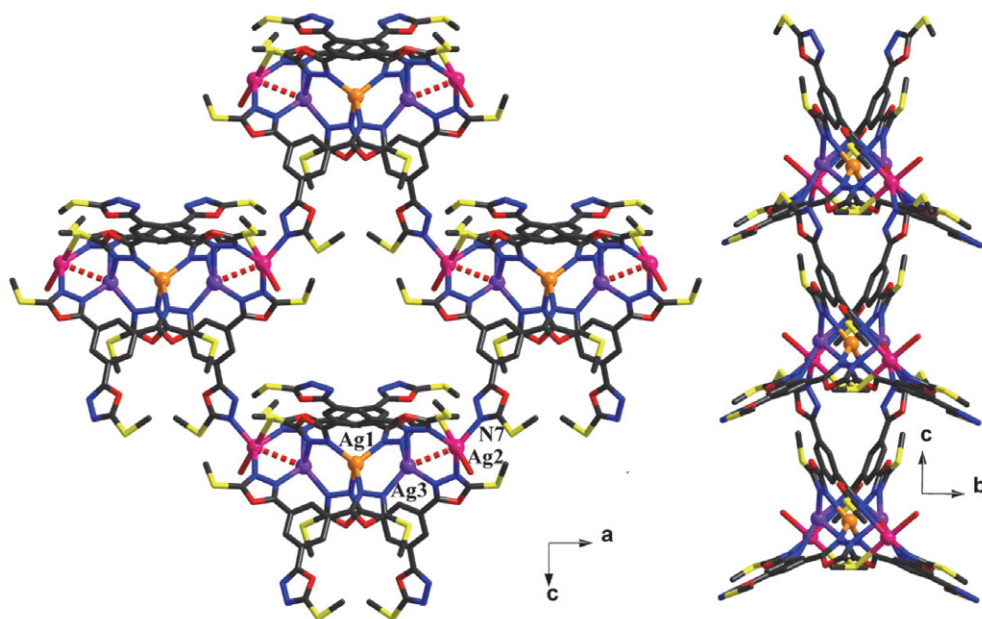


Figure 6. View of 2D network in **2**, front and side views are presented.

τ of 0.33. Therefore, Ag3 is best described as distorted square pyramidal with N10 in axial positions and the other N donors (N1, N3ⁱ, N6^{iv}, and N12ⁱ) forming the equatorial plane. The bond angles around the Ag⁺ center range from 79.2(2) to 152.4(2)° in the equatorial positions and from 82.7(2) to 132.2(2)° for the apical positions. Ag3-N bond lengths are 2.325(7)–2.548(6) Å, which is the longest among these Ag-N bonds.

have been used as antimicrobials since the successful use of silver-containing creams for burn treatment.²² We have reported the antibacterial activities of silver complexes based on quinoline or hydrazone scaffolds.^{18,23,24} As a continuation of our efforts in exploring new antibacterial reagents to supplement structure–activity information, the *in vitro* antibacterial activities of the synthesized compounds were assessed. The IC₅₀ (half minimum inhibitory concen-

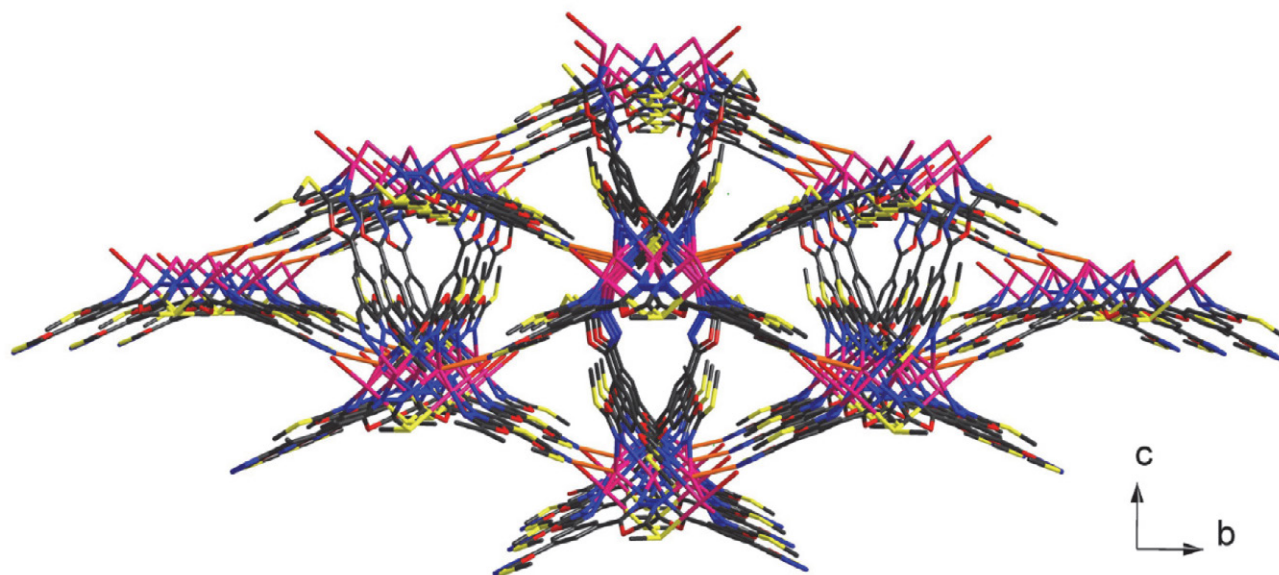


Figure 7. View of 3D network of **2** along *a* axis (anions and THF molecules are omitted for clarity).

The {Ag₂N₄} dinuclear moieties were also found in compound **2**. The shortest Ag2...Ag3 distance is 3.2013(8) Å (while the Ag3...Ag1 separation is 3.713(1) Å), indicating weak Ag...Ag interactions. In the solid state, four {Ag₂N₄} units are interlocked together into a butterfly-like penta-nuclear sub-building block (as shown in Figure S3). These sub-building blocks are strung together by the Ag2-N7 bond into a two-dimensional sheet extending in the crystallographic *ac* plane, as shown in Figure 6. These 2D layers are further connected by Ag3-N6 linkages into a three-dimensional network with triangular channels along the crystallographic *a* axis, in which uncoordinated SbF₆⁻ counteranions and THF guest molecules are located in place of CH₂Cl₂ (Figure 7). Principally, one of the L ligand in compound **2** acts as a hexa-dentate ligand, binding to six Ag⁺ via N1, N2, N3, N4, N6, and S1, while the other ligand acts as a penta-dentate ligand, binding to five Ag⁺ via N7, N9, N10, N11, and N12.

3. 2. Antibacterial Activity

Among the diverse transition metals, silver has fundamental importance in bioinorganic chemistry, and the use of silver metal complexes for medicinal applications has been well documented.^{20,21} Silver-based complexes

(values of the test compounds are presented in Table 4. Known antibiotic, such as streptomycin, was used as control drug.

Table 4 Antimicrobial activity of the tested compounds.

Compounds	Half maximal inhibitory concentrations (µg/mL)			
	Gram-negative		Gram-positive	
	<i>E.coli</i>	<i>Paeruginosa</i>	<i>B.subtilis</i>	<i>S.aureus</i>
L	>50	>50	>50	>50
1	8.62	9.35	13.41	10.41
2	9.43	7.56	15.23	6.74
AgSO₃CF₃	3.53	3.27	8.21	4.67
AgSbF₆	2.03	0.19	7.02	3.87
Streptomycin	3.94	>50	4.12	5.24

As shown in Table 4, against all the tested bacteria, the free ligand **L** was inactive under the tested conditions. However, the introduction of Ag⁺ on the ligand resulted in improved antibacterial activity, especially against the tested gram-negative strains, with IC₅₀ values of 7.56 to 9.43 µg mL⁻¹. For the tested gram-negative strains, the IC₅₀ values ranged from 6.74 to 15.23 µg mL⁻¹. It is evident that the

activity of the two complexes is dependent primarily on the presence of the Ag^+ ion. It has been found that the nature of ligands, chelate effect of ligands, nuclearity, and total charge are the main factors contributing to the biological activity of the Ag-compounds.²⁵ Compared with our previously reported quinoline-silver(I) complexes and hydrazone-silver(I) complexes, the bioactivities of **1** and **2** are slightly lower. This can be attributed to the lack of a chelate effect because the $\text{N}_{\text{oxadiazole}}$ donors of **L** in **1** and **2** are all in the bridging mode.

4. Conclusions

In conclusion, we synthesized and characterized two novel 3D Ag(I) coordination polymers generated from the oxadiazole-containing tri-armed ligand **L**. Complexes **1** and **2** are both three-dimensional frameworks, but **L** features different coordination modes in them. **L** in complex **1** acts as a hexa-dentate ligand (binding to six Ag^+ atoms *via* all the N donors), while in **2**, one of the ligands acts as a hexa-dentate ligand (binding to six Ag^+ atoms *via* five N donors and one S donor), and the other **L** acts as a penta-dentate ligand (binding to five Ag^+ *via* five N donors). The structural diversity reveals that inorganic counter anions play an important role in building up the coordination framework. In addition, complexes **1** and **2** exhibited potent antibacterial activity.

5. References

1. E. G. R. de Arruda, M. A. de Farias, S. A. V. Jannuzzi, S. D. A. Gonsales, R. A. Timm, S. Sharma, G. Zoppellaro, L. T. Kubota, M. Knobel, A. L. B. Formiga, *Inorg. Chim. Acta* **2017**, *466*, 456–463. DOI:10.1016/j.ica.2017.06.073
2. A. Rühling, H. J. Galla, F. Glorius, *Chem. Eur. J.* **2015**, *21*, 12291–12294. DOI:10.1002/chem.201502542
3. J. Rodriguez, D. Bourissou, *Angew. Chem. Int. Ed.* **2018**, *57*, 386–388. DOI:10.1002/anie.201710105
4. T. P. Latendresse, V. Vieru, B. O. Wilkins, N. S. Bhuvanesh, L. F. Chibotaru, M. Nippe, *Angew. Chem. Int. Ed.* **2018**, *57*, 8164–8169. DOI:10.1002/anie.201804075
5. M. B. Coban, E. Gungor, H. Kara, U. Baisch, Y. Acar, *J. Mol. Struct.* **2018**, *1154*, 579–586. DOI:10.1016/j.molstruc.2017.10.049
6. A. T. Baryshnikova, B. F. Minaev, G. V. Baryshnikov, H. Ågren, *Inorg. Chim. Acta* **2019**, *485*, 73–79. DOI:10.1016/j.ica.2018.09.086
7. I. Ahmed, S. H. Jhung, *Chem. Eng. J.* **2017**, *310*, 197–215. DOI:10.1016/j.cej.2016.10.115
8. Y. Y. Jia, X. T. Liu, R. Feng, S. Y. Zhang, P. Zhang, Y. B. He, Y. H. Zha-ng, X. H. Bu, *Inorg. Chem. Front* **2016**, *3*, 1510–1515. DOI:10.1039/C6QI00191B
9. W. P. Lustig, S. Mukherjee, N. D. Rudd, A. V. Desai, J. Li, S. K. Ghosh, *Chem. Soc. Rev.* **2017**, *46*, 3242–3285. DOI:10.1039/C6CS00930A
10. M. Gon, K. Tanaka, Y. Chujo, *Bull. Chem. Soc. Jpn.* **2019**, *92*, 7–18. DOI:10.1246/bcsj.20180245
11. L. N. Wang, L. Fu, J. W. Zhu, Y. Xu, M. Zhang, Q. You, P. Wang, J. Qin, *Acta Chim. Slov.* **2017**, *64*, 202–207. DOI: 10.17344/acsi.2016.3109
12. C. W. Zhao, J. P. Ma, Q. K. Liu, X. R. Wang, Y. Liu, J. Yang, J. S. Yang, Y. B. Dong, *Chem. Commun.* **2016**, *52*, 5238–5241. DOI:10.1039/C6CC00189K
13. Y. B. Dong, Q. Zhang, L. L. Liu, J. P. Ma, B. Tang, R. Q. Huang, *J. Am. Chem. Soc.* **2007**, *129*, 1514–1515. DOI:10.1021/ja067384z
14. Y. B. Dong, H. X. Xu, J. P. Ma, R. Q. Huang, *Inorg. Chem.* **2006**, *45*, 3325–3343. DOI:10.1021/ic052158w
15. Bruker, SMART and SAINT. Bruker AXS Inc., Madison, Wisconsin, USA, **2002**.
16. G. M. Sheldrick, SADABS. Program for Empirical Absorption Correction of Area Detector, University of Göttingen, Germany, **1996**.
17. G. M. Sheldrick, *Acta Crystallogr.* **2008**, *A64*, 112–122. DOI:10.1107/S0108767307043930
18. L. Zhang, Z. W. Man, Y. Zhang, J. Hong, M. R. Guo, J. Qin, *Acta Chim. Slov.* **2016**, *63*, 891–898. DOI:10.17344/acsi.2016.2895
19. A. W. Addison, T. N. Rao, *J. Chem. Soc., Dalton Trans.* **1984**, 1349–1356. DOI:10.1039/DT9840001349
20. K. Gholivand, F. Molaei, N. Oroujzadeh, R. Mobasseri, H. Naderi-Manesh, *Inorg. Chim. Acta* **2014**, *423*, 107–116. DOI:10.1016/j.ica.2014.07.029
21. J. H. B. Nunes, R. E. F. de Paiva, A. Cuin, W. R. Lustri, P. P. Corbi, *Polyhedron* **2015**, *85*, 437–444. DOI:10.1016/j.poly.2014.09.010
22. S. Silver, L. T. Phung, G. Silver, *J. Ind. Microbiol. Biotechnol.*, **2006**, *33*, 627–634. DOI:10.1007/s10295-006-0139-7
23. S. S. Zhao, P. Wang, L. N. Wang, L. Fu, X. M. Han, J. Qin, S. S. Qian, *J. Coord. Chem.* **2017**, *70*, 885–897. DOI:10.1080/00958972.2017.1281915
24. Q. L. Ren, S. S. Zhao, L. X. Song, S. S. Qian, J. Qin, *J. Coord. Chem.* **2016**, *69*, 227–237. DOI:10.1080/00958972.2015.1110240
25. M. Zampakou, S. Balala, F. Perdih, S. Kalogiannis, I. Turel, G. Psomas, *RSC Adv.* **2015**, *5*, 11861–11872. DOI:10.1039/C4RA11682H

Povzetek

Z reakcijo med triveznim ligandom z oksadiazolom, 1,3,5-tri(2-metiltio-1,3,4-oxadiazol-5il) benzen (**L**), in srebrovimi solmi v mediju CH₂Cl₂/THF smo sintetizirali dva koordinacijska polimera, [Ag₂(**L**)(SO₃CF₃)(H₂O)](SO₃CF₃)•CH₂Cl₂ (**1**) in [Ag₅(**L**)₄(H₂O)₂](SbF₆)₅•5THF (**2**). Spojini kristalizirata v tetragonalni prostorski skupini *I*₄₁/*a* oziroma ortoromb-ski prostorski skupini *Fdd*2. Rentgenska difrakcija na monokristalu je pokazala bistvene razlike med 3D polimernima strukturama obeh spojin, kar lahko pripišemo različnim protionom. V spojini **1** je ligand **L** šestvezen in koordiniran na dve vrsti Ag⁺ ionov s katerimi tvori 3D polimerno strukturo. V spojini **2** je ligand **L** pet- in šestvezen in koordiniran na tri vrste Ag⁺ ionov s katerimi prav tako tvori 3D polimerno strukturo. Raziskovali smo tudi protibakterijsko učinkovitost novih koordinacijskih spojin.



Except when otherwise noted, articles in this journal are published under the terms and conditions of the Creative Commons Attribution 4.0 International License

Scientific paper

Prediction of Biological Activities, Structural Investigation and Theoretical Studies of *meta*-cyanobenzyl Substituted Benzimidazolium Salts

Duygu Barut Celepci^{1,*} and Aydın Aktaş^{2,3}¹ Dokuz Eylül University, Faculty of Science, Department of Physics, İzmir, Turkey² İnönü University, Vocational School of Health Service, 44280, Malatya, Turkey³ İnönü University, Faculty of Science, Department of Chemistry 44280, Malatya, Turkey

* Corresponding author: E-mail: duygu.barut@deu.edu.tr

Received: 12-18-2019

Abstract

The structural properties of *meta*-cyanobenzyl substituted *N*-heterocyclic carbene (NHC) precursors were investigated theoretically. The molecular and crystal structure of one of the compounds was determined by using the single-crystal X-ray diffraction method. Global reactivity descriptors were analyzed to understand the biological activity behaviors of the compounds with *Density Functional Theory* (DFT) B3LYP method with 6-31G* basis set. Vibrational frequencies, chemical shifts and absorption wavelengths were computed and compared to experimental data. A predictive study for the biological activities was done using PASS (prediction of activity spectra for biologically active structures) online software. Biological activity predictions showed the analgesic, substance P antagonist, non-opioid and antiinflammatory activities of the compounds.

Keywords: *N*-heterocyclic precursors; crystal structure; DFT; PASS online

1. Introduction

N-heterocyclic carbenes (NHC) are cyclic carbenes containing at least one amino substituent.¹ NHCs were first pioneered by Öfele, Wanzlick, and Schönherr in 1968 and the isolation of the first stable crystalline carbene was performed by Arduengo in 1991.^{2–4} After the stability of the NHC ligands was registered, they have been attracted great interest in the field of organic and organometallic chemistry. Especially, in medical applications, there have been various studies of metal-NHCs.^{5–7} The chelating effect of NHC precursors with unique sigma donor properties could be effective in biological activity.^{8,9} In our previous study, the investigations on the biological activity of NHC compounds containing cyanobenzyl substituents show that these compounds have exhibited biological activity.¹⁰

Biological experiments are often limited in terms of sample, time and cost. In this context, DFT-based reactivity descriptors are advantageous and generally be consistent with the experimental observations.¹¹ In recent years, the prediction of the reactivity of chemical systems is one

of the main purposes of theoretical chemistry. Density functional theory (DFT) has been quite successful in providing the theoretical groundwork of this purpose. For analyzing and understanding the biological reactivity of the chemical systems, several reactivity descriptors have been proposed. In this work, biological reactivity studies of three compounds **2b**, **2f** and **2g** were carried out through these global reactivity descriptors. Geometries of the compounds were optimized and bonding parameters were compared to the experimental data. Frontier molecule orbitals (HOMO and LUMO) and the energy values were computed. Natural bond orbital (NBO) analysis was used to analyze the stability of the molecules arising from hyperconjugative interactions and charge delocalization. The vibrational frequencies, chemical shifts and absorption wavelengths were calculated and compared to the experimental ones. Also, PASS (prediction of activity spectra for biologically active structures) online software was used to predict the putative biological activity spectra of the compounds. DFT studies and PASS online predictions point out the similar activity results for the compounds.

It is believed that this kind of study will contribute to getting a better understanding of the chemical behavior of *meta*-cyanobenzyl substituted benzimidazolium salts. As proved by enzyme inhibition studies,¹⁰ these compounds can be a candidate as new drugs for therapy of some diseases such as glaucoma, epilepsy, gastric and duodenal ulcers, osteoporosis, mountain sickness, or neurological disturbances.

2. Experimental

The synthesis, some spectroscopic results and enzyme inhibition studies of the compounds **2b**, **2f**, **2g** and single-crystal X-ray diffraction studies of the **2f** and **2g** were reported previously.¹⁰ In this work, firstly, we determined the crystal structure of **2b** by single-crystal X-ray diffraction method. Then, the theoretical studies were performed for all structures.

2.1. X-ray Crystallography

The single-crystal X-ray diffraction study of the compound **2b** was performed by ω -scan technique, using a Rigaku-Oxford Xcalibur diffractometer with an EOS-CCD area detector operated at 50 kV and 40 mA using graphite-monochromated MoK α radiation ($\lambda = 0.71073$ Å) from an enhance X-ray source with CrysAlis^{Pro} software.¹² Data reduction and analytical absorption corrections were carried out by CrysAlis^{Pro} program.¹³ The structure was solved by the *Intrinsic Phasing* method with SHELXT and refined utilizing the SHELXL program^{14,15}

incorporated in the OLEX2 program package.¹⁶ The crystallographic data and some parameters of refinement are placed in Table 1. Anisotropic thermal parameters were applied to all non-hydrogen atoms. All the hydrogen atoms were placed using standard geometric models and with their thermal parameters riding on those of their parent atoms.

2.2. Computational Details

The compounds **2b**, **2f** and **2g** were optimized, chemical shifts and frontier molecular orbital energies were carried out by using DFT/B3LYP with the basis set 6-31G* by Gaussian 09W and GaussView 6.0 molecular visualization programs.^{17,18} Natural bond orbital (NBO) analysis was performed using NBO 3.1 program as implemented in the Gaussian 09 package at the same level of the theory.¹⁹ The normal mode assignments of the compounds were employed by VEDA²⁰ program and verified by GaussView 6.0. The NMR chemical shifts were computed in the gaseous state within GIAO (Gauge-Independent Atomic Orbital) approach by subtracting the shielding constants of TMS.²¹ The biological activity spectra of studied compounds **2b**, **2f** and **2g** were obtained by the PASS Online Program (<http://www.way2drug.com/PASSOnline/>).

3. Results & Discussions

3.1. Crystal Structure of Compound 2b

Single-crystal X-ray diffraction analyses reveal that the compound **2b** crystallizes in the orthorhombic space

Table 1. Crystal data and experimental details for the compound **2b**.

Empirical Formula	C ₂₃ H ₂₀ BrN ₃
Formula Weight	418.33
Temperature (K)	293(2)
Crystal System, space group	Orthorhombic, <i>Pca</i> 2 ₁
<i>a</i> , <i>b</i> , <i>c</i> (Å)	14.6406(7), 7.9998(4), 17.0884(9)
α , β , γ (°)	90, 90, 90
<i>V</i> (Å ³)	2001.43(17)
<i>Z</i>	4
Density (calculated) (g/cm ³)	1.388
Absorption coefficient (μ , mm ⁻¹)	2.066
<i>F</i> (000)	856
Crystal size (mm ³)	0.360 × 0.259 × 0.253
Radiation	MoK α ($\lambda = 0.71073$)
2 θ range for data collection (°)	6.054 to 51.364
Index ranges	-10 ≤ <i>h</i> ≤ 17, -9 ≤ <i>k</i> ≤ 9, -20 ≤ <i>l</i> ≤ 20
Reflections collected	8295
Independent reflections	3441 [<i>R</i> _{int} = 0.0322, <i>R</i> _{sigma} = 0.0441]
Restraints/Parameters	4/245
Goodness-of-fit on <i>F</i> ²	1.015
Final <i>R</i> indices [<i>I</i> ≥ 2 σ (<i>I</i>)]	<i>R</i> ₁ = 0.0335, <i>wR</i> ₂ = 0.0599
<i>R</i> indices	<i>R</i> ₁ = 0.0529, <i>wR</i> ₂ = 0.0661
Largest diff. peak/hole (eÅ ⁻³)	0.20/-0.20

group $Pca2_1$. The asymmetric unit of the compound contains a *meta*-cyanobenzyl-substituted benzimidazolium cation and a bromide anion (Fig. 1). The single-crystal X-ray diffraction studies reveal that the benzimidazolium ring system is almost coplanar with the r.m.s. deviation of 0.007(6) Å. Cyanobenzyl and methylbenzyl fragments lie to the different sides of the benzimidazole ring system, giving the cation a Z-shape. The dihedral angles between the benzimidazolium ring and the mean plane of these fragments are 67.83(9)° and 69.27(2)°, respectively. Two

C–H...Br type intermolecular interactions are observed in the crystal structure; one is between the most acidic proton of the imidazolium cation and the bromide anion [C1–H1...Br1, H1...Br1 = 2.61 Å, C1–Br1 = 3.545(5) Å, C1–H1...Br1=155°], the other interaction is C16–H16B...Br1ⁱ [H16B...Br1ⁱ=2.85 Å, C16–Br1ⁱ=3.813(6) Å, C1–H1...Br1ⁱ = 170°]. Fig.2 displays the infinite chain occurs *via* these hydrogen bonds along the *b*-axis. The molecules stacked in the crystal structure to form a *pincers-like* packing motif, as shown in Fig. 3.

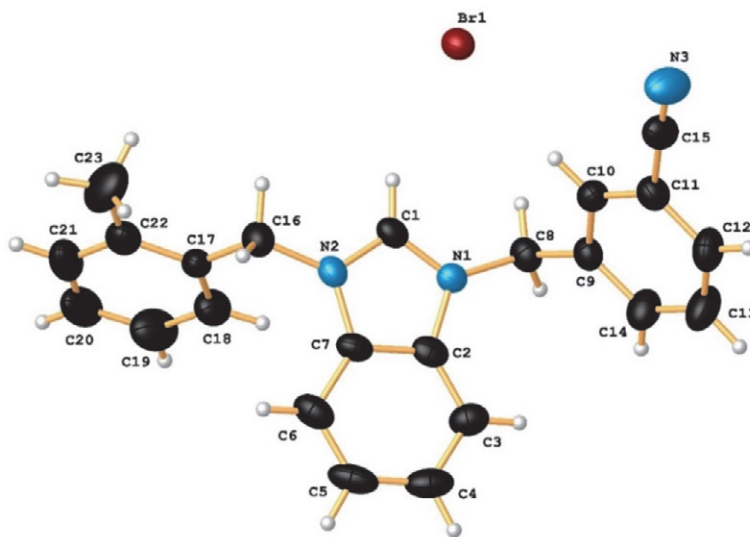


Fig. 1. Structure of **2b** with ellipsoids plotted at 30% probability. Selected bond parameters (Å,°): N1–C1 1.327(6), N1–C2 1.389(5), N1–C8 1.472(5), N2–C1 1.326(5), N2–C7 1.389(6), N2–C16 1.459(6), N3–C15 1.138(7); N1–C1–N2 111.0(4), C1–N1–C8 125.6(4), N1–C8–C9 113.2(4), C2–N1–C8 126.3(4), C1–N2–C16 125.4(4), C7–N2–C16 127.0(4), N2–C16–C17 113.0(4), C11–C15–N3 177.2(8).

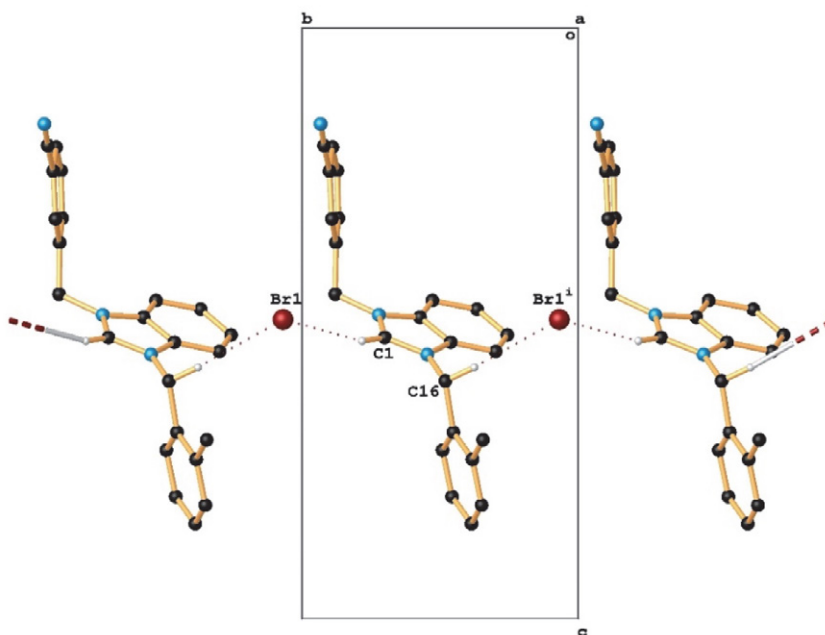


Fig. 2. Packing of the cation molecules of **2b** through the intermolecular hydrogen bonds bridged by the bromide anions, which lead to the infinite chain along the *b* axes. All hydrogen atoms except those participating in the hydrogen bonds were omitted for clarity. Cation molecules are shown in the stick drawing style.

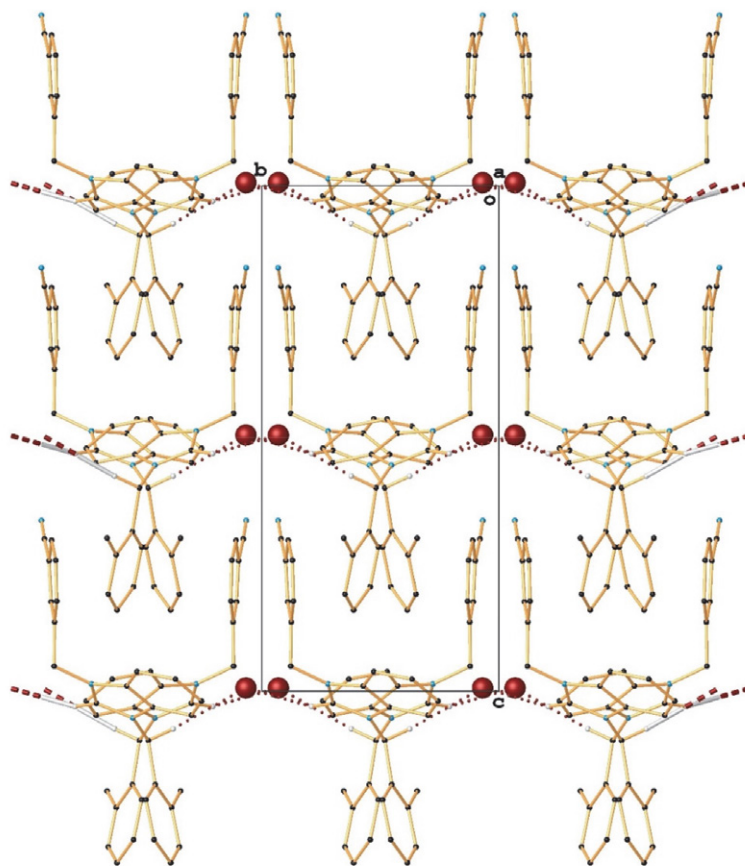


Fig. 3. Graphical representation of *pincers-like* packing motif the molecules within the unit cell for **2b**.

3. 2. Geometry Optimization, Frontier Molecular Orbitals and Global Reactivity Descriptors

The optimized ground state geometry of the compounds at DFT/B3LYP/6-31G* level of the theory is shown in Fig. 4. The correlations between the theoretical and experimental bonding parameters were displayed in Fig. S1 (see supplementary information file). It is clearly

understood from the figure that there are some discrepancies between the experimental and computed bond parameters. While the theoretical calculations of the isolated structure were carried out in the gas phase, the fact that the experimental molecular structures were in a solid-state form likely caused these differences. Also, the experimental structures have intermolecular interactions, which may cause discrepancies in the bonding parameters.

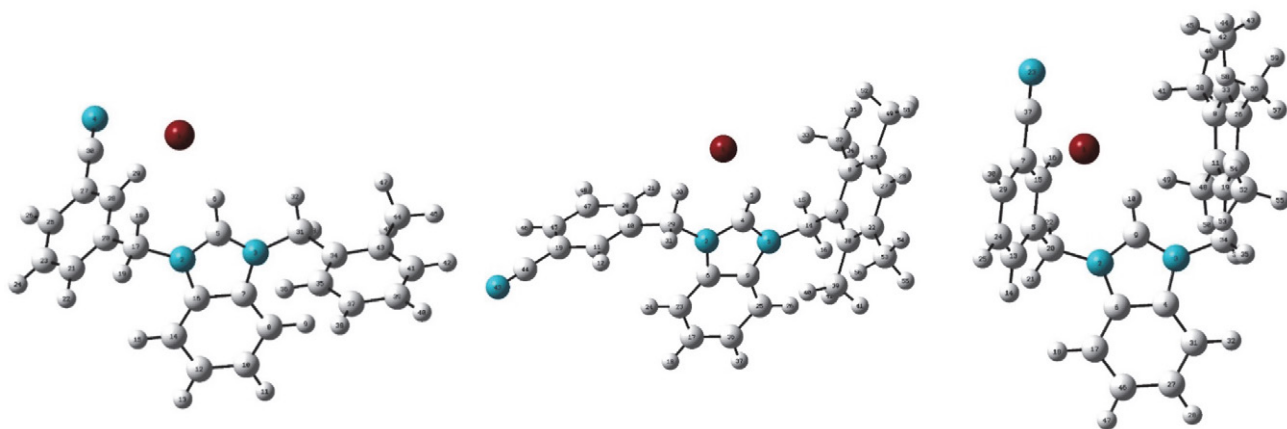


Fig. 4. Optimized geometries of the compounds **2b**, **2f** and **2g**, respectively.

The FMOs theory involving HOMO and LUMO is one of the best theories to get an insight into the chemical stability of a molecule.²² The highest occupied molecular orbital (HOMO) represents the distribution and energy of the least tightly held electrons in the molecule and the lowest unoccupied molecular orbital (LUMO) describes the easiest route to the addition of more electrons to the system. The high value of E_{HOMO} indicates the ease of donating an electron to the unoccupied orbital of the receptor molecule, and the small value of E_{LUMO} means that it has small resistance to accept electrons so it will be more able to accept electrons. The difference between HOMO and LUMO energy values gives the HOMO-LUMO energy gap (E_{gap}) and it is an important stability index.²³ A molecule with large E_{gap} is described as a hard molecule, much less polarizable, and implies high molecular stability and aromaticity low reactivity in chemical reactions.^{24,25} The soft systems have small E_{gap} , they are highly polarizable and exhibit a significant degree of intramolecular charge transfer from the electron donor to the electron acceptor and conjugation that may influence the biological activity of the molecule.²⁶

To evaluate the energetic behavior of the compounds, the HOMO-LUMO analysis was carried out by using B3LYP/6-31G* method, and the plots are depicted in Table 2. As can be seen, compounds show different localization of the HOMOs and LUMOs. The HOMO of the **2b** and **2g** is located on the bromide anions, while in **2f**, it is distributed to the bromide anion and the benzimidazolium fragment of the cation molecule. Similarly, LUMO electron density of **2f** is spread over the cyanobenzyl moiety, but for **2b** and **2g**, the LUMO electrons are mainly located on the benzimidazolium ring. The values of energy separation between the HOMO-LUMO were found as 2.930, 3.845 and 3.011 eV, respectively.

The global reactivity descriptors calculated using the DFT method play an essential and reliable role to understand the biological activities in many studies. Some of these descriptors are; the global hardness (η), which measures the resistance to change in electron density; chemical potential (μ), measures the escaping tendency of an electron; electronegativity (χ), describes the ability of a molecule to attract electrons towards itself; electrophilicity index (ω), measures the susceptibility of chemical species to accept electrons; softness (S), is the inverse of hardness; the maximum charge transfer (ΔN_{max}), describes the propensity of the system to acquire additional electronic charge from the environment.^{27,28} These global reactivity parameters can be defined as:

$$\mu = -\frac{(I+A)}{2} \quad \chi = -\mu \quad \eta = \frac{(I-A)}{2} \quad (1)$$

$$\omega = \frac{\mu^2}{2\eta} \quad S = \frac{1}{2\eta} \quad \Delta N_{\text{max}} = -\frac{\mu}{\eta} \quad (2)$$

where I is the ionization potential ($I = -E_{\text{HOMO}}$) and A is the electron affinity ($A = -E_{\text{LUMO}}$).

The calculated values of reactivity descriptors of the compounds are listed in Table 3. The hardness (η) values of the compounds are following the order **2f** > **2g** > **2b**. It is expected that the high value of softness (S), defined as the inverse of hardness, is the representative of high reactivity. According to these parameters, **2b** seems the most reactive compound. Also, the E_{gap} of **2b** is the smallest one, this indicates that **2b** is softer than other compounds, its electronic chemical potential (μ) and electrophilicity index (ω) values are the greatest and the maximum charge transfer capability (ΔN_{max}) is the highest. The dipole moments of the compounds are 15.136 Debye for **2b**, 7.264 Debye for **2f** and 13.600 Debye for **2g**, proved that the most stable compound is **2f**, while the **2b** is the most reactive.

3. 3. Mulliken Population Analysis, Natural Population Analysis (NPA) and Molecular Electrostatic Potential (MEP)

Mulliken atomic charges and natural population analysis (NPA) play an important role in quantum chemistry. The atomic charge distribution of acceptor and donor atoms in molecules is directly affected by parameters such as polarizability, refractivity, dipole moment, and other electronic structural parameters.²⁹ Mulliken population charge analysis and natural population analysis of structures were performed using B3LYP/6-31G* level of calculation and a list of all calculated atomic charges are given in Table S1 (see supplementary file). The analyses reveal the presence of electrophilic and nucleophilic atomic charges. According to the results, the bromide anions of the compounds display high nucleophilic behavior with their negative donor atomic charges, while the 2-C-H protons have the highest positive charge value. So, bromide anions attack the hydrogen atom of 2-C carbons, which is the most reactive site of the molecules.

The molecular electrostatic potential (MEP) is related to the electron density and is a useful descriptor in understanding the reactive behavior in both electrophilic and nucleophilic reactions and hydrogen bonding reactions.³⁰ In the MEP profile, the areas with major positive potential are specified by blue color, which demonstrates the strongest attraction, whereas the maximum negative potential sections have been presented red color, indicates the repulsion. Comparing with the X-ray data it was concluded that the MEP plots proved the intermolecular hydrogen bonds between the bromide anion and cation molecules for all structures (Table 2). The negative potential regions are over the electronegative bromide anions, which are responsible for the intermolecular C–H...Br hydrogen bonds. Also, the N≡C of cyanobenzyl groups of all structures have red colors which means these regions are the electron-rich nucleophilic regions. The net charges of the nitrogen atoms of cyanobenzyl groups confirmed the MEP output.

Table 2. The molecular orbitals for HOMO-LUMO and MEP diagrams of the compounds.

	2b	2f	2g
LUMO+2			
LUMO+1			
LUMO			
HOMO			
HOMO-1			
HOMO-2			
MEP			

Table 3. Global descriptors of chemical reactivity of *meta*-cyanobenzyl substituted benzimidazolium salts.

(eV)	2b	2f	2g
$E_{HOMO} (-I)$	-4.799	-5.335	-4.861
$E_{LUMO} (-A)$	-1.869	-1.490	-1.850
E_{gap}	2.930	3.845	3.011
Electronegativity χ	3.334	3.413	3.356
Chemical hardness η	1.465	1.923	1.506
Electronic chemical potential μ	-3.334	-3.413	-3.356
Electrophilicity index ω	3.794	3.029	3.739
Softness S	0.341	0.260	0.332
Maximum charge transfer capability ΔN_{max}	2.276	1.775	2.228

3. 4. Natural Bond Orbital (NBO) Analysis

The natural bond orbital analysis (NBO) is an effective method for predicting the stereoelectronic interactions on the reactivity and dynamic behaviors of chemical compounds.³¹ It provides a convenient basis for investigating charge transfer or conjugative interaction in molecular systems. The interactions depend on the energy difference between interacting orbitals, and the strong interactions arise between predominant donor and acceptor. The second-order perturbation analysis of the Fock matrix is used to calculate stabilization energy for each donor (i) and acceptor (j) within $i \rightarrow j$ delocalization. The estimated energy can be determined as $E(2) = \Delta E_{ij} = q_i \frac{F_{ij}^2}{E_j - E_i}$, where q_i is donor orbital occupancy, E_i and E_j are diagonal elements and F_{ij} is the off-diagonal NBO Fock matrix element. The larger the $E(2)$ value means the more intensive interaction between electron donors and acceptors.³² The natural bond orbitals' (NBO) calculations for the structures were

performed at the DFT/B3LYP/6-31G* method. The stabilization energies of the most important interactions between donor and acceptor along with occupancy are given in Table 4. According to the table, the strongest interactions ($\pi \rightarrow \pi^*$) occur in the NHC ligand for all structures. In the **2b** and **2g**, the electron donation from a lone-pair orbital on the carbon atom of benzimidazole, LP(1) C16 and LP(1) C6, to the antibonding acceptors π^* N3–C7 (233.49 kJ/mol), π^* C12–C14 (58.10 kJ/mol) and π^* N3–C4 (219.31 kJ/mol), π^* C17–C46 (58.79) orbitals have also high stabilization energies. In the compound **2f**, from the lone-pair orbital of LP(1) N3 to the π^* N2–C4 has the energy of 82.11 kJ/mol.

3. 5. UV-Vis Analysis of the Compounds **2b**, **2f** and **2g**

The UV-Vis spectra of the *meta*-cyanobenzyl substituted benzimidazolium salts **2b**, **2f** and **2g** were recorded

Table 4. The Second Order Perturbation Theory Analysis Results of the Fock Matrix in NBO Basis for **2b**, **2f** and **2g** at B3LYP/6-31G* level of the theory.

Donor(i)	Acceptor(j)	ED _i (e)	ED _j (e)	E(2) kJ/mol	$E_j - E_i$ (a.u)	F_{ij} (a.u)
2b						
π^* N3–C7	π^* N2–C5	0.8166	0.4510	245.94	0.01	0.063
LP(1) C16	π^* N3–C7	1.0440	0.8166	233.49	0.08	0.123
LP(1) C16	π^* C12–C14	1.0440	0.3062	58.10	0.16	0.104
2f						
π^* C6–C9	π^* C25–C36	0.4719	0.3343	217.58	0.02	0.082
π^* C10–C11	π^* C20–C47	0.3349	0.2821	190.65	0.01	0.081
π^* C6–C9	π^* C17–C23	0.4719	0.3274	188.55	0.02	0.082
π^* C19–C45	π^* C20–C47	0.3848	0.2821	179.27	0.02	0.082
LP(1) N3	π^* N2–C4	1.5551	0.5650	82.11	0.21	0.122
2g						
π^* N3–C4	π^* N2–C9	0.8011	0.4644	321.23	0.01	0.064
π^* C12–C26	π^* C8–C33	0.3536	0.3265	261.24	0.01	0.081
LP(1) C6	π^* N3–C4	1.0410	0.8011	219.31	0.08	0.122
π^* C11–C19	π^* C8–C33	0.3938	0.3265	177.46	0.02	0.084
LP(1) C6	π^* C17–C46	1.0410	0.3086	58.79	0.16	0.104

with Shimadzu UV-1601 instrument in ethyl alcohol solutions at a concentration of 15 or 20 μM at 25 $^{\circ}\text{C}$ and they were depicted with a range of 200–400 nm. The calculations of the title molecules were performed in ethyl alcohol solvent by using TD-DFT/B3LYP/6-31G* method. Table 5 shows the experimental and calculated UV-Vis spectroscopic parameters (absorption wavelengths (λ), excitation energies and oscillator strengths (f)). Also, Fig. S2 displays the theoretical UV-Vis spectra of the compounds. The UV-Vis spectra of *meta*-cyanobenzyl substituted benzimidazolium salts **2b**, **2f** and **2g** display four absorption peaks at 220, 230, 250 and 270 nm (Fig. 5). As can be seen in

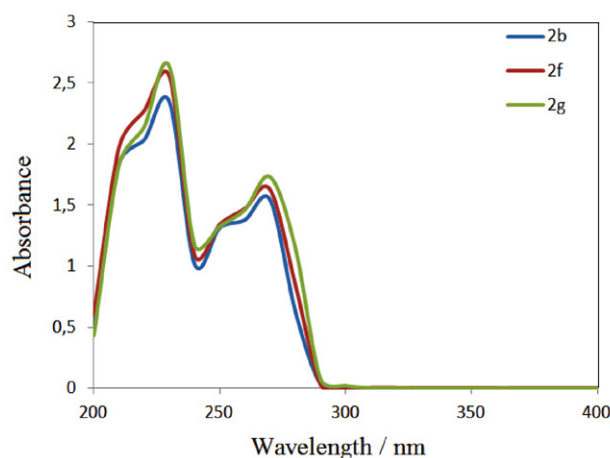


Fig. 5. UV-Vis spectra of the **2b**, **2f** and **2g**

Table 5, the calculated absorption peaks are found to be in close agreement with the experimental ones. The absorption bands between 202 and 288 nm in ethyl alcohol are practically identical and can be attributed to π - π^* transitions in the benzene and benzimidazole ring or azomethine (C=N) groups.^{33,34} The UV absorbance at an observed excitation wavelength (at 230 and 270 nm) indicates the lowest value for **2b**. These data show that **2b** possesses the lowest molar absorptivity and hence produces the highest quantum yield when compared with **2f** and **2g**.

3. 6. Vibrational Analysis

The experimental and calculated FT-IR spectra of the compounds are illustrated in Fig. 6. The unscaled theoretical frequencies using the B3LYP level of theory with 6-31G* basis set along with their IR intensities, probable assignments and potential energy distribution (PED) performed employing VEDA program for all structures are presented in Table S2. As seen in Fig. 6, the experimental fundamentals are nearly consistent with the calculated ones. The probable discrepancies can arise as a result of anharmonic and finite temperature effects.³⁵ As it is expected that C-H stretching modes belonging to the aromatic ring of the NHC salts were observed and calculated above 3000 cm^{-1} .³⁶ The 2-C-H stretching modes occur at 2960 cm^{-1} for **2b** and **2f** and 2956 cm^{-1} for **2g**. The calculated assignments are 2772, 3256 and 3025 cm^{-1} , respectively. The benzonitrile N-C stretching vibrations have the

Table 5. The experimental and calculated UV-Vis parameters of the compounds **2b**, **2f** and **2g**.

2b			
Experimental	The calculated with B3LYP/6-311G(d,p) level in ethyl alcohol		
λ (nm)	λ (nm)	Excitation energy (eV)	f (oscillator strength)
220.00	199.98	6.1999	0.0001
230.00	200.45	6.1853	0.0001
250.00	223.58	5.5454	0.0028
270.00	245.19	5.0566	0.1320
2f			
Experimental	The calculated with B3LYP/6-311G(d,p) level in gas phase		
λ (nm)	λ (nm)	Excitation energy (eV)	f (oscillator strength)
220.00	201.77	6.1450	0.0208
230.00	203.81	6.0836	0.1032
250.00	221.07	5.6087	0.0046
270.00	232.95	5.3223	0.0015
2g			
Experimental	The calculated with B3LYP/6-311G(d,p) level in gas phase		
λ (nm)	λ (nm)	Excitation energy (eV)	f (oscillator strength)
220.00	200.45	6.1853	0.0001
230.00	201.06	6.1667	0.0000
250.00	234.01	5.2983	0.0062
270.00	245.19	5.0566	0.1320

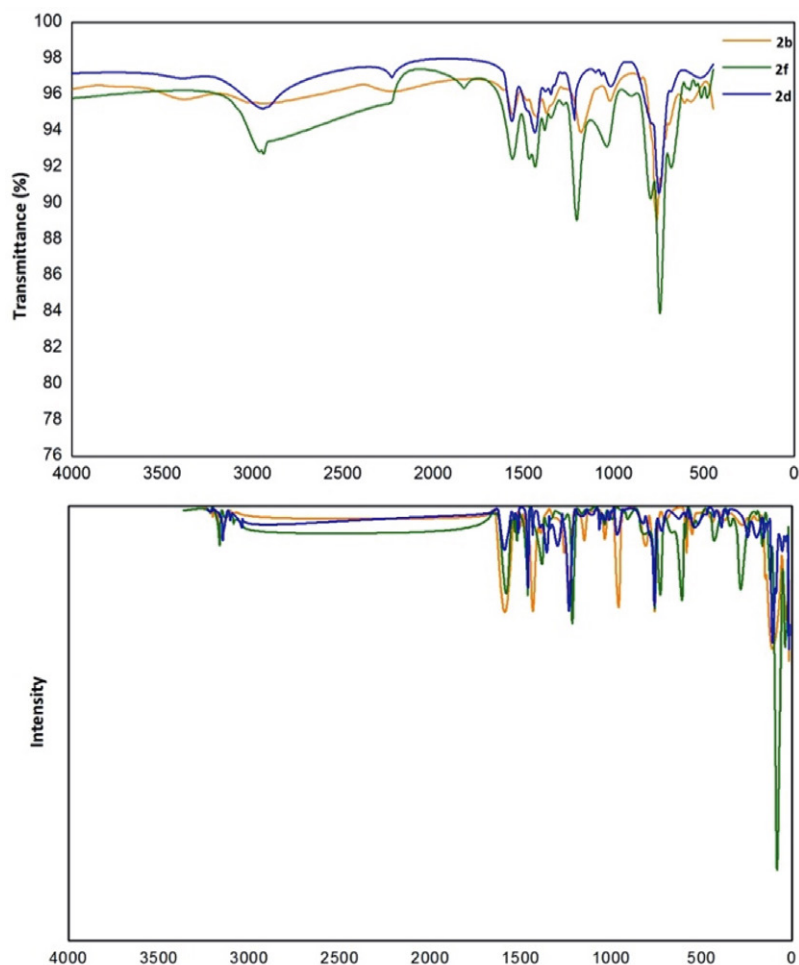


Fig. 6. The experimental (above) and calculated (below) IR spectra of the *meta*-cyanobenzyl substituted benzimidazolium salts.

PED contributions of 89% for all structures; the modes assigned at 2227, 2228 and 2229 cm^{-1} , while they were calculated at 2352, 2348 and 2351 cm^{-1} , respectively.

3. 7. Nuclear Magnetic Resonance (NMR) Studies

The compounds were characterized by ^1H , ^{13}C NMR spectroscopy (Figs. S3-8). The theoretical GIAO ^1H and ^{13}C chemical shift calculations (with respect to TMS in ppm) were carried out using the DFT/B3LYP method with 6-31G* basis set and compared with experimental chemical shift values (Tables S3, S4). The chemical shifts are converted to the TMS scale by subtracting the calculated absolute chemical shielding of TMS ($\delta = \Sigma_0 - \Sigma$) where δ is the chemical shift, Σ is the absolute shielding and Σ_0 is the absolute shielding of TMS, whose values are 32.18 and 189.73 ppm for B3LYP/6-31G*, respectively. There are some deviations of the chemical shift values, which may be due to the chemical environment of the C and H atoms in the molecules.

According to the tables, the signals of the 2-C carbons appeared at 143.55, 142.2 and 134.4 ppm, while they were calculated at 139.27, 127.10 and 124.52 ppm, respec-

tively. Hydrogen bonding has been recognized as the main interaction between the cations and anions of azolium salts leading to close arrangement between the counter anions and the most acidic 2-C-H proton.³⁷⁻⁴⁰ A strong hydrogen bond acceptor is expected to polarize the 2-C-H bond and slightly increase the acidity of the salt. As anticipated, bromide anions with four lone pairs of electrons are the hydrogen bonding acceptors that lead to the most downfield shifts of the ^1H NMR for 2-C-H signal. These hydrogen bonding interactions were also determined by single-crystal X-ray diffraction studies.¹⁰ The most acidic protons (2-C-H) were observed at 10.13, 9.42 and 9.34 ppm, and calculated at 16.14, 9.81 and 12.79 ppm, respectively. The data also showed that the methylene carbon atoms had the least chemical shift values.

3. 8. Computer-Aided Prediction of Biological Activities of the *Meta*-cyanobenzyl-substituted Benzimidazolium Salts

The PASS (Prediction of Activity Spectra for Substances) computer program is an estimation tool, which allows predicting the probable profile of biological activity of a

Table 6. Biological activity assessment using PASS online software.

Activity	2b		2f		2g	
	P_a	P_i	P_a	P_i	P_a	P_i
Analgesic	0.885	0.004	0.854	0.005	0.874	0.004
Substance P antagonist	0.880	0.002	0.859	0.002	0.880	0.002
Analgesic, non-opioid	0.843	0.004	0.805	0.005	0.827	0.005
Antiinflammatory	0.769	0.009	0.787	0.008	0.751	0.010
CYP2H substrate	0.653	0.049	0.633	0.055	0.653	0.049
CYP2C19 inducer	0.557	0.008	0.546	0.008	0.557	0.008
Acetylcholine neuromuscular blocking agent	0.557	0.041	0.529	0.057	0.557	0.041

drug-like organic compound based on its structural formula. The average accuracy of prediction is about 95% according to leave-one-out-cross validation (LOOCV) estimation.^{41,42}

The biological activity spectra of the *meta*-cyanobenzyl substituted benzimidazolium salts were theoretically obtained by the PASS Online program and the analysis results were enlisted in Table 6. According to the data, all compounds are very likely to be analgesic, Substance P antagonist, non-opioid analgesic and anti-inflammatory with corresponding P_a values, which are higher than 0.7. Compounds also exhibit activity to the CYP2H substrate and CYP2C19 inducer. In our previous study, potential AChE inhibition properties of the compounds were investigated.¹⁰ PASS online studies proved that these compounds can be used as acetylcholine neuromuscular blocking agents, as well.

4. Conclusion

As a result, this study contains theoretical aspects of three *meta*-cyanobenzyl substituted NHC precursors. The biological reactivity of the compounds was predicted by global reactivity descriptors and using PASS (prediction of activity spectra for biologically active structures) online. DFT and PASS online studies pointed out the activation of the compounds. The compound **2b** was found to be the most reactive structure by both computational methods. These results were found to be compatible with the experimental biological activity studies. The molecular and crystal structure of **2b** was also determined by using the single-crystal X-ray diffraction method. Natural bond orbital (NBO) analysis was used to analyze the stability of the molecules arising from hyperconjugative interactions and charge delocalization. The vibrational frequencies, chemical shifts and absorption wavelengths were calculated and compared to the experimental ones. Biological activity predictions showed that all structures have a high analgesic, substance P antagonist and non-opioid analgesic activities.

Supplementary

Crystallographic data as .cif files for the structure reported in this paper have been deposited at the Cambridge

Crystallographic Data Center with CCDC 1971777 for **2b**. Copies of the data can be obtained free of charge at <http://www.ccdc.cam.ac.uk/conts/retrieving.html> or from the Cambridge Crystallographic Data Center, 12, Union Road, Cambridge CB2 1EZ, UK. Fax: (+44) 1223-336-033, email: deposit@ccdc.cam.ac.uk.

Acknowledgments

The authors acknowledge İnönü University Scientific and Technology Center for the spectroscopic data and Dokuz Eylül University for the use of the Oxford Rigaku Xcalibur Eos Diffractometer (purchased under University Research Grant No: 2010.KB.FEN.13). The authors also thank Assoc. Prof. Dr. Muhittin Aygün for the use of the Gaussian 09W/Gauss View package program.

5. References

1. S. Diez-Gonzalez, N. Marion, S. P. Nolan, *Chem. Rev.* **2009**, *109*, 3612–3676. DOI:10.1021/cr900074m
2. H. W. Wanzlick, H. J. Schönherr, *Angew. Chem. Int. Ed. Engl.* **1968**, *7*, 141–142. DOI:10.1002/anie.196801412
3. K. Öfele, *J. Organomet. Chem.* **1968**, *12*, 42–43. DOI:10.1016/S0022-328X(00)88691-X
4. A. J. III Arduengo, R. L. Harlow, M. Kline, *J. Am. Chem. Soc.* **1991**, *113*, 361–363. DOI:10.1021/ja00001a054
5. S. Akkoç, V. Kayser, I. Ö. İlhan, D. E. Hibbs, Y. Gök, P. A. Williams, B. Hawkins, F. Lai, *J. Organomet. Chem.* **2017**, *839*, 98–107. DOI:10.1016/j.jorganchem.2017.03.037
6. I. Yıldırım, A. Aktaş, D. Barut Celepci, S. Kırbağ, T. Kutlu, Y. Gök, M. Aygün, *Res. Chem. Intermed.* **2017**, *43*, 6379–6393. DOI:10.1007/s11164-017-2995-3
7. Y. Gök, S. Akkoç, H. Erdoğan, S. Albayrak, *J. Enzyme Inhib. Med. Chem.* **2016**, *31*, 1322–1327. DOI:10.3109/14756366.2015.1132210
8. S. Budagumpi, S. Endud, *Organometallics* **2013**, *32*, 1537–1562. DOI:10.1021/om301091p
9. Y. Sarı, A. Aktaş, P. Taslimi, Y. Gök, İ. Gülçin, *J. Biochem. Mol. Toxicol.* **2018**, *32*, e22009. DOI:10.1002/jbt.22009
10. F. Türker, D. Barut Celepci, A. Aktaş, P. Taslimi, Y. Gök,

- M. Aygün, İ. Gülçin, *Arch Pharm Chem Life Sci.* **2018**, *351*, e1800029. DOI:10.1002/ardp.201800029
11. P. K. Chattaraj, S. Nath, and B. Maiti, *Computational Medicinal Chemistry for Drug Discovery*, **2003**, Marcel Dekker, New York.
12. CrysAlis^{Pro} Software System, Version 1.171.38.43, **2015**, Rigaku Corporation, Oxford, UK.
13. R. C. Clark, J. S. Reid, *Acta Crystallogr. A.* **1995**, *51*, 887–897. DOI:10.1107/S0108767395007367
14. G. M. Sheldrick, *Acta Crystallogr. A.* **2015**, *71*, 3–8. DOI:10.1107/S2053273314026370
15. G. M. Sheldrick, *Acta Crystallogr. C.* **2015**, *71*, 3–8. DOI:10.1107/S2053273314026370
16. O. V. Dolomanov, L. J. Bourhis, R. J. Gildea, J. A. K. Howard, H. Puschmann, *J. Appl. Cryst.* **2009**, *42*, 339–341. DOI:10.1107/S0021889808042726
17. M. J. Frisch, G. W. Trucks, H. B. Schlegel, G. E. Scuseria, M. A. Robb, J. R. Cheeseman, G. Scalmani, V. Barone, G. A. Petersson, H. Nakatsuji, X. Li, M. Caricato, A. Marenich, J. Bloino, B. G. Janesko, R. Gomperts, B. Mennucci, H. P. Hratchian, J. V. Ortiz, A. F. Izmaylov, J. L. Sonnenberg, D. Williams-Young, F. Ding, F. Lipparini, F. Egidi, J. Goings, B. Peng, A. Petrone, T. Henderson, D. Ranasinghe, V. G. Zakrzewski, J. Gao, N. Rega, G. Zheng, W. Liang, M. Hada, M. Ehara, K. Toyota, R. Fukuda, J. Hasegawa, M. Ishida, T. Nakajima, Y. Honda, O. Kitao, H. Nakai, T. Vreven, K. Throssell, J. A. Montgomery, Jr., J. E. Peralta, F. Ogliaro, M. Bearpark, J. J. Heyd, E. Brothers, K. N. Kudin, V. N. Staroverov, T. Keith, R. Kobayashi, J. Normand, K. Raghavachari, A. Rendell, J. C. Burant, S. S. Iyengar, J. Tomasi, M. Cossi, J. M. Millam, M. Klene, C. Adamo, R. Cammi, J. W. Ochterski, R. L. Martin, K. Morokuma, O. Farkas, J. B. Foresman, and D. J. Fox, Gaussian 09, Revision D.01. **2013**, Gaussian, Inc., Wallingford CT.
18. R. Dennington, T. A. Keith, J.M. Millam, GaussView, Version 6, **2016**, Semichem Inc., Shawnee Mission, KS.
19. E.D. Glendening, J.K. Badenhoop, A.E. Reed, J.E. Carpenter, F. Weinhold, NBO Version 3.1. **1995**, Theoretical Chemistry Institute, University of Wisconsin, Maddison.
20. M. H. Jamroz, *Vibrational Energy Distribution Analysis VEDA 4.* **2004–2010**, Warsaw.
21. R. Ditchfield, *J. Chem. Phys.* **1972**, *56*, 5688–5691. DOI:10.1063/1.1677088
22. S. Gunasekaran, R. A. Balaji, S. Kumeresan, G. Anand, S. Srinivasan, *Can. J. Anal. Sci. Spectrosc.* **2008**, *53*, 149–162.
23. J. Fleming, *Frontier Orbitals and Organic Chemical Reactions.* **1976**, John Wiley & Sons, New York.
24. V. Arjunan, L. Devi, R. Subbalakshmi, T. Rani, S. Mohan, *Spectrochim. Acta A.* **2014**, *130*, 164–177. DOI:10.1016/j.saa.2014.03.121
25. O. A. El-Gammal, T. H. Rakha, H. M. Metwally, G. M. Abu El-Reash, *Spectrochim. Acta A.* **2014**, *127*, 144–156. DOI:10.1016/j.saa.2014.02.008
26. R. Bahnasawy, E. Shereafy, T. Kashar, *J. Thermal Anal. Calorimetry*, **1993**, *39*, 65–74. DOI:10.1007/BF02235447
27. H. Chermette, *J. Comput. Chem.* **1999**, *20*, 129–154. DOI:10.1002/(SICI)1096-987X(19990115)20:1<129::AID-JCC13>3.0.CO;2-A
28. L. H. Mendoza-Huizar, *Acta Chim. Slov.* **2014**, *61*, 694–702.
29. R. S. Mulliken, *J. Chem. Phys.* **1955**, *23*, 1833–1840. DOI:10.1063/1.1740588
30. N. Okulik, A. H. Jubert, *Internet Electron. J. Mol. Des.* **2005**, *4*, 17–21.
31. P. Singh, S.S. Islam, H. Ahmad, A. Prabakaran, *J. Mol. Struct.* **2018**, *1154*, 39–50. DOI:10.1016/j.molstruc.2017.10.012
32. R. J. Xavier, E. Gobinath, *Spectrochim Acta A.* **2012**, *86*, 242–251. DOI:10.1016/j.saa.2011.10.031
33. A. Kılıç, E. Tas, İ. Yılmaz, *J. Chem. Sci.* **2009**, *121*, 43–56. DOI:10.1007/s12039-009-0005-z
34. A. Aktas, D. Barut Celepci, Y. Gök, *J. Chin Chem Soc.* **2019**, *66*, 1389–1396. DOI:10.1002/jccs.201900020
35. M. Katari, E. Nicol, V. Steinmetz, G. van der Rest, D. Carmichael, G. Frison, *Chem. Eur. J.* **2017**, *23*, 8414–8423. DOI:10.1002/chem.201700340
36. S. Gunasekaran, S. Ponnusamy, *Indian J. Pure Ap. Phy.* **2005**, *43*, 838–843.
37. A. G. Avent, P. A. Chaloner, M. P. Day, K. R. Seddon, T. Welton, *J. Chem. Soc. Dalton Trans.* **1994**, *23*, 3405–3413. DOI:10.1039/dt9940003405
38. J. A. Cowan, J. A. C. Clyburne, M. G. Davidson, R. L. W. Harris, J. A. K. Howard, P. Kupper, M. A. Leech, S. P. Richards, *Angew. Chem. Int. Ed.* **2002**, *41*, 1432–1434. DOI:10.1002/1521-3773(20020415)41:8<1432::AID-ANIE1432>3.0.CO;2-M
39. N. Kuhn, A. Alsheikh, *Coord. Chem. Rev.* **2005**, *249*, 829–857. DOI:10.1016/j.ccr.2004.10.003
40. H. V. Huynh, T. T. Lam, H. T. T. Luong, *RSC Adv.* **2018**, *8*, 34960–34966. DOI:10.1039/C8RA05839C
41. D. A. Filimonov, A. A. Lagunin, T. A. Glorizova, A. V. Rudik, D. S. Druzhilovskii, P. V. Pogodin, V. V. Poroikov, *Chem Heterocyc Compd.* **2014**, *50*, 444–457. DOI:10.1007/s10593-014-1496-1
42. D. A. Filimonov, V. V. Poroikov, *RSC Publishing*, **2008**, Cambridge, 182–216.

Povzetek

Teoretično smo preučevali strukturne lastnosti prekurzorjev *N*-heterocikličnih karbenov (NHC), ki so bili substituirani z meta-cianobenzilom. Molekularno in kristalno strukturo ene od spojin smo določili z rentgensko difrakcijsko metodo. Deskriptorje globalne reaktivnosti smo analizirali z metodo gostotnega funkcionala (DFT) B3LYP z baznim setom 6-31G*, da bi razumeli biološko aktivnost spojin. Izračunali smo vibracijske frekvence, kemične premike in absorpcijske valovne dolžine in jih primerjali z eksperimentalnimi podatki. Napovedovalna študija biološke aktivnosti je bila narejena s pomočjo spletne programske opreme PASS (= prediction of activity spectra for biologically active structures) in je pokazala, da imajo spojine analgetično, antagonistično (na snov P), neopioidno in protivnetno aktivnost.



Except when otherwise noted, articles in this journal are published under the terms and conditions of the Creative Commons Attribution 4.0 International License

Scientific paper

Effects of Amino Acids on the Crystallization of Calcium Tartrate Tetrahydrate

Sevgi Polat, Elif Aytan-Goze and Perviz Sayan*

Department of Chemical Engineering, Faculty of Engineering, Marmara University, 34722, İstanbul, Turkey.

* Corresponding author: E-mail: perviz.sayan@marmara.edu.tr,

Phone: +90-2167773703, Fax: +90-2167773501

Received: 01-05-2020

Abstract

This work assesses the effects of various amino acids, including serine, alanine, methionine, and proline, on calcium tartrate tetrahydrate (CTT) crystals. The crystallization experiments were performed in batch mode at 25 °C, pH 9 with three amino acid concentrations. The CTT crystals were characterized by XRD, FTIR, SEM, particle size and zeta potential analysis. All of the amino acids used in this study were found to significantly affect the surface electrical charge, size, and morphology of the obtained crystals. In addition, the thermal decomposition of the produced crystals obtained in pure media was examined and the obtained data were used to investigate the decomposition kinetics of the crystals with the help of three different model-free kinetic methods, namely Flynn–Wall–Ozawa (FWO), Kissinger–Akahira–Sunose (KAS), and Starink. The average activation energy of the crystals for the first, second, third, and fourth stages using the FWO, KAS, and Starink methods was calculated to be 91.0, 158.0, 249.1, and 224.8 kJ/mol; 89.6, 155.9, 250.7, and 221.1 kJ/mol; 88.6, 156.8, 250.5, and 220.4 kJ/mol, respectively. Thus, the results of this work are useful for selecting CTT morphology modifiers and explaining the decomposition kinetics of CTT crystals.

Keywords: Calcium tartrate; crystallization; amino acid; kinetics, model-free

1. Introduction

The physical properties of tartrate crystals hold significant research interest. Ferroelectric and piezoelectric tartrate crystals have been reported, and tartrate crystals are often used for controlling laser emissions.^{1,2} Among tartrate crystals, calcium tartrate has drawn the attention of many researchers because of its various applications in science and technology as well as in the field of pharmaceutical science, in addition to industrial uses.³ Besides these practical applications, calcium tartrate tetrahydrate (CTT) crystals are also reported as novel kidney stones in animals.⁴

CTT crystals are orthorhombic with a tetra molecular unit cell of dimensions $a = 9.24$, $b = 10.63$, and $c = 9.66$ Å with space group $P2_12_12_1$. There are two asymmetric carbons in calcium tartrate, so it forms three isomers: two chiral and one non-chiral (meso-form). The chiral levorotatory (–) isomer is the most common form in nature. CTT crystals have been shown to have ferroelectric and non-linear optical properties.⁵

In recent years, researchers in the field of solid-state science have shown significant interest in the growth and

characterization of CTT crystals, either pure crystallization media or with added dopants, such as barium, strontium, cobalt, nickel, manganese, zinc, and cadmium.^{6–9} To date, most studies on pure CTT crystals have aimed at understanding the basic principles and the nature of the crystal growth phenomenon.² In the present study, we investigated the crystallization of CTT in the presence of the amino acid additives serine, alanine, methionine, and proline. These additives were selected because so far only limited studies have been reported on CTT crystallization in the presence of various amino acids; our work should clarify their roles as crystallization-modifying additives. Thus, in this work, we assessed the crystalline structure, morphology, and particle size of crystals prepared using solutions with and without an amino acid additive. In addition, we hope to address the lack of literature on the thermal decomposition kinetics of CTT crystals using the model-free kinetic models of Flynn–Wall–Ozawa (FWO), Kissinger–Akahira–Sunose (KAS), and Starink models. Therefore, the thermal decomposition behavior of the prepared crystals was investigated in detail and used to explain the kinetic characteristics and calculate the activation energies for the decomposition of CTT crystals.

2. Experimental

2.1. Materials

Calcium chloride dihydrate (CCD, $\text{CaCl}_2 \cdot 2\text{H}_2\text{O}$) and tartaric acid (TA, $\text{C}_4\text{H}_6\text{O}_6$) of analytical reagent grade were supplied by Merck, Darmstadt, Germany and used for the precipitation of CTT crystals. The amino acid additives alanine ($\text{C}_3\text{H}_7\text{NO}_2$), methionine ($\text{C}_5\text{H}_{11}\text{NO}_2\text{S}$), serine ($\text{C}_3\text{H}_7\text{NO}_3$), and proline ($\text{C}_5\text{H}_9\text{NO}_2$) of analytical reagent grade were also provided by Merck. Distilled water was used for the experiments.

2.2. Preparation of Calcium Tartrate Tetrahydrate Crystals

The CTT crystallization was carried out in batch mode at 25°C in a double-jacketed crystallizer with an active volume of 500 ml. CCD and TA were used as the reactants for CTT precipitation. The experimental setup is illustrated in Figure 1.

suspension in the crystallizer was stirred at a rate of 300 rpm. During the crystallization process, the pH of the solution was continuously monitored and maintained at pH 9 by adding NaOH solution using an automatic pH control system.

The influence of different types and concentrations of amino acid on the crystallization of CTT was investigated in this study. At the beginning of the experiments, alanine, methionine, serine, and proline were added to the TA solution to provide the desired concentrations of 50, 100, and 200 ppm in the crystallizer. After all of the reactants had been added to the crystallizer, the suspension was left to stir for half an hour. At the end of this time, the crystallizer contents were filtered and washed thoroughly with distilled water. The washing repeated was continued until no chloride ions remained. The presence of chloride ions was checked using 0.1 M silver nitrate solution. The washed CTT crystals were then dried at room temperature and subjected to various characterization processes.

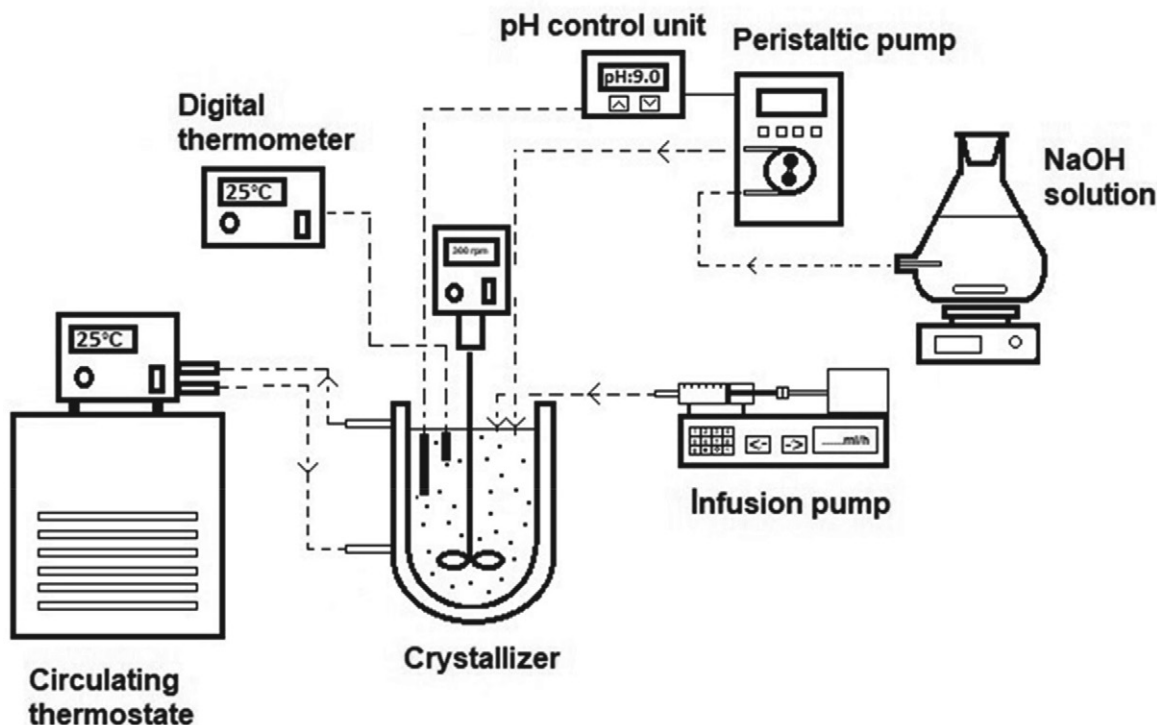


Figure 1. Experimental setup.

Firstly, 0.25 M CCD and 0.25 M TA solutions were prepared. To start the crystallization, 200 ml of TA solution was placed into the crystallizer, followed by the addition of 0.1 M NaOH solution to adjust the pH to 9. The solution was maintained at a constant temperature of $25 \pm 0.5^\circ\text{C}$ using a thermostat. After thermal equilibrium was reached, 200 ml of CCD solution was fed into the crystallizer via an infusion pump at a flow rate of 1 ml/min. The

2.3. Characterization of the Calcium Tetrahydrate Crystals

The structures of the prepared crystal samples were determined using a Bruker D2 Phaser benchtop X-ray diffractometer (30 kV, 10 mA) with $\text{CuK}\alpha$ radiation ($\lambda = 1.5418 \text{ \AA}$) in the 2θ range of $10\text{--}60^\circ$. Fourier transform infrared spectrometry (FTIR; Shimadzu) was used to determine the functional groups of the crystals and to clarify their structures. The spectra were record-

ed at room temperature in the wavenumber range of 600–4000 cm^{-1} . The morphology of the CTT crystals was observed using a scanning electronic microscope (SEM, Zeiss EVO LS 10). The length and width of the samples were determined using Data Translation Image-Pro Plus image analysis software; at least 50 particles were counted to calculate the average aspect ratio of CTT. Zeta potential analysis was performed using a Malvern Zetasizer Nano ZS instrument to determine the surface charge of the CTT crystals obtained in pure and additive media. Measurements were repeated at least 10 times and the mean value was taken. The thermal behavior of the CTT crystals obtained in pure and amino acid-supplemented media was determined using a Setaram LABSYS Evo thermogravimetric analyzer in a nitrogen atmosphere between 30 °C and 850 °C with a heating rate of 5, 10, 20 °C/min. Using the obtained data, the thermal decomposition kinetics for the CTT crystals obtained in pure media were investigated and activation energy was calculated.

2. 4. Kinetic Model Equations

Thermogravimetric analysis is a common method used to investigate the thermal decomposition behavior of solids and to determine activation energy:

The decomposition rate of a solid can be defined as:

$$\frac{dx}{dt} = k(T)f(x) \quad (1)$$

where $f(x)$, $k(T)$, and t represent the reaction model, the reaction rate constant, and time, respectively. The rate constant, $k(T)$, can be defined by the Arrhenius equation, as shown in Eq. (2).

$$k(T) = A \exp\left(-\frac{E}{RT}\right) \quad (2)$$

where A is the pre-exponential or frequency factor (min^{-1}), E is the activation energy (kJ/mol), T is the absolute temperature (K), and R is the ideal gas constant (8.314 J/mol K).

The conversion x is shown in Eq. (3):

$$x = \frac{W_0 - W_t}{W_0 - W_f} \quad (3)$$

where W_0 and W_f are the initial and final sample mass, respectively, and W_t is the sample weight at time t . For a constant heating rate, β (K/min) can be defined as:

$$\beta = \frac{dT}{dt} \quad (4)$$

For non-isothermal analysis, by substituting Eq. (4) into Eq. (1), the equation is given by Eq. (5).

$$\frac{dx}{dT} = k(T)f(x) = \frac{A}{\beta} \exp\left(-\frac{E}{RT}\right)f(x) \quad (5)$$

Integrating Eq. (5) gives Eq. (6):

$$\int_0^x \frac{dx}{f(x)} = g(x) = \frac{A}{\beta} \int_{T_0}^T \exp\left(-\frac{E}{RT}\right)dT = \frac{AE}{\beta R} p(u) \quad (6)$$

where $p(u)$ and $g(x)$ show the temperature integral and the integrated reaction model, respectively. The solution of this equation can be obtained by some approximations depending on the applied kinetic method. In this study, three common isoconversional kinetic methods, namely the Flynn–Wall–Ozawa (FWO),^{10,11} Kissinger–Akahira–Sunose (KAS),¹² and Starink¹³ methods, were used to determine the activation energies of the CTT crystals. Their linear equations are presented in Eqs. (7)–(9), respectively.

$$\text{FWO: } \ln(\beta) = \ln\left(\frac{AE}{Rg(x)}\right) - 5.331 - 1.052 \frac{E}{R} \frac{1}{T} \quad (7)$$

$$\text{KAS: } \ln\left(\frac{\beta}{T^2}\right) = \ln\left(\frac{AR}{Eg(x)}\right) - \frac{E}{RT} \quad (8)$$

$$\text{Starink: } \ln\left(\frac{\beta}{T^{1.92}}\right) = C - 1.008 \frac{E}{RT} \quad (9)$$

For any given value, it is possible to estimate E based on the gradients of the lines obtained from the plot of $\ln(\beta)$ versus $1/T$, $\ln(\beta/T^2)$ versus $1/T$, $\ln(\beta/T^{1.92})$ versus $1/T$ for the FWO, KAS, and Starink, models, respectively.

3. Results and Discussion

3. 1. XRD Analysis

The XRD patterns of the CTT crystals obtained with and without different amino acids are presented in Figure 2. The experimentally observed XRD patterns for the crystals closely matched the patterns simulated using Rietveld refinement. The XRD results showed that the crystals obtained in pure media were in the form of CTT. Consistent with the literature,¹⁴ the main peaks detected at 13.274, 15.700, 16.740, 18.397, 29.0250, 29.418, 33.269, 40.165, and 48.721° corresponded to the (101), (111), (020), (200), (310), (301), (132), (104), and (342) planes of the orthorhombic structure, respectively, with space group P212121.

Unit cell dimensions of $a = 9.637 \text{ \AA}$, $b = 10.583 \text{ \AA}$, $c = 9.216 \text{ \AA}$, $\alpha = \beta = \gamma = 90^\circ$ were calculated for the CTT crystals using Materials Analysis Using Diffraction (MAUD) software, which was in agreement with the results of a previous study.¹⁵

Similar to the crystals prepared in pure media, all of the XRD peaks, regardless of the amino acids used, were attributed to CTT crystals and no other phase formations were observed. In other words, the addition of amino acids

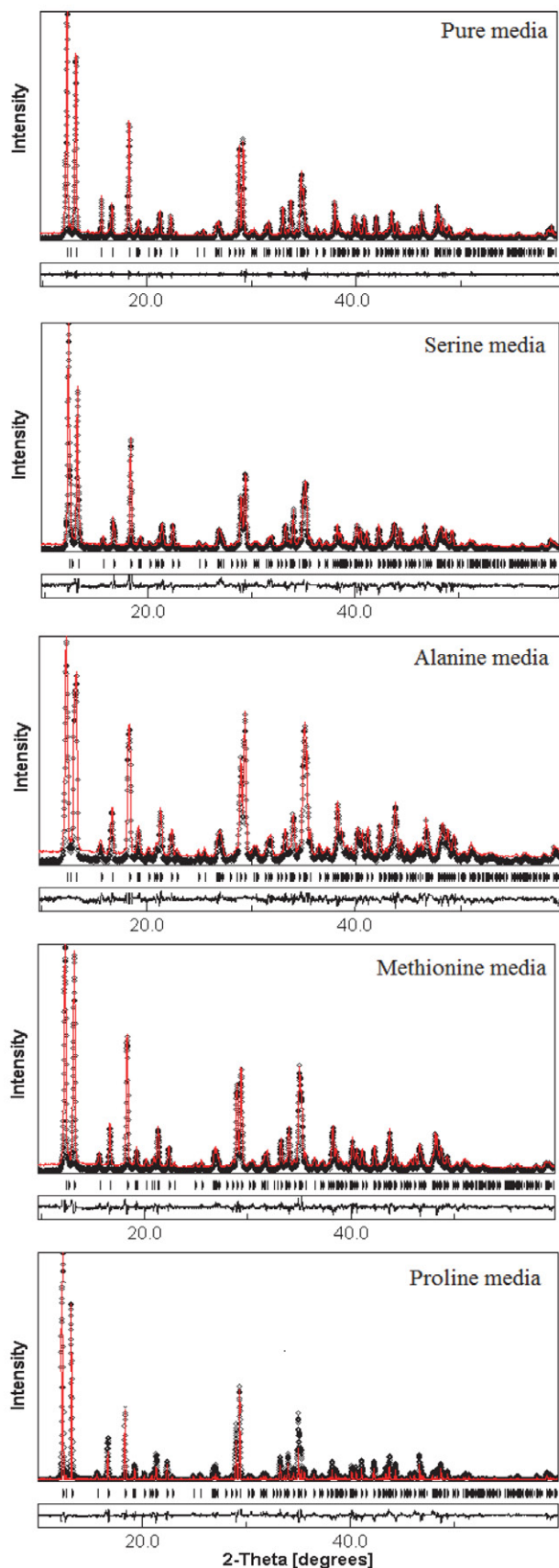


Figure 2. XRD patterns of the CTT crystals obtained in pure media and media supplemented with various amino acids.

to the crystallization media did not lead to any change in the crystal structure. Figure 2 shows that the diffraction peaks were slightly shifted to the right and the intensity of these peaks also changed with the addition of amino acids. This could be due to the adsorption of the additives on the crystal faces, which could lead to the formation of imperfections and internal strain in the resulting crystals. The unit cell dimensions for crystals prepared in media supplemented with serine, alanine, methionine, and proline were calculated and the results are shown in Table 1.

Table 1. The unit cell dimensions for crystals obtained in pure media and media supplemented with various amino acids.

Media	Cell Units		
	<i>a</i> (Å)	<i>b</i> (Å)	<i>c</i> (Å)
Pure	9.637	10.583	9.216
Serine	9.638	10.581	9.226
Alanine	9.647	10.593	9.233
Methionine	9.645	10.594	9.233
Proline	9.645	10.585	9.230

3. 2. FTIR Analysis

FTIR analysis was performed to identify and quantify certain functional groups on the surface of the CTT crystals. Figure 3 shows the FTIR spectra of CTT crystals obtained without and with the different amino acid additives. The FTIR spectrum for the crystals prepared in pure media was in accordance with the literature.¹⁵ O–H, C=O, C–O, and metal–oxygen bonds were the main functional groups in the CTT crystals. The three peaks positioned at 3556, 3414, and 3257 cm^{-1} were assigned to the O–H stretching vibrations. The peak at 2986 cm^{-1} belongs to the C–H stretching vibration. The peaks observed at 1575 and 1381 cm^{-1} were attributed to the C=O stretching vibration and $\lambda(\text{C=O}) + \delta(\text{O–C=O})$ vibrations, respectively. The peak located at 1281 cm^{-1} indicated the O–H plane bending vibration and the peak at 1146 cm^{-1} was ascribed to the $\delta(\text{C–H}) + \pi(\text{C–H})$. In addition, the two peaks at 1061 cm^{-1} and 1012 cm^{-1} were assigned to the O–H deformation and C–O stretching vibrations, respectively. Finally, the peaks located at 964 and 707 cm^{-1} were assigned to Ca–O bending vibrations. In agreement with the XRD results, FTIR analysis showed that the crystals were in the CTT form.

In order to determine whether the addition of amino acids to the crystallization media affects the functional groups of the CTT and also to analyze the adsorption of these amino acids on the surface of the CTT crystals, FTIR analysis was also performed for the crystals obtained in the presence of amino acids. The FTIR spectra of the crystals prepared in media supplemented with amino acids closely matched the spectra for the crystals prepared in pure media, with all the characteristic peaks of CTT crystals present.

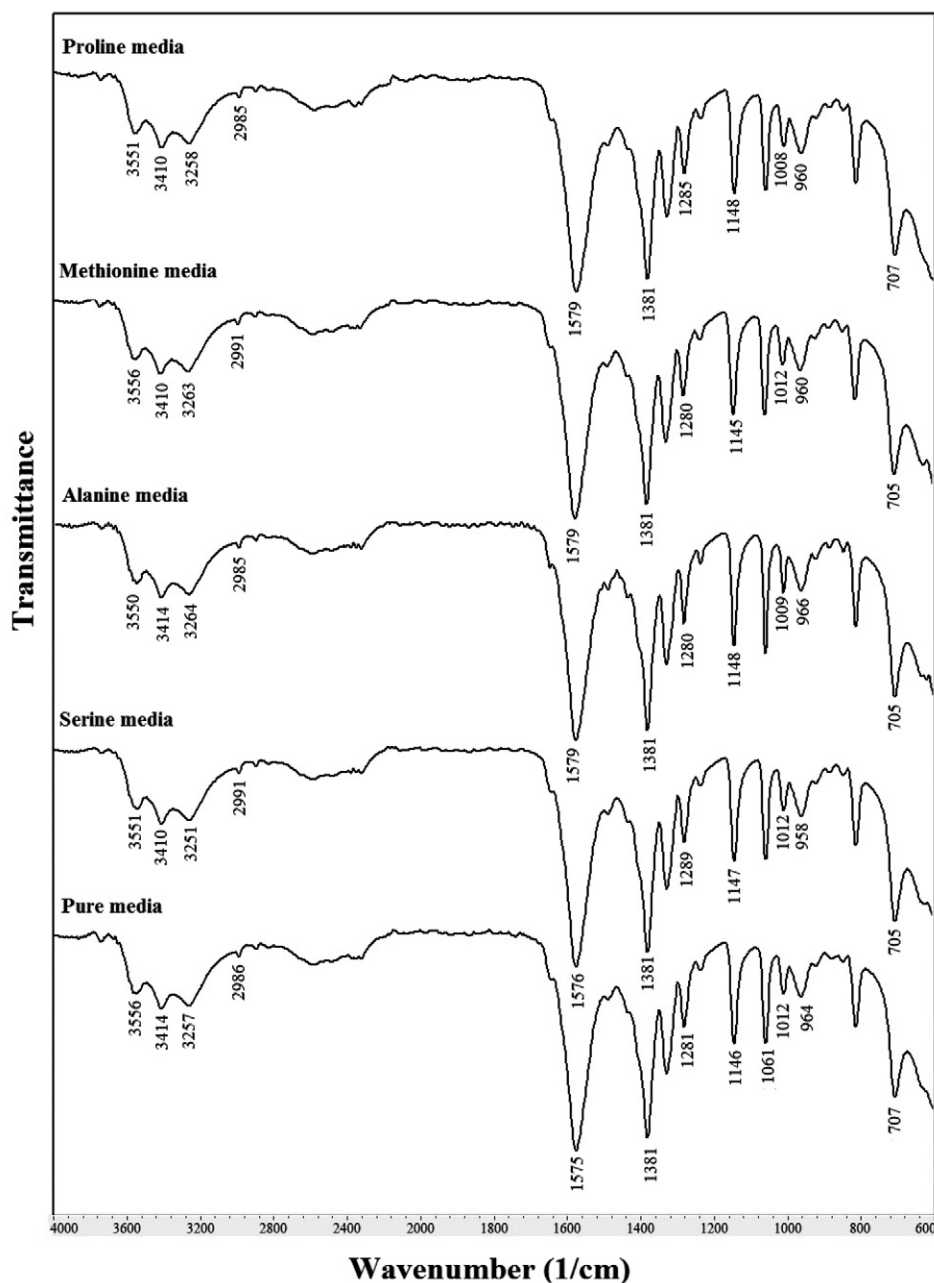


Figure 3. FTIR spectra of the CTT crystals obtained in pure media and media supplemented with various amino acids.

We did not detect any additional peaks relating to the amino acids, which could be because the small amounts of amino acids adsorbed on the surface of the crystals were below the instrument's limit of detection. This may be also attributed to the amino acids being physically adsorbed on the surface of the CTT crystals at the studied concentrations through weak Van der Waals forces.

3. 3. Morphology Analysis

The effects of the different amino acids on the crystal morphology of CTT are shown in Figure 4 and the corre-

sponding length, width, and aspect ratio are shown in Figure 5.

As shown in Figure 4a, the crystals acquired in pure media consisted of prismatic shaped crystals with a smooth surface. There was a high tendency for twin and triplet crystal formation. These crystals had a tendency to break under hydrodynamic conditions and then to form twins and triplets again. The tips of the crystals lost their sharp corners as a result of collisions with each other, the crystallizer wall, and the stirrer. As shown in Figure 5, the aspect ratio of the CTT crystals acquired using pure media was calculated to be 0.255 by dividing the width of the crystal by its length.

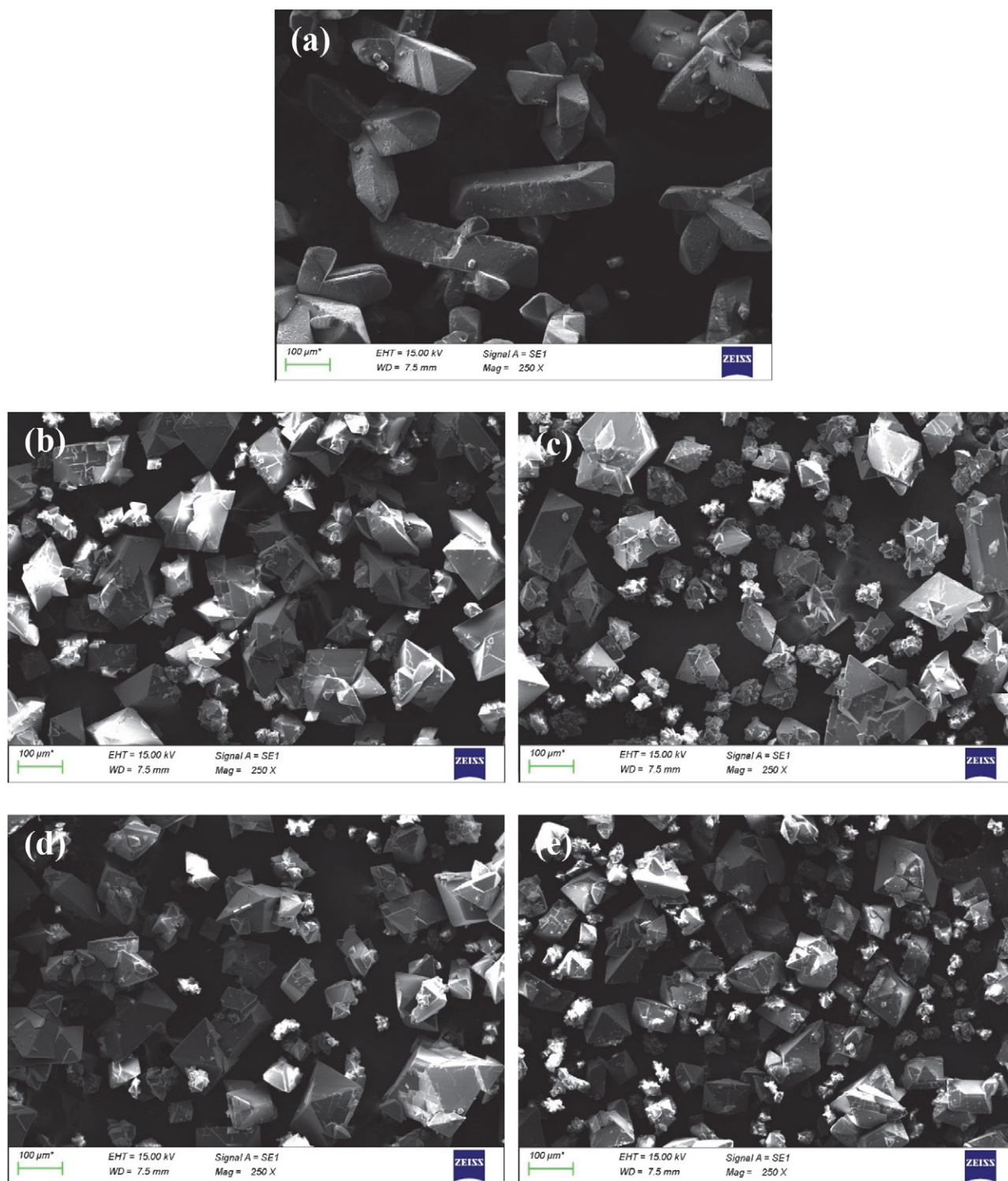


Figure 4. SEM images of the CTT crystals obtained in pure media (a) and in the presence of 200 ppm serine (b), alanine (c), methionine (d), and proline (e).

The morphology of the CTT crystals was significantly affected by the amino acids used. Figures 4b–d clearly show the morphological transformation of CTT crystals from long prismatic to short pyramidal and the surface morphology changed from smooth to rough, indicating

that the addition of amino acids affected the crystal structure and led to the formation of defective crystals. The amino acids used as the additive molecules may have greater affinity with certain faces of a particular surfaces. They preferentially interact with kinks on the crystal nu-

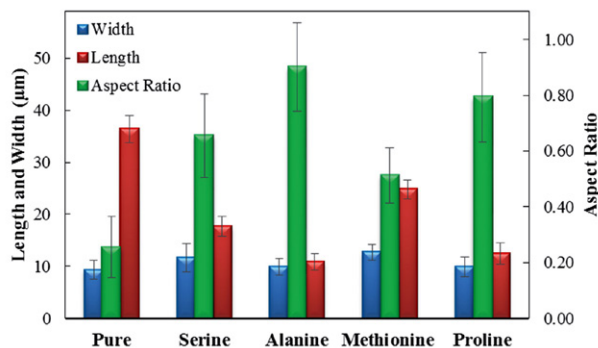


Figure 5. The width, length, and aspect ratio of CTT crystals obtained in pure media and in the presence of 200 ppm serine, alanine, methionine, and proline.

cleus surface and adsorb onto the sites of active growth. These additives interact with Ca^{2+} ions of the crystal surface with their side terminal carboxyl groups or through hydrogen bonding. This interaction influences the crystallization rate and change the morphology of CTT crystals.

In the presence of serine at a concentration of 200 ppm, the CTT crystals were shortened in length and enlarged in width, resulting in an increased aspect ratio of 0.655. In addition, rhomboid crystals were formed, compared to the prismatic crystals obtained in pure media. The formed rhomboid crystals tended to grow on top of each other and they had a different appearance. Although the surfaces of the crystals were generally smooth, the one surface in particular was affected differently from the other surfaces. Serine can selectively adsorb on the surface of CTT crystals and inhibit the crystal growth. When the SEM image for the crystals prepared with alanine added to the media was examined, it could be clearly seen that this additive had a greater effect than serine. The crystals acquired in the presence of 200 ppm alanine were defective as well as being much smaller and more agglomerated than those obtained in pure media, with an aspect ratio of 0.901.

As shown in Figure 4d, the presence of methionine in the crystallization media resulted in the formation of a larger amount of irregular, rhomboid-shaped CTT crystals of non-uniform size with a smooth surface. The aspect ratio of the crystals was 0.512. When proline was used as the additive, nearly all of the crystals converted from prismatic form to short pyramidal form and some of the crystals were fractured. There were less deformations on the crystal surface than with the other amino acid additives used. In the presence of proline, there was a tendency for surface nucleation. Compared to the other additives, the tendency for surface nucleation was highest in the presence of proline. When the concentration of proline was 200 ppm, the aspect ratio was 0.793.

Accordingly, it can be concluded that the addition of the amino acids serine, alanine, methionine, and proline as effective crystal modifiers results in CTT crystals with different crystal size and morphology. The most effective additive for varying the crystal shape was alanine.

3. 4. Zeta Potential Analysis

To further reveal the adsorption characteristics of amino acids on CTT crystals zeta potential measurements were performed. The zeta potential analysis results for the crystals prepared with the addition of various amino acids at concentrations from 0 to 200 ppm are presented in Figure 6. The CTT crystals obtained in pure media exhibited a zeta potential of -21 ± 1.5 mV. The results showed that the addition of amino acids significantly changed the electrical surface charge of the crystals and their zeta potentials were less negative compared to the crystals obtained in pure media.

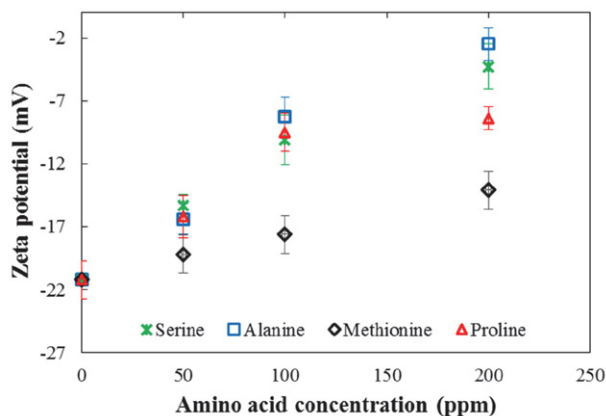
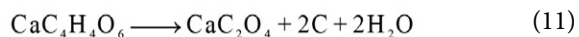


Figure 6. Variation of zeta potential with amino acid concentration.

When the concentration of serine was 50 ppm, the zeta potential value was -15.3 ± 0.9 mV, reaching -4.3 ± 1.8 mV at a serine concentration of 200 ppm. The zeta potentials of the CTT crystals obtained in 200 ppm alanine, methionine, and proline media were -2.5 ± 1.3 mV, -14.1 ± 1.2 mV, and -8.4 ± 0.8 mV, respectively. The zeta potential results show that alanine has the greatest effect on the surface charge of the CTT crystals and that amino acids are adsorbed onto the crystal surface. Moreover, the zeta potentials for the crystals prepared in media supplemented with amino acids increased with the agglomeration tendency of the crystals, in accordance with the SEM results.

3. 5. Thermal Analysis

We applied thermogravimetric analysis to study the structural evolution and thermal decomposition of the CTT crystals. The thermogravimetric (TG) and differential thermogravimetric (DTG) analysis curves for the crystals obtained in the absence and the presence of the various amino acids at a heating rate of 10 °C/min are shown in Figure 7. In accordance with the literature,^{1,5} the thermal decomposition of CTT crystals obtained in pure media proceeded through four different main stages, which can be expressed as follows:



The first decomposition stage included two different peaks at 137 and 191 °C, corresponding to the main weight loss, which were attributed to the loss of four molecules of water of crystallization and the formation of calcium tartrate anhydride ($\text{CaC}_4\text{H}_4\text{O}_6$), respectively. In the second (260–356 °C) and third (400–451 °C) decomposition stages, the crystals decomposed into calcium oxalate (CaC_2O_4) and were further converted into calcium carbonate

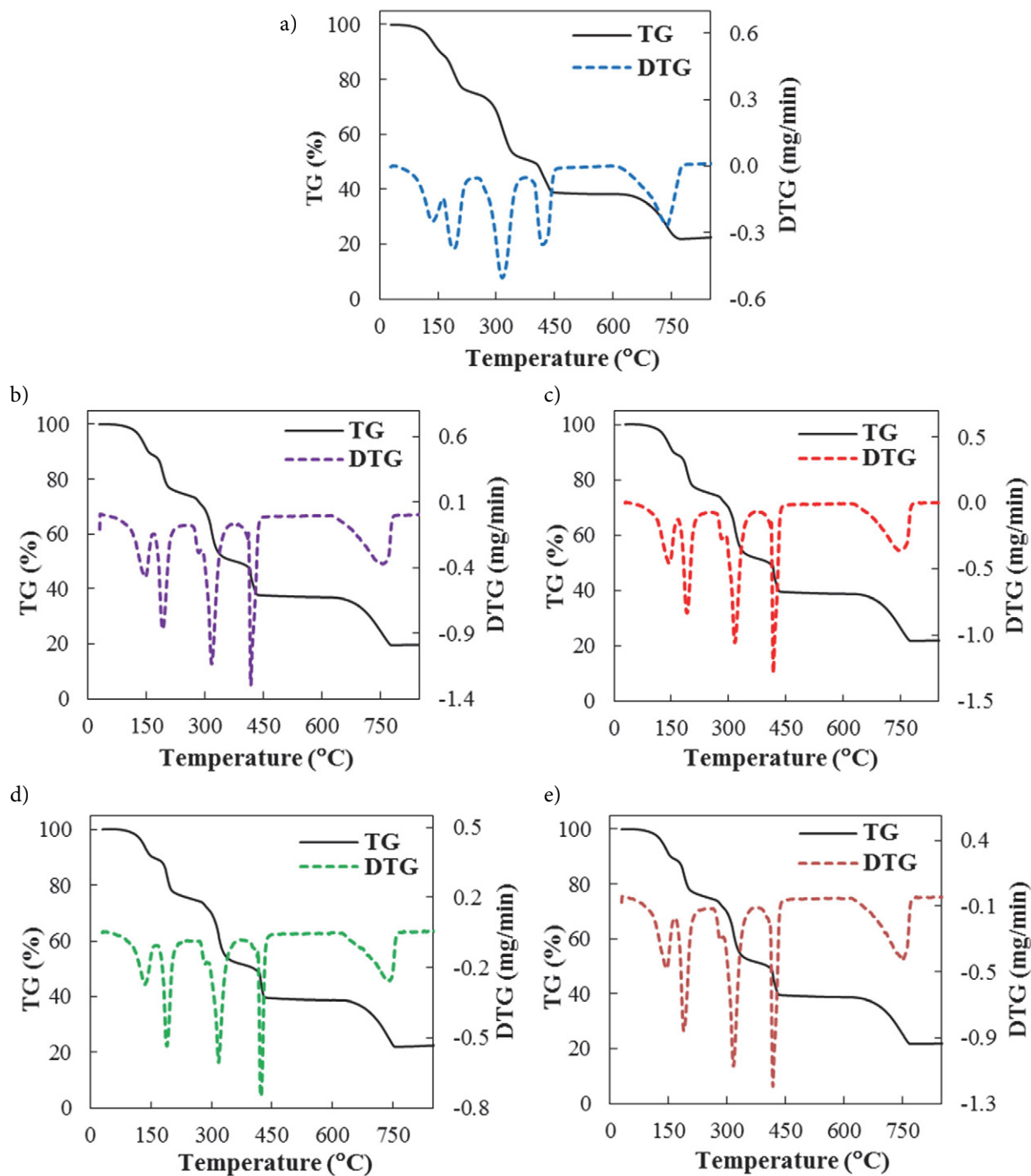


Figure 7. TG/DTG curves of the CTT crystals obtained in pure media (a) and media supplemented with serine (b), alanine (c), methionine (d), and proline (e).

(CaCO₃) and carbon monoxide (CO) gas, respectively. The final stage was attributed to the transformation of calcium carbonate (CaCO₃) to calcium oxide (CaO) and carbon dioxide (CO₂) gas in the temperature range of 623–776 °C. Above this temperature, the weight loss remained stable until the end of the decomposition process. The TG/DTG results showed that the obtained crystals were in tetrahydrate form.

As can be seen in Figure 7, similar to the crystals obtained in pure media, the four main decomposition stages were detected for all the amino acids used. Unlike the crystals from the pure media, a low-intensity shoulder was detected at ~297 °C owing to the decomposition of the amino acid additives. This may be attributed to the loss of amino group from the amino acid molecules. The weight loss from the CTT crystals obtained in pure media was 77.9%, which was in agreement with the literature.¹⁶ Increments of 1.5%, 0.8%, 0.3%, and 0.6% were observed for CTT crystals obtained in serine, alanine, methionine, and proline, respectively. The increased weight loss indicated that the amino acids had been adsorbed onto and interacted with the surface of the CTT crystals. The amino acids used had a significant effect on the temperatures of the decomposition peaks during the thermal decomposition of CTT. The peaks shifted towards the higher temperature region in the presence of the additives.

3. 6. Kinetic Analysis

The FWO, KAS and Starink methods were applied to determine the activation energy of CTT was calculated in the four decomposition zones. Table 2 shows the specific decomposition temperatures, namely initial temperature, T_i , maximum peak temperature, T_{max} , and final temperature, T_f , for the CTT crystals obtained in pure media.

Table 2. Specific temperatures of the CTT crystals decomposition process.

Media	Heating Rate (°C/min)	T_i (°C)	T_{max} (°C)	T_f (°C)
Stage I	5	82	183	202
	10	88	191	222
	20	124	198	235
Stage II	5	255	306	328
	10	260	315	356
	20	278	324	366
Stage III	5	390	412	429
	10	400	419	451
	20	409	427	470
Stage IV	5	611	722	757
	10	623	737	774
	20	659	773	814

Table 2 clearly shows that as the heating rate was increased, the characteristic temperatures for each decom-

position stage were shifted to higher values, which was attributed to the effect of the different heat-transfer rates on the thermal decomposition kinetics.

Figure 8 presents the plots of the three models of the CTT for conversion degrees from 0.1 to 0.9 at different heating rates for the first decomposition stage. The experimental results show high correlation with the three models, with R^2 values of 0.9324–0.9999, which suggests that the results are highly reliable (Figure 8). The parallel lines indicate that there is similar kinetic behavior in the range of 0.10–0.40, which suggests that all of the tested models follow the same reaction mechanism for CTT decomposition. However, the reaction mechanism is not similar for all conversion values, particularly at higher conversions, which suggests that there may be a complex multi-step mechanism involving parallel, competitive, and consecutive reactions with different energies.

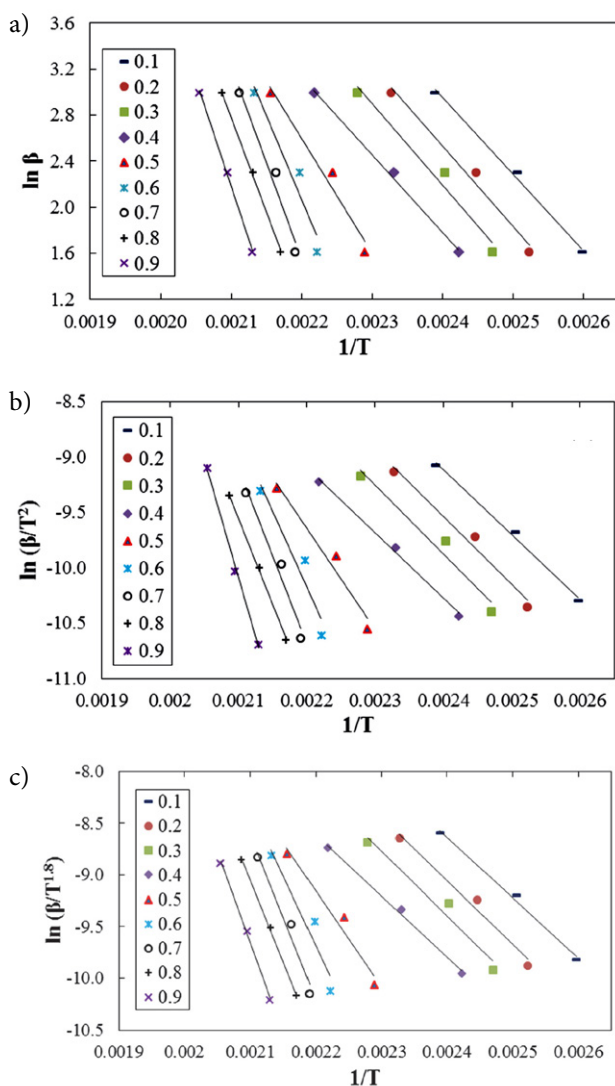


Figure 8. Plots of (a) FWO, (b) KAS, and (c) Starink methods for the first decomposition stage of the CTT crystals obtained in pure media.

The activation energy (i.e., the minimum amount of energy required to initiate a reaction) is plotted as a function of the degree of CTT conversion for four different stages in Figure 9.

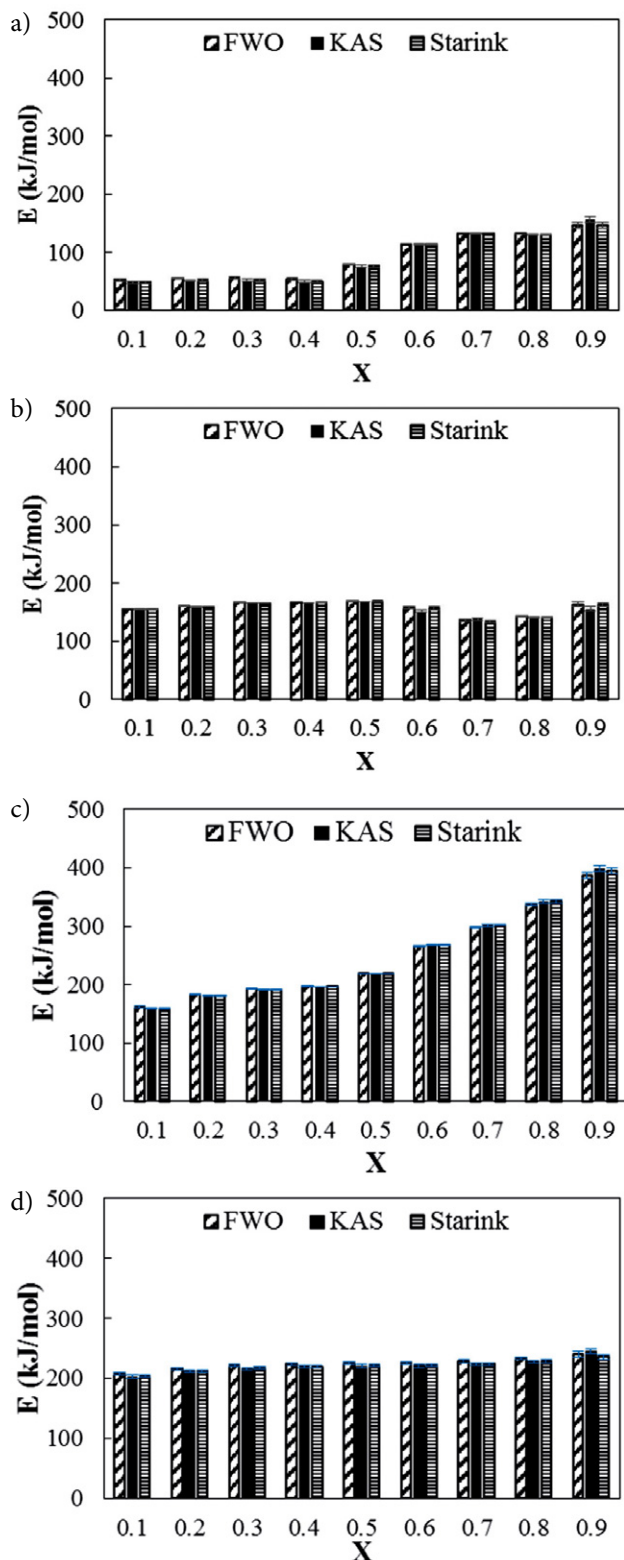


Figure 9. Activation energy versus conversion degree for the CTT crystals for a) Stage I b) Stage II c) Stage III d) Stage IV.

The results show that the minimum mean activation energy values from the FWO, KAS, and Starink methods for the first decomposition stage were 91.0, 89.6, and 88.6 kJ/mol, respectively, which are similar to the activation energy reported in the literature for the dehydration of CTT crystals.^{16,17} There is good agreement among the calculated values with little deviation, demonstrating the consistency and reliability of the activation energies calculated using the three different kinetic models and various heating rates. The minor differences in the activation energy values arose from the approximations, assumptions, and mathematical formulations used in the different models. The mean activation energies for the second, third and fourth decomposition stages were calculated to be 158.0, 155.9, and 156.8 kJ/mol; 249.1, 250.7, and 250.5 kJ/mol; 224.8, 221.1, and 220.4 kJ/mol, respectively, using the FWO, KAS, and Starink models. According to the calculated activation energy values, less energy was needed for the first decomposition stage but the third decomposition stage related to the decomposition of carbon monoxide required a higher amount of energy to proceed.

4. Conclusions

Different concentrations of various amino acids were used to regulate the crystal size and morphology of CTT crystals, which were characterized in detail. Moreover, the thermal decomposition kinetics of the crystals obtained in pure media were examined. The general conclusions obtained can be summarized as follows:

- The XRD results showed that CTT was the only detectable crystalline phase for the crystals obtained in the absence and the presence of the amino acids.
- SEM analysis results indicated that the amino acids used have the ability to change the morphology of CTT crystals. The SEM images showed that the crystal surface varied from smooth to rough, which suggested that the amino acids used affected the crystal morphology, causing the formation of defective and irregular crystals.
- The morphology analysis results revealed that the CTT crystals obtained in the presence of all of the tested amino acids were shortened in length and enlarged in width, resulting in an increased aspect ratio.
- With increasing amino acid concentration, the surface charge of the crystals became more positive. For instance, the zeta potential value changed from -21.2 ± 1.5 mV for crystals prepared in pure media to -2.5 ± 1.3 mV for the crystals prepared in media supplemented with 200 ppm alanine.
- Thermal decomposition kinetics for pure media were examined using different iso-conversional methods. Increasing the conversion from 0.1 to 0.9 changed the calculated activation energy values, which led to the different decomposition characteristics of the CTT crystals.

Using the different kinetic methods, the average activation energies for the first, second, third, and fourth stages were calculated to be 89.7, 156.9, 250.1, and 222.1 kJ/mol, respectively.

Acknowledgements

This work was supported by Marmara University Scientific Research Projects Commission under the funding FEN-C-YLP-230119-0009.

5. References

1. X. Sahaya Shajan, C. Mahadevan, *Cryst. Res. Technol.* **2005**, *40*(6), 598–602. DOI:10.1002/crat.200410389
2. S. S. Sonawane, S. J. Nandre, R. R. Ahire, S. J. Shitole, *Der Pharma Chem.* **2014**, *6*(3), 33–38.
3. M. Tailor, V. Joshi, *Adv. Appl. Sci. Res.* **2014**, *5*(6), 115–119.
4. C. Kleinguetl, J. C. Williams Jr, J. C. Lieske, M. Daudon, M. E. Rivera, P. J. Jannetto, J. Bornhorst, D. Rokke, E. T. Bird, J. E. Lingeman, M. M. El Tayeb, *Urology.* **2019**, *126*, 49–53. DOI:10.1016/j.urology.2019.01.005
5. X. Sahaya Shajan, C. Mahadevan, *Bull. Mater. Sci.* **2004**, *27*(4), 327–331. DOI:10.1007/BF02704767
6. M. E. Torres, T. López, J. Stockel, X. Solans, M. García-Vallés, E. Rodríguez-Castellón, C. González-Silgo, *J. Solid State Chem.* **2002**, *163*, 491–497. DOI:10.1006/jssc.2001.9435
7. K. Suryanarayana, S.M. Dharmaparakash, *Mater. Lett.* **2000**, *42*, 92–96. DOI:10.1016/S0167-577X(99)00165-2
8. E.V. Shlyakhova, N. F. Yudanov, Y. V. Shubin, L. I. Yudanova, L. G. Bulusheva, A. V. Okotrub, *Carbon.* **2009**, *47*(7), 1701–1707. DOI:10.1016/j.carbon.2009.02.018
9. C. Gonzalez-Silgo, M. E. Torres, T. Lopez, J. Gonzalez-Platas, A. C. Yanes, J. D. Castillo, J. F. Peraza, X. Solan, *Mater. Lett.* **2006**, *60*(12), 1509–1514. DOI:10.1016/j.matlet.2005.11.068
10. T. Ozawa, *Bulletin Chem. Soc. Japan.* **1965**, *38*, 1881–1886. DOI:10.1246/bcsj.38.1881
11. J. H. Flynn, L. A. Wall, *J. Res. Nat. Bur. Stand.* **1966**, *70*, 487–523. DOI:10.6028/jres.070A.043
12. T. Akahira, T. Sunose, *Res. Rep. Chiba Inst. Technol (Sci Technol).* **1971**, *16*, 22–31.
13. M. Starink, *Thermochim. Acta.* **1966**, *288*, 97–104. DOI:10.1016/S0040-6031(96)03053-5
14. P. P. Pradyumnan, C. Shini, *Indian J. Pure Ap. Phy.* **2009**, *47*, 199–205.
15. B. B. Parekh, V. S. Joshi, V. Pawar, V. S. Thaker, M. J. Joshi, *Cryst. Res. Technol.* **2009**, *44*(1), 31–35. DOI:10.1002/crat.200800405
16. V. S. Joshi, *Int. J. Innov. Res. Sci. Eng. Technol.* **2016**, *5*(5), 8191–8197.
17. V. S. Joshi, M. Joshi, *Indian J. Phys.* **2001**, *75A*(2), 159–163.

Povzetek

S to raziskavo smo preučili vpliv nekaterih aminokislin, konkretno serina, alanina, metionina in prolina na kristale kalcijevega tartrata tetrahidrata (CTT). Kristalizacijo smo izvajali šaržno, pri temperaturi 25 °C, pH vrednosti 9, dodali pa aminokislino v treh različnih koncentracijah. Kristale CTT smo okarakterizirali z XRD, FTIR, SEM, njihovo velikostjo in zeta potencialom. Za vse uporabljene aminokislino se je izkazalo, da znatno vplivajo na površinski naboj, velikost in morfologijo kristalov. Kristale dobljene brez dodanih aminokislin smo termično razkrojili, pri čemer smo spremljali kinetiko razkroja. Kinetiko smo preučili z uporabo treh različnih kinetičnih modelov, Flynn–Wall–Ozawa (FWO), Kissinger–Akahira–Sunose (KAS) in Starink. Povprečne aktivacijske energije kristalov za prvo, drugo, tretjo in četrto stopnjo razklopa so bile za FWO model 91.0, 158.0, 249.1, in 224.8 kJ/mol, za KAS model 89.6, 155.9, 250.7 in 221.1 kJ/mol ter za Starink model 88.6, 156.8, 250.5 in 220.4 kJ/mol. Rezultati študije nam omogočijo, da lahko izberemo aminokislino, s katero dobimo željeno morfologijo CTT kristalov, preučena pa je tudi kinetika razklopa.



Except when otherwise noted, articles in this journal are published under the terms and conditions of the Creative Commons Attribution 4.0 International License

Scientific paper

Synthesis, Crystal Structures and Catalytic Property of Dioxidomolybdenum(VI) Complexes with Tridentate Hydrazones

Xiao-Qiang Luo,^{1,2} Yong-Jun Han¹ and Ling-Wei Xue^{1,2,*}¹ School of Chemical and Environmental Engineering, Pingdingshan University, Pingdingshan Henan 467000, P.R. China² Henan Key Laboratory of Research for Central Plains Ancient Ceramics, Pingdingshan University, Pingdingshan Henan 467000, P.R. China

* Corresponding author: E-mail: pdsuchemistry@163.com

Received: 01-07-2020

Abstract

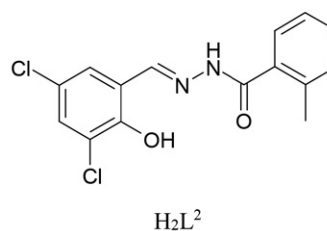
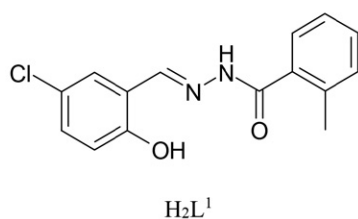
New dioxidomolybdenum(VI) complexes with the formula $[\text{MoO}_2\text{L}(\text{MeOH})]$, derived from N^2 -(5-chloro-2-hydroxybenzylidene)-2-methylbenzohydrazide (H_2L^1) and N^2 -(3,5-dichloro-2-hydroxybenzylidene)-2-methylbenzohydrazide (H_2L^2) were prepared. Crystal and molecular structures of the complexes were determined by single crystal X-ray diffraction method. Both complexes were further characterized by elemental analysis and FT-IR spectra. Single crystal X-ray structural studies indicate that the hydrazones L^1 and L^2 coordinate to the MoO_2 cores through the enolate oxygen, phenolate oxygen and azomethine nitrogen. The Mo atoms in both complexes are in octahedral coordination. Catalytic properties for epoxidation of styrene by the complexes using PhIO and NaOCl as oxidant have been studied.

Keywords: Molybdenum; hydrazine; crystal structure; hydrogen bonding; catalytic property

1. Introduction

The oxidation of organic compounds is an important chemical process in the chemical industry to synthesize a large variety of organic materials. Due to the slow rate of most oxidation reactions in the absence of catalysts, the catalytic oxidation of organic substrates by metal complexes has received much attention in organic synthesis. Many transition metals have been used as homogenous or heterogeneous catalysts in various oxidation systems.¹ The epoxidation products of olefins have widely applications in various fields. They are intermediates or precursors for the synthesis of pharmaceuticals, agrochemicals, and many other compounds.² Among various metal complexes, those with Mo centers have been attracted considerable attention due

to their recently discovered biochemical significance³ as well as their efficient catalytic properties in several organic synthesis procedures.⁴ Schiff bases are widely used as ligands in the construction of metal complexes.⁵ In recent years, a large number of molybdenum complexes with Schiff bases derived from salicylaldehyde and primary amines have been reported.⁶ Hydrazones, bearing $-\text{C}(\text{O})-\text{NH}-\text{N}=\text{CH}-$ groups, are a kind of special Schiff bases, which are of particular interest in coordination chemistry and biological applications.⁷ However, due to the search of the Crystallographic Structural Database, the number of molybdenum(VI) complexes with hydrazone ligands are much less than other metal complexes with such type of ligands. In this paper, two new dioxidomolybdenum(VI) complexes with the formula $[\text{MoO}_2\text{L}(\text{MeOH})]$, derived



from *N'*-(5-chloro-2-hydroxybenzylidene)-2-methylbenzohydrazide (H_2L^1) and *N'*-(3,5-dichloro-2-hydroxybenzylidene)-2-methylbenzohydrazide (H_2L^2) are reported.

2. Experimental

2.1. Materials and Measurements

5-Chlorosalicylaldehyde, 3,5-dichlorosalicylaldehyde and 2-methylbenzohydrazide were purchased from Aldrich and used without further purification. $[MoO_2(acac)_2]$ and other solvents and reagents were made in China and used as received. C, H and N elemental analyses were performed with a Perkin-Elmer elemental analyser. GC experiments were performed with Agilent 5977A Network GC systems. Infrared spectra were recorded on a Nicolet AVATAR 360 spectrometer as KBr pellets in the 4000–400 cm^{-1} region.

2.2. Synthesis of H_2L^1

5-Chlorosalicylaldehyde (1.0 mmol, 0.156 g) and 2-methylbenzohydrazide (1.0 mmol, 0.150 g) were dissolved in methanol (30 mL) with stirring. The mixture was stirred for about 30 min at room temperature to give a colorless solution. The solvent was evaporated to give colorless crystalline product of H_2L^1 . Yield, 91%. For $C_{15}H_{13}ClN_2O_2$: anal. calcd., %: C, 62.4; H, 4.5; N, 9.7. Found, %: C, 62.2; H, 4.6; N, 9.8.

2.3. Synthesis of H_2L^2

3,5-Dichlorosalicylaldehyde (1.0 mmol, 0.190 g) and 2-methylbenzohydrazide (1.0 mmol, 0.150 g) were dissolved in methanol (30 mL) with stirring. The mixture was stirred for about 30 min at room temperature to give a colorless solution. The solvent was evaporated to give colorless crystalline product of H_2L^2 . Yield, 95%. For $C_{15}H_{12}Cl_2N_2O_2$: anal. calcd., %: C, 55.8; H, 3.7; N, 8.7. Found, %: C, 55.7; H, 3.8; N, 8.6.

2.4. Synthesis of $[MoO_2L^1(MeOH)]$ (1)

A methanolic solution (10 mL) of $[MoO_2(acac)_2]$ (0.1 mmol, 32.6 mg) was added to a methanolic solution (10 mL) of H_2L^1 (0.1 mmol, 28.9 mg) with stirring. The mixture was stirred for 20 min to give a yellow solution. The resulting solution was allowed to stand in air for a few days. Yellow block-shaped crystals suitable for X-ray single crystal analysis were formed at the bottom of the vessel. The isolated product was washed three times with cold methanol, and dried in a vacuum over anhydrous $CaCl_2$. Yield, 63%. For $C_{16}H_{15}ClMoN_2O_5$: anal. calcd., %: C, 43.0; H, 3.4; N, 6.3. Found, %: C, 43.2; H, 3.4; N, 6.2.

2.5. Synthesis of $[MoO_2L^2(MeOH)]$ (2)

A methanolic solution (10 mL) of $[MoO_2(acac)_2]$ (0.1 mmol, 32.6 mg) was added to a methanolic solution

Table 1. Crystallographic data and refinement parameters for the complexes

	1	2
Chemical formula	$C_{16}H_{15}ClMoN_2O_5$	$C_{16}H_{14}Cl_2MoN_2O_5$
<i>Mr</i>	446.7	481.1
Crystal color, habit	Yellow, block	Yellow, block
Crystal size (mm^3)	$0.32 \times 0.30 \times 0.27$	$0.20 \times 0.20 \times 0.17$
Crystal system	Monoclinic	Monoclinic
Space group	$P2_1/c$	$P2_1/c$
Unit cell parameters		
<i>a</i> (Å)	7.957(1)	7.961(2)
<i>b</i> (Å)	14.073(1)	14.123(2)
<i>c</i> (Å)	15.172(1)	15.981(2)
β (°)	92.767(2)	92.277(2)
<i>V</i> (Å ³)	1697.0(3)	1795.4(6)
<i>Z</i>	4	4
<i>D</i> _{calc} ($g\ cm^{-3}$)	1.748	1.780
Temperature (K)	298(2)	298(2)
μ (mm^{-1})	0.960	1.058
<i>F</i> (000)	896	960
Number of unique data	3702	3919
Number of observed data [$I > 2\sigma(I)$]	2963	3151
Number of parameters	231	240
Number of restraints	1	1
<i>R</i> ₁ , <i>wR</i> ₂ [$I > 2\sigma(I)$]	0.0261, 0.0595	0.0313, 0.0688
<i>R</i> ₁ , <i>wR</i> ₂ (all data)	0.0388, 0.0668	0.0466, 0.0764
Goodness of fit on <i>F</i> ²	1.080	1.043
Max and min electron density ($e\ \text{Å}^{-3}$)	0.699, -0.436	0.881, -0.710

(10 mL) of H_2L^2 (0.1 mmol, 32.2 mg) with stirring. The mixture was stirred for 20 min to give a yellow solution. The resulting solution was allowed to stand in air for a few days. Yellow block-shaped crystals suitable for X-ray single crystal analysis were formed at the bottom of the vessel. The isolated product was washed three times with cold methanol, and dried in a vacuum over anhydrous $CaCl_2$. Yield, 45%. For $C_{16}H_{14}Cl_2MoN_2O_5$; anal. calcd., %: C, 39.9; H, 2.9; N, 5.8. Found, %: C, 40.0; H, 3.0; N, 5.6.

2. 6. Data Collection, Structural Determination and Refinement

Diffraction intensities for the complexes were collected at 298(2) K using a Bruker Smart 1000 CCD area diffractometer with MoKa radiation ($\lambda = 0.71073 \text{ \AA}$). The collected data were reduced using SAINT,⁸ and multi-scan absorption corrections were performed using SADABS.⁹ Structures of the complexes were solved by direct methods and refined against F^2 by full-matrix least-squares methods using SHELXTL.¹⁰ All of the non-hydrogen atoms were refined anisotropically. The methanol H atoms in the complexes were located in difference Fourier maps and refined isotropically, with O–H distances restrained to 0.85(1) \AA . All other H atoms were placed in idealized positions and constrained to ride on their parent atoms. The crystallographic data for the complexes are summarized in Table 1. Selected bond lengths and angles are given in Table 2.

Table 2. Selected bond distances (\AA) and angles ($^\circ$) for the complexes

1			
Mo1–O1	1.918(2)	Mo1–O2	2.012(2)
Mo1–O3	2.360(2)	Mo1–O4	1.695(2)
Mo1–O5	1.692(2)	Mo1–N1	2.234(2)
O1–Mo1–O2	149.57(7)	O1–Mo1–N1	81.23(7)
O4–Mo1–O1	103.03(8)	O4–Mo1–O2	97.65(7)
O4–Mo1–N1	156.30(8)	O2–Mo1–N1	71.12(6)
O5–Mo1–O1	99.90(9)	O5–Mo1–O2	95.61(9)
O5–Mo1–O4	105.77(9)	O5–Mo1–N1	96.26(8)
O5–Mo1–O3	170.96(8)	O4–Mo1–O3	81.89(7)
O1–Mo1–O3	82.69(8)	O2–Mo1–O3	78.37(7)
N1–Mo1–O3	75.49(6)		
2			
Mo1–O1	1.941(2)	Mo1–O2	2.022(2)
Mo1–O3	2.326(2)	Mo1–O4	1.686(2)
Mo1–O5	1.697(2)	Mo1–N1	2.246(2)
O1–Mo1–O2	149.21(8)	O1–Mo1–N1	80.87(8)
O2–Mo1–N1	70.86(8)	O1–Mo1–O3	82.57(8)
O4–Mo1–O1	98.35(10)	O4–Mo1–O2	96.19(10)
O4–Mo1–O5	105.94(11)	O4–Mo1–N1	95.25(9)
O4–Mo1–O3	170.55(9)	O2–Mo1–O3	78.86(8)
O5–Mo1–O1	103.64(9)	O5–Mo1–O2	98.19(9)
O5–Mo1–N1	157.24(9)	O5–Mo1–O3	82.86(9)
N1–Mo1–O3	75.56(7)		

2. 7. General Method for Styrene Oxidation

The oxidation reactions were carried out according to the literature method.¹¹ The composition of the reaction mixture was 2.00 mmol of styrene, 2.00 mmol of chlorobenzene (internal standard), 0.10 mmol of the complex (catalyst) and 2.00 mmol iodosylbenzene (PhIO) or sodium hypochlorite (NaClO) as the oxidant in 5.00 mL freshly distilled acetonitrile. When the oxidant was sodium hypochlorite, the solution was buffered to pH 11.2. The composition of reaction medium was determined by GC with styrene and styrene epoxide quantified by the internal standard method (chlorobenzene).

3. Results and Discussion

3. 1. Chemistry

The complexes were prepared by mixing $[MoO_2(a-cac)_2]$ with the hydrazones H_2L^1 and H_2L^2 in methanol. Single crystal structures were obtained by slow evaporation of the complexes in methanol. The difference of the molecular packing modes of the complexes may be caused by the hindrance effects of the chloro-substituent groups. There is only one chloro-substituent group in complex **1**, while two in complex **2**. The complexes are soluble in methanol, ethanol, and acetonitrile. The molar conductance of the complexes **1** and **2** at the concentrations of 10^{-4} M are 25 and $20 \text{ } \Omega^{-1} \text{ cm}^2 \text{ mol}^{-1}$, respectively, indicating they are non-electrolytes.¹²

3. 2. Structure Description of the Complexes

The molecular structures and atom numbering schemes of complexes **1** and **2** are shown in Figures 1 and 2, respectively. The coordination geometry around the Mo atoms in both complexes is highly distorted octahedral. The dianionic hydrazones L^1 and L^2 adopt planar tridentate manner, forming five- and one six-membered chelate rings involving the MoO_2 cores. The hydrazones L^1 and L^2 in the complexes are bonded to the MoO_2 cores in planar fashion, coordinating through the phenolate O, imino N, and enolate O, and an oxo group lying *trans* to the nitrogen donor. In each complex, a methanol molecule completes the distorted octahedral coordination sphere which lying *trans* to the other oxo group. The Mo–O(methanol) bonds are significantly longer than the other Mo–O bonds, indicating that the methanol molecules are weakly bonded to the MoO_2 cores and this position holds the possibility of functioning as a substrate binding site. The atoms O1, O2, O4, and N1 show high degree of planarity from the equatorial plane, the Mo atoms displaced by 0.332(1) \AA for complex **1** and 0.320(1) \AA for complex **2** toward the axial oxo groups. The Mo=O bonds in the complexes are almost equal within the standard deviations, and are within previously reported ranges.^{4f,13} The angular distortion in the

octahedral environment around Mo atoms come from the five- and six-membered chelate rings taken by the hydrazones L^1 and L^2 . For the same reason, the *trans* angles are significantly deviate from the ideal values of 180° . The hydrazones L^1 and L^2 in the complexes are distorted, with the two benzene rings make dihedral angles of $12.6(3)^\circ$ for complex **1** and $9.2(3)^\circ$ for complex **2**. The bond lengths of C6–C7, C7–N1, N1–N2, N2–C8 and C8–O2 are comparable to those observed in similar hydrazone complexes.¹⁴

In the crystal structure of complex **1** (Figure 3), two symmetry related adjacent molecules are linked by the methanol molecules of each other through two intermolecular O3–H3A...N2 hydrogen bonds (Table 3), to form a dimeric moiety. The dimeric moieties are further linked *via* C–H...O interactions (Table 3), to form 3D network. In the crystal structure of complex **2** (Figure 4), two symme-

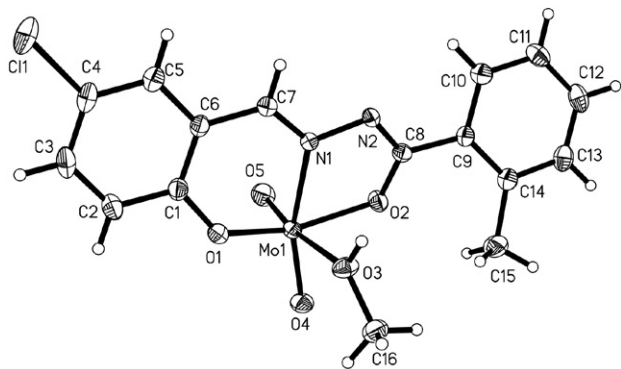


Figure 1. ORTEP plot of the crystal structure of **1**. Displacement ellipsoids of non-hydrogen atoms are drawn at the 30% probability level.

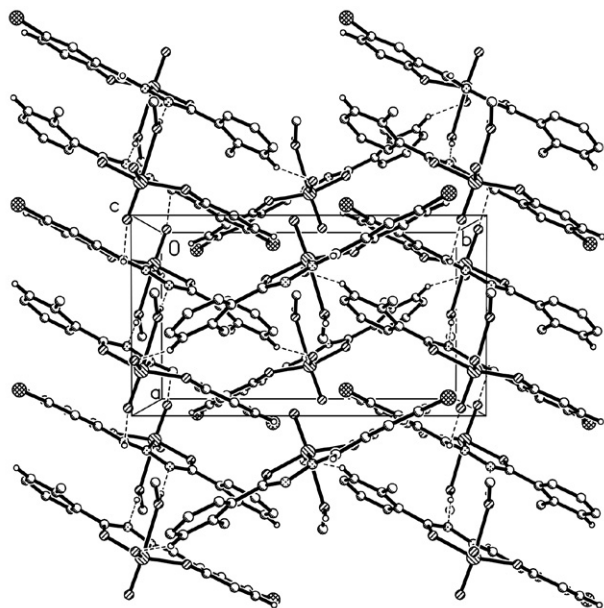


Figure 2. ORTEP plot of the crystal structure of **2**. Displacement ellipsoids of non-hydrogen atoms are drawn at the 30% probability level.

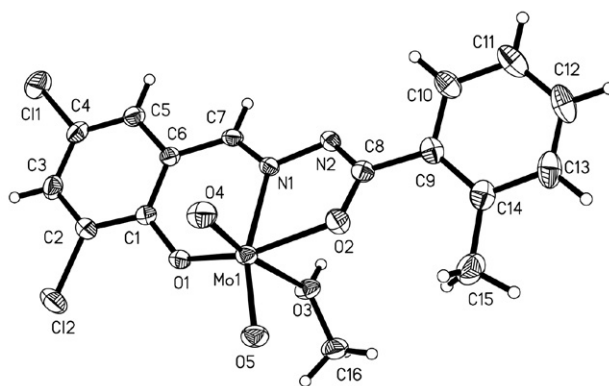


Figure 3. Molecular packing arrangement of **1** displayed in the unit cell. Hydrogen bonds are shown as dashed lines.

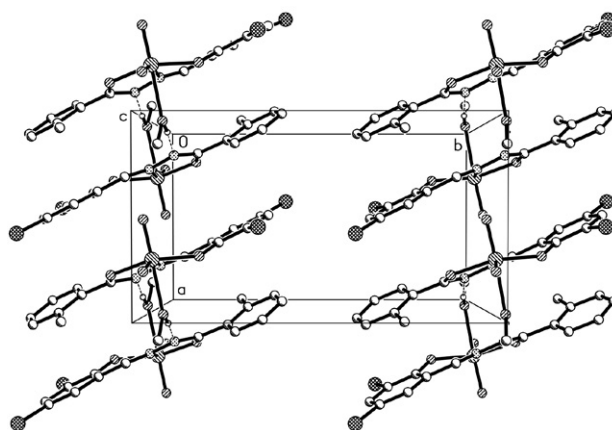


Figure 4. Molecular packing arrangement of **2** displayed in the unit cell. Hydrogen bonds are shown as dashed lines.

Table 3. Geometrical Parameters for Hydrogen Bonds

Hydrogen bonds	D–H (Å)	H...A (Å)	D...A (Å)	D–H...A ($^\circ$)
1				
O3–H3A...N2 ^{#1}	0.85(1)	1.97(1)	2.811(2)	173(4)
C3–H3...O4 ^{#2}	0.93	2.59(1)	3.419(2)	148(4)
C7–H7...O5 ^{#3}	0.93	2.55(1)	3.243(2)	131(4)
C13–H13...O4 ^{#4}	0.93	2.53(1)	3.408(2)	157(4)
2				
O3–H3A...N2 ^{#5}	0.90(1)	1.89(1)	2.788(3)	175(5)

^{#1} $1 - x, 1 - y, -z$; ^{#2} $2 - x, -1 + y, 1/2 - z$; ^{#3} $2 - x, 1 - y, -z$; ^{#4} $1 - x, 1/2 + y, 1/2 - z$; ^{#5} $-x, -y, 1 - z$.

try related adjacent molecules are linked by the methanol molecules of each other through two intermolecular O3–H3A...N2 hydrogen bonds (Table 3), to form a dimeric moiety. In addition, there are π ... π interactions among the rings Mo1–O2–C8–N2–N1, C1–C2–C3–C4–C5–C6 and C9–C10–C11–C12–C13–C14, with centroid to centroid distances of 3.67–4.58 Å for complex **1** and 3.69–4.41 Å for

complex **2**. The C4-Cl1... π interactions between Cl1 atom with the ring C9-C10-C11-C12-C13-C14 also contribute to the crystal packing of both complexes, with distances of 3.705(3) Å for complex **1** and 3.944(3) Å for complex **2**.

3. 3. Infrared and Electronic Spectra

The hydrazones showed stretching bands attributed to C=O, C=N, C-OH and NH at about 1654, 1629, 1150 and 1225, and 3253 cm^{-1} . In addition, strong bands observed at 1612 cm^{-1} for H_2L^1 and H_2L^2 are attributed to CH=N groups.¹⁵ Both complexes exhibit intense bands at ca. 920 cm^{-1} , assigned to the vibrations of the MoO_2 cores.¹⁶ The bands due to $\nu_{\text{C=O}}$ and ν_{NH} are absent in the complexes, but new C–O stretches appeared at 1261 cm^{-1} for both complexes. Keto-imine tautomerism is present in molecules H_2L^1 and H_2L^2 . Upon coordination to Mo atom, enol-imine tautomerism is present in ligands L^1 and L^2 . The $\nu_{\text{C=N}}$ absorption observed at 1629 cm^{-1} in the free hydrazones shifted to 1603 cm^{-1} for the complexes upon coordination to Mo atoms.¹⁶ The weak peaks in the low wave numbers in the region 450–800 cm^{-1} may be attributed to Mo–O and Mo–N bonds of the complexes.¹⁷

In the electronic spectra of the two complexes, the bands ranging from 250 to 340 nm are assigned to $n \rightarrow \pi^*$ transitions, and those at 210–230 nm assigned to $\pi \rightarrow \pi^*$ transitions.¹⁸ The bands with the maximum absorption at 400–410 nm are due to the ligand to metal charge transfer transition.¹⁸

3. 4. Catalytic Property

Oxidation of styrene was carried out at room temperature with the complexes as the catalysts and PhIO and NaOCl as oxidants. The orange color of the solutions containing the complexes and the substrate was intensified after the addition of oxidant indicating the formation of oxo-metallic intermediates of the catalysts. After completion of oxidation reaction of the alkene, the solution regains its initial color which suggests that the regeneration of the catalysts takes place.

The two complexes as catalysts convert styrene most efficiently in the presence of PhIO or NaOCl. There is no obvious difference for the catalytic properties between the two complexes, as a result of similar structures. The complexes are selective towards the formation of styrene epoxide. When the reactions were carried out with PhIO, styrene conversions are 83% and 85% for **1** and **2**, respectively. When the reactions were carried out with NaOCl, styrene conversions are 71% and 74% for **1** and **2**, respectively. It is evident that between the oxidants PhIO and NaOCl, the former acts as a better oxidant with respect to the styrene conversion. The two complexes have similar catalytic properties on the oxidation of styrene when compared to the manganese(III) complexes with the ligand *N,N'*-*o*-phenylenebis(3-ethoxysalicylaldehyde).¹¹

Reaction of the oxidants with the complexes would likely generate a Mo–Cl or Mo–I entity, which further exchange Cl or I for ClO or IO, and homolytic cleavage of Mo–OCl or Mo–OI bond, generate effective epoxidising agent ClO· or IO·. Then, ClO· or IO· reacts with styrene to give the styrene epoxide.

4. Conclusion

New dioxidomolybdenum(VI) complexes with similar hydrazones have been prepared and structurally characterized by single crystal X-ray diffraction method, as well as elemental analysis and FT-IR spectra. The hydrazones coordinate to the MoO_2 cores through the enolate oxygen, phenolate oxygen and azomethine nitrogen. Methanol is a suitable solvent for the preparation of such complexes, which readily coordinates to the Mo atom as a co-ligand. Different substituent groups in the benzene rings of the ligands can result in different molecular packing modes of the final molybdenum(VI) complexes. Both complexes have similar and effective catalytic oxidation property on styrene.

Supplementary Material

CCDC–943080 (**1**) and 943081 (**2**) contain the supplementary crystallographic data for this paper. These data can be obtained free of charge at <http://www.ccdc.cam.ac.uk/const/retrieving.html> or from the Cambridge Crystallographic Data Centre (CCDC), 12 Union Road, Cambridge CB2 1EZ, UK; fax: +44(0)1223-336033 or e-mail: deposit@ccdc.cam.ac.uk.

5. References

- (a) J. A. L. da Silva, J. J. R. F. da Silva, A. J. L. Pombeiro, *Coord. Chem. Rev.* **2011**, 255, 2232–2248; DOI:10.1016/j.ccr.2011.05.009
- (b) A. G. J. Ligtenbarg, R. Hage, B. L. Feringa, *Coord. Chem. Rev.* **2003**, 237, 89–101; DOI:10.1016/S0010-8545(02)00308-9
- (c) Z. Moradi-Shoeili, M. Zare, M. Bagherzadeh, M. Kubicki, D. M. Boghaei, *J. Coord. Chem.* **2015**, 68, 548–559; DOI:10.1080/00958972.2014.993321
- (d) N. C. Jana, M. Patra, P. Brandao, A. Panja, *Polyhedron* **2019**, 164, 23–34; DOI:10.1016/j.poly.2019.02.024
- (e) V. Vrdoljak, J. Pisk, D. Agustin, P. Novak, J. P. Vukovic, D. Matkovic-Calogovic, *New J. Chem.* **2014**, 38, 6176–6185. DOI:10.1039/C4NJ01394H
2. R. Bikas, V. Lippolis, N. Noshiranzadeh, H. Farzaneh-Bonab, A. J. Blake, M. Siczek, H. Hosseini-Monfared, T. Lis, *Eur. J. Inorg. Chem.* **2017**, 6, 999–1006. DOI:10.1002/ejic.201601359
3. (a) S. Quintal, M. J. P. da Silva, S. R. M. Martins, R. Sales, V. Felix, M. G. B. Drew, M. Meireles, A. C. Mourato, C. D.

- Nunes, M. S. Saraiva, M. Machuqueiro, M. J. Calhorda, *Dalton Trans.* **2019**, 48, 8449–8463; DOI:10.1039/C9DT00469F
- (b) J. Pisk, L. Bilic, M. Dakovic, D. Cvijanovic, V. Damjanovic, J. Lovric, M. Rubcic, V. Vrdoljak, M. Cindric, *Polyhedron* **2018**, 145, 70–79; DOI:10.1016/j.poly.2018.02.003
- (c) H. Pfeiffer, M. Dragoun, A. Prokop, U. Schatzschneider, *Z. Anorg. Allg. Chem.* **2013**, 639, 1568–1576. DOI:10.1002/zaac.201300055
4. (a) T. Leischner, L. A. Suarez, A. Spannenberg, K. Junge, A. Nova, M. Beller, *Chem. Sci.* **2019**, 10, 10566–10576; DOI:10.1039/C9SC03453F
- (b) M. R. Maurya, N. Jangra, F. Avecilla, N. Ribeiro, I. Correia, *ChemistrySelect* **2019**, 4, 12743–12756; DOI:10.1002/slct.201903678
- (c) R. Tran, S. M. Kilyanek, *Dalton Trans.* **2019**, 48, 16304–16311; DOI:10.1039/C9DT03759D
- (d) T. M. Asha, M. Sithambaresan, M. R. P. Kurup, *Polyhedron* **2019**, 171, 530–541. DOI:10.1016/j.poly.2019.08.006
5. (a) K. Dankhoff, B. Weber, *Dalton Trans.* **2019**, 48, 15376–15380; DOI:10.1039/C9DT00846B
- (b) H. Y. Qian, N. Sun, *Transition Met. Chem.* **2019**, 44, 501–506; DOI:10.1007/s11243-018-00296-x
- (c) S. Thakur, M. G. B. Drew, A. Franconetti, A. Frontera, S. Chattopadhyay, *RSC Advances* **2019**, 9, 35165–35175; DOI:10.1039/C9RA07006K
- (d) H. Y. Qian, *Inorg. Nano-Met. Chem.* **2018**, 48, 615–619; DOI:10.1080/24701556.2019.1567542
- (e) M. S. C. Manna, S. Mistri, A. Patra, M. K. Mahish, D. Saren, R. K. Manne, M. K. Santra, E. Zangrando, H. Puschmann, *Polyhedron* **2019**, 171, 77–85; DOI:10.1016/j.poly.2019.06.049
- (f) H. Y. Qian, *Russ. J. Coord. Chem.* **2018**, 44, 32–38. DOI:10.1134/S1070328418010074
6. (a) N. Monadi, E. Moradi, *Transition Met. Chem.* **2018**, 43, 161–170; DOI:10.1007/s11243-018-0204-x
- (b) M. Bagherzadeh, S. Ataie, H. Mahmoudi, J. Janczak, *Inorg. Chem. Commun.* **2017**, 84, 63–67; DOI:10.1016/j.inoche.2017.07.025
- (c) S. Rakshit, D. Palit, S. K. S. Hazari, S. Rabi, T. G. Roy, F. Olbrich, D. Rehder, *Polyhedron* **2016**, 117, 224–230; DOI:10.1016/j.poly.2016.05.053
- (d) G. Romanowski, J. Kira, *Polyhedron* **2016**, 117, 352–358; DOI:10.1016/j.poly.2016.06.015
- (e) Z. Moradi-Shoeili, M. Zare, M. Bagherzadeh, S. Ozkar, S. Akbayrak, *J. Coord. Chem.* **2016**, 69, 668–677; DOI:10.1080/00958972.2015.1137290
- (f) S. Y. Ebrahimipour, H. Khabazadeh, J. Castro, I. Sheikhshoae, A. Crochet, K. M. Fromm, *Inorg. Chim. Acta* **2015**, 427, 52–61. DOI:10.1016/j.ica.2014.11.023
7. (a) A. A. El-Sherif, A. Fetoh, Y. K. Abdulhamed, G. M. Abu El-Reash, *Inorg. Chim. Acta* **2018**, 480, 1–15; DOI:10.1016/j.ica.2018.04.038
- (b) H. Y. Qian, *Inorg. Nano-Met. Chem.* **2018**, 48, 461–466; DOI:10.1080/24701556.2019.1569689
- (c) S. Parveen, S. Govindarajan, H. Puschmann, R. Revathi, *Inorg. Chim. Acta* **2018**, 477, 66–74; DOI:10.1016/j.ica.2018.02.022
- (d) H. Y. Qian, *Russ. J. Coord. Chem.* **2017**, 43, 780–786; DOI:10.1134/S1070328417110070
- (e) H.-Y. Qian, *Acta Chim. Slov.* **2019**, 66, 995–1001; DOI:10.4149/neo_2019_190112N36
- (f) S. M. Soliman, J. H. Albering, M. Farooq, M. A. M. Wadaan, A. El-Faham, *Inorg. Chim. Acta* **2017**, 466, 16–29. DOI:10.1016/j.ica.2017.05.045
8. Bruker, SMART and SAINT. Bruker AXS Inc., Madison, Wisconsin, USA (2002).
9. G. M. Sheldrick, SADABS. Program for Empirical Absorption Correction of Area Detector, University of Göttingen, Germany, 1996.
10. G. M. Sheldrick, SHELXTL V5.1 Software Reference Manual, Bruker AXS, Inc., Madison, Wisconsin, USA, 1997.
11. S. Majumder, S. Hazra, S. Dutta, P. Biswas, S. Mohanta, *Polyhedron* **2009**, 28, 2473–2479. DOI:10.1016/j.poly.2009.04.034
12. W. J. Geary, *Coord. Chem. Rev.* **1971**, 7, 81–122. DOI:10.1016/S0010-8545(00)80009-0
13. (a) M. Bagherzadeh, M. Zare, V. Amani, A. Ellern, L. K. Woo, *Polyhedron* **2013**, 53, 223–229; DOI:10.1016/j.poly.2013.01.054
- (b) M. Ghorbanloo, R. Bikas, G. Malecki, *Inorg. Chim. Acta* **2016**, 445, 8–16; DOI:10.1016/j.ica.2016.02.018
- (c) Z. Moradi-Shoeili, M. Zare, S. Akbayrak, S. Ozkar, *Transition Met. Chem.* **2017**, 42, 357–363. DOI:10.1007/s11243-017-0139-7
14. (a) R. Dinda, P. Sengupta, S. Ghosh, H. Mayer-Figge, W. S. Sheldrick, *J. Chem. Soc., Dalton Trans.* **2002**, 4434–4439; DOI:10.1039/b207129k
- (b) S. Alghool, C. Slebodnick, *Polyhedron* **2014**, 67, 11–18; DOI:10.1016/j.poly.2013.08.059
- (c) R. Dinda, S. Ghosh, L. R. Falvello, M. Tomas, T. C. W. Mak, *Polyhedron* **2006**, 25, 2375–2382. DOI:10.1016/j.poly.2006.02.002
15. P. Paciorek, J. Szklarzewicz, A. Jasińska, B. Trzewik, W. Nitek, M. Hodorowicz, *Polyhedron* **2015**, 87, 226–232. DOI:10.1016/j.poly.2014.11.018
16. (a) T. M. Asha, M. R. P. Kurup, *Polyhedron* **2019**, 169, 151–161; DOI:10.1016/j.poly.2019.04.045
- (b) S. Gupta, A. K. Barik, S. Pal, A. Hazra, S. Roy, R. J. Butcher, S. K. Kar, *Polyhedron* **2007**, 26, 133–141. DOI:10.1016/j.poly.2006.08.001
17. (a) T. Glowiak, L. Jerzykiewicz, J. M. Sobczak, J. J. Ziolkowski, *Inorg. Chim. Acta* **2003**, 356, 387–392; DOI:10.1016/S0020-1693(03)00301-3
- (b) M. R. Maurya, L. Rana, F. Avecilla, *Inorg. Chim. Acta* **2015**, 429, 138–147; DOI:10.1016/j.ica.2015.01.040
- (c) E. Zamanifar, F. Farzaneh, J. Simpson, M. Maghami, *Inorg. Chim. Acta* **2014**, 414, 63–70. DOI:10.1016/j.ica.2014.01.028
18. H.-Y. Liu, Y.-S. Yin, L.-J. Yang, X.-L. Zou, Y.-F. Ye, *Acta Chim. Slov.* **2020**, 67, 130–136. DOI:10.17344/acsi.2019.5286

Povzetek

Sintetizirali smo nove dioksidomolibdenove(VI) komplekse s formulo $[\text{MoO}_2\text{L}(\text{MeOH})]$ z uporabo ligandov N^2 -(5-kloro-2-hidroksibenziiden)-2-metilbenzohidrazid (H_2L^1) in N^2 -(3,5-dikloro-2-hidroksibenziliden)-2-metilbenzohidrazid (H_2L^2). Z rentgensko analizo na monokristalu smo določili kristalno in molekulsko strukturo obeh kompleksov. Obe spojini smo karakterizirali tudi z elementno analizo in FT-IR spektroskopijo. Strukturna analiza je pokazala, da se hidrazona L^1 in L^2 koordinirata na MoO_2 orko enolatnega kisika, fenolatnega kisika in azometinskega dušika. Atomi Mo so v obeh spojinah oktaedrično koordinirani. Preučevali smo katalitske lastnosti obeh spojin pri epoksidaciji stirena z uporabo oksidantov PhIO in NaOCl.



Except when otherwise noted, articles in this journal are published under the terms and conditions of the Creative Commons Attribution 4.0 International License

Scientific paper

Synthesis and X-Ray Crystal Structures of Trinuclear Nickel(II) Complexes Derived from Schiff Bases and Acetate Ligands with Biological Activity

Jin-Long Hou,* Hong-Yuan Wu, Cheng-Bin Sun, Ye Bi and Wei Chen

College of Chemistry and Chemical Engineering, Qiqihar University, Qiqihar 161006, P. R. China

* Corresponding author: E-mail: houjinlong09@163.com

Received: 01-11-2020

Abstract

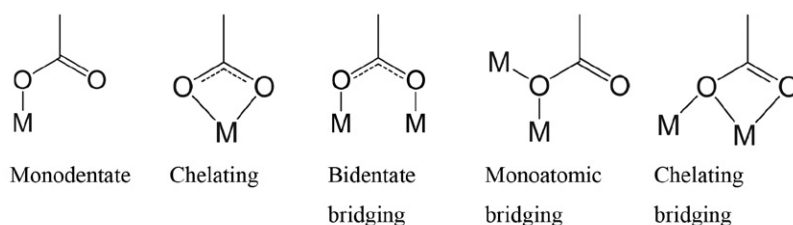
The reactions of $\text{Ni}(\text{OAc})_2 \cdot 2\text{H}_2\text{O}$ with Schiff base ligands 5-bromo-2-((cyclopentylimino)methyl)phenol (HL^1) and 5-bromo-2-(((2-(isopropylamino)ethyl)imino)methyl)phenol (HL^2) in methanol afforded two discrete trinuclear complexes $[\text{Ni}_3(\text{L}^1)_2(\mu_2\text{-}\eta^1\text{-}\eta^1\text{-OAc})_2(\text{DMF})_2(\text{BrSal})_2]$ (1) and $[\text{Ni}_3(\text{L}^2)_2(\mu_2\text{-}\eta^1\text{-}\eta^1\text{-OAc})_2(\mu_2\text{-}\eta^2\text{-}\eta^1\text{-OAc})_2]$ (2), where BrSal is the monoanionic form of 4-bromosalicylaldehyde. The complexes were characterized by elemental analysis, IR and UV-Vis spectroscopy. The crystal structures of the complexes have been determined by X-ray crystallography. In both complexes, the nickel atoms are in octahedral coordination geometries. The L^1 ligand coordinates to the nickel atoms through the phenolate O and imino N atoms, and the L^2 ligand coordinates to the nickel atoms through the phenolate O, imino N and amino N atoms. The antimicrobial activities of the complexes were assayed.

Keywords: Nickel complexes; schiff bases; crystal structures; trinuclear complexes; antimicrobial activity

1. Introduction

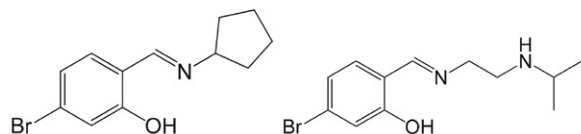
Studies on supramolecular interaction and the self-assembly resulting from them have attracted remarkable attention in recent years. Schiff bases and their metal complexes exhibit biological activity as antibiotics, antiviral, antibacterial and antitumour agents because of their specific structures.¹ Among Schiff bases, those derived from the mono-condensation of organic amines with carbonyl compounds, are a group of classical NO or NNO donor ligands.² These ligands react readily with nickel salts to occupy its equatorial coordination sites whereas several anionic or neutral ligands can be coordinated to the fourth

coordination site of the square plane to yield different type of complexes.³ Among the co-ligands, acetate has received remarkable attention because it can coordinate to the metal centers through versatile modes, such as monodentate, chelating, bidentate bridging, monoatomic bridging, chelating bridging, *etc* (Scheme 1).⁴ To combine Schiff bases and acetate ligands together in the complexes, a number of nickel complexes have been prepared. The complexes show interesting structures, biological, magnetic, and catalytic properties.⁵ However, it is still a great challenge to prepare acetate bridged multi-nuclear complexes with aiming structures. Herein, we report the synthesis and crystal structures of two new nickel(II) complexes, $[\text{Ni}_3(\text{L}^1)_2(\mu_2\text{-}$



Scheme 1. Chelating modes of acetate ligand.

$\eta^1:\eta^1\text{-OAc}_2(\text{DMF})_2(\text{BrSal})_2$] (1) and $[\text{Ni}_3(\text{L}^2)_2(\mu_2\text{-}\eta^1:\eta^1\text{-OAc})_2(\mu_2\text{-}\eta^2:\eta^1\text{-OAc})_2]$ (2), where $\text{L}^1 = 5\text{-bromo-2-}((\text{cyclopentylimino})\text{methyl})\text{phenolate}$, $\text{L}^2 = 5\text{-bromo-2-}(((2\text{-}(\text{isopropylamino})\text{ethyl})\text{imino})\text{methyl})\text{phenolate}$ (Scheme 2), $\text{BrSal} = 4\text{-bromosalicylaldehyde}$.



Scheme 2. HL^1 and HL^2 .

2. Experimental Section

2.1. Materials and Physical Measurements

4-Bromosalicylaldehyde, cyclopentylamine, *N*-isopropylethane-1,2-diamine and nickel acetate were purchased from Sigma-Aldrich. All other chemicals were commercially available and used as received. Elemental analysis was carried out using model 2400 Perkin-Elmer CHN analyzer. Infrared spectra were collected by using KBr pellets on a Jasco-5300 FT-IR spectrophotometer. Electronic spectra were carried out with a Lambda 35 spectrometer.

2.2. Preparation of Complex 1

4-Bromosalicylaldehyde (0.20 g, 10 mmol) and cyclopentylamine (0.085 g, 10 mmol) were dissolved and stirred at ambient temperature in methanol (30 mL). Thirty minutes later, nickel acetate tetrahydrate (0.50 g, 20 mmol) was added to the solution. The color turned from yellow to deep green, and some insoluble residue was produced. Then, a few drops of DMF was added until the insoluble residue has disappeared. The reaction mixture was stirred for about 1 h and filtered. The filtrate was allowed to slow evaporate for a few days, generating green block shaped single crystals. Yield: 0.13 g (38%). Anal. Calcd for $\text{C}_{48}\text{H}_{54}\text{Br}_4\text{N}_4\text{Ni}_3\text{O}_{12}$: C, 41.94; H, 3.96; N, 4.08. Found: C, 41.72; H, 4.11; N, 3.97. IR data (KBr; ν_{max} , cm^{-1}): 3097, 3052, 2936, 2868, 1643, 1581, 1517, 1456, 1429, 1408, 1285, 1183, 1101, 1064, 914, 863, 785, 672, 601, 553, 451. UV-Vis data in methanol (λ , nm (ϵ , $\text{L mol}^{-1} \text{cm}^{-1}$): 220 (1.71×10^4), 245 (1.34×10^4), 273 (9.17×10^3), 380 (3.70×10^3).

2.3. Preparation of Complex 2

4-Bromosalicylaldehyde (0.20 g, 10 mmol) and *N*-isopropylethane-1,2-diamine (0.102 g, 10 mmol) were dissolved and stirred at ambient temperature in methanol (30 mL). Thirty minutes later, nickel acetate tetrahydrate (0.50 g, 20 mmol) was added to the solution. The color turned from yellow to deep green. The reaction mixture was stirred for about 1 h and filtered. The filtrate was al-

lowed to slow evaporate for a few days, generating green block shaped single crystals. Yield: 0.21 g (43%). Anal. Calcd for $\text{C}_{32}\text{H}_{44}\text{Br}_2\text{N}_4\text{Ni}_3\text{O}_{10}$: C, 39.19; H, 4.52; N, 5.71. Found: C, 38.96; H, 4.61; N, 5.82. IR data (KBr; ν_{max} , cm^{-1}): 3107, 3075, 2935, 2858, 1627, 1582, 1550, 1473, 1430, 1409, 1396, 1295, 1188, 1157, 1102, 987, 862, 785, 667, 610, 565, 463. UV-Vis data in methanol (λ , nm (ϵ , $\text{L mol}^{-1} \text{cm}^{-1}$): 222 (1.56×10^4), 240 (1.70×10^4), 265 (5.32×10^3), 335 (4.81×10^3).

2.4. X-ray Crystallography

X-ray data for the complexes were collected on a Bruker SMART 1000 CCD single crystal diffractometer at 298(2) K, equipped with a graphite monochromator and a Mo $\text{K}\alpha$ fine-focus sealed tube ($\lambda = 0.71073 \text{ \AA}$) by the ω scan method. Reflections were corrected for Lorentz and polarization effects, and for absorption by semi-empirical methods based on symmetry-equivalent and repeated reflections. The SMART software was used for data acquisition and the SAINT-PLUS software was used for data extraction.⁶ The absorption corrections were performed with the help of SADABS program.⁷ The structures were solved by direct methods and refined on F^2 by full-matrix least-squares procedures. All non-hydrogen atoms were refined using anisotropic thermal parameters. Hydrogen atoms were included at idealized positions by using a riding model. The SHELX-97 programs were used for structure solution and refinement.⁸ Selected crystallographic data for the complexes are listed in Table 1.

Table 1. Crystal data and structure refinement parameters for complexes 1 and 2

	1	2
Formula	$\text{C}_{12}\text{H}_{14}\text{BrCuN}_3\text{OS}$	$\text{C}_{32}\text{H}_{44}\text{Br}_2\text{N}_4\text{Ni}_3\text{O}_{10}$
<i>M</i>	391.8	980.7
Temperature (K)	298(2)	298(2)
Crystal system	Orthorhombic	Monoclinic
Space group	<i>Pca</i> 2 ₁	<i>P</i> 2 ₁ / <i>c</i>
<i>a</i> (Å)	12.875(1)	11.4402(13)
<i>b</i> (Å)	6.788(1)	19.8179(17)
<i>c</i> (Å)	16.531(1)	8.6384(15)
β (°)		100.8150(10)
<i>V</i> (Å ³)	1444.8(2)	1923.7(4)
<i>Z</i>	4	2
<i>D</i> _c (g/cm ³)	1.801	1.693
μ (mm ⁻¹)	4.416	3.588
<i>F</i> (000)	780	996
Reflections collected	12900	10436
Independent reflections	2978	3581
<i>R</i> _{int}	0.0448	0.0998
Reflections with $F^2 > 2\sigma(F^2)$	2644	1552
<i>R</i> ₁ [$F^2 > 2\sigma(F^2)$]	0.0405	0.0491
<i>wR</i> ₂ (all data)	0.1020	0.0907
Goodness-of-fit on F^2	1.082	0.931

3. Results and Discussion

3. 1. Chemistry

Both complexes were readily prepared by reacting nickel acetate tetrahydrate with Schiff base ligands. The elemental analysis data are consistent with the general molecular formulae of the complexes. In complex **1**, the acetate ligands act as bidentate bridging groups. In complex **2**, two acetate ligands act as bidentate bridging groups, and the other two act as chelating bridging groups. The complexes are soluble in common organic solvents like dimethyl sulphoxide, dimethylformamide, methanol, and ethanol.

3. 2. Infrared and Electronic Spectra of the Complexes

In the spectra of the free Schiff bases HL¹ and HL², the bands at 1650 and 1645 cm⁻¹, respectively, are assigned to the azomethine groups, $\nu_{C=N}$,⁹ and the broad and weak absorptions at about 3430 cm⁻¹ are assigned to the hydroxyl groups, ν_{O-H} . In the complexes, the absence of the O–H stretching and bonding vibrations indicates coordination through the phenolate groups. The C=N stretches of the complexes are observed at lower frequencies (1643 and 1627 cm⁻¹) when compared to the free Schiff bases.¹⁰ The phenolic $\nu(Ar-O)$ in the free ligands exhibit bands at about 1270 cm⁻¹. However, in the complexes it appears at about 1283 cm⁻¹. The shift to higher wave number is an indication of C–O–M bond formation. The bands at about 1582 and 1408 cm⁻¹ are assigned to the acetate ligands.^{4a,5b} The occurrence of new bands in the 450–670 cm⁻¹ region confirms the presence of metal-nitrogen and metal-oxygen bonds, respectively.¹¹

In the electronic spectra of the free Schiff bases and the complexes, the absorption frequencies ascribed to the aromatic $\pi-\pi^*$ and $n-\pi^*$ transitions are located in the region 240–290 nm.¹² In the electronic spectra of the complexes, the absorption centered at 380 nm for complex **1** and 335 nm for complex **2** are assigned to ligand-to-metal charge transfer.¹³

3. 3. Structure Description of Complex 1

The molecular structure of complex **1** is depicted in Fig. 1. Bond parameters associated with the metal atom are listed in Table 2. The molecular structure is centrosymmetric with Ni2 atom on an inversion center. The structure shows a trinuclear complex consisting of three Ni atoms in a linear array, which is bridged by two acetate ligands and four phenolate groups. The Ni...Ni distance is 3.053(2) Å. The Schiff base ligand coordinates to the Ni atoms through phenolate O and imino N atoms. The ligand 4-bromosalicylaldehyde coordinates to the Ni atoms through carbonyl O and phenolate O atoms. The acetate ligand acts as a bidentate bridging group. The Ni2 atom is located at the

inversion centre of the complex in an octahedral geometry. This atom is coordinated by four phenolate O atoms from the Schiff base and 4-bromosalicylaldehyde ligands that form a plane and, near-perpendicularly to it, by two O atoms from two acetate bridging ligands that connect the central Ni atom to the outer Ni atoms. The greatest deviation of the bond angles from those expected for an ideal octahedral geometry is found for O1–Ni2–O3 with 79.3(3)° and O1–Ni2–O3A with 100.7(3)°. The remaining bond angles are close to the ideal values for the octahedral coordination. The *cis* and *trans* coordinate bond angles for Ni2 are in the region 79.3(3)–100.7(3)° and 180°. The terminal Ni1 atom is in an octahedral environment and is coordinated by the four donor atoms of the Schiff base and 4-bromosalicylaldehyde ligands in the equatorial plane, and by two O atoms from one bridging acetate group and one coordinated DMF ligand in the axial positions. The greatest deviations from an ideal octahedral geometry are found in the O2–Ni1–O6 (84.9(3)°) and in N1–Ni1–O2 (100.8(4)°) angles. The remaining bond angles are close to the ideal values for the octahedral coordination. The *cis* and *trans* coordinate bond angles for Ni1 are in the region 84.9(3)–100.8(4)° and 168.8(3)–176.6(3)°. The Ni–O and Ni–N bond lengths are similar to those reported previously.¹⁴

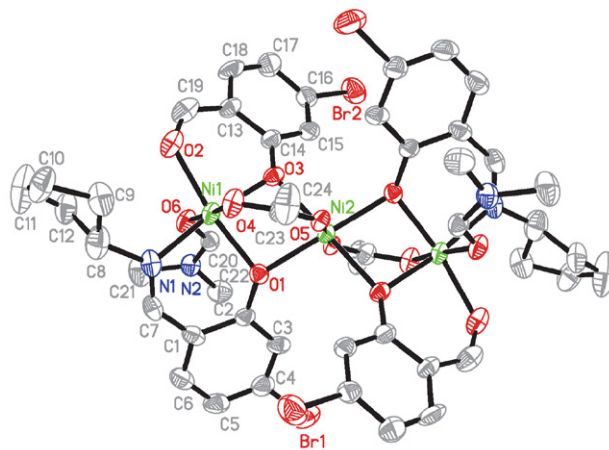


Figure 1. ORTEP diagram of complex **1** with thermal ellipsoids at 30% probability level. Selected bond lengths and angles are given in Table 2. Unlabeled atoms are related to the symmetry operation $1 - x, 1 - y, 1 - z$.

3. 4. Structure Description of Complex 2

The molecular structure of complex **2** is depicted in Fig. 2. Bond parameters associated with the metal atom are listed in Table 2. The molecular structure is centrosymmetric with Ni2 atom on an inversion center. The structure shows a trinuclear complex consisting of three Ni atoms in a linear array, which are bridged by four acetate ligands and two phenolate groups. The Ni...Ni distance is 3.043(2) Å. The Schiff base ligand coordinates to the Ni atoms through phenolate O, imino N and amino N atoms. Two of the acetate ligands act as bidentate bridging groups, and the other

two act as chelating bridging groups. The Ni2 atom is located at the inversion centre of the complex in an octahedral geometry. This atom is coordinated by two phenolate O atoms from the Schiff base ligands and two O atoms from two bidentate bridging acetate groups that form a plane and, near-perpendicularly to it, by two O atoms from two chelating bridging acetate groups that connect the central Ni atom to the outer Ni atoms. The greatest deviation of the bond angles from those expected for an ideal octahedral geometry is found for O1–Ni2–O2 with 79.97(16)° and O1–Ni2–O2A with 100.03(16)°. The remaining bond angles are close to the ideal values for the octahedral coordination. The *cis* and *trans* coordinate bond angles for Ni2 are in the region 79.97(16)–100.03(16)° and 180°. The terminal Ni1 atom is in an octahedral environment and is coordinated by the three donor atoms of the Schiff base ligand and the O2 atom of the chelating bridging acetate group in the equatorial plane, and by O3 atom of the chelating bridging acetate group and O4 atom of the bidentate bridging acetate group in the axial positions. The greatest deviations from an ideal octahedral geometry are found in O2–Ni1–O3 (60.69(19)°) and in O2–Ni1–N2 (103.6(3)°) angles. The remaining bond angles are close to the ideal values for the octahedral coordination. The *cis* and *trans* coordinate bond angles for Ni1 are in the region 60.69(19)–103.6(3)° and 157.1(2)–174.1(2)°. The Ni–O and Ni–N bond lengths are comparable to those of complex 1.

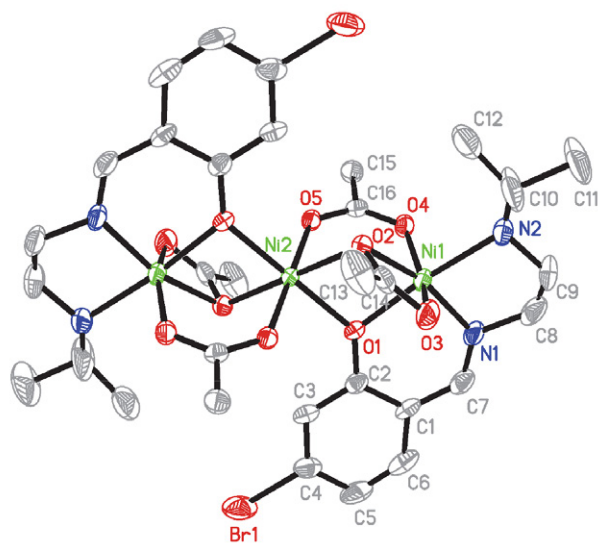


Figure 2. ORTEP diagram of complex 2 with thermal ellipsoids at 30% probability level. Selected bond lengths and angles are given in Table 2. Unlabeled atoms are related to the symmetry operation 1 – *x*, 1 – *y*, 1 – *z*.

3. 5. Antimicrobial Activity

The complexes were assayed against the bacteria *Escherichia coli* and *Salmonella typhi*, and the fungi *Aspergillus niger* and *Candida albicans* by MIC (Minimum In-

hibitory Concentration) method with three different concentrations of 100, 50 and 25 µg.¹⁵ The activity was also assayed for the free Schiff bases, the pure solvent DMF and the standard gentamycine for each of antibacterial and flucanazole for antifungal cultures. Final adjustments were made using optical density measurement for bacteria (absorbance 0.05 at 580 nm). The zones of inhibition in millimeter for the compounds are presented in Table 3. The two complexes have similar activities against the bacteria and fungi, and they are more susceptible toward bacterial cells than fungicidal cells. In general, both complexes have better activities than the free Schiff bases. The trends are in

Table 2. Selected bond distances (Å) and angles (°) for complexes 1 and 2

1			
Bond distances			
Ni1–N1	2.035(10)	Ni1–O1	2.014(7)
Ni1–O2	2.062(9)	Ni1–O3	2.023(7)
Ni1–O4	2.023(7)	Ni1–O6	2.125(8)
Ni2–O5	2.022(7)	Ni2–O1	2.048(6)
Ni2–O3	2.071(6)		
Bond angles			
O1–Ni1–O4	91.2(3)	O1–Ni1–O3	81.3(3)
O4–Ni1–O3	90.9(3)	O1–Ni1–N1	89.7(4)
O4–Ni1–N1	93.2(4)	O3–Ni1–N1	170.2(4)
O1–Ni1–O2	168.8(3)	O4–Ni1–O2	92.0(3)
O3–Ni1–O2	88.0(3)	N1–Ni1–O2	100.8(4)
O1–Ni1–O6	92.1(3)	O4–Ni1–O6	176.6(3)
O3–Ni1–O6	90.5(3)	N1–Ni1–O6	85.8(4)
O2–Ni1–O6	84.9(3)	O5–Ni2–O5A	180
O5–Ni2–O1A	92.3(3)	O5–Ni2–O1	87.7(3)
O1–Ni2–O1A	180	O5–Ni2–O3A	90.7(3)
O1–Ni2–O3A	100.7(3)	O5–Ni2–O3	89.3(3)
O1–Ni2–O3	79.3(3)	O3–Ni2–O3A	180
2			
Bond distances			
Ni1–N1	1.976(6)	Ni1–N2	2.152(8)
Ni1–O1	2.010(4)	Ni1–O2	2.100(4)
Ni1–O3	2.201(6)	Ni1–O4	2.015(4)
Ni2–O5	2.009(4)	Ni2–O1	2.057(4)
Ni2–O2	2.117(4)		
Bond angles			
N1–Ni1–O1	90.5(3)	N1–Ni1–O4	100.9(2)
O1–Ni1–O4	93.11(17)	N1–Ni1–O2	159.8(2)
O1–Ni1–O2	81.45(16)	O4–Ni1–O2	98.00(18)
N1–Ni1–N2	83.7(3)	O1–Ni1–N2	174.1(2)
O4–Ni1–N2	89.3(2)	O2–Ni1–N2	103.6(3)–
N1–Ni1–O3	101.4(2)	O1–Ni1–O3	91.91(19)
O4–Ni1–O3	157.1(2)	O2–Ni1–O3	60.69(19)
N2–Ni1–O3	88.0(3)	O5–Ni2–O5A	180
O5–Ni2–O1	90.09(16)	O5–Ni2–O1A	89.91(16)
O1–Ni2–O1A	180	O5–Ni2–O2A	90.16(17)
O1–Ni2–O2A	100.03(16)	O5–Ni2–O2	89.84(17)
O1–Ni2–O2	79.97(16)	O2–Ni2–O2A	180

Symmetry operation for A: 1 – *x*, 1 – *y*, 1 – *z*.

Table 3. Antimicrobial activities of the compounds (zone of inhibition in mm)

Compound	Bacteria		Fungi	
	<i>Escherichia coli</i>	<i>Salmonella typhi</i>	<i>Aspergillus niger</i>	<i>Candida albicans</i>
1	29	31	15	18
2	30	30	16	18
HL ¹	15	11	–	–
HL ²	13	12	–	–
Gentamycine	28	28	–	–
Flucanazole	–	–	23	23
DMF	12	14	12	12

The concentration is 100 µg L⁻¹.

accordance with the literature that metal complexes are more active in the biological potential than the ligands used in the synthesis.¹⁶ When comparing the antimicrobial activity of the studied complexes to those of reference antibiotics, the inhibitory ability is found to be good. For example, the two complexes have similar or even higher activity on the bacteria *Escherichia coli* and *Salmonella typhi* than gentamycine, and have effective activity on *Aspergillus niger* and *Candida albicans*, which is seldom seen in the literature. The results indicate that the two complexes can possibly be used in the treatment of diseases caused by the bacteria that were tested.

4. Conclusion

A pair of novel acetato-bridged nickel(II) complexes derived from the Schiff base ligands 5-bromo-2-((cyclopentylimino)methyl)phenol and 5-bromo-2-(((2-(isopropylamino)ethyl)imino)methyl)phenol were prepared. Single crystal structures of the complexes indicates that both complexes are trinuclear nickel(II) compounds. All of the nickel atoms in the complexes are in octahedral coordination geometries. The complexes have good antimicrobial activities against *Escherichia coli*, *Salmonella typhi*, *Aspergillus niger* and *Candida albicans*.

Supplementary Material

CCDC Nos. 1974759 (1) and 1974760 (2) contain the supplementary crystallographic data for this paper. These data can be obtained free of charge from the Cambridge Crystallographic Data Centre via www.ccdc.cam.ac.uk/data_request/cif. Crystal data and details of the data collection and refinement for the complexes are collected in Table 1.

5. References

- (a) H. Keypour, F. Forouzandeh, S. Salehzadeh, F. Hajibabaei, S. Feizi, R. Karamian, N. Ghiasi, R. W. Gable, *Polyhedron* **2019**, *170*, 584–592; DOI:10.1016/j.poly.2019.06.023
- (b) L. Saghatforoush, K. Moeini, S. A. Hosseini-Yazdi, Z. Mardani, A. Bakhtiari, A. Hajabbas-Farshchi, S. Honarvar, M. S. M. Abdelbaky, *Polyhedron* **2019**, *170*, 312–324; DOI:10.1016/j.poly.2019.05.057
- (c) S. C. Manna, S. Mistri, A. Patra, M. K. Mahish, D. Saren, R. K. Manne, M. K. Santra, E. Zangrando, H. Puschmann, *Polyhedron* **2019**, *171*, 77–85; DOI:10.1016/j.poly.2019.06.049
- (d) M. S. S. Adam, O. M. El-Hady, F. Ullah, *RSC Advances* **2019**, *9*, 34311–34329; DOI:10.1039/C9RA06816C
- (e) K. Dankhoff, M. Gold, L. Kober, F. Schmitt, L. Pfeifer, A. Durrmann, H. Kostrhunova, M. Rothemund, V. Brabec, R. Schobert, *Dalton Trans.* **2019**, *48*, 15220–15230. DOI:10.1039/C9DT02571E
- (a) H.-Y. Qian, *Acta Chim. Slov.* **2019**, *66*, 995–1001; DOI:10.4149/neo_2019_190112N36
- (b) H. Y. Qian, *Russ. J. Coord. Chem.* **2018**, *44*, 32–38; DOI:10.1134/S1070328418010074
- (c) H.-Y. Qian, *Inorg. Nano-Met. Chem.* **2018**, *48*, 615–619. DOI:10.1080/24701556.2019.1567542
- (a) K. Ghosh, S. Banerjee, S. Chattopadhyay, *CrystEngComm* **2019**, *21*, 6026–6037; DOI:10.1039/C9CE00922A
- (b) H. Kargar, V. Torabi, A. Akbari, R. Behjatmanesh-Ardakani, A. Sahraei, M. N. Tahir, *Struct. Chem.* **2019**, *30*, 2289–2299; DOI:10.1007/s11224-019-01350-9
- (c) R. Ogawa, T. Suzuki, M. Hirotsu, N. Nishi, Y. Shimizu, Y. Sunatsuki, Y. Teki, I. Kinoshita, *Dalton Trans.* **2019**, *48*, 13622–13629. DOI:10.1039/C9DT03007G
- (a) B.-H. Ye, X.-Y. Li, I. D. Williams, X.-M. Chen, *Inorg. Chem.* **2002**, *41*, 6426–6431; DOI:10.1021/ic025806+
- (b) U. Kumar, J. Thomas, N. Thirupathi, *Inorg. Chem.* **2010**, *49*, 62–72. DOI:10.1021/ic901100z
- (a) A. Majumder, G. M. Rosair, A. Mallick, N. Chattopadhyay, S. Mitra, *Polyhedron* **2006**, *25*, 1753–1762; DOI:10.1016/j.poly.2005.11.029
- (b) P. Li, M. J. Niu, M. Hong, S. Cheng, J. M. Dou, *J. Inorg. Biochem.* **2014**, *137*, 101–108; DOI:10.1016/j.jinorgbio.2014.04.005
- (c) M. Salehi, F. Rahimifar, M. Kubicki, A. Asadi, *Inorg. Chim. Acta* **2016**, *443*, 28–35; DOI:10.1016/j.ica.2015.12.016
- (d) X.-S. Zhou, X.-S. Cheng, Y.-N. Li, F.-Y. Tian, F.-Y. Xu, Z.-L. You, *Chin. J. Inorg. Chem.* **2013**, *29*, 397–402;
- (e) J.-C. Zhang, Y. Lu, X.-H. Li, Z.-L. You, *Chin. J. Inorg. Chem.* **2012**, *28*, 1259–1264.

6. SMART version 5.63 and SAINT-PLUS version 6.45, Bruker–Nonius Analytical X-ray Systems Inc., Madison, WI, USA, 2003.
7. G. M. Sheldrick. SADABS, Empirical Absorption Correction Program, University of Göttingen, Göttingen, Germany, 1997.
8. G. M. Sheldrick. SHELX-97, Structure Determination Software, University of Göttingen, Göttingen, Germany, 1997.
9. (a) M. Zhang, D.-M. Xian, H.-H. Li, J.-C. Zhang, Z.-L. You, *Aust. J. Chem.* **2012**, *65*, 343–350; DOI:10.1071/CH11424
(b) M. Duan, Y. Li, L. Xu, H. Yang, F. Luo, Y. Guan, B. Zhang, C. Jing, Z. You, *Inorg. Chem. Commun.* **2019**, *100*, 27–31. DOI:10.1016/j.inoche.2018.12.009
10. (a) H.-Y. Qian, N. Sun, *Transition Met. Chem.* **2019**, *44*, 501–506; DOI:10.1007/s11243-018-00296-x
(b) H. Y. Qian, *Russ. J. Coord. Chem.* **2017**, *43*, 780–786. DOI:10.1134/S1070328417110070
11. H.-Y. Qian, *Inorg. Nano-Met. Chem.* **2018**, *48*, 461–466. DOI:10.1080/24701556.2019.1569689
12. H. Liu, D. Niu, Z. Lu, *J. Coord. Chem.* **2009**, *62*, 3763–3771. DOI:10.1080/00958970903159131
13. A. Ray, D. Sadhukhan, G. M. Rosair, C. J. Gomez-Garcia, S. Mitra, *Polyhedron* **2009**, *28*, 3542–3550. DOI:10.1016/j.poly.2009.07.017
14. (a) M. K. Taylor, J. Reglinski, D. Wallace, *Polyhedron* **2004**, *23*, 3201–3209; DOI:10.1016/j.poly.2004.10.002
(b) R. Sanyal, S. K. Dash, P. Kundu, D. Mandal, S. Roy, D. Das, *Inorg. Chim. Acta* **2016**, *453*, 394–401; DOI:10.1016/j.ica.2016.08.047
(c) L. Rigamonti, A. Forni, *Inorg. Chim. Acta* **2018**, *473*, 216–222. DOI:10.1016/j.ica.2018.01.007
15. M. A. Phaniband, S. D. Dhumwad, *J. Coord. Chem.* **2009**, *62*, 2399–2410. DOI:10.1080/00958970902803341
16. (a) L.-W. Xue, H.-J. Zhang, P.-P. Wang, *Acta Chim. Slov.* **2019**, *66*, 190–195; DOI:10.17344/acsi.2018.4868
(b) G.-X. He, L.-W. Xue, Q.-L. Peng, P.-P. Wang, H.-J. Zhang, *Acta Chim. Slov.* **2019**, *66*, 570–575;
(c) S. Daravath, A. Rambabu, N. Vamsikrishna, N. Ganji, S. Raj, *J. Coord. Chem.* **2019**, *72*, 1973–1993; DOI:10.1080/00958972.2019.1634263
(d) M. A. Shaheen, W. Xiao, M. Aziz, A. Karim, M. Saleem, M. Mustaqeem, T. Mehmood, M. N. Tahir, A. Sltan, A. Simair, C. Lu, *Russ. J. Gen. Chem.* **2019**, *89*, 1691–1695. DOI:10.1134/S1070363219080231

Povzetek

Z reakcijo $\text{Ni}(\text{OAc})_2 \cdot 2\text{H}_2\text{O}$ s Schiffovo bazo 5-bromo-2-((ciklopentilimino)metil)fenolom (HL^1) in 5-bromo-2-(((2-(izopropilamino)etil)imino)metil)fenolom (HL^2) v metanolu smo izolirali dva diskretna trijedrna kompleksa $[\text{Ni}_3(\text{L}^1)_2(\mu_2\text{-}\eta^1\text{-}\eta^1\text{-OAc})_2(\text{DMF})_2(\text{BrSal})_2]$ (**1**) in $[\text{Ni}_3(\text{L}^2)_2(\mu_2\text{-}\eta^1\text{-}\eta^1\text{-OAc})_2(\mu_2\text{-}\eta^2\text{-}\eta^1\text{-OAc})_2]$ (**2**), kjer je BrSal monoanionska oblika 4-bromosalicilaldehida. Kompleksa sta bila okarakterizirana z elementno analizo, IR in UV-Vis spektroskopijo. Strukture kompleksov so bile določene z rentgensko monokristalno difrakcijo. V obeh kompleksih je nikeljev atom v oktaedrični koordinaciji. Ligand L^1 se koordinira na nikeljev atom preko fenolatnega O in imino N atoma, ligand L^2 se koordinira na nikeljev atom preko fenolatnega O, imino N in amino N atomov. Določena je bila tudi protimikrobna aktivnost kompleksov.



Except when otherwise noted, articles in this journal are published under the terms and conditions of the Creative Commons Attribution 4.0 International License

Scientific paper

Molybdcic Acid-Functionalized Nano-Fe₃O₄@TiO₂ as a Novel and Magnetically Separable Catalyst for the Synthesis of Coumarin-Containing Sulfonamide Derivatives

Jamileh Etemad Gholtash, Mahnaz Farahi,* Bahador Karami and Mahsa Abdollahi

Department of Chemistry, Yasouj University, P. O. Box 353, Yasouj 75918-74831, Iran

* Corresponding author: E-mail: farahimb@yu.ac.ir

Received: 01-11-2020

Abstract

Supported molybdcic acid on nano-Fe₃O₄@TiO₂ (Fe₃O₄@TiO₂@(CH₂)₃OMoO₃H) has been successfully prepared, characterized and applied as a catalyst for the synthesis of sulfonamide containing coumarin moieties. The prepared Fe₃O₄ nanoparticles by coprecipitation of Fe²⁺ and Fe³⁺ ions were treated with tetraethyl orthotitanate to obtain Fe₃O₄@TiO₂. By anchoring 3-chloropropyltriethoxysilan on Fe₃O₄@TiO₂ followed by reacting with molybdcic acid, the desired catalyst was produced. The synthesized catalyst was characterized using XRD, SEM, EDS, FT-IR and VSM analysis. Fe₃O₄@TiO₂@(CH₂)₃OMoO₃H was used as a catalyst for the synthesis of sulfonamide containing coumarin moieties *via* a three-component reaction of aryl aldehydes, *para*-toluenesulfonamide and 4-hydroxycoumarin or 5,7-dihydroxy-4-methylcoumarin. The catalyst recovery test showed the catalyst is highly reusable without losing its activity.

Keywords: Nanocatalyst; *para*-toluenesulfonamide; aromatic aldehydes; 4-hydroxycoumarin; 5,7-dihydroxy-4-methylcoumarin

1. Introduction

Nanochemistry is becoming increasingly significant which involves the synthesis and application of nanoparticles of different sizes and shapes.^{1–9} Nanoparticles are different from their bulk counterparts and show special properties. A considerable amount of attention to nanoparticles is due to their unique properties such as ease of availability, chemical inertness, high surface area to volume ratio, high activity and selectivity, thermal stability and low toxicity.^{10, 11} Nanomaterials have been widely utilized as solid support material for the design of environmentally benign heterogeneous catalysts to address various economic and green chemistry issues.^{12–15} Among them, magnetic nanoparticles (MNPs), especially nano-Fe₃O₄, have been more desirable because of their remarkable advantages. Nano-Fe₃O₄ has been intensively used as catalytic supports owing to the capability of separation from the reaction mixture *via* an external magnet which achieves a simple separation without filtration.^{16,17} Supported catalysts on nano-Fe₃O₄ show not only high catalytic activity but

also a high degree of chemical stability and they do not swell in organic solvents.

Nano-TiO₂ owing to its nontoxicity, long-term photostability, and high effectiveness has broadly been applied as catalyst in many organic transformations.^{18,19} It has good mechanical resistance and stability in acidic and oxidative environments. Nano-TiO₂ is broadly utilized in fuel processing because of its tunable porous surface and distribution, high thermal stability and mechanical strength.²⁰ Despite the several mentioned advantages of TiO₂ nanoparticles, they are difficult to separate from the reaction media because of their small size. To simplify the separation and in order to increase the surface area, TiO₂ can be immobilized on magnetic nanoparticles to produce magnetically recoverable heterogeneous catalysts.^{21–23}

In recent years, there has been an increased interest on the utilization of sulfonamide derivatives as basic constituents of numerous drugs include anticancer, anti-inflammatory, antiviral agents and HIV-protease inhibitors.^{24–26} Antibacterial agents with sulfonamide structure, *e.g.* sulfadiazine have been therapeutically used for many decades.²⁷ They

have also been applied as azo dyes for achieving improved light stability, water solubility, and fixation of fibers. Sulfonamides are also known as inhibitors of the activity of the enzymes, such as dihydropteroate synthase (DHPS), matrix metalloproteinase, and carbonic anhydrase (CA).²⁸

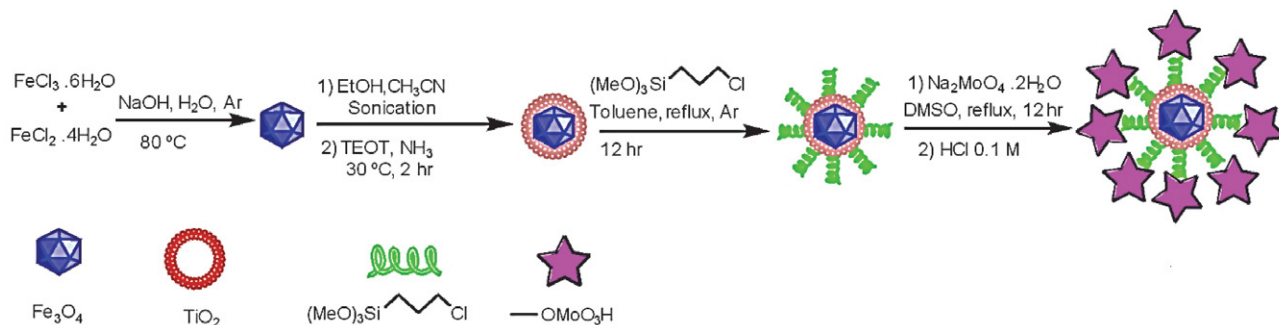
Coumarins as a class of lactones are important heterocycles that not only have many biological activities, but are also found in the structure of a large number of natural compounds.²⁹ With an entirely looking at medicinally important heterocycles, we find numerous drugs containing coumarin moiety.^{30–32} Their easy synthetic modifications cause the design and synthesis of various coumarin-based derivatives with diverse activities against cancer.³³ Also, coumarins are widely employed as cosmetics, pigments and agrochemicals. They can be fused with different classes of heterocycles to obtain novel useful compounds. The unique properties and wide applications of coumarins have promoted extensive studies for the synthesis of these heterocycles.

Due to these benefits and as a continuation of our studies on the preparation of new heterogeneous catalysts,^{34–36} herein we have developed synthesis and characterization of $\text{Fe}_3\text{O}_4@\text{TiO}_2@(\text{CH}_2)_3\text{OMoO}_3\text{H}$ as a novel recoverable nanocatalyst. Then, its application was investigated for the synthesis of sulfonamide containing coumarin moieties.

2. Results and Discussion

Because of reasonable needs for clean and green heterogeneous catalysts, $\text{Fe}_3\text{O}_4@\text{TiO}_2@(\text{CH}_2)_3\text{OMoO}_3\text{H}$ was synthesized following the procedure shown in Scheme 1. In the first step, the magnetic Fe_3O_4 nanoparticles were synthesized by coprecipitation of iron(II) and iron(III) ions.¹⁷ Consequently, the TiO_2 shell was prepared by the hydrolysis of tetraethyl orthotitanate (TEOT) in an absolute ethanol/acetonitrile mixture in the presence of the well-dispersed Fe_3O_4 nanocrystals.³⁷ In continuation, the OH groups on the titanium coating magnetic nanoparticles ($\text{Fe}_3\text{O}_4@\text{TiO}_2$) can be functionalized with 3-chloropropyltriethoxysilan molecule.³⁸ Next, the new catalyst **1** was obtained by replacing chloride group using molybdic acid. The structure of the nanocatalyst **1** was studied and fully characterized using SEM, EDX, VSM, XRD, and FT-IR.

Fig. 1 shows the wide-angle XRD patterns of nano- Fe_3O_4 , $\text{Fe}_3\text{O}_4@\text{TiO}_2$ and $\text{Fe}_3\text{O}_4@\text{TiO}_2@(\text{CH}_2)_3\text{OMoO}_3\text{H}$. As shown in Figure 1a, all the peaks agreed on face-centered cubic (fcc) Fe_3O_4 . The data showed diffraction peaks at $2\theta = 37.158, 43.173, 66.98, 74.188, \text{ and } 79.171$ which can be indexed to (222), (400), (442), (533), and (444) with the JCPD 01-88-0315. Additionally, the peak of the highest in-



Scheme 1. Synthesis of $\text{Fe}_3\text{O}_4@\text{TiO}_2@(\text{CH}_2)_3\text{OMoO}_3\text{H}$ (**1**).

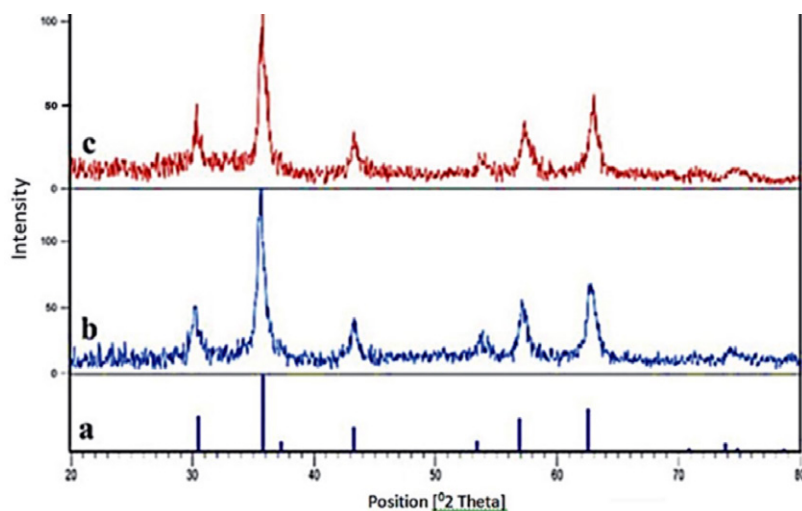


Figure 1. The XRD patterns of (a) nano- Fe_3O_4 , (b) $\text{Fe}_3\text{O}_4@\text{TiO}_2$ and (c) $\text{Fe}_3\text{O}_4@\text{TiO}_2@(\text{CH}_2)_3\text{OMoO}_3\text{H}$.

tensity (311 , $2\theta = 35.522$) was picked out to evaluate the particle diameter of the nanoparticles. Furthermore, in Figure 1b a broad diffraction peak appeared at $2\theta = 20$ – 30 nm that can be indexed to amorphous TiO_2 .³⁹ The main peaks for the $\text{Fe}_3\text{O}_4@/\text{TiO}_2$ are similar to the standard Fe_3O_4 particles, which reveals that the crystal structure of $\text{Fe}_3\text{O}_4@/\text{TiO}_2$ is well coated. No obvious diffraction peak for the TiO_2 is observed, suggesting amorphous TiO_2 coating is formed by the hydrolysis of tetraethyl titanate (TEOT) in the presence of the well-dispersed Fe_3O_4 nanocrystals by a sol-gel process.⁴⁰ In Figure 1c, the confirming peak showing the presence of molybdate group has appeared in the range of $2\theta = 20$ – 30° which is covered by the broad peak of TiO_2 .^{39, 41}

The FT-IR spectra of Fe_3O_4 , $\text{Fe}_3\text{O}_4@/\text{TiO}_2$, $\text{Fe}_3\text{O}_4@/\text{TiO}_2@(\text{CH}_2)_3\text{Cl}$ and $\text{Fe}_3\text{O}_4@/\text{TiO}_2@(\text{CH}_2)_3\text{OMoO}_3\text{H}$ were compared to analyze the progress of catalyst synthesis (Fig. 2). The observed characteristic peaks due to Fe–O stretching vibration at 583 cm^{-1} in all compared spectra is a confirmation of which nanostructure of Fe_3O_4 is preserved during the process. The appeared peaks at 1118 and 1400 cm^{-1} in Fig. 2b could be associated with stretching vibration modes of Ti–O and Fe–O–Ti bonds, respectively.³⁵ In Fig. 2c, the CH_2 bending as broadband and symmetric CH_2 and asymmetric CH_2 of the alkyl chains appear at 1480 cm^{-1} and 2860 – 2923 cm^{-1} , respectively. Fig. 2d shows new bands at 1623 and 3297 – 3436 cm^{-1} attributable to stretching vibration of Mo–O and OH.^{43,44}

The vibrating sample magnetometer (VSM) was applied to evaluate the magnetic measurement of the prepared catalyst (Fig. 3). Based on the results, the saturation magnetization for $\text{Fe}_3\text{O}_4@/\text{TiO}_2@(\text{CH}_2)_3\text{OMoO}_3\text{H}$ and $\text{Fe}_3\text{O}_4@/\text{TiO}_2$ are 22.98 and 77.85 emu g^{-1} , respectively. The decrease of the saturation magnetization of $\text{Fe}_3\text{O}_4@/\text{TiO}_2$

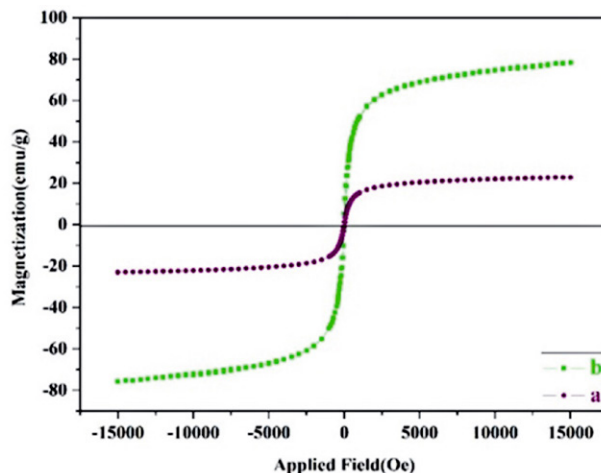


Figure 3. Room-temperature magnetization curves of (a) $\text{Fe}_3\text{O}_4@/\text{TiO}_2@(\text{CH}_2)_3\text{OMoO}_3\text{H}$ and (b) $\text{Fe}_3\text{O}_4@/\text{TiO}_2$.

after surface coating with molybdic acid was ascribed to the increase of particle size of $\text{Fe}_3\text{O}_4@/\text{TiO}_2$. This evidence indicates that molybdic acid immobilized on modified TiO_2 -coated Fe_3O_4 has been successfully obtained.

The surface morphology of $\text{Fe}_3\text{O}_4@/\text{TiO}_2@(\text{CH}_2)_3\text{OMoO}_3\text{H}$ was observed *via* a scanning electron microscopy (Fig. 4). The result demonstrates that nearly spherical nanoparticles with a narrow distribution were obtained with an average diameter of about 43.25 nm . Energy-dispersive X-ray spectroscopy (EDS) analysis of $\text{Fe}_3\text{O}_4@/\text{TiO}_2@(\text{CH}_2)_3\text{OMoO}_3\text{H}$ (Fig. 5) contains all expected elemental cases including Fe, Ti, Mo, C, Si and O. The EDS spectra of the catalyst confirmed the existence of molybdate and hence indicated that molybdic acid grafted successfully on the catalyst surface.

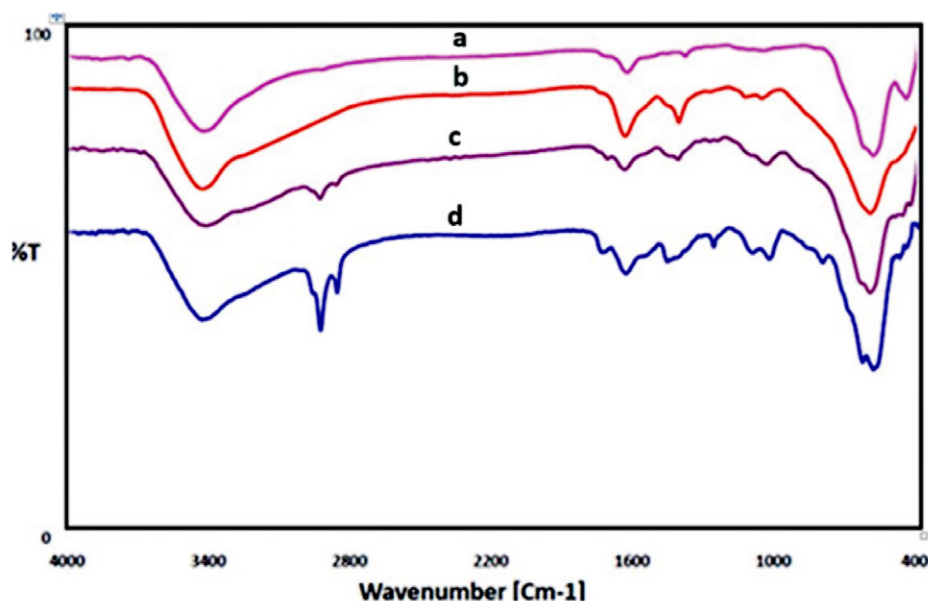


Figure 2. The FT-IR spectra of (a) Fe_3O_4 , (b) $\text{Fe}_3\text{O}_4@/\text{TiO}_2$, (c) $\text{Fe}_3\text{O}_4@/\text{TiO}_2@(\text{CH}_2)_3\text{Cl}$, and (d) $\text{Fe}_3\text{O}_4@/\text{TiO}_2@(\text{CH}_2)_3\text{OMoO}_3\text{H}$.

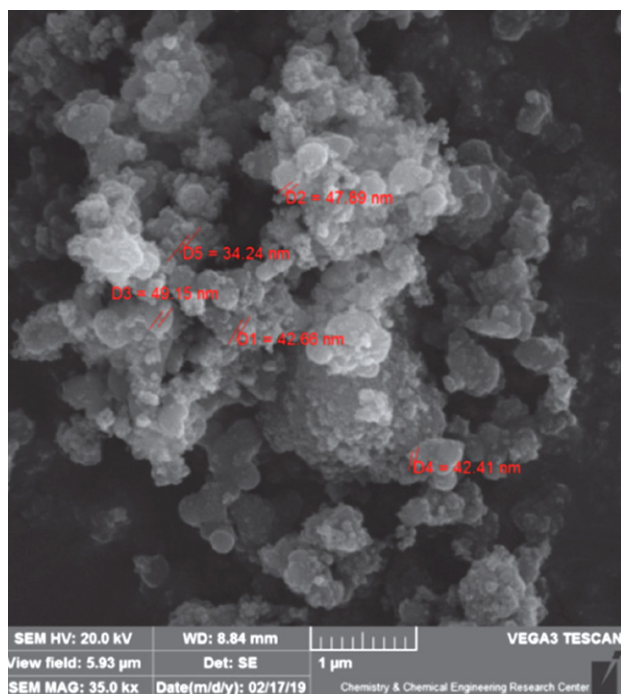


Figure 4. The SEM image of $\text{Fe}_3\text{O}_4@ \text{TiO}_2@ (\text{CH}_2)_3\text{OMoO}_3\text{H}$.

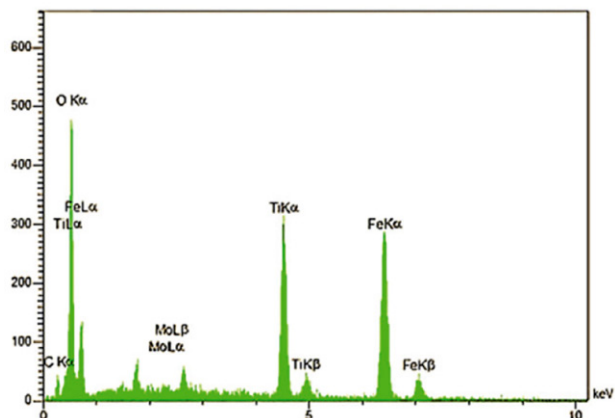
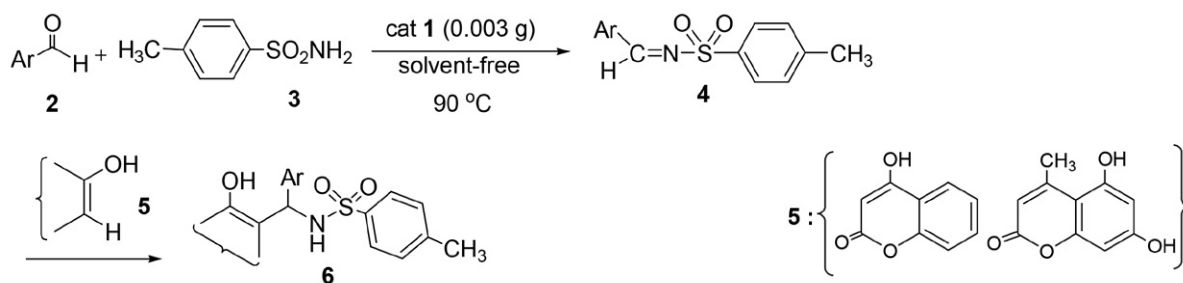


Figure 5. EDS analysis of $\text{Fe}_3\text{O}_4@ \text{TiO}_2@ (\text{CH}_2)_3\text{OMoO}_3\text{H}$.

The catalytic activity of $\text{Fe}_3\text{O}_4@ \text{TiO}_2@ (\text{CH}_2)_3\text{O-MoO}_3\text{H}$ was investigated in the synthesis of sulfonamide containing coumarins **6** via the reaction of aryl aldehydes (**2**), *para*-toluenesulfonamide (**3**) and compound **5** (4-hydroxycoumarin or 5,7-dihydroxy-4-methylcoumarin) (Scheme 2).



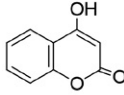
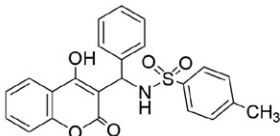
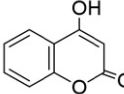
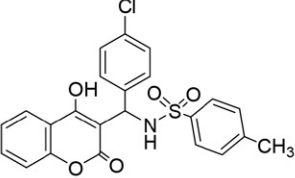
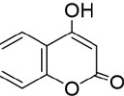
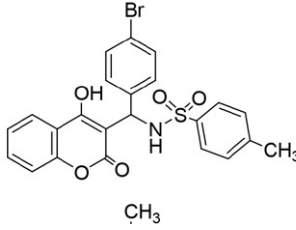
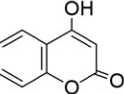
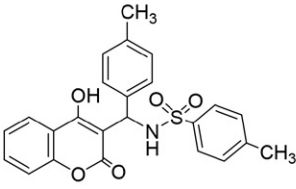
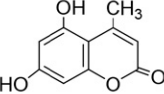
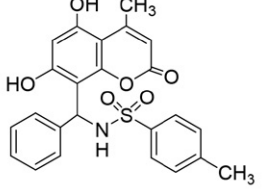
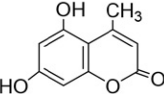
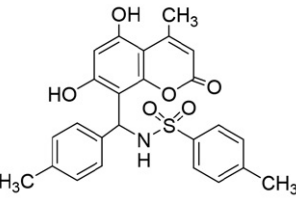
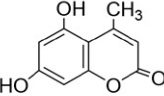
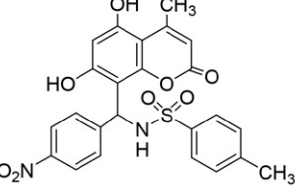
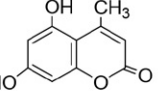
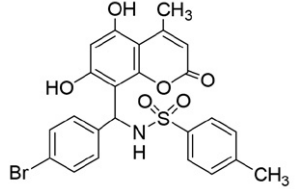
Scheme 2. Synthesis of sulfonamide containing coumarins by nanocatalyst **1**.

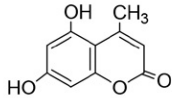
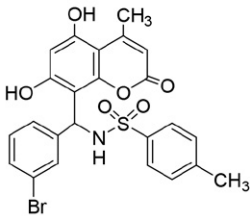
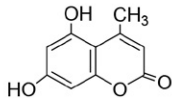
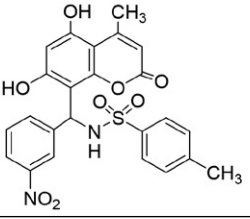
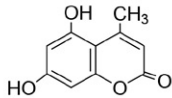
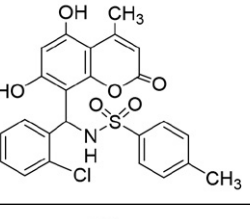
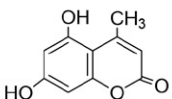
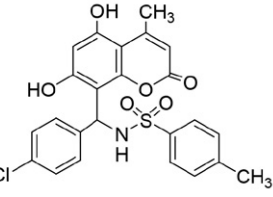
Table 1. Optimization of the model reaction.^a

Entry	Catalyst 1 (g)	Solvent	Temp. (°C)	Time (h)	Yield ^b (%)
1	–	–	25	24	–
2	–	–	80	24	5
3	–	–	100	24	9
4	–	Toluene	reflux	24	3
5	–	EtOH	reflux	24	5
6	0.001	–	60	3	50
7	0.003	–	60	3	65
8	0.005	–	60	3	60
9	0.007	–	60	3	57
10	0.003	EtOH	reflux	3	60
11	0.003	Toluene	reflux	3	55
12	0.003	H ₂ O	reflux	3	48
13	0.003	CHCl ₃	reflux	3	53
14	0.003	–	80	1.5	75
15	0.003	–	90	1.5	85
16	0.003	–	110	1.5	80

^a Reaction conditions: benzaldehyde (1 mmol), *para*-toluenesulfonamide (1 mmol) and 4-hydroxycoumarin (1 mmol). ^b Isolated yields.

Table 2. Synthesis of **6** in the presence of $\text{Fe}_3\text{O}_4@(\text{TiO}_2@(\text{CH}_2)_3\text{OMoO}_3\text{H})$.

Entry	Compound 5	Ar	Product	Mp (°C)	Time (min)
6a		C_6H_5		231–233	90
6b		4-ClC ₆ H ₄		251–253	85
6c		4-BrC ₆ H ₄		176–177	85
6d		4-CH ₃ C ₆ H ₄		263–264	120
6e		C_6H_5		260–262 ⁴⁶	240
6f		4-CH ₃ C ₆ H ₄		255–256 ⁴⁶	260
6g		4-NO ₂ C ₆ H ₄		219–221 ⁴⁶	200
6h		4-BrC ₆ H ₄		268–269 ⁴⁶	210

Entry	Compound 5	Ar	Product	Mp (°C)	Time (min)
6i		3-BrC ₆ H ₄		270–271 ⁴⁶	210
6j		3-NO ₂ C ₆ H ₄		230–232 ⁴⁶	200
6k		2-ClC ₆ H ₄		215–216 ⁴⁶	230
6l		4-ClC ₆ H ₄		208–210 ⁴⁶	220

^a Isolated yields.

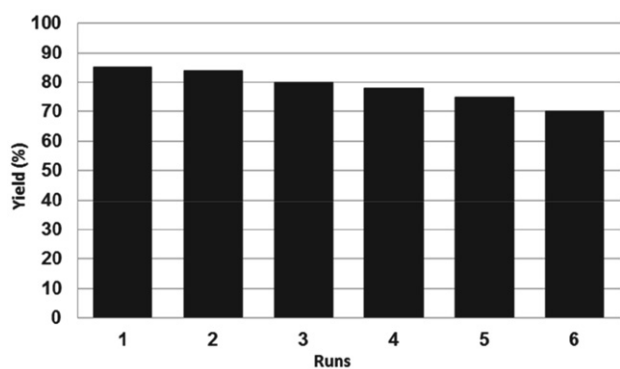


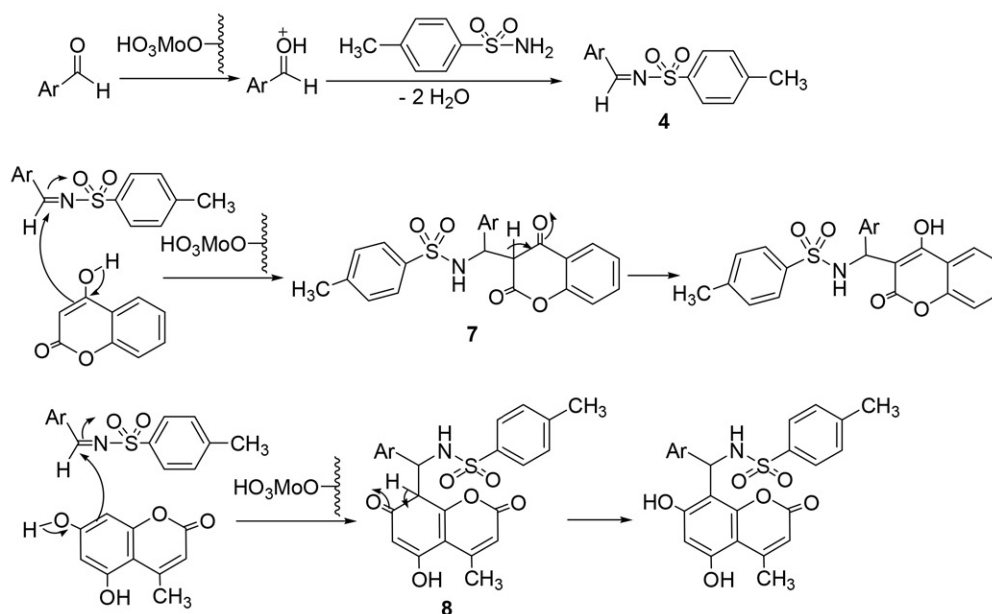
Figure 6. Reusability study of nanocatalyst **1** in the synthesis of **6a** at 90 °C under solvent-free conditions.

In a preliminary study, the reaction of benzaldehyde, *para*-toluenesulfonamide and 4-hydroxycoumarin was selected as a model reaction to determine suitable conditions. To illustrate the need of Fe₃O₄@TiO₂@(CH₂)₃OMoO₃H for this condensation, we examined the model reaction in the absence of this catalyst at various conditions. The results show clearly that Fe₃O₄@TiO₂@(CH₂)₃OMoO₃H is an effective catalyst for this reaction

and in the absence of this catalyst the reaction did not take place, even after 24 h. Next, the model reaction was conducted in the presence of several amounts of catalyst **1** at different conditions (Table 1). Through screening we found that this reaction was efficiently completed in the presence of 0.003 g of Fe₃O₄@TiO₂@(CH₂)₃OMoO₃H at 90 °C under solvent-free conditions.

To investigate the generality of this protocol, the reaction of different aryl aldehydes, containing both electron-donating and electron-withdrawing groups were employed in the reaction. In general, the reaction proceeded smoothly to afford the desired products **6** in good to excellent yields. Furthermore, under similar conditions, aryl aldehydes and *para*-toluenesulfonamide were reacted with 5,7-dihydroxy-4-methylcoumarin in the presence of the catalyst **1** (Table 2). According to the reported procedure in the literature,⁴⁵ 5,7-dihydroxy-4-methylcoumarin was synthesized *via* the ZrOCl₂/SiO₂-catalyzed condensation of phloroglucinol and ethyl acetoacetate.

Recovery and reuse of the catalysts after catalytic reactions are important factors for sustainable process management. The recovered nanomagnetic catalyst **1** from the model reaction for the synthesis of **6a** was separated by an



Scheme 3. Proposed mechanism for the synthesis of **6** in the presence of $\text{Fe}_3\text{O}_4@\text{TiO}_2@(\text{CH}_2)_3\text{OMoO}_3\text{H}$.

external magnet, washed with MeOH and reused in the next run. As outlined in Fig. 6, $\text{Fe}_3\text{O}_4@\text{TiO}_2@(\text{CH}_2)_3\text{OMoO}_3\text{H}$ exhibited no considerable decrease in activity after six cycles. This advantage besides the recoverability of the biodegradable and green catalyst makes this research highly favorable for large-scale synthesis.

A plausible mechanism for the synthesis of product **6** is outlined in Scheme 3. It is reasonable to assume that *para*-toluenesulfonamide attacks the activated arylaldehyde by the acid catalyst to give sulfonyl aldimines **4**. Then, intermediate **7** or **8** is generated from the condensation of **5** (5,7-dihydroxy-4-methylcoumarin or 4-hydroxycoumarin) with **4** which rearranges into the desired product.

The filtration test was performed to show the heterogeneity of the catalyst. For this purpose, after the development of about 40% of the model reaction (synthesis of **6a**), the catalyst was removed and the progress of the residual mixture was monitored. Interestingly, no further conversion was observed in this case. Therefore, we found that the catalyst operates in a heterogeneous manner and no leaching of molybdic acid as active species occurs under the applied conditions.

3. Experimental

All chemicals used in this research were purchased from Fluka and Merck chemical companies. The monitoring of the reaction progress and the purity of the compounds were accomplished using TLC performed with silica gel SIL G/UV254 plates. Melting points were determined by an electrothermal KSB1N apparatus and are uncorrected. ^1H NMR spectra were recorded in DMSO- d_6 on

a Bruker Avance Ultra Shield 400 MHz instrument spectrometers and ^{13}C NMR spectra were recorded at 100 MHz. X-ray powder diffraction (XRD) patterns were recorded using a Bruker AXS (D8 Advance) X-ray diffractometer with Cu K α radiation ($\lambda = 0.15418$ nm). The measurement was made in 2θ ranging from 10° to 80° at the speed of $0.05^\circ \text{ min}^{-1}$. For the preparation of the sample for XRD, after synthesis, the sample was powder, which was clumpy, and then XRD was measured. Analysis conditions includes: voltage: 40 kV and current: 30 mA. Energy dispersive spectroscopy (EDS) was performed using a TESCAN Vega model instrument. The morphology of the particles was observed by scanning electron microscopy (SEM) under an acceleration voltage of 26 kV. Before SEM characterization, the sample was powdered and then coated with gold. The magnetic measurement was carried out in a vibrating sample magnetometer (VSM) at Kashan University (Kashan, Iran) at room temperature.

Synthesis of Fe_3O_4 MNPs

A solution of $\text{FeCl}_3 \cdot 6\text{H}_2\text{O}$ (1.35 g, 5 mmol) and $\text{FeCl}_2 \cdot 4\text{H}_2\text{O}$ (0.5 g, 2.5 mmol) (dissolved in 22 mL double distilled water) stirred under argon atmosphere at 80°C for 30 min. Next the sodium hydroxide solution (2.5 mL, 10 M) was added dropwise to the reaction mixture with stirring for 1 h under argon atmosphere. Finally, the formed nanoparticles were collected using an external magnet. The nano particles were washed with distilled water repeatedly and then dried at 60°C .⁴⁷

Synthesis of nano- $\text{Fe}_3\text{O}_4@\text{TiO}_2$

Fe_3O_4 nanoparticles were added to a mixture of ethanol and acetonitrile (250:90 mL) and sonicated for 25

min. Next an aqueous ammonia solution (1.5 mL, 25 W%) was added and the resulting mixture was stirred at 25 °C for 30 min. Then, tetraethyl orthotitanate (3 mL) dissolved in absolute ethanol (20 mL) was added. After stirring for 2 h the obtained mixture was washed completely with absolute ethanol and was collected with an external magnet.³⁷

Synthesis of $\text{Fe}_3\text{O}_4@\text{TiO}_2@(\text{CH}_2)_3\text{Cl}$

Nano- $\text{Fe}_3\text{O}_4@\text{TiO}_2$ (0.6 g) was added in 3-chloropropyltrimethoxysilane (6 mL) and stirred for 12 h under argon atmosphere and reflux conditions. This product was then separated *via* a magnet and washed repeatedly using toluene, ethanol-water and distilled water. Finally, $\text{Fe}_3\text{O}_4@\text{TiO}_2@(\text{CH}_2)_3\text{Cl}$ was dried in an oven at 60 °C.⁴⁸

Preparation of $\text{Fe}_3\text{O}_4@\text{TiO}_2@(\text{CH}_2)_3\text{OMoO}_3\text{H}$

A mixture of $\text{Fe}_3\text{O}_4@\text{TiO}_2@(\text{CH}_2)_3\text{Cl}$ (1 g) and $\text{Na}_2\text{MoO}_4 \cdot 2\text{H}_2\text{O}$ (0.5 g) in DMSO (10 mL) was stirred at reflux under argon atmosphere for 12 h. The resulting product was decanted and washed twice with DMSO, once with distilled water and was dried at 50 °C for 18 h. Then, it was added to the flask containing HCl (60 mL, 0.1 N) and stirred for 2 h at room temperature. The resulting catalyst was decanted, washed with DMSO and water, afterwards dried at room temperature.

General Procedure for the Synthesis of **6**

Catalyst **1** (0.003 g) was added to the mixture of *para*-toluenesulfonamide (1 mmol), aldehyde (1 mmol) and 4-hydroxycoumarin (1 mmol) or 5,7-dihydroxy-4-methylcoumarin (1 mmol). The resulting mixture was stirred in an oil bath (90 °C) under solvent-free conditions. The reaction progress was monitored by TLC (*n*-hexane/EtOAc, 2:1). After completion of the reaction, boiling methanol (10 mL) was added, and the catalyst was separated by an external magnet. The obtained powder was recrystallized from hot EtOH.

Compound 6a: Yield: 0.357 g (85%), FT-IR (KBr) ($\bar{\nu}_{\text{max}}$, cm^{-1}): 3438, 1660, 1616, 1569, 1496, 1348, 1303, 1093, 759, 816. ^1H NMR (400 MHz, $\text{DMSO}-d_6$) δ (ppm): 2.51 (s, 3H), 6.39 (s, 1H), 7.15–7.19 (t, 3H), 7.23–7.27 (t, 2H), 7.33–7.40 (m, 4H), 7.60–7.64 (m, 2H), 7.92 (dd, $J_1 = 9.2$ Hz, $J_2 = 1.2$ Hz, 2H). ^{13}C NMR (100 MHz, $\text{DMSO}-d_6$) δ (ppm): 208.8, 166.0, 153.6, 152.1, 140.5, 139, 133.5, 132.6, 131.7, 128.6, 127.1, 126.0, 124.4, 124.3, 118.0, 116.5, 104.5, 57.0, 36.4.

Compound 6b: Yield: 0.409 g (90%), FT-IR (KBr) ($\bar{\nu}_{\text{max}}$, cm^{-1}): 3438, 1668, 1616, 1562, 1494, 1438, 1351, 1311, 887, 757. ^1H NMR (400 MHz, $\text{DMSO}-d_6$) δ (ppm): 2.07 (s, 3H), 6.28 (s, 1H), 7.13–7.15 (d, 2H), 7.25–7.27 (d, 2H), 7.30–7.36 (m, 4H), 7.57–7.61 (m, 2H), 7.88 (dd, $J_1 = 8$ Hz, $J_2 = 7.2$ Hz, 2H), 7.92–8.5 (m, 2H). ^{13}C NMR (100 MHz, $\text{DMSO}-d_6$) δ (ppm): 208.3, 165.7, 165.3, 153.6, 152.9, 139.4, 138.7, 132.5, 131.3, 130.3, 127.4, 124.4, 123.3, 119.0, 118.2, 116.4, 115.7, 104, 31.3.

Compound 6c: Yield: 0.773 g (84%), FT-IR (KBr) ($\bar{\nu}_{\text{max}}$, cm^{-1}): 3438, 3255, 1664, 1631, 1604, 1567, 1492, 1330, 1164, 736, 673. ^1H NMR (400 MHz, $\text{DMSO}-d_6$) δ (ppm): 2.31 (s, 3H), 6.32 (s, 1H), 7.16–7.37 (t, 8H), 7.57–7.61 (m, 2H), 7.89–8.10 (m, 4H). ^{13}C NMR (100 MHz, $\text{DMSO}-d_6$) δ (ppm): 208.10, 173.16, 172.32, 162.62, 143.15, 142.42, 138.37, 129.05, 128.62, 125.37, 124.32, 122.42, 120.42, 108.15, 31.10.

Compound 6d: Yield: 0.326 g (75%), FT-IR (KBr) ($\bar{\nu}_{\text{max}}$, cm^{-1}): 3438, 1668, 1616, 1604, 1563, 1351, 1311, 1095, 736, 673. ^1H NMR (400 MHz, $\text{DMSO}-d_6$) δ (ppm): 2.24 (s, 3H), 2.34 (s, 3H), 6.39 (s, 1H), 7.17–7.27 (m, 3H), 7.34–7.41 (m, 8H), 7.61–7.95 (m, 3H). ^{13}C NMR (100 MHz, $\text{DMSO}-d_6$) δ (ppm): 208.10, 173.16, 172.32, 162.62, 143.15, 142.42, 138.37, 129.05, 128.62, 125.37, 124.32, 122.42, 120.42, 108.15, 36.11, 31.10.

Compound 6k: Yield: 0.392 g (81%), FT-IR (KBr) ($\bar{\nu}_{\text{max}}$, cm^{-1}): 3471, 3338, 3170, 1673, 1610, 1575, 1413, 1157, 1091. ^1H NMR (400 MHz, $\text{DMSO}-d_6$) δ (ppm): 10.45 (s, 1H), 10.43 (s, 1H), 7.95 (d, 1H, $J = 10.9$ Hz), 7.87 (d, 1H, $J = 10.0$ Hz), 7.52 (d, 2H, $J = 10.8$ Hz), 7.28–7.08 (m, 5H), 6.20 (d, 1H, $J = 10.8$ Hz), 6.15 (s, 1H), 5.75 (s, 1H), 2.39 (s, 3H), 2.25 (s, 3H). ^{13}C NMR (100 MHz, $\text{DMSO}-d_6$) δ (ppm): 159.2, 158.8, 157.2, 154.8, 153.6, 142.0, 138.8, 138.4, 131.4, 130.9, 128.9, 128.7, 128.2, 126.3, 125.9, 108.6, 103.9, 101.8, 98.5, 49.19, 23.6, 20.9.

Compound 6l: Yield: 0.412 g (85%), FT-IR (KBr) ($\bar{\nu}_{\text{max}}$, cm^{-1}): 3477, 3423, 3315, 1702, 1619, 1524, 1432, 1292, 1182. ^1H NMR (400 MHz, $\text{DMSO}-d_6$) δ (ppm): 10.45 (s, 1H, OH), 7.88 (d, 1H, $J = 8$ Hz), 7.53 (d, 2H, $J = 8$ Hz), 7.11–7.28 (m, 6H), 6.20 (s, 1H), 6.16 (s, 1H), 5.77 (s, 1H), 2.41 (s, 3H), 2.28 (s, 3H). ^{13}C NMR (100 MHz, $\text{DMSO}-d_6$) δ (ppm): 159.14, 157.17, 154.73, 141.98, 138.91, 138.31, 131.33, 130.90, 129.14, 128.80, 128.66, 128.12, 126.24, 125.90, 108.64, 104.12, 98.57, 49.12, 23.54, 20.88. MS (EI): m/z 485 (M^+), 301 ($\text{C}_{16}\text{H}_9\text{ClO}_4^+$), 279 ($\text{C}_{17}\text{H}_{12}\text{O}_4^+$), 258 ($\text{C}_{15}\text{H}_{11}\text{ClO}_2^+$).

4. Conclusion

In summary, we have introduced $\text{Fe}_3\text{O}_4@\text{TiO}_2@(\text{CH}_2)_3\text{OMoO}_3\text{H}$ as a novel modified Fe_3O_4 MNPs. It was fully characterized by XRD, SEM, EDS, FT-IR and VSM analysis. Furthermore, the first application of this reusable nanocatalyst for the synthesis of sulfonamide containing coumarin derivatives was successfully examined. The use of $\text{Fe}_3\text{O}_4@\text{TiO}_2@(\text{CH}_2)_3\text{OMoO}_3\text{H}$ as a green and safe catalyst under solvent-free conditions, high yield of pure products, short reaction times and a simple recovery procedure are the main promising points of this work.

Acknowledgements

The authors gratefully acknowledge the partial support of this work by Yasouj University, Iran.

5. References

1. C. Sanchez, P. Belleville, M. Popalld, L. Nicole, *Chem. Soc. Rev.* **2011**, *40*, 696–753. DOI:10.1039/c0cs00136h
2. D. Zhang, X. Du, L. Shi, R. Gao, *Dalton Trans.* **2012**, *41*, 14455–14475. DOI:10.1039/c2dt31759a
3. M. B. Gawande, S. N. Shelke, R. Zboril, R. S. Varma, *Acc. Chem. Res.* **2014**, *47*, 1338–1348. DOI:10.1021/ar400309b
4. S. R. Bankar, S. Shelke, *Res. Chem. Intermed.* **2018**, *44*, 3507–3521. DOI:10.1007/s11164-018-3321-4
5. S. R. Bankar, *Curr. Organocatal.* **2018**, *5*, 42–50. DOI:10.2174/2213337205666180611112941
6. M. B. Gawande, P. S. Branco, R. S. Varma, *Chem. Soc. Rev.* **2013**, *42*, 3371–3393. DOI:10.1039/c3cs35480f
7. S. N. Shelke, S. R. Bankar, G. R. Mhaske, S. S. Kadam, D. K. Murade, S. B. Bhorkade, A. K. Rathi, N. Bundaleski, O. M. N. D. Teodoro, R. Zboril, R. S. Varma, M. B. Gawande, *ACS Sustainable Chem. Eng.* **2014**, *2*, 1699–1706. DOI:10.1021/sc500160f
8. S. R. Bankar, *Curr. Organocatal.* **2019**, *6*, 238–247. DOI:10.2174/2213337206666190415125053
9. V. Polshettiwar, R. S. Varma, *Green Chem.* **2010**, *5*, 743–754. DOI:10.1039/b921171c
10. S. Shylesh, V. Schnemann, W. R. Thiel, *Angew. Chem. Int. Ed.* **2010**, *49*, 3428–3459. DOI:10.1002/anie.200905684
11. R. Hudson, Y. Feng, R. S. Varma, A. Moores, *Green Chem.* **2014**, *16*, 4493–4505. DOI:10.1039/C4GC00418C
12. Z. C. Zhang, B. Xu, X. Wang, *Chem. Soc. Rev.* **2014**, *43*, 7870–7886. DOI:10.1039/C3CS60389J
13. I. I. Slowing, J. L. V. Escoto, B. G. Trewyn, V. S. Y. Lin, *J. Mater. Chem.* **2010**, *20*, 7924–7937. DOI:10.1039/c0jm00554a
14. P. Das, N. Aggarwal, N. R. Guha, *Tetrahedron Lett.* **2013**, *54*, 2924–2928. DOI:10.1016/j.tetlet.2013.03.106
15. A. Corma, H. Garcia, *Chem. Soc. Rev.* **2008**, *37*, 2096–2126. DOI:10.1039/b707314n
16. B. Karimi, F. Mansouri, H. M. Mirzaei, *ChemCatChem* **2015**, *7*, 1736–1789. DOI:10.1002/cctc.201403057
17. M. A. Zolfigol, M. Yarie, *Appl. Organometal. Chem.* **2017**, *31*, 3598–3609.
18. T. O. Eschemann, J. H. Bitter, K. P. de Jong, *Catal. Today* **2014**, *228*, 89–95. DOI:10.1016/j.cattod.2013.10.041
19. H. Kominami, M. Kohno, Y. Takada, M. Inoue, T. Inui, Y. Kera, *Ind. Eng. Chem. Res.* **1999**, *38*, 3925–3931. DOI:10.1021/ie9901170
20. B. Kraeutler, A. J. Bard, *J. Amer. Chem. Soc.* **1978**, *100*, 4317–4318. DOI:10.1021/ja00481a059
21. C. Gannoun, R. Delaigle, A. Ghorbel, E. M. Gaigneaux, *Catal. Sci. Technol.* **2019**, *9*, 2344–2350. DOI:10.1039/C9CY00099B
22. R. Palcheva, L. Dimitrov, G. Tyuliev, A. Spojakina, K. Jiratova, *Appl. Surf. Sci.* **2013**, *265*, 309–316. DOI:10.1016/j.apsusc.2012.11.001
23. W. P. Kwan, B. M. Voelker, *Environ. Sci. Tech.* **2003**, *37*, 1150–1158. DOI:10.1021/es020874g
24. E. De Clercq, *Curr. Med. Chem.* **2001**, *8*, 1543–1572. DOI:10.2174/0929867013371842
25. M. Lopez, L. F. Bornaghi, A. Innocenti, D. Vullo, S. A. Charman, C. T. Supuran, S. A. Poulsen, *J. Med. Chem.* **2010**, *53*, 2913–2926. DOI:10.1021/jm901888x
26. J. Mun, A. A. Jabbar, N. S. Devi, S. Yin, Y. Wang, C. Tan, D. Culver, J. P. Snyder, E. G. Van Meir, M. M. Goodman, *J. Med. Chem.* **2012**, *55*, 6738–6750. DOI:10.1021/jm300752n
27. S. Mc Mahon, R. Kennedy, P. Duffy, J. M. Vasquez, J. G. Wall, H. Tai, W. Wang, *ACS Appl. Mater. Interfaces* **2016**, *8*, 26648–26656. DOI:10.1021/acsami.6b11371
28. M. Bavadi, K. Niknam, M. Gharibi, *Monatsh. Chem.* **2017**, *148*, 1025–1034. DOI:10.1007/s00706-016-1847-y
29. A. Cristina, S. Baetas, M. S. P. Arruda, A. H. Müller, A. C. Arruda, *J. Braz. Chem. Soc.* **1999**, *10*, 181–183. DOI:10.1590/S0103-50531999000300004
30. C. Spino, M. Dodier, S. Sotheeswaran, *Bioorg. Med. Chem.* **1998**, *8*, 3475–3478. DOI:10.1016/S0960-894X(98)00628-3
31. M. Z. Hassan, H. Osman, M. A. Ali, M. J. Ahsan, *Eur. J. Med. Chem.* **2016**, *123*, 236–255. DOI:10.1016/j.ejmech.2016.07.056
32. D. C. Pinto, A. M. Silva, *Curr. Top. Med. Chem.* **2017**, *17*, 3190–3198.
33. A. Lacy, R. O’Kennedy, *Curr. Pharm. Des.* **2004**, *10*, 3797–3811. DOI:10.2174/1381612043382693
34. J. Etemad Gholtash, M. Farahi, *RSC Adv.* **2018**, *8*, 40962–40967. DOI:10.1039/C8RA06886K
35. M. Farahi, F. Tamaddon, B. Karami, S. Pasdar, *Tetrahedron Lett.* **2015**, *56*, 1887–1890. DOI:10.1016/j.tetlet.2015.02.105
36. M. Farahi, B. Karami, R. Keshavarz, F. Khosravian, *RSC Adv.* **2017**, *7*, 46644–46650. DOI:10.1039/C7RA08253C
37. A. Amoozadeh, S. Golian, S. Rahimi, *RSC Adv.* **2015**, *5*, 45974–45982. DOI:10.1039/C5RA06515A
38. A. A. Elmekawy, J. B. Sweeney, D. R. Brown, *Catal. Sci. Technol.* **2015**, *5*, 690–696. DOI:10.1039/C4CY00970C
39. H. Yin, Y. Wada, T. Kitamura, S. Kambe, S. Murasawa, H. Mori, T. Sakatac, S. Yanagida, *J. Mater. Chem.* **2001**, *11*, 1694–1703. DOI:10.1039/b008974p
40. F. Nemati, M. Heravi, A. Elhampour, *RSC Adv.* **2015**, *5*, 45775–45784. DOI:10.1039/C5RA06810J
41. F. Khosravian, B. Karami, M. Farahi, *New J. Chem.* **2017**, *41*, 11584–11590. DOI:10.1039/C7NJ02390A
42. T. Xin, M. Ma, H. Zhang, J. Gu, S. Wang, M. Liu, Q. Zhang, *Appl. Surf. Sci.* **2014**, *288*, 51–59. DOI:10.1016/j.apsusc.2013.09.108
43. N. Divsalar, N. Monadi, M. Tajbaksh, *J. Nanostruct.* **2016**, *6*, 312–321.
44. B. Karami, M. Kiani, *Monatsh. Chem.* **2016**, *147*, 1117–1124. DOI:10.1007/s00706-015-1551-3
45. B. Karami, M. Kiani, *Catal. Commun.* **2011**, *14*, 62–67. DOI:10.1016/j.catcom.2011.07.002

46. M. Farahi, B. Karami, H. Mohamadi Tanuraghaj, *Tetrahedron Lett.* **2015**, *56*, 1833–1836. DOI:10.1016/j.tetlet.2015.02.087
47. M. C. Mascolo, Y. Pei, T. A. Ring, *Materials* **2013**, *6*, 5549–5567. DOI:10.3390/ma6125549
48. A. A. Elmekawy, J. B. Sweeney, D. R. Brown, *Catal. Sci. Technol.* **2015**, *5*, 690–696. DOI:10.1039/C4CY00970C

Povzetek

Uspešno smo pripravili molibdensko kislino imobilizirano na nano- $\text{Fe}_3\text{O}_4@\text{TiO}_2$ ($\text{Fe}_3\text{O}_4@\text{TiO}_2@(\text{CH}_2)_3\text{OMoO}_3\text{H}$), jo karakterizirali in uporabili kot katalizator za sintezo sulfonamidov, vsebujočih kumarinski fragment. Pripravi Fe_3O_4 nanodelcev s so-obarjanjem Fe^{2+} in Fe^{3+} ionov je sledila obdelava s tetraetil ortotitanatom, ki je vodila do nastanka $\text{Fe}_3\text{O}_4@\text{TiO}_2$. Tako dobljene delce smo nato obdelali s 3-kloropropiltrioksosilanom, nato pa reagirali še z molibdensko kislino ter dobili željeni katalizator, ki smo ga karakterizirali z XRD, SEM, EDS, FT-IR in VSM analizami. $\text{Fe}_3\text{O}_4@\text{TiO}_2@(\text{CH}_2)_3\text{OMoO}_3\text{H}$ smo uporabili kot katalizator za sintezo sulfonamidov, vsebujočih kumarinski fragment, ki smo jo izvedli v obliki trokomponentne reakcije med aril aldehydi, *para*-toluensulfonamidom in 4-hidroksikumarinom (ali 5,7-dihidroksi-4-metilkumarinom). Izolacija katalizatorja po končani reakciji in njegova ponovna uporaba ni pokazala nobene izgube njegove aktivnosti.



Except when otherwise noted, articles in this journal are published under the terms and conditions of the Creative Commons Attribution 4.0 International License

Scientific paper

Quantum Mechanics/Molecular Mechanics Study on Caspase-2 Recognition by Peptide Inhibitors

Petar M. Mitrasinovic*

Center for Biophysical and Chemical Research, Belgrade Institute of Science and Technology, 11060 Belgrade, Serbia

* Corresponding author: E-mail: pmitrasinovic.ist-belgrade.edu.rs@tech-center.com

Received: 01-17-2020

Abstract

For a variety of biological and medical reasons, the ongoing development of humane caspase-2 inhibitors is of vital importance. Herein, a hybrid (Quantum Mechanics/Molecular Mechanics – QM/MM), two-layered molecular model is derived in order to understand better the affinity and specificity of peptide inhibitor interaction with caspase-2. By taking care of both the unique structural features and the catalytic activity of human caspase-2, the critical enzyme residues (E217, R378, N379, T380, and Y420) with the peptide inhibitor are treated at QM level (the Self-Consistent-Charge Density-Functional Tight-Binding method with the Dispersion correction (SCC-DFTB-D)), while the remaining part of the complex is treated at MM level (AMBER force field). The QM/MM binding free energies (BFEs) are well-correlated with the experimental observations and indicate that caspase-2 uniquely prefers a penta-peptide such as VDVAD. The sequence of VDVAD is varied in a systematic fashion by considering the physicochemical properties of every constitutive amino acid and its substituent, and the corresponding BFE with the inhibition constant (K_i) is evaluated. The values of K_i for several caspase-2:peptide complexes are found to be within the experimental range (between 0.01 nM and 1 μ M). The affinity order is: VELAD ($K_i = 0.081$ nM) > VDVAD ($K_i = 0.23$ nM) > VEIAD ($K_i = 0.61$ nM) > VEVAD ($K_i = 3.7$ nM) > VDIAD ($K_i = 4.5$ nM) etc. An approximate condition needed to be satisfied by the kinetic parameters (the Michaelis constant – K_M and the specificity constant – k_{cat}/K_M) for competitive inhibition is reported. The estimated values of k_{cat}/K_M , being within the experimentally established range (between 10^{-4} and 10^{-1} μ M $^{-1}$ s $^{-1}$), indicate that VELAD and VDVAD are most specific to caspase-2. These two particular peptides are nearly 1.5, 3 and 4 times more specific to the receptor than VEIAD, VEVAD and VDIAD respectively. Additional kinetic threshold, aimed to discriminate tightly bound inhibitors, is given.

Keywords: Enzyme; human caspase-2; inhibition; peptide inhibitor; QM/MM; SCC-DFTB-D

1. Introduction

Homologues that make up the caspase (casp) family of cysteine proteases are essential mediators of cellular processes, such as apoptosis, proliferation, and differentiation.^{1,2} They are synthesized and stored as inactive zymogens, as well as divided into inflammatory (caspase-1, -4, -5, -12 in humans and caspase-1, -11, and -12 in mice) and apoptotic (caspase-3, -6, -7, -8, and -9 in mammals) caspases according to their function and pro-domain structure. The functions of caspase-2, -10, and -14 can not be easily categorized. Apoptotic caspases are further subclassified by their mechanism of action as initiators (caspase-8 and -9) and executioners (caspase-3, -6, and -7).

The first identified mammalian member is caspase-2 and its physiological role is not quite clear. Caspase-2, one of the most evolutionarily conserved caspases, is inclined to behave as either executioner or initiator. In terms of

substrate specificity, caspase-2 is similar to caspase-3 and -7 (executioner caspases). However, the long N-terminal caspase recruitment domain (CARD) of caspase-2 indicates its potential role as an initiator caspase.³ While the function of caspase-2 in the embryonic development of mice is questionable,⁴ its important role in stress-induced cell death pathways and tumor suppression is more certain.⁵ The potential roles of caspase-2 in mediating nonapoptotic pathways (cell-cycle regulation and DNA repair) have been reported in terms of whether caspase-2 is mandatory for apoptosis under specific circumstances,^{6,7} or whether it primarily functions in cell-cycle regulation.⁵ An elevated expression level of caspase-2 has been observed in the brain of patients with some neurodegenerative disorders.⁸ In addition, the critical role of caspase-2 in mediating nonalcoholic steatohepatitis (NASH) pathogenesis, a chronic and aggressive liver condition not only in mice but probably in humans, has been highlighted.⁹

Whereas many questions on caspase-2 physiology remain enigmatic, one of the key aspects for developing caspase-2 specific probes is related to the way in which caspase-2 gets activated.

Peptide bonds are hydrolyzed using caspases (endo-proteases) in a reaction that depends on catalytic cysteine residues in the caspase active site and occurs only after certain aspartic acid residues in the substrate. Besides resulting in substrate inactivation, caspase-mediated processing may generate active signaling molecules that participate in apoptosis and inflammation. Caspase activities are strictly regulated by protein-protein interactions and by proteolysis.¹ The crystal structures of caspase-2 in complex with several peptide inhibitors and comparison of the apo (substrate-free) and inhibited caspase-2 structures have revealed a recognition via several discrete catalytic steps: (i) activation of caspase-2 by breaking a nonconserved salt bridge between Glu217 (caspase-2 is the only human caspase with glutamate at position 217) and the invariant Arg378, (ii) formation of a catalytically competent conformation upon binding to a single substrate, and (iii) formation of the enzyme-substrate complex after having both active sites occupied by the substrate.¹⁰ Caspase-2 has been suggested to uniquely prefer a penta-peptide rather than a tetra-peptide, as required for efficient cleavage by other caspases.¹⁰ To gain more complete insights into the caspase-2/peptide recognition and further facilitate the design of caspase-2 inhibitors, a hybrid QM/MM approach is employed in this work.

2. Methods

To obtain the initial atomic coordinates of the apo and inhibited caspase-2 structures, the experimental structures were retrieved from the Research Collaboratory for Structural Bioinformatics (RCSB) Protein Data Bank (PDB): 3R7S.PDB (apo caspase-2), 3R6G.PDB (caspase-2/

VDVAD), 3R5J.PDB (caspase-2/ADVAD), 3R7B.PDB (caspase-2/DVAD), and 3R6L.PDB (T380A/VDVAD).¹⁰ The sequence of the penta-peptide inhibitor was varied using single point mutations generated by applying the Mutagenesis engine of PyMol-v0.99 to the experimental structure 3R6G.PDB in a backbone-dependent fashion.¹¹

Before running QM/MM calculations, the systems were prepared using the Amber 11 suite of programs.^{12,13} The solute was prepared using the Amber11 utility program tLeap in association with the ff99sb force field.¹⁴ Every inhibitor was initially prepared by parameterizing its atom types, charges, and connectivity in order to be treated as part of the solute. The molecular geometry was optimized by Gaussian 98 at the MP2/6-31G* level of theory.¹⁵ The molecular electrostatic potential was calculated by Gaussian 98 at the HF/6-31G* level of theory,¹⁵ while the atomic charges were derived by means of the RESP fitting technique,¹⁶ which is part of AmberTools 1.5.^{12,13} Remaining parameters were assigned from the General Amber Force Field (GAFF),¹⁷ being entirely compatible with the ff99sb macromolecular force field.¹⁴ Every solute was solvated using a 10 Å (1 Å = 10⁻¹⁰ m) pad of TIP3P water molecules (\approx 11500) and the counter ions Na⁺ were added to neutralize each system. To remove clashes and bad contacts, two-stage geometric minimization was performed using the Sander module of Amber11.^{12,13} At the outset, the positions of the solute atoms were kept fixed, while the positions of the water atoms were minimized by gradually reducing an initial harmonic restraint of 2 kcal mol⁻¹ Å⁻² on all non-hydrogen non-water atoms via 5000 combined steepest descent (2500 steps) and conjugate gradient (2500 steps) minimization steps. Afterwards, the entire system was minimized without restrains by means of 10000 combined steepest descent (5000 steps) and conjugate gradient (5000 steps) minimization steps.

A two-layered hybrid approach was employed to assess the binding affinities within the caspase-2:peptide complexes. The outer layer of the complex (Figure 1) was

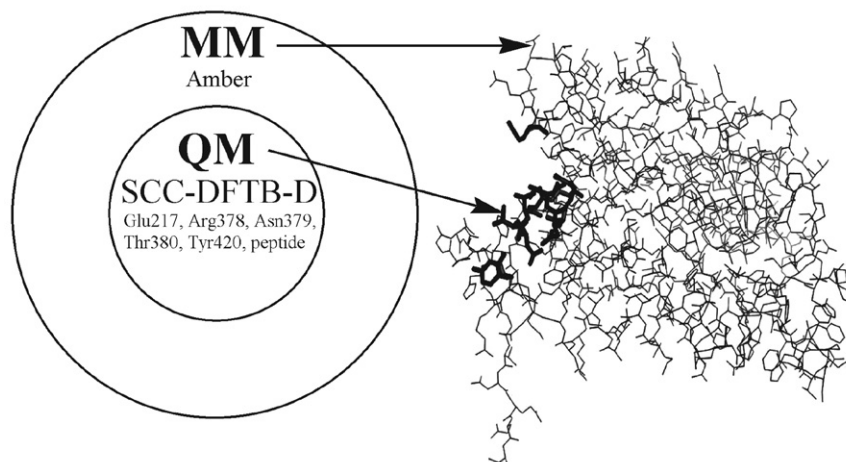


Figure 1. The two-layered QM/MM (SCC-DFTB-D/AMBER) model was used to evaluate the efficacy of peptide inhibitors towards caspase-2 (PDB ID: 3R6G).

kept at the low level of theory (MM) with an Amber force field. The central layer of the complex (bold sticks; Figure 1) was treated at the high level of theory (QM), employing SCC-DFTB-D, the Self-Consistent-Charge Density-Functional Tight-Binding method^{18,19} with Dispersion energy,²⁰ as implemented in Amber11.^{21,22} The inclusion of the empirical correction for dispersion energy into SCC-DFTB provided a balanced and reliable description of the interactions inside the systems.²³ Pure Density Functional Theory (DFT) methods are known for their modest computational costs, but they are not able to adequately describe dispersive forces, especially within unconventional systems,^{24,25} as many density functionals are empirical.²⁰ DFT was extended to include dispersion correction (DFT-D),^{26,27} and as such DFT-D became suitable for performing energy minimizations and vibrational analyses of extended molecular complexes containing hundreds of atoms. By being a few orders of magnitude faster than DFT-D,^{23,28–33} SCC-DFTB-D was suggested to be applicable to both quantumchemical simulations and calculations pertaining to a large number of extended molecular complexes.²³

The total interaction energies were defined as:

$$\Delta E_{\text{interaction}} = \Delta E_{\text{model,high}} + \Delta E_{\text{real,low}} - \Delta E_{\text{model,low}} \quad (1)$$

where ΔE_{model} denote the energies of the model system defined at high and low level of theory and ΔE_{real} denotes the whole (real) system. Therefore, the equivalent binding free energies of the complex systems were determined as:

$$\Delta G_{\text{binding}} \approx \Delta G = G_{\text{casp-2:peptide}} - [G_{\text{casp-2}} + G_{\text{peptide}}] \quad (2)$$

The thermodynamic quantities (enthalpies, entropies, and different entropic contributions) were obtained from frequency calculations done by the Nmode module of Amber11.^{12,13} The different entropic contributions (translation, rotation, and vibration) for caspase-2:peptide complexes were calculated as:

$$\Delta S = S_{\text{casp-2:peptide}} - [S_{\text{casp-2}} + S_{\text{peptide}}] \quad (3)$$

3. Results and Discussion

Kinetic measurements of competitive inhibition associated with the initial experimental structures¹⁰ are summarized in Table 1. The specificity constant ($k_{\text{cat}}/K_{\text{M}}$) identified the penta-peptide VDVAD as a preferred inhibitor, while two residues, Thr380 and Tyr420, were identified as critical for recognizing a residue at the P5 position – the first position at the left end in the peptide sequence (Figures 2b & 2c). The salt bridge between Glu217 and Arg378, which is present in the apo caspase-2 (3.37 Å, Figure 2a), is broken in the caspase-2:VDVAD complex (8.05 Å, Figure 2b), because Thr380 and Tyr420 in P5 rec-

ognition move 2.1 and 3.6 Å, respectively (Figure 2d). Furthermore, the specificity constant revealed that mutation of Thr380 to Ala reduces the catalytic efficiency of caspase-2 by about 40 fold (Table 1), as Thr380Ala (Figure 2c) causes the loss of the hydrogen bond between Thr380 and the P5 side chain (3.51 Å, Figure 2b) due to a 2.3 Å movement in the main chain in residue 380. Structurally speaking in a similar manner, mutation of Tyr420 to Ala reduces the catalytic efficiency of caspase-2 by about 4 fold (Table 1), as Tyr420Ala causes a 0.5 Å movement of the side chain of residue 420 and the loss of the hydrophobic interaction between Tyr420 and the P5 side chain.¹⁰

Table 1. Kinetic data¹⁰ for experimental caspase-2:peptide inhibitor complexes: K_{M} – Michaelis constant, k_{cat} – catalytic constant, $k_{\text{cat}}/K_{\text{M}}$ – specificity constant, and IC_{50} – inhibitory concentration

Complex ^(a) PDB ID	K_{M} ^(b) (μM)	k_{cat} (s^{-1})	$k_{\text{cat}}/K_{\text{M}}$ ($\mu\text{M}^{-1} \text{s}^{-1}$)	IC_{50} ^{(b),(c)} (nM)
wt:VDVAD 3R6G	25	0.60	0.024	25
wt:ADVAD 3R5J	150	0.81	0.0055	110
wt:DVAD 3R7B	92	0.12	0.0013	710
Y420A:VDVAD Y420A of 3R6G	84	0.52	0.0062	314
T380A:VDVAD 3R6L	220	0.13	0.00060	347
T380A/Y420A:VDVAD Y420A of 3R6L	> 400	< 0.000014	N/A ^(d)	574

^(a) wild-type (wt) casp-2, Ala (A), Asp (D), Thr (T), Tyr (Y), Val (V)
^(b) $1 \mu\text{M} = 10^{-6} \text{ M}$, $1 \text{ nM} = 10^{-9} \text{ M}$ ^(c) IC_{50} represents the concentration at which a substance exerts half of its maximal inhibitory effect.
^(d) It is unreliable to measure the catalytic efficiency values for the slowest ($k_{\text{cat}}/K_{\text{M}} < 10^{-4} \mu\text{M}^{-1} \text{ s}^{-1}$) and fastest ($k_{\text{cat}}/K_{\text{M}} > 10^{-1} \mu\text{M}^{-1} \text{ s}^{-1}$) reactions.³⁶

To perform physically realistic QM/MM calculations, the first important aspect is how to define a QM region, or what caspase-2 residues need to be included in the QM region. There are no good universal rules here. Binding site residues of caspase-2 that are involved in non-covalent interactions with a peptide inhibitor are: Arg219, His277, Gly278, Gln318, Cys320, Ala376, Arg378, Asn379, Thr380, Trp385, Arg417, Glu418, and Tyr420.¹⁰ Caspase-2 is the only human caspase with glutamate at position 217 forming a salt bridge with Arg378 in the apo caspase-2 (Figure 2a). The inhibition of caspase-2 was related to breaking the Glu217-Arg378 salt bridge, while residues Thr380 and Tyr420 were pointed out as the key elements for recognizing a preferred penta-peptide along a catalytic pathway (Figure 2b).¹⁰ An intention to define a QM region to mimic the active site has to take into account all these experimental and structural arguments. Knowing that inclusion of a different number of caspase-2 residues in the QM region is associated with different thermodynamic

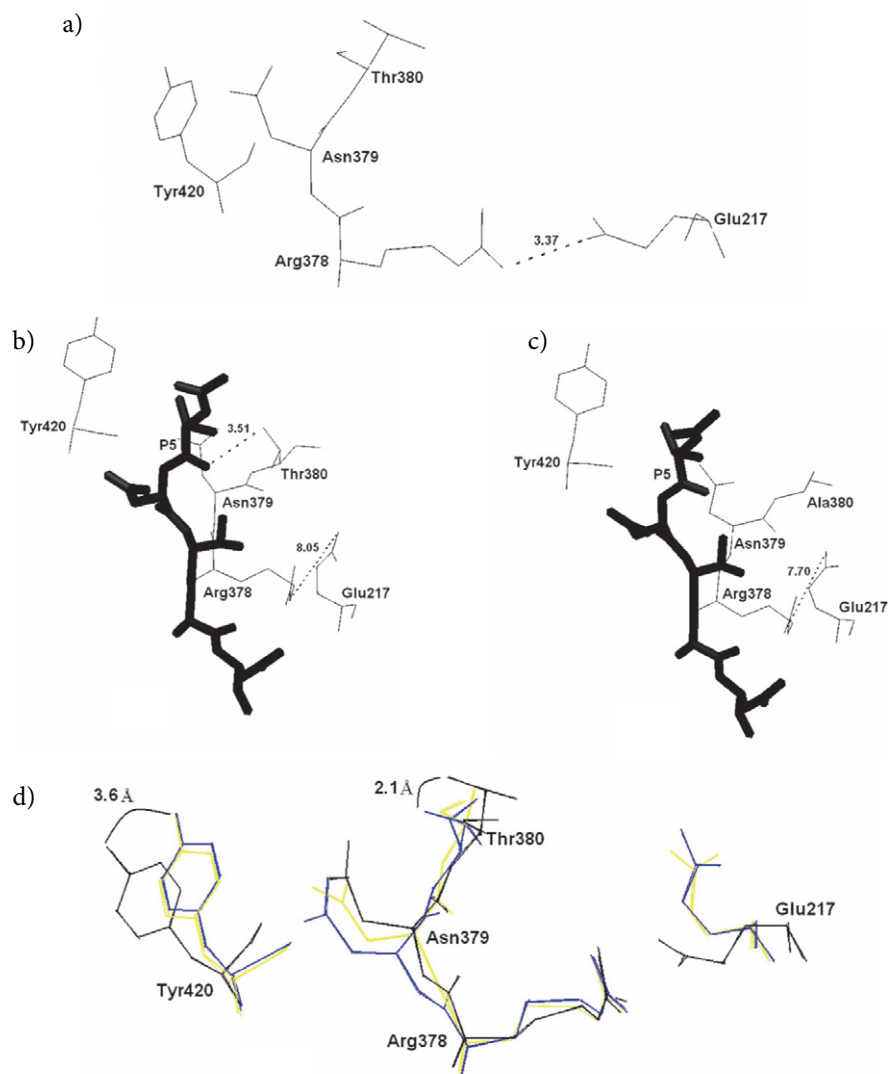


Figure 2. QM region is based upon some important experimental facts¹⁰ associated with caspase-2/peptide recognition: (a) apo (ligand-free) caspase-2 with Glu217-Arg378 salt bridge (3.37 Å), (b) caspase-2:VDVAD without Glu217-Arg378 (8.05 Å) salt bridge, (c) Thr380Ala:VDVAD without Glu217-Arg378 (7.70 Å) salt bridge, and (d) the overlay of the enzyme residues of apo caspase-2 (black), caspase-2:VDVAD (blue), and Thr380Ala:VDVAD (yellow). VDVAD is denoted by bold sticks in (b) and (c), P5 – the first position at the left end in the peptide sequence.

Table 2. Binding free energies that are evaluated using QM/MM (SCC-DFTB-D/AMBER) method for experimental caspase-2:peptide structures

Complex ^(a) PDB ID	$\Delta G_{\text{bind}}^{(b)}$ (kcal mol ⁻¹)	ΔH (kcal mol ⁻¹)	$T\Delta S_{\text{total}}$ (kcal mol ⁻¹)	$T\Delta S_{\text{trans}}$ (kcal mol ⁻¹)	$T\Delta S_{\text{rot}}$ (kcal mol ⁻¹)	$T\Delta S_{\text{vib}}$ (kcal mol ⁻¹)
wt:VDVAD 3R6G	-13.22	-31.85	-18.63	-12.90	-10.61	4.88
wt:ADVAD 3R5J	-9.83	-30.35	-20.52	-12.87	-10.56	2.91
Y420A:VDVAD Y420A of 3R6G	-9.17	-30.29	-21.12	-12.87	-10.38	2.13
T380A:VDVAD 3R6L	-8.71	-29.74	-21.03	-12.90	-10.80	2.67
T380A/Y420A:VDVAD Y420A of 3R6L	-5.53	-25.69	-20.16	-12.81	-10.53	3.18
wt:DVAD 3R7B	-2.75	-24.28	-21.53	-12.81	-10.58	1.86

^(a) wild-type (wt) casp-2, Ala (A), Asp (D), Thr (T), Tyr (Y), Val (V) ^(b) Gibbs's free energy (ΔG), enthalpy (ΔH), entropy ($T\Delta S$) and entropic contribution, translational ($T\Delta S_{\text{trans}}$), rotational ($T\Delta S_{\text{rot}}$), vibrational ($T\Delta S_{\text{vib}}$) are derived from Eqs. 2 and 3.

properties such as the binding free energies means that an appropriate QM region is supposed to generate results in agreement with experimental data. Even though one might want to have as large a QM region as possible, having more than 80–100 atoms in a QM region lead to simulations that are computationally very expensive.^{12,13} To reconcile all the structural, functional, and computational standpoints as much as possible, the present choice of including Glu217, Arg378, Asn379, Thr380, Tyr420, and the peptide inhibitor in the QM region (Figure 1) is carefully made in order to

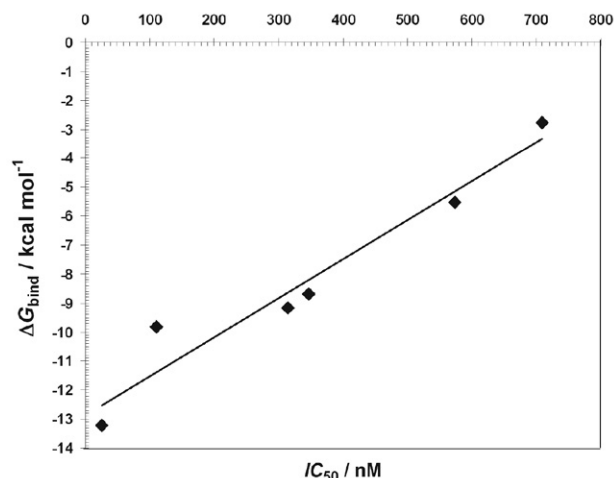


Figure 3. Correlation of the calculated binding free energy (ΔG_{bind}) with the measured inhibitory concentration (IC_{50}) for the experimental caspase-2:peptide structures. $\Delta G_{\text{bind}} = 0.013 IC_{50} - 12.85$, $R = 0.97$.

generate the inhibition constants that are within an experimental range – from 1 μM ($1 \mu\text{M} = 10^{-6} \text{ M}$) to 0.01 nM ($1 \text{ nM} = 10^{-9} \text{ M}$) for inhibited caspase-2 structures.³⁴

QM/MM binding free energies for the experimental structures are given in Table 2. Figure 3 shows quite a satisfactory linear correlation between the calculated ΔG_{bind} (Table 2) and the experimental inhibitory concentration IC_{50} (Table 1): $\Delta G_{\text{bind}} = 0.013 IC_{50} - 12.85$, $R = 0.97$. The most negative BFE for the caspase-2:VDVAD complex ($-13.22 \text{ kcal mol}^{-1}$) signifies that VDVAD is a favorable inhibitor. The enthalpy contribution (ΔH) for the complexes ranges from -31.85 to $-24.28 \text{ kcal mol}^{-1}$, indicating that the noncovalent complexation process is exothermic. In case of the entropy contribution ($T\Delta S$), the less negative entropy change is, the more reduced degrees of freedom of an inhibitor in the protein active pocket are. The least negative entropy ($-18.63 \text{ kcal mol}^{-1}$) is associated with caspase-2:VDVAD, of which vibrational contribution ($4.88 \text{ kcal mol}^{-1}$) makes a most conspicuous difference with respect to the other complexes (Table 2). The increased and thermodynamically favorable vibrational entropy change upon binding of VDVAD to caspase-2 is the signature of preferred noncovalent complexation.

To search for more effective penta-peptides, the sequence of VDVwAD is systematically varied by means of single point mutations of its constitutive residues. To make such a procedure consistent, each amino acid is mutated to its counterpart observed from a physicochemical standpoint. Val (V), an aliphatic and hydrophobic amino acid, is mutated to either Ile (I) or Leu (L). Asp (D), a polar and

Table 3. QM/MM binding free energies that are within experimental range (between -8.23 and $-15.09 \text{ kcal mol}^{-1}$) for caspase-2:peptide complexes

Complex ^(a)	$\Delta G_{\text{bind}}^{(b)}$ (kcal mol^{-1})	ΔH (kcal mol^{-1})	$T\Delta S_{\text{total}}$ (kcal mol^{-1})	$K_i^{(b)}$ (μM)
casp-2:VELAD	-13.84	-33.49	-19.65	0.000081
casp-2:VDVAD	-13.22	-31.85	-18.63	0.00023
casp-2:VEIAD	-12.64	-30.91	-18.27	0.00061
casp-2:VEVAD	-11.57	-29.60	-18.03	0.0037
casp-2:VDIAD	-11.45	-32.75	-21.30	0.0045
casp-2:VDLAE	-11.09	-29.12	-18.03	0.0083
casp-2:IEIAD	-10.85	-26.60	-15.75	0.012
casp-2:IDVAD	-10.72	-29.35	-18.63	0.015
casp-2:LDIAD	-10.54	-31.87	-21.33	0.021
casp-2:VDLGE	-10.52	-28.82	-18.30	0.022
casp-2:VEIGE	-10.21	-29.29	-19.08	0.036
casp-2:IDLAD	-10.07	-29.96	-19.89	0.045
casp-2:IEIGE	-10.01	-33.26	-23.25	0.050
casp-2:IDIAD	-9.80	-29.63	-19.83	0.072
casp-2:LELAD	-9.75	-32.91	-23.16	0.078
casp-2:VELGE	-9.33	-28.38	-19.05	0.16
casp-2:VDLAD	-9.27	-29.52	-20.25	0.17
casp-2:LELAE	-8.55	-29.13	-20.58	0.59

^(a) Ala (A), Asp (D), Glu (E), Ile (I), Leu (L), Val (V) ^(b) Gibbs' free energy (ΔG), enthalpy (ΔH), entropy ($T\Delta S$), inhibition constant (K_i), $\Delta G_{\text{bind}} = RT \ln(K_i)$, R – the gas constant ($1.9872 \text{ kcal K}^{-1} \text{ mol}^{-1}$), T – the absolute temperature (300 K), $1 \mu\text{M} = 10^{-6} \text{ M}$

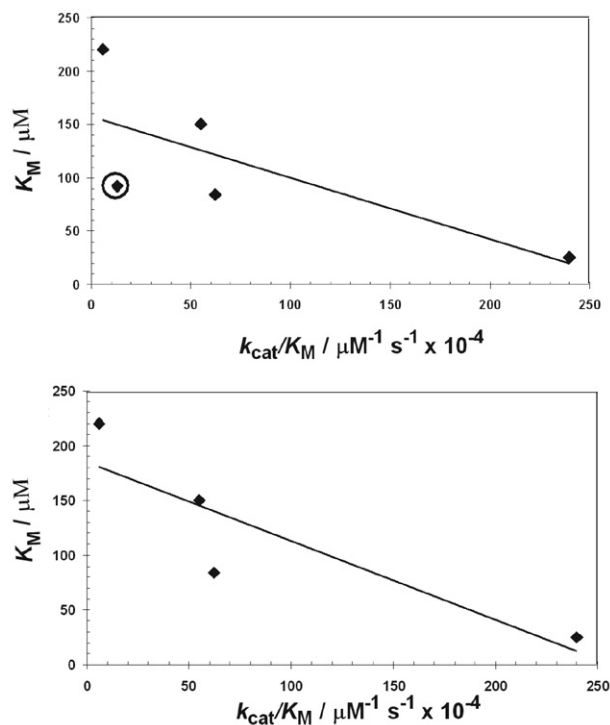


Figure 4. Correlation of the Michaelis constant (K_M) with the specificity constant (k_{cat}/K_M) for the experimental caspase-2:peptide structures: $K_M = -0.58 k_{\text{cat}}/K_M + 157.51$, $R = 0.74$ (top). If a data point (denoted by circle, top) is removed, the correlation becomes: $K_M = -0.72 k_{\text{cat}}/K_M + 184.99$, $R = 0.88$ (bottom).

negatively charged amino acid, is mutated to Glu (E). Ala (A), a tiny and hydrophobic amino acid, is mutated to Gly (G). The estimated BFE and K_i for each generated complex are reported in Table S1 (Supplementary Material). On the basis of the relation $\Delta G_{\text{bind}} = RT \ln(K_i)$ (R – the gas constant = $1.9872 \text{ kcal K}^{-1} \text{ mol}^{-1}$), T – the absolute temperature = 300 K), the experimental range of K_i in between $1 \mu\text{M}$ and 0.01 nM corresponds to the BFE (ΔG_{bind}) range in between -8.23 and $-15.09 \text{ kcal mol}^{-1}$ for inhibited caspase-2 structures. Numerical inspection of the data in Table S1 identified the complexes that have the BFEs inside of this specific range (Table 3). Thus, as far as affinity issue for the receptor is concerned, the order of preferred inhibitors is: VELAD ($K_i = 0.081 \text{ nM}$) > VDVAAD ($K_i = 0.23 \text{ nM}$) > VEIAD ($K_i = 0.61 \text{ nM}$) > VEVAD ($K_i = 3.7 \text{ nM}$) > VDIAD ($K_i = 4.5 \text{ nM}$) etc.

In order to evaluate the specificity constant for the complexes (Table 3), the correlation of the Michaelis constant with the specificity constant for the experimental caspase-2:peptide structures (Table 1) is observed. Even though two linear correlations are established (Figure 4), the first one ($K_M = -0.58 k_{\text{cat}}/K_M + 157.51$, $R = 0.74$; Figure 4, top) is slightly more suitable because it reproduces the experimental value of the specificity constant for the caspase-2:VDVAAD complex more accurately than the second one (Figure 4, bottom). Due to the negative slope (-0.58) of the linear regression line, $K_M < 157.51 \mu\text{M}$ rep-

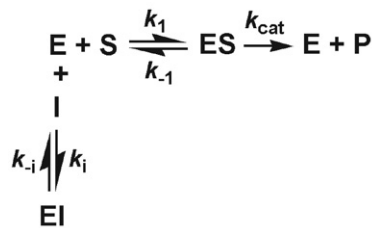


Figure 5. Reaction of competitive inhibition.³⁵

presents an approximate condition for the physically meaningful estimate of k_{cat}/K_M .

To evaluate the functional efficiency of the complexes (Table 3) in terms of the specificity constant (k_{cat}/K_M), a competitive inhibition mechanism is considered (Figure 5). For such a reaction, the inhibition constant is defined as:

$$K_i = \frac{IC_{50}}{\left(\frac{[S]}{K_M} + 1\right)} = \begin{cases} \text{if } [S] = K_M, K_i = IC_{50}/2 \\ \text{if } [S] \gg K_M, K_i \ll IC_{50} \\ \text{if } [S] \ll K_M, K_i \cong IC_{50} \end{cases} \quad (4)$$

where IC_{50} is the inhibitory concentration, K_M is the Michaelis constant, and $[S]$ is the substrate concentration.³⁵ Solving Eq. 4 for the Michaelis constant gives:

$$K_M = \frac{[S]}{\left(\frac{IC_{50}}{K_i} - 1\right)} \quad (5)$$

The kinetic data are analyzed as follows. IC_{50} is evaluated using its linear correlation with ΔG_{bind} (Figure 3). K_M is evaluated using Eq. 5 with $[S] \approx 2.7 \text{ mM}$ ($1 \text{ mM} = 10^{-3} \text{ M}$) – a typical experimental value.¹⁰ Of these complexes (Table 3), those having $K_M < 157.51 \mu\text{M}$ are selected (Table 4) and may be considered as competitively inhibited structures. The comparison of the values of K_M (Table 4) with respect to $[S]$ shows that $[S] \gg K_M$, what is in line with $K_i \ll IC_{50}$ according to Eq. 4. The estimate of k_{cat}/K_M (Table 4) is made by way of the linear correlation $K_M = -0.58 k_{\text{cat}}/K_M + 157.51$ (Figure 4, top). The specificity constants (k_{cat}/K_M) are within the experimental range (between 10^{-4} and $10^{-1} \mu\text{M}^{-1} \text{ s}^{-1}$),³⁶ indicating that VELAD and VDVAAD are most specific to caspase-2. These two particular peptides are approximately 1.5, 3 and 4 times more specific to the enzyme than VEIAD, VEVAD and VDIAD respectively.

In case of simple enzyme reaction with one substrate, if $k_{\text{cat}} \ll k_{-1}$, K_M is conceivable as the dissociation constant that quantifies the strength of the ES complex formation. If the K_M value gets smaller then the ES complex gets stronger (or more stable). In other words, the more pronounced enzyme affinity to the substrate is lined up with the more specific inhibition of the enzyme. The values of ΔG_{bind} (Table 3), K_M (Table 4) and k_{cat}/K_M (Table 4) conform to the trend.

Table 4. Evaluated competitive inhibition data for caspase-2:peptide complexes: K_i – inhibition constant, IC_{50} – inhibitory concentration, K_M – Michaelis constant, k_{cat} – catalytic constant, and k_{cat}/K_M – specificity constant

Complex ^(a)	ΔG_{bind} (kcal mol ⁻¹)	K_i (μ M) ^(b)	IC_{50} (nM) ^(b)	K_M (μ M) ^{(b), (c)}	k_{cat} (s ⁻¹)	k_{cat}/K_M (μ M ⁻¹ s ⁻¹)
casp-2:VELAD	-13.84	0.000081	23.88	9.19	0.24	0.026
casp-2:VDVAD	-13.22	0.00023	25.00	25.00	0.58	0.023
casp-2:VEIAD	-12.64	0.00061	26.15	64.48	1.03	0.016
casp-2:VEVAD	-11.57	0.0037	98.46	105.43	0.94	0.0089
casp-2:VDIAD	-11.45	0.0045	107.69	117.75	0.80	0.0068

^(a) Ala (A), Asp (D), Glu (E), Ile (I), Leu (L), Val (V) ^(b) 1 μ M = 10⁻⁶ M, 1 nM = 10⁻⁹ M ^(c) Of the complexes given in Table 3, those having $K_M < 157.51$ μ M are reported here. $K_M < 157.51$ μ M is an approximate condition for the physically meaningful estimate of k_{cat}/K_M (Figure 4, top).

For tightly bound inhibitors, the inhibition constant is:

$$K_i = \frac{(IC_{50} - [E]/2)}{\left(\frac{[S]}{K_M} + 1\right)} \quad (6)$$

where $[E]$ is the enzyme concentration.³⁵ For tightly bound inhibitors, the equation 6 takes into account the larger amounts of inhibitor bound species, thus making that the Michaelis-Menten assumption of the total enzyme concentration being equal does not hold.^{35,37}

The Michaelis constant for tightly bound inhibitors is:

$$K_M = \frac{[S]}{\left(\frac{IC_{50} - [E]/2}{K_i} - 1\right)} \quad (7)$$

The condition $K_M < 157.51$ μ M for tightly bound peptides means:

$$\frac{[S]}{\left(\frac{IC_{50} - [E]/2}{K_i} - 1\right)} < 157.51 \mu\text{M} \quad (8)$$

Therefore,

$$\frac{IC_{50} - [E]/2}{K_i} - 1 > \frac{[S]}{157.51} \quad (9)$$

Solving Eq. 9 for IC_{50} gives:

$$IC_{50} > \frac{[S]}{157.51} K_i + [E]/2 \quad (10)$$

For $[S] \approx 2.7$ mM and $[E] \approx 50$ nM – typical experimental values,¹⁰ Eq. 10 gives an approximate condition, IC_{50} (nM) > 17.14 K_i (nM) + 25, which should be satisfied by the tight binding of penta-peptides to caspase-2. The values of IC_{50} and K_i (Table 4) indicate that VEVAD and VDIAD satisfy this condition. By reducing $[E]$ from 50 to 44.8 nM, the condition becomes IC_{50} (nM) > 17.14 K_i (nM) + 22.4 and is satisfied by VELAD, VEVAD and VDIAD. If $[E]$ is additionally lowered to 42 nM then the condition gets IC_{50} (nM) > 17.14 K_i (nM) + 21, indicating

that VELAD, VDVAD, VEVAD and VDIAD may be considered as tightly bound inhibitors.

In most experimental investigations of enzyme kinetics, the total concentration of substrate is in excess of the enzyme concentration, thus making the free and total substrate concentrations essentially equal.³⁵ For a set of inhibitor candidates, comparison of K_M or IC_{50} values is only assumed to be valid when these values are evaluated under identical experimental conditions.^{35,38} Only few data exist on the catalytic efficiencies of caspase substrates, so that a more complete understanding of their true substrate preferences is impossible.³⁶ The present results are imagined to facilitate additional experiments, which are needed to understand better the kinetics of caspase-2/peptide recognition for further research or therapeutic product development. The fact that caspase inhibition-based drug has not been approved on the market so far means that the development of therapeutic approaches that specifically target caspases is a substantial challenge of particular biological and clinical interest.³⁹

4. Conclusions

QM/MM model derived and exploited in this work has been shown to correlate with the existing experimental observations to an appreciable extent, indicating that caspase-2 uniquely prefers a penta-peptide such as VDVAD.

This approach has enabled the extensive and systematic investigations of some of the important aspects both of the thermodynamics and of the kinetics of caspase-2 recognition by a large number of penta-peptides. The sequence of VDVAD has been consistently varied and the corresponding binding free energies with the inhibition constants have been evaluated. The values of the inhibition constants, being within the experimental range for several caspase-2:peptide complexes, have indicated that the affinity order is: VELAD > VDVAD > VEIAD > VEVAD > VDIAD etc. The specificity constants for competitive inhibition have been estimated to fit the experimentally predicted range, thereby suggesting that VELAD and VDVAD are most specific to caspase-2; also both are about 1.5, 3 and 4 times more specific to the receptor than VEIAD, VEVAD and VDIAD respectively. An approximate kinetic

threshold, supposed to discriminate tightly bound peptide inhibitors, has been reported.

This study has demonstrated that a well-calibrated computational work may yield information inaccessible by other methods or suggest new experimental procedures.

Acknowledgment

Prof. David A. Case of Rutgers University is acknowledged for granting the author an academic license for using the molecular dynamics software package Amber11 in combination with AmberTools 1.5.

Supplementary Material

QM/MM binding free energies for all studied caspase-2:peptide complexes are available.

5. References

- D. R. McIlwain, T. Berger, T. W. Mak, *Cold Spring Harb. Perspect. Biol.* **2013**, 5, a008656. DOI:10.1101/cshperspect.a008656
- S. Nagata, *Annu. Rev. Immunol.* **2018**, 36, 489–517. DOI:10.1146/annurev-immunol-042617-053010
- G. Krumschnabel, B. Sohm, F. Bock, C. Manzl, A. Villunger, *Cell Death Differ.* **2009**, 16, 195–207. DOI:10.1038/cdd.2008.170
- L. Bergeron, G. I. Perez, G. Macdonald, L. Shi, Y. Sun, A. Jurisicova, S. Varmuza, K. E. Latham, J. A. Flaws, J. C. Salter, H. Hara, M. A. Moskowitz, E. Li, A. Greenberg, J. L. Tilly, J. Yuan, *Genes Dev.* **1998**, 12, 1304–1314. DOI:10.1101/gad.12.9.1304
- L. Bouchier-Hayes, *J. Cell. Mol. Med.* **2010**, 14, 1212–1224. DOI:10.1111/j.1582-4934.2010.01037.x
- S. Kumar, *Nat. Rev. Cancer* **2009**, 9, 897–903. DOI:10.1038/nrc2745
- H. Vakifahmetoglu-Norberg, B. Zhivotovsky, *Trends Cell Biol.* **2010**, 20, 150–159. DOI:10.1016/j.tcb.2009.12.006
- S. Shimohama, H. Tanino, S. Fujimoto, *Biochem. Biophys. Res. Commun.* **1999**, 256, 381–384. DOI:10.1006/bbrc.1999.0344
- J. Y. Kim, R. Garcia-Carbonell, S. Yamachika, P. Zhao, D. Dhar, R. Loomba, R. J. Kaufman, A. R. Saltiel, M. Karin, *Cell* **2018**, 75(1), 133–145.e15. DOI:10.1016/j.cell.2018.08.020
- Y. Tang, J. A. Wells, M. R. Arkin, *J. Biol. Chem.* **2011**, 286(39), 34147–34154. DOI:10.1074/jbc.M111.247627
- PyMol, Version 0.99, W. L. DeLano, DeLano Scientific LLC, South San Francisco CA, **2006**.
- D. A. Case, T. Cheatham, T. Darden, H. Gohlke, R. Luo, K. M. Merz, A. Onufriev, C. Simmerling, B. Wang, R. Woods, *J. Comput. Chem.* **2005**, 26, 1668–1688. DOI:10.1002/jcc.20290
- Amber 11, D. A. Case, T. A. Darden, T. E. Cheatham III, C. L. Simmerling, J. Wang, R. E. Duke, R. Luo, R. C. Walker, W. Zhang, K. M. Merz, B. P. Roberts, B. Wang, S. Hayik, A. Roitberg, G. Seabra, I. Kolossváry, K. F. Wong, F. Paesani, J. Vanicek, J. Liu, X. Wu, S. R. Brozell, T. Steinbrecher, H. Gohlke, Q. Cai, X. Ye, J. Wang, M. J. Hsieh, G. Cui, D. R. Roe, D. H. Mathews, M. G. Seetin, C. Sagui, V. Babin, T. Luchko, S. Gusarov, A. Kovalenko, and P. A. Kollman, University of California, San Francisco CA. **2010**.
- V. Hornak, R. Abei, A. Okur, B. Strockbine, A. Roitberg, C. Simmerling, *Proteins* **2006**, 65, 712–725. DOI:10.1002/prot.21123
- Gaussian 98, Revision A.9, M. J. Frisch, G. W. Trucks, H. B. Schlegel, G. E. Scuseria, M. A. Robb, J. R. Cheeseman, V. G. Zakrzewski, J. A. Montgomery, R. E. Stratmann, J. C. Burant, S. Dapprich, J. M. Millam, A. D. Daniels, K. N. Kudin, M. C. Strain, O. Farkas, J. Tomasi, V. Barone, M. Cossi, R. Cammi, B. Mennucci, C. Pomelli, C. Adamo, S. Clifford, J. Ochterski, G. A. Petersson, P. Y. Ayala, Q. Cui, K. Morokuma, D. K. Malick, A. D. Rabuck, K. Raghavachari, J. B. Foresman, J. Cioslowski, J. V. Ortiz, A. G. Baboul, B. Stefanov, G. Liu, A. Liashenko, P. Piskorz, I. Komaromi, R. Gomperts, R. L. Martin, D. J. Fox, T. A. Keith, M. A. Al-Laham, C. Y. Peng, A. Nanayakkara, M. Challacombe, P. M. W. Gill, B. Johnson, W. Chen, M. W. Wong, J. L. Andres, C. Gonzalez, M. Head-Gordon, E. S. Replogle, and J. A. Pople, Gaussian, Inc., Pittsburgh PA, **1998**.
- C. I. Bayly, P. Cieplak, W. Cornell, P. A. Kollman, *J. Phys. Chem.* **1993**, 97, 10269–10280. DOI:10.1021/j100142a004
- J. Wang, R. M. Wolf, J. W. Caldwell, P. A. Kollman, D. A. Case, *J. Comput. Chem.* **2004**, 25, 1157–1174. DOI:10.1002/jcc.20035
- M. Elstner, D. Porezag, G. Jungnickel, J. Elsner, M. Haugk, T. Frauenheim, S. Suhai, G. Seifert, *Phys. Rev. B* **1998**, 58, 7260–7268. DOI:10.1103/PhysRevB.58.7260
- M. Elstner, P. Hobza, T. Frauenheim, S. Suhai, E. Kaxiras, *J. Chem. Phys.* **2001**, 114, 5149–5155. DOI:10.1063/1.1329889
- S. Grimme, J. Antony, T. Schwabe, C. Muck-Lichtenfeld, *Org. Biomol. Chem.* **2007**, 5, 741–758. DOI:10.1039/B615319B
- G. M. Seabre, R. C. Walker, M. Elstner, D. A. Case, A. E. Roitberg, *J. Phys. Chem. A* **2007**, 111(26), 5655–5664. DOI:10.1021/jp070071l
- R. C. Walker, M. F. Crowley, D. A. Case, *J. Comp. Chem.* **2008**, 29(7), 1019–1031. DOI:10.1002/jcc.20857
- T. Kubar, P. Jurecka, J. Cerny, J. Rezac, M. Otyepka, H. Valdes, P. Hobza, *J. Phys. Chem. A* **2007**, 111, 5642–5647. DOI:10.1021/jp068858j
- S. Kristyan, P. Pulay, *Chem. Phys. Lett.* **1994**, 229, 175–180. DOI:10.1016/0009-2614(94)01027-7
- P. Hobza, J. Sponer, T. Reschel, *J. Comp. Chem.* **1995**, 16, 1315–1325. DOI:10.1002/jcc.540161102
- P. Jurecka, J. Sponer, J. Cerny, P. Hobza, *Phys. Chem. Chem. Phys.* **2006**, 8, 1985–1993. DOI:10.1039/B600027D
- P. Jurecka, J. Cerny, P. Hobza, D. R. Salahub, *J. Comp. Chem.* **2007**, 28, 555–569. DOI:10.1002/jcc.20570
- A. Pavlov, P. M. Mitrasinovic, *Curr. Org. Chem.* **2010**, 14, 129–138. DOI:10.2174/138527210790069866
- P. M. Mitrasinovic, *Curr. Drug Targ.* **2013**, 14, 817–829. DOI:10.2174/1389450111314070009
- P. M. Mitrasinovic, *Med. Chem.* **2014**, 10, 46–58. DOI:10.2174/157340641001131226122124
- P. M. Mitrasinovic, *Med. Chem.* **2014**, 10, 252–270. DOI:10.2174/157340641003140304143442

32. P. M. Mitrasinovic, *Can. J. Chem.* **2003**, *81*, 542–554. DOI:10.1139/v03-043
33. P. M. Mitrasinovic, *Curr. Org. Chem.* **2010**, *14*, 198–211. DOI:10.2174/138527210790069857
34. M. Garcia-Calvo, E. P. Peterson, B. Leiting, R. Rue, D. W. Nicholson, N. A. Thornberry, *J. Biol. Chem.* **1998**, *273*(49), 32608–32613. DOI:10.1074/jbc.273.49.32608
35. R. Z. Cer, U. Mudunuri, R. Stephens, F. J. Lebeda, *Nucl. Acids Res.* **2009**, *37*, W441–W445. DOI:10.1093/nar/gkp253
36. O. Julien, M. Zhuang, A. P. Wiita, A. J. O'Donoghue, G. M. Knudsen, C. S. Craik, J. A. Wells, *Proc. Natl. Acad. Sci. U. S. A.* **2016**, *113*(14), E2001–E2010. DOI:10.1073/pnas.1524900113
37. P. J. Henderson, *Biochem. J.* **1972**, *127*, 321–333. DOI:10.1042/bj1270321
38. P. J. Munson, D. Rodbard, *J. Recept. Res.* **1988**, *8*, 533–546. DOI:10.3109/10799898809049010
39. J. Kudelova, J. Fleischmannova, E. Adamova, E. Matalova, *J. Physiol. Pharmacol.* **2015**, *66*(4), 473–482.

Povzetek

Zaradi različnih bioloških in zdravstvenih razlogov je razvoj humanih zaviralcev kaspaze-2 ključnega pomena. V članku je izpeljan hibridni (kvantno mehanski / molekularno mehanski – QM / MM), dvoplastni molekulski model s ciljem boljšega razumevanja afinitete in specifičnosti interakcije peptidnih zaviralcev s kaspazo-2. Z upoštevanjem edinstvenih strukturnih značilnosti in katalitične aktivnosti človeške kaspaze-2 se kritični aminokislinski preostanki encima (E217, R378, N379, T380 in Y420) s peptidnim zaviralcem obravnavajo na ravni QM (z uporabo t.i. Self-Consistent-Charge Density-Functional Tight-Binding method with the Dispersion correction (SCC-DFTB-D)), preostali del kompleksa pa se obravnava na ravni MM (t.i. AMBER force field). QM/MM vezavne proste energije (VPE) dobro korelirajo z eksperimentalnimi opazovanji in kažejo, da kaspaza-2 daje prednost penta-peptidu, kot je VDVAD. Zaporedje VDVAD smo sistematično spreminjali tako, da smo upoštevali fizikalno-kemijske lastnosti vsake aminokislina in njenega substituenta, pri čemer smo ovrednotili ustrezne VPE z inhibicijsko konstanto (K_i). Vrednosti K_i za več kompleksov kaspaza-2:peptidni inhibitor se nahajajo v eksperimentalnem območju (med 0,01 nM in 1 μ M). Zaporedje afinitet je: VELAD ($K_i = 0,081$ nM) > VDVAD ($K_i = 0,23$ nM) > VEIAD ($K_i = 0,61$ nM) > VEVAD ($K_i = 3,7$ nM) > VDIAD ($K_i = 4,5$ nM) itd. Navajamo pogoj aproksimacije, ki mu je potrebno zadostiti s kinetičnimi parametri (Michaelisova konstanta – K_M in konstanta specifičnosti – k_{cat} / K_M) za kompetitivno inhibicijo. Ocenjene vrednosti k_{cat} / K_M v eksperimentalno določenem območju (med 10^{-4} in 10^{-1} μ M $^{-1}$ s $^{-1}$) kažejo, da sta VELAD in VDVAD najbolj specifična za kaspazo-2. Ta dva peptida sta skoraj 1,5, 3 in 4-krat bolj specifična za receptor od peptidov VEIAD, VEVAD in VDIAD. Naveden je tudi dodatni kinetični prag, ki je namenjen razločevanju med tesno vezanimi zaviralci.



Except when otherwise noted, articles in this journal are published under the terms and conditions of the Creative Commons Attribution 4.0 International License

Scientific paper

Antimüllerian Hormone and Oxidative Stress Biomarkers as Predictors of Successful Pregnancy in Polycystic Ovary Syndrome, Endometriosis and Tubal Infertility Factor

Teja Fabjan,^{1,3} Eda Vrtačnik-Bokal,² Irma Virant-Klun,² Jure Bedenk,²
Kristina Kumer^{1,3} and Joško Osredkar^{1,3,*}

¹ University Medical Centre Ljubljana, Institute of Clinical Chemistry and Biochemistry, Njogoševa 4,
1000 Ljubljana, Slovenia

² University Medical Centre Ljubljana, Division of Gynaecology, Department of Human Reproduction, Šljajmerjeva 3,
1000 Ljubljana, Slovenia

³ University of Ljubljana, Faculty of Pharmacy, Aškerčeva cesta 7, 1000 Ljubljana

* Corresponding author: E-mail: josko.osredkar@kclj.si

Received: 01-29-2020

Abstract

Oxidative stress in the follicular fluid (FF) is thought to be responsible for the abnormal development of oocytes. In our study patients with polycystic ovarian syndrome (PCOS), endometriosis, and tubal infertility factor (TIF), and healthy women with a male factor of infertility, were prospectively enrolled. From each patient, a sample of individual FF was collected from a dominant follicle. Concentration levels of TAS, 8-IP, 8-OHdG, and AMH were determined.

In women with PCOS, we found significantly lower values of oxidative stress markers in the FF. 8-IP and TAS levels were lower in the FF of women with endometriosis. In women with TIF, we also found significantly lower values of all tested markers in the FF, except for 8-OHdG and AMH. We wanted to see whether the biomarker measured in the FF in an individual diagnosis could predict a successfully obtained embryo from this particular follicle. The FF 8-OHdG result in PCOS patients stood out and proved to be a good predictive marker of matured and fertilized oocytes in these patients. Further research is needed to be able to apply the acquired knowledge in improving the outcome of IVF procedures.

Keywords: Oxidative stress; Antimüllerian hormone; Polycystic ovary syndrome; Endometriosis; Tubal infertility factor; Infertility

1. Introduction

The overall prevalence of infertility is 12.5% among women and 10.1% among men, and this rate is rising. The causes vary; among female diagnoses the most common are ovulation disorders, including PCOS, as well as endometriosis and various fallopian tubes defects. The prevalence of those seeking help has been reported even above 50%.¹ Environmental and lifestyle factors affect the couple's fertility status through a series of known and unknown mechanisms.

The reproductive organs have the highest number of mitochondria in the human body.² This is needed because of the high requirement of energy production via ATP. On

the other hand, this makes these organs highly susceptible to elevated levels of reactive oxygen or nitrogen species (ROS/RNS). Oxidative stress (OS) has received extensive attention in the past two decades due to the discovery that abnormal oxidation status is related to patients with chronic diseases, such as diabetes, cardiovascular, polycystic ovary syndrome (PCOS), endometriosis, cancer, and neurological diseases.^{3–6} Oxidative stress occurs when oxidants outnumber antioxidants, then products of peroxidation develop, and then pathological effects are caused by these phenomena. ROS are produced mainly within the mitochondrial electron transport chain and must be constantly deactivated to avoid excess formation to maintain normal cell function.⁷

In vitro fertilization (IVF) is a widely accepted infertility treatment and is often the only option for infertile couples to have a baby. Unfortunately, the success of this technique, measured as an average pregnancy rate per cycle, is only 30–40% for women under age 40.^{8–10} Several studies have reported signs of oxidative stress in the FF of infertile women.^{7,11–14} It has been suggested that OS is responsible for normal oocyte development, due to DNA and cell membrane damage, which would then result in reduced oocyte quality, altered fertilization, and different embryo quality, implantation, and embryonic development. Elevated OS is also associated with ovarian ageing. Low-quality oocytes contain increased amounts of damaged DNA and chromosomal aneuploidy, secondary to age-related dysfunctions.¹⁵

It has been predicted that the concentration of AMH influences the number of oocytes retrieved during the IVF process. However, to date, the relationship between FF AMH and oocyte quality is unclear. The AMH level in the individual follicle was found to inversely correlate with the oocyte's maturity and developmental potential.¹⁶ In contrast, it was observed that oocytes capable of producing high levels of AMH were much easier to fertilize in normo-ovulatory females.¹⁷ In PCOS patients, however, it has even been shown that the proportion of mature oocytes, as well as fertilization success, does not correlate with FF AMH.¹⁸ In their study, Fanchin et al. showed that FF AMH is a better predictor of fertilization and implantation of embryo than serum AMH in normo-ovulatory women.¹⁹ In Korea, these results have recently been confirmed on a smaller sample.²⁰ However, there have been very few studies on the relationship between FF AMH levels and the quality of oocyte and embryo.

The tubal factor of infertility, PCOS, and endometriosis are the main indications in patients undergoing IVF procedures. PCOS is a disease with high heterogeneity, and its clinical features mainly include menstrual disorder, secondary amenorrhea, serum hormone abnormalities, hirsutism, acne, obesity, and infertility.²² It is estimated that it affects 3–15% of all women.²³ The primary cause of the disorder is an abnormality in the ovaries, but additional agents, such as obesity and environmental factors, affect the development of individual symptoms.²⁴

Endometriosis is also one of the most common gynecologic diseases in women of reproductive age. It is characterized by implantation and growth of endometrial tissue (glands and stroma) outside the uterine cavity. Endometriosis is an estrogen-dependent pelvic inflammatory disease. The prevalence in women with pelvic pain ranges from 30–40% of the infertile population. Endometriosis can be also asymptomatic or accompanied by symptoms such as dysmenorrhea and dyspareunia.^{25,26} Many studies widely accepted that oxidative stress might be implicated in the pathophysiology of endometriosis causing a general inflammatory response in the peritoneal cavity.^{27–31}

It is not known exactly how endometriosis causes

infertility, but it is probably related to the inflammatory response resulting from the overproduction of prostaglandins, cytokines and macrophages, and natural killer cells. The inflammatory process thus impairs the function of the ovaries, peritoneal system, fallopian tubes, and endometrium and leads to impaired folliculogenesis, fertilization, and other conditions. Tubal infertility factor (TIF) accounts for about 35% of all infertility cases.³² Pregnancy does not occur due to mechanical obstruction in the fallopian tube. There are several causes for tubal blockage: infection, inflammation, surgery due to ectopic pregnancy, adhesions due to abnormal immunochemical environment, or rarely a congenital anomaly.³³ Many studies use TIF patients as a control group because the obstacle is considered purely mechanical. We decided to include it as a pathological group because the causes of tubal infertility may also be hormonal (e.g. endometriosis) and inflammatory and this could have a significant impact on oxidative stress measurements.

The aim of this study was to evaluate OS in patients undergoing IVF procedure according to various indications, capabilities of fertilization, and embryo quality. We determined three different OS biomarkers and AMH in the FF of the dominant follicle containing oocyte. We have examined how their combination affects success rates in obtaining mature and fertilized oocytes in patients with PCOS, endometriosis, and TIF during IVF procedure.

2. Selected Biomarkers

Antimüllerian hormone (AMH)

AMH is produced in the granulosa cells and is a member of the transforming growth factor β family. AMH is an excellent marker of ovarian reserves.³⁴ The hormone levels in both the peripheral blood and intrafollicular fluid correspond with the rate of follicular maturation. AMH affects oocyte development during folliculogenesis, and the levels of AMH in the follicular fluid may affect the oocyte and embryo quality.^{20,35–37}

8-Isoprostane (8-IP)

Free radical attack induces lipid peroxidation. Lipid peroxidation is a self-propagating phenomenon terminated by antioxidants and the measurement of products of lipid peroxidation has commonly been used to assess OS. Isoprostanes are a series of prostaglandin F₂-like compounds, in vitro and in vivo formed by free radical-catalyzed peroxidation of phospholipid-bound arachidonic acid, a pathway that is independent of the cyclooxygenase pathway.^{38–40} F₂-Isoprostanes are considered the best available biomarkers of oxidative stress status and lipid peroxidation. Measurement of the level of lipid peroxidation as reflected by F₂-isoprostane concentrations in biological fluids may help to identify those patients most likely to benefit from antioxidant treatment.^{41,42}

8-hydroxy-2'-deoxyguanosine (8-OHdG)

An oxidized derivative of deoxyguanosine is one of the most common oxidative modification in mutagenic damage and is used as a biomarker of OS. Oxidation of DNA occurs normally in vivo but also increases with exposure to oxidizing agents. Guanosines are very susceptible to oxidation, and this reaction can lead to G:C→T:A mutations. These mutations could have serious consequences. Oxidized bases are usually recognized and excised by special DNA repair machinery.^{43,44}

Total antioxidant status (TAS)

The antioxidant defense system has many components. The total antioxidant status (TAS) of follicular fluid samples was determined using a special metric. The Randox TAS kit measures the total antioxidant capacity of a sample, i.e. anything that has an antioxidant effect, including both enzymatic and non-enzymatic antioxidants. The reaction rate is calibrated with Trolox, which is widely used as a traditional standard for TAS measurement assays, and the assay results are expressed in mmol Trolox equivalent/L.^{45,46}

3. Materials and Methods

3.1. Participants

A total of 197 women with an indication for IVE/ICSI treatment were prospectively enrolled in this study from March 2013 to April 2014 at University Medical Centre Ljubljana, Reproductive Medicine Unit. The research was approved by the ethics committee from the Slovenian National committee on medical ethics. Written informed consent was obtained from all participants. The study included four different groups: 36 patients with polycystic ovarian syndrome (PCOS), 72 with endometriosis, 41 with TIF, and 48 healthy controls. Healthy women whose in-

fertility issues were caused by male partners were enrolled as controls. The demographic characteristics of the patient groups and control group are presented in Table 1.

Figure 1 shows the number and share of all eggs collected and further the embryos during observation in this study. In our study, 197 dominant follicles were aspirated. Oocytes were obtained in 54% of these follicles. 81% of the oocytes were mature and 74% of these were fertilized. In this study group, 64 embryos were obtained and of these, 54 were successfully transferred at the end.

3.2. Samples Collection

All women underwent ovarian stimulation using a combination of GnRH analogues and gonadotrophins. On the day of oocyte retrieval, the FF from the dominant follicle was aspirated. FF aspiration was performed transvaginally using a transvaginal ultrasound probe as a guide, and a specific oocyte aspiration needle connected to a closed vacuum system. Only FF samples without blood clots were used for the measurements, so as to minimize any possible interference with the photometric assay. Blood contamination was evaluated by visual inspection, and samples that appeared cloudy or bloodstained were discarded. The FF samples collected were centrifuged at 3500 rpm for 10 min (to precipitate blood cells and to remove cellular components). All samples were stored at -80 °C until assayed.

3.3. Sample Analysis

The effect of oxidative stress was measured by 8-isoprostane and 8-hydroxy-2'-deoxyguanosine and enzymatic antioxidant activity by TAS (the combined effect of all antioxidants). Expression levels of AMH, 8-IP, 8-OHdG and TAS levels were determined by using commercially available enzyme-linked immunosorbent assay (ELISA)

Table 1: Demographic characteristics of the participants (mean or median of individual biomarkers are statistically analyzed and the p values indicating the significance of differences between different infertility groups individually with control group obtained by the t test or Mann-Whitney test as appropriate)

	Endometriosis		PCOS		Tubal factor of infertility		Control group
N	72		36		41		48
Age [years]; (95% CI for the mean)	33.8 (33.1–34.5)	P = 0.0013	30.8 (29.4–32.2)	P = 0.3621	32.3 (31–33.5)	P = 0.1597	31.62 (30.5–32.7)
Height [cm]; (95% CI for the mean)	165.9 (164.3–167.5)	P = 0.1746	164.8 (162.8–166.7)	P = 0.0310	167.5 (165.8–169.2)	P = 0.9985	167.4 (165.9–169.1)
Weight [kg]; (95% CI for the mean)	60.3 (58.5–62.0)	P = 0.0292	70.7 (65.1–76.3)	P = 0.0582	65.3 (61.6–69)	P = 0.6207	63.4 (61.1–65.8)
BMI (95% CI for the median)	21.65 (21.2–22.5)	P = 0.3831	24.5 (23–27)	P = 0.0111	22.45 (21.2–24)	P = 0.7096	22.45 (21.4–23.3)

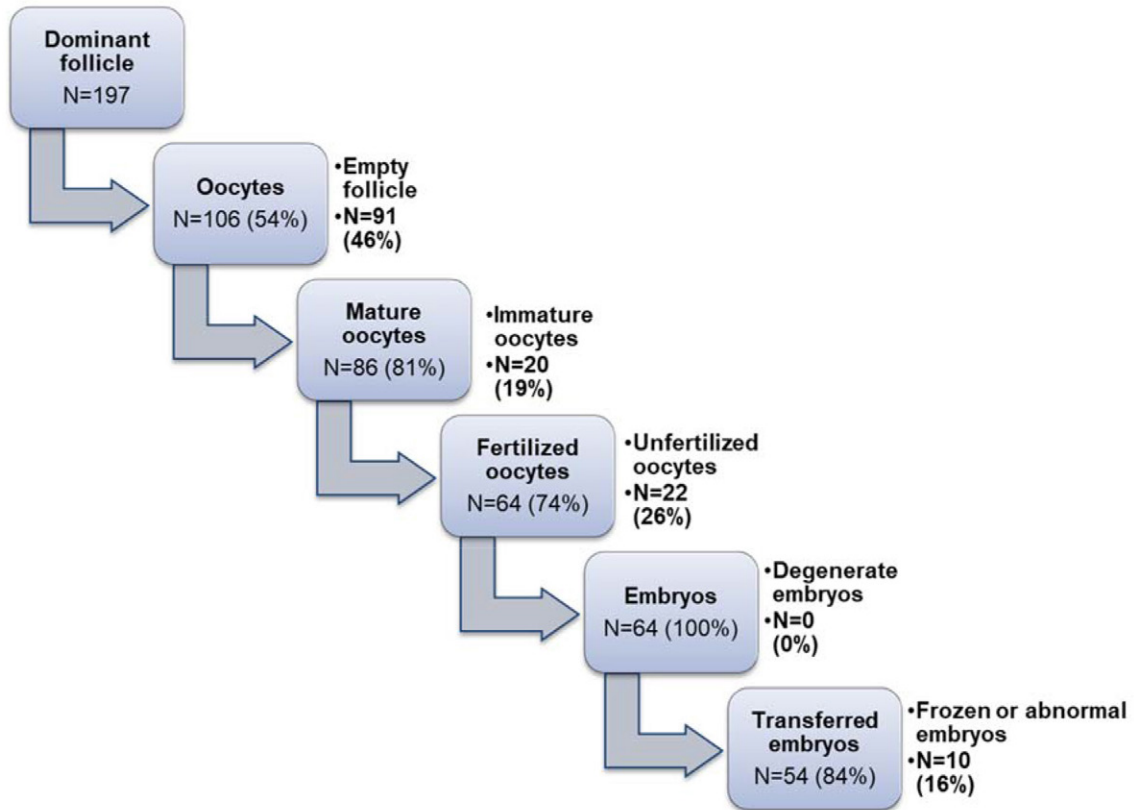


Figure 1: Outcome of IVF procedure in patients enrolled in the study by stages

kits according to the manufacturer's instructions. For 8-IP (Cayman Chemical Company, USA),⁴⁷ 8-OHdG (Ja-ICA - Japan Institute for the Control of Aging, Japan)⁴⁸ and AMH (Anshlab)⁴⁹ the lower and upper detection limits were estimated as 0.8–500 ng/L; 0.5–200 ng/mL and 3.8–1091 ng/L, respectively. Total antioxidant status (TAS) was evaluated by colourimetric method with Randox assay (Randox Laboratories Limited, UK).⁵⁰

The results of the tests used are presented in Table 2.

3. 4. Statistical Analysis

Statistical significance was calculated by two different tests: the Mann–Whitney U test. This test is non-parametric and does not require the groups to be normally distributed; it is more stable to outliers. The predictive value of biomarkers was determined using the “Receiver Operating Characteristic” analysis (ROC). P-values <0.05 were considered as significant. All analyses were made with statistical program Medcalc.

Table 2: Characteristic of the tests

		Measuring Range	Intra-assay variation (%CV)	Inter-assay variation (%CV)
AMH [pg/mL]	Low	14.2–15.5	4.7	6.9
	Medium	80.0–80.8	2.9	4.3
	High	609.6–942.8	3.0	4.5
8-IP [pg/mL]	Low	0.80–5.10	20.0	11.1
	Medium	12.80–32.00	7.7	17.4
	High	80.00–500.00	12.2	13.5
8-OHdG [ng/mL]	Low	8.6–10.2	2.9	6.1
	Medium	28.5–32.2	1.8	4.0
	High	107.3–129.7	5.5	5.4
TAS	Low	0.9–1.23	5.1	4.1
	Medium	1.59–1.75	1.8	3.0
	High	2.10–2.40	1.3	3.9

4. Results

Follicular fluid from the dominant follicle of 197 women undergoing IVF was analyzed in this study. The groups were generally comparable with each other; only patients with endometriosis were slightly older on average. The BMI index is higher in patients with PCOS as

expected. The basal levels of serum hormones that affect the characteristics of infertility indications are presented in Table 3. The different diagnosis groups show variations in the levels of different hormones where it is typically expected, e.g. LH is elevated in the PCOS group.

The analyzed data are summarized in Table 4 and presented graphically in Figure 2.

Table 3: Hormonal status of the participants

	Endometriosis N = 72		PCOS N = 36		TIF N = 41		Control group N = 48
S-FSH	7.4	P = 0.5454	6.0	P = 0.0085	6.6	P = 0.2103	7.1
S-LH	4.1	P = 0.9681	11.2	P < 0.0001	3.8	P = 0.4426	4.1
S-PRL	10.2	P = 0.7682	10.5	P = 0.9602	10.4	P = 0.9093	10.6

Table 4: Medians of individual biomarkers and interquartile ranges analyzed and the p values indicating the significance of differences between different groups of patients obtained by the Mann-Whitney U test

	PCOS (N = 36)		Endometriosis (N = 72)	Endometriosis (N = 72)	TIF (N = 41)	
8-OHdG [ng/mL]	6.82 (4.66–11.45)	P = 0.0001	15.11 (8.76–23.45)	8-OHdG [ng/mL]	15.11 (8.76–23.45)	P = 0.7539 16.32 (9.77–22.41)
8-IP [pg/mL]	85.97 (58.81–313.12)	P = 0.9682	91.07 (60.15–170.09)	8-IP [pg/mL]	91.07 (60.15–170.09)	P = 0.5985 91.78 (47.14–213.51)
TAS [mmol/L]	0.965 (0.880–1.010)	P = 0.0001	1.08 (0.945–1.160)	TAS [mmol/L]	1.08 (0.945–1.160)	P = 0.0002 0.92 (0.858–1.008)
AMH [U/mL]	6.85 (3.49–11.26)	P = 0.0093	3.52 (2.06–6.56)	AMH [U/mL]	3.52 (2.06–6.56)	P = 0.0340 5.54 (3.63–8.15)
	PCOS (N = 36)		TIF (N = 41)	Endometriosis (N = 72)	Healthy (N = 48)	
8-OHdG [ng/mL]	6.82 (4.66–11.45)	P = 0.0001	16.32 (9.77–22.41)	8-OHdG [ng/mL]	15.11 (8.76–23.45)	P = 0.8262 14.81 (9.12–25.59)
8-IP [pg/mL]	85.97 (58.81–313.12)	P = 0.6357	91.78 (47.14–213.51)	8-IP [pg/mL]	91.07 (60.15–170.09)	P < 0.0001 253.36 (125.47–556.10)
TAS [mmol/L]	0.965 (0.880–1.010)	P = 0.3712	0.92 (0.858–1.008)	TAS [mmol/L]	1.08 (0.945–1.160)	P < 0.0001 1.275 (1.150–1.355)
AMH [U/mL]	6.85 (3.49–11.26)	P = 0.3814	5.54 (3.63–8.15)	AMH [U/mL]	3.52 (2.06–6.56)	P = 0.0895 4.64 (2.69–8.18)
	PCOS (N = 36)		Healthy (N = 48)	TIF (N = 41)	Healthy (N = 48)	
8-OHdG [ng/mL]	6.82 (4.66–11.45)	P = 0.0001	14.81 (9.12–25.59)	8-OHdG [ng/mL]	16.32 (9.77–22.41)	P = 0.9672 14.81 (9.12–25.59)
8-IP [pg/mL]	85.97 (58.81–313.12)	P = 0.0005	253.35 (125.47–556.10)	8-IP [pg/mL]	91.78 (47.14–213.51)	P < 0.0001 253.35 (125.47–556.10)
TAS [mmol/L]	0.965 (0.880–1.010)	P < 0.0001	1.275 (1.150–1.355)	TAS [mmol/L]	0.92 (0.858–1.008)	P < 0.0001 1.275 (1.150–1.355)
AMH [U/mL]	6.85 (3.49–11.26)	P = 0.2306	4.64 (2.69–8.18)	AMH [U/mL]	5.54 (3.63–8.15)	P = 0.6537 4.64 (2.69–8.18)

In women with PCOS, we found significantly lower values of oxidative stress markers in the FF (8-IP: 73.21 vs. 253.36 pg/mL, $P = 0.0001$; 8-hydroxy-2-deoxyguanosine: 6.82 vs. 14.81 ng/mL, $P = 0.0001$ and total antioxidant status: 0.97 vs. 1.28 mmol/L, $P < 0.0001$) and no difference in AMH concentration (6.9 vs. 4.6 U/mL, $P = 0.2306$) compared with the control group.

8-IP levels were also significantly lower in the FF of women with endometriosis (90.11 vs. 253.36 pg/mL, $P < 0.0001$) compared to control group. TAS levels were also lower in FF of endometriosis patients (1.08 vs. 1.28 mmol/L, $P < 0.0001$). No significant differences were found in FF-8-OHdG (15.11 vs. 14.81 ng/mL, $P = 0.8262$) and in FF-AMH (3.5 vs. 4.6 U/mL, $P = 0.0895$) between endometriosis and control group. In women with TIF, we also found significantly lower values of oxidative stress markers in the FF (8-IP: 57.18 vs. 253.36 pg/mL, $P = 0.0001$; and TAS: 0.97 vs. 1.28 mmol/L, $P < 0.0001$) and no difference in 8-OHdG concentration: 16.32 vs. 14.81 ng/mL, $P = 0.0001$ and AMH concentration (5.5 vs. 4.6 U/mL, $P = 0.6537$) compared with the control group.

In the second part, we aimed to relate our results to the outcome of the IVF procedure and determine whether a single biomarker measured in the follicular fluid in an individual diagnosis could predict a successfully obtained matured and fertilized cell from that particular follicle.

Figure 2 shows the accuracy measured by the area under the ROC curve (AUC). The area measures discrimination, i.e. the test's ability to correctly classify those with and without high-quality embryos ready for transfer. An area of 1 represents a perfect test; an area of 0.5 represents a worthless test. Of all the analyses shown, the FF 8-OHdG result in PCOS patients stood out and proved to be a very good predictive marker of obtaining a mature oocyte and of successful fertilization in these patients. At the limit of

6.18 ng/mL, with a sensitivity of 85.7% and a specificity of 86.4%, 8-OHdG separated those with a mature and those with immature oocyte ($p < 0.0001$). 8-OHdG also separated those PCOS patients with a fertilized and those with unfertilized oocyte ($p < 0.0001$), also at the limit 6.18 ng/mL, with sensitivity of 84.62% and specificity of 82.61%. Figure 2 graphically shows both ROC curves for this biomarker. All other markers of OS and also AMH showed poor predictive value both in predicting obtaining a mature cell from a particular follicle and in obtaining fertilization.

5. Discussion

In this study we confirmed for the first time that FF 8-OHdG is a good predictive biomarker for oocyte maturity and fertilization in PCOS patients.

The evaluation of the pathophysiology of a couple's infertility has shown that oxidative stress (OS) may be one of the causative factors of female infertility, as recent studies shown.^{11,28,51-53} But so far there is still a big gap in our knowledge and understanding of individual mechanisms, and further research is needed to be able to use the acquired knowledge to improve the outcome of IVF procedures. Many degenerative changes to the oocytes during ageing are due to oxidative stress. We evaluate OS in patients attended to IVF procedure according to different indicators and we have come up with some very interesting results.

We therefore decided in the present study also to include AMH as one of the investigated markers in the FF. AMH levels did not differ significantly between subjects with PCOS, endometriosis, TIF, and the control. However, an interesting trend suggesting lower concentrations

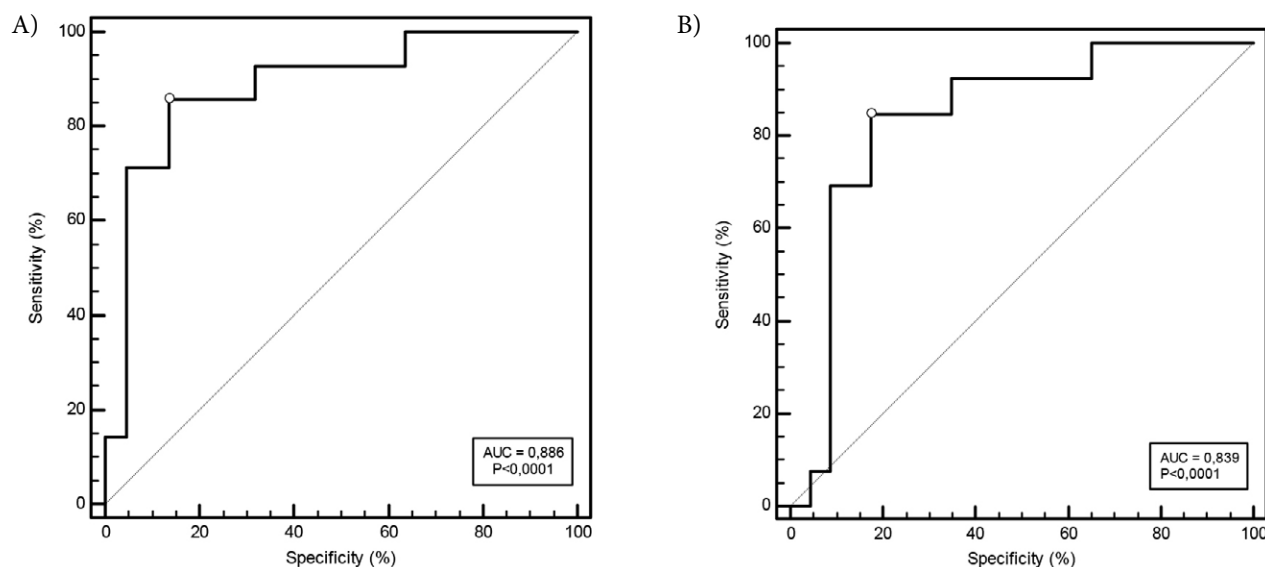


Figure 2: ROC curve for 8-OHdG in PCOS patient group classify on two different outcomes (A-mature oocytes; B-fertilized oocytes)

of AMH is in the group of patients with endometriosis. Lower concentrations of AMH in FF of the leading follicle in patients with endometriosis were also detected in the Spanish research group.⁵⁴ They also observed that the presence of the endometrioma itself reduce even further AMH concentration in the surrounding follicles and suggest that these results could be useful when counselling patients regarding their reproductive outcome. In the PCOS group, we detected slightly higher concentrations of AMH in FF, which is comparable to the study conducted by Liu et al.⁵⁵ AMH production starts in the very small follicles. The peak of production is reached and then the production rapidly declines. AMH production within the follicles is the part of the mechanism responsible for selection of the pre-ovulatory follicle.⁵⁶ All follicles in our study were leading follicles of similar size, so a similar concentration of AMH is expected. In the TIF group, we did not detect a significant difference in the concentration of AMH in the follicular fluid as expected. Similarly, others have noted this, although they regarded this group as a control group.^{57,58}

Another objective of our study was to determine the degree of oxidative stress *in vivo* in follicular fluid. Our results show some interesting differences between patients with PCOS, endometriosis, and TIF compared with healthy controls. The measured 8-IP concentration was found to be significantly higher in the control group than in all three patient groups. It is unclear why we obtained such results. One would expect to see less harmful OS products in healthy patients. A possible reason would be that patients are more concerned about the process and are taking more antioxidant supplements. There are known examples in the literature where vitamin supplements affect the concentration of lipid peroxidation products. Obesity and smoking can also affect the concentration of 8-IP.⁵⁹ A recent meta-analysis showed that the intake of various antioxidant supplements can alter plasma F2-isoprostane concentrations.⁶⁰ However, we do not know what this means for concentrations in follicular fluid. There are only a few studies in which the concentration of FF 8-IP is measured. Malhotra et al. found that the 8-IP concentration is associated with abortion rates and is higher in patients with PCOS. But, unlike us, they took the whole pool of follicle fluid and not just the leading follicle. However, TIF patients were taken as the control group. In these patients, we also have a slightly lower 8-IP concentration, but the difference is not significant.⁶¹ In their pilot study, Lin and colleagues found a lack of correlation between 8-IP levels and age, and further found that similar 8-IP levels between the right and left follicles suggests that oxidative stress affects both ovaries equally.⁶² Pier analyzed the concentration of 8-IP in the follicular fluid using mass spectrometry and reached a similar conclusion, namely, the 8-IP concentration did not significantly increase with the age of the patients. Additionally, he also did not detect an increase in 8-IP concentration associated with PCOS

or endometriosis. They concluded that these findings are at odds with the conventional assumption that 8-IP is a marker for oxidative stress. Instead, they suggested that F2-isoprostanes in FF may have functions unrelated to stress or inflammation.⁶³ To date, we have not found any other researches that would measure 8-IP in follicular fluid. Some studies measured peritoneal fluid and plasma levels of 8-IP *in vivo* in patients with endometriosis. They found that concentrations in both the urine and peritoneal fluid of patients with endometriosis were significantly elevated compared to those of controls.^{64,65} Calzada et al. measured plasma 8-IP concentrations in patients with PCOS. They found that the level of 8-IP in patients was significantly increased. Our results in follicular fluid did not confirm this, as in our case the concentration of 8-IP was significantly increased in the control group. Based on all this information, it is difficult to conclude exactly what our results mean. Perhaps the 8-IP concentration in the follicular fluid from the leading follicle is not similar to that in other body fluids. Our study also shows that the concentration of 8-IP in the leading follicle has a weak effect on the effectiveness of the IVF procedure. It should be emphasized that our results of 8-IP measurements were very scattered in all groups, and some cross-reactivity might have occurred. According to the manufacturer's instructions, some types of sample may contain contaminants that interfere with the analysis. It is also known that several different prostaglandin derivatives are present in the follicular fluid.^{47,66} We estimate that this assay is not good for testing in follicle fluid and therefore no significant conclusions can be drawn from concentrations in this analyze. Due to the lack of clarity and poor research, further studies are needed.

Our measurements of 8-OHdG in the leading follicle show similar concentration in controls and patients with endometriosis. This runs contrary to a study done in Brazil,⁶⁷ where higher follicular concentrations of 8-OHdG were found in the endometriosis group compared to controls. A more recent study of OS in endometriosis patients led to results similar to ours.⁶⁸ The concentration of 8-OHdG was similar in the control group to that of patients with endometriosis. But in both studies, all of the follicular fluid was used, not only from the leading follicle. In discussing the reasons for such a result it is worth mentioning the very interesting information that 8-OHdG also exhibited ROS-suppressing properties in several *in vitro* models, suggesting its possible involvement in the fine tuning of the response to OS.⁶⁹ In fact, there are already several studies that investigate the mechanism where 8-OHdG sometimes show antioxidant or anti-inflammatory-like activity that can be attributed to the Rac1-GTP pathway.^{70–72} We further failed to find a difference in the concentration of 8-OHdG between the TIF and control groups, which is consistent with extant findings.⁵⁷ In patients with PCOS, the concentration of 8-OHdG in leading follicular fluid is significantly lower. Our result is consistent with other

studies, where authors have claimed that decreased serum levels of 8-OHdG can reflect an enfeebled repair of oxidative DNA damage or enhanced antioxidant defense rather than low ROS production in PCOS tissue. High ROS levels are well known to promote the expression of antioxidant enzymes.⁷³ Therefore, overexpression of these antioxidants may lead to suppression of the extent of oxidative stress and consequently to the prevention of ROS interactions with DNA, thereby diminishing 8-OHdG formation. Several studies have reported that major antioxidant enzymes are significantly induced in subjects with PCOS compared to healthy subjects.^{74,75} Metformin therapies have also been shown to have the effect of lowering 8-OHdG levels in the serum of patients with PCOS, which also might be a reason for our results in follicular fluid. Metformin is a drug commonly used in the treatment of insulin resistance, which is very common in obese patients with PCOS, so a correlation is possible but as yet unverified.⁷⁶ It would certainly be necessary to investigate further and determine in more detail the causes of such results. To begin with, the activity of the DNA glycosylase-repairing enzymes in FF should be checked.

The results of our antioxidant status measurements show statistically significant higher TAS concentrations in the FF of healthy women compared to individual patients group (PCOS, endometriosis and also TIF). Our results are in perfect agreement with the rest of the literature. Some also found a positive association between FF TAS and clinical pregnancy rates.^{77,78}

A very interesting and maybe most important finding that our research showed was that the concentration of 8-OHdG in PCOS group in the particular follicle showed a strong association with a mature and with a fertilized oocyte. As far as we know, to date, no one has tried to relate the concentration of 8-OHdG to the outcome of the IVF procedure in patients with PCOS. We have found that 8-OHdG, measured in a particular follicular fluid, can very well predict the acquisition of a mature egg and the successful fertilization of that egg. Anyway, our study alone is not enough and this link must be checked further on a larger sample. But if these results hold, the FF 8-OHdG could be a useful predictive marker for the individual oocyte in the artificial insemination procedure in PCOS patients.

6. Conclusion

OS plays a role in several physiological processes, from oocyte maturation to fertilization and embryo development. There is burgeoning literature on the involvement of OS in the pathophysiology of infertility, assisted fertility, and female reproduction. What we do know is that the role of OS in female reproduction cannot be underestimated. Our study revealed a few significant differences in the concentrations of individual markers of oxidative stress

and AMH between groups with different diagnoses. But the most interesting finding, one that is definitely worth exploring further, is the strong relationship between the concentration of 8-OHdG in follicular fluid and the obtaining of a useful mature cell from this follicle in PCOS patients, as well as the successful fertilization in the end of IVF procedure.

Acknowledgments

The authors would like to thank all the women in IVF programs who agreed to participate in the study, and to Vera Troha who processed samples in lab.

Research funding: This study was financed by the Ministry of Science and Education through the Young Researchers program. The funding organizations played no role in the study design, in the collection, analysis, and interpretation of data, in the writing of the report, or in the decision to submit the report for publication. Ethical approval for this study was obtained from the Republic of Slovenia's National Medical Ethics Committee (108/02/13).

7. References

1. J. Datta, M. J. Palmer, C. Tanton, L. J. Gibson, K. G. Jones, W. Macdowall, A. Glasier, P. Sonnenberg, N. Field, C. H. Mercer, et al., *Hum. Reprod.* **2016**, *31*, 2108–18. DOI:10.1093/humrep/dew123
2. S. Gupta, G. Ahmad, M. Tran, G. Al Hayaza, Z. Kayali, in: A. Agarwal (Ed.), R. Sharma, S. Gupta, A. Harlev, G. Ahmad, S. S. du Plessis, S. C. Esteves, S. M. Wang: Oxidative stress in Human Reproduction, Springer Nature, Cham, Switzerland, **2017**, pp. 107–128
3. S. Reuter, S. C. Gupta, M. M. Chaturvedi, B. B. Aggarwal, *Free Radic. Biol. Med.* **2010**, *49*, 1603–16. DOI:10.1016/j.freeradbiomed.2010.09.006
4. R. De Bont, N. van Larebeke, *Mutagenesis* **2004**, *19*, 169–85. DOI:10.1093/mutage/geh025
5. G. Scutiero, P. Iannone, G. Bernardi, G. Bonaccorsi, S. Spadaro, C. A. Volta, P. Greco, L. Nappi, *Oxid. Med. Cell. Longev.* **2017**, *2017*, 1–7. DOI:10.1155/2017/7265238
6. I. Dalle-Donne, R. Rossi, R. Colombo, D. Giustarini, A. Milzani, *Clin. Chem.* **2006**, *52*, 601–23. DOI:10.1373/clinchem.2005.061408
7. A. Agarwal, A. Aponte-Mellado, B. J. Premkumar, A. Shaman, S. Gupta, *Reprod. Biol. Endocrinol.* **2012**, *10*, 49. DOI:10.1186/1477-7827-10-49
8. D. R. Meldrum, K. M. Silverberg, M. Bustillo, L. Stokes, *Fertil. Steril.* **1998**, *69*, 1005–1009. DOI:10.1016/S0015-0282(98)00083-1
9. J. J. Wade, V. MacLachlan, G. Kovacs, *Aust. New Zeal. J. Obstet. Gynaecol.* **2015**, *55*, 473–476. DOI:10.1111/ajo.12356
10. R. Nuñez-Calonge, S. Cortés, L. M. Gutierrez Gonzalez, R. Kireev, E. Vara, L. Ortega, P. Caballero, L. Rancan, J. Tres-

- guerres, *Reprod. Biomed. Online* **2016**, *32*, 446–456.
DOI:10.1016/j.rbmo.2015.12.010
11. P. J. Devine, S. D. Perreault, U. Luderer, *Biol. Reprod.* **2012**, *86*, 27. DOI:10.1095/biolreprod.111.095224
 12. A. Agarwal, S. Gupta, R. Sharma, *Reprod. Biomed. Online* **2005**, *11*, 641–50. DOI:10.1016/S1472-6483(10)61174-1
 13. O. Oyawoye, A. Abdel Gadir, A. Garner, N. Constantinovici, C. Perrett, P. Hardiman, *Hum. Reprod.* **2003**, *18*, 2270–4.
 14. M. Becatti, R. Fucci, A. Mannucci, V. Barygina, M. Mugnaini, L. Criscuoli, C. Giachini, F. Bertocci, R. Picone, G. Emmi, et al., *Int. J. Mol. Sci.* **2018**, *19*. DOI:10.3390/ijms19020592
 15. A. Agarwal, A. Aponte-Mellado, B. J. Premkumar, A. Shaman, S. Gupta, *Reprod. Biol. Endocrinol.* **2012**, *10*, 49. DOI:10.1186/1477-7827-10-49
 16. S. Cupisti, R. Dittrich, A. Mueller, R. Strick, E. Stiegler, H. Binder, M. W. Beckmann, P. Strissel, *Eur. J. Med. Res.* **2007**, *12*, 604–8.
 17. C. Takahashi, A. Fujito, M. Kazuka, R. Sugiyama, H. Ito, K. Isaka, *Fertil. Steril.* **2008**, *89*, 586–591. DOI:10.1016/j.fertnstert.2007.03.080
 18. R. Mashiach, A. Amit, J. Hasson, S. Amzalag, B. Almog, D. Ben-Yosef, J. B. Lessing, R. Limor, F. Azem, *Fertil. Steril.* **2010**, *93*, 2299–2302. DOI:10.1016/j.fertnstert.2009.01.125
 19. R. Fanchin, D. H. Mendez Lozano, N. Frydman, A. Gougeon, N. di Clemente, R. Frydman, J. Taieb, *J. Clin. Endocrinol. Metab.* **2007**, *92*, 1796–1802. DOI:10.1210/jc.2006-1053
 20. J. H. Kim, J. R. Lee, H. J. Chang, B. C. Jee, C. S. Suh, S. H. Kim, *J. Korean Med. Sci.* **2014**, *29*, 1266. DOI:10.3346/jkms.2014.29.9.1266
 21. S. Arabzadeh, G. Hossein, B. H. Rashidi, M. A. Hosseini, H. Zeraati, *Ann. Saudi Med.* **2010**, *30*, 442–447. DOI:10.4103/0256-4947.71063
 22. Rotterdam ESHRE/ASRM-Sponsored PCOS Consensus Workshop Group, *Fertil. Steril.* **2004**, *81*, 19–25.
 23. S. Wolczyński, W. Zgliczyński, in: Large Interna – Endocrinology, Medical Tribune Poland, Warsaw, **2012**, pp. 561–567. DOI:10.17219/acem/59380
 24. S. Bednarska, A. Siejka, *Adv. Clin. Exp. Med.* **2017**, *26*, 359–367.
 25. A. Augoulea, A. Alexandrou, M. Creatsa, N. Vrachnis, I. Lambrinouadaki, *Arch. Gynecol. Obstet.* **2012**, *286*, 99–103. DOI:10.1007/s00404-012-2357-8
 26. N. Singh, K. Lata, M. Naha, N. Malhotra, A. Tiwari, P. Vanamail, *J. Hum. Reprod. Sci.* **2014**, *7*, 143–7. DOI:10.4103/0974-1208.138874
 27. G. Christodoulakos, A. Augoulea, I. Lambrinouadaki, V. Sioulas, G. Creatsas, *Eur. J. Contracept. Reprod. Heal. Care* **2007**, *12*, 194–202. DOI:10.1080/13625180701387266
 28. A. Augoulea, G. Mastorakos, I. Lambrinouadaki, G. Christodoulakos, G. Creatsas, *Gynecol. Endocrinol.* **2009**, *25*, 75–81. DOI:10.1080/09513590802485012
 29. G. Scutiero, P. Iannone, G. Bernardi, G. Bonaccorsi, S. Spadaro, C. A. Volta, P. Greco, L. Nappi, *Oxid. Med. Cell. Longev.* **2017**, *2017*, 1–7. DOI:10.1155/2017/7265238
 30. A. Mulgund, S. Doshi, A. Agarwal, in: Handbook of Fertility, Elsevier, Amsterdam, **2015**, pp. 273–281. DOI:10.1016/B978-0-12-800872-0.00025-1
 31. Yavuz, N. E. Aydin, O. Celik, E. Yilmaz, E. Ozerol, K. Tanbek, *J. Cancer Res. Ther.* **2014**, *10*, 324. DOI:10.4103/0973-1482.136619
 32. M. G. Hull, C. M. Glazener, N. J. Kelly, D. I. Conway, P. A. Foster, R. A. Hinton, C. Coulson, P. A. Lambert, E. M. Watt, K. M. Desai, *Br. Med. J. (Clin. Res. Ed.)*. **1985**, *291*, 1693–7. DOI:10.1136/bmj.291.6510.1693
 33. G. D. Adamson, V. L. Baker, *Best Pract. Res. Clin. Obstet. Gynaecol.* **2003**, *17*, 169–185. DOI:10.1016/S1521-6934(02)00146-3
 34. E. W. Freeman, M. D. Sammel, H. Lin, C. R. Gracia, *J. Clin. Endocrinol. Metab.* **2012**, *97*, 1673–1680. DOI:10.1210/jc.2011-3032
 35. B. Abu-Fakher, F. Al-Quobaili, M. Alhalabi, *Middle East Fertil. Soc. J.* **2013**, *18*, 110–114. DOI:10.1016/j.mefs.2012.12.005
 36. B. Wiweko, U. Anggraheni, E. Mansyur, T. Yuningsih, A. K. Harzief, G. Pratama, K. Sumapraja, M. Natadisastra, A. Hestiantoro, *Asian Pacific J. Reprod.* **2016**, *5*, 361–364. DOI:10.1016/j.apjr.2016.07.011
 37. R. Fanchin, J. Taieb, D. H. M. Lozano, B. Ducot, R. Frydman, J. Bouyer, *Hum. Reprod. Oxford Engl.* **2005**, *20*, 923–927. DOI:10.1093/humrep/deh688
 38. B. Piłacik, T. W. Nofer, W. Wąsowicz, *Int. J. Occup. Med. Environ. Health* **2002**, *15*, 19–27.
 39. M. Janicka, A. Kot-Wasik, J. Kot, J. Namieśnik, *Int. J. Mol. Sci.* **2010**, *11*, 4631–59. DOI:10.3390/ijms11114631
 40. M. Comporti, C. Signorini, B. Arezzini, D. Vecchio, B. Monaco, C. Gardi, *Mol. Aspects Med.* **2008**, *29*, 43–49. DOI:10.1016/j.mam.2007.09.011
 41. M. Comporti, C. Signorini, B. Arezzini, D. Vecchio, B. Monaco, C. Gardi, *Free Radic. Biol. Med.* **2008**, *44*, 247–56. DOI:10.1016/j.freeradbiomed.2007.10.004
 42. P. Montuschi, P. J. Barnes, L. J. Roberts, *FASEB J.* **2004**, *18*, 1791–800. DOI:10.1096/fj.04-2330rev
 43. Y. Guo, J. Weck, R. Sundaram, A. E. Goldstone, G. Buck Louis, K. Kannan, *Environ. Sci. Technol.* **2014**, *48*, 9804–9811. DOI:10.1021/es5024898
 44. A. C. Pereira, F. Martel, *Cell Biol. Toxicol.* **2014**, *30*, 301–312. DOI:10.1007/s10565-014-9285-2
 45. O. Erel, *Clin. Biochem.* **2005**, *38*, 1103–1111. DOI:10.1016/j.clinbiochem.2005.08.008
 46. I. Marrocco, F. Altieri, I. Peluso, *Oxid. Med. Cell. Longev.* **2017**, *2017*, 6501046. DOI:10.1155/2017/6501046
 47. Cayman Chemical, 8-Isoprostane ELISA Kit, <https://www.caymanchem.com/product/516351>, (assessed: March 20, 2019).
 48. Japan Institute for the Control of Aging (JaICA), Highly Sensitive 8-OHdG Check ELISA kit, http://www.jaica.com/e/products_dna_8ohdg_kit_hs.html, (assessed: March 20, 2019).
 49. Ansh Labs, AMH(pico) ELISA kit, <https://www.anshlabs.com/product/picoamh-elisa/>, (assessed: March 21, 2019)
 50. Randox Laboratories, Total Antioxidant Status reagent,

- <https://www.randox.com/total-antioxidant-status/>, (assessed: March 20, 2019)
51. E. Ozturk, T. Oge, Y. Aydin, O. Isiklar, H. Hassa, **2018**, *49*, 136–139.
 52. Á. Várnagy, T. Kőszegi, E. Györgyi, S. Szegedi, E. Sulyok, V. Prémusz, J. Bódis, *Hum. Fertil.* **2018**, 1–9. DOI:10.1080/14647273.2018.1535719
 53. M. Becatti, R. Fucci, A. Mannucci, V. Barygina, M. Mugnaini, L. Criscuoli, C. Giachini, F. Bertocci, R. Picone, G. Emmi, et al., *Int. J. Mol. Sci.* **2018**, *19*, 592. DOI:10.3390/ijms19020592
 54. J. A. Garcia-Velasco, L. Motta, S. Rodriguez, M. Toribio, J. Martinez-Salazar, A. Pacheco, *J. Endometr.* **2009**, *1*, 52–56. DOI:10.1177/228402650900100108
 55. X. Y. Liu, Y. J. Yang, C. L. Tang, K. Wang, J. J. Chen, X. M. Teng, Y. C. Ruan, J. Z. Yang, *Fertil. Steril.* **2019**, *111*, 157–167. DOI:10.1016/j.fertnstert.2018.09.022
 56. J. V. Jeppesen, R. A. Anderson, T. W. Kelsey, S. L. Christiansen, S. G. Kristensen, K. Jayaprakasan, N. Raine-Fenning, B. K. Campbell, C. Yding Andersen, *Mol. Hum. Reprod.* **2013**, *19*, 519–527. DOI:10.1093/molehr/gat024
 57. C. S. Campos, D. Vaamonde, C. Andreoli, A. C. Martins, V. K. Genro, C. A. Souza, R. Chapon, J. S. L. Cunha-Filho, *Reprod. Biomed. Online* **2010**, *21*, 470–473. DOI:10.1016/j.rbmo.2010.05.007
 58. R. Kucera, V. Babuska, Z. Ulcova-Gallova, V. Kulda, O. Topolcan, *Syst. Biol. Reprod. Med.* **2018**, *64*, 220–223. DOI:10.1080/19396368.2018.1450906
 59. G. Block, C. D. Jensen, J. D. Morrow, N. Holland, E. P. Nor-kus, G. L. Milne, M. Hudes, T. B. Dalvi, P. B. Crawford, E. B. Fung, et al., *Free Radic. Biol. Med.* **2008**, *45*, 377–84. DOI:10.1016/j.freeradbiomed.2008.04.005
 60. T. J. van 't Erve, *Redox Biol.* **2018**, *17*, 284–296. DOI:10.1016/j.redox.2018.05.003
 61. N. Malhotra, K. Gongadashetti, R. Dada, N. Singh, *Fertil. Steril.* **2014**, *102*, 86. DOI:10.1016/j.fertnstert.2014.07.291
 62. K. Lin, K. Barnhart, A. Shaunik, S. Butts, G. A. Fitzgerald, C. Coutifaris, *Fertil. Steril.* **2005**, *84*, 47. DOI:10.1016/j.fertnstert.2005.07.112
 63. B. Pier, J. W. Edmonds, L. Wilson, A. Arabshahi, R. Moore, G. W. Bates, J. K. Prasain, M. A. Miller, *Prostaglandins Other Lipid Mediat.* **2018**, *134*, 7–15. DOI:10.1016/j.prostaglandins.2017.11.001
 64. I. Sharma, L. K. Dhaliwal, S. C. Saha, S. Sangwan, V. Dhawan, *Fertil. Steril.* **2010**, *94*, 63–70. DOI:10.1016/j.fertnstert.2009.01.141
 65. G. Polak, I. Wertel, B. Barczyński, W. Kwaśniewski, W. Bednarek, J. Kotarski, *Eur. J. Obstet. Gynecol. Reprod. Biol.* **2013**, *168*, 187–190. DOI:10.1016/j.ejogrb.2012.12.043
 66. B. Pier, J. W. Edmonds, L. Wilson, A. Arabshahi, R. Moore, G. W. Bates, J. K. Prasain, M. A. Miller, *Prostaglandins Other Lipid Mediat.* **2018**, *134*, 7–15. DOI:10.1016/j.prostaglandins.2017.11.001
 67. M. G. Da Broi, F. O. de Albuquerque, A. Z. de Andrade, R. L. Cardoso, A. A. Jordão Junior, P. A. Navarro, *Cell Tissue Res.* **2016**, *366*, 231–242. DOI:10.1007/s00441-016-2428-4
 68. Á. Várnagy, T. Kőszegi, E. Györgyi, S. Szegedi, E. Sulyok, V. Prémusz, J. Bódis, *Hum. Fertil.* **2018**, 1–9. DOI:10.1080/14647273.2018.1535719
 69. C. Y. Ock, K. S. Hong, K.-S. Choi, M.-H. Chung, Y. Kim, J. H. Kim, K.-B. Hahm, *Biochem. Pharmacol.* **2011**, *81*, 111–122. DOI:10.1016/j.bcp.2010.08.023
 70. J. Y. Huh, D. J. Son, Y. Lee, J. Lee, B. Kim, H. M. Lee, H. Jo, S. Choi, H. Ha, M. H. Chung, *Free Radic. Biol. Med.* **2012**, *53*, 109–121. DOI:10.1016/j.freeradbiomed.2012.03.023
 71. D. H. Kim, I. H. Cho, H. S. Kim, J. E. Jung, J. E. Kim, K. H. Lee, T. Park, Y. M. Yang, S. Y. Seong, S. K. Ye, M. H. Chung, *J. Chinese Med. Assoc.* **2006**, *38*, 417. DOI:10.1038/emm.2006.49
 72. H. S. Kim, S. K. Ye, I. H. Cho, J. E. Jung, D. H. Kim, S. Choi, Y. S. Kim, C. G. Park, T. Y. Kim, J. W. Lee, M. H. Chung, *Free Radic. Biol. Med.* **2006**, *41*, 1392. DOI:10.1016/j.freeradbiomed.2006.07.018
 73. H. Sova, L. Morin-Papunen, U. Puistola, P. Karihtala, *Fertil. Steril.* **2010**, *94*, 2670–3. DOI:10.1016/j.fertnstert.2010.03.049
 74. W. Atiomo, S. Khalid, S. Parameshwaran, M. Houda, R. Layfield, *BJOG An Int. J. Obstet. Gynaecol.* **2009**, *116*, 137–143. DOI:10.1111/j.1471-0528.2008.02041.x
 75. N. K. Kuşçu, A. Var, *Acta Obstet. Gynecol. Scand.* **2009**, *88*, 612–617. DOI:10.1080/00016340902859315
 76. H. Sova, U. Puistola, L. Morin-Papunen, P. Karihtala, *Fertil. Steril.* **2013**, *99*, 593–598. DOI:10.1016/j.fertnstert.2012.10.013
 77. A. K. Singh, R. Chattopadhyay, B. Chakravarty, K. Chaudhury, *Reprod. Toxicol.* **2013**, *42*, 116–124. DOI:10.1016/j.reprotox.2013.08.005
 78. N. Yilmaz, H. A. Inal, U. Gorkem, A. Sargin Oruc, S. Yilmaz, A. Turkkani, *J. Obstet. Gynaecol. (Lahore)*. **2016**, *36*, 654–657. DOI:10.3109/01443615.2016.1148683

Povzetek

Oksidativni stres v folikularni tekočini (FF) naj bi bil odgovoren za nenormalen razvoj oocitov. V našo raziskavo so bile prospektivno vključene pacientke s sindromom policističnih jajčnikov (PCOS), endometriozo in tubarnim dejavnikom neplodnosti (TIF) ter zdrave ženske z dejavnikom moške neplodnosti. Od vsake bolnice je bil odvzet vzorec FF iz dominantnega folikla. Določene so bile koncentracije TAS, 8-IP, 8-OHdG in AMH.

Pri ženskah s PCOS smo ugotovili bistveno nižje vrednosti označevalcev oksidativnega stresa v FF. Stopnje 8-IP in TAS so bile v FF žensk z endometriozo nižje. Pri ženskah s TIF smo ugotovili tudi bistveno nižje vrednosti vseh testiranih označevalcev v FF, razen za 8-OHdG in AMH. Želeli smo videti, ali lahko označevalec, izmerjen v FF pri posamezni diagnozi, napoveduje uspešnost pridobitve zarodka iz tega folikla. Rezultat 8-OHdG v FF pri pacientkah s PCOS je izstopal in se je izkazal za dober napovedni označevalec dozorelih in oplojenih oocitov pri teh pacientkah. Potrebne so nadaljnje raziskave, da bi lahko pridobljeno znanje uporabili za izboljšanje rezultatov postopkov IVF.



Except when otherwise noted, articles in this journal are published under the terms and conditions of the Creative Commons Attribution 4.0 International License

Scientific paper

Syntheses, Crystal Structures and Catalytic Property of Oxidovanadium(V) Complexes Derived from Tridentate Hydrazone Ligands

Ya-Jun Cai,^{1,2} Yuan-Yuan Wu,^{1,2} Fei Pan,^{1,2} Qi-An Peng^{1,2}
and Yong-Ming Cui^{3,*}

¹ School of Environmental Engineering, Wuhan Textile University, Wuhan 430073, P. R. China

² Engineering Research Center for Clean Production of Textile Printing, Ministry of Education, Wuhan 430073, P. R. China

³ National Local Joint Engineering Laboratory for Advanced Textile Processing and Clean Production, Wuhan Textile University, Wuhan 430073, P. R. China

* Corresponding author: E-mail: fcym981248@sohu.com

Received: 02-08-2020

Abstract

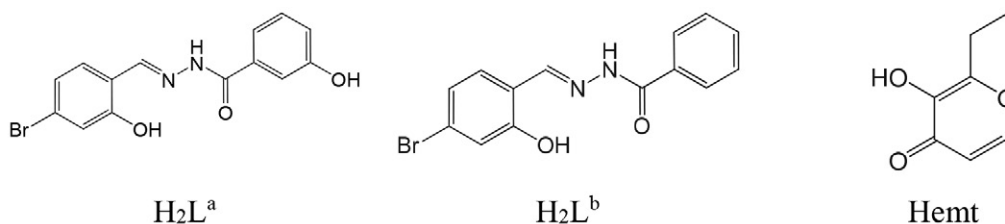
Two new ethyl maltolato coordinated mononuclear oxidovanadium(V) complexes [VOL^a(emt)]·DMF (1) and [VOL^b(emt)] (2), where H₂L^a = N²-(4-bromo-2-hydroxybenzylidene)-3-hydroxybenzohydrazide, H₂L^b = N²-(4-bromo-2-hydroxybenzylidene)benzohydrazide, Hemt = ethyl maltol, have been synthesized and characterized on the basis of CHN elemental analysis, FT-IR and UV-Vis spectroscopy and powder XRD analysis. Structures of the complexes were further characterized by single crystal X-ray diffraction, which indicated that the V atoms in the complexes adopt octahedral coordination. The hydrazones behave as NOO tridentate ligands. The catalytic epoxidation properties on cyclooctene of the complexes were investigated.

Keywords: Hydrazone; oxidovanadium complex; crystal structure; catalytic epoxidation

1. Introduction

Schiff bases are interesting ligands in the formation of versatile complexes with various metal ions.¹ The complexes with Schiff base ligands have received particular attention for their facile synthesis and remarkable biological, catalytic and magnetic applications.² Catalytic epoxidation of olefins is an important type of reactions in industrial chemistry. A number of complexes with transition metal

ions are active catalysts for this process.³ In particular, among the complexes, vanadium and molybdenum complexes seem more interesting because of their excellent catalytic ability in the oxidation of olefins and sulfides.⁴ Vanadium complexes with hydrazones are reported to possess catalytic properties. In order to study the influence of the substituent groups of the hydrazones on the catalytic property of the vanadium complexes, in this paper, two new oxidovanadium(V) complexes, [VOL^a(emt)]·DMF



Scheme 1. The hydrazones and Hemt.

(1) and [VOL^b(emt)] (2), where H₂L^a = *N*'-(4-bromo-2-hydroxybenzylidene)-3-hydroxybenzohydrazide, H₂L^b = *N*'-(4-bromo-2-hydroxybenzylidene)benzohydrazide, Hemt = ethyl maltol (Scheme 1), are presented.

2. Experimental

2.1. Materials and Methods

3-Hydroxybenzohydrazide, benzohydrazide, 4-bromosalicylaldehyde, ethyl maltol and VO(acac)₂ were purchased from Alfa Aesar and used as received. Reagent grade solvents were used as received. Microanalyses of the complexes were performed with a Vario EL III CHNOS elemental analyzer. Infrared spectra were recorded as KBr pellets with an FTS-40 spectrophotometer. Electronic spectra were recorded on a Lambda 900 spectrometer. The powder XRD spectra were recorded in a 2θ range of 2–50° using a Bruker D8 Advance detector under ambient conditions. The catalytic reactions were followed by gas chromatography on an Agilent 6890A chromatograph equipped with an FID detector and a DB5-MS capillary column (30 m × 0.32 mm, 0.25 μm). Molar conductance measurements were made by means of a Metrohm 712 conductometer in acetonitrile.

2.2. Synthesis of the Complex [VOL^a(emt)]·DMF

3-Hydroxybenzohydrazide (10 mmol, 1.52 g) and 4-bromosalicylaldehyde (10 mmol, 2.01 g) were refluxed in methanol (50 mL). Then, VO(acac)₂ (10 mmol, 2.63 g) and ethyl maltol (10 mmol, 1.40 g) dissolved in methanol (30 mL) were added to the mixture and refluxed for 1 h in oil bath to give a deep brown solution with some insoluble substance. Then, a few drops of DMF were added until the insoluble substance dissolved. Single crystals of the complex were formed during slow evaporation of the reaction mixture in air. The crystals were isolated by filtration, washed with cold methanol and dried over anhydrous CaCl₂. Yield: 0.38 g (61%). IR data (KBr pellet, cm⁻¹): 1667 ν(C=O), 1592 ν(C=N), 1524, 1455, 1408, 1353, 1250 ν(C–O_{phenolate}), 1188 ν(N–N), 1107, 1066, 1030, 973 ν(V=O), 926, 850, 796, 727, 630, 522, 468. UV-Vis data in methanol (nm): 210, 269, 320, 398. Molar conductance (10⁻³ mol L⁻¹, methanol): 25 Ω⁻¹ cm² mol⁻¹. Analysis: Found: C 46.89, H 3.85, N 6.77%. Calculated for C₂₄H₂₃BrN₃O₈V: C 47.08, H 3.79, N 6.86%.

2.3. Synthesis of the Complex [VOL^b(emt)]

Benzohydrazide (10 mmol, 1.36 g) and 4-bromosalicylaldehyde (10 mmol, 2.01 g) were refluxed in methanol (50 mL). Then, VO(acac)₂ (10 mmol, 2.63 g) and ethyl maltol (10 mmol, 1.40 g) dissolved in methanol (30 mL) were added to the mixture and refluxed for 1 h in oil bath

to give a deep brown solution. Single crystals of the complex were formed during slow evaporation of the reaction mixture in air. The crystals were isolated by filtration, washed with cold methanol and dried over anhydrous CaCl₂. Yield: 0.21 g (40%). IR data (KBr pellet, cm⁻¹): 1595 ν(C=N), 1529, 1458, 1407, 1338, 1252 ν(C–O_{phenolate}), 1196 ν(N–N), 1131, 1070, 973 ν(V=O), 919, 835, 786, 695, 639, 598, 515, 466. UV-Vis data in methanol (nm): 210, 267, 322, 396. Molar conductance (10⁻³ mol L⁻¹, methanol): 33 Ω⁻¹ cm² mol⁻¹. Analysis: Found: C 48.37, H 3.16, N 5.22%. Calculated for C₂₁H₁₆BrN₂O₆V: C 48.21, H 3.08, N 5.35%.

2.4. Crystal Structure Determination

Data were collected on a Bruker SMART 1000 CCD area diffractometer using a graphite monochromator Mo Kα radiation (λ = 0.71073 Å) at 298(2) K. The data were corrected with SADABS programs and refined on F² with Siemens SHELXL software.⁵ The structures of the complexes were solved by direct methods and difference Fourier syntheses. All non-hydrogen atoms were refined anisotropically. The hydrogen atoms were placed in calculated positions and included in the last cycles of refinement. Crystal data and details of the data collection and refinement are listed in Table 1. Selected coordinate bond lengths and angles are listed in Table 2.

Table 1. Crystallographic data for the complexes

Parameters	1	2
Empirical formula	C ₂₄ H ₂₃ BrN ₃ O ₈ V	C ₂₁ H ₁₆ BrN ₂ O ₆ V
Formula weight	612.30	523.21
Crystal system	Triclinic	Monoclinic
Space group	<i>P</i> -1	<i>P</i> 2 ₁ / <i>n</i>
<i>a</i> [Å]	10.0508(11)	12.2708(11)
<i>b</i> [Å]	11.6192(12)	7.4066(7)
<i>c</i> [Å]	12.8769(12)	22.6657(12)
α [°]	63.7350(10)	90
β [°]	68.8460(10)	94.5300(10)
γ [°]	86.6150(10)	90
<i>V</i> [Å ³]	1248.5(2)	2053.5(3)
<i>Z</i>	2	4
ρ _{calcd.} [g cm ⁻³]	1.629	1.692
μ [mm ⁻¹]	2.052	2.471
<i>F</i> (000)	620	1048
Measured reflections	27647	11744
Independent reflections	4646	3809
Observed reflections (<i>I</i> > 2σ(<i>I</i>))	3541	2765
Parameters	338	281
Restraints	0	0
Final R indices [<i>I</i> > 2σ(<i>I</i>)]	0.0491, 0.1387	0.0385, 0.0914
R indices (all data)	0.0674, 0.1518	0.0632, 0.1020
Goodness-of-fit on F ²	1.037	1.030
Largest difference in peak and hole (e Å ⁻³)	0.941, -0.696	0.542, -0.482

Table 2. Selected bond lengths (Å) and angles (°) for the complexes

1			
V1–O1	1.843(3)	V1–O2	1.918(3)
V1–O4	1.585(3)	V1–O5	2.263(3)
V1–O6	1.862(2)	V1–N1	2.094(3)
O4–V1–O1	100.49(16)	O4–V1–O6	100.18(12)
O1–V1–O6	95.62(11)	O4–V1–O2	94.89(14)
O1–V1–O2	155.78(12)	O6–V1–O2	99.96(11)
O4–V1–N1	101.11(12)	O1–V1–N1	83.47(12)
O6–V1–N1	158.50(11)	O2–V1–N1	75.24(11)
O4–V1–O5	174.17(14)	O1–V1–O5	85.16(13)
O6–V1–O5	77.68(10)	O2–V1–O5	80.23(11)
N1–V1–O5	80.84(10)		
2			
V1–O1	1.849(2)	V1–O2	1.922(2)
V1–O3	1.588(2)	V1–O4	1.872(2)
V1–O5	2.255(2)	V1–N1	2.083(2)
O3–V1–O1	99.32(12)	O3–V1–O4	98.75(11)
O1–V1–O4	102.31(9)	O3–V1–O2	99.79(11)
O1–V1–O2	153.12(10)	O4–V1–O2	93.26(9)
O3–V1–N1	98.47(11)	O1–V1–N1	83.71(9)
O4–V1–N1	160.56(10)	O2–V1–N1	74.93(9)
O3–V1–O5	176.08(11)	O1–V1–O5	83.49(10)
O4–V1–O5	77.91(9)	O2–V1–O5	78.47(9)
N1–V1–O5	84.52(9)		

2. 5. Catalytic Epoxidation Process

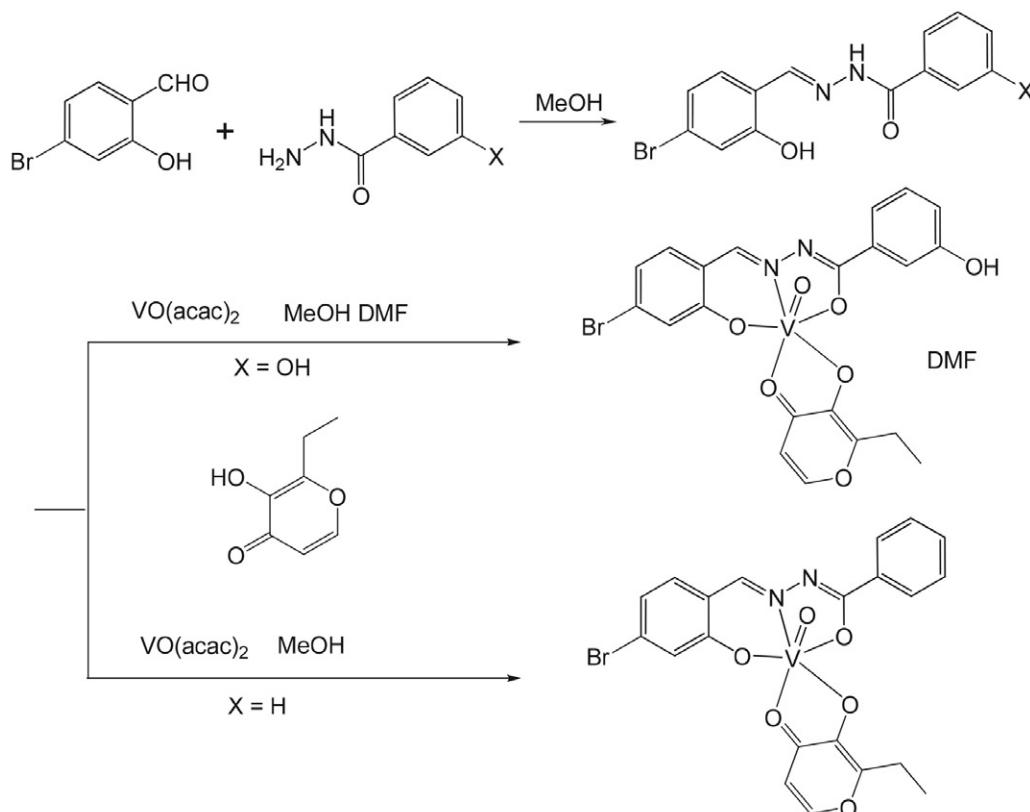
A mixture of cyclooctene (2.76 mL, 20 mmol), acetophenone (internal reference) and the complex as the catalyst (0.05 mmol) was stirred and heated up to 80 °C before addition of aqueous *tert*-butyl hydroperoxide (TBHP; 70% w/w, 5.48 mL, 40 mmol). The mixture is initially an emulsion, but two phases become clearly visible as the reaction progresses, a colorless aqueous one and a yellowish organic one. The reaction was monitored for 5 h with withdrawal and analysis of organic phase aliquots (0.1 mL) at required times. Each withdrawn sample was mixed with 2 mL of diethylether, treated with a small quantity of MnO₂ and then filtered through silica and analyzed by GC.

3. Results and Discussion

3. 1. Synthesis

The hydrazone compounds and the complexes were synthesized in a facile and analogous way (Scheme 2).

The hydrazones H₂L^a and H₂L^b act as tridentate dianionic NOO donor ligands toward the VO³⁺ cores. The two complexes were obtained from refluxing mixtures of the hydrazones with VO(acac)₂ in 1:1 molar proportion in the presence of ethyl maltol in methanol. Complex **1** is not soluble well in methanol, so DMF was added to improve the solubility. The complexes were isolated as single crystals from

**Scheme 2.** The syntheses of the hydrazones and the complexes

the reaction mixtures by slow evaporation at room temperature. Crystals of the complexes are stable at room temperature. The low molar solution conductance of the complexes in methanol indicates their non-electrolyte behavior.

Theoretical diffractograms were calculated using the PowderCell program.⁶ The experimental X-ray powder diffraction patterns of the bulk samples of the complexes agree well with the simulated patterns calculated from single crystal X-ray diffraction (Figures 1 and 2). The results prove the purity of the bulk samples.

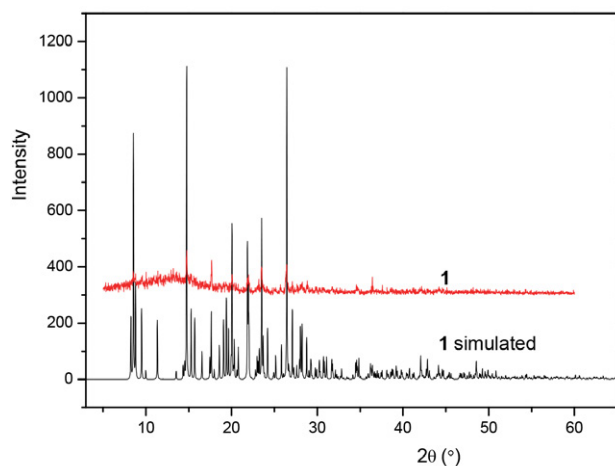


Figure 1. Experimental and simulated powder XRD patterns of complex 1.

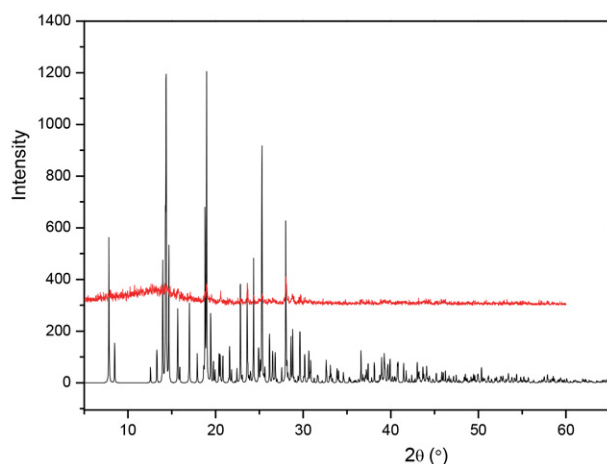


Figure 2. Experimental and simulated powder XRD patterns of complex 2.

3. 2. IR and Electronic Spectra

The IR spectra of the hydrazones show bands centered at about 3215 cm^{-1} for $\nu(\text{N-H})$, 3537 cm^{-1} for $\nu(\text{O-H})$, and 1655 cm^{-1} for $\nu(\text{C=O})$.⁷ The peaks attributed to $\nu(\text{N-H})$ and $\nu(\text{C=O})$ are absent in the spectra of the complexes as the ligands bind in dianionic form resulting

in losing proton from carbohydrazide group. An intense band at 1667 cm^{-1} for complex 1 ascribes to the C=O band of DMF molecule. Strong bands observed at 1592 and 1595 cm^{-1} for the vanadium complexes are attributed to $\nu(\text{C=N})$, which are located at lower frequencies as compared to the free hydrazones.⁸ The complexes exhibit characteristic bands at 973 cm^{-1} for the stretching of V=O bonds.⁹ Based on the IR absorption, it is obvious that the hydrazone ligands exist in the uncoordinated form in *ke-to*-amino tautomer form and in the complexes in imino-enol tautomeric form. This is not uncommon in the coordination of the hydrazone compounds.¹⁰ The absorptions at about 1525 and 1460 cm^{-1} are assigned to the $\nu(\text{C=O})$ and $\nu(\text{C=C})$ of the maltolate groups.¹¹

The UV-Vis spectra of the hydrazones and the complexes recorded in methanol are shown in Figures 3 and 4, respectively. The absorptions at about 300 nm for the hydrazones are assigned to the $n-\pi^*$ transitions. The strong absorption bands centered at about 400 nm for the complexes are assigned as charge transfer transitions of $\text{N}(p\pi)-\text{V}(d\pi)$ LMCT. The medium absorption bands centered at about 320 nm for the complexes are assigned as charge transfer transitions of $\text{O}(p\pi)-\text{V}(d\pi)$ LMCT.¹²

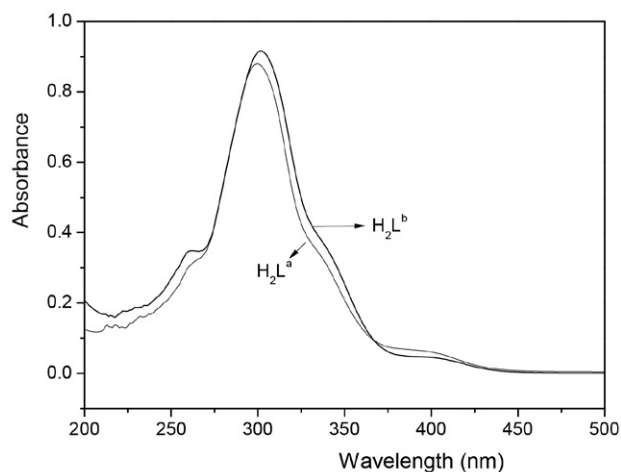


Figure 3. The UV-Vis spectra of H_2L^a and H_2L^b .

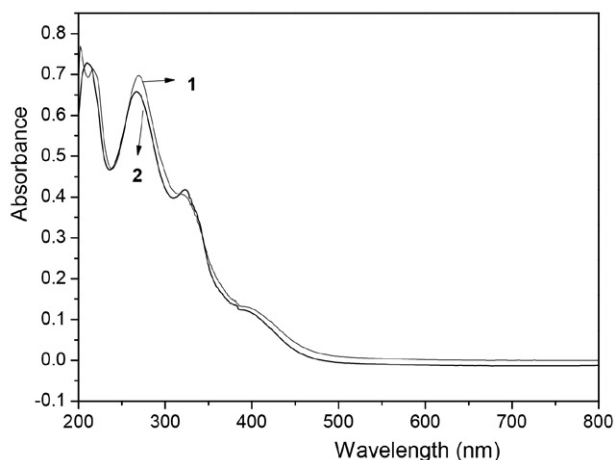


Figure 4. The UV-Vis spectra of complexes 1 and 2.

3. 3. Description of the Structures of the Complexes

The molecular structures of complexes **1** and **2** are depicted in Figures 5 and 6, respectively. There is a solvated DMF molecule in complex **1**. The V atoms in both complexes are in distorted octahedral coordination with NO₅ chromophore. The dianionic tridentate hydrazones coordinate to the V atoms with the phenolate oxygen (O1), the enolate oxygen (O2) and the imine nitrogen (N1). The emt ligand coordinates to the V atom with the carbonyl oxygen (O5) and phenolate oxygen (O6). The octahedral coordination is defined by the three donor atoms of the hydrazone and the O6 atom at the equatorial plane, and by the oxido oxygen (O4 for **1** and O3 for **2**) and the O5 atom at the axial positions. The V atoms in complex **1** and **2** deviated from the least-squares planes defined by the equatorial donor atoms by 0.306(1) Å and 0.302(1) Å, respectively. The V1–O5 bond lengths (2.26 Å) in both complexes are longer than the remaining V–O bonds (1.58–2.10 Å), which is caused by the *trans* effects generated by the oxido groups. The bond lengths of V–O and V–N are within the values observed in other vanadium(V) complexes.^{2f,4e,13} The bond lengths of C8–O2 (1.31 Å) indicate they are more close to single bonds, which is due to the conjugation effects of the ligands.¹⁴ In addition, the bond lengths of C8–N2 (1.30 Å) and N1–N2 (1.40 Å) are intermediate between single and double bonds, which also supports the electron cloud delocalization in the hydrazone ligands. The five-membered chelate rings (V1–N1–N2–C8–O2) are nearly planar, while the six-membered chelate rings (V1–O1–C2–C1–C7–N1) are obviously distorted from planarity. The benzene rings of the hydrazone ligands form dihedral angles of 1.8(3)° (**1**) and 8.7(4)° (**2**). The distortion of the octahedral coordination can be observed from the *trans* angles (157.8(1)–174.2(1)° for **1** and 153.8(1)–176.1(1)° for **2**).

In the crystal structures of complexes **1** and **2** (Figures 7 and 8), the complexes molecules are linked together by hydrogen bonds (Table 3).

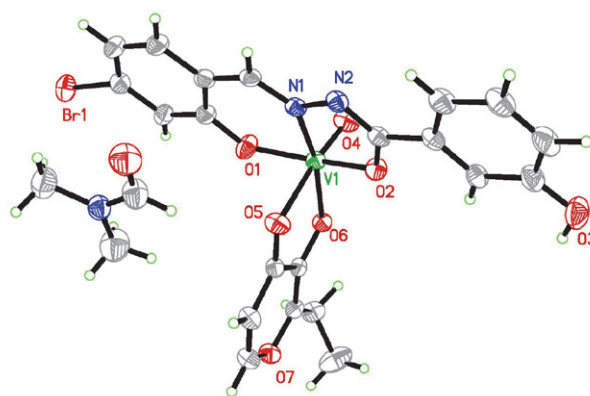


Figure 5. ORTEP plots (30% probability level) and numbering scheme for complex **1**.

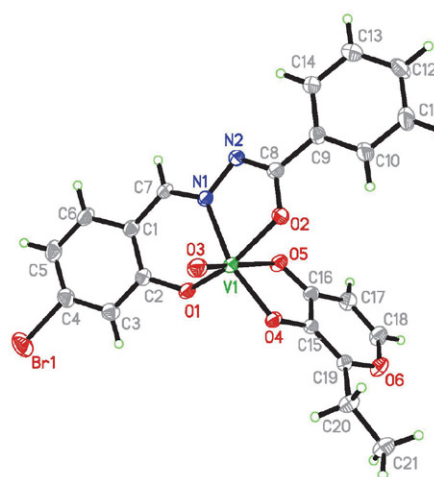


Figure 6. ORTEP plots (30% probability level) and numbering scheme for complex **2**.

3. 4. Catalytic Epoxidation Property

The complexes showed good properties on the cyclooctene epoxidation reaction by using aqueous TBHP as oxidant with no extra addition of organic solvents. Kinetic profiles of complexes **1** and **2** as the catalysts are presented

Table 3. Hydrogen bond distances (Å) and bond angles (°) for the complexes

<i>D</i> –H... <i>A</i>	<i>d</i> (<i>D</i> –H), Å	<i>d</i> (H... <i>A</i>), Å	<i>d</i> (<i>D</i> ... <i>A</i>), Å	Angle (<i>D</i> –H... <i>A</i>), °
1				
O3–H3...O8 ⁱ	0.82	1.81	2.628(5)	178(3)
C19–H19...O5 ⁱⁱ	0.93	2.51	3.357(5)	151(3)
C20–H20A...O4 ⁱⁱⁱ	0.97	2.53	3.264(5)	132(3)
2				
C17–H17...O3 ^{iv}	0.93	2.48	3.330(5)	153(3)
C21–H21B...O5 ^v	0.96	2.52	3.440(5)	160(3)

Symmetry codes: i) $-1 + x, y, z$; ii) $1 - x, -y, 1 - z$; iii) $1 - x, 1 - y, -z$; iv) $x, 1 + y, z$; v) $-x, 2 - y, -z$.

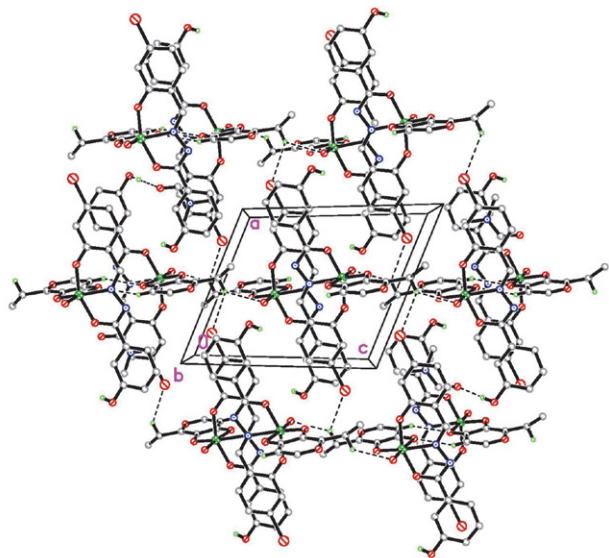


Figure 7. The molecular packing diagram of complex 1, viewed down the *b* axis. Hydrogen bonds are shown as dashed lines.

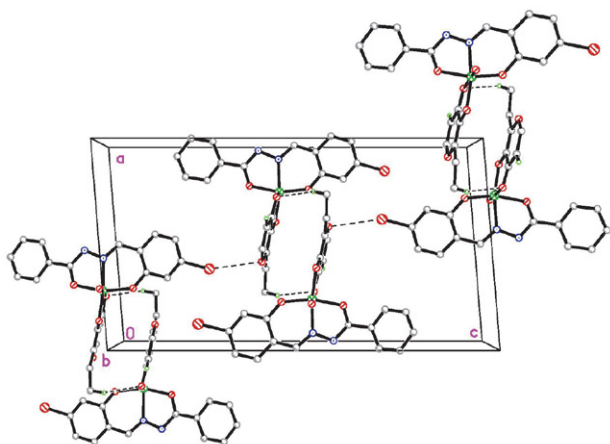


Figure 8. The molecular packing diagram of complex 2, viewed down the *b* axis. Hydrogen bonds are shown as dashed lines.

in Figure 9. The cyclooctene conversions for complexes 1 and 2 are 91% and 90% after 5 h, and the selectivities for cyclooctene oxide are 67 and 69%. The proposed mechanism is shown in Scheme 3. The TBHP molecule was considered to be coordinated to the V atom with the formation of an O–H...O hydrogen bond. Interestingly, the vanadium complexes in this work have higher conversions and selectivities for the epoxidation reaction of cyclooctene than the molybdenum complexes with hydrazone ligands.¹⁵ From the results, it is not obvious difference between the conversions of the complexes, but the selectivity of complex 2 with benzene as the terminal group of the hydrazone ligand (L^b) is a little higher than complex 1 with *p*-hydroxybenzene as the terminal groups of the hydrazone ligand (L^a).

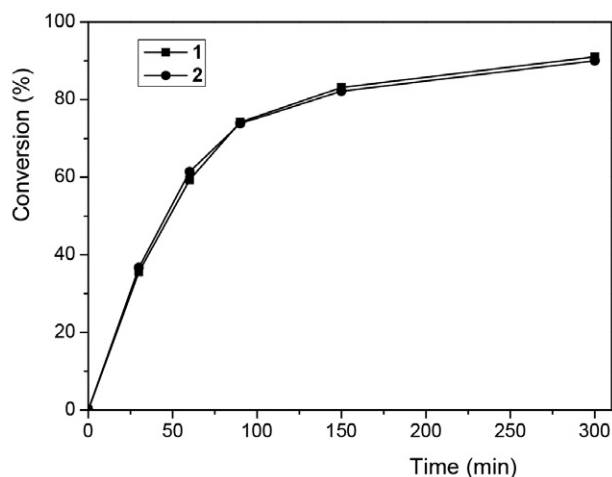
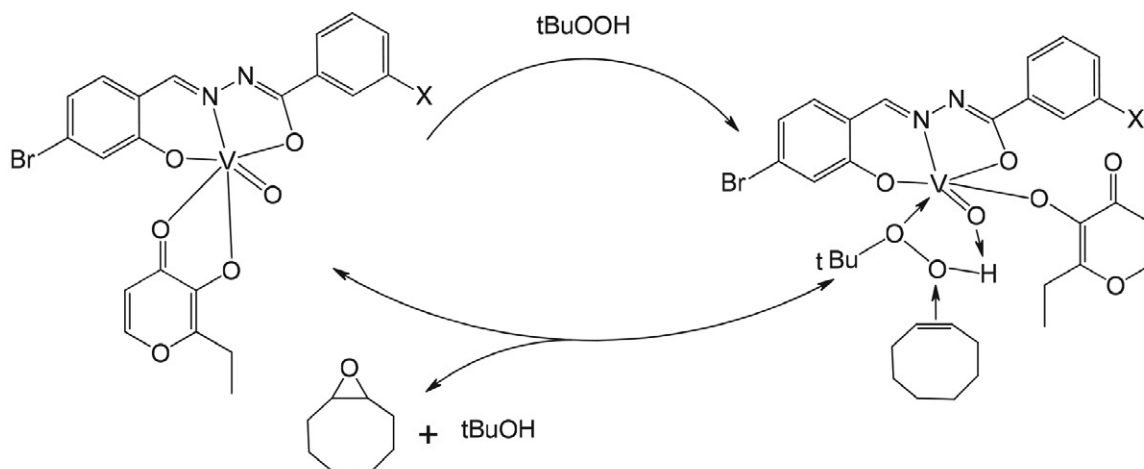


Figure 9. Kinetic monitoring of *cis*-cyclooctene epoxidation with TBHP–H₂O in the presence of the complexes 1 and 2.

4. Conclusion

In summary, two new structurally similar oxidovanadium(V) complexes derived from the tridentate hydra-



Scheme 3. Proposed mechanism for the catalytic reaction. X = OH for 1, and X = H for 2.

zones *N'*-(4-bromo-2-hydroxybenzylidene)-3-hydroxybenzohydrazide and *N'*-(4-bromo-2-hydroxybenzylidene)benzohydrazide, and the bidentate ligand ethyl maltol were prepared and structurally characterized. The hydrazone ligands coordinate to the vanadium atoms through the NOO donor set. The V atoms of the complexes are in octahedral coordination. The ethyl maltol ligand can be substituted by TBHP during the catalytic processes. The complexes have effective catalytic epoxidation properties on cyclooctene with high conversions.

5. Supplementary data

CCDC numbers 1979493 for **1** and 1979494 for **2** contain the supplementary crystallographic data. These data can be obtained free of charge via <http://www.ccdc.cam.ac.uk/conts/retrieving.html>, or from the Cambridge Crystallographic Data Center, 12, Union Road, Cambridge CB2 1EZ, UK; fax: +44 1223 336 033; or e-mail: deposit@ccdc.cam.ac.uk.

Acknowledgments

This work was supported by the Collaborative Innovation Plan of Hubei Province for Key Technology of Eco-Ramie Industry.

6. References

- (a) S. V. F. Beddoe, R. F. Loneragan, M. B. Pitak, J. R. Price, S. J. Coles, J. A. Kitchen, T. D. Keene, *Dalton Trans.* **2019**, 48, 15553–15559; DOI:10.1039/C9DT01527B
(b) S. Thakur, M. G. B. Drew, A. Franconetti, A. Frontera, S. Chattopadhyay, *RSC Advances* **2019**, 9, 35165–35175; DOI:10.1039/C9RA07006K
(c) H.-Y. Qian, N. Sun, *Transition Met. Chem.* **2019**, 44, 501–506; DOI:10.1007/s11243-018-00296-x
(d) C.-L. Zhang, X.-Y. Qiu, S.-J. Liu, *Acta Chim. Slov.* **2019**, 66, 484–489; DOI:10.17344/acsi.2019.5019
(e) H.-Y. Qian, *Inorg. Nano-Met. Chem.* **2018**, 48, 615–619; DOI:10.1080/24701556.2019.1567542
(f) Y. Li, L. Xu, M. Duan, B. Zhang, Y. Wang, Y. Guan, J. Wu, C. Jing, Z. You, *Polyhedron* **2019**, 166, 146–152. DOI:10.1016/j.poly.2019.03.051
- (a) T. A. Bazhenova, V. S. Mironov, I. A. Yakushev, R. D. Svetogorov, O. V. Maximova, Y. V. Manakin, A. B. Kornev, A. N. Vasiliev, E. B. Yagubskii, *Inorg. Chem.* **2020**, 59, 563–578; DOI:10.1021/acs.inorgchem.9b02825
(b) H.-Y. Qian, *Inorg. Nano-Met. Chem.* **2018**, 48, 461–466; DOI:10.1080/24701556.2019.1569689
(c) H. Y. Qian, *Russ. J. Coord. Chem.* **2017**, 43, 780–786; DOI:10.1134/S1070328417110070
(d) K. Dankhoff, M. Gold, L. Kober, F. Schmitt, L. Pfeifer, A. Durrmann, H. Kostrhunova, M. Rothemund, V. Brabec, R. Schobert, B. Weber, *Dalton Trans.* **2019**, 48, 15220–15230; DOI:10.1039/C9DT02571E
(e) H. Y. Qian, *Russ. J. Coord. Chem.* **2018**, 44, 32–38; DOI:10.1134/S1070328418010074
(f) M. Duan, Y. Li, L. Xu, H. Yang, F. Luo, Y. Guan, B. Zhang, C. Jing, Z. You, *Inorg. Chem. Commun.* **2019**, 100, 27–31; DOI:10.1016/j.inoche.2018.12.009
(g) E. Zarenezhad, S. Esmailzadeh, *Acta Chim. Slov.* **2018**, 65, 416–428. DOI:10.17344/acsi.2018.4159
- (a) K. Moghe, A. K. Sutar, I. K. Kang, K. C. Gupta, *RSC Advances* **2019**, 9, 30823–30834; DOI:10.1039/C9RA05811G
(b) G. Tseberlidis, L. Demonti, V. Pirovano, M. Scavini, S. Cappelli, S. Rizzato, R. Vicente, A. Caselli, *ChemCatChem* **2019**, 11, 4907–4915; DOI:10.1002/cctc.201901045
(c) Y. Kobayashi, R. Obayashi, Y. Watanabe, H. Miyazaki, I. Miyata, Y. Suzuki, Y. Yoshida, T. Shioiri, M. Matsugi, *Eur. J. Org. Chem.* **2019**, 13, 2401–2408; DOI:10.1002/ejoc.201900146
(d) X. Engelmann, D. D. Malik, T. Corona, K. Warm, E. R. Farquhar, M. Swart, W. Nam, K. Ray, *Angew. Chem. Int. Ed.* **2019**, 58, 4012–4016. DOI:10.1002/anie.201812758
- (a) M. Safaiee, M. Moeinimehr, M. A. Zolfigol, *Polyhedron* **2019**, 170, 138–150; DOI:10.1016/j.poly.2019.05.007
(b) R. J. Comito, Z. W. Wu, G. H. Zhang, J. A. Lawrence, M. D. Korzynski, J. A. Kehl, J. T. Miller, M. Dinca, *Angew. Chem. Int. Ed.* **2018**, 57, 8135–8139; DOI:10.1002/anie.201803642
(c) H. Hayashibara, X. H. Hou, K. Nomura, *Chem. Commun.* **2018**, 54, 13559–13562; DOI:10.1039/C8CC07974A
(d) M. Q. E. Mubarak, S. P. de Visser, *Dalton Trans.* **2019**, 48, 16899–16910; DOI:10.1039/C9DT03048D
(e) M. Liang, N. Sun, D.-H. Zou, *Acta Chim. Slov.* **2018**, 65, 964–969; DOI:10.17344/acsi.2018.4625
(f) L.-W. Xue, Q.-L. Peng, P.-P. Wang, H.-J. Zhang, *Acta Chim. Slov.* **2019**, 66, 694–700. DOI:10.17344/acsi.2019.5151
- G. M. Sheldrick, SHELXS97 Program for solution of crystal structures, University of Göttingen, Germany, **1997**.
- W. Kraus, G. Nolze, PowderCell 2.3, Federal Institute for Materials Research and Testing, Berlin, Germany, **1999**.
- (a) Y.-T. Ye, F. Niu, Y. Sun, D. Qu, X.-L. Zhao, J. Wang, D.-M. Xian, H. Jurg, Z.-L. You, *Chinese J. Inorg. Chem.* **2015**, 31, 1019–1026;
(b) Z.-L. You, D.-M. Xian, M. Zhang, *Cryst. Eng. Comm.* **2012**, 14, 7133–7136. DOI:10.1039/c2ce26201k
- (a) R. A. Lal, M. Chakrabarty, S. Choudhury, A. Ahmed, R. Borthakur, A. Kumar, *J. Coord. Chem.* **2010**, 63, 163–175; DOI:10.1080/00958970903259451
(b) T. Glowiak, L. Jerzykiewicz, J. A. Sobczak, J. J. Ziolkowski, *Inorg. Chim. Acta* **2003**, 356, 387–392. DOI:10.1016/S0020-1693(03)00301-3
- C. A. Koellner, N. A. Piro, W. S. Kassel, C. R. Goldsmith, C. R. Graves, *Inorg. Chem.* **2015**, 54, 7139–7141. DOI:10.1021/acs.inorgchem.5b01136
- (a) L.-X. Li, Y. Sun, Q. Xie, Y.-B. Sun, K.-H. Li, W. Li, Z.-L. You, *Chinese J. Inorg. Chem.* **2016**, 32, 369–376;
(b) L. Pan, C. Wang, K. Yan, K.-D. Zhao, G.-H. Sheng, H.-L. Zhu, X.-L. Zhao, D. Qu, F. Niu, Z.-L. You, *J. Inorg. Biochem.*

- 2016, 159, 22–28; DOI:10.1016/j.jinorgbio.2016.02.017
(c) D. Qu, F. Niu, X. Zhao, K.-X. Yan, Y.-T. Ye, J. Wang, M. Zhang, Z. You, *Bioorg. Med. Chem.* **2015**, 23, 1944–1949. DOI:10.1016/j.bmc.2015.03.036
11. P. Caravan, L. Gelmini, N. Glover, F. G. Herring, H. Li, J. H. McNeill, S. J. Rettig, I. A. Setyawati, E. Shuter, Y. Sun, A. S. Tracey, V. G. Yuen, C. Orvig, *J. Am. Chem. Soc.* **1995**, 117, 12759–12770. DOI:10.1021/ja00156a013
12. (a) R. Hahn, U. Kusthardt, W. Scherer, *Inorg. Chim. Acta* **1993**, 210, 177–182; DOI:10.1016/S0020-1693(00)83325-3
(b) S. Gupta, A. K. Barik, S. Pal, A. Hazra, S. Roy, R. J. Butcher, S. K. Kar, *Polyhedron* **2007**, 26, 133–141. DOI:10.1016/j.poly.2006.08.001
13. (a) M. R. Maurya, S. Agarwal, C. Bader, M. Ebel, D. Rehder, *Dalton Trans.* **2005**, 537–544;
(b) H.-Y. Qian, *Acta Chim. Slov.* **2019**, 66, 995–1001; DOI:10.4149/neo_2019_190112N36
(c) Y. Li, L. Xu, M. Duan, J. Wu, Y. Wang, K. Dong, M. Han, Z. You, *Inorg. Chem. Commun.* **2019**, 105, 212–216; DOI:10.1016/j.inoche.2019.05.011
(d) L. Xu, Y. Li, M. Duan, Y. Li, M. Han, J. Wu, Y. Wang, K. Dong, Z. You, *Polyhedron* **2019**, 165, 138–142. DOI:10.1016/j.poly.2019.03.016
14. T. M. Asha, M. R. P. Kurup, *Polyhedron* **2019**, 169, 151–161. DOI:10.1016/j.poly.2019.04.045
15. Q. Liu, J. Lin, J. Liu, W. Chen, Y. Cui, *Acta Chim. Slov.* **2016**, 63, 279–286.

Povzetek

Sintetizirali smo dva nova etil maltolato koordinacijska enojedrna oksidovanadijeva(V) kompleksa [VOL^a(emt)]·DMF (**1**) in [VOL^b(emt)] (**2**), kjer je H₂L^a = N⁷-(4-bromo-2-hidroksibenziliden)-3-hidroksibenzohidrazid, H₂L^b = N⁷-(4-bromo-2-hidroksibenziliden)benzohidrazid, Hemt = etil maltol, ter ju okarakterizirali s CHN elementno analizo, FT-IR in UV-Vis spektroskopijo ter praškovno XRD analizo. Strukture smo določili z monokristalno rentgensko difrakcijo, ki razkrije, da imajo V atomi v kompleksu oktaedrično koordinacijo. Hidrazona sta NOO trivezna liganda. Katalitične lastnosti obeh kompleksov smo raziskali z reakcijo epoksidacije ciklooktena.



Except when otherwise noted, articles in this journal are published under the terms and conditions of the Creative Commons Attribution 4.0 International License

Scientific paper

Students' Achievements in Solving Authentic Tasks with 3D Dynamic Sub-Microscopic Animations About Specific States of Water and their Transition

Miha Slapničar*, Valerija Tompa, Saša A. Glažar, Iztok Devetak and Jerneja Pavlin*

University of Ljubljana, Faculty of Education, Kardeljeva pl. 16, 1000 Ljubljana

* Corresponding authors: E-mails: miha.slapnicar@pef.uni-lj.si and jerneja.pavlin@pef.uni-lj.si

Received: 02-13-2020

Abstract

This paper aims to identify differences in the justification of the selection of 3D dynamic submicroscopic-representation (SMR) of the solid and liquid states of water, as well as the freezing of water presented in selected authentic tasks. According to students' achievements in solving these tasks at different levels of education, their explanations were identified. To explain in greater detail how students attempted to solve the authentic tasks, an eye-tracking method was used to identify the differences in the total fixation durations on specific areas of interest at the specific SMRs between successful and unsuccessful students in three age groups. A total of 79 students participated in this research. The data were collected with a structured interview conducted with students when solving three authentic tasks displayed on the computer screen. The tasks comprise text (as problem and questions), macro-images (photos of the phenomena) and SMRs of the phenomena. The eye-tracker was also used to measure the students' gaze fixations at the particular area of interest. The results show that successful students' justifications for a correct SMR include macroscopic and sub-microscopic representations of the chosen concepts. Along different stages of education, the selection success increases and sufficient justifications comprise the sub-microscopic level. It could be concluded that there are mostly no significant differences between successful and unsuccessful students within the same age group in the total fixation duration at the correct SMR. Further studies are needed to investigate the information-processing strategies between high and low achievers in solving various authentic tasks comprising SMRs and those that integrate all three levels of the representation of chemical concepts.

Keywords: States of water; freezing of water; authentic tasks; 3D dynamic SMR; eye tracking.

1. Introduction

Most chemical concepts are comprehended as abstract for teaching and learning because they can be represented on three different levels of representation: macroscopic, sub-microscopic, and symbolic. The teaching and learning of chemical concepts can be facilitated by context-based chemistry approaches that usually start from contexts (topics, questions) that are close to students' everyday life (authentic context). These approaches increase students' interest, activate their pre-knowledge on certain topics and offer situations in which newly developed knowledge can be applied and linked to basic concepts.¹ Several authors have taken this into account when designing activities and tasks for students.^{2–5}

However, facilitating the understanding of the specific level of representation of chemical concepts is related

to the use of different visualisation tools.⁶ Therefore, teachers should pay more attention to the representation of structures of different substances at the sub-microscopic level so that students can develop an adequate understanding of specific chemical concepts.⁷ For visualisation at the sub-microscopic level, teachers could use static and dynamic 2D or 3D submicro-representations.^{8,9} However, some researchers¹⁰ have reported that students using 3D dynamic representations constructed a better understanding of the chemical concepts than students using static 3D representations did, while other researchers¹¹ have reported that 3D representations help students improve incomplete understandings of the concepts and influence the construction of more complete concepts.

For an adequate understanding of the chemical concept, students must integrate all three levels of chemical concept simultaneously: the macroscopic, the sub-micro-

scopic, and the symbolic.¹² Many studies have shown that students at all levels of education have problems in interpreting and applying SMRs.^{9,13,14} These difficulties indicate a lack of connection between all three levels of the representation of the chemical concept. Researchers^{15–17} have found that primary school, secondary school, and university students have problems in explaining the process (represented at the macroscopic level) at the sub-microscopic level. Nevertheless, knowledge about the particulate nature of matter in different stages of education is improving.¹⁸ Based on research,^{19,20} primary school students have problems in understanding SMRs for states of matter and transitions between them. Sixteen-year-old students achieved higher scores in tasks about states of water when concepts regarding the gaseous state of water at the sub-microscopic level were included.^{21,22}

It is reported that most students can explain particle motion in the liquid and solid states of matter.^{23,24} Students aged 10 to 12 years have problems in applying particle theory to justify everyday events. Even if the students had previous theoretical knowledge about the particulate nature of matter, problems with explaining everyday events or using it to explain observed phenomena were common.²⁵ Other researchers²⁶ have stated that the students were unable to transfer the obtained knowledge about the particulate nature of matter to situations in everyday life. Students have problems explaining events (based on particle theory) that are related to physical changes, even if they have formed adequate particle conceptions. Teachers should use the particulate nature of matter to explain events in everyday life, which enables learning and facilitates the conceptual understanding of particle theory.²⁴ Difficulties in the conceptual understanding of state changes have been reported in recent decades.²⁷ However, the representation of chemical concepts using dynamic SMRs has an impact on improving students' understanding of the particulate nature of matter,²⁸ e.g., motion^{29–32} and particle arrangement.^{33–35}

The process of an individual's solving a task can be identified with eye-tracking because cognitive information processing is related to eye movements, which are used as an observable measure of visual attention.^{36–38} Eye-tracking studies have shown that unsuccessful task solvers have had difficulty distinguishing between relevant and irrelevant factors and in focusing on relevant factors to solve the task. Success in selecting information is crucial for successful task solving,³⁹ and it is similar to the observation of 3D-SMRs.⁴⁰ Which information is processed by the cognitive system is indicated by fixations,⁴¹ which are periods of eye stability. The eyes can only be in a stable condition for a limited time (100–500 ms).^{36,41,42} The most commonly used measure of eye movement is fixation duration, including a variable total fixation duration (TFD).^{42,43} Fixation duration measures 'the duration of each fixation within an area of interest (AOI)'.^{37,44} Longer fixation durations indicate the greater complexity of visual

material.⁴⁵ The duration of the fixation on the individual components of a display can be used to identify the AOIs. Fixation duration also indicates the time in which the information is processed.³⁷ A longer fixation time indicates a deeper and more complex processing of the information.⁴⁶

2. Research Problem and Research Questions

The research results⁴⁷ showed an improvement in the knowledge of the states of matter at the sub-microscopic level through years of schooling. Based on research findings, primary school students have problems understanding SMRs for states of matter and transitions between them.^{19,20} Unsuccessful problem-solvers had difficulty in distinguishing between relevant and irrelevant factors and in focusing on the relevant factors to solve the scientific task. Success in selecting information is crucial for successful task solving.³⁹ From the literature presented in the introduction, it is evident that difficulties in explaining the particular nature of different states of water are found among students on different stages of education.

The objectives of the research were to determine whether successful and unsuccessful students' justifications at different stages of education and aged 12 years (primary school), 16 years (upper secondary school) and 23 years (university education) differ and to identify whether successful students fix their gaze for longer times on the correct 3D-SMR than non-successful students do when solving the tasks. Two research questions were set in the research:

RQ 1: How do successful and unsuccessful students of different age groups (12, 16, and 23 years) differ in the justifying of the selection of 3D dynamic SMRs (for the solid and liquid states of water and the freezing of water)?

RQ 2: How do successful and unsuccessful students of different age groups (12, 16, and 23 years) differ in TFD on AOI with 3D dynamic SMRs in authentic tasks, including the solid and liquid states of water and the freezing of water?

3. Methods

A quantitative non-experimental research approach with descriptive methods was used.

3.1. Participants

A non-random, convenience sample of participants was formed from a mixed urban population, including seventy-nine Slovenian students from three different age groups. The students came from the Ljubljana region and voluntarily participated in the research. The first group included thirty students who attended the seventh grade of primary school ($Mdn = 12.0$ years, $IQR = 0.43$ years). The

participants of the second group ($N = 29$) attended the first year of upper secondary school ($Mdn = 16.0$ years, $IQR = 1.0$ years). The third group consisted of 20 students (future teachers) of the double-majors study programme of chemistry and biology/physics from the Faculty of Education of the University of Ljubljana ($Mdn = 23.0$ years, $IQR = 2.0$ years).

The approval for primary and upper secondary students was obtained from school authorities, teachers, and parents/caregivers, according to the Ethics Committee for Pedagogy Research of the Faculty of Education of the University of Ljubljana. All participants had normal or corrected-to-normal vision, and all were competent readers. To ensure anonymity, each student was assigned a code consisting of the letter 'S' with the number of the age group and a student number (e.g., S1_7).

The group of successful students included students who selected the correct 3D dynamic SMR for a particular state of water or freezing of water and gave the correct justifications for their decisions, while the group of unsuccessful students included students who were unsuccessful in selecting and/or justifying the selection of a correct 3D dynamic SMR.

3. 2. Instruments

The problem set consisted of three authentic tasks. These specific tasks are three of eleven authentic science tasks that were studied from different aspects in the Slovenian Research Agency project entitled 'Explaining effec-

tive and efficient problem solving of the triplet relationship in science concepts representations'. The starting point for the selection of ideas for curriculum content for the preparation of tasks was made by the review of TIMMS (Trends in International Mathematics and Science Study), the PISA Programme for International Student Assessment, and the tasks of the Slovenian national external assessment for chemistry and physics. The group of the project designed authentic context-based tasks, including 3D dynamic SMRs of chemistry concepts. The 3D dynamic SMRs were designed by science educators, as well as the authors of this paper, and, according to their developed ideas, the computer specialist completed them. The 3D dynamic SMRs were developed only for this research. The time in which the participants looked at them was not limited. When the participants needed more time to solve the tasks, the animations started again from the beginning. However, the participants did not have the possibility of controlling the animations. The text of the tasks was in the Slovenian language. For the purpose of this paper, the task texts were translated into English (see Figures 1–3).

Task 1 (Figure 1) includes macroscopic and sub-microscopic levels of representation for the solid state of water, Task 2 for the liquid state of water, and Task 3 for the freezing of water. Each task was presented by displaying a screen image (slide) in the PowerPoint presentation. Task 1 and Task 2 each consisted of two slides.

Task 1 included a photo of an iceberg, three 3D dynamic SMRs, and two questions related to the selection

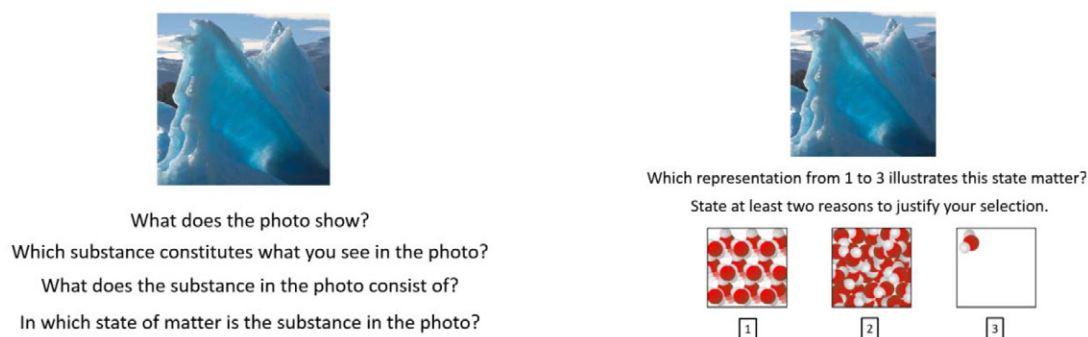


Figure 1. Screen images of the first authentic task, part 1 (left) and part 2 (right). (Image of an iceberg from hdwpics.com).



Figure 2. Screen images of the second authentic task, Part 1 (left) and Part 2 (right). (Image of flowing water from www.goingmobo.com).

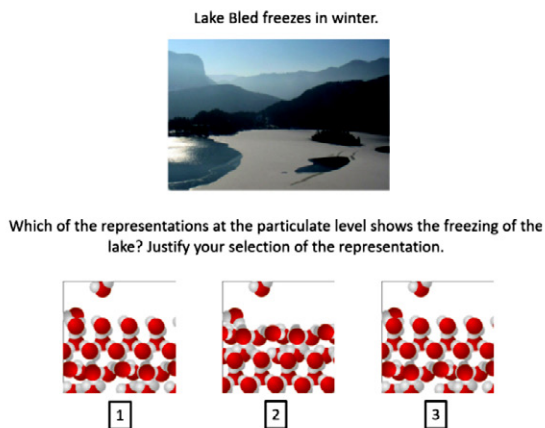


Figure 3. Screen image of the third authentic task. (Image of lake Bled from www.wikipedia.org). All SMRs represented the movement of water molecules in three different states of matter. All SMRs represented the correct movement and arrangement of particles (water molecules) in the gaseous state of water (on the top of SMR). The correct one is SMR 1 representing the liquid state in the lower part, the solid state in the middle part of the SMR, and the gaseous state in the upper part. SMR 2 did not represent the arrangement of the particles in the correct order (solid state in the lower part, liquid state in the middle part of the SMR, and gaseous state in the upper). SMR 3 is incorrect because particles do not move in the solid state of water.

and justification of the selected sub-micro-representation. Task 2 (Figure 2) consists of a photo of liquid water, three 3D dynamic SMRs, and two questions related to the selection and justification of the selected SMR. The 3D dynamic SMRs in Tasks 1 and 2 represented the correct arrangement and movement of particles in all three states of water (solid, liquid and gaseous state) in a different order. Task 3 (Figure 3) included a photo of partially frozen Lake Bled, two questions (to select and explain selected 3D sub-micro-representation) and three animations that could represent a process of water freezing.

3. 3 Research Design

To determine the time required by successful and unsuccessful students for a certain AOI (3D dynamic SMRs for the solid, liquid state of water and freezing of water), TFDs were measured with eye-tracking. ‘Fixations’ refer to maintaining one’s gaze on a specific AOI, while ‘saccades’ refer to rapid eye movements from one AOI to another.⁴⁸ The identification of saccades/fixations is based on the motion of gaze during each collected sample. If both the velocity and acceleration threshold (in our case: 30 degrees per second and 8000 degrees per second squared) or are exceeded, a saccade begins; otherwise, the sample was labelled as a fixation. The screen-based Eye-Link 1000 (35 mm lens, horizontal orientation) eye tracker apparatus and associated software (Experiment Builder for preparation of the experiment and a connection to Eye-Link; Data Viewer for data acquisition and basic analysis) for recordings and analyses of students’ eye movements when solving authentic tasks were used. Data were collected from the right eye (monocular data collection following corneal reflection and student responses) at 500 Hz.⁴⁹

The data were collected using the eye-tracking method in the laboratory of the Department of Psychology, of

the Faculty of Arts, of the University of Ljubljana. The data collection was performed between November 2017 and January 2018. Before the individual testing with the eye tracker, each student was informed about the eye-tracking method, the purpose of the research, and their role in it. During testing with the eye tracker, a student sat in the front of the computer screen with chin and forehead held on a special head-supporting stand, which enabled the optimal measurement, recording and stability of the head and recordings. The distance between the participants’ eyes and the computer screen was approximately 60 centimetres. After calibrating and validating the eye tracker using a nine-point algorithm, the student solved the tasks and gave the answers to the tester (structured interview), who transcribed them. The tasks were represented in the form of slides in a PowerPoint presentation. When the student solved the task presented on a slide, the tester switched to another slide (task).⁵⁰

A basic analysis of the collected eye movement data was performed in the Data Viewer software. Further data analysis was conducted in the Statistical Package for Social Sciences (SPSS), version 22. The participants of all three age groups (12-, 16-, and 23-year-old students) were divided into successful and unsuccessful groups based on their successful justification together with the selection of the correct 3D dynamic SMR for the liquid and solid states of water and the freezing of water, as well as the reasons for their selection. The students’ justifications (written down by the tester) were read several times by two authors independently, identifying and coding the most important meanings concerning the level of the chemical concept representations and correctness of the justification. The authors then met to compare and confirm the results. Any disagreements were resolved by discussion between the authors. The planned recourse to the third author for arbitration did not prove necessary.

The mean values of the TFDs were described by a median (*Mdn*) and an interquartile range (*IQR*) for the specific 3D SMR. The distribution of data was non-normal, and the sample was small. Therefore, the Mann-Whitney U and Kruskal-Wallis non-parametric tests were used to explain the relationship between the (un)successfully solved authentic task, including SMRs, and TFD on AOs with SMRs. Statistical hypotheses were tested at a 5% alpha error rate. To describe whether the effects have a relevant magnitude, the effect size measure eta squared η^2 was used to describe the strength of a phenomenon. Benchmarks for effects size are small (0.01), medium (0.06), and large (0.14).^{51,52}

4. Results and Discussion

The results are presented according to the research questions.

4.1. Students' Achievements in Justifications Altogether with the Selection of SMR

Research Question 1 focused on the differences between successful and unsuccessful students in three age groups in the justification of selected 3D dynamic SMRs for the solid and liquid state of water or the freezing of water.

The results showed that all students in Groups 2 and 3 chose the correct SMR for the solid and liquid state of water, while one student in Group 1 chose the incorrect SMR for the solid state of water and two of them chose the incorrect SMR for the liquid state of water; 23.33% of the students in Group 1, 58.62% in Group 2, and 75.00% in Group 3 chose the correct 3D dynamic SMR for the freezing of water.

Table 1 presents the relative frequencies for students' achievements in justifications of the selected SMS in three tasks related to the solid and liquid state of water or the freezing of water. It is evident that the percentage of successful students' justification for the correct SMR for the solid state of water is increasing according to the stage of education from 10.00% in Group 1 to 20.00% in Group 3. In Task 2, on the liquid state of water, the ability to correctly justify the choice rose from 17.24% to 55.00% according to the years of schooling. The relative frequencies of suc-

cessful students related to the task in water freezing increased among the years of schooling from 13.33% in Group 1 to 40.00% in Group 3. The results are coherent with researchers¹⁸ who noted that knowledge about the particulate nature of matter improves according to the stages of education. Other researchers^{19,20,48} have also argued about improved knowledge among the stages of education.

The level at which the justification of selected SMR (sub-microscopic, macroscopic, a combination of both levels) was argued is shown in Table 2 by absolute frequencies of justifications at the specific level of representation of chemical concepts in Tasks 1 (solid state of water), 2 (liquid state of water) and 3 (freezing of water).

The majority (70.00%) of successful and unsuccessful students in Group 1 justified their selection for the SMR of the solid state of water (Task 1) at the macroscopic level and a combination of macroscopic and sub-microscopic levels, while most (70.00%) successful and unsuccessful students in Group 3 justified their selection at the sub-microscopic level. It is evident that the majority of successful and unsuccessful students in all three groups listed the justifications for selecting the SMR for the liquid state of water (Task 2) at the macroscopic and sub-microscopic levels, except for the unsuccessful students in Group 3, who gave the same number of justifications at the sub-microscopic or macroscopic and sub-microscopic levels.

Successful and unsuccessful students in Group 1 explained the majority of the justifications in Task 3 (freezing of water) at the macroscopic level. Most of the successful and unsuccessful students of Group 2 discussed a selection of a correct SMR at the macroscopic and sub-microscopic levels. Successful students in Group 3 argued about the selection of an SMR for freezing of water at the macroscopic and sub-microscopic levels or at the macroscopic level, while unsuccessful students in Group 3 argued at the macroscopic and sub-microscopic levels.

This is shown by examples of justifications for Task 3 (freezing of water) that were identified as incorrect. They are listed below by age group.

Examples of incorrect justification of students of Group 1.

SI_3: The ice surface is at rest, and the water underneath moves normally.

SI_8: The ice does not freeze everywhere. It only freezes on the surface. Water vapour still evaporates.

Table 1. Relative frequencies of successful and unsuccessful students at solving tasks on solid (Task 1), liquid state of water (Task 2) and freezing of water (Task 3).

Group of students	Task 1: Solid state of water			Task 2: Liquid state of water			Task 3: Freezing of water		
	1	2	3	1	2	3	1	2	3
Successful (f%)	10.00	13.79	20.00	17.24	50.00	55.00	13.33	31.03	40.00
Unsuccessful (f%)	90.00	86.21	80.00	82.76	50.00	45.00	86.67	68.97	60.00

Group 1: Students aged 12. Group 2: Students aged 16. Group 3: Students aged 23.

S1_17: The layer is freezing, and not all the particles are moving. Some particles are at rest.

S1_23: Because the lake above is icy and solid and the particles are not moving. Below is liquid.

Examples of incorrect justification of students of Group 2.

S2_2: Because the top layer freezes. In the lower layer, the particles are still in motion (flowing water).

S2_6: The upper layer is still moving a little bit. Especially when we slide from the pressure, this part melts. The water freezes. A layer of water remains on top.

S2_11: Because there is ice on the surface, solid state. The particles do not move. Underneath, the water is in a liquid state, and the particles move.

S2_18: Because there is ice in the upper part, particles stand still; they do not move, and the lower part is liquid, particles move. This layer does not freeze.

Some examples of incorrect justification from students of Group 3.

S3_3: I chose animation number three because the ice structure on it is firmer because the molecules don't wobble. The molecules are connected to stronger forces during their movement than in the first animation. The ice is firmer in the third presentation and, therefore, does not break as fast as in the first presentation.

S3_5: What is the difference between 1 and 3? I do not see any difference. I will say 3. The top layer represents ice, the particles do not move, they are arranged.

S3_12: We have gaseous molecules at the top. In the middle, the lake is frozen, below it is running water.

S3_13: The bottom layer is liquid, and the top layer is ice. Here the particles are arranged and do not move. In the liquid state, the particles move in a disorderly fashion.

An example per age group of the correct justification is given as well.

Example of correct justification of students of Group 1.

S1_2: In this animation, water exists in three states of matter. I see this because the molecules move differently, even if they are the same. They move mainly in the gaseous state of water, then in liquid and then only around them in the solid state.

Example of correct justification of students of Group 2.

S2_19: In the first animation, the water in the lower part of the box is in a liquid state. In the middle of the box is ice, and on top is water vapour. The molecules in the water vapour move freely, in the solid state the water molecules in the liquid state of the water vibrate, there is something between them.

Example of correct justification of students of Group 3.

S3_7: 3D Animation 1 is correct. In Animation 1, we see that the water at the bottom of the window is in a liquid state, which illustrates that flowing water has a higher density than the ice above it. Above the ice or the solid state of water is the gaseous state of water or water vapour. Solid-state water molecules also oscillate in this representation of particle motion, which correctly illustrates the solid state.

As can be seen from the justifications for the selections of the SMRs, students of all age groups, including Group 3 (pre-service chemistry teachers), have problems describing the sub-microscopic level with the macroscopic level and misunderstandings within the sub-microscopic level, which is in line with research findings;^{19,20} primary school students have problems in understanding SMRs for states of matter and transitions between them, and most students can explain the motion of particles in the liquid and solid states of matter.^{23,24} It was found that the proportion of tested students who used macroscopic levels to represent the state of water decreased with age.⁴⁸ Other studies^{15–17} have also shown that primary school, secondary school, and university students have problems explaining the process (represented at the macroscopic level) at the sub-microscopic level, as the present study shows. Stu-

Table 2. Relative frequencies of successful and unsuccessful students' arguments at a specific level of representation, m – macroscopic level; m & s – macroscopic and sub-microscopic level; s – sub-microscopic level.

		Group 1			Group 2			Group 3		
		m (f)	m & s (f)	s (f)	m (f)	m & s (f)	s (f)	m (f)	m & s (f)	s (f)
Successful students	Task 1: Solid state of water	–	6.67	3.33	–	6.89	6.89	–	15.00	40.00
	Task 2: Liquid state of water	–	20.00	–	–	10.34	6.89	–	40.00	10.00
	Task 3: Freezing of water	13.33	–	–	13.79	17.24	–	20.00	20.00	–
Unsuccessful students	Task 1: Solid state of water	13.33	50.00	26.67	3.45	48.28	34.48	–	15.00	30.00
	Task 2: Liquid state of water	6.67	40.00	33.33	–	55.17	27.59	–	25.00	25.00
	Task 3: Freezing of water	66.67	16.67	3.33	27.59	41.38	–	25.00	35.00	–

Group 1: Students aged 12. Group 2: Students aged 16. Group 3: Students aged 23.

dents often assign macroscopic properties to particulate matter, revealing their misunderstandings about the macroscopic and sub-microscopic levels of particulate matter representations.^{21,53,54} In terms of teacher awareness, it is important to note that switching between the macroscopic and sub-microscopic levels is generally difficult for students. It is the teachers' task to accustom the students to sub-microscopic representations gradually and to present them with different examples so that they do not only recognise what they already know. Pre-service chemistry teachers should pay particular attention to the level of chemical concept representation so that they will be able to teach their students confidently.

4. 2. TFDs of Successful and Unsuccessful Students at AOIs with SMRs of Authentic Tasks, Including the Solid, Liquid State of Water and the Freezing of Water.

The second research question related to the identification of differences between successful and unsuccessful students of different age groups in the TFD on AOIs, including 3D dynamic SMRs in tasks dealing with the solid, the liquid state of water and the freezing of water.

Table 3 presents *Mdns* and *IQRs* for *TFD* at different AOIs – 3D dynamic SMRs for successful and unsuccessful students of three age groups for Task 1 about the solid state of water. Differences in TFDs of successful and unsuccessful students of Group 1, Group 2, and Group 3 on the correct SMR 1 are not statistically significant ($U = 49.000, p = 0.600; U = 20.000, p = 0.060; U = 50.000, p = 1.000$, respectively). However, differences in TFDs on the incorrect SMRs of successful and unsuccessful students for students from certain age groups are statistically significant only for Group 3 on AOI with the SMR 3 ($U = 22.000, p = 0.038, \eta^2$

$= 0.218$). The results show that Task 1 of a solid aggregate state is well known for both successful and unsuccessful students of each age group, which is reflected in the fact that there are no statistically significant differences in the processing time of the information provided by TFD.

Differences in TFDs of successful and unsuccessful including all 79 students together on AOI with the correct SMR in Task 1 (SMR 1) were not statistically significant (successful students: $Mdn = 11.015, IQR = 9.055$; unsuccessful students: $Mdn = 13.788, IQR = 9.858; U = 435.500, p = 0.185$) as well as on the incorrect SMR 3 (successful students: $Mdn = 0.812, IQR = 0.969$; unsuccessful students: $Mdn = 1.430, IQR = 2.178; U = 384.500, p = 0.054$). However, statistically significant differences in TFDs between all successful and unsuccessful students appear on AOI with SMR 2 (successful students: $Mdn = 4.530, IQR = 7.462$; unsuccessful students: $Mdn = 7.322, IQR = 8.470; U = 373.000, p = 0.040, \eta^2 = 0.054$). The size effect is small.

Differences in TFDs of successful students regarding the age group on the AOI with the correct SMR in Task 1 were not statistically significant (Kruskal-Wallis $\chi^2(2) = 5.720, p = 0.075, \eta^2 = 0.248$), whereas they are statistically significant for incorrect SMRs, concretely on the AOI with SMR 2 (Kruskal-Wallis $\chi^2(2) = 7.126, p = 0.028, \eta^2 = 0.342$), and AOI with the SMR 3 (Kruskal-Wallis $\chi^2(2) = 10.724, p = .005, \eta^2 = 0.582$) (Table 3). This reflects the fact that successful students of all age groups observe the correct AOI for the same amount of time. It can be anticipated that this SMR is well known to the students.

Differences in the TFDs of unsuccessful students regarding the age group on the AOI with the correct SMR in Task 1 were not statistically significant (Kruskal-Wallis $\chi^2(2) = 4.451, p \leq 0.000, \eta^2 = 0.042$), whereas they are statistically significant for incorrect SMRs, concretely on the AOI with SMR 2 (Kruskal-Wallis $\chi^2(2) = 20.090, p \leq 0.001$,

Table 3. Median (*Mdn*) and interquartile range (*IQR*) of TFDs on areas of interest for successful and unsuccessful students of 3 age groups for Task 1 (solid state of water). The correct SMR is SMR 1.

Variable	SMR 1		AOI SMR 2		SMR 3		
	<i>Mdn</i> ₁	<i>IQR</i> ₁	<i>Mdn</i> ₂	<i>IQR</i> ₂	<i>Mdn</i> ₃	<i>IQR</i> ₃	
Group 1	Successful (<i>n</i> = 3)	16.40	–	15.79	–	7.55	–
	Unsuccessful (<i>n</i> = 27)	16.18	11.62	13.15	14.03	2.67	2.72
Group 2	Successful (<i>n</i> = 4)	6.60	5.52	7.15	16.44	1.36	1.55
	Unsuccessful (<i>n</i> = 25)	12.49	9.83	5.46	4.23	0.93	0.89
Group 3	Successful (<i>n</i> = 11)	10.82	8.92	2.53	3.83	0.38	0.93
	Unsuccessful (<i>n</i> = 9)	12.86	7.57	5.64	4.06	1.22	0.90

Group 1: Students aged 12. Group 2: Students aged 16. Group 3: Students aged 23.

$\eta^2 = 0.312$), and AOI with the SMR 3 (Kruskal-Wallis $\chi^2(2) = 17.884$, $p \leq 0.001$, $\eta^2 = 0.274$) (Table 3). It is evident that the correct AOI is similarly interesting for unsuccessful students of different age groups.

Table 4 shows medians and IQR for TFDs on different AOIs with 3D dynamic SMRs for successful and unsuccessful students of three age groups for Task 2 on the liquid state of water. Similar to Task 1 (solid state of water), Task 2 (including the liquid state of water) shows that there are no statistically significant differences in the TFD between successful and unsuccessful students of each age group on the correct SMR 3 ($U = 73.000$, $p = 1.000$; $U = 68.000$, $p = 0.674$; $U = 40.000$, $p = 0.481$). This might be justified by the fact that tasks containing three typical SMRs of water with only one aggregate state and that are well known to the students reflect the similar value of the TFD for successful and unsuccessful students. From this, it can be concluded that for easier and better known authentic tasks, successful and unsuccessful students within the age group have a similar processing time.

Differences in the TFDs of successful and unsuccessful 79 students on AOI with the correct SMR in Task 2 (SMR 3) were not statistically significant (successful students: $Mdn = 12.014$, $IQR = 9.601$; unsuccessful students: $Mdn = 13.186$, $IQR = 13.988$; $U = 594.000$, $p = 0.860$) as well as on the AOI with SMR 1 (successful students: $Mdn = 1.988$, $IQR = 1.622$; unsuccessful students: $Mdn = 2.475$, $IQR = 2.859$; $U = 568.000$, $p = 0.649$) and on the AOI with SMR 2 (successful students: $Mdn = 4.504$, $IQR = 3.530$; unsuccessful students: $Mdn = 4.441$, $IQR = 4.454$; $U = 582.000$, $p = 0.764$).

Differences in TFDs of only the successful students regarding the age group on the AOI with the correct SMR in Task 1 (SMR 3) were not statistically significant (Kruskal-Wallis $\chi^2(2) = 2.202$, $p = 0.333$); it is similar on the AOI with the SMR 1 (Kruskal-Wallis $\chi^2(2) = 1.856$, $p = 0.395$).

However, statistically significant differences in TFDs of successful students regarding the age group are determined on the AOI with SMR 2 (Kruskal-Wallis $\chi^2(2) = 7.425$, $p = 0.024$, $\eta^2 = 0.301$) (Table 4).

Differences in TFDs of unsuccessful students regarding the age group on the AOI with the correct SMR (SMR 3) in task 2 were not statistically significant (Kruskal-Wallis $\chi^2(2) = 3.325$, $p = 0.190$), whereas they are statistically significant for incorrect SMRs, concretely on the AOI with SMR 1 (Kruskal-Wallis $\chi^2(2) = 10.326$, $p = 0.006$, $\eta^2 = 0.151$), and AOI with the SMR 2 (Kruskal-Wallis $\chi^2(2) = 14.518$, $p = 0.001$, $\eta^2 = 0.228$) (Table 4).

Table 5 shows medians and interquartile range for TFDs on AOIs (3D dynamic SMRs) for successful and unsuccessful students of three age groups for Task 3 on the freezing of water. Differences in TFDs of successful and unsuccessful students for students from the certain age group on the correct (SMR 1) and other two incorrect SMRs were not statistically significant (SMR 1: Group 1: $U = 83.000$, $p = 0.061$; Group 3: $U = 141.000$, $p = 0.015$; SMR 2: Group 1: $U = 53.000$, $p = 0.734$; Group 2: $U = 78.000$, $p = 0.594$; Group 3: $U = 36.000$, $p = 0.384$; SMR 3: Group 1: $U = 38.000$, $p = 0.425$; Group 2: $U = 83.000$, $p = 0.764$; Group 3: $U = 32.000$, $p = 0.238$). An exception appears in Group 2 on the AOI with the correct SMR ($U = 141.00$, $p = 0.015$, $\eta^2 = 0.199$). The results obtained show that the interpretation of the results for the liquid aggregate state of water is highly similar to the interpretation of the results for the solid aggregate state of water, which is confirmed by the fact that the successful and unsuccessful students of each age group, individual and known SMR, are similarly interested in solving the problem.

Differences in TFDs of the successful and unsuccessful 79 students on AOI with the correct SMR in Task 3 (SMR 1) were statistically significant with large effect (successful students: $Mdn = 22.648$, $IQR = 18.018$; unsuccessful students:

Table 4. Median (Mdn) and interquartile range (IQR) of interest for successful and unsuccessful students of 3 age groups in Task 2 (liquid state of water). The correct SMR is SMR 3.

	Variable	SMR 1		AOI SMR 2		SMR 3	
		Mdn_1	IQR_1	Mdn_2	IQR_2	Mdn_3	IQR_3
Group 1	Successful ($n = 6$)	2.30	3.30	6.17	5.28	16.85	13.32
	Unsuccessful ($n = 24$)	4.21	6.56	6.20	4.98	17.05	16.24
Group 2	Successful ($n = 5$)	1.56	1.18	3.61	3.08	9.51	10.92
	Unsuccessful ($n = 24$)	1.73	2.18	3.22	3.88	9.81	10.66
Group 3	Successful ($n = 10$)	2.28	2.20	3.59	2.72	11.47	8.90
	Unsuccessful ($n = 10$)	1.78	2.62	2.26	3.18	13.97	11.10

Group 1: Students aged 12. Group 2: Students aged 16. Group 3: Students aged 23.

$Mdn = 12.518$, $IQR = 12.481$; $U = 918.000$, $p = 0.001$, $\eta^2 = 0.149$); they were not statistically significant for the AOI with the SMR 2 (successful students: $Mdn = 6.694$, $IQR = 6.301$; unsuccessful students: $Mdn = 7.414$, $IQR = 8.076$; $U = 524.000$, $p = 0.346$) and AOI with the SMR 3 (successful students: $Mdn = 9.408$, $IQR = 9.218$; unsuccessful students: $Mdn = 13.407$, $IQR = 14.987$; $U = 446.000$, $p = 0.070$, $\eta^2 = 0.041$). Successful students spent more time on the correct SMR, which might be interpreted as successful students helping with the correct SMR when justifying the selection.

Differences in TFDs of successful students regarding the age group on the AOI with the correct SMR in Task 3 (SMR 1) and incorrect SMRs were not statistically significant (Kruskal-Wallis $\chi^2(2) = 0.532$, $p = 0.766$; Kruskal-Wallis $\chi^2(2) = 1.583$, $p = 0.453$; Kruskal-Wallis $\chi^2(2) = 0.396$, $p = 0.820$) (Table 5). The result shows that successful students, regardless of age group, spend similar time with AOIs, which shows that the effort for processing the visible information of successful students is similarly high when solving the task.

Differences in TFDs of unsuccessful students regarding the age group on the AOI with the correct SMR in Task 3 were statistically significant (Kruskal-Wallis $\chi^2(2) = 9.225$, $p = 0.010$, $\eta^2 = 0.131$), whereas they were not statistically significant for incorrect SMRs, concretely on the AOI with SMR 2 (Kruskal-Wallis $\chi^2(2) = 0.070$, $p = 0.965$), and AOI with the SMR 3 (Kruskal-Wallis $\chi^2(2) = 5.143$, $p = 0.076$) (Table 5).

It can be concluded that successful students (of all age groups) spend more time with the correct SMR when justifying their choice, which leads them to correctly solve the task, while the irrelevant information on the screen image is observed for less time. Unsuccessful task-solvers have difficulty in distinguishing between relevant and irrelevant factors and in focusing on the relevant factors to

solve the authentic task, which is (to some extent) consistent with the results of this research. Success in selecting information is crucial for successful task-solving, which is similar to the observation of 3D dynamic SMRs.^{39,40}

5. Conclusions

The focus of the presented research was to explore and explain students' justifications for the selection of the correct SMR in solving context-based tasks on the solid and liquid states of water and the process of freezing water, which include macroscopic and sub-microscopic levels of chemical concepts, and to identify differences between successful and unsuccessful students in justifying the selection of 3D dynamic SMRs and differences in the TFDs in solving the task among students in different groups.

The first research question referred to the students' justification of the selected correct SMR in three tasks related to states of matter and the impact of the stages of education in the justifications for the decision of selecting 3D dynamic SMRs for the solid and liquid states of water or the freezing of water between successful and unsuccessful students. It is evident that along the stages of education, the percentage of correct justifications of the selected SMR of the tasks increase and the justifications in the combination of sub-microscopic and macroscopic levels are mostly dominant for students of all ages for the solid and liquid states of water. The students in Group 1 stated the majority of the justifications at the macroscopic level. In contrast, most successful students in Groups 2 and 3 mentioned the choice of an SMR for the freezing of water at the macroscopic and sub-microscopic levels.

The second set of findings is related to the identification of differences in TFDs between successful and unsuccess-

Table 5. Median (Mdn) and interquartile range (IQR) of interest for successful and unsuccessful students of three age groups in Task 3 (freezing of water). The correct SMR is SMR 1.

	Variable	SMR 1		AOI SMR 2		SMR 3	
		Mdn_1	IQR_1	Mdn_2	IQR_2	Mdn_3	IQR_3
Group 1	Successful ($n = 4$)	22.51	29.30	9.46	9.64	9.93	13.9
	Unsuccessful ($n = 26$)	8.53	10.96	8.75	9.02	14.44	13.94
Group 2	Successful ($n = 9$)	25.76	15.90	7.79	5.04	9.41	8.98
	Unsuccessful ($n = 20$)	12.29	8.82	7.11	5.80	9.10	10.26
Group 3	Successful ($n = 8$)	20.82	23.36	5.69	6.62	9.22	14.42
	Unsuccessful ($n = 12$)	19.46	25.44	7.05	9.94	18.08	16.06

Group 1: Students aged 12. Group 2: Students aged 16. Group 3: Students aged 23.

successful students of the same and different age groups in solving tasks, including the solid and liquid states of water and the freezing of water. From the results of the TFDs in all tasks for the AOI with the correct SMR, it can be concluded that successful and unsuccessful students of the same age group observe SMRs for a similar amount of time while solving the task.

In justifying the choice of the correct SMR for the solid and liquid aggregate states of water, it is assumed that there are no differences between all successful and unsuccessful students, while in the case of the freezing water task, there are no differences, which indicates that easy and well-known SMRs do not require significant differences in observation time while students are justifying them. This is not the case for SMRs that are unknown to the students and, therefore, more difficult. In this case, the differences in SMR observation time are greater. The results suggest that successful students need more time to justify the choice of the right SMR for more difficult tasks that require greater cognitive effort, which is not true for unsuccessful students whose excessive cognitive effort hinders the path to the correct justification of the choice of the correct SMR.

A comparison of successful students of different age groups shows that all of them observe SMRs a similar time while explaining the choice. From this, it can be concluded that all successful students, regardless of age group, have a similar cognitive effort to justify the choice of the correct SMR, as evidenced by the similar processing of visible information on a computer screen image.

The limitations of this research are differences in the size of the groups of successful and unsuccessful students and the criteria used to classify students into successful and unsuccessful.

Based on the research results, we can make some recommendations for chemistry or science teaching: teachers who teach chemistry and other science subjects at different stages of education should strive to formulate the justification of the chosen SMRs appropriately in their teaching by including SMRs. The justification must combine the macroscopic and sub-microscopic levels of the chemical concept representation.

For unsuccessful students, it is useful that teachers, when observing the SMRs, gradually guide students to find key facts relevant to formulating an appropriate justification.

For further research, it will be necessary to carry deeper analyses of eye-tracker measures on an unknown task, as well as more tasks that also examine the other changing states of matter, information about the level of logical thinking of the students and their visual abilities, information about the way that SMRs were presented to them during the classes, etc. We will examine how future chemistry teachers, as well as those teachers who already teach chemistry and have extensive practical experience in teaching SMRs, explain the chosen SMR orally. The comparison of the results can aid in providing guidelines for

the proper training of future chemistry teachers.

Acknowledgement

This research was supported by the project 'Explaining effective and efficient problem solving of the triplet relationship in science concepts representations' (J5-6814), funded by the ARRS - Slovenian research agency.

6. References

1. I. Parchmann, R. Blonder, K. Broman, in: L. Leite, L. Dourado, A. S. Afonso, S. Morgado (Eds.): Contextualizing Teaching to Improve Learning the Case of Science and Geography, Nova Science Publishers, New York, United States of America, **2017**, pp. 25–39.
2. K. Broman, I. Parchmann, *Chem. Educ. Res. Pract.* **2014**, *15*, 516–529. DOI:10.1039/C4RP00051J
3. J. Majer, M. Slapničar, I. Devetak, *Acta Chim. Slov.* **2019**, *66*, 659–667. DOI:10.17344/acsi.2019.5087
4. M. Slapničar, I. Devetak, S. A. Glažar, J. Pavlin, *J. Balt. Sci. Edu.* **2017**, *16*, 308–323.
5. M. Slapničar, V. Tompa, S. A. Glažar, I. Devetak, *J. Balt. Sci. Edu.* **2018**, *17*, 620–632.
6. I. Devetak: Provision of high quality scientific knowledge through submicro-representations, Ljubljana, Univerza v Ljubljani, Pedagoška fakulteta. **2012**, pp. 13–16.
7. I. Devetak, M. Hajzeri, S. A. Glažar, J. Vogrinc, *Acta Chim. Slov.* **2010**, *57*, 904–911.
8. J. Trumbo, *Sci. Commun.* **1999**, *20*, 409–425. DOI:10.1177/1075547099020004004
9. H. K. Wu, J. S. Krajcik, E. Soloway, *J. Res. Sci. Teach.* **2001**, *38*, 821–842. DOI:10.1002/tea.1033
10. S. C. Chen, H. C. She, M. S. Hsiao, *Comput. Human. Behav.* **2015**, *53*, 169–180. DOI:10.1016/j.chb.2015.07.003
11. C. F. Wu, M. C. Chiang, *Comput. Educ.* **2013**, *63*, 28–42. DOI:10.1016/j.compedu.2012.11.012
12. A. H. Johnstone, *Sch. Sci. Rev.* **1982**, *64*, 377–379.
13. M. Heitzman, J. Krajcik, Urban Seventh-grader's Translations of Chemical Equations: What Parts of the Translation Process do Students Have Trouble? http://www.project2061.org/research/ccms/site.archive/documents/Translations_of_Chemical_Equations.pdf, (assessed: December 27, 2019).
14. R. Kozma, E. Chin, J. Russell, N. Marx, *J. Learn. Sci.* **2000**, *9*, 105–143. DOI:10.1207/s15327809jls0902_1
15. E. Adadan, F. Savasci, *Int. J. Sci. Educ.* **2011**, *34*, 513–544. DOI:10.1080/09500693.2011.636084
16. K. de Berg, *Chem. Educ. Res. Pract.* **2012**, *13*, 8–16. DOI:10.1039/C1RP90056K
17. A. I. Kern, N. B. Wood, G. H. Roehrig, J. Nyachwaya, *Chem. Educ. Res. Pract.* **2010**, *11*, 165–172. DOI:10.1039/C005465H
18. D. Özalp, A. Kahveci, *Chem. Educ. Res. Pract.* **2015**, *16*, 619–639. DOI:10.1039/C5RP00096C
19. I. Devetak, J. Vogrinc, S. A. Glažar, *Res. Sci. Educ.* **2009**, *39*, 157–179. DOI:10.1007/s11165-007-9077-2

20. V. Kind, Beyond appearances: students' misconceptions about basic chemical ideas, 2nd edition, <http://modeling.asu.edu/modeling/KindVanessaBarkerchem.pdf>, (assessed: December 27, 2019).
21. M. L. Chiu, M. H. Chiu, C. Y. Ho, *Proc. Natl. Sci. Counc.* **2002**, *12*, 91–99.
22. I. Devetak: *Explaining the latent structure of understanding submicrorepresentations in science*. Ph. D. Thesis, Ljubljana: University of Ljubljana. **2005**.
23. K. Adbo, K. S. Taber, *Int. J. Sci. Educ.* **2009**, *31*, 757–786. DOI:10.1080/09500690701799383
24. Y. Boz, *J. Sci. Educ. Tech.* **2006**, *15*, 203–213. DOI:10.1007/s10956-006-9003-9
25. H. Özmen, *Eurasian J. Phys. Chem. Educ.* **2013**, *5*, 81–90.
26. L. Löfgren, G. Hellden, *Int. J. Sci. Educ.* **2009**, *31*, 1631–1655. DOI:10.1080/09500690802154850
27. G. Tsitsipis, D. Stamovlasis, G. Papageorgiou, *Int. J. Sci. Educ.* **2010**, *32*, 987–1016. DOI:10.1080/09500690902893605
28. E. E. Olakanmi, *J. Balt. Sci. Edu.* **2015**, *14*, 627–640.
29. V. M. Williamson, M. R. Abraham, *J. Res. Sci. Teach.* **1995**, *32*, 521–534. DOI:10.1002/tea.3660320508
30. J. W. Russell, R. B. Kozma, T. Jones, J. Wykoff, N. Marx, J. Davis, *J. Chem. Educ.* **1997**, *74*, 330–334. DOI:10.1021/ed074p330
31. M. J. Sanger, *J. Chem. Educ.* **2000**, *77*, 762–766. DOI:10.1021/ed077p762
32. D. M. Bunce, D. Gabel, *J. Res. Sci. Teach.* **2002**, *39*, 911–927. DOI:10.1002/tea.10056
33. M. Barak, Y. J. Dori, *Sci. Educ.* **2005**, *89*, 117–139. DOI:10.1002/sce.20027
34. E. J. Yeziarski, J. P. Birk, *J. Chem. Educ.* **2006**, *83*, 954–960. DOI:10.1021/ed083p954
35. M. B. Nakhleh, *J. Chem. Educ.* **1992**, *69*, 191–196. DOI:10.1021/ed069p191
36. S. Eivazi, R. Bednarik, Predicting problem-solving behaviour and performance levels from visual attention data, https://pdfs.semanticscholar.org/25c0/b17194ce09f600c766867e8962e4ee4f7784.pdf?_ga=2.206226385.334794364.1575983244-1516362230.1550597977, (assessed: December 5, 2019).
37. K. L. Havanki, J. R. VandenPlas in: D. M. Bunce, R. S. Cole (Ed.): *Tools of Chemistry Education Research*, ACS Symposium Series, American Chemical Society, Washington DC, **2014**, pp. 191–218. DOI:10.1021/bk-2014-1166.ch011
38. K. Rayner, *Q. J. Exp. Psychol.* **2009**, *62*, 1457–1506. DOI:10.1080/17470210902816461
39. M. Tsai, H. Hou, M. Lai, W. Liu, F. Yang, *Comput. Educ.* **2011**, *58*, 375–385. DOI:10.1016/j.compedu.2011.07.012
40. B. B. Koning, H. K. Tabbers, R. M. J. P. Rikers, F. Paas, *Educ. Psychol. Rev.* **2009**, *2*, 113–140. DOI:10.1007/s10648-009-9098-7
41. G. Underwood, R. Radach, in: G. Underwood (Ed.): *Eye Guidance in Reading and Scene Perception*, Elsevier Science, Oxford, UK, **1998**, pp. 1–27. DOI:10.1016/B978-008043361-5/50002-X
42. K. Holmqvist, M. Nystrom, R. Andersson, R. Dewhurst, H. Jarodzka, H. in Van de Weijer, J. (2011). *Eye tracking: A comprehensive guide to methods and measures*. Oxford University Press, Oxford, UK, **2011**.
43. V. Ferik Savec, Š. Hrast, I. Devetak, G. Torkar, *Acta Chim. Slov.* **2016**, *63*, 864–873. DOI:10.17344/acsi.2016.2835
44. Timing guide for Tobii eye trackers and eye tracking software, **2010**. Tobii technology, <https://www.tobii.com/siteassets/tobii-pro/learn-and-support/design/eye-tracker-timing-performance/tobii-eye-tracking-timing.pdf>, (assessed: December 5, 2019).
45. H. J. Green, P. Lemaire, S. Dufau, *Acta Psychol.* **2007**, *125*, 257–278. DOI:10.1016/j.actpsy.2006.08.001
46. J. Hyönä, R. F. Jr. Lorch, J. K. Kaakinen, *J. Educ. Psychol.* **2002**, *94*, 44–55. DOI:10.1037/0022-0663.94.1.44
47. M. P. Pereira, M. E. M. Pestana, *Int. J. Sci. Educ.* **1991**, *13*, 313–319. DOI:10.1080/0950069910130309
48. A. T. Duchowski, *Eye tracking methodology*, Springer, London, UK, **2007**.
49. G. Torkar, M. Veldin, S. A. Glažar, A. Podlesek, *Eurasia J. Math. Sci. Technol. Educ.* **2018**, *14*, 2265–2276. DOI: 10.29333/ejmste/87119
50. J. Pavlin, S. A. Glažar, M. Slapničar, I. Devetak, *Chem. Educ. Res. Pract.* **2019**, *20*, 633–649. DOI: 10.1039/c8rp00189h
51. J. Pallant, *SPSS survival manual: A step by step guide to data analysis using SPSS*, Allen & Unwin, Crows Nest, Australia, **2011**. DOI:10.1039/C8RP00189H
52. J. Cohen, *Statistical power analysis for the behavioral sciences*, Lawrence Erlbaum Associates, Hillsdale, NJ, **1988**.
53. A. G. Harrison, D. F. Treagust, *Sci. Educ.* **2000**, *84*, 352–381. DOI:10.1002/(SICI)1098-237X(200005)84:3<352::AID-SCE3>3.0.CO;2-J
54. G. Nicoll, *Int. J. Sci. Educ.* **2001**, *23*, 707–730. DOI:10.1080/09500690010025012

Povzetek

V članku predstavljena raziskava se ukvarja z identifikacijo razlik med udeleženci raziskave, ki so uspešno oz. neuspešno utemeljili izbiro 3 D dinamične submikroskopske predstavitve (SMR) trdnega in tekočega agregatnega stanja vode ter zmrzovanja vode. Preučevane so bile tudi razlike v času trajanja fiksacij na izbranih interesnih področjih med njimi. V raziskavi je sodelovalo 79 udeležencev treh starostnih skupin. Podatki so bili zbrani s strukturiranim intervjujem, ki je vključeval računalniške zaslonske slike treh avtentičnih nalog. Naloga je vsebovala besedilo (problem ali vprašanje), fotografijo pojava na makroskopski ravni in SMR pojava. Metoda očesnega sledilca je bila uporabljena za merjenje fiksacij med reševanjem avtentičnih nalog na določenem interesnem področju. Rezultati kažejo, da so uspešni posamezniki pri utemeljitvah vključevali predvsem makroskopske in submikroskopske predstavitve izbranega pojma. Po vertikali izobraževanja narašča uspešnost izbire in pravilnost utemeljitve prevladujoče na submikroskopski ravni. Med uspešnimi in neuspešnimi učečimi se iste starostne skupine, se po večini ne pojavijo razlike v času trajanja fiksacij na izbranem interesnem področju (pravilni SMR). Potrebne so nadaljnje raziskave, s katerimi bo preučeno procesiranje informacij uspešnih in neuspešnih učečih se, pri reševanju različnih avtentičnih nalog s SMR.



Except when otherwise noted, articles in this journal are published under the terms and conditions of the Creative Commons Attribution 4.0 International License

Scientific paper

Cyanide-Bridged Polynuclear and One-Dimensional Fe^{III}-Mn^{III/II} Bimetallic Complexes Based-on Pentacyanoferrite(III) Building Block: Synthesis, Crystal Structures, and Magnetic Properties

Xiaoyun Hao,¹ Yong Dou,¹ Tong Cao,¹ Lan Qin,¹ Zhen Zhou,^{1,*} Lu Yang,¹ Dacheng Li,² Qingyun Liu,³ Yueyun Li¹ and Daopeng Zhang^{1,*}

¹ College of Chemistry and Chemical Engineering, Shandong University of Technology, Zibo 255049, China.

² College of Chemical Engineering, Liaocheng University, Liaocheng 252059, China.

³ College of Chemical and Environmental Engineering, Shandong University of Science and Technology, Qingdao 266510, PR China.

* Corresponding author: E-mail: dpzhang73@126.com

Received: 02-14-2020

Abstract

In this contribution, based-on the structurally confirmed pentacyanometallate (PPh₄)₂[Fe(CN)₅(imidazole)]·(imidazole)·H₂O (1) and the manganese compounds [Mn(L)(H₂O)₂]ClO₄ (L = N,N-ethylenebis(3-methoxysalicylideneimine) or [Mn(MAC)(H₂O)Cl]ClO₄ (MAC = 2,13-dimethyl-3,6,9,12,18-pentaazabicyclo-[12.3.1]octadeca-1(18),2,12,14,16-pentaene), two new cyanide-bridged bimetallic Fe^{III}-Mn^{III/II} complexes {[Mn(L)(H₂O)]₃[Fe(CN)₅(imidazole)]}(ClO₄) (2) and {[Mn(MAC)][Fe(CN)₅(imidazole)]·CH₃OH}_n (3) were successfully synthesized and characterized by elemental analysis, IR spectroscopy and X-ray structure determination. Single X-ray diffraction analysis reveals the cationic FeMn₃ tetranuclear entity for complex 2, which can be further assembled into supramolecular 1D ladder-like double chain by the strong intermolecular hydrogen bond interactions. For complex 3, it can be structurally characterized as neutral one-dimensional linear single infinite chain. The magnetic investigations discover the ferromagnetic coupling between the Fe^{III}-Mn^{III} units in complex 2 and the antiferromagnetic coupling in complex 3 between the Fe^{III}-Mn^{II} units through the bridging cyanide group, respectively.

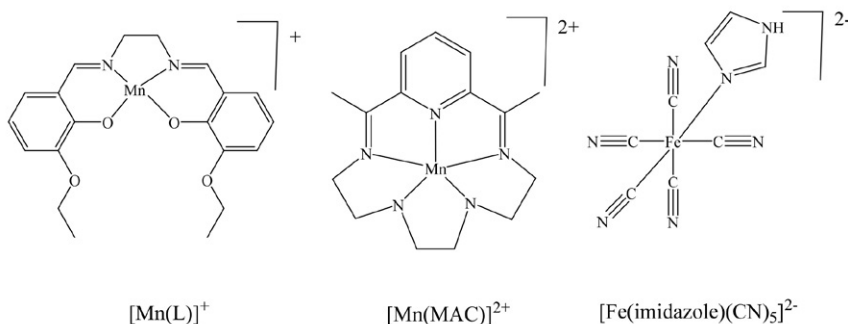
Keywords: Pentacyanoferrite; cyanide-bridged; crystal structure; magnetic property

1. Introduction

In the past several decades, due to their great potential in high-tech fields including quantum compute, information storage, etc., more and more attention have been paid to the research of the molecular-based magnetism.^{1–8} As one of the most important building block for the rational construction of molecular magnetic systems, cyanide-bridged magnetic complexes have all along received intense attention since their readily controlled molecular topological structures and theoretically predicted magnetic properties.^{9–13} Up to now, a great deal of cyanide-bridged molecular materials structural ranging from 0-dimensional cluster to three-dimensional beautiful networks have been rationally designed and structurally characterized.

Among those, some systems with interesting magnetic properties, such as single chain magnets (SCMs) and single molecule magnets (SMMs),^{14–20} spin crossover materials,^{21–23} high-T_c magnets,^{24–25} photomagnetic materials,^{26–29} ferromagnetic materials,³⁰ chirality magnets^{31–33} et al, have been detailed magnetically studied.

One of the most successful strategies used to prepare cyanide-bridged magnetic complexes^{34–35} is based on the assemble reactions of the decorated polycyanometallates [M(L)(CN)_x]ⁿ⁻ ((M = Fe, Cr, W, Mo, Mn, Ru; x = 1–8, L = mono- or multi-dentate organic ligand) with other counterpart paramagnetic metal compounds. Because the blocking organic ligand(s) in either the cyano precursors or the counterpart assemble segments can contribute obvious steric effect and therefore efficiently lower the dimen-



Scheme 1. The starting materials used in this paper.

sionality of the target product, many low-dimensional $[M(L)(CN)_x]^{n-}$ -based complexes have been expectedly obtained.^{36–38} Among all the polycyanoferrite(III) building blocks, the pentacyanoferrite(III) $[Fe(L)(CN)_5]^{2-}$ (L = monodentate ligand) precursors have been comparatively limited employed in cyanide-bridged molecule magnetism field.^{39–43} In this paper, we are focusing on the designed preparation of new cyanide-bridged magnetic complexes with the exploitation of pentacyanoferrite(III) compound $[Fe(CN)_5(imidazole)]^{2-}$ as building block and manganese compounds as assemble segments (Scheme 1). The synthesis, structural characterization and magnetic study for the two new obtained $Mn^{II/III}$ - Fe^{III} bimetallic magnetic complexes $\{[Mn(L)(H_2O)]_3[Fe(CN)_5(imidazole)]\}(ClO_4)$ (**2**) and $\{[Mn(MAC)][Fe(CN)_5(imidazole)] \cdot CH_3OH\}_n$ (**3**), as well as the structure of the cyano precursor $(PPh_4)_2[Fe(CN)_5(imidazole)] \cdot (imidazole) \cdot H_2O$ (**1**), will be presented in the current contribution.

2. Experimental Section

2.1. General Procedures and Materials

All the reactions were carried out at room temperature under air atmosphere with the solvents and chemicals used reagent grade without additional purification. $[Ca(imidazole)(H_2O)][Fe(CN)_5(imidazole)]$ was prepared as black crystals according to the literature method for $[Ca(1-CH_3im)(H_2O)][Fe(CN)_5(1-CH_3im)]$.⁴¹ $[Mn(L)(H_2O)_2]ClO_4$ ⁴² (L = *N,N*-ethylenebis(3-methoxysalicylideneimine)) and $[Mn(MAC)(H_2O)Cl]ClO_4$ ⁴⁴ (MAC = 2,13-dimethyl-3,6,9,12,18-pentaazabicyclo-[12. 3.1]octadeca-1(18),2,12,14,16-pentaene) were available from the previous works.

Caution! KCN is hypertoxic and hazardous. Perchlorate salts with organic ligands are potentially explosive. They should be handled in small quantities with care.

Synthesis of $(PPh_4)_2[Fe(CN)_5(imidazole)] \cdot (imidazole) \cdot H_2O$ (**1**):

$[Ca(imidazole)(H_2O)][Fe(CN)_5(imidazole)]$ (1.9 g, 5 mmol) was dissolved in water (20 ml), and PPh_4Br (4.0 g,

10 mmol) was added to the solution. Then, the mixture was stirred in the dark overnight before the yellow powder formed was filtered out. Yield: 3.57g (70%). Recrystallization of the powder in MeOH afforded yellow single crystals. Main IR bands(cm^{-1}): 2110, 2121(s, $\nu_{C=N}$). The elemental analysis (experimental and theoretical) and some physical properties are given in Table 1.

Synthesis of $\{[Mn(L)(H_2O)]_3[Fe(CN)_5(imidazole)]\}(ClO_4)$ (**2**):

The complex was prepared by using three layers diffusion procedure. A solution containing $(PPh_4)_2[Fe(CN)_5(imidazole)] \cdot (imidazole) \cdot H_2O$ (102 mg, 0.10 mmol) dissolved in 5 mL H_2O was laid in the bottom of a tube, and then carefully upon addition of a mixture solvent of water and methanol (5 mL) with a ratio of 1:1. Finally, a solution of $[Mn(L)(H_2O)_2]ClO_4$ (112 mg, 0.2 mmol) in 5 mL of CH_3OH was carefully added to the top of the mixture solvent layer above formed. The dark-brown crystal appeared in the middle of the tube was filtered out 2–3 weeks later, washed by methanol and dried in air. $\{[Mn(L)(H_2O)]_3[Fe(CN)_5(imidazole)]\}(ClO_4)$ (**2**): Yield: 49.6 mg (44.6%). Main IR bands(cm^{-1}): 2150 (s, $\nu_{C=N}$), 2122 (s, $\nu_{C=N}$), 1620 (m, $\nu_{C=N}$), 1100 (s, $\nu_{Cl=O}$). The elemental analysis (experimental and theoretical) and some physical properties are given in Table 1.

Synthesis of $\{[Mn(MAC)][Fe(CN)_5(imidazole)] \cdot CH_3OH\}_n$ (**3**):

A solution of $(PPh_4)_2[Fe(CN)_5(imidazole)] \cdot (imidazole) \cdot H_2O$ (102 mg, 0.10 mmol) dissolved in 5 mL H_2O was laid in the bottom of a tube, and then carefully upon addition of a mixture solvent of water and methanol (5 mL) with a ratio of 1:1. Finally, a solution of $[Mn(MAC)(H_2O)Cl]ClO_4$ (48 mg, 0.1 mmol) in 5 mL of CH_3OH was carefully added to the top of the mixture solvent layer above formed. The yellow crystal appeared in the middle of the tube 2–3 weeks later, which was filtered out, washed by methanol and dried in air. $\{[Mn(MAC)][Fe(CN)_5(imidazole)] \cdot CH_3OH\}_n$ (**3**): Yield: 43.6 mg, 70.9%. Main IR bands (cm^{-1}): 2150, 2120(s, $\nu_{C=N}$), 1630 (m, $\nu_{C=N}$). The elemental analysis (experimental and theoretical) and some physical properties are given in Table 1.

Table 1. The elemental analysis (experimental and theoretical) and some physical properties for complexes 1–3.

Formula	Elemental Analysis(Cal.)	Elemental Analysis(Found)	Color	Solubility	Melting Point
C ₅₉ H ₅₀ N ₉ O P ₂ Fe	C, 69.55; H, 4.95; N, 12.37	C, 69.62; H, 5.01; N, 12.31	Yellow	MeOH	> 573K
C ₆₉ H ₈₀ N ₁₃ O ₂₀ ClFeMn ₃	C, 49.70; H, 4.84; N, 10.92.	C, 49.77; H, 4.91; N, 11.00	Dark- Brown	MeOH DMF	> 573K
C ₂₄ H ₃₁ N ₁₂ OFeMn	C, 46.92; H, 5.09; N, 27.36	C, 46.86; H, 5.16; N, 27.47	Yellow	MeOH DMF	> 573K

2. 2. X-ray Data Collection and Structure Refinement

Single crystals with suitable dimensions for complexes 1–3 for X-ray diffraction analysis were mounted on the glass rod and the crystal data were collected on a Bruker APEX II CCD area-detector with a Mo K α sealed tube ($\lambda = 0.71073 \text{ \AA}$) at room temperature using a ω scan mode. The structures were solved by direct method and expanded using Fourier difference techniques with the SHELX-TL-2018/3 program package.⁴⁵ While all the hydrogen atoms were introduced as fixed contributors, the non-hydrogen atoms were refined anisotropically with anisotropic displacement coefficients. Hydrogen atoms except some ones from the solvent molecules were assigned isotropic displacement coefficients $U(H) = 1.2U(C)$ or $1.5U(C)$ and their coordinates were allowed to ride on their respective carbon/nitrogen atoms using SHELXL 2018/3. For the solvent H atoms, they were refined isotropically with fixed U values, during which the DFIX command was used to rationalize the bond parameter. The CCDC 1978692–1978694 for complexes 1–3 contain the

supplementary crystallographic data for this paper. These data can be obtained free of charge from the Cambridge Crystallographic Data Centre via www.ccdc.cam.ac.uk/data_request/cif. Details of the crystallographic parameter, data collection, and refinement are summarized in Table 2.

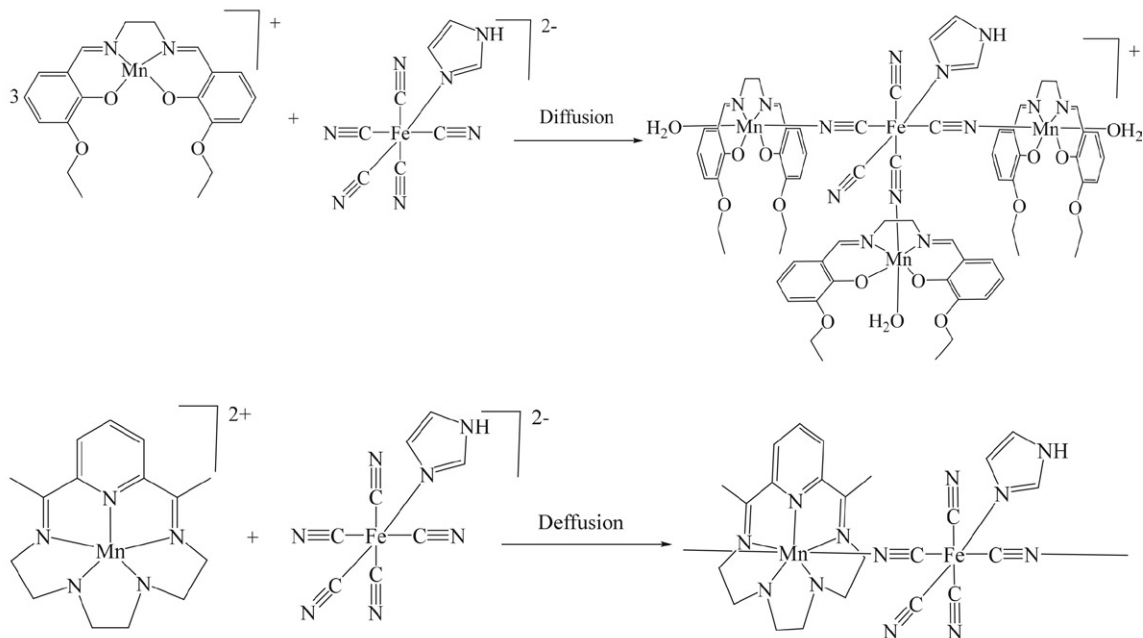
3. Results and Discussion

3. 1. Synthesis

With comparison to the widely used hexacyanoiron(III) in cyanide-bridged molecular magnetism field, the pentacyanoiron(III) has been relatively less used to assemble magnetic complex, and only several pentacyanoiron(III)-based heterometallic magnetic systems have been reported.^{39–42, 45} By using the three-layers diffusion method, which has been shown to be a powerful way for growing single crystals,^{43–44} one cationic tetranuclear Fe^{III}Mn^{III}₃ entity and one neutral one-dimensional Fe^{III}Mn^{II} complex have been successfully prepared from the reactions of $[\text{Fe}(\text{imidazole})(\text{CN})_5]^{2-}$ and the manganese

Table 2. Details of the crystal parameters, data collection, and refinement for compounds 1–3.

	1	2	3
Formula	C ₅₉ H ₅₀ N ₉ O ₂ Fe	C ₆₉ H ₈₀ N ₁₃ O ₂₀ ClFeMn ₃	C ₂₄ H ₃₁ N ₁₂ OFeMn
Fw	1018.87	1667.58	614.4
Crystal system	monoclinic	monoclinic	Triclinic
Space group	P21/c	C 2/c	P-1
a/ \AA	12.8623(7)	45.062(5)	10.883(3)
b/ \AA	23.5860(13)	13.5410(14)	11.521(3)
c/ \AA	18.4068(9)	29.308(4)	13.284(3)
α/deg	90	90	90.578(4)
β/deg	106.7580(10)	116.647(4)	105.693(4)
γ/deg	90	90	114.939(4)
Z	4	8	2
V/ \AA^3	5346.9(5)	15984(3)	1439.1(6)
F(000)	2124	6904	636
θ/deg	1.65–25.01	1.59–25.01	1.61–25.01
Goodness-of-fit	1.016	1.019	1.046
R ₁ [$I > 2\sigma(I)$]	0.0459	0.0659	0.0692
wR ₂ (all data)	0.1166	0.2125	0.2086



Scheme 2. The preparation diagram for the complex 2 and 3.

Schiff-base $[\text{Mn}(\text{L})]^+$ or the macrocyclic $[\text{Mn}(\text{MAC})]^{2+}$ compound, respectively (Scheme 2).

The cyanide-bridged heterometallic complexes have been characterized by IR spectroscopy. Compared to the cyanide precursor with only one peak at about 2125 cm^{-1} , two sharp peaks in the IR spectra of complexes 2 and 3 due to the cyanide-stretching vibration ^[42, 43] were observed at about 2120 and 2160 cm^{-1} , respectively, indicating the presence of bridging and nonbridging cyanide ligands in these complexes. For complex 2, the strong peak centered at 1100 cm^{-1} is attributed to the free ClO_4^- anions.

3. 2. Crystal Structure Descriptions

The crystal structure of the cyano precursor:

The selected bond lengths and angles for complex 1 are given in Table 3. The molecular structure and the H-bond resulted 1D supramolecular structure are shown in

Figures 1 and 2, respectively. The asymmetric unit of $(\text{PPh}_4)_2[\text{Fe}(\text{CN})_5(\text{imidazole})]\cdot(\text{imidazole})\cdot\text{H}_2\text{O}$ (1), which crystallizes in monoclinic space group $\text{P}2_1/c$, is comprised

Table 3. Selected bond lengths (Å) and angles (°) for complex 1.

Complex 1			
Fe(1)-N(1)	2.002(2)	P(1)-C(12)	1.793(3)
Fe(1)-C(4)	1.951(3)	P(1)-C(18)	1.786(3)
Fe(1)-C(5)	1.949(3)	P(1)-C(24)	1.789(3)
Fe(1)-C(6)	1.925(3)	P(1)-C(30)	1.797(3)
Fe(1)-C(7)	1.951(3)	P(2)-C(36)	1.789(3)
Fe(1)-C(8)	1.958(3)	P(2)-C(42)	1.797(3)
Fe(1)-C(4)-N(3)	179.2(3)	P(2)-C(48)	1.793(3)
Fe(1)-C(5)-N(4)	175.4(3)	P(2)-C(54)	1.787(3)
Fe(1)-C(6)-N(5)	176.3(3)	Fe(1)-C(8)-N(7)	178.4(2)
Fe(1)-C(7)-N(6)	177.9(3)		

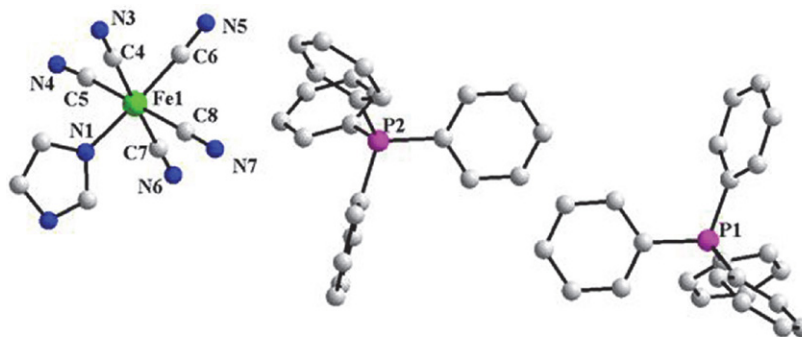


Figure 1. The molecular structure of complex 1. The solvent molecule, the co-crystallized imidazole and all the H atoms have been omitted for clarity.

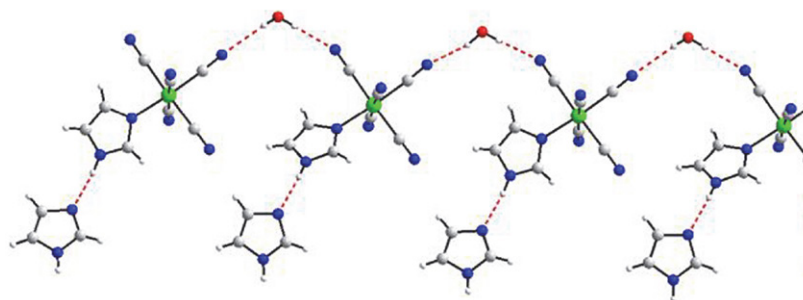


Figure 2. The H-bond resulted 1D anionic supramolecular structure of the complex 1. The balanced $[\text{PPh}_4]^+$ cations have been omitted for clarity.

Table 4. The selected hydrogen bond parameters (\AA , $^\circ$) for complexes 1–3.

Complex 1			
D-H...A	d(H...A)	d(D...A)	$\angle(\text{DHA})$
O1-H1A...N3	2.116	2.941	175.22
O1-H1B...N5#1	2.317	3.042	138.02
N2-H2...N9#2	1.988	2.820	162.61
N8-H8...N5#3	2.419	3.174	146.94
Complex 2			
O1-H1A...O8#1	2.257	3.029	153.15
O1-H1B...O7#1	2.435	3.119	142.07
O10-H10A...O5#1	2.279	3.033	151.02
O10-H10B...O3#1	2.155	2.984	161.87
O15-H15A...O12#1	2.461	3.022	125.88
O10-H15B...O14#1	2.416	3.022	129.69
Complex 3			
O1-H1A...N8	2.390	2.804	110.57

Symmetry transformations used to generate equivalent atoms: #1 $x, -y+1/2, z+1/2$; #2 $x, -y+1/2, z+1/2$; #3 $x+1, y, z$ (1); #1 $x, -y, z-1/2$ (2).

by five moieties: an anionic Fe complex, one water molecule, one imidazole molecule and two tetraphenylphosphonium cations. The $[\text{Fe}(\text{CN})_5(\text{imidazole})]^{2-}$ anion contains a low-spin Fe^{III} center coordinated by one imidazole unit and five CN units, in which four CN groups occupy the four equatorial positions with the fifth CN group collinearly axial with the imidazole group. The Fe–C bond lengths in a narrow range 1.925(3)–1.958(3) \AA are slightly shorter than the Fe–N_{imidazole} bond with the value 2.002(2) \AA . The Fe–C \equiv N angles are within the range of 175.4(3)–179.3(3) $^\circ$, indicating the almost linear conformation of these atoms. Under the O–H...N H-bond interactions from the host anion and the co-crystallized water molecules (Table 4), the $[\text{Fe}(\text{CN})_5(\text{imidazole})]^{2-}$ moieties are linked into 1D supramolecular single chain structure (Figure 2).

3. 3. The Crystal Structure of the Complex 2

The cationic tetranuclear structure and the one-dimensional ladder-like double-chain structure formed by

the intermolecular hydrogen bonds for complex 2 are shown in Figures 3 and 4, respectively. The selected important bond parameters for complex 2 are listed in Table 5.

The complex 2 is a neutral tetranuclear cluster comprised by the cationic FeMn_3 unit and an additional disordered ClO_4^- as counter anion. In the FeMn_3 core, $[\text{Fe}(\text{imidazole})(\text{CN})_5]^{2-}$ acting as a *mer-m*₃-coordinating-donor building block is coordinated by three $[\text{Mn}(\text{L})(\text{H}_2\text{O})]^+$ through three cyanide groups and forming a *T*-like arrangement. Each $[\text{Mn}(\text{L})(\text{H}_2\text{O})]^+$ moiety has an elongated octahedral geometry with Jahn-Teller distortion along the $(\text{H}_2\text{O})\text{-Mn-N}_{\text{cyanide}}$ axis, in which the four equatorial positions are coordinated by N_2O_2 unit from the Schiff-base ligand and the two axial ones occupied by one N atom of the bridge cyanide group and one O atom from the H_2O molecule. The average $\text{Mn-N}_{\text{Schiff-base}}/\text{O}_{\text{Schiff-base}}$ bond lengths are 1.988(5) \AA and 1.874(3) \AA , which are obviously shorter than the $\text{Mn-N}_{\text{cyanide}}$ 2.245(5) \AA and $\text{Mn-O}_{\text{water}}$ 2.298(4) \AA . The $\text{Mn}(1)\text{-N}(1)\text{-C}(1)$ angle (156.5(4) $^\circ$) is slightly bigger than the other two $\text{Mn-N}\equiv\text{C}$ angles with values of 146.(4) $^\circ$ and 149.2(4) $^\circ$. The intramolecular $\text{Mn}^{\text{III}}\text{-Fe}^{\text{III}}$ distances through bridge-cyanides are very close to each other with values 5.100, 5.100 and 5.154 \AA , respectively, which are slightly longer than the shortest intermo-

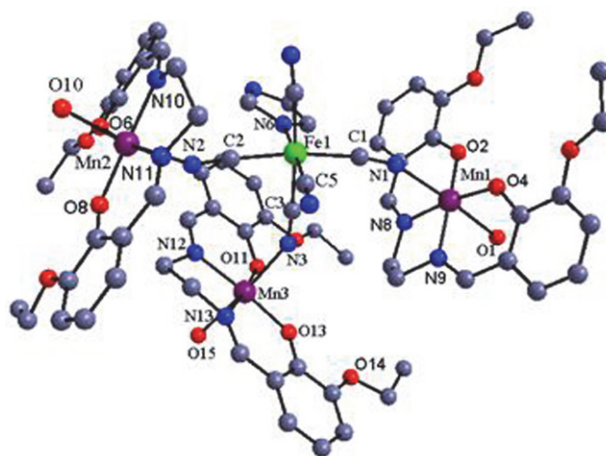
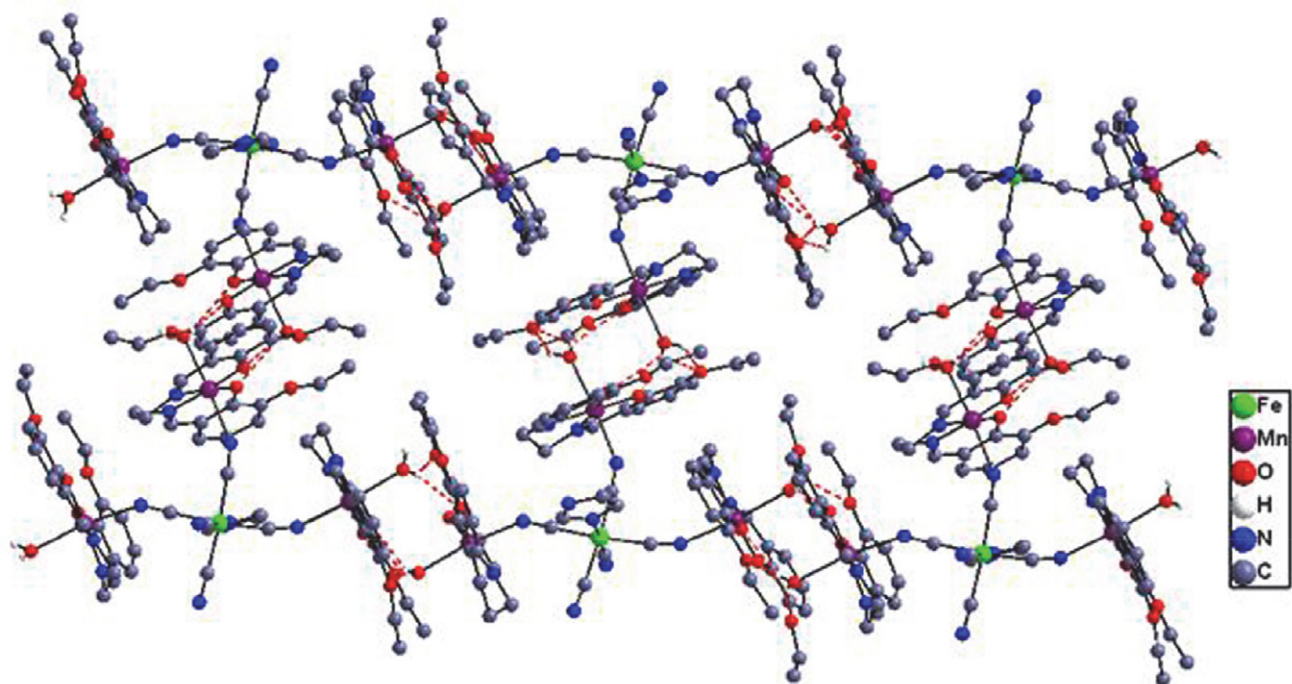


Figure 3. The cationic crystal structure of complex 2. All H atoms and the counter ClO_4^- anion have been omitted for clarity.

Table 5. Selected bond lengths (Å) and angles (°) for complexes 2–3.

Complex 2					
Fe(1)-C(1)	1.941(5)	Mn(1)-O(2)	1.889(3)	Mn(2)-O(8)	1.871(3)
Fe(1)-C(2)	1.928(5)	Mn(1)-O(4)	1.863(4)	Mn(2)-N(2)	2.247(4)
Fe(1)-C(3)	1.914(5)	Mn(2)-O(6)	1.873(3)	Mn(2)-N(10)	1.986(4)
Fe(1)-C(4)	1.958(6)	Mn(1)-N(1)	2.253(5)	Mn(2)-N(11)	1.982(4)
Fe(1)-C(5)	1.922(6)	Mn(1)-N(8)	1.996(5)	Mn(2)-O(10)	2.273(3)
Fe(1)-N(6)	1.986(4)	Mn(1)-N(9)	1.980(5)	Mn(1)-O(1)	2.336(4)
Mn(1)-N(1)-C(1)		156.1(4)	Mn(2)-N(2)-C(2)		146.4(4)
Mn(3)-N(3)-C(3)		149.1(4)	Fe(1)-C(1)-N(1)		171.1(5)
Fe(1)-C(2)-N(2)		175.3(5)	Fe(1)-C(3)-N(3)		175.9(5)
Fe(1)-C(4)-N(4)		175.3(5)	Fe(1)-C(5)-N(5)		176.5(5)
C(1)-Fe(1)-C(2)		172.0(2)	N(3)-Mn(3)-O(15)		175.7(2)
N(2)-Mn(2)-O(10)		170.6(1)	N(1)-Mn(1)-O(1)		174.3(1)
Complex 3					
Fe(1)-C(1)	1.936(5)	Fe(2)-C(7)	1.946(6)	Mn(1)-N(1)	2.199(5)
Fe(1)-C(2)	1.941(7)	Fe(2)-C(8)	1.939(6)	Mn(1)-N(6)	2.220(5)
Fe(1)-C(3)	1.958(6)	Fe(2)-C(9)	1.940(6)	Mn(1)-N(11)	2.251(5)
Fe(1)-N(4)	1.958(6)	Fe(2)-N(9)	1.940(6)	Mn(1)-N(12)	2.294(4)
Mn(1)-N(13)	2.299(4)	Mn(1)-N(14)	2.242(5)		
Fe(1)-C(1)-N(1)		179.3(5)	Fe(2)-C(7)-N(6)		177.1(5)
Fe(1)-C(2)-N(2)		178.9(6)	Fe(2)-C(8)-N(7)		179.8(6)
Fe(1)-C(3)-N(3)		173.2(9)	Fe(2)-C(9)-N(8)		176.5(11)
Mn(1)-N(1)-C(1)		161.7(5)	Mn(1)-N(12)-C(16)		112.0(4)
Mn(1)-N(6)-C(7)		152.6(4)	Mn(1)-N(12)-C(17)		110.8(4)
Mn(1)-N(11)-C(13)		123.9(5)	Mn(1)-N(13)-C(18)		115.1(5)
Mn(1)-N(11)-C(15)		116.6(4)	Mn(1)-N(13)-C(19)		109.6(3)

**Figure 4.** One-dimensional double-chain structure of complex 2 formed by intermolecular hydrogen-bond interactions. All the H atoms except those used to form hydrogen bonds and the balance ClO_4^- have been omitted for clarity.

lecular metal-metal separation. Because of the excellent encapsulation ability of the O_4 compartment for the water molecule, one-dimensional ladder-like double chain structure is formed under the help of the intermolecular H-bond interactions (Table 3) between the O_{H_2O} atoms and the O atoms of the Schiff-base ligand.

3. 4. The Crystal Structure of the Complex 3

The asymmetry binuclear unit and 1D neutral chain structure of complex 3 is presented in Figure 5. The important bond parameters are given in Table 5. As can be found, complex 3 possesses one-dimensional neutral single chain structure comprising of the repeating $[-NC-Fe(imidazole)(CN)_3-CN-Mn(MAC)-]$ units. In this complex, each $[Fe(imidazole)(CN)_5]^{2-}$ unit, functioning as bidentate ligand through its two cyanide groups in *trans* position, connects the Mn(II) ions of two independent macrocyclic manganese units. Similar to that in compounds 1 and 2, the coordination geometry of the Fe atom is also a slightly distorted octahedral. As listed in Table 5, the bond angle of $Fe-C\equiv N$ in the range of $171.1(5)$ – $176.5(5)^\circ$ clearly indicates that the three atoms are in a good linear configuration. The Mn^{II} ion displays the hep-

ta-coordinates mode and involved in a pentagonal-bipyramidal geometry with the macrocyclic ligand forming the equatorial plane. The five equatorial positions are occupied by N_5 unit from the macrocyclic ligand, while the axial positions are occupied by two N atoms of the bridging cyanide groups. The $Mn-N_{MAC}$ distances within the range 2.196 – 2.299 Å are with no conspicuous with the $Mn-N_{cyanide}$ bond lengths ($2.199(5)$ and $2.220(5)$ Å), indicating the only slightly distorted pentagonal-bipyramidal geometry of the Mn(II) ion. With comparison to the $Fe-C\equiv N$ angle distributed in a very narrow range of $179.3(5)$ – $177.1(5)^\circ$, the bridging cyanide ligands coordinated to the Mn(II) ions in a bent fashion with the $Mn-N\equiv C$ angles are $152.6(4)$ and $161.7(5)^\circ$, respectively.

3. 5. The Magnetic Properties of Complexes 2 and 3

The temperature dependences of the $c_m T$ product per $Fe^{III}Mn^{III}_3$ and $Fe^{III}Mn^{II}$ unit for 2 and 3 measured from 2 to 300 K under an applied magnetic field of 2000 Oe are shown in Figures 6 and 7. The $c_m T$ value at room temperature is 9.11 emu K mol $^{-1}$ ($\mu_{eff} = 8.57$ BM) for 2 and 4.33 emu K mol $^{-1}$ ($\mu_{eff} = 5.91$ BM) for 3, which are slightly

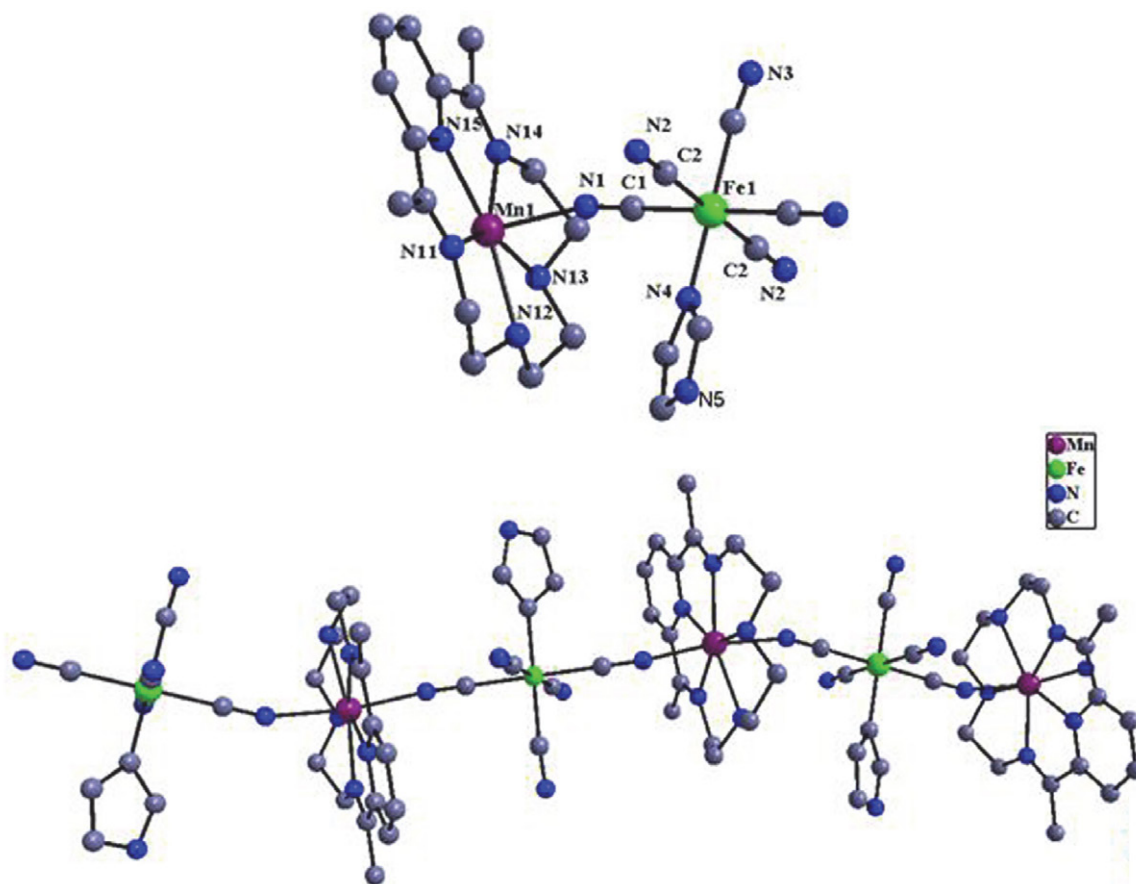


Figure 5. Asymmetry neutral unit and 1D neutral chain structure of complex 3. All the hydrogen atoms and solvent molecules have been omitted for clarity.

lower than the spin only value of 9.375/4.75 emu K mol⁻¹ for uncoupled three high spin Mn(III) ($S = 2$)/one high spin Mn(II) ($S = 5/2$) and one low spin Fe(III) ($S = 1/2$) based on $g = 2.00$, respectively. For these two complexes, the $c_m T$ values maintains nearly constant until the temperature lowering to 20 K for 2 and 50 K for 3. After that, the $c_m T$ value for complex 2 starts to increase smoothly and reaches its highest value 10.12 emu K mol⁻¹, and then decreases rapidly to the lowest value about 0.87 emu K mol⁻¹ at 2 K. The suddenly decrease for the $c_m T$ value in the low temperature range can maybe attributed to the comparable strong intermolecular H-bond interaction and/or the zero field splitting of the Mn(III) ion. Different from that for complex 2, the $c_m T$ value of complex 3 presents the obvious decreasing tendency from 50 K, and attains its minimum value 2.19 emu K mol⁻¹ at 2 K, implying the different coupling nature in these two complexes. The magnetic susceptibilities of 2 and 3 conform well to Curie-Weiss law and give the positive Weiss constant $q = 1.87$ K, Curie constant $C = 8.90$ emu K mol⁻¹ for 2 and negative $q = -1.90$ K, $C = 4.54$ emu K mol⁻¹ for 3. On the basis of the Weiss constant and with the combination of change tendency of $c_m T$ - T curves, the overall ferromagnetic magnetic coupling between Fe(III) and Mn(III) ions in complex 2 and antiferromagnetic coupling between Fe(III) and Mn(II) ion in 3 can be concluded.

In view of the situation that the three Mn-N≡C-Fe bridges are structurally independent and the coordination environment of the three Mn(III) ions are not completely same to each other with the Mn-N≡C angles 146.4(4)–156.1(4)° and the Mn-N_{CN} bond lengths 1.980(5)–2.253(5) Å, the simulation of the magnetic susceptibility for this compound should be based on three different J values ($J_1 \neq J_2 \neq J_3$), where the three J values represent the Mn(1)...Fe(1), Mn(2)...Fe(1) and Mn(3)...Fe(1) interactions through cyanide bridges, respectively. On the other hand, according to the method successfully employed to simu-

late the magnetic susceptibilities of 1D chain compound with alternating spins 1/2 and 2,^{30b} the one-dimensional chain structure of the complex 3 can be considered as isotropic Heisenberg chain containing alternating spins 1/2 and 5/2 with two antiferromagnetic exchange interactions J_1 and J_2 . In this case, the magnetic susceptibility of this complex can be calculated rationally based on a closed ring cluster model consisting of five 1/2–5/2 spin pairs,

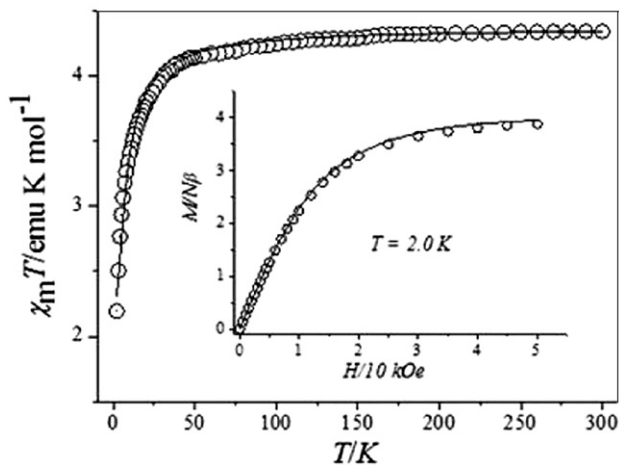


Figure 7. Temperature dependence of $c_m T$ of complex 3 (the solid line represents the best fit based on the parameters discussed in the text). Inset: Field dependence of magnetization at 2 K (the dotted line is the Brillouin curve for antiferromagnetically coupled Fe(III) and Mn(II) ions with $g = 2.0$).

Scheme 4.

Evaluation of the exchange coupling between the iron(III) ion and manganese(III/II) ions bridged by cyanide group in complexes 2 and 3 are carried out by MAGPACK program.⁴⁷ The best-fit parameters obtained are $J_1 = 1.12$, $J_2 = 1.65$, $J_3 = 0.91$ cm⁻¹, $D = -1.81$ cm⁻¹, $g = 2.02$, R

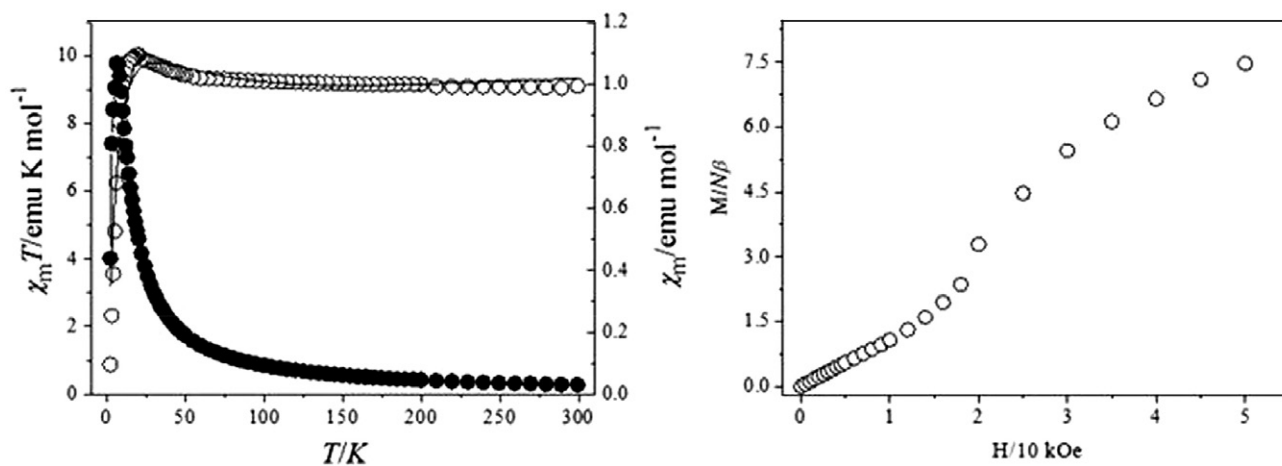
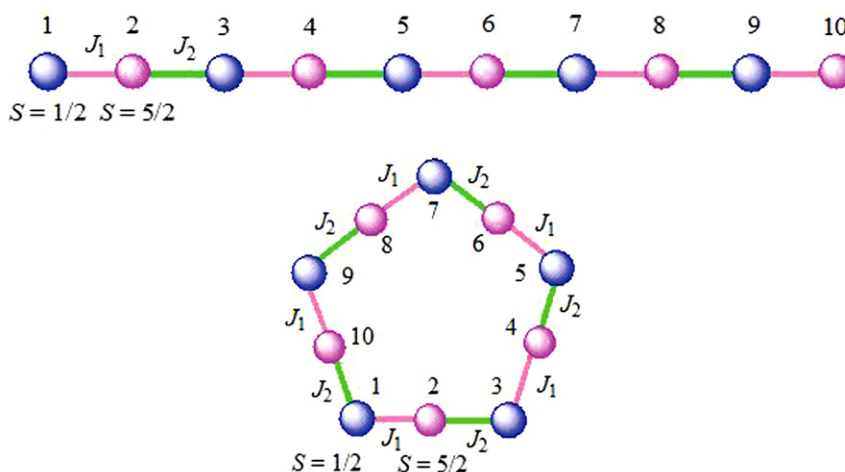


Figure 6. Left: The $c_m T$ - T (the solid line represents the best fit based on the parameters discussed in the text) and $c_m T$ curve for complex 2. Right: The field-dependent magnetization for complex 2.



Scheme 4. The magnetic simulation model for the complex 3.

$= \Sigma(c_{\text{obsd}}T - c_{\text{cald}}T)^2 / \Sigma(c_{\text{obsd}}T)^2 = 1.61 \times 10^{-5}$ for complex 2 and $J_1 = -1.34$, $J_2 = -0.54(1) \text{ cm}^{-1}$, $g = 1.99$, $R = 3.01 \times 10^{-5}$ for complex 3, respectively. All the theoretical fitting results are comparable to those found in the previously reported cyanide-bridged $\text{Fe}^{\text{III}}\text{-Mn}^{\text{III/II}}$ complexes.^{42–44, 48} The field-dependent magnetizations measured up to 50 kOe at 2 K for complexes 2 and 3 are shown in Figure 6 and the inset of Figure 7, respectively. The field-dependent magnetization curve for complex 2 has a sigmoid shape, implying maybe the metamagnetic behavior: The magnetization first increases slowly with increasing magnetic field until 20 kOe because of the relatively strong intermolecular hydrogen bond interaction, then increases abruptly for a phase transition at about 20 kOe, and finally attains the highest value about $7.45 N\beta$, which is slightly higher than the saturated value for three Mn(III) ion ($S = 2$) and one low spin Fe(III) ion ($S = 1/2$). For complex 3, the magnetization quickly increases with the field increasing until about 15 kOe, then increases smoothly up to about $3.9 N\beta$ until 50 kOe. This data is very close to the saturated value of $4.0 N\beta$ but obviously lower than the value of uncoupled low spin Fe(III) and Mn(II) based on $g = 2.0$, confirming again the overall antiferromagnetic coupling interaction between Fe(III) and Mn(II) ions bridged by cyanide group.

4. Conclusion

In summary, two new heterobimetallic cyanide-bridged complexes have been prepared with pentacyanoiron(III) as building block and manganese(III/II) compounds as the counterpart assemble segment. The single crystal X-ray analysis revealed the cationic tetranuclear FeMn_3 entity or one-dimensional infinite chain structure, respectively. For the polynuclear cluster, it can be self-complementary through coordinated aqua ligand from one complex and the free O_4 compartment from the neighboring complex, therefore giving interesting supramolecular

one-dimensional ladders. The experimental and theoretical investigation on their magnetic properties disclose the ferro- or antiferromagnetic coupling in cyanide-bridged $\text{Fe}^{\text{III}}\text{-Mn}^{\text{III}}$ or $\text{Fe}^{\text{III}}\text{-Mn}^{\text{II}}$ units, respectively. The present results can further enrich the pentacyanometallate-based molecule magnetic system, which is helpful for fully discover the magneto-structural relation from the molecule magnetism.

Acknowledgement

We are very thankful for the support from the National Nature Science Foundation of China (21671121) and Natural Science Foundation of Shandong Province (grant No. ZR2018BB002).

5. References

- M. Andruh, *Chem. Commun.* **2018**, 54, 3559–3577. DOI:10.1039/C8CC00939B
- B. M. Pires, F. E. Galdino, J. A. Bonacin, *Inorg. Chim. Acta* **2017**, 466, 166–173. DOI:10.1016/j.ica.2017.06.003
- F. Liu, C. L. Gao, Q. Deng, X. Zhu, A. Kostanyan, R. Westerström, A. A. Popov, *J. Am. Chem. Soc.* **2016**, 138, 14764–14771. DOI:10.1021/jacs.6b09329
- T. Gong, X. Lou, J. J. Fang, E. Q. Gao, B. Hu, *Dalton Trans.* **2016**, 45, 19109–19116. DOI:10.1039/C6DT03637F
- E. Coronado, M. Yamashita, *Dalton Trans.* **2016**, 45, 16553–16555. DOI:10.1039/C6DT90183B
- A. Bleuzen, V. Marvaud, C. Mathoniere, B. Sieklucka, M. Verdaguer, *Inorg. Chem.* **2009**, 48, 3453–3466. DOI:10.1021/ic802007g
- Z. Zhu, M. Guo, X. L. Li, J. Tang, *Coord. Chem. Rev.* **2019**, 378, 350–364. DOI:10.1016/j.ccr.2017.10.030
- M. Andruh, *Chem. Comm.* **2018**, 54, 3559–3577. DOI:10.1039/C8CC00939B
- K. Wang, S. Y. Zeng, H. L. Wang, J. M. Dou, J. Z. Jiang, *Inorg.*

- Chem. Front.* **2014**, *1*, 167–171. DOI:10.1039/c3qi00097d
10. (a) W. L. Lan, X. T. Wang, L. Yang, Si, W., S. J. Zhuang, H. Liu, D. P. Zhang, *Trans. Met. Chem.* **2019**, *44*, 383–389. DOI:10.1007/s11243-019-00304-8
(b) F. Fei, Y. Dou, X. Y. Hao, W. L. Lan, Z. Zhou, L. Yang, D. P. Zhang, *Inorg. Chem. Commun.* **2019**, *106*, 22–26. DOI:10.1016/j.inoche.2019.05.024
(c) D. P. Zhang, H. Y. Zhang, *Polyhedron* **2015**, *100*, 36–42. DOI:10.1016/j.poly.2015.07.024
11. A. H. Yuan, X. P. Shen, H. Zhou, *Trans. Met. Chem.* **2008**, *33*, 133–136. DOI:10.1007/s11243-007-9032-0
12. N. Pradhan, S. Das Adhikari, A. Nag, D. D. Sarma, *Angew Chem Int. Edit.* **2017**, *56*, 7038–7054. DOI:10.1002/anie.201611526
13. Z. Sofer, D. Sedmidubský, Š. Huber, J. Luxa, D. Bouša, C. Boothroyd, M. Pumera, *Angew Chem Int. Edit.* **2016**, *55*, 3382–3386. DOI:10.1002/anie.201511309
14. (a) Y. Zhang, C. Luo, X. Wu, *Inorg. Chem.* **2014**, *53*, 3503–3510. DOI:10.1021/ic402945j
(b) D. P. Zhang, J. Cano, W. L. Lan, H. Liu, F. G. Sun, Y. H. Dong, J. Z. Jiang, *J. Mater. Chem. C* **2019**, *7*, 3623–3633. DOI:10.1039/C8TC05650A
15. Y. Liu, Y. C. Chen, J. Liu, W. B. Chen, G. Z. Huang, S. G. Wu, M. L. Tong, *Inorg. Chem.* **2020**, *59*, 687–694. DOI:10.1021/acs.inorgchem.9b02948
16. V. D. Sasnovskaya, V. A. Kopotkov, A. D. Talantsev, R. B. Morgunov, E. B. Yagubskii, S. V. Simonov, V. S. SMironov, *Inorg. Chem.* **2017**, *56*, 8926–8943. DOI:10.1021/acs.inorgchem.7b00676
17. A. B. Canaj, M. K. Singh, E. R. Marti, M. Damjanović, C. Wilson, O. Céspedes, M. Murrie, *Chem. Commun.* **2019**, *55*, 5950–5953. DOI:10.1039/C9CC00965E
18. J. Long, Y. Guari, R. A. Ferreira, L. D. Carlos, J. Larionova, *Coord. Chem. Rev.* **2018**, *363*, 57–70. DOI:10.1016/j.ccr.2018.02.019
19. C. A. Gould, L. E. Darago, M. I. Gonzalez, S. Demir, J. R. Long, *Angew. Chem. Int. Edit.* **2017**, *56*, 10103–10107. DOI:10.1002/anie.201612271
20. T. Pugh, N. F. Chilton, R. A. Layfield, *Chem. Sci.* **2017**, *8*, 2073–2080. DOI:10.1039/C6SC04465D
21. E. Trzop, D. P. Zhang, L. Piñero-Lopez, F. J. Valverde-Muñoz, M. Carmen Muñoz, L. Palatinus, E. Collet, *Angew. Chem. Int. Ed.* **2016**, *55*, 8675–8679. DOI:10.1002/anie.201602441
22. F. J. Valverde-Muñoz, M. Sereyuk, M. C. Muñoz, K. Znovjyak, I. O. Fritsky, J. A. Real, *Inorg. Chem.* **2016**, *55*, 10654–10665. DOI:10.1021/acs.inorgchem.6b01901
23. J. E. Clements, J. R. Price, S. M. Neville, C. J. Kepert, *Angew. Chem. Int. Ed.* **2016**, *55*, 15105–15109. DOI:10.1002/anie.201605418
24. X. Yin, C. S. Tang, S. Zeng, T. C. Asmara, P. Yang, M. A. Nardipa, P. E. Trevisanutto, T. Shirakawa, B. H. Kim, S. Yunoki, M. B. H. Breese, T. Venkatesan, A. T. S. Wee, A. Ariando, A. Rusydi, *ACS Photonics* **2019**, *6*, 3281–3289. DOI:10.1021/acsp Photonics.9b01294
25. Y. Q. Wang, Q. Yue, E. Q. Gao, *Chem. - Eur. J.* **2017**, *23*, 896–904. DOI:10.1002/chem.201604202
26. M. Magott, M. Reczynski, B. Gawel, B. Sieklucka, D. A. Pinkowicz, *J. Am. Chem. Soc.* **2018**, *140*, 15876–15882. DOI:10.1021/jacs.8b09322
27. R. Kulmaczewski, E. Trzop, L. J. Kershaw Cook, E. Collet, G. Chastanet, M. A. Halcrow, *Chem. Comm.* **2017**, *53*, 13268–13271. DOI:10.1039/C7CC07990G
28. V. García-López, M. Palacios-Corella, S. Cardona-Serra, M. Clemente-León, E. Coronado, *Chem. Comm.* **2019**, *55*, 12227–12230. DOI:10.1039/C9CC05988A
29. A. Bleuzen, V. Marvaud, C. Mathoniere, B. Sieklucka, M. Verdaguier, *Inorg. Chem.* **2009**, *48*, 3453–3466. DOI:10.1021/ic802007g
30. (a) L. Cui, Z. P. Lv, C. F. Leong, J. Ru, D. M. D'Alessandro, Y. Song, J. L. Zuo, *Dalton Trans.* **2016**, *45*, 16575–16584. DOI:10.1039/C6DT01756H
(b) A. M. Madalan, N. Avarvari, M. Fourmigue, R. Clerac, L. F. Chibotaru, S. Clima, M. Andruh, *Inorg. Chem.* **2008**, *47*, 940–950. DOI:10.1021/ic701738z
31. (a) M. X. Yao, Q. Zheng, X. M. Cai, Y. Z. Li, Y. Song, J. L. Zuo, *Inorg. Chem.* **2012**, *51*, 2140–2149. DOI:10.1021/ic201982d
(b) J. Ru, F. Gao, T. Wu, M. X. Yao, Y. Z. Li, J. L. Zuo, *Dalton Trans.* **2014**, *43*, 933–936. DOI:10.1039/C3DT52951G
32. X. Chen, W. L. Lan, X. Y. Hao, Y. Liu, Z. Zhou, S. J. Zhuang, D. P. Zhang, *Acta Chim. Slov.* **2019**, *66*, 308–314. DOI:10.17344/acsi.2018.4790
33. D. P. Zhang, S. P. Zhuo, H. Y. Zhang, P. Wang, J. J. Jiang, *Dalton Trans.* **2015**, *44*, 4655–4664. DOI:10.1039/C4DT03274H
34. A. Bleuzen, C. Lomenech, V. Escax, F. Villain, F. Varret, M. Verdaguier, *J. Am. Chem. Soc.* **2000**, *122*, 6648–6652. DOI:10.1021/ja000348u
35. R. Xiang, Y. Duan, C. Tong, L. Peng, J. Wang, S. S. A. Shah, Z. Wei, *Electrochimica Acta* **2019**, *302*, 45–55. DOI:10.1016/j.electacta.2019.01.170
36. X. He, L. Tian, M. Qiao, J. Zhang, W. Geng, Q. Zhang, *J. Mater. Chem. A* **2019**, *7*, 11478–11486. DOI:10.1039/C9TA02265A
37. J. R. Jiménez, A. Sugahara, M. Okubo, A. Yamada, L. M. Chamoreau, L. Lisnard, R. Lescouëzec, *Chem. Comm.* **2018**, *54*, 5189–5192. DOI:10.1039/C8CC01374H
38. J. W. Shi, Q. G. Meng, C. C. Xue, Q. Y. Liu, D. P. Zhang, *Trans. Met. Chem.* **2018**, *43*, 45–52. DOI:10.1007/s11243-017-0192-2
39. (a) W. W. Ni, Z. H. Ni, A. L. Cui, X. Liang, H. Z. Kou, *Inorg. Chem.* **2017**, *46*, 22–33. (b) M. C. Monteiro, K. C. Toledo, B. M. Pires, R. Wick, J. A. Bonacin, *Eur. J. Inorg. Chem.* **2017**, *2017*, 1979–1988. DOI:10.1002/ejic.201601540
(c) H. Tchouka, A. Meetsma, W. R. Browne, *Inorg. Chem.* **2010**, *49*, 10557–10570. DOI:10.1021/ic101447q
40. H. Miyasaka, T. Madanbashi, A. Saitoh, N. Motokawa, R. Ishikawa, M. Yamashita, R. Clérac, *Chem. - Eur. J.* **2012**, *18*, 3942–3954. DOI:10.1002/chem.201102738
41. C. C. Zhao, W. W. Ni, J. Tao, A. L. Cui, H. Z. Kou, *CrystEngComm* **2009**, *11*, 632–637. DOI:10.1039/B812117F
42. D. P. Zhang, H. Wang, Y. Chen, Z. H. Ni, L. Tian, J. J. Jiang, *Inorg. Chem.* **2009**, *48*, 11215–11225.

- DOI:10.1021/ic901530p
43. H. Y. Zhang, C. C. Xue, J. W. Shi, H. Liu, Y. H. Dong, Z. D. Zhao, D. P. Zhang, J. J. Jiang, *Crystal Growth & Des.* **2016**, *16*, 5753–5761. DOI:10.1021/acs.cgd.6b00820
44. D. P. Zhang, H. Wang, Y. Chen, Z. H. Ni, L. Tian, J. J. Jiang, *Inorg. Chem.* **2009**, *48*, 5488–5496. DOI:10.1021/ic900483z
45. Sheldrick G. M. (1997) SHELXTL97, Program for the Refinement of Crystal Structure, University of Göttingen, Germany.
46. J. W. Shi, W. L. Lan, Q. Y. Liu, D. P. Zhang, *Russ. J. General Chem.* **2018**, *88*, 319–324. DOI:10.1134/S1070363218020202
47. J. J. Borrás-Almenar, J. M. Clemente-Juan, E. Coronado, B. S. Tsukerblat, *J. Comput. Chem.* **2001**, *22*, 985–991. DOI:10.1002/jcc.1059
48. W. L. Lan, X. Y. Hao, Y. Dou, Z. Zhou, L. Yang, H. Liu, D. P. Zhang, *Polymers* **2019**, *11*, 1585–1598. DOI:10.3390/polym111101585

Povzetek

V tem prispevku je na osnovi strukturno potrjenega pentacianidometalata $(\text{PPh}_4)_2[\text{Fe}(\text{CN})_5(\text{imidazol})] \cdot (\text{imidazol}) \cdot \text{H}_2\text{O}$ (**1**) in manganovih spojin $[\text{Mn}(\text{L})(\text{H}_2\text{O})_2]\text{ClO}_4$ ($\text{L} = \text{N,N}$ -etilenbis(3-metoksisalicilideniminat) in $[\text{Mn}(\text{MAC})(\text{H}_2\text{O})\text{Cl}]\text{ClO}_4$ ($\text{MAC} = 2,13$ -dimetil-3,6,9,12,18-pentaazabicyklo-[12.3.1]oktadeka-1(18),2,12,14,16-pentaen) opisana sinteza dveh novih $\text{Fe}^{\text{III}}\text{-Mn}^{\text{III/II}}$ kompleksov s cianidnim mostom, $\{[\text{Mn}(\text{L})(\text{H}_2\text{O})_2][\text{Fe}(\text{CN})_5(\text{imidazol})]\}(\text{ClO}_4)$ (**2**) in $\{[\text{Mn}(\text{MAC})][\text{Fe}(\text{CN})_5(\text{imidazol})] \cdot \text{CH}_3\text{OH}\}_n$ (**3**), njihova karakterizacija z elementno analizo, IR spektroskopijo in rentgensko strukturno analizo. Rentgenska analiza na monokristalu je pokazala, da je spojina **2** zgrajena iz tetranuklearnih enot FeMn_3 , ki se z močnimi vodikovimi vezmi povezujejo v supramolekularne 1D dvojne verige v obliki lestve, medtem ko spojino **3** sestavljajo nevtralne enodimenzionalne enojne verige. Magnetne meritve so pokazale feromagnetno sklopitev med $\text{Fe}^{\text{III}}\text{-Mn}^{\text{III}}$ enotami in antiferomagnetno sklopitev med $\text{Fe}^{\text{III}}\text{-Mn}^{\text{II}}$ enotami preko mostovnih cianidnih skupin v spojinah **2** in **3**.



Except when otherwise noted, articles in this journal are published under the terms and conditions of the Creative Commons Attribution 4.0 International License

Scientific paper

Synthesis, Crystal Structures and Catalytic Property of Oxidovanadium(V) Complexes with *N*'-(4-Oxopentan-2-ylidene)nicotinohydrazide and 4-Bromo-*N*'-(4-oxopentan-2-ylidene)benzohydrazide

Qiwen Yang,^{1,*} Pu Wang¹ and Yan Lei^{1,2}¹ College of Environment and Ecology, Chongqing University, Chongqing 400030, P. R. China² College of Environmental and Chemistry Engineering, Chongqing Three Gorges University, Chongqing 404000, P. R. China

* Corresponding author: E-mail: yangqiwen222@126.com

Received: 02-21-2020

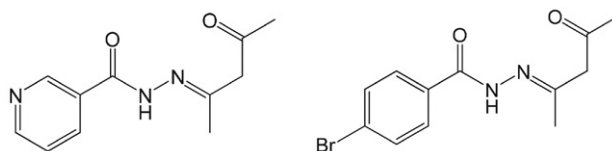
Abstract

A pair of structurally similar oxidovanadium(V) complexes with the general formula [VOL¹L], with the hydrazone compounds *N*'-(4-oxopentan-2-ylidene)nicotinohydrazide (H₂L¹) and 4-bromo-*N*'-(4-oxopentan-2-ylidene)benzohydrazide (H₂L²), and the acetohydroxamic acid (HL) as ligands, have been synthesized and structurally characterized by physico-chemical methods and single crystal X-ray determination. Single crystal X-ray analysis indicates that the V atoms in the complexes are in octahedral coordination, with the ONO donor atoms of the hydrazone ligands, and the OO donor atoms of the acetohydroxamate ligands, as well as an oxido O atom. The complexes showed good property for the catalytic epoxidation of styrene.

Keywords: Oxidovanadium(V) complex; hydrazone ligand; crystal structure; catalytic property

1. Introduction

In recent years, due to the environmental and economic issues, green chemistry became the principle for chemical syntheses. One of the major goals in recent research is to find new and efficient catalysts for the industrially important reactions. Hydrazone compounds, the aldehyde- or ketone analogs in which the carbonyl group is replaced by an imine or azomethine group, are considered privileged ligands, because of their simple preparation in an one-pot condensation of aldehydes (or ketones) and primary amines in an alcohol solvent.¹ The metal complexes of hydrazones have been widely studied for their structures, biological activities and catalytic properties.² Among the complexes, those with V centers are of particular interest for their biological and catalytic properties.³ The epoxidation of alkenes is one of the most widely studied reactions in organic chemistry since epoxides are key starting materials for a wide variety of products. The catalytic epoxidation of olefins by various complexes is a hot research



Scheme 1. The hydrazone compounds H₂L¹ and H₂L².

topic.⁴ A number of vanadium complexes with Schiff base ligands are reported for the oxidation of various organic substrates.⁵ However, the vanadium complexes with hydrazones derived from hydrazides with acetylacetone have seldom been reported. Herein we report the syntheses, crystal structures and catalytic epoxidation properties of a pair of structurally similar oxidovanadium(V) complexes, [VOL¹L'] (1) and [VOL²L'] (2), where L¹ and L² are the enolate form of *N*'-(4-oxopentan-2-ylidene)nicotinohydrazide (H₂L¹) and 4-bromo-*N*'-(4-oxopentan-2-ylidene)benzohydrazide (H₂L²), respectively (Scheme 1), and L' is the anionic form of acetohydroxamic acid (HL).

2. Experimental

2.1. Materials

[VO(acac)₂], nicotinohydrazide and 4-bromobenzohydrazide were purchased from Aldrich. All other reagents with AR grade were used as received without further purification.

2.2. Physical Measurements

Infrared spectra (4000–400 cm⁻¹) were recorded as KBr discs with a FTS-40 BioRad FT-IR spectrophotometer. The electronic spectra were recorded on a Lambda 35 spectrometer. Microanalyses (C, H, N) of the complex were carried out on a Carlo-Erba 1106 elemental analyzer. Solution electrical conductivity was measured at 298K using a DDS-11 conductivity meter. GC analyses were performed on a Shimadzu GC-2010 gas chromatograph.

2.3. X-ray Crystallography

Crystallographic data of the complexes were collected on a Bruker SMART CCD area diffractometer with graphite monochromated Mo-K α radiation ($\lambda = 0.71073$ Å) at 298(2) K. Absorption corrections were applied by using the multi-scan program.⁶ The structures of the complexes were solved by direct methods and successive Fourier difference syntheses, and anisotropic thermal parameters for all nonhydrogen atoms were refined by full-matrix least-squares procedure against F^2 .⁷ All non-hydrogen atoms were refined anisotropically. The amino H atoms were located from difference Fourier maps and refined isotropically. The N–H distances were restrained to 0.86(1) Å. The crystallographic data and experimental details for the

Table 1. Crystallographic data for the single crystal of the complexes

	1	2
Empirical formula	C ₁₃ H ₁₅ N ₄ O ₅ V	C ₁₄ H ₁₅ BrN ₃ O ₅ V
Formula weight	358.23	436.14
Temperature (K)	298(2)	298(2)
Crystal system	Monoclinic	Triclinic
Space group	$P2_1/n$	$P\bar{1}$
<i>a</i> (Å)	7.658(1)	7.952(1)
<i>b</i> (Å)	23.873(1)	10.371(1)
<i>c</i> (Å)	8.556(1)	11.613(1)
α (°)	90	110.733(1)
β (°)	96.883(1)	96.007(1)
γ (°)	90	102.030(1)
<i>V</i> (Å ³)	1552.9(3)	859.2(2)
<i>Z</i>	4	2
<i>F</i> (000)	736	436
Data/restraints/parameters	2891/1/214	3187/1/222
Goodness-of-fit on F^2	1.132	1.023
R_1, wR_2 [$I > 2\sigma(I)$]	0.0491, 0.1072	0.0488, 0.1047
R_1, wR_2 (all data)	0.0618, 0.1126	0.0762, 0.1189

structural analysis are summarized in Table 1, and the selected bond lengths and angles are listed in Table 2.

Table 2. Selected bond distances (Å) and bond angles (°) for the complexes

	1	2
V1–O1	1.896(2)	1.886(3)
V1–O2	1.938(2)	1.975(3)
V1–O3	2.228(2)	2.201(3)
V1–O4	1.854(2)	1.869(3)
V1–O5	1.588(2)	1.588(3)
V1–N1	2.059(2)	2.046(3)
C2–O1	1.310(4)	1.315(5)
C2–C3	1.351(4)	1.357(6)
C4–N1	1.314(4)	1.329(5)
N1–N2	1.398(3)	1.393(5)
C6–N2	1.291(4)	1.302(5)
C6–O2	1.303(3)	1.321(5)
O5–V1–O4	96.20(11)	95.96(14)
O5–V1–O1	98.02(12)	98.50(14)
O4–V1–O1	104.00(9)	103.84(12)
O5–V1–O2	101.39(12)	100.24(13)
O4–V1–O2	90.23(9)	100.24(13)
O1–V1–O2	154.51(10)	154.79(12)
O5–V1–N1	100.96(11)	101.32(14)
O4–V1–N1	159.58(10)	159.63(12)
O1–V1–N1	84.58(9)	84.29(12)
O2–V1–N1	75.66(9)	75.62(12)
O5–V1–O3	171.30(10)	171.74(13)
O4–V1–O3	75.52(8)	75.87(11)
O1–V1–O3	81.69(9)	82.57(12)
O2–V1–O3	81.58(9)	81.31(11)
N1–V1–O3	87.68(9)	86.92(12)

2.4. Synthesis of [VOL1L'] (1)

Nicotinohydrazide (1.00 mmol, 0.135 g) and [VO(acac)₂] (1.00 mmol, 0.265 g) were mixed and stirred in methanol (50 mL) for 30 min at 25 °C. Then, acetohydroxamic acid (1.00 mmol, 0.0750 g) was added. The final mixture was further stirred for 30 min. The brown solution was evaporated to remove three quarters of the solvents under reduced pressure, yielding deep brown solid of the complex. Yield: 0.26 g (72%). Well-shaped single crystals suitable for X-ray diffraction were obtained by recrystallization of the solid from methanol. Elemental analysis found: C, 43.75; H, 4.31; N, 15.56%. C₁₃H₁₅N₄O₅V calcd: C, 43.59; H, 4.22; N, 15.64%. IR data (KBr, cm⁻¹): 3287, 3119, 2917, 2850, 1628, 1556, 1490, 1400, 1332, 1280, 1168, 1116, 1033, 961, 806, 712, 585. UV-Vis data in methanol [λ_{\max} (nm), ϵ (L mol⁻¹ cm⁻¹): 235, 1.62 × 10⁴; 273, 1.58 × 10⁴; 345, 9.67 × 10³; 460, 7.72 × 10³].

2.5. Synthesis of [VOL²L'] (2)

4-Bromobenzohydrazide (1.00 mmol, 0.214 g) and [VO(acac)₂] (1.00 mmol, 0.265 g) were mixed and stirred

in methanol (50 mL) for 30 min at 25 °C. Then, acetohydroxamic acid (1.00 mmol, 0.0750 g) was added. The final mixture was further stirred for 30 min. The brown solution was evaporated to remove three quarters of the solvents under reduced pressure, yielding deep brown solid of the complex. Yield: 0.34 g (77%). Well-shaped single crystals suitable for X-ray diffraction were obtained by recrystallization of the solid from methanol. Elemental analysis found: C, 38.37; H, 3.53; N, 9.72%. $C_{14}H_{15}BrN_3O_5V$ calcd: C, 38.55; H, 3.47; N, 9.63%. IR data (KBr, cm^{-1}): 3272, 3105, 2913, 2880, 1636, 1422, 1145, 1085, 958, 846, 532. UV-Vis data in methanol [λ_{max} (nm), ϵ ($L\ mol^{-1}\ cm^{-1}$)]: 275, 1.73×10^4 ; 343, 1.05×10^4 ; 435, 5.62×10^3 .

2. 6. Styrene Epoxidation

The epoxidation reaction was carried out at room temperature in acetonitrile under N_2 atmosphere with constant stirring. The composition of the reaction mixture was 2.00 mmol of styrene, 2.00 mmol of chlorobenzene (internal standard), 0.10 mmol of the complexes (catalyst) and 2.00 mmol iodosylbenzene or sodium hypochlorite (oxidant) in 5.00 mL freshly distilled acetonitrile. When the oxidant was sodium hypochlorite, the solution was buffered to pH 11.2 with NaH_2PO_4 and NaOH. The composition of reaction medium was determined by GC with styrene and styrene epoxide quantified by the internal standard method (chlorobenzene). All other products detected by GC were mentioned as others. For each complex the reaction time for maximum epoxide yield was determined by withdrawing periodically 0.1 mL aliquots from the reaction mixture and this time was used to monitor the efficiency of the catalyst on performing at least two independent experiments. Blank experiments with each oxidant and using the same experimental conditions except catalyst were also performed.

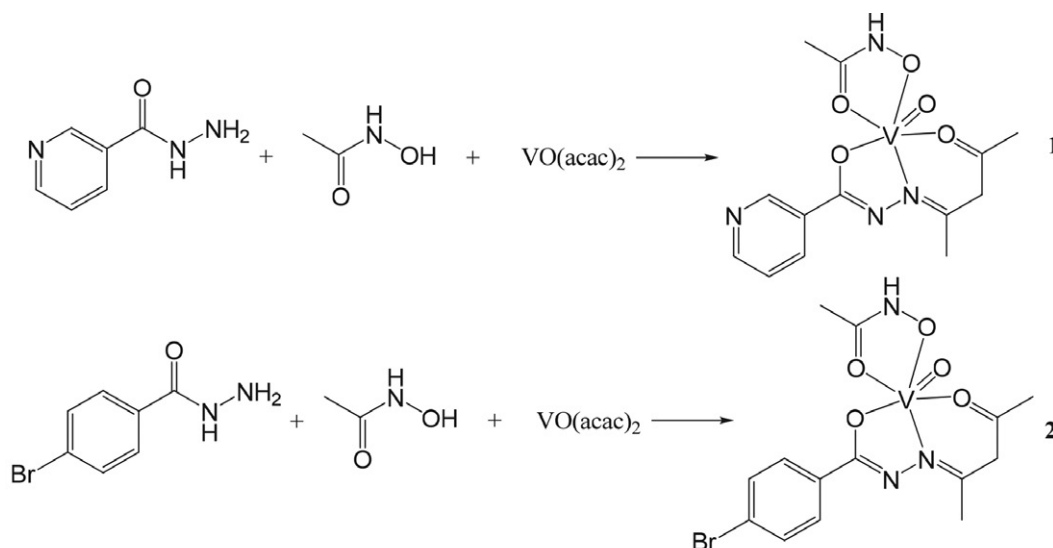
3. Results and Discussion

3. 1. Chemistry

Complexes **1** and **2** were readily prepared by reaction of $VO(acac)_2$, acetohydroxamic acid with nicotinohydrazide and 4-bromobenzohydrazide, respectively, in methanol (Scheme 2). The hydrazone ligands were formed by the condensation reactions of the hydrazides with the acetylacetone ligand of $VO(acac)_2$. The reaction progresses are accompanied by an immediate color change of the solution from colorless to brown. The molar conductivities ($\Lambda_M = 37\ \Omega^{-1}\ cm^2\ mol^{-1}$ for **1** and $43\ \Omega^{-1}\ cm^2\ mol^{-1}$ for **2**) measured in methanol are consistent with the values expected for non-electrolyte.⁸ The structure of complex **2** has been reported but with different crystal system and space group (orthorhombic $Pbca$).⁸

3. 2. Crystal Structure Description of the Complexes

Single-crystal X-ray analysis shows that both complexes are structurally similar mononuclear oxidovanadium(V) compounds. The differences between the two complexes are the terminal groups, *viz.* pyridinyl for **1** and bromophenyl for **2**. The ORTEP plots of the complexes **1** and **2** are shown in Figs. 1 and 2, respectively. The V atom is in distorted octahedral geometry, which is coordinated by the NO_2 donor atoms of the hydrazone ligand and the hydroxyl O atom of the acetylhydroxamate ligand in the equatorial plane, and by the carbonyl O atom of the acetylhydroxamate ligand and the oxido O atom at the two axial positions. The metal atoms are displaced toward the axial oxido O atoms (O5) by 0.29–0.30 Å from the equatorial planes of both complexes. The distortion of the octahedral coordination of the complexes can be observed from the bond angles (Table 2) related to the V atoms. The *cis*- and



Scheme 2. The preparation of the complexes.

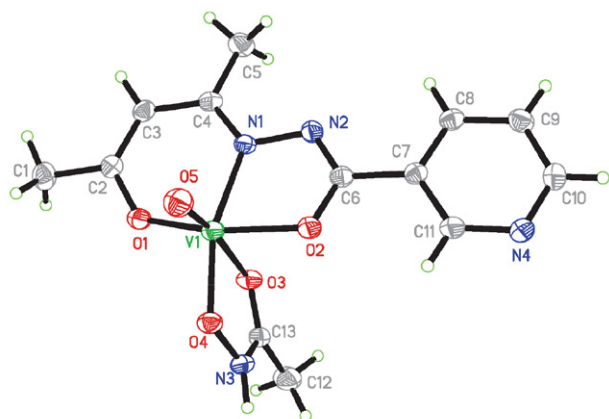
Table 3. Hydrogen bond distances (Å) and bond angles (°) for the complexes

<i>D</i> –H... <i>A</i>	<i>d</i> (<i>D</i> –H)	<i>d</i> (H... <i>A</i>)	<i>d</i> (<i>D</i> ... <i>A</i>)	Angle (<i>D</i> –H... <i>A</i>)
1				
N3–H3A...N4 ^{#1}	0.86(1)	1.96(1)	2.813(4)	171(4)
C8–H8...O4 ^{#2}	0.93	2.55	3.053(3)	114(5)
2				
N3–H3A...O2 ^{#3}	0.86(1)	1.99(1)	2.838(4)	170(5)
C1–H1A...O1 ^{#4}	0.96	2.58	3.492(5)	159(6)
C12–H12...O3 ^{#5}	0.93	2.57	3.253(5)	131(6)

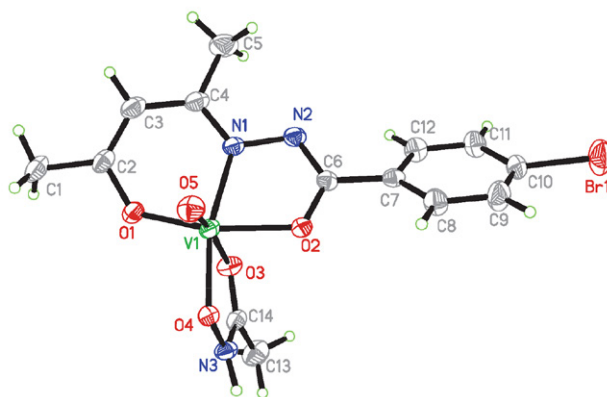
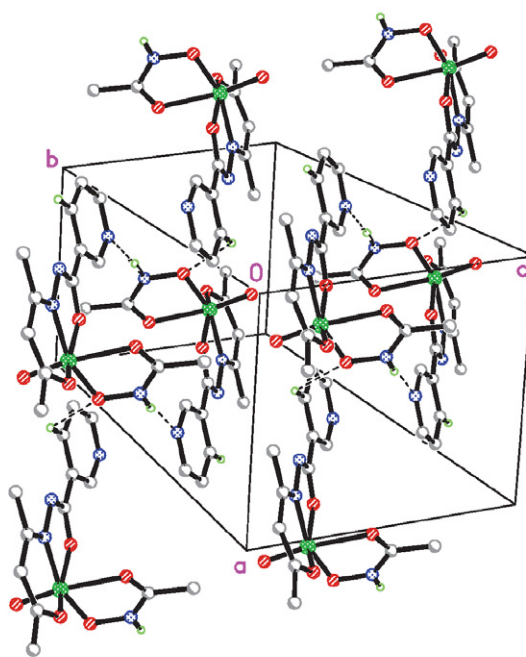
Symmetry codes: #1: 2 – *x*, –*y*, 1 – *z*; #2: –1 + *x*, *y*, *z*; #3: 2 – *x*, –*y*, 1 – *z*; #4: 2 – *x*, –*y*, –*z*; #5: 2 – *x*, 1 – *y*, 1 – *z*.

trans- angles related to the V atoms at the equatorial planes are in the range of 75.52(8)–104.00(9)° and 154.51(10)–171.30(10)° for **1** and 75.62(12)–103.84(12)° and 154.79(12)–171.74(13)° for **2**. The deviations from the ideal octahedral geometry are mainly origin from the strain created by the five-membered chelate rings N1–V1–O2 and O3–V1–O4. The bond lengths of V–O and V–N (Table 2) of both complexes are similar to each other, and comparable to those in other V complexes in literature.^{9,10} The terminal V1–O5 [1.588(2) Å] bond distances of both complexes agree well with the corresponding values reported for related systems.¹¹ Because of the *trans* influence of the oxido groups, the distances to the O3 atoms (2.20–2.23 Å) are considerably elongated, making the O3 atoms weakly coordinated to the V atoms. Such elongation has previously been observed in other complexes with similar structures.¹² The hydrazone ligands coordinate to the V atoms through dianionic form, which can be seen from the bond lengths of C6–O2, N1–N2, C2–C3 and C2–O1. The bonds C6–O2 and C2–O1 are obviously longer than typical double bonds, and the bonds C6–N2 and C2–C3 are obviously shorter than typical single bonds. This phenomenon is not uncommon for hydrazone complexes.¹³

In the crystal structures of complex **1**, the molecules are linked through N–H...N hydrogen bonds between the amino group of the acetohydroxamate ligand and the pyridine N atom, as well as the C–H...O hydrogen bonds be-

**Fig. 1.** ORTEP diagram of complex **1** with 30% thermal ellipsoid.

tween the pyridine C–H group and the hydroxyl O atom of the acetohydroxamate ligand (Table 3), to form one dimensional zigzag chains running along the *a* axis (Fig. 3). In the crystal structures of complex **2**, the molecules are

**Fig. 2.** ORTEP diagram of complex **2** with 30% thermal ellipsoid.**Fig. 3.** Molecular packing structure of complex **1** linked by hydrogen bonds.

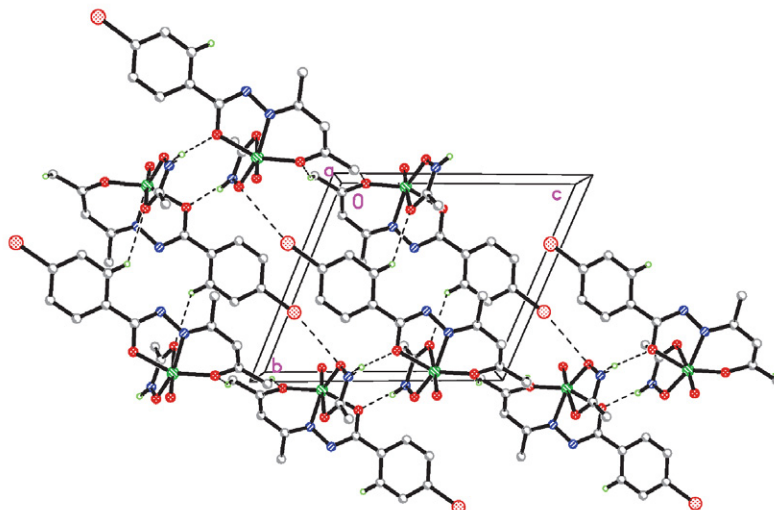


Fig. 4. Molecular packing structure of complex 2 linked by hydrogen bonds.

linked through N-H...O hydrogen bonds between the amino group of the acetohydroxamate ligand and the carbonyl O atom of the hydrazone ligand, as well as the C-H...O hydrogen bonds between the benzene C-H group and the carbonyl O atom of the acetohydroxamate ligand (Table 3), to generate layers parallel to the *bc* direction (Fig. 4).

3. 3. Infrared and Electronic Spectra

The sharp absorptions at about 3280 cm^{-1} for the spectra of both complexes are attributed to the N–H bonds of the amino groups. The bands in the region 3120–2850 cm^{-1} are assigned to the C–H bonds. The intense bands at about 1630 cm^{-1} are assigned to the vibration of the C=N group.^{1,12b} The characteristic of the spectra of both complexes is the exhibition of sharp bands at about 960 cm^{-1} , corresponding to the V=O stretching vibration.^{1,13b} The appearance of a single band in this region indicates the existence of monomeric six-coordinated V=O units instead of the polymeric units.¹⁴ This is approved by the single crystal structure determination.

In the UV-Vis spectra of the complexes, the bands at about 345 nm and 275 nm are attributed to the π - π^* and n - π^* transitions.^{13b,15} The weak bands at 430–470 nm are attributed to intramolecular charge transfer transitions from the p_π orbital on the nitrogen and oxygen to the empty d orbitals of the V atoms.^{12b,13b}

3. 4. Catalytic Property

The percentage of conversion of styrene, selectivity for styrene oxide, yield of styrene oxide and reaction time to obtain maximum yield using both the oxidants are shown in Fig. 5. The data reveals that the complexes as catalysts convert styrene most efficiently in the presence of both oxidants. Nevertheless, the catalysts are selective (over 90%) towards the formation of styrene epoxides de-

spite of the formation of by-products like benzaldehyde, phenylacetaldehyde, styrene epoxides derivative, alcohols *etc.* From the data it is also clear that the complexes exhibit high efficiency for styrene epoxide yields. When the reactions were carried out with PhIO at 2 h, styrene conversions of complexes 1 and 2 are 95% and 87%, respectively. When the reactions were carried out with NaOCl at 3 h, styrene conversions of complexes 1 and 2 are 93% and 84%, respectively. It is evident that between PhIO and NaOCl, the former acts as a better oxidant with respect to both styrene conversion and styrene epoxide selectivity. Moreover, complex 2 has better conversion values than complex 1, which is in accordance with that the presence of electronegative groups in the ligands increases the catalytic efficiency of the complexes.¹⁶ The epoxide yields for the complexes 1 and 2 using PhIO and NaOCl as oxidants are about 80% and 75%, respectively. Thus, both complexes have good and similar catalytic properties on the oxidation of styrene.

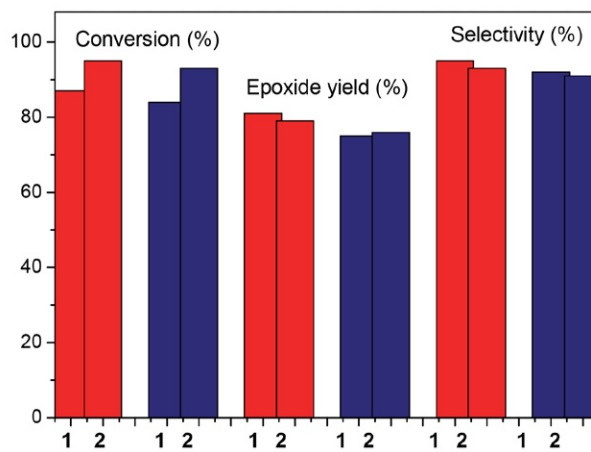


Fig. 5. Catalytic epoxidation results. The red and blue columns represent the results catalyzed by PhIO (2 h) and NaOCl (3 h), respectively.

4. Conclusion

In summary, two oxidovanadium(V) complexes derived from hydrazone and acetylhydroxamate ligands were prepared and characterized. The V atoms in the complexes are in octahedral coordination. Both complexes have good catalytic property for the epoxidation of styrene with the good selectivity (over 90%) and high styrene epoxide and epoxide yields. The presence of electronegative groups in the ligands can increase the catalytic efficiency of the complexes.

Supplementary Material

CCDC 1985429 (1) and 1985432 (2) contain the supplementary crystallographic data for this paper. These data can be obtained free of charge via <http://www.ccdc.cam.ac.uk/conts/retrieving.html>, or from the Cambridge Crystallographic Data Centre, 12 Union Road, Cambridge CB2 1EZ, UK; fax: (+44) 1223-336-033; or e-mail: deposit@ccdc.cam.ac.uk.

Acknowledgements

This project was supported by the Scientific and Technological Research Program of Chongqing Municipal Education Commission (Grant No. KJQN201801222), the Chunhui Project from Education Ministry of China (Grant No. Z2015140), the Key Laboratory of Water Environment Evolution and Pollution Control in Three Gorges Reservoir (Chongqing Three Georges University) (Grant No. 0969809) and the Key Cultivation Project of Chongqing Three Gorges University (Grant No. 17ZD12).

5. References

- Grivani, G. Bruno, H. A. Rudbari, A. D. Khalaji, P. Pourteimouri, *Inorg. Chem. Commun.* **2012**, *18*, 15–20.
DOI:10.1016/j.inoche.2011.12.044
- (a) S. Dasgupta, S. Karim, S. Banerjee, M. Saha, K. Das Saha, D. Das, *Dalton Trans.* **2020**, *49*, 1232–1240;
DOI:10.1039/C9DT04636D
(b) M. Cuccioloni, L. Bonfili, V. Cecarini, M. Nabissi, R. Pettinari, F. Marchetti, R. Petrelli, L. Cappellacci, M. Angeletti, A. M. Eleuteri, *ChemMedChem* **2020**, *15*, 105–113;
DOI:10.1002/cmdc.201900551
(c) A. A. Khandar, Z. M. Azar, M. Eskandani, C. B. Hubschle, S. van Smaalen, B. Shaabani, Y. Omid, *Polyhedron* **2019**, *171*, 237–248; DOI:10.1016/j.poly.2019.06.026
(d) M. Sutradhar, M. V. Kirillova, M. F. C. G. da Silva, C. M. Liu, A. J. L. Pombeiro, *Dalton Trans.* **2013**, *42*, 16578–16587;
DOI:10.1039/c3dt52453a
(e) D. Sadhukhan, A. Ray, G. Pilet, C. Rizzoli, G. M. Rosair, C. J. Gomez-Garcia, S. Signorella, S. Bellu, S. Mitra, *Inorg. Chem.* **2011**, *50*, 8326–8339; DOI:10.1021/ic200846j
- (f) O. Pouralimardan, A. C. Chamayou, C. Janiak, H. Hosseini-Monfared, *Inorg. Chim. Acta* **2007**, *360*, 1599–1608.
DOI:10.1016/j.ica.2006.08.056
- (a) H. H. Monfared, S. Kheirabadi, N. A. Lalami, P. Mayer, *Polyhedron* **2011**, *30*, 1375–1384; DOI:10.1016/j.poly.2011.02.005
(b) H. Hosseini-Monfared, R. Bikas, P. Mahboubi-Anarjan, A. J. Blake, V. Lippolis, N. B. Arslan, C. Kazak, *Polyhedron* **2014**, *69*, 90–102; DOI:10.1016/j.poly.2013.11.020
(c) H. Y. Qian, *Inorg. Nano-Met. Chem.* **2018**, *48*, 461–466;
DOI:10.1080/24701556.2019.1569689
(d) H. Y. Qian, *Russ. J. Coord. Chem.* **2017**, *43*, 780–786;
DOI:10.1134/S1070328417110070
(e) H.-Y. Qian, *Acta Chim. Slov.* **2019**, *66*, 995–1001;
DOI:10.4149/neo_2019_190112N36
(f) E.-C. Liu, W. Li, X.-S. Cheng, *Acta Chim. Slov.* **2019**, *66*, 971–977;
(g) C.-L. Zhang, X.-Y. Qiu, S.-J. Liu, *Acta Chim. Slov.* **2019**, *66*, 719–725; DOI:10.17344/acsi.2019.5241
(h) L.-W. Xue, Y.-J. Han, X.-Q. Luo, *Acta Chim. Slov.* **2019**, *66*, 622–628. DOI:10.17344/acsi.2019.5039
- (a) K. Moghe, A. K. Sutar, I. K. Kang, K. C. Gupta, *RSC Advances* **2019**, *9*, 30823–30834; DOI:10.1039/C9RA05811G
(b) B. Rezazadeh, A. R. Pourali, A. Banaei, H. Behniafar, *J. Coord. Chem.* **2019**, *72*, 3401–3416.
DOI:10.1080/00958972.2019.1691724
- (a) M. S. S. Adam, O. M. El-Hady, F. Ullah, *RSC Advances* **2019**, *9*, 34311–34329; DOI:10.1039/C9RA06816C
(b) A. Najafian, T. R. Cundari, *Inorg. Chem.* **2019**, *58*, 12254–12263; DOI:10.1021/acs.inorgchem.9b01696
(c) N. C. Jana, M. Patra, P. Brandao, A. Panja, *Polyhedron* **2019**, *164*, 23–34. DOI:10.1016/j.poly.2019.02.024
- L. Krause, R. Herbst-Irmer, G. M. Sheldrick, D. Stalke, *J. Appl. Crystallogr.* **2015**, *48*, 3–10.
DOI:10.1107/S1600576714022985
- (a) G. M. Sheldrick, *Acta Crystallogr.* **2015**, *A71*, 3–8;
DOI:10.1107/S2053273314026370
(b) G. M. Sheldrick, *Acta Crystallogr.* **2015**, *C71*, 3–8.
- W. J. Geary, *Coord. Chem. Rev.* **1971**, *7*, 81–122.
DOI:10.1016/S0010-8545(00)80009-0
- X. Y. Qiu, S. J. Liu, J. X. Lei, Y. T. Ye, *Russ. J. Coord. Chem.* **2017**, *43*, 396–403. DOI:10.1134/S1070328417060069
- (a) N. Lotfi, I. Sheikhshoeai, S. Y. Ebrahimipour, H. Krautscheid, *J. Mol. Struct.* **2017**, *1149*, 432–438;
DOI:10.1016/j.molstruc.2017.08.010
(b) S. K. Mal, M. Mitra, H. R. Yadav, C. S. Purohit, A. R. Choudhury, R. Ghosh, *Polyhedron* **2016**, *111*, 118–122.
DOI:10.1016/j.poly.2016.03.033
- (a) S. Guo, N. Sun, Y. Ding, A. Li, Y. Jiang, W. Zhai, Z. Li, D. Qu, Z. You, *Z. Anorg. Allg. Chem.* **2018**, *644*, 1172–1176;
DOI:10.1002/zaac.201800060
(b) L. Li, K.-W. Lv, Y.-T. Li, G.-F. Jiang, Y. Xin, L. Ye, Y. Zhang, H. Liu, C.-N. Shang, Z.-L. You, *Chinese J. Inorg. Chem.* **2017**, *33*, 905–912;
(c) Z. You, B. Zheng, T. Yang, F. Liu, X.-S. Cheng, *J. Coord. Chem.* **2016**, *69*, 1371–1379.
DOI:10.1080/00958972.2016.1171856

12. (a) M. R. Maurya, S. Agarwal, C. Bader, M. Ebel, D. Rehder, *Dalton Trans.* **2005**, 537–544;
(b) H. H. Monfared, S. Alavi, R. Bikas, M. Vahedpour, P. Mayer, *Polyhedron* **2010**, *29*, 3355–3362. DOI:10.1016/j.poly.2010.09.029
13. (a) Y. M. Li, L. Y. Xu, M. M. Duan, J. H. Wu, Y. H. Wang, K. X. Dong, M. X. Han, Z. L. You, *Inorg. Chem. Commun.* **2019**, *105*, 212–216; DOI:10.1016/j.inoche.2019.05.011
(b) L. Y. Xu, Y. M. Li, M. M. Duan, Y. X. Li, M. X. Han, J. H. Wu, Y. H. Wang, K. X. Dong, Z. L. You, *Polyhedron* **2019**, *165*, 138–142. DOI:10.1016/j.poly.2019.03.016
14. (a) R. Ando, S. Mori, M. Hayashi, T. Yagyu, M. Maeda, *Inorg. Chim. Acta* **2004**, *357*, 1177–1184; DOI:10.1016/j.ica.2003.09.033
(b) C. J. Chang, J. A. Labinger, H. B. Gray, *Inorg. Chem.* **1997**, *36*, 5927–5930; DOI:10.1021/ic970824q
(c) R. Ando, H. Ono, T. Yagyu, M. Maeda, *Inorg. Chim. Acta* **2004**, *357*, 2237–2244. DOI:10.1016/j.ica.2003.12.031
15. S. Mondal, M. Mukherjee, K. Dhara, S. Ghosh, J. Ratha, P. Banerjee, A. K. Mukherjee, *Cryst. Growth Des.* **2007**, *7*, 1716–1721. DOI:10.1021/cg060753i
16. (a) J. Rahchamani, M. Behzad, A. Bezaatpour, V. Jahed, G. Dutkiewicz, M. Kubicki, M. Salehi, *Polyhedron* **2011**, *30*, 2611–2618; DOI:10.1016/j.poly.2011.07.011
(b) D. M. Boghaei, A. Bezaatpour, M. Behzad, *J. Mol. Catal. A: Chem.* **2006**, *245*, 12–16. DOI:10.1016/j.molcata.2005.09.022

Povzetek

Sintetizirali smo dva strukturno sorodna oksidovanadijeva(V) kompleksa s splošno formulo [VOLL], s hidrazonoma N^2 -(4-oksopentan-2-iliden)nikotinohidrazid (H_2L^1) in 4-bromo- N^2 -(4-oksopentan-2-iliden)benzohidrazid (H_2L^2) in z acetohidroksamsko kislino (HL') kot ligandi ter ju okarakterizirali z fiziko-kemijskimi metodami in monokristalno rentgensko difrakcijo. Kristalna analiza razkriva, da je V atom v oktaedričnem okolju z ONO donorskimi atomi hidrazonskega liganda, z OO donorskima atomoma acetohidroksamatnega liganda ter oksido O atomom. Kompleksa izkazujeta dobre lastnosti pri katalitični epoksidaciji stirena.



Except when otherwise noted, articles in this journal are published under the terms and conditions of the Creative Commons Attribution 4.0 International License

Scientific paper

Synthesis and Evaluation on Anticonvulsant and Antidepressant Activities of Naphthoquinone Derivatives Containing Pyrazole and Pyrimidine Fragments

Nataliia Polish,¹ Mariia Nesterkina,^{2,*} Nataliia Marintsova,¹ Andriy Karkhut,¹
Iryna Kravchenko,² Volodymyr Novikov¹ and Andrei Khairulin³

¹ Department of Technology Biologically Compounds, Pharmacy and Biotechnology, Lviv Polytechnic National University, Lviv 79013, Ukraine

² Department of Organic and Pharmaceutical Technology, Odessa National Polytechnic University, Odessa 65044, Ukraine

³ Laboratory of Condensed Heterocyclic Compounds, Department of Sulfur Chemistry, Institute of Organic Chemistry NAS of Ukraine, Kyiv 02660, Ukraine

* Corresponding author: E-mail: mashaneutron@gmail.com;
ORCID 0000-0002-3201-7961

Received: 02-22-2020

Abstract

Novel heterocyclic dichloronaphthoquinone derivatives have been synthesized by chlorine atom substitution in 2,3-dichloro-1,4-naphthoquinone to pyrazole or pyrimidine fragments. The structures of these compounds have been confirmed by FT-IR, ESI-MS, ¹H-NMR, ¹³C-NMR and elementary analysis. Synthesized compounds were evaluated for their anticonvulsant action in a pentylenetetrazole (PTZ)-convulsion model and antidepressant activity in the forced swimming test (FST). All naphthoquinone derivatives at a dose 100 mg/kg indicated anticonvulsant effect in PTZ-induced test at 3 h and 24 h after oral administration. In addition, these compounds possessed prolonged antidepressant properties significantly reducing the duration of immobility time when compared to the reference drug amitriptyline.

Keywords: 2,3-dichloro-1,4-naphthoquinone; pyrazole and pyrimidine fragments; anticonvulsant activity; antidepressant action

1. Introduction

The development of novel compounds possessing combined action on central nervous system (CNS) and, thus, capable of being used simultaneously in treatment of various CNS disorders, still remains an active field in drug discovery. Such CNS disease state as depression is concomitant pathology in patients with epilepsy while some antidepressants were found to increase the risk of seizures (bupropion) or exhibit both the anticonvulsant and proconvulsant effect in experimental study (venlafaxine).¹ In this context, synthesis of compounds contemporaneously demonstrating antidepressant and anticonvulsant activity is feasible approach to reduce aforementioned side effects. In this context, significant interest is attracted by naphthoquinones and their derivatives as building blocks for rational drug design. A considerable amount of these com-

pounds have already been reported as antifungal, anti-inflammatory, anticancer and antibacterial agents.^{2–6} Surprisingly, only a limited number of publications are devoted to investigation of naphthoquinones influence on CNS. For example, amide derivatives of 4-amino-1,2-naphthoquinone were examined for anticonvulsant activity by the maximal electroshock (MES) and subcutaneous pentylenetetrazole (sc. PTZ) tests.⁷ The antidepressant potential of plumbagin, a medicinal plant-derived naphthoquinone, was explored in unstressed and stressed mice and explained by inhibition of brain monoamine oxidase A (MAO-A) activity.⁸ Naphthoquinones derived from *Lithospermum erythrorhizon* (acetylshikonin and shikonin) were isolated and proven as inhibitors of MAO-A and MAO-B in a competitive manner that might be further used in the treatment of depression.⁹ Obviously, the nature and position of substituents in naphthoquinone core are

the crucial factors affecting the pharmacological evaluation of the structures. Bearing in mind that five- and six-membered heterocycles, pyrazole and pyrimidine, are important scaffold for CNS-active compounds,^{10–13} our attention was paid to the naphthoquinones containing these moieties. Thus, here we report the synthesis of aminopyrazole- and aminopyrimidine derivatives of 2,3-dichloro-1,4-naphthoquinone and their anticonvulsant and antidepressant activity determined by pentylenetetrazole (PTZ) and forced swim test (FST), accordingly.

2. Experimental

2. 1. Chemistry

IR spectrum was measured with a Thermo Scientific Nicolet iS10 FT-IR Spectrometer using Nicolet iZ10 module (Thermo Fisher Scientific, Madison, WI, USA) equipped with a diamond window in a range of 4000–525 cm^{-1} . ^1H NMR and ^{13}C NMR spectra were recorded on Varian Mercury-400 (Varian Inc., Palo Alto, CA) 300 MHz/75 MHz spectrometer with $\text{DMSO}-d_6$ or CDCl_3 as solvents and TMS as an internal standard; the coupling constants are given in Hz. The elemental analysis was performed on a Euro Vector EA-3000 (Eurovector SPA, Re-davalle, Italy) microanalyzer. Elemental analyses were within $\pm 0.4\%$ of the theoretical values. Electrospray ionization mass spectrometry (ESI-MS) was measured by Agilent 1100 Series (LC/MSD Trap) Spectrometer applying isocratic elution of acetonitrile : 0.01% formic acid aqueous solution (70:30). Separation column: Rapid Resolutionn HT Cartige 4.6x30 mm, 1.8-Micron, Zorbax SB-C18. Melting points (uncorrected) were measured in an open capillary tube using a Stuart SMP30 melting point apparatus.

2. 1. 1. General Procedure for the Synthesis of Aminopyrazole Derivatives of Naphthoquinone (3a–d)

To a magnetically stirred solution of 2,3-dichloro-1,4-naphthoquinone (**1**) (0.68 g, 0.3 mmol) in ethanol (50 mL) was added a solution of aminopyrazole **2a–d** (0.3 mmol) in ethanol (20 mL). The reaction was carried out at 78 °C in the presence of an equivalent amount of Na_2CO_3 with constant stirring for 3 h. Reaction progress was monitored by TLC analysis. After reaction completion the obtained precipitate was filtered, washed several times with water and dried. The precipitate was suspended in 20 ml of ethanol, heated to boiling, filtered from impurities, the filtrate was cooled with ice to 0 °C, the precipitated crystals were filtered, dried in vacuum over CaCl_2 to afford compounds **3a–c** as red and **3d** as orange colored crystals.

2-Chloro-3-((1-(difluoromethyl)-1-H-pyrazol-3-yl)-amino)-naphthalene-1,4-dione (3a)

Yield 42%, red crystals, m.p. = 123–125 °C. IR (KBr, cm^{-1}):

3642 (N-H), 2968, 2895 ($\text{CH}_{\text{aliphatic}}$), 1681 (C=O), 1059, 1083 (C-F). ^1H NMR (300 MHz, $\text{DMSO}-d_6$): δ 9.01 (s, 1H, NH), 7.93–8.05 (m, 4H, Ar-H), 7.12 (d, $J = 4.4$ Hz, 1H, CH-pyraz.), 5.95 (d, $J = 4.4$ Hz, 1H, CH-pyraz.), 6.63 (s, 1H, CH). ^{13}C NMR (75 MHz, $\text{DMSO}-d_6$) δ , ppm: 180.03 (C), 176.9 (C), 149.1 (C), 147.9 (C), 133.1 (CH), 133.2 (CH), 131.0 (CH), 130.6 (C), 129.1 (C), 123.9 (CH), 123.8 (CH), 114.7 (CH), 106.1 (C), 94.8 (CH). MS (ESI), m/z (%): calculated for $\text{C}_{14}\text{H}_8\text{ClF}_2\text{N}_3\text{O}_2$ $[\text{M}]^+$ 323, found 323 (100). Calcd: C 58.45; H 3.50; Cl 12.32; N 14.61; O 11.12. Found: C 58.32; H 3.40; Cl 12.24; N 14.50. HPLC: $t_r = 0.879$ min.

2-Chloro-3-((1-methyl-1H-pyrazol-3-yl)amino)naphthalene-1,4-dione (3b)

Yield 78%, red crystals, m.p. = 215–217 °C. IR (KBr, cm^{-1}): 3200 (N-H); 1680, 1652 (C=O), 2967, 2894 ($\text{CH}_{\text{aliphatic}}$), 717 (C-Cl). ^1H NMR (300 MHz, CDCl_3): δ 9.03 (s, 1H, NH), 7.96–8.07 (m, 2H, Ar-H), 7.71–7.91 (m, 2H, Ar-H), 7.60 (d, $J = 2.2$ Hz, 1H, CH-pyraz.), 6.04 (d, $J = 2.2$ Hz, 1H, CH-pyraz.), 3.76 (s, 3H, CH_3). ^{13}C NMR (75 MHz, $\text{DMSO}-d_6$) δ , ppm: 180.1 (C), 177.1 (C), 149.2 (C), 147.5 (C), 133.3 (CH), 133.2 (CH), 132.2 (CH), 131.2 (C), 130.8 (C), 125.0 (CH), 124.8 (CH), 106.7 (C), 92.7 (CH), 37.7 (CH_3). MS (ESI), m/z (%): calculated for $\text{C}_{14}\text{H}_{10}\text{ClN}_3\text{O}_2$ $[\text{M}]^+$ 287, found 287 (100). Calcd: C 58.45; H 3.50; Cl 12.32; N 14.61; O 11.12. Found: C 58.30; H 3.42; Cl 12.21; N 14.50. HPLC: $t_r = 0.961$ min.

2-Chloro-3-((3-(p-tolyl)-1H-pyrazol-5-yl)amino)naphthalene-1,4-dione (3c)

Yield 56%, red crystals, m.p. = 238–240 °C. IR (KBr, cm^{-1}): 3500 (N-H), 1672 (C=O), 1600–1572 (C=C), 720 (C-Cl). ^1H NMR (300 MHz, $\text{DMSO}-d_6$): δ 12.95 (s, 1H, NH), 9.07 (s, 1H, NH), 7.97–8.06 (m, 2H, Ar-H), 7.86 (t, 1H, Ar-H), 7.79 (t, 1H, Ar-H), 7.63 (d, $J = 7.8$ Hz, 2H, Ar-H), 7.26 (d, $J = 7.9$ Hz, 2H, Ar-H), 6.49 (s, 1H, CH-pyraz.), 2.33 (s, 3H, CH_3). ^{13}C NMR (75 MHz, $\text{DMSO}-d_6$) δ , ppm: 179.9 (C), 176.8 (C), 148.2 (C), 144.3 (C), 142.1 (C), 138.1 (C), 132.9 (CH), 132.8 (CH), 131.2 (C), 131.1 (C), 129.8 (2CH), 125.9 (2CH), 125.6 (CH), 125.2 (CH), 124.9 (C), 105.3 (C), 94.2 (CH), 22.0 (CH_3). MS (ESI), m/z (%): calculated for $\text{C}_{20}\text{H}_{14}\text{ClN}_3\text{O}_2$ $[\text{M}]^+$ 363, found 363 (100). Calcd: C 66.03; H 3.88; Cl 9.74; N 11.55; O 8.80. Found: C 65.62; H 3.77; Cl 9.63; N 11.25. HPLC: $t_r = 1.389$ min.

Ethyl-4-((3-chloro-1,4-dioxo-1,4-dihydronaphthalen-2-yl)amino)-1-phenyl-1H-pyrazol-3-carboxylate (3d)

Yield 76%, orange crystals, m.p. = 162–165 °C. IR (KBr, cm^{-1}): 3300 (N-H), 1712 (C=O), 1676, 1652 (C=O), 1604–1576 (C=C), 720 (C-Cl). ^1H NMR (300 MHz, $\text{DMSO}-d_6$): δ 9.38 (br.s, 1H, NH), 8.12 (s, 1H, CH-pyraz.), 8.01 (t, 2H, Ar-H), 7.89 (d, $J = 7.4 \times 2$ Hz, 1H, Ar-H), 7.82 (d, $J = 7.4 \times 2$ Hz, 1H, Ar-H), 7.66 (d, $J = 7.9$ Hz, 2H, Ar-H), 7.51 (t, 2H, Ar-H), 7.42 (t, 1H, Ar-H), 4.04 (q, CH_2CH_3 , 2H), 1.02 (t, CH_2CH_3 , 3H). ^{13}C NMR (75 MHz, $\text{DMSO}-d_6$) δ , ppm: 180.2 (C), 176.9 (C), 161.9 (C), 149.3 (C), 147.5 (C), 140.9 (C), 133.2 (CH), 133.1 (CH), 131.1 (C), 131.0 (C), 130.8 (CH), 130.0 (2CH), 127.1

(CH), 125.7 (CH), 125.3 (CH), 118.2 (2CH), 106.1 (C), 96.8 (C), 59.5 (CH₂), 14.3 (CH₃). MS (ESI), *m/z* (%): calculated for C₂₂H₁₆ClN₃O₄ [M]⁺ 422, found 422 (100). Calcd: C 62.64; H 3.83; Cl 8.40; N 9.96; O 15.17. Found: C 62.35; H 3.71; Cl 8.29; N 9.85. HPLC: *t_r* = 1.059 min.

2. 1. 2. General Procedure for the Synthesis Aminopyrimidine Derivatives of Naphthoquinone (3e–f)

To a magnetically stirred solution of 2,3-dichloro-1,4-naphthoquinone (1) (0.27 g, 0.1 mmol) in DMF (15 mL) was added a solution of aminopyrimidine 2e–f (0.1 mmol) in DMF (10 mL). The reaction was carried out at 65 °C in the presence of an equivalent amount of K₂CO₃ with constant stirring for 4 h. Reaction progress was monitored by TLC analysis. The mixture was left to cool to room temperature (25 °C), then the reaction mixture diluted with water (30 ml) and acidified with 5% HCl to pH 6–7; the formed precipitate was filtered off. The precipitate was suspended in 20 ml of ethanol, heated to boiling, filtered from impurities, the filtrate was cooled with ice to 0 °C, the precipitated crystals were filtered and dried in vacuum over CaCl₂ to afford compounds 3a–f as orange colored crystals.

2-Chloro-3-((2-(4-methyl-6-(trifluoromethyl)pyrimidin-2-yl)ethyl)amino)naphthalene-1,4-dione (3e)

Yield 73%, orange crystals, m.p. = 121–123 °C. IR (KBr, cm⁻¹): 3656 (N-H), 2981, 2889 (CH_{aliphatic}), 1677 (C=O), 1138 (C-F). ¹H NMR (300 MHz, DMSO-*d*₆): δ 7.91–7.99 (m, 2H, Ar-H), 7.86–7.71 (m, 2H, Ar-H), 7.54 (br.s, NH, 1H), 4.21 (t, 2H, CH₂), 3.28 (t, 2H, CH₂), 2.53 (s, 3H, CH₃). ¹³C NMR (75 MHz, DMSO-*d*₆) δ, ppm: 180.2 (C), 177.2 (C), 168.1 (C), 166.7 (C), 149.6 (C), 139.5 (C), 133.4 (CH), 133.3 (CH), 131.8 (C), 130.4 (C), 123.1 (CH), 122.7 (CH), 122.0 (C), 112.5 (CH), 107.8 (C), 42.9 (CH₂), 31.8 (CH₂), 21.3 (CH₃). MS (ESI), *m/z* (%): calculated for C₁₈H₁₃ClF₃N₃O₂ [M]⁺ 395, found 395 (100). Calcd: C 54.63; H 3.30; Cl 8.96; F 14.40; N 10.62; O 8.09. Found: C 54.36; H 3.19; Cl 8.87; F 14.29 N 10.50. HPLC: *t_r* = 1.090 min.

2-Chloro-3-((2-(4-(trifluoromethyl)-5,6,7,8-tetrahydroquinazolin-2-yl)ethyl)amino) naphthalene-1,4-dione (3f)

Yield 53%, orange crystals, m.p. = 118–120 °C. IR (KBr, cm⁻¹): 3659 (N-H), 2980, 2889 (CH_{aliphatic}), 1679 (C=O), 1144, 1123 (C-F). ¹H NMR (300 MHz, DMSO-*d*₆): δ 8.04–7.67 (m, 4H, Ar-H), 7.48 (br.s, 1H, NH), 4.19 (t, 2H, CH₂), 3.20 (t, 2H, CH₂), 2.62–2.93 (m, 4H, 2CH₂), 1.90–1.65 (m, 4H, 2CH₂). ¹³C NMR (75 MHz, DMSO-*d*₆) δ, ppm: 180.6 (C), 177.1 (C), 168.1 (C), 165.9 (C), 153.0 (C), 139.8 (C), 133.2 (CH), 133.1 (CH), 131.3 (C), 130.7 (C), 122.8 (CH), 122.3 (CH), 121.7 (C), 119.8 (C), 106.9 (C), 42.8 (CH₂), 32.1 (CH₂), 30.8 (CH₂), 23.7 (CH₂), 22.5 (CH₂), 22.8 (CH₂). MS (ESI), *m/z* (%): calculated for C₂₁H₁₇ClF₃N₃O₂ [M]⁺ 435, found 435 (100). Calcd: C 57.87; H 3.93; Cl 8.13; F 13.08; N 9.65; O 7.34. Found: C 56.89; H 3.89; Cl 8.07 F 12.21; N 9.58. HPLC: *t_r* = 1.199 min.

2. 2. Pharmacological Evaluation

2. 2. 1. Animals

Pharmacological investigations of compound 3a–f were studied using outbred male white mice (18–22 g) as experimental animals purchased from Odessa National Medical University, Ukraine. All animals were kept under 12 h light regime and in a standard animal facility with free access to water and food, in compliance with the European Convention for the Protection of Vertebrate Animals Used for Experimental and Other Specific Purposes (Strasbourg, 1986).

2. 2. 2. Drug Administration

Anticonvulsant and antidepressant activities of compounds 3a–f were evaluated at 3 h and 24 h after administration. The compounds were administered orally to mice in Tween 80/water emulsion at a dose of 100 mg/kg and Tween 80/water emulsion has been used as a vehicle control. Valproic acid (VPA, 400 mg/kg, p.o.) and amitriptyline (20 mg/kg, p.o.) served as reference drugs, respectively.

2. 2. 3. Anticonvulsant Activity

The anticonvulsant activity of 1,4-naphthoquinone derivatives was evaluated by pentylenetetrazole model (PTZ) as described in.^{14,15} Doses of PTZ for inducing clonic-tonic convulsions (DCTC) and tonic extension (DTE) were calculated relative to control. The anticonvulsant effect of compounds was estimated at 3 h and 24 h after their administration from the increase of pentylenetetrazole MED compared with a control group. MED in percent was calculated using the formula:

$$\text{MED} = V/m \times 10^4$$

where MED – minimum effective dose of PTZ inducing DCTC or DTE; V – volume of PTZ solution, ml; m – animal weight, g.

2. 2. 4. Antidepressant Effect

Forced swim test (FST) was used to determine antidepressant action of 1,4-naphthoquinone derivatives 3a–f according to procedure.¹⁶ Briefly, mice were placed individually into glass cylinder filled with water (24 ± 3 °C) and total duration of their immobility during 5 minutes has been recorded.

2. 2. 5. Statistical Analysis

All results are expressed as mean ± standard error mean (SEM). One-way analysis of variance (ANOVA) was used to determine the statistical significance of the results followed by Tukey's *post hoc* comparison. ** *p* < 0.01 and * *p* < 0.05 was considered as significant.

3. Results and Discussion

3. 1. Chemistry

Naphthoquinones are highly reactive compounds due to the activation of unsaturated bond by two conjugated electron-withdrawing carbonyl groups. 2,3-Dichloro-1,4-naphthoquinone readily reacts with nucleophiles with substitution of one chlorine atom by one-step mechanism. A nucleophilic attack results in the formation of σ -complex and then the chlorine anion is eliminated with the regeneration of quinoid structure.^{17,18} The activity of the second chlorine atom depends on the electronic effect of the first substituent. It reduces greatly when an electron-donating group such as an amine is bonded to a C₂ atom. However, the second substitution can occur if electron-withdrawing substituent is introduced.^{19,20}

Currently, minor information is available on the reaction of 2,3-dichloro-1,4-naphthoquinone with aminopyrazole derivatives. Hassan et al.²¹ investigated methods for the synthesis of aminopyrazole derivatives of 2,3-dichloro-1,4-naphthoquinone, 2,3-dicyano-1,4-naphthoquinone and its isomer 2-(dicyanomethylene)indan-1,3-dione. According to the described method, reaction of 2 eq. of 2,3-dichloro-1,4-naphthoquinone with 1 eq. of aminopyrazole derivatives without using a base proceeds with the formation of cyclization product involving both nucleophilic centers of 2,3-dichloro-1,4-naphthoquinone. However, in our case the aforementioned method was ineffective - only the products of monosubstitution instead of cyclization derivatives were formed and isolated with low yield after heating with triethylamine.

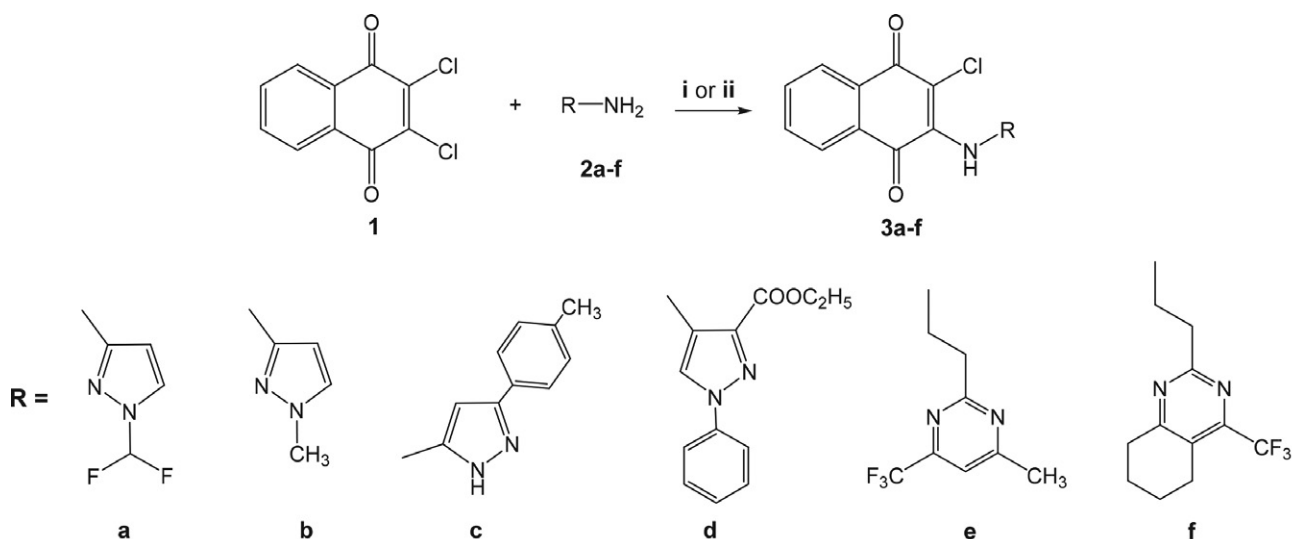
Given the above, synthesis of novel heterocyclic dichloronaphthoquinone derivatives (**3a-f**) was carried out by chlorine atom substitution of 2,3-dichloro-1,4-naphthoquinone (**1**) to pyrazole (**3a-d**) or pyrimidine (**3e-f**) fragments. As illustrated in Scheme 1, target compounds

(**3a-f**) were obtained by mixing equimolar ratios of 2,3-dichloro-1,4-naphthoquinone with heterocyclic amines (**2a-f**) in ethanol with further mixture refluxing for 2 h in the presence of Na₂CO₃ as a base or using DMF as solvent and K₂CO₃ as a base with constant stirring of reaction mixture at 65 °C during 4 h.

Novel heterocyclic N-derivatives naphthoquinone (**3a-f**) were obtained in the range of 42–78% yield as red or orange solids. The structures of products **3a-f** were reliably confirmed and elucidated on the basis of spectral and analytical data. The FTIR spectra exhibited absorption peaks at 3200–3659 cm⁻¹ (NH), 1652–1712 cm⁻¹ (C=O), 2895–2980 cm⁻¹ (CH_{aliphatic}), 717–720 cm⁻¹ (C-Cl) and 1059–1144 cm⁻¹ (C-F). The ¹H-NMR spectral data of naphthoquinone **3a-f** contain resonance signals described by their chemical shift, integration and multiplicity that are in full agreement with the presented molecular formulas.

3. 2. Pharmacological Studies

In the present study, a non-competitive GABA antagonist pentylenetetrazole (PTZ) has been used to investigate anticonvulsant activity of 1,4-naphthoquinone derivatives (**3a-f**). PTZ-induced seizure model is positioned as a model of generalized convulsions and extensively used for evaluating the excitability of central nervous system (CNS) and, consequently, activity of gamma-aminobutyric acid (GABA).²² Valproic acid (VPA), an established antiepileptic drug possessing anticonvulsive effect on PTZ-induced model, served as reference drug.²³ Anticonvulsant activity of heterocyclic compounds **3a-f** was estimated after single oral administration (100 mg/kg, p.o.) at short (3 h) and long (24 h) time periods. As shown in Figure 1, all synthesized compounds and VPA were found to protect animals from clonic-tonic convulsions and tonic extension at 3 h after their oral administration as evidenced by in-



Scheme 1. Synthesis of aminopyrazole- (**3a-d**) and aminopyrimidine (**3e-f**) derivatives of dichloronaphthoquinone. Reagents and conditions: i) EtOH/Na₂CO₃, reflux, 2 h; ii) DMF/K₂CO₃, 65 °C, 4 h

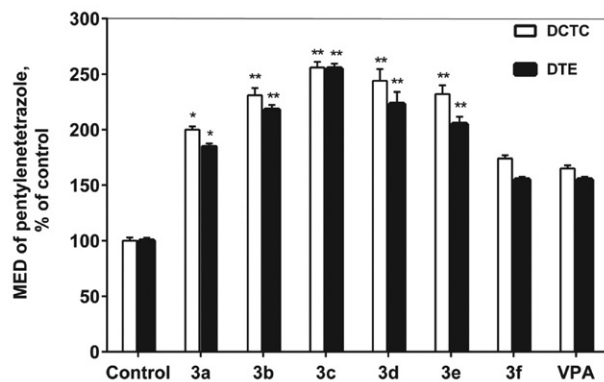


Figure 1. Anticonvulsant activity of compounds **3a-f** at 3 h after oral administration. Values are given as mean \pm SEM, $n = 5$ mice; for all groups $p < 0.01$ compared with control; * $p < 0.05$ and ** $p < 0.01$ compared with VPA

creasing of DCTC and DTE values ($p < 0.01$ vs control). At this time point, DCTC and DTE values of 1,4-naphthoquinones **3a** ($p < 0.05$ vs VPA) and **3b-e** ($p < 0.01$ vs VPA) are statistically different from those defined for reference drug (VPA) indicating a decrease of seizure threshold.

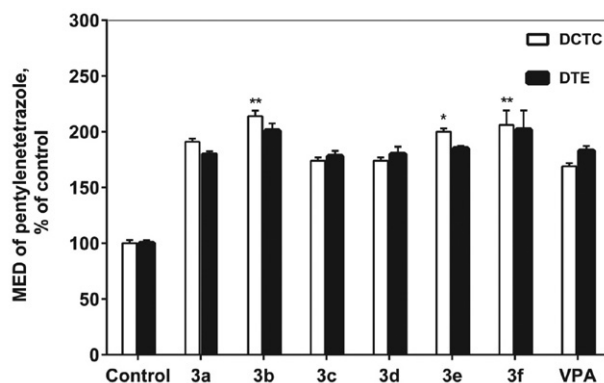


Figure 2. Anticonvulsant activity of compounds **3a-f** at 24 h after oral administration. Values are given as mean \pm SEM, $n = 5$ mice; for all groups $p < 0.01$ compared with control; * $p < 0.05$ and ** $p < 0.01$ compared with VPA

Evaluation of pentylenetetrazole-induced seizure susceptibility of compounds **3a-f** was also carried out at long time period (24 h), as depicted in Figure 2. In this case, statistically significant difference was observed only in tonic phase of clonic-tonic seizures between naphthoquinones **3b** ($p < 0.01$ vs VPA), **3e** ($p < 0.05$ vs VPA), **3f** ($p < 0.01$ vs VPA) and reference drug. It is noteworthy that antiseizure effect of compounds **3a**, **3c**, **3d** were also demonstrated prolonged anticonvulsant action at 24 h after administration that is indicated as DCTC and DTE increase in 2 times when compared to control.

As demonstrated in Table 1, mean immobility period was reduced in animals treated both with naphthoquinone derivatives **3a-f** and reference drug amitriptyline compared to control at 3 h after oral administration. When

compared with amitriptyline, the antidepressant activity of compounds **3a-f** did not exceed that of reference drug.

Table 1. Antidepressant activity of compounds **3a-f** in forced swim test (FST).

Compound	Immobility time, s	
	3 h after administration	24 h after administration
Control	95.0 \pm 8.7	95.0 \pm 8.7
3a	51.7 \pm 7.8	34.7 \pm 4.9**
3b	16.0 \pm 6.7	39.3 \pm 8.7**
3c	46.3 \pm 7.8	53.7 \pm 3.2**
3d	70.7 \pm 5.2	20.0 \pm 4.5**
3e	39.0 \pm 4.4	45.7 \pm 4.7**
3f	27.3 \pm 3.7	47.7 \pm 3.0**
Amitriptyline	25.7 \pm 3.5	93.7 \pm 4.4

All values are expressed as mean \pm SEM; $n = 5$ mice; for all groups $p < 0.01$ compared with control; * $p < 0.05$ and ** $p < 0.01$ compared with amitriptyline.

However, there was no statistically significant difference in immobility time between control groups of animals and that treated with amitriptyline at long time period (24 h). At this time point, all synthesized naphthoquinone derivatives were found to possess significant antidepressant-like effect ($p < 0.01$ vs. amitriptyline) indicating a prolonged action of compounds **3a-f**.

4. Conclusion

Heterocyclic N-derivatives naphthoquinone containing pyrazole and pyrimidine moieties have been synthesized in good yield and characterized by a series of analytical and spectroscopic methods (^1H NMR, ^{13}C NMR, FT-IR, ESI-MS, LC and elementary analysis). The activity of synthesized compounds as potential anticonvulsant and antidepressant agents was investigated on the models of PTZ-induced seizures and forced swim test (FST), accordingly. Pharmacological analyses showed that compounds **3a-f** exhibit anticonvulsant and antidepressant properties at a dose 100 mg/kg both at short and long time period (3 h and 24 h after oral administration). Thus, naphthoquinone derivatives obtained at the present study demonstrate combined action on CNS and might be further studied as compounds useful for treating depressive disorders in patients with seizures.

5. References

1. A. K. Sharma, N. Dahiya, A. Khanapure, J. K. Kairi, *Int. J. Basic Clin. Pharmacol.* **2016**, *5*, 850–854.
DOI:10.18203/2319-2003.ijbcp20161533

2. M. Á. Castro, A. M. Gamito, V. Tangarife-Castaño, B. Zapata, J. M. Miguel del Corral, A. C. Mesa-Arango, L. Betancur-Galvis, A. San Feliciano, *Eur. J. Med. Chem.* **2013**, *67*, 19–27. DOI:10.1016/j.ejmech.2013.06.018
3. P. Ravichandiran, M. Maslyk, S. Sheet, M. Janeczko, D. Premnath, A. R. Kim, B. H. Park, M. K. Han, D. J. Yoo, *Chemistry-Open* **2019**, *8*, 589–600. DOI:10.1002/open.201900077
4. I. Milackova, M. S. Prnova, M. Majekova, R. Sotnikova, M. Stasko, L. Kovacikova, S. Banerjee, M. Veverka, M. Stefek, *J. Enzyme Inhib. Med. Chem.* **2015**, *30*, 107–113. DOI:10.3109/14756366.2014.892935
5. V. Prachayasittikul, R. Pingaew, A. Worachartcheewan, C. Nantasenamat, S. Prachayasittikul, S. Ruchirawat, V. Prachayasittikul, *Eur. J. Med. Chem.* **2014**, *84*, 247–263. DOI:10.1016/j.ejmech.2014.07.024
6. K. Kobayashi, S. Nishiumi, M. Nishida, M. Hirai, T. Azuma, H. Yoshida, Y. Mizushina, M. Yoshida, *Med. Chem.* **2011**, *7*, 37–44. DOI:10.2174/157340611794072742
7. M. Bansal, B. Goel, S. Shukla, R. S. Srivastava, *Med. Chem. Res.* **2013**, *22*, 5349–5355. DOI:10.1007/s00044-013-0531-6
8. D. Dhingra, S. Bansal, *Pharmacol. Rep.* **2015**, *67*, 1024–1032. DOI:10.1016/j.pharep.2015.03.001
9. W. H. Choi, S. S. Hong, S. A. Lee, X. H. Han, K. S. Lee, M. K. Lee, B. Y. Hwang, J. S. Ro, *Arch. Pharm. Res.* **2005**, *28*, 400–404. DOI:10.1007/BF02977668
10. H. Zhang, S. Wang, X. Wen, J.-Z. Li, Z.-S. Quan, *Med. Chem. Res.* **2016**, *25*, 1287–1298. DOI:10.1007/s00044-016-1559-1
11. K. Karrouchi, S. Radi, Y. Ramli, J. Taoufik, Y. N. Mabkhot, F. A. Al-Aizari, M. Ansar, *Molecules* **2018**, *23*, 1–86. DOI:10.3390/molecules23010134
12. M. J. Naim, O. Alam, F. Nawaz, M. J. Alam, P. Alam, *J. Pharm. Bioallied. Sci.* **2016**, *8*, 2–17. DOI:10.4103/0975-7406.171694
13. S. B. Wang, X. Q. Deng, Y. Zheng, Y. P. Yuan, Z. S. Quan, L. P. Guan, *Eur. J. Med. Chem.* **2012**, *56*, 139–144. DOI:10.1016/j.ejmech.2012.08.027
14. M. V. Nesterkina, I. A. Kravchenko, *Chem. Nat. Compd.* **2016**, *52*, 237–239. DOI:10.1007/s10600-016-1604-9
15. M. V. Nesterkina, E. A. Alekseeva, I. A. Kravchenko, *Pharm. Chem. J.* **2014**, *48*, 82–84. DOI:10.1007/s11094-014-1052-4
16. G. Gupta, T. J. Jia, L. Y. Woon, D. K. Chellappan, M. Candamy, K. Dua, *Adv. Pharmacol. Sci.* **2015**, *2015*, 1–6. DOI:10.1155/2015/164943
17. A. A. Kutyrev, *Tetrahedron* **1991**, *47*, 8043–8065. DOI:10.1016/S0040-4020(01)91002-6
18. G.M. Neelgund, M. L. Budni, *Spectrochim Acta A* **2005**, *61*, 1729–1735. DOI:10.1016/j.saa.2004.07.003
19. M. Delarmelina, S. J. Greco, J. W. Carneiro, *Tetrahedron* **2017**, *73*, 4363–4370. DOI:10.1016/j.tet.2017.05.095
20. L. R. Domingo, J. A. Saez, R. J. Zaragoza, M. Arno, *J. Org. Chem.* **2008**, *73*, 8791–8799.
21. A. A. Hassan, N. K. Mohamed, Y. R. Ibrahim, A. F. E. Mourad, *Liebigs Ann. Chem.* **1993**, *6*, 695–697. DOI:10.1002/jlac.1993199301112
22. A. V. Kalueff, *Neurochem. Int.* **2007**, *50*, 61–68. DOI:10.1016/j.neuint.2006.07.004
23. D. Calderón Guzmán, I. Espitia Vázquez, G. Barragán Mejía, N. Labra Ruiz, R. Rodríguez Pérez, D. Santamaria del Angel, F. Ayala Guerrero, H. Juárez Olguín, *Proc. West Pharmacol. Soc.* **2003**, *46*, 48–50.

Povzetek

Novi heterociklični derivati dikloronaftokinona so bili sintetizirani s substitucijo klorovega atoma v 2,3-dikloro-1,4-naftokinonu s fragmenti pirazola ali pirimidina. Strukture teh spojin so bile potrjene s FT-IR, ESI-MS, ¹H-NMR, ¹³C-NMR in elementno analizo. Antikonvulzivno delovanje sintetiziranih spojin je bilo ocenjeno v pentilentetrazol (PTZ) konvulzijskem modelu in z antidepresivnim delovanjem v testu prisilnega plavanja (FST). Vsi derivati naftokinona so v odmerku 100 mg/kg izkazovali antikonvulzivni učinek v PTZ-induciranem testu 3 ure in 24 ur po peroralni uporabi. Poleg tega so te spojine izkazovale dolgotrajne antidepresivne lastnosti in znatno zmanjšale čas nepremičnosti v primerjavi z referenčno učinkovino amitriptilin.



Except when otherwise noted, articles in this journal are published under the terms and conditions of the Creative Commons Attribution 4.0 International License

Scientific paper

A Simple and Effective Synthesis of 3- and 4-((Phenylcarbamoyl)oxy)benzoic Acids

Urban Košak¹ and Stanislav Gobec^{1,*}¹ Faculty of Pharmacy, University of Ljubljana, Aškerčeva 7, 1000 Ljubljana, Slovenia

* Corresponding author: E-mail: stanislav.gobec@ffa.uni-lj.si

Tel.: + 386 (1)4769585; fax: + 386 (1)4258031

Received: 03-23-2020

Abstract

Phenserine, posiphen, tolserine and cymserine and its derivatives are experimental Alzheimer's disease drugs that contain a phenyl phenylcarbamate moiety that is responsible for their anti-Alzheimer activities. We have developed a simple (3 steps) and effective (overall yields 76–90%) method for preparing 3- and 4-((phenylcarbamoyl)oxy)benzoic acids which can be reacted with amines to produce phenyl phenylcarbamate moiety containing amides as new potential anti-Alzheimer disease drugs. The synthesized carboxylic acids are thus important building blocks with potential use in medicinal chemistry and drug discovery.

Keywords: ((Phenylcarbamoyl)oxy)benzoic acids; phenyl isocyanates; carbamates; building blocks; Alzheimer's disease.

1. Introduction

Alzheimer's disease (AD) is a progressive neurodegenerative brain disorder.¹ The synaptic dysfunction and neurodegeneration in AD most severely affects the cholinergic system.² This decreases the levels of the neurotransmitter acetylcholine (ACh),³ which then produces cognitive impairment and memory loss,⁴ characteristic for patients with AD. Several compounds are currently being evaluated in preclinical and clinical trials for efficacy in AD, including cholinesterase (ChE) inhibitors which increase the levels of ACh in the brain: phenserine, posiphen, tolserine and cymserine and its derivatives (Figure 1).⁵ These experimental Alzheimer's disease drugs all contain the phenyl phenylcarbamate moiety or its derivative. Phenserine⁶ and posiphen⁷ contain a phenyl phenylcarbamate moiety, tolserine⁸ contains a phenyl *ortho*-tolylcarbamate moiety and cymserine and its derivatives^{9,10} contain a phenyl (4-isopropylphenyl)carbamate moiety (Figure 1).

Phenserine, posiphen, tolserine and cymserine and its derivatives are pseudo-irreversible carbamate inhibitors of ChEs where the phenyl phenylcarbamate moiety is responsible for their biological activity. Their mechanism of inhibition involves a rapid initial covalent reaction between their carbamate carbonyl group and the catalytic serine in the active site of ChEs (carbamoylation). The inhibited (carbamoylated) ChE is then reactivated by a slow

hydrolysis (decarbamylation) of the active enzyme serine (Scheme 1).^{11,12}

As part of our development of new ChE inhibitors as potential anti-Alzheimer disease drugs, we designed compounds with the general formula **1** that contain the phenyl phenylcarbamate moiety (Scheme 2A). These compounds were designed based on the structures of our previously reported ChE inhibitors.^{13–15} We planned to synthesize compounds with the general formula **1** by utilizing one of several methods for the synthesis of carbamates,^{16,17} i.e. reacting phenols with the general formula **2** with various phenyl isocyanates (**3**) in the presence of a catalytic amount of 4-dimethylamino pyridine (4-DMAP) in CH₂Cl₂ or DMF (Scheme 2A).^{18,19} However, this reaction did not produce the desired carbamates as no reaction was observed. Therefore, we had to plan an alternative synthetic route. We decided to use 3- and 4-((phenylcarbamoyl)oxy)benzoic acids (**4**) and react them with various amines (**5**) which we have previously used to synthesize amide^{13,14} and sulfonamide^{14,15} ChE inhibitors, in the presence of coupling reagent TBTU and *N,N*-diisopropylethylamine (DIPEA) in CH₂Cl₂²⁰ to produce the designed amides (Scheme 2B).

The problem was that 3- and 4-((phenylcarbamoyl)oxy)benzoic acids (**4**; Scheme 2B) are not commercially available and procedures for their preparation have also not been reported yet. Herein we describe how we solved

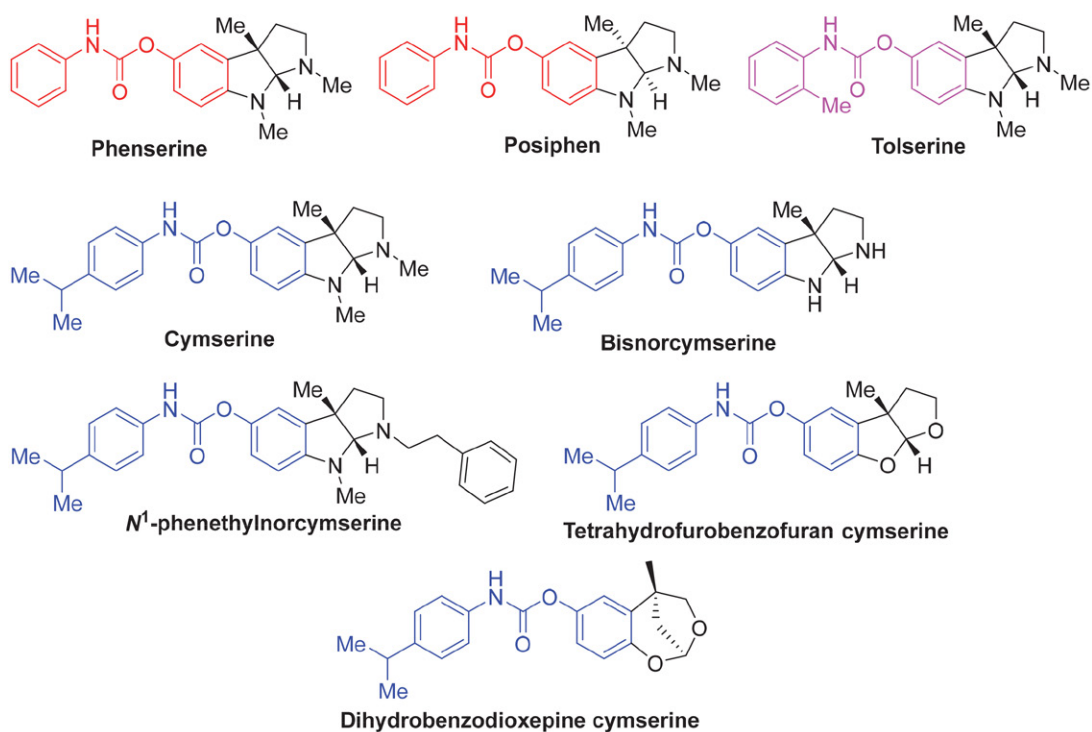
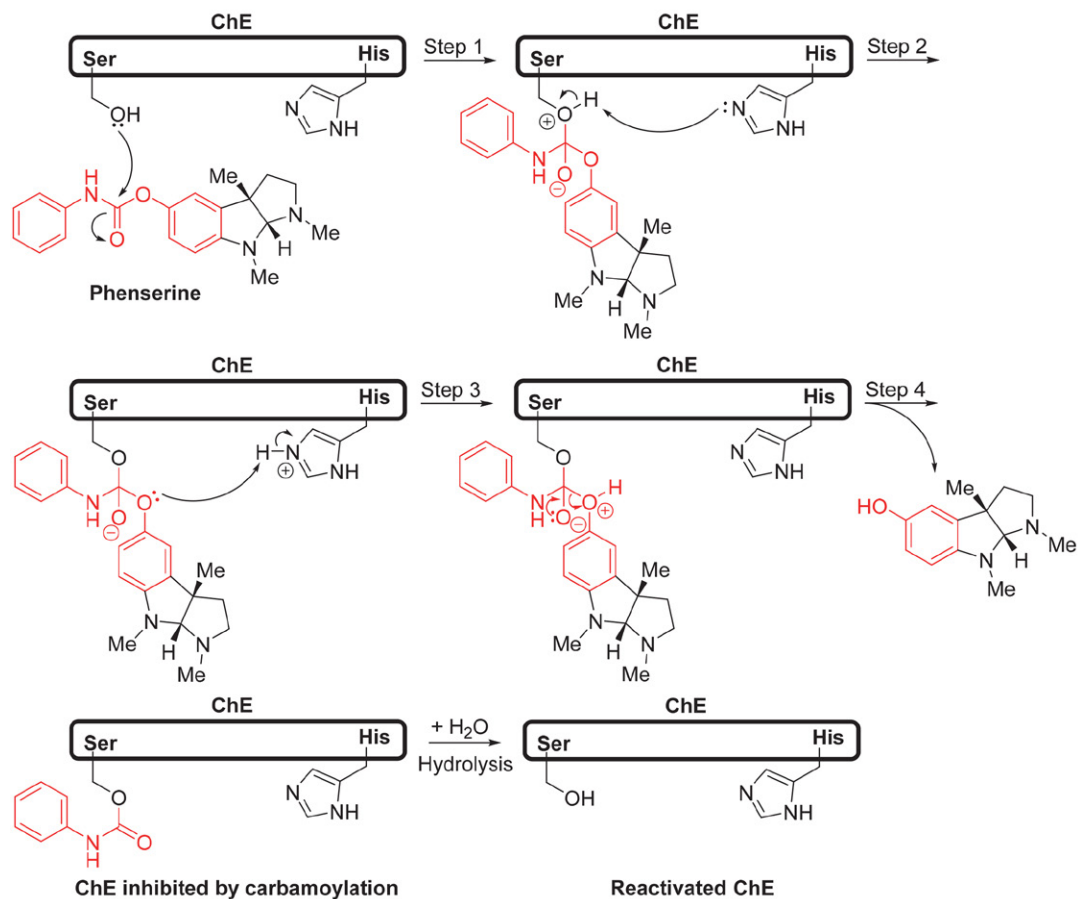
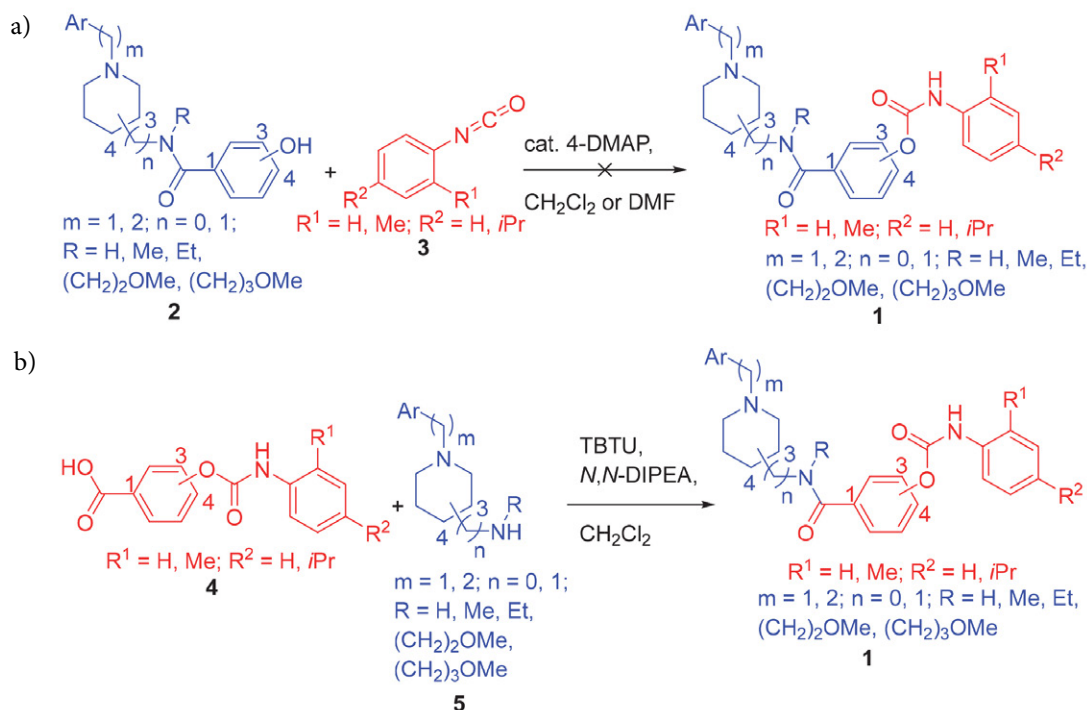


Figure 1. Structures of phenyl phenylcarbamate containing experimental Alzheimer's disease drugs.



Scheme 1. Mechanism of ChE inhibition by phenserine.



Scheme 2. Synthesis of new ChE inhibitors as potential anti-Alzheimer disease drugs with the general formula 1.

this problem by developing a simple procedure to produce these building blocks in high overall yields.

2. Experimental

2.1. General Chemistry Methods

1H NMR and ^{13}C NMR were recorded at 400.130 MHz and 100.613 MHz, respectively, on an NMR spectrophotometer (Bruker Avance III). The chemical shifts (δ) are reported in parts per million (ppm) and are referenced to the deuterated solvent used. The coupling constants (J) are reported in Hz, and the splitting patterns are indicated as: s, singlet; br. s, broad singlet; d, doublet; dd, doublet of doublets; td, triplet of doublets; h, hextet; m, multiplet; t, triplet; br. t, broad triplet; dt, doublet of triplets; tt, triplet of triplets; q, quartet; qd, quartet of doublets. Infrared (IR) spectra were recorded on a FT-IR spectrometer (System Spectrum BX; Perkin-Elmer). ATR IR spectra were recorded on a FT-IR spectrometer (Thermo Nicolet Nexus 470 ESP). Micro-analyses were performed on a Perkin-Elmer C, H, N Analyzer 240 C. The analyses are indicated by the symbols of the elements and they were within $\pm 0.4\%$ of the theoretical values. Mass spectra were recorded on a LC-MS/MS system (Q Executive Plus; Thermo Scientific, MA, USA). Melting points were determined on a Leica hot-stage microscope and are uncorrected. Evaporation of the solvents was performed under reduced pressure. Reagents and solvents were purchased from Acros Organics, Alfa Aesar, Euriso-Top, Fluka, Merck, Sigma-Aldrich, and TCI Europe, and were used without further purification,

unless otherwise stated. Flash column chromatography was performed on silica gel 60 for column chromatography (particle size, 230–400 mesh). Analytical thin-layer chromatography was performed on silica gel aluminum sheets (0.20 mm; 60 F254; Merck), with visualization using ultraviolet light and/or visualization reagents. Analytical reversed-phase UPLC method A was performed on an LC system (Dionex Ultimate 3000 Binary Rapid Separation; Thermo Scientific) equipped with an autosampler, a binary pump system, a photodiode array detector, a thermostated column compartment, and the Chromeleon Chromatography Data System. The detector on UPLC system was set to 210 nm and 254 nm. The column used for method A was a C18 analytical column (50 \times 2.1 mm, 1.8 μ m; Acquity UPLC HSS C18SB). The column was thermostated at 40 $^{\circ}C$.

Method A: The sample solution (1 μ L; 0.2 mg/mL in MeCN) was injected and eluted at a flow rate of 0.4 mL/min, using a linear gradient of mobile phase A (MeCN) and mobile phase B (0.1% [v/v] aqueous TFA). The gradient for method A (for mobile phase A) was: 0–2 min, 20%; 2–5 min, 20–90%; 5–8 min, 90%.

2.2. General Synthetic Procedures

2.2.1. General Procedure for Synthesis of Benzyl Esters 6 and 8 (General Procedure 1)

To a 100-mL round-bottom flask equipped with a stirring bar, hydroxybenzoic acid (5.000 g, 36.177 mmol, 1.0 mol. equiv.) and DMF (50 mL) were added. The resulting solution was stirred and Na_2CO_3 (3.837 g, 36.177

mmol, 1.0 mol. equiv.) was added. Benzyl bromide (4.297 mL, 36.177 mmol, 1.0 mol. equiv.) was added dropwise to the suspension and the reaction mixture was stirred for 24 hours at room temperature, then poured into a 500-mL separating funnel. Water (100 mL) was added and the mixture was extracted with Et₂O (3 × 150 mL). The combined organic phases were transferred into a 1-L separating funnel, washed with water (3 × 450 mL) followed by sat. brine solution (450 mL), dried over anhyd. Na₂SO₄, and evaporated to produce the benzyl hydroxybenzoate as a colourless oil which solidified into a white solid after cooling. This product was used in the next step without further purification.

2. 2. 2. General Procedure for Synthesis of Carbamates 10–15 (General Procedure 2)

To a round-bottom flask equipped with a stirring bar, benzyl hydroxybenzoate (1.0 mol. equiv.) and CH₂Cl₂ (*c* = 0.3 M) were added. The resulting solution was stirred and 4-DMAP (0.01 mol. equiv.) was added. Phenyl isocyanate, 2-methylphenyl isocyanate or 4-isopropylphenyl isocyanate (1.0 mol. equiv.) was added dropwise and the reaction mixture was stirred for 24 hours at room temperature, then evaporated to produce the carbamates. These products were used in the next step without further purification.

2. 2. 3. General Procedure for Debenzylation of Benzyl Esters Yielding 16–21 (General Procedure 3)

To a round-bottom flask equipped with a stirring bar, benzyl ester (1.0 mol. equiv.) and inhibitor-free THF (*c* = 0.02 g/mL) were added. The resulting solution was stirred and agitated with a stream of argon for 30 min. 10% Pd/C (5% mass of benzyl ester) was added and the resulting suspension was agitated with a stream of hydrogen for 30 min. The reaction mixture was stirred under an atmosphere of hydrogen for 24 hours then agitated with a stream of argon for 30 min, filtered with suction through a pad of Celite and evaporated to produce the carboxylic acid.

2. 3. Synthesis and Characterization of Compounds

2. 3. 1. Synthesis of Benzyl 3-Hydroxybenzoate (6)

Synthesized from 3-hydroxybenzoic acid (7) (5.000 g, 36.177 mmol, 1.0 mol. equiv.), Na₂CO₃ (3.837 g, 36.177 mmol, 1.0 mol. equiv.) and benzyl bromide (4.297 mL, 36.177 mmol, 0.01 mol. equiv.) in DMF (50 mL) via general procedure 1 to produce 7.750 g of **6** as a white solid (94% yield). *R*_f = 0.52 (CH₂Cl₂/MeOH, 20:1, v/v). ¹H NMR (400.130 MHz, CDCl₃): δ 5.17 (s, 1H), 5.36 (s, 2H), 7.05

(dd, *J*₁ = 8.0 Hz, *J*₂ = 2.4 Hz, 1H), 7.30–7.45 (m, 6H), 7.56 (s, 1H), 7.66 (d, *J* = 7.8 Hz, 1H).

2. 3. 2. Synthesis of Benzyl 4-Hydroxybenzoate (8)

Synthesized from 4-hydroxybenzoic acid (9) (5.000 g, 36.177 mmol, 1.0 mol. equiv.), Na₂CO₃ (3.837 g, 36.177 mmol, 1.0 mol. equiv.) and benzyl bromide (4.297 mL, 36.177 mmol, 1.0 mol. equiv.) in DMF (50 mL) via general procedure 1 to produce 7.073 g of **8** as a white solid (86% yield). *R*_f = 0.46 (CH₂Cl₂/MeOH, 20:1, v/v). ¹H NMR (400.130 MHz, CDCl₃): δ 5.34 (s, 2H), 5.58 (s, 1H), 6.86 (d, *J* = 8.7 Hz, 2H), 7.32–7.45 (m, 5H), 8.00 (d, *J* = 8.7 Hz, 2H).

2. 3. 3. Synthesis of Benzyl 3-((phenylcarbamoyl)oxy)benzoate (10)

Synthesized from **6** (3.249 g, 14.235 mmol, 1.0 mol. equiv.), phenyl isocyanate (1.547 mL, 14.235 mmol, 1.0 mol. equiv.) and 4-DMAP (0.017 g, 0.142 mmol, 0.01 mol. equiv.) in CH₂Cl₂ (47 mL) via general procedure 2 to produce 4.750 g of **10** as a white solid (96% yield). *R*_f = 0.44 (CH₂Cl₂). mp 121–123 °C. IR (ATR): 3319, 1707, 1544, 1440, 1278, 1202, 1107, 732, 692 cm⁻¹. ¹H NMR (400.130 MHz, CDCl₃): δ 5.37 (s, 2H), 6.96 (br. s, 1H), 7.13 (t, *J* = 7.3 Hz, 1H), 7.33–7.49 (m, 11H), 7.89 (s, 1H), 7.97 (d, *J* = 7.6 Hz, 1H). ¹³C NMR (100 MHz, DMSO-*d*₆): δ 66.41, 118.51, 122.52, 123.06, 126.23, 127.03, 127.97, 128.10, 128.46, 128.81, 129.98, 130.93, 135.90, 138.39, 150.60, 151.35, 164.82. HRMS (ESI+): *m/z* calcd for C₂₁H₁₈NO₄: 348.12303; found: 348.12410. Anal. Calcd for C₂₁H₁₇NO₄: C, 72.61; H, 4.93; N, 4.03. Found: C, 72.65; H, 4.96; N, 4.00.

2. 3. 4. Synthesis of Benzyl 3-((ortho-Tolylcarbamoyl)oxy)benzoate (11)

Synthesized from **6** (3.463 g, 15.172 mmol, 1.0 mol. equiv.), 2-methylphenyl isocyanate (1.881 mL, 15.172 mmol, 1.0 mol. equiv.) and 4-DMAP (0.019 g, 0.152 mmol, 0.01 mol. equiv.) in CH₂Cl₂ (50 mL) via general procedure 2 to produce 5.373 g of **11** as a white solid (98% yield). *R*_f = 0.32 (CH₂Cl₂). mp 78–80 °C. IR (ATR): 3273, 1712, 1531, 1289, 1270, 1232, 1189, 1069, 1022, 747 cm⁻¹. ¹H NMR (400.130 MHz, CDCl₃): δ 2.34 (s, 3H), 5.37 (s, 2H), 6.75 (br. s, 1H), 7.08 (t, *J* = 7.3 Hz, 1H), 7.22 (t, *J* = 7.6 Hz, 2H), 7.33–7.49 (m, 7H), 7.83 (br. s, 1H), 7.89 (s, 1H), 7.96 (d, *J* = 7.5 Hz, 1H). ¹³C NMR (100 MHz, DMSO-*d*₆): δ 17.72, 66.41, 115.66, 119.88, 120.41, 122.42, 126.08, 126.12, 126.93, 127.91, 127.97, 128.02, 128.09, 128.45, 129.92, 130.37, 130.90, 135.65, 135.91, 150.92, 152.33, 164.85. HRMS (ESI+): *m/z* calcd for C₂₂H₂₀NO₄: 362.13868; found: 362.13802. Anal. Calcd for C₂₂H₁₉NO₄: C, 73.12; H, 5.30; N, 3.88. Found: C, 73.11; H, 5.26; N, 3.92.

2. 3. 5. Synthesis of Benzyl 3-(((4-Isopropylphenyl) carbamoyl)oxy)benzoate (12)

Synthesized from **6** (3.242 g, 14.204 mmol, 1.0 mol. equiv.), 4-isopropylphenyl isocyanate (2.267 mL, 14.204 mmol, 1.0 mol. equiv.) and 4-DMAP (0.017 g, 0.142 mmol, 0.01 mol. equiv.) in CH₂Cl₂ (47 mL) via general procedure 2 to produce 5.278 g of **12** as a white solid (95% yield). *R_f* = 0.45 (CH₂Cl₂). mp 99–101 °C. IR (ATR): 3322, 2963, 1710, 1529, 1445, 1275, 1231, 1100, 741 cm⁻¹. ¹H NMR (400.130 MHz, CDCl₃): δ 1.24 (d, *J* = 6.8 Hz, 6H), 2.84–2.94 (m, 1H), 5.37 (s, 2H), 6.92 (br. s, 1H), 7.20 (d, *J* = 8.3 Hz, 2H), 7.33–7.49 (m, 9H), 7.88 (s, 1H), 7.96 (d, *J* = 7.5 Hz, 1H). ¹³C NMR (100 MHz, DMSO-*d*₆): δ 23.82, 32.74, 66.39, 118.63, 122.46, 126.13, 126.50, 126.98, 127.95, 128.07, 128.43, 129.94, 130.88, 135.88, 136.06, 143.13, 150.65, 151.35, 164.80. HRMS (ESI+): *m/z* calcd for C₂₄H₂₄NO₄: 390.16998; found: 390.16931. Anal. Calcd for C₂₄H₂₃NO₄: C, 74.02; H, 5.95; N, 3.60. Found: C, 74.05; H, 5.92; N, 3.58.

2. 3. 6. Synthesis of Benzyl 4-((Phenylcarbamoyl)oxy)benzoate (13)

Synthesized from **8** (3.010 g, 13.187 mmol, 1.0 mol. equiv.), phenyl isocyanate (1.433 mL, 13.187 mmol, 1.0 mol. equiv.) and 4-DMAP (0.016 g, 0.132 mmol, 0.01 mol. equiv.) in CH₂Cl₂ (44 mL) via general procedure 2 to produce 4.415 g of **13** as a white solid (96% yield). *R_f* = 0.33 (CH₂Cl₂). mp 103–105 °C. IR (ATR): 3331, 1706, 1543, 1264, 1216, 1102, 1007, 752, 690 cm⁻¹. ¹H NMR (400.130 MHz, CDCl₃): δ 5.34 (s, 2H), 6.95 (br. s, 1H), 7.10 (t, *J* = 7.3 Hz, 1H), 7.24 (d, *J* = 3.4 Hz, 2H), 7.30–7.43 (m, 9H), 8.10 (d, *J* = 8.6 Hz, 2H). ¹³C NMR (100 MHz, DMSO-*d*₆): δ 66.16, 115.35, 118.15, 118.55, 122.08, 123.13, 126.58, 127.86, 128.02, 128.43, 128.82, 130.82, 131.50, 136.06, 138.32, 150.93, 154.43, 164.89. HRMS (ESI+): *m/z* calcd for C₂₁H₁₈NO₄: 348.12303; found: 348.12249. Anal. Calcd for C₂₁H₁₇NO₄: C, 72.61; H, 4.93; N, 4.03. Found: C, 72.64; H, 4.96; N, 4.05.

2. 3. 7. Synthesis of Benzyl 4-((ortho-Tolylcarbamoyl)oxy)benzoate (14)

Synthesized from **8** (3.453 g, 15.128 mmol, 1.0 mol. equiv.), 2-methylphenyl isocyanate (1.876 mL, 15.128 mmol, 1.0 mol. equiv.) and 4-DMAP (0.018 g, 0.131 mmol, 0.01 mol. equiv.) in CH₂Cl₂ (50 mL) via general procedure 2 to produce 4.975 g of **14** as a white solid (91% yield). *R_f* = 0.27 (CH₂Cl₂). mp 87–89 °C. IR (ATR): 3264, 1705, 1531, 1454, 1272, 1207, 1232, 1016, 753, 696 cm⁻¹. ¹H NMR (400.130 MHz, CDCl₃): δ 2.34 (s, 3H), 5.37 (s, 2H), 6.76 (br. s, 1H), 7.09 (t, *J* = 7.2 Hz, 1H), 7.22 (t, *J* = 8.1 Hz, 2H), 7.29 (d, *J* = 8.6 Hz, 2H), 7.33–7.45 (m, 5H), 7.83 (br. s, 1H), 8.12 (d, *J* = 8.7 Hz, 2H). ¹³C NMR (100 MHz, DMSO-*d*₆): δ 17.70, 66.14, 115.34, 121.98, 124.91, 126.14, 126.40, 126.98, 127.77, 127.87, 128.03, 128.39, 128.44, 130.39, 130.79, 131.48, 135.54, 136.06, 136.42, 151.89, 154.74,

164.90. HRMS (ESI+): *m/z* calcd for C₂₂H₂₀NO₄: 362.13868; found: 362.13803. Anal. Calcd for C₂₂H₁₉NO₄: C, 73.12; H, 5.30; N, 3.88. Found: C, 73.16; H, 5.33; N, 3.91.

2. 3. 8. Synthesis of Benzyl 4-(((4-Isopropylphenyl) carbamoyl)oxy)benzoate (15)

Synthesized from **8** (2.988 g, 13.091 mmol, 1.0 mol. equiv.), 4-isopropylphenyl isocyanate (2.089 mL, 13.091 mmol, 1.0 mol. equiv.) and 4-DMAP (0.016 g, 0.131 mmol, 0.01 mol. equiv.) in CH₂Cl₂ (44 mL) via general procedure 2 to produce 4.960 g of **15** as a white solid (97% yield). *R_f* = 0.37 (CH₂Cl₂). mp 112–114 °C. IR (ATR): 3329, 2962, 1717, 1537, 1415, 1202, 1113, 1006, 831, 689 cm⁻¹. ¹H NMR (400.130 MHz, CDCl₃): δ 1.24 (d, *J* = 7.0 Hz, 6H), 2.84–2.95 (m, 1H), 5.37 (s, 2H), 6.91 (br. s, 1H), 7.21 (d, *J* = 8.3 Hz, 2H), 7.27 (d, *J* = 8.3 Hz, 2H), 7.33–7.45 (m, 7H), 8.12 (d, *J* = 8.6 Hz, 2H). ¹³C NMR (100 MHz, DMSO-*d*₆): δ 23.81, 32.75, 66.13, 115.32, 118.24, 118.67, 122.02, 126.52, 127.84, 128.01, 128.42, 131.47, 136.05, 143.24, 150.92, 154.50, 164.88. HRMS (ESI+): *m/z* calcd for C₂₄H₂₄NO₄: 390.16998; found: 390.17214. Anal. Calcd for C₂₄H₂₃NO₄: C, 74.02; H, 5.95; N, 3.60. Found: C, 73.99; H, 5.99; N, 3.57.

2. 3. 9. Synthesis of 3-((Phenylcarbamoyl)oxy)benzoic Acid (16)

Synthesized from **10** (5.163 g, 14.863 mmol, 1.0 mol. equiv.) and 10% Pd/C (0.258 g, 5% mass of **10**) in inhibitor-free THF (258 mL) via general procedure 3 to produce 3.720 g of **16** as a white solid (96% yield). *R_f* = 0.00 (CH₂Cl₂). mp 151–153 °C. IR (ATR): 3337, 2564, 1685, 1523, 1439, 1302, 1208, 1016, 754 cm⁻¹. ¹H NMR (400.130 MHz, acetone-*d*₆): δ 7.09 (t, *J* = 7.3 Hz, 1H), 7.35 (t, *J* = 7.9 Hz, 2H), 7.50 (d, *J* = 8.3 Hz, 1H), 7.57 (t, *J* = 7.9 Hz, 1H), 7.63 (d, *J* = 8.1 Hz, 2H), 7.86 (s, 1H), 7.93 (d, *J* = 7.6 Hz, 1H), 9.25 (s, 1H), 11.43 (br. s, 1H). ¹³C NMR (100 MHz, acetone-*d*₆): δ 120.50, 124.77, 125.13, 128.32, 128.34, 130.74, 131.35, 133.91, 140.54, 152.98, 153.37, 167.96. HRMS (ESI+): *m/z* calcd for C₁₄H₁₂NO₄: 258.07608; found: 258.07740. UPLC purity, 99% at 254 nm (method A, *t_R* = 4.130 min).

2. 3. 10. Synthesis of 3-((ortho-Tolylcarbamoyl)oxy)benzoic Acid (17)

Synthesized from **11** (5.292 g, 14.643 mmol, 1.0 mol. equiv.) and 10% Pd/C (0.265 g, 5% mass of **11**) in inhibitor-free THF (265 mL) via general procedure 3 to produce 3.902 g of **17** as a white solid (98% yield). *R_f* = 0.00 (CH₂Cl₂). mp 176–178 °C. IR (ATR): 3298, 2565, 1686, 1530, 1449, 1306, 1221, 1023, 942, 750 cm⁻¹. ¹H NMR (400.130 MHz, acetone-*d*₆): δ 2.39 (s, 3H), 7.11 (t, *J* = 7.5 Hz, 1H), 7.19–7.26 (m, 2H), 7.49 (d, *J* = 8.3 Hz, 1H), 7.56 (t, *J* = 7.9 Hz, 1H), 7.63 (d, *J* = 7.9 Hz, 1H), 7.85 (s,

1H), 7.92 (d, $J = 7.6$ Hz, 1H), 8.50 (br. s, 1H), 11.32 (br. s, 1H). ^{13}C NMR (100 MHz, DMSO- d_6): δ 17.76, 122.54, 124.87, 125.48, 126.18, 126.34, 129.72, 130.43, 132.07, 132.28, 135.71, 150.85, 152.45, 166.64. HRMS (ESI+): m/z calcd for $\text{C}_{15}\text{H}_{14}\text{NO}_4$: 272.09173; found: 272.09150. UPLC purity, 96% at 254 nm (method A, $t_R = 4.193$ min).

2. 3. 11. Synthesis of 3-(((4-Isopropylphenyl) carbamoyl)oxy)benzoic Acid (18)

Synthesized from **12** (5.193 g, 13.334 mmol, 1.0 mol. equiv.) and 10% Pd/C (0.260 g, 5% mass of **12**) in inhibitor-free THF (260 mL) via general procedure 3 to produce 3.795 g of **18** as a white solid (95% yield). $R_f = 0.00$ (CH_2Cl_2). mp 174–176 °C. IR (ATR): 3320, 2961, 2541, 1715, 1682, 1538, 1450, 1274, 1225, 1017, 840 cm^{-1} . ^1H NMR (400.130 MHz, acetone- d_6): δ 1.23 (d, $J = 7.0$ Hz, 6H), 2.84–2.94 (m, 1H), 7.23 (d, $J = 8.4$ Hz, 2H), 7.48 (m, 4H), 7.85 (s, 1H), 7.92 (d, $J = 7.7$ Hz, 1H), 9.18 (s, 1H), 11.41 (br. s, 1H). ^{13}C NMR (100 MHz, acetone- d_6): δ 25.35, 35.19, 120.65, 124.76, 128.28, 128.31, 128.53, 131.32, 133.82, 138.18, 145.68, 153.03, 153.39, 167.98. HRMS (ESI+): m/z calcd for $\text{C}_{17}\text{H}_{18}\text{NO}_4$: 300.12303; found: 300.12463. UPLC purity, 99% at 254 nm (method A, $t_R = 4.723$ min).

2. 3. 12. Synthesis of 4-((Phenylcarbamoyl)oxy)benzoic Acid (19)

Synthesized from **13** (4.334 g, 12.477 mmol, 1.0 mol. equiv.) and 10% Pd/C (0.217 g, 5% mass of **13**) in inhibitor-free THF (217 mL) via general procedure 3 to produce 3.194 g of **19** as a white solid (99% yield). $R_f = 0.00$ (CH_2Cl_2). mp 195–197 °C. IR (ATR): 3305, 2557, 1682, 1527, 1502, 1427, 1292, 1198, 1012, 752 cm^{-1} . ^1H NMR (400.130 MHz, acetone- d_6): δ 7.10 (t, $J = 7.3$ Hz, 1H), 7.34–7.38 (m, 4H), 7.63 (d, $J = 7.9$ Hz, 2H), 8.10 (d, $J = 8.1$ Hz, 2H), 9.28 (s, 1H), 11.10 (br. s, 1H). ^{13}C NMR (100 MHz, DMSO- d_6): δ 115.07, 118.53, 121.89, 123.14, 127.90, 128.87, 130.82, 131.49, 138.33, 151.04, 153.98, 166.67. HRMS (ESI+): m/z calcd for $\text{C}_{14}\text{H}_{12}\text{NO}_4$: 258.07608; found: 258.07647. UPLC purity, 98% at 254 nm (method A, $t_R = 4.153$ min).

2. 3. 13. Synthesis of 4-((ortho-Tolylcarbamoyl)oxy)benzoic Acid (20)

Synthesized from **14** (4.640 g, 12.839 mmol, 1.0 mol. equiv.) and 10% Pd/C (0.232 g, 5% mass of **14**) in inhibitor-free THF (232 mL) via general procedure 3 to produce 3.384 g of **20** as a white solid (97% yield). $R_f = 0.00$ (CH_2Cl_2). mp 183–185 °C. IR (ATR): 3280, 2555, 1685, 1529, 1426, 1291, 1234, 1208, 1161, 748 cm^{-1} . ^1H NMR (400.130 MHz, acetone- d_6): δ 2.39 (s, 3H), 7.11 (t, $J = 7.5$ Hz, 1H), 7.20–7.27 (m, 2H), 7.36 (d, $J = 8.6$ Hz, 2H), 7.62 (d, $J = 7.7$ Hz, 1H), 8.09 (d, $J = 8.6$ Hz, 2H), 8.53 (br. s, 1H), 11.14 (br. s, 1H). ^{13}C NMR (100 MHz, DMSO- d_6): δ 17.77, 115.14, 121.81, 124.99, 125.56, 126.61, 127.80,

130.46, 130.86, 131.55, 135.63, 152.08, 154.37, 166.75. HRMS (ESI+): m/z calcd for $\text{C}_{15}\text{H}_{14}\text{NO}_4$: 272.09173; found: 272.09436. UPLC purity, 97% at 254 nm (method A, $t_R = 4.213$ min).

2. 3. 14. Synthesis of 4-(((4-Isopropylphenyl) carbamoyl)oxy)benzoic Acid (21)

Synthesized from **15** (4.864 g, 12.489 mmol, 1.0 mol. equiv.) and 10% Pd/C (0.243 g, 5% mass of **15**) in inhibitor-free THF (243 mL) via general procedure 3 to produce 3.720 g of **21** as a white solid (99% yield). $R_f = 0.00$ (CH_2Cl_2). mp 196–198 °C. IR (ATR): 3362, 2964, 2547, 1720, 1676, 1501, 1198, 1011, 828, 758 cm^{-1} . ^1H NMR (400.130 MHz, acetone- d_6): δ 1.23 (d, $J = 6.8$ Hz, 6H), 2.84–2.94 (m, 1H), 7.24 (d, $J = 8.3$ Hz, 2H), 7.36 (d, $J = 8.4$ Hz, 2H), 7.53 (d, $J = 8.2$ Hz, 2H), 8.09 (d, $J = 8.6$ Hz, 2H), 9.19 (s, 1H), 11.19 (br. s, 1H). ^{13}C NMR (100 MHz, DMSO- d_6): δ 23.90, 32.83, 118.75, 121.85, 126.60, 127.87, 130.87, 136.08, 143.31, 151.12, 154.14, 166.75. HRMS (ESI+): m/z calcd for $\text{C}_{17}\text{H}_{18}\text{NO}_4$: 300.12303; found: 300.12476. UPLC purity, 99% at 254 nm (method A, $t_R = 4.743$ min).

2. 3. 15. Synthesis of 3-((1-(2,3-Dihydro-1H-inden-2-yl)piperidin-3-yl)carbamoyl)phenyl Phenylcarbamate (22)

To a 50-mL round-bottom flask equipped with a stirring bar, compound **16** (0.100 g, 0.389 mmol, 1.0 equiv) was added followed by CH_2Cl_2 (10 mL). The resulting suspension was stirred and cooled to 0 °C. *N,N*-Diisopropylethylamine (0.135 mL, 0.778 mmol, 2.0 equiv) was added dropwise and the suspension transformed into a solution. TBTU was added and 30 min later solution A (see below) was added dropwise. The reaction mixture was allowed to warm to room temperature and then stirred for 24 hours. During this time a white precipitate formed. The suspension was filtered with suction to produce 0.133 g of compound **22** as a white solid (75% yield).

Preparation of solution A: To 25-mL round-bottom flask equipped with a stirring bar, compound **23** (0.112 g, 0.389 mmol, 1.0 equiv) was added followed by CH_2Cl_2 (11 mL). The resulting suspension was stirred and cooled to 0 °C. *N,N*-Diisopropylethylamine (0.135 mL, 0.778 mmol, 2.0 equiv) was added dropwise and the suspension transformed into a solution.

Characterization of compound 22: $R_f = 0.46$ ($\text{CH}_2\text{Cl}_2/\text{MeOH}$, 10:1, v/v). mp 137–139 °C. IR (ATR): 3293, 2953, 1716, 1629, 1538, 1226, 1211, 1021, 694 cm^{-1} . ^1H NMR (400.130 MHz, DMSO- d_6): δ 1.33–1.43 (m, 1H), 1.48–1.60 (m, 1H), 1.73 (d, $J = 13.3$ Hz, 1H), 1.83 (d, $J = 10.5$ Hz, 1H), 1.96–2.01 (m, 2H), 2.75–2.86 (m, 3H), 2.98–3.05 (m, 3H), 3.20 (t, $J = 7.7$ Hz, 1H), 3.97 (br. s, 1H), 7.04–7.12 (m, 3H), 7.17–7.18 (m, 2H), 7.33 (t, $J = 7.7$ Hz, 2H), 7.39 (d, $J = 8.4$ Hz, 1H), 7.50–7.53 (m, 3H), 7.70 (s, 1H),

7.76 (d, $J = 7.7$ Hz, 1H), 8.27 (d, $J = 7.7$ Hz, 1H), 10.29 (s, 1H). ^{13}C NMR (100 MHz, $\text{DMSO}-d_6$): δ 23.75, 29.80, 36.19, 36.28, 46.47, 50.70, 55.99, 66.07, 118.42, 120.79, 123.00, 124.17, 124.44, 124.72, 126.19, 128.81, 129.27, 135.81, 138.42, 141.27, 150.28, 151.54, 164.55. HRMS (ESI+): m/z calcd for $\text{C}_{28}\text{H}_{30}\text{N}_3\text{O}_3$: 456.22817; found: 456.22717. UPLC purity, 96% at 254 nm (method A, $t_R = 4.420$ min).

3. Results and Discussion

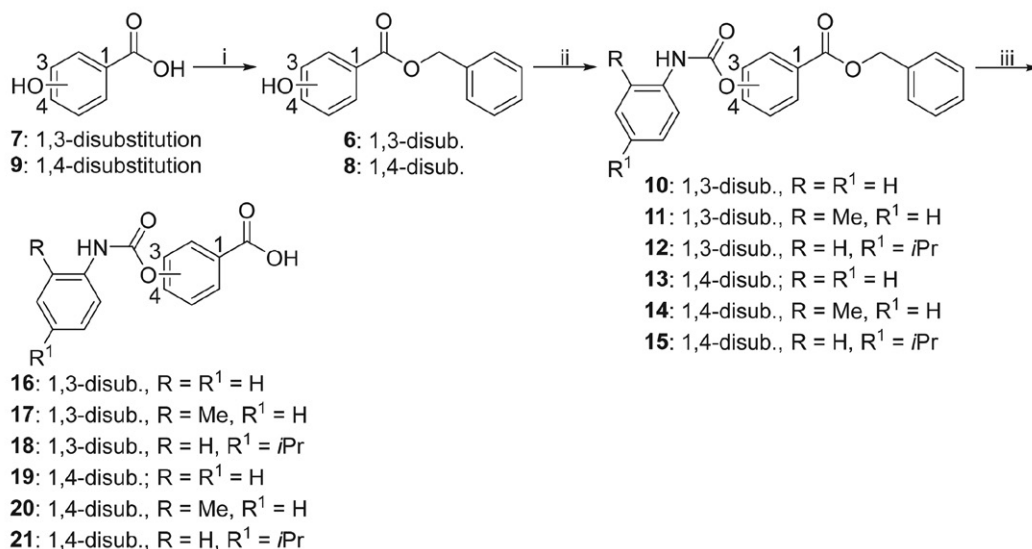
For the synthesis of 3-((phenylcarbamoyl)oxy)benzoic acid (**16**), commercially available 3-hydroxybenzoic acid (**7**) was treated with benzyl bromide in the presence of Na_2CO_3 in DMF,²¹ to provide benzyl 3-hydroxybenzoate (**6**) in 86% yield. No further purification of compound **6** was required and the diethyl ether used for the extraction of compound **6** was reused for the extraction in the synthesis of benzyl 4-hydroxybenzoate (**8**) (Scheme 3).

In the second step, compound **6** was converted into carbamate **10** with one equivalent of phenyl isocyanate in the presence of a catalytic amount (0.01 equivalent) of 4-DMAP in CH_2Cl_2 ^{18,19} in 96% yield. Again, no further

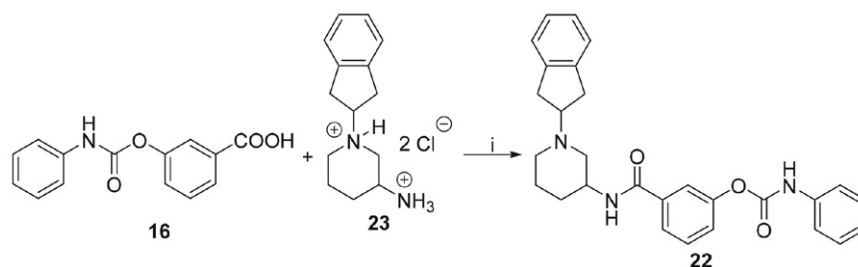
purification of carbamate **10** was required. Using one equivalent of phenyl isocyanate, rather than 1.10¹⁹ or 1.20 equivalent,¹⁸ was found to be an advantage as no over-reaction occurred. As reported previously, excess phenyl isocyanate can undergo an $\text{S}_{\text{E}}\text{Ar}$ substitution in the phenyl moiety of the carbamate to produce an amide, which can be difficult to separate from the desired carbamate.¹⁹ Additionally, 1.0 mol% rather than 5 mol%^{18,19} of 4-DMAP was enough to produce the desired carbamate in excellent yield (Scheme 3).

In the third and final step, the benzyl ester **10** was debenzylated using classic catalytic hydrogenation with gaseous hydrogen and a catalytic amount of 10% Pd/ C^{22} (5% mass of benzyl ester **10**) in inhibitor-free THF to produce carboxylic acid **16** in 99% yield (Scheme 3). The hydrogenation was a very clean reaction: no further purification of acid **16** was required and the inhibitor-free THF was reused for the debenzylation of benzyl esters **11–15**.

The overall yield for the preparation of compound **16** from 3-hydroxybenzoic acid (**7**) using this procedure was 87% (Table 1). The same procedure was then used to prepare compounds **17–21** from the corresponding hydroxybenzoic acids **7** or **9** via **11–15** (Scheme 3). Overall yields ranged from 76–90% and are reported in Table 1.



Scheme 3. Reagents and conditions: (i) PhCH_2Br , Na_2CO_3 , DMF, rt, 24 h, 94% (for **8**) and 86% (for **9**); (ii) aryl isocyanate, 4-DMAP, CH_2Cl_2 , rt, 24 h, 91–98%; (iii) $\text{H}_2(\text{g})$, 10% Pd/C, THF, rt, 24 h, 95–99%.



Scheme 4. Reagents and conditions: (i) TBTU, N,N-DIPEA, CH_2Cl_2 , 0 °C to rt, 24 h, 75%.

Table 1. The synthesized 3- and 4-((phenylcarbamoyl)oxy)benzoic acids.

Starting hydroxybenzoic acid	Final ((phenylcarbamoyl)oxy) benzoic acid	Overall yield %
		87
		90
		85
		82
		76
		83

As a proof of concept that the synthesized 3- and 4-((phenylcarbamoyl)oxy)benzoic acids **16–21** can be used in the next reaction to prepare amides, carboxylic acid **16** was reacted with amine **23** (which we have previously used to synthesize amide^{13,14} and sulfonamide^{14,15} ChE inhibitors), in the presence of coupling reagent TBTU and *N,N*-diisopropylethylamine (*N,N*-DIPEA) in CH₂Cl₂²⁰ to produce amide **22** in 75% yield (Scheme 4).

4. Conclusions

In summary, we have developed method for the synthesis of previously unreported 3- and 4-((phenylcarbamoyl)oxy)benzoic acids from commercially available 3- and 4-hydroxybenzoic acids, respectively. The main advantages of our method are the simplicity, as no purification of intermediates or final acids is required, and effectiveness, as the overall yields are very good to excellent (76–90%). As we have shown, the synthesized carboxylic acids can be converted further, e.g. reacted with amines to produce amides with potential application in drug discovery.

oyl)oxy)benzoic acids from commercially available 3- and 4-hydroxybenzoic acids, respectively. The main advantages of our method are the simplicity, as no purification of intermediates or final acids is required, and effectiveness, as the overall yields are very good to excellent (76–90%). As we have shown, the synthesized carboxylic acids can be converted further, e.g. reacted with amines to produce amides with potential application in drug discovery.

Acknowledgements

The authors declare that there is no conflict of interest. This work was supported by the Slovenian Research Agency ARRS (grant No. Z1-9195 and core funding P1-0208).

5. References

- C. L. Masters, R. Bateman, K. Blennow, C. C. Rowe, R. A. Sperling, J. L. Cummings, *Nat. Rev. Dis. Primers* **2015**, *1*, 15056. DOI:10.1038/nrdp.2015.56
- E. Scherder, in: *Aging and dementia: neuropsychology, motor Skills, and pain*, 1st ed; VU University Press, Amsterdam, Netherlands, **2011**, pp. 9–32.
- E. Scarpini, P. Schelterns, H. Feldman, *Lancet Neurol.* **2003**, *2*, 539–547. DOI:10.1016/S1474-4422(03)00502-7
- E. K. Perry, B. E. Tomlinson, G. Blessed, K. Bergmann, P. H. Gibson, R.H. Perry, *Br. Med. J.* **1978**, *2*, 1457–1459. DOI:10.1136/bmj.2.6150.1457
- J. L. Cummings, G. Lee, A. Ritter, M. Sabbagh, K. Zhong, *Alzheimers Dement.* **2019**, *5*, 272–293. DOI:10.1016/j.trci.2019.05.008
- D. Lecca, M. Bader, D. Tweedie, A. F. Hoffman, Y. J. Jung, S. C. Hsueh, B. J. Hoffer, R. E. Becker, C. G. Pick, C. R. Lupica, N. H. Greig, *Neurobiol. Dis.* **2019**, *130*, 104528. DOI:10.1016/j.nbd.2019.104528
- M. L. Maccacchini, M. Y. Chang, C. Pan, J. Varghese, H. Zetterberg, N. H. Greig, *J. Neurol. Neurosurg. Psychiatry.* **2012**, *83*, 894–902. DOI:10.1136/jnnp-2012-302589
- M. A. Kamal, N. H. Greig, A. S. Alhomida, A. A. Al-Jafari, *Biochem. Pharmacol.* **2000**, *60*, 561–70. DOI:10.1016/S0006-2952(00)00330-0
- N. H. Greig, T. Utsuki, D. K. Ingram, Y. Wang, G. Pepeu, C. Scali, Q. S. Yu, J. Mamczarz, H. W. Holloway, T. Giordano, D. Chen, K. Furukawa, K. Sambamurti, A. Brossi, D. K. Lahiri, *Proc. Natl. Acad. Sci.* **2005**, *102*, 17213–17218. DOI:10.1073/pnas.0508575102
- M. A. Kamal, X. Qu, Q. S. Yu, D. Tweedie, H. W. Holloway, Y. Li, Y. Tan, N. H. Greig, *J. Neural. Transm.* **2008**, *115*, 889–898. DOI:10.1007/s00702-008-0022-y
- C. Bartolucci, J. Stojan, Q. Yu, N. H. Greig, D. Lamba, *Biochem. J.* **2012**, *444*, 269–277. DOI:10.1042/BJ20111675
- G. L. Patrick, in: *An Introduction to Medicinal Chemistry*, Oxford Univeristy Press Inc., New York, United States, **2009**, pp. 601–603.
- U. Košak, B. Brus, D. Knez, S. Žakelj, J. Trontelj, A. Pišlar, R.

- Šink, M. Jukić, M. Živin, A. Podkova, F. Nachon, X. Brazzolotto, J. Stojan, J. Kos, N. Coquelle, K. Sałat, J. P. Colletier, S. Gobec, *J. Med. Chem.* **2018**, *61*, 119–139. DOI:10.1021/acs.jmedchem.7b01086
14. U. Košak, D. Knez, N. Coquelle, B. Brusa, A. Pišlar, F. Nachon, X. Brazzolotto, J. Kos, J. P. Colletier, S. Gobec, *Bioorg. Med. Chem.* **2017**, *25*, 633–645. DOI:10.1016/j.bmc.2016.11.032
15. U. Košak, B. Brus, D. Knez, R. Šink, S. Žakelj, J. Trontelj, A. Pišlar, J. Šlenc, M. Gobec, M. Živin, L. Tratnjek, M. Perše, K. Sałat, A. Podkova, B. Filipek, F. Nachon, X. Brazzolotto, A. Więckowska, B. Malawska, J. Stojan, I. Mlinarič Raščan, J. Kos, N. Coquelle, J.-P. Colletier, S. Gobec, *Sci. Rep.* **2016**, *6*, 39495. DOI:10.1038/srep39495
16. A. K. Ghosh, M. Brindisi, *J. Med. Chem.* **2015**, *58*, 2895–2940. DOI:10.1021/jm501371s
17. M. T. Leffler, E. J. Matson, *J. Am. Chem. Soc.* **1948**, *70*, 3439–3442. DOI:10.1021/ja01190a065
18. C. Stock, R. Brückner, *Synlett* **2010**, *16*, 2429–2434. DOI:10.1055/s-0030-1258552
19. C. Stock, R. Brückner, *Adv. Synth. Catal.* **2012**, *354*, 2309–2330. DOI:10.1002/adsc.201200303
20. S. Balalaie, M. Mahdidoust, R. Eshaghi-Najafabadi, *J. Iran. Chem. Soc.* **2007**, *4*, 364–369. DOI:10.1007/BF03245987
21. B. Laursen, M. P. Denieul, T. Skrydstrup, *Tetrahedron* **2002**, *58*, 2231–2238. DOI:10.1016/S0040-4020(02)00096-0
22. T. W. Greene, P. G. M. Wuts, in: *Protective Groups in Organic Synthesis*, John Wiley and Sons, Inc., New York, United States **1999**, pp. 416–418. DOI:10.1002/0471220574

Povzetek

Fenserin, posifen, tolserin in cimserin ter njegovi derivati so eksperimentalne učinkovine za zdravljenje Alzheimerjeve bolezni. Te učinkovine vsebujejo fenil fenilkarbamatno skupino, ki je odgovorna za njihovo delovanje proti Alzheimerjevi bolezni. Razvili smo preprost (trije koraki) in učinkovit (skupni izkoristek 76–90%) postopek za pripravo 3- in 4-((fenilkarbamoil)oksi)benzojske kisline, ki ju lahko pri reakciji z amini pretvorimo v amide s fenil fenilkarbamatno skupino. Ti amidi so nove potencialne učinkovine za zdravljenje Alzheimerjevi bolezni. Sintetizirane karboksilne kisline so tako pomembni gradniki, ki se lahko uporabljajo v farmacevtski kemiji in pri odkrivanju zdravilnih učinkovin.



Except when otherwise noted, articles in this journal are published under the terms and conditions of the Creative Commons Attribution 4.0 International License

Scientific paper

Prediction of Single Point Mutations in Human Coronavirus and Their Effects on Binding to 9-O-Acetylated Sialic Acid and Hydroxychloroquine

Petar M. Mitrasinovic*

Center for Biophysical and Chemical Research, Belgrade Institute of Science and Technology, 11060 Belgrade, Serbia

* Corresponding author: E-mail: pmitrasinovic.ist-belgrade.edu.rs@tech-center.com

Received: 05-19-2020

Abstract

Due to the current spreading of the new disease CoViD-19, the World Health Organization formally declared a world pandemic on March 11, 2020. The present trends indicate that the pandemic will have an enormous clinical and economic impact on population health. Infections are initiated by the transmembrane spike (S) glycoproteins of human coronavirus (hCoV) binding to host receptors. Ongoing research and therapeutic product development are of vital importance for the successful treatment of CoViD-19. To contribute somewhat to the overall effort, herein, single point mutations (SPMs) of the binding site residues in hCoV-OC43 S that recognizes cellular surface components containing 9-O-acetylated sialic acid (9-O-Ac-Sia) are explored using an *in silico* protein engineering approach, while their effects on the binding of 9-O-Ac-Sia and Hydroxychloroquine (Hcq) are evaluated using molecular docking simulations. Thr31Met and Val84Arg are predicted to be the critical – most likely SPMs in hCoV-OC43 S for the binding of 9-O-Ac-Sia and Hcq, respectively, even though Thr31Met is a very likely SPM in the case of Hcq too. The corresponding modes of interaction indicate a comparable strength of the Thr31Met/9-O-Ac-Sia and Val84Arg/Hcq (or Thr31Met/Hcq) complexes. Given that the binding site is conserved in all CoV S glycoproteins that associate with 9-O-acetyl-sialoglycans, the high hydrophobic affinity of Hcq to hCoV-OC43 S speaks in favor of its ability to competitively inhibit rapid S-mediated virion attachment in high-density receptor environments, but its considerably low specificity to hCoV-OC43 S may be one of the key obstacles in considering the potential of Hcq to become a drug candidate.

Keywords: CoViD-19; coronavirus, hydroxychloroquine; pandemic; single point mutation

1. Introduction

A number of enveloped, positive single-stranded RNA viruses, denoted by CoV, are involved in respiratory, enteric, hepatic and neuronal infectious diseases both in animals and in humans. Among four CoV genera (alpha, beta, gamma and delta), the beta genus comprises bCoV, hCoV-OC43, MHV, SARS-CoV and MERS-CoV.¹ A new infectious disease CoViD-19, caused by a new severe acute respiratory syndrome coronavirus 2 (SARS-CoV-2; also referred to as hCoV-19), was first identified in 2019 in Wuhan, China,² and has since spread through interpersonal contacts globally. The World Health Organization officially declared a world 2019-20 coronavirus pandemic on March 11, 2020.³ The rate of deaths per number of diagnosed cases varies on a daily basis and currently ranges from 0.2% to 15%, depending on age and other health problems.⁴ If SARS-CoV-2 continues to adapt genetically, initiating person-to-person transmission, it will presum-

ably spread like wildfire throughout the globe. Such pandemic might well arise by a still-undiscovered mechanism, making coronavirus fundamental research and therapeutic product development urgent. The US FDA – United States Food and Drug Administration is testing coronavirus treatments, including hydroxychloroquine and chloroquine, by looking at widespread clinical trials of the drugs.⁵ As initial therapy for patients infected with SARS-CoV-2, the use of Hcq is, presumably, more preferential than the use of Cq.⁶ According to the sources from the pharmaceutical industry, a vaccine will be available on the market in the next 12 to 18 months.⁷

SARS-CoV-2 binds the angiotensin-converting enzyme 2 (ACE2) at the surface of respiratory cells. There are biophysical and structural evidences that the SARS-CoV-2 S protein binds ACE2 with higher affinity than does SARS-CoV S.⁸ The shape of SARS-CoV-2 S and the size of the protein (SARS-CoV-2 S)/protein (ACE2) interaction interface make the bi-protein complex unsuitable as a mo-

lecular model for exploring competitive inhibition mechanism, by which a small ligand (such as Hcq) is supposed to interfere with the binding of beta CoV S glycoproteins to host receptors, particularly in terms of affinity and specificity. Structural and molecular modeling studies have suggested that the SARS-CoV-2 S protein displays two distinct domains, the receptor-binding domain (RBD) that interacts with ACE2 and the N-terminal domain (NTD) that interacts with the ganglioside-rich domain of the plasma membrane.⁶ Amino acid residues (111–158) of the NTD of SARS-CoV-2 S define a functional ganglioside-binding domain (GBD) being completely conserved in clinical isolates worldwide. Hcq has been found to bind sialic acids (linked to gangliosides) with pronounced affinity, indicating its potential to block the interaction of GBD with lipid rafts.⁶ Therefore, specificity issue underlying the dual recognition of gangliosides and ACE2 by SARS-CoV-2 S has not been raised.

One of the most representative CoV prototypes of this genus that causes common cold and pneumonia in elderly population, as well as severe lower respiratory tract infection in patients with compromised immune system is hCoV-OC43.^{1,9} Based on some structural knowledge of hCoV-OC43 S,¹⁰ in the present communication, the recognition modes of the hCoV-OC43 S protein by 9-O-Ac-Sia and Hcq, which share the same binding site (Figure 1), are investigated using molecular docking simulations. A computer-based protein engineering approach^{11,12} is employed to predict single point mutations to which the virus is prone during its genetic adaptation. A question, how the most likely SPMs affect the affinity and specificity of the hCoV-OC43/9-O-Ac-Sia and hCoV-OC43/Hcq interactions, is consequently analyzed.

2. Methods

To obtain the initial coordinates of atoms, the experimental structure of the trimeric hCoV-OC43 S in complex with 9-O-Ac-Sia (PDB ID: 6NZK) was retrieved from the Research Collaboratory for Structural Bioinformatics (RCSB) Protein Data Bank (PDB).¹⁰

The FoldX molecular design toolkit version 5.0^{13–21} was employed to systematically perform single point mutations of each residue being in the binding site of hCoV-OC43 S. FoldX provides a fast quantitative estimation of the importance of the interactions contributing to the stability of proteins and protein complexes. The algorithm uses a full atomic description of the structure of the proteins, while different energy terms taken into account are weighted using empirical data obtained from protein engineering experiments. The code mutates one amino acid to the other 24, including phosphorylated Tyr, Ser and Thr, as well as hydroxyl Proline in addition to 20 standard amino acids, and repairs the neighbor residues. The way it functions is: it mutates the selected position to Ala and anno-

tates all neighbor residues; it mutates the wild-type (wt) residue to itself, and then the neighbors to themselves followed each time by the wt residue to itself. In this way it ensures that, when mutating, any residue that has not been moved in the wt reference will not move. Once this is done, the new wt reference is mutated at the selected position to the target amino acids. To prevent problems, neighbor side chains are only optimized when creating the wt reference after self mutation, but not when making the individual mutants unless a new rotamer for the neighbor is selected.^{11–21} The predictive power was tested on a very large set of point mutants (1088) that comprise most of the structural environments found in proteins.²² A training database of 339 mutants in nine different proteins was initially considered and the set of parameters and weighting factors that best accounted for the changes in stability of the mutants was optimized. The predictive power was then tested using a blind test mutant database of 667 mutants, as well as a database of 82 protein-protein complex mutants. The global correlation for 95% of the entire mutant database (1030 mutants) was 0.83, with a standard deviation of 0.81 kcal mol⁻¹ and a slope of 0.76.²² In the present work, single point mutations of the binding site residues in the hCoV-OC43 S protein were predicted at pH 8, which was used for the experimental determination of the starting structure (PDB ID: 6NZK).¹⁰ It was shown that pH acidification of the medium, such as the one occurring in the endosomal compartment, does not trigger hCoV-OC43 S fusogenic conformational changes.¹⁰

Docking calculations were performed using the AScore/ShapeDock protocol from the ArgusLab 4.0.1 suite of programs.²³ AScore is based on the decomposition

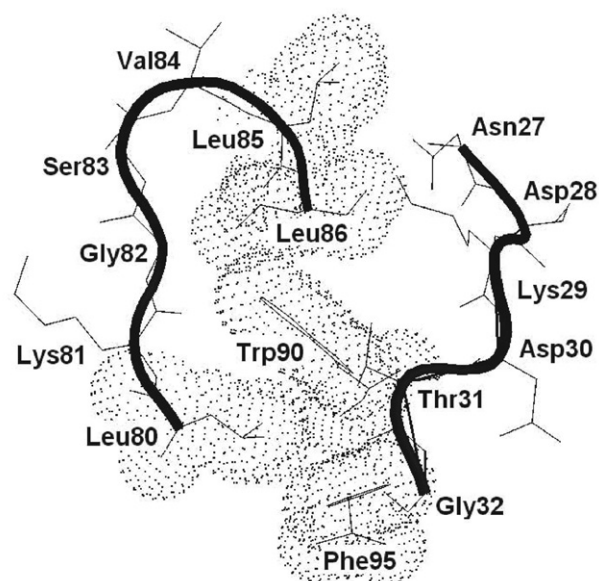


Figure 1. The binding site of hCoV-OC43 S (PDB ID: 6NZK) consists of two loops, L1 (27-Asn-Asp-Lys-Asp-Thr-Gly-32) and L2 (80-Leu-Lys-Gly-Ser-Val-Leu-Leu-86), and two hydrophobic pockets, P1 (Leu85, Leu86 and Trp90) and P2 (Leu80, Trp90 and Phe95) given by dots.

of the total protein-ligand binding free energy into the following contributions: the van der Waals interaction between the ligand and the protein, the hydrophobic effect, the hydrogen bonding between the ligand and the protein, the hydrogen bonding that involves charged donor and/or acceptor groups, the deformation effect, and the effects of the translational and rotational entropy loss in binding process, respectively. Flexible ligand docking was done by describing the ligand as a torsion tree. Groups of bonded atoms that do not have rotatable bonds are nodes, while torsions are connections between the nodes. Topology of a torsion tree is a determinative factor influencing efficient docking. The AScore/ShapeDock protocol is fast, reproducible and formally explores all energy minima.²³ This particular protocol was shown to be very consistent for docking ligands into the crystal structures of viral proteins,^{24–28} while the calculated binding free energies were well-correlated with the experimental inhibitory concentrations.²⁶

3. Results and Discussion

Infections are mediated by the transmembrane S glycoproteins, binding to host receptors and fusing the viral and cellular membranes.¹⁰ Cell surface components that contain 9-O-Ac-Sia are recognized by hCoV-OC43 S.^{29,30} The interacting site of hCoV-OC43 S (PDB ID: 6NZK) contains the following amino acids: Asn27, Asp28, Lys29, Asp30, Thr31, Gly32, Leu80, Lys81, Gly82, Ser83, Val84, Leu85, Leu86, Trp90 and Phe95 (Figure 1). These residues are mainly located in two loops, L1 (27-Asn-Asp-Lys-Asp-Thr-Gly-32) and L2 (80-Leu-Lys-Gly-Ser-Val-Leu-Leu-86). The P1 hydrophobic pocket is defined by Leu85, Leu86 and Trp90 (Figure 1), accommodating the 9-O-Ac-Sia methyl (Figure 2, center). The P2 hydrophobic pocket is defined by Leu80, Trp90 and Phe95 (Figure 1), suiting

the 5-N-acetyl methyl (Figure 2, center). The 9-O-acetyl carbonyl makes a hydrogen bond with Asn27 (2.85 Å, Figure 2, right), while the 5-N atom makes a hydrogen bond with the Lys81 backbone carbonyl (2.79 Å, Figure 2, right). The 9-O-Ac-Sia C1-carboxylate makes both a salt bridge with the Lys81 side chain amine (3.24 Å, Figure 2, right) and a hydrogen bond with the Ser83 side chain hydroxyl (2.71 Å, Figure 2, right). Thus, the specificity of the hCoV-OC43/9-O-Ac-Sia complex formation is Asn27Lys81Lys81Ser83. Evaluated strength of the hCoV-OC43/9-O-Ac-Sia interaction, seen through a dissociation constant $K_d = 48.7 \mu\text{M}$ (Table 1), is in agreement with an experimental observation of $49.7 \pm 10.7 \mu\text{M}$,¹⁰ indicating rapid S-mediated virion attachment, especially in high-density receptor environments.³¹ The binding site is conserved in all CoV S glycoproteins that associate with 9-O-acetyl-sialoglycans, including hCoV-OC43 S, hCoV-HKU1 S, bCoV S and PHEV S.¹⁰ The particular topology of the residues that is similar to those of the ligand-binding pockets of CoV hemagglutinin esterases (HEs) and influenza virus C/D hemagglutinin-esterase fusion (HEF) glycoproteins means that the CoV S glycoproteins share the ligand specificity of influenza C/D HEF but are functionally more compatible to influenza A/B hemagglutinin.¹⁰

Each of the binding site residues is mutated to the other 24 (20 standard amino acids, phosphorylated Tyr, Ser and Thr, as well as hydroxyl Proline). All the single point mutants are energetically evaluated with reference to the original receptor (PDB ID: 6NZK). SPMs that stabilize the wt receptor structure for more than 2 kcal mol⁻¹ are extracted as likely ones (Table 1). An average level of thermochemical accuracy of 2 kcal mol⁻¹ is acceptable for the structure-based drug (or ligand) design purposes.^{32–44}

A careful inspection of the values in Table 1 shows that the SPM Thr31Met stabilizes the wt/9-O-Ac-Sia complex to a largest extent. The introduction of Met31 (Figure 3), instead of Thr31 (Figure 2), in the binding site is asso-

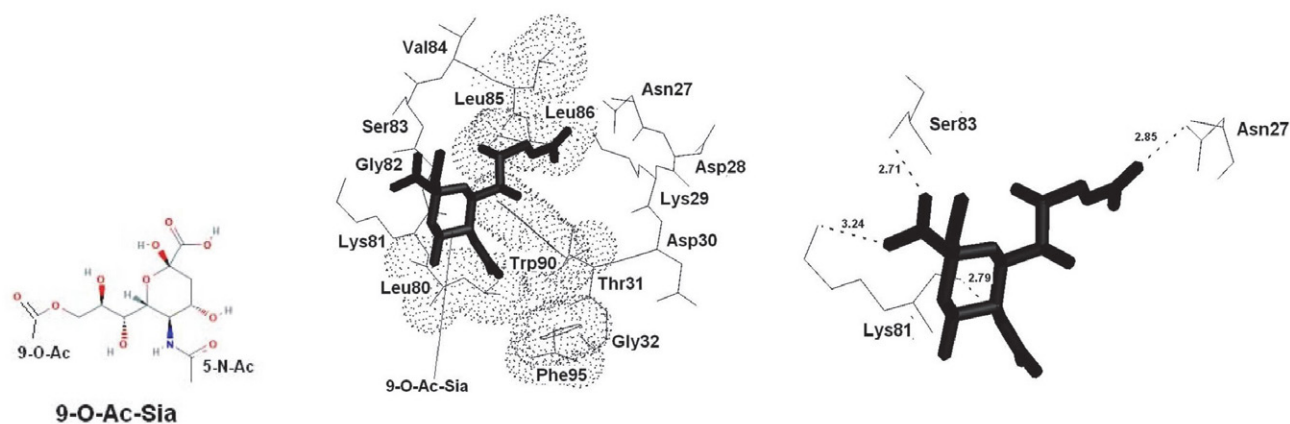


Figure 2. The chemical structure of 9-O-acetylated sialic acid (9-O-Ac-Sia) (left). 9-O-Ac-Sia (bold sticks) in interaction with the binding site residues of hCoV-OC43 S (PDB ID: 6NZK). The P1 (Leu85, Leu86 and Trp90) hydrophobic pocket (dots) accommodates the 9-O-Ac-Sia methyl, while the P2 (Leu80, Trp90 and Phe95) hydrophobic pocket (dots) accommodates the 5-N-acetyl methyl (center). 4 electrostatic contacts of 9-O-Ac-Sia with Asn27, Lys81, Lys81 and Ser83, respectively (right).

Table 1. The Binding Free Energies Obtained by Docking 9-O-Ac-Sia and Hcq in the Single Point Mutants of hCoV-OC43 S (PDB ID: 6NZK)

Ligand: 9-O-Acetylated Sialic Acid			Ligand: Hidroxychloroquine		
Receptor ^(a)	ΔG_{bind} (kcal mol ⁻¹)	K_{d} (μM) ^(b)	Receptor ^(a)	ΔG_{bind} (kcal mol ⁻¹)	K_{d} (μM) ^(b)
wt hCoV-OC43 S	-5.92	48.68	wt hCoV-OC43 S	-6.21	29.93
Asp28Phe	-6.79	11.31	Ser83Gly	-7.93	1.67
Ser83Gly	-6.79	11.31	Asn27Ile	-7.94	1.64
Ser83Val	-6.80	11.12	Asp28Arg	-7.94	1.64
Gly82Ser	-6.85	10.23	Asp28Gln	-7.94	1.64
Asp28Tyr	-6.93	8.94	Asp28Glu	-7.94	1.64
Val84Leu	-6.94	8.80	Asp28Leu	-7.94	1.64
Ser83Arg	-6.98	8.22	Asp28Lys	-7.94	1.64
Leu80Ile	-7.01	7.82	Asp28Met	-7.94	1.64
Asn27Leu	-7.06	7.19	Asp28Phe	-7.94	1.64
Leu86Met	-7.07	7.07	Asp28Ptr	-7.94	1.64
Ser83Tpo	-7.09	6.84	Asp28Tyr	-7.94	1.64
Lys81Met	-7.12	6.50	Leu80Ile	-7.94	1.64
Ser83Glu	-7.12	6.50	Lys81Met	-7.94	1.64
Asp28Leu	-7.13	6.40	Leu86Met	-7.94	1.64
Asp28Met	-7.13	6.40	Asn27Leu	-7.95	1.62
Val84Arg	-7.24	5.32	Ser83Thr	-7.95	1.62
Ser83Lys	-7.28	4.97	Ser83Arg	-7.96	1.59
Ser83Leu	-7.32	4.65	Ser83Tpo	-7.96	1.59
Thr31Leu	-7.35	4.42	Thr31Leu	-7.98	1.54
Asp28Arg	-7.50	3.44	Ser83Glu	-7.98	1.54
Asp28Ptr	-7.50	3.44	Ser83Leu	-8.02	1.44
Asn27Ile	-7.60	2.91	Gly82Ser	-8.06	1.34
Asp28Lys	-7.77	2.19	Val84Leu	-8.07	1.32
Asp28Glu	-7.77	2.19	Ser83Lys	-8.08	1.30
Asp28Gln	-7.77	2.19	Thr31Met	-8.11	1.24
Ser83Thr	-7.89	1.79	Ser83Val	-8.11	1.24
Thr31Met	-7.95	1.62	Val84Arg	-8.25	0.98

^(a) wild-type (wt), Ptr – phosphorylated Thr, Tpo – phosphorylated Tyr; ^(b) ΔG_{bind} – the binding free energy, K_{d} – the dissociation constant, $\Delta G_{\text{bind}} = RT \ln(K_{\text{d}})$, R – the gas constant (1.9872×10^{-3} kcal K⁻¹ mol⁻¹), T – the absolute temperature (300 K), 1 $\mu\text{M} = 10^{-6}$ M

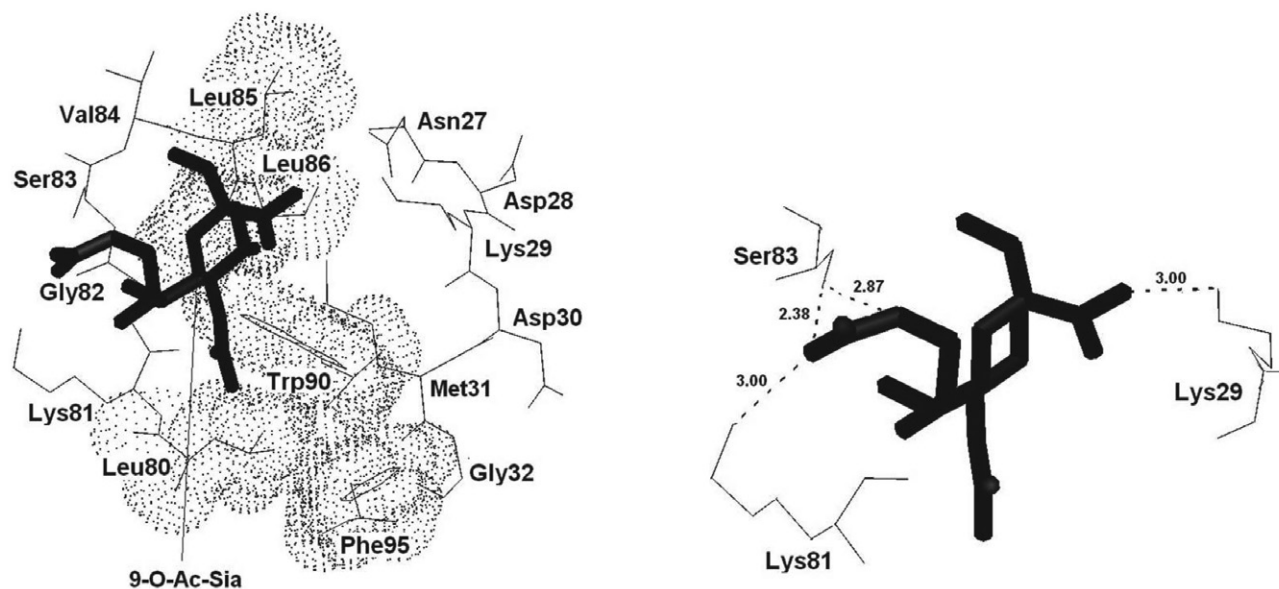


Figure 3. 9-O-Ac-Sia (bold sticks) that is docked in the binding site of the Thr31Met mutant of hCoV-OC43 S. The P2 (Leu80, Trp90 and Phe95) hydrophobic pocket (dots) accommodates the 5-N-acetyl methyl (left). 4 electrostatic contacts of 9-O-Ac-Sia with Lys29, Lys81, Ser83 and Ser83, respectively (right).

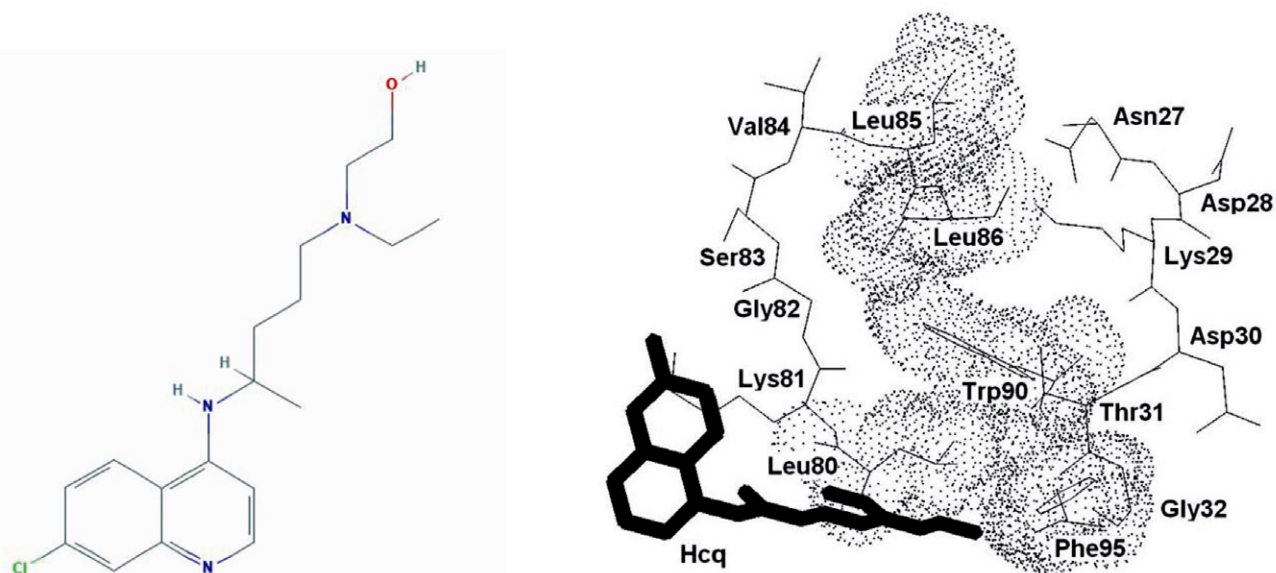


Figure 4. The chemical structure of Hydroxychloroquine (Hcq) (left). Hcq (bold sticks) that is docked in the binding site of hCoV-OC43 S (PDB ID: 6NZK). Hydrophobic interaction of the P2 (Leu80, Trp90 and Phe95) pocket (dots) with the Hcq side chain (right). No electrostatic contacts are detected.

ciated with the horizontal conformational flip of 9-O-Ac-Sia, making the 9-O hydrophobic side chain face outside of the active cavity (Figure 3, left). The P2 (Leu80, Trp90 and Phe95) hydrophobic pocket (dots) accommodates the 5-N-acetyl methyl (Figure 3, left). The 9-O-Ac-Sia C1-carboxylate makes a hydrogen bond with the Lys29 side chain (3.00 Å, Figure 3, right); the 9-O-acetyl carbonyl makes two hydrogen bonds with the Lys81 and Ser83 side chains (3.00 Å and 2.38 Å, Figure 3, right), while the 9-O makes a hydrogen bond with the Ser83 side chain (2.87 Å, Figure 3, right). Thus, Thr31Met changes the specificity, Asn27Lys81Lys81Ser83, of the original hCoV-OC43/9-O-Ac-Sia complex to Lys29Lys81Ser83Ser83. The specificity difference is in the substitution of an Asn by a Ser, that is, in the substitution of a small amino acid by a tiny one. Met31 is a larger and more hydrophobic amino acid than Thr31 being almost indifferent in terms of its hydrophobicity. Among aliphatic amino acids, Met is unique by having a sulphur atom in its side chain. A water molecule in bulk water can rotate in many directions. The presence of a nonpolar residue such as Met in the binding site restricts the movement of the water, causing an entropy loss that can be regained through the hydrophobic effect and the release of protein-bound water molecules.

The chemical structure of Hcq (Figure 4, left) contains an aromatic core scaffold to which both a Cl atom and a large side chain are bound, indicating a pronounced hydrophobic character of the ligand. The binding mode obtained by docking Hcq in the binding site of hCoV-OC43 S (PDB ID: 6NZK) is illustrated in Figure 4 (right). The P2 (Leu80, Trp90 and Phe95) hydrophobic pocket is in interaction with the Hcq side chain, while the Hcq aromatic core is oriented outside of the active

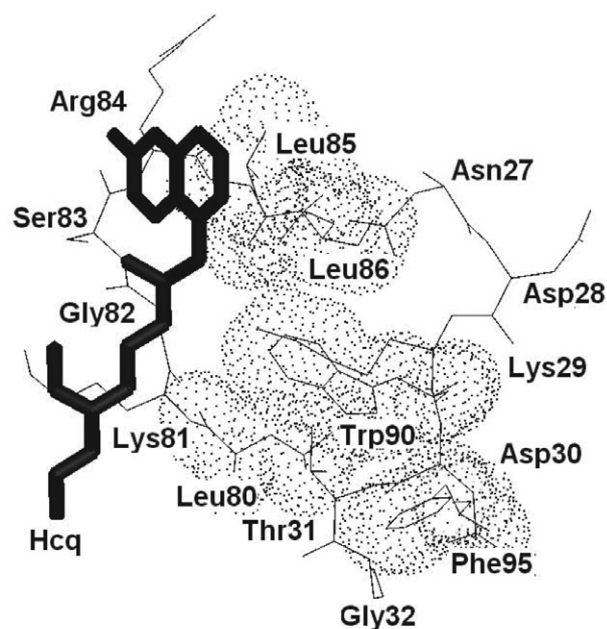


Figure 5. Hcq (bold sticks) that is docked in the binding site of the Val84Arg mutant of hCoV-OC43 S. The P1 (Leu85, Leu86 and Trp90) hydrophobic pocket (dots) accommodates the aromatic core scaffold of Hcq. No electrostatic contacts are detected.

cavity. Noteworthy is that electrostatic interactions are not involved in formation of the hCoV-OC43/Hcq complex.

The values in Table 1 illustrate that the SPM Val84Arg is the most stabilizing one in the wt/Hcq complex. The introduction of Arg84 (Figure 5), instead of Val84 (Figure 4), in the binding site causes the vertical conformational

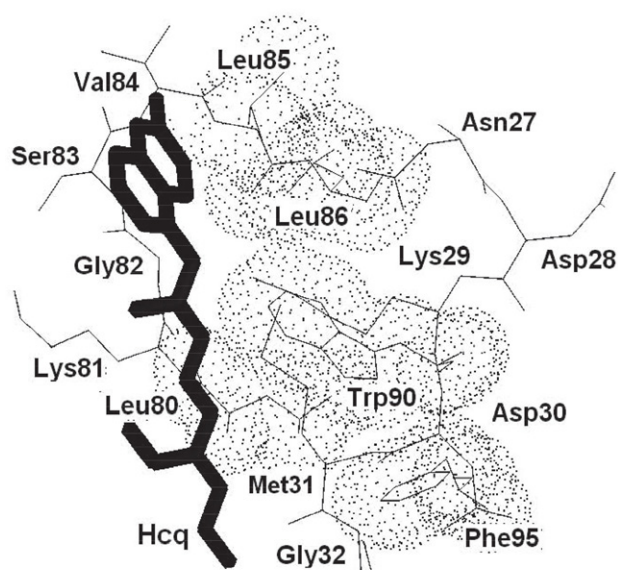


Figure 6. Hcq (bold sticks) that is docked in the binding site of the Thr31Met mutant of hCoV-OC43 S. The P1 (Leu85, Leu86 and Trp90) hydrophobic pocket (dots) accommodates the aromatic core scaffold of Hcq. No electrostatic contacts are detected.

switch (rotation by around 90° clockwise) of Hcq, making the aromatic core scaffold of Hcq interact with the P1 hydrophobic pocket containing Leu85, Leu86 and Trp90 (Figure 5). No electrostatic interactions are detected at the Val84Arg/Hcq interface, indicating the very low (or almost negligible) specificity of Hcq binding.

The values in Table 1 indicate that Thr31Met, which is the most likely SPM for the binding of 9-O-Ac-Sia, is a very likely one for the binding of Hcq as well. The hydrophobic nature of the Thr31Met/Hcq interaction mode (Figure 6) is similar to that of the Val84Arg/Hcq interaction mode (Figure 5) qualitatively.

Comparing the binding free energies (Table 1) of the complexes, formed by docking 9-O-Ac-Sia and Hcq to the same receptor such as the Thr31Met mutant of hCoV-OC43 S, shows that Hcq has slightly higher affinity to hCoV-OC43 S than does 9-O-Ac-Sia. This standpoint can be accounted for by the almost-pure hydrophobic recognition of hCoV-OC43 S by Hcq with very low specificity. However, rapid kinetics underlying S-mediated virion attachment to 9-O-Ac-Sia is associated with recognition being hydrophobic and very specific at the same time. In view of this, it is useful to contrast the chemical structures of 9-O-Ac-Sia and Hcq and to consider entropy loss upon ligand binding. Flexible docking of ligand is based on active torsions in ligand structure, which can be conceivable as particular sp^3 bonds that are directly involved in finding the lowest energy receptor/ligand conformations. Entropy loss due to ligand binding is related to the loss of its degrees of freedom. The torsional potential indirectly takes care of the particular entropy amount by being proportional to the number of active torsions in ligand structure.

An active torsion has been estimated to cost circa 0.3 kcal mol⁻¹ energetically.^{45,46} It means that the structure of 9-O-Ac-Sia having eleven active torsions experiences a negative entropy change that roughly costs -3.3 kcal mol⁻¹. By having only one active torsion in its structure, the binding of Hcq is associated with a tiny entropic decrease of about -0.3 kcal mol⁻¹. The dissociation constants of the hCoV-OC43/Hcq complexes are in the micromolar (10⁻⁶ M) range (Table 1), which is acceptable for hit ligand molecule but not for drug candidate. Knowing that the binding site is conserved in all CoV S glycoproteins that associate with 9-O-acetyl-sialoglycans,¹⁰ the very low specificity of Hcq to hCoV-OC43 S does not speak in favor of the potential of Hcq to be a drug candidate.

4. References

1. J. Reguera, G. Mudgal, C. Santiago, J. M. Casasnovas, *Virus Res.* **2014**, *194*, 3–15. DOI:10.1016/j.virusres.2014.10.005
2. D. S. Hui, E. I. Azhar, T. A. Madani, C. Drosten, A. Zumla, E. Petersen, *Int. J. Infect. Dis.* **2020**, *91*, 264–266. DOI:10.1016/j.ijid.2020.01.009
3. <https://www.who.int/dg/speeches/detail/who-director-general-s-opening-remarks-at-the-media-briefing-on-covid-19---11-march-2020> (accessed on 18 May 2020)
4. <https://www.worldometers.info/coronavirus/coronavirus-death-rate/> (accessed on 18 May 2020)
5. <https://techcrunch.com/2020/03/19/fda-testing-coronavirus-treatments-including-chloroquine-plasma-from-recovered-covid-19-patients/> (accessed on 18 May 2020)
6. J. Fantini, C. Di Scala, H. Chahinian, N. Yahi, *Int. J. Antimicrob. Agents* **2020**, 105960. DOI:10.1016/j.ijantimicag.2020.105960
7. <https://medicalxpress.com/news/2020-03-pharma-chiefs-coronavirus-vaccine-.html> (accessed on 18 May 2020)
8. D. Wrapp, N. Wang, K. S. Corbett, J. A. Goldsmith, C. L. Hsieh, O. Abiona, B. S. Graham, J. S. McLellan, *Science* **2020**, *367*(6483), 1260–1263. DOI:10.1126/science.abb2507
9. J. S. Kahn, K. McIntosh, *Pediatr. Infect. Dis. J.* **2005**, *24* (11 Suppl.), S223–S227. DOI:10.1097/01.inf.0000188166.17324.60
10. M. Alejandra Tortorici, A. C. Walls, Y. Lang, C. Wang, Z. Li, D. Koerhuis, G.-J. Boons, B.-J. Bosch, F. A. Rey, R. J. de Groot, D. Veasler, *Nat. Struct. & Mol. Biol.* **2019**, *26*, 481–489. DOI:10.1038/s41594-019-0233-y
11. P. M. Mitrasinovic, *Med. Chem.* **2014**, *10*, 252–270. DOI:10.2174/157340641003140304143442
12. P. M. Mitrasinovic, *Med. Chem.* **2014**, *10*, 46–58. DOI:10.2174/157340641001131226122124
13. P. Vanhee, E. Verschuere, L. Baeten, F. Stricher, L. Serrano, F. Rousseau, J. Schymkowitz, *Nucleic Acids Res.* **2011**, *39*, D435–D442. DOI:10.1093/nar/gkq972
14. M. Petukhov, D. Cregut, C. M. Soares, L. Serrano, *Protein Sci.* **1999**, *8*, 1982–1989. DOI:10.1110/ps.8.10.1982
15. V. Muñoz, L. Serrano, *Proteins* **1994**, *20*, 301–311. DOI:10.1002/prot.340200403

16. R. Abagyan, M. Totrov, *J. Mol. Biol.* **1994**, *235*, 983–1002. DOI:10.1006/jmbi.1994.1052
17. M. Vijayakumar, K. Y. Wong, G. Schreiber, A. R. Fersht, A. Szabo, H. X. Zhou, *J. Mol. Biol.* **1998**, *278*, 1015–1024. DOI:10.1006/jmbi.1998.1747
18. J. W. H. Schymkowitz, F. Rousseau, I. C. Martins, J. Ferkinghoff-Borg, F. Stricher, L. Serrano, *Proc. Natl. Acad. Sci. U. S. A.* **2005**, *102*, 10147–10152. DOI:10.1073/pnas.0501980102
19. J. Van Durme, J. Delgado, F. Stricher, L. Serrano, J. Schymkowitz, F. Rousseau, *Bioinformatics* **2011**, *27*, 1711–1712. DOI:10.1093/bioinformatics/btr254
20. J. Schymkowitz, J. Borg, F. Stricher, R. Nys, F. Rousseau, L. Serrano, *Nucleic Acids Res.* **2005**, *33*, W382–W388. DOI:10.1093/nar/gki387
21. L. Baeten, J. Reumers, V. Tur, F. Stricher, T. Lenaerts, L. Serrano, F. Rousseau, J. Schymkowitz, *PLoS Comput. Biol.* **2008**, *4*, e1000083. DOI:10.1371/journal.pcbi.1000083
22. R. Guerois, J. E. Nielsen, L. Serrano, *J. Mol. Biol.* **2002**, *320*(2), 369–387. DOI:10.1016/S0022-2836(02)00442-4
23. ArgusLab 4.0.1, M. A. Thompson, Planaria Software, LLC, Seattle WA, **2004**.
24. P. M. Mitrasinovic, *Biophys. Chem.* **2009**, *140*, 35–38. DOI:10.1016/j.bpc.2008.11.004
25. P. M. Mitrasinovic, *Curr. Drug Targets*, **2010**, *11*, 315–326. DOI:10.2174/138945010790711932
26. M. L. Mihajlovic, P. M. Mitrasinovic, *Mol. Simulation* **2009**, *35*, 311–324. DOI:10.1080/08927020802430752
27. M. L. Mihajlovic, P. M. Mitrasinovic, *Biophys. Chem.* **2008**, *136*, 152–158. DOI:10.1016/j.bpc.2008.06.003
28. M. L. Mihajlovic, P. M. Mitrasinovic, *J. Serb. Chem. Soc.* **2009**, *74*, 1–13. DOI:10.2298/JSC0901001M
29. G. Herrler, S. Szepanski, B. Schultze, *Behring Inst. Mitt.* **1991**, *89*, 177–184.
30. F. Kunkel, G. Herrler, *Virology* **1993**, *195*, 195–202. DOI:10.1006/viro.1993.1360
31. R. J. G. Hulswit, Y. Lang, M. J. G. Bakkers, W. Li, Z. Li, A. Schouten, B. Ophorst, F. J. M. Kuppeveld, G.-J. Boons, B.-J. Bosch, E. G. Huizinga, R. J. de Groot, *Proc. Natl. Acad. Sci. U. S. A.* **2019**, *116*, 2681–2690. DOI:10.1073/pnas.1809667116
32. A. D. Becke, *J. Chem. Phys.* **2002**, *117*, 6935–6938. DOI:10.1063/1.1503772
33. S. Cosconati, S. Forli, A. L. Perryman, R. Harris, D. S. Goodsell, A. J. Olson, *Expert Opin. Drug Discov.* **2010**, *5*(6), 597–607. DOI:10.1517/17460441.2010.484460
34. N. Deng, L. Wickstrom, P. Cieplak, C. Lin, D. Yang, *J. Phys. Chem. B* **2017**, *121*(46), 10484–10497. DOI:10.1021/acs.jpcc.7b09406
35. P. M. Mitrasinovic, *Chem. Phys.* **2003**, *286*, 1–13. DOI:10.1016/S0301-0104(02)00902-3
36. P. M. Mitrasinovic, *Acta Chim. Slov.* **2020**, *67*, 386–395. DOI:10.17344/acsi.2019.5105
37. P. M. Mitrasinovic, *Acta Chim. Slov.* **2020**, *67*, 683–700. DOI: 10.17344/acsi.2020.5823
38. P. M. Mitrasinovic, *Acta Chim. Slov.* **2020**, *67*, 876–884. DOI:10.17344/acsi.2020.5847
39. P. M. Mitrasinovic, *Croat. Chem. Acta* **2019**, *92*(1), 43–57. DOI:10.5562/cca3456
40. P. M. Mitrasinovic, *J. Biomol. Struct. Dyn.* **2018**, *36*(9), 2292–2302. DOI:10.1080/07391102.2017.1358670
41. P. M. Mitrasinovic, *J. Chem. Inf. Model.* **2015**, *55*(2), 421–433. DOI:10.1021/ci5006965
42. A. Pavlov, P. M. Mitrasinovic, *Curr. Org. Chem.* **2010**, *14*, 129–138. DOI:10.2174/138527210790069866
43. P. M. Mitrasinovic, *Curr. Org. Chem.* **2010**, *14*, 198–211. DOI:10.2174/138527210790069857
44. P. M. Mitrasinovic, *Curr. Drug Targets* **2013**, *14*, 817–829. DOI:10.2174/1389450111314070009
45. G. M. Morris, D. S. Goodsell, R. S. Halliday, R. Huey, W. E. Hart, R. K. Belew, A. J. Olson, *J. Comput. Chem.* **1998**, *19*, 1639–1662. DOI:10.1002/(SICI)1096-987X(19981115)19:14<1639::AID-JCC10>3.0.CO;2-B
46. G. M. Morris, R. Huey, W. Lindstrom, M. F. Sanner, R. K. Belew, D. S. Goodsell, A. J. Olson, *J. Comput. Chem.* **2009**, *30*, 2785–2791. DOI:10.1002/jcc.21256

Povzetek

Zaradi trenutnega širjenja nove bolezni CoViD-19 je Svetovna zdravstvena organizacija 11. marca 2020 uradno razglasila svetovno pandemijo. Sedanji trendi kažejo, da bo imela pandemija izjemen klinični in gospodarski vpliv na zdravje prebivalstva. Okužbo sproži konica (S) transmembranskega glikoproteina humanega koronavirusa (hCoV), ki se veže na gostiteljski receptor. Raziskave v teku in razvoj terapevtskih izdelkov so bistvenega pomena za uspešno zdravljenje CoViD-19. Da bi prispevali k skupnemu naporu, smo v tej študiji z uporabo *in silico* proteinskega inženiringa proučili točkovne mutacije preostankov vezavnega mesta pri hCoV-OC43 S, ki prepoznajo celične površinske komponente, ki vsebujejo 9-O-acetilirano sialično kislino (9-O-Ac-Sia), medtem ko smo njihove učinke na vezavo 9-O-Ac-Sia in hidrosiklorokina (Hcq) ocenili z uporabo simulacij molekulskega sidranja. Thr31Met in Val84Arg naj bi bili kritični – najverjetnejši točkovni mutaciji v hCoV-OC43 S za vezavo 9-O-Ac-Sia oz. Hcq, pri čemer je Thr31Met zelo verjetna mutacija tudi v primeru Hcq. Načini interakcije kažejo na primerljivo moč kompleksov Thr31Met / 9-O-Ac-Sia in Val84Arg / Hcq (ali Thr31Met / Hcq). Glede na to, da je pri vseh CoV ohranjeno mesto vezave S glikoproteinov, ki se povezujejo z 9-O-acetil-sialoglikani, visoka hidrofobna afiniteta Hcq do hCoV-OC43 S govori v prid njegovi sposobnosti kompetitivne inhibicije hitre S-posredovane pritrditve viriona v okoljih z visoko gostoto receptorja, vendar je lahko njegova občutno nizka specifičnost za hCoV-OC43 S ena ključnih ovir za upoštevanje potenciala Hcq, da postane kandidat za zdravilo.



Except when otherwise noted, articles in this journal are published under the terms and conditions of the Creative Commons Attribution 4.0 International License

Scientific paper

Synthesis, Characterization and Biological Application of Pyrazolo[1,5-a]pyrimidine Based Organometallic Re(I) Complexes

Reena R. Varma,¹ Juhee G. Pandya,² Foram U. Vaidya,³ Chandramani Pathak,³ Bhupesh S. Bhatt¹ and Mohan N. Patel^{1,*}

¹ Department of Chemistry, Sardar Patel University, Vallabh Vidyanagar–388 120, Gujarat (INDIA)

² Department of Biosciences, Sardar Patel University, Vallabh Vidyanagar, Gujarat, (INDIA)

³ Department of Cell Biology, School of Biological Sciences and Biotechnology, Indian Institute of Advanced Research, Koba Institutional Area, Gandhinagar-382007, Gujarat (INDIA)

* Corresponding author: E-mail: jeenen@gmail.com
Phone number: (+912692) 226856*218

Received: 03-30-2020

Abstract

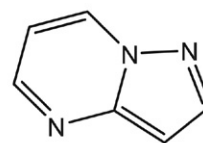
The neutral rhenium(I) complexes (I–VI) of type $[\text{ReCl}(\text{CO})_3\text{L}^n]$ {where $\text{L}^1 = 7\text{-phenyl-5-(pyridin-2-yl)pyrazolo[1,5-a]pyrimidine}$, $\text{L}^2 = 7\text{-(4-bromophenyl)-5-(pyridin-2-yl)pyrazolo[1,5-a]pyrimidine}$, $\text{L}^3 = 7\text{-(4-chlorophenyl)-5-(pyridin-2-yl)pyrazolo[1,5-a]pyrimidine}$, $\text{L}^4 = 7\text{-(2-chlorophenyl)-5-(pyridin-2-yl)pyrazolo[1,5-a]pyrimidine}$, $\text{L}^5 = 7\text{-(4-methoxyphenyl)-5-(pyridin-2-yl)pyrazolo[1,5-a]pyrimidine}$, $\text{L}^6 = 5\text{-(pyridin-2-yl)-7-(p-tolyl)pyrazolo[1,5-a]pyrimidine}$ } were synthesized and characterized by ^{13}C -APT, ^1H -NMR, IR, electronic spectra, magnetic moment and conductance measurement. The anti-proliferative activity on HCT116 cells by MTT assay suggests potent cytotoxic nature of complexes, some complexes even have better activity than standard drug cisplatin, oxaliplatin, and carboplatin. The complexes were found to have better antimicrobial activity compare to pyrazolo pyrimidine ligands. The theoretical study of compounds–DNA interactions was examined by molecular docking as a supportive tool to the experimental data, which suggests the groove mode of binding. The values of docking energy for compounds–DNA interaction were found in the range of -230.31 to -288.34 kJ/mol. The intrinsic binding constant values of complexes ($1.1\text{--}3.5 \times 10^5 \text{ M}^{-1}$) were found higher than the ligands ($0.32\text{--}1.8 \times 10^5 \text{ M}^{-1}$).

Keywords: *In vitro* cytotoxicity; Molecular modelling; Anti-proliferative activity; Groove binding

1. Introduction

Metal carbonyl moieties, such as $\{\text{M}(\text{CO})_3\}$ ($\text{M} = \text{Cr}, \text{Mn}, \text{Re}, \text{Fe}$), can attach to the biomolecules capable of molecular recognition, to label and assay, specific biological receptors. When $\text{M} = \text{Tc}$ or Re , the same idea is used to introduce radioactive $^{99\text{m}}\text{Tc}$, ^{186}Re , or ^{188}Re at a receptor for radiopharmaceutical applications.^{1,2} There has been considerable interest in testing metal carbonyls for anticancer activity.³ For example, $[\text{Co}_2(\text{CO})_6(\text{HC}_2\text{C-CH}_2\text{O}_2\text{CC}_6\text{H}_4\text{-2-OH})]$ is more active than cisplatin on the human mammary tumor cell lines MCF-7 and MDA-MB-231.⁴ Also $[\{\eta^5\text{-}(4\text{-Me}_2\text{N}\{\text{CH}_2\}_4\text{OC}_6\text{H}_4)\text{-}(4\text{-HOC}_6\text{H}_4)\text{CHCHEtC}_5\text{H}_4\}\text{Re}(\text{CO})_3]$ has been shown to behave similarly to tamoxifen,

and it appears that the observed antiproliferative effect is dependent on the oestradiol receptor α .⁵



pyrazolo[1,5-a]pyrimidine

Pyrazole and pyrimidine derivatives attracted organic chemists very much due to their biological and chemotherapeutic importance. Pyrazolo pyrimidines and related fused heterocycles are of interest as potential bioactive molecules. They are known to exhibit pharmacological ac-

tivities such as CNS depressant,⁶ neuroleptic,⁷ and tuberculostatic.⁸ Recently, the chemistry of pyrazolo[1,5-a]pyrimidines attracted great attention as a synthetically important class of compounds.⁹ They represent biologically important compounds of purine analogues and this class has attracted wide pharmaceutical interest as inhibitors of lymphocyte-specific kinase (Lck) with enzymatic, cellular, and *in vivo* potency.¹⁰ In 2003, a research group from NRC synthesized some pyrazolo[1,5-a]pyrimidines and studied their biological effects as an anti-inflammatory, analgesic, and antipyretic drugs in comparison to nivalgin.¹¹ The choice of the ligand is very important for the development of new radiopharmaceuticals reagents; thus, studies on rhenium(I) complexes with ligands as aromatic N-heterocycles have shown a great effectiveness.¹²

In continuation of our earlier work,¹³ the present study illustrates the synthesis of new heterocyclic ligands and their organometallic rhenium complexes. Heterocyclic compounds have significant biological importance upon chelation with pentacarbonyl chloro rhenium(I) and presence of carbonyl group attached with metal which further enhanced the biological activity.

2. Experimental

Materials and methods: All the chemicals and solvents were of reagent grade, 2-acetyl thiophene, substituted aldehyde were purchased from Merck Limited (India), different substituted phenyl hydrazine were purchased from Thirumalai Chemicals Ltd. (TCL), potassium-tert-butoxide, potassium hydroxide purchased from Sisco Research Laboratories Pvt. Ltd. (SRL), pentacarbonyl chloro rhenium(I) purchased from Sigma Aldrich (USA). Luria broth and nutrient broth were purchased from Himedia (India). Agarose and Luria Broth (LB) were purchased from Hi-media Laboratories Pvt. Ltd., India. Culture of two Gram(+ve), i.e. *Staphylococcus aureus* (*S. aureus*) (MTCC-3160) and *Bacillus subtilis* (MTCC-7193), and three Gram(-ve), i.e. *Serratia marcescens* (MTCC-7103), *Pseudomonas aeruginosa* (MTCC-1688) and *Escherichia coli* (MTCC-433), were purchased from Institute of Microbial Technology (Chandigarh, India). *S. cerevisiae* Var. Paul Linder 3360 was obtained from IMTECH, Chandigarh, India. HS DNA was purchased from Sigma Aldrich Chemical Co. (India). Human colorectal carcinoma (HCT 116) cells were obtained from the cell repository, National Center for Cell Science (NCCS), Pune, Maharashtra, India.

Physical measurements: The ¹H and ¹³C NMR spectra were recorded on a Bruker Avance (400 MHz). Infrared spectra were recorded on an FT-IR ABB Bomen MB 3000 spectrophotometer in the range 4000–400 cm⁻¹. C, H, and N elemental analyses were performed with a Heraeus, Germany CHNO RAPID. Molar conductance was meas-

ured using a conductivity meter model no. EQ-660A, Mumbai (India). Melting points (°C, uncorrected) were determined in open capillaries on the ThermoCal10 melting point apparatus (Analab Scientific Pvt. Ltd, India). The electronic spectra were recorded on a UV-160A UV-Vis spectrophotometer, Shimadzu (Japan). The minimum inhibitory concentration (MIC) study was carried out using laminar airflow cabinet (Toshiba, Delhi, India). Hydrodynamic chain length study was carried out by a viscometric measurement bath. Photo quantization of the gel after electrophoresis was carried out on AlphaDigiDoc™ RT. Version V.4.0.0 PC-Image software.

General method for synthesis of pyrazolo[1,5-a]pyrimidines ligands (L¹-L⁶): The α,β unsaturated carbonyl compounds (3a-3f) were synthesized using literature procedure.¹⁴ Syntheses of the pyrazolo[1,5-a]pyrimidines based ligands (L¹-L⁶) were carried out using Lipson and co-workers method.¹⁵ To a solution of the α,β-unsaturated carbonyl compounds (3a-3f) (~2.391 mmol) in 10 mL of DMF, 1H-pyrazol-3-amine (4a) (~198.7 mg, ~2.391 mmol) and KOH (~15 mg, ~2.391 mmol) solution were added. The reaction mixture was refluxed for 30 min. Completion of the reaction was checked by TLC plates, the excess of solvent was removed under reduced pressure and the reaction mixture was cooled on an ice bath. The reaction mixture was extracted with ethyl acetate (20 mL × 2) and washed thoroughly with water (25 mL × 2). The brine solution of sodium chloride was added to it and dried over sodium sulphate. The resulting mixture was concentrated under vacuum to obtain pyrazolo[1,5-a]pyrimidine based ligands as products. The ¹H and ¹³C NMR spectra are shown in supplementary material 1 and 2 respectively.

Synthesis of 7-phenyl-5-(pyridin-2-yl)pyrazolo[1,5-a]pyrimidine (L¹): The ligand (L¹) was prepared by using enone (3a) (500 mg, 2.391 mmol) and 1H-pyrazole-3-amine (4a) (198.7 mg, 2.391 mmol). Yield: 84.2%; Color: yellowish amorphous solid; mp 170 °C; Mol. wt.: 272.31g/mol; **Empirical formula:** C₁₇H₁₂N₄; **Elemental analysis:** Calc. (%): C, 74.98; H, 4.44; N, 20.58; found. C, 74.88; H, 4.40; N, 20.58; **Mass spectra (m/z %):** 272.20 (100) [M⁺]; **¹H NMR (400 MHz, CDCl₃) δ/ppm:** 8.75 (1H, d, J = 4.0 Hz, H₆), 8.59 (1H, d, J = 8.0 Hz, H₄), 8.22 (1H, s, H₇), 8.16 (2H, dd, J = 4.4 Hz, J = 3.2 Hz, H₃, 5), 7.89 (2H, d, J = 1.6 Hz, H_{2,6}), 7.60 (1H, d, J = 3.6 Hz, H₃), 7.41 (3H, m, H_{3, 4, 5}), 6.86 (1H, d, J = 2.4 Hz, H₄). **¹³C NMR (100 MHz, CDCl₃) δ/ppm:** 155.1 (C₈, Cquat.), 154.5 (C₂, Cquat.), 149.8 (C₆, Cquat.), 149.2 (C₆, CH), 146.9 (C_{5a}, Cquat.), 145.2 (C₄, -CH), 136.4 (C₃, -CH), 131.6 (C₁, Cquat.) 130.9 (C_{3,5}, -CH), 129.4 (C₄, -CH), 128.6 (C_{2, 6}, -CH), 124.8 (C₅, -CH), 121.6 (C₃, -CH), 105.2 (C₇, -CH), 97.5 (C₄, -CH). [**Total signal observed** = 15: signal of C = 5 (phenyl ring-C = 1, pyrazolo[1,5-a]pyrimidine-C = 3, pyridine ring-C = 1), signal of CH = 10 (pyrazolo[1,5-a]pyrimidine-CH = 3, phenylring-CH = 3, pyridine ring-CH = 4)]; **IR (KBr, 4000–400 cm⁻¹):** 2930 ν(C-H)ar., 1551 ν(C=N),

1504 (C-H) bending, 1251 ν (C-N), 1597 ν (C=C) conjugated alkenes, 763 ν (Ar-H) adjacent hydrogen.

7-(4-Bromophenyl)-5-(pyridin-2-yl)pyrazolo[1,5-a]pyrimidine (L²): The ligand (L²) was prepared by using enone (3b) (500 mg, 1.730 mmol) and 1H-pyrazole-3-amine (4a) (143.8 mg, 1.730 mmol). Yield: 84.2%; Color: yellowish amorphous solid; **mp** 182 °C; **Mol. wt.:** 351.21 g/mol; **Empirical formula:** C₁₇H₁₁BrN₄; **Elemental analysis:** Calc. (found) (%): C, 58.14; H, 3.16; N, 15.95; found. C, 58.08; H, 3.11; N, 15.90; **Mass spectra (m/z %):** 350.4 (100) [M⁺], 352.4 [M+2]; **¹H NMR (400 MHz, CDCl₃) δ /ppm:** 8.75 (1H, d, *J* = 4.4 Hz, H_{6^a}), 8.59 (1H, d, *J* = 8.0, H_{4^a}), 8.21 (1H, s, H₇), 8.14 (2H, dd, *J* = 3.2 Hz, 2 Hz, H_{3^a,5^a}), 7.94 (1H, d, *J* = 6.4 Hz, H_{6^c}), 7.91 (1H, d, *J* = 7.6 Hz, H₂), 7.76 (2H, d, *J* = 2.0 Hz, H_{3^b,5^b}), 7.43 (1H, dd, *J* = 8.0 Hz, 1.6 Hz, H₃), 6.87 (1H, d, *J* = 1.2 Hz, H₄). **¹³C NMR (100 MHz, CDCl₃) δ /ppm:** 160.6 (C₆, Cquat.), 153.9 (C_{2^a}, Cquat.), 153.1 (C_{5a}, Cquat.), 148.8 (C₈, Cquat.), 148.9 (C_{6^b}, -CH), 145.7 (C₁, Cquat.), 145.2 (C_{4^b}, -CH), 137.9 (C₃, -CH), 130.9 (C_{3^b,5^b}, -CH), 125.5 (C_{2^b,6^b}, -CH), 122.3 (C_{4^a}, Cquat.), 121.1 (C_{5^b}, -CH), 117.6 (C_{3^a}, -CH), 103.3 (C₇, -CH), 97.9 (C₄, -CH). [**Total signal observed** = 15: signal of C = 6 (*p*-Br-phenyl ring-C = 2, pyrazolo[1,5-a]pyrimidine-C = 3, pyridine ring-C = 1), signal of CH = 9 (pyrazolo[1,5-a]pyrimidine-CH = 3, *p*-Br phenyl ring-CH = 2, pyridine ring-CH = 4)]; **IR (KBr, 4000–400 cm⁻¹):** 2925 ν (C-H)ar., 1558 ν (C=N), 1490 (C-H) bending, 1204 ν (C-N), 1597 ν (C=C) conjugated alkenes, 764 ν (Ar-H) adjacent hydrogen.

7-(4-Chlorophenyl)-5-(pyridin-2-yl)pyrazolo[1,5-a]pyrimidine (L³): The ligand (L³) was prepared by using enone (3c) (500 mg, 2.044 mmol) and 1H-pyrazole-3-amine (4a) (169.8 mg, 2.044 mmol). Yield: 85.4%; Color: yellowish amorphous solid; **mp** 178 °C; **Mol. wt.:** 306.75 g/mol; **Empirical formula:** C₁₇H₁₁ClN₄; **Calc. (%)**: C, 66.56; H, 3.61; N, 18.26; found. C, 66.55; H, 3.58; N, 18.24; **Mass spectra (m/z %):** 306.20 (100) [M⁺], 308.20 [M+2]; **¹H NMR (400 MHz, CDCl₃) δ /ppm:** 8.75 (1H, d, *J* = 4.8 Hz, H_{6^a}), 8.59 (1H, d, *J* = 8.0 Hz, H_{4^a}), 8.22 (1H, s, H₇), 8.17 (2H, dd, *J* = 8.4, 4.0 Hz, H_{3^a,5^a}), 7.93 (2H, d, *J* = 2.0 Hz, H_{2^b,6^b}), 7.58 (1H, d, *J* = 8.4 Hz, H₃), 7.44 (2H, d, *J* = 4.0 Hz, H_{3^b,5^b}), 6.87 (1H, d, *J* = 2.4 Hz, H₄). **¹³C NMR (100 MHz, CDCl₃) δ /ppm:** 155.1 (C₈, Cquat.), 154.3 (C_{2^a}, Cquat.), 149.6 (C₆, Cquat.), 149.2 (C_{6^b}, -CH), 145.7 (C_{4^b}, -CH), 145.2 (C_{4^a}, Cquat.), 137.2 (C₃, -CH), 130.8 (C_{5a}, Cquat.), 129.9 (C_{3^b,5^b}, -CH), 129.4 (C₁, Cquat.), 129.0 (C_{2^b,6^b}, -CH), 124.9 (C_{5^b}, -CH), 121.7 (C_{3^a}, -CH), 104.9 (C₇, -CH), 97.68 (C₄, -CH). [**Total signal observed** = 15: signal of C = 6 (*p*-Cl-phenyl ring-C = 2, pyrazolo[1,5-a]pyrimidine-C = 3, pyridine ring-C = 1), signal of CH = 9 (pyrazolo[1,5-a]pyrimidine-CH = 3, *p*-Cl-phenyl ring-CH = 2, pyridine ring-CH = 4)]; **IR (KBr, 4000–400 cm⁻¹):** 2922 ν (C-H)ar., 1551 ν (C=N), 1504 (C-H) bending, 1190 ν (C-N), 1605 ν (C=C) conjugated alkenes, 756 ν (Ar-H) adjacent hydrogen.

7-(2-Chlorophenyl)-5-(pyridin-2-yl)pyrazolo[1,5-a]pyrimidine (L⁴): This ligand (L⁴) was prepared by using

enone (3d) (500 mg, 2.044 mmol) and 1H-pyrazole-3-amine (4a) (169.8 mg, 2.044 mmol). Yield: 79.5%; Color: yellowish amorphous solid; **mp** 180 °C; **Mol. wt.:** 306.75 g/mol; **Empirical formula:** C₁₇H₁₁ClN₄; **Calc. (found) (%)**: C, 66.56; H, 3.61; N, 18.26; found. C, 66.50; H, 3.60; N, 18.23; **Mass spectra (m/z %):** 306.82 (100) [M⁺], 308.82 [M+2]; **¹H NMR (400 MHz, CDCl₃) δ /ppm:** 8.73 (1H, d, *J* = 3.6 Hz, H_{6^a}), 8.61 (1H, d, *J* = 8.0 Hz, H_{4^a}), 8.19 (1H, d, *J* = 2.4 Hz, H_{5^a}), 8.09 (1H, s, H₇), 7.93 (1H, d, *J* = 1.6 Hz, H_{3^a}), 7.62 (2H, m, H_{4^b,5^b}), 7.51 (2H, m, H_{3^b,6^b}), 7.41 (1H, d, *J* = 5.2 Hz, H₃), 6.88 (1H, d, *J* = 2.4 Hz, H₄). **¹³C NMR (100 MHz, CDCl₃) δ /ppm:** 154.9 (C₈, Cquat.), 153.01 (C_{2^a}, Cquat.), 149.28 (C_{6^b}, -CH), 148.9 (C₆, Cquat.), 145.5 (C_{4^b}, -CH), 145.1 (C_{5a}, Cquat.), 137.10 (C₃, -CH), 133.7 (C_{2^a}, Cquat.), 131.57 (C_{3^b}, -CH), 131.1 (C_{5^b}, -CH), 130.2 (C_{4^b}, -CH), 128.6 (C₁, Cquat.), 127.1 (C_{6^b}, -CH), 124.9 (C_{5^b}, -CH), 121.8 (C_{3^a}, -CH), 105.2 (C₇, -CH), 97.72 (C₄, -CH). [**Total signal observed** = 17: signal of C = 6 (*o*-Cl-phenyl ring-C = 2, pyrazolo[1,5-a]pyrimidine-C = 3, phenyl ring-C = 1), signal of CH = 11 (pyrazolo[1,5-a]pyrimidine-CH = 3, *o*-Cl phenyl ring-CH = 4, pyridine ring-CH = 4)]; **IR (KBr, 4000–400 cm⁻¹):** 2922 ν (C-H)ar., 1551 ν (C=N), 1504 ν (C-H) bending, 1190 ν (C-N), 1605 ν (C=C) conjugated alkenes, 758 ν (Ar-H) adjacent hydrogen.

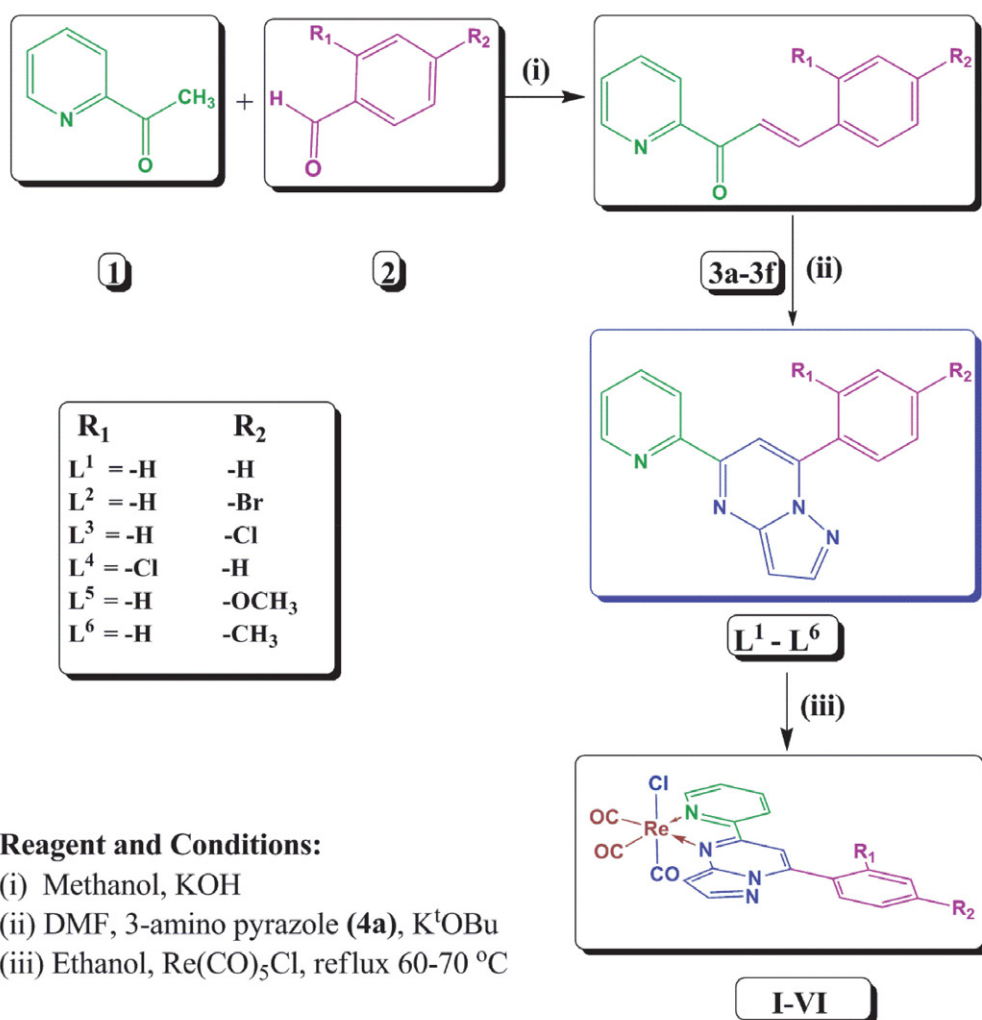
7-(4-Methoxyphenyl)-5-(pyridin-2-yl)pyrazolo[1,5-a]pyrimidine (L⁵): The ligand (L⁵) was prepared by using enone (3e) (500 mg, 2.082 mmol) and 1H-pyrazole-3-amine (4a) (173 mg, 2.082 mmol). Yield: 87.6%; Color: yellowish amorphous solid; **mp** 178 °C; **Mol. wt.:** 302.34 g/mol; **Empirical formula:** C₁₈H₁₄N₄O; **Calc. (found) (%)**: C, 71.51; H, 4.67; N, 18.53; found. C, 71.48; H, 4.62; N, 18.56; **Mass spectra (m/z %):** 302.20 (100) [M⁺]; **¹H NMR (400 MHz, CDCl₃) δ /ppm:** 8.78 (1H, d, *J* = 4.4 Hz, H_{6^a}), 8.51 (1H, d, *J* = 8.0 Hz, H_{4^a}), 8.33 (1H, s, H₇), 8.25 (2H, d, *J* = 8.8 Hz, H_{3^a,5^a}), 8.10 (1H, d, *J* = 10.4 Hz, H_{6^c}), 8.03 (1H, d, *J* = 7.6 Hz, H₂), 7.58 (1H, d, *J* = 5.2 Hz, H₃), 7.19 (2H, d, *J* = 8.8 Hz, H_{3^b,5^b}), 6.92 (1H, d, *J* = 2.0 Hz, H₄), 3.09 (3H, s, -OCH₃). **¹³C NMR (100 MHz, CDCl₃) δ /ppm:** 161.9 (C_{4^b}, Cquat.), 154.7 (C₈, Cquat.), 154.01 (C_{2^a}, Cquat.), 149.9 (C_{6^b}, -CH), 149.7 (C₆, Cquat.), 146.7 (C_{4^a}, -CH), 146.3 (C_{5a}, Cquat.), 138.1 (C₃, -CH), 131.7 (C_{2^b,6^b}, -CH), 125.8 (C_{5^b}, -CH), 123.4 (C₁, Cquat.), 121.5 (C_{3^a}, -CH), 114.5 (C₇, -CH), 103.8 (C_{3^b,5^b}, -CH), 97.6 (C₄, -CH), 55.9 (-OCH₃). [**Total signal observed** = 16: signal of C = 6 (*p*-OCH₃-phenyl ring-C = 2, pyrazolo[1,5-a]pyrimidine-C = 3, pyridine ring-C = 1), signal of CH = 9 (pyrazolo[1,5-a]pyrimidine-CH = 3, *p*-OCH₃ phenyl ring-CH = 2, pyridine ring-CH = 4), -OCH₃ = 1]; **IR (KBr, 4000–400 cm⁻¹):** 2922 ν (C-H)ar., 1551 ν (C=N), 1514 (C-H) bending, 1188 ν (C-N), 1597 ν (C=C) conjugated alkenes, 764 ν (Ar-H) adjacent hydrogen.

5-(Pyridin-2-yl)-7-(*p*-tolyl)pyrazolo[1,5-a]pyrimidine (L⁶): The ligand (L⁶) was prepared by using enone (3f) (500 mg, 2.231 mmol) and 1H-pyrazole-3-amine (4a) (185.4 mg, 2.231 mmol). Yield: 82.5%; Color: yellowish amorphous solid; **mp** 175 °C; **Mol. wt.:** 286.34 g/mol; **Em-**

empirical formula: $C_{18}H_{14}N_4$. Calc. (found) (%): C, 75.50; H, 4.93; N, 19.57; found. C, 75.46; H, 4.90; N, 19.55; **Mass spectra (m/z %):** 286.60 (100) $[M^+]$; **1H NMR (400 MHz, $CDCl_3$) δ/ppm :** 8.75 (1H, d, $J = 4.4$ Hz, H_{6^a}), 8.59 (1H, d, $J = 8.0$ Hz, H_{4^a}), 8.23 (1H, s, H_7), 8.22 (2H, dd, $J = 2.4$ Hz, 1.6 Hz, $H_{3^a, 5^a}$), 8.08 (2H, dd, $J = 10.0$ Hz, 8.0 Hz, $H_{2^a, 6^a}$), 7.41 (3H, d, $J = 7.6$ Hz, $H_{3, 3', 5'}$), 6.85 (1H, d, $J = 2.0$ Hz, H_4), 2.49 (3H, s, $-CH_3$). **^{13}C NMR (100 MHz, $CDCl_3$) δ/ppm :** 155.0 (C_8 , Cquat.), 154.6 (C_{2^a} , Cquat.), 149.7 (C_6 , Cquat.), 149.2 (C_{6^a} , $-CH$), 147.07 (C_{5a} , Cquat.), 145.1 (C_4 , $-CH$), 141.3 (C_4 , Cquat.), 137.0 (C_3 , $-CH$), 129.3 ($C_{3', 5'}$, $-CH$), 129.2 (C_{1^a} , Cquat.), 128.6 ($C_{2', 6'}$, $-CH$), 124.7 (C_{5^a} , $-CH$), 121.6 (C_{3^a} , $-CH$), 104.73 (C_7 , $-CH$), 97.4 (C_4 , $-CH$), 21.5 ($-CH_3$). [**Total signal observed** = 16: signal of C = 6 (p - CH_3 phenyl ring-C = 2, pyrazolo[1,5- a]pyrimidine-C = 3, pyridine ring-C = 1), signal of CH = 9 (pyrazolo[1,5- a]pyrimidine-CH = 3, p - CH_3 -phenylring-CH = 2, pyridine ring-CH = 4), $-CH_3$ = 1]; **IR (KBr, 4000–400 cm^{-1}):** 2923 ν (C-H)ar., 1551 ν (C=N), 1512 (C-H) bending, 1196 ν (C-N), 1597 ν (C=C) conjugated alkenes, 764 ν (Ar-H) adjacent hydrogen.

General synthesis of complexes: The metal carbonyl complexes (I–VI) were synthesized using pentacarbonyl chloro rhenium(I) and ligands (L^1 – L^6) in ethanol in a 1:1 proportion.¹⁶

Synthesis of $[Re(CO)_3(L^1)Cl]$ (I): Ethanolic solution of the precursor of $[Re(CO)_5Cl]$ (100 mg, 0.276 mmol) was refluxed for 10 minutes. Then a solution of ligand (L^1) (75 mg, 0.276 mmol in 10mL ethanol), was added and the reaction was stirred yielding a solution. The resulting mixture was stirred at 60 °C for 5–6 hr. Progress of reaction was monitored by TLC after completion of reaction the solution was filtered through celite in order to remove solid particles and the solvent was removed under reduced pressure the orange red product was obtained. The proposed reaction for the synthesis of complexes (I–VI) is shown in scheme 1. Yield: 62.9%; Color: yellowish amorphous solid; **mp** 380 °C; **Mol. wt.:** 578.00 g/mol; **Empirical formula:** $C_{20}H_{12}ClN_4O_3Re$, **Elemental analysis: Calc. (%)**: C, 41.56; H, 2.00; N, 9.69; Re, 32.22; **Found. (%)**: C, 41.52; H, 1.98; N, 9.67; Re, 32.20; **Conductance:** 2.83 S $cm^2 mol^{-1}$. **1H NMR (400 MHz, $DMSO-d_6$) δ/ppm :** 9.18



Scheme 1. Reaction scheme for the synthesis of ligands and rhenium complexes.

(2H, dd, $J = 8.4$ Hz, 6.4 Hz, $H_{3,6}$), 8.60 (1H, s, H_7), 8.45 (2H, dd, $J = 11.2$ Hz, 8.0 Hz, $H_{4,5}$), 8.3 (2H, d, $J = 7.6$ Hz, $H_{2,6}$), 7.91 (1H, d, $J = 6.8$ Hz, H_3), 7.72 (3H, m, $H_{3,4,5}$), 7.25 (1H, d, $J = 2.4$ Hz, H_4). $^{13}\text{C NMR}$ (100 MHz, DMSO- d_6) δ/ppm : 203.1 (M-CO, Cquat.), 197.5 (2M-CO, Cquat.), 157.5 (C_8 , Cquat.), 154.7 ($C_{2,3}$, Cquat.), 153.9 ($C_{6,7}$, -CH), 149.8 (C_6 , Cquat.), 149.1 (C_{5a} , Cquat.), 147.1 ($C_{4,5}$, -CH), 140.9 (C_3 , -CH), 132.8 ($C_{3,5}$, -CH), 131.0 ($C_{4,5}$, -CH), 130.0 ($C_{1,3}$, Cquat.), 129.4 ($C_{2,6}$, -CH), 129.0 ($C_{5,7}$, -CH), 127.6 ($C_{3,7}$, -CH), 106.1 (C_7 , -CH), 99.7 (C_4 , -CH). [Total signal observed = 17: signal of C = 7 (M-CO = 2, phenyl ring-C = 1, pyrazolo[1,5-a]pyrimidine-C = 3, pyridine ring-C = 1), signal of CH = 10 (pyrazolo[1,5-a]pyrimidine-CH = 3, phenylring-CH = 3, pyridine ring-CH = 4)]; IR (KBr, 4000–400 cm^{-1}): 2014, 1898 $\nu(\text{Re}(\text{CO}))$, 1550 $\nu(\text{C}=\text{N})$, 1504 (C-H) bending, 1250 $\nu(\text{C}-\text{N})$, 1604 $\nu(\text{C}=\text{C})$ conjugated alkenes, 763 $\nu(\text{Ar}-\text{H})$ adjacent hydrogen.

Synthesis of $[\text{Re}(\text{CO})_3(\text{L}^2)\text{Cl}]$ (II): It was synthesized using ligand (L^2) (97 mg, 0.276 mmol). Yield: 77.2%; Color: yellowish amorphous solid; mp 385 °C; Mol. wt.: 656.89 g/mol; Empirical formula: $\text{C}_{20}\text{H}_{11}\text{BrClN}_4\text{O}_3\text{Re}$; Elemental analysis: Calc. (%): C, 36.57; H, 1.69; N, 8.83; Re, 28.35; Found. (%): C, 36.55; H, 1.67; N, 8.80; Re, 8.33; Conductance: 5.12 $\text{S cm}^2 \text{mol}^{-1}$. $^1\text{H NMR}$ (400 MHz, DMSO- d_6) δ/ppm : 9.16 (2H, dd, $J = 8.4$ Hz, 7.6 Hz, $H_{4,6}$), 8.60 (1H, s, H_7), 8.46 (2H, dd, $J = 6.4$ Hz, 4.4 Hz, $H_{3,5}$), 8.28 (2H, d, $J = 8.4$ Hz, $H_{2,6}$), 7.95 (2H, d, $J = 8.4$ Hz, H_3), 7.73 (1H, d, $J = 7.6$ Hz, H_3), 7.25 (1H, d, $J = 1.2$ Hz, H_4). $^{13}\text{C NMR}$ (100 MHz, DMSO- d_6) δ/ppm : 198.9 (M-CO, Cquat.), 197.6 (2M-CO, Cquat.), 157.5 (C_6 , Cquat.), 154.6 ($C_{2,3}$, Cquat.), 153.9 ($C_{6,7}$, -CH), 149.8 (C_{5a} , Cquat.), 149.2 (C_8 , Cquat.), 147.1 ($C_{4,5}$, -CH), 140.9 (C_3 , -CH), 132.7 ($C_{3,5}$, -CH), 132.1 ($C_{2,6}$, -CH), 130.9 ($C_{5,7}$, -CH), 129.5 ($C_{1,3}$, Cquat.), 129.06 ($C_{3,7}$, -CH), 126.6 ($C_{4,5}$, -Cquat.), 106.1 (C_7 , -CH), 99.82 (C_4 , -CH). [Total signal observed = 17: signal of C = 8 (M-CO = 2, *p*-Br-phenyl ring-C = 2, pyrazolo[1,5-a]pyrimidine-C = 3, pyridine ring-C = 1), signal of CH = 9 (pyrazolo[1,5-a]pyrimidine-CH = 3, *p*-Br phenylring-CH = 2, pyridine ring-CH = 4)]; IR (KBr, 4000–400 cm^{-1}): 2021, 1898 $\nu(\text{Re}(\text{CO}))$, 1558 $\nu(\text{C}=\text{N})$, 1481 (C-H) bending, 1196 $\nu(\text{C}-\text{N})$, 1597 $\nu(\text{C}=\text{C})$ conjugated alkenes, 764 $\nu(\text{Ar}-\text{H})$ adjacent hydrogen.

Synthesis of $[\text{Re}(\text{CO})_3(\text{L}^3)\text{Cl}]$ (III): It was synthesized using ligand (L^3) (84 mg, 0.276 mmol). Yield: 140 mg, 76.1%; Color: yellowish amorphous solid; mp 378 °C; Mol. wt.: 612.44 g/mol; Empirical formula: $\text{C}_{20}\text{H}_{11}\text{Cl}_2\text{N}_4\text{O}_3\text{Re}$; Elemental analysis: Calc. (%): C, 39.22; H, 1.81; N, 9.15; Re, 30.40; Found. (%): C, 39.20; H, 1.78; N, 9.12; Re, 30.36; Conductance: 11.16 $\text{S cm}^2 \text{mol}^{-1}$. $^1\text{H NMR}$ (400 MHz, DMSO- d_6) δ/ppm : 9.17 (2H, dd, $J = 8.4$ Hz, 6.4 Hz, $H_{4,6}$), 8.61 (1H, s, H_7), 8.48 (2H, dd, $J = 8.4$ Hz, 8.0 Hz, $H_{3,5}$), 8.36 (2H, d, $J = 8.8$ Hz, $H_{2,6}$), 7.91 (1H, d, $J = 6.4$ Hz, H_3), 7.81 (2H, d, $J = 8.4$ Hz, $H_{3,5}$), 7.26 (1H, d, $J = 2.0$ Hz, H_4). $^{13}\text{C NMR}$ (100 MHz, DMSO- d_6) δ/ppm : 195.5 (M-CO, Cquat.), 189.2 (M-2CO, Cquat.), 157.5 (C_8 , Cquat.), 154.7

($C_{2,3}$, Cquat.), 153.9 ($C_{6,7}$, -CH), 149.3 (C_6 , Cquat.), 148.6 ($C_{4,5}$, Cquat.), 147.2 ($C_{4,5}$, -CH), 140.9 (C_3 , -CH), 137.6 (C_{5a} , Cquat.), 132.8 ($C_{3,5}$, -CH), 129.5 ($C_{2,6}$, -CH), 129.2 ($C_{5,7}$, -CH), 128.7 ($C_{1,3}$, Cquat.), 127.5 ($C_{3,7}$, -CH), 106.2 (C_7 , -CH), 99.8 (C_4 , -CH). [Total signal observed = 17: signal of C = 8 (M-CO = 2, *p*-Cl-phenyl ring-C = 2, pyrazolo[1,5-a]pyrimidine-C = 3, pyridine ring-C = 1), signal of CH = 9 (pyrazolo[1,5-a]pyrimidine-CH = 3, *p*-Cl phenyl ring-CH = 2, pyridine ring-CH = 4)]; IR (KBr, 4000–400 cm^{-1}): 2021, 1898 $\nu(\text{Re}(\text{CO}))$, 1551 $\nu(\text{C}=\text{N})$, 1504 (C-H) bending, 1165 $\nu(\text{C}-\text{N})$, 1597 $\nu(\text{C}=\text{C})$ conjugated alkenes, 764 $\nu(\text{Ar}-\text{H})$ adjacent hydrogen.

Synthesis of $[\text{Re}(\text{CO})_3(\text{L}^4)\text{Cl}]$ (IV): It was synthesized using ligand (L^4) (84 mg, 0.276 mmol). Yield: 76.1%; Color: yellowish amorphous solid; mp 368 °C; Mol. wt.: 612.44 g/mol; Empirical formula: $\text{C}_{20}\text{H}_{11}\text{Cl}_2\text{N}_4\text{O}_3\text{Re}$; Elemental analysis: Calc. (%): C, 39.22; H, 1.81; N, 9.15; Re, 30.40; Found. (%): C, 39.20; H, 1.78; N, 9.12; Re, 30.36; Conductance: 11.30 $\text{S cm}^2 \text{mol}^{-1}$. $^1\text{H NMR}$ (400 MHz, DMSO- d_6) δ/ppm : 9.20 (1H, d, $J = 3.6$ Hz, H_6), 9.01 (1H, d, $J = 12.8$ Hz, H_4), 8.54 (2H, d, $J = 2.0$ Hz, $H_{3,5}$), 8.44 (1H, s, H_7), 7.89 (2H, m, $H_{4,5}$), 7.77 (2H, m, $H_{3,6}$), 7.68 (1H, d, $J = 7.6$ Hz, H_3), 7.27 (1H, d, $J = 2.4$ Hz, H_4). $^{13}\text{C NMR}$ (100 MHz, DMSO- d_6) δ/ppm : 198.8 (M-CO, Cquat.), 197.6 (2M-CO, Cquat.), 157.6 (C_8 , Cquat.), 154.5 ($C_{2,3}$, Cquat.), 154.02 ($C_{6,7}$, -CH), 148.40 (C_6 , Cquat.), 147.9 (C_{5a} , Cquat.), 147.3 ($C_{4,5}$, -CH), 141.1 (C_3 , -CH), 133.3 ($C_{3,7}$, -CH), 133.1 ($C_{2,6}$, Cquat.), 132.3 ($C_{5,7}$, -CH), 130.2 ($C_{4,5}$, -CH), 130.1 ($C_{1,3}$, Cquat.), 129.6 ($C_{6,7}$, -CH), 128.1 ($C_{5,7}$, -CH), 127.5 ($C_{3,7}$, -CH), 107.8 (C_7 , -CH), 99.9 (C_4 , -CH). [Total signal observed = 19: signal of C = 8 (M-CO = 2, *o*-Cl-phenyl ring-C = 2, pyrazolo[1,5-a]pyrimidine-C = 3, pyridine ring-C = 1), signal of CH = 11 (pyrazolo[1,5-a]pyrimidine-CH = 3, *o*-Cl phenyl ring-CH = 4, pyridine ring-CH = 4)]; IR (KBr, 4000–400 cm^{-1}): 2021, 1898 $\nu(\text{Re}(\text{CO}))$, 1551 $\nu(\text{C}=\text{N})$, 1504 (C-H) bending, 1165 $\nu(\text{C}-\text{N})$, 1605 $\nu(\text{C}=\text{C})$ conjugated alkenes, 756 $\nu(\text{Ar}-\text{H})$ adjacent hydrogen.

Synthesis of $[\text{Re}(\text{CO})_3(\text{L}^5)\text{Cl}]$ (V): It was synthesized using ligand (L^5) (84 mg, 0.276 mmol). Yield: 89.7%; Color: yellowish amorphous solid; mp 370 °C; Mol. wt.: 608.02 g/mol; Empirical formula: $\text{C}_{21}\text{H}_{14}\text{ClN}_4\text{O}_4\text{Re}$; Elemental analysis: Calc. (%): C, 41.48; H, 2.32; N, 9.21; Re, 30.62; Found. (%): C, 41.45; H, 2.30; N, 9.18; Re, 30.60; Conductance: 15.18 $\text{S cm}^2 \text{mol}^{-1}$. $^1\text{H NMR}$ (400 MHz, DMSO- d_6) δ/ppm : 9.19 (2H, dd, $J = 8.0$ Hz, 6.0 Hz, $H_{4,6}$), 8.60 (1H, s, H_7), 8.46 (4H, dd, $J = 7.6$ Hz, 4.8 Hz, $H_{2,6,3,5}$), 7.89 (1H, d, $J = 6.4$ Hz, H_3), 7.27 (2H, d, $J = 8.8$ Hz, $H_{3,5}$), 7.22 (1H, d, $J = 2.4$ Hz, H_4), 3.94 (3H, s, $-\text{OCH}_3$). $^{13}\text{C NMR}$ (100 MHz, DMSO- d_6) δ/ppm : 199.0 (M-CO, Cquat.), 198.2 (2M-CO, Cquat.), 163.1 ($C_{4,5}$, Cquat.), 157.2 (C_8 , Cquat.), 154.8 ($C_{2,3}$, Cquat.), 153.8 ($C_{6,7}$, -CH), 149.4 (C_6 , Cquat.), 147.0 ($C_{4,5}$, CH), 140.9 (C_3 , -CH), 133.2 ($C_{2,6}$, -CH), 129.4 ($C_{5,7}$, -CH), 127.5 ($C_{3,7}$, -CH), 123.2 (C_{5a} , -Cquat.), 121.9 ($C_{1,3}$, Cquat.), 114.7 (C_7 , -CH), 105.0 ($C_{3,5}$, -CH), 99.4 (C_4 , -CH), 56.2 ($-\text{OCH}_3$). [Total signal ob-

served = 18: signal of C = 8 (M-CO = 2, *p*-OCH₃-phenyl ring-C = 2, pyrazolo[1,5-*a*]pyrimidine-C = 3, pyridin ring-C = 1), signal of CH = 9 (pyrazolo[1,5-*a*]pyrimidine-CH = 3, *p*-OCH₃ phenylring-CH = 2, pyridine ring-CH = 4), -OCH₃ = 1]; IR (KBr, 4000–400 cm⁻¹): 2021, 1921, 1898 ν(Re(CO)), 1551 ν(C=N), 1512 (C-H) bending, 1180 ν(C-N), 1597 ν(C=C) conjugated alkenes, 764 ν(Ar-H) adjacent hydrogen.

Synthesis of [Re(CO)₃(L⁶)Cl] (VI): It was synthesized using ligand (L⁶) (79 mg, 0.276 mmol). Yield: 84.9%; Color: yellowish amorphous solid; mp 374 °C; Mol. wt.: 592.03 g/mol; Empirical formula: C₂₁H₁₄ClN₄O₃Re, Elemental analysis: C, 42.60; H, 2.38; N, 9.46; Re, 31.45; Found. (%): C, 42.40; H, 2.20; N, 9.35; Re, 31.42; Conductance: 13.25 S cm² mol⁻¹. ¹H NMR (400 MHz, DMSO-*d*₆) δ/ppm: 9.17 (2H, dd, *J* = 8.0 Hz, 7.6 Hz, H_{4^a,6^a}), 8.59 (1H, s, H₇), 8.44 (2H, dd, *J* = 8.4 Hz, 6.4 Hz, H_{3^a,5^a}), 8.27 (2H, d, *J* = 8.0 Hz, H_{2^a,6^a}), 7.90 (1H, d, *J* = 6.4 Hz, H₃), 7.53 (2H, d, *J* = 8.4 Hz, H_{3^a,5^a}), 7.23 (1H, d, *J* = 2.4 Hz, H₄), 2.49 (3H, s, -CH₃). ¹³C NMR (100 MHz, DMSO-*d*₆) δ/ppm: 198.9 (M-CO, Cquat.), 197.7 (2M-CO, Cquat.), 157.3 (C₈, Cquat.), 154.7 (C_{2^a}, Cquat.), 153.8 (C_{6^a}, -CH), 149.7 (C₆, -Cquat.), 149.2 (C_{5^a}, Cquat.), 147.1 (C₄, -CH), 143.3 (C₄, Cquat.), 140.9 (C₃, -CH), 130.9 (C_{3^a,5^a}, -CH), 129.6 (C_{2^a,6^a}, -CH), 129.4 (C_{5^a}, -CH), 127.5 (C_{3^a}, -CH), 126.9 (C_{1^a}, Cquat.), 105.6 (C₇, -CH), 99.54 (C₄, -CH), 21.7 (-CH₃). [Total signal observed = 18: signal of C = 8 (M-CO = 2, *p*-CH₃-phenyl ring-C = 2, pyrazolo[1,5-*a*]pyrimidine-C = 3, pyridine ring-C = 1), signal of CH = 9 (pyrazolo[1,5-*a*]pyrimidine-CH = 3, *p*-CH₃-phenylring-CH = 2, pyridine ring-CH = 4, CH₃ = 1)]; IR (KBr, 4000–400 cm⁻¹): 2021, 1913 ν(Re(CO)), 1551 ν(C=N), 1512 (C-H) bending, 1196 ν(C-N), 1597 ν(C=C) conjugated alkenes, 764 ν(Ar-H) adjacent hydrogen.

Biological activities:

In vitro antimicrobial assay: The synthesized ligands and complexes were evaluated for their antimicrobial properties according to literature.¹⁷

In vivo brine shrimp lethality bioassay (BSLB): The brine shrimp (*Artemia* cysts) lethality bioassay for the synthesized compounds were carried out according to literature.^{17, 18}

Cellular level bioassay using *S. cerevisiae*: The *in vitro* cytotoxicity assay was performed in the eukaryotic system where a yeast cell, *S. cerevisiae* was taken as a model test organism. The cytotoxic effect of compounds was determined by viability staining and represented as % viability. Lower % viability indicates high toxicity of compound on that particular biological system.

Antiproliferative study: The Re(I) tricarbonyl complexes I-VI were tested for *in vitro* cytotoxicity against colon carcinoma (HCT116) cancerous cell lines. The MTT (3-(4,5-dimethylthiazol-2-yl)-2,5-diphenyltetrazolium bromide) assay was used to determine the cytotoxicity of

the compounds.¹⁹ The extent of inhibition is displayed as an IC₅₀ value, which is defined as the concentration required to inhibit cell growth to half.^{20,21} Stock solutions of 10–100 mg/mL of test complexes (I-VI) were prepared in dimethyl sulfoxide (DMSO). Twenty-four hours after cell plating, media was removed and replaced with fresh media containing 10, 25, 50, 100, 500 μg/mL of test compounds DMSO vehicle control, for the indicated exposure times.

DNA binding activity: Binding of metal complexes with DNA can be understood by absorption spectral analysis of DNA. The binding mode and binding constant (K_b) of a complex toward DNA give an idea about the strength of interaction, which can be obtained by studying UV-Vis absorbance titration.²² The binding constant values were estimated by the following equation,

$$\frac{[DNA]}{(\epsilon_a - \epsilon_f)} = \frac{[DNA]}{(\epsilon_b - \epsilon_f)} + \frac{1}{K_b(\epsilon_b - \epsilon_f)} \quad (1)$$

Where, [DNA] = concentration of DNA in base pairs, ε_a = extinction coefficient observed for the MLCT absorption band at the given DNA concentration, ε_f = the extinction coefficient of the complex in solution and ε_b = the extinction coefficient of the complex when fully bound to DNA.

Viscometric experiments were performed using Ubbelohde viscometer, maintained at 25.0 (±0.5) °C in a thermostatic water bath. The total system was 3 mL, containing 100 μM of DNA, and metal complexes were varied from 5 to 50 μM. The flow time of solutions in phosphate buffer (pH 7.0) was recorded, and an average flow time was calculated. Data were presented as (η/η⁰)^{1/3} versus [Compound]/[DNA], where η is the viscosity of DNA in the presence of complex and η⁰ is the viscosity of DNA alone. All the experiment was done in triplicate. The hydrodynamic length of DNA generally increases upon partial intercalation while it does not lengthen upon groove binding.^{23,24}

Molecular docking: Docking study was measured for Re(I) complexes with deoxyribonucleic acid (DNA) sequence d(ACCGACGTCGGT)₂. The main purpose of molecular docking is to identify the binding mode of metal complexes using Hex 8.0 software. The detailed process of this study is described in literature.²⁵

Integrity of compounds on the DNA: For DNA integrity of compounds, the treated test organism's DNA subjected to Agarose gel electrophoresis. The DNA of *S. cerevisiae* was extracted according to the protocol described by Michael R. Green and Joseph Sambrook.²⁶ The detailed process is described in literature.²⁷

3. Results and Discussion

¹³C-APT, ¹H-NMR, IR, magnetic moments, conductance measurements, and electronic spectra: The ¹H

NMR spectra of ligands L¹–L⁶ and complexes I–VI demonstrate peak at 6.0 – 8.0 δ ppm confirms protons of pyrazolo[1,5-a]pyrimidine aromatic ring. ¹³C-APT data of ligands L¹–L⁶ and complexes I–VI show signals at 97–160 δ ppm confirm the presence of aromatic environment.¹⁶ The crystal structure of Re(CO)₅Cl show four CO at equatorial position, and one CO along with Cl atom at axial position.²⁸ The heterocyclic bidentate ligand approach from equatorial position and replace two CO molecules to form Re(I) complexes. In keeping with the *facial* arrangement of the CO ligands, the ¹³C (APT) NMR spectra show two low-field signals in the range of 189.2–198.2 ppm and 195.5–203.1 ppm for axial and equatorial carbonyl groups of Re(I) complexes, respectively.²⁹

Results of the FT-IR spectra of free ligands (L¹–L⁶) show the bands at \sim 2922 cm⁻¹ ν (=C-H)ar, and \sim 1196 cm⁻¹ for ν -CN stretching of pyrazolo[1,5-a]pyridine ring. The band \sim 590–620 cm⁻¹ is observed due to carbon-halogen bond and band at \sim 977–1062 cm⁻¹ is observed due to the *para*-substituted benzene ring. The bands at \sim 1551, and \sim 1597 cm⁻¹ are assigned to ν (C=N) and ν (C=C) conjugated alkene.²⁷ In complexes, the ν (Re-N) band are appeared at around 570 – 578 cm⁻¹.³⁰ The IR spectra of Re(I) complexes exhibit three strong ν (CO) bands in the range of 2020–1898 cm⁻¹.³¹ The strong ν (CO) bands centered at 2000 cm⁻¹ suggests expected *fac*-geometry around the Re metal.^{31,32}

The observed magnetic moment values of rhenium(I) complexes are zero due to absence of unpaired electron i.e. low spin t_{2g}⁶ e_g⁰ configuration makes rhenium(I) complexes diamagnetic, and the oxidation state of rhenium is +1 in complexes.

Molar conductance values of all the low spin Re(I) complexes are found in the range of 2.83–19.25 S cm² mol⁻¹. It suggests that the Re(I) complexes are non-ionic and non-electrolytic with absence of any counter ions surrounding the coordination sphere.

The electronic spectra of compounds were recorded in DMSO solution (Figure 1). The ground state for t_{2g}⁶ electronic configuration of rhenium(I) metal ion is ¹A_{1g}. Three bands are observed in the electronic spectrum: one band ranging in 436.0–442.50 nm region assign to MLCT, second band ranging from 332.5–354.5 nm region attribute to n– π^* , and third band ranging from 286–296 nm assign to ultra-ligand charge transfer (π – π^*). It suggests that Re(I) metal complexes possess octahedral geometry.³³

Biological applications of synthesized ligands and complexes:

In vitro antimicrobial screening: The data reveals that all the complexes have higher antimicrobial activity than neutral bidentate ligands and a metal salt (Figure 2). The antimicrobial activity of all complexes against different microorganisms is found better than that of the respective ligands are shown in supplementary material 3. The MIC values of the complexes, ligands, and metal salt are observed in the range of 60–90 μ M, 280–320 μ M, and 2500 μ M, respectively. A comparative of antimicrobial activity (MIC) values among all synthesized metal complexes and their ligands in decreasing order are as V > II > IV > VI > III > I > L⁵ > L⁴ > L³ > L¹ > L² > L⁶ > Re(CO)₅Cl for gram positive bacteria, and V > IV > III > I > VI > II > L⁴ > L⁵ > L³ > L⁶ > L² > L¹ > Re(CO)₅Cl for gram negative bacteria. The complex V is the most active amongst all the complexes, due to the presence of the methoxy group to the pyridine ring in pyrazolo[1,5-a]pyrimidine ligand.

The presence of a more electronegative environment in complex V and VI improves their biological properties. Two factors are applicable, that are, the ligands bound to metal ions in a multidentate fashion, and the nature of the ligand, for improving MIC values of the synthesized compounds. These may be the main reasons for the diverse antibacterial activity shown by the complexes. The pharmaco-

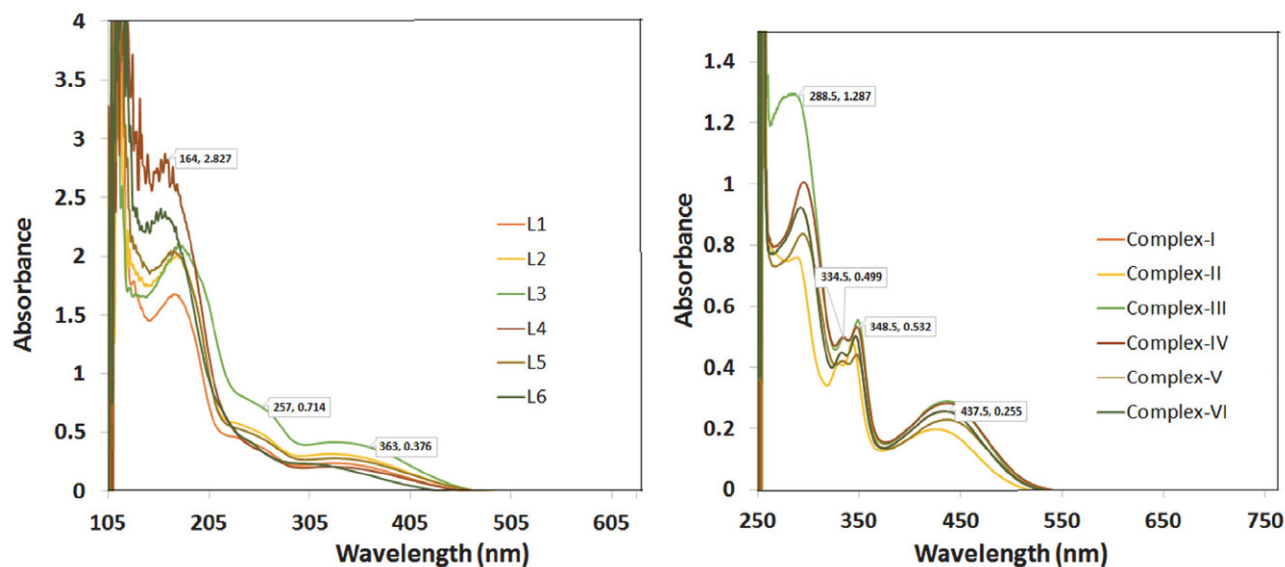


Figure 1. Electronic transition spectra of the ligands (L¹–L⁶) and complexes (I–VI).

logical activities of these metal compounds depend on the metal ion, its ligands, and the structure of the compounds. These factors are responsible for reaching them at the proper target site in the body. It is known that certain metal ions penetrate into bacteria and inactivate their enzymes, or some metal ions can generate hydrogen peroxide, thus killing bacteria. According to overtone's concept of cell permeability, the lipid membrane that surrounds a cell favours the passage of only lipid soluble materials so that lipo-solubility is an important factor which contributes to bactericidal activity.³⁴

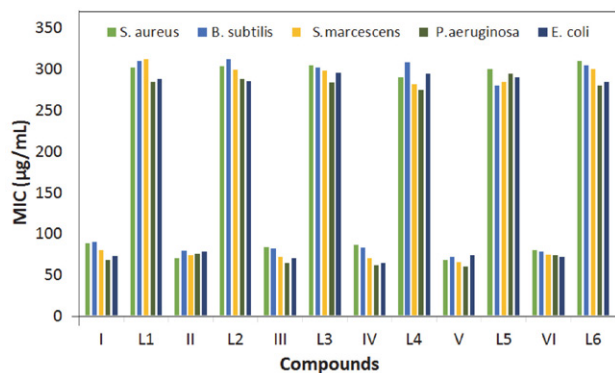


Figure 2. Antibacterial study of ligands and complexes by broth dilution method in terms of MIC in μM .

Cellular level bioassay using S. cerevisiae: The *in vitro* cellular level cytotoxicity of ligands L¹–L⁶ and complexes I–VI was found to vary with the type of substituent present in the synthesized complexes. From the results, it was found that, as the concentration of compound increases from 20 $\mu\text{g}/\text{mL}$ to 100 $\mu\text{g}/\text{mL}$, cytotoxicity also increases which can be exhibited by decreasing % viability shown in supplementary material 4. The complexes I and II show the maximum cytotoxic effect on cells, while complexes III and IV exhibit moderate cytotoxicity, and complexes V and VI exhibit less cytotoxicity (Figure 3 and 4). The increasing order

of % viability of ligands and complexes is $L^5 < L^3 < L^6 = L^4 < L^1 < L^2 < V < VI < IV < III < II < I$, respectively.

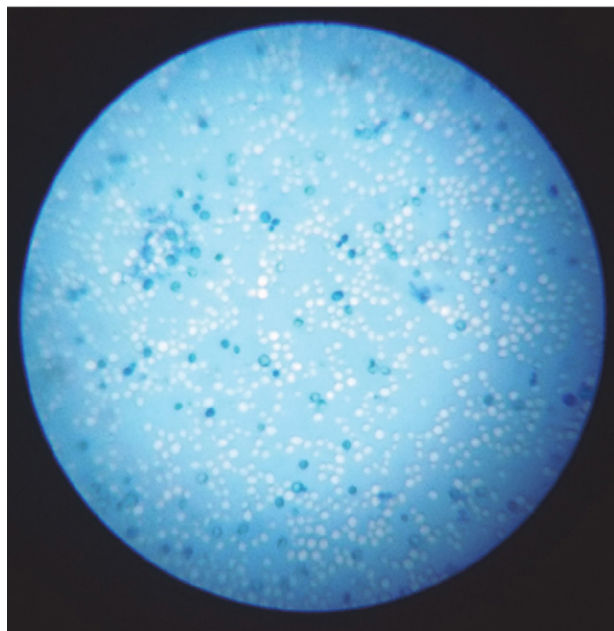


Figure 3. Cellular level cytotoxicity of synthesized compounds using *S. cerevisiae*, dead cells are seen dark whereas live cells are seen transparent.

In vitro brine shrimp lethality bioassay (BSLB): This method is reliable, rapid, and economical. A plot of the log of the sample's concentration versus percentage (%) mortality of brine shrimp larvae showed a linear correlation. These results suggest that the mortality rate of brine shrimp larvae increases with increasing the concentration of the compounds. The synthesized ligands have less mortality rate as compared to the synthesized complexes. The increasing mortality rate of ligands (LC_{50}) and complexes (LC_{50}) is $L^1 (19.95) < L^3 (17.96) < L^5 (17.83) < L^4 (16.00) < L^2 (11.95) < L^6 (9.84) < II (9.78) < III = V (8.03) < I (7.96)$

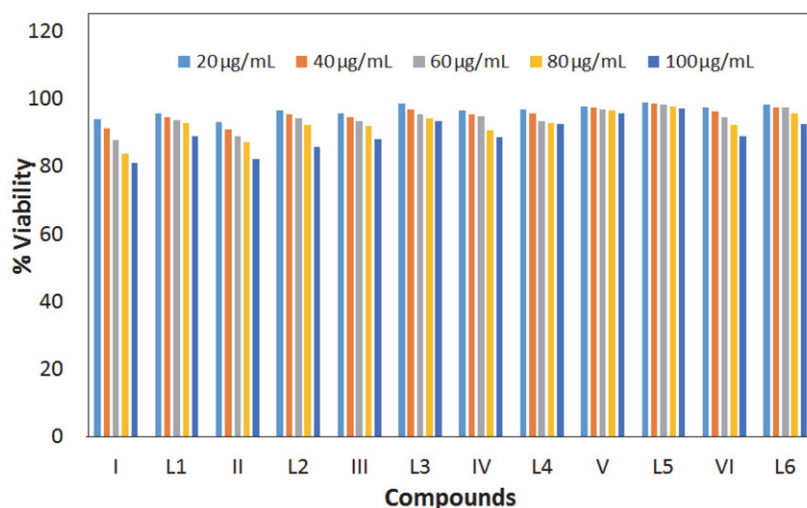


Figure 4. Effect of compounds on *S. cerevisiae* cells as increasing concentration.

< VI (4.01) < IV (3.98). The LC_{50} values of the compounds are shown in brackets in $\mu\text{g/mL}$. Complex IV is the most potent amongst all the compounds.

DNA binding activities: Binding of metal complexes with DNA via intercalation generally results in hypochromism and a redshift (bathochromism) in the absorption band.³⁵ Complex bind to DNA through major or minor groove results in hypochromism and redshift. The charged rhenium complex shows intercalation due to a strong stacking interaction between an aromatic moiety of the ligand and the base pair of the DNA,³⁶ while neutral Re(I) complex shows groove binding.³⁷ The increasing order of K_b is $L^2 < L^5 < L^6 < \text{II} < \text{V} < L^3 < \text{VI} < L^1 = L^4 < \text{I} < \text{IV} < \text{III}$. The observed result shows that upon successive addition of DNA (100 μL) at every 10 minutes time interval, a decrease in absorption intensity (hypochromism) and small redshift (1–6 nm) was observed (Figure 5). It suggests that all synthesized complexes show groove binding, which

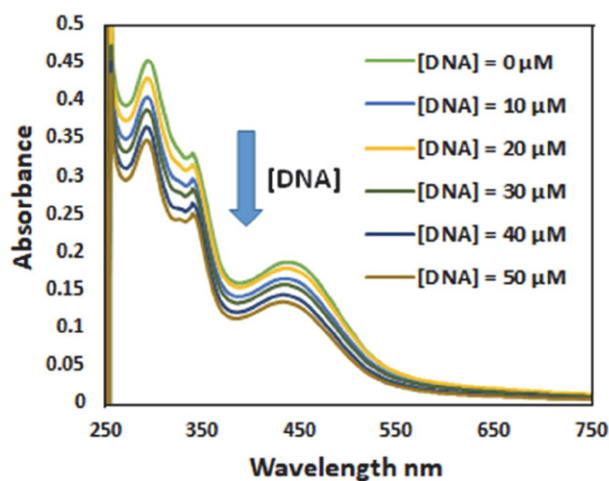


Figure 5. UV-Vis absorption spectral changes on the addition of HS DNA to the solution of complex (ligand L^1 and complex I).

was also confirmed by viscosity measurement and molecular docking. The organic antitumor drug netropsin has to bind within the DNA minor groove. The drug is held in place by amide hydrogen bonds to adenine N-3 and thymine O-2 atoms.³⁸

The binding constant (K_b) values estimated from the ratio of the slope to the intercept ratio. The absorption spectral changes were monitored at around 273–296 nm for the investigation of the DNA binding mode and strength. As the DNA concentration was increased, the transition bands of the complexes I–VI exhibited hypochromicity [hypochromicity, $H\% = [(A_{\text{free}} - A_{\text{bound}})/A_{\text{free}}] \times 100\%$] of about 11.0–40.5%, and bathochromicity of 1–6 nm. The complex IV and the ligand L^4 have the highest percentage hypochromicity (IV–28.5%, L^4 –40.5%). The Gibbs free energies of the synthesized compounds are found negative values in the range of -34.30 to -42.20 kJ mol^{-1} (Table 1). The negative value of Gibbs free energy change (ΔG°) reveals that the binding process is spontaneous.

Viscosity measurement was carried out on DNA by varying the concentration of the added Re(I) complex to get an idea of the binding mode. Groove binding typically causes less pronounced or only a minor change in the viscosity.³⁹ The values of relative specific viscosity $(\eta/\eta^0)^{1/3}$ (η and η^0 are the specific viscosities of DNA in the presence and absence of the Re(I) complex) are plotted against $[\text{Re(I) complex}]/[\text{DNA}]$ in Figure 6. The decreasing order of the $(\eta/\eta^0)^{1/3}$ to the DNA is $\text{III} > \text{VI} > \text{II} > \text{IV} > \text{V} > \text{I} > L^6 > L^5 > L^4 > L^1 > L^2 > L^3$, which parallels the DNA binding affinity. The increase in viscosity, observed in the presence of I–VI is small compared to the classical DNA intercalator EtBr.⁴⁰ Similar enhancement in viscosity has been observed for DNA groove binding simple and mixed ligand Fe(II) and Ru(II) complexes containing 5,6-dmp (5,6-dimethyl-1,10-phenanthroline) as a co-ligand.^{41,42} The enhancement in viscosity observed in the present study is

Table 1 Binding constant (K_b), percentage hypochromicity (%H), bathochromicity ($\Delta\lambda$), and Gibbs free energy (ΔG°) values of free ligands and synthesized complexes

Compounds	λ_{max} (nm)		$^a\Delta\lambda$ (nm)	bK_b ($\text{M}^{-1}) \times 10^5$	$^cH\%$	$^d\Delta G^\circ$ (Jmol^{-1})
	Free	Bound				
L^1	277	278	1	1.8	27.8	-40,040.91
L^2	279	280	1	0.3	39.2	-34,325.59
L^3	281	282	1	1.3	30.1	-38,964.10
L^4	277	279	2	1.8	40.5	-40,040.91
L^5	276	277	1	0.5	14.9	-35,802.34
L^6	272	273	1	0.7	35.4	-36,915.72
I	292	294	2	2.0	16.8	-40,389.55
II	289	291	3	1.1	15.2	-38,411.32
III	290	296	6	3.5	16.7	-42,241.30
IV	291	295	4	3.1	28.5	-41,839.72
V	286	291	5	1.2	11.2	-38,699.24
VI	286	287	1	1.7	15.1	-39,851.78

^a $\Delta\lambda$ = Difference between bound wavelength and free wavelength; ^b K_b = Intrinsic DNA binding constant determined from the UV-visible absorption spectral titration; ^c $H\% = [(A_{\text{free}} - A_{\text{bound}})/A_{\text{free}}] \times 100\%$; ^d ΔG° = Change in Gibbs free energy

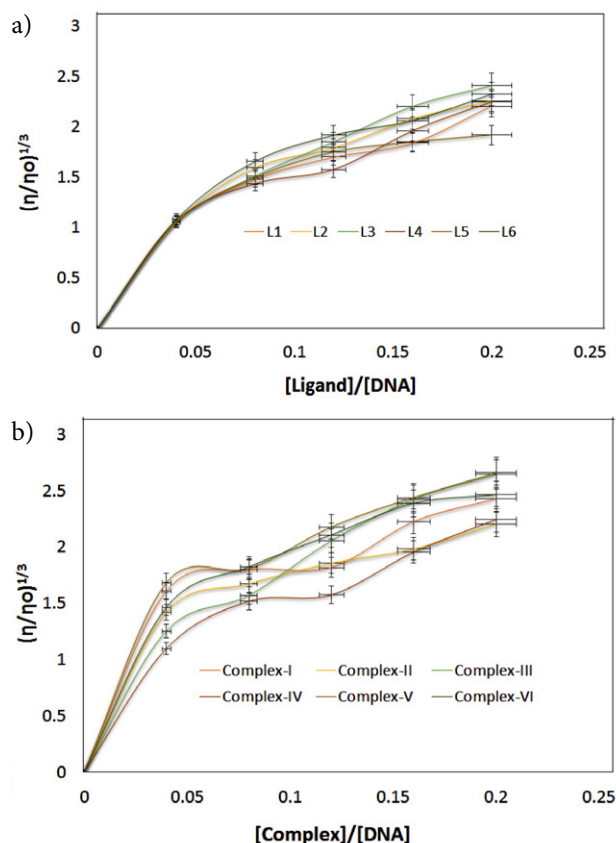


Figure 6. Effect of increasing concentration of (a) ligands and (b) complexes on the relative viscosity of HS DNA at 27 (± 0.1) °C in phosphate buffer at pH = 7.2:

also similar to minor groove binder netropsin.⁴³ These show that complexes I–VI is more likely to have a DNA groove binding propensity.^{33,43}

Molecular Docking with DNA sequence d(ACCGA CGTCGGT)₂: Molecular docking study is attempted to have an idea on the binding sites and favoured orientation of the

ligand inside the DNA groove.^{44, 45} The complexes and ligands are shown by the ball and stick model and DNA base pair shown by the VDW sphere using Hex 8.0 software shown in supplementary material 5. Structure of ligands and complexes were drawn in .CDX format using ChemBioDraw Ultra 14.0 then converted to PDB format using Chem3D (Cambridge Soft). For docking studies, the structural coordinates of DNA were obtained from the protein data bank (pdb id: 423D).⁴⁶ Figure 7 shows that Re(I) complexes bind with the base pair A–T, C–G, G–C, A–T (B-DNA) minor grooves of the DNA. The energy of the docked structure (I–VI and L¹–L⁶) is –279.72, –280.28, –283.51, –288.34, –278.84, –281.34, and –233.32, –254.18, –253.77, –252.77, –251.48, –230.31 kJ/mol. The increasing order of energy is L⁶ < L¹ < L⁵ < L⁴ < L³ < L² < V < I < II < VI < III < IV.

Effect of compounds on the integrity of DNA of *S. cerevisiae* cells: To determine the DNA damaging potential of the compounds a characteristic picture of comets was observed when yeast cells were exposed to increasing concentrations of compounds, increasing in smearing was observed. Agarose gel electrophoresis is a convenient method to assess the cleavage of DNA by metal-based drugs,⁴⁷ to determine the factors affecting the nucleolytic efficiency of a compound, and to compare the nucleolytic properties of different compounds. Figure 8 shows the electrophoretic separation of *S. cerevisiae* DNA when reacted with compounds under aerobic conditions. These clearly show that the relative binding efficacy of the complexes to DNA is much higher than the binding efficacy of pyrazolo[1,5-a]pyrimidine ligands. The difference in the DNA-cleavage efficiency of the complexes and ligands is due to the difference in binding affinity of the ligands and complexes to the DNA. In Figure 8 ligands show lesser smearing as compared to the complexes. It suggests that the cleavage efficiency of DNA is higher in the presence of complexes than the ligands. Complexes III, IV and VI show better cleavage effect of DNA, complex II shows

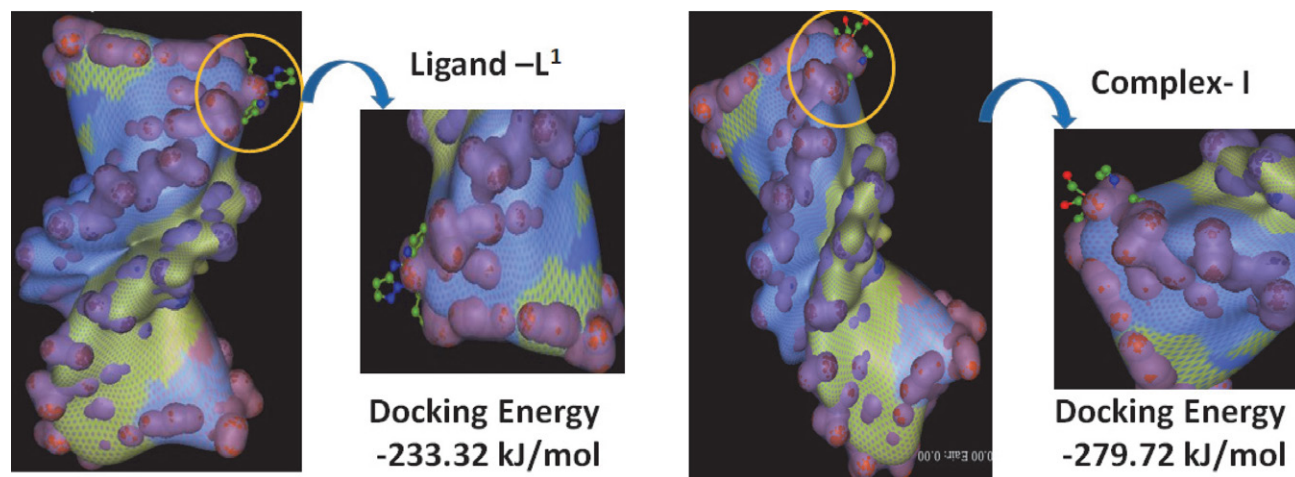


Figure 7. Molecular docking of complex I (ball and stick) with the DNA duplex (VDW spheres) of sequence d(CGCGAATTGCGG)₂. The complex is docked inside the DNA groove.

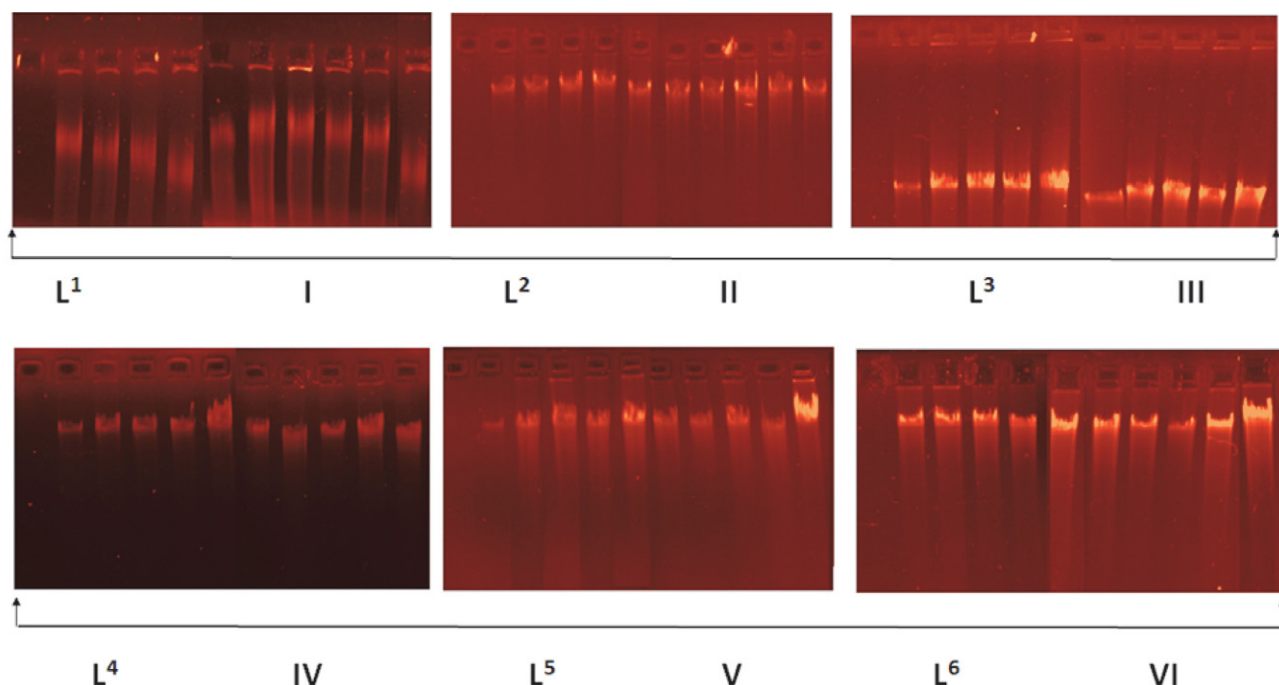


Figure 8. Photogenic view of the cleavage of *S. cerevisiae* DNA with a series of compounds using % agarose gel containing 0.5 µg/L EtBr for 24 h at 37 °C.

moderate cleavage effect of DNA, and complexes I and IV show lesser cleavage effect of DNA.

Antiproliferative study: Metal carbonyls as anticancer drugs in clinical and pharmaceutical trials has wide scope because of its good solubility, and carbonyl releasing ability in the biological system. The synthesized complexes tested as MTT assay using HCT 116 cell line (Supplementary material 6). As the concentration increases the % cell proliferation is decreases means inhibit the tumor cells. The increasing order of IC_{50} values is $III > carboplatin > I > oxaliplatin > II > cisplatin > IV = V = VI$. Above 500 µg/mL concentration solution becomes turbid, coloration, and visibility not seen properly, from these, we can conclude that below 500 µg/mL concentration, all synthesized complexes gives good anticancer activity. The IC_{50} value of synthesised complex (I-VI) and standard drugs like cisplatin, carboplatin, oxaliplatin is 44.66 µg/mL, 20.50 µg/mL, >500 µg/mL, <10 µg/mL, <10 µg/mL, <10 µg/mL, 15.49 µg/mL, >111.37 µg/mL, and 22.66 µg/mL, respectively. The complexes IV, V, and VI are most cytotoxic than other complexes and standard drugs. The approach of metal complexes having carbon monoxide (CO) and heterocyclic compound with three to four bond distance presence of hetero atom chelated with rhenium metal is promising in terms of enhancing anticancer activity.

4. Conclusion

A series of substituted pyrazolo[1,5-a]pyrimidine nucleus based organometallic rhenium(I) complexes were

synthesized and characterized, in search of new organo-metallic complexes with better antibacterial, cytotoxicity, genotoxicity, DNA binding, and DNA cleavage study. The synthesis was carried out by pentacarbonyl chloro rhenium(I) as a starting material. The spectral and analytical data are in good agreement with the proposed structure and revealed the octahedral geometry, and non-electrolytic nature of complexes. Re(I) compounds treatment to *Saccharomyces cerevisiae* yeast cells induced genotoxicity and changes in the conformation of cell DNA. DNA binding study was carried out by absorption titration, viscosity measurement, and molecular modelling. Binding constant (K_b) values of complexes were higher than the ligands, and the studies showed groove mode of DNA binding. There was a minor change in the relative specific viscosity ($(\eta/\eta^0)^{1/3}$) (η and η^0 are the specific viscosities) of DNA in presence and absence of the Re(I) complex, which supports absorption spectroscopy titration data of groove mode of DNA binding. In molecular modelling, docking energies of complexes were observed higher than the ligands. The presence of a more electronegative environment improves the antibacterial activity of complexes than ligands. The increasing order of LC_{50} values evaluated by brine shrimp lethality bioassay is $L^1 < L^3 < L^5 < L^4 < L^2 < L^6 < II < III = V < I < VI < IV$. All the complexes show potent *in vitro* cytotoxicity in cellular level bioassay compared to free ligands.

Acknowledgement

The authors are thankful to the Head, Department of Chemistry, Sardar Patel University, Vallabh Vidyanagar,

Gujarat, India, for providing necessary research facilities, Sardar Patel University, Vallabh Vidyanagar, CPEPA, UGC, New Delhi for providing chemicals facility, DST-PURSE Sardar Patel University, Vallabh Vidyanagar for LC-MS analysis.

6. References

- G. Jaouen, S. Top, A. Vessières and R. Alberto, *Journal of Organometallic Chemistry* **2000**, *600*, 23–36. DOI:10.1016/S0022-328X(00)00036-X
- J. Wald, R. Alberto, K. Ortner and L. Candrea, *Angewandte Chemie International Edition* **2001**, *40*, 3062–3066. DOI:10.1002/1521-3773(20010817)40:16<3062::AID-ANIE3062>3.0.CO;2-O
- W. H. Mahmoud, N. F. Mahmoud and G. G. Mohamed, *Journal of Organometallic Chemistry* **2017**, *848*, 288–301. DOI:10.1016/j.jorganchem.2017.08.001
- K. Schmidt, M. Jung, R. Keilitz, B. Schnurr and R. Gust, *Inorganica Chimica Acta* **2000**, *306*, 6–16. DOI:10.1016/S0020-1693(00)00139-0
- T. R. Johnson, B. E. Mann, J. E. Clark, R. Foresti, C. J. Green and R. Motterlini, *Angewandte Chemie International Edition* **2003**, *42*, 3722–3729. DOI:10.1002/anie.200301634
- B. S. Holla, M. Mahalinga, M. S. Karthikeyan, P. M. Akberali and N. S. Shetty, *Bioorganic & medicinal chemistry* **2006**, *14*, 2040–2047. DOI:10.1016/j.bmc.2005.10.053
- R. Filler, *Chemtech* **1974**, *12*, 752–757.
- M. Ghorab, Z. H. Ismail, S. M. Abdel-Gawad and A. A. Azim, *Heteroatom Chemistry* **2004**, *15*, 57–62. DOI:10.1002/hc.10212
- A. E. Rashad, M. Abdelmegid, A. H. Shamroukh and F. M. Abdelmegeid, *Org. Chem. Ind. J.* **2014**, *10*, 224–250.
- N. Gommermann, P. Buehlmayer, A. Von Matt, W. Breitenstein, K. Masuya, B. Pirard, P. Furet, S. W. Cowan-Jacob and G. Weckbecker, *Bioorganic & medicinal chemistry letters* **2010**, *20*, 3628–3631. DOI:10.1016/j.bmcl.2010.04.112
- O. Fathalla, M. Zaki, S. Swelam, S. Nofal and W. El-Eraky, *Acta poloniae pharmaceutica* **2003**, *60*, 51–60.
- S. Tzanopoulou, M. Sagnou, M. Paravatou-Petsotas, E. Gourni, G. Loudos, S. Xanthopoulos, D. Lafkas, H. Kiaris, A. Varvarigou and I. C. Pirmettis, *Journal of medicinal chemistry* **2010**, *53*, 4633–4641. DOI:10.1021/jm1001293
- P. S. Karia, P. A. Vekariya, A. P. Patidar, D. N. Kanthecha, B. S. Bhatt and M. N. Patel, *Acta Chimica Slovenica* **2019**, *66*, 944–949. DOI:10.17344/acsi.2019.5159
- A. Guida, M. H. Lhouty, D. Tichit, F. Figueras and P. Geneste, *Applied Catalysis A: General* **1997**, *164*, 251–264. DOI:10.1016/S0926-860X(97)00175-0
- V. Lipson, S. Desenko, V. Borodina and M. Shirobokova, *Chemistry of Heterocyclic Compounds* **2007**, *43*, 1544–1550. DOI:10.1007/s10593-007-0071-4
- R. R. Varma, B. H. Pursuwani, E. Suresh, B. S. Bhatt and M. N. Patel, *Journal of Molecular Structure* **2020**, *1200*, 127068. DOI:10.1016/j.molstruc.2019.127068
- M. N. Patel, B. S. Bhatt, P. A. Dosi, N. V. Amaravady and H. V. Movaliya, *Applied Organometallic Chemistry* **2012**, *26*, 217–224. DOI:10.1002/aoc.2841
- G. Zhao, Y. Hui, J. K. Rupprecht, J. L. McLaughlin and K. V. Wood, *Journal of Natural Products* **1992**, *55*, 347–356. DOI:10.1021/np50081a011
- S. J. S. Franchi, R. A. de Souza, A. E. Mauro, I. Z. Carlos, L. C. de Abreu Ribeiro, F. V. Rocha and A. V. de Godoy-Netto, *Acta Chimica Slovenica* **2018**, *65*, 547–553. DOI:10.17344/acsi.2017.4112
- M. A. M. Basha and S. Rishikesan, *Acta Chimica Slovenica* **2020**.
- E. H. El-Sayed and A. A. Fadda, *Acta Chimica Slovenica* **2018**, *65*, 853–864. DOI:10.17344/acsi.2018.4506
- P. A. Vekariya, P. S. Karia, B. S. Bhatt and M. N. Patel, *Applied Organometallic Chemistry* **2019**, *33*, e5152.
- F. Leng, W. Priebe and J. B. Chaires, *Biochemistry* **1998**, *37*, 1743–1753. DOI:10.1021/bi9720742
- J. V. Mehta, S. B. Gajera, D. D. Patel and M. N. Patel, *Applied Organometallic Chemistry* **2015**, *29*, 357–367. DOI:10.1002/aoc.3299
- T. Sato, H. Awano, O. Haba, H. Katagiri, Y.-J. Pu, T. Takahashi and K. Yonetake, *Dalton Transactions* **2012**, *41*, 8379–8389. DOI:10.1039/c2dt30071k
- J. Sambrook and D. W. Russell, *Cold Spring Harbor Protocols* **2006**, *2006*, pdb. prot4039. DOI:10.1101/pdb.prot3847
- D. A. Kanthecha, B. S. Bhatt and M. N. Patel, *Heliyon* **2019**, *5*, e01968. DOI:10.1016/j.heliyon.2019.e01968
- F. Cotton and L. Daniels, *Acta Crystallographica Section C: Crystal Structure Communications* **1983**, *39*, 1495–1496. DOI:10.1107/S0108270183009014
- R. Kia, V. Mirkhani, A. Kálmán and A. Deák, *Polyhedron* **2007**, *26*, 1711–1716. DOI:10.1016/j.poly.2006.12.025
- A. Karaküçük-İyidoğan, D. Taşdemir, E. E. Oruç-Emre and J. Balzarini, *European Journal of Medicinal Chemistry* **2011**, *46*, 5616–5624. DOI:10.1016/j.ejmech.2011.09.031
- K. Chanawanno, J. T. Engle, K. X. Le, R. S. Herrick and C. J. Ziegler, *Dalton transactions* **2013**, *42*, 13679–13684. DOI:10.1039/c3dt50894c
- A. Núñez-Montenegro, R. Carballo and E. M. Vázquez-López, *Journal of inorganic biochemistry* **2014**, *140*, 53–63. DOI:10.1016/j.jinorgbio.2014.06.012
- G. Balakrishnan, T. Rajendran, K. S. Murugan, M. S. Kumar, V. K. Sivasubramanian, M. Ganesan, A. Mahesh, T. Thirunalasundari and S. Rajagopal, *Inorganica Chimica Acta* **2015**, *434*, 51–59. DOI:10.1016/j.ica.2015.04.036
- M. Rizzotto: A search for antibacterial agents, *InTech*, **2012**.
- F. L. Thorp-Greenwood, M. P. Coogan, L. Mishra, N. Kumari, G. Rai and S. Saripella, *New Journal of Chemistry* **2012**, *36*, 64–72. DOI:10.1039/C1NJ20662A
- H.-K. Liu and P. J. Sadler, *Accounts of Chemical Research* **2011**, *44*, 349–359. DOI:10.1021/ar100140e
- M. Kaplanis, G. Stamatakis, V. D. Papakonstantinou, M. Paravatou-Petsotas, C. A. Demopoulos and C. A. Mitsopoulou, *Journal of inorganic biochemistry* **2014**, *135*, 1–9. DOI:10.1016/j.jinorgbio.2014.02.003

38. M. L. Kopka, C. Yoon, D. Goodsell, P. Pjura and R. E. Dickerson, *Journal of molecular biology* **1985**, *183*, 553–563. DOI:10.1016/0022-2836(85)90171-8
39. S. S. Mati, S. S. Roy, S. Chall, S. Bhattacharya and S. C. Bhattacharya, *The Journal of Physical Chemistry B* **2013**, *117*, 14655–14665. DOI:10.1021/jp4090553
40. B. Nordén and F. Tjerneld, *Biopolymers: Original Research on Biomolecules* **1982**, *21*, 1713–1734. DOI:10.1002/bip.360210904
41. P. Uma Maheswari, V. Rajendiran, H. Stoeckli-Evans and M. Palaniandavar, *Inorganic chemistry* **2006**, *45*, 37–50. DOI:10.1021/ic050940q
42. S. Ramakrishnan, E. Suresh, A. Riyasdeen, M. A. Akbarsha and M. Palaniandavar, *Dalton Transactions* **2011**, *40*, 3524–3536. DOI:10.1039/c0dt00466a
43. A. K. Patra, T. Bhowmick, S. Roy, S. Ramakumar and A. R. Chakravarty, *Inorganic chemistry* **2009**, *48*, 2932–2943. DOI:10.1021/ic8017425
44. R. Bera, B. K. Sahoo, K. S. Ghosh and S. Dasgupta, *International journal of biological macromolecules* **2008**, *42*, 14–21. DOI:10.1016/j.ijbiomac.2007.08.010
45. Y. Gilad and H. Senderowitz, *Journal of chemical information and modeling* **2013**, *54*, 96–107. DOI:10.1021/ci400352t
46. D. Shao, M. Shi, Q. Zhao, J. Wen, Z. Geng and Z. Wang, *Zeitschrift für anorganische und allgemeine Chemie* **2015**, *641*, 454–459. DOI:10.1002/zaac.201400410
47. A. Pyle, J. Rehmann, R. Meshoyrer, C. Kumar, N. Turro and J. K. Barton, *Journal of the American Chemical Society* **1989**, *111*, 3051–3058. DOI:10.1021/ja00190a046

Povzetek

Sintetizirali smo nevtralne komplekse renija(I) tipa $[\text{ReCl}(\text{CO})_3\text{L}^n]$ ($\text{L}^1 = 7\text{-fenil-5-(piridin-2-il)pirazolo[1,5-a]pirimidin}$, $\text{L}^2 = 7\text{-(4-bromofenil)-5-(piridin-2-il)pirazolo[1,5-a]pirimidin}$, $\text{L}^3 = 7\text{-(4-klorofenil)-5-(piridin-2-il)pirazolo[1,5-a]pirimidin}$, $\text{L}^4 = 7\text{-(2-klorofenil)-5-(piridin-2-il)pirazolo[1,5-a]pirimidin}$, $\text{L}^5 = 7\text{-(4-metoksifenil)-5-(piridin-2-il)pirazolo[1,5-a]pirimidin}$, $\text{L}^6 = 5\text{-(piridin-2-il)-7-(p-tolil)pirazolo[1,5-a]pirimidin}$) in jih karakterizirali s ^{13}C -APT, ^1H -NMR, IR, meritvami elektronskih spektrov, magnetnimi meritvami in meritvijo predvodnosti. Anti-proliferativna aktivnost merjena na celicah HCT116 z metodo MTT nakazuje na močno citotoksično delovanje kompleksov, ki pri nekaterih presega celo aktivnost standardnih učinkovin kot so cisplatina, oksaliplatina in karboplatina. Antimikrobno delovanje kompleksov je večje kot pri pirazolo pirimidinskih ligandih. Teoretične študije interakcij med novimi spojinami in DNK smo preučevali z metodo molekularnega priklapljanja. Vrednost interakcij DNK-kompleks je med -230.31 in -288.34 kJ/mol. Vrednosti veznih konstant za komplekse ($1.1\text{--}3.5 \times 10^5 \text{ M}^{-1}$) so višje od vrednosti za ustrezne ligande ($0.32\text{--}1.8 \times 10^5 \text{ M}^{-1}$).



Except when otherwise noted, articles in this journal are published under the terms and conditions of the Creative Commons Attribution 4.0 International License

Scientific paper

A New Reagent for Spectrophotometric Determination of Ir(IV): 5-[2-(4-Hydroxyphenyl)hydrazineylidene]-4-iminothiazolidin-2-one (HPIT)

Oleksandr Tymoshuk,¹ Lesia Oleksiv,^{1,*} Orest Fedyshyn,¹ Petro Rydchuk,¹
Vasyl Matiychuk¹ and Taras Chaban²

¹ Department of Chemistry, Ivan Franko National University of Lviv, Kyryla and Mefodiya Str., 6, 79005 Lviv, Ukraine;

² Faculty of Pharmacy, Danylo Halytsky Lviv National Medical University, Pekarska Str., 69, 79010 Lviv, Ukraine

* Corresponding author: E-mail: l_lozynska@ukr.net

Received: 06-15-2020

Abstract

The paper presents a new azolidone derivative – 5-[2-(4-hydroxyphenyl)hydrazineylidene]-4-iminothiazolidin-2-one (HPIT) studies and its interaction results with iridium(IV) ions. The Ir(IV) with this reagent in the pH = 5.0 without heating forms a stable complex ($\lambda_{\max} = 328$ nm). The stoichiometric ratio of Ir(IV) to the reagent in complex is 1:1. The molar absorptivity and Sandell's sensitivity are 5.57×10^3 L mol⁻¹ cm⁻¹ and 0.034 $\mu\text{g cm}^{-2}$ respectively. The calibration curve is linear in the range of 1.0–11.5 $\mu\text{g mL}^{-1}$ of Ir(IV) ($R = 0.9996$). The limit of detection is 0.4 $\mu\text{g mL}^{-1}$. Based on the conducted investigation a rapid and simple, spectrophotometric method for the determination of Ir(IV) using 5-[2-(4-hydroxyphenyl)hydrazineylidene]-4-iminothiazolidin-2-one as a chromophoric reagent was developed. The iridium(IV) was determined in various synthetic mixtures and alloys.

Keywords: Iridium(IV); spectrophotometry; 5-[2-(4-hydroxyphenyl)hydrazineylidene]-4-iminothiazolidin-2-one; azolidones.

1. Introduction

The relevance of platinum metals and their compounds usage encourages the development of simple, rapid, inexpensive, selective, and sensitive methods for the determination of trace amounts of these metals in complex samples. Spectrophotometric methods of analysis are successfully used to solve this problem in analytical chemistry with the use of organic reagents containing functional-analytical groups.^{1,2}

Spectrophotometric methods are one of the most widely used physical-chemical analysis methods in industrial and research laboratories. The main advantages of spectrophotometry are versatility, sufficient sensitivity to solve specific analytical problems, simplicity, the possibility of analysis automation, which provides it a leading place in the modern analytical chemistry. Spectrophotometric methods of platinum determination are characterized by different sensitivity ($\epsilon_{\lambda} \sim 10^3 - 10^5$ L mol⁻¹ cm⁻¹) depending on the choice of reagent. Their sensitivity is significantly increased using organic reagents, namely heterocyclic azo

derivatives and sulfur-containing compounds.¹⁻³ Among a large number of azo dyes, azolidones and their derivatives are of particular interest. The color reactions of noble metals with this group of reagents are highly sensitive ($\epsilon = (0.4-1.5) \times 10^4$ L mol⁻¹ cm⁻¹) and contrast ($\Delta\lambda = 70-80$ nm). Azorodanines contain several functional-analytical groups in their molecules, which makes it possible to use them as group reagents for the precious metals determination.³⁻⁶

Our scientific group first investigated the analytical properties of several azolidone derivatives and successfully used them to determine the number of ions: Cu(II), Ni(II), Cd(II), Zn(II), Hg(II), Pd(II), Pt(IV), Rh(III), Ir(IV), Ru(IV).⁷⁻²¹

Due to the wide usage of iridium in various industries (such as jewelry, electrical equipment, dental alloys, automobile, chemical, and electronics industries, the field of photography and aviation), it is important to develop efficient analytical methods for this metal determination in various samples.^{22,23} Most of spectrophotometric methods for the Iridium determination are not enough sensi-

tive, selective and need heating or extraction.^{1,2,4,11,24–27} For this reasons the goal of our research was to find the effective analytical reagents for spectrophotometric Ir(IV) determination using azolidones derivatives. One of them was a new reagent – 5-[2-(4-hydroxyphenyl)hydrazineylidene]-4-iminothiazolidin-2-one (HPIT).

2. Experimental

2.1. Equipment

Spectrophotometric measurements were performed with a computerized spectrophotometer, model ULAB 108-UV, fitted with 1.0 cm quartz cells.

Computerized device MTech OVA-410 with a linear potential sweep was used for voltammetric measurements.²⁸ A three-electrode system including dropping mercury electrode (working electrode), a saturated calomel electrode (reference electrode), and platinum (counter electrode) were used.

The pH-150 M pH-meter equipped with a combined glass electrode was used to measure the pH values of solutions.

¹H NMR spectra were registered on the spectrometer Varian Mercury UX-400, DMSO-d₆ was used as a solvent, tetramethylsilane as a standard.

2.2. Reagents

The stock solution of iridium(IV) chloride was prepared by melting the exact mass of pure iridium (99.99%) with the oxidizing mixture of NaNO₃ + NaOH (1:3, v/v), and BaO₂ at 950 K for 45–60 min. Then the fusion was dissolved in 3.0 mol L⁻¹ hydrochloric acid. The existence form of Ir(IV) ([IrCl₆]²⁻) in the obtained solution was confirmed by comparing its absorption spectra with the transferred data.²⁹ The obtained solution of Ir(IV) was additionally standardized using the titration method – iodometry, due to possible losses during sintering.^{1,2} Standard transferred solutions of Ir(IV) were prepared by diluting an aliquot of Ir(IV) initial stock solution in 1.0 mol L⁻¹ HCl.

The solution of 5-[2-(4-hydroxyphenyl)hydrazineylidene]-4-iminothiazolidin-2-one was prepared by dissolving the exact mass of the pre-purified reagent in dimethyl sulfoxide. Working solutions of HPIT were prepared by diluting an aliquot of the stock solution in dimethyl sulfoxide. The 5-[2-(4-hydroxyphenyl)hydrazineylidene]-4-iminothiazolidin-2-one was synthesized by the following procedure: 0.01 mol of 4-aminophenol was dissolved in 3 ml of concentrated hydrochloric acid, after which 5 ml of water was added. The solution obtained at this stage, with cooling, was diazotized with 0.72 g of transferred nitrite dissolved in 3 mL of water. The resulting diazonium salt was added over 30 minutes to a solution of 0.01 mol of 4-iminothiazolidin-2-one previously dissolved in 80 ml of glacial acetate acid containing 4 g of anhydrous

sodium acetate (pH = 4.5–5.0) with stirring and was cooled. The mixture was left at 12 h, after which it was poured into 200 mL of water. The precipitate was filtered, washed on the filter with water, dried, and recrystallized. ¹H NMR (400 MHz, DMSO-d₆; δ, ppm): 6.70 (d, J = 9.0 Hz, 2H, C₆H₄), 7.28 (d, J = 9.0 Hz, 2H, C₆H₄), 8.71 (s, 1H, NH), 8.97 (s, 1H, NH), 10.17 (s, 1H, NH). The purity of HPIT was determined by chromatography-mass spectrometry.

The solution of HCl was prepared by dilution of concentrated HCl. The solutions of sodium salts (to study the effect of anions), NaCl and NaOH were prepared by dissolving an appropriate amount of respective salts and NaOH in distilled water. The Britton–Robinson buffer (BRB) was prepared by mixing solutions of boric, phosphoric and acetic acids.³⁰ The solutions of various metals (to study the effect of cations) were prepared by dissolving the exact mass of the corresponding metal in HCl or HNO₃ acids either its mixture, or their salts in distilled water or dilute hydrochloric or nitric acids. The solutions of Rh(III) and Ru(IV) were prepared by sintering corresponding metal with the oxidizing mixture NaNO₃ + NaOH (1:3, v/v) with further dissolving the fusion in 3.0 mol · L⁻¹ HCl.

All chemicals used were of analytical grade and distilled water was used for the preparation of the aqueous solution.

2.3. Procedure

Research of the HPIT spectral characteristics

Aliquots of 2.0 mL HPIT working solution (2.5 × 10⁻⁴ mol L⁻¹) were transferred into a series of 25.0 mL transferred flasks, then 2.0 mL BRB (1.5 mol L⁻¹), 1.25 mL NaCl (2.0 mol L⁻¹) and water (~15–20 mL) were added to each flask. The pH values (2.0–12.0) were adjusted using NaOH (4.0 mol L⁻¹) and then diluted to volume with distilled water. The solution with pH = 1.0 was prepared as described above but without BRB addition and pH value was adjusted using HCl (6.0 mol L⁻¹). The absorption spectra were measured against distilled water as blank.

General procedure for the determination of Ir(IV) with HPIT

An aliquot of Ir(IV) solution (in the range of 1.0–11.5 μg mL⁻¹ in the final volume), 2.5 mL (1.0 × 10⁻³ mol L⁻¹) HPIT, 1.0 mL (1.5 mol L⁻¹) BRB and 1.25 mL (2.0 mol L⁻¹) NaCl were placed into 25.0 mL calibrated flasks and then distilled water was added (~15 mL). The pH was adjusted to ~5.0 with NaOH solution and diluted to the mark with distilled water. The absorbance was measured at 328 nm against a reagent blank.

Determination the stoichiometric ratio of the Ir(IV)-HPIT complex

The equimolar solutions of Ir(IV) and HPIT (1.0 × 10⁻³ mol L⁻¹) were used to determine the metal to ligand ratio by Job's method of continuous variation. The total concentration C_{Ir(IV)} + C_{HPIT} was equal 1.0 × 10⁻⁴ mol L⁻¹

in a 25.0 mL volumetric flask. Then 1.0 mL (1.5 mol L^{-1}) BRB, 1.25 mL (2.0 mol L^{-1}) NaCl, and distilled water ($\sim 15 \text{ mL}$) were added. The pH was adjusted to 5.0 by NaOH and diluted with distilled water to the calibration mark. The absorbance values were recorded at 328 nm.

The mole-ratio method was performed in the transferred way: into a series of 25.0 mL volumetric flasks the Ir(IV) solution with fixed concentration (0.5 mL of $1.0 \times 10^{-3} \text{ mol L}^{-1}$), an aliquot $0.10\text{--}10.0 \text{ mL}$ ($5.0 \times 10^{-4} \text{ mol L}^{-1}$) HPIT, 1.0 mL (1.5 mol L^{-1}) BRB, 1.25 mL (2.0 mol L^{-1}) NaCl, and distilled water $\sim 20 \text{ mL}$ were added. The pH was adjusted to $\text{pH} = 5.0$ by adding NaOH and diluted up to the mark with water. Then, the absorbance at 328 nm was measured.

Alloys samples preparation

The alloys ($\text{Gd}_2\text{Ir}_3\text{Al}_9$, $\text{Tb}_2\text{Ir}_3\text{Al}_9$) were synthesized by arc melting of pure metals ($\text{Gd} \geq 99.86\%$, $\text{Tb} \geq 99.83\%$, $\text{Ir} \geq 99.9\%$, $\text{Al} \geq 99.998\%$) under an argon atmosphere and heated to 873 K , held at that temperature for 720 h and then cooled to room temperature.³¹

The solutions of alloys samples were prepared by dissolving of $0.05\text{--}0.1 \text{ g}$ of sample in $10\text{--}20 \text{ mL}$ of HCl and HNO_3 ($10:1$, v/v) mixture and heating for $\sim 2 \text{ h}$. Then the black residue was filtered and filtrate transferred to a 200.0 mL volumetric flask. The residue was sintered with a NaNO_3 and NaOH ($1:3$, v/v) mixture at 950 K (60 min). The melt was dissolved in 3.0 mol L^{-1} HCl. The obtained solution was transferred to the previous filtrate and distilled water was added to the mark. The $0.4\text{--}1.5 \text{ mL}$ of alloys aliquots were taken for Ir(IV) determination with HPIT as described above.¹¹

3. Results and Discussion

3.1. Research Spectral Characteristics of the HPIT

We researched a new reagent – 5-[2-(4-hydroxyphenyl)hydrazineylidene]-4-iminothiazolidin-2-one, which is a derivative of azolidone (Fig. 1). HPIT is the crystalline yellow powder poorly soluble in water and ethanol but well soluble in dimethylformamide and dimethyl sulfoxide. The melting point is 515 K .

In our previous work,³² we investigated the effect of the medium acidity on the absorption spectra of HPIT

over the pH range $1.0\text{--}12.0$. As shown by the results of the experiment, the HPIT absorption maximum depends on the pH of the solution, which is associated with different existence forms depending on the medium acidity (Fig. 2). At $\text{pH} = 1.0$, the absorption spectrum is characterized by a maximum at a wavelength of 418 nm , which corresponds to the protonated form of the reagent; at $\text{pH} 2.0\text{--}10.0$, the maximum of absorbance shifts slightly to the region of smaller wavelengths (400 nm), and in the alkaline medium ($\text{pH} > 10.0$) (Fig. 3), there is a course of hydrolysis reaction with the release of ammonia (Scheme 1). The molar absorptivity at $\lambda = 418 \text{ nm}$ is $2.04 \times 10^4 \text{ L mol}^{-1} \text{ cm}^{-1}$ ($\text{pH} = 1.0$); at $\lambda = 400 \text{ nm}$ is $(1.14\text{--}1.85) \times 10^4 \text{ L mol}^{-1} \text{ cm}^{-1}$ ($\text{pH} 2.0\text{--}9.0$) and $1.02 \times 10^3 \text{ L mol}^{-1} \text{ cm}^{-1}$ ($\text{pH} = 10.0$).

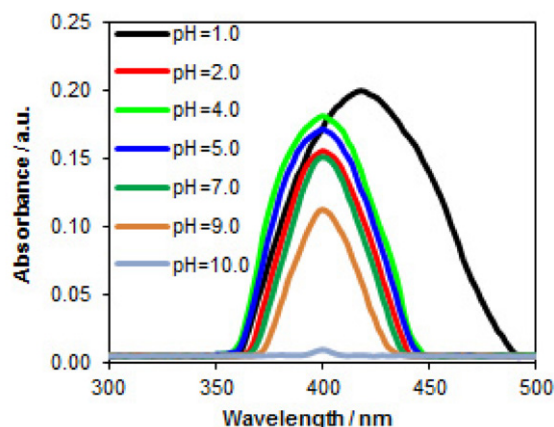


Fig. 2. Absorbance spectra of HPIT at different pH

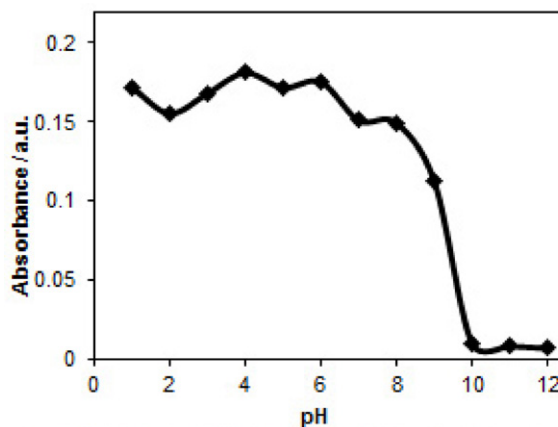


Fig. 3. Effect pH on the absorbance of HPIT at 400 nm

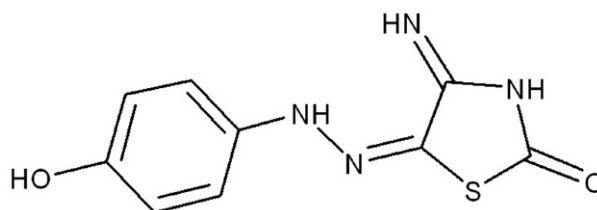
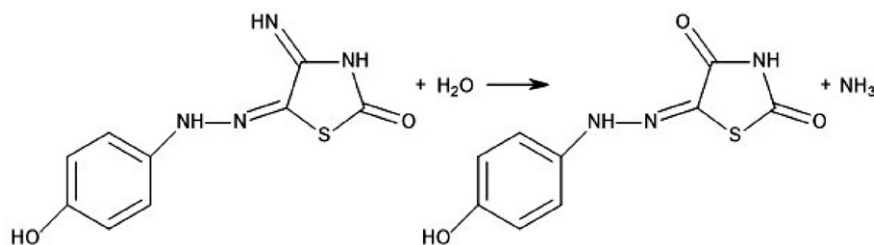


Fig. 1. Structural formula of the HPIT



Scheme 1. Hydrolysis of 5-[2-(4-hydroxyphenyl)hydrazineylidene]-4-iminothiazolidin-2-one

HPIT does not polymerize and does not form tautomeric forms at pH = 1.0 in the concentration range of 5.0×10^{-6} – 8.0×10^{-5} mol L⁻¹, since in this range the Beer's law is applicable and only one maximum is observed.

3. 2. Investigation of the Interaction of Ir(IV) with HPIT

It was found that the Ir(IV) ions form a complex with HPIT (Fig. 4). The absorption spectra of HPIT, Ir(IV), and Ir(IV)-HPIT were recorded over the range 200 to 550 nm. As shown on Fig. 4 the maximum of the reagent at 400 nm (pH = 5.0) is reduced in the presence of iridium(IV) ions. Instead, there was an increase in the absorption of Ir(IV)-HPIT in the wavelength range from 250 to 360 nm compared to the absorption of the reagent, which indicates the interaction. The largest difference in absorption of the reagent and compound is at $\lambda = 328$ nm.

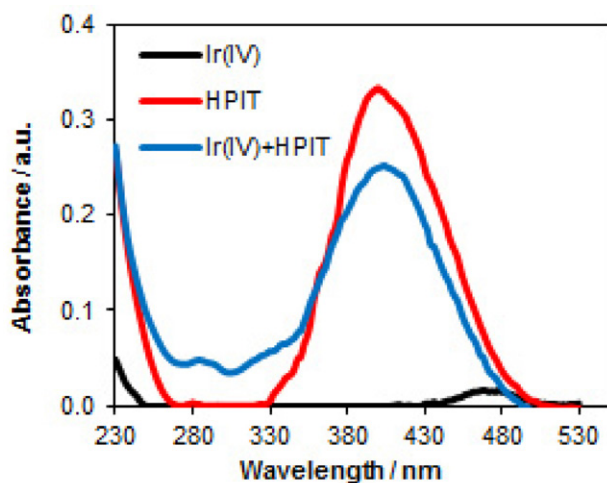


Fig. 4. Absorbance spectra of Ir(IV), reagent and complex Ir(IV) with HPIT (pH = 5.0, $C_{\text{Ir(IV)}} = 8.0 \times 10^{-6}$ mol L⁻¹, $C_{\text{HPIT}} = 2.0 \times 10^{-5}$ mol L⁻¹)

The effect of various parameters on the formed products absorption intensity was studied and the reaction conditions were optimized.

Effect of pH

The acidity of the medium is one of the important parameters that affect the complexation. Within the pH

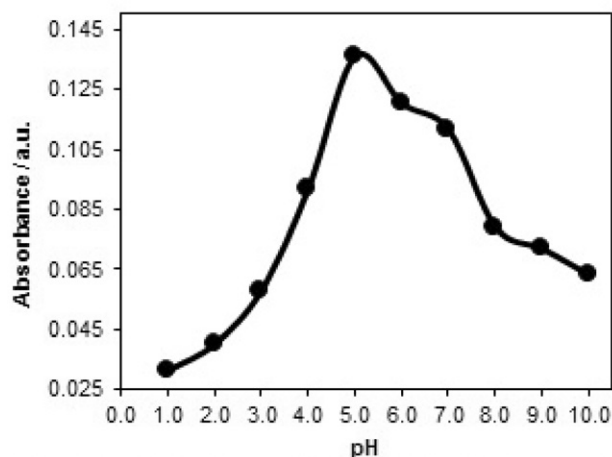


Fig. 5. Effect of pH on the maximum yield of Ir(IV) with HPIT complex ($\lambda = 328$ nm, $C_{\text{Ir(IV)}} = 2 \times 10^{-5}$ mol L⁻¹, $C_{\text{HPIT}} = 4 \times 10^{-5}$ mol L⁻¹)

range from 2.0 to 10.0 Ir(IV) ions form a complex with HPIT (Fig. 5). The maximum yield of complex is at pH = 5.0. Hence this value of pH was selected for further studies.

Effect of time and temperature

The process of iridium(IV) ions complexation with HPIT occurred at room temperature (~ 291 – 296 K) immediately after the acidity of the medium was established. The effect of heating time on the maximum yield of the colored compound was investigated. The solutions heating in a boiling water bath (~ 371 K) caused a decrease in the absorption of the solutions, but the complex compound Ir(IV)–HPIT was not destroyed even when heated for 60 min. Therefore it is recommended that the reaction should be carried out at room temperature. The absorbance of obtained Ir(IV)–HPIT complex was stable up to 72 h.

The stoichiometric ratio of complex

The Job's method of continuous variations (Fig. 6) and the mole-ratio method were used to determine the stoichiometric ratio of the complex. These methods indicate that complex with stoichiometry 1:1 was formed. A 1.5 fold excess of reagent is required for full complexation. The formal stability constant of the Ir(IV)–HPIT complex was calculated and it is equal to 8.9×10^5 .

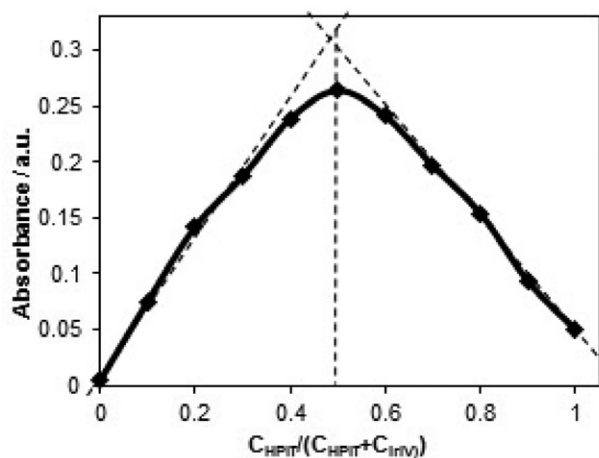


Fig. 6. The method of continuous variations

Calibration curve

The calibration graph for Ir(IV) determination with HPIT was constructed using the optimal conditions (pH = 5.0, $\lambda = 328$ nm, $C_{\text{HPIT}} = 1.0 \times 10^{-4}$ mol L⁻¹, $C_{\text{NaCl}} = 0.1$ mol L⁻¹, $C_{\text{BRB}} = 0.06$ mol L⁻¹) and showed that the system obeys Beer's law in the concentration range of 1.0–11.5 $\mu\text{g mL}^{-1}$ of Ir(IV). The linear equation is $\Delta A = (0.011 \pm 0.004) + (0.0292 \pm 0.0007) \times C_{\text{Ir(IV)}}$ (ΔA – absorbance, C – concentration of Ir(IV) in $\mu\text{g mL}^{-1}$) with correlation coefficient equal 0.9996, $N = 6$, $SD = 2.37 \times 10^{-3}$. The molar absorptivities and Sandell sensitivity are 5.57×10^3 L mol⁻¹ cm⁻¹ and 0.034 $\mu\text{g cm}^{-2}$ respectively. The limit of detection is 0.4 $\mu\text{g mL}^{-1}$.

3. 3. Selectivity of the Ir(IV) Determination

The various cations and anions influence on the iridium(IV) determination were studied under the conditions of the standard procedure. The tolerance limits of tested interfering ions were calculated as the maximum concentrations that do not cause an error of more than $\pm 5\%$ in an absorbance value. The tolerance limits for foreign ions are shown in Table 1. It has been found that the majority of cations do not interfere significantly. The iridium(IV) ions can be easily determined in the presence of Tb(III), Gd(II), Cd(II), Zn(II), Mn(II), Ni(II), Cu(II), Ca(II), Mg(II), Ba(II) and the studied anions. However, several ions such as Pd(II), Rh(III), Pt(IV), Ru(IV) interfere seriously. Their effect can be eliminated by using some of the studied anions as masking agents. For example, Pd(II) and Ru(IV) were masked using EDTA (the tolerance limits reach 1 for Pd(II) and 2 for Ru(IV)). This method has higher selectivity than most of the spectrophotometric methods of Iridium determination.^{1, 2, 4, 11, 24–27}

3. 4. Analytical Application

The developed spectrophotometric method was applied to the determination of Ir(IV) in synthetic mixtures and alloys to validate it.

Analysis of Ir(IV) in synthetic mixtures

Different synthetic mixtures were prepared and analyzed using the proposed developed method in order to research the precision and accuracy (Table 2). As can be seen in Table 2, the obtained results are consistent with the

Table 1. Selectivity of Ir(IV) spectrophotometric determination ($C_{\text{Ir(IV)}} = 2.5 \times 10^{-5}$ mol L⁻¹; $C_{\text{HPIT}} = 1.0 \times 10^{-4}$ mol L⁻¹; $C_{\text{NaCl}} = 0.1$ mol L⁻¹; $C_{\text{BRB}} = 0.06$ mol L⁻¹; pH = 5.0; $\lambda = 328$ nm; $l = 1.0$ cm)

Foreign ion	Tolerance limit $C_{\text{ion}} : C_{\text{Ir(IV)}}$	Foreign ion	Tolerance limit $C_{\text{ion}} : C_{\text{Ir(IV)}}$	Foreign ion	Tolerance limit $C_{\text{ion}} : C_{\text{Ir(IV)}}$
Pd(II)	0.1	Ni(II)	150	Ca(II), Mg(II)	>200
Pt(IV)	0.25	Fe(III)	15	$\text{C}_2\text{O}_4^{2-}$ *	100
Rh(III)	0.1	Cd(II)*	75	F^- *	100
Ru(IV)	0.25	Pb(II)*	75	EDTA*	100
Tb(III)	100	Mn(II)*	100	Sal*	100
Gd(III)	75	Zn(II)	75	Citr ³⁻ *	100
Cu(II)	50	Al(III)	8	Tart ²⁻ *	100
Co(II)	30	Ba(II)	75	PO_4^{3-} *	100

*These ions decrease the absorbance value by $\pm 5\%$, and the others all increase.

Table 2. Determination of Iridium(IV) in synthetic mixtures, $n = 3$; $P = 0.95$

Composition of synthetic mixture	Added Ir(IV), μg	Found Ir(IV), $\bar{x} \pm \frac{s \times t_\alpha}{\sqrt{n}}$, μg	RSD, %
12.6 μg Ru(IV), 0.7 mg Co(II)	96	98 \pm 5	2.0
3.3 μg Pd(II), 2.8 mg Ni(II), 9.7 mg Pb(II)	96	101 \pm 7	2.8
24.4 μg Pt(IV), 3.4 mg Mn(II)	96	100 \pm 8	3.2

Table 3. Results of the determination of Ir(IV) in alloys, n = 3, P = 0,95

Alloy	ω_{Ir}^{calc}	Spectrophotometry		Voltammetry	
		$\omega_{Ir}^{pr} \pm \frac{S \times t_{\alpha}}{\sqrt{n}}$, %	RSD, %	$\omega_{Ir}^{pr} \pm \frac{S \times t_{\alpha}}{\sqrt{n}}$, %	RSD, %
Gd ₂ Ir ₃ Al ₉	50.9	51.5 ± 1.8	1.4	51.2 ± 1.4	1.1
Tb ₂ Ir ₃ Al ₉	50.7	51.0 ± 1.5	1.2	50.8 ± 1.6	1.3

added amounts of Ir(IV). The calculated values of the relative standard deviation and the absence of a significant systematic error indicate a good reproducibility and accuracy of this spectrophotometric method.

Analysis of Ir(IV) in the alloys

The results of Iridium determination in the alloys are given in Table 3. The data obtained by the spectrophotometric method were compared with Ir(IV) contents determined by the voltammetric method. As seen, the results of both methods are agreed. The results in Table 3 show that the relative error and relative standard deviation do not exceed 1.5%.

4. Conclusions

The results of this research indicate that the developed spectrophotometric method based on the complexation of Ir(IV) with the new azolidone derivative (5-[2-(4-hydroxyphenyl)-hydrazineylidene]-4-iminothiazolidin-2-one) can be successfully used for the determination of iridium(IV) in different samples. This method is simple, sensitive, selective towards many ions, reproducible, and rapid because it does not require heating or separation from a large number of foreign ions (such as REE, Cu(II), Ni(II), Mn(II), Zn(II), Cd(II), et al.), which are associated with Ir(IV) in its objects. The time needed for analysis about 30 min, which makes this method much faster than other spectrophotometric methods for determining Iridium, which are described in the literature.

6. References

- Ya. A. Zolotov, G. M. Varshal, V. M. Ivanov, *Analiticheskaya Khimiya Metallov Platinovoi Gruppy*, Editorial URSS, Moscow, Russia, 2003, p. 592.
- S. I. Ginzburg, N. A. Yezerskaya, I. V. Prokof'eva, N. V. Fedorenko, V. I. Shlenskaya, N. K. Belsky, *Analiticheskaya Khimiya Platinovykh Metallov*, Nauka, Moscow, Russia, 1972, p. 613.
- R. F. Gur'eva, S. B. Savvin, *Zh. Anal. Khim.* **2002**, 57, 980–996. DOI:10.1023/A:1020917221896
- R. F. Gur'eva, S. B. Savvin, *Usp. Khim.* **1998**, 67, 236–251. DOI:10.1070/RC1998v067n03ABEH000375
- S. B. Savvin, R. F. Gur'eva, *Talanta* **1987**, 34, 87–101. DOI:10.1016/0039-9140(87)80012-7
- E. Tang, G. Yang, J. Yin, *Spectrochim. Acta, Part A.* **2003**, 59, 651–656. DOI:10.1016/S1386-1425(02)00209-3
- L. Lozynska, O. Tymoshuk, *Chem. Chem. Technol.* **2013**, 7, 391–395. DOI:10.23939/chcht07.04.391
- L. Lozynska, O. Tymoshuk, In: O. L. Berezko, *The Interaction of 5-hydroxyimino-4-imino-1,3-thiazolidin-2-one with Platinum(IV) Ions*, 3rd International Conference of Young Scientists CCT-13, Lviv, Ukraine, **2013**, 166.
- L. V. Lozynska, O. S. Tymoshuk, T. I. Chaban, *Methods Objects Chem. Anal.* **2014**, 9, 50–54. DOI:10.17721/moca.2014.50-54
- L. V. Lozynska, O. S. Tymoshuk, *Issues Chem. Chem. Technol.*, **2014**, 1, 80–85.
- L. V. Lozynska, O. S. Tymoshuk, T. Ya. Vrublevs'ka, *Materials Science* **2015**, 6, 870–876. DOI:10.1007/s11003-015-9795-y
- L. Lozynska, O. Tymoshuk, T. Chaban, *Acta Chim Slov.* **2015**, 62, 159–167. DOI:10.17344/acsi.2014.866
- A. Tupys, O. Tymoshuk, P. Rydchuk, *Chem. Chem. Technol.* **2016**, 10, 19–25. DOI:10.23939/chcht10.01.019
- A. Tupys, J. Kalemkiewicz, Y. Bazel, L. Zapala, M. Dranka, Y. Ostapiuk, O. Tymoshuk, E. Woźnicka, *J. Mol. Struct.* **2017**, 1127, 722–733. DOI:10.1016/j.molstruc.2016.07.119
- A. Tupys, J. Kalemkiewicz, Y. Ostapiuk, V. Matiichuk, O. Tymoshuk, E. Woźnicka, L. Byczyński, *J. Therm. Anal. Calorim.* **2017**, 127, 2233–2242. DOI:10.1007/s10973-016-5784-0
- M. Fizer, V. Sidey, A. Tupys, Y. Ostapiuk, O. Tymoshuk, Y. Bazel, *J. Mol. Struct.* **2017**, 1149, 669–682. DOI:10.1016/j.molstruc.2017.08.037
- Y. Bazel, A. Tupys, Y. Ostapiuk, O. Tymoshuk, V. Matyichuk, *J. Mol. Liq.*, **2017**, 242, 471–477. DOI:10.1016/j.molliq.2017.07.047
- Y. Bazel, A. Tupys, Y. Ostapiuk, O. Tymoshuk, J. Imricha, J. Šandrejová, *RSC Adv.*, **2018**, 8, 15940–15950. DOI:10.1039/C8RA02039F
- O. Tymoshuk, L. Oleksiv, L. Khvalbota, T. Chaban, I. Patsay, *Acta Chim Slov.* **2019**, 66, 62–69. DOI:10.17344/acsi.2018.4448
- P. V. Rydchuk, O. S. Tymoshuk, L. V. Oleksiv, T. I. Chaban, V. S. Matyichuk, *Methods Objects Chem. Anal.* **2019**, 14, 130–139. DOI:10.17721/moca.2019.130-139
- O. S. Tymoshuk, O. S. Fedyshyn, L. V. Oleksiv, P. V. Rydchuk, I. O. Patsai, *Materials Science* **2019**, 55, 455–459. DOI:10.1007/s11003-019-00325-9
- V. Drušković, V. Vojković, S. Miko, *Talanta* **2004**, 62, 489–495. DOI:10.1016/j.talanta.2003.08.031
- L. Zhang, N. Li, P. Fan, X. Chu, S. An, J. Zhang, X. Wang, Hy-

- drometallurgy* **2012**, 127–128, 8–15.
DOI:10.1016/j.hydromet.2012.06.012
24. V. Drušković, V. Vojković, *Croat. Chem. Acta* **2003**, 76, 49–54.
25. A. S. Amin, I. A. Zaafarany, *Anal. Chem. Res.* **2015**, 3, 77–81.
DOI: 10.1016/j.ancr.2014.10.001
26. M. A. Taher, S. Puri, R. K. Bansal, B. K. Puri, *Talanta* **1997**, 45, 411–416. DOI:10.1016/S0039-9140(97)00149-5
27. S. Kuchekar, S. Bhumkar, H. Aher, S. H. Han, *J. Mater. Environ. Sci.* **2019**, 10, 1200–1213. DOI:10.20959/wjpps20174-8960
28. I. Patsay, P. Rydchuk, O. Tymoshuk, *Visnyk of the Lviv University. Series Chemistry* **2017**, 58, 219–224.
29. N. E. Ezerskaya, I. N. Kiseleva, *Zh. Anal. Khim.* **2001**, 967–970, 855–858. DOI:10.1023/A:1016768614942
30. Yu.Yu. Lur'è, *Spravochnik po analiticheskoj khimii*, Khimiya, Moscow, Russia, 1971, p. 456.
31. Yu. Lutsyshyn, Ya. Tokaychuk, P. Demchenko, R. Gladyshevskii, *Visnyk of the Lviv University. Series Chemistry* **2010**, 51, 52–59.
32. L. Khvalbota, O. Tymoshuk, V. Matyichuk, *Visnyk of the Lviv University. Series Chemistry* **2016**, 57, 219–225.

Povzetek

V prispevku je predstavljen nov derivat azolidona – 5-[2-(4-hidroksifenil)hidrazineiliden]-4-iminotiazolidin-2-on (HPIT) in rezultati njegove interakcije z ioni iridija(IV). Ir(IV) ion s tem reagentom pri pH = 5,0 brez segrevanja tvori stabilen kompleks ($\lambda_{\max} = 328$ nm). Stehiometrično razmerje Ir(IV) in reagenta v kompleksu je 1:1. Molarna absorptivnost in Sandellova občutljivost sta $5,57 \times 10^3$ L mol⁻¹ cm⁻¹ in 0,034 µg cm⁻². Kalibracijska krivulja je linearna v območju 1,0–11,5 µg mL⁻¹ Ir(IV) (R = 0,9996). Meja zaznave je 0,4 µg mL⁻¹. Na podlagi izvedene raziskave je bila razvita hitra in enostavna spektrofotometrična metoda za določanje Ir(IV) z uporabo 5-[2-(4-hidroksifenil)hidrazineilidena]-4-iminotiazolidin-2-ona kot kromofornega reagenta. Ir(IV) je bil določen v različnih sintetičnih mešanica in zlitinah.



Except when otherwise noted, articles in this journal are published under the terms and conditions of the Creative Commons Attribution 4.0 International License

Scientific paper

The Influence of Ionic Liquids on Micellization of Sodium Dodecyl Sulfate in Aqueous Solutions

Bojan Šarac* and Marija Bešter-Rogač

University of Ljubljana, Faculty of Chemistry and Chemical Technology, Večna pot 113, SI-1000 Ljubljana

* Corresponding author: E-mail: bojan.sarac@fkkt.uni-lj.si

Received: 04-22-2020

Abstract

The micellization of sodium dodecyl sulfate (SDS) in water and in aqueous solutions of three imidazolium based ionic liquids with different side-chain length, i.e. 1,3-dimethylimidazolium chloride ([C₁mim]Cl), 1-ethyl-3-methylimidazolium chloride ([C₂mim]Cl), and 1-butyl-3-methylimidazolium chloride ([C₄mim]Cl) was investigated by isothermal titration calorimetry (ITC) in the temperature range from 288.15 to 328.15 K. For comparison, the micellization of SDS in the presence of NaCl was studied also. ITC experimental data were analysed by the two-state mass-action model, yielding the values of critical micelle concentration (cmc), aggregation number (*n*), standard heat capacity ($\Delta_M c_p^\circ$), enthalpy ($\Delta_M H^\circ$), entropy ($\Delta_M S^\circ$), and Gibbs free energy ($\Delta_M G^\circ$) of the micellization process. It was found that the micellization of SDS in all the studied systems is an entropy-driven at lower temperatures and an enthalpy-driven at higher temperatures. In addition, it was assumed that with the increasing nonpolar character of IL, the interactions between the SDS are stronger, leading to more negative values of $\Delta_M H^\circ$ and $\Delta_M G^\circ$. To obtain more information about the micellar charge, the conductivity and zeta-potential measurements were performed at 298.15 K. Presumably the micellar charge is more positive in the presence of ILs due to their stronger interaction and possible incorporation into the micellar structure. This reflects in less negative zeta-potential comparing to SDS in water and consequently higher degrees of micelle ionization due to the larger portion of sodium ions in solution.

Keywords: Sodium dodecyl sulfate; ionic liquids; isothermal titration calorimetry; thermodynamics; micelle ionization; zeta-potential

1. Introduction

Sodium dodecyl sulfate (SDS), also known as sodium lauryl sulfate (SLS), is a well-known anionic surfactant, widely used in cleaning and hygiene products,¹ as a food additive² and also in research, as a cell disruptor, denaturing agent etc.^{3–5} It belongs to one of the most studied surfactants and consequently several characteristics of its micellization processes in aqueous solutions as, for example, the influence of inorganic electrolytes on critical micelle concentration (cmc), the shape of micelles and thermodynamic parameters of micellization of SDS are well-known.^{6–12} However, the presence of organic electrolytes usually affects these parameters in much more dramatic way if their hydrophobic chains can penetrate the micelles,¹³ as was already observed for many other surfactant systems.^{14–20} For an investigation of these effects, ionic liquids (ILs) as the most studied organic electrolytes in the last decades^{21,22} seem to be the most appropriate. Because of their bulky cation and anion structure over which the charge is distributed

by the resonance, they tend to be liquids at temperatures below 100 °C. Due to the amphiphilic character, some of the ILs can also be classified as cationic hydrotropes, and they can enhance the solubility of hydrophobic compounds in water.²³ Their behaviour in a pure state, mixtures or solutions is unlike conventional molecular solvents by forming amphiphilic nanostructures which offer great potential as designer solvents.²⁴ Properties of many pure protic and aprotic ILs are already well-investigated,^{25–27} but the knowledge of their influence on aggregation process of SDS or any other surfactant is rather scarce.^{28–30} Beyaz *et al.*, for example, showed that hydrophobic ILs (e.g. 30 mM solution of 1-hexyl-3-methylimidazolium chloride ([C₆mim]Cl)) decreased cmc of SDS, whereas hydrophilic ones (e.g. 30 mM [C₄mim]Cl) increased it.²⁸ Such a trend was also obtained for SDS in solutions of 1-pentyl-3-methylimidazolium hexafluorophosphate ([C₅mim][PF₆]), where cmc increased with increasing concentration of IL due to the solvophobic interactions around the surfactant hydrocarbon chains.²⁹ On the contrary, Javadian *et al.* observed a

decrease of cmc of SDS in up to 5.72 mM of $[C_4mim]Cl$. They also demonstrated that longer-chained ILs modify the structural properties of aggregates inducing the formation of wormlike micelles. It appears that the cmc values and morphology of the surfactant systems are strongly dependent upon the concentration and amphiphilicity of ILs which is still the area of extensive investigation.^{31,32}

In the present work, the systematic study of the influence of the increasing hydrophobicity of ILs on the micellization process of SDS in aqueous solutions was carried out by using isothermal titration calorimetry (ITC), conductivity and zeta-potential measurements. Although SDS is one of the most studied surfactants, there is limited temperature-dependent data in the literature. Thus, the micellization of SDS in water was studied first, followed by the investigation of the micellization of SDS in the presence of three ILs, i.e. 1,3-dimethylimidazolium ($[C_1mim]Cl$), 1-ethyl-3-methylimidazolium ($[C_2mim]Cl$) and, 1-butyl-3-methylimidazolium chloride ($[C_4mim]Cl$), where the concentration of ILs was kept constant at 0.01 M. Because the comparison between ILs and “classical” electrolytes is always interesting and needed, we decided to include also the investigations of micellization of SDS in NaCl solutions. But it turned out, that NaCl affects the process in considerably less extend as ILs. Almost no difference between the thermodynamic parameters for micellization of SDS in water and in 0.01 M NaCl solution was found namely, so the experiments were performed in 0.1 M NaCl solutions. On the contrary, the effect of ILs on micellization of SDS is much stronger and already at the concentration of 0.01 M the difference (in comparison to that in water) was considerable and compared to those in 0.1 M NaCl solutions.

Experimental ITC data were analysed by the two-state mass-action model yielding the corresponding standard thermodynamic parameters: Gibbs free energy ($\Delta_M G^\circ$), enthalpy ($\Delta_M H^\circ$), and entropy ($\Delta_M S^\circ$) of micellization together with cmc and aggregation number (n). From conductivity measurements, we estimated a degree of micelle ionization (α) which will be discussed in the light of the determined zeta-potentials (ζ).

2. Experimental

2.1. Chemicals

Sodium dodecyl sulfate (purity > 98.5 %, $M = 288.37 \text{ g mol}^{-1}$) and sodium chloride (> 99.5 %, $M = 58.44 \text{ g mol}^{-1}$) were purchased from Sigma-Aldrich (St. Louis, MO, USA) and used as received. 1,3-dimethyl- (>98 %, $M = 132.59 \text{ g mol}^{-1}$), 1-ethyl- (>98 %, $M = 146.62 \text{ g mol}^{-1}$) and 1-butyl-3-methylimidazolium chloride (>99 %, $M = 174.67 \text{ g mol}^{-1}$) were obtained from IoLiTec (Ionic Liquids Technologies GmbH, Heilbronn, Germany) and used as received. The chemicals were stored in a desiccator over P_2O_5 . For preparation of solutions, MiliQ water was used.

2.2. Isothermal Titration Calorimetry

The heat changes associated with (de)micellization of SDS were measured using a VP-ITC microcalorimeter (MicroCal Inc., Malvern, UK). The sample cell was filled with corresponding “solvent” (water, a solution of 0.1 M NaCl or 0.01 M of IL) and successive aliquots of 6 μL of the surfactant solution, prepared in the same “solvent”, were injected at 10–15 minutes intervals by a motor-driven syringe into the sample cell while stirring at 300 rpm. For each system, experiments at five temperatures between 288.15 and 328.15 K in step of 10 K were carried out. Each added aliquot produced a heat effect (raw signal) mainly due to the demicellization of surfactant micelles, dilution of monomers, and corresponding counterions. When the cmc of surfactant was exceeded in the sample cell, the heat effects evolved only due to dilution of micelles and ions. From the integration of the raw signal (an example in Figure S1a in Supporting information) the enthalpies of dilution (ΔH) of the surfactant expressed per mole of added SDS were obtained by using software Origin 7.0. According to our experience, the ITC gives highly reproducible results, thus, the experiments were not repeated.

2.3. Conductivity Measurements

Electrical conductivity of solutions was recorded with a PC-interfaced LCR Meter Agilent 4284 A connected to a three-electrode measuring cell described elsewhere.³³ The cell constant was determined with dilute potassium chloride solutions.³⁴ The cell was immersed in the high precision thermostat bath (containing polydimethylsiloxane) set to 298.15 K. The temperature was additionally checked with a calibrated Pt100 resistance thermometer (MPMI 1004/300 Merz) connected to an HP 3458 A multimeter.³³

After measuring the resistance of appropriate “solvent” (water, 0.1 M NaCl, 0.01 M IL) at a set temperature, successive aliquots of a stock solution of the surfactant in the same “solvent” were added by a programmable syringe pump (Model 1250, J-KEM Scientific, MO, USA) and the resistance of the solution was measured. Afterwards, the specific conductivities were calculated using previously determined cell constant. The specific conductivities of solutions were corrected by the specific conductivities of “solvent” and plotted as a function of the molar concentration of SDS in the cell. From the slopes before and after the cmc, the values of degree of micelle ionization (α) were estimated.³⁵ The applied method for determination of electrical conductivity of solutions supplies highly reproducible data, thus, the experiments were not repeated.

2.4. Zeta-Potential Determination

Electrophoretic measurements were performed by Litesizer 500 (Anton Paar GmbH, Graz, Austria) in cuvette using Univette accessory. All the measurements were per-

formed at 298.15 K, after a 1-minute temperature equilibration period. For each solution, which was prepared directly in cuvette by diluting a stock solution of surfactant (20 mM) with solvent, we performed 3 series (triplicates) of measurements, each containing 120 runs. All the zeta-potentials (ζ) were calculated using Smoluchowski approximation corrected by Henry:^{36, 37}

$$\zeta = \frac{\mu\eta}{\varepsilon\varepsilon_0 f(\kappa a)} \quad (1)$$

where μ is measured electrophoretic mobility, η the viscosity of the medium, ε the relative dielectric constant of the medium, ε_0 the vacuum permittivity, κ the inverse of the Debye distance, and a the radius of the micelles.

Function $f(\kappa a)$ is for spherical micelles given by:

$$f(\kappa a) = \frac{2}{3} \left[1 + \frac{1}{2(1 + 2.5/\kappa a \{1 + 2 \exp(-\kappa a)\})^3} \right] \quad (2)$$

The viscosities and relative permittivities of all the solvents were taken the same as for the water (0.890 mPa s, 78.4). The radius of the micelles $a = 1.81$ nm for all investigated systems was taken.³⁸

3. Thermodynamics of Micellization

According to the two-state mass-action model, the process of micellization of SDS can be described as the equilibrium between negatively charged surfactant monomers (S^-), corresponding positive counterions (C^+), and micelles (M^{an-}):



where n represents the aggregation number and α the degree of micelle ionization. The apparent constant of micellization (K_M) expressed by the molalities of corresponding species, can be connected to the Gibbs free energy of micellization ($\Delta_M G^\circ$) by:

$$\Delta_M G^\circ = -\frac{RT}{n} \ln K_M = -\frac{RT}{n} \ln \frac{m_M}{m_S^n (m_C + m_X)^{n(1-\alpha)}} \quad (4)$$

where m_X represents the molality of added electrolyte (0.1 M NaCl or 0.01 M IL).

By ITC experiment, the heat effects accompanying the titration of stock solution in the sample cell are measured, presented usually in form so called enthalpograms as the enthalpy of dilution (ΔH) versus the concentration of surfactant in the solution (Figure S1b). ΔH can be expressed in terms of partial molar enthalpies of surfactant (\bar{H}_s), counterions (\bar{H}_c) and the enthalpy of micellization ($\Delta_M H^\circ$) by the use of thermodynamic laws and mass-balance equations as:³⁹

$$\Delta H = (\bar{H}_s + \bar{H}_c) + \Delta_M H^\circ \left(\frac{\partial n_M}{\partial n_2} \right)_{n_1, p, T} \quad (5)$$

where the last term represents the change of the amount of surfactant in the micellar form at every addition of surfactant and is connected to K_M or $\Delta_M G^\circ$. \bar{H}_s and \bar{H}_c were determined from the extrapolation of the lines through the plateaus of the enthalpograms before the cmc, as it is shown on Figure S1b. $\Delta_M H^\circ$ and $\Delta_M G^\circ$ were the fitting parameters primarily determined at 298.15 K (reference temperature, T_0). At other temperatures (T), their values were obtained from the Kirchhoff and integrated Gibbs-Helmholtz equations

$$\begin{aligned} \Delta_M H^\circ(T) &= \Delta_M H^\circ(T_0) + \Delta_M c_p^\circ \cdot (T - T_0) \\ \Delta_M G^\circ(T) &= T(\Delta_M G^\circ(T)/T_0 + \Delta_M H^\circ(T) \cdot [1/T - 1/T_0]) + \\ &+ \Delta_M c_p^\circ \cdot [1 - T/T_0 - \ln(T/T_0)] \end{aligned} \quad (6)$$

where $\Delta_M c_p^\circ$ was treated as a temperature-independent fitting parameter.

The model function (right-hand side of equation (5)) was fitted to the ITC experimental data simultaneously at all temperatures (global fitting), using the Levenberg-Marquardt nonlinear regression algorithm.⁴⁰ A detailed derivation of equation (5) is given in our previous work.³⁹ From the global analysis of ITC data, the best-fit thermodynamic parameters were extracted, i.e., enthalpy, $\Delta_M H^\circ$, Gibbs free energy, $\Delta_M G^\circ$, and heat capacity, $\Delta_M c_p^\circ$, of the micellization. Aggregation number (n) was set as the temperature-independent fitting parameter during the global analysis. The values of α were estimated from conductivity measurements at 298.15 K. Since the values of fitting parameters in the ITC data analysis are not correlated strongly to α , it was taken as a temperature-independent parameter. The entropy of micellization was calculated from the Gibbs-Helmholtz equation

$$\Delta_M S^\circ = \frac{\Delta_M H^\circ - \Delta_M G^\circ}{T} \quad (7)$$

4. Results and Discussion

The dependence of experimental enthalpy of dilution (ΔH) on surfactant concentration (enthalpogram) for titration of SDS in water from 288.15 K to 328.15 K is shown in Figure 1a. The precipitation of SDS (Krafft point) at 278.15 K takes place immediately after the cmc in the sample cell is reached (Figure S2 in Supporting information), therefore this temperature was excluded from the temperature range in further experiments. Enthalpograms for titration of SDS in 0.1 M NaCl and 0.01 M solutions of [C₁mim]Cl, [C₂mim]Cl and [C₄mim]Cl in the investigated temperature range are presented in Figure S3 in Supporting information.

The comparison of enthalpograms for the micellization process of SDS in all studied systems at 308.15 K is shown in Figure 1b. From Figures 1 and S3 in Supporting information, it is evident, that the energetics of the micellization process is highly dependent on the temperature and a type and/or concentration of added electrolyte. As explained already in Introduction, the impact of lower concentrations of NaCl (e.g. 0.01 M)¹² on the micellization process of SDS is less pronounced in terms of cmc and thermodynamic parameters comparing to investigated ILs, therefore all experiments were performed in 0.1 M NaCl solutions. Resulting cmc values are similar comparing to 10-times less concentrated solutions of ILs which furthermore emphasize the effect of organic additives on micellization process.

By applying the global fitting of the model equation (5) to the experimental ITC data, denoted on the graphs as full lines, the values of $\Delta_M H^\circ$, $\Delta_M G^\circ$, $\Delta_M c_p^\circ$, and n were obtained as the best fitting parameters. $\Delta_M S^\circ$ was calculated by help of equation (7), whereas the cmc values were

determined from the inflection point of the fitting curves. All estimated parameters at 298.15 K are listed in Table 1, together with available literature data. In Table S1 in Supporting information also the data at other temperatures are gathered.

The temperature dependence of cmc for SDS in all investigated systems shows nearly U-shaped form (Figure 2a). Evidently, cmc is systematically decreasing by increasing polarity of counterions from [C₁mim]Cl to [C₄mim]Cl. Our results are in agreement with the findings of Javadian *et al.*,³⁰ but Beyaz *et al.* reported a higher value of cmc in solution of 30 mM of [C₄mim]Cl.²⁸ The cmc values in water and 0.1 M NaCl agree quite well with available ITC literature data (see Table 1 for an overview).^{8, 12, 41}

The smallest aggregation number (n , Table 1) for the micelles of SDS in water was found. In the presence of ILs the micelles should be slightly bigger, but the structure of ILs does not have an expressed influence on n . For SDS in 0.1 M NaCl aqueous solutions the highest n was estimated, supporting the reported sphere-rod transition.^{42,43}

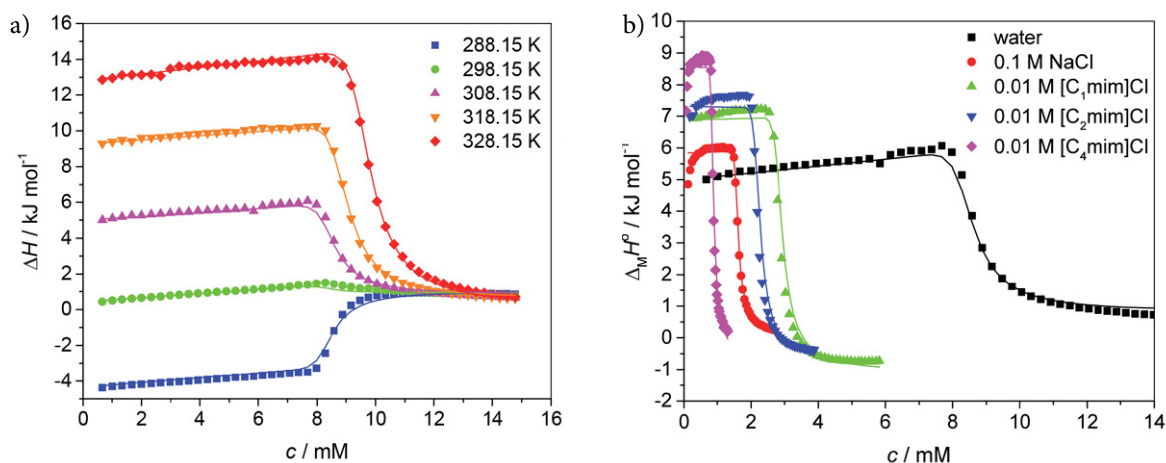


Figure 1. (a) Enthalpograms of SDS titrations in water from 288.15 K to 328.15 K in the step of 10 K and (b) enthalpograms of SDS in all investigated systems at 308.15 K. Symbols represent the experimental data, and solid lines are the best-fits according to two-state mass action model (eq. (5)).

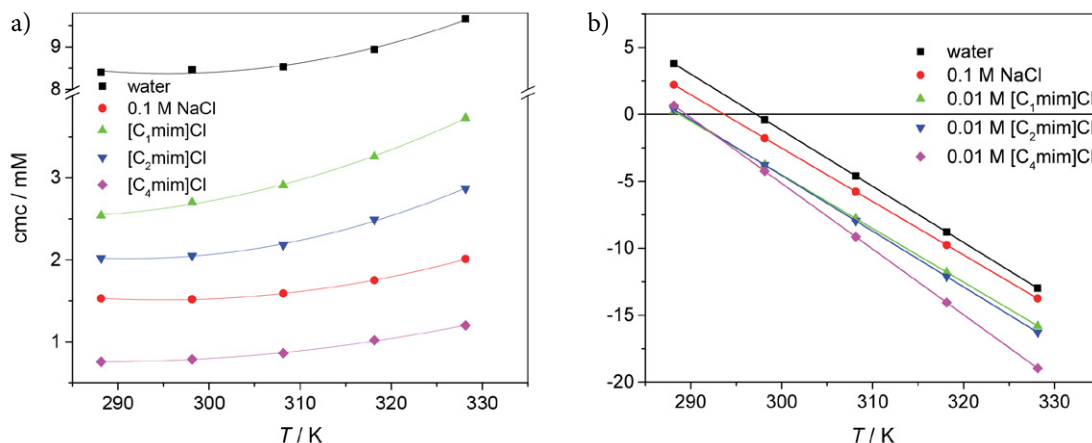


Figure 2. (a) The values of cmc and (b) $\Delta_M H^\circ$ as a function of temperature for all investigated systems. Lines in (a) present guides to the eye (polynomial fits) and in (b) linear fits from which the heat capacities of micellization were extracted.

The micellization process is endothermic at low temperatures and exothermic at higher temperatures, as it is evident from Figure 2b and Table S1 in Supporting information. Similar behaviour has already been observed at micellization process of alkyltrimethylammonium chlorides in water and aqueous solutions of NaCl or hydroxybenzoates.^{17,19,44,45} Evidently, the temperature at which $\Delta_M H^0 = 0$ is ~ 297 K for SDS in water and ~ 290 K in the presence of ILs. The change in the sign of $\Delta_M H^0$ is related to the sensitive balance between the main two processes accompanying the micellization: (de)hydration of nonpolar parts of surfactants' monomers, which are then held together by cooperative noncovalent interactions, and condensation of counterions onto the micellar surface upon the micellization. The first process is energetically unfavourable (endothermic), and it is prevailing at lower temperatures, whereas the condensation of counterions is an exothermic process and only weakly temperature-dependent. With increasing temperature- as a consequence of increasing thermal energy in the systems- the binding of surrounding water molecules to the nonpolar parts is weaker leading to the overall exothermic process of micellization.

Gibbs free energy ($\Delta_M G^0$) of the micellization process of SDS is negative in all studied systems, as it is characteristically for spontaneous processes (Table 1). From Table 1 in Supporting information is evident, that the micellization of SDS in all media is entropically driven process at lower temperatures whereas at higher temperatures the entropy and enthalpy contribute both to the negative value of $\Delta_M G^0$ as it is usually found for ionic surfactants.^{45–49} The main contribution to the entropy change stems from desolvation of the cations and anions upon the

micellization, which is obviously comparable among the investigated systems, leading to only small differences in $T\Delta_M S^0$. Furthermore, the last diminishes with temperature, due to rising thermal energy of the water molecules, leading to the prevalence of enthalpy ($\Delta_M H^0$) connected to the electrostatic interactions between the positive counterions and negative sulfate heads.

The values of $\Delta_M c_p^0$ for studied micellization process of SDS in different media are strongly negative, which is characteristic for the processes at removal of water surrounding nonpolar chains upon the micellization. The largest value (in the absolute sense) is obtained for SDS in [C₄mim]Cl solution. Since the most expressed nonpolar character of [C₄mim]⁺ cation, it can be assumed that the butyl chain is partly dehydrated and incorporated into the micellar structure. The interactions (noncovalent and electrostatic) between the SDS and ILs are therefore rising with the increasing length of the nonpolar chain which is also evident from the increasing exothermicity of the micellization process ($\Delta_M H^0$) at a fixed temperature (Tables 1 and S2).

The value of α is in 0.1 M NaCl higher than in water which was already observed for SDS and also DTAC in high salinity systems and can be attributed to increased charge screening in a diffuse layer around micelles at higher ionic strength.^{7,50} In the presence of 0.01 M ILs the values of α are also higher than in water and are interestingly rising in the order from [C₁mim]Cl to [C₄mim]Cl. With the assumption that the contribution of the micelles to the specific conductivity of solutions is negligible, the slopes of specific conductivities before and after the cmc, from which the α values were determined, depend mainly upon the mobility of small ions,⁵¹ such as Na⁺ and IL cations in

Table 1. The values of critical micelle concentration (cmc), aggregation number (n), enthalpy ($\Delta_M H^0$), Gibbs free energy ($\Delta_M G^0$), entropy contribution ($T\Delta_M S^0$), heat capacity ($\Delta_M c_p^0$) of micellization, and a degree of micelle ionization (α) for SDS in all the investigated systems at 298.15 K. Where possible, the literature data are given (the numbers in parentheses denote the temperature at which the values were determined).^a

	Water	0.1 M NaCl	0.01 M [C ₁ mim]Cl	0.01 M [C ₂ mim]Cl	0.01 M [C ₄ mim]Cl
cmc	8.47 ± 0.04 8.1 (301 K) ^b 8.73 (293 K) ^c	1.52 ± 0.01 1.54 ^b 1.72 (303 K) ^d	2.70 ± 0.04	2.05 ± 0.03	0.79 ± 0.01
n	24 ± 1	42 ± 1	30 ± 1	29 ± 1	30 ± 2
$\Delta_M H^0$	-0.40 ± 0.06 0.22 ^{b*} -0.82 ^{c*} -0.81 ^e	-1.78 ± 0.04 -1.90 (301 K) ^b	-3.77 ± 0.06	-3.78 ± 0.05	-4.24 ± 0.08
$\Delta_M G^0$	-18.04 ± 0.03	-16.97 ± 0.06	-19.00 ± 0.01	-19.23 ± 0.01	-21.57 ± 0.05
$T\Delta_M S^0$	17.64 ± 0.07	15.19 ± 0.08	15.24 ± 0.07	15.45 ± 0.05	17.33 ± 0.09
$\Delta_M c_p^0$	-0.419 ± 0.004	-0.399 ± 0.004	-0.401 ± 0.004	-0.417 ± 0.002	-0.491 ± 0.005
α	0.379 ± 0.005	0.70 ± 0.05	0.496 ± 0.007	0.536 ± 0.003	0.549 ± 0.007

^aUnits: cmc, mM; $\Delta_M H^0$, $\Delta_M G^0$, $T\Delta_M S^0$, kJ · mol⁻¹; $\Delta_M c_p^0$, kJ mol⁻¹ · K⁻¹] ^bref.⁸; ^cref.⁴¹; ^dref.¹²; ^eref.⁹; *obtained by interpolation of existing literature data

our case. Due to the partial nonpolar (hydrophobic) character, IL cations interact more strongly with sulfate headgroups of SDS than Na^+ ions. Consequently, the micellar surface potential is lower leading to the lower condensation of Na^+ ions on the micellar surface than in water. In other words, a larger portion of Na^+ ions are free in the bulk, which gives rise to the α values.

To affirm such a hypothesis and to gain insight into the micellar charge, we performed ζ -potential measurements. Figure 3 shows the values of ζ -potential as a function of SDS concentration in water, 0.1 M NaCl, and 0.01 M IL solutions. Our values for SDS in water and 0.1 M NaCl correspond well to the literature data (around -100 mV and -60 mV, respectively),^{12, 52} whereas for SDS in IL solutions no data was found. From Figure 3, it is evident that the values of ζ -potential after cmc in 0.01 M IL and 0.1 M NaCl solutions are less negative (or more positive) than in water. This can be attributed to the lower micellar charge, due to possible incorporation of IL cations, or more efficient screening around SDS micelles. On the other hand, the least negative value of ζ -potential was encountered for $[\text{C}_2\text{mim}]\text{Cl}$, which is somewhat surprising. ζ -potential is an experimentally determined potential (or electrical charge) of micelles within the region to some distance from the micellar surface, also abbreviated as a shear plane. The difference in the values between ILs could be prescribed to the shifting of the position of the shear plane due to their different depths of incorporation into the micellar structure. Probably the $[\text{C}_4\text{mim}]^+$ cation is incorporated more deeply than $[\text{C}_2\text{mim}]^+$ cation meaning that imidazolium ring of the last is farther from the micellar surface. Therefore, the shear plane is extended towards the bulk solution leading to less negative ζ -potential. Interestingly, the ζ -potential for SDS in $[\text{C}_1\text{mim}]\text{Cl}$ is similar as in $[\text{C}_4\text{mim}]\text{Cl}$. The possible explanation for this could be a different orientation of $[\text{C}_1\text{mim}]^+$ cation at the micellar surface since the cation is more symmetrical than the oth-

er two, but this needs further investigation. It is also interesting that after cmc all the ζ -potential values are monotonically decreasing with SDS concentration except in the case of SDS in 0.1 M NaCl solutions where it is almost constant throughout the whole concentration range of SDS. Here it has to be emphasized that at high concentrations of the additives the SDS could form cylindrical or rod-like micelles^{42, 43} which makes the interpretation of ζ -potential dubious and needs further exploration. For example, if we employ function $f(ka)$ for cylindrical micelles³⁶ in equation (1) we obtain ζ -potential around -100 mV for 20 mM SDS in 0.1 M NaCl.

5. Conclusions

The micellization process of SDS in water, 0.1 NaCl, and 0.01 M solutions of $[\text{C}_1\text{mim}]\text{Cl}$, $[\text{C}_2\text{mim}]\text{Cl}$, and $[\text{C}_4\text{mim}]\text{Cl}$ was studied from 288.15 to 328.15 K using ITC. From the fitting of the model equation from two-state mass-action model to the ITC experimental data the thermodynamic parameters – enthalpy ($\Delta_{\text{M}}H^\circ$), Gibbs free energy ($\Delta_{\text{M}}G^\circ$), entropy ($\Delta_{\text{M}}S^\circ$), heat capacity ($\Delta_{\text{M}}c_p^\circ$), critical micelle concentrations (cmc) and aggregation numbers (n) – were determined. The micellization of SDS is a spontaneous (negative $\Delta_{\text{M}}G^\circ$ values) and entropically driven process at lower temperatures whereas at higher temperatures, $\Delta_{\text{M}}H^\circ$ becomes prevalent. The spontaneity is more expressed in the case of SDS in ionic liquids (ILs) solutions which is also reflected in lower cmc values than in water. The same can also be observed for SDS in 0.1 M NaCl. In the last case, we also observed higher n than at others which could be due to the formation of rod-like micelles.

The values of α were estimated from conductivity measurements at 298.15 K in all investigated systems. Interestingly, we observed the increase of α values in the case of added electrolytes. Furthermore, zeta-potential (ζ) of micelles at different concentrations of SDS was determined at 298.15 K. It turned out that all the values are less negative than in water. This can be attributed to the condensation and partial incorporation of IL cations to the micelle surface and consequently lowering the micelle surface potential. In this way, the charge of the micelles is lower than in the water, where Na^+ ions are the only counterions, which leads to a greater portion of the last ions in the bulk and consequently higher α values.

Acknowledgements

The financial support by the Slovenian Research Agency through Grant No. P1-0201 is gratefully acknowledged. The authors would also like to thank Ph. D. student Nevena Đekić for her help at the laboratory work.

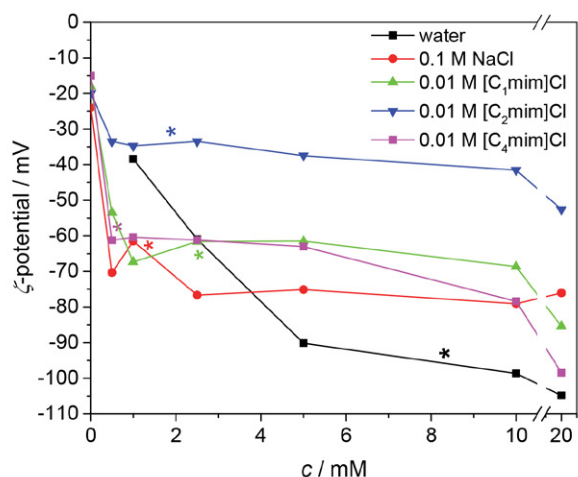


Figure 3. ζ -potential values for all investigated systems as a function of SDS concentration at 298.15 K. Asterisks denote the corresponding cmc values.

6. References

- C. A. Bondi, J. L. Marks, L. B. Wroblewski, H. S. Raatikainen, S. R. Lenox, K. E. Gebhardt, *Environ. Health Insights* **2015**, *9*, 27–32. DOI:10.4137/EHI.S31765
- S. R. Igoe, *Dictionary Of Food Ingredients*, Springer, San Diego, USA, **2011**, pp. 131. DOI:10.1007/978-1-4419-9713-5
- H. Schägger, in: C. Hunte, G. von Jagow and H. Schägger (Eds.): *Membrane Protein Purification and Crystallization*, Elsevier, Amsterdam, Netherlands, **2003**, pp. 85–103. DOI:10.1016/B978-0-12-361776-7.X5000-1
- R. E. Farrell, *RNA Methodologies*, Elsevier, Amsterdam, Netherlands, **2010**, pp. 155–172. DOI:10.1016/B978-0-12-374727-3.00007-3
- K. T. Naidu, N. P. Prabhu, *J. Phys. Chem. B* **2011**, *115*, 14760–14767. DOI:10.1021/jp2062496
- G. C. Krescheck, W. A. Hargraves, *J. Colloid Interface Sci.* **1974**, *48*, 481–493. DOI:10.1016/0021-9797(74)90193-3
- P. C. Shanks, E. I. Franses, *J. Phys. Chem.* **1992**, *96*, 1794–1805. DOI:10.1021/j100183a055
- S. Paula, W. Sus, J. Tuchtenhagen, A. Blume, *J. Phys. Chem.* **1995**, *99*, 11742–11751. DOI:10.1021/j100030a019
- A. Chatterjee, S. P. Moulik, S. K. Sanyal, B. K. Mishra, P. M. Puri, *J. Phys. Chem. B* **2001**, *105*, 12823–12831. DOI:10.1021/jp0123029
- E. Dutkiewicz, A. Jakubowska, *Colloid Polym. Sci.* **2002**, *280*, 1009–1014. DOI:10.1007/s00396-002-0723-y
- R. F. P. Pereira, A. J. M. Valente, H. D. Burrows, *J. Mol. Liq.* **2010**, *156*, 109–114. DOI:10.1016/j.molliq.2010.02.007
- B. Naskar, A. Dey, S. P. Moulik, *J. Surfactants Deterg.* **2013**, *16*, 785–794. DOI:10.1007/s11743-013-1449-1
- B. C. Paul, S. S. Islam, K. Ismail, *J. Phys. Chem. B* **1998**, *102*, 7807–7812. DOI:10.1021/jp9812381
- C. Manohar, U. R. K. Rao, B. S. Valaulikar, R. M. Lyer, *J. Chem. Soc., Chem. Commun.* **1986**, 379–381. DOI:10.1039/c39860000379
- L. J. Magid, Z. Han, G. G. Warr, M. A. Cassidy, P. D. Butler, W. A. Hamilton, *J. Phys. Chem. B* **1997**, *101*, 7919–7927. DOI:10.1021/jp970864f
- K. Bijma, M. J. Blandamer, J. B. F. N. Engberts, *Langmuir* **1998**, *14*, 79–83. DOI:10.1021/la970216n
- B. Šarac, J. Cerkovnik, B. Ancian, G. Mériquet, G. M. Roger, S. Durand-Vidal, M. Bešter-Rogač, *Colloid Polym. Sci.* **2011**, *289*, 1597–1607. DOI:10.1007/s00396-011-2480-2
- T. K. Hodgdon, E. W. Kaler, *Curr. Opin. Colloid Interface Sci.* **2007**, *12*, 121–128. DOI:10.1016/j.cocis.2007.06.004
- B. Šarac, G. Meriquet, B. Ancian, M. Bešter-Rogač, *Langmuir* **2013**, *29*, 4460–4469. DOI:10.1021/la400161n
- I. Čobanov, B. Šarac, Ž. Medoš, A. Tot, M. Vraneš, S. Gadžurić, M. Bešter-Rogač, *J. Mol. Liq.* **2020**, *301*, 112419. DOI:10.1016/j.molliq.2019.112419
- T. Welton, *Biophys. Rev.* **2018**, *10*, 691–706. DOI:10.1007/s12551-018-0419-2
- M. Bešter-Rogač, *Acta Chim. Slov.* **2020**, *67*, 1–14. DOI:10.17344/acsi.2020.5870
- A. F. M. Claudio, M. C. Neves, K. Shimizu, J. N. C. Lopes, M. G. Freire, J. A. P. Coutinho, *Green Chem.* **2015**, *17*, 3948–3963. DOI:10.1039/C5GC00712G
- H. J. Jiang, R. Atkin, G. G. Warr, *Curr. Opin. Green Sustain. Chem.* **2018**, *12*, 27–32. DOI:10.1016/j.cogsc.2018.05.003
- R. Hayes, G. G. Warr, R. Atkin, *Chem. Rev.* **2015**, *115*, 6357–6426. DOI:10.1021/cr500411q
- S. Zhang, N. Sun, X. He, X. Lu, X. Zhang, *J. Phys. Chem. Ref. Data* **2006**, *35*, 1475–1517. DOI:10.1063/1.2204959
- T. L. Greaves, A. Weerawardena, C. Fong, C. J. Drummond, *Langmuir* **2007**, *23*, 402–404. DOI:10.1021/la062895k
- A. Beyaz, W. S. Oh, V. P. Reddy, *Colloids Surf., B* **2004**, *35*, 119–124. DOI:10.1016/j.colsurfb.2004.02.014
- A. Pal, S. Chaudhary, *Colloids Surf., A* **2013**, *430*, 58–64. DOI:10.1016/j.colsurfa.2013.04.001
- S. Javadian, F. Nasiri, A. Heydari, A. Yousefi, A. A. Shahir, *J. Phys. Chem. B* **2014**, *118*, 4140–4150. DOI:10.1021/jp5010049
- M. T. Lam, W. D. Adamson, S. Miao, R. Atkin, G. G. Warr, *J. Colloid Interface Sci.* **2019**, *552*, 597–603. DOI:10.1016/j.jcis.2019.05.082
- S. J. Bryant, C. J. Jafta, R. Atkin, M. Gradziński, G. G. Warr, *J. Colloid Interface Sci.* **2019**, *540*, 515–523. DOI:10.1016/j.jcis.2019.01.048
- M. Bešter-Rogač, D. Habe, *Acta Chim. Slov.* **2006**, *53*, 391–395.
- J. Barthel, F. Feuerlein, R. Neueder, R. Wachter, *J. Solution Chem.* **1980**, *9*, 209–219. DOI:10.1007/BF00648327
- J. P. Marcolongo, M. Mirenda, *J. Chem. Educ.* **2011**, *88*, 629–633. DOI:10.1007/BF00648327
- M. A. Morini, P. C. Schulz, *Colloid Polym. Sci.* **1997**, *275*, 802–805. DOI:10.1007/s003960050151
- D. C. Henry, *Proc. R. Soc. Lond. A* **1931**, *133*, 106–129. DOI:10.1098/rspa.1931.0133
- M. Almgren, S. Swarup, *J. Phys. Chem.* **1982**, *86*, 4212–4216. DOI:10.1021/j100218a024
- A. Kroflič, B. Šarac, M. Bešter-Rogač, *Langmuir* **2012**, *28*, 10363–10371. DOI:10.1021/la302133q
- W. H. Press, S. A. Teukolsky, W. T. Vetterling, B. P. Flannery, *Numerical Recipes in Fortran 77: The Art of Scientific Computing*, Cambridge University Press, New York, **2001**, pp. 678
- P. R. Majhi, A. Blume, *Langmuir* **2001**, *17*, 3844–3851. DOI:10.1021/la001660k
- A. Coello, F. Meijide, M. A. Mougán, E. Núñez Rodríguez, J. Tato Vázquez, *J. Chem. Educ.* **1995**, *72*, 73–75. DOI:10.1021/ed072p73
- S. Hayashi, S. Ikeda, *J. Phys. Chem.* **1980**, *84*, 744–751. DOI:10.1021/j100444a011
- T. M. Perger, M. Bešter-Rogač, *J. Colloid Interface Sci.* **2007**, *313*, 288–295. DOI:10.1016/j.jcis.2007.04.043
- B. Šarac, M. Bešter-Rogač, *J. Colloid Interface Sci.* **2009**, *338*, 216–221. DOI:10.1016/j.jcis.2009.06.027
- K. Beyer, D. Leine, A. Blume, *Colloids Surf., B* **2006**, *49*, 31–39. DOI:10.1016/j.colsurfb.2006.02.003
- R. Zielinski, *J. Colloid Interface Sci.* **2001**, *235*, 201–209. DOI:10.1006/jcis.2000.7364

48. A. Kroflič, B. Šarac, M. Bešter-Rogač, *J. Chem. Thermodyn.* **2011**, *43*, 1557–1563. DOI:10.1016/j.jct.2011.05.015
49. Ž. Medoš, M. Bešter-Rogač, *Langmuir* **2017**, *33*, 7722–7731. DOI:10.1021/acs.langmuir.7b01700
50. A. Kroflič, B. Šarac, M. Bešter-Rogač, *Acta Chim. Slov.* **2012**, *59*, 564–570.
51. K. D. Danov, P. A. Kralchevsky, K. P. Ananthapadmanabhan, *Adv. Colloid Interface Sci.* **2014**, *206*, 17–45. DOI:10.1016/j.cis.2013.02.001
52. D. Stigter, K. J. Mysels, *J. Phys. Chem.* **1955**, *59*, 45–51. DOI:10.1021/j150523a014

Povzetek

Z izotermno titracijsko kalorimetrijo (ITC) smo v temperaturnem območju med 15 in 55 °C proučevali micelizacijo natrijevega dodecil sulfata (SDS) v vodi in vodnih raztopinah treh imidazolijevih ionskih tekočin (IL) z različnimi dolžinami stranskih verig, in sicer 1,3-dimetil imidazolijevga klorida ($[C_1\text{mim}]\text{Cl}$), 1-etil-3-metil imidazolijevga klorida ($[C_2\text{mim}]\text{Cl}$) ter 1-butil-3-metil imidazolijevga klorida ($[C_4\text{mim}]\text{Cl}$). Za primerjavo smo proučili tudi micelizacijo SDS v prisotnosti NaCl. Eksperimentalne ITC podatke smo analizirali s pomočjo dvostopenjskega ravnotežnega modela, iz česar smo dobili vrednosti kritične micelne koncentracije (cmc), agregacijskega števila (n) ter vrednosti sprememb standardne toplotne kapacitete ($\Delta_M c_p^\circ$), standardne entalpije ($\Delta_M H^\circ$), standardne entropije ($\Delta_M S^\circ$) in Gibbsove proste entalpije ($\Delta_M G^\circ$) za proces micelizacije. Ugotovili smo, da je micelizacija SDS v vseh proučevanih sistemih entropijsko voden proces pri nizkih temperaturah in entalpijsko voden proces pri visokih temperaturah. Predpostavimo lahko, da so z naraščajočim nepolarnim značajem ionskih tekočin interakcije z SDS bolj izražene, s čimer vrednosti $\Delta_M H^\circ$ in $\Delta_M G^\circ$ postanejo bolj negativne. Da bi pridobili več informacij o naboju micel, smo izvedli meritve električne prevodnosti in zeta-potenciala pri 25 °C. Zaradi močnejše interakcije in možnega vgrajevanja IL v micelno strukturo SDS je naboj micel bolj pozitiven. To se odraža v manj negativnih vrednostih zeta-potenciala v primerjavi s SDS v vodi, kar vodi do višjih vrednostih stopnje ionizacije micel zaradi večjega deleža natrijevih ionov v raztopini.



Except when otherwise noted, articles in this journal are published under the terms and conditions of the Creative Commons Attribution 4.0 International License

Short communication

Arsenic in Sediments, Soil and Plants in a Remediated Area of the Iron Quadrangle, Brazil, and its Accumulation and Biotransformation in *Eleocharis geniculata*

Maria Ângela de B. C. Menezes,¹ Ingrid Falnoga,² Zdenka Šlejkovec,²
Radojko Jaćimović,² Nilton Couto,³ Eleonora Deschamps⁴ and Jadran Faganeli^{5,*}

¹ Nuclear Technology Development Centre/Brazilian Commission for Nuclear Energy (CDTN/CNEN),
Division for Analytical Techniques, Caixa Postal 941, CEP 30161-970, Belo Horizonte, Minas Gerais, Brazil

² Jožef Stefan Institute, Department of Environmental Sciences, Jamova cesta 39, SI-1000 Ljubljana, Slovenia

³ Fundação Ezequiel Dias (FUNED), Rua Conde Pereira Carneiro, 80, Gameleira, CEP 30510-010,
Belo Horizonte, Minas Gerais, Brazil

⁴ FUMEC (Universidade Fundação Mineira de Educação e Cultura), Rua Cobre, 200, CEP: 30.310-190
Belo Horizonte, Minas Gerais, Brazil

⁵ National Institute of Biology, Marine Biology Station, Fornace 41. SI-6330 Piran, Slovenia

* Corresponding author: E-mail: jadran.faganeli@nib.si,
Tel.: +386 5 9232911

Received: 12-04-2019

Abstract

Since arsenic (As) exposure is largely due to geochemical contamination, this study focused on the remediated area of Santana do Morro, a district of Santa Bárbara, Minas Gerais, Brazil, which was previously contaminated with As due to gold mining. Total As concentrations in sediment, soil and plants were determined, next to As species, anionic arsenic compounds As(III), As(V), monomethylarsonic acid (MMA) and dimethylarsinic acid (DMA), in plants samples. Total As concentrations in soil and sediments were slightly elevated (16–18 $\mu\text{g g}^{-1}$) and most of the plants contained low levels of As (< 1 $\mu\text{g g}^{-1}$). The exception was a native plant *Eleocharis geniculata* (L.) which contained elevated levels of As (4 $\mu\text{g g}^{-1}$). The exposure of this plant to As under controlled conditions (hydroponics) indicated its possible tolerance to elevated As levels and suggesting its potential use in phytomonitoring of As-contaminated sites. This plant is able to metabolize arsenate to arsenite and contained MMA and DMA, both in its natural habitat and under controlled conditions.

Keywords: Arsenic species; soil; sediments; plants; Cyperacea; Iron Quadrangle

1. Introduction

The presence of arsenic (As) in soil, water, plants and food presents a potential risk to human health^{1,2} due to its toxicity. Due to its potential risk, As is considered as one of the most toxic elements to human health according to the ATSDR Substance Priority List³ and has received special attention worldwide.⁴ The toxicity and bioavailability of As in the environment depend not only on total concentration, but also on chemical species. In soil, As is relatively

immobilized due to insoluble complexes with iron and aluminum oxides.⁵ Generally, the toxicity decreases in the order As^{3+} inorganic compounds > As^{5+} inorganic compounds > As^{3+} organic compounds > As^{5+} organic compounds. The order of their phytotoxicity is less clear and may be plant species dependent. Finnegan and Chen⁶ reported that “no As form appears to be consistently most phytotoxic”.

In Brazil, the most significant presence of As is restricted to the state of Minas Gerais, specifically in the Iron

Quadrangle region and in the city of Paracatu. The Iron Quadrangle is a known gold-producing area, where As commonly occurs as arsenopyrite (FeAsS) and as a trace element in pyrite associated with gold mineralization.⁷ In this region, there are many active and abandoned gold mines where the As: Au ratios range from 300 to 3000. In this region, As is also present due to past anthropogenic activities, when it was discharged into drainage systems and stored in tailing piles on the banks of several local rivers.^{1,8} Large dams have recently been built to store the tailings and the effluents are treated in compliance with environmental regulations since most of the mining and smelting operations, apart from some small-scale mining operations (*garimpo*), are carried out by large companies with modern infrastructures and facilities.⁸ The spring water, previously used by local inhabitants, was contaminated with As prevalently bonded onto soil particulates. In 2007, water treatment plants were constructed and water became potable.⁹

Various studies related to the Iron Quadrangle have described the environmental impact of As pollution from several old gold mines on stream sediments, surface water and run-off water. The impact of As pollution on the population of the municipalities of Santa Bárbara and Nova Lima^{1,8,10,11} has also been detected in the frame of ARSENEX project.¹² Results showed that As in soil ranges from between 13–467 mg kg⁻¹.

In this study, levels of As and its species were determined in soil, sediments and some plants from Santana do Morro, district of Santa Bárbara, to assess the level of As contamination in this remediated area. The main objective of the study was to evaluate if certain plants are able to methylate As⁵⁺ and if they can be potential accumulators of As and used in phytomonitoring of As-contaminated sites.

2. Materials and Methods

2.1. Study Area

Samples were collected in the surroundings of the small village of Santana do Morro (Water spring coordinates: 20°1'15"S 43°28'79"W), located in the district of Santa Bárbara, Minas Gerais, Brazil (Fig. 1). This village has approximately 200 inhabitants and lacks basic services. Until 2006, the water supply originated from the local spring contaminated with As (3.3–21.5 µg L⁻¹).⁸ From 2006 onwards, the water has been treated in the water treatment plant constructed during the ARSENEX project and from there it is distributed to several houses and the As concentration varies between <0.08 and 0.64 µg L⁻¹.¹³ The climatological, hydrological and geological features of the study area were described by Almeida et al.⁷



Figure 1. Sampling locations in Santana do Morro (Santa Bárbara district, Minas Gerais, Brazil) (<https://earth.google.com/web/@-20.02021163,43.47656815,739.64086466a,578.07324732d,35y,0h,0t,0r>)

2. 2. Collection and Preparation of Soil and Sediment

Soil samples were taken from surface to the depth of 20 cm at 14 locations (Fig. 1) in the vicinity where plants were collected. From each location approximately 100 g of soil was sampled and stored in plastic bags for further analysis. Sediment samples were collected from 14 locations at the edge of the spring pool (Fig. 1) and were also stored in plastic bags. Soil and sediment samples were air-dried, homogenized and sieved to five granulometric fractions. The finest-grained fraction (<0.06 mm) was analyzed after rehomogenization.

2. 3. Collection and Preparation of Plants

A total of 14 species (Table 1) were collected in the vicinity of the spring pool in Santana do Morro (Fig. 1). One part of the plants sampled was set aside for taxonomical identification and the other part was used for As determination and speciation. The samples for plant identification were stored in paper and pressed. For chemical analysis, all plants collected were first vigorously washed with tap water, immersed in deionized water for some minutes, air dried and weighed. Plant samples were successively frozen, freeze-dried and weighed again. Dried plants were ground to a fine powder in a laboratory mill (Knife Mill GRINDOMIX GM 200, Retsch) and analyzed for As as described below.

2. 4. As Exposure Study of *Eleocharis Geniculata*

After identifying the plant which contained As in the environmental survey, a Cyperacea *Eleocharis geniculata* (L.) was exposed to As in a hydroponic system according to a procedure described by Moreno-Jimenez et al.¹⁴ Seedlings from the field were grown in a vessel with nutrient solution with commercial fertilizers prepared according to instructions (SUPERthrive[®], a highly concentrated non-toxic vitamin solution suited for hydro-seeding, hydroponics and foliar spraying) without As. After producing several seedlings in As-free conditions, these seedlings were transferred to a container with fresh commercial nutrient solution and 50 µg of As(V) per container. Ten plastic containers (capacity of 2 L each) were prepared, each one containing 3 seedlings. After one month of growth, the plants were cleaned by washing them with tap water, followed by immersion in deionized water for several minutes. The roots were separated from the shoots (leaves and stems), compounding two samples, one of shoots (22.97 g dry weight) and one of roots (3.43 g dry weight). This material was frozen, freeze-dried, homogenized and analyzed for total As and its species as described below.

2. 5. Determination of As and its Species

Determination of total As in soil, sediment and plants The k_0 -INAA method (Instrumental Neutron Activation Analysis) was applied to determine total As concentrations. After being weighed in polyethylene vials suitable for neutron irradiation, the samples were co-irradiated in a TRIGA Mark II reactor together with flux monitor disks of Al - 0.1 % Au from the Central Bureau for Nuclear Measurements, Geel, Belgium. After a suitable cooling time the gamma spectra were obtained in a HPGe gamma counting system with 40% efficiency^{15,16} and evaluated by HyperLab software.¹⁷ Concentrations were calculated using the Kayzero software.¹⁸ Standard Reference Materials from the National Research Centre for CRM (China) (GBW 07604, Poplar Leaves, 0.4 ± 0.1 mg kg⁻¹, certified 0.37 ± 0.06 mg kg⁻¹) and the International Atomic Energy Agency (IAEA-SOIL-7, 13 ± 1 mg kg⁻¹, certified 13.4 ± 0.85 mg kg⁻¹) were analyzed together with our samples to verify the accuracy of the k_0 -method. Detection limits were in a range of few ng g⁻¹.

Determination of As species in plant samples Powdered plant samples were extracted with 25 mL of a Milli-Q water/methanol mixture (1:1) at 25 °C for 3 h. After extraction the samples were centrifuged, decanted and re-extracted using the same conditions. Both extracts were joined and evaporated to dryness using a rotary evaporator (45 °C, ~ 30 min). Dry residue was taken up into 2.00 mL of Milli-Q water, filtered through a 0.45 µm membrane PVDF syringe filter and kept frozen until analysis. An HPLC-HG-AFS (high performance liquid chromatography-hydride generation – atomic fluorescence spectroscopy) system¹⁹ was used for determination of the anionic arsenic compounds As(III), As(V), monomethylarsonic acid (MMA) and dimethylarsinic acid (DMA) in extracts. An anion exchange column (Hamilton PRP X-100, with 15 mmol L⁻¹ KH₂PO₄, pH 6.1) was used to separate compounds prior to hydride generation (4.4 mol L⁻¹ HCl, 3.0 mL min⁻¹ and 1.5% NaBH₄ in 0.1% NaOH, 3 mL min⁻¹). An Excalibur (PS Analytical, Kent, UK) AFS detector was used for the detection of volatile arsenic hydrides. Detection limits were 1 µg kg⁻¹ for MMA and As(III) and 2 µg kg⁻¹ for DMA and As(V).

3. Results and Discussion

3. 1. Total As in Soil and Sediments

The mean As concentrations in soil (16 mg kg⁻¹) and sediment (18 mg kg⁻¹) in the vicinity of the spring water pool showed slight contamination. According to Brazilian legislation regarding soil²⁰ they were close to prevention values (15 mg kg⁻¹) but below the levels for residential use (55 mg kg⁻¹). However, the concentrations were higher than the average values for world soils (5 mg kg⁻¹) but comparable to average values for world sediments (2–22

mg kg⁻¹).²¹ According to Adriano²², As concentrations typically vary from below 10 mg kg⁻¹ in uncontaminated to as high as 30000 mg kg⁻¹ in contaminated world soils. It appears therefore that mining activities did not greatly contribute to As levels in local soil and sediments.²³

3. 2. Total As in Plants

The taxonomic determination of the dominant species (Table 1) in the vicinity of the spring water was performed to characterize the vegetation and identify species that might be able to accumulate or exclude As. Only *E. geniculata*,^{24,25} a wetland annual or short-lived perennial plant commonly known as spike rush, was identified as a native species. Most of the plants investigated contained no detectable As concentrations, as may be expected for unexposed plants.^{22,26} Only *E. geniculata* contained higher levels of As, i.e. 4 mg kg⁻¹, suggesting that this species is likely tolerant or able to accumulate As. The rather low As concentrations in plant can be associated with rather low As levels in the corresponding soil (16 ± 1 mg kg⁻¹) and sediment (18 ± 1 mg kg⁻¹).

E. geniculata is known to be metal-tolerant and its metal accumulation ability was previously confirmed for lead²⁷ but there are no data for As. Cyperaceae family is widely distributed around the world and some of the species of *Eleocharis* genus were suggested to be of potential use in aquatic weed management and pollution abatement²⁸. For example, *Eleocharis sp.*, naturally colonizing abandoned copper – tailings ponds at the Rakha mines in India, was found to accumulate copper up to 1493 mg kg⁻¹ dry weight, with greater amounts in roots than in shoots.²⁹ The potential for accumulation of various metals, i.e. Cu, Zn, As, Pb, Cd, and phytoremediation was reported for *Eleocharis acicularis* in laboratories and field experiments^{30,31} and for *Eleocharis equisetina* in an abandoned acid mine tailing pond in NE Australia.³² Experiments

with As performed with *Eleocharis macrostachya* revealed that a part of As can be removed from water by rhizofiltration.³³

3. 3. As Species in Native and Cultivated *Eleocharis Genuculata*

Once it was verified that *E. geniculata* can accumulate more As than other plants, a systematic study of As uptake was performed. Table 2 shows the results of total As and its species determined in roots and shoots of *E. geniculata* collected in its natural habitat at the spring water pool and in samples after 30 days of cultivation in As enriched nutrient solution in a hydroponic system. Extractability of As from *E. geniculata* grown in the field or after hydroponic exposure to As(V) was rather low, 30% from roots and approximately 60% from shoots, as is often in plant material.⁴

Samples of *E. geniculata* from the field contained more total As in the roots than in the shoots. The root:shoot ratio was 16.4, which is comparable to data from the literature regarding other plants from the same family. For example, *E. equisetina* contained from 10–146 µg kg⁻¹ As in roots and from 3.3–17.3 µg kg⁻¹ As in shoots³² and *E. macrostachya* contained 17–47 times more As in roots compared to shoots.³³ This similarity indicates that all three plant species are able to exclude As from above-ground tissues. Poor translocation might be the result of sequestration of As into vacuoles of the root cells, helping the plant to alleviate the potentially toxic effects of As.³⁴ However, such comparisons could be misleading due to differences in exposure conditions. Sequestration into vacuoles of the root cells during exposure to low levels is likely more efficient than at high levels of As exposure.

As speciation in the *E. geniculata* samples highlighted the presence of mainly As(III) and small amounts of As(V) and MMA in roots while shoots from the pilot parallel ex-

Table 1. Total arsenic in freeze dried plants collected around the spring water pool in Santana do Morro

Species	Family	As (mg kg ⁻¹)
<i>Baccharis retusa</i> DC.	Asteraceae	< 1
<i>Baccharis calvescens</i> DC.	Asteraceae	< 1
<i>Cyrtocymura scorpioides</i> (Lam.) H. Rob.	Asteraceae	< 1
<i>Jacquemontia rufa</i> (Choisy) Hallier f.	Convolvulaceae	< 1
<i>Eleocharis geniculata</i> (L.) Roem. & Schult.	Cyperaceae	4
<i>Rhynchospora marisculus</i> Lindl. & Nees	Cyperaceae	< 1
<i>Hyptis lanceolata</i> Poir.	Lamiaceae	< 1
<i>Hyptis suaveolens</i> Poit.	Lamiaceae	< 1
<i>Triunfetta semitriloba</i> Jacq.	Malvaceae	< 1
<i>Rhynchanthera grandiflora</i> (Aubl.) DC.	Melastomataceae	< 1
<i>Trembleya parviflora</i> (D. Don) Cogn.	Melastomataceae	< 1
<i>Ludwigia lagunae</i> (Morong) H. Hara	Onagraceae	< 1
<i>Melinis minutiflora</i> P. Beauv.	Poaceae	< 1
<i>Borreria capitata</i> (Ruiz & Pav.) DC.	Rubiaceae	< 1

Table 2. Arsenic and its species in *Eleocharis geniculata* from its natural habitat and cultivated in a hydroponic system with the addition of As(V)

Sample	Part of the plants	Total As (mg kg ⁻¹)	As(III) (mg kg ⁻¹)	DMA (mg kg ⁻¹)	MMA (mg kg ⁻¹)	As(V) (mg kg ⁻¹)
From natural habitat (n=5)	Roots	4.6 ± 0.2	0.79 ± 0.03	< 0.001	0.005 ± 0.001	0.010 ± 0.001
	Shoots	0.28 ± 0.05	Na	Na	Na	Na
From hydroponic system (n=5)	Roots	11.5 ± 0.4	2.67 ± 0.08	0.09 ± 0.01	0.05 ± 0.01	1.64 ± 0.11
	Shoots	25 ± 1	4.55 ± 0.16	0.39 ± 0.06	0.06 ± 0.01	9.62 ± 0.87

Na – not analyzed due to insufficient mass

periment also contained low but detectable amounts of DMA (data not shown). It is known that As(V) is readily reduced to As(III) by plants, while biomethylation issues are less clear³⁵ and attributed to microorganisms, in particular bacteria living in soil.³⁵

In the hydroponic system, the seedling was subjected to a total of 500 µg of As(V) for one month and the growing plants took up all the available As. In the hydroponic system (absence of soil), the roots contained less As than shoots, which is contradictory to natural conditions and possibly related to different exposure conditions³⁵ including additional exposure to higher concentrations in a shorter time. In such conditions the plant was able to translocate As from roots to shoots very efficiently. It is believed that in the tolerant plants a much higher amount of assimilated As is transported to the shoots than in nontolerant plants.³⁶ Concerning the species studied, the results also showed the presence of As(III), pointing out the ability of the plant to metabolize As(V) to As(III) as previously observed by Finnegan and Chen⁶ and to produce MMA and DMA. All four arsenic species were identified in roots and shoots. In the same plants growing in the field we identified three arsenic species, without DMA, in roots only. Involvement of bacterial methylation of As could not be excluded since we did not use axenic conditions. Arsenosugars and other arsenic species were not detected in any of the samples.

4. Conclusions

Total As concentrations in soil and sediments in a remediated area in Santana do Morro, a district of Santa Bárbara, Minas Gerais, Brazil, were slightly elevated (16–18 µg g⁻¹) but most plants contained low levels of As (< 1 µg g⁻¹). The analysis of vegetation, mostly consisting of alien species, showed that only *E. geniculata*, a native plant, contained elevated levels of As. *E. geniculata* exposed to As in its habitat and to inorganic As (As⁵⁺) under controlled conditions (hydroponic system) was able to accumulate

As. As from the treatment solution was removed completely suggesting its potential use in phytomonitoring and removing As from contaminated soils³⁷ and further exploration is suggested. This plant was able to metabolize As(V) to As(III) and produced minor amounts of MMA and DMA in both situations.

Acknowledgements

The authors wish to thank Prof. Alexandre Salino and colleagues, the Botanic Department, Institute for Biological Sciences, Federal University of Minas Gerais (UFMG) for floristic analysis. This study was financially supported by CNPq (National Counsel of Technological and Scientific Development), Process n. 490059/2009-0 (Edital CNPq N 015/2009) and by the Slovenian Research Agency (ARRS) through Slovenian-Brazilian scientific cooperation (BI-BR/10-12-002).

5. References

1. E. Smith, R. Naidu, A. M. Alston, *Adv. Agron.* **1998**, *64*, 149–195. DOI:10.1016/S0065-2113(08)60504-0
2. A. L. Juhasz, E. Smith, J. Weber, M. Rees, A. Rofe, T. Kuchel, L. Sansom, R. Naidu, *Chemosphere* **2008**, *71*, 1963–1969. DOI:10.1016/j.chemosphere.2007.12.021
3. ATSDR, Agency for Toxic Substances & Disease Registry, <http://www.atsdr.cdc.gov/spl/>, 2013.
4. A. Sarkar, B. Paul, *Chemosphere* **2016**, *158*, 37–49. DOI:10.1016/j.chemosphere.2016.05.043
5. I. Arčon, H. J. Van Elteren, A. Glass, A. Kodre, Z. Šlejkovec, *X-Ray Spectrom.* **2005**, *34*, 435–438. DOI:10.1002/xrs.857
6. P. M. Finnegan, W. Chen, *Front. Physiol.* **2012**, *3*, 182, doi.org/10.3389/fphys.2012.00182.
7. K. Almeida, J. Matschullat, J. Mello, I. Meneses, Z. Viola, in: E. Deschamps, J. Matschullat (Ed.): *Arsenic: Natural and Anthropogenic*, CRC Press, Boca Raton, **2011**, pp. 81–90.
8. O. Vasconcelos, S. Oberda, E. Deschamps, J. Matschullat, in:

- E. Deschamps, J. Matschullat (Ed.): *Arsenic: Natural and Anthropogenic*, CRC Press, Boca Raton, **2011**, pp. 119–126. DOI:10.1201/b10772-15
9. E. Deschamps, N. Assuncao, in: E. Deschamps, J. Matschullat (Ed.): *Arsenic: Natural and Anthropogenic*, CRC Press, Boca Raton, **2011**, pp. 183–192. DOI:10.1201/b10772-21
10. L. V. Cruz, Avaliação Geoquímica ambiental da Estação Ecológica do Tripuí e adjacências, sudeste do Quadrilátero Ferrífero, MG. Universidade Federal de Ouro Preto, M.Sc. Thesis, **2002**.
11. J. Matschullat, R. P. Borba, E. Deschamps, B. R. Figueiredo, T. Gabrio, M. Schwenk, *Appl. Geochem.* **2000**, *15*, 181–190. DOI:10.1016/S0883-2927(99)00039-6
12. N. Couto, S. Mattos, J. Matschullat, in: E. Deschamps, J. Matschullat (Ed.): *Arsenic: Natural and Anthropogenic*, CRC Press, Boca Raton, **2011**, pp. 153–167.
13. C. A. Ferreira, H. E. L. Palmieri, M. Â. B. C. Menezes, L. M. L. A. Auler, *Amer. Jour. Water Res.* **2017**, *5*, 29–40.
14. E. Moreno-Jimenez, E. Esteban, T. Fresno, C. Lopez de Egea, J. M. Penalosa, *Chemosphere* **2010**, *79*, 513–517. DOI:10.1016/S0883-2927(99)00039-6
15. R. Jaćimović, V. Stibilj, L. Benedik, B. Smodiš, *Jour. Radioanal. Nucl. Chem.* **2003**, *257*, 545–549. DOI:10.1023/A:1025484313986
16. M. Â. B. C. Menezes, R. Jaćimović, *Jour. Radioanal. Nucl. Chem.* **2008**, *278*, 607–611. DOI:10.1007/s10967-008-1201-x
17. HyperLab. System. Installation and Quick Start Guide, HyperLabs Software, Budapest, Hungary, **2009**.
18. Kayzero for Windows® User's Manual, for reactor neutron activation analysis (NAA) using the k_0 standardisation method, Ver. 2.42, **2008**.
19. Z. Šlejkovec, J. T van Elteren, H. J. Glass, Z. Jeran, R. Jaćimović, *Int. Jour. Environ. Anal. Chem.* **2010**, *90*, 784–796. DOI:10.1080/03067310902977542
20. Brasil. Conselho Nacional de Meio Ambiente – CONAMA, Resolução 420/2009, de 28 de dezembro de 2009. “Dispõe sobre critérios e valores orientadores de qualidade do solo quanto à presença de substâncias químicas e estabelece diretrizes para o gerenciamento ambiental de áreas contaminadas por essas substâncias em decorrência de atividades antrópicas”, Brasília. **2009**.
21. C. Reimann, P. de Caritat, Chemical elements in the environment Factsheets for the geochemists and environmental scientists, Springer, New York, **1998**.
22. D. C. Adriano, Trace Elements in the Terrestrial Environment. Springer, New York, **2001**. DOI:10.1007/978-0-387-21510-5
23. E. Deschamps, J. Meillo, J. Matschullat, in: E. Deschamps, J. Matschullat (Ed.): *Arsenic: Natural and Anthropogenic*, CRC Press, Boca Raton, **2011**, pp. 127–139. DOI:10.1201/b10772
24. M. L. L. Martins, R. M. Carvalho-Okano, M. Luceño, *Acta Bot. Bras.* **1999**, *13*, 187–222. DOI:10.1590/S0102-33061999000200008
25. A. S. B. Gil, C. P. O. Bove, *Arq. Mus. Nac. Rio de Janeiro* **2004**, *62*, 131–150.
26. R. Eisler, *Eisler's Encyclopedia of Environmentally Hazardous Priority Chemicals*, Elsevier, 9999Amsterdam, **2007**.
27. J. Yang, Z. Ye, *Environ. Sci. Pollut. Res.* **2015**, *22*, 1931–1939. DOI:10.1007/s11356-014-3610-4
28. M. S. Gonzales-Elizondo, P. M. Peterson, *Taxon* **1997**, *46*, 433–449. DOI:10.2307/1224386
29. M. Das, S. K. Maiti, *Land Contam. Reclam.* **2008**, *16*, 135–153. DOI:10.2462/09670513.691
30. M. Sakahibara, Y. Ohmori, N. T. H. Sano, K. Sera, *Clean - Soil, Water* **2011**, *39*, 735–741. DOI:10.1002/clen.201000488
31. A. G. Nurfitiri, S. Masayuki, S. Koichiro, *Environ. Sci. Ind. Jour.* **2017**, *13*, 131.
32. B. A. Lottermoser, P. A. Ashley, *Environ. Pollut.* **2011**, *159*, 3028–3035. DOI:10.1016/j.envpol.2011.04.014
33. M. A. Olmos-Márquez, M. T. Alarcón-Herrera, I. R. Martín-Domínguez, *Environ. Sci. Pollut. Res.* **2012**, *19*, 763–771. DOI:10.1007/s11356-011-0598-x
34. A. K. Shankar, C. Cervantes, H. Loza-Tavera, S. Avudainayagam, *Sci. Total Environ.* **2005**, *31*, 739–753. DOI:10.1016/j.envint.2005.02.003
35. P. Wang, G. Sun, Y. S. Jia, A. A. Meharg, Y. Zhu, *Jour. Environ. Sci.* **2014**, *26*, 371–381. DOI:10.1016/S1001-0742(13)60432-5
36. N. Singh, L. Q. Ma, in: N. Willey (ed.): *Phytoremediation: Methods and Reviews*, Biotechnology, Humana Press, Totowa, **2007**.
37. L. Q. Ma, K. M. Komar, C. Tu, W. Zhang, Y. Cai, E. D. Kennelley, *Nature*, **2001**, *409*, 579. DOI:10.1038/35054664

Povzetek

V področju kontaminiranem z arzenom (As) Santana do Morro (Santa Bárbara, Minas Gerais, Brazilija), kot posledica rudarjenja zlata, smo določili koncentracije celotnega As v sedimentu, prsti in rastlinah. V rastlinah smo analizirali tudi zvrsti As: As(III), As(V), metilarzonsko (MMA) in dimetilarzinsko kislino (DMA). Koncentracije As v prsti in sedimentu so bile le rahlo povečane ($16\text{--}18\ \mu\text{g g}^{-1}$) in večina rastlin je vsebovala nizke koncentracije As ($<1\ \mu\text{g g}^{-1}$). Izjema je bila avtohtona rastlina *Eleocharis geniculata* (L.) s povečanimi koncentracijami As ($4\ \mu\text{g g}^{-1}$). Poskusi v kontroliranih pogojih (hidroponika) kažejo na njeno odpornost na povečane koncentracije As in možnost uporabe v fitomonitoringu in bioremediaciji kontaminiranih področij z As. Rastlina metabolizira arzenat v arzenit in vsebuje MMA in DMA v naravnih in laboratorijskih pogojih.



Except when otherwise noted, articles in this journal are published under the terms and conditions of the Creative Commons Attribution 4.0 International License

**DRUŠTVENE VESTI IN DRUGE AKTIVNOSTI
SOCIETY NEWS, ANNOUNCEMENTS, ACTIVITIES**

Vsebina

Navodila za avtorje S80

Contents

Instructions for authors S80

Acta Chimica Slovenica

Author Guidelines

Submissions

Submission to ACSi is made with the implicit understanding that neither the manuscript nor the essence of its content has been published in whole or in part and that it is not being considered for publication elsewhere. All the listed authors should have agreed on the content and the corresponding (submitting) author is responsible for having ensured that this agreement has been reached. The acceptance of an article is based entirely on its scientific merit, as judged by peer review. There are no page charges for publishing articles in ACSi. The authors are asked to read the Author Guidelines carefully to gain an overview and assess if their manuscript is suitable for ACSi.

Additional information

- Citing spectral and analytical data
- Depositing X-ray data

Submission material

Typical submission consists of:

- full manuscript (PDF file, with title, authors, abstract, keywords, figures and tables embedded, and references)
- supplementary files
 - **Full manuscript** (original Word file)
 - **Statement of novelty** (Word file)
 - **List of suggested reviewers** (Word file)
 - **ZIP file containing graphics** (figures, illustrations, images, photographs)
 - **Graphical abstract** (single graphics file)
 - **Proposed cover picture** (optional, single graphics file)
 - **Appendices** (optional, Word files, graphics files)

Incomplete or not properly prepared submissions will be rejected.

Submission process

Before submission, authors should go through the checklist at the bottom of the page and prepare for submission.

Submission process consists of 5 steps.

Step 1: Starting the submission

- Choose one of the journal sections.
- Confirm all the requirements of the **checklist**.
- Additional plain text comments for the editor can be provided in the relevant text field.

Step 2: Upload submission

- Upload full manuscript in the form of a Word file (with title, authors, abstract, keywords, figures and tables embedded, and references).

Step 3: Enter metadata

- First name, last name, contact email and affiliation for all authors, in relevant order, must be provided. Corresponding author has to be selected. Full postal address and phone number of the corresponding author has to be provided.

- **Title and abstract** must be provided in plain text.
- Keywords must be provided (max. 6, separated by semicolons).
- Data about contributors and supporting agencies may be entered.
- **References** in plain text must be provided in the relevant text field.

Step 4: Upload supplementary files

- Original Word file (original of the PDF uploaded in the step 2)
- **Statement of novelty** in a Word file must be uploaded
- All **graphics** have to be uploaded in a single ZIP file. Graphics should be named Figure 1.jpg, Figure 2.eps, etc.
- **Graphical abstract image** must be uploaded separately
- **Proposed cover picture** (optional) should be uploaded separately.
- Any additional **appendices** (optional) to the paper may be uploaded. Appendices may be published as a supplementary material to the paper, if accepted.
- For each uploaded file the author is asked for additional metadata which may be provided. Depending of the type of the file please provide the relevant title (Statement of novelty, List of suggested reviewers, Figures, Graphical abstract, Proposed cover picture, Appendix).

Step 5: Confirmation

- Final confirmation is required.

Article Types

Feature Articles are contributions that are written on editor's invitation. They should be clear and concise summaries of the most recent activity of the author and his/her research group written with the broad scope of ACSi in mind. They are intended to be general overviews of the authors' subfield of research but should be written in a way that engages and informs scientists in other areas. They should contain the following (see also general directions for article structure in ACSi below): (1) an introduction that acquaints readers with the authors' research field and outlines the important questions to which answers are being sought; (2) interesting, new, and recent contributions of the author(s) to the field; and (3) a summary that presents possible future directions. Manuscripts normally should not exceed 40 pages of one column format (letter size 12, 33 lines per page). Generally, experts in a field who have made important contribution to a specific topic in recent years will be invited by an editor to contribute such an **Invited Feature Article**. Individuals may, however, send a proposal (one-page maximum) for an Invited Feature Article to the Editor-in-Chief for consideration.

Scientific articles should report significant and innovative achievements in chemistry and related sciences and should exhibit a high level of originality. They

should have the following structure:

1. Title (max. 150 characters),
2. Authors and affiliations,
3. Abstract (max. 1000 characters),
4. Keywords (max. 6),
5. Introduction,
6. Experimental,
7. Results and Discussion,
8. Conclusions,
9. Acknowledgements,
10. References.

The sections should be arranged in the sequence generally accepted for publications in the respective fields and should be successively numbered.

Short communications generally follow the same order of sections as Scientific articles, but should be short (max. 2500 words) and report a significant aspect of research work meriting separate publication. Editors may decide that a Scientific paper is categorized as a Short Communication if its length is short.

Technical articles report applications of an already described innovation. Typically, technical articles are not based on new experiments.

Preparation of Submissions

Text of the submitted articles must be prepared with Microsoft Word. Normal style set to single column, 1.5 line spacing, and 12 pt Times New Roman font is recommended. Line numbering (continuous, for the whole document) must be enabled to simplify the reviewing process. For any other format, please consult the editor. Articles should be written in English. Correct spelling and grammar are the sole responsibility of the author(s). Papers should be written in a concise and succinct manner. The authors shall respect the ISO 80000 standard [1], and IUPAC Green Book [2] rules on the names and symbols of quantities and units. The Système International d'Unités (SI) must be used for all dimensional quantities.

Graphics (figures, graphs, illustrations, digital images, photographs) should be inserted in the text where appropriate. The captions should be self-explanatory. Lettering should be readable (suggested 8 point Arial font) with equal size in all figures. Use common programs such as MS Excel or similar to prepare figures (graphs) and ChemDraw to prepare structures in their final size. Width of graphs in the manuscript should be 8 cm. Only in special cases (in case of numerous data, visibility issues) graphs can be 17 cm wide. All graphs in the manuscript should be inserted in relevant places and **aligned left**. The same graphs should be provided separately as images of appropriate resolution (see below) and submitted together in a ZIP file (Graphics ZIP). Please do not submit figures as a Word file. In **graphs**, only the graph area determined by both axes should be in the frame, while a frame around the whole graph should be omitted. The graph area should be white. The legend should be inside the graph area. The style of all graphs should be the same. **Figures and illustrations** should be of sufficient quality for the printed version, i.e. 300 dpi minimum. **Digital images and photographs** should be of high quality (minimum 250 dpi resolution). On submission, figures should be of good enough resolution to be assessed by the referees, ideally as JPEGs. High-resolution figures (in JPEG,

TIFF, or EPS format) might be required if the paper is accepted for publication.

Tables should be prepared in the Word file of the paper as usual Word tables. The captions should appear above the table and should be self-explanatory.

References should be numbered and ordered sequentially as they appear in the text, likewise methods, tables, figure captions. When cited in the text, reference numbers should be superscripted, following punctuation marks. It is the sole responsibility of authors to cite articles that have been submitted to a journal or were in print at the time of submission to ACSi. Formatting of references to published work should follow the journal style; please also consult a recent issue:

1. J. W. Smith, A. G. White, *Acta Chim. Slov.* **2008**, *55*, 1055–1059.
2. M. F. Kemmere, T. F. Keurentjes, in: S. P. Nunes, K. V. Peinemann (Ed.): *Membrane Technology in the Chemical Industry*, Wiley-VCH, Weinheim, Germany, **2008**, pp. 229–255.
3. J. Levec, Arrangement and process for oxidizing an aqueous medium, US Patent Number 5,928,521, date of patent July 27, **1999**.
4. L. A. Bursill, J. M. Thomas, in: R. Sersale, C. Collela, R. Aiello (Eds.), *Recent Progress Report and Discussions: 5th International Zeolite Conference*, Naples, Italy, 1980, Gianini, Naples, **1981**, pp. 25–30.
5. J. Szegezdi, F. Csizmadia, Prediction of dissociation using microconstants, http://www.chemaxon.com/conf/Prediction_of_dissociation_constant_using_microconstants.pdf, (assessed: March 31, 2008)

Titles of journals should be abbreviated according to Chemical Abstracts Service Source Index (CASSI).

Special Notes

- Complete characterization, **including crystal structure**, should be given when the synthesis of new compounds in crystal form is reported.
- Numerical **data should be reported with the number of significant digits corresponding to the magnitude** of experimental uncertainty.
- **The SI system of units and IUPAC recommendations** for nomenclature, symbols and abbreviations should be followed closely. Additionally, the authors should follow the general guidelines when citing spectral and analytical data, and depositing crystallographic data.
- **Characters** should be correctly represented throughout the manuscript: for example, 1 (one) and l (ell), 0 (zero) and O (oh), x (ex), D7 (times sign), B0 (degree sign). Use Symbol font for all Greek letters and mathematical symbols.
- The rules and recommendations of the **IUBMB** and the **International Union of Pure and Applied Chemistry (IUPAC)** should be used for abbreviation of chemical names, nomenclature of chemical compounds, enzyme nomenclature, isotopic compounds, optically active isomers, and spectroscopic data.
- **A conflict of interest** occurs when an individual (author, reviewer, editor) or its organization is involved in multiple interests, one of which could possibly corrupt the motivation for an act in the

other. Financial relationships are the most easily identifiable conflicts of interest, while conflicts can occur also as personal relationships, academic competition, etc. **The Editors** will make effort to ensure that conflicts of interest will not compromise the evaluation process; potential editors and reviewers will be asked to exempt themselves from review process when such conflict of interest exists. When the manuscript is submitted for publication, **the authors** are expected to disclose any relationships that might pose potential conflict of interest with respect to results reported in that manuscript. In the Acknowledgement section the source of funding support should be mentioned. The statement of disclosure must be provided as Comments to Editor during the submission process.

- **Published statement of Informed Consent.** Research described in papers submitted to ACSi must adhere to the principles of the Declaration of Helsinki (<http://www.wma.net/e/policy/b3.htm>). These studies must be approved by an appropriate institutional review board or committee, and informed consent must be obtained from subjects. The Methods section of the paper must include: 1) a statement of protocol approval from an institutional review board or committee and 2), a statement that informed consent was obtained from the human subjects or their representatives.
- **Published Statement of Human and Animal Rights.** When reporting experiments on human subjects, authors should indicate whether the procedures followed were in accordance with the ethical standards of the responsible committee on human experimentation (institutional and national) and with the Helsinki Declaration of 1975, as revised in 2008. If doubt exists whether the research was conducted in accordance with the Helsinki Declaration, the authors must explain the rationale for their approach and demonstrate that the institutional review body explicitly approved the doubtful aspects of the study. When reporting experiments on animals, authors should indicate whether the institutional and national guide for the care and use of laboratory animals was followed.
- To avoid conflict of interest between authors and referees we expect that not more than one referee is from the same country as the corresponding author(s), however, not from the same institution.
- Contributions authored by **Slovenian scientists** are evaluated by non-Slovenian referees.
- Papers describing **microwave-assisted reactions** performed in domestic microwave ovens are not considered for publication in *Acta Chimica Slovenica*.
- *Manuscripts that are **not prepared and submitted** in accord with the instructions for authors are not considered for publication.*

Appendices

Authors are encouraged to make use of supporting information for publication, which is supplementary material (appendices) that is submitted at the same time as the manuscript. It is made available on the Journal's web site and is linked to the article in the

Journal's Web edition. The use of supporting information is particularly appropriate for presenting additional graphs, spectra, tables and discussion and is more likely to be of interest to specialists than to general readers. When preparing supporting information, authors should keep in mind that the supporting information files will not be edited by the editorial staff. In addition, the files should be not too large (upper limit 10 MB) and should be provided in common widely known file formats to be accessible to readers without difficulty. All files of supplementary materials are loaded separately during the submission process as supplementary files.

Proposed Cover Picture and Graphical Abstract Image

Graphical content: an ideally full-colour illustration of resolution 300 dpi from the manuscript must be proposed with the submission. Graphical abstract pictures are printed in size 6.5 x 4 cm (hence minimal resolution of 770 x 470 pixels). Cover picture is printed in size 11 x 9.5 cm (hence minimal resolution of 1300 x 1130 pixels)

Authors are encouraged to submit illustrations as candidates for the journal Cover Picture*. The illustration must be related to the subject matter of the paper. Usually both proposed cover picture and graphical abstract are the same, but authors may provide different pictures as well.

* The authors will be asked to contribute to the costs of the cover picture production.

Statement of novelty

Statement of novelty is provided in a Word file and submitted as a supplementary file in step 4 of submission process. Authors should in no more than 100 words emphasize the scientific novelty of the presented research. Do not repeat for this purpose the content of your abstract.

List of suggested reviewers

List of suggested reviewers is a Word file submitted as a supplementary file in step 4 of submission process. Authors should propose the names, full affiliation (department, institution, city and country) and e-mail addresses of three potential referees. Field of expertise and at least two references relevant to the scientific field of the submitted manuscript must be provided for each of the suggested reviewers. The referees should be knowledgeable about the subject but have no close connection with any of the authors. In addition, referees should be from institutions other than (and preferably countries other than) those of any of the authors.

How to Submit

Users registered in the role of author can start submission by choosing USER HOME link on the top of the page, then choosing the role of the Author and follow the relevant link for starting the submission process. Prior to submission we strongly recommend that you familiarize yourself with the ACSi style by browsing the journal, particularly if you have not submitted to the ACSi before or recently.

Correspondence

All correspondence with the ACSi editor regarding the paper goes through this web site and emails. Emails are sent and recorded in the web site database. In the correspondence with the editorial office please provide ID number of your manuscript. All emails you receive from the system contain relevant links. **Please do not answer the emails directly but use the embedded links in the emails for carrying out relevant actions.** Alternatively, you can carry out all the actions and correspondence through the online system by logging in and selecting relevant options.

Proofs

Proofs will be dispatched via e-mail and corrections should be returned to the editor by e-mail as quickly as possible, normally within 48 hours of receipt. Typing errors should be corrected; other changes of contents will be treated as new submissions.

Submission Preparation Checklist

As part of the submission process, authors are required to check off their submission's compliance with all of the following items, and submissions may be returned to authors that do not adhere to these guidelines.

1. The submission has not been previously published, nor is it under consideration for publication in any other journal (or an explanation has been provided in Comments to the Editor).
2. All the listed authors have agreed on the content and the corresponding (submitting) author is responsible for having ensured that this agreement has been reached.
3. The submission files are in the correct format: manuscript is created in MS Word but will be **submitted in PDF** (for reviewers) as well as in original MS Word format (as a supplementary file for technical editing); diagrams and graphs are created in Excel and saved in one of the file formats: TIFF, EPS or JPG; illustrations are also saved in one of these formats. The preferred position of graphic files in a document is to embed them close to the place where they are mentioned in the text (See **Author guidelines** for details).
4. The manuscript has been examined for spelling and grammar (spell checked).
5. The **title** (maximum 150 characters) briefly explains the contents of the manuscript.
6. Full names (first and last) of all authors together with the affiliation address are provided. Name of author(s) denoted as the corresponding author(s), together with their e-mail address, full postal address and telephone/fax numbers are given.
7. The **abstract** states the objective and conclusions of the research concisely in no more than 150 words.
8. Keywords (minimum three, maximum six) are provided.
9. **Statement of novelty** (maximum 100 words) clearly explaining new findings reported in the manuscript should be prepared as a separate Word file.
10. The text adheres to the stylistic and bibliographic requirements outlined in the **Author guidelines**.
11. Text in normal style is set to single column, 1.5 line spacing, and 12 pt. Times New Roman font is

recommended. All tables, figures and illustrations have appropriate captions and are placed within the text at the appropriate points.

12. Mathematical and chemical equations are provided in separate lines and numbered (Arabic numbers) consecutively in parenthesis at the end of the line. All equation numbers are (if necessary) appropriately included in the text. Corresponding numbers are checked.
13. Tables, Figures, illustrations, are prepared in correct format and resolution (see **Author guidelines**).
14. The lettering used in the figures and graphs do not vary greatly in size. The recommended lettering size is 8 point Arial.
15. Separate files for each figure and illustration are prepared. The names (numbers) of the separate files are the same as they appear in the text. All the figure files are packed for uploading in a single ZIP file.
16. Authors have read **special notes** and have accordingly prepared their manuscript (if necessary).
17. References in the text and in the References are correctly cited. (see **Author guidelines**). All references mentioned in the Reference list are cited in the text, and vice versa.
18. Permission has been obtained for use of copyrighted material from other sources (including the Web).
19. The names, full affiliation (department, institution, city and country), e-mail addresses and references of three potential referees from institutions other than (and preferably countries other than) those of any of the authors are prepared in the word file. At least two relevant references (important papers with high impact factor, head positions of departments, labs, research groups, etc.) for each suggested reviewer must be provided.
20. Full-colour illustration or graph from the manuscript is proposed for graphical abstract.
21. **Appendices** (if appropriate) as supplementary material are prepared and will be submitted at the same time as the manuscript.

Privacy Statement

The names and email addresses entered in this journal site will be used exclusively for the stated purposes of this journal and will not be made available for any other purpose or to any other party.

ISSN: 1580-3155

Koristni naslovi

Slovensko kemijsko društvo
Slovenian Chemical Society



Slovensko kemijsko društvo

www.chem-soc.si

e-mail: chem.soc@ki.si



Wessex Institute of Technology

www.wessex.ac.uk



SETAC

www.setac.org



European Water Association

<http://www.ewa-online.eu/>



European Science Foundation

www.esf.org



European Federation of Chemical Engineering

<https://efce.info/>



I U P A C

INTERNATIONAL UNION OF
PURE AND APPLIED CHEMISTRY

International Union of Pure and Applied Chemistry

<https://iupac.org/>

Novice evropske zveze kemijskih društev EuChemS najdete na:

 **EuChemS**
European Chemical Society

Brussels News Updates

<http://www.euchems.eu/newsletters/>

Sistemi za čisto in ultračisto vodo

Kvaliteta vode 1 do 3*

*v skladu s standardom ISO 3696 in ustreznimi ASTM ter CLSI



DONAU LAB Ljubljana
Member of LPPgroup

Donau Lab d.o.o., Ljubljana
Tbilisjska 85
SI-1000 Ljubljana
www.donaulab.si
office-si@donaulab.com



Že od
3.214€+DDV
(B30 Trace s 25 L Pro rezerv.
Slika je simbolična)

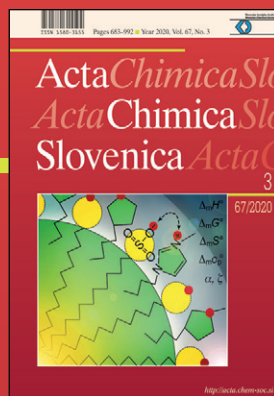


adrona

ActaChimicaSlovenica

ActaChimicaSlovenica

The micellization process of sodium dodecyl sulfate in the presence of three imidazolium based ionic liquids (ILs) with different side-chain length is investigated by calorimetric, conductivity and zeta-potential measurements. The impact of ILs on critical micelle concentration, thermodynamics of micellization and charge of the micelles is discussed in terms of hydrophobic and electrostatic interactions between the species in the solution. (see page 977)



Year 2020, Vol. 67, No. 3

